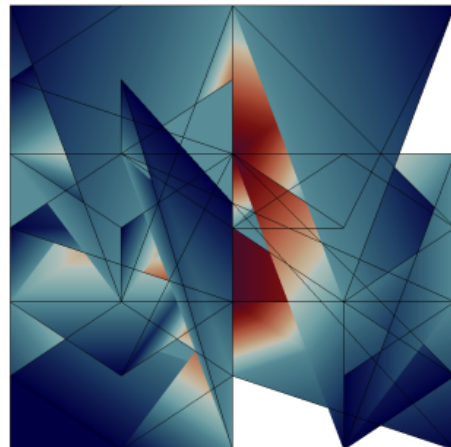


FieldStone

[Finite Elements (duh!) applied to Stones]



C. Thieulot

With contributions from: Wolfgang Bangerth, Eric van den Hoogen, Job Mos, Lukas van de Wiel, Alraune Zech, Wim Spakman.

If you find anything in this document useful for your research please cite it as follows (*please* include the doi!):

```
@article{Thieulot2019,  
author = "C.A.P. (Cedric) Thieulot",  
title = "{Fieldstone: The Finite Element Method in Computational Geodynamics}",  
year = "2019",  
month = "8",  
url = "https://uu.figshare.com/articles/manual_pdf/9209393",  
doi = "10.23644/uu.9209393.v1"}
```

Why do I have to promise where I am going while I am not there yet?

You can't google something you don't know exists.

You can be correct or you can get stuff done.

Computational Geodynamics

C. Thieulot

October 23, 2019

Contents

1	Introduction	11
1.1	Philosophy	11
1.2	ambition & motivation	11
1.3	Acknowledgements	11
1.4	About the author	11
1.5	Essential/relevant literature	12
1.6	Installation	12
1.7	What is a fieldstone?	12
1.8	Why the Finite Element method?	13
1.9	Oldies but goodies	13
1.10	Notations	14
1.11	Colour maps for visualisation	15
1.12	Bibliography	15
2	List of stones	16
3	The physical equations	20
3.1	Coordinate systems	20
3.1.1	Cartesian coordinates	20
3.1.2	Cylindrical coordinates	20
3.1.3	Spherical coordinates	20
3.2	A continuum mechanics primer	21
3.2.1	Stress tensor and tractions	22
3.3	Strain rate and spin tensor	23
3.3.1	Compressible Newtonian Fluid	23
3.3.2	Incompressible Newtonian Fluid	23
3.4	The heat transport equation - energy conservation equation	24
3.5	The momentum conservation equations	24
3.6	The mass conservation equations	25
3.7	The equations in ASPECT manual	25
3.8	The Boussinesq approximation	27
3.9	Stokes equation for elastic medium	28
3.10	The strain rate tensor in all coordinate systems	29
3.10.1	Cartesian coordinates	29
3.10.2	Polar coordinates	29
3.10.3	Cylindrical coordinates	29
3.10.4	Spherical coordinates	30
3.11	Boundary conditions	31
3.11.1	The Stokes equations	31
3.11.2	The heat transport equation	31
3.12	Meaningful physical quantities	32
3.13	Principal stress	34
3.13.1	In two dimensions	34

3.13.2	In three dimensions	36
3.14	The need for numerical modelling	39
3.15	Rheology in geodynamics	39
3.15.1	Linear viscous aka Newtonian	39
3.15.2	Power-law model	39
3.15.3	Carreau model	40
3.15.4	Bingham model	40
3.15.5	Herschel-Bulkley visco-plastic model	41
3.15.6	The Casson model	42
3.15.7	One model to rule them all?	42
3.15.8	Dislocation and Diffusion creep	42
3.15.9	Combining diffusion and dislocation creep	45
3.15.10	The von Mises failure criterion	47
3.15.11	The Tresca failure criterion	48
3.15.12	The Drucker-Prager failure criterion	49
3.15.13	The Mohr-Coulomb failure criterion	50
3.15.14	The Griffith-Murrell failure criterion	51
3.15.15	The failure envelope, or yield surface	51
3.15.16	Peierls creep	52
3.15.17	Arrhenius law	52
3.15.18	Simple parametrisation of the mantle	53
3.15.19	Glen's law for ice	53
3.15.20	Elasto-Visco-Plasticity	54
3.15.21	Anisotropic viscosity	54
3.15.22	Rheology of the lithosphere	55
3.16	Moment of inertia	55
4	The building blocks of the Finite Element Method	57
4.1	Numerical integration	57
4.1.1	in 1D - theory	57
4.1.2	in 1D - examples	60
4.1.3	in 2D/3D - theory	60
4.1.4	quadrature on triangles	61
4.1.5	quadrature on tetrahedra	61
4.1.6	The Gauss-Lobatto approach	62
4.2	The mesh	63
4.3	A bit of FE terminology	63
4.4	Elements and basis functions in 1D	64
4.4.1	Linear basis functions (Q_1)	64
4.4.2	Quadratic basis functions (Q_2)	65
4.4.3	Cubic basis functions (Q_3)	65
4.4.4	Quartic basis functions (Q_4)	68
4.5	Elements and basis functions in 2D	70
4.5.1	Bilinear basis functions in 2D (Q_1)	71
4.5.2	Biquadratic basis functions in 2D (Q_2)	73
4.5.3	Eight node serendipity basis functions in 2D ($Q_2^{(8)}$)	74
4.5.4	Bicubic basis functions in 2D (Q_3)	76
4.5.5	Biquartic basis functions in 2D (Q_4)	77
4.5.6	Linear basis functions for triangles in 2D (P_1)	77
4.5.7	Linear basis functions for quadrilaterals in 2D (P_1)	79
4.5.8	Enriched linear basis functions in triangles (P_1^+)	80
4.5.9	Quadratic basis functions for triangles in 2D (P_2)	82
4.5.10	Enriched quadratic basis functions in triangles (P_2^+)	83
4.5.11	Cubic basis functions for triangles (P_3)	85
4.6	Elements and basis functions in 3D	85
4.6.1	Linear basis functions in tetrahedra (P_1)	85

4.6.2	Enriched linear in tetrahedra(P_1^+)	86
4.6.3	Triquadratic basis functions in 3D (Q_2)	88
4.6.4	Enriched quadratic basis functions in tetrahedra (P_2^+)	89
4.6.5	Linear basis functions for tetrahedra (P_1)	89
4.6.6	20-node serendipity basis functions in 3D ($Q_2^{(20)}$)	90
5	Solving the heat transport equation with linear Finite Elements	91
5.1	The diffusion equation in 1D	91
5.2	The advection-diffusion equation in 1D	98
5.3	The advection-diffusion equation in 2D	100
5.3.1	Dealing with the time discretisation	101
5.3.2	On steady states	103
5.3.3	Anisotropic heat conduction	103
6	Solving the flow equations with the FEM	104
6.1	Strong and weak forms	104
6.2	Which velocity-pressure pair for Stokes?	104
6.2.1	The compatibility condition (or LBB condition)	104
6.2.2	Families	104
6.2.3	The bi/tri-linear velocity - constant pressure element ($Q_1 \times P_0$)	105
6.2.4	The bi/tri-quadratic velocity - discontinuous linear pressure element ($Q_2 \times P_{-1}$)	105
6.2.5	The bi/tri-quadratic velocity - bi/tri-linear pressure element ($Q_2 \times Q_1$)	105
6.2.6	The stabilised bi/tri-linear velocity - bi/tri-linear pressure element ($Q_1 \times Q_1\text{-stab}$)	106
6.2.7	The MINI triangular element ($P_1^+ \times P_1$) in 2D	106
6.2.8	The quadratic velocity - linear pressure triangle ($P_2 \times P_1$)	107
6.2.9	The Crouzeix-Raviart triangle ($P_2^+ \times P_{-1}$)	107
6.2.10	The Rannacher-Turek element - rotated $Q_1 \times P_0$	108
6.2.11	Other elements	108
6.2.12	A note about incompressibility and standard mixed methods	108
6.3	The penalty approach for viscous flow	108
6.4	The mixed FEM for viscous flow	112
6.4.1	in three dimensions	112
6.4.2	Going from 3D to 2D	118
6.5	Solving the elastic equations	120
6.6	A quick tour of similar literature	120
6.7	The case against the $Q_1 \times P_0$ element	120
6.8	Isoviscous Stokes for incompressible flow	121
7	The Discontinuous Galerkin Finite Element Method (DG-FEM)	123
7.1	First-order advection ODE in 1D	123
7.2	Steady state diffusion in 1D	126
8	Additional techniques and features	128
8.1	Dealing with a free surface (and mesh deformation)	129
8.1.1	The fully Lagrangian approach	129
8.1.2	The Eulerian approach: using sticky air	130
8.1.3	The Arbitrary Lagrangian Eulerian (ALE) approach	132
8.1.4	On the topic of moving internal nodes	137
8.2	Convergence criterion for nonlinear iterations	138
8.3	Strain weakening	139
8.4	The gravity vector	141
8.5	The SUPG formulation for the energy equation	142
8.5.1	Linear elements	142
8.6	The method of manufactured solutions	144
8.6.1	Analytical benchmark I - "DH"	144
8.6.2	Analytical benchmark II - "DB2D"	146

8.6.3	Analytical benchmark III - "DB3D"	146
8.6.4	Analytical benchmark IV - "Bercovier & Engelman"	148
8.6.5	Analytical benchmark V - "VJ1"	149
8.6.6	Analytical benchmark VI - "Ilinca & Pelletier"	150
8.6.7	Analytical benchmark VII - "grooves"	150
8.6.8	Analytical benchmark VIII - "Kovasznay"	153
8.6.9	Analytical benchmark IX - "VJ2"	153
8.6.10	Analytical benchmark X - "VJ3"	153
8.6.11	Analytical benchmark XI - "PPC1"	156
8.6.12	Analytical benchmark XII - "PPC2"	156
8.6.13	Annulus with kinematical b.c.	156
8.7	Geodynamical benchmarks	158
8.7.1	Relaxation of sinusoidal topography	160
8.7.2	the plastic brick	160
8.7.3	Infinite plate with a circular hole [1346]	163
8.7.4	Slope stability for elasto-plastic materials a la [1346]	164
8.7.5	Time-dependent benchmark in an annulus	164
8.7.6	Convection in 2D-box	165
8.7.7	The sinker problem	166
8.7.8	The hot blob problem	167
8.7.9	The punch/indentor problem in 2D	167
8.7.10	Lid driven cavity with analytical solution	169
8.7.11	Flow around a cylinder	170
8.7.12	Thin layer entrainment	170
8.7.13	Heat flow around a cylinder	173
8.7.14	Thermal diffusion of half-cooling space	173
8.7.15	Laplace equation on a semi infinite plate	174
8.7.16	Slab detachment benchmark	176
8.8	Assigning values to quadrature points	177
8.9	Matrix (Sparse) storage	180
8.9.1	2D domain - One degree of freedom per node	180
8.9.2	2D domain - Two degrees of freedom per node	181
8.9.3	in fieldstone	182
8.10	Mesh generation	183
8.10.1	Quadrilateral-based meshes	183
8.10.2	Delaunay triangulation and Voronoi cells, and triangle-based meshes	185
8.10.3	Tetrahedra	188
8.10.4	Hexahedra	188
8.10.5	Adaptive Mesh Refinement	188
8.10.6	Conformal Mesh Refinement	191
8.10.7	Meshes in an annulus	191
8.10.8	Meshes in a hollow sphere	191
8.11	Visco-Plasticity	195
8.11.1	Tensor invariants	195
8.11.2	Scalar viscoplasticity	196
8.11.3	About the yield stress value Y	196
8.12	Pressure smoothing	197
8.13	Pressure scaling	199
8.14	Pressure normalisation	200
8.14.1	Basic idea and naive implementation	200
8.14.2	Implementation – the real deal	200
8.15	Solving the Stokes system	201
8.15.1	when using the penalty formulation	201
8.15.2	Conjugate gradient and the Schur complement approach	202
8.15.3	Conjugate gradient and the Schur complement approach	203
8.15.4	The Augmented Lagrangian approach	207

8.15.5	The GMRES approach	208
8.16	The consistent boundary flux (CBF)	209
8.16.1	The CBF applied to the Stokes equation	209
8.16.2	The CBF applied to the heat transport equation	210
8.16.3	Some implementation details for the Stokes equation	210
8.17	The value of the timestep	213
8.18	Mappings	214
8.18.1	Linear mapping on a triangle	214
8.18.2	Bilinear mapping on a linear quadrilateral	214
8.18.3	biquadratic mapping of a straight-line face Q_2 element	218
8.18.4	biquadratic mapping of a not-so straight-line face Q_2 element	219
8.18.5	bilinear, biquadratic and bicubic mapping in an annulus	219
8.19	Exporting data to vtk format	222
8.20	Runge-Kutta methods	224
8.20.1	Using RK methods to advect particles/markers	225
8.21	Am I in or not? - finding reduced coordinates	227
8.21.1	Two-dimensional space	227
8.21.2	Three-dimensional space	227
8.22	Error measurements and convergence rates	230
8.22.1	About extrapolation	231
8.23	The initial temperature field	232
8.23.1	Single layer with imposed temperature b.c.	232
8.23.2	Single layer with imposed heat flux b.c.	233
8.23.3	Single layer with imposed heat flux and temperature b.c.	233
8.23.4	Half cooling space	233
8.23.5	Plate model	233
8.23.6	McKenzie slab	233
8.23.7	Initial temperature for global mantle convection models	235
8.24	Kinematic boundary conditions	236
8.24.1	In-out flux boundary conditions for lithospheric models	236
8.25	Computing gradients - the recovery process	237
8.25.1	Global recovery	237
8.25.2	Local recovery - centroid average over patch	237
8.25.3	Local recovery - nodal average over patch	237
8.25.4	Local recovery - least squares over patch	237
8.25.5	Link to pressure smoothing	237
8.26	Tracking materials and/or interfaces	238
8.26.1	The Particle-in-cell technique	239
8.26.2	The level set function technique	242
8.26.3	The field/composition technique	242
8.26.4	The Volume-of-Fluid method	243
8.26.5	The method of characteristics	243
8.26.6	The Marker Chain method	244
8.26.7	Hybrid methods	244
8.26.8	Boundary fitted mesh	244
8.27	Static condensation	246
8.28	Measuring incompressibility	247
8.29	Periodic boundary conditions	248
8.30	Removing rotational nullspace	249
8.30.1	Three dimensions	250
8.30.2	Two dimensions	250
8.31	Picard and Newton	252
8.31.1	Picard iterations	252
8.32	Defect correction formulation	253
8.33	Parallel or not?	254
8.34	Stream function	255

8.34.1	In Cartesian coordinates	255
8.34.2	In Cylindrical coordinates	255
8.35	Corner flow	256
8.36	Surface processes	258
8.36.1	In 1D - simple nonlinear diffusion a la [268]	258
8.36.2	In 1D - not so simple, a la [33]	258
8.37	Geometric multigrid	260
8.38	Computing depth	262
8.39	Imposing boundary conditions	263
8.40	The Geoid	264
8.40.1	What is the geoid?	264
8.40.2	How to compute it?	264
8.40.3	Interesting modelling	264
9	Gravity and co	265
	Stone 01: simple analytical solution (D&H)	266
	Stone 02: Stokes sphere	268
	Stone 03: Convection in a 2D box	269
	Stone 04: The lid driven cavity	272
	Stone 05: SolCx benchmark	274
	Stone 06: SolKz benchmark	276
	Stone 07: SolVi benchmark	277
	Stone 08: the indentor benchmark	279
	Stone 09: the annulus benchmark	281
	Stone 10: Stokes sphere (3D) - penalty	283
	Stone 11: stokes sphere (3D) - mixed formulation	284
	Stone 12: consistent pressure recovery	285
	Stone 13: the Particle in Cell technique (1) - the effect of averaging	287
	Stone 14: solving the full saddle point problem	291
	Stone 15: saddle point problem with Schur complement approach - benchmark	294
	Stone 16: saddle point problem with Schur complement approach - Stokes sphere	297
	Stone 17: solving the full saddle point problem in 3D	299
	Stone 18: solving the full saddle point problem with $Q_2 \times Q_1$ elements	304
	Stone 19: solving the full saddle point problem with $Q_3 \times Q_2$ elements	306
	Stone 20: the Busse benchmark	308
	Stone 22: The stabilised $Q_1 \times Q_1$ element	311
	Stone 23: compressible flow (1) - analytical benchmark	315

Stone 24: compressible flow (2) - convection box	318
Stone 25: Rayleigh-Taylor instability (1) - instantaneous	334
Stone 26: Slab detachment benchmark (1) - instantaneous	336
Stone 27: Consistent Boundary Flux	338
Stone 28: convection 2D box - Tosi et al, 2015	342
Stone 29: open boundary conditions	354
Stone 30: conservative velocity interpolation	357
Stone 31: conservative velocity interpolation 3D	358
Stone 32: 2D analytical sol. from stream function	359
Stone 33: Convection in an annulus	363
Stone 34: the Cartesian geometry elastic aquarium	365
Stone 35: 2D analytical sol. in annulus from stream function	367
Stone 36: the annulus geometry elastic aquarium	373
Stone 37: marker advection and population control	376
Stone 38: Critical Rayleigh number	377
Stone 39: chpe15	379
Stone 40: Rayleigh-Taylor instability	389
Stone 42: 1D diffusion	391
Stone 43: the rotating cone	392
Stone 44: the flat slab	395
Stone 45: the corner flow	396
Stone 46: MMS1 with Crouzeix-Raviart ($P_2^+ \times P_{-1}$) elements	400
Stone 47: MMS1 with MINI ($P_1^+ \times P_1$) elements	401
Stone 48: D&H with $Q_1 \times P_0$, $Q_2 \times Q_1$, $Q_3 \times Q_2$ and $Q_4 \times Q_3$ elements	403
Stone 49: Consistent Boundary Flux method on D&H benchmark with 4 elements	409
Stone 50: Lithosphere extension	410
Stone 51: Triangular domain benchmark with MINI element	411
Stone 52: Serendipity element in 2D	415
Stone 53: the sinking block benchmark	417
Stone 54: ALEs	418
Stone 55: Subduction as a thin-sheet problem	428

Stone 56: Dynamics of the Salt Water - Fresh Water Interface	430
Stone 57: 1D diffusion with DG-FEM	431
10 fieldstone: Gravity: buried sphere	432
11 Problems, to do list and projects for students	434
A Three-dimensional applications	436
B Codes in geodynamics	437
C Matrix properties	444
C.1 Symmetric matrices	444
C.2 Schur complement	444
D Dont be a hero - unless you have to	446
E A FANTOM, an ELEFANT and a GHOST	448
F Some useful Python commands	452
F.1 Sparse matrices	452
F.2 condition number	452
G Some useful maths	453
G.1 Inverse of a 3x3 matrix	453
G.2 Inverse of a 3x3 matrix	453
H Topics in (computational) geodynamics	454
H.1 Seismo-tectonics, subduction earthquakes	464
I Elemental mass matrices for simple geometries	468
I.1 1D segments	468
I.1.1 Linear basis functions	468
I.1.2 Quadratic basis functions	468
I.1.3 Cubic basis functions	469
I.1.4 Quartic basis functions	471
I.2 Quadrilaterals: rectangular elements	472
I.3 Hexahedra: cuboid elements	472
J Finite element terminology in various languages	473
K Fun modelling	474
L Beautiful/interesting images from computational geodynamics	475
M People	476

WARNING: this is work in progress

1 Introduction

1.1 Philosophy

This document was written with my students in mind, i.e. 3rd and 4th year Geology/Geophysics students at Utrecht University. I have chosen to use as little jargon as possible unless it is a term that is commonly found in the geodynamics literature (methods paper as well as application papers). There is no mathematical proof of any theorem that may be mentioned but I will try to refer to the appropriate sources, i.e. generic Numerical Analysis, Finite Element and Linear Algebra books. If you find that this book lacks references to Sobolev spaces, Hilbert spaces, and other spaces, this book is just not for you.

The codes I provide here are by no means optimised as I have chosen code readability over code efficiency. I have also chosen to avoid resorting to multiple code files or even functions in order to favour a sequential reading of the codes. These codes are not designed to form the basis of a real life application: Existing open source highly optimised codes should be preferred, such as ASPECT [1009, 809], CITCOM [1765, 1761], LAMEM [950], PTATIN [1154, 1151], PYLITH, ...

All kinds of feedback is welcome on the text (grammar, typos, ...), on the text, the equations or on the code(s). You will have my eternal gratitude if you wish to contribute an example, a benchmark, a cookbook.

All the python scripts and this document are freely available at

<https://github.com/cedriict/fieldstone>

1.2 ambition & motivation

I wish to provide the community with:

- an enormous bibliography data base - simply search the pdf for keywords. The \LaTeX file is also available next to the manual.tex file on github;
- a go-to document for anybody who wants to know more about a particular topic in computational geodynamics;
- a useful teaching tool for researchers, teachers, students and PhD students alike;
- small, readable, educative codes.

1.3 Acknowledgements

I have benefitted from many discussions, lectures, tutorials, coffee machine discussions, debugging sessions, conference poster sessions, etc ... over the years. I wish to name these instrumental people in particular and in alphabetic order: Wolfgang Bangerth, Jean Braun, Rens Elbertsen, Philippe Fullsack, Menno Fraters, Anne Glerum, Timo Heister, Dave May, Robert Myhill, John Naliboff, E. Gerry Puckett, Melchior Schuh-Senlis, Michael Tetley, Lukas van de Wiel, Arie van den Berg, Eric van den Hoogen, Tom Weir, and the whole ASPECT family/team.

1.4 About the author

I have BSc in mathematics, and an MSc diploma in physics (with a specialization in musical acoustics [458]). I did my PhD at the university of Groningen (The Netherlands) title *Thermodynamically consistent fluid particle modelling of phase separating mixtures*¹. Although half of the thesis deals with the re-derivation of the Navier-Stokes equations for such systems[525], the second half is concerned with the implementation of these equations with the Smoothed Particle Hydrodynamics method [1546, 1547, 1545].

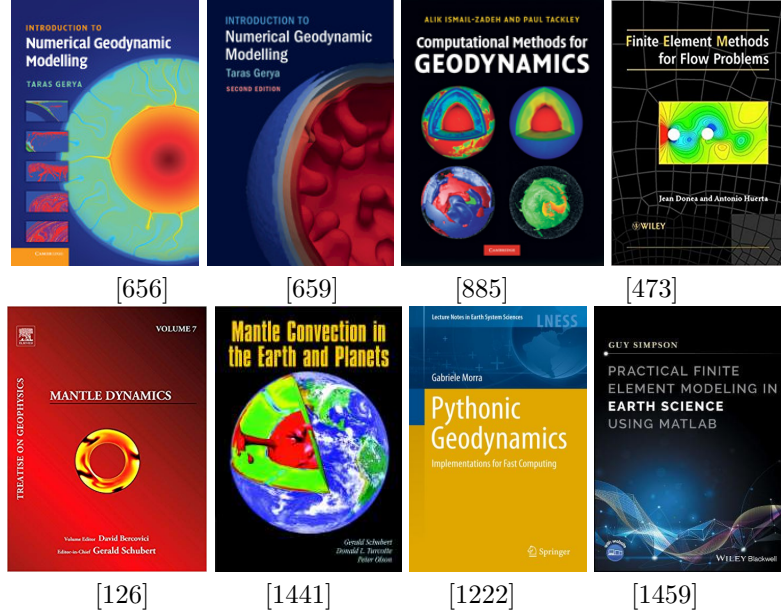
I then taught physics and programming at the University of Rennes (France) for a year, after which I did a 2-year post-doc with Prof. J. Braun² in the Geosciences department. I then did a 4-year post-doc

¹<http://cedriictheulot.net/thesis.html>

²<https://www.gfz-potsdam.de/en/staff/jean-braun/>

with prof. R. Huismans³ at the University of Bergen (Norway), followed by a 3-year post-doc with profs. T. Torsvik and W. Spakman at the Utrecht University (The Netherlands). Since June 2015 I am assistant professor there in the geophysics group.

1.5 Essential/relevant literature



- *Numerical modeling of Earth Systems* by Thorsten W. Becker and Boris J. P. Kaus, <http://www-udc.ig.utexas.edu/external/becker/teaching-557.html>
- *Myths & Methods in Modeling* by M. Spiegelman, <https://www.1deo.columbia.edu/~mspieg/mmm/>
- *Computational Science I* by Matthew G. Knepley, <https://cse.buffalo.edu/~knepley/classes/caam519/Syllabus.html>
- *Introduction to Numerical Methods for Variational Problems* by Hans Petter Langtangen and Kent-Andre Mardal, <https://hplgit.github.io/fem-book/doc/pub/book/pdf/fem-book-4print.pdf>

1.6 Installation

If numpy, scipy or matplotlib are not installed on your machine, here is how you can install them:

```
python3.6 -m pip install --user numpy scipy matplotlib
```

To install the umfpack solver:

```
pip install --upgrade scikit-umfpack --user
```

1.7 What is a fieldstone?

Simply put, it is stone collected from the surface of fields where it occurs naturally. It also stands for the bad acronym: finite element deformation of stones which echoes the primary application of these codes: geodynamic modelling.

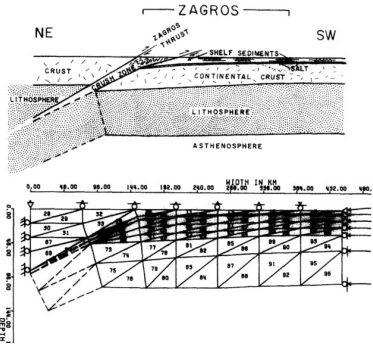
³<https://folk.uib.no/huismans/>

1.8 Why the Finite Element method?

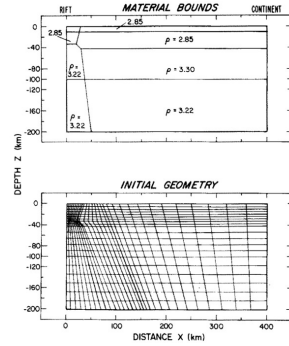
The Finite Element Method (FEM) is by no means the only method to solve PDEs in geodynamics, nor is it necessarily the best one. Other methods are employed very successfully, such as the Finite Difference Method (FDM), the Finite Volume Method (FVM), and to a lesser extent the Discrete Element Method (DEM) [1522, 504, 505, 621], the Lattice-Boltzmann method [853], the Rigid Element Method [1020], or the Element Free Galerkin Method (EFGM) [788]. I have been using FEM since 2008 and I do not have real experience to speak of in FVM or FDM so I concentrate in this book on what I know best.

1.9 Oldies but goodies

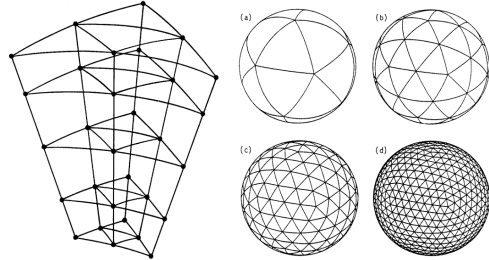
The first papers I could find showcasing the FEM in geodynamics are listed hereafter (I arbitrarily stop at 1995): [630], [28][1171][212] [515] [1534] [516][1220] [1790] [177] [203] [206]. I hereunder show a few plots taken from early geodynamics papers.



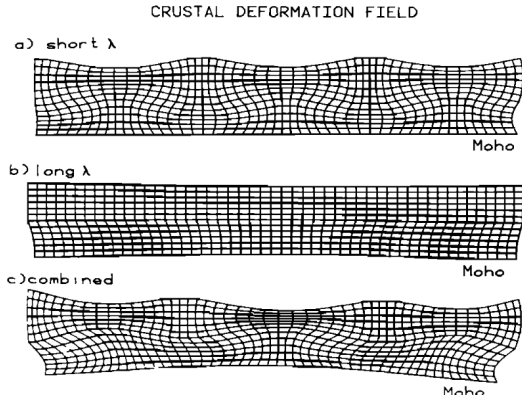
1978: Finite element modelling of lithosphere deformation: the Zagros collision orogeny [150]



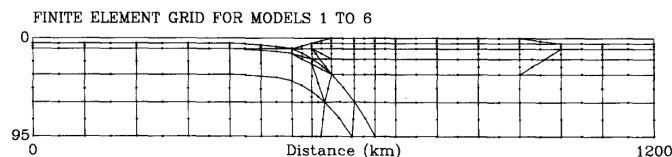
1981: Thermal regimes, mantle diapirs and crustal stresses of continental rifts [213]



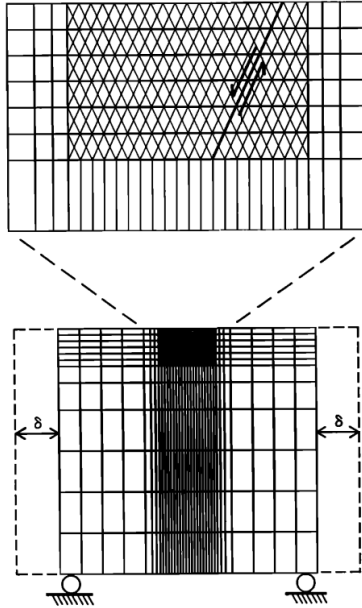
1985: Three-Dimensional Treatment of Convective Flow in the Earth's Mantle. [88]



1986: Lithospheric necking: a dynamic model for rift morphology [1791]

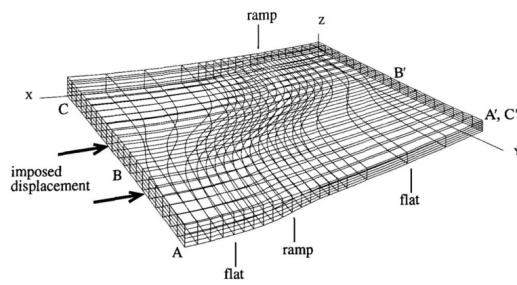


1989: Plate boundary forces at subduction zones and trench-arc compression [177]

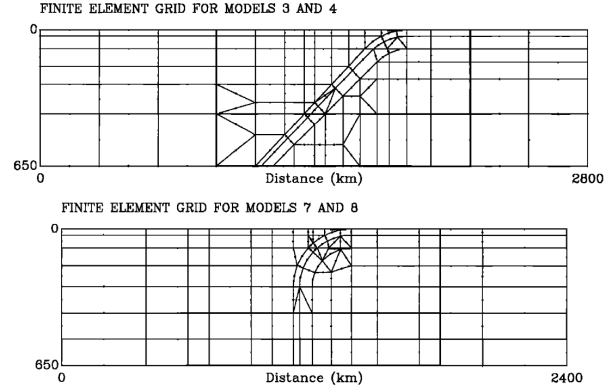


1989: Mechanics of graben formation in crustal rocks

[1172]

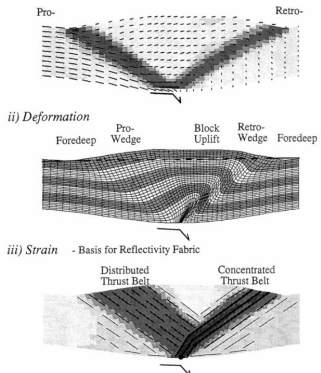


1993: 3D numerical modeling of compressional orogenies: Thrust geometry and oblique convergence [202]

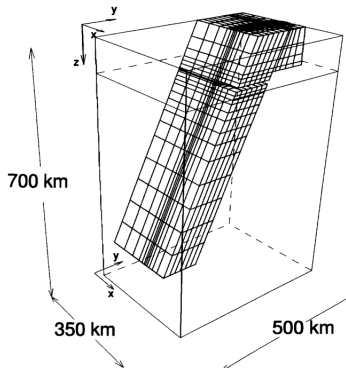


1992: Stresses and plate boundary forces associated with subduction plate margins

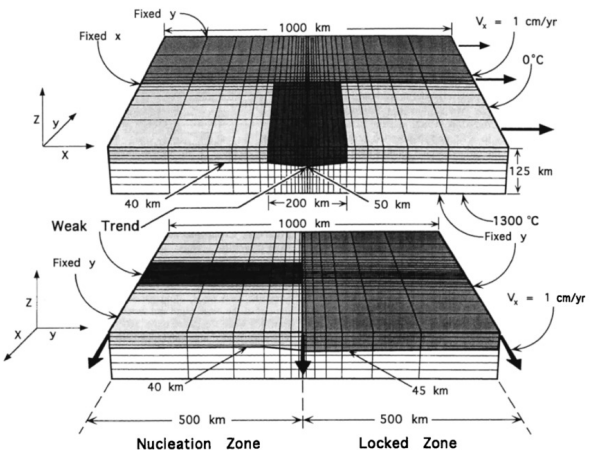
[1685]



Crustal-scale compressional orogens [100]



1995: 3D numerical modeling of detachment of subducted lithosphere [1734]



1996: 3D dynamical model of continental rift propagation and margin plateau formation [484]

1.10 Notations

Scalars such as temperature, density, pressure, etc ... are simply obtained in L^AT_EX by using the math mode, e.g. T , ρ , p . Although it is common to lump vectors and matrices/tensors together by using bold

fonts, I have decided in the interest of clarity to distinguish between those: vectors are denoted by an arrow atop the quantity, e.g. \vec{v} , \vec{g} , while matrices and tensors are in bold M , σ , etc ...

Also I use the \cdot notation between two vectors to denote a dot product $\vec{u} \cdot \vec{v} = u_i v_i$ or a matrix-vector multiplication $M \cdot \vec{a} = M_{ij} a_j$. If there is no \cdot between vectors, it means that the result $\vec{a}\vec{b} = a_i b_j$ is a matrix (it is a dyadic product⁴. Case in point, $\vec{\nabla} \cdot \vec{v}$ is the velocity divergence while $\vec{\nabla}\vec{v}$ is the velocity gradient tensor.

1.11 Colour maps for visualisation

In an attempt to homogenise the figures obtained with ParaView, I have decided to use a fixed colour scale for each field throughout this document. These colour scales were obtained from this link and are Perceptually Uniform Colour Maps [1003].

Field	colour code
Velocity/displacement	CET-D1A
Pressure	CET-L17
Velocity divergence	CET-L1
Density	CET-D3
Strain rate	CET-R2
Viscosity	CET-R3
Temperature	CET-D9

1.12 Bibliography

If the paper is a single-author paper, say by Garfield, published in 1978, its code in my bibliography file is *garf78* (i.e. the first four letters of the name, followed by the two digits of the publication year).

If the paper was written by two authors, say Garfield and Odie, in 1987, its code will be *gaod87*, i.e. the first two letters of the first author followed by the two first letters of the second author followed by two digits.

If the paper was written by three or more authors, say Garfield, Odie, John and Irene in 2003, its code will be *gaoj03*, i.e. the first two letters of the first author followed by the first letter of the second author, the first letter of the third author and the year.

Remark. Dutch names such as '*van Hunen*' or '*van den Berg*' are classified under letter '*v*', not '*h*' or '*d*' nor '*b*'.

⁴<https://en.wikipedia.org/wiki/Dyadics>

2 List of stones

I AM NOT HAPPY ABOUT THIS ... WILL CHANGE THIS SOON-ISH

stone number	element	outer solver	formulation	physical problem	3D	temperature	time stepping	nonlinear	compressible	analytical benchmark	numerical benchmark	elastomechanics
1	$Q_1 \times P_0$		penalty	analytical benchmark MMS1					†			
2	$Q_1 \times P_0$		penalty	Stokes sphere								
3	$Q_1 \times P_0$		penalty	Blankenbach et al., 1989		†	†					
4	$Q_1 \times P_0$		penalty	Lid driven cavity								
5	$Q_1 \times P_0$		penalty	SolCx benchmark								
6	$Q_1 \times P_0$		penalty	SolKz benchmark								
7	$Q_1 \times P_0$		penalty	SolVi benchmark								
8	$Q_1 \times P_0$		penalty	Indentor				†				
9	$Q_1 \times P_0$		penalty	annulus benchmark								
10	$Q_1 \times P_0$		penalty	Stokes sphere	†							
11	$Q_1 \times P_0$	full matrix	mixed	Stokes sphere	†							
12	$Q_1 \times P_0$		penalty	analytical benchmark + consistent press recovery								
13	$Q_1 \times P_0$		penalty	Stokes sphere + markers averaging								
14	$Q_1 \times P_0$	full matrix	mixed	analytical benchmark								
15	$Q_1 \times P_0$	Schur comp. CG	mixed	analytical benchmark								
16	$Q_1 \times P_0$	Schur comp. PCG	mixed	Stokes sphere								
17	$Q_2 \times Q_1$	full matrix	mixed	Burstedde benchmark	†							
18	$Q_2 \times Q_1$	full matrix	mixed	analytical benchmark								
19	$Q_3 \times Q_2$	full matrix	mixed	analytical benchmark								
20	$Q_1 \times P_0$		penalty	Busse et al., 1993	†	†	†					
21	$Q_1 \times P_0$ R-T		penalty	analytical benchmark								
22	$Q_1 \times Q_1$ -stab	full matrix	mixed	analytical benchmark								
23	$Q_1 \times P_0$		mixed	analytical benchmark					†			
24	$Q_1 \times P_0$		mixed	convection box	†	†			†			

Analytical benchmark means that an analytical solution exists while numerical benchmark means that a comparison with other code(s) has been carried out.

3 The physical equations

Symbol	meaning	unit
t	Time	s
x, y, z	Cartesian coordinates	m
r, θ	Polar coordinates	m,-
r, θ, z	Cylindrical coordinates	m,-,m
r, θ, ϕ	Spherical coordinates	m,-,-
\vec{v}	velocity vector	$\text{m} \cdot \text{s}^{-1}$
\vec{u}	displacement vector	m
ρ	mass density	kg/m^3
η	dynamic viscosity	$\text{Pa} \cdot \text{s}$
λ	penalty parameter	$\text{Pa} \cdot \text{s}$
T	temperature	K
$\vec{\nabla}$	gradient operator	m^{-1}
$\vec{\nabla} \cdot$	divergence operator	m^{-1}
p	pressure	Pa
$\dot{\epsilon}(\vec{v})$	strain rate tensor	s^{-1}
α	thermal expansion coefficient	K^{-1}
k	thermal conductivity	$\text{W}/(\text{m} \cdot \text{K})$
C_p	Heat capacity	J/K
H	intrinsic specific heat production	W/kg
β_T	isothermal compressibility	Pa^{-1}
τ	deviatoric stress tensor	Pa
σ	full stress tensor	Pa

3.1 Coordinate systems

3.1.1 Cartesian coordinates

3.1.2 Cylindrical coordinates

We have $r > 0$ and $\theta = [0, 2\pi[, defined in the (x, y) -plane.$

The relation between the unit vector in Cartesian and Polar/Cylindrical coordinates is given by:

$$\begin{pmatrix} \vec{e}_r \\ \vec{e}_\theta \end{pmatrix} = \begin{pmatrix} \cos \theta & \sin \theta \\ -\sin \theta & \cos \theta \end{pmatrix} \cdot \begin{pmatrix} \vec{e}_x \\ \vec{e}_y \end{pmatrix}$$

which yields

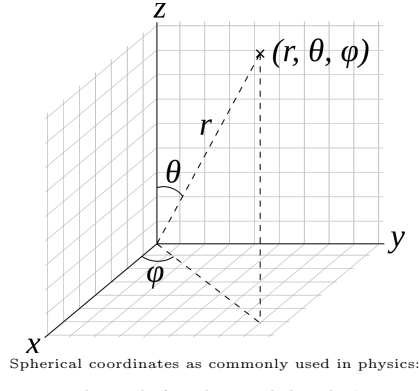
$$\begin{pmatrix} \vec{e}_x \\ \vec{e}_y \end{pmatrix} = \begin{pmatrix} \cos \theta & -\sin \theta \\ \sin \theta & \cos \theta \end{pmatrix} \cdot \begin{pmatrix} \vec{e}_r \\ \vec{e}_\theta \end{pmatrix}$$

so that for any vector \vec{V}

$$\begin{aligned} \vec{V} &= V_x \vec{e}_x + V_y \vec{e}_y \\ &= V_x[(\cos \theta) \vec{e}_r - (\sin \theta) \vec{e}_\theta] + V_y[(\sin \theta) \vec{e}_r + (\cos \theta) \vec{e}_\theta] \\ &= [V_x(\cos \theta) + V_y(\sin \theta)] \vec{e}_r + [-V_x(\sin \theta) + V_y(\cos \theta)] \vec{e}_\theta \end{aligned} \tag{1}$$

3.1.3 Spherical coordinates

On the following figure are represented the three cartesian axis, a point and its spherical coordinates r, θ, ϕ :



Spherical coordinates as commonly used in physics:

polar angle θ , and azimuthal angle ϕ .

In this case $\theta \in [0 : \pi]$ and $\phi \in] -\pi : \pi]$ and we have the following relationships:

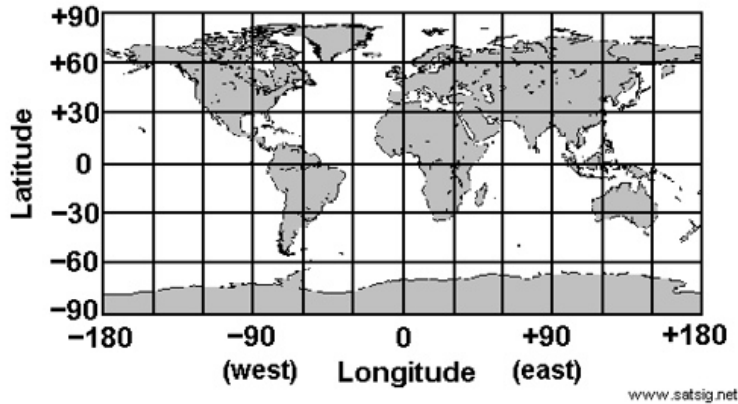
$$r = \sqrt{x^2 + y^2 + z^2} \quad (2)$$

$$\theta = \arccos(z/r) \quad (3)$$

$$\phi = \arctan(y/x) \quad (4)$$

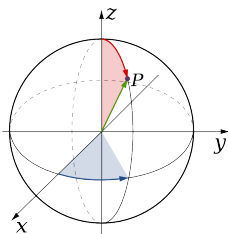
The inverse tangent used to compute ϕ must be suitably defined, taking into account the correct quadrant of (x, y) , which is why the atan2 intrinsic function is used in fortran for example.

In geography one uses latitude and longitude, represented hereunder:



- Latitude $\in [-90 : 90]$, or $\in [-\pi/2 : \pi/2]$
- Longitude $\in] -180 : 180]$, or $\in] -\pi : \pi]$

Since the colatitude is the complementary angle of the latitude, i.e. the difference between 90 and the latitude, where southern latitudes are denoted with a minus sign, θ as shown above is actually the colatitude. The co-latitude is shown in red on the following figure:



3.2 A continuum mechanics primer

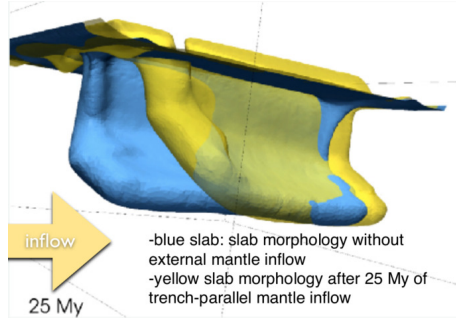
Contains contributions by W. Spakman

In continuum mechanics we make a distinction between two broad classes of forces:

- Body forces defined as force per unit volume (N/m^3): gravity, electro-magnetic forces
- Traction: Surface forces defined as force per unit surface area (N/m^2): Contact forces, elastic forces per unit area, internal flow friction, pressure, ...

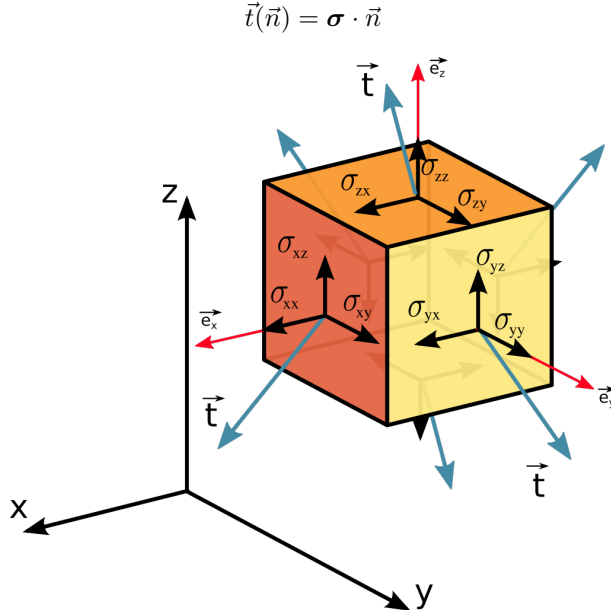
A traction is the surface average of all atomic forces exerted by atoms on the one side on atoms on the other side of the surface. For real-Earth processes, internal tractions are ultimately caused by the body forces, usually gravity.

Existing mantle flow(i.e. flow that is forced elsewhere) can exert tractions (shear stresses) on the subducting slab or for instance at the base of lithosphere plates. In HPT-laboratory experiments external tractions (pressure, shear traction) are applied to a rock sample, which cause internal tractions to balance the exerted forces.



3.2.1 Stress tensor and tractions

The Cauchy tensor⁵ consists of nine components σ_{ij} that completely define the state of stress at a point inside a material. The tensor relates a unit-length direction vector \vec{n} to the so-called 'stress vector' (most commonly called 'traction') $\vec{t}(\vec{n})$ across an imaginary surface perpendicular to \vec{n} :



With respect to an orthonormal basis $\{\vec{e}_x, \vec{e}_y, \vec{e}_z\}$, the Cauchy stress tensor is given by:

$$\boldsymbol{\sigma} = \begin{pmatrix} \sigma_{xx} & \sigma_{xy} & \sigma_{xz} \\ \sigma_{yx} & \sigma_{yy} & \sigma_{yz} \\ \sigma_{zx} & \sigma_{zy} & \sigma_{zz} \end{pmatrix} \quad (5)$$

⁵https://en.wikipedia.org/wiki/Cauchy_stress_tensor

⁶https://commons.wikimedia.org/wiki/File:Components_stress_tensor_cartesian.svg

The three diagonal elements are called normal stresses while the off-diagonal terms are called shear stresses.

One can easily prove (see for instance Section 3.3.6 of [745]) that the balance of angular momentum leads reduces to the statement that the Cauchy stress tensor is symmetric, i.e. $\boldsymbol{\sigma} = \boldsymbol{\sigma}^T$. Therefore, the stress state of the medium at any point and instant can be specified by only six independent parameters, rather than nine:

$$\boldsymbol{\sigma} = \begin{pmatrix} \sigma_{xx} & \sigma_{xy} & \sigma_{xz} \\ \sigma_{xy} & \sigma_{yy} & \sigma_{yz} \\ \sigma_{xz} & \sigma_{yz} & \sigma_{zz} \end{pmatrix} \quad \text{or sometimes} \quad \boldsymbol{\sigma} = \begin{pmatrix} \sigma_x & \tau_{xy} & \tau_{xz} \\ \tau_{xy} & \sigma_y & \tau_{yz} \\ \tau_{xz} & \tau_{yz} & \sigma_z \end{pmatrix} \quad (6)$$

where the elements $\sigma_x, \sigma_y, \sigma_z$ are called the orthogonal normal stresses (relative to the chosen coordinate system), and $\tau_{xy}, \tau_{xz}, \tau_{yz}$ the orthogonal shear stresses.

As seen above, the SI units of both stress tensor and traction are N/m².

3.3 Strain rate and spin tensor

The velocity gradient is given in Cartesian coordinates by:

$$\vec{\nabla}\vec{v} = \begin{pmatrix} \frac{\partial u}{\partial x} & \frac{\partial v}{\partial x} & \frac{\partial w}{\partial x} \\ \frac{\partial u}{\partial y} & \frac{\partial v}{\partial y} & \frac{\partial w}{\partial y} \\ \frac{\partial u}{\partial z} & \frac{\partial v}{\partial z} & \frac{\partial w}{\partial z} \end{pmatrix} \quad (7)$$

It can be decomposed into its symmetric and skew-symmetric parts according to:

$$\vec{\nabla}\vec{v} = \vec{\nabla}^s\vec{v} + \vec{\nabla}^w\vec{v} \quad (8)$$

The symmetric part is called the strain rate (or rate of deformation):

$$\dot{\boldsymbol{\epsilon}}(\vec{v}) = \frac{1}{2} (\vec{\nabla}\vec{v} + \vec{\nabla}\vec{v}^T) \quad (9)$$

The skew-symmetric tensor is called spin tensor (or vorticity tensor):

$$\dot{\boldsymbol{R}}(\vec{v}) = \frac{1}{2} (\vec{\nabla}\vec{v} - \vec{\nabla}\vec{v}^T) \quad (10)$$

Remark. In the mathematical literature a different notation for the strain rate tensor is often used, i.e. $D(\vec{v})$, such as for instance in [614].

3.3.1 Compressible Newtonian Fluid

For the compressible case, $\boldsymbol{\sigma}$ depends linearly on the strain rate tensor $\dot{\boldsymbol{\epsilon}}$:

$$\boldsymbol{\sigma} = -p(\rho, T)\mathbf{1} + \lambda \operatorname{tr}(\dot{\boldsymbol{\epsilon}})\mathbf{1} + 2\eta\dot{\boldsymbol{\epsilon}} \quad (11)$$

where p is the thermodynamic pressure which is a function of the density ρ and the temperature T (an equation of state is then needed). λ and η are the coefficients of viscosity. We also have:

$$\boldsymbol{\sigma} = -p(\rho, T)\mathbf{1} + \zeta \operatorname{tr}(\dot{\boldsymbol{\epsilon}})\mathbf{1} + 2\eta\dot{\boldsymbol{\epsilon}}^d \quad (12)$$

where $\zeta = \lambda + 2\eta/3$ is the bulk viscosity and η is the shear viscosity.

3.3.2 Incompressible Newtonian Fluid

In this case the stress tensor is

$$\boldsymbol{\sigma} = -p\mathbf{1} + \boldsymbol{\tau} \quad (13)$$

where $p = -1/3 \operatorname{tr}(\boldsymbol{\sigma})$ and $\boldsymbol{\tau}$ is the deviatoric stress tensor:

$$\boldsymbol{\tau} = 2\eta\dot{\boldsymbol{\epsilon}}^d \quad (14)$$

3.4 The heat transport equation - energy conservation equation

Let us start from the heat transport equation as shown in Schubert, Turcotte and Olson [1441]:

$$\rho C_p \frac{DT}{Dt} - \alpha T \frac{Dp}{Dt} = \vec{\nabla} \cdot k \vec{\nabla} T + \Phi + \rho H \quad (15)$$

with D/Dt being the total derivatives so that

$$\frac{DT}{Dt} = \frac{\partial T}{\partial t} + \vec{v} \cdot \vec{\nabla} T \quad \frac{Dp}{Dt} = \frac{\partial p}{\partial t} + \vec{v} \cdot \vec{\nabla} p \quad (16)$$

Solving for temperature, this equation is often rewritten as follows:

$$\rho C_p \frac{DT}{Dt} - \vec{\nabla} \cdot k \vec{\nabla} T = \alpha T \frac{Dp}{Dt} + \Phi + \rho H \quad (17)$$

where Φ is the shear heating [1361, p287]. In many publications, Φ is given by $\Phi = \tau_{ij} \partial_j u_i = \boldsymbol{\tau} : \vec{\nabla} \vec{v}$.

$$\begin{aligned} \Phi &= \tau_{ij} \partial_j u_i \\ &= 2\eta \dot{\epsilon}_{ij}^d \partial_j u_i \\ &= 2\eta \frac{1}{2} (\dot{\epsilon}_{ij}^d \partial_j u_i + \dot{\epsilon}_{ji}^d \partial_i u_j) \\ &= 2\eta \frac{1}{2} (\dot{\epsilon}_{ij}^d \partial_j u_i + \dot{\epsilon}_{ij}^d \partial_i u_j) \\ &= 2\eta \dot{\epsilon}_{ij}^d \frac{1}{2} (\partial_j u_i + \partial_i u_j) \\ &= 2\eta \dot{\epsilon}_{ij}^d \dot{\epsilon}_{ij} \\ &= 2\eta \dot{\epsilon}^d : \dot{\epsilon} \\ &= 2\eta \dot{\epsilon}^d : \left(\dot{\epsilon}^d + \frac{1}{3} (\vec{\nabla} \cdot \vec{v}) \mathbf{1} \right) \\ &= 2\eta \dot{\epsilon}^d : \dot{\epsilon}^d + 2\eta \dot{\epsilon}^d : \mathbf{1} (\vec{\nabla} \cdot \vec{v}) \\ &= 2\eta \dot{\epsilon}^d : \dot{\epsilon}^d \end{aligned} \quad (18)$$

Finally

$$\Phi = \boldsymbol{\tau} : \vec{\nabla} \vec{v} = 2\eta \dot{\epsilon}^d : \dot{\epsilon}^d = 2\eta ((\dot{\epsilon}_{xx}^d)^2 + (\dot{\epsilon}_{yy}^d)^2 + 2(\dot{\epsilon}_{xy}^d)^2)$$

3.5 The momentum conservation equations

Because the Prandlt number is virtually zero in Earth science applications the Navier Stokes equations reduce to the Stokes equation:

$$\vec{\nabla} \cdot \boldsymbol{\sigma} + \rho \vec{g} = \vec{0} \quad (19)$$

Since

$$\boldsymbol{\sigma} = -p \mathbf{1} + \boldsymbol{\tau} \quad (20)$$

it also writes

$$-\vec{\nabla} p + \vec{\nabla} \cdot \boldsymbol{\tau} + \rho \vec{g} = \vec{0} \quad (21)$$

Using the relationship $\boldsymbol{\tau} = 2\eta \dot{\epsilon}^d$ we arrive at

$$-\vec{\nabla} p + \vec{\nabla} \cdot (2\eta \dot{\epsilon}^d) + \rho \vec{g} = \vec{0} \quad (22)$$

3.6 The mass conservation equations

The mass conservation equation is given by

$$\frac{D\rho}{Dt} + \rho \vec{\nabla} \cdot \vec{v} = 0$$

or,

$$\frac{\partial \rho}{\partial t} + \vec{\nabla} \cdot (\rho \vec{v}) = 0$$

In the case of an incompressible flow, then $\partial \rho / \partial t = 0$ and $\vec{\nabla} \rho = 0$, i.e. $D\rho/Dt = 0$ and the remaining equation is simply:

$$\vec{\nabla} \cdot \vec{v} = 0$$

A vector field that is divergence-free is also called solenoidal⁷.

3.7 The equations in ASPECT manual

The following is lifted off the ASPECT manual. We focus on the system of equations in a $d = 2$ - or $d = 3$ -dimensional domain Ω that describes the motion of a highly viscous fluid driven by differences in the gravitational force due to a density that depends on the temperature. In the following, we largely follow the exposition of this material in Schubert, Turcotte and Olson [1441].

Specifically, we consider the following set of equations for velocity \mathbf{u} , pressure p and temperature T :

$$-\vec{\nabla} \cdot \left[2\eta \left(\dot{\varepsilon}(\vec{v}) - \frac{1}{3}(\vec{\nabla} \cdot \vec{v})\mathbf{1} \right) \right] + \vec{\nabla} p = \rho \vec{g} \quad \text{in } \Omega, \quad (23)$$

$$\vec{\nabla} \cdot (\rho \vec{v}) = 0 \quad \text{in } \Omega, \quad (24)$$

$$\begin{aligned} \rho C_p \left(\frac{\partial T}{\partial t} + \vec{v} \cdot \vec{\nabla} T \right) - \vec{\nabla} \cdot k \vec{\nabla} T &= \rho H \\ &+ 2\eta \left(\dot{\varepsilon}(\mathbf{v}) - \frac{1}{3}(\vec{\nabla} \cdot \vec{v})\mathbf{1} \right) : \left(\dot{\varepsilon}(\mathbf{v}) - \frac{1}{3}(\vec{\nabla} \cdot \vec{v})\mathbf{1} \right) \\ &+ \alpha T (\mathbf{v} \cdot \vec{\nabla} p) \end{aligned} \quad (25)$$

in Ω ,

where $\dot{\varepsilon}(\vec{v}) = \frac{1}{2}(\vec{\nabla} \vec{v} + \vec{\nabla} \vec{v}^T)$ is the symmetric gradient of the velocity (often called the *strain rate*).

In this set of equations, (672) and (673) represent the compressible Stokes equations in which $\mathbf{v} = \mathbf{v}(\mathbf{x}, t)$ is the velocity field and $p = p(\mathbf{x}, t)$ the pressure field. Both fields depend on space \mathbf{x} and time t . Fluid flow is driven by the gravity force that acts on the fluid and that is proportional to both the density of the fluid and the strength of the gravitational pull.

Coupled to this Stokes system is equation (674) for the temperature field $T = T(\mathbf{x}, t)$ that contains heat conduction terms as well as advection with the flow velocity \mathbf{v} . The right hand side terms of this equation correspond to

- internal heat production for example due to radioactive decay;
- friction (shear) heating;
- adiabatic compression of material;

In order to arrive at the set of equations that ASPECT solves, we need to

- neglect the $\partial p / \partial t$. **WHY?**
- neglect the $\partial \rho / \partial t$. **WHY?**

⁷https://en.wikipedia.org/wiki/Solenoidal_vector_field

from equations above.

Also, their definition of the shear heating term Φ is:

$$\Phi = k_B(\nabla \cdot \mathbf{v})^2 + 2\eta\dot{\epsilon}^d : \dot{\epsilon}^d$$

For many fluids the bulk viscosity k_B is very small and is often taken to be zero, an assumption known as the Stokes assumption: $k_B = \lambda + 2\eta/3 = 0$. Note that η is the dynamic viscosity and λ the second viscosity. Also,

$$\boldsymbol{\tau} = 2\eta\dot{\epsilon} + \lambda(\nabla \cdot \mathbf{v})\mathbf{1}$$

but since $k_B = \lambda + 2\eta/3 = 0$, then $\lambda = -2\eta/3$ so

$$\boldsymbol{\tau} = 2\eta\dot{\epsilon} - \frac{2}{3}\eta(\nabla \cdot \mathbf{v})\mathbf{1} = 2\eta\dot{\epsilon}^d$$

3.8 The Boussinesq approximation

As nicely explained in Spiegel & Veronis [1472]: "In the study of problems of thermal convection it is a frequent practice to simplify the basic equations by introducing certain approximations which are attributed to Boussinesq (1903). The Boussinesq approximations can best be summarized by two statements: (1) The fluctuations in density which appear with the advent of motion result principally from thermal (as opposed to pressure) effects. (2) In the equations for the rate of change of momentum and mass, density variations may be neglected except when they are coupled to the gravitational acceleration in the buoyancy force." Note that their paper examines the Boussinesq approximation for compressible fluids.

[from ASPECT manual] The Boussinesq approximation assumes that the density can be considered constant in all occurrences in the equations with the exception of the buoyancy term on the right hand side of (672). The primary result of this assumption is that the continuity equation (673) will now read

$$\nabla \cdot \mathbf{v} = 0$$

This implies that the strain rate tensor is deviatoric. Under the Boussinesq approximation, the equations are much simplified:

$$-\nabla \cdot [2\eta\dot{\epsilon}(\mathbf{v})] + \nabla p = \rho\mathbf{g} \quad \text{in } \Omega, \quad (26)$$

$$\nabla \cdot (\rho\mathbf{v}) = 0 \quad \text{in } \Omega, \quad (27)$$

$$\rho_0 C_p \left(\frac{\partial T}{\partial t} + \mathbf{v} \cdot \nabla T \right) - \nabla \cdot k \nabla T = \rho H \quad \text{in } \Omega \quad (28)$$

Note that all terms on the rhs of the temperature equations have disappeared, with the exception of the source term.

3.9 Stokes equation for elastic medium

What follows is mostly borrowed from Becker & Kaus lecture notes.

The strong form of the PDE that governs force balance in a medium is given by

$$\vec{\nabla} \cdot \boldsymbol{\sigma} + \vec{f} = \vec{0}$$

where $\boldsymbol{\sigma}$ is the stress tensor and \vec{f} is a body force.

The stress tensor is related to the strain tensor through the generalised Hooke's law⁸:

$$\sigma_{ij} = \sum_{kl} C_{ijkl} \epsilon_{kl} \quad \text{or} \quad \boldsymbol{\sigma} = \mathbf{C} : \boldsymbol{\epsilon} \quad (29)$$

where \mathbf{C} is the fourth-order elastic tensor.

Due to the inherent symmetries of $\boldsymbol{\sigma}$, $\boldsymbol{\epsilon}$, and \mathbf{C} , only 21 elastic coefficients of the latter are independent. For isotropic media (which have the same physical properties in any direction), \mathbf{C} can be reduced to only two independent numbers (for example the bulk modulus K and the shear modulus G that quantify the material's resistance to changes in volume and to shearing deformations, respectively).

One often then write Eq. as follows:

$$\sigma_{ij} = \lambda \epsilon_{kk} \delta_{ij} + 2\mu \epsilon_{ij} \quad \text{or}, \quad \boldsymbol{\sigma} = \lambda (\vec{\nabla} \cdot \vec{u}) \mathbf{1} + 2\mu \boldsymbol{\epsilon} \quad (30)$$

where λ is the Lamé parameter and μ is the shear modulus⁹. The term $\vec{\nabla} \cdot \vec{u}$ is the isotropic dilation.

The strain tensor is related to the displacement as follows:

$$\boldsymbol{\epsilon} = \frac{1}{2} (\vec{\nabla} \vec{u} + \vec{\nabla} \vec{u}^T)$$

The incompressibility (bulk modulus), K , is defined as $p = -K \vec{\nabla} \cdot \vec{u}$ where p is the pressure with

$$\begin{aligned} p &= -\frac{1}{3} \text{tr}(\boldsymbol{\sigma}) \\ &= -\frac{1}{3} [\lambda (\vec{\nabla} \cdot \vec{u}) \text{tr}[\mathbf{1}] + 2\mu \text{tr}[\boldsymbol{\epsilon}]] \\ &= -\frac{1}{3} [\lambda (\vec{\nabla} \cdot \vec{u}) 3 + 2\mu (\vec{\nabla} \cdot \vec{u})] \\ &= -\left[\lambda + \frac{2}{3}\mu \right] (\vec{\nabla} \cdot \vec{u}) \end{aligned} \quad (31)$$

so that $K = \lambda + \frac{2}{3}\mu$.

Remark. Eq. (3.9) and (30) are analogous to the ones that one has to solve in the context of viscous flow using the penalty method. In this case λ is the penalty coefficient, \mathbf{u} is the velocity, and μ is then the dynamic viscosity.

The Lamé parameter and the shear modulus are also linked to ν the poisson ratio, and E , Young's modulus:

$$\lambda = \mu \frac{2\nu}{1-2\nu} = \frac{\nu E}{(1+\nu)(1-2\nu)} \quad \text{with} \quad E = 2\mu(1+\nu)$$

The shear modulus, expressed often in GPa, describes the material's response to shear stress. The poisson ratio describes the response in the direction orthogonal to uniaxial stress. The Young modulus, expressed in GPa, describes the material's strain response to uniaxial stress in the direction of this stress.

⁸[https://en.wikipedia.org/wiki/Hooke's_law](https://en.wikipedia.org/wiki/Hooke%27s_law)

⁹It is also sometimes written G

3.10 The strain rate tensor in all coordinate systems

The strain rate tensor $\dot{\varepsilon}$ is given by

$$\dot{\varepsilon} = \frac{1}{2}(\vec{\nabla}\vec{v} + \vec{\nabla}\vec{v}^T) \quad (32)$$

3.10.1 Cartesian coordinates

$$\dot{\varepsilon}_{xx} = \frac{\partial u}{\partial x} \quad (33)$$

$$\dot{\varepsilon}_{yy} = \frac{\partial v}{\partial y} \quad (34)$$

$$\dot{\varepsilon}_{zz} = \frac{\partial w}{\partial z} \quad (35)$$

$$\dot{\varepsilon}_{yx} = \dot{\varepsilon}_{xy} = \frac{1}{2} \left(\frac{\partial u}{\partial y} + \frac{\partial v}{\partial x} \right) \quad (36)$$

$$\dot{\varepsilon}_{zx} = \dot{\varepsilon}_{xz} = \frac{1}{2} \left(\frac{\partial u}{\partial z} + \frac{\partial w}{\partial x} \right) \quad (37)$$

$$\dot{\varepsilon}_{zy} = \dot{\varepsilon}_{yz} = \frac{1}{2} \left(\frac{\partial v}{\partial z} + \frac{\partial w}{\partial y} \right) \quad (38)$$

3.10.2 Polar coordinates

$$\dot{\varepsilon}_{rr} = \frac{\partial v_r}{\partial r} \quad (39)$$

$$\dot{\varepsilon}_{\theta\theta} = \frac{v_r}{r} + \frac{1}{r} \frac{\partial v_\theta}{\partial \theta} \quad (40)$$

$$\dot{\varepsilon}_{\theta r} = \dot{\varepsilon}_{r\theta} = \frac{1}{2} \left(\frac{\partial v_\theta}{\partial r} - \frac{v_\theta}{r} + \frac{1}{r} \frac{\partial v_r}{\partial \theta} \right) \quad (41)$$

3.10.3 Cylindrical coordinates

$$\dot{\varepsilon}_{rr} = \frac{\partial v_r}{\partial r} \quad (42)$$

$$\dot{\varepsilon}_{\theta\theta} = \frac{v_r}{r} + \frac{1}{r} \frac{\partial v_\theta}{\partial \theta} \quad (43)$$

$$\dot{\varepsilon}_{\theta r} = \dot{\varepsilon}_{r\theta} = \frac{1}{2} \left(\frac{\partial v_\theta}{\partial r} - \frac{v_\theta}{r} + \frac{1}{r} \frac{\partial v_r}{\partial \theta} \right) \quad (44)$$

$$\dot{\varepsilon}_{zz} = \frac{\partial w}{\partial z} \quad (45)$$

$$\dot{\varepsilon}_{rz} = \dot{\varepsilon}_{zr} = \frac{1}{2} () \quad (46)$$

$$\dot{\varepsilon}_{\theta z} = \dot{\varepsilon}_{z\theta} = \frac{1}{2} \left(\frac{1}{r} \frac{\partial w}{\partial \theta} + \frac{\partial v_\theta}{\partial z} \right) \quad (47)$$

$$(48)$$

CHECK AND HOMOGENIZE NOTATIONS

<http://eml.ou.edu/equation/FLUIDS/STRAIN/STRAIN.HTM>

3.10.4 Spherical coordinates

$$\dot{\varepsilon}_{rr} = \frac{\partial v_r}{\partial r} \quad (49)$$

$$\dot{\varepsilon}_{\theta\theta} = \frac{v_r}{r} + \frac{1}{r} \frac{\partial v_\theta}{\partial \theta} \quad (50)$$

$$\dot{\varepsilon}_{\phi\phi} = \frac{1}{r \sin \theta} \frac{\partial v_\phi}{\partial \phi} \quad (51)$$

$$\dot{\varepsilon}_{\theta r} = \dot{\varepsilon}_{r\theta} = \frac{1}{2} \left(r \frac{\partial}{\partial r} \left(\frac{v_\theta}{r} \right) + \frac{1}{r} \frac{\partial v_r}{\partial \theta} \right) \quad (52)$$

$$\dot{\varepsilon}_{\phi r} = \dot{\varepsilon}_{r\phi} = \frac{1}{2} \left(\frac{1}{r \sin \theta} \frac{\partial v_r}{\partial \phi} + r \frac{\partial}{\partial r} \left(\frac{v_\phi}{r} \right) \right) \quad (53)$$

$$\dot{\varepsilon}_{\phi\theta} = \dot{\varepsilon}_{\theta\phi} = \frac{1}{2} \left(\frac{\sin \theta}{r} \frac{\partial}{\partial \theta} \left(\frac{v_\phi}{\sin \theta} \right) + \frac{1}{r \sin \theta} \frac{\partial v_\theta}{\partial \phi} \right) \quad (54)$$

3.11 Boundary conditions

In mathematics, the Dirichlet (or first-type) boundary condition is a type of boundary condition, named after Peter Gustav Lejeune Dirichlet. When imposed on an ODE or PDE, it specifies the values that a solution needs to take on along the boundary of the domain. Note that a Dirichlet boundary condition may also be referred to as a fixed boundary condition.

The Neumann (or second-type) boundary condition is a type of boundary condition, named after Carl Neumann. When imposed on an ordinary or a partial differential equation, the condition specifies the values in which the derivative of a solution is applied within the boundary of the domain.

It is possible to describe the problem using other boundary conditions: a Dirichlet boundary condition specifies the values of the solution itself (as opposed to its derivative) on the boundary, whereas the Cauchy boundary condition, mixed boundary condition and Robin boundary condition are all different types of combinations of the Neumann and Dirichlet boundary conditions.

3.11.1 The Stokes equations

You may find the following terms in the computational geodynamics literature:

- free surface: this means that no force is acting on the surface, i.e. $\sigma \cdot \vec{n} = \vec{0}$. It is usually used on the top boundary of the domain and allows for topography evolution.
- free slip: $\vec{v} \cdot \vec{n} = 0$ and $(\sigma \cdot \vec{n}) \times \vec{n} = \vec{0}$. This condition ensures a frictionless flow parallel to the boundary where it is prescribed.
- no slip: this means that the velocity (or displacement) is exactly zero on the boundary, i.e. $\vec{v} = \vec{0}$.
- prescribed velocity: $\vec{v} = \vec{v}_{bc}$
- stress b.c.:
- open .b.c.: see fieldstone 29.

3.11.2 The heat transport equation

There are two types of boundary conditions for this equation: temperature boundary conditions (Dirichlet boundary conditions) and heat flux boundary conditions (Neumann boundary conditions).

3.12 Meaningful physical quantities

- Velocity \vec{v} (m/s): This is a vector quantity and both magnitude and direction are needed to define it. It is the rate of change of position with respect to a frame of reference.
- Root mean square velocity v_{rms} (m/s):

$$v_{rms} = \left(\frac{\int_{\Omega} |\vec{v}|^2 d\Omega}{\int_{\Omega} d\Omega} \right)^{1/2} = \left(\frac{1}{V_{\Omega}} \int_{\Omega} |\vec{v}|^2 d\Omega \right)^{1/2} \quad (55)$$

Remark. V_{Ω} is usually computed numerically at the same time v_{rms} is computed.

In Cartesian coordinates, for a cuboid domain of size $L_x \times L_y \times L_z$, the v_{rms} is simply given by:

$$v_{rms} = \left(\frac{1}{L_x L_y L_z} \int_0^{L_x} \int_0^{L_y} \int_0^{L_z} (u^2 + v^2 + w^2) dx dy dz \right)^{1/2} \quad (56)$$

In the case of an annulus domain, although calculations are carried out in Cartesian coordinates, it makes sense to look at the radial velocity component v_r and the tangential velocity component v_{θ} , and their respective root mean square averages:

$$v_r|_{rms} = \left(\frac{1}{V_{\Omega}} \int_{\Omega} v_r^2 d\Omega \right)^{1/2} \quad (57)$$

$$v_{\theta}|_{rms} = \left(\frac{1}{V_{\Omega}} \int_{\Omega} v_{\theta}^2 d\Omega \right)^{1/2} \quad (58)$$

- Pressure p (Pa):
- Stress tensor σ (Pa):
- Strain tensor ϵ (dimensionless):
- Strain rate tensor $\dot{\epsilon}$ (s⁻¹):
- Rayleigh number Ra (X): It is a dimensionless number that expresses the ratio of the driving forces to the opposing forces. The buoyancy force comes from the volumetric thermal expansion while the viscous forces and the heat diffusivity oppose convection (the latter one smoothes out thermal gradients).

The Rayleigh number for convection driven by a constant temperature hot base and a cold surface in a domain of thickness D is:

$$Ra = \frac{\rho_0 g \alpha D^3}{\eta \kappa} \cdot \Delta T = \frac{\rho_0^2 C_p g \alpha D^3 \Delta T}{\eta k}$$

The Rayleigh number for convection driven by a hot base (constant basal heat flow q_b) and a colder surface is:

$$Ra = \frac{\rho_0 g \alpha D^3}{\eta \kappa} \cdot \frac{q_b D}{k}$$

The Rayleigh number for convection driven by internal heating H (production per cubic meter) is:

$$Ra = \frac{\rho_0 g \alpha D^3}{\eta \kappa} \cdot \frac{H D^2}{k}$$

The Rayleigh number for convection driven by both basal heat flow and internal heating is:

$$Ra = \frac{\rho_0 g \alpha D^3}{\eta \kappa} \cdot \frac{q_b D + H D^2}{k}$$

For convection to occur, the Rayleigh number must be larger than the so-called critical Rayleigh number, which ranges from 600 to 3000 (it depends on the boundary conditions and the geometry).

- Prandtl number Pr (X): It is named after the German physicist Ludwig Prandtl and is defined as the ratio of momentum diffusivity to thermal diffusivity. It is given as:

$$Pr = \frac{\text{momentum diffusivity}}{\text{thermal diffusivity}} = \frac{\eta/\rho}{k/(\rho C_p)} = \frac{\eta C_p}{k}$$

For Earth materials, we have $Pr \sim (10^{21} 1000)/3 \gg 1$, which means that momentum diffusivity dominates.

- Nusselt number N_u (X): the Nusselt number (Nu) is the ratio of convective to conductive heat transfer across (normal to) the boundary. The conductive component is measured under the same conditions as the heat convection but with a (hypothetically) stagnant (or motionless) fluid.

In practice the Nusselt number Nu of a layer (typically the mantle of a planet) is defined as follows:

$$\text{Nu} = \frac{q}{q_c} \quad (59)$$

where q is the heat transferred by convection while $q_c = k\Delta T/D$ is the amount of heat that would be conducted through a layer of thickness D with a temperature difference ΔT across it with k being the thermal conductivity.

For 2D Cartesian systems of size (L_x, L_y) the Nu is computed [158]

$$\text{Nu} = \frac{\frac{1}{L_x} \int_0^{L_x} k \frac{\partial T}{\partial y}(x, y = L_y) dx}{-\frac{1}{L_x} \int_0^{L_x} k T(x, y = 0) / L_y dx} = -L_y \frac{\int_0^{L_x} \frac{\partial T}{\partial y}(x, y = L_y) dx}{\int_0^{L_x} T(x, y = 0) dx}$$

i.e. it is the mean surface temperature gradient over the mean bottom temperature.

finish, not happy with definition. Look at literature

Note that in the case when no convection takes place then the measured heat flux at the top is the one obtained from a purely conductive profile which yields $\text{Nu}=1$.

Note that a relationship $\text{Ra} \propto \text{Nu}^\alpha$ exists between the Rayleigh number Ra and the Nusselt number Nu in convective systems, see [1703] and references therein.

Turning now to cylindrical geometries with inner radius R_1 and outer radius R_2 , we define $f = R_1/R_2$. A small value of f corresponds to a high degree of curvature. We assume now that $R_2 - R_1 = 1$, so that $R_2 = 1/(1-f)$ and $R_1 = f/(1-f)$. Following [909], the Nusselt number at the inner and outer boundaries are:

$$\text{Nu}_{inner} = \frac{f \ln f}{1-f} \frac{1}{2\pi} \int_0^{2\pi} \left(\frac{\partial T}{\partial r} \right)_{r=R_1} d\theta \quad (60)$$

$$\text{Nu}_{outer} = \frac{\ln f}{1-f} \frac{1}{2\pi} \int_0^{2\pi} \left(\frac{\partial T}{\partial r} \right)_{r=R_2} d\theta \quad (61)$$

Note that a conductive geotherm in such an annulus between temperatures T_1 and T_2 is given by

$$T_c(r) = \frac{\ln(r/R_2)}{\ln(R_1/R_2)} = \frac{\ln(r(1-f))}{\ln f}$$

so that

$$\frac{\partial T_c}{\partial r} = \frac{1}{r \ln f}$$

We then find:

$$\text{Nu}_{inner} = \frac{f \ln f}{1-f} \frac{1}{2\pi} \int_0^{2\pi} \left(\frac{\partial T_c}{\partial r} \right)_{r=R_1} d\theta = \frac{f \ln f}{1-f} \frac{1}{R_1 \ln f} = 1 \quad (62)$$

$$\text{Nu}_{outer} = \frac{\ln f}{1-f} \frac{1}{2\pi} \int_0^{2\pi} \left(\frac{\partial T_c}{\partial r} \right)_{r=R_2} d\theta = \frac{\ln f}{1-f} \frac{1}{R_2 \ln f} = 1 \quad (63)$$

As expected, the recovered Nusselt number at both boundaries is exactly 1 when the temperature field is given by a steady state conductive geotherm.

[derive formula for Earth size R1 and R2](#)

- Temperature (K):
- Viscosity (Pa.s):
- Density (kg/m³):
- Heat capacity C_p (J.K⁻¹): It is the measure of the heat energy required to increase the temperature of a unit quantity of a substance by unit degree. Note that the specific heat capacity c_p of a substance is the heat capacity of a sample of the substance divided by the mass of the sample, with units $J \cdot K \cdot kg^{-1}$.
- Heat conductivity, or thermal conductivity k (W.m⁻¹.K⁻¹). It is the property of a material that indicates its ability to conduct heat. It appears primarily in Fourier's Law for heat conduction. Note that it is a function of temperature, especially in mantle convection settings [1190]. See also [171] and refs therein.
- Heat diffusivity: $\kappa = k/(\rho C_p)$ (m².s⁻¹). Substances with high thermal diffusivity rapidly adjust their temperature to that of their surroundings, because they conduct heat quickly in comparison to their volumetric heat capacity or 'thermal bulk'.
- thermal expansion α (K⁻¹): it is the tendency of a matter to change in volume in response to a change in temperature. Note that it is a function of temperature, especially in mantle convection settings [1190].
- Urey Ratio: mantle heat production divided by heat loss) is a key constraint for thermal history models. Recent Urey ratio estimates are in the range of 0.210.49. [1043]

[check aspect manual The 2D cylindrical shell benchmarks by Davies et al. 5.4.12](#)

3.13 Principal stress

As seen before (see Section 3.2.1) the stress tensor is a symmetric 3×3 real matrix, and linear algebra tells us that it therefore has three mutually orthogonal unit-length eigenvectors $\vec{n}_1, \vec{n}_2, \vec{n}_3$ and three real eigenvalues $\lambda_1, \lambda_2, \lambda_3$ such that $\sigma \cdot \vec{n}_i = \lambda_i \vec{n}_i$.

As a consequence, in a coordinate system with axes $\vec{n}_1, \vec{n}_2, \vec{n}_3$, the stress tensor is a diagonal matrix, and has only the three normal components $\lambda_1, \lambda_2, \lambda_3$ i.e. the principal stresses. If the three eigenvalues are equal, the stress is an isotropic compression or tension, always perpendicular to any surface, there is no shear stress, and the tensor is a diagonal matrix in any coordinate frame.

3.13.1 In two dimensions

We are looking for the stress tensor eigenvector vector $\vec{n} = (n_x, n_y)$ associated to the eigenvalue λ such that

$$\begin{pmatrix} \sigma_{xx} & \sigma_{xy} \\ \sigma_{xy} & \sigma_{yy} \end{pmatrix} \cdot \begin{pmatrix} n_x \\ n_y \end{pmatrix} = \lambda \begin{pmatrix} n_x \\ n_y \end{pmatrix}$$

or,

$$\begin{pmatrix} \sigma_{xx} & \sigma_{xy} \\ \sigma_{xy} & \sigma_{yy} \end{pmatrix} \cdot \begin{pmatrix} n_x \\ n_y \end{pmatrix} - \begin{pmatrix} \lambda & 0 \\ 0 & \lambda \end{pmatrix} \cdot \begin{pmatrix} n_x \\ n_y \end{pmatrix} = \vec{0}$$

i.e.,

$$\begin{pmatrix} \sigma_{xx} - \lambda & \sigma_{xy} \\ \sigma_{xy} & \sigma_{yy} - \lambda \end{pmatrix} \cdot \begin{pmatrix} n_x \\ n_y \end{pmatrix} = \vec{0}$$

which yields

$$(\sigma_{xx} - \lambda)(\sigma_{yy} - \lambda) - \sigma_{xy}^2 = 0$$

or,

$$\lambda^2 - (\sigma_{xx} + \sigma_{yy})\lambda + (\sigma_{xx}\sigma_{yy} - \sigma_{xy}^2) = 0$$

The discriminant Δ is

$$\begin{aligned}\Delta &= (\sigma_{xx} + \sigma_{yy})^2 - 4(\sigma_{xx}\sigma_{yy} - \sigma_{xy}^2) \\ &= (\sigma_{xx} - \sigma_{yy})^2 + 4\sigma_{xy}^2\end{aligned}$$

The roots are given by:

$$\begin{aligned}\lambda_{\pm} &= \frac{(\sigma_{xx} + \sigma_{yy}) \pm \sqrt{(\sigma_{xx} - \sigma_{yy})^2 + 4\sigma_{xy}^2}}{2} \\ &= \frac{\sigma_{xx} + \sigma_{yy}}{2} \pm \sqrt{\left(\frac{\sigma_{xx} - \sigma_{yy}}{2}\right)^2 + \sigma_{xy}^2}\end{aligned}\tag{64}$$

The two principal stresses are then:

$$\begin{aligned}\sigma_1 &= \frac{\sigma_{xx} + \sigma_{yy}}{2} + \sqrt{\left(\frac{\sigma_{xx} - \sigma_{yy}}{2}\right)^2 + \sigma_{xy}^2} \\ \sigma_2 &= \frac{\sigma_{xx} + \sigma_{yy}}{2} - \sqrt{\left(\frac{\sigma_{xx} - \sigma_{yy}}{2}\right)^2 + \sigma_{xy}^2}\end{aligned}\tag{65}$$

with the convention $\sigma_1 > \sigma_2$. The maximum shear stress is defined as one-half the difference between the two principal stresses

$$\tau_{max} = \frac{\sigma_1 - \sigma_2}{2} = \sqrt{\left(\frac{\sigma_{xx} - \sigma_{yy}}{2}\right)^2 + \sigma_{xy}^2}$$

The eigenvector \vec{n}_1 corresponding to σ_1 is obtained by solving

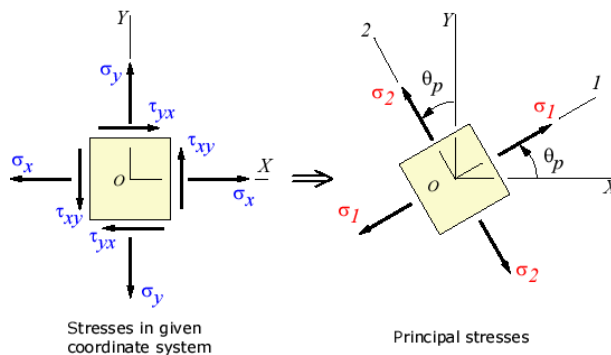
$$\boldsymbol{\sigma} \cdot \vec{n}_1 = \sigma_1 \vec{n}_1$$

and same for the other eigenvalue/vector:

$$\boldsymbol{\sigma} \cdot \vec{n}_2 = \sigma_2 \vec{n}_2$$

Each is a system of two equations with two unknowns. These are not difficult to solve, but can prove cumbersome. Note that linear algebra tells us that $\vec{n}_1 \cdot \vec{n}_2 = 0$, i.e. the eigenvectors form a basis of \mathbb{R}^2 .

This is the reason why often people go another route. One can ask the question: what is the value of the angle θ_p which, if used to perform a rotation of the axis system, yields a stress tensor that is diagonal, with the principal stresses on the diagonal?



Taken from https://www.efunda.com/formulae/solid_mechanics/mat_mechanics/plane_stress_principal.cfm

The rotation matrix is

$$\mathbf{R} = \begin{pmatrix} \cos \theta_p & -\sin \theta_p \\ \sin \theta_p & \cos \theta_p \end{pmatrix}$$

and the image of σ by means of the axis rotation is $\sigma' = \mathbf{R} \cdot \sigma \cdot \mathbf{R}^{-1}$, i.e.

$$\begin{aligned} \sigma' &= \begin{pmatrix} \cos \theta_p & -\sin \theta_p \\ \sin \theta_p & \cos \theta_p \end{pmatrix} \cdot \begin{pmatrix} \sigma_{xx} & \sigma_{xy} \\ \sigma_{xy} & \sigma_{yy} \end{pmatrix} \cdot \begin{pmatrix} \cos \theta_p & \sin \theta_p \\ -\sin \theta_p & \cos \theta_p \end{pmatrix} \\ &= \begin{pmatrix} \cos \theta_p & -\sin \theta_p \\ \sin \theta_p & \cos \theta_p \end{pmatrix} \cdot \begin{pmatrix} \sigma_{xx} \cos \theta_p - \sigma_{xy} \sin \theta_p & \sigma_{xx} \sin \theta_p + \sigma_{xy} \cos \theta_p \\ \sigma_{xy} \cos \theta_p - \sigma_{yy} \sin \theta_p & \sigma_{xy} \sin \theta_p + \sigma_{yy} \cos \theta_p \end{pmatrix} \\ &= \begin{pmatrix} \dots & \cos \theta_p (\sigma_{xx} \sin \theta_p + \sigma_{xy} \cos \theta_p) - \sin \theta_p (\sigma_{xy} \sin \theta_p + \sigma_{yy} \cos \theta_p) \\ \dots & \dots \end{pmatrix} \end{aligned}$$

In the matrix above I have only computed the off diagonal term since we are actually looking for θ_p such that $\sigma'_{xy} = 0$, or

$$\begin{aligned} \cos \theta_p (\sigma_{xx} \sin \theta_p + \sigma_{xy} \cos \theta_p) - \sin \theta_p (\sigma_{xy} \sin \theta_p + \sigma_{yy} \cos \theta_p) &= 0 \\ \sin \theta_p \cos \theta_p (\sigma_{xx} - \sigma_{yy}) + (\cos^2 \theta_p - \sin^2 \theta_p) \sigma_{xy} &= 0 \end{aligned}$$

and then

$$\frac{\sin \theta_p \cos \theta_p}{\cos^2 \theta_p - \sin^2 \theta_p} = \frac{\sigma_{xy}}{\sigma_{xx} - \sigma_{yy}}$$

The left hand term is actually a trigonometric identity¹⁰:

$$\frac{\sin \theta_p \cos \theta_p}{\cos^2 \theta_p - \sin^2 \theta_p} = \frac{1}{2} \tan 2\theta_p$$

and finally:

$$\tan 2\theta_p = \frac{2\sigma_{xy}}{\sigma_{xx} - \sigma_{yy}} \quad \text{or} \quad \theta_p = \frac{1}{2} \tan^{-1} \frac{2\sigma_{xy}}{\sigma_{xx} - \sigma_{yy}}$$

Once θ_p has been found the other direction is given by $\theta_p + \pi/2$.

Example: Let us start with

$$\sigma = \begin{pmatrix} a & 0 \\ 0 & b \end{pmatrix}$$

then $\tan 2\theta_p = 0$, and then $\theta_p = 0$. The principal directions are the horizontal and vertical directions, i.e. the Cartesian axis system, which is consistent.

3.13.2 In three dimensions

We are looking for the stress tensor eigenvector vector $\vec{n} = (n_x, n_y, n_z)$ associated to the eigenvalue λ such that

$$\begin{pmatrix} \sigma_{xx} & \sigma_{xy} & \sigma_{xz} \\ \sigma_{xy} & \sigma_{yy} & \sigma_{yz} \\ \sigma_{xz} & \sigma_{yz} & \sigma_{zz} \end{pmatrix} \cdot \begin{pmatrix} n_x \\ n_y \\ n_z \end{pmatrix} = \lambda \begin{pmatrix} n_x \\ n_y \\ n_z \end{pmatrix}$$

or,

$$\begin{aligned} \begin{pmatrix} \sigma_{xx} & \sigma_{xy} & \sigma_{xz} \\ \sigma_{xy} & \sigma_{yy} & \sigma_{yz} \\ \sigma_{xz} & \sigma_{yz} & \sigma_{zz} \end{pmatrix} \cdot \begin{pmatrix} n_x \\ n_y \\ n_z \end{pmatrix} - \begin{pmatrix} \lambda & 0 & 0 \\ 0 & \lambda & 0 \\ 0 & 0 & \lambda \end{pmatrix} \cdot \begin{pmatrix} n_x \\ n_y \\ n_z \end{pmatrix} &= \vec{0} \\ \begin{pmatrix} \sigma_{xx} - \lambda & \sigma_{xy} & \sigma_{xz} \\ \sigma_{xy} & \sigma_{yy} - \lambda & \sigma_{yz} \\ \sigma_{xz} & \sigma_{yz} & \sigma_{zz} - \lambda \end{pmatrix} \cdot \begin{pmatrix} n_x \\ n_y \\ n_z \end{pmatrix} &= \vec{0} \end{aligned}$$

¹⁰https://en.wikipedia.org/wiki/List_of_trigonometric_identities

Non-trivial solutions of this equation require

$$\begin{vmatrix} \sigma_{xx} - \lambda & \sigma_{xy} & \sigma_{xz} \\ \sigma_{yx} & \sigma_{yy} - \lambda & \sigma_{yz} \\ \sigma_{zx} & \sigma_{zy} & \sigma_{zz} - \lambda \end{vmatrix} = 0$$

Expanding the determinant results in the cubic equation

$$\lambda^3 - K_1\lambda^2 + K_2\lambda - K_3 = 0 \quad (66)$$

where:

$$\begin{aligned} K_1 &= \sigma_{xx} + \sigma_{yy} + \sigma_{zz} \\ K_2 &= \sigma_{xx}\sigma_{yy} + \sigma_{yy}\sigma_{zz} + \sigma_{zz}\sigma_{xx} - \sigma_{xy}\sigma_{yx} - \sigma_{xz}\sigma_{zx} - \sigma_{yz}\sigma_{zy} \\ K_3 &= \det(\boldsymbol{\sigma}) \end{aligned}$$

Very often we will find ourselves interested in the principal components of the deviatoric stress tensor \mathbf{s} . In this case the cubic equation becomes

$$\lambda^3 - J_2\lambda - J_3 = 0 \quad (67)$$

where J_2 and J_3 are the second and third invariants of deviatoric stress tensor \mathbf{s} .

Noting the trigonometric identity

$$\sin^3 \theta - \frac{3}{4} \sin \theta + \frac{1}{4} \sin 3\theta = 0 \quad (68)$$

and substituting $\lambda = r \sin \theta$ into (67) we have

$$\sin^3 \theta - \frac{J_2}{r^2} \sin \theta - \frac{J_3}{r^3} = 0 \quad (69)$$

Comparing (68) and (69) gives

$$r = \frac{2}{\sqrt{3}} \sqrt{J_2} \quad (70)$$

$$\sin 3\theta = -\frac{4J_3}{r^3} = -\frac{3\sqrt{3}}{2} \frac{J_3}{(J_2)^{3/2}} \quad (71)$$

The first root of (71) with θ determined for 3θ in the range $\pm\pi/2$ is a convenient alternative to the third invariant, J_3 . By noting the cyclic nature of $\sin(3\theta + 2n\pi)$ we have immediately the three (and only three) possible values of $\sin \theta$ which define the three principal stresses. The deviatoric principal stresses are given by $t = r \sin \theta$ on substitution of the three values of $\sin \theta$ in turn. Substituting for r from (70) and adding the mean hydrodynamic stress component gives the total principal stresses to be

The so-called Lode angle [1781] is then given by

$$\theta = \frac{1}{3} \sin^{-1} \left(-\frac{3\sqrt{3}}{2} \frac{J_3}{J_2^{3/2}} \right)$$

with $-\pi/6 < \theta < \pi/6$. Note that the Lode angle is one of the Lode coordinates¹¹, or HaighWestergaard coordinates.

SOMETHING missing HERE

$$\begin{Bmatrix} \sigma_1 \\ \sigma_2 \\ \sigma_3 \end{Bmatrix} = \sqrt{J_2} \begin{Bmatrix} \cos \theta + \frac{1}{\sqrt{3}} \sin \theta \\ \frac{2}{\sqrt{3}} \sin \theta \\ \frac{1}{\sqrt{3}} \sin \theta - \cos \theta \end{Bmatrix} + \frac{J_1}{3} \begin{Bmatrix} 1 \\ 1 \\ 1 \end{Bmatrix} \quad (72)$$

¹¹https://en.wikipedia.org/wiki/Lode_coordinates

with $\sigma_1 > \sigma_2 > \sigma_3$.

We will later need $\sigma_1 - \sigma_3$ and $\sigma_1 + \sigma_3$ so let's compute these quantities now:

$$\begin{aligned}\sigma_1 - \sigma_3 &= \left(\frac{1}{3}J_1 + \sqrt{J_2}(\cos\theta + \frac{1}{\sqrt{3}}\sin\theta) \right) - \left(\frac{1}{3}J_1 + \sqrt{J_2}(\frac{1}{\sqrt{3}}\sin\theta - \cos\theta) \right) \\ &= \sqrt{J_2} \left((\cos\theta + \frac{1}{\sqrt{3}}\sin\theta) - (\frac{1}{\sqrt{3}}\sin\theta - \cos\theta) \right) \\ &= 2\sqrt{J_2}\cos\theta\end{aligned}\tag{73}$$

$$\begin{aligned}\sigma_1 + \sigma_3 &= \left(\frac{1}{3}J_1 + \sqrt{J_2}(\cos\theta + \frac{1}{\sqrt{3}}\sin\theta) \right) + \left(\frac{1}{3}J_1 + \sqrt{J_2}(\frac{1}{\sqrt{3}}\sin\theta - \cos\theta) \right) \\ &= \frac{2}{3}J_1 + \sqrt{J_2}\frac{2}{\sqrt{3}}\sin\theta\end{aligned}\tag{74}$$

Note that the expression for the Lode angle is different in [1785, p101] than in [1781] or [1784, p62]

3.14 The need for numerical modelling

The governing equations we have seen in this chapter require the use of numerical solution techniques for three main reasons:

- the advection term in the energy equation couples velocity and temperature;
- the constitutive law (the relationship between stress and strain rate) often depends on velocity (or rather, strain rate), temperature, pressure, ...
- Even when the coefficients of the PDE's are linear, often their spatial variability, coupled to potentially complex domain geometries prevent arriving at the analytical solution.

3.15 Rheology in geodynamics

For now what follows only deals with viscous behavior. The reader is referred to Barnes [77] for a discussion and review of non-linear viscous rheologies.

Here is a quick recap of notations:

σ	(full) stress tensor
$\sigma_1, \sigma_2, \sigma_3$	principal stresses
τ	deviatoric stress tensor
τ_1, τ_2, τ_3	principal stresses
$\mathcal{I}_1(\mathbf{T})$	first invariant of tensor \mathbf{T}
$\mathcal{I}_2(\mathbf{T})$	first invariant of tensor \mathbf{T}
$\mathcal{I}_3(\mathbf{T})$	first invariant of tensor \mathbf{T}
$\tau_e = \sqrt{\mathcal{I}_2(\boldsymbol{\tau})}$	effective deviatoric stress
$\dot{\varepsilon}_e = \sqrt{\mathcal{I}_2(\boldsymbol{\varepsilon}^d)}$	effective deviatoric strain rate

Note that for incompressible flow, the stress tensor is given by $\sigma = -p\mathbf{1} + \tau$ so that $\mathcal{I}_1(\sigma) = -p\mathcal{I}_1(\mathbf{1}) + \mathcal{I}_1(\tau)$. Since τ is deviatoric, its first invariant is zero. We then have $\mathcal{I}_1(\sigma) = -pn_D$ where n_D is the number of dimensions.

3.15.1 Linear viscous aka Newtonian

Simply put, a Newtonian fluid is a fluid in which the viscous stresses at every point are linearly proportional to the local strain rate. Mathematically speaking, this means that the fourth-order tensor \mathbf{C} relating the viscous stress tensor to the strain rate tensor does not depend on the stress state and velocity of the flow.

$$\tau = \mathbf{C} : \boldsymbol{\varepsilon}$$

One very often make the assumption that the fluid is isotropic, i.e. its mechanical properties are the same along any direction. As a consequence the fourth order viscosity tensor \mathbf{C} is symmetric and will have only two independent real parameters: a bulk viscosity coefficient, that defines the resistance of the medium to gradual uniform compression; and a dynamic viscosity coefficient η that expresses its resistance to gradual shearing, (we here neglect the so-called rotational viscosity coefficient which results from a coupling between the fluid flow and the rotation of the individual particles).

Rather logically we denote by non-Newtonian fluids with are not Newtonian, i.e. their viscosity (tensor) depends on stress. Such fluids are part of our daily life, e.g. honey, toothpaste, paint, blood, and shampoo. They are also sometimes denoted as Generalized Newtonian Fluid .

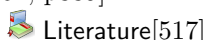
3.15.2 Power-law model

One of the simplest non-Newtonian viscosity model is the power-law model:

$$\eta = K \dot{\varepsilon}_e^{(n-1)/2} \quad (75)$$

where n and K are parameters. n is called the power-law index.

Note that a Newtonian viscosity is recovered when $n = 1$. Also n and K may depend on temperature [1361, p339].



Literature[517]

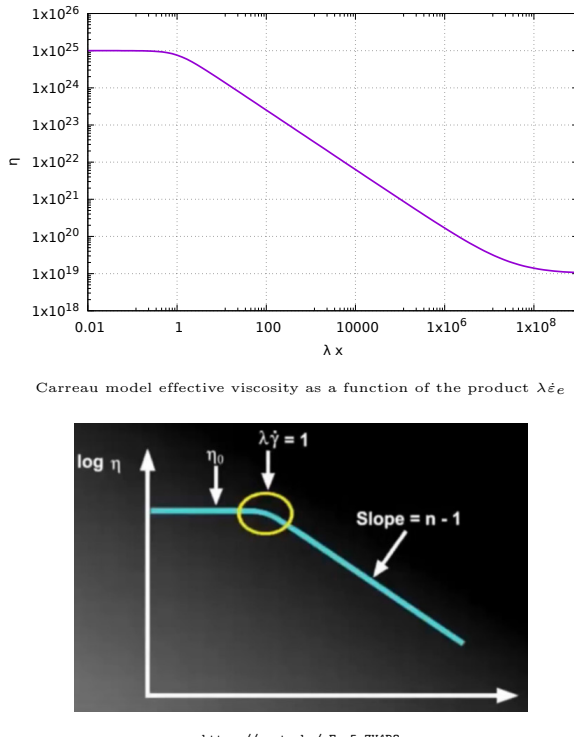
3.15.3 Carreau model

Note that this model is sometimes called Bird-Carreau in the literature. As explained in [1361], the power-law model poses no restriction on how small or large the viscosity may become, which may prove problematic once implemented as it can lead to runaway effects (strain rate becomes large \rightarrow viscosity becomes smaller \rightarrow strain rate becomes larger, etc ...). This problem is alleviated in the so-called Carreau¹² model [1787]. The viscosity is then given by

$$\eta = \eta_\infty + (\eta_0 - \eta_\infty) (1 + (\lambda\dot{\varepsilon}_e)^2)^{(n-1)/2} \quad (76)$$

where η_0 , η_∞ , λ and $n \in [0, 1]$ are material parameters. λ is called the relaxation time: it is the inverse of the shear rate at which the fluid changes from Newtonian to power-law behavior.

At low strain rate a Carreau fluid behaves as a Newtonian fluid with viscosity η_0 . At intermediate strain rates $\dot{\varepsilon}_e\lambda \sim 1$ a Carreau fluid behaves as a Power-law fluid. At high strain rate, a Carreau fluid behaves as a Newtonian fluid again with viscosity η_∞ .



Note that the (Bird)-Carreau-Yasuda model [1285] is very similar to the standard (Bird)-Carreau:

$$\eta = \eta_\infty + (\eta_0 - \eta_\infty) (1 + (\lambda\dot{\varepsilon}_e)^a)^{(n-1)/a} \quad (77)$$

3.15.4 Bingham model

Bingham fluids can sustain an applied stress without any motion occurring. Only when the applied stress exceeds a yield stress τ_0 then the fluid flows. This translates as follows [1361]:

$$s = \left(\frac{\tau_0}{\dot{\varepsilon}} + 2\eta_0 \right) \dot{\varepsilon} \quad \text{if } s_{II} > \tau_0 \quad (78)$$

$$s = 0 \quad \text{if } s_{II} \leq \tau_0 \quad (79)$$

¹²https://en.wikipedia.org/wiki/Carreau_fluid

When flow occurs, the effective viscosity is then given by:

$$\eta_{eff} = \frac{\tau_0}{\dot{\varepsilon}_e} + 2\eta_0$$

and when the strain rate is large we recover a Newtonian behaviour. Typical Bingham fluids are mud, slurry, toothpaste.

When using a velocity-based FEM code, the implementation of this rheological behaviour is complicated by the no-flow condition under a given stress. However, our codes require a relationship between stress and strain rate in the form of an effective viscosity which cannot be zero. This difficulty can be circumvented by implementing Bingham fluids as follows [1361]:

$$s = \left(\frac{\tau_0(1 - \eta/\eta_r)}{\dot{\varepsilon}_e} + 2\eta_0 \right) \dot{\varepsilon} \quad \text{if } s_{II} > \tau_0 \quad (80)$$

$$s = 2\eta_r \dot{\varepsilon} \quad \text{if } s_{II} \leq \tau_0 \quad (81)$$

where η_r is a pre-yield viscosity and $\eta/\eta_r \ll 1$ (typically 1% or less). This is a form of regularisation, and we will see a similar one in the next section.

 Literature: [156, 1188, 1112, 1495, 148, 73]

3.15.5 Herschel-Bulkley visco-plastic model

The Herschel-Bulkley model is effectively a combination of the power-law model and a simple plastic model:

$$s = 2 \left(K \dot{\varepsilon}_e^{n-1} + \frac{\tau_0}{\dot{\varepsilon}} \right) \dot{\varepsilon} \quad \text{if } \tau_e > \tau_0 \quad (82)$$

$$\dot{\varepsilon} = \mathbf{0} \quad \text{if } \tau_e \leq \tau_0 \quad (83)$$

in which τ_0 is the yield stress, K the consistency, and n is the flow index [446]. The flow index measures the degree to which the fluid is shear-thinning ($n < 1$) or shear-thickening ($n > 1$). If $n = 1$ and $\tau_0 = 0$ the model reduces to the Newtonian model.

The term between parenthesis above is the nonlinear effective viscosity. Concretely, the implementation goes as follows¹³:

$$\eta_{eff} = \begin{cases} \eta_0 & \dot{\varepsilon}_e \leq \dot{\varepsilon}_0 \\ K \dot{\varepsilon}_e^{n-1} + \frac{\tau_0}{\dot{\varepsilon}_e} & \dot{\varepsilon}_e \geq \dot{\varepsilon}_0 \end{cases}$$

The limiting viscosity η_0 is chosen such that $\eta_0 = K \dot{\varepsilon}_0^{n-1} + \frac{\tau_0}{\dot{\varepsilon}_0}$

A large limiting viscosity means that the fluid will only flow in response to a large applied force. This feature captures the Bingham-type behaviour of the fluid. Note that when strain rates are large, the power-law behavior dominates.

As we have seen for Bingham fluids, the equations above are not easily amenable to implementation so that one usually resorts to regularisation, which is a modification of the equations by introducing a new material parameter which controls the exponential growth of stress. This way the equation is valid for both yielded and unyielded areas [156, 1291, 1787]:

$$\eta_{eff} = K \dot{\varepsilon}_e^{n-1} + \frac{\tau_0}{\dot{\varepsilon}_e} [1 - \exp(-m\dot{\varepsilon}_e)] \quad (84)$$

When the strain rate becomes (very) small a Taylor expansion of the regularisation term yields $1 - \exp(-m\dot{\varepsilon}) \sim m\dot{\varepsilon}$ so that $\eta_{eff} \rightarrow m\tau_0$.

Channel flow of wikipedia with analytical solution!

 Literature: [1146]. Check dam break problem of [27, 374, 72, 1517, 1187].

(MSc Thesis): redo the sinking sphere in Bingham or herschel-Bulkley fluid experiment [446].

¹³https://en.wikipedia.org/wiki/Herschel-Bulkley_fluid

3.15.6 The Casson model

It is described by [77]

$$\sqrt{\sigma} = \sqrt{\sigma_y} + \sqrt{\eta_p \dot{\varepsilon}_e}$$

or, when squaring it:

$$\sigma = \sigma_y + \eta_p \dot{\varepsilon}_e + 2\sqrt{\sigma_y \eta_p \dot{\varepsilon}_e}$$

This model has been found to accurately describe the behaviour of synthetic based muds [5].

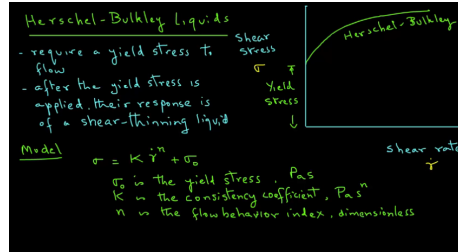
3.15.7 One model to rule them all?

Let us consider the base equation

$$\frac{\eta - \eta_\infty}{\eta_0 - \eta_\infty} = [1 + (K \dot{\varepsilon}_e)^a]^{-(1-n)/a}$$

This equation is purposefully generic and specific parameter combination choices allow to recover any of the above models (and more) [1285].

Similar conclusions are reached in the following video:



3.15.8 Dislocation and Diffusion creep

The standard dislocation creep effective viscosity is given by:

$$\eta_{eff}^{ds} = \frac{1}{2} f A^{-1/n} \dot{\varepsilon}_e^{(1-n)/n} \exp\left(\frac{Q + pV}{nRT}\right)$$

where A is the pre-exponential scaling factor, f is a scaling factor representing viscous weakening or strengthening, Q is the activation energy, V is the activation volume, T is the absolute temperature, n is the power-law exponent, R is the universal gas constant.

The coefficients A, n, Q, V are material parameters and are obtained in the laboratory by means of high pressure/temperature experiments[935]. Unfortunately these experiments cannot be run at Earth-like strain rate values ($\sim 10^{-15} \text{s}^{-1}$) so that extrapolations must be carried out over several orders of magnitude to arrive at values we can use in our numerical models. The 1/2 factor arises from the relationship between deviatoric stress and strain rate which involves a factor 2.

The factor f is in fact a tuning parameter used to explore end members (e.g. 'weak crust' vs 'strong crust'), see discussion in the supplementary material in [865]. This approach has been extensively used by the SOPALE users community, see for instance [1668, 1669, 1670, 737].

Furthermore, we know that several other factors will strongly affect the rheology:

- water content, or as often mentioned: 'dry' vs 'wet'. Following [935], dry means water-free and wet means water-saturated conditions.

Mechanism	Dry	Wet
<i>Dislocation creep</i>		
A (s^{-1})	3.5×10^{22}	2.0×10^{18}
n	3.5	3.0
m	0	0
E^* (kJ mol^{-1})	540	430
V^* ($\text{cm}^3 \text{mol}^{-1}$)	15 to 25†	10 to 20†
<i>Diffusion creep</i>		
A (s^{-1})	8.7×10^{15}	5.3×10^{15}
n	1.0	1.0
m	2.5‡	2.5‡
E^* (kJ mol^{-1})	300	240
V^* ($\text{cm}^3 \text{mol}^{-1}$)	6§	5§

†The activation volume for dislocation creep is not well constrained. Values from $13 \text{ cm}^3 \text{mol}^{-1}$ at wet conditions to $27 \text{ cm}^3 \text{mol}^{-1}$ at nearly dry conditions have been reported [33]. Considering this uncertainty, we used a range of activation volumes, 15 to 25 $\text{cm}^3 \text{mol}^{-1}$, for dry olivine and 10 to 20 $\text{cm}^3 \text{mol}^{-1}$ for wet olivine. ‡The grain-size exponent is fixed at 2 for dry olivine and 3 for wet olivine [16]. However, during extrapolation to a large grain size, the grain-size exponent may change from 2 to 3 or from 3 to 2 [16]. Taking this uncertainty into account, we chose a grain-size exponent of 2.5, and the preexponential factors were modified accordingly. §The activation volume for diffusion is determined as $6 \text{ cm}^3 \text{mol}^{-1}$ at dry conditions [26]. No data are available for the activation volume for diffusion at wet conditions; we assumed that this value is $\sim 80\%$ of the activation volume at dry conditions.

Taken from Karato and Wu [935].

 Literature: [1340] and refs therein for the effects of water migration on models of subduction dynamics.

- composition: while one typically assigns olivine properties to the mantle in models, the mineral olivine¹⁴ is actually a magnesium iron silicate with the formula $(\text{Mg}^{2+}, \text{Fe}^{2+})_2\text{SiO}_4$. and the ratio of magnesium to iron varies between the two endmembers of the solid solution series: forsterite (Mg-endmember: Mg_2SiO_4) and fayalite (Fe-endmember: Fe_2SiO_4).
- grain size: this only affects diffusion creep mechanisms [935]. Grain size varies over several orders of magnitude and also evolves over time and its evolution is affected by the ambient deformation and the deformation history. Dannberg et al [427] then used a diffusion creep effective viscosity given by:

$$\eta_{eff}^{df} = \frac{1}{2} A_{df}^{-1} d^m \exp\left(\frac{Q_{df} + pV_{df}}{RT}\right)$$

where d is the (variable) grain size and m the grain size exponent. Grain growth/evolution is usually approximated using semi-empirical expressions [427, section 2.2]. Smaller grains facilitating faster creep.

The evolution of grain size in the lower mantle is discussed in detail by Solomatov [1464, 1467, 1469] and Cerpa et al [320].

 Literature: [1237]

- anisotropy, LPO:
- phase changes:

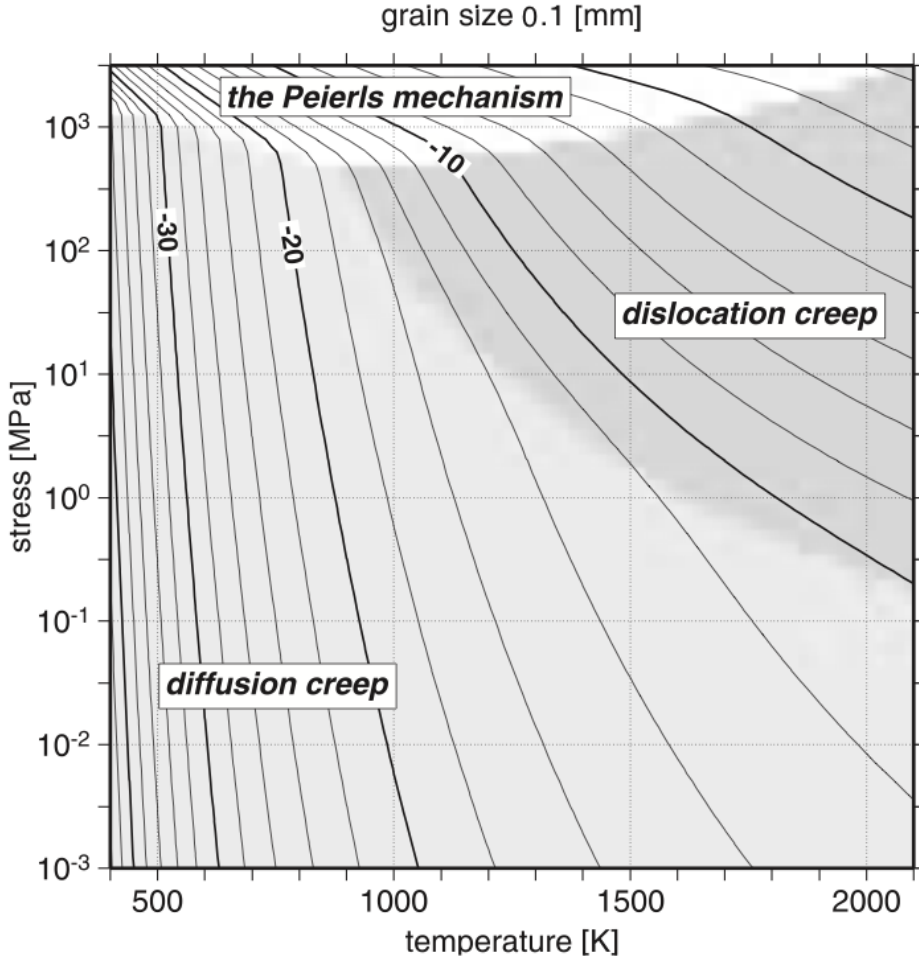
Remark. It is not uncommon to find in the literature effective viscosity formulations written as a function of B with $B = A^{-1/n}$ [1668, 1669, 1670]. Also, this B coefficient often contains the conversion factor of the next remark.

Remark. uniaxial stuff An additional coefficient is added to the effective viscosity formula(s ??) [737, 739].

$$3^{-(1+n)/2n} 2^{(1-n)/n}$$

[1351]

¹⁴<https://en.wikipedia.org/wiki/Olivine>



Deformation mechanism map calculated for grain size $a = 0.1\text{mm}$. The lightly shaded area indicates that deformation mainly occurs by diffusion creep. The densely shaded area indicates that deformation mainly occurs by power-law creep. The white region indicates that deformation mainly occurs by the Peierls mechanism. The solid curves are lines of constant strain rate. The numbers attached to each contour indicate the logarithm of the strain rate in the unit of s^{-1} [929].

A closer look at the diffusion creep of Karato & Wu (1993) In the article, the following equation is used:

$$\dot{\varepsilon} = A \left(\frac{\tau}{\mu} \right) \left(\frac{b}{d} \right)^m \exp \left(-\frac{Q + pV}{RT} \right)$$

where μ is the shear modulus ($\sim 80\text{GPa}$), b is the length of the Burgers vector ($\sim 0.5\text{nm}$) and d is the grain size. One can express the above equation in terms of second invariants (see Section 8.11.1):

$$\dot{\varepsilon}_e = A \left(\frac{\tau_e}{\mu} \right) \left(\frac{b}{d} \right)^m \exp \left(-\frac{Q + pV}{RT} \right)$$

and assuming a Newtonian linearisation/relation between deviatoric stress and strain rate $\tau_e = 2\eta_{df}\dot{\varepsilon}_e$, one arrive at

$$\eta_{df} = \frac{1}{2} \left(\frac{A}{\mu} \right)^{-1} \left(\frac{b}{d} \right)^{-m} \exp \left(\frac{Q + pV}{RT} \right)$$

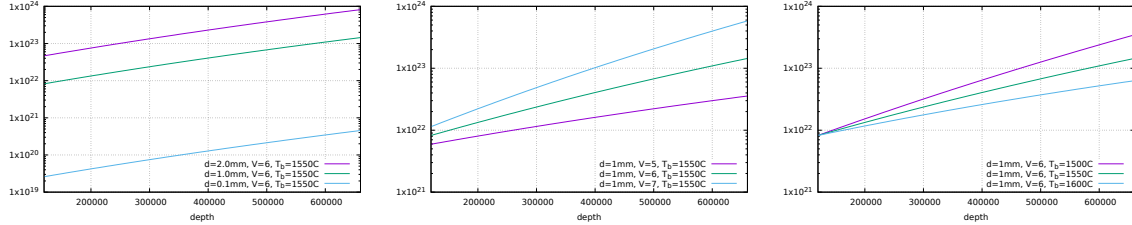
or,

$$\eta_{df} = \frac{1}{2} \left[\frac{A}{\mu} \left(\frac{b}{d} \right)^m \right]^{-1} \exp \left(\frac{Q + pV}{RT} \right)$$

The effective diffusion creep viscosity is independent of strain-rate so that one could substitute the total pressure for lithostatic pressure in the equation, assume a geotherm and easily compute the predicted viscosity as a function of grain size d .

Let us assume that the 1D profile starts from the base of the lithosphere (say 120km depth) and ends at the 660 boundary. Assume the temperature to increase linearly from 1300°C to T_{bottom} . At the bottom of the lithosphere, the lithostatic pressure is of the order of $\rho \cdot g \cdot L \simeq 3000 \cdot 10 \cdot 120e3 \simeq 4\text{GPa}$. At the bottom of the domain, the pressure has increased by $3300 \cdot 10 \cdot 630e3 \simeq 21\text{GPa}$.

The viscosity profile is plotted hereunder for three different grain sizes, bottom temperature and activation volumes ($4,5,6 \text{ cm}^3/\text{mol}$).



Although this exercise only provides us with first-order results, we can conclude that one can essentially change the diffusion creep effective viscosity by up to 2 orders of magnitude simply by choosing key parameters within acceptable ranges.

3.15.9 Combining diffusion and dislocation creep

It is rather common in the computational geodynamics to combine both viscosities into one so-called 'effective viscous viscosity' (as opposed to the so-called 'effective plastic viscosity'). The harmonic average is then used:

$$\eta_{eff} = \frac{\eta_{df}\eta_{ds}}{\eta_{df} + \eta_{ds}} = \left(\frac{1}{\eta_{df}} + \frac{1}{\eta_{ds}} \right)^{-1} \quad (85)$$

See for instance [966].

However, although this formula seems simple enough, it hides an important fact: strain rates are supposed to be additive, i.e. the total strain rate $\dot{\varepsilon}_T$ of the deformation is the sum of the dislocation strain rate $\dot{\varepsilon}_{ds}$ and the diffusion strain rate $\dot{\varepsilon}_{df}$:

$$\dot{\varepsilon}_T = \dot{\varepsilon}_{df} + \dot{\varepsilon}_{ds}$$

and so are the effective strain rates (the underscore e has been dropped for convenience - see section 8.11.1 for definitions):

$$\dot{\varepsilon}_T = \dot{\varepsilon}_{df} + \dot{\varepsilon}_{ds}$$

i.e.,

$$\dot{\varepsilon}_T = A_{df}\tau \exp\left(-\frac{Q_{df} + pV_{df}}{RT}\right) + A_{ds}\tau^n \exp\left(-\frac{Q_{ds} + pV_{ds}}{RT}\right)$$

where τ is the effective shear stress.

We know all the coefficients in this equation with the exception of the scalar τ (the total strain rate is obtained from the previous nonlinear iteration velocity or previous time-step velocity) so that it can be cast under the form $f(\tau) = 0$

$$f(\tau) = \dot{\varepsilon}_T - A_{df}\tau \exp\left(-\frac{Q_{df} + pV_{df}}{RT}\right) - A_{ds}\tau^n \exp\left(-\frac{Q_{ds} + pV_{ds}}{RT}\right)$$

A Newton method can be used where and the iterations will be of the form:

$$\tau_{n+1} = \tau_n - \frac{f(\tau_n)}{f'(\tau_n)}$$

where the derivative of the function f with respect to τ reads:

$$f'(\tau) = \frac{\partial f}{\partial \tau} = -A_{df} \exp\left(-\frac{Q_{df} + pV_{df}}{RT}\right) - A_{ds}n\tau^{n-1} \exp\left(-\frac{Q_{ds} + pV_{ds}}{RT}\right)$$

Also, from the additivity of strain rates follows the harmonic averaging of viscosities:

$$\dot{\varepsilon}_T = \dot{\varepsilon}_{df} + \dot{\varepsilon}_{ds} \quad \Rightarrow \quad \frac{\tau}{2\eta_{eff}} = \frac{\tau}{2\eta_{df}} + \frac{\tau}{2\eta_{ds}} \quad \Rightarrow \quad \frac{1}{\eta_{eff}} = \frac{1}{\eta_{df}} + \frac{1}{\eta_{ds}}$$

so that the algorithm simply writes:

1. compute τ iteratively
2. compute $\dot{\varepsilon}_{df}$, $\dot{\varepsilon}_{ds}$
3. compute $\eta_{ds} = \tau/(2\dot{\varepsilon}_{ds})$, $\eta_{df} = \tau/(2\dot{\varepsilon}_{df})$
4. compute η_{eff}

Note that one can also directly compute η_{eff} as $\eta_{eff} = \frac{\tau}{2\dot{\varepsilon}_T}$ since

$$\eta_{eff} = \frac{\tau}{2\dot{\varepsilon}_T} = \frac{\tau}{2\dot{\varepsilon}_{ds} + 2\dot{\varepsilon}_{df}} = \frac{1}{2\dot{\varepsilon}_{ds}/\tau + 2\dot{\varepsilon}_{df}/\tau} = \frac{1}{1/\eta_{ds} + 1/\eta_{df}}$$

In the case where many deformation mechanisms are present, the total strain rate is seen as the sum of the strain rates associated to each mechanism:

$$\dot{\varepsilon}_T = \dot{\varepsilon}_1 + \dot{\varepsilon}_2 + \dot{\varepsilon}_3 + \dots$$

and then

$$\dot{\varepsilon}_T = \dot{\varepsilon}_1 + \dot{\varepsilon}_2 + \dot{\varepsilon}_3 + \dots \quad \Rightarrow \quad \frac{\tau}{2\eta_{eff}} = \frac{\tau}{2\eta_1} + \frac{\tau}{2\eta_2} + \frac{\tau}{2\eta_3} + \dots \quad \Rightarrow \quad \frac{1}{\eta_{eff}} = \frac{1}{\eta_1} + \frac{1}{\eta_2} + \frac{1}{\eta_3} + \dots$$

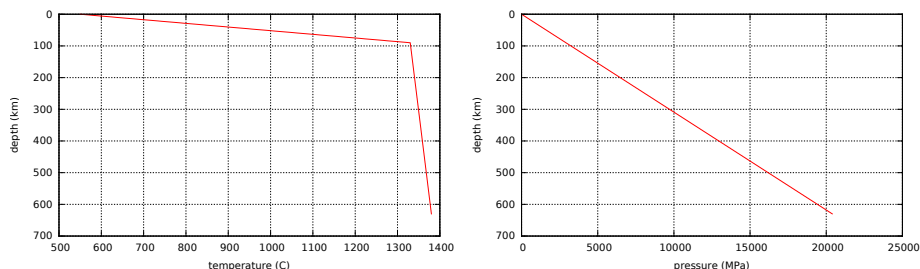
Rather importantly, as we will see hereafter, the following variant is implemented in some codes (e.g. DOUAR, FANTOM, SOPALE) so as to bypass the costly Newton iterations:

1. compute η_{ds} and η_{df} with the *same* strainrate, pressure and temperature values
2. average them by means of an harmonic average

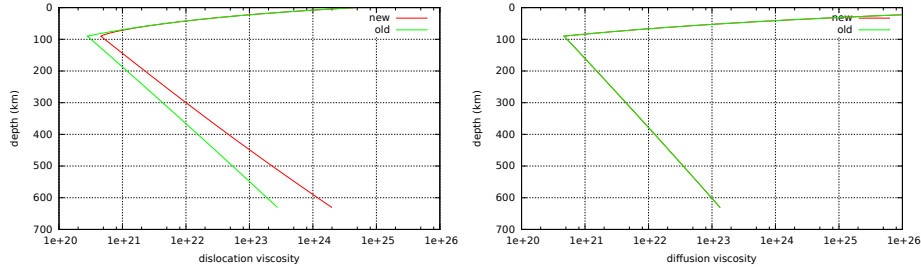
In this case, we have

$$\dot{\varepsilon}_T = A_{df}\tau_{df} \exp\left(-\frac{Q_{df} + pV_{df}}{RT}\right) \quad \dot{\varepsilon}_T = A_{ds}\tau_{ds}^n \exp\left(-\frac{Q_{ds} + pV_{ds}}{RT}\right)$$

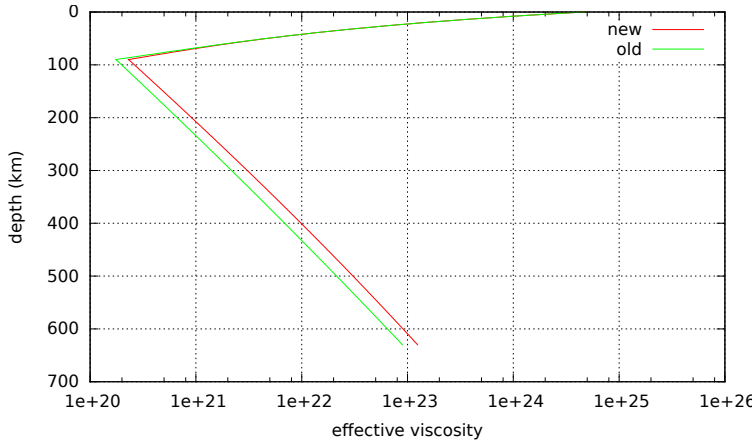
A concrete example Let us consider a vertical section of upper mantle, from 660km depth to 30km depth. The lithosphere is assumed to be 90km thick. The temperature at the moho (the top of the domain) is set to 550C, 1330C at the LMB and 1380C at the bottom. A constant strainrate $\dot{\varepsilon}$ is assumed. The density is set to a constant 3300kg/m³ and we assume a lithostatic pressure. The temperature and pressure fields are shown hereunder:



In what follows, the values obtained with Newton iterations are coined 'new' and those obtained without are coined 'old'. The diffusion and dislocation creep viscosities can be computed for both old and new algorithms and are shown hereunder (the diffusion creep viscosity is independent of strain rate so is the same for both):



Using the algorithm highlighted hereabove we can compute the composite effective viscosity and compare it with the 'standard' effective viscosity:



look at folder, codes, clean up, change labels new and old

3.15.10 The von Mises failure criterion

The von Mises yield criterion suggests that the yielding of materials begins when the second deviatoric stress invariant $\mathcal{I}_2(\boldsymbol{\tau})$ reaches a critical value. For this reason, it is sometimes called the J_2 -plasticity or J_2 flow theory¹⁵. It is part of a plasticity theory that applies best to ductile materials, such as metals.

In material science and engineering the von Mises yield criterion can be also formulated in terms of the von Mises stress or equivalent tensile stress, σ_v , a scalar stress value that can be computed from the stress tensor. In this case, a material is said to start yielding when its von Mises stress reaches a critical value known as the yield strength, σ_Y . The von Mises stress is used to predict yielding of materials under any loading condition from results of simple uniaxial tensile tests. The von Mises stress satisfies the property that two stress states with equal distortion energy have equal von Mises stress.

Because the von Mises yield criterion is independent of the first stress invariant, $\mathcal{I}_1(\boldsymbol{\sigma})$, it is applicable for the analysis of plastic deformation for ductile materials such as metals, as the onset of yield for these materials does not depend on the hydrostatic component of the stress tensor.

Although formulated by Maxwell in 1865, it is generally attributed to von Mises [1648]. Huber (1904), in a paper in Polish, anticipated to some extent this criterion. Heinrich Hencky formulated the same criterion as von Mises independently in 1924 [810, 1523]. This criterion is also referred to as the Maxwell-Huber-Hencky-von Mises theory.

The von Mises yield criterion (also known as Prandtl-Reuss yield criterion) is expressed in the principal stresses as

$$\sigma_v = \sqrt{3J'_2} = \sigma_Y \quad \text{or,} \quad (\sigma_1 - \sigma_2)^2 + (\sigma_2 - \sigma_3)^2 + (\sigma_3 - \sigma_1)^2 = 2\sigma_y^2$$

where σ_Y is the yield stress in uniaxial tension.

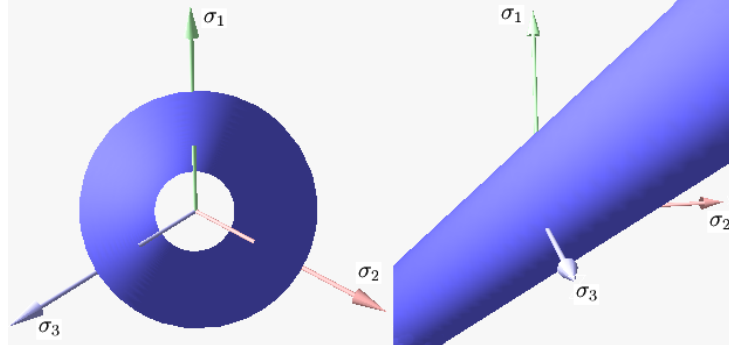
The von Mises yield criterion writes:

¹⁵ J_2 is the common notation for $\mathcal{I}_2(\boldsymbol{\tau})$

$$F^{VM} = \sqrt{J_2} - \frac{2c}{\sqrt{3}} \quad (86)$$

which is purposely the Drucker-Prager criterion with $\phi = 0$.

The following figure shows the von Mises yield surface in the three-dimensional space of principal stresses.



It is a circular cylinder of infinite length with its axis inclined at equal angles to the three principal stresses.

3.15.11 The Tresca failure criterion

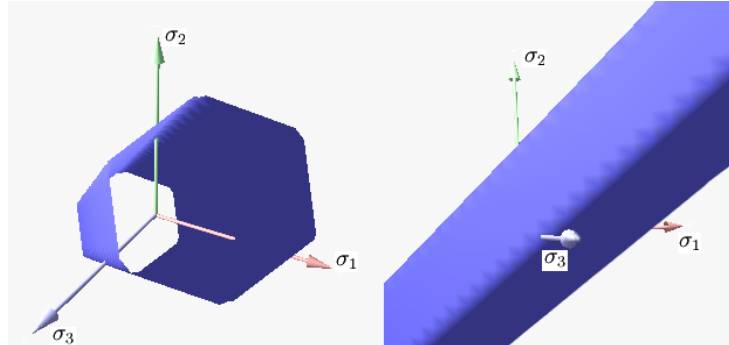
The Tresca or maximum shear stress yield criterion is taken to be the work of Henri Tresca. It is also referred as the Tresca-Guest (TG) criterion. The functional form of this yield criterion is

$$f(\sigma_1, \sigma_2, \sigma_3) = 0$$

In terms of the principal stresses the Tresca criterion is expressed as

$$\max(|\sigma_1 - \sigma_2|, |\sigma_2 - \sigma_3|, |\sigma_3 - \sigma_1|) = \sigma_0$$

The following figure shows the Tresca-Guest yield surface in the three-dimensional space of principal stresses.



It is a prism of six sides and having infinite length. This means that the material remains viscous when all three principal stresses are roughly equivalent (a hydrostatic pressure), no matter how much it is compressed or stretched. However, when one of principal stresses becomes smaller (or larger) than the others the material is subject to shearing. In such situations, if the shear stress reaches the yield limit then the material enters the plastic domain.

Remark. *The yield function is non-continuous, making its numerical implementation more difficult (directional derivatives are needed)*

two-dimensional space Using the values of the principal stresses in a two dimensional space, the criterion becomes

$$|\sigma_1 - \sigma_2| = \sqrt{J'_2} = \sigma_0$$

which is equivalent to the von Mises criterion.

three-dimensional space We have already established that

$$\sigma_1 - \sigma_3 = 2\sqrt{J_2} \cos \theta$$

with $\sigma_1 > \sigma_3$, so that the failure criterion is given by

$$F^{TR,3D} = 2\sqrt{J_2} \cos \theta - c$$

Obviously, the Tresca criterion corresponds to the case where the friction angle $\phi = 0$.

3.15.12 The Drucker-Prager failure criterion

The von Mises yield criterion is not suitable for modelling the yielding of frictional material as it does not include the effect of mean stress as observed in experiments. To overcome this limitation, Drucker and Prager [479] proposed a revised function for frictional materials.

The Drucker-Prager yield criterion has the function form

$$F(\boldsymbol{\sigma}) = F\mathcal{I}_1(\boldsymbol{\sigma}), \mathcal{I}_2(\boldsymbol{\sigma})) = 0 \quad (87)$$

This criterion is most often used for concrete where both normal and shear stresses can determine failure. The Drucker-Prager yield criterion may be expressed as

$$F^{DP} = \tau_e - (\alpha\mathcal{I}_1(\boldsymbol{\sigma}) + k) \quad (88)$$

Since the Drucker-Prager yield surface is a smooth version of the Mohr-Coulomb yield surface, it is often expressed in terms of the cohesion c and the angle of internal friction ϕ that are used to describe the Mohr-Coulomb yield surface. One then wishes to relate α and k to c and ϕ : $\alpha = fct(\phi)$ and $k = fct(c, \phi)$.

two-dimensional space By choosing $k = c \cos \phi$ and $\alpha = \frac{1}{2} \sin \phi$ and seeing that that $p = \frac{1}{2}\mathcal{I}_1(\boldsymbol{\sigma})$, we can make the Drucker-Prager yield criterion coincide with the Mohr-Coulomb yield criterion so that

$$F^{DP,2D} = \tau_e - (p \sin \phi + c \cos \phi)$$

three-dimensional space Let us first assume that the Drucker-Prager yield surface circumscribes the Mohr-Coulomb yield surface such that the two surfaces coincide at $\theta = \frac{\pi}{3}$. The expression for the Mohr-Coulomb yield criterion is

$$F^{MC,3D} = -\frac{1}{3}J_1 \sin \phi + \sqrt{J_2}(\cos \theta - \frac{1}{\sqrt{3}} \sin \theta \sin \phi) - c \cos \phi$$

Taking $\theta = \pi/6$ yields:

$$\begin{aligned} F^{MC,3D} &= -\frac{1}{3}J_1 \sin \phi + \sqrt{J_2}(\frac{\sqrt{3}}{2} - \frac{1}{\sqrt{3}} \frac{1}{2} \sin \phi) - c \cos \phi \\ &= -\frac{1}{3}J_1 \sin \phi + \frac{1}{2\sqrt{3}} \sqrt{J_2}(3 - \sin \phi) - c \cos \phi \\ &= -\frac{1}{3}J_1 \sin \phi + \frac{1}{6} \sqrt{J_2} \sqrt{3}(3 - \sin \phi) - c \cos \phi \\ &= \frac{\sqrt{3}(3 - \sin \phi)}{6} \left(-\frac{2 \sin \phi}{\sqrt{3}(3 - \sin \phi)} J_1 + \sqrt{J_2} - \frac{6c \cos \phi}{\sqrt{3}(3 - \sin \phi)} \right) \end{aligned}$$

The constant in front of the brackets (which always strictly positive) does not matter since we look at the sign of F . Comparing with

$$F^{DP} = \sqrt{J_2} - (\alpha J_1 + k)$$

we naturally set

$$\alpha = \frac{2 \sin \phi}{\sqrt{3}(3 - \sin \phi)} \quad k = \frac{6c \cos \phi}{\sqrt{3}(3 - \sin \phi)}$$

and since $p = \frac{1}{3}\mathcal{I}_1(\boldsymbol{\sigma})$:

$$F^{DP,3D} = \tau_e - \left[\frac{6 \sin \phi}{\sqrt{3}(3 - \sin \phi)} p + \frac{6c \cos \phi}{\sqrt{3}(3 - \sin \phi)} \right]$$

which is the formula used in [697].

TO VERIFY If the Drucker-Prager surface inscribes the Mohr-Coulomb surface, then matching the two surfaces at $\theta = 0$ gives

$$k = \frac{6 c \cos \phi}{\sqrt{3}(3 - \sin \phi)} ; \quad \alpha = \frac{2 \sin \phi}{\sqrt{3}(3 - \sin \phi)}$$

In the principal stress space, the Drucker-Prager surface has the form of a circular cone, whilst the von Mises yield surface is an infinitely long cylinder.

3.15.13 The Mohr-Coulomb failure criterion

Mohr-Coulomb theory is a model describing the response of a material such as rubble piles or concrete to shear stress as well as normal stress. Most of the classical engineering materials somehow follow this rule in at least a portion of their shear failure envelope. In geology it is used to define shear strength of soils at different effective stresses.

In structural engineering it is used to determine failure load as well as the angle of fracture of a displacement fracture in concrete and similar materials. Coulomb's friction hypothesis is used to determine the combination of shear and normal stress that will cause a fracture of the material. Mohr's circle is used to determine which principal stresses that will produce this combination of shear and normal stress, and the angle of the plane in which this will occur. According to the principle of normality the stress introduced at failure will be perpendicular to the line describing the fracture condition.

The Mohr-Coulomb failure criterion represents the linear envelope that is obtained from a plot of the shear strength of a material versus the applied normal stress. This relation is expressed as

$$\tau = \sigma \tan(\phi) + c$$

where τ is the shear strength, σ is the normal stress, c is the intercept of the failure envelope with the τ axis, and ϕ is the slope of the failure envelope. The quantity c is often called the cohesion and the angle ϕ is called the angle of internal friction. Compression is assumed to be positive in the following discussion. If compression is assumed to be negative then σ should be replaced with $-\sigma$.

From Mohr's circle we have

$$\sigma = \sigma_m - \tau_m \sin \phi \quad \tau = \tau_m \cos \phi$$

where

$$\tau_m = \frac{\sigma_1 - \sigma_3}{2} ; \quad \sigma_m = \frac{\sigma_1 + \sigma_3}{2}$$

and σ_1 is the maximum principal stress and σ_3 is the minimum principal stress. Therefore the Mohr-Coulomb criterion may also be expressed as

$$\tau_m = \sigma_m \sin \phi + c \cos \phi$$

The Mohr-Coulomb failure (yield) surface is often expressed in Haigh-Westergaard coordinates. For example, the last equation rewrites

$$\frac{\sigma_1 - \sigma_3}{2} = \frac{\sigma_1 + \sigma_3}{2} \sin \phi + c \cos \phi$$

two-dimensional space The principal stress values are given by

$$\sigma_{1,2} = \frac{\sigma_{xx} + \sigma_{yy}}{2} \pm \sqrt{\frac{1}{4}(\sigma_{xx} - \sigma_{yy})^2 + \sigma_{xy}^2} = \frac{J_1}{2} \pm \sqrt{J_2'}$$

The Mohr-Coulomb criterion simply writes:

$$F^{MC,2D} = -\frac{J_1}{2} \sin \phi + \sqrt{J_2} - c \cos \phi$$

three-dimensional space We have already established that

$$\sigma_1 - \sigma_3 = 2\sqrt{J_2} \cos \theta \quad \sigma_1 + \sigma_3 = \frac{2}{3}J_1 + \sqrt{J_2} \frac{2}{\sqrt{3}} \sin \theta$$

$$\begin{aligned} \frac{\sigma_1 - \sigma_3}{2} &= \frac{\sigma_1 + \sigma_3}{2} \sin \phi + c \cos \phi \\ \Rightarrow \sqrt{J_2} \cos \theta &= \left(\frac{1}{3}J_1 + \sqrt{J_2} \frac{1}{\sqrt{3}} \sin \theta \right) \sin \phi + c \cos \phi \\ \Rightarrow -\frac{1}{3}J_1 \sin \phi + \sqrt{J_2} \left(\cos \theta - \frac{1}{\sqrt{3}} \sin \theta \sin \phi \right) - c \cos \phi &= 0 \end{aligned}$$

$$F^{MC,3D} = -\frac{1}{3}J_1 \sin \phi + \sqrt{J_2} \left(\cos \theta - \frac{1}{\sqrt{3}} \sin \theta \sin \phi \right) - c \cos \phi$$

Note that the expression for F in the Mohr-Coulomb case in [1781] contains errors which is later corrected in [1785, p102].

3.15.14 The Griffith-Murrell failure criterion

The Griffith-Murrell yield criterion [203, 206, 82] is not often used. Extending the work of Griffith (1921) to three dimensional stress distributions, Murrell (1963) suggested the following criterion for rock failure expressed in terms of the principal stresses:

$$(\sigma_1 - \sigma_2)^2 + (\sigma_2 - \sigma_3)^2 + (\sigma_3 - \sigma_1)^2 + 24T_0(\sigma_1 + \sigma_2 + \sigma_3) = 0$$

where T_0 is a material property called the tensile strength. In principal stress space, this criterion is represented by a paraboloid of revolution around the pressure (or hydrostatic) axis.

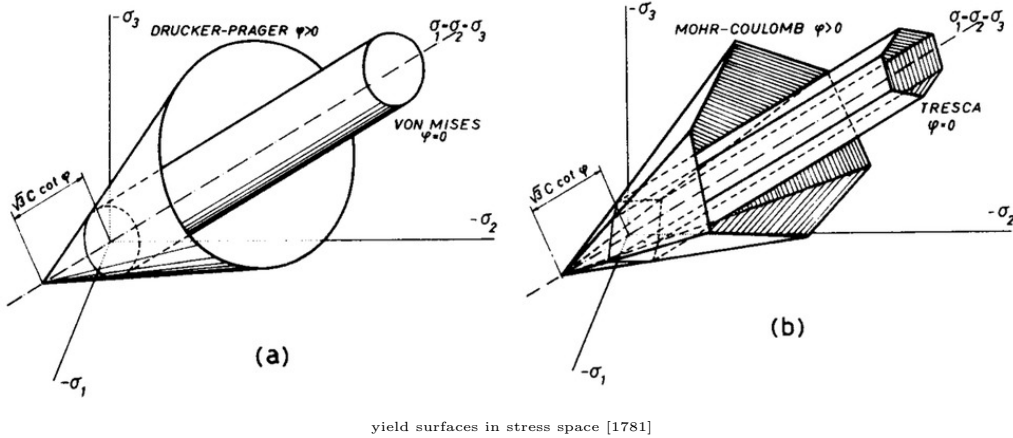
Also found:

$$J_{2D} + 12T_0 p = 0$$

3.15.15 The failure envelope, or yield surface

A yield surface is a five-dimensional surface in the six-dimensional space of stresses. The state of stress of inside the yield surface is elastic. When the stress state lies on the surface the material is said to have reached its yield point and the material is said to have become plastic. Further deformation of the material causes the stress state to remain on the yield surface, even though the surface itself may change shape and size as the plastic deformation evolves, this is because stress states that lie outside the yield surface are non-permissible.

The yield surface is usually expressed in terms of (and visualized in) a three-dimensional principal stress space $(\sigma_1, \sigma_2, \sigma_3)$, a two- or three-dimensional space spanned by stress invariants or a version of the three-dimensional Haigh-Westergaard space.



yield surfaces in stress space [1781]

3.15.16 Peierls creep

Looking at the literature, there seems to be many formulations for the Peierls creep deformation mechanism but it appears that a standard formulation for the Peierls creep writes:

$$\dot{\epsilon} = A\sigma^n \exp \left[-\frac{Q+pV}{RT} \left(1 - \left(\frac{\sigma}{\sigma_P} \right)^k \right)^q \right]$$

and it seems common to take $k = 1$, and $n = 2$ [656, 938]

$$\dot{\epsilon} = A\sigma^2 \exp \left[-\frac{Q+pV}{RT} \left(1 - \frac{\sigma}{\sigma_P} \right)^q \right]$$

In Chenin et al. (2019) [332] the authors state that their Peierls creep implementation relies on parameters from Evans and Goetze (1979) [527] using the approach of Kameyama et al (1999) [929]:

$$\eta^{pe} = \frac{2}{3} \frac{(1-s)/s}{(1+s)/2s} A (\varepsilon_e^{ds})^{\frac{1}{n}-1}$$

with A for this formulation:

$$A = \left[A_p \exp \left(-\frac{Q(1-\gamma)^2}{RT} \right) \right]^{-1/s} \gamma \sigma_p$$

where s is an effective stress exponent that depends on the temperature:

$$s = 2\gamma \frac{Q}{RT} (1-\gamma)$$

where γ is a fitting parameter.

Literature[56, 278, 545, 628, 656, 701, 938, 954, 932, 1169, 1762, 331]

3.15.17 Arrhenius law

A purely temperature-dependent dimensional Arrhenius law that emulates the temperature dependence of viscosity in silicate rock is often employed for mantle rocks [13, 1748, 1600, 186, 1243, 160, 754]:

$$\eta(T) = \eta_0 \exp \left(\frac{Q}{R} \left(\frac{1}{T} - \frac{1}{T_0} \right) \right) \quad (89)$$

where η_0 is a reference viscosity and T_0 its corresponding reference temperature.

It can also account for pressure effects as in [1099] where the diffusion creep viscosity (under the assumption of homogeneous grain size) is temperature- and pressure-dependent:

$$\eta(T) = \eta_0 \exp \left(\frac{1}{R} \left(\frac{Q-pV}{T} - \frac{Q}{T_0} \right) \right)$$

(I find the minus sign rather suspicious)

3.15.18 Simple parametrisation of the mantle

Many CITCOMs-based publications [249, 248] have used the following (dimensionless) viscosity for the mantle:

$$\eta(T, z) = \eta_r(r) \exp(A(0.5 - T))$$

where η_r is a depth dependent viscosity profile (usually defined as discontinuous linear profiles for various shells)

The non-dimensional activation coefficient is chosen to be $A = 9.2103$ in [248] which leads to a temperature-induced viscosity contrast of 10^4 .

This is also called the FrankKamenetskii flow rule, as used in [1029]:

$$\eta' = \eta_0 \exp(-\theta T)$$

where the parameters η_0, θ account for the local chemical composition of the rock.

Another temperature-dependent common expression is as follows [563]:

$$\eta(T) = \eta_\infty \exp\left(\frac{Q}{R}\left(\frac{1}{T} - \frac{1}{T_\infty}\right)\right)$$

Also, following [563]: For studying transient convection in a non-Newtonian rheological fluid, it is expedient from a computational point of view to employ a law which behaves linearly for low stresses initially and becomes gradually non-Newtonian only after a certain threshold stress level has been surpassed [345, 353]:

$$\eta(T, p, \tau_2) = \eta(T, p) \frac{1}{A_2 + A_3 \tau_2^2}$$

where A_2 is a parameter describing the linear creep at low stress levels and A_3 governs the transition stress between Newtonian and non-Newtonian rheologies.

Coltice and Sheppard (2018) [389] use a depth- and temperature-dependent viscosity formulation:

$$\eta(z, T) = \eta_0(z) \exp \frac{Q}{RT}$$

Note that this expression is supplemented with a pseudo-plastic formulation [1400].

 Literature: [966]

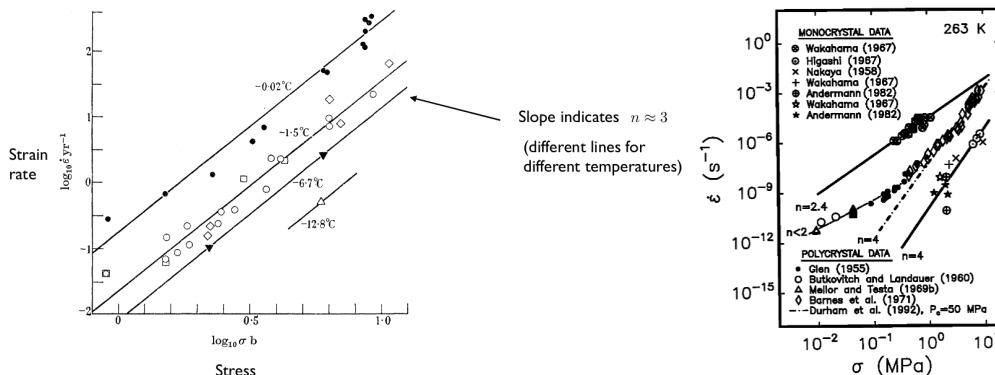
3.15.19 Glen's law for ice

As it turns out, ice and rocks share similarities in terms of rheology. Glens law is the most commonly used flow law for ice in glaciers and ice sheets [696] and it is actually a power-law type rheology:

$$\dot{\varepsilon} = A \tau^n$$

with $n \sim 3$ and $A \sim 2.4 \cdot 10^{-24} \text{ Pa}^{-3} \cdot \text{s}^{-1}$ at 0°C . The effective viscosity is then given by

$$\eta = \frac{1}{2A\tau_e^{n-1}}$$



Left: Taken from Glen [696]; Right: taken from [709].

Most of these studies suggest values of the power-law exponent $n \sim 2 - 4$, and there seems to be a general indication that the exponent is lower at lower stresses.

The A coefficient above has been found to depend on temperature and is reasonably described with an Arrhenius law:

$$A(T) = A_0 \exp\left(-\frac{Q}{RT}\right)$$

A standard formulation is the Paterson-Budd law with a fixed Glen exponent $n = 3$ and a split Arrhenius term [1293]:

$$A = 3.615 \cdot 10^{-13} \text{Pa}^{-3} \cdot \text{s}^{-1}, \quad Q = 60 \text{ kJ/mol}, \quad \text{if } T < 263\text{K}$$

$$A = 1.733 \cdot 10^3 \text{Pa}^{-3} \cdot \text{s}^{-1}, \quad Q = 139 \text{ kJ/mol}, \quad \text{if } T > 263\text{K}$$

Be careful that in these two equations the temperature T is the pressure-adjusted temperature [1293].

Note that A is also affected by the water content and the presence of impurities.

Finally, Glen's law is the standard rheology used for ice-sheet modelling but it does not account for the complex evolution of fabric and resulting anisotropy.

 Literature[744, 1005, 745]

3.15.20 Elasto-Visco-Plasticity

[33] [508]

Following [332], one can base the rheological model on the additive decomposition of the deviatoric strain rate tensor ε^d :

$$\varepsilon^d = \varepsilon^{el} + \varepsilon^{pl} + \varepsilon^{ds} + \varepsilon^{df} + \varepsilon^{pe}$$

where the five strain rate terms correspond respectively to the elastic, plastic, and viscous creep (dislocation, diffusion, peierls) contributions. Rather interestingly, Chenin et al [332] state that "this strain rate equation is nonlinear and solved locally on cell centroids and vertices in order to define the current effective viscosity and stress [1320]."

3.15.21 Anisotropic viscosity

Following the paper by Lev and Hager (2008) [1058], the anisotropic viscosity enters the equation of momentum through a 'correction' term added to the isotropic part of the constitutive equation relating stress and strain rate [1233]:

$$\sigma_{ij} = -p\delta_{ij} + 2\eta_N \dot{\varepsilon}_{ij} - 2(\eta_N - \eta_S) \Lambda_{ijkl} \dot{\varepsilon}_{kl}$$

where η_N is the normal viscosity and η_S is the shear viscosity. The fourth order tensor Λ reflects the orientation of the directors in space, denotes by \vec{n} :

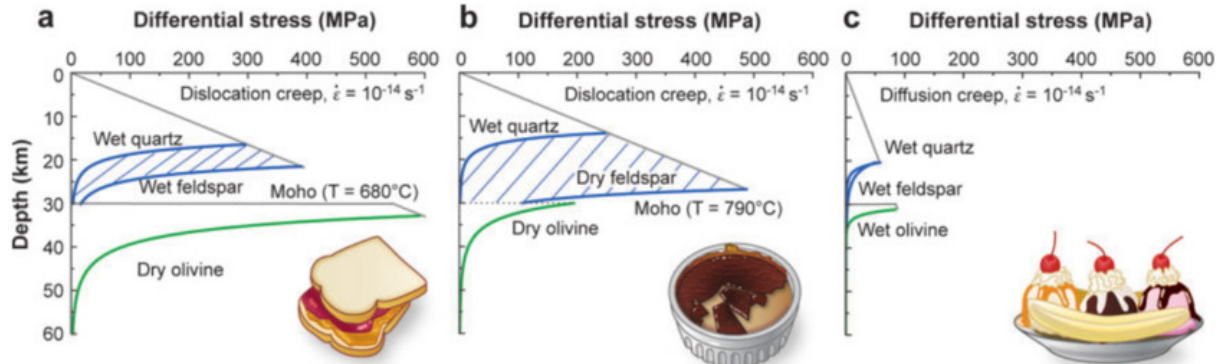
$$\Lambda_{ijkl} = \frac{1}{2}(n_i n_k \delta_{lj} + n_j n_k \delta_{il} + n_i n_l \delta_{kj} n_j n_l \delta_{ik}) - 2n_i n_j n_k n_l$$

Following [1208, 1233], the 'directors' are advected through the model and are analogous to particles. The directors are vector-particles pointing normal to the easy-glide plane or layer, thus defining the directions associated with η_N and η_S . In each time step of the calculation, the directors are advected and rotated by the flow, and in return determine the viscosity structure for the next time step [1232].

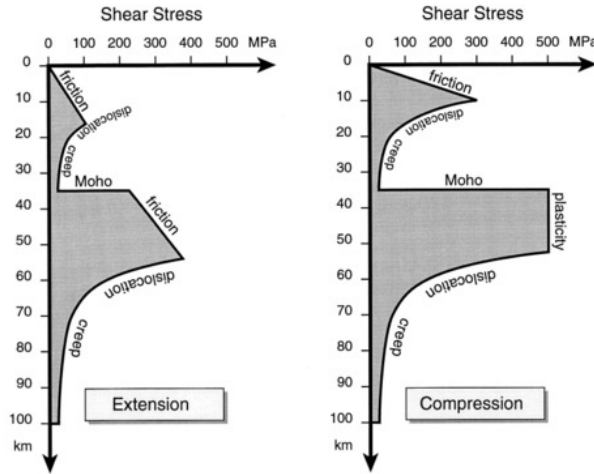
(**MSc Thesis**): redo the Rayleigh-Taylor instabilities with anisotropic lithospheric viscosity. experiments of Lev & Hager (2008) [1058].

 Literature: [1233, 1635, 1232, 1233, 1177, 1388, 1422]

3.15.22 Rheology of the lithosphere



Schematic view of the three most common first order rheological models of the continental lithosphere under a strain rate of 10^{-14} s^{-1} . In all three models the upper crust has its frictional strength increased with pressure and depth. (a) The jelly sandwich model has a weak mid-lower crust and a strong mantle composed of dry olivine. (b) The crème brûlée model assumes that the mantle is weak, due to the presence of water and high temperature deformation, and the dry and brittle crust determines the strength of the lithosphere. (c) The banana split model assumes that the lithosphere as a whole has its strength greatly reduced due to various strain weakening and feedback processes [263]



Taken from [152]. Typical vertical distribution of maximum shear stress in continental lithosphere undergoing compressional (right) or extensional (left) strain at 10^{-15} s . Friction controls level of shear stress in upper part of crust and sometimes in mantle lithosphere; then, below brittle/ductile transition, shear stress is controlled by thermally-activated dislocation creep.

Literature[276, 263, 1354, 1352]

3.16 Moment of inertia

Consider a rigid body rotating with fixed angular velocity ω about an axis which passes through the origin. Let \mathbf{r}_i be the position vector of the i th mass element, whose mass is m_i . We expect this position vector to precess about the axis of rotation (which is parallel to ω) with angular velocity ω .

$$\frac{d\mathbf{r}_i}{dt} = \boldsymbol{\omega} \times \mathbf{r}_i.$$

Thus, the above equation specifies the velocity, $\mathbf{v}_i = d\mathbf{r}_i/dt$, of each mass element as the body rotates with fixed angular velocity ω about an axis passing through the origin.

The total angular momentum of the body (about the origin) is written

$$\mathbf{L} = \sum_{i=1,N} m_i \mathbf{r}_i \times \frac{d\mathbf{r}_i}{dt} = \sum_{i=1,N} m_i \mathbf{r}_i \times (\boldsymbol{\omega} \times \mathbf{r}_i) = \sum_{i=1,N} m_i [\mathbf{r}_i^2 \boldsymbol{\omega} - (\mathbf{r}_i \cdot \boldsymbol{\omega}) \mathbf{r}_i]$$

The above formula can be written as a matrix equation of the form

$$\begin{pmatrix} L_x \\ L_y \\ L_z \end{pmatrix} = \begin{pmatrix} I_{xx} & I_{xy} & I_{xz} \\ I_{yx} & I_{yy} & I_{yz} \\ I_{zx} & I_{zy} & I_{zz} \end{pmatrix} \begin{pmatrix} \omega_x \\ \omega_y \\ \omega_z \end{pmatrix}$$

where

$$\begin{aligned} I_{xx} &= + \sum_{i=1,N} (y_i^2 + z_i^2) m_i = \int (y^2 + z^2) dm = \int_V (y^2 + z^2) \rho(x, y, z) dV \\ I_{yy} &= + \sum_{i=1,N} (x_i^2 + z_i^2) m_i = \int (x^2 + z^2) dm = \int_V (x^2 + z^2) \rho(x, y, z) dV \\ I_{zz} &= + \sum_{i=1,N} (x_i^2 + y_i^2) m_i = \int (x^2 + y^2) dm = \int_V (x^2 + y^2) \rho(x, y, z) dV \\ I_{xy} = I_{yx} &= - \sum_{i=1,N} x_i y_i m_i = - \int x y dm = - \int x y \rho(x, y, z) dV \\ I_{yz} = I_{zy} &= - \sum_{i=1,N} y_i z_i m_i = - \int y z dm = - \int y z \rho(x, y, z) dV \\ I_{xz} = I_{zx} &= - \sum_{i=1,N} x_i z_i m_i = - \int x z dm = - \int x z \rho(x, y, z) dV \end{aligned}$$

Here, I_{xx} is called the moment of inertia about the x -axis, I_{yy} the moment of inertia about the y -axis, I_{xy} the xy product of inertia, I_{yz} the yz product of inertia, etc. The matrix of the I_{ij} values is known as the moment of inertia tensor.

In general, the angular momentum vector, \mathbf{L} points in a different direction to the angular velocity vector, ω . In other words, \mathbf{L} is generally not parallel to ω .

Finally, although the above results were obtained assuming a fixed angular velocity, they remain valid at each instant in time if the angular velocity varies.

In the simplified case of a spherically symmetric planet, it is easy to see that $I_{xx} = I_{yy} = I_{zz}$ so that $I = \frac{1}{3}(I_{xx} + I_{yy} + I_{zz})$, and $\rho = \rho(r)$ with $dV = 4\pi r^2 dr$, leading to

$$I = \frac{8\pi}{3} \int_0^R \rho(r) r^4 dr$$

Assuming further that the planet has a constant density ρ_0 , we obtain

$$I = \frac{8\pi}{3} \rho_0 \int_0^R r^4 dr = \frac{8\pi}{3} \rho_0 \frac{R^5}{5} = \frac{2}{5} M R^2$$

where M is the mass of the planet and R is its radius.

Assuming now that the planet is composed of a core of radius R_c and density ρ_c surrounded by a mantle of density ρ_m , we have

$$I = \frac{8\pi}{3} \int_0^R \rho(r) r^4 dr = \frac{8\pi}{3} \left(\int_0^{R_c} \rho_c r^4 dr + \int_{R_c}^R \rho_m r^4 dr \right) = \frac{8\pi}{15} (\rho_c R_c^5 + \rho_m (R^5 - R_c^5))$$

The moment of inertia of the core is given in Table 2 of "Core Dynamics", Treatise on Geophysics, edited by Peter Olson: $I_{core} = 9.2 \times 10^{36} kg.m^2$. The total moment of inertia for the Earth is then given by $I = I_{core} + I_{mantle}$.

4 The building blocks of the Finite Element Method

4.1 Numerical integration

As we will see later, using the Finite Element method to solve problems involves computing integrals which are more often than not too complex to be computed analytically/exactly. We will then need to compute them numerically.

[wiki] In essence, the basic problem in numerical integration is to compute an approximate solution to a definite integral

$$\int_a^b f(x)dx$$

to a given degree of accuracy. This problem has been widely studied and we know that if $f(x)$ is a smooth function, and the domain of integration is bounded, there are many methods for approximating the integral to the desired precision.

There are several reasons for carrying out numerical integration.

- The integrand $f(x)$ may be known only at certain points, such as obtained by sampling. Some embedded systems and other computer applications may need numerical integration for this reason.
- A formula for the integrand may be known, but it may be difficult or impossible to find an antiderivative that is an elementary function. An example of such an integrand is $f(x) = \exp(-x^2)$, the antiderivative of which (the error function, times a constant) cannot be written in elementary form.
- It may be possible to find an antiderivative symbolically, but it may be easier to compute a numerical approximation than to compute the antiderivative. That may be the case if the antiderivative is given as an infinite series or product, or if its evaluation requires a special function that is not available.

4.1.1 in 1D - theory

The simplest method of this type is to let the interpolating function be a constant function (a polynomial of degree zero) that passes through the point $((a+b)/2, f((a+b)/2))$.

This is called the midpoint rule or rectangle rule.

$$\int_a^b f(x)dx \simeq (b-a)f\left(\frac{a+b}{2}\right)$$

insert here figure

The interpolating function may be a straight line (an affine function, i.e. a polynomial of degree 1) passing through the points $(a, f(a))$ and $(b, f(b))$.

This is called the trapezoidal rule.

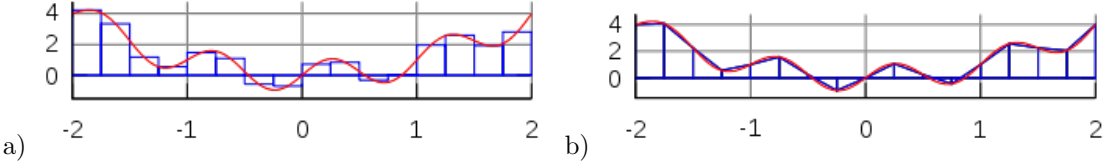
$$\int_a^b f(x)dx \simeq (b-a)\frac{f(a) + f(b)}{2}$$

insert here figure

For either one of these rules, we can make a more accurate approximation by breaking up the interval $[a, b]$ into some number n of subintervals, computing an approximation for each subinterval, then adding up all the results. This is called a composite rule, extended rule, or iterated rule. For example, the composite trapezoidal rule can be stated as

$$\int_a^b f(x)dx \simeq \frac{b-a}{n} \left(\frac{f(a)}{2} + \sum_{k=1}^{n-1} f(a + k \frac{b-a}{n}) + \frac{f(b)}{2} \right)$$

where the subintervals have the form $[kh, (k+1)h]$, with $h = (b-a)/n$ and $k = 0, 1, 2, \dots, n-1$.



The interval $[-2, 2]$ is broken into 16 sub-intervals. The blue lines correspond to the approximation of the red curve by means of a) the midpoint rule, b) the trapezoidal rule.

There are several algorithms for numerical integration (also commonly called 'numerical quadrature', or simply 'quadrature'). Interpolation with polynomials evaluated at equally spaced points in $[a, b]$ yields the NewtonCotes formulas, of which the rectangle rule and the trapezoidal rule are examples. If we allow the intervals between interpolation points to vary, we find another group of quadrature formulas, such as the Gauss(ian) quadrature formulas. A Gaussian quadrature rule is typically more accurate than a NewtonCotes rule, which requires the same number of function evaluations, if the integrand is smooth (i.e., if it is sufficiently differentiable).

An n -point Gaussian quadrature rule, named after Carl Friedrich Gauss, is a quadrature rule constructed to yield an exact result for polynomials of degree $2n - 1$ or less by a suitable choice of the points x_i and weights w_i for $i = 1, \dots, n$.

The domain of integration for such a rule is conventionally taken as $[-1, 1]$, so the rule is stated as

$$\int_{-1}^{+1} f(x) dx = \sum_{i_q=1}^n w_{i_q} f(x_{i_q})$$

In this formula the x_{i_q} coordinate is the i -th root of the Legendre polynomial $P_n(x)$.

It is important to note that a Gaussian quadrature will only produce good results if the function $f(x)$ is well approximated by a polynomial function within the range $[-1, 1]$. As a consequence, the method is not, for example, suitable for functions with singularities.

Number of points, n	Points, x_i	Weights, w_i
1	0	2
2	$\pm\sqrt{\frac{1}{3}}$	1
3	0	$\frac{8}{9}$
	$\pm\sqrt{\frac{3}{5}}$	$\frac{5}{9}$
4	$\pm\sqrt{\frac{3}{7} - \frac{2}{7}\sqrt{\frac{6}{5}}}$	$\frac{18+\sqrt{30}}{36}$
	$\pm\sqrt{\frac{3}{7} + \frac{2}{7}\sqrt{\frac{6}{5}}}$	$\frac{18-\sqrt{30}}{36}$
5	0	$\frac{128}{225}$
	$\pm\frac{1}{3}\sqrt{5 - 2\sqrt{\frac{10}{7}}}$	$\frac{322+13\sqrt{70}}{900}$
	$\pm\frac{1}{3}\sqrt{5 + 2\sqrt{\frac{10}{7}}}$	$\frac{322-13\sqrt{70}}{900}$

Gauss-Legendre points and their weights.

n	x_{iq}	w_{iq}	x_{iq} (approx)	w_{iq} (approx)
1	0	2	0	2
2	$\pm\sqrt{1/3}$	1	$\pm 0.577\ 350\ 269\ 189\ 626$	1
3	0	$8/9$	0	0.888 888 888 888 888
	$\pm\sqrt{3/5}$	$5/9$	$\pm 0.774\ 596\ 669\ 241\ 483$	0.555 555 555 555 555
4	$\pm\sqrt{\frac{3}{7} - \frac{2}{7}\sqrt{6/5}}$	$\frac{18+\sqrt{30}}{36}$	$\pm 0.339\ 981\ 043\ 584\ 856$	0.652 145 154 862 546
	$\pm\sqrt{\frac{3}{7} + \frac{2}{7}\sqrt{6/5}}$	$\frac{18-\sqrt{30}}{36}$	$\pm 0.861\ 136\ 311\ 594\ 953$	0.347 854 845 137 454
5	0	$128/225$	0	0.568 888 888 888 889
	$\pm\frac{1}{3}\sqrt{5 - 2\sqrt{\frac{10}{7}}}$	$\frac{322+13\sqrt{70}}{900}$	$\pm 0.538\ 469\ 310\ 105\ 683$	0.478 628 670 499 366
	$\pm\frac{1}{3}\sqrt{5 + 2\sqrt{\frac{10}{7}}}$	$\frac{322-13\sqrt{70}}{900}$	$\pm 0.906\ 179\ 845\ 938\ 664$	0.236 926 885 056 189
6	?	?	$\pm 0.238\ 619\ 186\ 083\ 197$ $\pm 0.661\ 209\ 386\ 466\ 265$ $\pm 0.932\ 469\ 514\ 203\ 152$	0.467 913 934 572 691 0.360 761 573 048 139 0.171 324 492 379 170
7			$\pm 0.946\ 107\ 912\ 342\ 759$ $\pm 0.741\ 531\ 185\ 599\ 394$ $\pm 0.405\ 845\ 151\ 377\ 397$ 0.000 000 000 000 000	0.129 484 966 168 870 0.279 705 391 489 277 0.381 830 050 505 119 0.417 959 183 673 469
8			$\pm 0.960\ 289\ 856\ 497\ 536$ $\pm 0.796\ 666\ 477\ 413\ 627$ $\pm 0.525\ 532\ 409\ 916\ 329$ $\pm 0.183\ 434\ 642\ 495\ 650$	0.101 228 536 290 376 0.222 381 034 453 374 0.313 706 645 877 887 0.362 683 783 378 362
9			$\pm 0.968\ 160\ 239\ 507\ 626$ $\pm 0.836\ 031\ 107\ 326\ 636$ $\pm 0.613\ 371\ 432\ 700\ 590$ $\pm 0.324\ 253\ 423\ 403\ 809$ 0.000 000 000 000 000	0.081 274 388 361 574 0.180 648 160 694 857 0.260 610 696 402 935 0.312 347 077 040 003 0.330 239 355 001 260
10			$\pm 0.973\ 906\ 528\ 517\ 172$ $\pm 0.865\ 063\ 366\ 688\ 985$ $\pm 0.679\ 409\ 568\ 299\ 024$ $\pm 0.433\ 395\ 394\ 129\ 247$ $\pm 0.148\ 874\ 338\ 981\ 631$	0.066 671 344 308 688 0.149 451 349 150 581 0.219 086 362 515 982 0.269 266 719 309 996 0.295 524 224 714 753

Abscissae and weights for Gauss quadratures up to $n = 10$. See [1060, p89]

As shown in the above table, it can be shown that the weight values must fulfill the following condition:

$$\sum_{iq} w_{iq} = 2 \quad (90)$$

and it is worth noting that all quadrature point coordinates are symmetrical around the origin.

Since most quadrature formula are only valid on a specific interval, we now must address the problem of their use outside of such intervals. The solution turns out to be quite simple: one must carry out a change of variables from the interval $[a, b]$ to $[-1, 1]$.

We then consider the reduced coordinate $r \in [-1, 1]$ such that

$$r = \frac{2}{b-a}(x-a) - 1$$

This relationship can be reversed such that when r is known, its equivalent coordinate $x \in [a, b]$ can be computed:

$$x = \frac{b-a}{2}(1+r) + a$$

From this it follows that

$$dx = \frac{b-a}{2}dr$$

and then

$$\int_a^b f(x)dx = \frac{b-a}{2} \int_{-1}^{+1} f(r)dr \simeq \frac{b-a}{2} \sum_{i_q=1}^n w_{i_q} f(r_{i_q})$$

4.1.2 in 1D - examples

example 1 Since we know how to carry out any required change of variables, we choose for simplicity $a = -1$, $b = +1$. Let us take for example $f(x) = \pi$. Then we can compute the integral of this function over the interval $[a, b]$ exactly:

$$I = \int_{-1}^{+1} f(x)dx = \pi \int_{-1}^{+1} dx = 2\pi$$

We can now use a Gauss-Legendre formula to compute this same integral:

$$I_{gq} = \int_{-1}^{+1} f(x)dx = \sum_{i_q=1}^{n_q} w_{i_q} f(x_{i_q}) = \sum_{i_q=1}^{n_q} w_{i_q} \pi = \pi \underbrace{\sum_{i_q=1}^{n_q} w_{i_q}}_{=2} = 2\pi$$

where we have used the property of the weight values of Eq.(90). Since the actual number of points was never specified, this result is valid for all quadrature rules.

example 2 Let us now take $f(x) = mx + p$ and repeat the same exercise:

$$I = \int_{-1}^{+1} f(x)dx = \int_{-1}^{+1} (mx + p)dx = [\frac{1}{2}mx^2 + px]_{-1}^{+1} = 2p$$

$$I_{gq} = \int_{-1}^{+1} f(x)dx = \sum_{i_q=1}^{n_q} w_{i_q} f(x_{i_q}) = \sum_{i_q=1}^{n_q} w_{i_q} (mx_{i_q} + p) = m \underbrace{\sum_{i_q=1}^{n_q} w_{i_q} x_{i_q}}_{=0} + p \underbrace{\sum_{i_q=1}^{n_q} w_{i_q}}_{=2} = 2p$$

since the quadrature points are symmetric w.r.t. to zero on the x-axis. Once again the quadrature is able to compute the exact value of this integral: this makes sense since an n -point rule exactly integrates a $2n - 1$ order polynomial such that a 1 point quadrature exactly integrates a first order polynomial like the one above.

example 3 Let us now take $f(x) = x^2$. We have

$$I = \int_{-1}^{+1} f(x)dx = \int_{-1}^{+1} x^2 dx = [\frac{1}{3}x^3]_{-1}^{+1} = \frac{2}{3}$$

and

$$I_{gq} = \int_{-1}^{+1} f(x)dx = \sum_{i_q=1}^{n_q} w_{i_q} f(x_{i_q}) = \sum_{i_q=1}^{n_q} w_{i_q} x_{i_q}^2$$

- $n_q = 1$: $x_{i_q}^{(1)} = 0$, $w_{i_q} = 2$. $I_{gq} = 0$
- $n_q = 2$: $x_q^{(1)} = -1/\sqrt{3}$, $x_q^{(2)} = 1/\sqrt{3}$, $w_q^{(1)} = w_q^{(2)} = 1$. $I_{gq} = \frac{2}{3}$
- It also works $\forall n_q > 2$!

4.1.3 in 2D/3D - theory

Let us now turn to a two-dimensional integral of the form

$$I = \int_{-1}^{+1} \int_{-1}^{+1} f(x, y) dxdy$$

The equivalent Gaussian quadrature writes:

$$I_{gq} \simeq \sum_{i_q=1}^{n_q} \sum_{j_q=1}^{n_q} f(x_{i_q}, y_{j_q}) w_{i_q} w_{j_q}$$

4.1.4 quadrature on triangles

Quadrature rules for triangles can be found in Dunavant, 1985 [483]. The following ones are identical to those in *ip_triangle.m* file of the MILAMIN code [426].

	r_q	s_q	w_q	
$iq = 1$	1/3	1/3	1/2	
$iq = 1$	1/6	1/6	1/6	
$iq = 2$	2/3	1/6	1/6	
$iq = 3$	1/6	2/3	1/6	
$iq = 1$	1/3	1/3	-27/96	
$iq = 2$	0.6	0.2	25/96	
$iq = 3$	0.2	0.6	25/96	
$iq = 4$	0.2	0.2	25/96	
$iq = 1$	$1 - 2g_1$	g_1	$w_1/2$	0.108103018168070
$iq = 2$	g_1	$1 - 2g_1$	$w_1/2$	0.445948490915965
$iq = 3$	g_1	g_1	$w_1/2$	0.445948490915965
$iq = 4$	$1 - 2g_2$	g_2	$w_2/2$	0.816847572980459
$iq = 5$	g_2	$1 - 2g_2$	$w_2/2$	0.091576213509771
$iq = 6$	g_2	g_2	$w_2/2$	0.091576213509771
$iq = 1$				0.091576213509771
$iq = 2$				0.816847572980459
$iq = 3$				0.091576213509771
$iq = 4$				0.445948490915965
$iq = 5$				0.108103018168070
$iq = 6$				0.445948490915965
$iq = 1$				0.091576213509771
$iq = 2$				0.091576213509771
$iq = 3$				0.816847572980459
$iq = 4$				0.091576213509771
$iq = 5$				0.445948490915965
$iq = 6$				0.108103018168070
$iq = 7$				0.223381589678011/2.0
$iq = 1$				0.091576213509771
$iq = 2$				0.091576213509771
$iq = 3$				0.091576213509771
$iq = 4$				0.091576213509771
$iq = 5$				0.091576213509771
$iq = 6$				0.091576213509771
$iq = 7$				0.091576213509771
$iq = 1$				0.1012865073235
$iq = 2$				0.7974269853531
$iq = 3$				0.1012865073235
$iq = 4$				0.4701420641051
$iq = 5$				0.4701420641051
$iq = 6$				0.0597158717898
$iq = 7$				0.3333333333333
$iq = 1$				0.1012865073235
$iq = 2$				0.7974269853531
$iq = 3$				0.1012865073235
$iq = 4$				0.4701420641051
$iq = 5$				0.4701420641051
$iq = 6$				0.0597158717898
$iq = 7$				0.3333333333333
$iq = 1$				0.3333333333333
$iq = 1$				5.01426509658179E - 01
$iq = 2$				2.49286745170910E - 01
$iq = 3$				2.49286745170910E - 01
$iq = 4$				8.73821971016996E - 01
$iq = 5$				6.30890144915020E - 02
$iq = 6$				6.30890144915020E - 02
$iq = 7$				5.31450498448170E - 02
$iq = 8$				6.36502499121399E - 01
$iq = 9$				3.10352451033784E - 01
$iq = 10$				5.31450498448170E - 02
$iq = 11$				6.36502499121399E - 01
$iq = 12$				3.10352451033784E - 01
$iq = 1$				5.83931378631895E - 02
$iq = 2$				5.83931378631895E - 02
$iq = 3$				5.83931378631895E - 02
$iq = 4$				2.54224531851035E - 02
$iq = 5$				2.54224531851035E - 02
$iq = 6$				2.54224531851035E - 02
$iq = 7$				2.54224531851035E - 02
$iq = 8$				2.54224531851035E - 02
$iq = 9$				2.54224531851035E - 02
$iq = 10$				2.54224531851035E - 02
$iq = 11$				2.54224531851035E - 02
$iq = 12$				2.54224531851035E - 02
$iq = 1$				5.83931378631895E - 02
$iq = 2$				5.83931378631895E - 02
$iq = 3$				5.83931378631895E - 02
$iq = 4$				0.109951743655322/2.0
$iq = 5$				0.109951743655322/2.0
$iq = 6$				0.109951743655322/2.0
$iq = 7$				0.109951743655322/2.0
$iq = 8$				0.109951743655322/2.0
$iq = 9$				0.109951743655322/2.0
$iq = 10$				0.109951743655322/2.0
$iq = 11$				0.109951743655322/2.0
$iq = 12$				0.109951743655322/2.0

where

$$g_1 = \left(8 - \sqrt{10} + \sqrt{38 - 44\sqrt{2/5}} \right) / 18 \quad g_2 = \left(8 - \sqrt{10} - \sqrt{38 - 44\sqrt{2/5}} \right) / 18$$

$$w_1 = \left(620 + \sqrt{213125 - 53320\sqrt{10}} \right) / 3720 \quad w_2 = \left(620 - \sqrt{213125 - 53320\sqrt{10}} \right) / 3720$$

4.1.5 quadrature on tetrahedra

Remark. In what follows the coefficients in the tables are not the reduced coordinates of the quadrature points but the coefficients corresponding to the 4 nodes.

Quadrature rules on tetrahedra take the form:

$$\int \int \int_{el} f(x, y, z) dx dy dz = V_{el} \sum_{iq=1}^{nqel} w_{iq} f(\xi_1^{iq}, \xi_2^{iq}, \xi_3^{iq}, \xi_4^{iq})$$

or, that is to say:

$$\int \int \int_{el} f(x, y, z) dx dy dz = \sum_{iq=1}^{nqel} (w_{iq} V_{el}) f(\xi_1^{iq}, \xi_2^{iq}, \xi_3^{iq}, \xi_4^{iq})$$

with in our case $V_{el} = 1/6$.

In the literature it can be found that a one point quadrature is characterised by

$$w_{iq} = 1 \quad \xi_1^{iq} = \xi_2^{iq} = \xi_3^{iq} = \xi_4^{iq} = 0.25$$

i.e, the coordinates of the single point are given by:

$$x_{iq} = \sum_{i=1}^4 \xi_i^{iq} x_i = \frac{1}{4}(x_1 + x_2 + x_3 + x_4)$$

Same for y and z coordinates.

A four-point quadrature rule is characterised by $w_{iq} = V_{el} * 0.25 = 1/24 \simeq 04166666666666667$ and

	ξ_1	ξ_2	ξ_3	ξ_4
$iq=1$	0.585410196624969	0.138196601125011	0.138196601125011	0.138196601125011
$iq=2$	0.138196601125011	0.585410196624969	0.138196601125011	0.138196601125011
$iq=3$	0.138196601125011	0.138196601125011	0.585410196624969	0.138196601125011
$iq=4$	0.138196601125011	0.138196601125011	0.138196601125011	0.585410196624969

We then have:

$$r_{iq} = \sum_{i=1}^4 \xi_i^{iq} x_i = (\xi_1^{iq}, \xi_2^{iq}, \xi_3^{iq}, \xi_4^{iq}) \cdot (r_1, r_2, r_3, r_4) = (\xi_1^{iq}, \xi_2^{iq}, \xi_3^{iq}, \xi_4^{iq}) \cdot (0, 1, 0, 0) = \xi_2^{iq}$$

$$s_{iq} = \sum_{i=1}^4 \xi_i^{iq} y_i = (\xi_1^{iq}, \xi_2^{iq}, \xi_3^{iq}, \xi_4^{iq}) \cdot (s_1, s_2, s_3, s_4) = (\xi_1^{iq}, \xi_2^{iq}, \xi_3^{iq}, \xi_4^{iq}) \cdot (0, 0, 1, 0) = \xi_3^{iq}$$

$$t_{iq} = \sum_{i=1}^4 \xi_i^{iq} z_i = (\xi_1^{iq}, \xi_2^{iq}, \xi_3^{iq}, \xi_4^{iq}) \cdot (t_1, t_2, t_3, t_4) = (\xi_1^{iq}, \xi_2^{iq}, \xi_3^{iq}, \xi_4^{iq}) \cdot (0, 0, 0, 1) = \xi_4^{iq}$$

Finally:

	r_q	s_q	t_q	w_q
$iq = 1$	0.138196601125011	0.138196601125011	0.138196601125011	0.04166666666666667
$iq = 2$	0.585410196624969	0.138196601125011	0.138196601125011	0.04166666666666667
$iq = 3$	0.138196601125011	0.585410196624969	0.138196601125011	0.04166666666666667
$iq = 4$	0.138196601125011	0.138196601125011	0.585410196624969	0.04166666666666667

4.1.6 The Gauss-Lobatto approach

All what we have seen above falls under the Gauss-Legendre quadrature method. There is however another somewhat common quadrature method: the Gauss-Lobatto quadrature. . It is similar to Gaussian quadrature with the following important differences: 1) There are integration points in the interval but they also always include the end points of the integration interval; 2) It is accurate for polynomials up to degree $2n - 3$, where n is the number of integration points.

In 1D, it reads:

$$\int_{-1}^{+1} f(x) dx = \frac{2}{n(n-1)} [f(-1) + f(1)] + \sum_{i=2}^{n-1} w_i f(x_i)$$

The locations and weights of the integration points are as follows:

n	x_{iq}	w_{iq}	x_{iq} (approx)	w_{iq} (approx)
3	0	4/3	4/3	1/3
	± 1	1/3		
4	$\pm \sqrt{\frac{1}{5}}$	5/6	5/6	1/6
	± 1	1/6		
5	0	32/45	32/45	49/90
	$\pm \sqrt{\frac{3}{7}}$	49/90		
	± 1	1/10		
6	$\pm \sqrt{\frac{1}{3} - \frac{2\sqrt{7}}{21}}$	$\frac{14+\sqrt{7}}{30}$	$\frac{14+\sqrt{7}}{30}$	$\frac{14-\sqrt{7}}{30}$
	$\pm \sqrt{\frac{1}{3} + \frac{2\sqrt{7}}{21}}$	$\frac{14-\sqrt{7}}{30}$		
	± 1	1/15		

4.2 The mesh

4.3 A bit of FE terminology

We introduce here some terminology for efficient element descriptions [743]:

- For triangles/tetrahedra, the designation $P_m \times P_n$ means that each component of the velocity is approximated by continuous piecewise complete Polynomials of degree m and pressure by continuous piecewise complete Polynomials of degree n . For example $P_2 \times P_1$ means

$$u \sim a_1 + a_2x + a_3y + a_4xy + a_5x^2 + a_6y^2$$

with similar approximations for v , and

$$p \sim b_1 + b_2x + b_3y$$

Both velocity and pressure are continuous across element boundaries, and each triangular element contains 6 velocity nodes and three pressure nodes.

- For the same families, $P_m \times P_{-n}$ is as above, except that pressure is approximated via piecewise discontinuous polynomials of degree n . For instance, $P_2 \times P_{-1}$ is the same as P_2P_1 except that pressure is now an independent linear function in each element and therefore discontinuous at element boundaries.
- For quadrilaterals/hexahedra, the designation $Q_m \times Q_n$ means that each component of the velocity is approximated by a continuous piecewise polynomial of degree m in each direction on the quadrilateral and likewise for pressure, except that the polynomial is of degree n . For instance, $Q_2 \times Q_1$ means

$$u \sim a_1 + a_2x + a_3y + a_4xy + a_5x^2 + a_6y^2 + a_7x^2y + a_8xy^2 + a_9x^2y^2$$

and

$$p \sim b_1 + b_2x + b_3y + b_4xy$$

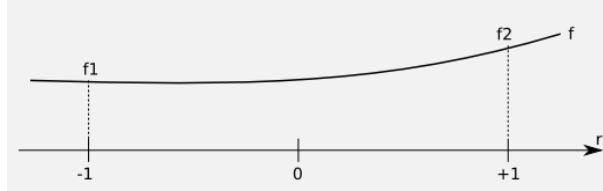
- For these same families, $Q_m \times Q_{-n}$ is as above, except that the pressure approximation is not continuous at element boundaries.
- Again for the same families, $Q_m \times P_{-n}$ indicates the same velocity approximation with a pressure approximation that is a discontinuous complete piecewise polynomial of degree n (not of degree n in each direction !)
- The designation P_m^+ or Q_m^+ means that some sort of bubble function was added to the polynomial approximation for the velocity. You may also find the term 'enriched element' in the literature.
- Finally, for $n = 0$, we have piecewise-constant pressure, and we omit the minus sign for simplicity.

Another point which needs to be clarified is the use of so-called 'conforming elements' (or 'non-conforming elements'). Following again [743], conforming velocity elements are those for which the basis functions for a subset of H^1 for the continuous problem (the first derivatives and their squares are integrable in Ω). For instance, the rotated $Q_1 \times P_0$ element of Rannacher and Turek (see section ??) is such that the velocity is discontinuous across element edges, so that the derivative does not exist there. Another typical example of non-conforming element is the Crouzeix-Raviart element [419].

4.4 Elements and basis functions in 1D

4.4.1 Linear basis functions (Q_1)

Let $f(r)$ be a C^1 function on the interval $[-1 : 1]$ with $f(-1) = f_1$ and $f(1) = f_2$.



Let us assume that the function $f(r)$ is to be approximated on $[-1, 1]$ by the first order polynomial

$$f(r) = a + br \quad (91)$$

Then it must fulfill

$$\begin{aligned} f(r = -1) &= a - b = f_1 \\ f(r = +1) &= a + b = f_2 \end{aligned}$$

This leads to

$$a = \frac{1}{2}(f_1 + f_2) \quad b = \frac{1}{2}(-f_1 + f_2)$$

and then replacing a, b in Eq. (91) by the above values on gets

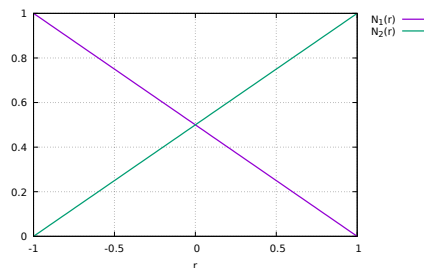
$$f(r) = \left[\frac{1}{2}(1 - r) \right] f_1 + \left[\frac{1}{2}(1 + r) \right] f_2$$

or

$$f(r) = \sum_{i=1}^2 N_i(r) f_i$$

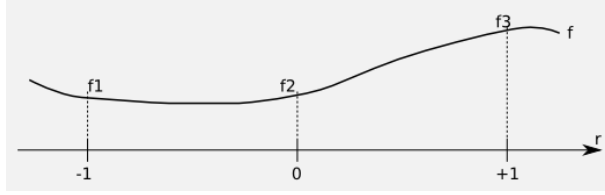
with

$N_1(r) = \frac{1}{2}(1 - r)$ $N_2(r) = \frac{1}{2}(1 + r)$	(92)
--	------



4.4.2 Quadratic basis functions (Q_2)

Let $f(r)$ be a C^1 function on the interval $[-1 : 1]$ with $f(-1) = f_1$, $f(0) = f_2$ and $f(1) = f_3$.



Let us assume that the function $f(r)$ is to be approximated on $[-1, 1]$ by the second order polynomial

$$f(r) = a + br + cr^2 \quad (93)$$

Then it must fulfill

$$\begin{aligned} f(r = -1) &= a - b + c = f_1 \\ f(r = 0) &= a = f_2 \\ f(r = +1) &= a + b + c = f_3 \end{aligned}$$

This leads to

$$a = f_2 \quad b = \frac{1}{2}(-f_1 + f_3) \quad c = \frac{1}{2}(f_1 + f_3 - 2f_2)$$

and then replacing a, b, c in Eq. (93) by the above values on gets

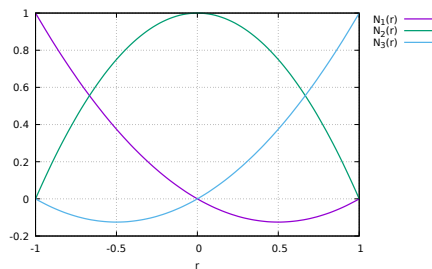
$$f(r) = \left[\frac{1}{2}r(r-1) \right] f_1 + (1-r^2)f_2 + \left[\frac{1}{2}r(r+1) \right] f_3$$

or,

$$f(r) = \sum_{i=1}^3 N_i(r) f_i$$

with

$\begin{aligned} N_1(r) &= \frac{1}{2}r(r-1) \\ N_2(r) &= (1-r^2) \\ N_3(r) &= \frac{1}{2}r(r+1) \end{aligned} \quad (94)$
--



4.4.3 Cubic basis functions (Q_3)

The 1D basis polynomial is given by

$$f(r) = a + br + cr^2 + dr^3$$

with the nodes at position $-1, -1/3, +1/3$ and $+1$.

$$\begin{aligned}
f(-1) &= a - b + c - d = f_1 \\
f(-1/3) &= a - \frac{b}{3} + \frac{c}{9} - \frac{d}{27} = f_2 \\
f(+1/3) &= a - \frac{b}{3} + \frac{c}{9} - \frac{d}{27} = f_3 \\
f(+1) &= a + b + c + d = f_4
\end{aligned}$$

Adding the first and fourth equation and the second and third, one arrives at

$$f_1 + f_4 = 2a + 2c \quad f_2 + f_3 = 2a + \frac{2c}{9}$$

and finally:

$$\begin{aligned}
a &= \frac{1}{16}(-f_1 + 9f_2 + 9f_3 - f_4) \\
c &= \frac{9}{16}(f_1 - f_2 - f_3 + f_4)
\end{aligned}$$

Combining the original 4 equations in a different way yields

$$2b + 2d = f_4 - f_1 \quad \frac{2b}{3} + \frac{2d}{27} = f_3 - f_2$$

so that

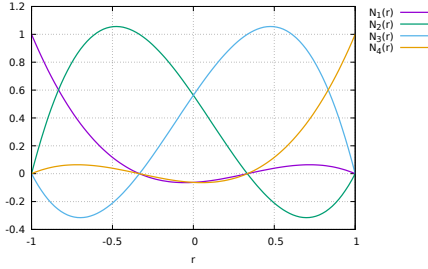
$$\begin{aligned}
b &= \frac{1}{16}(f_1 - 27f_2 + 27f_3 - f_4) \\
d &= \frac{9}{16}(-f_1 + 3f_2 - 3f_3 + f_4)
\end{aligned}$$

Finally,

$$\begin{aligned}
f(r) &= a + b + cr^2 + dr^3 \\
&= \frac{1}{16}(-1 + r + 9r^2 - 9r^3)f_1 \\
&\quad + \frac{1}{16}(9 - 27r - 9r^2 + 27r^3)f_2 \\
&\quad + \frac{1}{16}(9 + 27r - 9r^2 - 27r^3)f_3 \\
&\quad + \frac{1}{16}(-1 - r + 9r^2 + 9r^3)f_4 \\
&= \sum_{i=1}^4 N_i(r)f_i
\end{aligned}$$

where

$ \begin{aligned} N_1 &= \frac{1}{16}(-1 + r + 9r^2 - 9r^3) \\ N_2 &= \frac{1}{16}(9 - 27r - 9r^2 + 27r^3) \\ N_3 &= \frac{1}{16}(9 + 27r - 9r^2 - 27r^3) \\ N_4 &= \frac{1}{16}(-1 - r + 9r^2 + 9r^3) \end{aligned} $
--



These are identical to [1060, p49]

Verification:

- Let us assume $f(r) = C$, then

$$\hat{f}(r) = \sum_i N_i(r) f_i = \sum_i N_i C = C \sum_i N_i = C$$

so that a constant function is exactly reproduced, as expected.

- Let us assume $f(r) = r$, then $f_1 = -1$, $f_2 = -1/3$, $f_3 = 1/3$ and $f_4 = +1$. We then have

$$\begin{aligned}
\hat{f}(r) &= \sum_i N_i(r) f_i \\
&= -N_1(r) - \frac{1}{3}N_2(r) + \frac{1}{3}N_3(r) + N_4(r) \\
&= [-(-1 + r + 9r^2 - 9r^3) \\
&\quad - \frac{1}{3}(9 - 27r - 9r^2 - 27r^3) \\
&\quad + \frac{1}{3}(9 + 27r - 9r^2 + 27r^3) \\
&\quad + (-1 - r + 9r^2 + 9r^3)]/16 \\
&= [-r + 9r + 9r - r]/16 + \dots 0\dots \\
&= r
\end{aligned} \tag{95}$$

The basis functions derivative are given by

$\frac{\partial N_1}{\partial r}$	$=$	$\frac{1}{16}(1 + 18r - 27r^2)$
$\frac{\partial N_2}{\partial r}$	$=$	$\frac{1}{16}(-27 - 18r + 81r^2)$
$\frac{\partial N_3}{\partial r}$	$=$	$\frac{1}{16}(+27 - 18r - 81r^2)$
$\frac{\partial N_4}{\partial r}$	$=$	$\frac{1}{16}(-1 + 18r + 27r^2)$

Verification:

- Let us assume $f(r) = C$, then

$$\begin{aligned}
\frac{\partial \hat{f}}{\partial r} &= \sum_i \frac{\partial N_i}{\partial r} f_i \\
&= C \sum_i \frac{\partial N_i}{\partial r} \\
&= \frac{C}{16} [(1 + 18r - 27r^2) \\
&\quad + (-27 - 18r + 81r^2) \\
&\quad + (+27 - 18r - 81r^2) \\
&\quad + (-1 + 18r + 27r^2)] \\
&= 0
\end{aligned}$$

- Let us assume $f(r) = r$, then $f_1 = -1$, $f_2 = -1/3$, $f_3 = 1/3$ and $f_4 = +1$. We then have

$$\begin{aligned}
\frac{\partial \hat{f}}{\partial r} &= \sum_i \frac{\partial N_i}{\partial r} f_i \\
&= \frac{1}{16} [-(1 + 18r - 27r^2) \\
&\quad - \frac{1}{3}(-27 - 18r + 81r^2) \\
&\quad + \frac{1}{3}(+27 - 18r - 81r^2) \\
&\quad + (-1 + 18r + 27r^2)] \\
&= \frac{1}{16} [-2 + 18 + 54r^2 - 54r^2] \\
&= 1
\end{aligned}$$

4.4.4 Quartic basis functions (Q_4)

The 1D basis polynomial is given by

$$f(r) = a + br + cr^2 + dr^3 + er^4$$

with the nodes at position -1,-1/2, 0, +1/2 and +1.

$$\begin{aligned}
f(-1) &= a - b + c - d + e = f_1 \\
f(-1/2) &= a - \frac{b}{2} + \frac{c}{4} - \frac{d}{8} + \frac{e}{16} = f_2 \\
f(0) &= a = f_3 \\
f(+1/2) &= a - \frac{b}{2} + \frac{c}{4} - \frac{d}{8} + \frac{e}{16} = f_4 \\
f(+1) &= a + b + c + d + e = f_5
\end{aligned}$$

or,

$$\begin{pmatrix} 1 & -1 & 1 & -1 & 1 \\ 1 & -1/2 & 1/4 & -1/8 & 1/16 \\ 1 & 0 & 0 & 0 & 0 \\ 1 & 1/2 & 1/4 & 1/8 & 1/16 \\ 1 & 1 & 1 & 1 & 1 \end{pmatrix} \begin{pmatrix} a \\ b \\ c \\ d \\ e \end{pmatrix} = \begin{pmatrix} f_1 \\ f_2 \\ f_3 \\ f_4 \\ f_5 \end{pmatrix} \tag{96}$$

The third line gives $a = f_3$ so that

$$\underbrace{\begin{pmatrix} -1 & 1 & -1 & 1 \\ -1/2 & 1/4 & -1/8 & 1/16 \\ 1/2 & 1/4 & 1/8 & 1/16 \\ 1 & 1 & 1 & 1 \end{pmatrix}}_A \begin{pmatrix} b \\ c \\ d \\ e \end{pmatrix} = \begin{pmatrix} f_1 - f_3 \\ f_2 - f_3 \\ f_4 - f_3 \\ f_5 - f_3 \end{pmatrix} \quad (97)$$

The inverse of the matrix A is:

$$A^{-1} = \frac{1}{6} \begin{pmatrix} 1 & -8 & 8 & -1 \\ -1 & 16 & 16 & -1 \\ -4 & 8 & -8 & 4 \\ 4 & -16 & -16 & 4 \end{pmatrix}$$

so that

$$\begin{pmatrix} b \\ c \\ d \\ e \end{pmatrix} = \frac{1}{6} \begin{pmatrix} 1 & -8 & 8 & -1 \\ -1 & 16 & 16 & -1 \\ -4 & 8 & -8 & 4 \\ 4 & -16 & -16 & 4 \end{pmatrix} \cdot \begin{pmatrix} f_1 - f_3 \\ f_2 - f_3 \\ f_4 - f_3 \\ f_5 - f_3 \end{pmatrix}$$

and then

$$b = \frac{1}{6} (f_1 - 8f_2 + 8f_4 - f_5) \quad (98)$$

$$c = \frac{1}{6} (-f_1 + 16f_2 - 30f_3 + 16f_4 - f_5) \quad (99)$$

$$d = \frac{1}{6} (-4f_1 + 8f_2 - 8f_4 + 4f_5) \quad (100)$$

$$e = \frac{1}{6} (4f_1 - 16f_2 + 24f_3 - 16f_4 + 4f_5) \quad (101)$$

$$f(r) = a + br + cr^2 + dr^3 + er^4 \quad (102)$$

$$= f_3 + \frac{1}{6} (f_1 - 8f_2 + 8f_4 - f_5) r + \frac{1}{6} (-f_1 + 16f_2 - 30f_3 + 16f_4 - f_5) r^2 + \quad (103)$$

$$+ \frac{1}{6} (-4f_1 + 8f_2 - 8f_4 + 4f_5) r^3 + \frac{1}{6} (4f_1 - 16f_2 + 24f_3 - 16f_4 + 4f_5) r^4 \quad (104)$$

$$= \frac{1}{6} (r - r^2 - 4r^3 + 4r^4) f_1 \quad (105)$$

$$+ \frac{1}{6} (-8r + 16r^2 + 8r^3 - 16r^4) f_2 \quad (106)$$

$$+ (1 - 5r^2 + 4r^4) f_3 \quad (107)$$

$$+ \frac{1}{6} (8r + 16r^2 - 8r^3 - 16r^4) f_4 \quad (108)$$

$$+ \frac{1}{6} (-r - r^2 + 4r^3 + 4r^4) f_5 \quad (109)$$

Finally

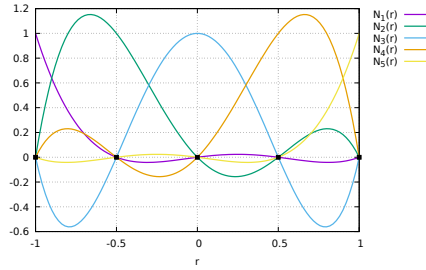
$$N_1(r) = \frac{1}{6} (r - r^2 - 4r^3 + 4r^4) \quad (110)$$

$$N_2(r) = \frac{1}{6} (-8r + 16r^2 + 8r^3 - 16r^4) \quad (111)$$

$$N_3(r) = (1 - 5r^2 + 4r^4) \quad (112)$$

$$N_4(r) = \frac{1}{6} (8r + 16r^2 - 8r^3 - 16r^4) \quad (113)$$

$$N_5(r) = \frac{1}{6} (-r - r^2 + 4r^3 + 4r^4) \quad (114)$$



The basis functions derivative are given by

$$\frac{\partial N_1}{\partial r} = \frac{1}{6} (1 - 2r - 12r^2 + 16r^3) \quad (115)$$

$$\frac{\partial N_2}{\partial r} = \frac{1}{6} (-8 + 32r + 24r^2 - 64r^3) \quad (116)$$

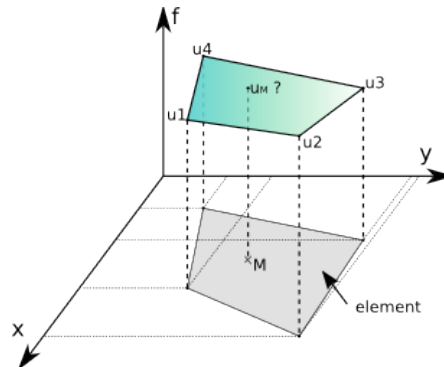
$$\frac{\partial N_3}{\partial r} = -10r + 16r^3 \quad (117)$$

$$\frac{\partial N_4}{\partial r} = \frac{1}{6} (8 + 32r - 24r^2 - 64r^3) \quad (118)$$

$$\frac{\partial N_5}{\partial r} = \frac{1}{6} (-1 - 2r + 12r^2 + 16r^3) \quad (119)$$

4.5 Elements and basis functions in 2D

Let us for a moment consider a single quadrilateral element in the xy -plane, as shown on the following figure:



Let us assume that we know the values of a given field u at the vertices. For a given point M inside the element in the plane, what is the value of the field u at this point? It makes sense to postulate that $u_M = u(x_M, y_M)$ will be given by

$$u_M = \phi(u_1, u_2, u_3, u_4, x_M, y_M)$$

where ϕ is a function to be determined. Although ϕ is not unique, we can decide to express the value u_M as a weighed sum of the values at the vertices u_i . One option could be to assign all four vertices the same weight, say $1/4$ so that $u_M = (u_1 + u_2 + u_3 + u_4)/4$, i.e. u_M is simply given by the arithmetic mean of the vertices values. This approach suffers from a major drawback as it does not use the location of point M inside the element. For instance, when $(x_M, y_M) \rightarrow (x_2, y_2)$ we expect $u_M \rightarrow u_2$.

In light of this, we could now assume that the weights would depend on the position of M in a continuous fashion:

$$u(x_M, y_M) = \sum_{i=1}^4 N_i(x_M, y_M) u_i$$

where the N_i are continuous ("well behaved") functions which have the property:

$$N_i(x_j, y_j) = \delta_{ij}$$

or, in other words:

$$N_3(x_1, y_1) = 0 \quad (120)$$

$$N_3(x_2, y_2) = 0 \quad (121)$$

$$N_3(x_3, y_3) = 1 \quad (122)$$

$$N_3(x_4, y_4) = 0 \quad (123)$$

The functions N_i are commonly called basis functions.

Omitting the M subscripts for any point inside the element, the velocity components u and v are given by:

$$\hat{u}(x, y) = \sum_{i=1}^4 N_i(x, y) u_i \quad (124)$$

$$\hat{v}(x, y) = \sum_{i=1}^4 N_i(x, y) v_i \quad (125)$$

Rather interestingly, one can now easily compute velocity gradients (and therefore the strain rate tensor) since we have assumed the basis functions to be "well behaved" (in this case differentiable):

$$\dot{\epsilon}_{xx}(x, y) = \frac{\partial u}{\partial x} = \sum_{i=1}^4 \frac{\partial N_i}{\partial x} u_i \quad (126)$$

$$\dot{\epsilon}_{yy}(x, y) = \frac{\partial v}{\partial y} = \sum_{i=1}^4 \frac{\partial N_i}{\partial y} v_i \quad (127)$$

$$\dot{\epsilon}_{xy}(x, y) = \frac{1}{2} \frac{\partial u}{\partial y} + \frac{1}{2} \frac{\partial v}{\partial x} = \frac{1}{2} \sum_{i=1}^4 \frac{\partial N_i}{\partial y} u_i + \frac{1}{2} \sum_{i=1}^4 \frac{\partial N_i}{\partial x} v_i \quad (128)$$

How we actually obtain the exact form of the basis functions is explained in the coming section.

4.5.1 Bilinear basis functions in 2D (Q_1)

In this section, we place ourselves in the most favorable case, i.e. the element is a square defined by $-1 < r < 1$, $-1 < s < 1$ in the Cartesian coordinates system (r, s) :

```
3=====2
|           |   (r_0,s_0)=(-1,-1)
|           |   (r_1,s_1)=(+1,-1)
|           |   (r_2,s_2)=(+1,+1)
|           |   (r_3,s_3)=(-1,+1)
|
0=====1
```

This element is commonly called the reference element. How we go from the (x, y) coordinate system to the (r, s) once and vice versa will be dealt later on. For now, the basis functions in the above reference element and in the reduced coordinates system (r, s) are given by:

$$\begin{aligned} N_1(r, s) &= 0.25(1 - r)(1 - s) \\ N_2(r, s) &= 0.25(1 + r)(1 - s) \\ N_3(r, s) &= 0.25(1 + r)(1 + s) \\ N_4(r, s) &= 0.25(1 - r)(1 + s) \end{aligned}$$

The partial derivatives of these functions with respect to r and s automatically follow:

$$\begin{aligned} \frac{\partial N_1}{\partial r}(r, s) &= -0.25(1 - s) & \frac{\partial N_1}{\partial s}(r, s) &= -0.25(1 - r) \\ \frac{\partial N_2}{\partial r}(r, s) &= +0.25(1 - s) & \frac{\partial N_2}{\partial s}(r, s) &= -0.25(1 + r) \\ \frac{\partial N_3}{\partial r}(r, s) &= +0.25(1 + s) & \frac{\partial N_3}{\partial s}(r, s) &= +0.25(1 + r) \\ \frac{\partial N_4}{\partial r}(r, s) &= -0.25(1 + s) & \frac{\partial N_4}{\partial s}(r, s) &= +0.25(1 - r) \end{aligned}$$

Let us go back to Eq.(125). And let us assume that the function $v(r, s) = C$ so that $v_i = C$ for $i = 1, 2, 3, 4$. It then follows that

$$\hat{v}(r, s) = \sum_{i=1}^4 N_i(r, s) v_i = C \sum_{i=1}^4 N_i(r, s) = C[N_1(r, s) + N_2(r, s) + N_3(r, s) + N_4(r, s)] = C$$

This is a very important property: if the v function used to assign values at the vertices is constant, then the value of \hat{v} anywhere in the element is exactly C . If we now turn to the derivatives of v with respect to r and s :

$$\frac{\partial \hat{v}}{\partial r}(r, s) = \sum_{i=1}^4 \frac{\partial N_i}{\partial r}(r, s) v_i = C \sum_{i=1}^4 \frac{\partial N_i}{\partial r}(r, s) = C[-0.25(1 - s) + 0.25(1 - s) + 0.25(1 + s) - 0.25(1 + s)] = 0$$

$$\frac{\partial \hat{v}}{\partial s}(r, s) = \sum_{i=1}^4 \frac{\partial N_i}{\partial s}(r, s) v_i = C \sum_{i=1}^4 \frac{\partial N_i}{\partial s}(r, s) = C[-0.25(1 - r) - 0.25(1 + r) + 0.25(1 + r) + 0.25(1 - r)] = 0$$

We reassuringly find that the derivative of a constant field anywhere in the element is exactly zero.

If we now choose $v(r, s) = ar + bs$ with a and b two constant scalars, we find:

$$\hat{v}(r, s) = \sum_{i=1}^4 N_i(r, s) v_i \tag{129}$$

$$= \sum_{i=1}^4 N_i(r, s)(ar_i + bs_i) \tag{130}$$

$$= \underbrace{a \sum_{i=1}^4 N_i(r, s)r_i}_{r} + \underbrace{b \sum_{i=1}^4 N_i(r, s)s_i}_{s} \tag{131}$$

$$\begin{aligned} &= a[0.25(1 - r)(1 - s)(-1) + 0.25(1 + r)(1 - s)(+1) + 0.25(1 + r)(1 + s)(+1) + 0.25(1 - r)(1 + s)(-1)] \\ &+ b[0.25(1 - r)(1 - s)(-1) + 0.25(1 + r)(1 - s)(-1) + 0.25(1 + r)(1 + s)(+1) + 0.25(1 - r)(1 + s)(+1)] \\ &= a[-0.25(1 - r)(1 - s) + 0.25(1 + r)(1 - s) + 0.25(1 + r)(1 + s) - 0.25(1 - r)(1 + s)] \\ &+ b[-0.25(1 - r)(1 - s) - 0.25(1 + r)(1 - s) + 0.25(1 + r)(1 + s) + 0.25(1 - r)(1 + s)] \\ &= ar + bs \end{aligned} \tag{132}$$

verify above eq. This set of bilinear shape functions is therefore capable of exactly representing a bilinear field. The derivatives are:

$$\frac{\partial \hat{v}}{\partial r}(r, s) = \sum_{i=1}^4 \frac{\partial N_i}{\partial r}(r, s) v_i \quad (133)$$

$$= a \sum_{i=1}^4 \frac{\partial N_i}{\partial r}(r, s) r_i + b \sum_{i=1}^4 \frac{\partial N_i}{\partial r}(r, s) s_i \quad (134)$$

$$= a [-0.25(1-s)(-1) + 0.25(1-s)(+1) + 0.25(1+s)(+1) - 0.25(1+s)(-1)]$$

$$+ b [-0.25(1-s)(-1) + 0.25(1-s)(-1) + 0.25(1+s)(+1) - 0.25(1+s)(+1)]$$

$$= \frac{a}{4} [(1-s) + (1-s) + (1+s) + (1+s)]$$

$$+ \frac{b}{4} [(1-s) - (1-s) + (1+s) - (1+s)]$$

$$= a \quad (135)$$

Here again, we find that the derivative of the bilinear field inside the element is exact: $\frac{\partial \hat{v}}{\partial r} = \frac{\partial v}{\partial r}$.

However, following the same methodology as above, one can easily prove that this is no more true for polynomials of degree strivtly higher than 1. This fact has serious consequences: if the solution to the problem at hand is for instance a parabola, the Q_1 shape functions cannot represent the solution properly, but only by approximating the parabola in each element by a line. As we will see later, Q_2 basis functions can remedy this problem by containing themselves quadratic terms.

4.5.2 Biquadratic basis functions in 2D (Q_2)

This element is part of the so-called LAgrange family.

citation needed

Inside an element the local numbering of the nodes is as follows:

3=====6=====2							
			(r_0,s_0)=(-1,-1)	(r_4,s_4)=(0,-1)			
			(r_1,s_1)=(+1,-1)	(r_5,s_5)=(+1, 0)			
7=====8=====5			(r_2,s_2)=(+1,+1)	(r_6,s_6)=(0,+1)			
			(r_3,s_3)=(-1,+1)	(r_7,s_7)=(-1, 0)			
				(r_8,s_8)=(0, 0)			
0=====4=====1							

Note that this numbering is also employed in [1060, 56]. The basis polynomial is then

$$f(r, s) = a + br + cs + drs + er^2 + fs^2 + gr^2s + hrs^2 + ir^2s^2$$

The velocity shape functions are given by:

$N_0(r, s) = \frac{1}{2}r(r-1)\frac{1}{2}s(s-1)$
$N_1(r, s) = \frac{1}{2}r(r+1)\frac{1}{2}s(s-1)$
$N_2(r, s) = \frac{1}{2}r(r+1)\frac{1}{2}s(s+1)$
$N_3(r, s) = \frac{1}{2}r(r-1)\frac{1}{2}s(s+1)$
$N_4(r, s) = (1-r^2)\frac{1}{2}s(s-1)$
$N_5(r, s) = \frac{1}{2}r(r+1)(1-s^2)$
$N_6(r, s) = (1-r^2)\frac{1}{2}s(s+1)$
$N_7(r, s) = \frac{1}{2}r(r-1)(1-s^2)$
$N_8(r, s) = (1-r^2)(1-s^2)$

These are identical to [1060, p57]. Their derivatives are given by:

$\frac{\partial N_0}{\partial r} = \frac{1}{2}(2r-1)\frac{1}{2}s(s-1)$	$\frac{\partial N_0}{\partial s} = \frac{1}{2}r(r-1)\frac{1}{2}(2s-1)$
$\frac{\partial N_1}{\partial r} = \frac{1}{2}(2r+1)\frac{1}{2}s(s-1)$	$\frac{\partial N_1}{\partial s} = \frac{1}{2}r(r+1)\frac{1}{2}(2s-1)$
$\frac{\partial N_2}{\partial r} = \frac{1}{2}(2r+1)\frac{1}{2}s(s+1)$	$\frac{\partial N_2}{\partial s} = \frac{1}{2}r(r+1)\frac{1}{2}(2s+1)$
$\frac{\partial N_3}{\partial r} = \frac{1}{2}(2r-1)\frac{1}{2}s(s+1)$	$\frac{\partial N_3}{\partial s} = \frac{1}{2}r(r-1)\frac{1}{2}(2s+1)$
$\frac{\partial N_4}{\partial r} = (-2r)\frac{1}{2}s(s-1)$	$\frac{\partial N_4}{\partial s} = (1-r^2)\frac{1}{2}(2s-1)$
$\frac{\partial N_5}{\partial r} = \frac{1}{2}(2r+1)(1-s^2)$	$\frac{\partial N_5}{\partial s} = \frac{1}{2}r(r+1)(-2s)$
$\frac{\partial N_6}{\partial r} = (-2r)\frac{1}{2}s(s+1)$	$\frac{\partial N_6}{\partial s} = (1-r^2)\frac{1}{2}(2s+1)$
$\frac{\partial N_7}{\partial r} = \frac{1}{2}(2r-1)(1-s^2)$	$\frac{\partial N_7}{\partial s} = \frac{1}{2}r(r-1)(-2s)$
$\frac{\partial N_8}{\partial r} = (-2r)(1-s^2)$	$\frac{\partial N_8}{\partial s} = (1-r^2)(-2s)$

4.5.3 Eight node serendipity basis functions in 2D ($Q_2^{(8)}$)

The serendipity elements are those rectangular elements which have no interior nodes [1361, p65].

Inside an element the local numbering of the nodes is as follows:

```
3=====6=====2
|       |       |   (r_0,s_0)=(-1,-1)   (r_4,s_4)=( 0,-1)
|       |       |   (r_1,s_1)=(+1,-1)   (r_5,s_5)=(+1, 0)
7=====+=====5   (r_2,s_2)=(+1,+1)   (r_6,s_6)=( 0,+1)
|       |       |   (r_3,s_3)=(-1,+1)   (r_7,s_7)=(-1, 0)
|       |       |
0=====4=====1
```

The main difference with the Q_2 element resides in the fact that there is no node in the middle of the element. The basis polynomial is then

$$f(r, s) = a + br + cs + drs + er^2 + fs^2 + gr^2s + hrs^2$$

Note that absence of the r^2s^2 term which was previously associated to the center node. We find that

$$N_0(r, s) = \frac{1}{4}(1-r)(1-s)(-r-s-1) \quad (136)$$

$$N_1(r, s) = \frac{1}{4}(1+r)(1-s)(r-s-1) \quad (137)$$

$$N_2(r, s) = \frac{1}{4}(1+r)(1+s)(r+s-1) \quad (138)$$

$$N_3(r, s) = \frac{1}{4}(1-r)(1+s)(-r+s-1) \quad (139)$$

$$N_4(r, s) = \frac{1}{2}(1-r^2)(1-s) \quad (140)$$

$$N_5(r, s) = \frac{1}{2}(1+r)(1-s^2) \quad (141)$$

$$N_6(r, s) = \frac{1}{2}(1-r^2)(1+s) \quad (142)$$

$$N_7(r, s) = \frac{1}{2}(1-r)(1-s^2) \quad (143)$$

The shape functions at the mid side nodes are products of a second order polynomial parallel to side and a linear function perpendicular to the side while shape functions for corner nodes are modifications of the bilinear quadrilateral element.

$$\frac{\partial N_0}{\partial r}(r, s) = -\frac{1}{4}(s-1)(2r+s) \quad (144)$$

$$\frac{\partial N_1}{\partial r}(r, s) = -\frac{1}{4}(s-1)(2r-s) \quad (145)$$

$$\frac{\partial N_2}{\partial r}(r, s) = \frac{1}{4}(s+1)(2r+s) \quad (146)$$

$$\frac{\partial N_3}{\partial r}(r, s) = \frac{1}{4}(s+1)(2r-s) \quad (147)$$

$$\frac{\partial N_4}{\partial r}(r, s) = r(s-1) \quad (148)$$

$$\frac{\partial N_5}{\partial r}(r, s) = \frac{1}{2}(1-s^2) \quad (149)$$

$$\frac{\partial N_6}{\partial r}(r, s) = -r(s+1) \quad (150)$$

$$\frac{\partial N_7}{\partial r}(r, s) = -\frac{1}{2}(1-s^2) \quad (151)$$

$$\frac{\partial N_0}{\partial s}(r, s) = -\frac{1}{4}(r-1)(r+2s) \quad (152)$$

$$\frac{\partial N_1}{\partial s}(r, s) = -\frac{1}{4}(r+1)(r-2s) \quad (153)$$

$$\frac{\partial N_2}{\partial s}(r, s) = \frac{1}{4}(r+1)(r+2s) \quad (154)$$

$$\frac{\partial N_3}{\partial s}(r, s) = \frac{1}{4}(r-1)(r-2s) \quad (155)$$

$$\frac{\partial N_4}{\partial s}(r, s) = -\frac{1}{2}(1-r^2) \quad (156)$$

$$\frac{\partial N_5}{\partial s}(r, s) = -(r+1)s \quad (157)$$

$$\frac{\partial N_6}{\partial s}(r, s) = \frac{1}{2}(1-r^2) \quad (158)$$

$$\frac{\partial N_7}{\partial s}(r, s) = (r-1)s \quad (159)$$

4.5.4 Bicubic basis functions in 2D (Q_3)

Inside an element the local numbering of the nodes is as follows:

12==13==14==15	$(r,s)_{\{00\}}=(-1,-1)$	$(r,s)_{\{08\}}=(-1,+1/3)$
	$(r,s)_{\{01\}}=(-1/3,-1)$	$(r,s)_{\{09\}}=(-1/3,+1/3)$
08==09==10==11	$(r,s)_{\{02\}}=(+1/3,-1)$	$(r,s)_{\{10\}}=(+1/3,+1/3)$
	$(r,s)_{\{03\}}=(+1,-1)$	$(r,s)_{\{11\}}=(+1,+1/3)$
04==05==06==07	$(r,s)_{\{04\}}=(-1,-1/3)$	$(r,s)_{\{12\}}=(-1,+1)$
	$(r,s)_{\{05\}}=(-1/3,-1/3)$	$(r,s)_{\{13\}}=(-1/3,+1)$
00==01==02==03	$(r,s)_{\{06\}}=(+1/3,-1/3)$	$(r,s)_{\{14\}}=(+1/3,+1)$
	$(r,s)_{\{07\}}=(+1,-1/3)$	$(r,s)_{\{15\}}=(+1,+1)$

The velocity shape functions are given by:

$$N_1(r) = (-1 + r + 9r^2 - 9r^3)/16$$

$$N_1(t) = (-1 + t + 9t^2 - 9t^3)/16$$

$$N_2(r) = (+9 - 27r - 9r^2 + 27r^3)/16$$

$$N_2(t) = (+9 - 27t - 9t^2 + 27t^3)/16$$

$$N_3(r) = (+9 + 27r - 9r^2 - 27r^3)/16$$

$$N_3(t) = (+9 + 27t - 9t^2 - 27t^3)/16$$

$$N_4(r) = (-1 - r + 9r^2 + 9r^3)/16$$

$$N_4(t) = (-1 - t + 9t^2 + 9t^3)/16$$

$N_{01}(r, s) = N_1(r)N_1(s) = (-1 + r + 9r^2 - 9r^3)/16 * (-1 + t + 9s^2 - 9s^3)/16$	(160)
$N_{02}(r, s) = N_2(r)N_1(s) = (+9 - 27r - 9r^2 + 27r^3)/16 * (-1 + t + 9s^2 - 9s^3)/16$	(161)
$N_{03}(r, s) = N_3(r)N_1(s) = (+9 + 27r - 9r^2 - 27r^3)/16 * (-1 + t + 9s^2 - 9s^3)/16$	(162)
$N_{04}(r, s) = N_4(r)N_1(s) = (-1 - r + 9r^2 + 9r^3)/16 * (-1 + t + 9s^2 - 9s^3)/16$	(163)
$N_{05}(r, s) = N_1(r)N_2(s) = (-1 + r + 9r^2 - 9r^3)/16 * (9 - 27s - 9s^2 + 27s^3)/16$	(164)
$N_{06}(r, s) = N_2(r)N_2(s) = (+9 - 27r - 9r^2 + 27r^3)/16 * (9 - 27s - 9s^2 + 27s^3)/16$	(165)
$N_{07}(r, s) = N_3(r)N_2(s) = (+9 + 27r - 9r^2 - 27r^3)/16 * (9 - 27s - 9s^2 + 27s^3)/16$	(166)
$N_{08}(r, s) = N_4(r)N_2(s) = (-1 - r + 9r^2 + 9r^3)/16 * (9 - 27s - 9s^2 + 27s^3)/16$	(167)
$N_{09}(r, s) = N_1(r)N_3(s) =$	
$N_{10}(r, s) = N_2(r)N_3(s) =$	
$N_{11}(r, s) = N_3(r)N_3(s) =$	
$N_{12}(r, s) = N_4(r)N_3(s) =$	
$N_{13}(r, s) = N_1(r)N_4(s) =$	
$N_{14}(r, s) = N_2(r)N_4(s) =$	
$N_{15}(r, s) = N_3(r)N_4(s) =$	
$N_{16}(r, s) = N_4(r)N_4(s) =$	

4.5.5 Biquartic basis functions in 2D (Q_4)

Inside an element the local numbering of the nodes is as follows:

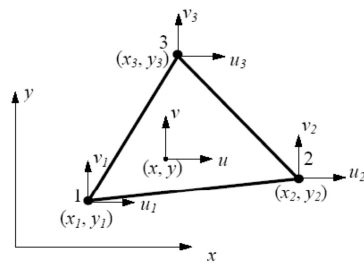
```
20====21====22====23====24
||    ||    ||    ||
15====16====17====18====19
||    ||    ||    ||
10====11====12====13====14
||    ||    ||    ||
05====06====07====08====09
||    ||    ||    ||
00====01====02====03====04
```

4.5.6 Linear basis functions for triangles in 2D (P_1)

Velocities (or displacements) (u, v) in a plane element are interpolated from nodal velocities (u_i, v_i) using shape functions N_i as follows,

$$\begin{pmatrix} u \\ v \end{pmatrix} = \begin{pmatrix} N_1 & 0 & N_2 & 0 & N_3 & 0 \\ 0 & N_1 & 0 & N_2 & 0 & N_3 \end{pmatrix} \cdot \begin{pmatrix} u_1 \\ v_1 \\ u_2 \\ v_2 \\ u_3 \\ v_3 \end{pmatrix}$$

This is the simplest 2D element, which is also called linear triangular element.



For this element, we have three nodes at the vertices of the triangle, which are numbered around the element in the counterclockwise direction. Each node has two degrees of freedom (can move in the x and y directions). The velocities u and v are assumed to be linear functions within the element, that is,

$$u = b_1 + b_2x + b_3y \quad v = b_4 + b_5x + b_6y$$

where b_i are constants to be determined and which depend on the triangle shape. Note that the strain rate components are then given by

$$\dot{\varepsilon}_{xx} = b_2 \quad \dot{\varepsilon}_{yy} = b_6 \quad \dot{\varepsilon}_{xy} = (b_3 + b_5)/2$$

and are constant throughout the element.

The velocities should satisfy the following six equations:

$$\begin{aligned} u_1 &= b_1 + b_2x_1 + b_3y_1 \\ u_2 &= b_1 + b_2x_2 + b_3y_2 \\ u_3 &= b_1 + b_2x_3 + b_3y_3 \\ v_1 &= b_4 + b_5x_1 + b_6y_1 \\ v_2 &= b_4 + b_5x_2 + b_6y_2 \\ v_3 &= b_4 + b_5x_3 + b_6y_3 \end{aligned}$$

This can be re-written:

$$\begin{pmatrix} u_1 \\ u_2 \\ u_3 \end{pmatrix} = \begin{pmatrix} 1 & x_1 & y_1 \\ 1 & x_2 & y_2 \\ 1 & x_3 & y_3 \end{pmatrix} \cdot \begin{pmatrix} b_1 \\ b_2 \\ b_3 \end{pmatrix}$$

In order to obtain b_1, b_2, b_3 we need to solve this system, or simply to compute the inverse of the 3×3 \mathbf{M} matrix, as explained in G.2.

We define $D = \det(\mathbf{M})$ and we get

$$\begin{aligned} \begin{pmatrix} b_1 \\ b_2 \\ b_3 \end{pmatrix} &= \frac{1}{D} \tilde{\mathbf{M}} \cdot \begin{pmatrix} u_1 \\ u_2 \\ u_3 \end{pmatrix} \\ \begin{pmatrix} b_4 \\ b_5 \\ b_6 \end{pmatrix} &= \frac{1}{D} \tilde{\mathbf{M}} \cdot \begin{pmatrix} v_1 \\ v_2 \\ v_3 \end{pmatrix} \end{aligned}$$

The matrix $\tilde{\mathbf{M}}$ writes:

$$\tilde{\mathbf{M}} = \begin{pmatrix} x_2y_3 - x_3y_2 & -(y_3 - y_2) & x_3 - x_2 \\ -(x_1y_3 - x_3y_1) & y_3 - y_1 & -(x_3 - x_1) \\ x_1y_2 - x_2y_1 & -(y_2 - y_1) & x_2 - x_1 \end{pmatrix}$$

ie,

$$\tilde{\mathbf{M}} = \begin{pmatrix} x_2y_3 - x_3y_2 & y_2 - y_3 & x_3 - x_2 \\ x_3y_1 - x_1y_3 & y_3 - y_1 & x_1 - x_3 \\ x_1y_2 - x_2y_1 & y_1 - y_2 & x_2 - x_1 \end{pmatrix}$$

and finally the linear shape functions are given by:

$$\begin{aligned} N_1(x, y) &= \frac{1}{D}[(x_2y_3 - x_3y_2) + (y_2 - y_3)x + (x_3 - x_2)y] \\ N_2(x, y) &= \frac{1}{D}[(x_3y_1 - x_1y_3) + (y_3 - y_1)x + (x_1 - x_3)y] \\ N_3(x, y) &= \frac{1}{D}[(x_1y_2 - x_2y_1) + (y_1 - y_2)x + (x_2 - x_1)y] \end{aligned}$$

Note that the area A of the triangle is given by:

$$A = \frac{1}{2}D = \frac{1}{2} \begin{vmatrix} 1 & x_1 & y_1 \\ 1 & x_2 & y_2 \\ 1 & x_3 & y_3 \end{vmatrix}$$

If we now consider the reference element in the reduced coordinates space (r, s) :

```

2
| \
|   \      (r_0,s_0)=(0,0)
|     \    (r_1,s_1)=(1,0)
|       \  (r_2,s_2)=(0,2)
0=====1

```

The basis polynomial is then

$$f(r, s) = a + br + cs$$

and the shape functions:

$$N_0(r, s) = 1 - r - s \quad (168)$$

$$N_1(r, s) = r \quad (169)$$

$$N_2(r, s) = s \quad (170)$$

4.5.7 Linear basis functions for quadrilaterals in 2D (P_1)

```

.=====.
|       |       |
|       3       |      (r_1,s_1)=(0,0)
|       |       |      (r_2,s_2)=(1/2,0)
.=====1==2==.  (r_3,s_3)=(0,1/2)
|       |       |
|       |       |
|       |       |
.=====.

```

Let us assume that the function $f(r, s)$ is to be approximated on $[-1, 1] \times [-1, 1]$ by

$$f(r, s) = a + br + cs$$

The function f then must fulfil:

$$\begin{aligned} f(r_1, s_1) &= a = f_1 \\ f(r_2, s_2) &= a + \frac{b}{2} = f_2 \\ f(r_3, s_3) &= a + \frac{c}{2} = f_3 \end{aligned} \quad (171)$$

This leads to :

$$a = f_1 \quad b = 2(f_2 - f_1) \quad c = 2(f_3 - f_1)$$

Then

$$f(r, s) = f_1 + 2(f_2 - f_1)r + 2(f_3 - f_1)s$$

or,

$$f(r) = \sum_{i=1}^3 N_i(r, s) f_i$$

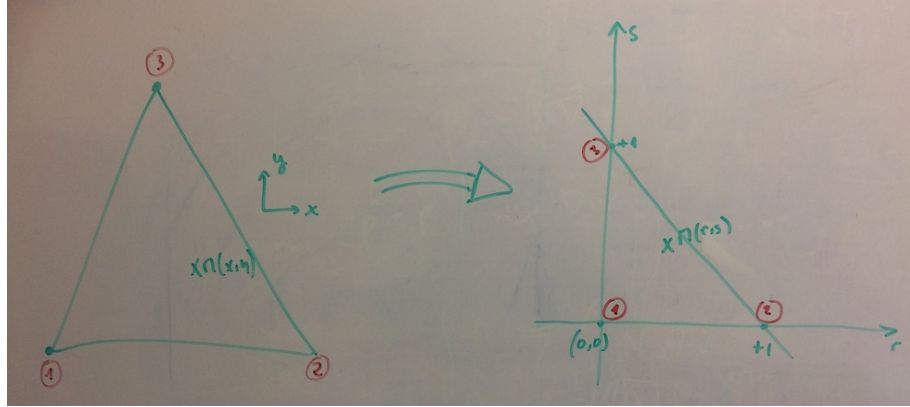
with

$$\begin{aligned} N_1(r) &= 1 - 2(r + s) \\ N_2(r) &= 2r \\ N_3(r) &= 2s \end{aligned} \quad (172)$$

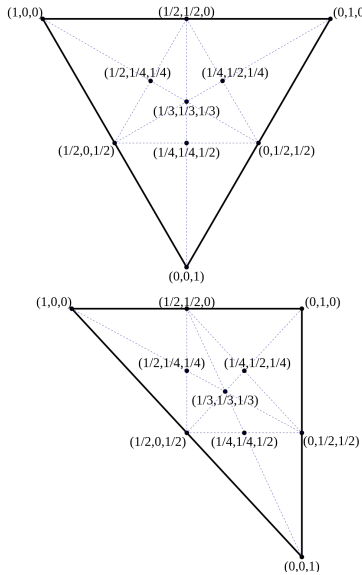
4.5.8 Enriched linear basis functions in triangles (P_1^+)

As we will see in Section 6.2.7 the above P_1 can be enriched with a so-called bubble function. The bubble function of the MINI element is described in [42] as being $\lambda_1\lambda_2\lambda_3$ where λ_i are the so-called barycentric coordinates¹⁶.

$$\begin{aligned}\lambda_1 &= \frac{(y_2 - y_3)(x - x_3) + (x_3 - x_2)(y - y_3)}{(y_2 - y_3)(x_1 - x_3) + (x_3 - x_2)(y_1 - y_3)} \\ \lambda_2 &= \frac{(y_3 - y_1)(x - x_3) + (x_1 - x_3)(y - y_3)}{(y_2 - y_3)(x_1 - x_3) + (x_3 - x_2)(y_1 - y_3)} \\ \lambda_3 &= 1 - \lambda_1 - \lambda_2\end{aligned}$$



representation of the element in the real coordinate system (x, y) and in the reduced coordinate system (r, s)



Barycentric coordinates $(\lambda_1, \lambda_2, \lambda_3)$ on an equilateral triangle and on a right triangle.

In the reference triangle, the barycentric coordinates write

$$\begin{aligned}\lambda_1 &= \frac{(s_2 - s_3)(r - r_3) + (r_3 - r_2)(s - s_3)}{(s_2 - s_3)(r_1 - r_3) + (r_3 - r_2)(s_1 - s_3)} = \frac{(-1)(r) + (-1)(s - 1)}{(-1)(0) + (-1)(-1)} = -r - s + 1 \\ \lambda_2 &= \frac{(s_3 - s_1)(r - r_3) + (r_1 - r_3)(s - s_3)}{(s_2 - s_3)(r_1 - r_3) + (r_3 - r_2)(s_1 - s_3)} = \frac{(1)(r) + (0)(s - 1)}{(-1)(0) + (-1)(-1)} = r \\ \lambda_3 &= 1 - \lambda_1 - \lambda_2 = 1 - (-r - s + 1) - r = s\end{aligned}$$

¹⁶https://en.wikipedia.org/wiki/Barycentric_coordinate_system

As we have seen before the bubble function is given by $\lambda_1\lambda_2\lambda_3 = (1 - r - s)rs$ and the polynomial form for the shape functions is given by:

$$f(r, s) = a + br + cs + d(1 - r - s)rs$$

Setting the location of the bubble at $r = s = 1/3$, i.e. $\lambda_1\lambda_2\lambda_3 = 1/3$, we then have

$$\begin{aligned} f(r_1, s_1) &= f_1 = a + br_1 + cs_1 + d(1 - r_1 - s_1)r_1s_1 = a \\ f(r_2, s_2) &= f_2 = a + br_2 + cs_2 + d(1 - r_2 - s_2)r_2s_2 = a + b \\ f(r_3, s_3) &= f_3 = a + br_3 + cs_3 + d(1 - r_3 - s_3)r_3s_3 = a + c \\ f(r_4, s_4) &= f_4 = a + br_4 + cs_4 + d(1 - r_4 - s_4)r_4s_4 = a + \frac{b}{3} + \frac{c}{3} + \frac{1}{27} \end{aligned}$$

where point 4 is the location of the bubble. This yields

$$a = f_1 \quad b = f_2 - a = f_2 - f_1 \quad c = f_3 - a = f_3 - f_1$$

and

$$d = 27(f_4 - a - \frac{b}{3} - \frac{c}{3}) = 27(f_4 - f_1 - \frac{f_2 - f_1}{3} - \frac{f_3 - f_1}{3}) = 27(f_4 - \frac{f_1}{3} - \frac{f_2}{3} - \frac{f_3}{3})$$

Finally

$$\begin{aligned} f(r, s) &= a + br + cs + d(1 - r - s)rs \\ &= f_1 + (f_2 - f_1)r + (f_3 - f_1)s + 27(f_4 - \frac{f_1}{3} - \frac{f_2}{3} - \frac{f_3}{3})(1 - r - s)rs \\ &= [1 - r - s - 9(1 - r - s)rs]f_1 + [r - 9(1 - r - s)rs]f_2 + [s - 9(1 - r - s)rs]f_3 + [27(1 - r - s)rs]f_4 \end{aligned}$$

so that

$$f(r, s) = \sum_{i=1}^4 N_i(r, s)f_i$$

with

$$\begin{aligned} N_1(r, s) &= 1 - r - s - 9(1 - r - s)rs \\ N_2(r, s) &= r - 9(1 - r - s)rs \\ N_3(r, s) &= s - 9(1 - r - s)rs \\ N_4(r, s) &= 27(1 - r - s)rs \end{aligned}$$

It is trivial to verify that $\sum_i N_i = 1$ for all values of r, s and the gradients of the shape functions are:

$$\frac{\partial N_1}{\partial r}(r, s) = -1 - 9(1 - 2r - s)s \quad (173)$$

$$\frac{\partial N_2}{\partial r}(r, s) = +1 - 9(1 - 2r - s)s \quad (174)$$

$$\frac{\partial N_3}{\partial r}(r, s) = -9(1 - 2r - s)s \quad (175)$$

$$\frac{\partial N_4}{\partial r}(r, s) = 27(1 - 2r - s)s \quad (176)$$

$$(177)$$

$$\frac{\partial N_1}{\partial s}(r, s) = -1 - 9(1 - r - 2s)r \quad (178)$$

$$\frac{\partial N_2}{\partial s}(r, s) = -9(1 - r - 2s)r \quad (179)$$

$$\frac{\partial N_3}{\partial s}(r, s) = +1 - 9(1 - r - 2s)r \quad (180)$$

$$\frac{\partial N_4}{\partial s}(r, s) = 27(1 - r - 2s)r \quad (181)$$

We have two coordinate systems for the element: the global coordinates (x, y) and the natural coordinates (r, s) . Inside the element, the relation between the two is given by

$$\begin{aligned} x &= N_1x_1 + N_2x_2 + N_3x_3 + N_4x_4 = \sum_i N_i(r, s)x_i \\ y &= N_1y_1 + N_2y_2 + N_3y_3 + N_4y_4 = \sum_i N_i(r, s)y_i \end{aligned} \quad (182)$$

or,

$$\begin{aligned} x &= [1 - r - s - 9(1 - r - s)rs]x_1 + [r - 9(1 - r - s)rs]x_2 + [s - 9(1 - r - s)rs]x_3 + [27(1 - r - s)rs]x_4 \\ &= x_1 - r(x_1 - x_2) - s(x_1 - x_3) + (1 - r - s)rs(-9x_1 - 9x_2 - 9x_3 + 27x_4) \\ &= x_1 - r(x_1 - x_2) - s(x_1 - x_3) + (1 - r - s)rs(-9x_1 - 9x_2 - 9x_3 + 27(x_1 + x_2 + x_3)/3) \\ &= x_1 - r(x_1 - x_2) - s(x_1 - x_3) \\ &= x_1 - rx_{12} - sx_{13} \\ y &= [1 - r - s - 9(1 - r - s)rs]y_1 + [r - 9(1 - r - s)rs]y_2 + [s - 9(1 - r - s)rs]y_3 + [27(1 - r - s)rs]y_4 \\ &= y_1 - r(y_1 - y_2) - s(y_1 - y_3) + (1 - r - s)rs(-9y_1 - 9y_2 - 9y_3 + 27y_4) \\ &= y_1 - r(y_1 - y_2) - s(y_1 - y_3) + (1 - r - s)rs(-9y_1 - 9y_2 - 9y_3 + 27(y_1 + y_2 + y_3)/3) \\ &= y_1 - r(y_1 - y_2) - s(y_1 - y_3) \\ &= y_1 - ry_{12} - sy_{13} \end{aligned}$$

4.5.9 Quadratic basis functions for triangles in 2D (P_2)

```

2
|\ \
| \   (r_0,s_0)=(0,0)  (r_3,s_3)=(1/2,0)
5   4   (r_1,s_1)=(1,0)  (r_4,s_4)=(1/2,1/2)
|     \   (r_2,s_2)=(0,1)  (r_5,s_5)=(0,1/2)
|       \
0====3====1

```

The basis polynomial is then

$$f(r, s) = c_1 + c_2r + c_3s + c_4r^2 + c_5rs + c_6s^2$$

We have

$$\begin{aligned} f_1 = f(r_1, s_1) &= c_1 \\ f_2 = f(r_2, s_2) &= c_1 + c_2 + c_4 \\ f_3 = f(r_3, s_3) &= c_1 + c_3 + c_6 \\ f_4 = f(r_4, s_4) &= c_1 + c_2/2 + c_4/4 \\ f_5 = f(r_5, s_5) &= c_1 + c_2/2 + c_3/2 \\ &\quad + c_4/4 + c_5/4 + c_6/4 \\ f_6 = f(r_6, s_6) &= c_1 + c_3/2 + c_6/4 \end{aligned}$$

This can be cast as $\mathbf{f} = \mathbf{A} \cdot \mathbf{c}$ where \mathbf{A} is a 6x6 matrix:

$$\mathbf{A} = \begin{pmatrix} 1 & 0 & 0 & 0 & 0 & 0 \\ 1 & 1 & 0 & 1 & 0 & 0 \\ 1 & 0 & 1 & 0 & 0 & 1 \\ 1 & 1/2 & 0 & 1/4 & 0 & 0 \\ 1 & 1/2 & 1/2 & 1/4 & 1/4 & 1/4 \\ 1 & 0 & 1/2 & 0 & 0 & 1/4 \end{pmatrix}$$

It is rather trivial to compute the inverse of this matrix:

$$\mathbf{A}^{-1} = \begin{pmatrix} 1 & 0 & 0 & 0 & 0 & 0 \\ -3 & -1 & 0 & 4 & 0 & 0 \\ -3 & 0 & -1 & 0 & 0 & 4 \\ 2 & 2 & 0 & -4 & 0 & 0 \\ 4 & 0 & 0 & -4 & 4 & -4 \\ 2 & 0 & 2 & 0 & 0 & -4 \end{pmatrix}$$

In the end, one obtains:

$$\begin{aligned} f(r, s) &= f_1 + (-3f_1 - f_2 + 4f_4)r + (-3f_1 - f_3 + 4f_6)s \\ &\quad + (2f_1 + 2f_2 - 4f_4)r^2 + (4f_1 - 4f_4 + 4f_5 - 4f_6)rs \\ &\quad + (2f_1 + 2f_3 - 4f_6)s^2 \\ &= \sum_{i=1}^6 N_i(r, s)f_i \end{aligned} \tag{183}$$

with

$N_1(r, s)$	$=$	$1 - 3r - 3s + 2r^2 + 4rs + 2s^2$
$N_2(r, s)$	$=$	$-r + 2r^2$
$N_3(r, s)$	$=$	$-s + 2s^2$
$N_4(r, s)$	$=$	$4r - 4r^2 - 4rs$
$N_5(r, s)$	$=$	$4rs$
$N_6(r, s)$	$=$	$4s - 4rs - 4s^2$

4.5.10 Enriched quadratic basis functions in triangles (P_2^+)

This is used by the Crouzeix-Raviart element, see Section 6.2.9.

```

03      (r_1,s_1)=(0,0)
|| \\
||  \\
||  \\
06  05      (r_5,s_5)=(1/2,1/2)
|| 07  \\
||    \\
01==04==02

```

The shape functions are given by:

[find reference](#)

$$N_1(r, s) = (1 - r - s)(1 - 2r - 2s + 3rs) \tag{184}$$

$$N_2(r, s) = r(2r - 1 + 3s - 3rs - 3s^2) \tag{185}$$

$$N_3(r, s) = s(2s - 1 + 3r - 3r^2 - 3rs) \tag{186}$$

$$N_4(r, s) = 4(1 - r - s)r(1 - 3s) \tag{187}$$

$$N_5(r, s) = 4rs[-2 + 3r + 3s] \tag{188}$$

$$N_6(r, s) = 4(1 - r - s)s(1 - 3r) \tag{189}$$

$$N_7(r, s) = 27(1 - r - s)rs \tag{190}$$

It is then easy to verify that for all shape functions we have $N_i(r_j, s_j) = \delta_{ij}$ where j denotes one of the seven nodes.

The derivatives are as follows:

$$\frac{\partial N_1}{\partial r}(r, s) = r(4 - 6s) - 3s^2 + 7s - 3 \quad (191)$$

$$\frac{\partial N_2}{\partial r}(r, s) = r(4 - 6s) - 3s^2 + 3s - 1 \quad (192)$$

$$\frac{\partial N_3}{\partial r}(r, s) = -3s(2r + s - 1) \quad (193)$$

$$\frac{\partial N_4}{\partial r}(r, s) = 4(3s - 1)(2r + s - 1) \quad (194)$$

$$\frac{\partial N_5}{\partial r}(r, s) = 4s(6r + 3s - 2) \quad (195)$$

$$\frac{\partial N_6}{\partial r}(r, s) = 4s(6r + 3s - 4) \quad (196)$$

$$\frac{\partial N_7}{\partial r}(r, s) = -27s(2r + s - 1) \quad (197)$$

$$\frac{\partial N_1}{\partial s}(r, s) = -3r^2 + r(7 - 6s) + 4s - 3 \quad (198)$$

$$\frac{\partial N_2}{\partial s}(r, s) = -3r(r + 2s - 1) \quad (199)$$

$$\frac{\partial N_3}{\partial s}(r, s) = -3r^2 + r(3 - 6s) + 4s - 1 \quad (200)$$

$$\frac{\partial N_4}{\partial s}(r, s) = 4r(3r + 6s - 4) \quad (201)$$

$$\frac{\partial N_5}{\partial s}(r, s) = 4r(3r + 6s - 2) \quad (202)$$

$$\frac{\partial N_6}{\partial s}(r, s) = 4(3r - 1)(r + 2s - 1) \quad (203)$$

$$\frac{\partial N_7}{\partial s}(r, s) = -27r(r + 2s - 1) \quad (204)$$

Note that the shape functions can also be expressed as a function of the barycentric coordinates, as in the MILAMIN code [426] or in Cuvelier et al, 1986 [425]¹⁷

```

03
|| \\
|| \\
||  \\
05  04
|| 07 \\
||      \\
01==06==02

```

$$N_1(\lambda_1, \lambda_2, \lambda_3) = \eta_1(2\eta_1 - 1) + 3\eta_1\eta_2\eta_3 \quad (205)$$

$$N_2(\lambda_1, \lambda_2, \lambda_3) = \eta_2(2\eta_2 - 1) + 3\eta_1\eta_2\eta_3 \quad (206)$$

$$N_3(\lambda_1, \lambda_2, \lambda_3) = \eta_3(2\eta_3 - 1) + 3\eta_1\eta_2\eta_3 \quad (207)$$

$$N_4(\lambda_1, \lambda_2, \lambda_3) = 4\eta_2\eta_3 - 12\eta_1\eta_2\eta_3 \quad (208)$$

$$N_5(\lambda_1, \lambda_2, \lambda_3) = 4\eta_1\eta_3 - 12\eta_1\eta_2\eta_3 \quad (209)$$

$$N_6(\lambda_1, \lambda_2, \lambda_3) = 4\eta_1\eta_2 - 12\eta_1\eta_2\eta_3 \quad (210)$$

$$N_7(\lambda_1, \lambda_2, \lambda_3) = 27\eta_1\eta_2\eta_3 \quad (211)$$

¹⁷Note that the numbering of the nodes in the book is different with respect to the one above.

VERIFY that when $\eta_1 = 1 - r - s$, $\eta_2 = r$ and $\eta_3 = s$ we find the above r, s shape functions

4.5.11 Cubic basis functions for triangles (P_3)

```

2
|\          (r_0,s_0)=(0,0)  (r_5,s_5)=(2/3,1/3)
| \        (r_1,s_1)=(1,0)  (r_6,s_6)=(1/3,2/3)
7   6      (r_2,s_2)=(0,1)  (r_7,s_7)=(0,2/3)
|   \
8   9   5    (r_3,s_3)=(1/3,0) (r_8,s_8)=(0,1/3)
|       \
0==3==4==1

```

The basis polynomial is then

$$f(r, s) = c_1 + c_2r + c_3s + c_4r^2 + c_5rs + c_6s^2 + c_7r^3 + c_8r^2s + c_9rs^2 + c_{10}s^3$$

$$N_0(r, s) = \frac{9}{2}(1 - r - s)(1/3 - r - s)(2/3 - r - s) \quad (212)$$

$$N_1(r, s) = \frac{9}{2}r(r - 1/3)(r - 2/3) \quad (213)$$

$$N_2(r, s) = \frac{9}{2}s(s - 1/3)(s - 2/3) \quad (214)$$

$$N_3(r, s) = \frac{27}{2}(1 - r - s)r(2/3 - r - s) \quad (215)$$

$$N_4(r, s) = \frac{27}{2}(1 - r - s)r(r - 1/3) \quad (216)$$

$$N_5(r, s) = \frac{27}{2}rs(r - 1/3) \quad (217)$$

$$N_6(r, s) = \frac{27}{2}rs(r - 2/3) \quad (218)$$

$$N_7(r, s) = \frac{27}{2}(1 - r - s)s(s - 1/3) \quad (219)$$

$$N_8(r, s) = \frac{27}{2}(1 - r - s)s(2/3 - r - s) \quad (220)$$

$$N_9(r, s) = 27rs(1 - r - s) \quad (221)$$

verify those

4.6 Elements and basis functions in 3D

4.6.1 Linear basis functions in tetrahedra (P_1)

$$(r_0, s_0) = (0, 0, 0)$$

$$(r_1, s_1) = (1, 0, 0)$$

$$(r_2, s_2) = (0, 2, 0)$$

$$(r_3, s_3) = (0, 0, 1)$$

The basis polynomial is given by

$$f(r, s, t) = c_0 + c_1r + c_2s + c_3t$$

$$f_1 = f(r_1, s_1, t_1) = c_0 \quad (222)$$

$$f_2 = f(r_2, s_2, t_2) = c_0 + c_1 \quad (223)$$

$$f_3 = f(r_3, s_3, t_3) = c_0 + c_2 \quad (224)$$

$$f_4 = f(r_4, s_4, t_4) = c_0 + c_3 \quad (225)$$

which yields:

$$c_0 = f_1 \quad c_1 = f_2 - f_1 \quad c_2 = f_3 - f_1 \quad c_3 = f_4 - f_1$$

$$\begin{aligned} f(r, s, t) &= c_0 + c_1 r + c_2 s + c_3 t \\ &= f_1 + (f_2 - f_1)r + (f_3 - f_1)s + (f_4 - f_1)t \\ &= f_1(1 - r - s - t) + f_2 r + f_3 s + f_4 t \\ &= \sum_i N_i(r, s, t) f_i \end{aligned}$$

Finally,

$N_1(r, s, t) = 1 - r - s - t$
$N_2(r, s, t) = r$
$N_3(r, s, t) = s$
$N_4(r, s, t) = t$

4.6.2 Enriched linear in tetrahedra(P_1^+)

These shape functions would be used in the MINI element, see Section 6.2.7.

In 3D the bubble function looks like $rst(1 - r - s - t)$ so that

$$f(r, s, t) = a + b r + c s + d t + e rst(1 - r - s - t)$$

We have node 1 at location $(r, s, t) = (0, 0, 0)$, node 2 at $(r, s, t) = (1, 0, 0)$, node 3 at $(r, s, t) = (0, 1, 0)$, node 4 at $(r, s, t) = (0, 0, 1)$ and we set the location of the bubble (node 5) at $r = s = t = 1/4$ so that

$$f(r_1, s_1, t_1) = f_1 = a + b r_1 + c s_1 + d t_1 + e r_1 s_1 t_1 (1 - r_1 - s_1 - t_1) \quad (226)$$

$$f(r_2, s_2, t_2) = f_2 = a + b r_2 + c s_2 + d t_2 + e r_2 s_2 t_2 (1 - r_2 - s_2 - t_2) \quad (227)$$

$$f(r_3, s_3, t_3) = f_3 = a + b r_3 + c s_3 + d t_3 + e r_3 s_3 t_3 (1 - r_3 - s_3 - t_3) \quad (228)$$

$$f(r_4, s_4, t_4) = f_4 = a + b r_4 + c s_4 + d t_4 + e r_4 s_4 t_4 (1 - r_4 - s_4 - t_4) \quad (229)$$

$$f(r_5, s_5, t_5) = f_5 = a + b r_5 + c s_5 + d t_5 + e r_5 s_5 t_5 (1 - r_5 - s_5 - t_5) \quad (230)$$

i.e.,

$$f_1 = a \quad (231)$$

$$f_2 = a + b \quad (232)$$

$$f_3 = a + c \quad (233)$$

$$f_4 = a + d \quad (234)$$

$$f_5 = a + b/4 + c/4 + d/4 + e/64(1 - 1/4 - 1/4 - 1/4) \quad (235)$$

$$= a + b/4 + c/4 + d/4 + e/256 \quad (236)$$

Then

$$a = f_1 \quad (237)$$

$$b = f_2 - f_1 \quad (238)$$

$$c = f_3 - f_1 \quad (239)$$

$$d = f_4 - f_1 \quad (240)$$

$$e = 256(f_5 - a - b/4 - c/4 - d/4) \quad (241)$$

$$= 256(f_5 - f_1 - (f_2 - f_1)/4 - (f_3 - f_1)/4 - (f_4 - f_1)/4) \quad (242)$$

$$= 256(-f_1/4 - f_2/4 - f_3/4 - f_4/4 + f_5) \quad (243)$$

$$= 64(-f_1 - f_2 - f_3 - f_4 + 4f_5) \quad (244)$$

Finally:

$$\begin{aligned}
f(r, s, t) &= a + br + cs + dt + erst(1 - r - s - t) \\
&= f_1 + (f_2 - f_1)r + (f_3 - f_1)s + (f_4 - f_1)t + 64(-f_1 - f_2 - f_3 - f_4 + 4f_5)rst(1 - r - s - t) \\
&= f_1[1 - r - s - t - 64rst(1 - r - s - t)] \\
&\quad + f_2[r - 64rst(1 - r - s - t)] \\
&\quad + f_3[s - 64rst(1 - r - s - t)] \\
&\quad + f_4[t - 64rst(1 - r - s - t)] \\
&\quad + f_5[256rst(1 - r - s - t)] \\
&= \sum_{i=1}^5 N_i(r, s, t) f_i
\end{aligned} \tag{245}$$

with

$$N_1(r, s, t) = 1 - r - s - t - 64rst(1 - r - s - t) \tag{246}$$

$$N_2(r, s, t) = r - 64rst(1 - r - s - t) \tag{247}$$

$$N_3(r, s, t) = s - 64rst(1 - r - s - t) \tag{248}$$

$$N_4(r, s, t) = t - 64rst(1 - r - s - t) \tag{249}$$

$$N_5(r, s, t) = +256rst(1 - r - s - t) \tag{250}$$

The derivatives are given by:

$$\frac{\partial N_1}{\partial r}(r, s, t) = -1 - 64st(1 - 2r - s - t)$$

$$\frac{\partial N_2}{\partial r}(r, s, t) = +1 - 64st(1 - 2r - s - t)$$

$$\frac{\partial N_3}{\partial r}(r, s, t) = -64st(1 - 2r - s - t)$$

$$\frac{\partial N_4}{\partial r}(r, s, t) = -64st(1 - 2r - s - t)$$

$$\frac{\partial N_5}{\partial r}(r, s, t) = 256st(1 - 2r - s - t)$$

$$\frac{\partial N_1}{\partial s}(r, s, t) = -1 - 64rt(1 - r - 2s - t)$$

$$\frac{\partial N_2}{\partial s}(r, s, t) = -64rt(1 - r - 2s - t)$$

$$\frac{\partial N_3}{\partial s}(r, s, t) = +1 - 64rt(1 - r - 2s - t)$$

$$\frac{\partial N_4}{\partial s}(r, s, t) = -64rt(1 - r - 2s - t)$$

$$\frac{\partial N_5}{\partial s}(r, s, t) = 256rt(1 - r - 2s - t)$$

$$\frac{\partial N_1}{\partial t}(r, s, t) = -1 - 64rs(1 - r - s - 2t)$$

$$\frac{\partial N_2}{\partial t}(r, s, t) = -64rs(1 - r - s - 2t)$$

$$\frac{\partial N_3}{\partial t}(r, s, t) = -64rs(1 - r - s - 2t)$$

$$\frac{\partial N_4}{\partial t}(r, s, t) = +1 - 64rs(1 - r - s - 2t)$$

$$\frac{\partial N_5}{\partial t}(r, s, t) = 256rs(1 - r - s - 2t)$$

4.6.3 Triquadratic basis functions in 3D (Q_2)

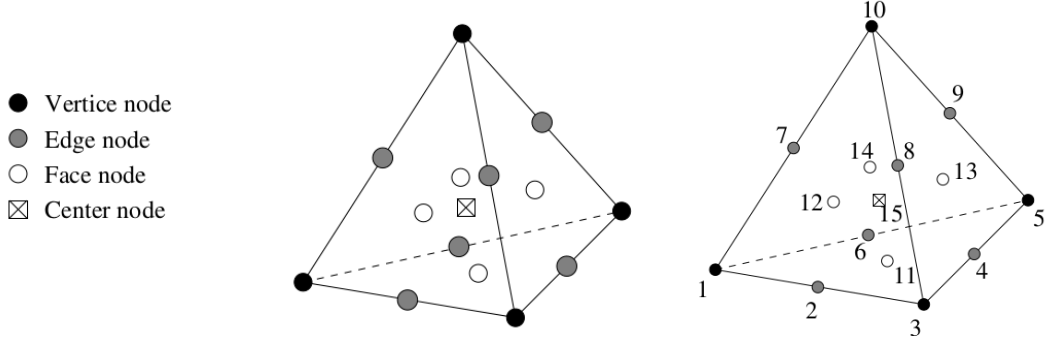
```

t
|
. --s
/
r
          05=====16=====08
          |       |       |
          |       |       |
13=====26=====15  17=====25=====20
          |       |       |
          |       |       |
06=====14=====07  22=====27=====24  01=====12=====04 @ r=-1
          |       |       |
          |       |       |
18=====23=====14  09=====21=====11 @ r=0
          |       |       |
          |       |       |
02=====10=====03 @ r=+1

```

$$\begin{aligned}
N_1 &= 0.5r(r-1) 0.5s(s-1) 0.5t(t-1) \\
N_2 &= 0.5r(r+1) 0.5s(s-1) 0.5t(t-1) \\
N_3 &= 0.5r(r+1) 0.5s(s+1) 0.5t(t-1) \\
N_4 &= 0.5r(r-1) 0.5s(s+1) 0.5t(t-1) \\
N_5 &= 0.5r(r-1) 0.5s(s-1) 0.5t(t+1) \\
N_6 &= 0.5r(r+1) 0.5s(s-1) 0.5t(t+1) \\
N_7 &= 0.5r(r+1) 0.5s(s+1) 0.5t(t+1) \\
N_8 &= 0.5r(r-1) 0.5s(s+1) 0.5t(t+1) \\
N_9 &= (1 - r^2) 0.5s(s-1) 0.5t(t-1) \\
N_{10} &= 0.5r(r+1) (1 - s^2) 0.5t(t-1) \\
N_{11} &= (1 - r^2) 0.5s(s+1) 0.5t(t-1) \\
N_{12} &= 0.5r(r-1) (1 - s^2) 0.5t(t-1) \\
N_{13} &= (1 - r^2) 0.5s(s-1) 0.5t(t+1) \\
N_{14} &= 0.5r(r+1) (1 - s^2) 0.5t(t+1) \\
N_{15} &= (1 - r^2) 0.5s(s+1) 0.5t(t+1) \\
N_{16} &= 0.5r(r-1) (1 - s^2) 0.5t(t+1) \\
N_{17} &= 0.5r(r-1) 0.5s(s-1) (1 - t^2) \\
N_{18} &= 0.5r(r+1) 0.5s(s-1) (1 - t^2) \\
N_{19} &= 0.5r(r+1) 0.5s(s+1) (1 - t^2) \\
N_{20} &= 0.5r(r-1) 0.5s(s+1) (1 - t^2) \\
N_{21} &= (1 - r^2) (1 - s^2) 0.5t(t-1) \\
N_{22} &= (1 - r^2) 0.5s(s-1) (1 - t^2) \\
N_{23} &= 0.5r(r+1) (1 - s^2) (1 - t^2) \\
N_{24} &= (1 - r^2) 0.5s(s+1) (1 - t^2) \\
N_{25} &= 0.5r(r-1) (1 - s^2) (1 - t^2) \\
N_{26} &= (1 - r^2) (1 - s^2) 0.5t(t+1) \\
N_{27} &= (1 - r^2) (1 - s^2) (1 - t^2)
\end{aligned}$$

4.6.4 Enriched quadratic basis functions in tetrahedra (P_2^+)



The velocity shape functions are:

$$\phi_i = \lambda_i(2\lambda_i - 1) + 3(\lambda_i\lambda_j\lambda_k + \lambda_i\lambda_j\lambda_l + \lambda_i\lambda_k\lambda_l) - 4\lambda_i\lambda_j\lambda_k\lambda_l \quad (251)$$

$$\phi_{ij} = 4\lambda_i\lambda_j - 12(\lambda_i\lambda_j\lambda_k + \lambda_i\lambda_j\lambda_l) + 32\lambda_i\lambda_j\lambda_k\lambda_l \quad (252)$$

$$\phi_{ijk} = 27\lambda_i\lambda_j\lambda_k - 108\lambda_i\lambda_j\lambda_k\lambda_l \quad (253)$$

$$\phi_c = 256\lambda_i\lambda_j\lambda_k\lambda_l \quad (254)$$

REFS ??? better definition of functions !

4.6.5 Linear basis functions for tetrahedra (P_1)

This is essentially in the $Q_2 \times P_{-1}$ element.

I choose the reduced coordinates of the pressure nodes to be :

point	r	s	t
1	1/2	-1/2	-1/2
2	-1/2	1/2	-1/2
3	-1/2	-1/2	1/2
4	1/2	1/2	1/2

Inside the element the pressure is given as a linear function of the reduced coordinates r, s, t :

$$p(r, s, t) = a + br + cs + dt$$

This expression must exactly interpolate the pressure at all four pressure nodes:

$$\begin{aligned} p_1 &= p(r_1, s_1, t_1) = a + br_1 + cs_1 + dt_1 = a + b/2 - c/2 - d/2 \\ p_2 &= p(r_2, s_2, t_2) = a + br_2 + cs_2 + dt_2 = a - b/2 + c/2 - d/2 \\ p_3 &= p(r_3, s_3, t_3) = a + br_3 + cs_3 + dt_3 = a - b/2 - c/2 + d/2 \\ p_4 &= p(r_4, s_4, t_4) = a + br_4 + cs_4 + dt_4 = a + b/2 + c/2 + d/2 \end{aligned}$$

or,

$$\begin{pmatrix} 1 & 1/2 & -1/2 & -1/2 \\ 1 & -1/2 & +1/2 & -1/2 \\ 1 & -1/2 & -1/2 & +1/2 \\ 1 & 1/2 & +1/2 & +1/2 \end{pmatrix} \begin{pmatrix} a \\ b \\ c \\ d \end{pmatrix} = \begin{pmatrix} p_1 \\ p_2 \\ p_3 \\ p_4 \end{pmatrix}$$

The matrix is invertible and we get:

$$\begin{pmatrix} a \\ b \\ c \\ d \end{pmatrix} = \begin{pmatrix} 1/4 & 1/4 & 1/4 & 1/4 \\ 1/2 & -1/2 & -1/2 & 1/2 \\ -1/2 & 1/2 & -1/2 & 1/2 \\ -1/2 & -1/2 & 1/2 & 1/2 \end{pmatrix} \begin{pmatrix} p_1 \\ p_2 \\ p_3 \\ p_4 \end{pmatrix}$$

so

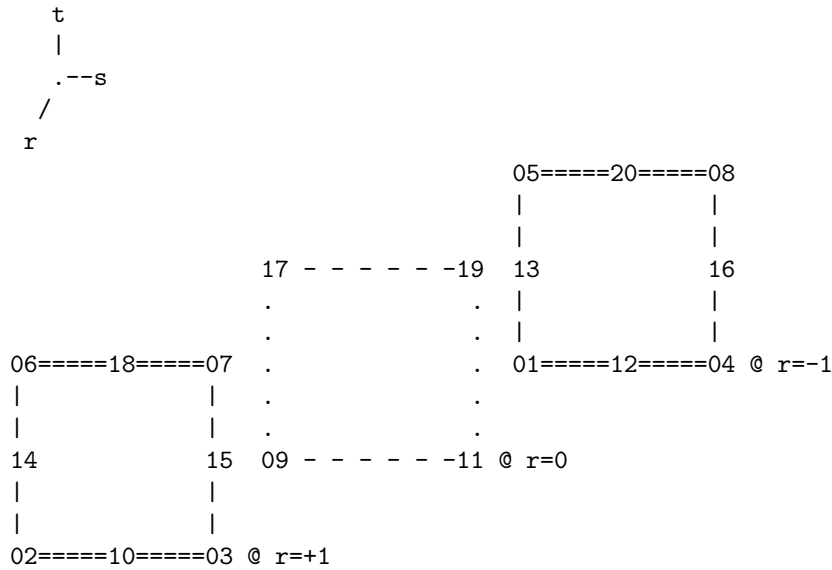
$$\begin{aligned}
 p(r, s, t) &= a + br + cs + dt \\
 &= \frac{1}{4}(p_1 + p_2 + p_3 + p_4) + \frac{1}{2}(p_1 - p_2 - p_3 + p_4)r + \frac{1}{2}(-p_1 + p_2 - p_3 + p_4)s + \frac{1}{2}(-p_1 - p_2 + p_3 + p_4)t \\
 &= \frac{1}{4}(1 + 2r - 2s - 2t)p_1 + \frac{1}{4}(1 - 2r + 2s - 2t)p_2 + \frac{1}{4}(1 - 2r - 2s + 2t)p_3 + \frac{1}{4}(1 + 2r + 2s + 2t)p_4 \\
 &= \sum_{i=1}^4 N_i(r, s, t)p_i
 \end{aligned} \tag{255}$$

with

$$\begin{aligned}
 N_1(r, s, t) &= \frac{1}{4}(1 + 2r - 2s - 2t) \\
 N_2(r, s, t) &= \frac{1}{4}(1 - 2r + 2s - 2t) \\
 N_3(r, s, t) &= \frac{1}{4}(1 - 2r - 2s + 2t) \\
 N_4(r, s, t) &= \frac{1}{4}(1 + 2r + 2s + 2t)
 \end{aligned}$$

4.6.6 20-node serendipity basis functions in 3D ($Q_2^{(20)}$)

The serendipity elements are those rectangular elements which have no interior nodes [1361, p91].

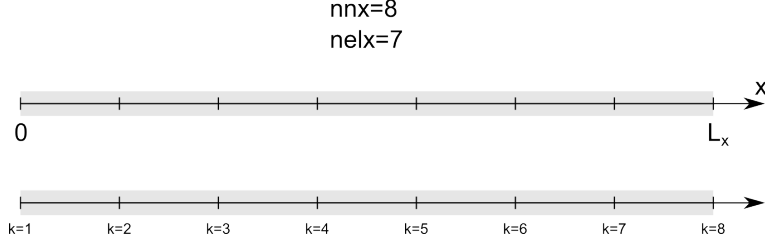


find/build shape functions!

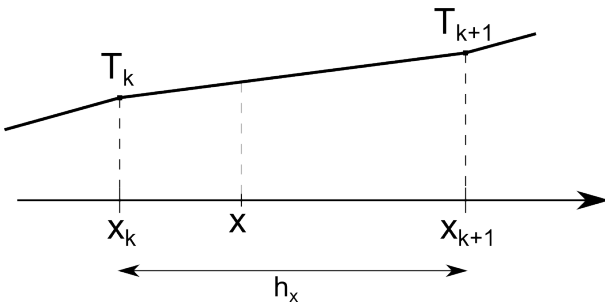
5 Solving the heat transport equation with linear Finite Elements

5.1 The diffusion equation in 1D

Let us consider the following one-dimensional grid:



Its spans the domain Ω of length L_x . It is discretised by means of n_{nx} nodes and $n_{elx} = n_{nx} - 1$ elements. Zooming in on element which is bounded by two nodes k and $k + 1$, its size (also sometimes called diameter) is $h_x = x_{k+1} - x_k$, and the temperature field we wish to compute is located on those nodes so that they are logically called T_k and T_{k+1} :



We focus here on the 1D diffusion equation (no advection, no heat sources):

$$\rho C_p \frac{\partial T}{\partial t} = \frac{\partial}{\partial x} \left(k \frac{\partial T}{\partial x} \right) \quad (256)$$

This is the **strong form** of the ODE to solve. I can multiply this equation by a function¹⁸ $f(x)$ and integrate it over Ω :

$$\int_{\Omega} f(x) \rho C_p \frac{\partial T}{\partial t} dx = \int_{\Omega} f(x) \frac{\partial}{\partial x} \left(k \frac{\partial T}{\partial x} \right) dx \quad (257)$$

Looking at the right hand side, it is of the form $\int uv'$ so that I naturally integrate it by parts:

$$\int_{\Omega} f(x) \frac{\partial}{\partial x} \left(k \frac{\partial T}{\partial x} \right) dx = \left[f(x) k \frac{\partial T}{\partial x} \right]_{\partial\Omega} - \int_{\Omega} \frac{\partial f}{\partial x} k \frac{\partial T}{\partial x} dx \quad (258)$$

Assuming there is no heat flux prescribed on the boundary (i.e. $q_x = -k \partial T / \partial x = 0$),

NOT happy with this statement!!

then:

$$\int_{\Omega} f(x) \frac{\partial}{\partial x} \left(k \frac{\partial T}{\partial x} \right) dx = - \int_{\Omega} \frac{\partial f}{\partial x} k \frac{\partial T}{\partial x} dx \quad (259)$$

We then obtain the **weak form** of the diffusion equation in 1D:

$$\int_{\Omega} f(x) \rho C_p \frac{\partial T}{\partial t} dx + \int_{\Omega} \frac{\partial f}{\partial x} k \frac{\partial T}{\partial x} dx = 0$$

(260)

¹⁸This function should be well-behaved with special properties, but we here assume it is a polynomial function.

We then use the additive property of the integral $\int_{\Omega} \dots = \sum_{elts} \int_{\Omega_e} \dots$ so that

$$\sum_{elts} \left(\underbrace{\int_{\Omega_e} f(x) \rho C_p \frac{\partial T}{\partial t} dx}_{\Lambda_f^e} + \underbrace{\int_{\Omega_e} \frac{\partial f}{\partial x} k \frac{\partial T}{\partial x} dx}_{\Upsilon_f^e} \right) = 0 \quad (261)$$

In order to compute these integrals (analytically or by means of a numerical quadrature), we will need to evaluate T inside the element. However, inside the element, the temperature is not known: all we have is the temperature at the nodes. For $x \in [x_k, x_{k+1}]$ we need to come up with a way to compute the temperature at this location. It makes sense to think that $T(x)$ will then be a function of the temperature at the nodes, i.e. $T(x) = \alpha T_k + \beta T_{k+1}$ where α and β are coefficients. One over-simplified approach would be to assign $T(x) = (T_k + T_{k+1})/2$ but this would make the temperature discontinuous from element to element. The rather logical solution to this problem is a linear temperature field between T_k and T_{k+1} :

$$T(x) = \underbrace{\frac{x_{k+1} - x}{h_x} T_k}_{N_k^\theta(x)} + \underbrace{\frac{x - x_k}{h_x} T_{k+1}}_{N_{k+1}^\theta(x)}$$

where $N_k^\theta(x)$ is the (temperature) shape function associated to node k and $N_{k+1}^\theta(x)$ is the shape function associated to node $k+1$.

Rather reassuringly, we have:

- $x = x_k$ yields $T(x) = T_k$
- $x = x_{k+1}$ yields $T(x) = T_{k+1}$
- $x = (x_k + x_{k+1})/2$ yields $T(x) = (T_k + T_{k+1})/2$

In what follows we abbreviate $\partial T / \partial x$ by \dot{T} . Let us compute Λ_f^e and Υ_f^e separately.

$$\begin{aligned} \Lambda_f^e &= \int_{x_k}^{x_{k+1}} f(x) \rho C_p \dot{T}(x) dx \\ &= \int_{x_k}^{x_{k+1}} f(x) \rho C_p [N_k^\theta(x) \dot{T}_k + N_{k+1}^\theta(x) \dot{T}_{k+1}] dx \\ &= \int_{x_k}^{x_{k+1}} f(x) \rho C_p N_k^\theta(x) \dot{T}_k dx + \int_{x_k}^{x_{k+1}} f(x) \rho C_p N_{k+1}^\theta(x) \dot{T}_{k+1} dx \\ &= \left(\int_{x_k}^{x_{k+1}} f(x) \rho C_p N_k^\theta(x) dx \right) \dot{T}_k + \left(\int_{x_k}^{x_{k+1}} f(x) \rho C_p N_{k+1}^\theta(x) dx \right) \dot{T}_{k+1} \end{aligned}$$

Taking $f(x) = N_k^\theta(x)$ and omitting '(x)' in the rhs:

$$\Lambda_{N_k^\theta}^e = \left(\int_{x_k}^{x_{k+1}} \rho C_p N_k^\theta N_k^\theta dx \right) \dot{T}_k + \left(\int_{x_k}^{x_{k+1}} \rho C_p N_k^\theta N_{k+1}^\theta dx \right) \dot{T}_{k+1}$$

Taking $f(x) = N_{k+1}^\theta(x)$ and omitting '(x)' in the rhs:

$$\Lambda_{N_{k+1}^\theta}^e = \left(\int_{x_k}^{x_{k+1}} \rho C_p N_{k+1}^\theta N_k^\theta dx \right) \dot{T}_k + \left(\int_{x_k}^{x_{k+1}} \rho C_p N_{k+1}^\theta N_{k+1}^\theta dx \right) \dot{T}_{k+1}$$

We can rearrange these last two equations as follows:

$$\begin{pmatrix} \Lambda_{N_k^\theta}^e \\ \Lambda_{N_{k+1}^\theta}^e \end{pmatrix} = \begin{pmatrix} \int_{x_k}^{x_{k+1}} N_k^\theta \rho C_p N_k^\theta dx & \int_{x_k}^{x_{k+1}} N_k^\theta \rho C_p N_{k+1}^\theta dx \\ \int_{x_k}^{x_{k+1}} N_{k+1}^\theta \rho C_p N_k^\theta dx & \int_{x_k}^{x_{k+1}} N_{k+1}^\theta \rho C_p N_{k+1}^\theta dx \end{pmatrix} \cdot \begin{pmatrix} \dot{T}_k \\ \dot{T}_{k+1} \end{pmatrix}$$

and we can take the integrals outside of the matrix:

$$\begin{pmatrix} \Lambda_{N_k^\theta}^e \\ \Lambda_{N_{k+1}^\theta}^e \end{pmatrix} = \left[\int_{x_k}^{x_{k+1}} \rho C_p \begin{pmatrix} N_k^\theta N_k^\theta & N_k^\theta N_{k+1}^\theta \\ N_{k+1}^\theta N_k^\theta & N_{k+1}^\theta N_{k+1}^\theta \end{pmatrix} dx \right] \cdot \begin{pmatrix} \dot{T}_k \\ \dot{T}_{k+1} \end{pmatrix}$$

Finally, we can define the vectors

$$\vec{N}^T = \begin{pmatrix} N_k^\theta(x) \\ N_{k+1}^\theta(x) \end{pmatrix}$$

and

$$\vec{T}^e = \begin{pmatrix} T_k \\ T_{k+1} \end{pmatrix} \quad \dot{\vec{T}}^e = \begin{pmatrix} \dot{T}_k \\ \dot{T}_{k+1} \end{pmatrix}$$

so that

$$\begin{pmatrix} \Lambda_{N_k^\theta}^e \\ \Lambda_{N_{k+1}^\theta}^e \end{pmatrix} = \left(\int_{x_k}^{x_{k+1}} \vec{N}^T \rho C_p \vec{N} dx \right) \cdot \dot{\vec{T}}^e$$

Back to the diffusion term:

$$\begin{aligned} \Upsilon_f^e &= \int_{x_k}^{x^{k+1}} \frac{\partial f}{\partial x} k \frac{\partial T}{\partial x} dx \\ &= \int_{x_k}^{x^{k+1}} \frac{\partial f}{\partial x} k \frac{\partial (N_k^\theta(x) T_k + N_{k+1}^\theta(x) T_{k+1})}{\partial x} dx \\ &= \left(\int_{x_k}^{x^{k+1}} \frac{\partial f}{\partial x} k \frac{\partial N_k^\theta}{\partial x} dx \right) T_k + \left(\int_{x_k}^{x^{k+1}} \frac{\partial f}{\partial x} k \frac{\partial N_{k+1}^\theta}{\partial x} dx \right) T_{k+1} \end{aligned}$$

Taking $f(x) = N_k^\theta(x)$

$$\Upsilon_{N_k^\theta}^e = \left(\int_{x_k}^{x^{k+1}} k \frac{\partial N_k^\theta}{\partial x} \frac{\partial N_k^\theta}{\partial x} dx \right) T_k + \left(\int_{x_k}^{x^{k+1}} k \frac{\partial N_k^\theta}{\partial x} \frac{\partial N_{k+1}^\theta}{\partial x} dx \right) T_{k+1}$$

Taking $f(x) = N_{k+1}^\theta(x)$

$$\begin{aligned} \Upsilon_{N_{k+1}^\theta}^e &= \left(\int_{x_k}^{x^{k+1}} k \frac{\partial N_{k+1}^\theta}{\partial x} \frac{\partial N_k^\theta}{\partial x} dx \right) T_k + \left(\int_{x_k}^{x^{k+1}} k \frac{\partial N_{k+1}^\theta}{\partial x} \frac{\partial N_{k+1}^\theta}{\partial x} dx \right) T_{k+1} \\ \begin{pmatrix} \Upsilon_{N_k^\theta}^e \\ \Upsilon_{N_{k+1}^\theta}^e \end{pmatrix} &= \begin{pmatrix} \int_{x_k}^{x^{k+1}} \frac{\partial N_k^\theta}{\partial x} k \frac{\partial N_k^\theta}{\partial x} dx & \int_{x_k}^{x^{k+1}} \frac{\partial N_k^\theta}{\partial x} k \frac{\partial N_{k+1}^\theta}{\partial x} dx \\ \int_{x_k}^{x^{k+1}} \frac{\partial N_{k+1}^\theta}{\partial x} k \frac{\partial N_k^\theta}{\partial x} dx & \int_{x_k}^{x^{k+1}} \frac{\partial N_{k+1}^\theta}{\partial x} k \frac{\partial N_{k+1}^\theta}{\partial x} dx \end{pmatrix} \cdot \begin{pmatrix} T_k \\ T_{k+1} \end{pmatrix} \end{aligned}$$

or,

$$\begin{pmatrix} \Upsilon_{N_k^\theta}^e \\ \Upsilon_{N_{k+1}^\theta}^e \end{pmatrix} = \left[\int_{x_k}^{x^{k+1}} k \begin{pmatrix} \frac{\partial N_k^\theta}{\partial x} \frac{\partial N_k^\theta}{\partial x} & \frac{\partial N_k^\theta}{\partial x} \frac{\partial N_{k+1}^\theta}{\partial x} \\ \frac{\partial N_{k+1}^\theta}{\partial x} \frac{\partial N_k^\theta}{\partial x} & \frac{\partial N_{k+1}^\theta}{\partial x} \frac{\partial N_{k+1}^\theta}{\partial x} \end{pmatrix} dx \right] \cdot \begin{pmatrix} T_k \\ T_{k+1} \end{pmatrix}$$

Finally, we can define the vector

$$\vec{B}^T = \begin{pmatrix} \frac{\partial N_k^\theta}{\partial x} \\ \frac{\partial N_{k+1}^\theta}{\partial x} \end{pmatrix}$$

so that

$$\begin{pmatrix} \Upsilon_{N_k^\theta}^e \\ \Upsilon_{N_{k+1}^\theta}^e \end{pmatrix} = \left(\int_{x_k}^{x_{k+1}} \vec{B}^T k \vec{B} dx \right) \cdot \vec{T}^e$$

The weak form discretised over 1 element becomes

$$\underbrace{\left(\int_{x_k}^{x_{k+1}} \vec{N}^T \rho C_p \vec{N} dx \right) \cdot \dot{\vec{T}}^e}_{\mathbf{M}^e} + \underbrace{\left(\int_{x_k}^{x_{k+1}} \vec{B}^T k \vec{B} dx \right) \cdot \vec{T}^e}_{\mathbf{K}_d^e} = 0$$

or,

$$\boxed{\mathbf{M}^e \cdot \dot{\vec{T}}^e + \mathbf{K}_d^e \cdot \vec{T}^e = 0}$$

or,

$$\boxed{\mathbf{M}^e \cdot \frac{\partial \vec{T}^e}{\partial t} + \mathbf{K}_d^e \cdot \vec{T}^e = 0}$$

\mathbf{M}^e is commonly called the mass matrix, or capacitance matrix [1361, p103].

Using a backward first order in time discretisation for the time derivative:

$$\dot{\vec{T}} = \frac{\partial \vec{T}}{\partial t} = \frac{\vec{T}^{new} - \vec{T}^{old}}{\delta t}$$

we get

$$\mathbf{M}^e \cdot \frac{\vec{T}^{new} - \vec{T}^{old}}{\delta t} + \mathbf{K}_d^e \cdot \vec{T}^{new} = 0$$

or,

$$\boxed{(\mathbf{M}^e + \mathbf{K}_d^e \delta t) \cdot \vec{T}^{new} = \mathbf{M}^e \cdot \vec{T}^{old}}$$

with

$$\mathbf{M}^e = \int_{x_k}^{x_{k+1}} \vec{N}^T \rho C_p \vec{N} dx \quad \mathbf{K}_d^e = \int_{x_k}^{x_{k+1}} \vec{B}^T k \vec{B} dx$$

Let us compute \mathbf{M} for an element:

$$\mathbf{M}^e = \int_{x_k}^{x_{k+1}} \vec{N}^T \rho C_p \vec{N} dx$$

with

$$\vec{N}^T = \begin{pmatrix} N_k(x) \\ N_{k+1}(x) \end{pmatrix} = \begin{pmatrix} \frac{x_{k+1}-x}{h_x} \\ \frac{x-x_k}{h_x} \end{pmatrix}$$

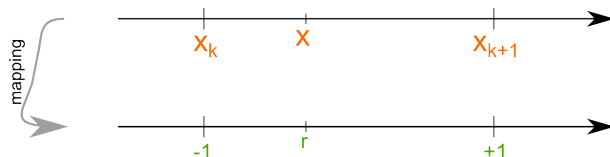
Then

$$\mathbf{M}^e = \begin{pmatrix} M_{11} & M_{12} \\ M_{21} & M_{22} \end{pmatrix} = \begin{pmatrix} \int_{x_k}^{x_{k+1}} \rho C_p N_k^\theta N_k^\theta dx & \int_{x_k}^{x_{k+1}} \rho C_p N_k^\theta N_{k+1}^\theta dx \\ \int_{x_k}^{x_{k+1}} \rho C_p N_{k+1}^\theta N_k^\theta dx & \int_{x_k}^{x_{k+1}} \rho C_p N_{k+1}^\theta N_{k+1}^\theta dx \end{pmatrix}$$

I only need to compute 3 integrals since $M_{12} = M_{21}$. Let us start with M_{11} :

$$M_{11} = \int_{x_k}^{x_{k+1}} \rho C_p N_k^\theta(x) N_k^\theta(x) dx = \int_{x_k}^{x_{k+1}} \rho C_p \frac{x_{k+1}-x}{h_x} \frac{x_{k+1}-x}{h_x} dx$$

It is then customary to carry out the change of variable $x \rightarrow r$ where $r \in [-1 : 1]$ as shown hereunder:



The relationships between x and r are:

$$r = \frac{2}{h_x}(x - x_k) - 1 \quad x = \frac{h_x}{2}(1 + r) + x_k$$

In what follows we assume for simplicity that ρ and C_p are constant within each element.

$$M_{11} = \rho C_p \int_{x_k}^{x_{k+1}} \frac{x_{k+1} - x}{h_x} \frac{x_{k+1} - x}{h_x} dx = \frac{\rho C_p h_x}{8} \int_{-1}^{+1} (1 - r)(1 - r) dr = \frac{h_x}{3} \rho C_p$$

Similarly we arrive at

$$M_{12} = \rho C_p \int_{x_k}^{x_{k+1}} \frac{x_{k+1} - x}{h_x} \frac{x - x_k}{h_x} dx = \frac{\rho C_p h_x}{8} \int_{-1}^{+1} (1 - r)(1 + r) dr = \frac{h_x}{6} \rho C_p$$

and

$$M_{22} = \rho C_p \int_{x_k}^{x_{k+1}} \frac{x - x_k}{h_x} \frac{x - x_k}{h_x} dx = \frac{\rho C_p h_x}{8} \int_{-1}^{+1} (1 + r)(1 + r) dr = \frac{h_x}{3} \rho C_p$$

Finally

$$\boxed{\mathbf{M}^e = \frac{h_x}{3} \rho C_p \begin{pmatrix} 1 & 1/2 \\ 1/2 & 1 \end{pmatrix}}$$

In the new coordinate system, the shape functions

$$N_k^\theta(x) = \frac{x_{k+1} - x}{h_x} \quad N_{k+1}^\theta(x) = \frac{x - x_k}{h_x}$$

become

$$N_k^\theta(r) = \frac{1}{2}(1 - r) \quad N_{k+1}^\theta(r) = \frac{1}{2}(1 + r)$$

Also,

$$\frac{\partial N_k^\theta}{\partial x} = -\frac{1}{h_x} \quad \frac{\partial N_{k+1}^\theta}{\partial x} = \frac{1}{h_x}$$

so that

$$\vec{B}^T = \begin{pmatrix} \frac{\partial N_k^\theta}{\partial x} \\ \frac{\partial N_{k+1}^\theta}{\partial x} \end{pmatrix} = \begin{pmatrix} -\frac{1}{h_x} \\ \frac{1}{h_x} \end{pmatrix}$$

We here also assume that k is constant within the element:

$$\mathbf{K}_d = \int_{x_k}^{x_{k+1}} \vec{B}^T k \vec{B} dx = k \int_{x_k}^{x_{k+1}} \vec{B}^T \vec{B} dx$$

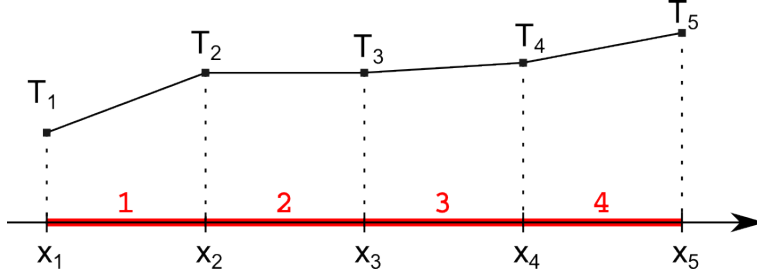
simply becomes

$$\mathbf{K}_d = k \int_{x_k}^{x_{k+1}} \frac{1}{h_x^2} \begin{pmatrix} 1 & -1 \\ -1 & 1 \end{pmatrix} dx$$

and then

$$\boxed{\mathbf{K}_d = \frac{k}{h_x} \begin{pmatrix} 1 & -1 \\ -1 & 1 \end{pmatrix}}$$

Let us consider this very simple grid consisting of 4 elements/5 nodes:



For each element we have

$$\underbrace{(\mathbf{M}^e + \mathbf{K}_d^e \delta t)}_{\mathbf{A}^e} \cdot \vec{\mathbf{T}}^{new} = \underbrace{\mathbf{M}^e \cdot \vec{\mathbf{T}}^{old}}_{\vec{\mathbf{b}}^e}$$

We can write this equation very explicitly for each element:

- element 1

$$\mathbf{A}^1 \cdot \begin{pmatrix} T_1 \\ T_2 \end{pmatrix} = \vec{\mathbf{b}}^1$$

$$\begin{cases} A_{11}^1 T_1 + A_{12}^1 T_2 = b_x^1 \\ A_{21}^1 T_1 + A_{22}^1 T_2 = b_y^1 \end{cases}$$

- element 2

$$\mathbf{A}^2 \cdot \begin{pmatrix} T_2 \\ T_3 \end{pmatrix} = \vec{\mathbf{b}}^2$$

$$\begin{cases} A_{11}^2 T_2 + A_{12}^2 T_3 = b_1^2 \\ A_{21}^2 T_2 + A_{22}^2 T_3 = b_2^2 \end{cases}$$

- element 3

$$\mathbf{A}^3 \cdot \begin{pmatrix} T_3 \\ T_4 \end{pmatrix} = \vec{\mathbf{b}}^3$$

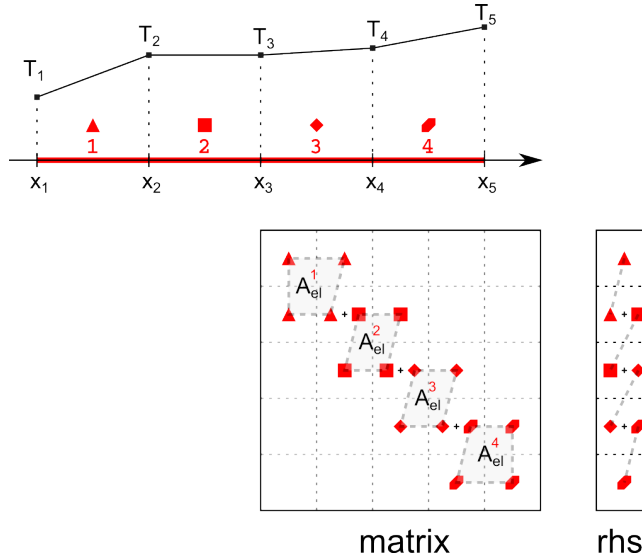
$$\begin{cases} A_{11}^3 T_3 + A_{12}^3 T_4 = b_1^3 \\ A_{21}^3 T_3 + A_{22}^3 T_4 = b_2^3 \end{cases}$$

- element 4

$$\mathbf{A}^4 \cdot \begin{pmatrix} T_4 \\ T_5 \end{pmatrix} = \vec{\mathbf{b}}^4$$

$$\begin{cases} A_{11}^4 T_4 + A_{12}^4 T_5 = b_1^4 \\ A_{21}^4 T_4 + A_{22}^4 T_5 = b_2^4 \end{cases}$$

All equations can be cast into a single linear system: this is the **assembly** phase. The process can also be visualised as shown hereunder. Because nodes 2,3,4 belong to two elements elemental contributions will be summed in the matrix and the rhs:



The assembled matrix and rhs are then:

$$\begin{pmatrix} A_{11}^1 & A_{12}^1 & 0 & 0 & 0 \\ A_{21}^1 & A_{22}^1 + A_{11}^2 & A_{12}^2 & 0 & 0 \\ 0 & A_{21}^2 & A_{22}^2 + A_{11}^3 & A_{12}^3 & 0 \\ 0 & 0 & A_{21}^3 & A_{22}^3 + A_{11}^4 & A_{12}^4 \\ 0 & 0 & 0 & A_{21}^4 & A_{22}^4 \end{pmatrix} \begin{pmatrix} T_1 \\ T_2 \\ T_3 \\ T_4 \\ T_5 \end{pmatrix} = \begin{pmatrix} b_1^1 \\ b_2^1 + b_1^2 \\ b_2^2 + b_1^3 \\ b_2^3 + b_1^4 \\ b_2^4 \end{pmatrix}$$

Ultimately the assembled matrix system also takes the form

$$\begin{pmatrix} A_{11} & A_{12} & 0 & 0 & 0 \\ A_{21} & A_{22} & A_{23} & 0 & 0 \\ 0 & A_{32} & A_{33} & A_{34} & 0 \\ 0 & 0 & A_{43} & A_{44} & A_{45} \\ 0 & 0 & 0 & A_{54} & A_{55} \end{pmatrix} \begin{pmatrix} T_1 \\ T_2 \\ T_3 \\ T_4 \\ T_5 \end{pmatrix} = \begin{pmatrix} b_1 \\ b_2 \\ b_3 \\ b_4 \\ b_5 \end{pmatrix}$$

and we see that it is sparse. Its sparsity structure is easy to derive: each row corresponds to a dof, and since nodes 1 and 2 'see' each other (they belong to the same element) there will be non-zero entries in the first and second column. Likewise, node 2 'sees' node 1 (in other words, there is an edge linking nodes 1 and 2), itself, and node 3, so that there are non-zero entries in the second row at columns 1, 2, and 3.

Before we solve the system, we need to take care of boundary conditions. Let us assume that we wish to fix the temperature at node 2, or in other words we wish to set

$$T_2 = T^{bc}$$

This equation can be cast as

$$(0 \ 1 \ 0 \ 0 \ 0) \begin{pmatrix} T_1 \\ T_2 \\ T_3 \\ T_4 \\ T_5 \end{pmatrix} = \begin{pmatrix} 0 \\ T^{bc} \\ 0 \\ 0 \\ 0 \end{pmatrix}$$

This replaces the second line in the previous matrix equation:

$$\begin{pmatrix} A_{11} & A_{12} & 0 & 0 & 0 \\ 0 & 1 & 0 & 0 & 0 \\ 0 & A_{32} & A_{33} & A_{34} & 0 \\ 0 & 0 & A_{43} & A_{44} & A_{45} \\ 0 & 0 & 0 & A_{54} & A_{55} \end{pmatrix} \begin{pmatrix} T_1 \\ T_2 \\ T_3 \\ T_4 \\ T_5 \end{pmatrix} = \begin{pmatrix} b_1 \\ T^{bc} \\ b_3 \\ b_4 \\ b_5 \end{pmatrix}$$

That's it, we have a linear system of equations which can be solved!

5.2 The advection-diffusion equation in 1D

We start with the 1D advection-diffusion equation

$$\rho C_p \left(\frac{\partial T}{\partial t} + u \frac{\partial T}{\partial x} \right) = \frac{\partial}{\partial x} \left(k \frac{\partial T}{\partial x} \right) + H \quad (262)$$

This is the **strong form** of the ODE to solve. As in the previous section, I multiply this equation by a function $f(x)$ and integrate it over the domain Ω :

$$\int_{\Omega} f(x) \rho C_p \frac{\partial T}{\partial t} dx + \int_{\Omega} f(x) \rho C_p u \frac{\partial T}{\partial x} dx = \int_{\Omega} f(x) \frac{\partial}{\partial x} \left(k \frac{\partial T}{\partial x} \right) dx + \int_{\Omega} f(x) H dx$$

As in the previous section I integrate the r.h.s. by parts:

$$\int_{\Omega} f(x) \frac{\partial}{\partial x} \left(k \frac{\partial T}{\partial x} \right) dx = \left[f(x) k \frac{\partial T}{\partial x} \right]_{\partial\Omega} - \int_{\Omega} \frac{\partial f}{\partial x} k \frac{\partial T}{\partial x} dx$$

Disregarding the boundary term for now, we then obtain the **weak form** of the diffusion equation in 1D:

$$\boxed{\int_{\Omega} f(x) \rho C_p \frac{\partial T}{\partial t} dx + \int_{\Omega} f(x) \rho C_p u \frac{\partial T}{\partial x} dx + \int_{\Omega} \frac{\partial f}{\partial x} k \frac{\partial T}{\partial x} dx = \int_{\Omega} f(x) H dx}$$

We then use the additive property of the integral $\int_{\Omega} \cdots = \sum_{elts} \int_{\Omega_e} \cdots$

$$\sum_{elts} \left(\underbrace{\int_{\Omega_e} f(x) \rho C_p \frac{\partial T}{\partial t} dx}_{\Lambda_f^e} + \underbrace{\int_{\Omega_e} f(x) \rho C_p u \frac{\partial T}{\partial x} dx}_{\Sigma_f^e} + \underbrace{\int_{\Omega_e} \frac{\partial f}{\partial x} k \frac{\partial T}{\partial x} dx}_{\Upsilon_f^e} - \underbrace{\int_{\Omega_e} f(x) H dx}_{\Omega_f^e} \right) = 0$$

In the element, we have seen that the temperature can be written:

$$T(x) = N_k^\theta(x) T_k + N_{k+1}^\theta(x) T_{k+1}$$

In the previous presentation we have computed Λ_f^e and Υ_f^e . Let us now turn to Σ_f^e and Ω_f^e .

$$\begin{aligned} \Sigma_f^e &= \int_{x_k}^{x_{k+1}} f(x) \rho C_p u \frac{\partial T}{\partial x} dx \\ &= \int_{x_k}^{x_{k+1}} f(x) \rho C_p u \frac{\partial [N_k^\theta(x) T_k + N_{k+1}^\theta(x) T_{k+1}]}{\partial x} dx \\ &= \int_{x_k}^{x_{k+1}} f(x) \rho C_p u \frac{\partial N_k^\theta}{\partial x} T_k dx + \int_{x_k}^{x_{k+1}} f(x) \rho C_p u \frac{\partial N_{k+1}^\theta}{\partial x} T_{k+1} dx \\ &= \left(\int_{x_k}^{x_{k+1}} f(x) \rho C_p u \frac{\partial N_k^\theta}{\partial x} dx \right) T_k + \left(\int_{x_k}^{x_{k+1}} f(x) \rho C_p u \frac{\partial N_{k+1}^\theta}{\partial x} dx \right) T_{k+1} \end{aligned}$$

Taking $f(x) = N_k^\theta(x)$ and omitting '(x)' in the rhs:

$$\Sigma_{N_k^\theta}^e = \left(\int_{x_k}^{x_{k+1}} \rho C_p u N_k^\theta \frac{\partial N_k^\theta}{\partial x} dx \right) T_k + \left(\int_{x_k}^{x_{k+1}} \rho C_p u N_{k+1}^\theta \frac{\partial N_{k+1}^\theta}{\partial x} dx \right) T_{k+1}$$

Taking $f(x) = N_{k+1}^\theta(x)$ and omitting '(x)' in the rhs:

$$\Sigma_{N_{k+1}^\theta}^e = \left(\int_{x_k}^{x_{k+1}} \rho C_p u N_{k+1}^\theta \frac{\partial N_k^\theta}{\partial x} dx \right) T_k + \left(\int_{x_k}^{x_{k+1}} \rho C_p u N_{k+1}^\theta \frac{\partial N_{k+1}^\theta}{\partial x} dx \right) T_{k+1}$$

$$\begin{pmatrix} \Sigma_{N_k^\theta} \\ \Sigma_{N_{k+1}^\theta} \end{pmatrix} = \begin{pmatrix} \int_{x_k}^{x_{k+1}} \rho C_p u N_k^\theta \frac{\partial N_k^\theta}{\partial x} dx & \int_{x_k}^{x_{k+1}} \rho C_p u N_k^\theta \frac{\partial N_{k+1}^\theta}{\partial x} dx \\ \int_{x_k}^{x_{k+1}} \rho C_p u N_{k+1}^\theta \frac{\partial N_k^\theta}{\partial x} dx & \int_{x_k}^{x_{k+1}} \rho C_p u N_{k+1}^\theta \frac{\partial N_{k+1}^\theta}{\partial x} dx \end{pmatrix} \cdot \begin{pmatrix} T_k \\ T_{k+1} \end{pmatrix}$$

or,

$$\begin{pmatrix} \Sigma_{N_k^\theta} \\ \Sigma_{N_{k+1}^\theta} \end{pmatrix} = \left[\int_{x_k}^{x_{k+1}} \rho C_p u \begin{pmatrix} N_k^\theta \frac{\partial N_k^\theta}{\partial x} & N_k^\theta \frac{\partial N_{k+1}^\theta}{\partial x} \\ N_{k+1}^\theta \frac{\partial N_k^\theta}{\partial x} & N_{k+1}^\theta \frac{\partial N_{k+1}^\theta}{\partial x} \end{pmatrix} dx \right] \cdot \begin{pmatrix} T_k \\ T_{k+1} \end{pmatrix}$$

Finally, we have already defined the vectors

$$\vec{N}^T = \begin{pmatrix} N_k^\theta(x) \\ N_{k+1}^\theta(x) \end{pmatrix} \quad \vec{B}^T = \begin{pmatrix} \frac{\partial N_k^\theta}{\partial x} \\ \frac{\partial N_{k+1}^\theta}{\partial x} \end{pmatrix} \quad \vec{T}^e = \begin{pmatrix} T_k \\ T_{k+1} \end{pmatrix}$$

so that

$$\begin{pmatrix} \Sigma_{N_k^\theta} \\ \Sigma_{N_{k+1}^\theta} \end{pmatrix} = \left(\int_{x_k}^{x_{k+1}} \vec{N}^T \rho C_p u \vec{B} dx \right) \cdot \vec{T}^e = \mathbf{K}_a \cdot \vec{T}^e$$

One can easily show that

$$\mathbf{K}_a^e = \rho C_p u \begin{pmatrix} -1/2 & 1/2 \\ -1/2 & 1/2 \end{pmatrix}$$

Note that the matrix \mathbf{K}_a^e is not symmetric.

Let us now look at the source term:

$$\Omega_f^e = \int_{x_k}^{x_{k+1}} f(x) H(x) dx$$

Taking $f(x) = N_k^\theta(x)$:

$$\Omega_{N_k^\theta} = \int_{x_k}^{x_{k+1}} N_k^\theta(x) H(x) dx$$

Taking $f(x) = N_{k+1}^\theta(x)$:

$$\Omega_{N_{k+1}^\theta} = \int_{x_k}^{x_{k+1}} N_{k+1}^\theta(x) H(x) dx$$

We can rearrange both equations as follows:

$$\begin{pmatrix} \Omega_{N_k^\theta} \\ \Omega_{N_{k+1}^\theta} \end{pmatrix} = \begin{pmatrix} \int_{x_k}^{x_{k+1}} N_k^\theta(x) H(x) dx \\ \int_{x_k}^{x_{k+1}} N_{k+1}^\theta(x) H(x) dx \end{pmatrix}$$

or,

$$\begin{pmatrix} \Omega_{N_k^\theta} \\ \Omega_{N_{k+1}^\theta} \end{pmatrix} = \left[\int_{x_k}^{x_{k+1}} \begin{pmatrix} N_k^\theta(x) H(x) \\ N_{k+1}^\theta(x) H(x) \end{pmatrix} dx \right]$$

so that

$$\begin{pmatrix} \Omega_{N_k^\theta} \\ \Omega_{N_{k+1}^\theta} \end{pmatrix} = \left(\int_{x_k}^{x_{k+1}} \vec{N}^T H(x) dx \right)$$

The weak form discretised over 1 element becomes

$$\underbrace{\left(\int_{x_k}^{x_{k+1}} \vec{N}^T \rho C_p \mathbf{N} dx \right)}_{\mathbf{M}^e} \cdot \dot{\vec{T}}^e + \underbrace{\left(\int_{x_k}^{x_{k+1}} \vec{N}^T \rho C_p u \mathbf{B} dx \right)}_{\mathbf{K}_a^e} \cdot \vec{T}^e + \underbrace{\left(\int_{x_k}^{x_{k+1}} \vec{B}^T k \mathbf{B} dx \right)}_{\mathbf{K}_d^e} \cdot \vec{T}^e = \underbrace{\left(\int_{x_k}^{x_{k+1}} \vec{N}^T H(x) dx \right)}_{\vec{F}^e}$$

or,

$$\mathbf{M}^e \cdot \dot{\vec{T}}^e + (\mathbf{K}_a^e + \mathbf{K}_d^e) \cdot \vec{T}^e = \vec{F}^e$$

or,

$$\mathbf{M}^e \cdot \frac{\partial \vec{T}^e}{\partial t} + (\mathbf{K}_a^e + \mathbf{K}_d^e) \cdot \vec{T}^e = \vec{F}^e$$

5.3 The advection-diffusion equation in 2D

We start from the 'bare-bones' heat transport equation (source terms are omitted):

$$\rho C_p \left(\frac{\partial T}{\partial t} + \vec{v} \cdot \vec{\nabla} T \right) = \vec{\nabla} \cdot k \vec{\nabla} T \quad (263)$$

In what follows we assume that the velocity field \vec{v} is known so that temperature is the only unknown. Let N^θ be the temperature basis functions so that the temperature inside an element is given by¹⁹:

$$T^h(\vec{r}) = \sum_{i=1}^{m_T} N_i^\theta(\vec{r}) T_i = \vec{N}^\theta \cdot \vec{T} \quad (264)$$

where \vec{T} is a vector of length m_T . The weak form is then

$$\begin{aligned} \int_{\Omega} N_i^\theta \left[\rho C_p \left(\frac{\partial T}{\partial t} + \vec{v} \cdot \vec{\nabla} T \right) \right] d\Omega &= \int_{\Omega} N_i^\theta \vec{\nabla} \cdot k \vec{\nabla} T d\Omega \\ \underbrace{\int_{\Omega} N_i^\theta \rho C_p \frac{\partial T}{\partial t} d\Omega}_{I} + \underbrace{\int_{\Omega} N_i^\theta \rho C_p \vec{v} \cdot \vec{\nabla} T d\Omega}_{II} &= \underbrace{\int_{\Omega} N_i^\theta \vec{\nabla} \cdot k \vec{\nabla} T d\Omega}_{III} \quad i = 1, m_T \end{aligned} \quad (265)$$

Looking at the first term:

$$\int_{\Omega} N_i^\theta \rho C_p \frac{\partial T}{\partial t} d\Omega = \int_{\Omega} N_i^\theta \rho C_p \vec{N}^\theta \cdot \dot{\vec{T}} d\Omega \quad (266)$$

(267)

so that when we assemble all contributions for $i = 1, m_T$ we get:

$$I = \int_{\Omega} \vec{N}^\theta \rho C_p \vec{N}^\theta \cdot \dot{\vec{T}} d\Omega = \left(\int_{\Omega} \rho C_p \vec{N}^\theta \vec{N}^\theta d\Omega \right) \cdot \dot{\vec{T}} = \mathbf{M}^T \cdot \dot{\vec{T}}$$

where \mathbf{M}^T is the mass matrix of the system of size $(m_T \times m_T)$ with

$$M_{ij}^T = \int_{\Omega} \rho C_p N_i^\theta N_j^\theta d\Omega$$

Turning now to the second term:

$$\int_{\Omega} N_i^\theta \rho C_p \vec{v} \cdot \vec{\nabla} T d\Omega = \int_{\Omega} N_i^\theta \rho C_p (u \frac{\partial T}{\partial x} + v \frac{\partial T}{\partial y}) d\Omega \quad (268)$$

$$= \int_{\Omega} N_i^\theta \rho C_p (u \frac{\partial \vec{N}^\theta}{\partial x} + v \frac{\partial \vec{N}^\theta}{\partial y}) \cdot \vec{T} d\Omega \quad (269)$$

(270)

¹⁹the θ superscript has been chosen to denote temperature so as to avoid confusion with the transpose operator

so that when we assemble all contributions for $i = 1, m_T$ we get:

$$II = \left(\int_{\Omega} \rho C_p \vec{N}^{\theta} (u \frac{\partial \vec{N}^{\theta}}{\partial x} + v \frac{\partial \vec{N}^{\theta}}{\partial y}) d\Omega \right) \cdot \vec{T} = \mathbf{K}_a \cdot \vec{T}$$

where \mathbf{K}_a is the advection term matrix of size $(m_T \times m_T)$ with

$$(K_a)_{ij} = \int_{\Omega} \rho C_p N_i^{\theta} \left(u \frac{\partial N_j^{\theta}}{\partial x} + v \frac{\partial N_j^{\theta}}{\partial y} \right) d\Omega$$

Now looking at the third term, we carry out an integration by part and neglect the surface term for now, so that

$$\int_{\Omega} N_i^{\theta} \vec{\nabla} \cdot k \vec{\nabla} T d\Omega = - \int_{\Omega} k \vec{\nabla} N_i^{\theta} \cdot \vec{\nabla} T d\Omega \quad (271)$$

$$= - \int_{\Omega} k \vec{\nabla} N_i^{\theta} \cdot \vec{\nabla} (\vec{N}^{\theta} \cdot \vec{T}) d\Omega \quad (272)$$

(273)

with

$$\vec{\nabla} \vec{N}^{\theta} = \begin{pmatrix} \partial_x N_1^{\theta} & \partial_x N_2^{\theta} & \dots & \partial_x N_{m_T}^{\theta} \\ \partial_y N_1^{\theta} & \partial_y N_2^{\theta} & \dots & \partial_y N_{m_T}^{\theta} \end{pmatrix}$$

so that finally:

$$III = - \left(\int_{\Omega} k (\vec{\nabla} \vec{N}^{\theta})^T \cdot \vec{\nabla} \vec{N}^{\theta} d\Omega \right) \cdot \vec{T} = - \mathbf{K}_d \cdot \vec{T}$$

where \mathbf{K}_d is the diffusion term matrix:

$$\mathbf{K}_d = \int_{\Omega} k (\vec{\nabla} \vec{N}^{\theta})^T \cdot \vec{\nabla} \vec{N}^{\theta} d\Omega$$

Ultimately terms I, II, III together yield:

$$\boxed{\mathbf{M}^{\theta} \cdot \dot{\vec{T}} + (\mathbf{K}_a + \mathbf{K}_d) \cdot \vec{T} = \vec{0}}$$

add source term!!

5.3.1 Dealing with the time discretisation

Essentially we have to solve a PDE of the type:

$$\frac{\partial T}{\partial t} = \mathcal{F}(\vec{v}, T, \vec{\nabla} T, \Delta T)$$

with $\mathcal{F} = \frac{1}{\rho C_p} (-\vec{v} \cdot \vec{\nabla} T + \vec{\nabla} \cdot k \vec{\nabla} T)$.

The (explicit) forward Euler method is:

$$\frac{T^{n+1} - T^n}{\delta t} = \mathcal{F}^n(T, \vec{\nabla} T, \Delta T)$$

The (implicit) backward Euler method is:

$$\frac{T^{n+1} - T^n}{\delta t} = \mathcal{F}^{n+1}(T, \vec{\nabla} T, \Delta T)$$

and the (implicit) Crank-Nicolson algorithm is:

$$\frac{T^{n+1} - T^n}{\delta t} = \frac{1}{2} [\mathcal{F}^n(T, \vec{\nabla} T, \Delta T) + \mathcal{F}^{n+1}(T, \vec{\nabla} T, \Delta T)]$$

where the superscript n indicates the time step. The Crank-Nicolson is obviously based on the trapezoidal rule, with second-order convergence in time.

In what follows, I omit the superscript on the mass matrix to simplify notations: $\mathbf{M}^{\theta} = \mathbf{M}$. In terms of Finite Elements, these become:

- Explicit Forward euler:

$$\frac{1}{\delta t}(\mathbf{M}^{n+1} \cdot \vec{T}^{n+1} - \mathbf{M}^n \cdot \vec{T}^n) = -(\mathbf{K}_a^n + \mathbf{K}_d^n) \cdot \vec{T}^n$$

or,

$$\boxed{\mathbf{M}^{n+1} \cdot \vec{T}^{n+1} = (\mathbf{M}^n + (\mathbf{K}_a^n + \mathbf{K}_d^n)\delta t) \cdot \vec{T}^n}$$

- Implicit Backward euler:

$$\frac{1}{\delta t}(\mathbf{M}^{n+1} \cdot \vec{T}^{n+1} - \mathbf{M}^n \cdot \vec{T}^n) = -(\mathbf{K}_a^{n+1} + \mathbf{K}_d^{n+1}) \cdot \vec{T}^{n+1}$$

or,

$$\boxed{(\mathbf{M}^{n+1} + (\mathbf{K}_a^{n+1} + \mathbf{K}_d^{n+1})\delta t) \cdot \vec{T}^{n+1} = \mathbf{M}^n \cdot \vec{T}^n}$$

- Crank-Nicolson

$$\frac{1}{\delta t}(\mathbf{M}^{n+1} \cdot \vec{T}^{n+1} - \mathbf{M}^n \cdot \vec{T}^n) = \frac{1}{2} [-(\mathbf{K}_a^{n+1} + \mathbf{K}_d^{n+1}) \cdot \vec{T}^{n+1} - (\mathbf{K}_a^n + \mathbf{K}_d^n) \cdot \vec{T}^n]$$

or,

$$\boxed{\left(\mathbf{M}^{n+1} + (\mathbf{K}_a^{n+1} + \mathbf{K}_d^{n+1}) \frac{\delta t}{2} \right) \cdot \vec{T}^{n+1} = \left(\mathbf{M}^n + (\mathbf{K}_a^n + \mathbf{K}_d^n) \frac{\delta t}{2} \right) \cdot \vec{T}^n}$$

Note that in benchmarks where the domain/grid does not deform, the coefficients do not change in space and the velocity field is constant in time, or in practice out of convenience, the \mathbf{K} and \mathbf{M} matrices do not change and the r.h.s. can be constructed with the same matrices as the FE matrix.

The Backward differentiation formula (see for instance [779] or Wikipedia²⁰. The second-order BDF (or BDF-2) as shown in [1009] is as follows: it is a finite-difference quadratic interpolation approximation of the $\partial T / \partial t$ term which involves t^n , t^{n-1} and t^{n-2} :

$$\frac{\partial T}{\partial t}(t^n) = \frac{1}{\tau_n} \left(\frac{2\tau_n + \tau_{n-1}}{\tau_n + \tau_{n-1}} T(t^n) - \frac{\tau_n + \tau_{n-1}}{\tau_{n-1}} T(t^{n-1}) + \frac{\tau_n^2}{\tau_{n-1}(\tau_n + \tau_{n-1})} T(t^{n-2}) \right) \quad (274)$$

where $\tau_n = t^n - t^{n-1}$. Starting again from $\mathbf{M}^\theta \cdot \dot{\vec{T}} + (\mathbf{K}_a + \mathbf{K}_d) \cdot \vec{T} = \vec{0}$, we write

$$\mathbf{M}^\theta \cdot \frac{1}{\tau_n} \left(\frac{2\tau_n + \tau_{n-1}}{\tau_n + \tau_{n-1}} \vec{T}^n - \frac{\tau_n + \tau_{n-1}}{\tau_{n-1}} \vec{T}^{n-1} + \frac{\tau_n^2}{\tau_{n-1}(\tau_n + \tau_{n-1})} \vec{T}^{n-2} \right) + (\mathbf{K}_a + \mathbf{K}_d) \cdot \vec{T}^n = \vec{0}$$

and finally:

$$\left[\frac{2\tau_n + \tau_{n-1}}{\tau_n + \tau_{n-1}} \mathbf{M}^\theta + \tau_n (\mathbf{K}_a + \mathbf{K}_d) \right] \cdot \vec{T}^n = \frac{\tau_n + \tau_{n-1}}{\tau_{n-1}} \mathbf{M}^\theta \cdot \vec{T}^{n-1} - \frac{\tau_n^2}{\tau_{n-1}(\tau_n + \tau_{n-1})} \mathbf{M}^\theta \cdot \vec{T}^{n-2}$$

Note that if all timesteps are equal, i.e. $\tau_n = \tau_{n-1} = \delta t$, this equation becomes:

$$\left[\frac{3}{2} \mathbf{M}^\theta + \delta t (\mathbf{K}_a + \mathbf{K}_d) \right] \cdot \vec{T}^n = \mathbf{M}^\theta \cdot \left(2\vec{T}^{n-1} - \frac{1}{2}\vec{T}^{n-2} \right)$$

or,

$$\left[\mathbf{M}^\theta + \frac{2}{3} \delta t (\mathbf{K}_a + \mathbf{K}_d) \right] \cdot \vec{T}^n = \mathbf{M}^\theta \cdot \left(\frac{4}{3} \vec{T}^{n-1} - \frac{1}{3} \vec{T}^{n-2} \right)$$

As mentioned before the backward differentiation formula (BDF) is a family of implicit methods for the integration of ODEs. Each BDF- s method achieves order s . The BDF-1 is simply the backward Euler method as seen above:

$$T^{n+1} - T^n = \delta t \mathcal{F}^{n+1}$$

²⁰https://en.wikipedia.org/wiki/Backward_differentiation_formula

The BDF-2 is given by

$$T^{n+2} - \frac{4}{3}T^{n+1} + \frac{1}{3}T^n = \frac{2}{3}\delta t \mathcal{F}^{n+2}$$

The BDF-3 is given by

$$T^{n+3} - \frac{18}{11}T^{n+2} + \frac{9}{11}T^{n+1} - \frac{2}{11}T^n = \frac{6}{11}\delta t \mathcal{F}^{n+3}$$

The BDF-4 is given by

$$T^{n+4} - \frac{48}{25}T^{n+1} + \frac{36}{25}T^{n+1} - \frac{16}{25}T^{n+1} + \frac{3}{25}T^n = \frac{12}{25}\delta t \mathcal{F}^{n+4}$$

5.3.2 On steady states

It is said that a system is in a steady state if the (state) variables which define the behavior of the system are unchanging in time. In continuous time, this means that the partial derivative with respect to time is zero and remains so:

$$\frac{\partial}{\partial t} = 0 \quad \forall t$$

This is irrelevant for the Stokes equations which do not contain an explicit time dependence but the heat transport equation can reach a steady state. Note that if one is only interested in the steady state solution (and not how the system gets there in time) then the heat transport equation should be solved with $\partial T / \partial t$ set to zero.

5.3.3 Anisotropic heat conduction

It is most often assumed that the heat conductivity is isotropic so that one speaks of heat conductivity as a scalar k . However many materials are orthotropic and in that case the heat conductivity is a tensor \mathbf{k} which (in 2D) writes [1361, p121]:

$$\mathbf{k} = \begin{pmatrix} k_{xx} & k_{xy} \\ k_{yx} & k_{yy} \end{pmatrix} = \begin{pmatrix} \cos \theta & \sin \theta \\ -\sin \theta & \cos \theta \end{pmatrix} \cdot \begin{pmatrix} k_1 & 0 \\ 0 & k_2 \end{pmatrix} \cdot \begin{pmatrix} \cos \theta & -\sin \theta \\ \sin \theta & \cos \theta \end{pmatrix}$$

where k_1 and k_2 are the conductivities in the principal axes system and θ is the local orientation. In that case the diffusion term in the heat trasport equation becomes $\vec{\nabla} \cdot (\mathbf{k} \cdot \vec{\nabla} T)$.

(MSc Thesis): [1361, p121], [1361, p143]

6 Solving the flow equations with the FEM

In the case of an incompressible flow, we have seen that the continuity (mass conservation) equation takes the simple form $\vec{\nabla} \cdot \vec{v} = 0$. In other word flow takes place under the constraint that the divergence of its velocity field is exactly zero everywhere (solenoidal constraint), i.e. it is divergence free.

We see that the pressure in the momentum equation is then a degree of freedom which is needed to satisfy the incompressibility constraint (and it is not related to any constitutive equation) [473]. In other words the pressure is acting as a Lagrange multiplier of the incompressibility constraint.

Various approaches have been proposed in the literature to deal with the incompressibility constraint but we will only focus on the penalty method (section 6.3) and the so-called mixed finite element method 6.4.

6.1 Strong and weak forms

The strong form consists of the governing equation and the boundary conditions, i.e. the mass, momentum and energy conservation equations supplemented with Dirichlet and/or Neumann boundary conditions on (parts of) the boundary.

To develop the finite element formulation, the partial differential equations must be restated in an integral form called the weak form. In essence the PDEs are first multiplied by an arbitrary function and integrated over the domain.

6.2 Which velocity-pressure pair for Stokes?

The success of a mixed finite element formulation crucially depends on a proper choice of the local interpolations of the velocity and the pressure.

6.2.1 The compatibility condition (or LBB condition)

'LBB stable' elements assure the existence of a unique solution and assure convergence at the optimal rate.

6.2.2 Families

The family of Taylor-Hood finite element spaces on triangular/tetrahedral grids is given by $P_k \times P_{k-1}$ with $k \geq 2$, and on quadrilateral/hexahedral grids by $Q_k \times Q_{k-1}$ with $k \geq 2$. This means that the pressure is then approximated by continuous functions.

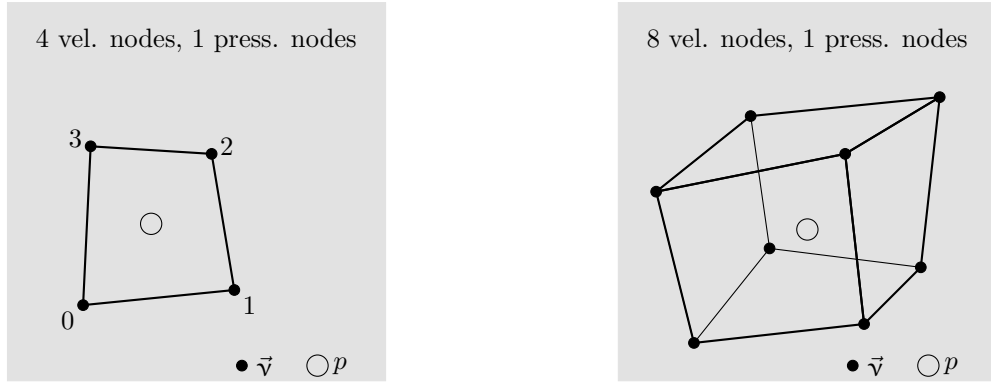
These finite elements are very popular, in particular the pairs for $k = 2$, i.e. $Q_2 \times Q_1$ and $P_2 \times P_1$. The reason why $k \geq 2$ comes from the fact that the $Q_1 \times Q_0$ (i.e. $Q_1 \times P_0$) and $P_2 \times P_1$ are not stable elements (they are not inf-sup stable).

Remark. Note that a similar element to $Q_2 \times Q_1$ has been proposed and used successfully used [1527, 842]: it is denoted by $Q_2^{(8)} \times Q_1$ since the center node (' x^2y^2 ') and its associated degrees of freedom have been removed. It has also been proved to be LBB stable.

The Raviart-Thomas family on triangles and quadrilaterals.

find literature

6.2.3 The bi/tri-linear velocity - constant pressure element ($Q_1 \times P_0$)



discussed in example 3.71 of [915]

However simple it may look, the element is one of the hardest elements to analyze and many questions are still open about its properties. The element does not satisfy the inf-sup condition [860]p211. In [743] it is qualified as follows: slightly unstable but highly usable.

The $Q_1 \times P_0$ mixed approximation is the lowest order conforming approximation method defined on a rectangular grid. It also happens to be the most famous example of an unstable mixed approximation method. [513, p235].

This element is discussed in [570], [572] and in [1309] in the context of multigrid use.

This element is plagued by so-called pressure checkerboard modes which have been thoroughly analysed [747], [324], [1425, 1426]. These can be filtered out [324]. Smoothing techniques are also discussed in [1035].

Literature[571]

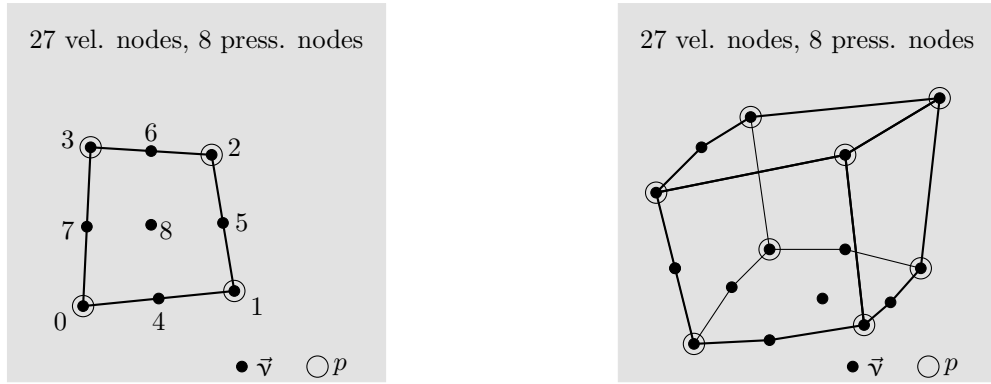
6.2.4 The bi/tri-quadratic velocity - discontinuous linear pressure element ($Q_2 \times P_{-1}$)

This element is crowned "probably the most accurate 2D element" in [743].

Piecewise Biquadratic velocities, piecewise linear discontinuous polynomial pressure. The element satisfies the inf-sup condition [860]p211. It is used in [1585]. See [165] over the two possible choices for the definition of the pressure space.. It is mentioned in [944], [165], [1295]. It is used in [594] to study 3D fold growth rates (see online supplementary material) and in [1434].

Note that the serendipity version of this pair, i.e. $Q_2^{(20)} \times P_{-1}$ is also LBB stable [1361, p180].

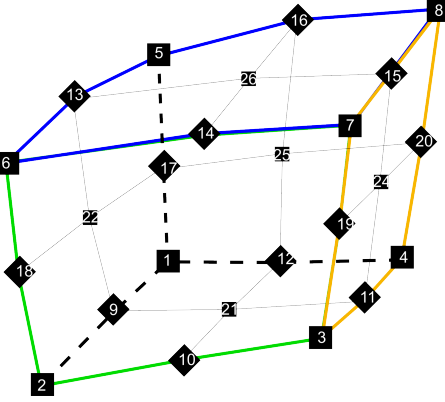
6.2.5 The bi/tri-quadratic velocity - bi/tri-linear pressure element ($Q_2 \times Q_1$)



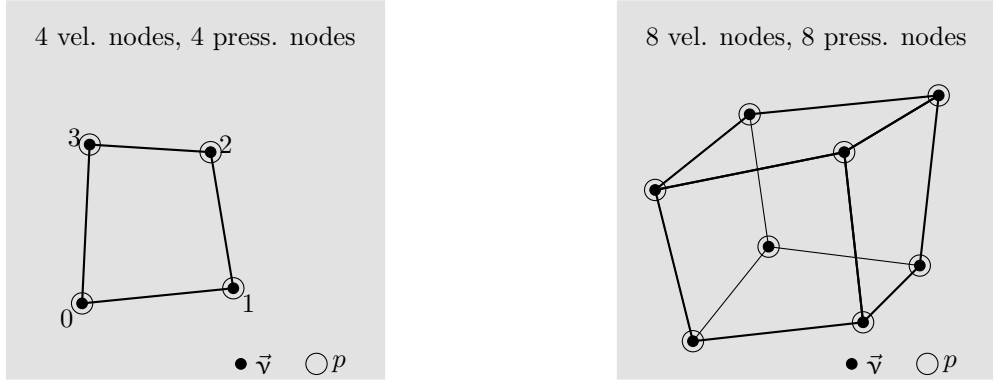
In [743] Gresho & Sani write that in their opinion $\text{div}(\vec{v}) = 0$ is not strong enough.

This element, implemented in penalised form, is discussed in [132] and the follow-up paper [133].
CHECK

Biquadratic velocities, bilinear pressure. See Hood and Taylor. The element satisfies the inf-sup condition [860]p215.



6.2.6 The stabilised bi/tri-linear velocity - bi/tri-linear pressure element ($Q_1 \times Q_1$ -stab)



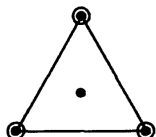
See [1270] for a fourier analysis of the normal and stabilised (a la [862]) $Q_1 - Q_1$ element. This element is used in [282, 283] in conjunction with AMR.

Stabilisation is worked out in [469, 163].

Literature: [740, 580]

6.2.7 The MINI triangular element ($P_1^+ \times P_1$) in 2D

The MINI element was first introduced in Arnold et al, 1984 [42]. It is also discussed in section 3.6.1 of [915]. It is schematically represented hereunder:



Mini element:
 Velocity: continuous linear
 + cubic bubble function,
 Pressure: continuous linear,
 Satisfies LBB condition,
 Linear convergence.

Nodes: • Velocity

○ Pressure

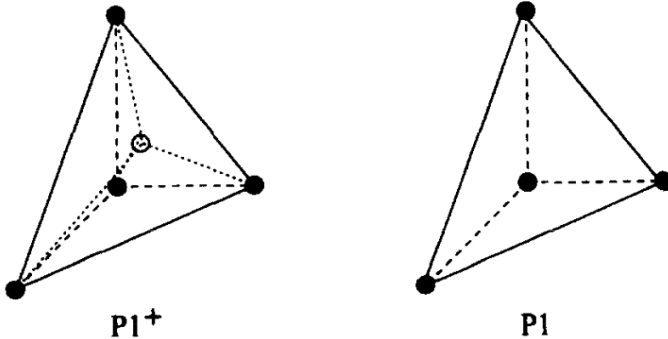
Figure taken from Donea and Huerta [473]

Remark. Note that [579] propose an equal-order-linear-continuous velocity-pressure variables which is enriched with velocity and pressure bubble functions to model the Stokes problem. They show by static condensation that these bubble functions give rise to a stabilized method involving least-squares forms of the momentum and of the continuity equations. In some cases their approach recovers the MINI element. Also check [624].

Remark. According to Braess[188], since the support of the bubble is restricted to the element, the associated variable (dofs living on the bubble) can be eliminated from the resulting system of linear equations by

static condensation. Also, the MINI element is cheaper than the Taylor-Hood element but it is commonly accepted that it yields a poorer approximation of the pressure.

The 3D MINI element is not very common but it is used for instance in [1304]. It is also said to be LBB stable in [1361, p180].



Velocity and pressure nodes for the 3D MINI element, taken from [1304]

Note that this element is used in [189] in the context of Arbitrary Lagrangian Eulerian finite element analysis of free surface flows.

6.2.8 The quadratic velocity - linear pressure triangle ($P_2 \times P_1$)

From [1446]: “Taylor-Hood elements [1527] are characterized by the fact that the pressure is continuous in the region Ω . A typical example is the quadratic triangle (P_2P_1 element). In this element the velocity is approximated by a quadratic polynomial and the pressure by a linear polynomial. One can easily verify that both approximations are continuous over the element boundaries.” It can be shown, Segal (1979), that this element is admissible if at least 3 elements are used. The quadrilateral counterpart of this triangle is the $Q_2 \times Q_1$ element. Reddy and Gartling [1361, p179] also report this element to be LBB stable.

6.2.9 The Crouzeix-Raviart triangle ($P_2^+ \times P_{-1}$)

Since the $P_2 \times P_{-1}$ pair is not LBB stable [1361, p179], it is enhanced by a cubic bubble and is therefore called $P_2^+ \times P_{-1}$.

This element was first introduced in [419]. It is the element used in the MILAMIN code [426]. It is a seven-node triangle with quadratic velocity shape functions enhanced by a cubic bubble function and discontinuous linear interpolation for the pressure field [425]. This element is LBB stable and no additional stabilization techniques are required[513]. The '+' in its name stands for the bubble while the '-' stands for the discontinuous character of the pressure field: once again, it is P_1 over the element, but discontinuous across element edges.

Remark. Cuvelier et al, 1986 [425] recommend a 6-point or 7-point quadrature rule for this element.

Remark. Segal [1446] explains for output purposes (printing, plotting etc.) the discontinuous pressures are averaged in vertices for all the adjoining elements. See also Fig. 7.3 of [425].

Remark. The simplest Crouzeix-Raviart element is the non-conforming linear triangle with constant pressure ($P_1 \times P_0$) [425].

It is worth noting that this element has more degrees of freedom than the Taylor-Hood element for the same order of accuracy. However, since the bubble can be eliminated, one can design a modified version of this element.

Check Cuvelier book chapter 8 for modified element

Remark. I have once asked the (main) author of MILAMIN why he chose this element, for example over the $P_2 \times P_1$. His answer is as follows: "Elements with continuous pressure are incapable of converging in the L^∞ norm for mechanical problems exhibiting pressure jumps such as the inclusion-host setup. During my MSc and PhD I was focusing on sharp heterogeneities, so this is why I decided to choose $P_2^+ \times P_{-1}$. You will see that it is also easy to invert the pressure mass matrix for such elements, which is really useful (both for the augmentation and preconditioning)."

This element is used by Poliakov and Podlachikov [1317] to study the deformation of the surface above a rising diapir. Note that they actually use a "13 point integration formula (Hughes 1987) for calculation of the stiffness matrix was used in order to conserve detailed information from the marker field in the coarse FEM mesh". It is also used in [32] in the context of a new free-surface stabilization scheme. It is the element used in LaCoDe [452].

6.2.10 The Rannacher-Turek element - rotated $Q_1 \times P_0$

p. 722 of [915]
[844, 980]

6.2.11 Other elements

- $P_1 \times P_0$: example 3.70 in [915], also [914].
- $P_1 \times P_1$
- Q2P0: : Quadratic velocities, constant pressure. The element satisfies the inf-sup condition, but the constant pressure assumption may require fine discretisation.
- Q2Q2: This element is never used, probably because a) it is unstable, b) it is very costly. There is one reference to it in [862].
- P2P2
- the MINI quadrilateral element $Q_1^+ \times Q_1$.
- Q1P-1 Bilinear velocities, piecewise linear discontinuous polynomial pressure.

6.2.12 A note about incompressibility and standard mixed methods

What follows is nicely explained and demonstrated in John et al [917]. In their example 1.1 they look at the velocity error of benchmark VJ2 (see Section 8.6.9) which analytical solution is a zero velocity field. They show that for the MINI, Taylor-Hood and Crouzeix-Raviart triangular elements the velocity error grows with the magnitude of the rhs. They also make this statement: "there are important applications, e.g., natural convection problems, where the pressure is larger than the velocity by orders of magnitude. In such situations, one cannot expect to compute accurate velocity fields with classical mixed methods, at least for low order methods."

6.3 The penalty approach for viscous flow

In order to impose the incompressibility constraint, two widely used procedures are available, namely the Lagrange multiplier method and the penalty method [81, 860]. The latter is implemented in ELEFANT, which allows for the elimination of the pressure variable from the momentum equation (resulting in a reduction of the matrix size).

Mathematical details on the origin and validity of the penalty approach applied to the Stokes problem can for instance be found in [425], [1360] or [759].

The penalty formulation of the mass conservation equation is based on a relaxation of the incompressibility constraint and writes

$$\vec{\nabla} \cdot \vec{v} + \frac{p}{\lambda} = 0 \quad (275)$$

where λ is the penalty parameter, that can be interpreted (and has the same dimension) as a bulk viscosity. It is equivalent to say that the material is weakly compressible. It can be shown that if one

chooses λ to be a sufficiently large number, the continuity equation $\vec{\nabla} \cdot \vec{v} = 0$ will be approximately satisfied in the finite element solution. The value of λ is often recommended to be 6 to 7 orders of magnitude larger than the shear viscosity [473, 863].

Equation (275) can be used to eliminate the pressure in the momentum equation so that the mass and momentum conservation equations fuse to become :

$$\vec{\nabla} \cdot (2\eta \dot{\epsilon}(\vec{v})) + \lambda \vec{\nabla}(\vec{\nabla} \cdot \vec{v}) = \rho \mathbf{g} = 0 \quad (276)$$

[1118] have established the equivalence for incompressible problems between the reduced integration of the penalty term and a mixed Finite Element approach if the pressure nodes coincide with the integration points of the reduced rule.

In the end, the elimination of the pressure unknown in the Stokes equations replaces the original saddle-point Stokes problem [124] by an elliptical problem, which leads to a symmetric positive definite (SPD) FEM matrix. This is the major benefit of the penalized approach over the full indefinite solver with the velocity-pressure variables. Indeed, the SPD character of the matrix lends itself to efficient solving strategies and is less memory-demanding since it is sufficient to store only the upper half of the matrix including the diagonal [710] .

list codes which use this approach

Since the penalty formulation is only valid for incompressible flows, then $\dot{\epsilon} = \dot{\epsilon}^d$ so that the d superscript is omitted in what follows. Because the stress tensor is symmetric one can also rewrite it the following vector format:

$$\begin{aligned} \begin{pmatrix} \sigma_{xx} \\ \sigma_{yy} \\ \sigma_{zz} \\ \sigma_{xy} \\ \sigma_{xz} \\ \sigma_{yz} \end{pmatrix} &= \begin{pmatrix} -p \\ -p \\ -p \\ 0 \\ 0 \\ 0 \end{pmatrix} + 2\eta \begin{pmatrix} \dot{\epsilon}_{xx} \\ \dot{\epsilon}_{yy} \\ \dot{\epsilon}_{zz} \\ \dot{\epsilon}_{xy} \\ \dot{\epsilon}_{xz} \\ \dot{\epsilon}_{yz} \end{pmatrix} \\ &= \lambda \begin{pmatrix} \dot{\epsilon}_{xx} + \dot{\epsilon}_{yy} + \dot{\epsilon}_{zz} \\ \dot{\epsilon}_{xx} + \dot{\epsilon}_{yy} + \dot{\epsilon}_{zz} \\ \dot{\epsilon}_{xx} + \dot{\epsilon}_{yy} + \dot{\epsilon}_{zz} \\ 0 \\ 0 \\ 0 \end{pmatrix} + 2\eta \begin{pmatrix} \dot{\epsilon}_{xx} \\ \dot{\epsilon}_{yy} \\ \dot{\epsilon}_{zz} \\ \dot{\epsilon}_{xy} \\ \dot{\epsilon}_{xz} \\ \dot{\epsilon}_{yz} \end{pmatrix} \\ &= \underbrace{\lambda \begin{pmatrix} 1 & 1 & 1 & 0 & 0 & 0 \\ 1 & 1 & 1 & 0 & 0 & 0 \\ 1 & 1 & 1 & 0 & 0 & 0 \\ 0 & 0 & 0 & 0 & 0 & 0 \\ 0 & 0 & 0 & 0 & 0 & 0 \\ 0 & 0 & 0 & 0 & 0 & 0 \end{pmatrix}}_{\mathbf{K}} + \underbrace{\eta \begin{pmatrix} 2 & 0 & 0 & 0 & 0 & 0 \\ 0 & 2 & 0 & 0 & 0 & 0 \\ 0 & 0 & 2 & 0 & 0 & 0 \\ 0 & 0 & 0 & 1 & 0 & 0 \\ 0 & 0 & 0 & 0 & 1 & 0 \\ 0 & 0 & 0 & 0 & 0 & 1 \end{pmatrix}}_{\mathbf{C}} \cdot \begin{pmatrix} \frac{\partial u}{\partial x} \\ \frac{\partial v}{\partial y} \\ \frac{\partial w}{\partial z} \\ \frac{\partial u}{\partial y} + \frac{\partial v}{\partial x} \\ \frac{\partial u}{\partial z} + \frac{\partial w}{\partial x} \\ \frac{\partial v}{\partial z} + \frac{\partial w}{\partial y} \end{pmatrix} \end{aligned}$$

Remember that

$$\frac{\partial u}{\partial x} = \sum_{i=1}^4 \frac{\partial N_i}{\partial x} u_i \quad \frac{\partial v}{\partial y} = \sum_{i=1}^4 \frac{\partial N_i}{\partial y} v_i \quad \frac{\partial w}{\partial z} = \sum_{i=1}^4 \frac{\partial N_i}{\partial z} w_i$$

and

$$\begin{aligned}\frac{\partial u}{\partial y} + \frac{\partial v}{\partial x} &= \sum_{i=1}^4 \frac{\partial N_i}{\partial y} u_i + \sum_{i=1}^4 \frac{\partial N_i}{\partial x} v_i \\ \frac{\partial u}{\partial z} + \frac{\partial w}{\partial x} &= \sum_{i=1}^4 \frac{\partial N_i}{\partial z} u_i + \sum_{i=1}^4 \frac{\partial N_i}{\partial x} w_i \\ \frac{\partial v}{\partial z} + \frac{\partial w}{\partial y} &= \sum_{i=1}^4 \frac{\partial N_i}{\partial z} v_i + \sum_{i=1}^4 \frac{\partial N_i}{\partial y} w_i\end{aligned}$$

so that

$$\left(\begin{array}{c} \frac{\partial u}{\partial x} \\ \frac{\partial v}{\partial y} \\ \frac{\partial w}{\partial z} \\ \frac{\partial u}{\partial y} + \frac{\partial v}{\partial x} \\ \frac{\partial u}{\partial z} + \frac{\partial w}{\partial x} \\ \frac{\partial v}{\partial z} + \frac{\partial w}{\partial y} \end{array} \right) = \underbrace{\left(\begin{array}{cccccccccccccccc} \frac{\partial N_1}{\partial x} & 0 & 0 & \frac{\partial N_2}{\partial x} & 0 & 0 & \frac{\partial N_3}{\partial x} & 0 & 0 & \dots & \frac{\partial N_4}{\partial x} & 0 & 0 \\ 0 & \frac{\partial N_1}{\partial y} & 0 & 0 & \frac{\partial N_2}{\partial y} & 0 & 0 & \frac{\partial N_3}{\partial y} & 0 & \dots & 0 & \frac{\partial N_4}{\partial y} & 0 \\ 0 & 0 & \frac{\partial N_1}{\partial z} & 0 & 0 & \frac{\partial N_2}{\partial z} & 0 & 0 & \frac{\partial N_3}{\partial z} & \dots & 0 & 0 & \frac{\partial N_4}{\partial z} \\ \frac{\partial N_1}{\partial y} & \frac{\partial N_1}{\partial x} & 0 & \frac{\partial N_2}{\partial y} & \frac{\partial N_2}{\partial x} & 0 & \frac{\partial N_3}{\partial y} & \frac{\partial N_3}{\partial x} & 0 & \dots & \frac{\partial N_4}{\partial y} & \frac{\partial N_4}{\partial x} & 0 \\ \frac{\partial N_1}{\partial z} & 0 & \frac{\partial N_1}{\partial x} & \frac{\partial N_2}{\partial z} & 0 & \frac{\partial N_2}{\partial x} & \frac{\partial N_3}{\partial z} & 0 & \frac{\partial N_3}{\partial x} & \dots & \frac{\partial N_4}{\partial z} & 0 & \frac{\partial N_4}{\partial x} \\ 0 & \frac{\partial N_1}{\partial z} & \frac{\partial N_1}{\partial y} & 0 & \frac{\partial N_2}{\partial z} & \frac{\partial N_2}{\partial y} & 0 & \frac{\partial N_3}{\partial z} & \frac{\partial N_3}{\partial y} & \dots & 0 & \frac{\partial N_4}{\partial z} & \frac{\partial N_4}{\partial y} \end{array} \right)}_{B(6 \times 24)} \cdot \underbrace{\left(\begin{array}{c} u1 \\ v1 \\ w1 \\ u2 \\ v2 \\ w2 \\ u3 \\ v3 \\ w3 \\ \dots \\ u8 \\ v8 \\ w8 \end{array} \right)}_{\vec{V}(24 \times 1)}.$$

Finally,

$$\vec{\sigma} = \begin{pmatrix} \sigma_{xx} \\ \sigma_{yy} \\ \sigma_{zz} \\ \sigma_{xy} \\ \sigma_{xz} \\ \sigma_{yz} \end{pmatrix} = (\lambda \mathbf{K} + \eta \mathbf{C}) \cdot \mathbf{B} \cdot \vec{V}$$

We will now establish the weak form of the momentum conservation equation. We start again from

$$\vec{\nabla} \cdot \boldsymbol{\sigma} + \vec{b} = \vec{0}$$

For the N_i 's 'regular enough', we can write:

$$\int_{\Omega_e} N_i \vec{\nabla} \cdot \boldsymbol{\sigma} d\Omega + \int_{\Omega_e} N_i \vec{b} d\Omega = 0$$

We can integrate by parts and drop the surface term²¹:

$$\int_{\Omega_e} \vec{\nabla} N_i \cdot \boldsymbol{\sigma} d\Omega = \int_{\Omega_e} N_i \vec{b} d\Omega$$

or,

$$\int_{\Omega_e} \left(\begin{array}{ccccc} \frac{\partial N_i}{\partial x} & 0 & 0 & \frac{\partial N_i}{\partial y} & \frac{\partial N_i}{\partial z} \\ 0 & \frac{\partial N_i}{\partial y} & 0 & \frac{\partial N_i}{\partial x} & 0 \\ 0 & 0 & \frac{\partial N_i}{\partial z} & 0 & \frac{\partial N_i}{\partial x} \end{array} \right) \cdot \begin{pmatrix} \sigma_{xx} \\ \sigma_{yy} \\ \sigma_{zz} \\ \sigma_{xy} \\ \sigma_{xz} \\ \sigma_{yz} \end{pmatrix} d\Omega = \int_{\Omega_e} N_i \vec{b} d\Omega$$

²¹We will come back to this at a later stage

Let $i = 1, 2, 3, 4, \dots, 8$ and stack the resulting eight equations on top of one another.

$$\begin{aligned} \int_{\Omega_e} \begin{pmatrix} \frac{\partial N_i}{\partial x} & 0 & 0 & \frac{\partial N_i}{\partial y} & \frac{\partial N_i}{\partial z} & 0 \\ 0 & \frac{\partial N_i}{\partial y} & 0 & \frac{\partial N_i}{\partial x} & 0 & \frac{\partial N_i}{\partial z} \\ 0 & 0 & \frac{\partial N_i}{\partial z} & 0 & \frac{\partial N_i}{\partial x} & \frac{\partial N_i}{\partial y} \end{pmatrix} \cdot \begin{pmatrix} \sigma_{xx} \\ \sigma_{yy} \\ \sigma_{zz} \\ \sigma_{xy} \\ \sigma_{xz} \\ \sigma_{yz} \end{pmatrix} d\Omega &= \int_{\Omega_e} N_1 \begin{pmatrix} b_x \\ b_y \\ b_z \end{pmatrix} d\Omega \\ \int_{\Omega_e} \begin{pmatrix} \frac{\partial N_i}{\partial x} & 0 & 0 & \frac{\partial N_i}{\partial y} & \frac{\partial N_i}{\partial z} & 0 \\ 0 & \frac{\partial N_i}{\partial y} & 0 & \frac{\partial N_i}{\partial x} & 0 & \frac{\partial N_i}{\partial z} \\ 0 & 0 & \frac{\partial N_i}{\partial z} & 0 & \frac{\partial N_i}{\partial x} & \frac{\partial N_i}{\partial y} \end{pmatrix} \cdot \begin{pmatrix} \sigma_{xx} \\ \sigma_{yy} \\ \sigma_{zz} \\ \sigma_{xy} \\ \sigma_{xz} \\ \sigma_{yz} \end{pmatrix} d\Omega &= \int_{\Omega_e} N_2 \begin{pmatrix} b_x \\ b_y \\ b_z \end{pmatrix} d\Omega \\ &\dots \\ \int_{\Omega_e} \begin{pmatrix} \frac{\partial N_8}{\partial x} & 0 & 0 & \frac{\partial N_8}{\partial y} & \frac{\partial N_8}{\partial z} & 0 \\ 0 & \frac{\partial N_8}{\partial y} & 0 & \frac{\partial N_8}{\partial x} & 0 & \frac{\partial N_8}{\partial z} \\ 0 & 0 & \frac{\partial N_8}{\partial z} & 0 & \frac{\partial N_8}{\partial x} & \frac{\partial N_8}{\partial y} \end{pmatrix} \cdot \begin{pmatrix} \sigma_{xx} \\ \sigma_{yy} \\ \sigma_{zz} \\ \sigma_{xy} \\ \sigma_{xz} \\ \sigma_{yz} \end{pmatrix} d\Omega &= \int_{\Omega_e} N_8 \begin{pmatrix} b_x \\ b_y \\ b_z \end{pmatrix} d\Omega \quad (277) \end{aligned}$$

We easily recognize \mathbf{B}^T inside the integrals! Let us define

$$\vec{N}_b^T = (N_1 b_x, N_1 b_y, N_1 b_z, \dots, N_8 b_x, N_8 b_y, N_8 b_z)$$

then we can write

$$\int_{\Omega_e} \mathbf{B}^T \cdot \begin{pmatrix} \sigma_{xx} \\ \sigma_{yy} \\ \sigma_{zz} \\ \sigma_{xy} \\ \sigma_{xz} \\ \sigma_{yz} \end{pmatrix} d\Omega = \int_{\Omega_e} \vec{N}_b d\Omega$$

and finally:

$$\int_{\Omega_e} \mathbf{B}^T \cdot [\lambda \mathbf{K} + \eta \mathbf{C}] \cdot \mathbf{B} \cdot \vec{V} d\Omega = \int_{\Omega_e} \vec{N}_b d\Omega$$

Since \vec{V} contains the vector of unknowns (i.e. the velocities at the corners), it does not depend on the x or y coordinates so it can be taken outside of the integral:

$$\underbrace{\left(\int_{\Omega_e} \mathbf{B}^T \cdot [\lambda \mathbf{K} + \eta \mathbf{C}] \cdot \mathbf{B} d\Omega \right)}_{\mathbf{A}_{el}(24 \times 24)} \cdot \underbrace{\vec{V}}_{(24 \times 1)} = \underbrace{\int_{\Omega_e} \vec{N}_b d\Omega}_{\vec{B}_{el}(24 \times 1)}$$

or,

$$\left[\underbrace{\left(\int_{\Omega_e} \lambda \mathbf{B}^T \cdot \mathbf{K} \cdot \mathbf{B} d\Omega \right)}_{\mathbf{A}_{el}^\lambda(24 \times 24)} + \underbrace{\left(\int_{\Omega_e} \eta \mathbf{B}^T \cdot \mathbf{C} \cdot \mathbf{B} d\Omega \right)}_{\mathbf{A}_{el}^\eta(24 \times 24)} \right] \cdot \underbrace{\vec{V}}_{(24 \times 1)} = \underbrace{\int_{\Omega_e} \vec{N}_b d\Omega}_{\vec{B}_{el}(24 \times 1)}$$

reduced integration

reduced integration [863]

write about 3D to 2D

6.4 The mixed FEM for viscous flow

6.4.1 in three dimensions

In what follows the flow is assumed to be incompressible, isoviscous and isothermal.

The methodology to derive the discretised equations of the mixed system is quite similar to the one we have used in the case of the penalty formulation. The big difference comes from the fact that we are now solving for both velocity and pressure at the same time, and that we therefore must solve the mass and momentum conservation equations together. As before, velocity inside an element is given by

$$\vec{v}^h(\vec{r}) = \sum_{i=1}^{m_v} N_i^v(\vec{r}) \vec{v}_i \quad (278)$$

where N_i^v are the polynomial basis functions for the velocity, and the summation runs over the m_v nodes composing the element. A similar expression is used for pressure:

$$p^h(\vec{r}) = \sum_{i=1}^{m_p} N_i^p(\vec{r}) p_i \quad (279)$$

Note that the velocity is a vector of size while pressure (and temperature) is a scalar. There are then $ndof_v$ velocity degrees of freedom per node and $ndof_p$ pressure degrees of freedom. It is also very important to remember that the numbers of velocity nodes and pressure nodes for a given element are more often than not different and that velocity and pressure nodes need not be colocated. Indeed, unless co-called 'stabilised elements' are used, we have $m_v > m_p$, which means that the polynomial order of the velocity field is higher than the polynomial order of the pressure field (usually by value 1).

insert here link(s) to manual and literature

Other notations are sometimes used for Eqs.(278) and (279):

$$u^h(\vec{r}) = \vec{N}^v \cdot \vec{u} \quad v^h(\vec{r}) = \vec{N}^v \cdot \vec{v} \quad w^h(\vec{r}) = \vec{N}^v \cdot \vec{w} \quad p^h(\vec{r}) = \vec{N}^p \cdot \vec{p} \quad (280)$$

where $\vec{v} = (u, v, w)$ and \vec{N}^v is the vector containing all basis functions evaluated at location \vec{r} :

$$\vec{N}^v = (N_1^v(\vec{r}), N_2^v(\vec{r}), N_3^v(\vec{r}), \dots, N_{m_v}^v(\vec{r})) \quad (281)$$

$$\vec{N}^p = (N_1^p(\vec{r}), N_2^p(\vec{r}), N_3^p(\vec{r}), \dots, N_{m_p}^p(\vec{r})) \quad (282)$$

and with

$$\vec{u} = (u_1, u_2, u_3, \dots, u_{m_v}) \quad (283)$$

$$\vec{v} = (v_1, v_2, v_3, \dots, v_{m_v}) \quad (284)$$

$$\vec{w} = (w_1, w_2, w_3, \dots, w_{m_v}) \quad (285)$$

$$\vec{p} = (p_1, p_2, p_3, \dots, p_{m_p}) \quad (286)$$

We will now establish the weak form of the momentum conservation equation. We start again from

$$\vec{\nabla} \cdot \boldsymbol{\sigma} + \vec{b} = \vec{0} \quad (287)$$

$$\vec{\nabla} \cdot \vec{v} = 0 \quad (288)$$

For the N_i^v 's and N_i^p 'regular enough', we can write:

$$\int_{\Omega_e} N_i^v \vec{\nabla} \cdot \boldsymbol{\sigma} d\Omega + \int_{\Omega_e} N_i^v \vec{b} d\Omega = \vec{0} \quad (289)$$

$$\int_{\Omega_e} N_i^p \vec{\nabla} \cdot \vec{v} d\Omega = 0 \quad (290)$$

We can integrate by parts and drop the surface term²²:

$$\int_{\Omega_e} \vec{\nabla} N_i^v \cdot \boldsymbol{\sigma} d\Omega = \int_{\Omega_e} N_i^v \vec{b} d\Omega \quad (291)$$

$$\int_{\Omega_e} N_i^p \vec{\nabla} \cdot \vec{v} d\Omega = 0 \quad (292)$$

²²We will come back to this at a later stage

or,

$$\int_{\Omega_e} \begin{pmatrix} \frac{\partial N_i^\gamma}{\partial x} & 0 & 0 & \frac{\partial N_i^\gamma}{\partial y} & \frac{\partial N_i^\gamma}{\partial z} & 0 \\ 0 & \frac{\partial N_i^\gamma}{\partial y} & 0 & \frac{\partial N_i^\gamma}{\partial x} & 0 & \frac{\partial N_i^\gamma}{\partial z} \\ 0 & 0 & \frac{\partial N_i^\gamma}{\partial z} & 0 & \frac{\partial N_i^\gamma}{\partial x} & \frac{\partial N_i^\gamma}{\partial y} \end{pmatrix} \cdot \begin{pmatrix} \sigma_{xx} \\ \sigma_{yy} \\ \sigma_{zz} \\ \sigma_{xy} \\ \sigma_{xz} \\ \sigma_{yz} \end{pmatrix} d\Omega = \int_{\Omega_e} N_i^\gamma \vec{b} d\Omega \quad (293)$$

The above equation can ultimately be written:

$$\int_{\Omega_e} \mathbf{B}^T \cdot \begin{pmatrix} \sigma_{xx} \\ \sigma_{yy} \\ \sigma_{zz} \\ \sigma_{xy} \\ \sigma_{xz} \\ \sigma_{yz} \end{pmatrix} d\Omega = \int_{\Omega_e} \vec{N}_b d\Omega \quad (294)$$

We have previously established that the strain rate vector $\vec{\varepsilon}$ is:

$$\vec{\varepsilon} = \begin{pmatrix} \frac{\partial u}{\partial x} \\ \frac{\partial v}{\partial y} \\ \frac{\partial w}{\partial z} \\ \frac{\partial u}{\partial y} + \frac{\partial v}{\partial x} \\ \frac{\partial u}{\partial z} + \frac{\partial w}{\partial x} \\ \frac{\partial v}{\partial z} + \frac{\partial w}{\partial y} \end{pmatrix} = \begin{pmatrix} \sum_i \frac{\partial N_i^\gamma}{\partial x} u_i \\ \sum_i \frac{\partial N_i^\gamma}{\partial y} v_i \\ \sum_i \frac{\partial N_i^\gamma}{\partial z} w_i \\ \sum_i (\frac{\partial N_i^\gamma}{\partial y} u_i + \frac{\partial N_i^\gamma}{\partial x} v_i) \\ \sum_i (\frac{\partial N_i^\gamma}{\partial z} u_i + \frac{\partial N_i^\gamma}{\partial x} w_i) \\ \sum_i (\frac{\partial N_i^\gamma}{\partial z} v_i + \frac{\partial N_i^\gamma}{\partial y} w_i) \end{pmatrix} = \underbrace{\begin{pmatrix} \frac{\partial N_1^\gamma}{\partial x} & 0 & 0 & \dots & \frac{\partial N_{m_v}^\gamma}{\partial x} & 0 & 0 \\ 0 & \frac{\partial N_1^\gamma}{\partial y} & 0 & \dots & 0 & \frac{\partial N_{m_v}^\gamma}{\partial y} & 0 \\ 0 & 0 & \frac{\partial N_1^\gamma}{\partial z} & \dots & 0 & 0 & \frac{\partial N_{m_v}^\gamma}{\partial z} \\ \frac{\partial N_1^\gamma}{\partial y} & \frac{\partial N_1^\gamma}{\partial x} & 0 & \dots & \frac{\partial N_{m_v}^\gamma}{\partial x} & \frac{\partial N_{m_v}^\gamma}{\partial x} & 0 \\ \frac{\partial N_1^\gamma}{\partial z} & 0 & \frac{\partial N_1^\gamma}{\partial x} & \dots & \frac{\partial N_{m_v}^\gamma}{\partial z} & 0 & \frac{\partial N_{m_v}^\gamma}{\partial x} \\ 0 & \frac{\partial N_1^\gamma}{\partial z} & \frac{\partial N_1^\gamma}{\partial y} & \dots & 0 & \frac{\partial N_{m_v}^\gamma}{\partial z} & \frac{\partial N_{m_v}^\gamma}{\partial y} \end{pmatrix}}_B \begin{pmatrix} u_1 \\ v_1 \\ w_1 \\ u_2 \\ v_2 \\ w_2 \\ u_3 \\ v_3 \\ \dots \\ u_{m_v} \\ v_{m_v} \\ w_{m_v} \end{pmatrix} \underbrace{\vec{V}}$$
(295)

or, $\vec{\varepsilon} = \mathbf{B} \cdot \vec{V}$ where \mathbf{B} is the gradient matrix and \vec{V} is the vector of all vector degrees of freedom for the element. The matrix \mathbf{B} is then of size $3 \times m_v \times ndim$ and the vector \vec{V} is $m_v * ndof$ long. we have

$$\sigma_{xx} = -p + 2\eta\dot{\varepsilon}_{xx}^d \quad (296)$$

$$\sigma_{yy} = -p + 2\eta\dot{\varepsilon}_{yy}^d \quad (297)$$

$$\sigma_{zz} = -p + 2\eta\dot{\varepsilon}_{zz}^d \quad (298)$$

$$\sigma_{xy} = 2\eta\dot{\varepsilon}_{xy}^d \quad (299)$$

$$\sigma_{xz} = 2\eta\dot{\varepsilon}_{xz}^d \quad (300)$$

$$\sigma_{yz} = 2\eta\dot{\varepsilon}_{yz}^d \quad (301)$$

Since we here only consider incompressible flow, we have $\dot{\varepsilon}^d = \dot{\varepsilon}$ so

$$\vec{\sigma} = - \begin{pmatrix} 1 \\ 1 \\ 1 \\ 0 \\ 0 \\ 0 \end{pmatrix} p + \mathbf{C} \cdot \vec{\varepsilon} = - \begin{pmatrix} 1 \\ 1 \\ 1 \\ 0 \\ 0 \\ 0 \end{pmatrix} \vec{N}^p \cdot \vec{P} + \mathbf{C} \cdot \mathbf{B} \cdot \vec{V} \quad (302)$$

with

$$\mathbf{C} = \eta \begin{pmatrix} 2 & 0 & 0 & 0 & 0 & 0 \\ 0 & 2 & 0 & 0 & 0 & 0 \\ 0 & 0 & 2 & 0 & 0 & 0 \\ 0 & 0 & 0 & 1 & 0 & 0 \\ 0 & 0 & 0 & 0 & 1 & 0 \\ 0 & 0 & 0 & 0 & 0 & 1 \end{pmatrix} \quad \vec{\varepsilon} = \begin{pmatrix} \dot{\varepsilon}_{xx} \\ \dot{\varepsilon}_{yy} \\ \dot{\varepsilon}_{zz} \\ 2\dot{\varepsilon}_{xy} \\ 2\dot{\varepsilon}_{xz} \\ 2\dot{\varepsilon}_{yz} \end{pmatrix} \quad (303)$$

Let us define matrix \mathbf{N}^p of size $6 \times m_p$:

$$\mathbf{N}^p = \begin{pmatrix} 1 \\ 1 \\ 1 \\ 0 \\ 0 \\ 0 \end{pmatrix} \quad \vec{N}^p = \begin{pmatrix} \vec{N}^p \\ \vec{N}^p \\ \vec{N}^p \\ 0 \\ 0 \\ 0 \end{pmatrix} \quad (304)$$

so that

$$\vec{\sigma} = -\mathbf{N}^p \cdot \vec{P} + \mathbf{C} \cdot \mathbf{B} \cdot \vec{V} \quad (305)$$

finally

$$\int_{\Omega_e} \mathbf{B}^T \cdot [-\mathbf{N}^p \cdot \vec{P} + \mathbf{C} \cdot \mathbf{B} \cdot \vec{V}] d\Omega = \int_{\Omega_e} \mathbf{N}_b d\Omega \quad (306)$$

or,

$$\underbrace{\left(- \int_{\Omega_e} \mathbf{B}^T \cdot \mathbf{N}^p d\Omega \right)}_{\mathbb{G}} \cdot \vec{P} + \underbrace{\left(\int_{\Omega_e} \mathbf{B}^T \cdot \mathbf{C} \cdot \mathbf{B} d\Omega \right)}_{\mathbb{K}} \cdot \vec{V} = \underbrace{\int_{\Omega_e} \vec{N}_b d\Omega}_{\vec{f}} \quad (307)$$

where the matrix \mathbb{K} is of size $(m_v * ndof_v \times m_v * ndof_v)$, and matrix \mathbb{G} is of size $(m_v * ndof_v \times m_p * ndof_p)$.

Turning now to the mass conservation equation:

$$\begin{aligned}
\vec{0} &= \int_{\Omega_e} \vec{N}^p \vec{\nabla} \cdot \vec{v} d\Omega \\
&= \int_{\Omega_e} \vec{N}^p \sum_{i=1}^{m_v} \left(\frac{\partial N_i^v}{\partial x} u_i + \frac{\partial N_i^v}{\partial y} v_i + \frac{\partial N_i^v}{\partial z} w_i \right) d\Omega \\
&= \int_{\Omega_e} \begin{pmatrix} N_1^p \left(\sum_{i=1}^{m_v} \frac{\partial N_i^v}{\partial x} u_i + \sum_{i=1}^{m_v} \frac{\partial N_i^v}{\partial y} v_i + \sum_{i=1}^{m_v} \frac{\partial N_i^v}{\partial z} w_i \right) \\ N_2^p \left(\sum_{i=1}^{m_v} \frac{\partial N_i^v}{\partial x} u_i + \sum_{i=1}^{m_v} \frac{\partial N_i^v}{\partial y} v_i + \sum_{i=1}^{m_v} \frac{\partial N_i^v}{\partial z} w_i \right) \\ N_3^p \left(\sum_{i=1}^{m_v} \frac{\partial N_i^v}{\partial x} u_i + \sum_{i=1}^{m_v} \frac{\partial N_i^v}{\partial y} v_i + \sum_{i=1}^{m_v} \frac{\partial N_i^v}{\partial z} w_i \right) \\ \vdots \\ N_{m_p}^p \left(\sum_{i=1}^{m_v} \frac{\partial N_i^v}{\partial x} u_i + \sum_{i=1}^{m_v} \frac{\partial N_i^v}{\partial y} v_i + \sum_{i=1}^{m_v} \frac{\partial N_i^v}{\partial z} w_i \right) \end{pmatrix} d\Omega \\
&= \int_{\Omega_e} \begin{pmatrix} N_1^p & N_1^p & N_1^p & 0 & 0 & 0 \\ N_2^p & N_2^p & N_2^p & 0 & 0 & 0 \\ N_3^p & N_3^p & N_3^p & 0 & 0 & 0 \\ \vdots & \vdots & \vdots & \vdots & \vdots & \vdots \\ N_{m_p}^p & N_{m_p}^p & N_{m_p}^p & 0 & 0 & 0 \end{pmatrix} \cdot \begin{pmatrix} \sum_i \frac{\partial N_i^v}{\partial x} u_i \\ \sum_i \frac{\partial N_i^v}{\partial y} v_i \\ \sum_i \frac{\partial N_i^v}{\partial z} w_i \\ \sum_i (\frac{\partial N_i^v}{\partial y} u_i + \frac{\partial N_i^v}{\partial x} v_i) \\ \sum_i (\frac{\partial N_i^v}{\partial z} u_i + \frac{\partial N_i^v}{\partial x} w_i) \\ \sum_i (\frac{\partial N_i^v}{\partial z} v_i + \frac{\partial N_i^v}{\partial y} w_i) \end{pmatrix} d\Omega \\
&= \int_{\Omega_e} \underbrace{\begin{pmatrix} N_1^p & N_1^p & N_1^p & 0 & 0 & 0 \\ N_2^p & N_2^p & N_2^p & 0 & 0 & 0 \\ N_3^p & N_3^p & N_3^p & 0 & 0 & 0 \\ \vdots & \vdots & \vdots & \vdots & \vdots & \vdots \\ N_{m_p}^p & N_{m_p}^p & N_{m_p}^p & 0 & 0 & 0 \end{pmatrix}}_{\mathbf{N}^p} \cdot \vec{\varepsilon} d\Omega \\
&= \left(\int \mathbf{N}^p \cdot \mathbf{B} d\Omega \right) \cdot \vec{V} \\
&= -\mathbb{G}_e^T \cdot \vec{V} \tag{308}
\end{aligned}$$

Note that it is common to actually start from $-\vec{\nabla} \cdot \vec{v} = 0$ (see Eq.(3) in [1154]) so as to arrive at $\mathbb{G}_e^T \cdot \vec{V} = \vec{0}$

Ultimately we obtain the following system for each element:

$$\begin{pmatrix} \mathbb{K}_e & \mathbb{G}_e \\ -\mathbb{G}_e^T & 0 \end{pmatrix} \cdot \begin{pmatrix} \vec{V} \\ \vec{P} \end{pmatrix} = \begin{pmatrix} \vec{f}_e \\ 0 \end{pmatrix}$$

Such a matrix is then generated for each element and then must be assembled into the global F.E. matrix. Note that in this case the elemental Stokes matrix is antisymmetric. One can also define the following symmetric modified Stokes matrix:

$$\begin{pmatrix} \mathbb{K}_e & \mathbb{G}_e \\ \mathbb{G}_e^T & 0 \end{pmatrix} \cdot \begin{pmatrix} \vec{V} \\ \vec{P} \end{pmatrix} = \begin{pmatrix} \vec{f}_e \\ 0 \end{pmatrix}$$

This matrix is symmetric, but indefinite. It is non-singular if $\ker(\mathbb{G}^T) = 0$, which is the case if the compatibility condition holds.

CHECK: Matrix \mathbb{K} is the viscosity matrix. Its size is $(ndof_v * N_v) \times (ndof_v * N_v)$ where $ndof_v$ is the number of velocity degrees of freedom per node (typically 1,2 or 3) and N_v is the number of velocity nodes. The size of matrix \mathbb{G} is $(ndof_v * N_v) \times (ndof_p * N_p)$ where $ndof_p (= 1)$ is the number of velocity degrees of freedom per node and N_p is the number of pressure nodes. Conversely, the size of matrix \mathbb{G}^T is $(ndof_p * N_p) \times (ndof_v * N_v)$. The size of the global FE matrix is $N = ndof_v * N_v + ndof_p * N_p$. Note that matrix \mathbb{K} is analogous to a discrete Laplacian operator, matrix \mathbb{G} to a discrete gradient operator, and matrix \mathbb{G}^T to a discrete divergence operator.

On the physical dimensions of the Stokes matrix blocks We start from the Stokes equations:

$$-\vec{\nabla} p + \vec{\nabla} \cdot (2\eta \dot{\boldsymbol{\varepsilon}}) + \rho \mathbf{g} = 0 \quad (309)$$

$$\vec{\nabla} \cdot \vec{v} = 0 \quad (310)$$

The dimensions of the terms in the first equation are: $ML^{-2}T^{-2}$. The blocks \mathbb{K} and \mathbb{G} stem from the weak form which obtained by multiplying the strong form equations by the (dimensionless) basis functions and integrating over the domain, so that it follows that

$$[\mathbb{K} \cdot \vec{V}] = [\mathbb{G} \cdot \vec{P}] = [\vec{f}] = ML^{-2}T^{-2}L^3 = MLT^{-2}$$

We can then easily deduce:

$$[\mathbb{K}] = MT^{-1} \quad [\mathbb{G}] = L^2$$

On elemental level mass balance. Note that in what is above no assumption has been made about whether the pressure basis functions are continuous or discontinuous from one element to another.

Indeed, as mentioned in [743], since the weak formulation of the momentum equation involves integration by parts of $\vec{\nabla} p$, the resulting weak form contains no derivatives of pressure. This introduces the possibility of approximating it by functions (piecewise polynomials, of course) that are not C^0 -continuous, and indeed this has been done and is quite popular/useful.

It is then worth noting that *only* discontinuous pressure elements assure an element-level mass balance [743]: if for instance N_i^p is piecewise-constant on element e (of value 1), the elemental weak form of the mass conservation equation is

$$\int_{\Omega_e} N_i^p \vec{\nabla} \cdot \vec{v} = \int_{\Omega_e} \vec{\nabla} \cdot \vec{v} = \int_{\Gamma_e} \vec{n} \cdot \vec{v} = 0$$

One potentially unwelcome consequence of using discontinuous pressure elements is that they do not possess uniquely defined pressure on the element boundaries; they are dual valued there, and often multi-valued at certain velocity nodes.

On the \boldsymbol{C} matrix The relationship between deviatoric stress and deviatoric strain rate tensor is

$$\boldsymbol{\tau} = 2\eta \dot{\boldsymbol{\varepsilon}}^d \quad (311)$$

$$= 2\eta \left(\dot{\boldsymbol{\varepsilon}} - \frac{1}{3} (\vec{\nabla} \cdot \vec{v}) \mathbf{1} \right) \quad (312)$$

$$= 2\eta \left[\begin{pmatrix} \dot{\varepsilon}_{xx} & \dot{\varepsilon}_{xy} & \dot{\varepsilon}_{xz} \\ \dot{\varepsilon}_{yx} & \dot{\varepsilon}_{yy} & \dot{\varepsilon}_{yz} \\ \dot{\varepsilon}_{zx} & \dot{\varepsilon}_{zy} & \dot{\varepsilon}_{zz} \end{pmatrix} - \frac{1}{3} (\dot{\varepsilon}_{xx} + \dot{\varepsilon}_{yy} + \dot{\varepsilon}_{zz}) \begin{pmatrix} 1 & 0 & 0 \\ 0 & 1 & 0 \\ 0 & 0 & 1 \end{pmatrix} \right] \quad (313)$$

$$= \frac{2}{3} \eta \begin{pmatrix} 2\dot{\varepsilon}_{xx} - \dot{\varepsilon}_{yy} - \dot{\varepsilon}_{zz} & 3\dot{\varepsilon}_{xy} & 3\dot{\varepsilon}_{xz} \\ 3\dot{\varepsilon}_{yx} & -\dot{\varepsilon}_{yy} + 2\dot{\varepsilon}_{yy} - \dot{\varepsilon}_{yy} & 3\dot{\varepsilon}_{yz} \\ 3\dot{\varepsilon}_{zx} & 3\dot{\varepsilon}_{zy} & -\dot{\varepsilon}_{xx} - \dot{\varepsilon}_{yy} - 2\dot{\varepsilon}_{zz} \end{pmatrix} \quad (314)$$

so that

$$\vec{\tau} = \frac{2}{3}\eta \begin{pmatrix} 2\dot{\varepsilon}_{xx} - \dot{\varepsilon}_{yy} - \dot{\varepsilon}_{zz} \\ -\dot{\varepsilon}_{yy} + 2\dot{\varepsilon}_{yy} - \dot{\varepsilon}_{yy} \\ -\dot{\varepsilon}_{xx} - \dot{\varepsilon}_{yy} + 2\dot{\varepsilon}_{zz} \\ 3\dot{\varepsilon}_{xy} \\ 3\dot{\varepsilon}_{xz} \\ 3\dot{\varepsilon}_{yz} \end{pmatrix} = \underbrace{\frac{\eta}{3} \begin{pmatrix} 4 & -2 & -2 & 0 & 0 & 0 \\ -2 & 4 & -2 & 0 & 0 & 0 \\ -2 & -2 & 4 & 0 & 0 & 0 \\ 0 & 0 & 0 & 3 & 0 & 0 \\ 0 & 0 & 0 & 0 & 3 & 0 \\ 0 & 0 & 0 & 0 & 0 & 3 \end{pmatrix}}_{C^d} \cdot \begin{pmatrix} \dot{\varepsilon}_{xx} \\ \dot{\varepsilon}_{yy} \\ \dot{\varepsilon}_{zz} \\ 2\dot{\varepsilon}_{xy} \\ 2\dot{\varepsilon}_{xz} \\ 2\dot{\varepsilon}_{yz} \end{pmatrix} = \mathbf{C}^d \cdot \vec{\varepsilon} \quad (315)$$

which is identical to the one in the Appendix A of [1434]. In two dimensions, we have

$$\vec{\tau} = \frac{1}{3}\eta \underbrace{\begin{pmatrix} 4 & -2 & 0 \\ -2 & 4 & 0 \\ 0 & 0 & 3 \end{pmatrix}}_{C^d}.$$

see for instance [32].

In the case where we assume incompressible flow from the beginning, i.e. $\dot{\varepsilon} = \dot{\varepsilon}^d$, then

$$\vec{\tau} = \eta \underbrace{\begin{pmatrix} 2 & 0 & 0 & 0 & 0 & 0 \\ 0 & 2 & 0 & 0 & 0 & 0 \\ 0 & 0 & 2 & 0 & 0 & 0 \\ 0 & 0 & 0 & 1 & 0 & 0 \\ 0 & 0 & 0 & 0 & 1 & 0 \\ 0 & 0 & 0 & 0 & 0 & 1 \end{pmatrix}}_C \cdot \begin{pmatrix} \dot{\varepsilon}_{xx} \\ \dot{\varepsilon}_{yy} \\ \dot{\varepsilon}_{zz} \\ 2\dot{\varepsilon}_{xy} \\ 2\dot{\varepsilon}_{xz} \\ 2\dot{\varepsilon}_{yz} \end{pmatrix} = \mathbf{C} \cdot \vec{\varepsilon} \quad (316)$$

Two slightly different formulations The momentum conservation equation can be written as follows:

$$\vec{\nabla} \cdot (2\eta \vec{\varepsilon}) - \vec{\nabla} p + \vec{b} = \vec{0}$$

When the viscosity η is constant this equation becomes

$$\eta \Delta \vec{v} - \vec{\nabla} p + \vec{b} = \vec{0}$$

In this case the matrix \mathbf{B} takes a different form [473, Eq. 6.24] and one should be aware that this can have consequences for the Neumann boundary conditions.

In [282] the authors state that when the Laplacian formulation is used it has the computational advantage that the velocity components are coupled only through the incompressibility condition. While the two formulations are equivalent only for constant viscosity, they state that they employ the Laplacian approach formulation as a preconditioner for the viscous term.

Concretely, we apply the same method as above, i.e. we reorganise the terms of the velocity gradient

tensor in a vector:

$$\vec{\nabla} \vec{v} \rightarrow \begin{pmatrix} \partial_x u \\ \partial_y u \\ \partial_z u \\ \partial_x v \\ \partial_y v \\ \partial_z v \\ \partial_x w \\ \partial_y w \\ \partial_z w \end{pmatrix} = \begin{pmatrix} \sum_i \partial_x N_i u_i \\ \sum_i \partial_y N_i u_i \\ \sum_i \partial_z N_i u_i \\ \sum_i \partial_x N_i v_i \\ \sum_i \partial_y N_i v_i \\ \sum_i \partial_z N_i v_i \\ \sum_i \partial_x N_i w_i \\ \sum_i \partial_y N_i w_i \\ \sum_i \partial_z N_i w_i \end{pmatrix}$$

$$= \underbrace{\begin{pmatrix} \partial_x N_1^Y & 0 & 0 & \partial_x N_2^Y & 0 & 0 & \dots & \partial_x N_{m_v}^Y & 0 & 0 \\ \partial_y N_1^Y & 0 & 0 & \partial_y N_2^Y & 0 & 0 & \dots & \partial_y N_{m_v}^Y & 0 & 0 \\ \partial_z N_1^Y & 0 & 0 & \partial_z N_2^Y & 0 & 0 & \dots & \partial_z N_{m_v}^Y & 0 & 0 \\ 0 & \partial_x N_1^Y & 0 & 0 & \partial_x N_2^Y & 0 & \dots & 0 & \partial_x N_{m_v}^Y & 0 \\ 0 & \partial_y N_1^Y & 0 & 0 & \partial_y N_2^Y & 0 & \dots & 0 & \partial_y N_{m_v}^Y & 0 \\ 0 & \partial_z N_1^Y & 0 & 0 & \partial_z N_2^Y & 0 & \dots & 0 & \partial_z N_{m_v}^Y & 0 \\ 0 & 0 & \partial_x N_1^Y & 0 & 0 & \partial_x N_2^Y & \dots & 0 & 0 & \partial_x N_{m_v}^Y \\ 0 & 0 & \partial_y N_1^Y & 0 & 0 & \partial_y N_2^Y & \dots & 0 & 0 & \partial_y N_{m_v}^Y \\ 0 & 0 & \partial_z N_1^Y & 0 & 0 & \partial_z N_2^Y & \dots & 0 & 0 & \partial_z N_{m_v}^Y \end{pmatrix}}_B \cdot \underbrace{\begin{pmatrix} u_1 \\ v_1 \\ w_1 \\ u_2 \\ v_2 \\ w_2 \\ u_3 \\ v_3 \\ \dots \\ u_{m_v} \\ v_{m_v} \\ w_{m_v} \end{pmatrix}}_{\vec{V}}$$

and in two dimensions:

$$\vec{\nabla} \vec{v} \rightarrow \begin{pmatrix} \partial_x u \\ \partial_y u \\ \partial_x v \\ \partial_y v \end{pmatrix} = \begin{pmatrix} \sum_i \partial_x N_i u_i \\ \sum_i \partial_y N_i u_i \\ \sum_i \partial_x N_i v_i \\ \sum_i \partial_y N_i v_i \end{pmatrix} = \underbrace{\begin{pmatrix} \partial_x N_1^Y & 0 & \partial_x N_2^Y & 0 & \dots & \partial_x N_{m_v}^Y & 0 \\ \partial_y N_1^Y & 0 & \partial_y N_2^Y & 0 & \dots & \partial_y N_{m_v}^Y & 0 \\ 0 & \partial_x N_1^Y & 0 & \partial_x N_2^Y & \dots & 0 & \partial_x N_{m_v}^Y \\ 0 & \partial_y N_1^Y & 0 & \partial_y N_2^Y & \dots & 0 & \partial_y N_{m_v}^Y \end{pmatrix}}_B \cdot \underbrace{\begin{pmatrix} u_1 \\ v_1 \\ u_2 \\ v_2 \\ u_3 \\ v_3 \\ \dots \\ u_{m_v} \\ v_{m_v} \end{pmatrix}}_{\vec{V}}$$

On the 'forgotten' surface terms

6.4.2 Going from 3D to 2D

The world is three-dimensional. However, for many different reasons one may wish to solve problems which are two-dimensional.

Following ASPECT manual, we will think of two-dimensional models in the following way:

- We assume that the domain we want to solve on is a two-dimensional cross section (in the $x - y$ plane) that extends infinitely far in both negative and positive z direction.
- We assume that the velocity is zero in the z direction and that all variables have no variation in the z direction.

As a consequence, two-dimensional models are three-dimensional ones in which the z component of the velocity is zero and so are all z derivatives. This allows to reduce the momentum conservation equations from 3 equations to 2 equations. However, contrarily to what is often seen, the 3D definition of the deviatoric strain rate remains, i.e. in other words:

$$\dot{\epsilon}^d = \dot{\epsilon} - \frac{1}{3}(\vec{\nabla} \cdot \vec{v})\mathbf{1} \quad (317)$$

and not $1/2$. In light of all this, the full strain rate tensor and the deviatoric strain rate tensor in 2D are given by:

$$\boldsymbol{\varepsilon} = \begin{pmatrix} \dot{\varepsilon}_{xx} & \dot{\varepsilon}_{xy} & \dot{\varepsilon}_{xz} \\ \dot{\varepsilon}_{yx} & \dot{\varepsilon}_{yy} & \dot{\varepsilon}_{yz} \\ \dot{\varepsilon}_{zx} & \dot{\varepsilon}_{zy} & \dot{\varepsilon}_{zz} \end{pmatrix} = \begin{pmatrix} \frac{\partial u}{\partial x} & \frac{1}{2} \left(\frac{\partial u}{\partial y} + \frac{\partial v}{\partial x} \right) & 0 \\ \frac{1}{2} \left(\frac{\partial u}{\partial y} + \frac{\partial v}{\partial x} \right) & \frac{\partial v}{\partial y} & 0 \\ 0 & 0 & 0 \end{pmatrix} \quad (318)$$

$$\dot{\boldsymbol{\varepsilon}}^d = \frac{1}{3} \begin{pmatrix} 2 \frac{\partial u}{\partial x} - \frac{\partial v}{\partial y} & \frac{1}{2} \left(\frac{\partial u}{\partial y} + \frac{\partial v}{\partial x} \right) & 0 \\ \frac{1}{2} \left(\frac{\partial u}{\partial y} + \frac{\partial v}{\partial x} \right) & -\frac{\partial u}{\partial x} + 2 \frac{\partial v}{\partial y} & 0 \\ 0 & 0 & -\frac{\partial u}{\partial x} - \frac{\partial v}{\partial y} \end{pmatrix} \quad (319)$$

Although the bottom right term may be surprising, it is of no consequence when this expression of the deviatoric strain rate is used in the Stokes equation:

$$\vec{\nabla} \cdot 2\eta \dot{\boldsymbol{\varepsilon}}^d =$$

FINISH!

In two dimensions the velocity is then $\vec{v} = (u, v)$ and the FEM building blocks and matrices are simply:

$$\vec{\dot{\boldsymbol{\varepsilon}}} = \begin{pmatrix} \dot{\varepsilon}_{xx} \\ \dot{\varepsilon}_{yy} \\ 2\dot{\varepsilon}_{xy} \end{pmatrix} = \begin{pmatrix} \frac{\partial u}{\partial x} \\ \frac{\partial v}{\partial y} \\ \frac{\partial u}{\partial y} + \frac{\partial v}{\partial x} \end{pmatrix} = \underbrace{\begin{pmatrix} \frac{\partial N_1^\gamma}{\partial x} & 0 & \frac{\partial N_2^\gamma}{\partial x} & 0 & \frac{\partial N_3^\gamma}{\partial x} & 0 & \dots & \frac{\partial N_{m_v}^\gamma}{\partial x} & 0 \\ 0 & \frac{\partial N_1^\gamma}{\partial y} & 0 & \frac{\partial N_2^\gamma}{\partial y} & 0 & \frac{\partial N_3^\gamma}{\partial y} & \dots & 0 & \frac{\partial N_{m_v}^\gamma}{\partial x} \\ \frac{\partial N_1^\gamma}{\partial y} & \frac{\partial N_1^\gamma}{\partial x} & \frac{\partial N_2^\gamma}{\partial y} & \frac{\partial N_2^\gamma}{\partial x} & \frac{\partial N_3^\gamma}{\partial y} & \frac{\partial N_3^\gamma}{\partial x} & \dots & \frac{\partial N_{m_v}^\gamma}{\partial y} & \frac{\partial N_{m_v}^\gamma}{\partial x} \end{pmatrix}}_B \cdot \underbrace{\begin{pmatrix} u_1 \\ v_1 \\ u_2 \\ v_2 \\ u_3 \\ v_3 \\ \dots \\ u_{m_v} \\ v_{m_v} \end{pmatrix}}_{\vec{V}} \quad (320)$$

we have

$$\sigma_{xx} = -p + 2\eta \dot{\varepsilon}_{xx} \quad (321)$$

$$\sigma_{yy} = -p + 2\eta \dot{\varepsilon}_{yy} \quad (322)$$

$$\sigma_{xy} = +2\eta \dot{\varepsilon}_{xy} \quad (323)$$

so

$$\vec{\sigma} = - \begin{pmatrix} 1 \\ 1 \\ 0 \end{pmatrix} p + \mathbf{C} \cdot \vec{\dot{\boldsymbol{\varepsilon}}} = - \begin{pmatrix} 1 \\ 1 \\ 0 \end{pmatrix} \vec{N}^p \cdot \vec{P} + \mathbf{C} \cdot \mathbf{B} \cdot \vec{V} \quad (324)$$

with

$$\mathbf{C} = \eta \begin{pmatrix} 2 & 0 & 0 \\ 0 & 2 & 0 \\ 0 & 0 & 1 \end{pmatrix} \quad \text{or} \quad \mathbf{C} = \frac{\eta}{3} \begin{pmatrix} 4 & -2 & 0 \\ -2 & 4 & 0 \\ 0 & 0 & 3 \end{pmatrix} \quad (325)$$

check the right C

Finally the matrix \mathbf{N}^p is of size $3 \times m_p$:

$$\mathbf{N}^p = \begin{pmatrix} 1 \\ 1 \\ 0 \end{pmatrix} \vec{N}^p = \begin{pmatrix} \vec{N}^p \\ \vec{N}^p \\ 0 \end{pmatrix} \quad (326)$$

6.5 Solving the elastic equations

6.6 A quick tour of similar literature

- *Treatise on Geophysics*, Volume 7, Edited by D. Bercovici and G. Schubert: "Numerical Methods for Mantle Convection", by S.J. Zhong, D.A. Yuen, L.N. Moresi and M.G. Knepley. Note that it is a revision of the previous edition chapter by S.J. Zhong, D.A. Yuen and L.N. Moresi, Volume 7, pp. 227-252, 2007.
- *Computational Science I*, Lecture Notes for CAAM 519, M.G. Knepley, 2017. <https://cse.buffalo.edu/~knepley/classes/caam519/>
- *Numerical Modeling of Earth Systems - An introduction to computational methods with focus on-solid Earth applications of continuum mechanics*, Th.W. Becker and B.J.P. Kaus, 2018. <http://www-udc.ig.utexas.edu/external/becker/Geodynamics557.pdf>
- *Myths and Methods in Modeling*, M. Spiegelman, 2000. https://earth.usc.edu/~becker/teaching/557/reading/spiegelman_mmm.pdf

6.7 The case against the $Q_1 \times P_0$ element

What follows was written by Dave May and sent to me by email in May 2014. It captures so well the problem at hand that I have decided to reproduce it hereunder.

In the case of the incompressible Stokes equations, we would like to solve

$$\begin{pmatrix} \mathbb{K} & \mathbb{G} \\ \mathbb{G}^T & 0 \end{pmatrix} \begin{pmatrix} \vec{\mathcal{V}} \\ \vec{\mathcal{P}} \end{pmatrix} = \begin{pmatrix} \vec{f} \\ 0 \end{pmatrix}$$

with an iterative method which is algorithmically scalable and optimal. Scalable here would mean that the number of iterations doesn't grow as the mesh is refined. Optimal means the solution time varies linearly with the total number of unknowns. When using a stable element, If we right precondition the above system with

$$P = \begin{pmatrix} \mathbb{K} & \mathbb{G} \\ 0 & -\mathbb{S} \end{pmatrix}$$

then convergence will occur in 2 iterations, however this requires an exact solve on \mathbb{K} and on $\mathbb{S} = \mathbb{G}^T \cdot \mathbb{K}^{-1} \cdot \mathbb{G}$ (\mathbb{S} is the pressure schur complement). In practice, people relax the ideal "two iteration" scenario by first replacing \mathbb{S} via $\mathbb{S}^* = \int \eta^{-1} \vec{N}^T \vec{N} dv$ (e.g. the pressure mass matrix scaled by the local inverse of viscosity).

$$P^* = \begin{pmatrix} \mathbb{K} & \mathbb{G} \\ 0 & -\mathbb{S}^* \end{pmatrix}$$

Using P^* , we obtain iteration counts which are larger than 2, but likely less than 10 - *however*, the number of iterations is independent of the mesh size. Replacing the exact \mathbb{K} solve in P^* again increases the iterations required to solve Stokes, but it's still independent of the number of elements. When you have this behaviour, we say the preconditioner (P^*) is spectrally equivalent to the operator (which here is Stokes)

The problem with $Q_1 \times P_0$ is that there are no approximations for \mathbb{S} which can be generated that ensure a spectrally equivalent P^* . Thus, as you refine the mesh using $Q_1 \times P_0$ elements, the iteration count ALWAYS grows. I worked on this problem during my thesis, making some improvements to the situation - however the problem still remains, it cannot be completely fixed and stems entirely from using unstable elements.

Citcom solvers works like this:

1. Solve $\mathbb{S} \cdot \mathcal{P} = \vec{f}'$ for pressure
2. Solve $\mathbb{K} \cdot \mathcal{V} = \vec{f} - \mathbb{G} \cdot \mathcal{P}$ for velocity

To obtain a scalable method, we need the number of iterations performed in (1) and (2) to be independent of the mesh. This means we need a spectrally equivalent preconditioner for \mathbb{S} and \mathbb{K} . Thus, we have the same issue as when you iterate on the full stokes system.

When we don't have a scalable method, it means increasing the resolution requires more cpu time in a manner which cannot be predicted. The increase in iteration counts as the mesh is refined can be dramatic.

If we can bound the number of iterations, AND ensure that the cost per iteration is linearly related to the number of unknowns, then we have a good method which can run on any mesh resolution with a predictable cpu time. Obtaining scalable and optimal preconditioners for \mathbb{K} is somewhat easier. Multigrid will provide us with this.

The reason citcom doesn't run with 400^3 elements is exactly due to this issue. I've added petsc support in citcom (when i was young and naive) - but the root cause of the non-scalable solve is directly caused by the element choice. Note that many of the high resolution citcom jobs are single time step calculations— there is a reason for that.

For many lithosphere dynamics problems, we need a reasonable resolution (at least 200^3 and realistically 400^3 to 800^3). Given the increase in cost which occurs when using Q1P0, this is not achievable, as the citcom code has demonstrated. Note that citcom is 20 years old now and for its time, it was great, but we know much more now and we know how to improve on it. As a result of this realization, I dumped all my old Q1P0 codes (and Q1Q1 codes, but for other reasons) in the trash and started from scratch. The only way to make something like 800^3 tractable is via iterative, scalable and optimal methods and that mandates stable elements. I can actually run at something like 1000^3 (nodal points) these days because of such design choices.

6.8 Isoviscous Stokes for incompressible flow

We start from the momentum equation:

$$-\vec{\nabla}p + \vec{\nabla} \cdot (2\eta\dot{\varepsilon}^d(\vec{v})) + \rho\vec{g} = \vec{0} \quad (327)$$

When the viscosity is constant in space, it can be taken out of the divergence operator:

$$-\vec{\nabla}p + 2\eta\vec{\nabla} \cdot \dot{\varepsilon}^d(\vec{v}) + \rho\vec{g} = \vec{0} \quad (328)$$

Let us for simplicity look at a 2D Cartesian formulation of this equation and for incompressible flow:

$$2\vec{\nabla} \cdot \dot{\varepsilon}^d(\vec{v}) = \vec{\nabla} \cdot (\vec{\nabla}\vec{v} + \vec{\nabla}\vec{v}^T) \quad (329)$$

$$= (\partial_x \partial_y) \cdot \begin{pmatrix} \partial_x u & \partial_x v \\ \partial_y u & \partial_y v \end{pmatrix} + (\partial_x \partial_y) \cdot \begin{pmatrix} \partial_x u & \partial_y u \\ \partial_x v & \partial_y v \end{pmatrix} \quad (330)$$

$$= (\partial_x^2 u + \partial_y^2 u, \partial_x^2 v + \partial_y^2 v) + (\partial_x \partial_x u + \partial_y \partial_x v, \partial_x \partial_y u + \partial_y \partial_y v) \quad (331)$$

$$= (\partial_x^2 u + \partial_y^2 u, \partial_x^2 v + \partial_y^2 v) + (\partial_x \underbrace{(\partial_x u + \partial_y v)}_{=0}, \partial_y \underbrace{(\partial_x u + \partial_y v)}_{=0}) \quad (332)$$

$$= (\partial_x^2 u + \partial_y^2 u, \partial_x^2 v + \partial_y^2 v) \quad (333)$$

and then finally the Stokes equation is:

$$-\vec{\nabla}p + \eta\Delta\vec{v} + \rho\vec{g} = \vec{0} \quad (334)$$

The mass conservation equation remains unchanged and so does the pressure gradient term. We shall then focus on the weak form of the previously obtained term. We multiply it by a velocity test function

N_i^ν and integrate over an element:

$$\begin{aligned}
& \int_{\Omega_e} N_i^\nu \Delta \vec{v}^h dV \\
&= \int_{\Omega_e} \begin{pmatrix} N_i^\nu \Delta u^h \\ N_i^\nu \Delta v^h \end{pmatrix} dV \\
&= \int_{\Omega_e} \begin{pmatrix} N_i^\nu \vec{\nabla} \cdot \vec{\nabla} u^h \\ N_i^\nu \vec{\nabla} \cdot \vec{\nabla} v^h \end{pmatrix} dV \\
&= \int_{\Omega_e} \begin{pmatrix} \vec{\nabla} N_i^\nu \cdot \vec{\nabla} u^h \\ \vec{\nabla} N_i^\nu \cdot \vec{\nabla} v^h \end{pmatrix} dV \\
&= \int_{\Omega_e} \begin{pmatrix} \partial_x N_i^\nu \partial_x u^h + \partial_y N_i^\nu \partial_y u^h \\ \partial_x N_i^\nu \partial_x v^h + \partial_y N_i^\nu \partial_y v^h \end{pmatrix} dV \\
&= \int_{\Omega_e} \begin{pmatrix} \partial_x N_i^\nu & \partial_y N_i^\nu & 0 & 0 \\ 0 & 0 & \partial_x N_i^\nu & \partial_y N_i^\nu \end{pmatrix} \cdot \begin{pmatrix} \partial_x u^h \\ \partial_y u^h \\ \partial_x v^h \\ \partial_y v^h \end{pmatrix} dV \\
&= \int_{\Omega_e} \begin{pmatrix} \partial_x N_i^\nu & \partial_y N_i^\nu & 0 & 0 \\ 0 & 0 & \partial_x N_i^\nu & \partial_y N_i^\nu \end{pmatrix} \cdot \begin{pmatrix} \partial_x N_1^\nu & 0 & \partial_x N_2^\nu & 0 & \cdots & \partial_x N_{m_\nu}^\nu & 0 \\ \partial_y N_1^\nu & 0 & \partial_y N_2^\nu & 0 & \cdots & \partial_y N_{m_\nu}^\nu & 0 \\ 0 & \partial_x N_1^\nu & 0 & \partial_x N_2^\nu & \cdots & 0 & \partial_x N_{m_\nu}^\nu \\ 0 & \partial_y N_1^\nu & 0 & \partial_y N_2^\nu & \cdots & 0 & \partial_y N_{m_\nu}^\nu \end{pmatrix} \cdot \underbrace{\begin{pmatrix} u_1 \\ v_1 \\ u_2 \\ v_2 \\ \vdots \\ u_{m_v} \\ v_{m_v} \end{pmatrix}}_{\vec{v}} dV
\end{aligned}$$

Writing this equation for $i = 1, \dots, m_\nu$, we obtain:

$$\int \underbrace{\begin{pmatrix} \partial_x N_1^\nu & \partial_y N_1^\nu & 0 & 0 \\ 0 & 0 & \partial_x N_1^\nu & \partial_y N_1^\nu \\ \partial_x N_2^\nu & \partial_y N_2^\nu & 0 & 0 \\ 0 & 0 & \partial_x N_2^\nu & \partial_y N_2^\nu \\ \vdots & \vdots & \vdots & \vdots \\ \partial_x N_{m_\nu}^\nu & \partial_y N_{m_\nu}^\nu & 0 & 0 \\ 0 & 0 & \partial_x N_{m_\nu}^\nu & \partial_y N_{m_\nu}^\nu \end{pmatrix}}_{\mathbf{B}} \cdot \underbrace{\begin{pmatrix} \partial_x N_1^\nu & 0 & \partial_x N_2^\nu & 0 & \cdots & \partial_x N_{m_\nu}^\nu & 0 \\ \partial_y N_1^\nu & 0 & \partial_y N_2^\nu & 0 & \cdots & \partial_y N_{m_\nu}^\nu & 0 \\ 0 & \partial_x N_1^\nu & 0 & \partial_x N_2^\nu & \cdots & 0 & \partial_x N_{m_\nu}^\nu \\ 0 & \partial_y N_1^\nu & 0 & \partial_y N_2^\nu & \cdots & 0 & \partial_y N_{m_\nu}^\nu \end{pmatrix}}_{\mathbf{B}^T} \cdot \underbrace{\begin{pmatrix} u_1 \\ v_1 \\ u_2 \\ v_2 \\ \vdots \\ u_{m_v} \\ v_{m_v} \end{pmatrix}}_{\vec{v}} dV$$

or,

$$\mathbf{K}_\eta = \eta \int_{\Omega_e} \mathbf{B}^T \cdot \mathbf{B} dV$$

where \mathbf{B} is a $(ndim * ndim) \times (m_v * ndofV)$ matrix (see also Eq. 6.24 of [473]).

In three dimensions, the matrix \mathbf{B} is given by

$$\begin{pmatrix} \partial_x N_1^\nu & 0 & \partial_x N_2^\nu & 0 & \cdots & \partial_x N_{m_\nu}^\nu & 0 \\ \partial_y N_1^\nu & 0 & \partial_y N_2^\nu & 0 & \cdots & \partial_y N_{m_\nu}^\nu & 0 \\ \partial_z N_1^\nu & 0 & \partial_z N_2^\nu & 0 & \cdots & \partial_z N_{m_\nu}^\nu & 0 \\ 0 & \partial_x N_1^\nu & 0 & \partial_x N_2^\nu & \cdots & 0 & \partial_x N_{m_\nu}^\nu \\ 0 & \partial_y N_1^\nu & 0 & \partial_y N_2^\nu & \cdots & 0 & \partial_y N_{m_\nu}^\nu \\ 0 & \partial_z N_1^\nu & 0 & \partial_z N_2^\nu & \cdots & 0 & \partial_z N_{m_\nu}^\nu \end{pmatrix}$$

7 The Discontinuous Galerkin Finite Element Method (DG-FEM)

7.1 First-order advection ODE in 1D

What follows is borrowed from the book "Discontinuous finite elements in fluid dynamics and heat transfer" by Ben Q. Li [1060].

To illustrate the basic ideas of the discontinuous finite element method, we consider a simple, one-dimensional, first order differential equation with u specified at one of the boundaries:

$$\frac{du}{dx} + g = 0 \quad x \in [a, b] \quad \text{and} \quad u(x = a) = u_a \quad (335)$$

where g is a constant (for simplicity). The domain is discretized such that : $\Omega_j = [x_j, x_{j+1}]$ with $j = 1, 2, \dots, nel$. Then, integrating the above equation over the element j with respect to a weighting function $f(x)$

$$\int_{x_j}^{x_{j+1}} \left(\frac{du}{dx} + g \right) f(x) dx = 0 \quad (336)$$

Remembering that $\int_c^d u(x)v'(x)dx = [u(x)v(x)]_c^d - \int_c^d u'(x)v(x)dx$, we can now perform an integration by parts on the differential operator and we obtain:

$$[u(x)f(x)]_{x_j}^{x_{j+1}} - \int_{x_j}^{x_{j+1}} \left(u \frac{df}{dx} - gf(x) \right) dx = 0 \quad (337)$$

or,

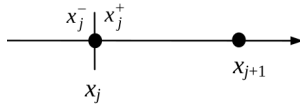
$$u(x_{j+1})f(x_{j+1}) - u(x_j)f(x_j) - \int_{x_j}^{x_{j+1}} \left(u \frac{df}{dx} - gf(x) \right) dx = 0 \quad (338)$$

On Ω_j u is approximated by $u_h \in H$, H being an appropriate function space of finite dimension, and f by f_h taken from the same function space as u_h . Upon substituting (u_h, f_h) for (u, f) in the equation above, we have the discontinuous Galerkin finite element formulation:

$$u_h(x_{j+1})f_h(x_{j+1}) - u_h(x_j)f_h(x_j) - \int_{x_j}^{x_{j+1}} \left(u_h \frac{df_h}{dx} - gf_h(x) \right) dx = 0 \quad (339)$$

In the continuous finite element approach, the field variable u_h is forced to be continuous across the boundary. The essential idea for the discontinuous method is that u_h is allowed to be discontinuous across the boundary. Therefore, across the element, the following two different values are defined at the two sides of the boundary:

$$u_j^+ = \lim_{x \searrow x_j^+} u_h(x) \quad u_j^- = \lim_{x \nearrow x_j^-} u_h(x) \quad (340)$$



An illustration of the jump across x_j of element j : x_j and x_{j+1} mark the boundaries of the element

Conversely, we also have:

$$u_{j+1}^+ = \lim_{x \searrow x_{j+1}^+} u_h(x) \quad u_{j+1}^- = \lim_{x \nearrow x_{j+1}^-} u_h(x) \quad (341)$$

It is key to remember that 1) u_h is discontinuous only at the element boundaries; 2) the solution u is smooth within (but excluding) the boundary. By this definition, the above equation contains the variables only within the integral limits of Ω_j . As a consequence, there is no direct coupling with other intervals or other elements. *The field values at a node, or the interface between two elements, are not unique.* They are calculated using the two limiting values approaching the interface from the two adjacent elements. This feature is certainly desirable for problems with internal discontinuities.

We can now write CHECK CHECK

$$u_{j+1}^- f_h(x_{j+1}) - u_j^+ f_h(x_j) - \int_{x_j}^{x_{j+1}} \left(u_h \frac{df_h}{dx} - g f_h(x) \right) dx = 0 \quad (342)$$

and we can integrate by parts again the term which contains a derivative:

$$\int_{x_j}^{x_{j+1}} u_h(x) \frac{df_h}{dx} dx = [u_h f_h] - \int_{x_j}^{x_{j+1}} f_h(x) \frac{du_h}{dx} dx$$

and then

$$u_{j+1}^- f_h(x_{j+1}) - u_j^+ f_h(x_j) - \int_{x_j}^{x_{j+1}} \left(u_h \frac{df_h}{dx} - g f_h(x) \right) dx = 0 \quad (343)$$

We start from the simplest ODE:

$$\frac{du}{dx} = 1 \quad x \in [0, 2] \quad \text{and} \quad u(x=0) = 0$$

As in the Continuous Galerkin case, the function f is replaced by a shape function $N_i(x)$:

How the hell do I arrive at:

$$\int_{x_j}^{x_{j+1}} \left(\frac{du_h}{dx} + g(u_h) \right) N_i(x) dx + (u_j^+ - u_j^-) N_i(x_j) = 0$$

7.2 Steady state diffusion in 1D

Let us start simple with the 1D steady state heat conduction problem in 1D, given by the following equation:

$$\frac{d^2T}{dx^2} = 0 \quad T(x=0) = 0 \quad T(x=1) = 1 \quad \text{on } x \in [0, 1] \quad (344)$$

Although this equation is usually solved as is with its second-order derivative, it can also be written in a mixed form, using the heat flux q (a scalar in 1D):

$$-\frac{dq}{dx} = 0 \quad q - \frac{dT}{dx} = 0 \quad x \in [0, 1]$$

and the boundary conditions remain unchanged.

We apply the standard approach to establish the weak forms of these two first-order ODEs, and we do so on an element e bound by nodes k and $k+1$ with coordinates x_k and x_{k+1}

$$\begin{aligned} -\int_{x_k}^{x_{k+1}} \frac{dq}{dx} \tilde{f}(x) dx &= -[q \tilde{f}]_{x_k}^{x_{k+1}} + \int_{x_k}^{x_{k+1}} \frac{d\tilde{f}}{dx} q(x) dx = 0 \\ \int_{x_k}^{x_{k+1}} \left(q - \frac{dT}{dx} \right) \bar{f}(x) dx &= \int_{x_k}^{x_{k+1}} q(x) \bar{f}(x) dx - [T \bar{f}]_{x_k}^{x_{k+1}} + \int_{x_k}^{x_{k+1}} \frac{d\bar{f}}{dx} T(x) dx = 0 \end{aligned}$$

where \tilde{f} and \bar{f} are test functions. We now must examine the term between square brackets. Inside the element, the test functions \tilde{f} and \bar{f} are well defined polynomials and we we coin:

$$\tilde{f}_k^+ = \tilde{f}(x_k^+) \quad \tilde{f}_{k+1}^- = \tilde{f}(x_{k+1}^-) \quad \bar{f}_k^+ = \bar{f}(x_k^+) \quad \bar{f}_{k+1}^- = \bar{f}(x_{k+1}^-)$$

Concerning q and T , we will for now give them values \hat{q}_k and \hat{T}_k at node k and \hat{q}_{k+1} and \hat{T}_{k+1} at node $k+1$, and we will specify the hat quantities as follows:

$$\begin{aligned} \hat{T}_k &= \begin{cases} T_k^- & k = 1 \\ \frac{1}{2}(T_k^- + T_k^+) + \mathcal{C}(T_k^- - T_k^+) & k = 2, \dots, N-1 \\ T_k^+ & k = N \end{cases} \\ \hat{q}_k &= \begin{cases} q_k^+ - \mathcal{E}(T_k^- - T_k^+) & k = 1 \\ \frac{1}{2}(q_k^+ + q_k^-) - \mathcal{E}(T_k^- - T_k^+) - \mathcal{C}(q_k^- - q_k^+) & k = 2, \dots, N-1 \\ q_k^- - \mathcal{E}(T_k^- - T_k^+) & k = N \end{cases} \end{aligned} \quad (345)$$

where N is the number of nodes and where \mathcal{C} and \mathcal{E} are two constants.

Remark. Note that $\hat{T}_k = T_1^-$ on the left boundary is consistent with $\hat{T}_k = \frac{1}{2}(T_k^- + T_k^+) + \mathcal{C}(T_k^- - T_k^+)$ provided $T_1^- = T_1^+$. The same goes for the right boundary, and the same reasoning applies for the heat flux terms \hat{q}_k .

Inside an element bounded by nodes k and $k+1$, the temperature T and heat flux q are interpolated over an isoparametric linear element:

$$T_h(x) = N_k(x)T_k^+ + N_{k+1}(x)T_{k+1}^-$$

$$q_h(x) = N_k(x)q_k^+ + N_{k+1}(x)q_{k+1}^-$$

As in the (Continuous) Galerkin case of section 5.1, the test functions are taken to be the shape functions, and in this case for both temperature and flux.

$$\begin{aligned}
0 &= -\hat{q}_{k+1}\tilde{f}(x_{k+1}^-) + \hat{q}_k\tilde{f}(x_k^+) + \int_{x_k}^{x_{k+1}} \frac{d\tilde{f}}{dx} q_h(x) dx \\
&= -\hat{q}_{k+1}\tilde{f}_{k+1}^- + \hat{q}_k\tilde{f}_k^+ + \int_{x_k}^{x_{k+1}} \frac{d\tilde{f}}{dx} (N_k(x)q_k^+ + N_{k+1}(x)q_{k+1}^-) dx \\
&= -\hat{q}_{k+1}\tilde{f}_{k+1}^- + \hat{q}_k\tilde{f}_k^+ + \int_{x_k}^{x_{k+1}} \frac{d\tilde{f}}{dx} N_k(x) dx \cdot q_k^+ + \int_{x_k}^{x_{k+1}} \frac{d\tilde{f}}{dx} N_{k+1}(x) dx \cdot q_{k+1}^- \\
&= -\left(\frac{1}{2}(q_{k+1}^+ + \textcolor{blue}{q}_{k+1}^-) - \mathcal{E}(T_{k+1}^- - T_{k+1}^+) - \mathcal{C}(\textcolor{blue}{q}_{k+1}^- - q_{k+1}^+)\right)\tilde{f}_{k+1}^- + \left(\frac{1}{2}(\textcolor{blue}{q}_k^+ + q_k^-) - \mathcal{E}(T_k^- - \textcolor{blue}{T}_k^+) - \mathcal{C}(q_k^- - \textcolor{blue}{q}_k^+)\right)\tilde{f}_k^+ \\
&\quad + \int_{x_k}^{x_{k+1}} \frac{d\tilde{f}}{dx} N_k(x) dx \cdot \textcolor{blue}{q}_k^+ + \int_{x_k}^{x_{k+1}} \frac{d\tilde{f}}{dx} N_{k+1}(x) dx \cdot \textcolor{blue}{q}_{k+1}^- \\
&= \left[-(0.5 + \mathcal{C})\tilde{f}_{k+1}^- + \int_{x_k}^{x_{k+1}} \frac{d\tilde{f}}{dx} N_{k+1}(x) dx\right] \textcolor{blue}{q}_{k+1}^- - \mathcal{E}\tilde{f}_{k+1}^- \textcolor{blue}{T}_{k+1}^- \\
&\quad + \left[(0.5 + \mathcal{C})\tilde{f}_k^+ + \int_{x_k}^{x_{k+1}} \frac{d\tilde{f}}{dx} N_{k+1}(x) dx\right] \textcolor{blue}{q}_k^+ + \mathcal{E}\tilde{f}_k^+ \textcolor{blue}{T}_k^+ \\
&\quad - \left(\frac{1}{2}q_{k+1}^+ + \mathcal{E}T_{k+1}^+ + \mathcal{C}q_{k+1}^+\right)\tilde{f}_{k+1}^- + \left(\frac{1}{2}q_k^- - \mathcal{E}T_k^- - \mathcal{C}q_k^-\right)\tilde{f}_k^+
\end{aligned} \tag{346}$$

$$\begin{aligned}
0 &= -[T\bar{f}]_{x_k}^{x_{k+1}} + \int_{x_k}^{x_{k+1}} q_h(x)\bar{f}(x) dx + \int_{x_k}^{x_{k+1}} \frac{d\bar{f}}{dx} T_h(x) dx \\
&= -\hat{T}_{k+1}\bar{f}(x_{k+1}^-) + \hat{T}_k\bar{f}(x_k^+) + \int_{x_k}^{x_{k+1}} q_h(x)\bar{f}(x) dx + \int_{x_k}^{x_{k+1}} \frac{d\bar{f}}{dx} T_h(x) dx \\
&= -\left(\frac{1}{2}(\textcolor{blue}{T}_{k+1}^- + T_{k+1}^+) + \mathcal{C}(\textcolor{blue}{T}_{k+1}^- - T_{k+1}^+)\right)\bar{f}_{k+1}^- + \left(\frac{1}{2}(T_k^- + \textcolor{blue}{T}_k^+) + \mathcal{C}(T_k^- - \textcolor{blue}{T}_k^+)\right)\bar{f}_k^+ \\
&\quad + \int_{x_k}^{x_{k+1}} (N_k(x)\textcolor{blue}{q}_k^+ + N_{k+1}(x)\textcolor{blue}{q}_{k+1}^-)\bar{f}(x) dx + \int_{x_k}^{x_{k+1}} \frac{d\bar{f}}{dx} (N_k(x)\textcolor{blue}{T}_k^+ + N_{k+1}(x)\textcolor{blue}{T}_{k+1}^-) dx
\end{aligned}$$

If I now rewrite both equations above by taking $\tilde{f} = \{N_k, N_{k+1}\}$ and $\bar{f} = \{N_k, N_{k+1}\}$ then we obtain four equations. For each element with the four unknowns $\textcolor{blue}{q}_k^+$, $\textcolor{blue}{q}_{k+1}^-$, $\textcolor{blue}{T}_k^+$ and $\textcolor{blue}{T}_{k+1}^-$. All other q and T quantities in the above equations will need to find their way to the rhs.

We will also use the results obtained in Appendix I:

$$\mathbf{M}^e = \int_{\Omega_e} \vec{N}^T \vec{N} dV = \int_{\Omega_e} \begin{pmatrix} N_k N_k & N_k N_{k+1} \\ N_{k+1} N_k & N_{k+1} N_{k+1} \end{pmatrix} dV = \frac{h}{2} \frac{1}{3} \begin{pmatrix} 2 & 1 \\ 1 & 2 \end{pmatrix} = \frac{h}{6} \begin{pmatrix} 2 & 1 \\ 1 & 2 \end{pmatrix}$$

and also

$$\int_{\Omega_e} \begin{pmatrix} \frac{dN_k}{dx} N_k & \frac{dN_k}{dx} N_{k+1} \\ \frac{dN_{k+1}}{dx} N_k & \frac{dN_{k+1}}{dx} N_{k+1} \end{pmatrix} dV = \frac{1}{2} \begin{pmatrix} -1 & -1 \\ 1 & 1 \end{pmatrix}$$

8 Additional techniques and features

Solving the Stokes equations and the energy equations is one thing. Doing it in a geodynamical context requires a lot of additional techniques.

8.1 Dealing with a free surface (and mesh deformation)

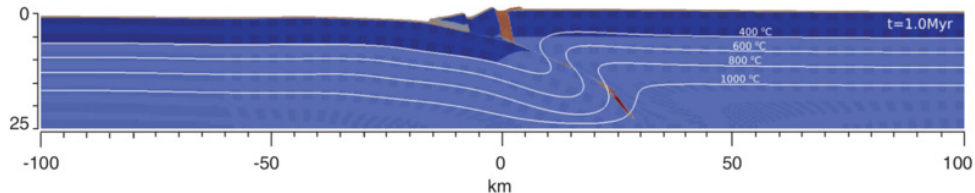
When carrying out global models, typically mantle convection, the effect of the free surface is often neglected/negligible: topography ranges from $\sim 10\text{km}$ depth to $\sim 10\text{km}$ height, which is very small compared to the depth of the mantle ($\sim 3000\text{km}$).

However, it has long been recognised that there is a feedback between topography and crust/lithosphere deformation: the surface of the Earth reflects the deeper processes, from orogeny, back-arc basins, rifts, mid-ocean ridges, etc ... (see for instance [205]).

Remark. Free surface flows are not unique to Earth sciences, and their modelling has given rise to many studies and textbooks. A typical free-surface flow problem in the CFD literature is the so-called 'dam break' problem [1192, 71, 1079, 1034, 835, 27]. Other occurrences involve sea waves, flow over structures, flow around ships, mould filling, flow with bubbles [1079].

What distinguishes geodynamics free surface modelling from its engineering counterpart is (i) the absence of surface tension, (ii) the fact that the fluids under consideration are Stokesian, (iii) their rheology is complex (the elastic and plastic components can be dominant at the surface).

The problem of dealing with a free surface can be deceptively simple at first glance: as mentioned before the amplitude of surface movement is often less than 1% of the domain size. Isostacy-driven movements are easy to deal with since the movement is vertical (and often characterised by long wavelength). However, computational problems quickly arise in subduction modelling: the downgoing lithosphere subducts below the overriding plate and the relative convergence of the two is likely to generate a cusp at the trench. The presence of shear bands intersecting the surface accentuates the problem:

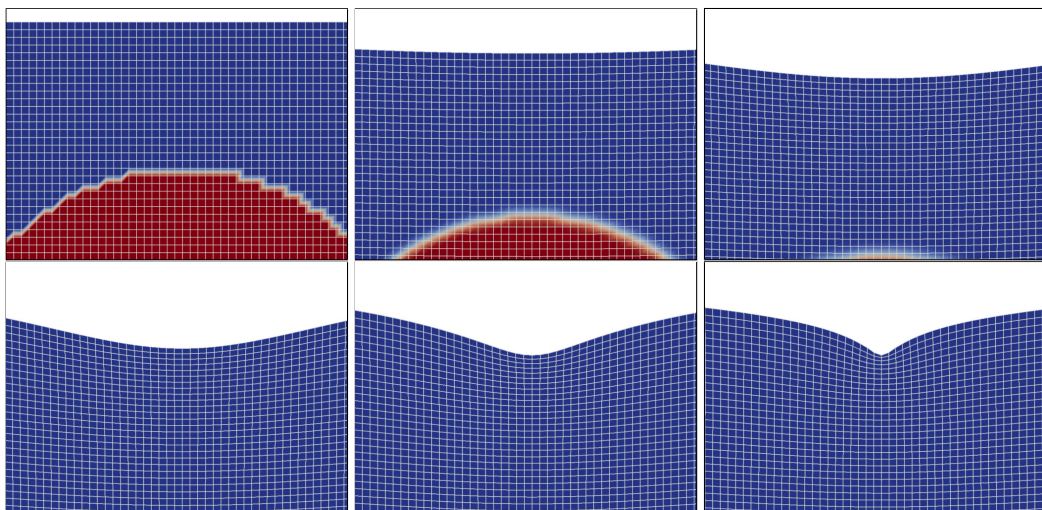


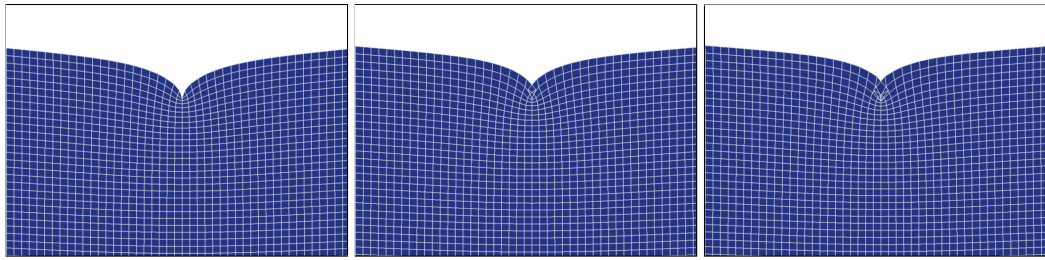
Taken from Maffione et al [1107]. Example of free surface deformation above intra-oceanic subduction initiation

Remark. It is difficult to talk about free surface without including the underlying mesh. What follows should be read alongside Section 8.10.

8.1.1 The fully Lagrangian approach

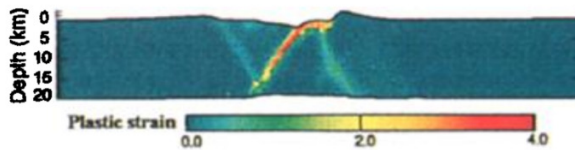
In this case the mesh is deformed with the velocity (or displacement) computed on its nodes. It is sometimes called 'body fitting' [409] or 'boundary fitted'. In the case when large deformation occurs (which is rather frequent in geodynamics - think about subduction or rifting processes where materials end up moving 100's or 1000's of km, horizontally and/or vertically), it leads to highly deformed elements, and in some cases even bow-tied:



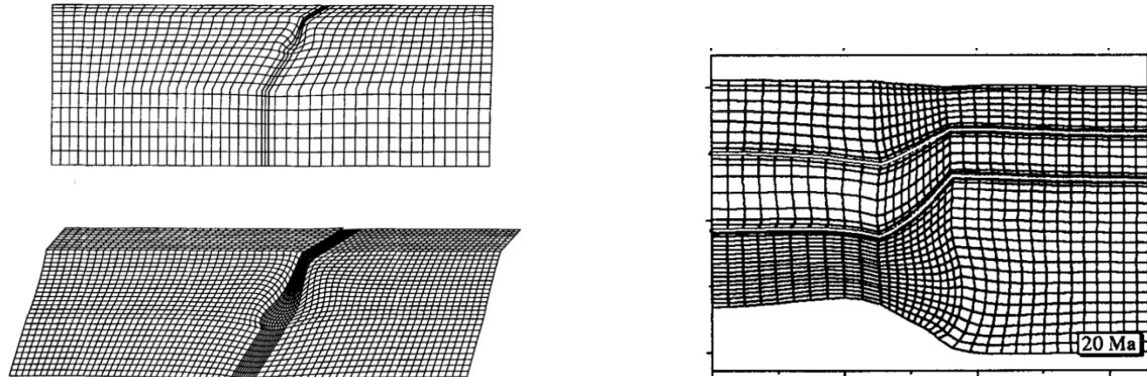


Example of a free surface evolution above a sinking sphere. The isostatic rebound above the sphere generates a cusp which, if no special measure is taken, ultimately leads to a bow-tied element. Once this occurs the simulation stops since the mapping of the bow-tied element to the reference element yields to wrong elemental matrix. Courtesy of M. Frater.

In the mildest cases this does not occur but it has long been established that large mesh deformation yields low accuracy calculations, especially when angles between edges become small or large. One way to overcome this problem is to remesh, i.e. generate a better mesh based on the available information on the deformed one. In 2D this is routinely done, especially when triangular elements are used. In 3D, multiple remeshing are very costly and it is generally avoided. Note also that re-meshing often involves some form of interpolation and therefore some unwanted numerical diffusion. When deformation is reasonably small, fully lagrangian methods work and have been used in geodynamics [802, 1171, 1025].



Taken from [1025]. Upper-crustal faulting, note that the bottom and the top surface are deformed.



Taken from [766]. Subduction model, topographic expression is shown without vertical exaggeration.

Taken from [723]. Asymmetric lithospheric extension.

GET: Crook et al. 2006, and references therein [416]) Beaumont et al. 1994; [94]

8.1.2 The Eulerian approach: using sticky air

Sticky air is the default option for numerical methods which mesh cannot be deformed (typically the finite difference method). In this case, the air above the crust/sediments is modelled as a zero-density fluid with very low viscosity (see for instance the early article by Zaleski and Julien [1743]). One problem quickly arises when one realises that the viscosity of the air ($\sim 18.5 \cdot 10^{-6}$ Pa·s²³) is almost 25-30 orders of magnitude lower than the (effective) viscosity of Earth materials. Real air viscosity cannot therefore be used because of 1) round-off errors, 2) extremely poorly-conditioned matrices. Low viscosities around $10^{16} - 10^{19}$ Pa·s are then commonly used as they are still negligible next to those of the (plastic) crust, and the flow of air parallel to Earth materials only generates extremely small shear and normal stress values (thereby approaching the true nature of a free surface). This approach is the one employed in all

²³<https://en.wikipedia.org/wiki/Viscosity>

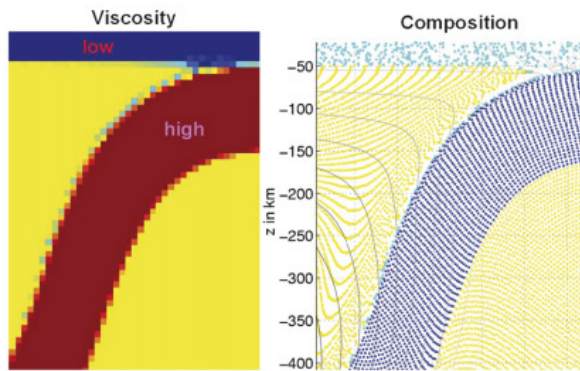
the papers based on the I2/I3(EL)VIS code (see Appendix B) and has been benchmarked in Crameri et al. [409].

This approach has a few advantages:

1. it is simple to implement
2. it is compatible with all the standard numerical methods (FEM, FDM,FVM)
3. it avoids (potentially complicated) remeshing

and quite a few drawbacks:

1. it increases the size of the computational domain, thereby adding more unknowns to the linear system: in [1436] the air layer is set to 50km while the lithospheric domain underneath is 700km thick;
2. it requires the use of averaging all along the free-surface where very large viscosity contrasts are present. Here is what Poliakov and Podlachikov [1317] say about the sticky air method: "Zaleski & Julien [1743] used a top layer with a very low viscosity and density to represent air or water above the surface. This allows a simple representation of the free surface. However, due to the very high viscosity and density contrast and diffusion between the top layer and the underlying layers, calculations sometimes become unstable and give significant errors."
3. it can showcase air entrainment:



Taken from [1436]. Details of the entrainment and lubrication of the soft surface layer. Light blue particles are sticky air particle and are found to greatly alter the viscosity of the subduction channel.

4. it is not clear how thick the air layer must be
5. it often requires to ascribe thermal parameters to the air;
6. it makes the implementation of Dirichlet or Neuman boundary conditions for temperature at the surface less obvious.
7. it makes the coupling with surface processes codes less straightforward.
8. its accuracy depends on the method used to track materials in the rest of the code (markers, level sets, ...). If markers are used, the free surface position is then known up to the average distance between markers.
9. it negatively impacts the condition number of the matrix.

The sticky air approach is employed by various codes in the subduction benchmark study [1436]

The term 'sticky water' is sometimes employed too. The dynamic viscosity of water is about 10^{-3} Pa·s so that it is also negligible compared to the viscosity of Earth materials and the same reasoning as air applies. However, in such a case a density of about 1000kg/m^3 is then assigned to the layer. REF?

In conclusion, as stated in [409]: "the sticky air method is a good way to simulate a free surface for Eulerian approaches, provided that its parameters are chosen carefully."

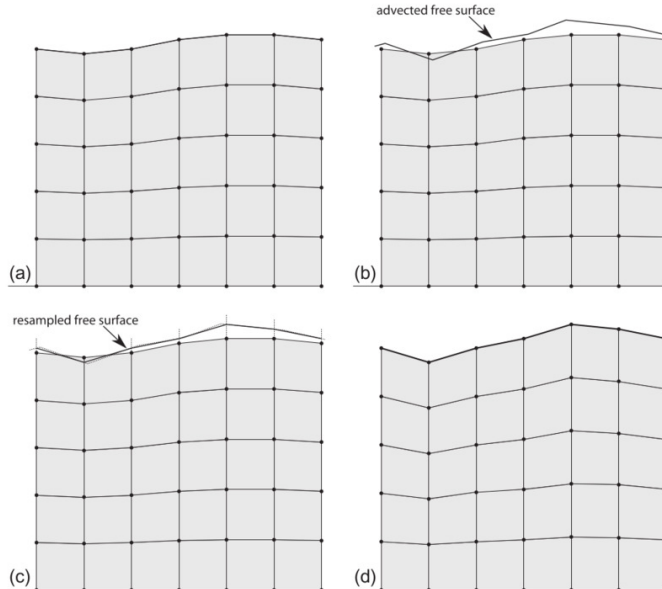
8.1.3 The Arbitrary Lagrangian Eulerian (ALE) approach

It is a very widely used approach in FEM-based geodynamics codes but originates in the field of CFD [829, 858] and is described at length in [1471, 472, 473]. To put it very simply, the key idea in the ALE formulation is the introduction of a computational mesh which can move and deform with a velocity independent of the velocity carried by the material particles.

The simple approach in [1538]. What follows is written with a 2D Cartesian model in mind ($Q_1 \times P_0$ elements are used). The computational domain is a rectangle of size $L_x \times L_y$ and a $n_{nx} \times n_{ny}$ rectangular grid spanning the simulation domain is generated. The grid points constituting the top row of the grid define the discrete free surface of the domain. Once the Eulerian velocity field has been computed on these, their position is first updated using a simple Eulerian advection step (see a,b on figure hereunder):

$$\vec{r}_i(t + \delta t) = \vec{r}_i(t) + \vec{v}_i \cdot \delta t \quad i = 1, \dots, n_{nx}$$

The other boundaries of the system remain fixed at locations $x = 0$, $x = L_x$ and $y = 0$. Even though the Eulerian grid must conform to the current domain shape, only vertical motion of grid nodes is allowed. It is therefore necessary to resample the predicted free surface given by \vec{r}_i at equidistant positions between $x = 0$ and $x = L_x$. The resampling is carried out either with Spline functions or a moving least square algorithm. Finally, the vertical position of all the nodes corresponding to column $i \in [1, n_{nx}]$ is recalculated so that they are equidistant, as sketched in Figure d. This has the advantage of keeping the mesh distortion to a minimum in the case of large deformation.



The ALE algorithm of [1538] in 2D. (a) Grid and free surface at a given time t ; (b) advection of the free surface; (c) resampling of the free surface at equidistant abscissae; (d) vertical adjustment of grid nodes in each column at equidistant ordinates.

The ALE method is used in the SOPALE, SULEC, FANTOM, ELEFANT, and ASPECT codes to name a few (see Appendix B).

The not-so-simple but rather elegant approach of ASPECT What follows is mostly borrowed from Rose et al [1406]. Their approach has the advantage that it does not presuppose a geometry (Cartesian, Spherical, ...) nor a number of dimensions. It is also designed to work in parallel and on octree-based meshes, and with various combinations of boundary conditions. Note that the authors specify that "for moderate mesh deformation, the mesh stays smooth and well conditioned, though it breaks down for large deformations".

This approach is obtained by simply imposing the obvious condition that no particle (fluid parcel) can cross the free surface (because it is a material surface). This can be imposed in a straightforward

manner by using a Lagrangian description along this surface. However, this condition may be relaxed by imposing only the necessary condition: \vec{v} equal to zero along the normal to the boundary (ie. $\vec{n} \cdot \vec{v} = 0$, where \vec{n} is the outward unit normal to the fluid domain). The mesh position, normal to the free surface, is determined from the normal component of the particle velocity and remeshing can be performed along the tangent; see, for instance Huerta and Liu, 1989 [856] or Braess and Wriggers, 2000 [189].

As mentioned above the mesh velocity in normal direction at the free surface (with unit normal \vec{n}) has to be consistent with the velocity of the Stokes velocity solution $\vec{v}(t)$:

$$\vec{v}_{\text{mesh}}(t) \cdot \vec{n} = \vec{v}(t) \cdot \vec{n} \quad \text{on } \Gamma_F \quad (347)$$

In ALE calculations the internal mesh velocity is usually undetermined, but one wants to smoothly deform the mesh so as to preserve its regularity, avoiding inverted or otherwise poorly conditioned cells. The mesh deformation can be calculated in many different ways, including algebraic (as mentioned in the previous paragraph) and PDE based approaches. The latter is chosen here. The Laplace equation is solved where the unknown in the mesh velocity, i.e. on must solve:

$$\Delta \vec{v}_{\text{mesh}} = 0 \quad (348)$$

subjected to the following boundary conditions:

$$\vec{v}_{\text{mesh}} = \vec{0} \quad \text{on } \Gamma_0 \quad (349)$$

$$\vec{v}_{\text{mesh}} = (\vec{v} \cdot \vec{n})\vec{n} \quad \text{on } \Gamma_F \quad (350)$$

$$\vec{v}_{\text{mesh}} \cdot \vec{n} = 0 \quad \text{on } \Gamma_{FS} \quad (351)$$

where Γ_{FS} is the part of the boundary with free slip boundary conditions, Γ_0 is the no-slip part and Γ_{FS} is the free slip part.

Once the mesh velocity has been obtained for all mesh points, these can be moved with said velocity. However, it must be noted that the multiple occurrences of the normal vector in the above equations is not without problem as the normal vectors are not well defined on the mesh vertices, which is where the mesh velocity is defined.

This yields what the author coin the 'quasi-implicit' scheme (we have so far neglected any kind of stabilisation):

1. Solve the Stokes system;
2. Solve for the surface mesh velocity using Equation 352;
3. Solve for the internal mesh velocity using Equations 348, 351;
4. Advect the mesh forward in time using displacements determined by the forward Euler scheme:
 $\vec{x}(t^{n+1}) = \vec{x}(t^n) + \vec{v}_{\text{mesh}}\delta t$.

Note that Rose et al (2017) [1406] go further than this, propose a 'nonstandard finite difference scheme' and make a link with the stabilisation presented in Kaus et al (2010) [946].

The authors list two simple methods of computing the normals:

- one can take \vec{n} as the direction of the local vertical,
- one could compute \vec{n} as some weighted average of the cell normals adjacent to a given vertex

but conclude that they have found that these schemes do not necessarily have good mass conservation properties.

A better approach is proposed in the form of an L_2 projection of the normal velocity $\vec{v} \cdot \vec{n}$ onto the free surface Γ_F . Multiplying the boundary conditions

$$\vec{v}_{\text{mesh}} = (\vec{v} \cdot \vec{n})\vec{n}$$

by a test function \vec{w} and integrating over the free surface part of the boundary, we find:

$$\int_{\Gamma_F} \vec{w} \cdot \vec{v}_{\text{mesh}} d\Gamma = \int_{\Gamma_F} \vec{w} \cdot (\vec{v} \cdot \vec{n})\vec{n} d\Gamma = \int_{\Gamma_F} (\vec{w} \cdot \vec{n})(\vec{v} \cdot \vec{n}) d\Gamma \quad (352)$$

When discretized, this forms a linear system which can be solved for the mesh velocity \vec{v}_{mesh} at the free surface. This system, being nonzero over only the free surface, is relatively computationally inexpensive to solve. The authors unfortunately fail to mention that this approach is particularly interesting since the numerical quadrature used to compute the above integrals require the normal \vec{n} between the nodes and these normals are well defined over each segment joining two nodes!²⁴

In what follows I present in some detail how to carry out the L_2 projection to arrive at the surface velocity for both Q_1 and Q_2 elements.

I start from the following integral over a Q_1 element:

$$\int_{\Gamma_e} N_i \vec{v}_{\text{mesh}} d\Gamma = \int N_i \begin{pmatrix} u_{\text{mesh}} \\ v_{\text{mesh}} \end{pmatrix} d\Gamma \quad (353)$$

$$= \int N_i \begin{pmatrix} N_1 & 0 & N_2 & 0 \\ 0 & N_1 & 0 & N_2 \end{pmatrix} \cdot \begin{pmatrix} u_1 \\ v_1 \\ u_2 \\ v_2 \end{pmatrix} d\Gamma \quad (354)$$

(355)

Writing this equation alternatively for $N_i = N_1, N_2$ yields:

$$\int_{\Gamma_e} \begin{pmatrix} N_1 N_1 & 0 & N_1 N_2 & 0 \\ 0 & N_1 N_1 & 0 & N_1 N_2 \\ N_2 N_1 & 0 & N_2 N_2 & 0 \\ 0 & N_2 N_1 & 0 & N_2 N_2 \end{pmatrix} \cdot \begin{pmatrix} u_1 \\ v_1 \\ u_2 \\ v_2 \end{pmatrix} d\Gamma = \int_{\Gamma_e} \begin{pmatrix} N_1 N_1 & 0 & N_1 N_2 & 0 \\ 0 & N_1 N_1 & 0 & N_1 N_2 \\ N_2 N_1 & 0 & N_2 N_2 & 0 \\ 0 & N_2 N_1 & 0 & N_2 N_2 \end{pmatrix} d\Gamma \cdot \begin{pmatrix} u_1 \\ v_1 \\ u_2 \\ v_2 \end{pmatrix}$$

Turning now to the right hand side $\int_{\Gamma_e} N_i (\vec{v} \cdot \vec{n}_e) \vec{n}_e d\Gamma$, it yields the following rhs:

$$\int_{\Gamma_e} (\vec{v} \cdot \vec{n}_e) \begin{pmatrix} N_1 n_x \\ N_1 n_y \\ N_2 n_x \\ N_2 n_y \end{pmatrix} d\Gamma$$

The elemental matrix and rhs must be built for each element and assembled in a global matrix and rhs. The solution is the mesh velocity vector at all surface nodes. the same approach can be taken for Q_2 elements:

$$\int_{\Gamma_e} N_i \vec{v}_{\text{mesh}} d\Gamma = \int N_i \begin{pmatrix} u_{\text{mesh}} \\ v_{\text{mesh}} \end{pmatrix} d\Gamma \quad (356)$$

$$= \int N_i \begin{pmatrix} N_1 & 0 & N_2 & 0 & N_3 & 0 \\ 0 & N_1 & 0 & N_2 & 0 & N_3 \end{pmatrix} \cdot \begin{pmatrix} u_1 \\ v_1 \\ u_2 \\ v_2 \\ u_3 \\ v_3 \end{pmatrix} d\Gamma \quad (357)$$

Writing this equation alternatively for $N_i = N_1, N_2, N_3$ yields:

$$\int_{\Gamma_e} \begin{pmatrix} N_1 N_1 & 0 & N_1 N_2 & 0 & N_1 N_3 & 0 \\ 0 & N_1 N_1 & 0 & N_1 N_2 & 0 & N_1 N_3 \\ N_2 N_1 & 0 & N_2 N_2 & 0 & N_2 N_3 & 0 \\ 0 & N_2 N_1 & 0 & N_2 N_2 & 0 & N_2 N_3 \\ N_3 N_1 & 0 & N_3 N_2 & 0 & N_3 N_3 & 0 \\ 0 & N_3 N_1 & 0 & N_3 N_2 & 0 & N_3 N_3 \end{pmatrix} \cdot \begin{pmatrix} u_1 \\ v_1 \\ u_2 \\ v_2 \\ u_3 \\ v_3 \end{pmatrix} d\Gamma$$

$$= \int_{\Gamma_e} \begin{pmatrix} N_1 N_1 & 0 & N_1 N_2 & 0 & N_1 N_3 & 0 \\ 0 & N_1 N_1 & 0 & N_1 N_2 & 0 & N_1 N_3 \\ N_2 N_1 & 0 & N_2 N_2 & 0 & N_2 N_3 & 0 \\ 0 & N_2 N_1 & 0 & N_2 N_2 & 0 & N_2 N_3 \\ N_3 N_1 & 0 & N_3 N_2 & 0 & N_3 N_3 & 0 \\ 0 & N_3 N_1 & 0 & N_3 N_2 & 0 & N_3 N_3 \end{pmatrix} d\Gamma \cdot \begin{pmatrix} u_1 \\ v_1 \\ u_2 \\ v_2 \\ u_3 \\ v_3 \end{pmatrix} \quad (358)$$

²⁴what if Q_k with $k > 1$ elements are used and nodes on the surface no more form a line?

The right hand side is then

$$\int_{\Gamma_e} (\vec{v} \cdot \vec{n}_e) \begin{pmatrix} N_1 n_x \\ N_1 n_y \\ N_2 n_x \\ N_2 n_y \\ N_3 n_x \\ N_3 n_y \end{pmatrix} d\Gamma$$

Having obtained the boundary condition velocity for the Laplace equation, we can now turn our attention to solving this ODE.

In what follows I omit the subscript 'mesh' and focus on the 2D case. The components of the (mesh) velocity are given by

$$u^h = \sum_{i=1}^{m_v} N_i^\nu u_i \quad v^h = \sum_{i=1}^{m_v} N_i^\nu v_i \quad \vec{v}^h = \begin{pmatrix} u^h \\ v^h \end{pmatrix}$$

We start from the ODE to solve in its strong form:

$$\Delta \vec{v}^h = \vec{0}$$

We multiply it by a velocity test function N_i^ν and integrate over an element:

$$\begin{aligned} & \vec{0} \\ &= \int_{\Omega_e} N_i^\nu \Delta \vec{v}^h \\ &= \int_{\Omega_e} N_i^\nu \Delta \vec{v}^h dV \\ &= \int_{\Omega_e} \begin{pmatrix} N_i^\nu \Delta u^h \\ N_i^\nu \Delta v^h \end{pmatrix} dV \\ &= \int_{\Omega_e} \begin{pmatrix} N_i^\nu \vec{\nabla} \cdot \vec{\nabla} u^h \\ N_i^\nu \vec{\nabla} \cdot \vec{\nabla} v^h \end{pmatrix} dV \\ &= \int_{\Omega_e} \begin{pmatrix} \vec{\nabla} N_i^\nu \cdot \vec{\nabla} u^h \\ \vec{\nabla} N_i^\nu \cdot \vec{\nabla} v^h \end{pmatrix} dV \\ &= \int_{\Omega_e} \begin{pmatrix} \partial_x N_i^\nu \partial_x u^h + \partial_y N_i^\nu \partial_y u^h \\ \partial_x N_i^\nu \partial_x v^h + \partial_y N_i^\nu \partial_y v^h \end{pmatrix} dV \\ &= \int_{\Omega_e} \begin{pmatrix} \partial_x N_i^\nu & \partial_y N_i^\nu & 0 & 0 \\ 0 & 0 & \partial_x N_i^\nu & \partial_y N_i^\nu \end{pmatrix} \cdot \begin{pmatrix} \partial_x u^h \\ \partial_y u^h \\ \partial_x v^h \\ \partial_y v^h \end{pmatrix} dV \\ &= \int_{\Omega_e} \begin{pmatrix} \frac{\partial N_i^\nu}{\partial x} & 0 & \frac{\partial N_i^\nu}{\partial x} & 0 & \cdots & \frac{\partial N_i^\nu}{\partial x} & 0 \\ \frac{\partial N_i^\nu}{\partial y} & 0 & \frac{\partial N_i^\nu}{\partial y} & 0 & \cdots & \frac{\partial N_i^\nu}{\partial y} & 0 \\ 0 & \frac{\partial N_i^\nu}{\partial x} & 0 & \frac{\partial N_i^\nu}{\partial x} & \cdots & 0 & \frac{\partial N_i^\nu}{\partial x} \\ 0 & \frac{\partial N_i^\nu}{\partial y} & 0 & \frac{\partial N_i^\nu}{\partial y} & \cdots & 0 & \frac{\partial N_i^\nu}{\partial y} \end{pmatrix} \cdot \begin{pmatrix} u_1 \\ v_1 \\ u_2 \\ v_2 \\ \vdots \\ u_{m_v} \\ v_{m_v} \end{pmatrix} dV \end{aligned}$$

Writing this equation for $i = 1, \dots, m_v$, we obtain:

$$\int \begin{pmatrix} \frac{\partial N_1^v}{\partial x} & \frac{\partial N_1^v}{\partial y} & 0 & 0 \\ 0 & 0 & \frac{\partial N_2^v}{\partial x} & \frac{\partial N_1^v}{\partial y} \\ \frac{\partial N_2^v}{\partial x} & \frac{\partial N_2^v}{\partial y} & 0 & 0 \\ 0 & 0 & \frac{\partial N_2^v}{\partial x} & \frac{\partial N_2^v}{\partial y} \\ \vdots & \vdots & \vdots & \vdots \\ \vdots & \vdots & \vdots & \vdots \\ \frac{\partial N_{m_v}^v}{\partial x} & \frac{\partial N_{m_v}^v}{\partial y} & 0 & 0 \\ 0 & 0 & \frac{\partial N_{m_v}^v}{\partial x} & \frac{\partial N_{m_v}^v}{\partial y} \end{pmatrix} \cdot \begin{pmatrix} \frac{\partial N_1^v}{\partial x} & 0 & \frac{\partial N_2^v}{\partial x} & 0 & \dots & \frac{\partial N_{m_v}^v}{\partial x} & 0 \\ \frac{\partial N_1^v}{\partial y} & 0 & \frac{\partial N_2^v}{\partial y} & 0 & \dots & \frac{\partial N_{m_v}^v}{\partial y} & 0 \\ 0 & \frac{\partial N_1^v}{\partial x} & 0 & \frac{\partial N_2^v}{\partial x} & \dots & 0 & \frac{\partial N_{m_v}^v}{\partial x} \\ 0 & \frac{\partial N_1^v}{\partial y} & 0 & \frac{\partial N_2^v}{\partial y} & \dots & 0 & \frac{\partial N_{m_v}^v}{\partial y} \end{pmatrix} \cdot \underbrace{\begin{pmatrix} u_1 \\ v_1 \\ u_2 \\ v_2 \\ \dots \\ u_{m_v} \\ v_{m_v} \end{pmatrix}}_{\vec{V}} dV = \vec{0}$$

or,

$$\left(\int_{\Omega_e} \mathbf{B}^T \cdot \mathbf{B} dV \right) \cdot \vec{V} = \vec{0}$$

where \mathbf{B} is a $(ndim * ndim) \times (m_v * ndofV)$ matrix. This is implemented in Stone 54.9.

Remark. The integration by parts should have a minus appear but since the left hand side is 0, it is not taken into account.

surface terms arising from the integration by parts are neglected. EXPLAIN WHY!

Yet another approach [472] The unknown position of free surfaces can be computed using the following approach: for the simple case of a single-valued function $h = h(x, y, t)$, a hyperbolic equation must be solved,

$$\frac{\partial h}{\partial t} + (\vec{v} \cdot \vec{\nabla}) h = 0 \quad (359)$$

This is the kinematic equation of the surface and has been used, for instance, by Ramaswamy and Kawahara (1987), Huerta and Liu, 1988b, 1990; Souli and Zolesio (2001).

Idea: Eq. (359) is a simple advection equation. One could also add a diffusion operator with a diffusion coefficient D . Low values of D could be used to stabilise the surface while higher values (possibly nonlinear ones) could be used to account for simple surface processes.

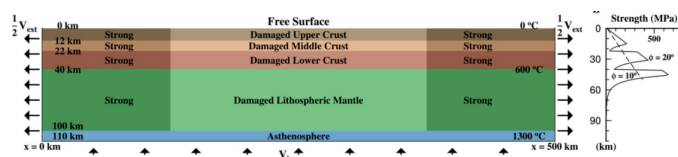
$$\frac{\partial h}{\partial t} + (\vec{v} \cdot \vec{\nabla}) h = D \Delta h \quad (360)$$

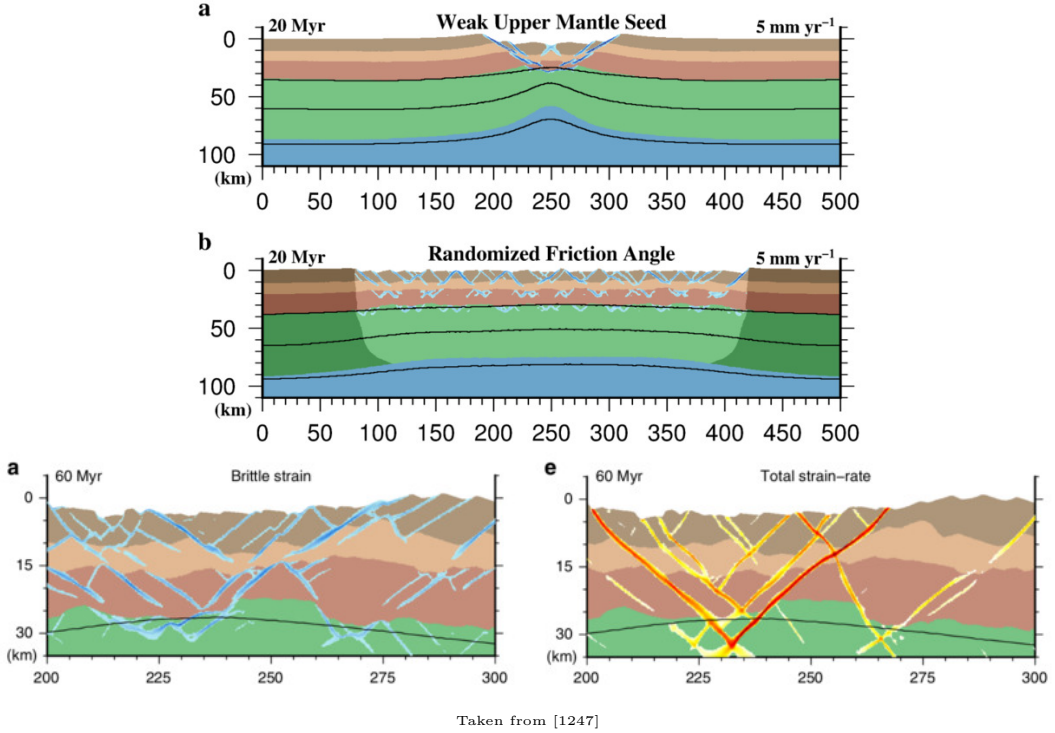
Also, Hansen and Nielsen [791, 790] write: During the entire model evolution surface processes act to re-distribute sediments. These processes are modelled by a diffusion equation with a source term enabling the transport of sediments to and from the model profile. The transport equation is written

$$\dot{h} = \nabla \cdot (\kappa \nabla h) + \dot{s}(w)$$

where $\kappa = 200 \text{ km}^2/\text{Ma}$ is the diffusivity of topography and $\dot{s}(w)$ is a linear function of water depth.

The following pictures are taken from Naliboff et al [1247] on the topic of how complex fault interaction controls continental rifting. It is a beautiful example (among many) of the importance of free surface geodynamical expression and large deformation:





8.1.4 On the topic of moving internal nodes

Braess & Wriggers [189] propose the following interesting algorithm: "A measure of the quality of a triangular mesh is the quotient of the outer radius r_{out} and the inner radius r_{in} of each element. This quotient is important because it plays a certain role in a priori error estimates. If an element degenerates this quotient will approach infinity. Another important feature of good mesh is that no element becomes very large. With these considerations in mind the penalty function W is defined:

$$W = \sum_{elts} \left(\frac{r_{out}}{r_{in}} \right)^m \left(\frac{r_{out}}{r_0} \right)^n \quad (361)$$

where m , n and r_0 are positive constants. For our calculations we chose $m = 3$, $n = 1$ and $r_0 = 1$, but the results seem to depend only slightly on this choice. Whenever a triangle is distorted or very large, this function becomes very large. A similar penalty function was presented in [?] for four-node elements. In that case the angles of the elements are used to construct the penalty function. In order to regularize a distorted mesh the coordinates of the internal nodes will be chosen such that W is minimized. It is not necessary to reach the global minimum, a rough approximation is sufficient. Therefore the minimization of the potential can be done efficiently with standard procedures and will not be discussed in any detail. This algorithm can also be applied to h -adaptive mesh-generation by choosing appropriate constants r_0 for each triangle."²⁵

This is still WORK IN PROGRESS. I Need to look at those papers: [856] [123] [490] [495] [32] [1006] [1477] [1113] [766][1759] [512] [189] and talk about free surface stabilisation [946, 1339, 490, 1406].

²⁵Indeed, if r_0 is the same for all elements this parameter will not play any role at all in the minimisation process.

8.2 Convergence criterion for nonlinear iterations

MEGA WORK in PROGRESS!!

Following [1473], one can monitor the relative changes in the solution from iteration to iteration. For instance,

$$\frac{\|\Delta \vec{V}\|_{L2}}{\|\vec{V}\|_{L2}} = \left(\frac{\int_{\Omega} (\vec{V}_i - \vec{V}_{i-1}) \cdot (\vec{V}_i - \vec{V}_{i-1}) dV}{\int_{\Omega} \vec{V}_i \cdot \vec{V}_i dV} \right)^{1/2}$$

is a measure of the relative change in the velocity field from iteration $i - 1$ to i . The same monitoring can be done for pressure:

$$\frac{\|\Delta \vec{P}\|_{L2}}{\|\vec{P}\|_{L2}} = \left(\frac{\int_{\Omega} (\vec{P}_i - \vec{P}_{i-1}) \cdot (\vec{P}_i - \vec{P}_{i-1}) dV}{\int_{\Omega} \vec{P}_i \cdot \vec{P}_i dV} \right)^{1/2}$$

Convergence is reached when both are below 0.001 [1037] or 0.0001 [944].

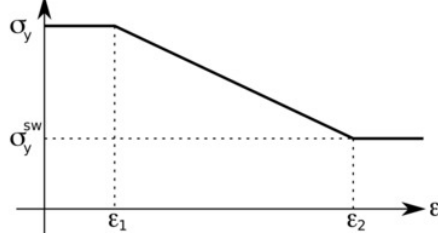
nonlinear residual .. see [1473] p2222.

check correlation of [1538]

8.3 Strain weakening

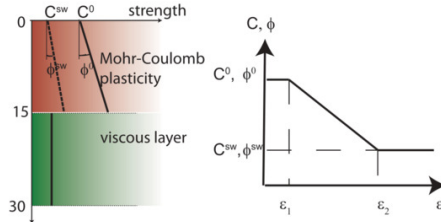
Several mechanisms may contribute to strain or strain rate dependent weakening but their relative and absolute importance is poorly constrained. Furthermore, weakening mechanisms are often crudely parameterised in geodynamical codes with simple mathematical functions and a limited number of parameters.

For example, in [20] the authors use a von Mises plasticity formulation so that the rheology is parameterised by the cohesion c , or $c = \sigma_y$ in their notations. The yield strength σ_y starts constant until the strain ε reaches the threshold value ε_1 . It then decreases linearly from σ_y to σ_y^{sw} between ε_1 and ε_2 . For strain values $\varepsilon > \varepsilon_2$, the yield strength remains constant at σ_y^{sw} .



Taken from [20]

The same authors in a subsequent study use a Drucker-Prager rheology parameterised by cohesion c and friction angle ϕ . They use the same approach as before but now both parameters are subjected to strain weakening:



Taken from [21], see also [1538]

They further define the factor $R = C^0/C^{sw} = \phi^0/\phi^{sw} \geq 1$ which is a proxy for the ratio σ_y/σ_y^{sw} where $\sigma_y = p \sin \phi + c \cos \phi$, and carry out 3D crustal extensional models for R between 2 and 5.

In [1029] the authors also define

$$\tau_y = p \sin(\phi(\varepsilon^p)) + c_0 \cos(\phi(\varepsilon^p))$$

but the cohesion is regarded to be constant. The angle of friction ϕ is assumed to decrease as a function of the accumulated plastic strain ε^p to

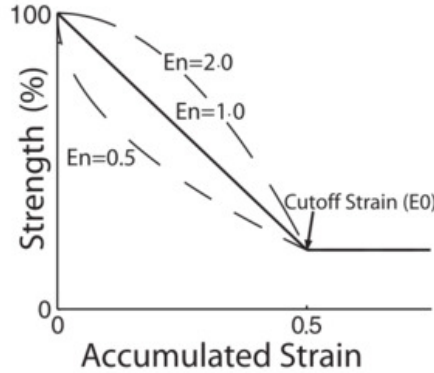
$$\phi(\varepsilon^p) = \max \left(\phi_\infty, \phi_0 - \frac{\varepsilon^p(\phi_0 - \phi_\infty)}{\varepsilon_\infty^p} \right)$$

This equation defines an empirical softening relation which reduces the friction angle linearly with accumulated plastic strain. ϕ_0 defines the initial friction angle, ε_∞^p represents the measure of plastic strain after which complete softening is achieved and internal friction angle reaches ϕ_∞ . Plastic strain represents an integrated, tensorial invariant measure of the deformation which has occurred due to plastic yielding. Thus, the quantity ε^p can be regarded as a simplified measure of material damage.

In Dyksterhuis et al [497] a variant of the above formulation is used:

$$f(\varepsilon) = \begin{cases} 1 - (1-a)(\varepsilon/\varepsilon_0)^n & \varepsilon \leq \varepsilon_0 \\ a & \varepsilon \geq \varepsilon_0 \end{cases}$$

where ε is the accumulated plastic strain, ε_0 is the saturation strain beyond which no further weakening takes place, n is an exponent that controls the shape of the function and a is a maximum value of strain weakening beyond which no further weakening occurs. This equation leads to the following plot:



Strain-softening behaviour showing strength weakening from 100 to 20% after an accumulated strain of 0.5, after which no further weakening occurs.

Dashed lines show the effect of the exponential parameter (E_n) on the curve. Taken from [497]

Although it is not specified in [497] what f is, other users of the code specify that the yield strength is given by

$$\sigma_y = (B_0 + B_1 p) f(\varepsilon)$$

where p is the pressure, B_0 is the cohesion, or yield stress at zero pressure, and B_p is the pressure dependence of the yield stress, equivalent to the friction coefficient in Byerlees law.

In [1724] the authors take a different approach:

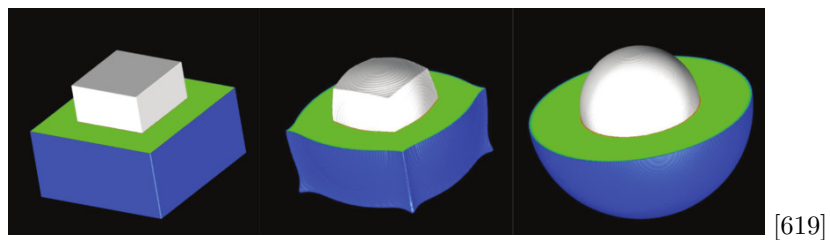
$$C = C_0 + C_1 \exp\left(-\frac{\varepsilon_{plast}}{\varepsilon_{ref}}\right)$$

$$\mu = \mu_0 + \mu_1 \exp\left(-\frac{\varepsilon_{plast}}{\varepsilon_{ref}}\right)$$

where C_0 and $C_0 + C_1$ represent the minimum and maximum cohesions, respectively; μ_0 and $\mu_0 + \mu_1$ represent the minimum and maximum frictional coefficients, respectively. ε_{plast} and ε_{ref} represent accumulated plastic strain and reference strain, respectively.

Literature: [1260]

8.4 The gravity vector



[619]

8.5 The SUPG formulation for the energy equation

As abundantly documented in the literature advection needs to be stabilised as it otherwise showcases non-negligible under- and overshoots. A standard approach is the Streamline Upwind Petrov Galerkin (SUPG) method.

 Literature[215][859]

8.5.1 Linear elements

When using linear elements, its implementation is rather trivial, as shown in the DOUAR paper [199] or the FANTOM paper [1538]. The advection matrix is simply modified and computed as follows:

$$(\mathbf{K}_a^e)_{SUPG} = \int_{x_k}^{x_{k+1}} (\mathbf{N}^*)^T \rho C_p \vec{v} \cdot \mathbf{B} dx \quad \text{with} \quad \mathbf{N}^* = \mathbf{N} + \tau \vec{v} \cdot \mathbf{B}$$

Note that we can also write

$$(\mathbf{K}_a^e)_{SUPG} = \int_{x_k}^{x_{k+1}} \mathbf{N}^T \rho C_p \vec{v} \cdot \mathbf{B} dx + \int_{x_k}^{x_{k+1}} \tau (\vec{v} \cdot \mathbf{B})^T \rho C_p (\vec{v} \cdot \mathbf{B}) dx$$

and we see that the SUPG method introduces an additional term that is akin to a diffusion term in the direction of the flow. This can be seen by looking at the advection matrix a regular grid of 1D elements of size h :

$$(\mathbf{K}_a^e)_{SUPG} = \mathbf{K}_a^e + \rho C_p \frac{\tau u^2}{h} \begin{pmatrix} 1 & -1 \\ -1 & 1 \end{pmatrix}$$

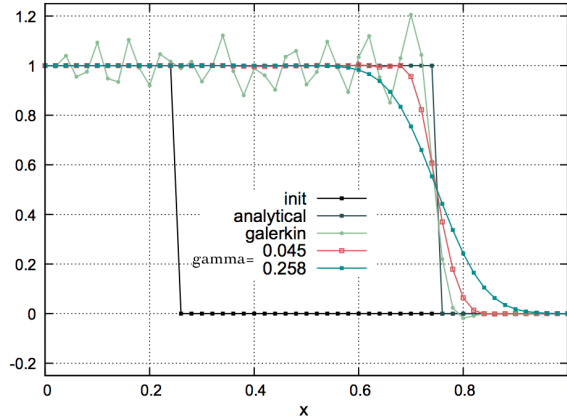
The additional matrix has the same structure as the 1D diffusion matrix matrix in 5.1.

The parameter τ is chosen as follows:

$$\tau = \gamma \frac{h}{\nu} \tag{362}$$

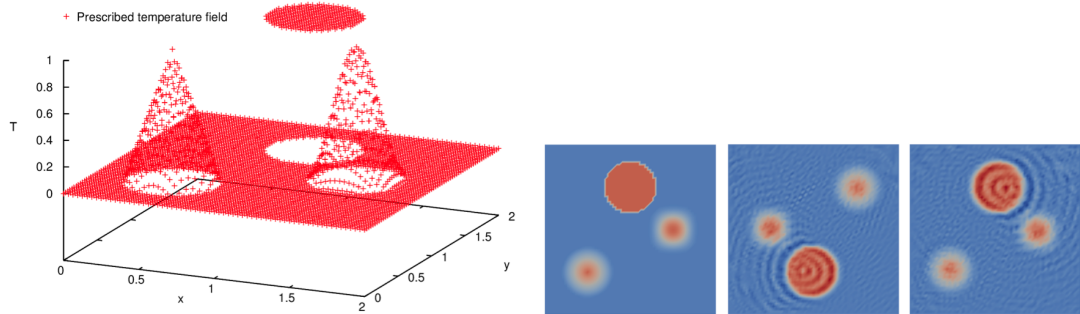
where γ is a user chosen parameter (see Appendix A of [1538]).

A typical test case for testing an advection scheme is the step advection benchmark (see for instance [473]). At $t = 0$, a field $T(x)$ is prescribed in a 1D domain of unit length. For $x \leq 1/4$ we have $T(x) = 1$ and $T(x) = 0$ everywhere else as shown on the following figure:



The prescribed velocity is $\nu = 1$, 50 elements are used and 250 time steps are carried out with $\delta t = 0.1h/\nu = 0.002$. As discussed in [1538], using Equation 362, one arrives to $\gamma = 0.045$, which leads to a desired removal of the oscillations through a small amount of numerical diffusion. Braun [195] argues for a constant $\gamma = 1/\sqrt{15} = 0.258$ (after [861]), which effect is also shown in the figure above. This value is arguably too large and introduces undesirable diffusion.

Another classic example of advection testing is a 2D problem where (for example) a cylinder, a Gaussian and a cone are prescribed and advected with a velocity field (see for instance [473]).



After a 2π rotation and in the absence of stabilisation we see that the temperature field showcases clearly visible ripples.

Remark. Note that ASPECT originally did not rely on the SUPG formulation to stabilise the advection(-diffusion) equations[1009]. It instead relied on the Entropy Viscosity formulation [753]. It is only during the 6th Hackathon in May 2019 that the SUPG was introduced on the code. Note that the ASPECT implementation is based on the deal.II step 63²⁶.

²⁶https://www.dealii.org/developer/doxygen/deal.II/step_63.html

8.6 The method of manufactured solutions

The method of manufactured solutions is a relatively simple way of carrying out code verification. In essence, one postulates a solution for the PDE at hand (as well as the proper boundary conditions), inserts it in the PDE and computes the corresponding source term. The same source term and boundary conditions will then be used in a numerical simulation so that the computed solution can be compared with the (postulated) true analytical solution.

Examples of this approach are to be found in [473, 283, 163, 1321, 159].

8.6.1 Analytical benchmark I - "DH"

Taken from [473]. We consider a two-dimensional problem in the square domain $\Omega = [0, 1] \times [0, 1]$, which possesses a closed-form analytical solution. The problem consists of determining the velocity field $\vec{v} = (u, v)$ and the pressure p such that

$$\eta \Delta \vec{v} - \vec{\nabla} p + \vec{b} = \vec{0} \quad \text{in } \Omega \quad (363)$$

$$\vec{\nabla} \cdot \vec{v} = 0 \quad \text{in } \Omega \quad (364)$$

$$\vec{v} = \vec{0} \quad \text{on } \Gamma_D \quad (365)$$

where the fluid viscosity is taken as $\eta = 1$. The components of the body force \vec{b} are prescribed as

$$\begin{aligned} b_x &= (12 - 24y)x^4 + (-24 + 48y)x^3 + (-48y + 72y^2 - 48y^3 + 12)x^2 \\ &\quad + (-2 + 24y - 72y^2 + 48y^3)x + 1 - 4y + 12y^2 - 8y^3 \\ b_y &= (8 - 48y + 48y^2)x^3 + (-12 + 72y - 72y^2)x^2 \\ &\quad + (4 - 24y + 48y^2 - 48y^3 + 24y^4)x - 12y^2 + 24y^3 - 12y^4 \end{aligned}$$

With this prescribed body force, the exact solution is

$$\begin{aligned} u(x, y) &= x^2(1-x)^2(2y-6y^2+4y^3) \\ v(x, y) &= -y^2(1-y)^2(2x-6x^2+4x^3) \\ p(x, y) &= x(1-x) - 1/6 \end{aligned}$$

Note that the pressure obeys $\int_{\Omega} p d\Omega = 0$. One can turn to the spatial derivatives of the fields:

$$\dot{\varepsilon}_{xx} = \frac{\partial u}{\partial x} = (2x - 6x^2 + 4x^3)(2y - 6y^2 + 4y^3) \quad (366)$$

$$\dot{\varepsilon}_{yy} = \frac{\partial v}{\partial y} = -(2x - 6x^2 + 4x^3)(2y - 6y^2 + 4y^3) \quad (367)$$

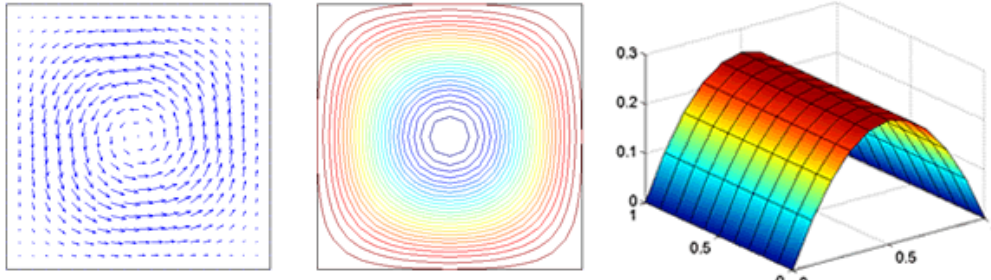
$$\dot{\varepsilon}_{xy} = \frac{1}{2} \left(\frac{\partial u}{\partial y} + \frac{\partial v}{\partial x} \right) = \frac{1}{2} (x^2(1-x)^2(2-12y+12y^2) - y^2(1-y)^2(2-12x+12x^2)) \quad (368)$$

with of course $\vec{\nabla} \cdot \vec{v} = 0$ and

$$\frac{\partial p}{\partial x} = 1 - 2x \quad (369)$$

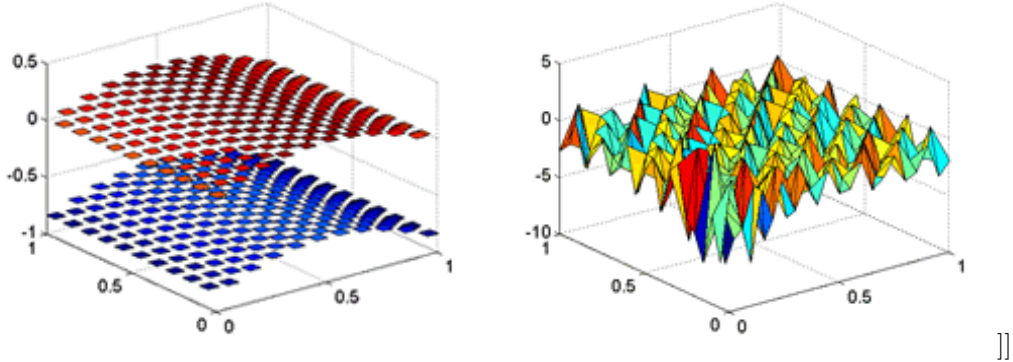
$$\frac{\partial p}{\partial y} = 0 \quad (370)$$

The velocity and pressure fields look like:



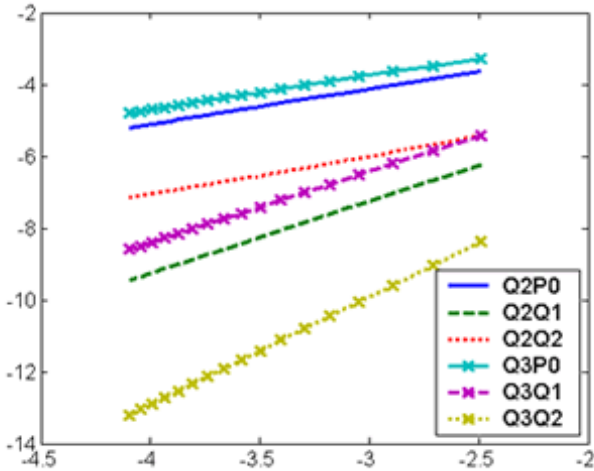
http://ww2.lacan.upc.edu/huerta/exercises/Incompressible/Incompressible_Ex1.htm

As shown in [473], If the LBB condition is not satisfied, spurious oscillations spoil the pressure approximation. Figures below show results obtained with a mesh of 20x20 Q1P0 (left) and P1P1 (right) elements:



http://ww2.lacan.upc.edu/huerta/exercises/Incompressible/Incompressible_Ex1.htm

Taking into account that the proposed problem has got analytical solution, it is easy to analyze convergence of the different pairs of elements:



http://ww2.lacan.upc.edu/huerta/exercises/Incompressible/Incompressible_Ex1.htm

One can also compute the stress components:

$$\sigma_{xx} = 2x^2(2x-2)(4y^3-6y^2+2y) + 4x(-x+1)^2 * (4y^3-6y^2+2y) - x(-x+1) + 1/6 \quad (371)$$

$$\sigma_{xy} = x^2(-x+1)^2 * (12y^2-12y+2) - y^2(-y+1)^2 * (12x^2-12x+2) \quad (372)$$

$$\sigma_{yy} = -x(-x+1) - 2y^2(2y-2)(4x^3-6x^2+2x) - 4y(-y+1)^2(4x^3-6x^2+2x) + 1/6 \quad (373)$$

All the necessary functions to do this benchmark are in `mms/dh.py`:

```
# functions for the Donea & Huerta benchmark (dh)

def u_th(x,y):
    return x**2*(1.-x)**2*(2*y-6*y**2+4*y**3)

def v_th(x,y):
    return -y**2*(1.-y)**2*(2*x-6*x**2+4*x**3)

def p_th(x,y):
    return x*(1-x)-1./6.

def dpdx_th(x,y):
    return 1.-2.*x
```

```

def dpdy_th(x,y):
    return 0.

def exx_th(x,y):
    return x**2*(2*x-2)*(4*y**3-6*y**2+2*y)+2*x*(-x+1)**2*(4*y**3-6*y**2+2*y)

def eyy_th(x,y):
    return (x**2*(-x+1)**2*(12*y**2-12*y+2)-y**2*(-y+1)**2*(12*x**2-12*x+2))/2

def bx(x,y):
    return ((12.-24.*y)*x**4+(-24.+48.*y)*x*x*x +
            (-48.*y+72.*y*y-48.*y*y*y+12.)*x*x +
            (-2.+24.*y-72.*y*y+48.*y*y*y)*x +
            1.-4.*y+12.*y*y-8.*y*y*y)

def by(x,y):
    return ((8.-48.*y+48.*y*y)*x*x*x+
            (-12.+72.*y-72.*y*y)*x*x+
            (4.-24.*y+48.*y*y-48.*y*y*y+24.*y**4)*x -
            12.*y*y+24.*y*y*y-12.*y**4)

```

This benchmark is implemented in ASPECT [75].

8.6.2 Analytical benchmark II - "DB2D"

Taken from [469, 163]. It is for a unit square with $\nu = \mu/\rho = 1$ and the smooth exact solution is

$$u(x,y) = x + x^2 - 2xy + x^3 - 3xy^2 + x^2y \quad (374)$$

$$v(x,y) = -y - 2xy + y^2 - 3x^2y + y^3 - xy^2 \quad (375)$$

$$p(x,y) = xy + x + y + x^3y^2 - 4/3 \quad (376)$$

Note that the pressure obeys $\int_{\Omega} p d\Omega = 0$

$$b_x = -(1 + y - 3x^2y^2) \quad (377)$$

$$b_y = -(1 - 3x - 2x^3y) \quad (378)$$

This benchmark is also used in [1708].

8.6.3 Analytical benchmark III - "DB3D"

This benchmark begins by postulating a polynomial solution to the 3D Stokes equation [469]:

$$\mathbf{v} = \begin{pmatrix} x + x^2 + xy + x^3y \\ y + xy + y^2 + x^2y^2 \\ -2z - 3xz - 3yz - 5x^2yz \end{pmatrix} \quad (379)$$

and

$$p = xyz + x^3y^3z - 5/32 \quad (380)$$

While it is then trivial to verify that this velocity field is divergence-free (see here under), the corresponding body force of the Stokes equation can be computed by inserting this solution into the momentum equation with a given viscosity $\eta(x, y, z)$ (constant or position/velocity/strain rate dependent). The domain is a unit cube and velocity boundary conditions simply use Eq. (645). Note that the pressure fulfills

$$\int_{\Omega} p(x, y, z) dV = 0.$$

Following [283], the viscosity is given by the smoothly varying function

$$\eta(x, y, z) = \exp(1 - \beta(x(1-x) + y(1-y) + z(1-z))) \quad (381)$$

Choosing $\beta = 0$ yields a constant velocity $\eta = e^1$ (and greatly simplifies the right-hand side). One can easily show that the ratio of viscosities η^* in the system follows $\eta^* = \exp(-3\beta/4)$ so that choosing $\beta = 10$ yields $\eta^* \simeq 1808$ and $\beta = 20$ yields $\eta^* \simeq 3.269 \times 10^6$.

$$\frac{\partial \mu}{\partial x} = -4\beta(1-2x)\mu(x, y, z) \quad (382)$$

$$\frac{\partial \mu}{\partial y} = -4\beta(1-2y)\mu(x, y, z) \quad (383)$$

$$\frac{\partial \mu}{\partial z} = -4\beta(1-2z)\mu(x, y, z) \quad (384)$$

We can compute the components of the strainrate tensor:

$$\dot{\varepsilon}_{xx} = 1 + 2x + y + 3x^2y \quad (385)$$

$$\dot{\varepsilon}_{yy} = 1 + x + 2y + 2x^2y \quad (386)$$

$$\dot{\varepsilon}_{zz} = -2 - 3x - 3y - 5x^2y \quad (387)$$

$$\dot{\varepsilon}_{xy} = \frac{1}{2}(x + y + 2xy^2 + x^3) \quad (388)$$

$$\dot{\varepsilon}_{xz} = \frac{1}{2}(-3z - 10xyz) \quad (389)$$

$$\dot{\varepsilon}_{yz} = \frac{1}{2}(-3z - 5x^2z) \quad (390)$$

and recover $\dot{\varepsilon}_{xx} + \dot{\varepsilon}_{yy} + \dot{\varepsilon}_{zz} = 0$ as expected.

We further have

$$\frac{\partial}{\partial x} 2\dot{\varepsilon}_{xx} = 2(2 + 6xy)$$

$$\frac{\partial}{\partial y} 2\dot{\varepsilon}_{xy} = 1 + 4xy$$

$$\frac{\partial}{\partial z} 2\dot{\varepsilon}_{xz} = -3 - 10xy$$

$$\frac{\partial}{\partial x} 2\dot{\varepsilon}_{xy} = 1 + 2y^2 + 3x^2$$

$$\frac{\partial}{\partial y} 2\dot{\varepsilon}_{yy} = 2(2 + 2x^2)$$

$$\frac{\partial}{\partial z} 2\dot{\varepsilon}_{yz} = -3 - 5x^2$$

$$\frac{\partial}{\partial x} 2\dot{\varepsilon}_{xz} = -10yz$$

$$\frac{\partial}{\partial y} 2\dot{\varepsilon}_{yz} = 0$$

$$\frac{\partial}{\partial z} 2\dot{\varepsilon}_{zz} = 2(0)$$

$$\frac{\partial p}{\partial x} = yz + 3x^2y^3z \quad (391)$$

$$\frac{\partial p}{\partial y} = xz + 3x^3y^2z \quad (392)$$

$$\frac{\partial p}{\partial z} = xy + x^3y^3 \quad (393)$$

Constant viscosity In this case, the right hand side writes:

$$f_x = -\frac{\partial p}{\partial x} + 2\eta \frac{\partial}{\partial x} \dot{\epsilon}_{xx} + 2\eta \frac{\partial}{\partial y} \dot{\epsilon}_{xy} + 2\eta \frac{\partial}{\partial z} \dot{\epsilon}_{xz} \quad (394)$$

$$= -(yz + 3x^2y^3z) + 2(2 + 6xy) + (1 + 4xy) + (-3 - 10xy) \quad (395)$$

$$f_y = -\frac{\partial p}{\partial y} + 2\mu \frac{\partial}{\partial x} \dot{\epsilon}_{xy} + 2\mu \frac{\partial}{\partial y} \dot{\epsilon}_{yy} + 2\mu \frac{\partial}{\partial z} \dot{\epsilon}_{yz} \quad (396)$$

$$= -(xz + 3x^3y^2z) + \mu(1 + 2y^2 + 3x^2) + \mu 2(2 + 2x^2) + \mu(-3 - 5x^2) \quad (397)$$

$$f_z = -\frac{\partial p}{\partial z} + 2\mu \frac{\partial}{\partial x} \dot{\epsilon}_{xz} + 2\mu \frac{\partial}{\partial y} \dot{\epsilon}_{yz} + 2\mu \frac{\partial}{\partial z} \dot{\epsilon}_{zz} \quad (398)$$

$$= -(xy + x^3y^3) + \mu(-10yz) + 0 + 0 \quad (399)$$

and finally

$$\begin{aligned} \mathbf{f} &= -\nabla p + \eta \begin{pmatrix} 2 + 6xy \\ 2 + 2x^2 + 2y^2 \\ -10yz \end{pmatrix} \\ &= - \begin{pmatrix} yz + 3x^2y^3z \\ xz + 3x^3y^2z \\ xy + x^3y^3 \end{pmatrix} + \eta \begin{pmatrix} 2 + 6xy \\ 2 + 2x^2 + 2y^2 \\ -10yz \end{pmatrix} \end{aligned}$$

Variable viscosity In this case, the right hand side is obtained through

$$\begin{aligned} \mathbf{f} &= -\nabla p + \eta \begin{pmatrix} 2 + 6xy \\ 2 + 2x^2 + 2y^2 \\ -10yz \end{pmatrix} \\ &+ \begin{pmatrix} 2\dot{\epsilon}_{xx} \\ 2\dot{\epsilon}_{xy} \\ 2\dot{\epsilon}_{xz} \end{pmatrix} \frac{\partial \eta}{\partial x} + \begin{pmatrix} 2\dot{\epsilon}_{xy} \\ 2\dot{\epsilon}_{yy} \\ 2\dot{\epsilon}_{yz} \end{pmatrix} \frac{\partial \eta}{\partial y} + \begin{pmatrix} 2\dot{\epsilon}_{xz} \\ 2\dot{\epsilon}_{yz} \\ 2\dot{\epsilon}_{zz} \end{pmatrix} \frac{\partial \eta}{\partial z} \end{aligned} \quad (400)$$

[283] has carried out this benchmark for $\beta = 4$, i.e.:

$$\mu(x, y, z) = \exp(1 - 4(x(1-x) + y(1-y) + z(1-z)))$$

In a unit cube, this yields a variable viscosity such that $0.1353 < \mu < 2.7182$, i.e. a ratio of approx. 20 within the domain. We then have:

$$\frac{\partial \mu}{\partial x} = -4(1 - 2x)\mu(x, y, z) \quad (401)$$

$$\frac{\partial \mu}{\partial y} = -4(1 - 2y)\mu(x, y, z) \quad (402)$$

$$\frac{\partial \mu}{\partial z} = -4(1 - 2z)\mu(x, y, z) \quad (403)$$

sort out mess wrt Eq 26 of busa13

8.6.4 Analytical benchmark IV - "Bercovier & Engelman"

From [132]. The two-dimensional domain is a unit square. The body forces are:

$$\begin{aligned} f_x &= 128[x^2(x-1)^2 12(2y-1) + 2(y-1)(2y-1)y(12x^2 - 12x + 2)] \\ f_y &= 128[y^2(y-1)^2 12(2x-1) + 2(x-1)(2x-1)y(12y^2 - 12y + 2)] \end{aligned} \quad (404)$$

The solution is

$$\begin{aligned} u &= -256x^2(x-1)^2y(y-1)(2y-1) \\ v &= 256y^2(y-1)^2x(x-1)(2x-1) \\ p &= 0 \end{aligned} \quad (405)$$

$$du/dx = 512(1-2x)(-1+x)x(-1+y)y(-1+2y) \quad (406)$$

$$du/dy = -256(-1+x)^2x^2(1-6y+6y^2) \quad (407)$$

$$dv/dx = 256y^2(y-1)^2x(x-1)(2x-1) \quad (408)$$

$$dv/dy = -512(-1+x)x(1-2x)(-1+y)y(-1+2y) \quad (409)$$

$$(410)$$

and we can easily verify that $\vec{\nabla} \cdot \vec{v} = du/dx + dv/dy = 0$.

CHECK RHS !

Another choice with a non-zero pressure:

$$\begin{aligned} f_x &= 128[x^2(x-1)^212(2y-1) + 2(y-1)(2y-1)y(12x^2-12x+2)] + y - 1/2 \\ f_y &= 128[y^2(y-1)^212(2x-1) + 2(x-1)(2x-1)y(12y^2-12y+2)] + x - 1/2 \end{aligned} \quad (411)$$

The solution is

$$\begin{aligned} u &= -256x^2(x-1)^2y(y-1)(2y-1) \\ v &= 256y^2(y-1)^2x(x-1)(2x-1) \\ p &= (x-1/2)(y-1/2) \end{aligned} \quad (412)$$

8.6.5 Analytical benchmark V - "VJ1"

This is taken from Appendix D1 of [915].

The domain Ω is a unit square. We consider the stream function

$$\phi(x, y) = 1000x^2(1-x)^4y^3(1-y)^2$$

The velocity field is defined by

$$u(x, y) = \partial_y \phi = 1000(x^2(1-x)^4y^2(1-y)(3-5y)) \quad (413)$$

$$v(x, y) = -\partial_x \phi = 1000(-2x(1-x)^3(1-3x)y^3(1-y)^2) \quad (414)$$

and it is easy to verify that $\vec{\nabla} \cdot \vec{v} = 0$.

The pressure is given by:

$$p(x, y) = \pi^2(xy^3 \cos(2\pi x^2 y) - x^2 y \sin(2\pi x y)) + \frac{1}{8}$$

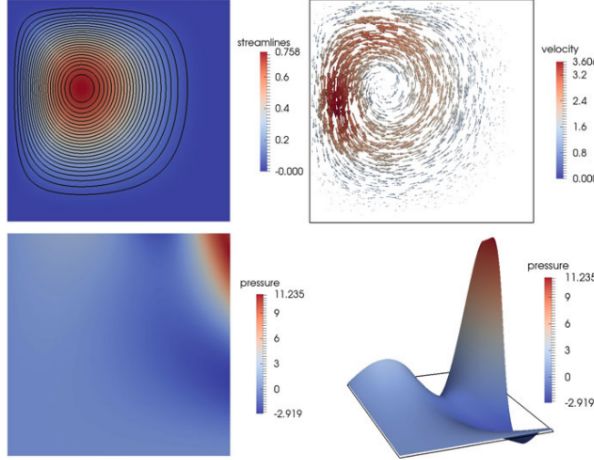


Fig. D.1 Example D.3. Stream function (top left) velocity (top right) and pressure (bottom). These plots are based on results obtained with numerical simulations

Taken from [915].

(BSc Thesis)

8.6.6 Analytical benchmark VI - "Ilinca & Pelletier"

This is taken from [878].

Let us consider the Poiseuille flow of a Newtonian fluid. The channel has isothermal flat walls located at $y = \pm h$. The velocity distribution is parabolic:

$$u = u_0 \left(1 - \frac{y^2}{h^2} \right) \quad v = 0$$

where u_0 is the maximum velocity. The (steady state) temperature field is the solution of the advection-diffusion equation:

$$\rho C_p \vec{v} \cdot \vec{\nabla} T = k \Delta T + \Phi$$

where Φ is the dissipation function given by

$$\Phi = \eta \left[2 \left(\frac{\partial u}{\partial x} \right)^2 + 2 \left(\frac{\partial v}{\partial y} \right)^2 + \left(\frac{\partial v}{\partial x} + \frac{\partial u}{\partial y} \right)^2 \right] = \eta \left(\frac{\partial u}{\partial y} \right)^2 = 4\eta \frac{u_0^2 y^2}{h^4}$$

We logically assume that $T = T(y)$ so that $\partial T / \partial x = 0$ and $\vec{v} \cdot \vec{\nabla} T = 0$. We then have to solve:

$$k \frac{\partial^2 T}{\partial y^2} + 4\eta \frac{u_0^2 y^2}{h^4} = 0$$

We can integrate twice and use the boundary conditions $T(y = \pm h) = T_0$ to arrive at:

$$T(y) = T_0 + \frac{1}{3} \frac{\eta u_0^2}{k} \left[1 - \left(\frac{y}{h} \right)^4 \right]$$

with a maximum temperature

$$T_M = T(y = 0) = T_0 + \frac{1}{3} \frac{\eta u_0^2}{k}$$

8.6.7 Analytical benchmark VII - "grooves"

This benchmark was designed by Dave May. The velocity and pressure fields are given by

$$\begin{aligned} u(x, y) &= x^3 y + x^2 + x y + x \\ v(x, y) &= -\frac{3}{2} x^2 y^2 - 2 x y - \frac{1}{2} y^2 - y \\ p(x, y) &= x^2 y^2 + x y + 5 + p_0 \end{aligned} \tag{415}$$

where p_0 is a constant to be determined based on the type of pressure normalisation. The viscosity is chosen to be

$$\eta(x, y) = -\sin(p) + 1 + \epsilon = -\sin(x^2y^2 + xy + 5) + 1 + \epsilon \quad (416)$$

where ϵ actually controls the viscosity contrast. Note that inserting the polynomial expression of the pressure inside the viscosity expression makes the problem linear. We have

$$\begin{aligned} \dot{\varepsilon}_{xx} &= \frac{\partial u}{\partial x} = 3x^2y + 2x + y + 1 \\ \dot{\varepsilon}_{yy} &= \frac{\partial v}{\partial y} = -3x^2y - 2x - y - 1 \\ \dot{\varepsilon}_{xy} &= \frac{1}{2} \left(\frac{\partial u}{\partial y} + \frac{\partial v}{\partial x} \right) = \frac{1}{2} (x^3 + x - 3xy^2 - 2y) \end{aligned} \quad (417)$$

and we can verify that the velocity field is incompressible since $\vec{\nabla} \cdot \vec{v} = \dot{\varepsilon}_{xx} + \dot{\varepsilon}_{yy} = 0$. The pressure gradient is given by

$$\begin{aligned} \frac{\partial p}{\partial x} &= 2xy^2 + y \\ \frac{\partial p}{\partial y} &= 2x^2y + x \end{aligned}$$

The right hand side term of the Stokes equation is such that

$$\begin{aligned} -\frac{\partial p}{\partial x} + \frac{\partial s_{xx}}{\partial x} + \frac{\partial s_{yx}}{\partial y} + f_x &= 0 \\ -\frac{\partial p}{\partial y} + \frac{\partial s_{xy}}{\partial x} + \frac{\partial s_{yy}}{\partial y} + f_y &= 0 \end{aligned} \quad (418)$$

with

$$\begin{aligned} \frac{\partial s_{xx}}{\partial x} &= \frac{\partial(2\eta\dot{\varepsilon}_{xx})}{\partial x} = 2\eta \frac{\partial\dot{\varepsilon}_{xx}}{\partial x} + 2\frac{\partial\eta}{\partial x}\dot{\varepsilon}_{xx} \\ \frac{\partial s_{zx}}{\partial z} &= \frac{\partial(2\eta\dot{\varepsilon}_{zx})}{\partial z} = 2\eta \frac{\partial\dot{\varepsilon}_{zx}}{\partial z} + 2\frac{\partial\eta}{\partial z}\dot{\varepsilon}_{zx} \\ \frac{\partial s_{xz}}{\partial x} &= \frac{\partial(2\eta\dot{\varepsilon}_{xz})}{\partial x} = 2\eta \frac{\partial\dot{\varepsilon}_{xz}}{\partial x} + 2\frac{\partial\eta}{\partial x}\dot{\varepsilon}_{xz} \\ \frac{\partial s_{zz}}{\partial z} &= \frac{\partial(2\eta\dot{\varepsilon}_{zz})}{\partial z} = 2\eta \frac{\partial\dot{\varepsilon}_{zz}}{\partial z} + 2\frac{\partial\eta}{\partial z}\dot{\varepsilon}_{zz} \\ \frac{\partial\eta}{\partial x} &= -z(2xz + 1) \cos(x^2z^2 + xz + 5) \\ \frac{\partial\eta}{\partial z} &= -x(2xz + 1) \cos(x^2z^2 + xz + 5) \\ \frac{\partial\dot{\varepsilon}_{xx}}{\partial x} &= 6xz + 2 \\ \frac{\partial\dot{\varepsilon}_{zx}}{\partial z} &= -3xz - 1 \\ \frac{\partial\dot{\varepsilon}_{xz}}{\partial x} &= \frac{1}{2}(3x^2 + 1 - 3z^2) \\ \frac{\partial\dot{\varepsilon}_{zz}}{\partial z} &= -3x^2 - 1 \end{aligned}$$

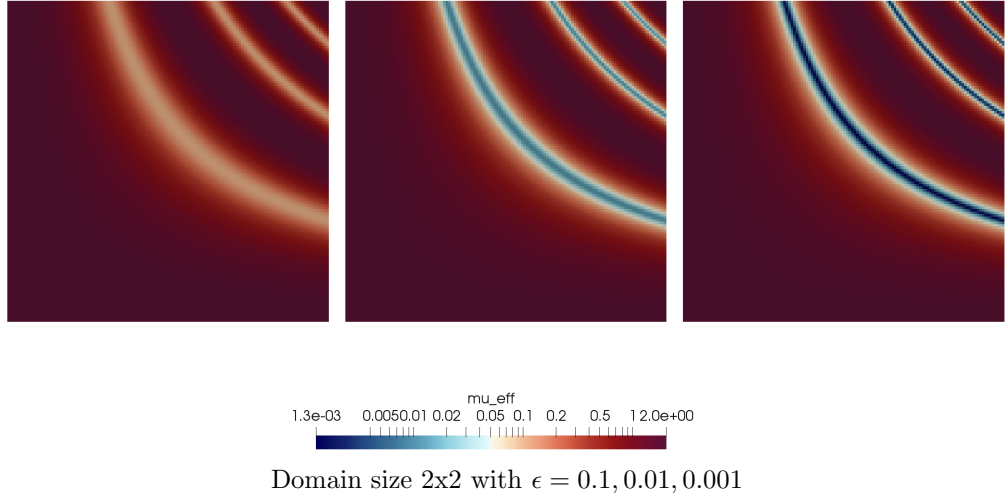
Velocity boundary conditions are prescribed on all four boundaries so that the pressure is known up to a constant (the pressure solution has a nullspace), and the p_0 constant can be determined by requiring that

$$\int_0^L \int_0^L p(x, y) dx dy = \int_0^L \int_0^L (x^2y^2 + xy + 5) dx dy + \int_0^L \int_0^L p_0 dx dy = \int_0^L \int_0^L (x^2y^2 + xy + 5) dx dy + p_0 L^2 = 0$$

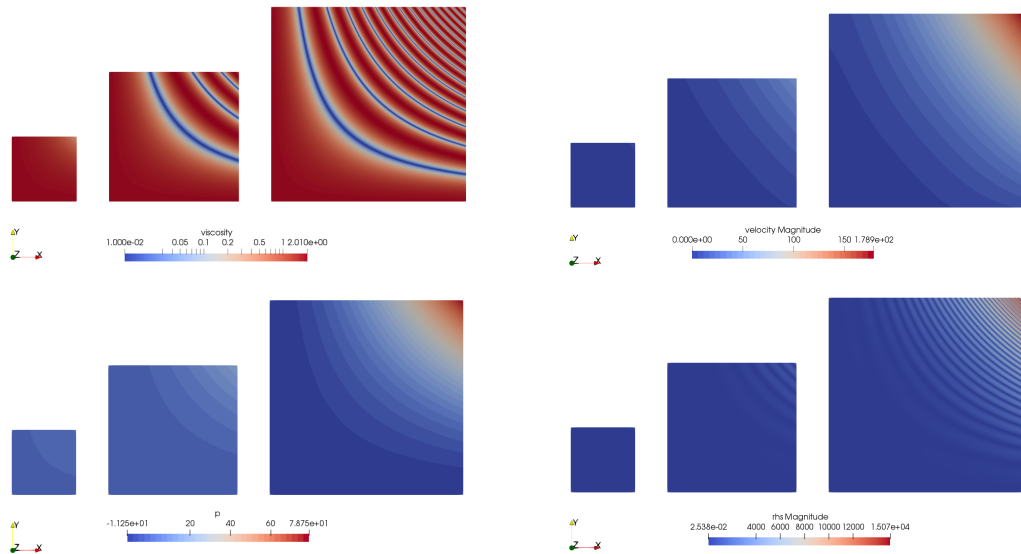
where L is the size of the square domain. Then

$$p_0 = -\frac{1}{L^2} \int_0^L \int_0^L (x^2y^2 + xy + 5) dx dy = -\frac{L^4}{9} - \frac{L^2}{4} - 5$$

As seen in the following figure, the value of ϵ controls the viscosity field amplitude. This is simply explained by the fact that when the sin term of the viscosity takes value 1, the viscosity is then equal to ϵ .



Another interesting aspect of this benchmark is the fact that increasing the domain size adds complexity to it as it increases the number of low viscosity zones and the spacing between them also decreases:



Three different domain sizes (1x1, 2x2, 3x3) with $\epsilon = 0.001$.

Finally, because the analytical expression for both components of the velocity is a polynomial, we can also compute the root mean square velocity exactly. For instance, for a 2x2 domain:

and we end up with (for $L = 2$)

$$v_{rms} = \sqrt{\frac{1}{L^2} \frac{861752}{1575}} = \sqrt{\frac{215438}{1575}} \simeq 11.6955560683$$

(BSc Thesis)

8.6.8 Analytical benchmark VIII - "Kovasznay"

This flow was published by L.I.G. Kovasznay in 1948 [1002]. This paper presents an exact two-dimensional solution of the Navier-Stokes equations with a periodicity in the vertical direction, gives an analytical solution to the steady-state Navier-Stokes equations that is similar which is a flow-field behind a periodic array of cylinders.

$$u(x, y) = 1 - \exp(\lambda x) \cos(2\pi y) \quad v(x, y) = \frac{\lambda}{2\pi} \exp(\lambda x) \sin(2\pi y) \quad \lambda = \frac{Re}{2} - \sqrt{\frac{Re^2}{4} + 4\pi^2}$$

Following step-55 of deal.II²⁷ we have to 'cheat' here since we are not solving the non-linear Navier-Stokes equations, but the linear Stokes system without convective term. Therefore, to recreate the exact same solution we move the convective term into the right-hand side.

The analytical solution is prescribed left and right, while free/no (?) slip is prescribed at top and bottom.

Solution as implemented in step-55:

```
const double pi2 = pi*pi;
u = -exp(x*(-sqrt(25.0 + 4*pi2) + 5.0))*cos(2*y*pi) + 1;
v = (1.0L/2.0L)*(-sqrt(25.0 + 4*pi2) + 5.0)*exp(x*(-sqrt(25.0 + 4*pi2) + 5.0))*sin(2*y*pi)/pi;
p = -1.0L/2.0L*exp(x*(-2*sqrt(25.0 + 4*pi2) + 10.0))
- 2.0*(-6538034.74494422 + 0.0134758939981709*exp(4*sqrt(25.0 + 4*pi2)))/(-80.0*exp(3*sqrt(25.0 + 4*pi2)))
+ 16.0*sqrt(25.0 + 4*pi2)*exp(3*sqrt(25.0 + 4*pi2)))
- 1634508.68623606*exp(-3.0*sqrt(25.0 + 4*pi2))/(-10.0 + 2.0*sqrt(25.0 + 4*pi2))
+ (-0.00673794699908547*exp(sqrt(25.0 + 4*pi2)))
+ 3269017.37247211*exp(-3*sqrt(25.0 + 4*pi2))/(-8*sqrt(25.0 + 4*pi2) + 40.0)
+ 0.00336897349954273*exp(1.0*sqrt(25.0 + 4*pi2))/(-10.0 + 2.0*sqrt(25.0 + 4*pi2));
```

8.6.9 Analytical benchmark IX - "VJ2"

It is presented in [917] and meant to be a peculiar case where the velocity solution is exactly zero. The viscosity is 1, the domain is a unit square, no-slip boundary conditions are prescribed everywhere. The buoyancy force is given by $\vec{b} = (0, Ra(1-y+3y^2))$ where $Ra > 0$ is a parameter. The flow is incompressible and the analytical pressure solution is given by $p = Ra(y^3 - y^2/2 + y - 7/12)$.

8.6.10 Analytical benchmark X - "VJ3"

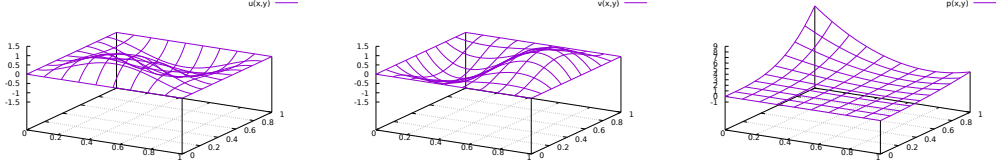
This benchmark comes from John et al. [917]. The domain is once again the unit square. The velocity field has the form of a large vortex.

²⁷https://www.dealii.org/current/doxygen/deal.II/step_55.html

$$u(x, y) = 200x^2(1-x)^2y(1-y)(1-2y) \quad (419)$$

$$v(x, y) = -200x(1-x)(1-2x)y^2(1-y)^2 \quad (420)$$

$$p(x, y) = 10 [(x-1/2)^3y^2 + (1-x)^3(y-1/2)^3] \quad (421)$$



$$\dot{\varepsilon}_{xx} = \frac{\partial u}{\partial x} = -400(1-x)x(2x-1)(y-1)y(2y-1) \quad (422)$$

$$\frac{\partial u}{\partial y} = 200(1-x)^2x^2(6y^2-6y+1) \quad (423)$$

$$\frac{\partial v}{\partial x} = -200(6x^2-6x+1)(1-y)^2y^2 \quad (424)$$

$$\dot{\varepsilon}_{yy} = \frac{\partial v}{\partial y} = 400(x-1)x(2x-1)(1-y)y(2y-1) \quad (425)$$

so that

$$\begin{aligned} \dot{\varepsilon}_{xy} &= \frac{1}{2} [200(1-x)^2x^2(6y^2-6y+1) - 200(6x^2-6x+1)(1-y)^2y^2] \\ &= 100(1-x)^2x^2(6y^2-6y+1) - 100(6x^2-6x+1)(1-y)^2y^2 \end{aligned} \quad (426)$$

Also

$$\begin{aligned} \frac{\partial \dot{\varepsilon}_{xx}}{\partial x} &= 400(6x^2-6x+1)y(2y^2-3y+1) \\ \frac{\partial \dot{\varepsilon}_{xy}}{\partial x} &= 200(-2x^2(1-x)(6y^2-6y+1) + 2x(1-x)^2(6y^2-6y+1) - 6(2x-1)(1-y)^2y^2) \\ &= 100(-2x^2(1-x)(6y^2-6y+1) + 2x(1-x)^2(6y^2-6y+1) - 6(2x-1)(1-y)^2y^2) \\ \frac{\partial \dot{\varepsilon}_{xy}}{\partial y} &= 400(6x^2-6x+1)(1-y)y^2 + 200(1-x)^2x^2(12y-6) - 400(6x^2-6x+1)(1-y)^2y \\ \frac{\partial \dot{\varepsilon}_{yy}}{\partial y} &= -400x(2x^2-3x+1)(6y^2-6y+1) \end{aligned} \quad (427)$$

$$\frac{\partial p}{\partial x} = 30(x-1/2)^2y^2 - 30(1-x)^2(y-1/2)^3 \quad (428)$$

$$\frac{\partial p}{\partial y} = 20(x-1/2)^3y + 30(1-x)^3(y-1/2)^2 \quad (429)$$

From $\vec{\nabla} \cdot \boldsymbol{\sigma} + \vec{b} = \vec{0}$ we can obtain the rhs as follows:

$$\begin{aligned} \vec{b} &= -\vec{\nabla} \cdot \boldsymbol{\sigma} \\ &= \vec{\nabla} p - \vec{\nabla} \cdot \boldsymbol{s} \\ &= \vec{\nabla} p - \vec{\nabla} \cdot (2\eta \dot{\varepsilon}) \end{aligned} \quad (430)$$

Assuming $\eta = 1$ we arrive at:

$$b_x = \frac{\partial p}{\partial x} - 2 \frac{\partial \dot{\varepsilon}_{xx}}{\partial x} - 2 \frac{\partial \dot{\varepsilon}_{xy}}{\partial y} \quad (431)$$

$$b_y = \frac{\partial p}{\partial y} - 2 \frac{\partial \dot{\varepsilon}_{xy}}{\partial x} - 2 \frac{\partial \dot{\varepsilon}_{yy}}{\partial y} \quad (432)$$

All the necessary functions to do this benchmark are in `mms/vj3.py`:

```

# functions for the Volker John III benchmark (vj3)

def u_th(x,y):
    return 200*x**2*(1-x)**2*y*(1-y)*(1-2*y)

def v_th(x,y):
    return -200*x*(1-x)*(1-2*x)*y**2*(1-y)**2

def p_th(x,y):
    return 10*( (x-1./2.)**3*y**2+(1-x)**3*(y-1./2.)**3 )

def dpdx_th(x,y):
    return 30*(x-1./2.)**2*y**2-30*(1-x)**2*(y-1./2.)**3

def dpdy_th(x,y):
    return 20*(x-1./2.)**3*y + 30*(1-x)**3*(y-1./2.)**2

def exx_th(x,y):
    return -400*(1-x)*x*(2*x-1)*(y-1)*y*(2*y-1)

def exy_th(x,y):
    return 100*(1-x)**2*x**2*(6*y**2-6*y+1)-100*(6*x**2-6*x+1)*(1-y)**2*y**2

def eyy_th(x,y):
    return 400*(x-1)*x*(2*x-1)*(1-y)*y*(2*y-1)

def dexxdx(x,y):
    return 400*(6*x**2-6*x+1)*y*(2*y**2-3*y+1)

def dexydx(x,y):
    return 100*(-2*x**2*(1-x)*(6*y**2-6*y+1) + 2*x*(1-x)**2*(6*y**2-6*y+1) - 6*(2*x-1)*(1-y)**2*y**2)

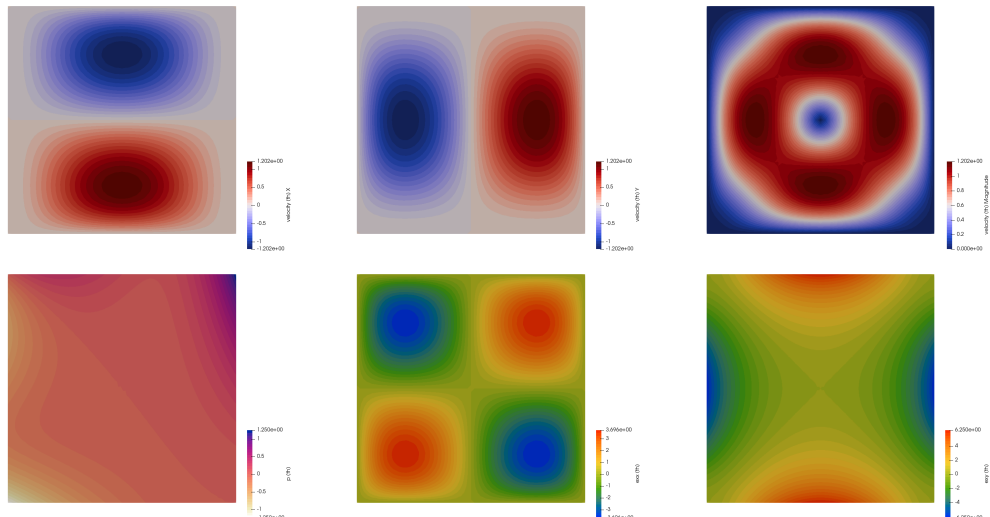
def dexydy(x,y):
    return 200*(6*x**2-6*x+1)*(1-y)*y**2 + 100*(1-x)**2*x**2*(12*y-6) - 200*(6*x**2-6*x+1)*(1-y)**2*y

def deyydy(x,y):
    return -400*x*(2*x**2-3*x+1)*(6*y**2-6*y+1)

def bx(x,y):
    return dpdx_th(x,y)-2*dexxdx(x,y)-2*dexydy(x,y)

def by(x,y):
    return dpdy_th(x,y)-2*dexydx(x,y)-2*deyydy(x,y)

```



8.6.11 Analytical benchmark XI - "PPC1"

8.6.12 Analytical benchmark XII - "PPC2"

8.6.13 Annulus with kinematical b.c.

The domain is a hollow cylinder or inner radius $R_i = 1$ and outside radius $R_o = 1$. Boundary conditions are prescribed both on the inside and the outside with $\vec{v} = (u, v) = (-y, x)$, or in polar coordinates $\vec{v} = r\vec{e}_\theta$.

The gravity is radial and is set to

$$g_x = -x/r \quad g_z = -y/r$$

where $r = \sqrt{x^2 + z^2}$, which in polar coordinates is $\vec{g} = -\vec{e}_r$. The viscosity is also set to 1, and the density is given by

$$\rho(r) = r^n$$

where n is a positive or null integer. The pressure is set to zero at the outer boundary.

The gradient operator in polar coordinates writes:

$$\vec{\nabla} = \frac{\partial}{\partial r}\vec{e}_r + \frac{1}{r}\frac{\partial}{\partial \theta}\vec{e}_\theta$$

and the Laplacian operator:

$$\Delta = \frac{\partial^2}{\partial r^2} + \frac{1}{r}\frac{\partial}{\partial r} + \frac{1}{r^2}\frac{\partial^2}{\partial \theta^2}$$

Note that in our case we need to take the Laplacian of a vector, and unfortunately the Laplacian of a vector is not the Laplacian of the vector's coordinates in polar coordinates (unlike cartesian coordinates). The Laplacian of a vector is given by²⁸

$$\nabla^2 \vec{A} = \nabla(\nabla \cdot \vec{A}) - \nabla \times (\nabla \times \vec{A}) = \begin{pmatrix} \frac{\partial^2 A_r}{\partial r^2} + \frac{1}{r}\frac{\partial A_r}{\partial r} - \frac{1}{r^2}A_r + \frac{1}{r^2}\frac{\partial^2 A_r}{\partial \theta^2} - \frac{2}{r^2}\frac{\partial A_\theta}{\partial \theta} \\ \frac{\partial^2 A_\theta}{\partial r^2} + \frac{1}{r}\frac{\partial A_\theta}{\partial r} - \frac{1}{r^2}A_\theta + \frac{1}{r^2}\frac{\partial^2 A_\theta}{\partial \theta^2} + \frac{2}{r^2}\frac{\partial A_r}{\partial \theta} \end{pmatrix} = \begin{pmatrix} \Delta A_r \\ \Delta A_\theta \end{pmatrix}$$

The Stokes equation writes:

$$\mu \Delta \vec{v} + \rho \vec{g} = \vec{0}$$

The velocity solution is expected to be $\vec{v} = r\vec{e}_\theta$. The Stokes equation in polar coordinates then writes:

$$\begin{aligned} -\frac{\partial p}{\partial r} + \Delta v_r + \rho(r)(-1) &= 0 \\ -\frac{1}{r}\frac{\partial p}{\partial \theta} + \Delta v_\theta &= 0 \end{aligned}$$

Since $\Delta v_\theta = 0$, then $\frac{\partial p}{\partial \theta} = 0$ and then the pressure is independent of θ , which is what we expect since the density distribution is radial. We then focus on the first equation, and since $v_r = 0$, we then obtain:

$$\frac{\partial p}{\partial r} = -\rho(r)$$

- If $\rho(r) = 1$, then

$$\frac{\partial p}{\partial r} = -1$$

yields $p(r) = -r + C$ where C is a constant determined by means of b.c. ($p(r=1) = 0$) so finally

$$p(r) = 1 - r$$

²⁸https://en.wikipedia.org/wiki/Vector_Laplacian

- If $\rho(r) = r$, then

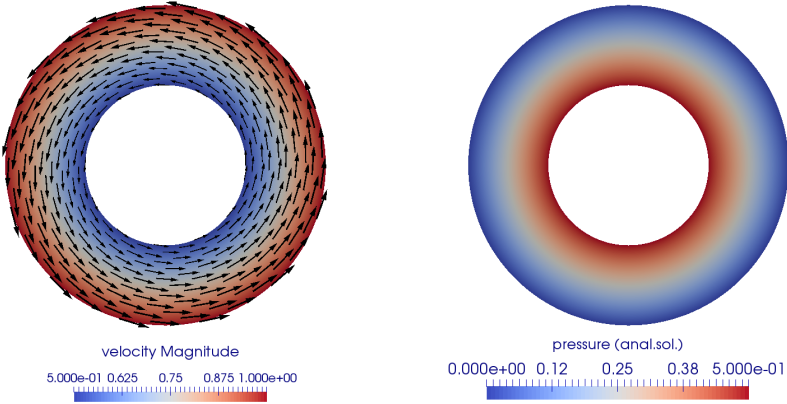
$$\frac{\partial p}{\partial r} = -r$$

so that $p(r) = -\frac{1}{2}r^2 + C$ and likewise

$$p(r) = \frac{1}{2}(1 - r^2)$$

In general, by taking $\rho(r) = r^n$ with $n = 0, 1, \dots$ one arrives to a pressure field given by

$$p(r) = \frac{1}{n+1}(1 - r^{n+1})$$



This benchmark is of course very simple and the fact that the solution is independent of θ renders it not so useful. It has successfully been implemented in ELEFANT.

8.7 Geodynamical benchmarks

Some published numerical experiments have over time become benchmarks for other codes, while some others showcased comparisons between codes. Here is a short list of 'famous' benchmarks' in the computational geodynamics community.

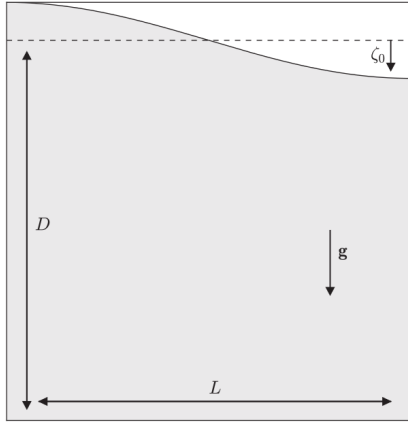
- the plastic brick [1037, 944, 1341, 1184, 1234, 1113, 1473, 697, 587]
- 2D Rayleigh-Benard convection (Blankenbach) [158, 1567, 336, 968, 1053, 1651, 1564, 136, 356]
- 2D Rayleigh-Benard convection with nonlinear rheology [1558, 75]
- 2D Rayleigh-Taylor convection/instability [1323, 1564, 1679, 1317, 1463, 57, 1513, 181] [84, 1341, 1423, 392, 1053, 1097, 1651, 1613, 181, 339, 466, 1184, 1113] [606, 454, 439, 452, 75]
- Thin layer entrainment (see Section 8.7.12)
- 3D Rayleigh-Taylor instability [620, 1649]
- subduction problems [1436, 1611, 319]
- numerical sandbox [237, 1113, 245, 697]
- the Stokes sphere [1017, 75], in visco-plastic fluid [446]
- the sinking block (sinker) [1538, 319, 656, 674, 1152, 1184, 622, 1113] (see Section 8.7.7)
- multiple sinkers [1154, 1151]
- 1D compression [1207]
- 2D compressible Stokes flow problem [886, 1519, 1051, 965, 1092]
- 3D convection at infinite Prandtl number (Busse) [288, 1567, 1279, 1009]
- Free surface evolution [409, 75]
- Love's problem [102]
- Poiseuille flow [569, 610, 1517]
- Couette flow with temperature dependent viscosity [508, 452]
- Couette flow with shear heating [508]
- Poiseuille-Couette flow [606]
- Lid driven Cavity [573, 682, 176, 953, 228]
- Lid driven cavity with analytical solution (see Section 8.7.10)
- Wannier flow [1663, 1729, 319]
- bending of elastic plate/beam [319, 168, 1649, 508, 452, 1207]
- flexure of finite length elastic plate [339]
- thermal diffusion of half-cooling space (see Section 8.7.14)
- thermal diffusion of Gaussian distribution (see compgeo notes, elefant manual)
- stress build-up in Maxwell visco-elastic material [655, 339, 508, 452]
- plastic oedometer test [339]
- SolCx [1152, 452, 75]

- SolKz [1152, 452, 75]
- SolVi, inclusion [948, 1113, 466, 136, 1649, 452, 75]
- channel flow (nonlinear) [1113, 587, 656, 508] ((**BSc Thesis**))
- indentor, punch problem (see Section 8.7.9) See also [854, 578, 644] for application.
- relaxation of sinusoidal topography [409, 1406]
- single layer visco-elastic folding [1649]
- Three-dimensional folding of an embedded viscous layer in pure shear [564]
- dam-break problem [1192, 71, 1079, 1034, 835, 27, 746, 830, 84]
- hot blob problem [282, 622] (see Section 8.7.8)
- viscous(-elastic) flow around a cylinder in a channel (see Section ??)
- Infinite plate with a circular hole [1346]
- Slope stability for elasto-plastic materials [1346]
- Time-dependent flow in an annulus [634] (see Section 8.7.5)
- Convection in 2D-box [634] (see Section 8.7.6)
- Onset of convection [75]
- Polydiapirism [1679, 75]
- Slab detachment benchmark (see Section 8.7.16)
- Hollow sphere benchmark [1540]
- Annulus benchmark [75]
- Viscosity grooves benchmark [75]
- Latent heat benchmark [75]
- Layered flow with viscosity contrast [75]
- Brittle thrust wedges benchmark [245, 75]
- 2D linear viscous subduction [1436, 697]
- mantle convection in 3D spherical shell [1356, 1765, 1731, 337, 1761, 928, 47, 1091]
- Benchmark of 3D numerical models of subduction against a laboratory experiment [1173]
- 3D subduction [1288]
- heat flow around a cylinder (see Section 8.7.13)
- Laplace equation on a semi infinite plate (see Section 8.7.15)

go through my papers and add relevant ones here

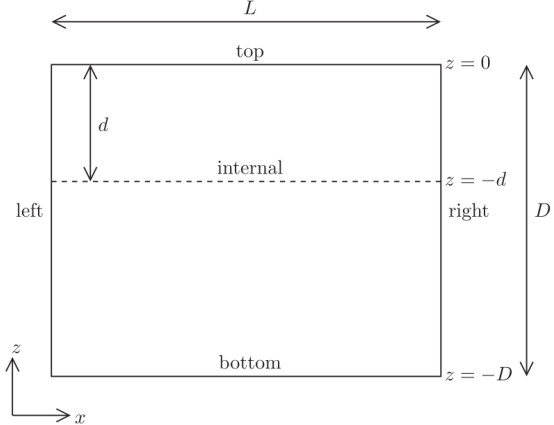
8.7.1 Relaxation of sinusoidal topography

Following Kramer et al. [1006, Section 3.1.1] and [1406] the benchmark consists of the relaxation of surface topography in a two-dimensional Cartesian box with an isoviscous fluid. Free slip boundary conditions are imposed on the sides and bottom of the domain. The setup is as follows:



Taken from [1406]. Setup for the free surface relaxation benchmark.

For the tests $\rho = \eta = g = L = D = 1$ and $\xi_0 = 0.005$.



Taken from [1006]. $D = 3 \cdot 10^6, \eta = 10^{21}, \rho = 4500, g = 10,$

$\xi_0 = 10^3 \text{m}$, and $L = D/4, D/2, D, 2D, 4D$.

and the infinitesimal sinusoidal perturbations to the free surface is given by

$$\xi(x, t = 0) = \xi_0 \cos\left(\frac{2\pi n x}{L}\right)$$

where n is a wavenumber which is an integer multiple of $1/2$ (taken to be $1/2$ exactly in both cases).

8.7.2 the plastic brick

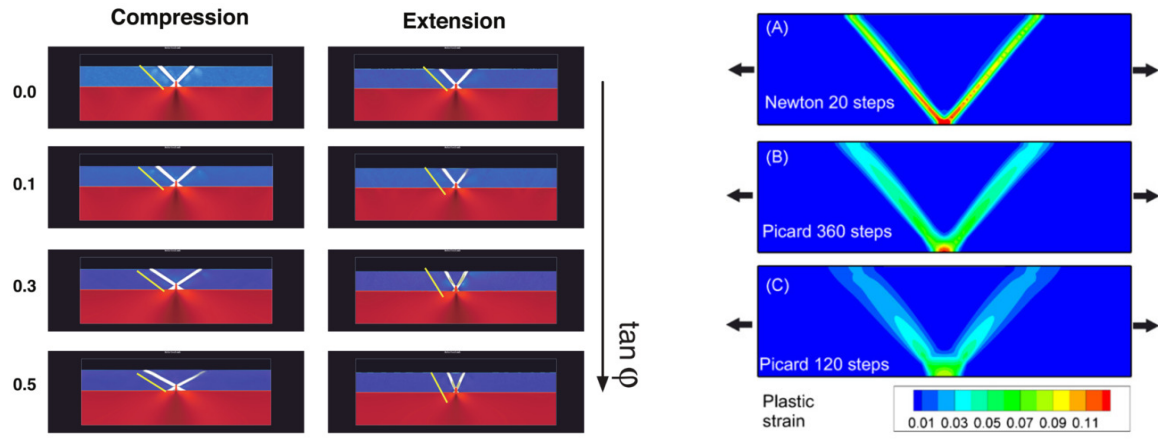


Literature[788, 1211, 1037, 944, 508, 1341, 1184, 1113, 1473, 697, 587, 75]

Pretty much all of the brick-type (elasto-)visco-plastic experiments in the literature introduce a weak seed at the bottom of the domain to seed deformation (the shear bands will ultimately stem from it). Dimensioned and dimensionless experiments have been carried out, with or without elastic behaviour, with or without adaptive mesh refinement, with first order and second order quadrilateral elements or Taylor-Hood triangles, with or without Newton algorithm, in extension and compression, with or without time-stepping, with or without viscous lower layer.

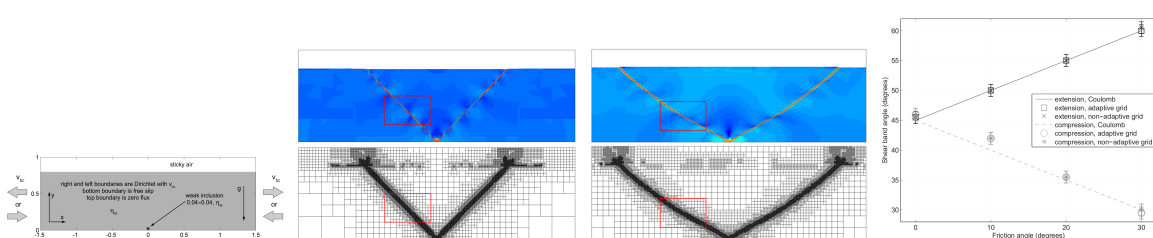
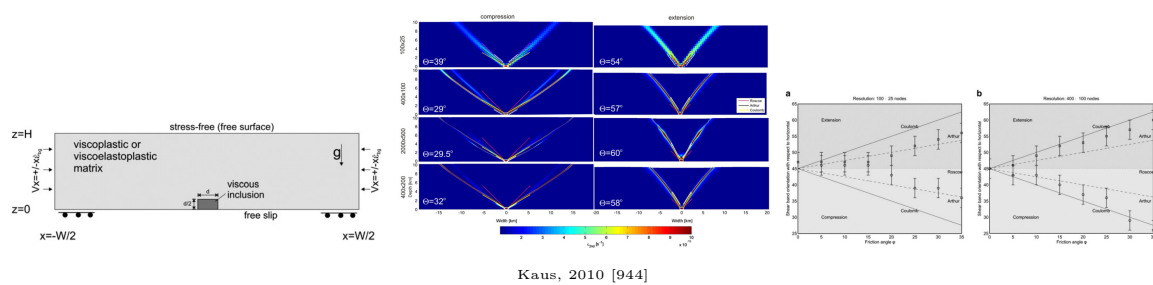
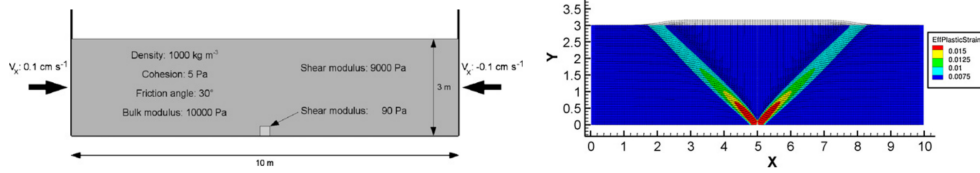
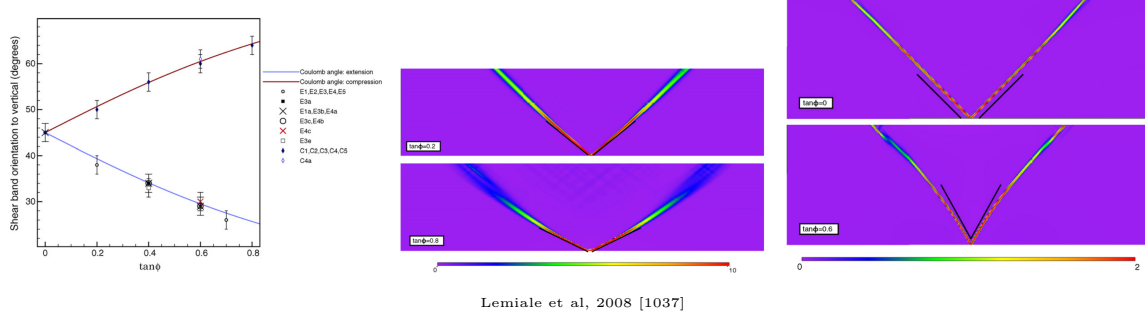


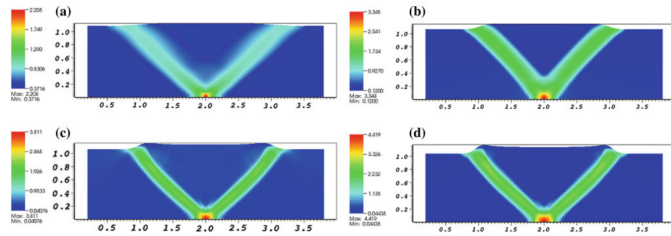
Moresi & Mühlhaus, 2006 [1210]



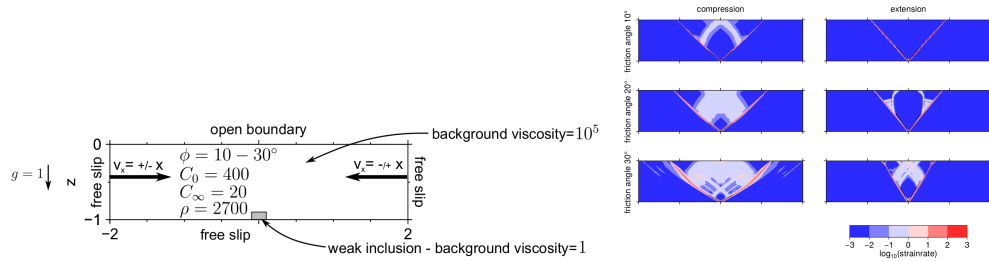
Moresi et al, 2007 [1211]

Popov et al, 2008 [1320]

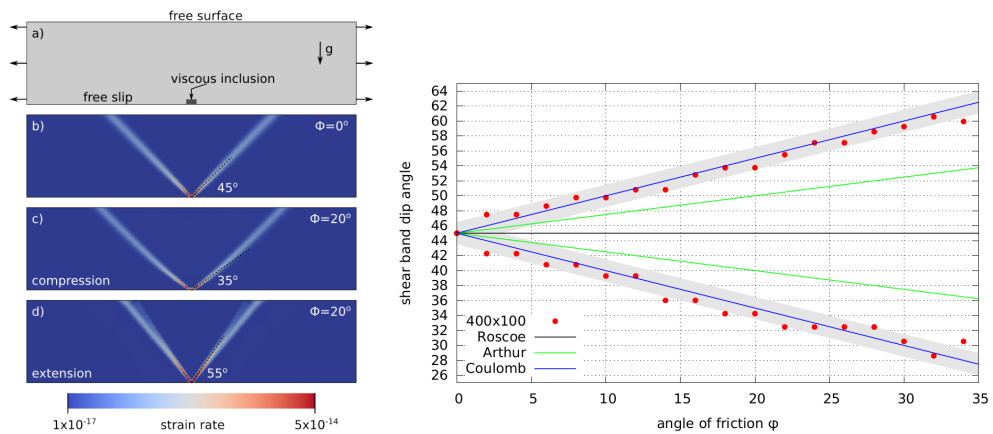




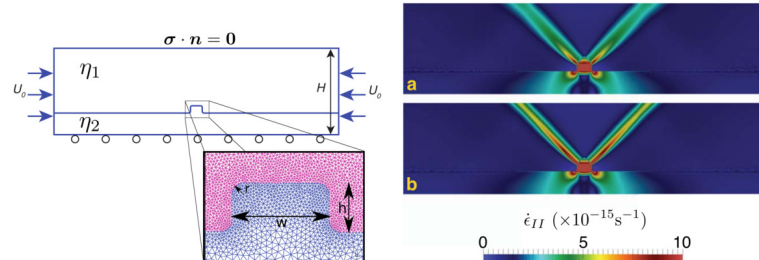
Mühlhaus et al, 2011 [1234].



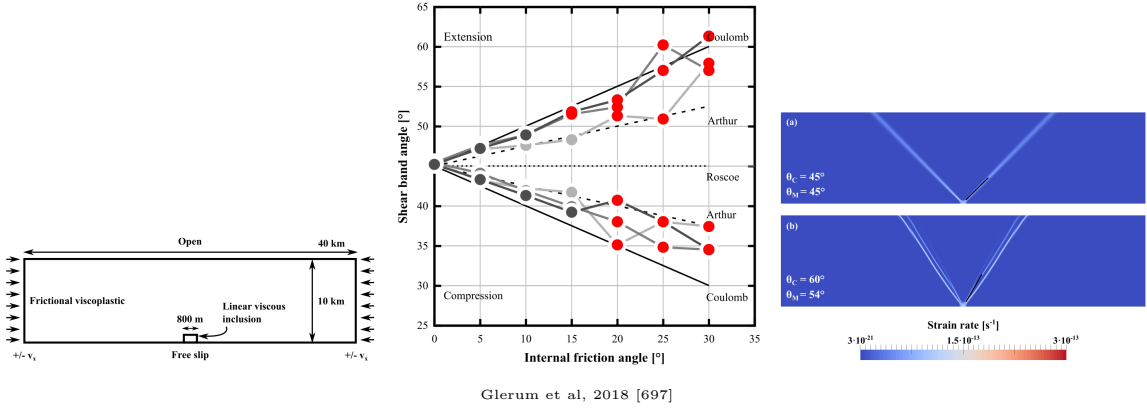
Maierova, phd thesis, 2012 [1113]



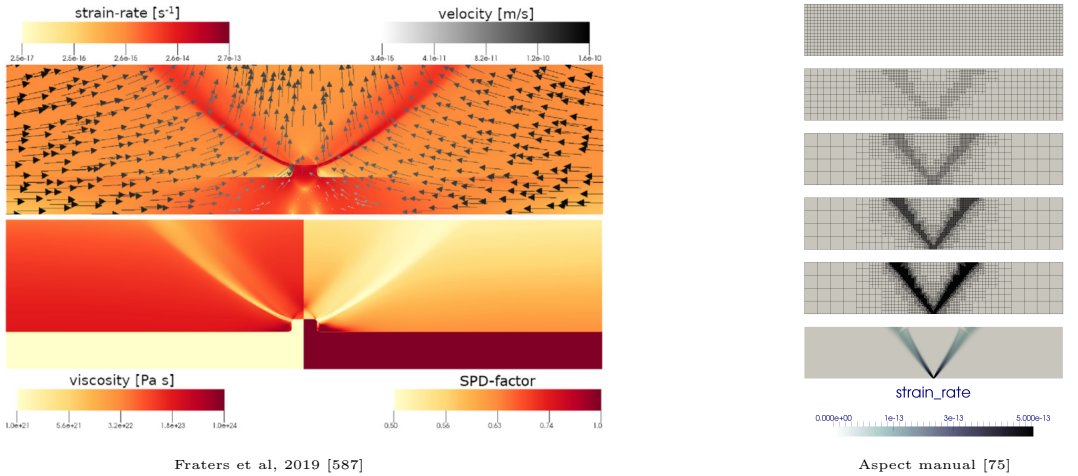
Thieulot, 2014 [1539]



Spiegelman et al, 2016 [1473]



Glerum et al, 2018 [697]



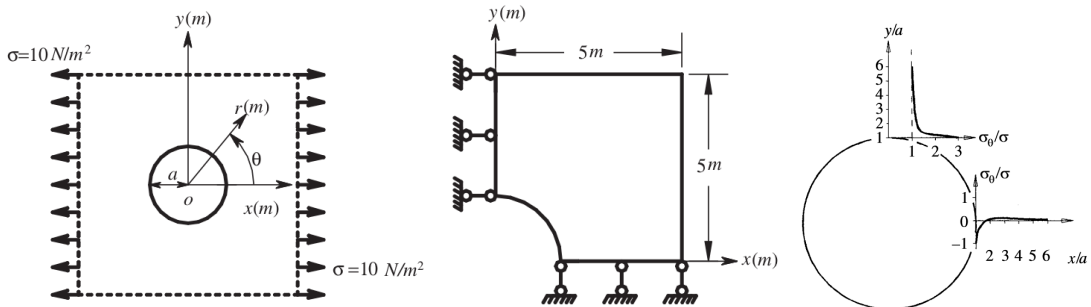
Fraters et al, 2019 [587]

Aspect manual [75]

8.7.3 Infinite plate with a circular hole [1346]

(MSc Thesis)

An infinite plate with a circular hole of radius a is subjected to a unidirectional tensile load of σ in the x direction as shown in the figure. In this case, only one quarter of the domain is analysed due to symmetry along x and y axis.



Left: An infinite plate with a circular hole subjected to unidirectional tension and its quarter model with symmetric conditions imposed on the left and bottom edges. Right: Tangential stress distribution for $\theta = 0$ and $\theta = \pi/2$. [1735]

The inner boundary of the hole is traction free and the right edge was imposed with the tractions based on the analytical solutions. The left edge is constrained in the x direction and the bottom edge is constrained in the y direction, respectively. The plane stress condition is considered and the parameters are: Young modulus $E = 3e7 \text{ MPa}$, Poisson Ratio $\nu = 0.3$, Load $\sigma = 10 \text{ N/m}^2$, $a = 1\text{m}$.

The analytical stress components for this problem are

$$\sigma_{xx}(x, y) = \sigma \left(1 - \frac{a^2}{r^2} \left(\frac{3}{2} \cos 2\theta + \cos 4\theta \right) + \frac{3a^4}{2r^4} \cos 4\theta \right) \quad (433)$$

$$\sigma_{yy}(x, y) = -\sigma \left(\frac{a^2}{r^2} \left(\frac{1}{2} \cos 2\theta - \cos 4\theta \right) - \frac{3a^4}{2r^4} \cos 4\theta \right) \quad (434)$$

$$\sigma_{xy}(x, y) = -\sigma \left(\frac{a^2}{r^2} \left(\frac{1}{2} \sin 2\theta + \sin 4\theta \right) + \frac{3a^4}{2r^4} \sin 4\theta \right) \quad (435)$$

Note that [1346] cites [325] which cites the book [1735, p772] which cites [234] for the solution!

there are discrepancies between [1346] and [325]

Following [1735], it can be shown, from linear elasticity, that the tangential stress throughout the plate is given by

$$\sigma_\theta = \frac{\sigma}{2} \left[1 + \frac{a^2}{r^2} - \left(1 + 3 \frac{a^4}{r^4} \right) \cos 2\theta \right]$$

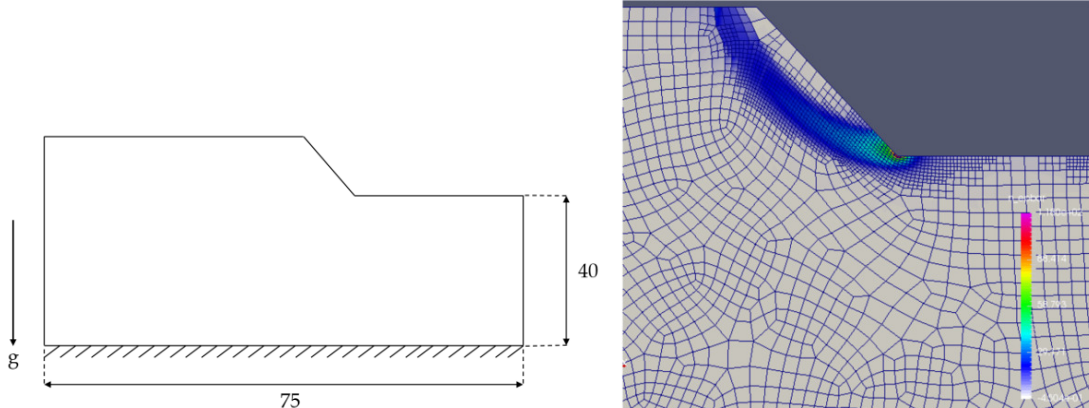
The maximum stress is $\sigma_\theta = 3\sigma$ at $r = a$ and $\theta = \pm\pi/2$. Along the surface of the hole, the tangential stress is $-\sigma$ at $y = 0$ and $\theta = \pi$, and increases, as θ increases, to 3σ at $\theta = \pi/2$ and $\theta = 3\pi/2$.

8.7.4 Slope stability for elasto-plastic materials a la [1346]

(MSc Thesis)

The bottom of the domain is constrained and the model is subjected to gravitational load. The material properties considered are

Young modulus 20e3 MPa, Poisson Ratio 0.49, Constitutive law Mohr-Coulomb (friction angle $\phi = 20^\circ$, dilatancy angle $\phi = 20^\circ$, cohesion $c=50$ Mpa).



Left: Slope stability problem setup; Right: Adaptive Refinement based on Plasticity Indicator

8.7.5 Time-dependent benchmark in an annulus

This benchmark is presented in Gassmöller et al [634]. The domain is a 2D annulus with inner and outer radii $R_1 = 1$ and $R_2 = 2$, respectively. In this situation, the incompressible isothermal Stokes equations and their solution can be expressed in a cylindrical coordinate system in terms of the radius r and the azimuthal angle θ . The viscosity is set to $\eta = 1$, and the density is given by

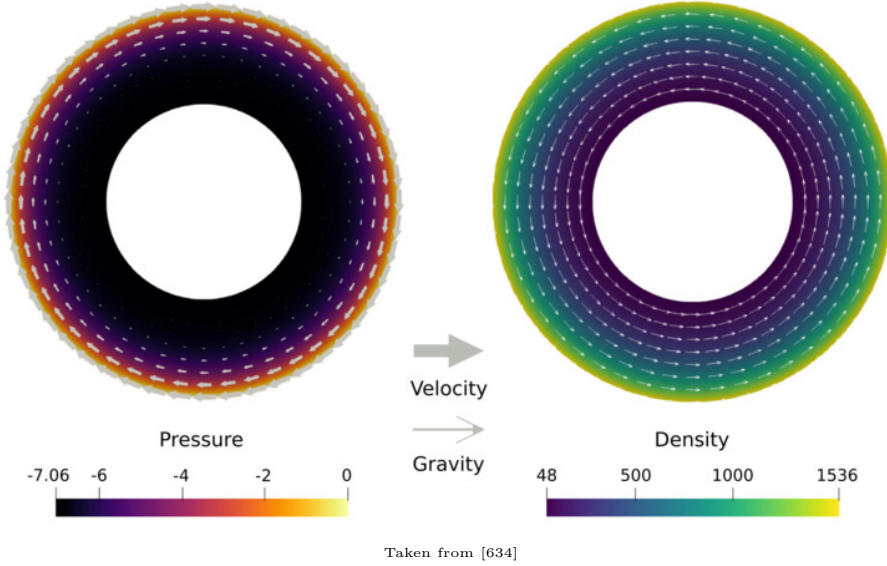
$$\rho(r, \theta) = 48r^5 \quad (436)$$

The gravity vector is set to

$$\vec{g}(r, \theta) = \frac{r^3}{384} \vec{e}_r + \vec{e}_\theta \quad (437)$$

Note that this gravity vector is not the gradient of a gravity potential and consequently not physical. The Stokes system can then be solved using a separation of variables approach and yields

$$\vec{v} = -r^7 \vec{e}_\theta \quad p(r, \theta) = \frac{r^9}{72} - \frac{512}{72} \quad (438)$$



Rather importantly, this benchmark was arrived at by means of a stream function (see Section 8.34) $\psi(r, \theta) = F(r)G(\theta)$ with $F(r) = r^8/8$ and $G(\theta) = 1$.

8.7.6 Convection in 2D-box

We start from the following stream function (see Section 8.34):

$$\psi(x, y) = \frac{1}{\pi} \sin \pi x \sin \pi y \quad (439)$$

which yields:

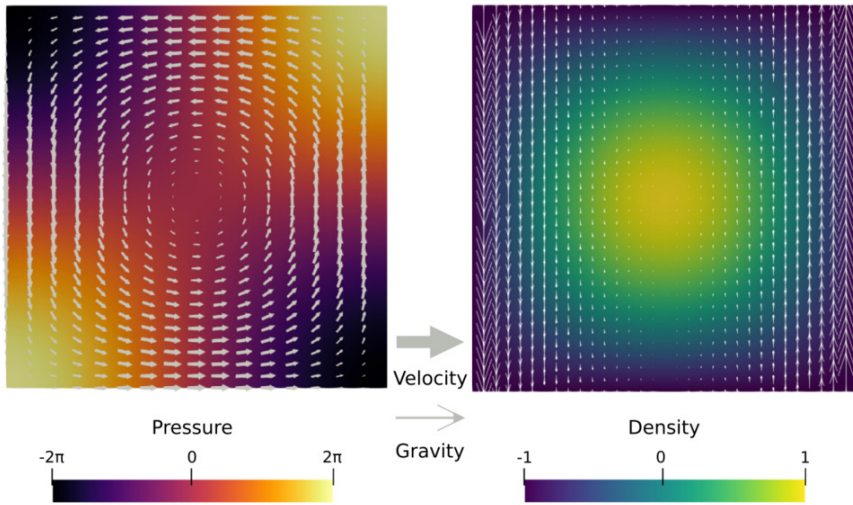
$$\begin{aligned} u(x, y) &= \frac{\partial \psi}{\partial y} = \sin \pi x \cos \pi y \\ v(x, y) &= -\frac{\partial \psi}{\partial x} = -\cos \pi x \sin \pi y \end{aligned} \quad (440)$$

The pressure field is

$$p(x, y) = 2\pi \cos(\pi x) \cos(\pi y) \quad (441)$$

with

$$\rho(x, y) = \sin(\pi x) \sin(\pi y) \quad g_y = -4\pi^2 \frac{\cos(\pi x)}{\sin(\pi x)} \quad (442)$$



Taken from [634]

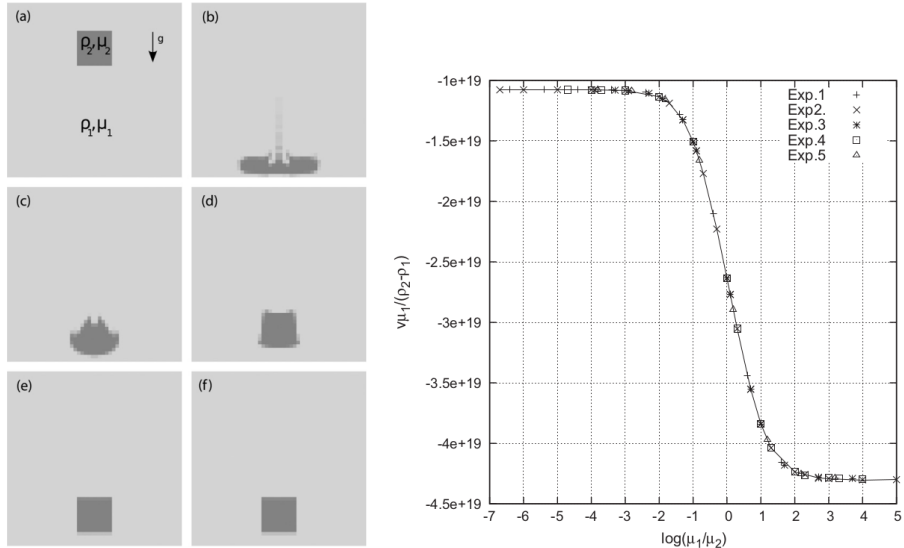
$$\begin{aligned}
v_{rms} &= \sqrt{\frac{1}{L_x L_y} \int_0^1 \int_0^1 (u^2 + v^2) dx dy} \\
&= \sqrt{\int_0^1 \int_0^1 (\sin^2(\pi x) \cos^2(\pi y) + \cos^2(\pi x) \sin^2(\pi y)) dx dy} \\
&= \sqrt{\int_0^1 \sin^2(\pi x) dx \cdot \int_0^1 \cos^2(\pi y) dy + \int_0^1 \cos^2(\pi x) dx \cdot \int \sin^2(\pi y) dy} \\
&= \sqrt{\frac{1}{2} \frac{1}{2} + \frac{1}{2} \frac{1}{2}} \\
&= \frac{\sqrt{2}}{2} \\
&\simeq 0.70711...
\end{aligned} \tag{443}$$

8.7.7 The sinker problem

This experiment is not a benchmark stricto sensu since there is no analytical solution. However, it is widely used in the technical literature because of its simple setup and since it allows to test solving strategies. Also, it can conveniently be carried out in both two and three dimensions.

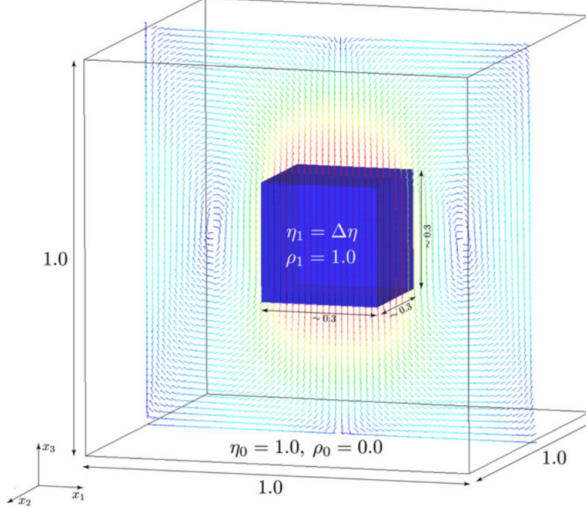
In two dimensions The time dependent version of the experiment is for instance to be found in Gerya [656] and the same is repeated in Thieulot [1538].

This simple benchmark provides challenging numerical experiments dealing with large viscosity variations within the simulation domain. It consists of a bulk of fluid 1 (η_1, ρ_1) in which a block of fluid 2 (η_2, ρ_2) falls under its own weight. The domain is a square of size $L_x = L_y = 500$ km and the block is initially centred at point ($x = 250$ km, $y = 400$ km) with size 100×100 km. Free slip boundary conditions are imposed on all sides of the domain. In [1538] five experiments have been conducted: $\eta_1 = 10^{20}$ Pa.s, $\rho_2 = 3220$ kg/m³; $\eta_1 = 10^{21}$ Pa.s, $\rho_2 = 3300$ kg/m³; $\eta_1 = 10^{22}$ Pa.s, $\rho_2 = 6600$ kg/m³; $\eta_1 = 10^{23}$ Pa.s, $\rho_2 = 3300$ kg/m³; $\eta_1 = 10^{24}$ Pa.s, $\rho_2 = 9900$ kg/m³, while in all experiments the density of the surrounding fluid is $\rho_1 = 3200$ kg/m³ and the viscosity of the block is varied between 10^{19} and $5 \cdot 10^{27}$ Pa.s.



Left: $\eta_1 = 10^{21}$ Pa.s, $\rho_2 = 3300$ kg/m³. (a) Initial setup; (b) $\eta_1 = 10^{21}$ Pa.s at time $t = 10$ Myrs; (c) $\eta_1 = 10^{22}$ Pa.s at time $t = 20$ Myrs; (d) $\eta_1 = 10^{23}$ Pa.s at time $t = 20$ Myrs; (e) $\eta_1 = 10^{25}$ Pa.s at time $t = 20$ Myrs; (f) $\eta_1 = 10^{27}$ Pa.s at time $t = 20$ Myrs. Right: Velocity measurements as a function of the viscosity contrast between surrounding medium and block for all experiments. Taken from [1538]

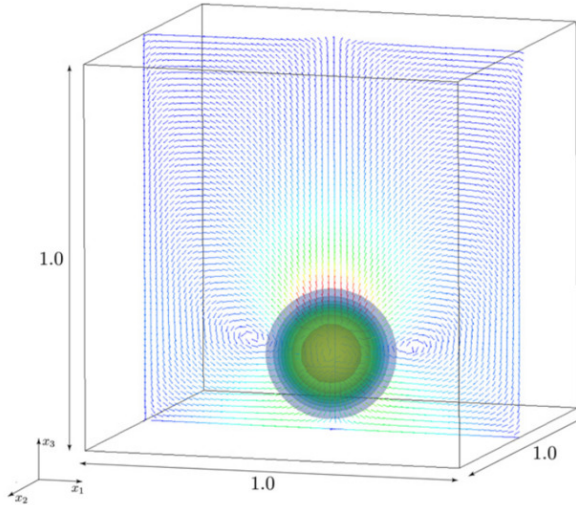
In three dimensions Let us look at the sinker experiment from Furuichi et al [622]: The domain is the unit box the origin at the center of the box. A cube with a viscosity $\eta_1 = \Delta\eta$ and density $\rho_1 = 1$ was placed at the middle of the domain defined by $-0.15 \leq x, y, z \leq 0.15$. The material surrounding the cube has the properties $\eta_0 = 1$ and $\rho_0 = 0$. The body force of the momentum equation was taken as $(0, 0, -\rho g)$ with $g = 1$. Along all walls on the domain, free-slip boundary conditions were employed.



Simulation setup for the 3D falling block (SINKER) problem. The vectors represent computed flow. Taken from [622]

8.7.8 The hot blob problem

This is a very similar setup as the 3D sinker from the same authors with higher but more diffusive variation of viscosity. The body force is given by $(0, 0, \beta T)$ and where the temperature field T is defined by $T = \exp(-\gamma(x^2 + y^2 + (z - 0.3)^2))$ with the constant parameters $\beta = 10^6$ and $\gamma = 200$. The temperature-dependent viscosity $\eta = \exp(-\alpha T)$ is employed with the parameter for viscosity contrast α .

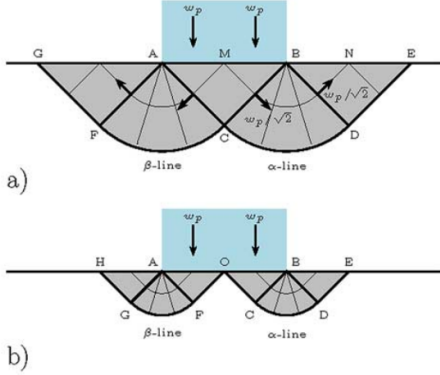


Simulation setting of BLOB problem. Isosurface and vectors represent temperature field and computed flow respectively. Taken from [622]

8.7.9 The punch/indentor problem in 2D

The punch benchmark is one of the few boundary value problems involving plastic solids for which there exists an exact solution. Such solutions are usually either for highly simplified geometries (spherical or axial symmetry, for instance) or simplified material models (such as rigid plastic solids) [924].

In this experiment, a rigid punch indents a rigid plastic half space; the slip line field theory gives exact solutions as shown hereunder:

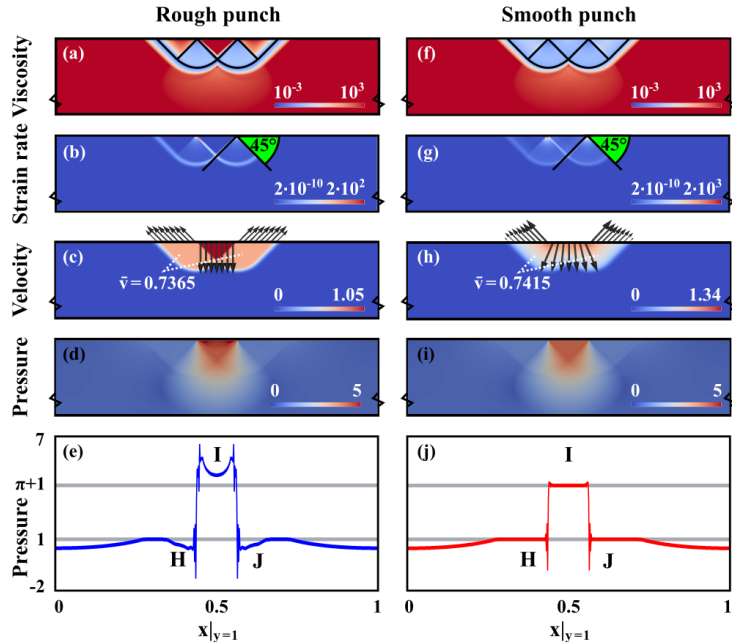


Two-dimensional rigid punch indenting a rigid plastic half space. (a) Prandtl's rigid plastic solution; (b) Hills solution. Taken from [1543]

The plane strain formulation of the equations and the detailed solution to the problem were derived in the Appendix of [1543] and are also presented in [649]. The two dimensional punch problem has been extensively studied numerically for the past 40 years [1783, 1782, 355, 354, 864, 1736, 236, 1343, 697] and has been used to draw a parallel with the tectonics of eastern China in the context of the India-Eurasia collision [1524, 1196, 515]. It is also worth noting that it has been carried out in one form or another in series of analogue modelling articles concerning the same region, with a rigid indenter colliding with a rheologically stratified lithosphere [1296, 445, 919].

Numerically, the one-time step punch experiment is performed on a two-dimensional domain of purely plastic von Mises material. Given that the von Mises rheology yield criterion does not depend on pressure, the density of the material and/or the gravity vector is set to zero. Sides are set to free slip boundary conditions, the bottom to no slip, while a vertical velocity $(0, -v_p)$ is prescribed at the top boundary for nodes whose x coordinate is within $[L_x/2 - \delta/2, L_x/2 + \delta/2]$.

The analytical solution predicts that the angle of the shear bands stemming from the sides of the punch is $\pi/4$, that the pressure right under the punch is $1 + \pi$, and that the velocity of the rigid blocks on each side of the punch is $v_p/\sqrt{2}$ (this is simply explained by invoking conservation of mass).



The punch benchmark results after 500 nonlinear iterations for a rough punch (left column) and a smooth punch (right column). (a,f) Viscosity field with analytical slip lines. (b,g) Strain rate norm $\dot{\epsilon}_e$ with measured shear band angles. (c,h) Velocity magnitude with velocity vectors along the surface of the domain. (d,i) Pressure field. (e,j) Pressure along the surface of the domain (colored line) and analytical solution values $\pi + 1$ and 1 (grey lines).

Taken from [697]

8.7.10 Lid driven cavity with analytical solution

This comes from [513](section 3.1.4). The velocity is prescribed to be

$$\vec{v} = (2y(1-x^2); -2x(1-y^2))$$

with a domain given by $\Omega = [-1 : 1] \times [-1 : 1]$. The strainrate tensor is then given by:

$$\dot{\epsilon} = \begin{pmatrix} -4xy & -x^2 + y^2 \\ -x^2 + y^2 & 4xy \end{pmatrix}$$

The Stokes equation is then:

$$-\frac{\partial p}{\partial x} + 2\mu(-4y + 2y) = \rho g_x \quad (444)$$

$$-\frac{\partial p}{\partial y} + 2\mu(-2x + 4x) = \rho g_y \quad (445)$$

where we assume the viscosity $\mu = 1$ to be constant in space. Assuming $g_x = 0$, the first equation is

$$\frac{\partial p}{\partial x} = -4y$$

i.e.

$$p(x, y) = -4yx + f(y)$$

Inserting this in the second equation:

$$4x - f'(y) + 4x = \rho g_y$$

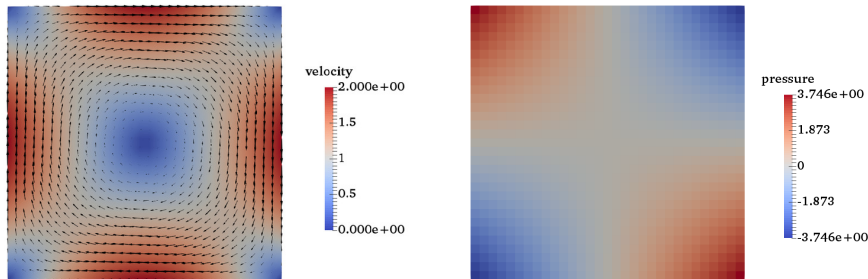
or,

$$-f'(y) + 8x = \rho g_y$$

Assuming $g_y = -1$, we get $\rho = -8x$ and then $f'(y) = 0$ so $f(y) = C$ where C is a constant. Finally the pressure is given by:

$$p(x, y) = -4yx + C$$

We add the following requirement: $\int_{\Omega} p(x, y) d\Omega = 0$ so that $C = 0$.



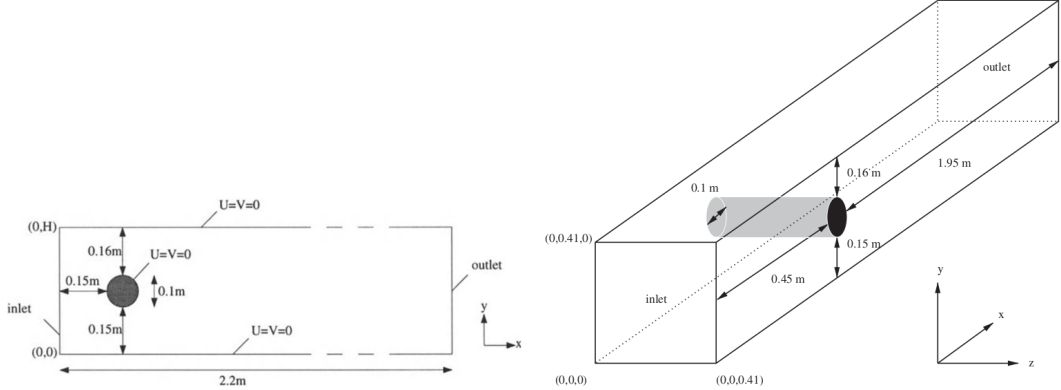
$$\begin{aligned}
 v_{rms}^2 &= \frac{1}{\Omega} \int_{\Omega} (u^2 + v^2) d\Omega \\
 &= \frac{1}{4} \int_{-1}^{+1} \int_{-1}^{+1} (u^2 + v^2) dx dy \\
 &= \frac{1}{4} \int_{-1}^{+1} \int_{-1}^{+1} [4y^2(1-x^2)^2 + 4x^2(1-y^2)^2] dx dy \\
 &=
 \end{aligned} \tag{446}$$

finish v_{rms} calculation of benchmark

8.7.11 Flow around a cylinder

??

There are many variants of this problem: 2D [1576], 3D [916]. Many studies focus on Navier-Stokes flow since the cylinder generates vortices at high Reynolds numbers. Steady state solutions at low Re are shown here²⁹. Note the interesting benchmark for 2D visco-elastic flow in [136].

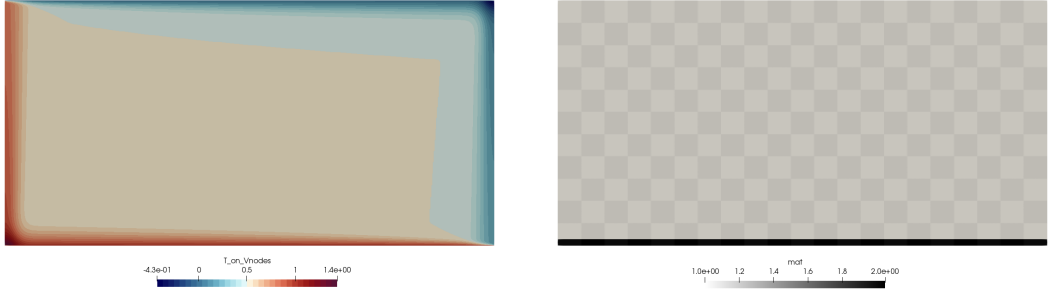


Left: taken from [1576]; Right: taken from [916]

8.7.12 Thin layer entrainment

This problem is a simulation to study the amount of entrainment by thermal convection of a dense, thin layer at the bottom of the model [1613]. To the author's knowledge only two other publications [1513, 1619] have presented results pertaining to this benchmark. The results shown here after are obtained with my ELEFANT code using the particle-in-cell technique.

The box is 2×1 , and contains two fluids:



Fluid 1 has a density $\rho_1 = 1$ and a viscosity $\eta = 1$. Fluid 2 is heavier ($\rho_2 = \rho_1 + \Delta\rho$) but has the same viscosity. Both fluids have a thermal expansion coefficient $\alpha = 10^{-10}$, a thermal conductivity $k = 1$, and a heat capacity coefficient $c_p = 1$. Fluid 2 is placed at the bottom of the box ($0 \leq y \leq 0.025$).

This experiment is parameterised by the thermal Rayleigh number $Ra = 300,000$ and the compositional Rayleigh number $Ra_c = 450,000$ which are defined as follows:

$$Ra_T = \frac{\alpha \rho g \Delta T L_y^3}{\kappa \eta} = \frac{\alpha \rho^2 g \Delta T L_y^3 c_p}{k \eta} = \alpha g \quad (447)$$

$$Ra_c = \frac{\Delta \rho g L_y^3}{\kappa \eta} = \frac{\rho \Delta \rho g L_y^3 c_p}{k \eta} = \Delta \rho g \quad (448)$$

where I have used the relationship $\kappa = k/\rho c_p$. B is defined as $B = Ra_T/Ra_c$ so The gravity acceleration is therefore set to $g = Ra/\alpha$ and this yields $\Delta \rho = Ra_c/g = BRa_T/g = B \times \alpha$.

²⁹upofthetestanddatameasurement

Free-slip boundary conditions are imposed on all sides of the domain. Temperature boundary conditions are $T(x, y = 0) = 1$ and $T(x, y = 1) = 0$. The analytical initial temperature field is given by

$$T(x, y) = T_u(x, y) + T_l(x, y) + T_r(x, y) + T_s(x, y) - \frac{3}{2} \quad (449)$$

where

$$\begin{aligned} T_u(x, y) &= \frac{1}{2} \operatorname{erf} \left(\frac{1-y}{2} \sqrt{\frac{u_0}{x}} \right) \\ T_l(x, y) &= 1 - \frac{1}{2} \operatorname{erf} \left(\frac{y}{2} \sqrt{\frac{u_0}{L_x - x}} \right) \\ T_r(x, y) &= \frac{1}{2} + \frac{Q}{2\sqrt{\pi}} \sqrt{\frac{u_0}{y+1}} \exp \left(-\frac{x^2 u_0}{4y+4} \right) \\ T_s(x, y) &= \frac{1}{2} - \frac{Q}{2\sqrt{\pi}} \sqrt{\frac{u_0}{2-y}} \exp \left(-\frac{(L_x-x)^2 u_0}{8-4y} \right) \end{aligned} \quad (450)$$

with

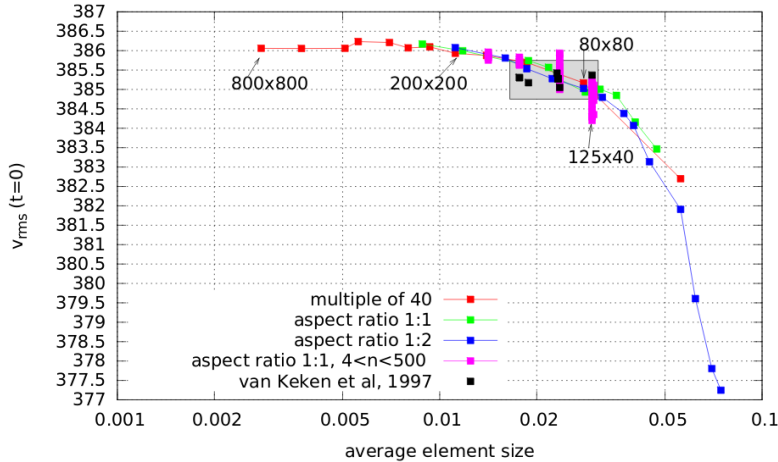
$$u_0 = \frac{L_x^{7/3}}{(1+L_x^4)^{2/3}} \left(\frac{Ra}{2\sqrt{\pi}} \right)^{2/3} \quad Q = 2\sqrt{\frac{L_x}{\pi u_0}} \quad (451)$$

Using $L_x = 2$, $Ra = 3 \times 10^5$, one gets $u_0 \simeq 1469.315$ and $Q \simeq 0.0416305$.

Given the small thickness of the bottom layer, it seems quite legitimate to investigate the influence of grid resolution on the simulation. I have therefore looked at the initial root mean square velocity measurement as a function of the element diagonal value (a proxy for the average resolution in the case where elements are not square).

Results are confirm that the element size plays a non negligible role at startup on the dynamics of the system. Superimposed on the figure are the measurements provided by Prof. van Keken (black squares in the gray box). They agree well with my measurements but also indicate that none of the authors in the original study ran the experiment at a high-enough resolution to start with (their results were therefore most likely resolution dependent).

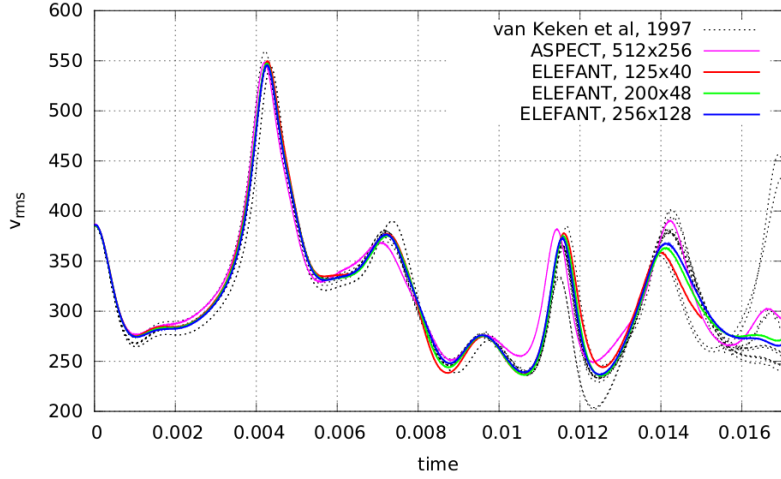
We see that the number of markers per element at startup is critical at (very) low resolution but that it does not lead to significant velocity variations at high resolution.



Thin layer entrainment experiment: root mean square velocity measurements at $t = 0$ as a function of the element diagonal size. The red square points correspond to resolutions where the number of elements in each direction is a multiple of 40 (i.e. L_y/d), so that no element would contain a mix of fluids 1 and 2. Pink points correspond to cases where the number of markers within each element was varied between 4 and 500 (random spatial distribution). Taken from [1539]

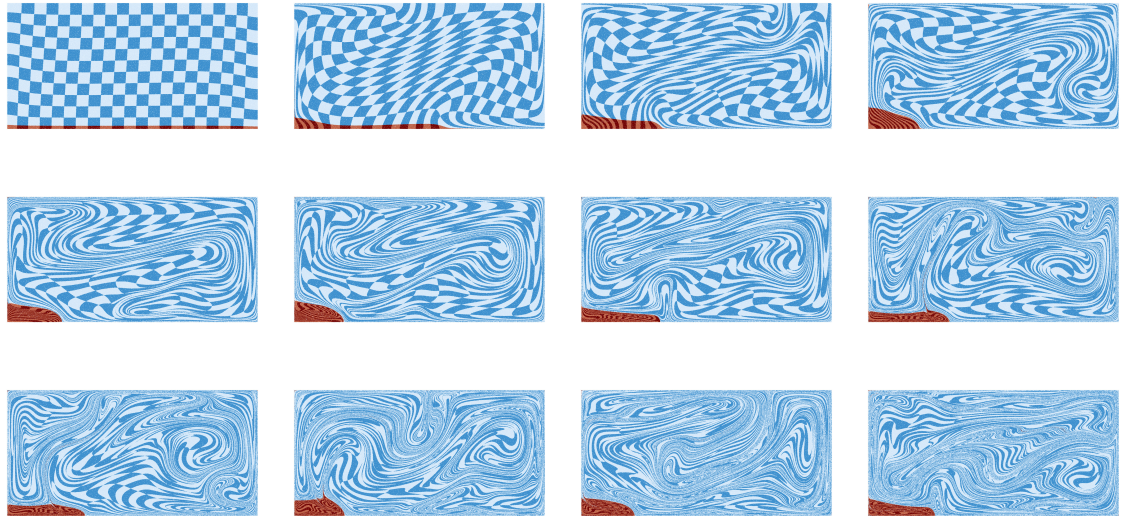
Looking at the root mean square velocity measurements, we see that the measurements done with ELEFANT agree nicely with those presented in [1613]. Past $t \sim 0.015$, the curves diverge clearly across all codes and authors, so I only need to focus the comparison for times $t < 0.015$. For the three tested

resolutions, measurements agree well and fall within the grey curves representing all results of van Keken et al. Additional tests have been carried out concerning the value of the Courant number (0.1 to 0.25) and the initial number of markers per element (100 or 200) and these parameters led to extremely similar results.



Thin layer entrainment experiment. Root mean square velocity as a function of time. All results presented in van Keken et al.(1997) are collapsed in dashed lines. All simulations were run with an initial marker density of 100 markers per element and with a Courant number of 0.25. Taken from [1539].

As observed in van Keken et al., the dense layer is first swept into the lower left corner. Thermal instabilities then further develop in an asymmetrical way and entrain the dense material. Past $t \simeq 0.015$ the system becomes more and more chaotic with markers being randomly mixed in the system in a non-orderly fashion.



marker distribution as obtained with ELEFANT for grid 240x120, init_marker_density=7, random distribution, CFL=0.25, rkmethod=2, m_to_q=2. Unpublished.

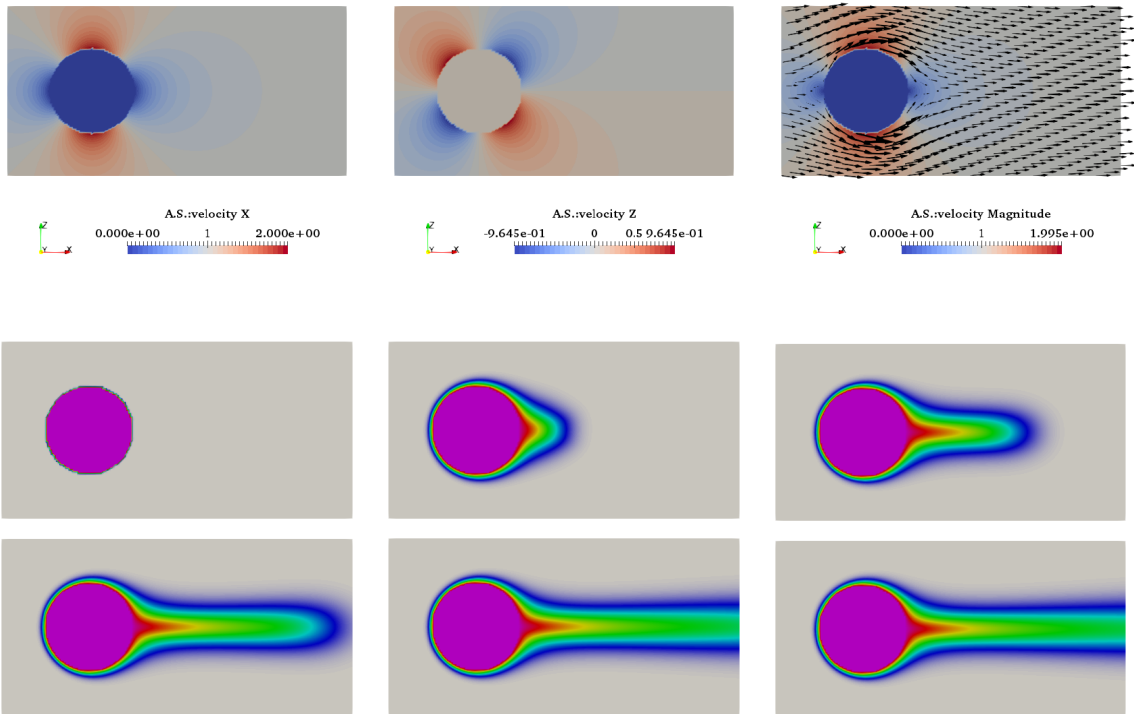
8.7.13 Heat flow around a cylinder

The domain is a 2D Cartesian box of size 8x4. The Stokes equations are not solved and the following velocity is prescribed:

$$u(x, y) = U_\infty \left(1 - \frac{x^2 - y^2}{(x^2 + y^2)^2} \right) \quad (452)$$

$$v(x, y) = -2U_\infty \frac{xy}{(x^2 + y^2)^2} \quad (453)$$

Boundary conditions are as follows: $T = 0$ is imposed at the top and bottom of the domain. $T = 1$ is imposed inside a disc centered at (2,2) with radius 1. Further: $k = 0.01$, $c_p = 1$, $\rho = 1$, CFL number is 0.1.



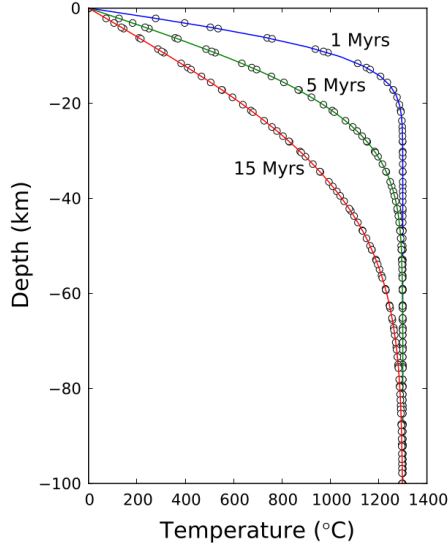
Time evolution of the temperature field. Results obtained with ELEFANT (unpublished)

8.7.14 Thermal diffusion of half-cooling space

This is a simple 1D experiment which solution is (for instance) available in Turcotte & Schubert [1575] and is also presented in [339].

The domain is 100km deep. $T_0 = 0^\circ\text{C}$ is prescribed at the surface and $T_m = 1300^\circ\text{C}$ is prescribed at the bottom. The initial temperature is $T(y) = 1300^\circ\text{C}$. The material is characterised by $\rho = 1000\text{kg/m}^3$, $C_p = 1000\text{J/kg/K}$, $k = 1\text{J/m/K}$. The time-dependent solution is given by:

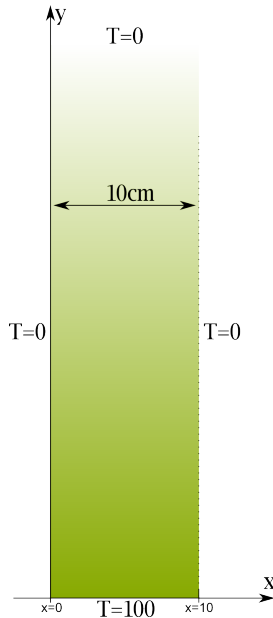
$$T(y, t) = T_0 + (T_0 - T_m) \operatorname{erf} \left(\frac{y}{2\sqrt{kt/\rho C_p}} \right) \quad (454)$$



Thermal diffusion of half space cooling plate. The temperature profiles in the analytical solution at 1, 5, and 15 Myrs are plotted in solid lines. The results from DynEarthSol2D are plotted in circles. Taken from [339]

8.7.15 Laplace equation on a semi infinite plate

) This experiment is based on a 2nd year mathematics lecture I give at Utrecht University. One wishes to solve the Laplace equation for temperature on the following plate subject to the indicated boundary conditions:



The temperature satisfies the 2D Laplace equation inside the plate:

$$\frac{\partial^2 T}{\partial x^2} + \frac{\partial^2 T}{\partial y^2} = 0 \quad (455)$$

We could try to solve the equation by using a tentative solution of the form:

$$T(x, y) = \theta(x)\Phi(y) \quad (456)$$

We do not *know* the solution is of this form.

We substitute (2) into (1) and obtain:

$$\Phi \frac{\partial^2 \theta}{\partial x^2} + \theta \frac{\partial^2 \Phi}{\partial y^2} = 0$$

Dividing by $\theta\Phi$ gives:

$$\frac{1}{\theta} \frac{\partial^2 \theta}{\partial x^2} + \frac{1}{\Phi} \frac{\partial^2 \Phi}{\partial y^2} = 0$$

Separation of variables: we say that each term is a constant because the first term is a function of x only and the second a function of y only. We then write

$$\frac{1}{\theta} \frac{\partial^2 \theta}{\partial x^2} = - \frac{1}{\Phi} \frac{\partial^2 \Phi}{\partial y^2} = -k^2$$

where k is called the separation constant. This leads to

$$\begin{aligned} \frac{\partial^2 \theta}{\partial x^2} + k^2 \theta &= 0 \\ \frac{\partial^2 \Phi}{\partial y^2} - k^2 \Phi &= 0 \end{aligned}$$

- The solution to the first one is $\theta(x) = \sin kx$ or $\theta(x) = \cos kx$
- The solution to the second one is $\Phi(y) = e^{ky}$ or $\Phi(y) = e^{-ky}$

The general solution writes:

$$T(x, y) = \theta(x)\Phi(y) = \left\{ \begin{array}{l} \sin kx \\ \cos kx \end{array} \right\} \left\{ \begin{array}{l} e^{ky} \\ e^{-ky} \end{array} \right\}$$

We can now use the b.c. to find the solution to the Laplace equation.

- Since $T \rightarrow 0$ when $y \rightarrow \infty$ then e^{ky} unacceptable.
- Since $T = 0$ when $x = 0$ then $\cos kx$ unacceptable.

so

$$T(x, y) = \sin(kx) e^{-ky}$$

We finally use $T = 0$ at $x = 10$ which leads to $10k = n\pi$, i.e.:

$$T(x, y) = \sin\left(\frac{n\pi x}{10}\right) e^{-n\pi y/10}$$

 Problem: the solution does not satisfy $T(x, 0) = 100$. However, a linear combination of solutions is still a solution ! Let's find such a combination which satisfies the b.c. at $y = 0$:

$$T(x, y) = \sum_{n=1}^{\infty} b_n \sin\left(\frac{n\pi x}{10}\right) e^{-n\pi y/10}$$

We impose then $T(x, 0) = 100$:

$$100 = \sum_{n=1}^{\infty} b_n \sin\left(\frac{n\pi x}{10}\right)$$

This is the Fourier sine series of $f(x) = 100$ with $l = 10$ (chapter 7.9 of Boas).

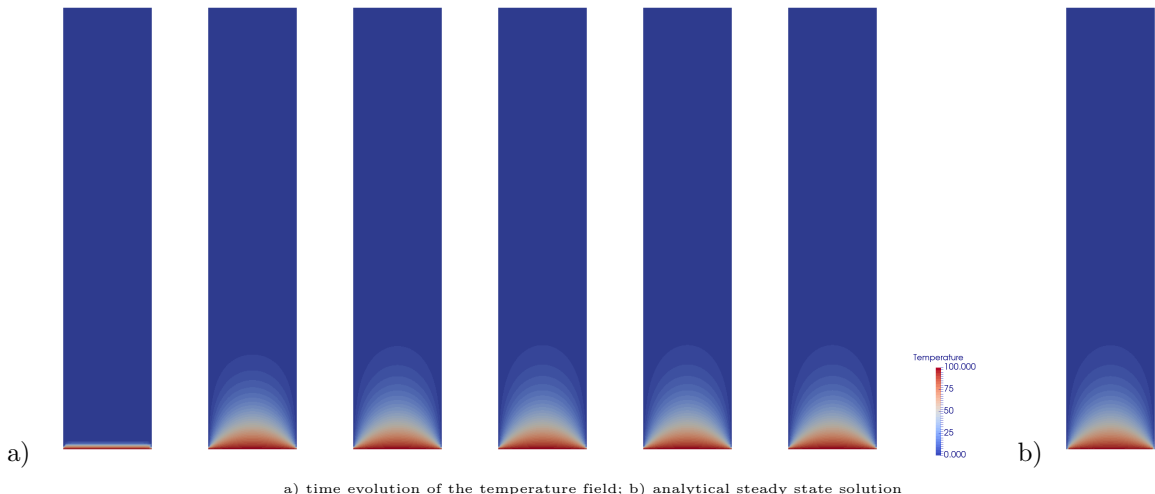
The coefficient b_n is then given by

$$b_n = \frac{2}{l} \int_0^l f(x) \sin \frac{n\pi x}{l} dx = \frac{2}{10} \int_0^{10} 100 \sin \frac{n\pi x}{10} dx = \begin{cases} 400/n\pi & \text{odd } n \\ 0 & \text{even } n \end{cases}$$

Finally (!):

$$T(x, y) = \frac{400}{\pi} \left(e^{-\pi y/10} \sin\left(\frac{\pi x}{10}\right) + \frac{1}{3} \sin\left(\frac{3\pi x}{10}\right) e^{-3\pi y/10} + \dots \right)$$

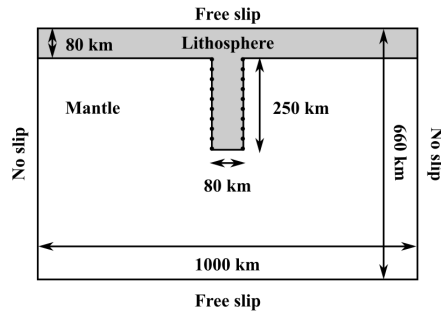
The simulation has been run with a 10x50 domain. All coefficients of the temperature equation are set to 1, and the Stokes equation is not solved. The timestep is fixed to $dt = 0.1$. Resolution is 32x160.



a) time evolution of the temperature field; b) analytical steady state solution

8.7.16 Slab detachment benchmark

[1432, 75, 697]



The detachment benchmark model setup of Schmalholz [1432]: a symmetric system of nonlinear viscous lithosphere with a vertical slab extending into a linear viscous mantle. The top and bottom boundaries are free slip, while the vertical boundaries are no slip. Taken from [697].

8.8 Assigning values to quadrature points

As we have seen in Section 6, the building of the elemental matrix and rhs requires (at least) to assign a density and viscosity value to each quadrature point inside the element. Depending on the type of modelling, this task can prove more complex than one might expect and have large consequences on the solution accuracy.

Here are several options:

- The simplest way (which is often used for benchmarks) consists in computing the 'real' coordinates (x_q, y_q, z_q) of a given quadrature point based on its reduced coordinates (r_q, s_q, t_q) , and passing these coordinates to a function which returns density and/or viscosity at this location. For instance, for the Stokes sphere:

```
def rho(x,y):
    if (x-.5)**2+(y-0.5)**2<0.123**2:
        val=2.
    else:
        val=1.
    return val

def mu(x,y):
    if (x-.5)**2+(y-0.5)**2<0.123**2:
        val=1.e2
    else:
        val=1.
    return val
```

This is very simple, but it has been shown to potentially be problematic. In essence, it can introduce very large contrasts inside a single element and perturb the quadrature. Please read section 3.3 of [809] and/or have a look at the section titled "Averaging material properties" in the ASPECT manual.

- another similar approach consists in assigning a density and viscosity value to the nodes of the FE mesh first, and then using these nodal values to assign values to the quadrature points. Very often ,and quite logically, the shape functions are used to this effect. Indeed we have seen before that for any point (r, s, t) inside an element we have

$$f_h(r, s, t) = \sum_i^m f_i N_i(r, s, t)$$

where the f_i are the nodal values and the N_i the corresponding basis functions.

In the case of linear elements (Q_1 basis functions), this is straightforward. In fact, the basis functions N_i can be seen as moving weights: the closer the point is to a node, the higher the weight (basis function value).

However, this is quite another story for quadratic elements (Q_2 basis functions). In order to illustrate the problem, let us consider a 1D problem. The basis functions are

$$N_1(r) = \frac{1}{2}r(r-1) \quad N_2(r) = 1 - r^2 \quad N_3(r) = \frac{1}{2}r(r+1)$$

Let us further assign: $\rho_1 = \rho_2 = 0$ and $\rho_3 = 1$. Then

$$\rho_h(r) = \sum_i^m \rho_i N_i(r) = N_3(r)$$

There lies the core of the problem: the $N_3(r)$ basis function is negative for $r \in [-1, 0]$. This means that the quadrature point in this interval will be assigned a negative density, which is nonsensical and numerically problematic!

use 2X Q1. write about it !

The above methods work fine as long as the domain contains a single material. As soon as there are multiple fluids in the domain a special technique is needed to track either the fluids themselves or their interfaces. Let us start with markers. We are then confronted to the infernal trio (a *menage à trois*?) which is present for each element, composed of its nodes, its markers and its quadrature points.

Each marker carries the material information (density and viscosity). This information must ultimately be projected onto the quadrature points. Two main options are possible: an algorithm is designed and projects the marker-based fields onto the quadrature points directly or the marker fields are first projected onto the FE nodes and then onto the quadrature points using the techniques above.

At a given time, every element e contains n^e markers. During the FE matrix building process, viscosity and density values are needed at the quadrature points. One therefore needs to project the values carried by the markers at these locations. Several approaches are currently in use in the community and the topic has been investigated by [466] and [490] for instance.

ELEFANT adopts a simple approach: viscosity and density are considered to be elemental values, i.e. all the markers within a given element contribute to assign a unique constant density and viscosity value to the element by means of an averaging scheme.

While it is common in the literature to treat the so-called arithmetic, geometric and harmonic means as separate averagings, I hereby wish to introduce the notion of generalised mean, which is a family of functions for aggregating sets of numbers that include as special cases the arithmetic, geometric and harmonic means.

If p is a non-zero real number, we can define the generalised mean (or power mean) with exponent p of the positive real numbers a_1, \dots, a_n as:

$$M_p(a_1, \dots, a_n) = \left(\frac{1}{n} \sum_{i=1}^n a_i^p \right)^{1/p} \quad (457)$$

and it is trivial to verify that we then have the special cases:

$$M_{-\infty} = \lim_{p \rightarrow -\infty} M_p = \min(a_1, \dots, a_n) \quad (\text{minimum}) \quad (458)$$

$$M_{-1} = \frac{n}{\frac{1}{a_1} + \frac{1}{a_2} + \dots + \frac{1}{a_n}} \quad (\text{harm. avrg.}) \quad (459)$$

$$M_0 = \lim_{p \rightarrow 0} M_p = \left(\prod_{i=1}^n a_i \right)^{1/n} \quad (\text{geom. avrg.}) \quad (460)$$

$$M_{+1} = \frac{1}{n} \sum_{i=1}^n a_i \quad (\text{arithm. avrg.}) \quad (461)$$

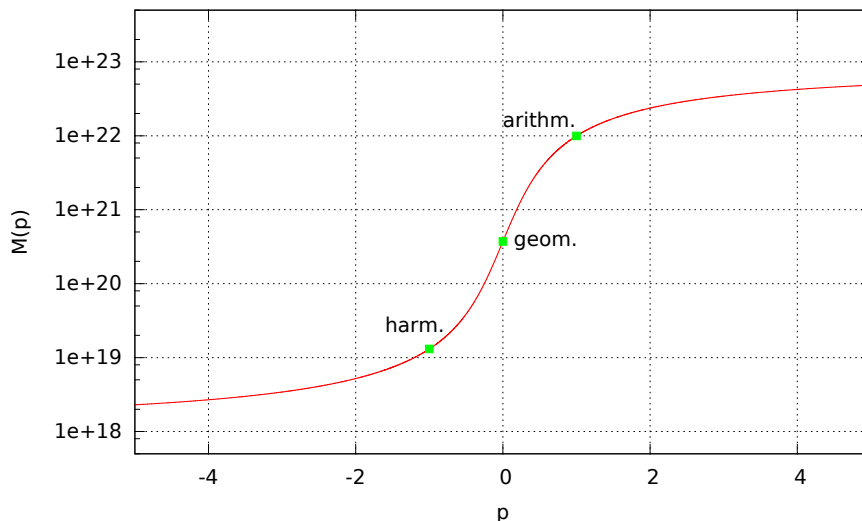
$$M_{+2} = \sqrt{\frac{1}{n} \sum_{i=1}^n a_i^2} \quad (\text{root mean square}) \quad (462)$$

$$M_{+\infty} = \lim_{p \rightarrow +\infty} M_p = \max(a_1, \dots, a_n) \quad (\text{maximum}) \quad (463)$$

Note that the proofs of the limit convergence are given in [250].

An interesting property of the generalised mean is as follows: for two real values p and q , if $p < q$ then $M_p \leq M_q$. This property has for instance been illustrated in Fig. 20 of [1436].

One can then for instance look at the generalised mean of a randomly generated set of 1000 viscosity values within $10^{18} Pa.s$ and $10^{23} Pa.s$ for $-5 \leq p \leq 5$. Results are shown in the figure hereunder and the arithmetic, geometric and harmonic values are indicated too. The function M_p assumes an arctangent-like shape: very low values of p will ultimately yield the minimum viscosity in the array while very high values will yield its maximum. In between, the transition is smooth and occurs essentially for $|p| \leq 5$.



```
▷ python_codes/fieldstone_markers_avrg
```

8.9 Matrix (Sparse) storage

The FE matrix is the result of the assembly process of all elemental matrices. Its size can become quite large when the resolution is being increased (from thousands of lines/columns to tens of millions).

One important property of the matrix is its sparsity. Typically less than 1% of the matrix terms is not zero and this means that the matrix storage can and should be optimised. Clever storage formats were designed early on since the amount of RAM memory in computers was the limiting factor 3 or 4 decades ago. [1419]

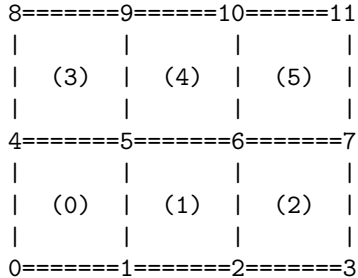
There are several standard formats:

- compressed sparse row (CSR) format
- compressed sparse column format (CSC)
- the Coordinate Format (COO)
- Skyline Storage Format
- ...

I focus on the CSR format in what follows.

8.9.1 2D domain - One degree of freedom per node

Let us consider again the 3×2 element grid which counts 12 nodes.



In the case there is only a single degree of freedom per node, the assembled FEM matrix will look like this:

$$\left(\begin{array}{cccccc|cc} X & X & & X & X & & & \\ X & X & X & X & X & X & & \\ & X & X & X & X & X & X & \\ & & X & X & & X & X & \\ X & X & & X & X & & X & X \\ X & X & X & X & X & X & X & X \\ & X & X & X & X & X & X & X \\ & & X & X & & X & X & \\ & & & X & X & X & X & X \\ & & & & X & X & X & X \\ & & & & & X & X & X \end{array} \right)$$

where the X stand for non-zero terms. This matrix structure stems from the fact that

- node 0 sees nodes 0,1,4,5
- node 1 sees nodes 0,1,2,4,5,6
- node 2 sees nodes 1,2,3,5,6,7
- ...

- node 5 sees nodes 0,1,2,4,5,6,8,9,10
- ...
- node 10 sees nodes 5,6,7,9,10,11
- node 11 sees nodes 6,7,10,11

In light thereof, we have

- 4 corner nodes which have 4 neighbours (counting themselves)
- $2(nnx-2)$ nodes which have 6 neighbours
- $2(nny-2)$ nodes which have 6 neighbours
- $(nnx-2) \times (nny-2)$ nodes which have 9 neighbours

In total, the number of non-zero terms in the matrix is then:

$$NZ = 4 \times 4 + 4 \times 6 + 2 \times 6 + 2 \times 9 = 70$$

In general, we would then have:

$$NZ = 4 \times 4 + [2(nnx - 2) + 2(nny - 2)] \times 6 + (nnx - 2)(nny - 2) \times 9$$

Let us temporarily assume $nnx = nny = n$. Then the matrix size (total number of unknowns) is $N = n^2$ and

$$NZ = 16 + 24(n - 2) + 9(n - 2)^2$$

A full matrix array would contain $N^2 = n^4$ terms. The ratio of NZ (the actual number of reals to store) to the full matrix size (the number of reals a full matrix contains) is then

$$R = \frac{16 + 24(n - 2) + 9(n - 2)^2}{n^4}$$

It is then obvious that when n is large enough $R \sim 1/n^2$.

CSR stores the nonzeros of the matrix row by row, in a single indexed array A of double precision numbers. Another array COLIND contains the column index of each corresponding entry in the A array. A third integer array RWPTR contains pointers to the beginning of each row, which an additional pointer to the first index following the nonzeros of the matrix A. A and COLIND have length NZ and RWPTR has length N+1.

In the case of the here-above matrix, the arrays COLIND and RWPTR will look like:

$$COLIND = (0, 1, 4, 5, 0, 1, 2, 4, 5, 6, 1, 2, 3, 5, 6, 7, \dots, 6, 7, 10, 11)$$

$$RWPTR = (0, 4, 10, 16, \dots)$$

8.9.2 2D domain - Two degrees of freedom per node

When there are now two degrees of freedom per node, such as in the case of the Stokes equation in two-dimensions, the size of the \mathbb{K} matrix is given by

<code>NfemV=nnp*ndofV</code>

In the case of the small grid above, we have `NfemV=24`. Elemental matrices are now 8×8 in size.

We still have

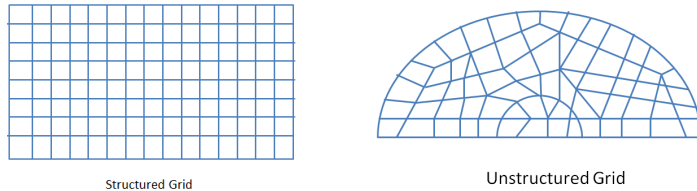
- 4 corner nodes which have 4 neighbours
- $2(nnx-2)$ nodes which have 6 neighbours
- $2(nny-2)$ nodes which have 6 neighbours

8.10 Mesh generation

Before basis functions can be defined and PDEs can be discretised and solved we must first tessellate the domain with polygons, e.g. triangles and quadrilaterals in 2D, tetrahedra, prisms and hexahedra in 3D.

When the domain is itself simple (e.g. a rectangle, a sphere, ...) the mesh (or grid) can be (more or less) easily produced and the connectivity array filled with straightforward algorithms [1541]. However, real life applications can involve extremely complex geometries (e.g. a bridge, a human spine, a car chassis and body, etc ...) and dedicated algorithms/softwares must be used (see [1549, 601, 1714]).

We usually distinguish between two broad classes of grids: structured grids (with a regular connectivity) and unstructured grids (with an irregular connectivity).



Remark. Various families of so-called meshless methods exist and are commonly employed in Computational Fluid Dynamics [1087, 1065, 1086, 1088]. They are however very rarely used in Computational geodynamics, with a noticeable exception [788].

8.10.1 Quadrilateral-based meshes

Let us now focus on the case of a rectangular computational domain of size $L_x \times L_y$ with a regular mesh composed of $\text{nelx} \times \text{nely} = \text{nel}$ quadrilaterals. There are then $\text{nmx} \times \text{nny} = \text{nnp}$ grid points. The elements are of size $\text{hx} \times \text{hy}$ with $\text{hx} = L_x / \text{nelx}$.

We have no reason to come up with an irregular/illogical node numbering so we can number nodes row by row or column by column as shown on the example hereunder of a 3×2 grid:

$\begin{array}{ccccccc} 8 & ===== & 9 & ===== & 10 & ===== & 11 \\ & & & & & & \\ & (3) & & (4) & & (5) & \\ & & & & & & \\ 4 & ===== & 5 & ===== & 6 & ===== & 7 \\ & & & & & & \\ & (0) & & (1) & & (2) & \\ & & & & & & \\ 0 & ===== & 1 & ===== & 2 & ===== & 3 \end{array}$	$\begin{array}{ccccccc} 2 & ===== & 5 & ===== & 8 & ===== & 11 \\ & & & & & & \\ & (1) & & (3) & & (5) & \\ & & & & & & \\ 1 & ===== & 4 & ===== & 7 & ===== & 10 \\ & & & & & & \\ & (0) & & (2) & & (4) & \\ & & & & & & \\ 0 & ===== & 3 & ===== & 6 & ===== & 9 \end{array}$
"row by row"	"column by column"

The numbering of the elements themselves could be done in a somewhat chaotic way but we follow the numbering of the nodes for simplicity. The row by row option is the adopted one in **fieldstone** and the coordinates of the points are computed as follows:

```
x = np.empty(nnp, dtype=np.float64)
y = np.empty(nnp, dtype=np.float64)
counter = 0
for j in range(0,nny):
    for i in range(0,nmx):
        x[counter]=i*hx
        y[counter]=j*hy
        counter += 1
```

The inner loop has i ranging from 0 to $\text{nmx}-1$ first for $j=0, 1, \dots$ up to $\text{nny}-1$ which indeed corresponds to the row by row numbering.

We now turn to the connectivity. As mentioned before, this is a structured mesh so that the so-called connectivity array, named `icon` in our case, can be filled easily. For each element we need to store the node identities of its vertices. Since there are `nel` elements and $m=4$ corners, this is a $m \times nel$ array. The algorithm goes as follows:

```
icon = np.zeros((m, nel), dtype=np.int16)
counter = 0
for j in range(0, nely):
    for i in range(0, nelx):
        icon[0, counter] = i + j * nnx
        icon[1, counter] = i + 1 + j * nnx
        icon[2, counter] = i + 1 + (j + 1) * nnx
        icon[3, counter] = i + (j + 1) * nnx
        counter += 1
```

In the case of the 3×2 mesh, the `icon` is filled as follows:

	element id→	0	1	2	3	4	5
node id↓							
0		0	1	2	4	5	6
1		1	2	3	5	6	7
2		5	6	7	9	10	11
3		4	5	6	8	9	10

It is to be understood as follows: element #4 is composed of nodes 5, 6, 10 and 9. Note that nodes are always stored in a counter clockwise manner, starting at the bottom left. This is very important since the corresponding basis functions and their derivatives will be labelled accordingly.

In three dimensions things are very similar. The mesh now counts `nelx×nely×nelz=nel` elements which represent a cuboid of size `Lx×Ly×Lz`. The position of the nodes is obtained as follows:

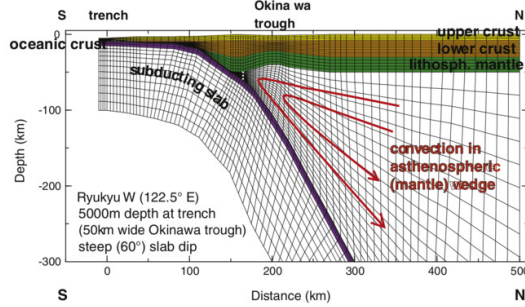
```
x = np.empty(nnp, dtype=np.float64)
y = np.empty(nnp, dtype=np.float64)
z = np.empty(nnp, dtype=np.float64)
counter=0
for i in range(0,nnx):
    for j in range(0,nny):
        for k in range(0,nnz):
            x[counter]=i*hx
            y[counter]=j*hy
            z[counter]=k*hz
            counter += 1
```

The connectivity array is now of size `m×nel` with `m=8`:

```
icon = np.zeros((m, nel), dtype=np.int16)
counter = 0
for i in range(0, nelx):
    for j in range(0, nely):
        for k in range(0, nelz):
            icon[0, counter]=nny*nnz*(i    )+nnz*(j    )+k
            icon[1, counter]=nny*nnz*(i+1)+nnz*(j    )+k
            icon[2, counter]=nny*nnz*(i+1)+nnz*(j+1)+k
            icon[3, counter]=nny*nnz*(i    )+nnz*(j+1)+k
            icon[4, counter]=nny*nnz*(i    )+nnz*(j    )+k+1
            icon[5, counter]=nny*nnz*(i+1)+nnz*(j    )+k+1
            icon[6, counter]=nny*nnz*(i+1)+nnz*(j+1)+k+1
            icon[7, counter]=nny*nnz*(i    )+nnz*(j+1)+k+1
            counter += 1
```

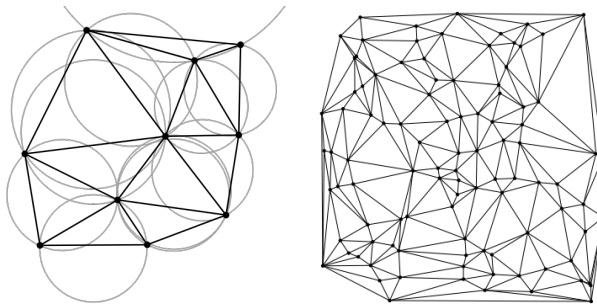
produce drawing of node numbering

Although it is not very common in geosciences, quadrilateral meshes are sometimes employed in a boundary-fitted way, as shown hereunder:



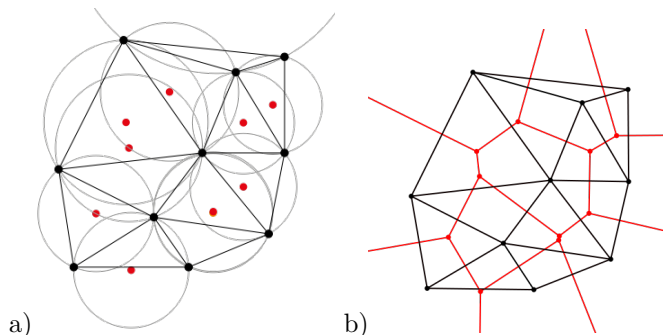
8.10.2 Delaunay triangulation and Voronoi cells, and triangle-based meshes

The topic of Delaunay³⁰ triangulation is vast, but a simple definition can be written as follows: "a Delaunay triangulation for a set P of points in a plane is a triangulation $DT(P)$ such that no point in P is inside the circumcircle of any triangle in $DT(P)$." [wikipedia] Other properties of such triangulations are that they maximize the minimum angle of all the angles of the triangles in the triangulation. Note that for four or more points on the same circle (e.g., the vertices of a rectangle) the Delaunay triangulation is not unique and that points on a line also cannot yield a valid triangulation (for the simple reason that they do not form a triangle).



a) A Delaunay triangulation in the plane with circumcircles shown. b) The Delaunay triangulation of a random set of 100 points in a plane.

The Delaunay triangulation of a discrete point set P in general corresponds to the dual graph of the Voronoi diagram for P . A Voronoi diagram is composed of non-overlapping Voronoi cells which make a partition of the plane. For each point there is a corresponding region consisting of all points closer to that point than to any other: this region is the Voronoi cell of that point.



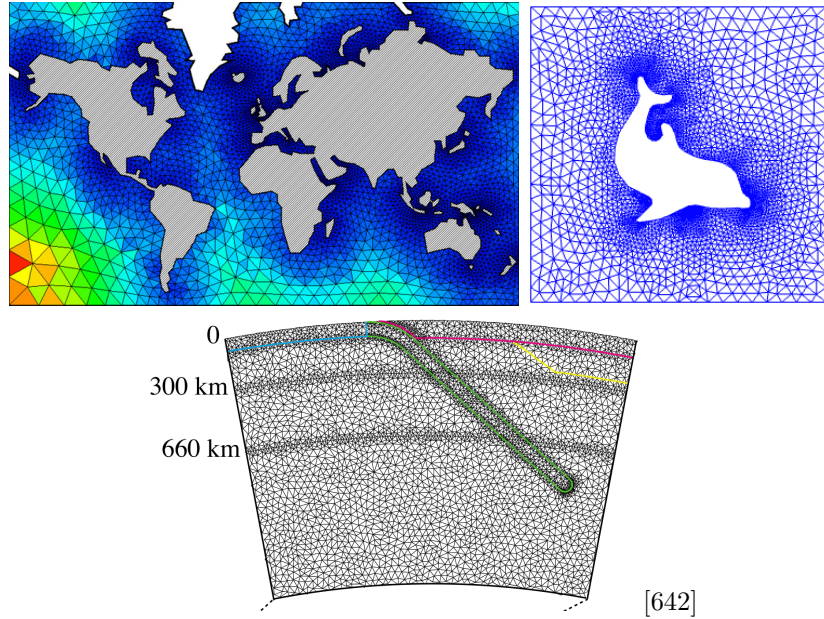
a) The Delaunay triangulation with all the circumcircles and their centers (in red). b) Connecting the centers of the circumcircles produces the Voronoi diagram (in red).

The Delaunay triangulation is used in the DOUAR code which is based on a particle levelset function to track materials. These particles are connected by means of a Delaunay triangulation (usually in a plane at startup, and then in a local Euclidean geometry once the surface is deformed) [199].

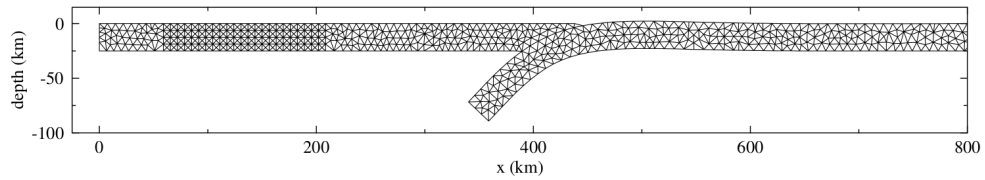
Literature: [640].

³⁰The triangulation is named after Boris Delaunay for his work on this topic from 1934.

Once a Delaunay triangulation has been obtained it can be used as a FEM mesh. Triangle-based meshes are obviously better suited for simulations of complex geometries:

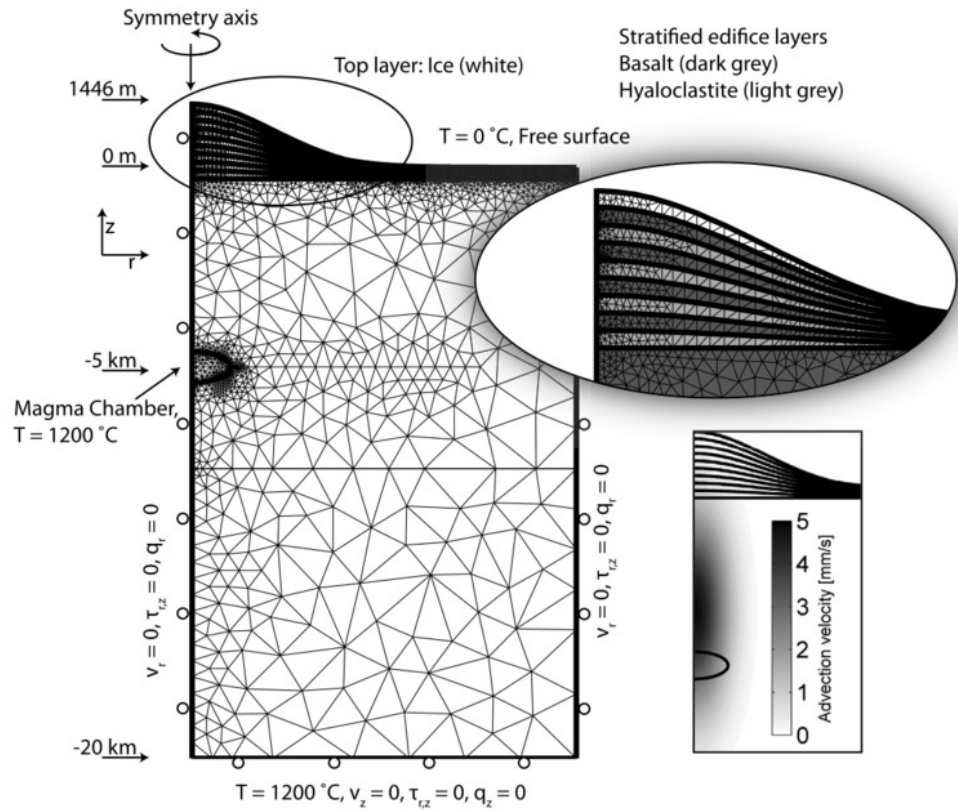


A very practical 2D triangle mesher is the code *Triangle*³¹ written by J.R. Shewchuk [1456]. Triangle is specialized for creating two-dimensional finite element meshes, but can also perform simpler related tasks such as forming Delaunay triangulations under various assumptions.



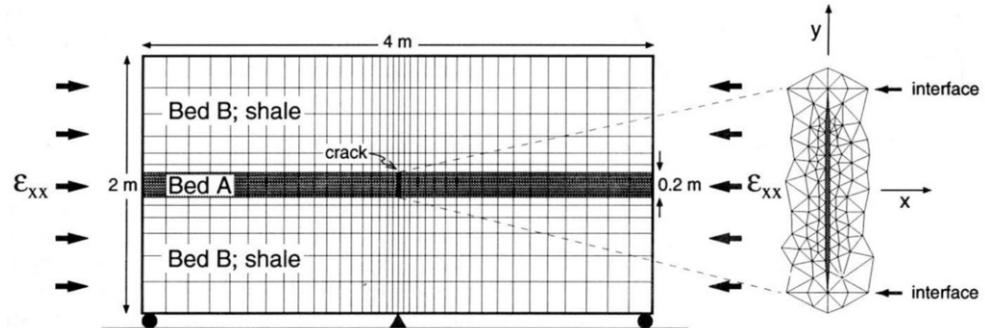
Taken from Buiter et al [240]. Finite element grid. The subducting plate initially extends to 1226 km in the horizontal direction and is not completely shown here. Discretization in the subducting plate is slightly coarser towards the right edge.

³¹<https://www.cs.cmu.edu/~quake/triangle.html>



Numerical model setup of the 2D axisymmetric half-space with all applied boundary conditions to study the effects of ice-cap unloading on shallow volcanic systems [64]

Although it is rarely used in practice it is possible to produce meshes which contain both quadrilateral and triangular elements:



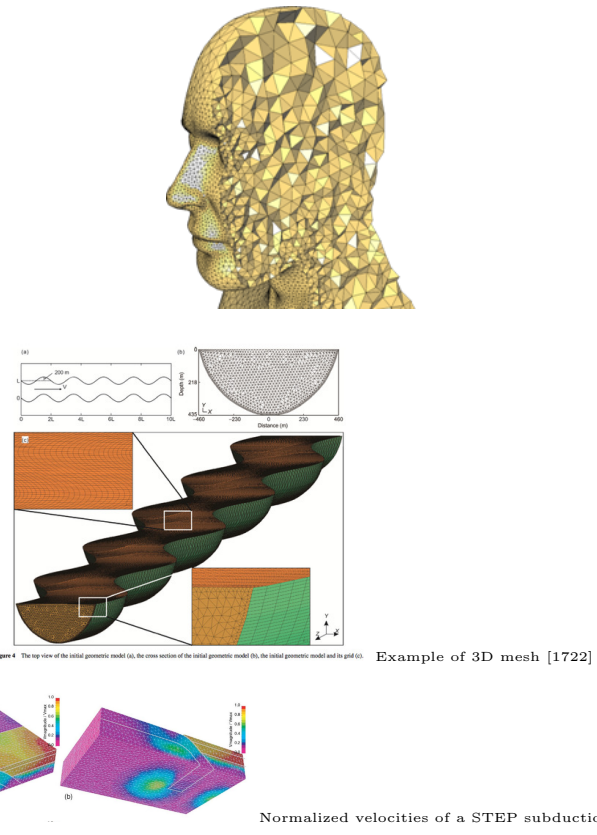
Mesh used to analyse the stress distribution around a pressurized crack in a layered elastic medium [559]

Literature[1238][1636]

mention stripack, plus paper moretti with it, and lithos1.0

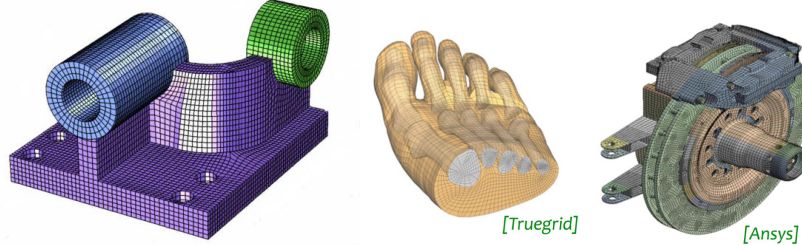
write about gmsh

8.10.3 Tetrahedra



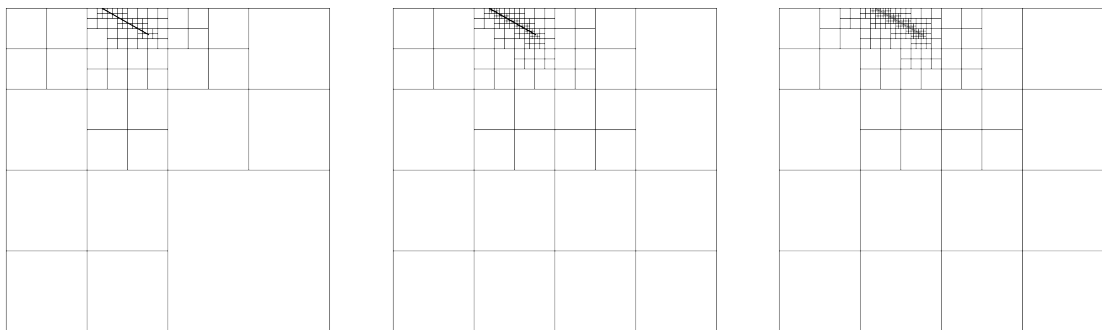
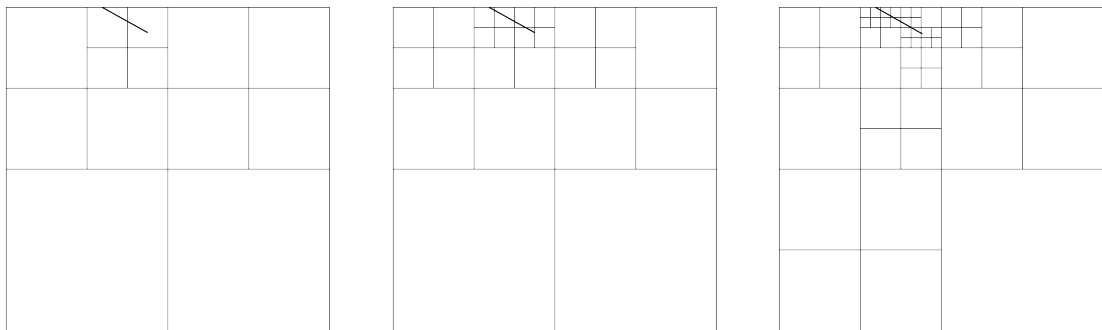
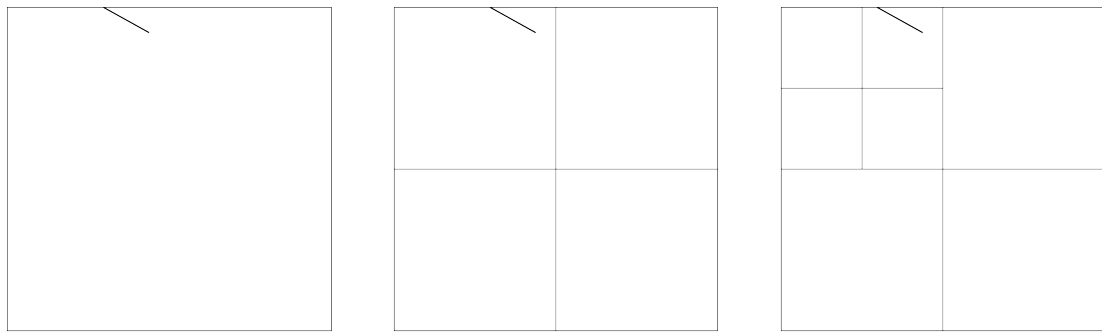
8.10.4 Hexahedra

A hexahedron is a convex polytope isomorphic to the cube $[0, 1]^3$. Edges are line segments, facets are strictly **planar** convex polygons.

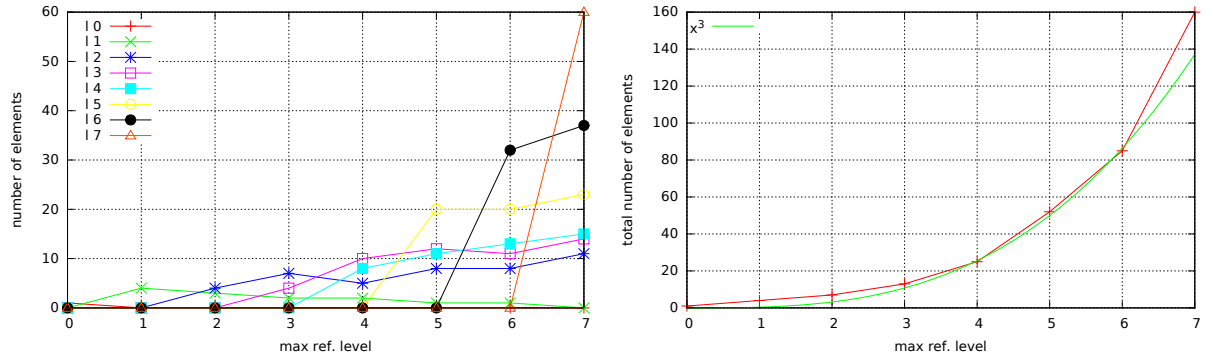


8.10.5 Adaptive Mesh Refinement

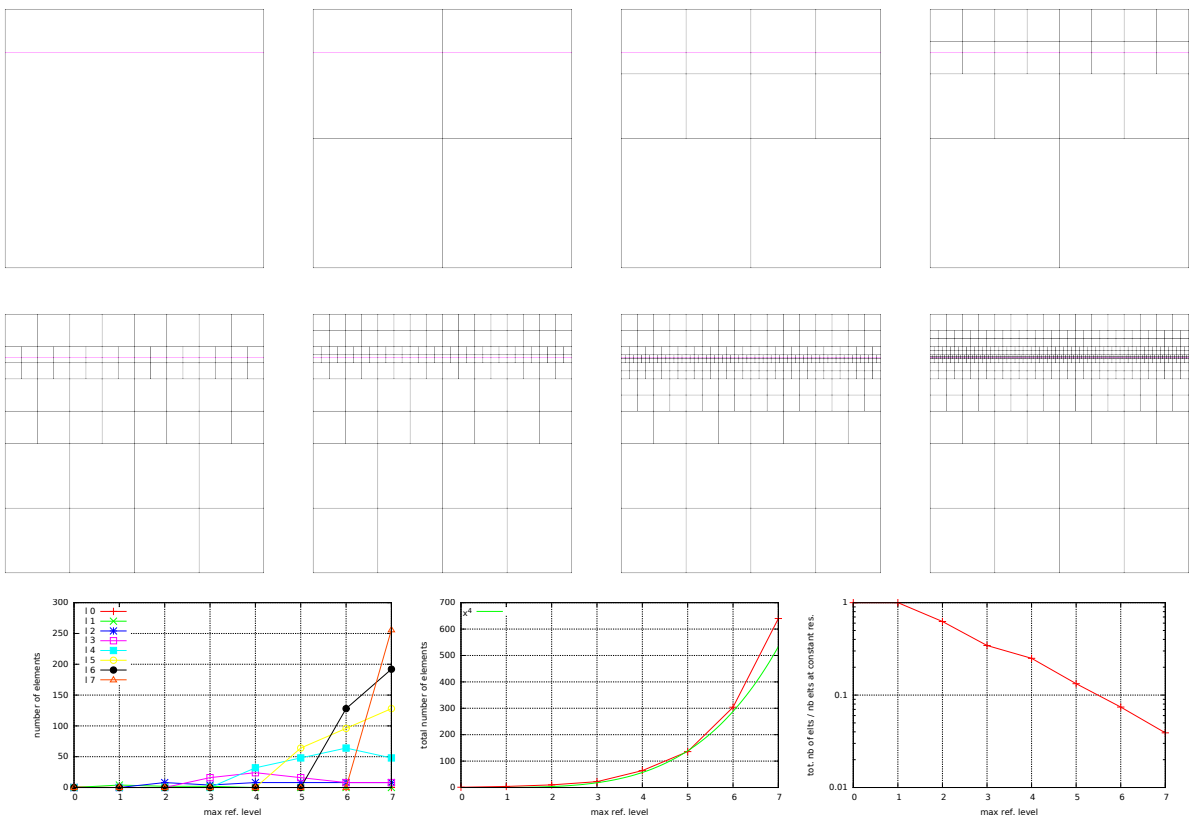
Literature: [285][104][1053] [282, sect 3] [104]



	# 10	# 11	# 12	# 13	# 14	# 15	# 16	# 17	# 18
max level= 0	1								
max level= 1	0	4							
max level= 2	0	3	4						
max level= 3	0	2	7	4					
max level= 4	0	2	5	10	8				
max level= 5	0	1	8	12	11	20			
max level= 6	0	1	8	11	13	20	32		
max level= 7	0	0	11	14	15	23	37	60	
max level= 8	0	0	11	13	17	27	43	72	116



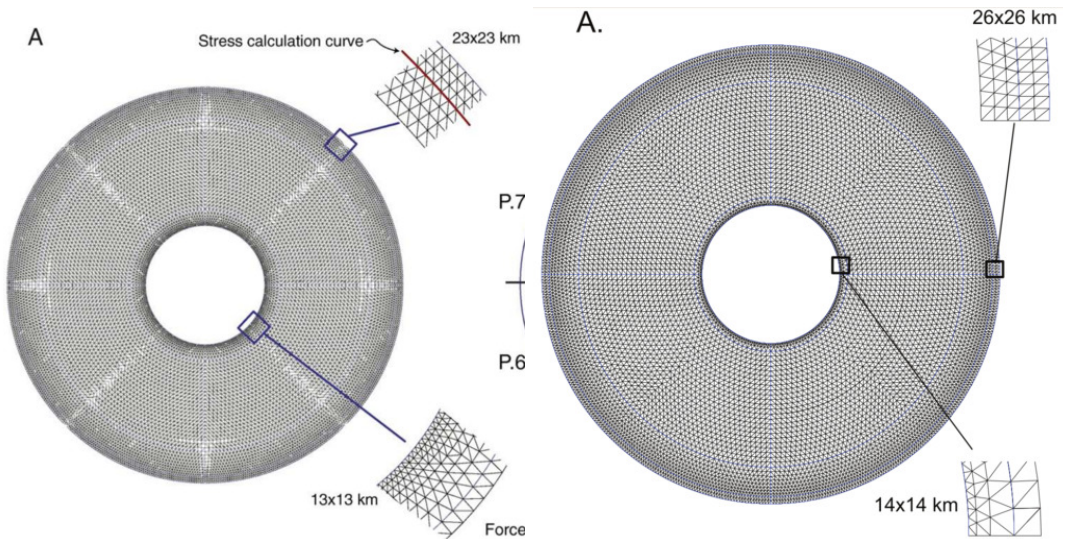
In the particular case presented here, even though the inclusion in a short two-dimensional line, the total number of elements grows faster than the third power of the refinement level. While of course the total number of elements remains much smaller than the constant resolution counterpart, this observation tells us that authorising a unit increase of the maximum refinement level can have a substantial effect on the total number of elements.



8.10.6 Conformal Mesh Refinement

Literature: [477][985]

8.10.7 Meshes in an annulus



The quadratic finite element mesh as used in [190, 192]

8.10.8 Meshes in a hollow sphere

The following is for the most part published in [1541].

To a first approximation the Earth is a sphere: the Earth's polar diameter is about 43 kilometers shorter than its equatorial diameter, a negligible difference of about 0.3%. As a consequence, modelling physical processes which take place in the planet require the discretisation of a sphere. Furthermore, because core dynamics occur on vastly different time scales than mantle dynamics, mantle modelling usually leaves the core out, thereby requiring simulations to be run on a hollow sphere mesh (with the noticeable exception of [655]).

Although so-called latitude-longitude grids would seem appealing, they suffer from the convergence of meridians at the poles (resulting in over sampling at poles) and the juxtaposition of triangles near the poles and quadrilaterals elsewhere. As a consequence more regular, but more complex, grids have been designed over the years which tessellate the surface of the sphere into triangles or quadrilaterals (sometimes overlapping). There is the 'cubed sphere' [1404, 337], the ying-yang grid [925, 1731, 928, 1511, 410, 411], the spiral grid [874], an icosahedron-based grid [89, 1496], or a grid composed of 12 blocks further subdivided into quadrilaterals [1765] as used in the CitcomS code. Note that [1271] have also presented a method for generating a numerical grid on a spherical surface which allows the grid to be based on several different regular polyhedrons (including octahedron, cube, icosahedron, and rhombic dodecahedron).

How such meshes are built is often not discussed in the literature. It is a tedious exercise of three-dimensional geometry and it can be time-consuming, especially the connectivity array generation. In [1541] I present an open source mesh generator for three hollow sphere meshes: the 'cubed sphere' mesh, the CitcomS mesh and the icosahedral mesh.

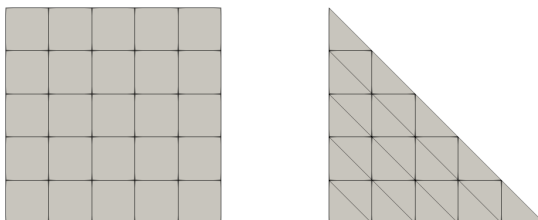
The open source code library GHOST[1541] allows three different types of hollow sphere meshes to be built , i.e. meshes bounded by two concentric spheres:

- The cubed sphere ('HS06'), composed of 6 blocks which are themselves subdivided into $N_b \times N_b$ quadrilateral shaped cells [1421, 1404, 1, 283]. Four types of cubed spheres meshes have been proposed: the conformal, elliptic, gnomonic and spring types [1328]. However only gnomonic meshes are considered here: these are obtained by inscribing a cube within a sphere and expanding to the surface of the sphere. The cubed sphere has recently been used in large-scale mantle convection simulation in conjunction with Adaptive Mesh Refinement [16, 283].
- The CitcomS mesh ('HS12') composed of 12 blocks also subdivided into $N_b \times N_b$ quadrilateral shaped cells [1765, 1486, 1761, 47]. Note that ASPECT [1009, 809], a relatively new code aimed at superseedng CitcomS can generate and use this type of mesh [1540] but is not limited to it.
- The icosahedral mesh ('HS20') composed of 20 triangular blocks [89, 88] subdivided into triangles, which is used in the TERRA code [252, 253, 251, 438].

Given the regularity and symmetry of these meshes determining the location of the mesh nodes in space is a relatively straightforward task. Building the mesh connectivity in an efficient manner is where the difficulty lies.

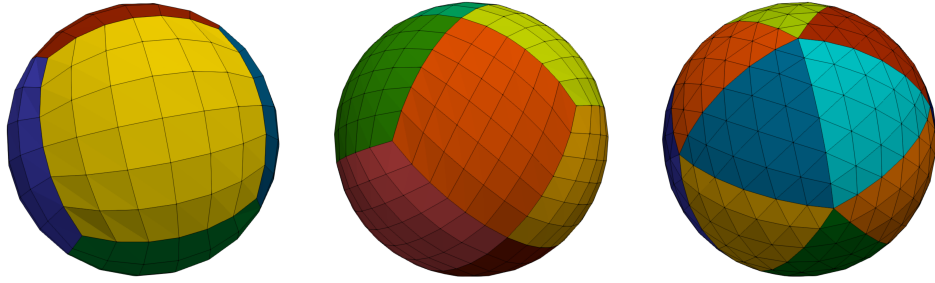
The approach to building all three meshes is identical:

1. A reference square or triangle is populated with cells, parametrised by a level l : the square is subdivided into $l \times l$ quadrilaterals while the triangle is subdivided into l^2 triangles.



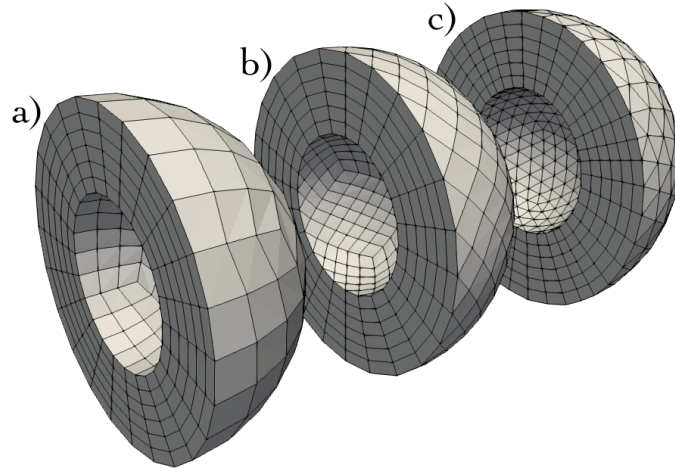
Reference square and triangles meshes at level 5.

2. This reference square or triangle is then replicated n_{block} times (6, 12 or 20) and mapped onto a portion of a unit sphere. The blocks are such that their union covers a full sphere but they cannot overlap except at the edges:



From left to right: HS06, HS12 and HS20 shells coloured by block number.

3. All block meshes are then merged together to generate a shell mesh. This task is rather complex as duplicate nodes must be removed and all connectivity arrays of the blocks must then be mended accordingly.
4. Shell meshes are replicated $n_{layer}+1$ times outwards with increasing radii. The n_{layer} shells are then merged together to form a hollow sphere mesh:



a) HS06 mesh composed of 6 blocks containing each 6^3 cells; b) HS12 mesh composed of 12 blocks containing each 6^3 cells; e) HS20 mesh composed of 20 blocks containing each 6^3 cells.

More information on these steps is available in the manual of the code. In the following table the number of nodes and cells for a variety of resolutions for all three mesh types is reported. Looking at the CitcomS literature of the past 20 years, we find that the mesh data presented in this table cover the various resolutions used, e.g. 12×48^3 [1164, 47], 12×64^3 [248] 12×96^3 [249], 12×128^3 [106, 1681, 1682]. Note that in the case of the HS06 and HS12 meshes the mesh nodes are mapped out to the 6 or 12 blocks following either an equidistant or equiangle approach (see [1328] for details on both approaches).

type	level	N	N_{el}	structure
HS06	2	78	48	6×2^3
HS06	4	490	384	6×4^3
HS06	8	3,474	3,072	6×8^3
HS06	16	26,146	24,576	6×16^3
HS06	32	202,818	196,608	6×32^3
HS06	64	1,597,570	1,572,864	6×64^3
HS06	128	12,681,474	12,582,912	6×128^3
HS06	256	101,057,026	100,663,296	6×256^3
HS12	2	150	96	12×2^3
HS12	4	970	768	12×4^3
HS12	8	6,930	6,144	12×8^3
HS12	16	52,258	49,152	12×16^3
HS12	32	405,570	393,216	12×32^3
HS12	48	1,354,850	1,327,104	12×48^3
HS12	64	3,195,010	3,145,728	12×64^3
HS12	128	25,362,690	25,165,824	12×128^3
HS12	256	202,113,538	201,326,592	12×256^3
HS20	2	126	160	20×2^3
HS20	4	810	1,280	20×4^3
HS20	8	5,778	10,240	20×8^3
HS20	16	43,554	81,920	20×16^3
HS20	32	337,986	655,360	20×32^3
HS20	64	2,662,530	5,242,880	20×64^3
HS20	128	21,135,618	41,943,040	20×128^3
HS20	256	168,428,034	335,544,320	20×256^3

Number of nodes N and elements/cells N_{el} for the three types of meshes and for various levels.

HS06: cubed sphere; HS12: CitcomS mesh; HS20: icosahedral mesh.

8.11 Visco-Plasticity

 Literature: [?, 338, 1210, 1234]

8.11.1 Tensor invariants

Before we dive into the world of nonlinear rheologies it is necessary to introduce the concept of tensor invariants since they are needed further on. Unfortunately there are many different notations used in the literature and these can prove to be confusing. Note that we only consider symmetric tensors in what follows.

Given a tensor \mathbf{T} , one can compute its (moment) invariants as follows [1361, p.339]:

- first invariant:

$$\begin{aligned}\mathcal{I}_1(\mathbf{T})|^{2D} &= \text{Tr}[\mathbf{T}] = T_{xx} + T_{yy} \\ \mathcal{I}_1(\mathbf{T})|^{3D} &= \text{Tr}[\mathbf{T}] = T_{xx} + T_{yy} + T_{zz}\end{aligned}\quad (464)$$

- second invariant:

$$\begin{aligned}\mathcal{I}_2(\mathbf{T})|^{2D} &= \frac{1}{2} \text{Tr}[\mathbf{T}^2] = \frac{1}{2} \sum_{ij} T_{ij} T_{ji} = \frac{1}{2} (T_{xx}^2 + T_{yy}^2) + T_{xy}^2 \\ \mathcal{I}_2(\mathbf{T})|^{3D} &= \frac{1}{2} \text{Tr}[\mathbf{T}^2] = \frac{1}{2} \sum_{ij} T_{ij} T_{ji} = \frac{1}{2} (T_{xx}^2 + T_{yy}^2 + T_{zz}^2) + T_{xy}^2 + T_{xz}^2 + T_{yz}^2\end{aligned}\quad (465)$$

- third invariant:

$$\mathcal{I}_3(\mathbf{T}) = \frac{1}{3} \text{Tr}[\mathbf{T}^3] = \frac{1}{3} \sum_i \sum_j \sum_k T_{ij} T_{jk} T_{ki}\quad (466)$$

The implementation of the plasticity criterions relies essentially on the second invariants of the (deviatoric) stress $\boldsymbol{\tau}$ and the (deviatoric) strainrate tensors $\dot{\boldsymbol{\varepsilon}}$:

$$\begin{aligned}\mathcal{I}_2(\boldsymbol{\tau})|^{2D} &= \frac{1}{2} (\tau_{xx}^2 + \tau_{yy}^2) + \tau_{xy}^2 \\ &= \frac{1}{4} (\sigma_{xx} - \sigma_{yy})^2 + \sigma_{xy}^2 \\ &= \frac{1}{4} (\sigma_1 - \sigma_2)^2 \\ \mathcal{I}_2(\boldsymbol{\tau})|^{3D} &= \frac{1}{2} (\tau_{xx}^2 + \tau_{yy}^2 + \tau_{zz}^2) + \tau_{xy}^2 + \tau_{xz}^2 + \tau_{yz}^2 \\ &= \frac{1}{6} [(\sigma_{xx} - \sigma_{yy})^2 + (\sigma_{yy} - \sigma_{zz})^2 + (\sigma_{xx} - \sigma_{zz})^2] + \sigma_{xy}^2 + \sigma_{xz}^2 + \sigma_{yz}^2 \\ &= \frac{1}{6} [(\sigma_1 - \sigma_2)^2 + (\sigma_2 - \sigma_3)^2 + (\sigma_1 - \sigma_3)^2] \\ \mathcal{I}_2(\dot{\boldsymbol{\varepsilon}}^d)|^{2D} &= \frac{1}{2} [(\dot{\varepsilon}_{xx}^d)^2 + (\dot{\varepsilon}_{yy}^d)^2] + (\dot{\varepsilon}_{xy}^d)^2 \\ &= \frac{1}{2} \left[\frac{1}{4} (\dot{\varepsilon}_{xx} - \dot{\varepsilon}_{yy})^2 + \frac{1}{4} (\dot{\varepsilon}_{yy} - \dot{\varepsilon}_{xx})^2 \right] + \dot{\varepsilon}_{xy}^2 \\ &= \frac{1}{4} (\dot{\varepsilon}_{xx} - \dot{\varepsilon}_{yy})^2 + \dot{\varepsilon}_{xy}^2 \\ \mathcal{I}_2(\dot{\boldsymbol{\varepsilon}}^d)|^{3D} &= \frac{1}{2} [(\dot{\varepsilon}_{xx}^d)^2 + (\dot{\varepsilon}_{yy}^d)^2 + (\dot{\varepsilon}_{zz}^d)^2] + (\dot{\varepsilon}_{xy}^d)^2 + (\dot{\varepsilon}_{xz}^d)^2 + (\dot{\varepsilon}_{yz}^d)^2 \\ &= \frac{1}{6} [(\dot{\varepsilon}_{xx} - \dot{\varepsilon}_{yy})^2 + (\dot{\varepsilon}_{yy} - \dot{\varepsilon}_{zz})^2 + (\dot{\varepsilon}_{xx} - \dot{\varepsilon}_{zz})^2] + \dot{\varepsilon}_{xy}^2 + \dot{\varepsilon}_{xz}^2 + \dot{\varepsilon}_{yz}^2\end{aligned}$$

Note that these (second) invariants are almost always used under a square root so we define:

$$\tau_e = \sqrt{\mathcal{I}_2(\boldsymbol{\tau})} \quad \dot{\varepsilon}_e = \sqrt{\mathcal{I}_2(\dot{\boldsymbol{\varepsilon}}^d)}$$

Note that these quantities have the same dimensions as their tensor counterparts, i.e. Pa for stresses and s^{-1} for strain rates.

The third (deviatoric) stress invariant is given by: (VERIFY!!)

$$\begin{aligned} \mathcal{I}_3(\boldsymbol{\tau})|^{3D} &= \frac{1}{3}s_{xx}(s_{xx}^2 + 3s_{xy}^2 + 3s_{xz}^2) \\ &+ \frac{1}{3}s_{yy}(3s_{xy}^2 + s_{yy}^2 + 3s_{yz}^2) \\ &+ \frac{1}{3}s_{zz}(3s_{xz}^2 + 3s_{yz}^2 + s_{zz}^2) \\ &+ 2s_{xy}s_{xz}s_{yz} \\ &= s_1s_2s_3 \end{aligned}$$

8.11.2 Scalar viscoplasticity

This formulation is quite easy to implement. It is widely used, e.g. [1690, 1543, 1473], and relies on the assumption that a scalar quantity η_p (the 'effective plastic viscosity') exists such that the deviatoric stress tensor

$$\boldsymbol{\tau} = 2\eta_p \dot{\boldsymbol{\varepsilon}} \quad (467)$$

is bounded by some yield stress value Y . From Eq. (467) it follows that $\underline{\tau}_{II} = 2\eta_p \dot{\underline{\varepsilon}}_{II} = Y$ which yields

$$\eta_p = \frac{Y}{2\underline{\dot{\varepsilon}}_{II}}$$

This approach has also been coined the Viscosity Rescaling Method (VRM) [924].

insert here the rederivation 2.1.1 of spmw16

It is at this stage important to realise that (i) in areas where the strainrate is low, the resulting effective viscosity will be large, and (ii) in areas where the strainrate is high, the resulting effective viscosity will be low. This is not without consequences since (effective) viscosity contrasts up to 8-10 orders of magnitude have been observed/obtained with this formulation and it makes the FE matrix very stiff, leading to (iterative) solver convergence issues. In order to contain these viscosity contrasts one usually resorts to viscosity limiters η_{min} and η_{max} such that

$$\eta_{min} \leq \eta_p \leq \eta_{max}$$

Caution must be taken when choosing both values as they may influence the final results.

▷ `python_codes/fieldstone_indentor`

8.11.3 About the yield stress value Y

In geodynamics the yield stress value is often given as a simple function. It can be constant (in space and time) and in this case we are dealing with a von Mises plasticity yield criterion. . We simply assume $Y_{vM} = C$ where C is a constant cohesion independent of pressure, strainrate, deformation history, etc ...

Another model is often used: the Drucker-Prager plasticity model. A friction angle ϕ is then introduced and the yield value Y takes the form

$$Y_{DP} = p \sin \phi + C \cos \phi$$

and therefore depends on the pressure p . Because ϕ is with the range $[0^\circ, 45^\circ]$, Y is found to increase with depth (since the lithostatic pressure often dominates the overpressure).

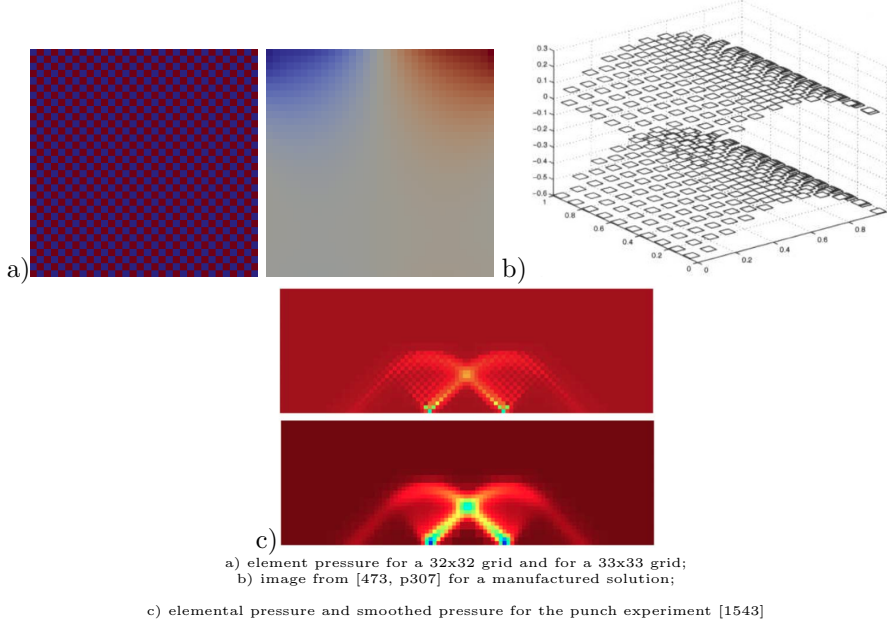
Note that a slightly modified version of this plasticity model has been used: the total pressure p is then replaced by the lithostatic pressure p_{lith} .

8.12 Pressure smoothing

It has been widely documented that the use of the $Q_1 \times P_0$ element is not without problems. Aside from the consequences it has on the FE matrix properties, we will here focus on another unavoidable side effect: the spurious pressure checkerboard modes.

These modes have been thoroughly analysed [747, 324, 1425, 1426]. They can be filtered out [324] or simply smoothed [1035].

On the following figure (a,b), pressure fields for the lid driven cavity experiment are presented for both an even and un-even number of elements. We see that the amplitude of the modes can sometimes be so large that the 'real' pressure is not visible and that something as simple as the number of elements in the domain can trigger those or not at all.



The easiest post-processing step that can be used (especially when a regular grid is used) is explained in [1543]: "The element-to-node interpolation is performed by averaging the elemental values from elements common to each node; the node-to-element interpolation is performed by averaging the nodal values element-by-element. This method is not only very efficient but produces a smoothing of the pressure that is adapted to the local density of the octree. Note that these two steps can be repeated until a satisfying level of smoothness (and diffusion) of the pressure field is attained."

In the codes which rely on the $Q_1 \times P_0$ element, the (elemental) pressure is simply defined as

```
p=np.zeros(nel, dtype=np.float64)
```

while the nodal pressure is then defined as

```
q=np.zeros(nnp, dtype=np.float64)
```

The element-to-node algorithm is then simply (in 2D):

```
count=np.zeros(nnp, dtype=np.int16)
for iel in range(0,nel):
    q[icon[0,iel]]+=p[iel]
    q[icon[1,iel]]+=p[iel]
    q[icon[2,iel]]+=p[iel]
    q[icon[3,iel]]+=p[iel]
    count[icon[0,iel]]+=1
    count[icon[1,iel]]+=1
    count[icon[2,iel]]+=1
    count[icon[3,iel]]+=1
q=q/count
```

Pressure smoothing is further discussed in [863].

[produce figure to explain this](#)

[link to proto paper](#)

[link to least square and nodal derivatives](#)

8.13 Pressure scaling

As perfectly explained in the step 32 of deal.ii³², we often need to scale the \mathbb{G} term since it is many orders of magnitude smaller than \mathbb{K} , which introduces large inaccuracies in the solving process to the point that the solution is nonsensical. This scaling coefficient is η/L where η and L are representative viscosities and lengths. We start from

$$\begin{pmatrix} \mathbb{K} & \mathbb{G} \\ \mathbb{G}^T & -\mathbb{C} \end{pmatrix} \cdot \begin{pmatrix} \vec{\mathcal{V}} \\ \vec{\mathcal{P}} \end{pmatrix} = \begin{pmatrix} \vec{f} \\ \vec{h} \end{pmatrix}$$

and introduce the scaling coefficient as follows (which in fact does not alter the solution at all):

$$\begin{pmatrix} \mathbb{K} & \frac{\eta}{L}\mathbb{G} \\ \frac{\eta}{L}\mathbb{G}^T & -\frac{\eta^2}{L^2}\mathbb{C} \end{pmatrix} \cdot \begin{pmatrix} \vec{\mathcal{V}} \\ \underline{\mathcal{P}} \end{pmatrix} = \begin{pmatrix} \vec{f} \\ \underline{h} \end{pmatrix}$$

We then end up with the modified Stokes system:

$$\begin{pmatrix} \mathbb{K} & \mathbb{G} \\ \underline{\mathbb{G}}^T & \underline{\mathbb{C}} \end{pmatrix} \cdot \begin{pmatrix} \vec{\mathcal{V}} \\ \underline{\mathcal{P}} \end{pmatrix} = \begin{pmatrix} \vec{f} \\ \underline{h} \end{pmatrix}$$

where

$$\underline{\mathbb{G}} = \frac{\eta}{L}\mathbb{G} \quad \underline{\mathcal{P}} = \frac{L}{\eta}\vec{\mathcal{P}} \quad \underline{\mathbb{C}} = \frac{\eta^2}{L^2}\mathbb{C} \quad \underline{h} = \frac{\eta}{L}\vec{h}$$

After the solve phase, we recover the real pressure with $\vec{\mathcal{P}} = \frac{\eta}{L}\underline{\mathcal{P}}$.

³²https://www.dealii.org/9.0.0/doxygen/deal.II/step_32.html

8.14 Pressure normalisation

8.14.1 Basic idea and naive implementation

When Dirichlet boundary conditions are imposed everywhere on the boundary, pressure is only present by its gradient in the equations. It is thus determined up to an arbitrary constant (one speaks then of a nullspace of size 1). In such a case, one commonly impose the average of the pressure over the whole domain or on a subset of the boundary to have a zero average, i.e.

$$\int_{\Omega} p dV = 0 \quad (468)$$

Another possibility is to impose the pressure value at a single node.

Let us assume for example that we are using $Q_1 \times P_0$ elements. Then the pressure is constant inside each element. The integral above becomes:

$$\int_{\Omega} p dV = \sum_e \int_{\Omega_e} p dV = \sum_e p_e \int_{\Omega_e} dV = \sum_e p_e A_e = 0 \quad (469)$$

where the sum runs over all elements e of area A_e . This can be rewritten

$$\mathbb{L}^T \cdot \vec{\mathcal{P}} = 0$$

and it is a constraint on the pressure solution which couples *all* pressure dofs. We can associate to it a Lagrange multiplier λ so that we must solve the modified Stokes system:

$$\begin{pmatrix} \mathbb{K} & \mathbb{G} & 0 \\ \mathbb{G}^T & 0 & \mathbb{L} \\ 0 & \mathbb{L}^T & 0 \end{pmatrix} \cdot \begin{pmatrix} \vec{\mathcal{V}} \\ \vec{\mathcal{P}} \\ \lambda \end{pmatrix} = \begin{pmatrix} \vec{f} \\ \vec{h} \\ 0 \end{pmatrix}$$

When higher order spaces are used for pressure (continuous or discontinuous) one must then carry out the above integration numerically by means of (usually) a Gauss-Legendre quadrature.

Although valid, this approach has one main disadvantage: it makes the Stokes matrix larger (although marginally so – only one row and column are added), but more importantly it prevents the use of some of the solving strategies of Section 8.15.

8.14.2 Implementation – the real deal

The idea is actually quite simple and requires two steps:

1. remove the null space by prescribing the pressure at one location and solve the system;
2. post-process the pressure so as to arrive at a pressure field which fulfills the required normalisation (surface, volume, ...)

The reason why it works is as follows: a constant pressure value lies in the null space, so that one can add or delete any value to the pressure field without consequence. As such I can choose said constant such that the pressure at a given node/element is zero. All other computed pressures are then relative to that one. The post-processing step will redistribute a constant value to all pressures (it will shift them up or down) so that the normalising condition is respected.

8.15 Solving the Stokes system

Let us start again from the (full) Stokes system:

$$\begin{pmatrix} \mathbb{K} & \mathbb{G} \\ \mathbb{G}^T & -\mathbb{C} \end{pmatrix} \cdot \begin{pmatrix} \vec{\mathcal{V}} \\ \vec{\mathcal{P}} \end{pmatrix} = \begin{pmatrix} \vec{f} \\ \vec{h} \end{pmatrix} \quad (470)$$

We need to solve this system in order to obtain the solution, i.e. the $\vec{\mathcal{V}}$ and $\vec{\mathcal{P}}$ vectors. But how? Unfortunately, this question is not simple to answer and the appropriate method depends on many parameters, but mainly on how big the matrix blocks are and what the condition number of the matrix \mathbb{K} is.

In what follow I cover:

- solving when the penalty approach is used
- the Schur complement approach
- the FGMRES approach



8.15.1 when using the penalty formulation

In this case we are only solving for velocity since pressure is recovered in a post-processing step:

$$(\mathbb{K}_\eta + \mathbb{K}_\lambda) \cdot \vec{\mathcal{V}} = \vec{f}$$

We also know that the penalty factor is many orders of magnitude higher than the viscosity and in combination with the use of the $Q_1 \times P_0$ element the resulting matrix condition number is very high so that the use of iterative solvers is precluded. Indeed codes such as SOPALE [614], DOUAR [199], or FANTOM [1538] relying on the penalty formulation all use direct solvers. The most popular are BLKFCT³³, MUMPS³⁴ [23, 25, 24, 26], WSMP³⁵ [760, 761], UMFPACK and CHOLMOD³⁶, SuperLU, PARDISO³⁷ [448, 1637, 1001], or those inside PETSc ??.

Braun et al [199] list the following features of such solvers:

- Robust
- Black-box operation
- Difficult to parallelize
- Memory consumption
- Limited scalability

The main advantage of direct solvers is used in this case: They can solve ill-conditioned matrices. However memory requirements for the storage of number of nonzeros in the Cholesky matrix grow very fast as the number of equations/grid size increases, especially in 3D, to the point that even modern computers with tens of Gb of RAM cannot deal with a 100^3 element mesh. This explains why direct solvers are often used for 2D problems and rarely in 3D with noticeable exceptions [1543, 1718, 201, 1098, 20, 21, 22, 1683, 1254].

³³<http://dm.unife.it/blkfclt/>

³⁴<http://mumps.enseeiht.fr/>

³⁵<http://www.research.ibm.com/projects/wsmp>

³⁶<http://faculty.cse.tamu.edu/davis/suitesparse.html>

³⁷<https://www.pardiso-project.org/>

8.15.2 Conjugate gradient and the Schur complement approach

Let us write the above system as two equations:

$$\mathbb{K} \cdot \vec{\mathcal{V}} + \mathbb{G} \cdot \vec{\mathcal{P}} = \vec{f} \quad (471)$$

$$\mathbb{G}^T \cdot \vec{\mathcal{V}} = \vec{h} \quad (472)$$

The first line can be re-written $\vec{\mathcal{V}} = \mathbb{K}^{-1} \cdot (\vec{f} - \mathbb{G} \cdot \vec{\mathcal{P}})$ and can be inserted in the second:

$$\mathbb{G}^T \cdot \vec{\mathcal{V}} = \mathbb{G}^T \cdot [\mathbb{K}^{-1} \cdot (\vec{f} - \mathbb{G} \cdot \vec{\mathcal{P}})] = \vec{h} \quad (473)$$

or,

$$(\mathbb{G}^T \cdot \mathbb{K}^{-1} \cdot \mathbb{G}) \cdot \vec{\mathcal{P}} = \mathbb{G}^T \cdot \mathbb{K}^{-1} \cdot \vec{f} - \vec{h} \quad (474)$$

The matrix $\mathbb{S} = \mathbb{G}^T \cdot \mathbb{K}^{-1} \cdot \mathbb{G}$ is called the Schur complement. It is Symmetric (since \mathbb{K} is symmetric) and Positive-Definite³⁸ (SPD) if $\text{Ker}(\mathbb{G}) = 0$. [look in donea-huerta book for details](#) Having solved this equation (we have obtained $\vec{\mathcal{P}}$), the velocity can be recovered by solving $\mathbb{K} \cdot \vec{\mathcal{V}} = \vec{f} - \mathbb{G} \cdot \vec{\mathcal{P}}$.

For now, let us assume that we have built the \mathbb{S} matrix and the right hand side $\vec{f} = \mathbb{G}^T \cdot \mathbb{K}^{-1} \cdot \vec{f} - \vec{h}$. We must solve $\mathbb{S} \cdot \vec{\mathcal{P}} = \vec{f}$.

One can resort to so-called Richardson iterations, defined as follows (e.g., see [1632], p141): in solving the matrix equation $\mathbf{A} \cdot \vec{X} = \vec{b}$, the Richardson iterative method is defined by:

$$\vec{X}_{k+1} = \vec{X}_k + \alpha_k (-\mathbf{A} \cdot \vec{X}_k + \vec{b}) \quad m \geq 0 \quad (475)$$

where the α_k 's are real scalars. It is easy to see that when the method converges then $\vec{X}_{k+1} \simeq \vec{X}_k$ and then $\mathbf{A} \cdot \vec{X} = \vec{b}$ is satisfied. In our case, it writes:

$$\begin{aligned} \vec{\mathcal{P}}_{k+1} &= \vec{\mathcal{P}}_k + \alpha_k (-\mathbb{S} \cdot \vec{\mathcal{P}}_k + \vec{f}) \\ &= \vec{\mathcal{P}}_k + \alpha_k (-\mathbb{G}^T \cdot \mathbb{K}^{-1} \cdot \mathbb{G} \cdot \vec{\mathcal{P}}_k + \mathbb{G}^T \cdot \mathbb{K}^{-1} \cdot \vec{f} - \vec{h}) \\ &= \vec{\mathcal{P}}_k + \alpha_k [\mathbb{G}^T \cdot \mathbb{K}^{-1} \cdot (-\mathbb{G} \cdot \vec{\mathcal{P}}_k + \vec{f}) - \vec{h}] \\ &= \vec{\mathcal{P}}_k + \alpha_k [\mathbb{G}^T \cdot \mathbb{K}^{-1} \cdot (\mathbb{K} \cdot \vec{\mathcal{V}}_k) - \vec{h}] \\ &= \vec{\mathcal{P}}_k + \alpha_k (\mathbb{G}^T \cdot \vec{\mathcal{V}}_k - \vec{h}) \end{aligned} \quad (476)$$

The above iterations are then carried out and for each new pressure field the associated velocity field is computed. The method of using Richardson iterations applied to the Schur complement is commonly called the Uzawa algorithm [188, p221].

Uzawa algorithm (1):

$$\text{solve } \mathbb{K} \cdot \vec{\mathcal{V}}_k = \vec{f} - \mathbb{G} \cdot \vec{\mathcal{P}}_{k-1} \quad (477)$$

$$\vec{\mathcal{P}}_k = \vec{\mathcal{P}}_{k-1} + \alpha (\mathbb{G}^T \cdot \vec{\mathcal{V}}_k - \vec{h}) \quad k = 1, 2, \dots \quad (478)$$

This method is rather simple to implement, although what makes an appropriate set of α_k values is not straightforward, which is why the conjugate gradient is often preferred, as detailed in the next subsection.

It is known that such iterations will converge for $0 < \alpha < \rho(\mathbb{S}) = \lambda_{max}(\mathbb{S})$ where $\rho(\mathbb{S})$ is the spectral radius of the matrix \mathbb{S} which is essentially the largest, in absolute value, eigenvalue of \mathbb{S} (neither of which can be computed easily). It can also be proven that the rate of convergence depends on the condition number of the matrix.

Richardson iterations are part of the family of stationary iterative methods, since it can be rewritten

$$\vec{X}_{k+1} = (\mathbf{I} - \alpha_k \mathbf{A}) \cdot \vec{X}_k + \alpha_k \vec{b} \quad (479)$$

³⁸ M positive definite $\iff x^T M x > 0 \forall x \in \mathbb{R}^n \setminus \mathbf{0}$

which is the definition of a stationary method.

Since the α parameter is the key to a successful Uzawa algorithm, this issue has of course been looked into. What follows is presented in [188, p221]. For the analysis of the Uzawa algorithm, we define the residue

$$\vec{\mathcal{R}}_k = \vec{h} - \mathbb{G}^T \cdot \vec{\mathcal{V}}_k$$

In addition, suppose the solution of the saddle point problem is denoted by $(\mathcal{V}^*, \mathcal{P}^*)$. Now substituting the iteration formula for \mathcal{V}_k , we get

$$\mathcal{R}_k = \mathbb{G}^T \cdot \vec{\mathcal{V}}^* - \mathbb{G}^T \cdot \mathbb{K}^{-1}(\vec{f} - \mathbb{G} \cdot \mathcal{P}_{k-1}) \quad (480)$$

$$= \mathbb{G}^T \cdot \vec{\mathcal{V}}^* - \mathbb{G}^T \cdot \mathbb{K}^{-1}(\mathbb{K} \cdot \vec{\mathcal{V}}^* + \mathbb{G} \cdot \vec{\mathcal{P}}^* - \mathbb{G} \cdot \mathcal{P}_{k-1}) \quad (481)$$

$$= \mathbb{G}^T \cdot \mathbb{K}^{-1} \cdot \mathbb{G} \cdot (\vec{\mathcal{P}}_{k-1} - \vec{\mathcal{P}}^*) \quad (482)$$

From Eq. 478 it follows that:

$$\mathcal{P}_k - \mathcal{P}_{k-1} = \alpha(\mathbb{G}^T \cdot \vec{\mathcal{V}}_k - \vec{h}) \quad (483)$$

$$= -\alpha \vec{\mathcal{R}}_k \quad (484)$$

$$= -\alpha \mathbb{G}^T \cdot \mathbb{K}^{-1} \cdot \mathbb{G} \cdot (\vec{\mathcal{P}}_{k-1} - \vec{\mathcal{P}}^*) \quad (485)$$

$$= \alpha \mathbb{G}^T \cdot \mathbb{K}^{-1} \cdot \mathbb{G} \cdot (\vec{\mathcal{P}}^* - \vec{\mathcal{P}}_{k-1}) \quad (486)$$

Thus the Uzawa algorithm is equivalent to applying the gradient method to the reduced equation using a fixed step size. In particular, the iteration converges for $\alpha < 2\|\mathbb{G}^T \cdot \mathbb{K}^{-1} \cdot \mathbb{G}\|^{-1}$ and one can show that the good step size α_k is given by

$$\alpha_k = \frac{\mathcal{R}_k \cdot \mathcal{R}_k}{(\mathbb{G} q_k) \cdot (\mathbb{K}^{-1} \mathbb{G} q_k)} \quad (487)$$

However, if we were to use this rule formally, we would need an additional multiplication by \mathbb{K}^{-1} in every step of the iteration. This can be avoided by storing an auxiliary vector.

Note that in [698] it is stated: the convergence of this algorithm is proved for $\alpha \in (0, 2\mu/d)$ (where d is the number of dimensions).

check this, and report page number

Note that this algorithm is presented in [1786] in the context of viscoplastic flow.

As mentioned above, there is a way to rework the original Uzawa algorithm to include Eq. (487). It yields a modified Uzawa algorithm [188, p221]:

Uzawa algorithm (2): Solve $\mathbb{K} \cdot \vec{\mathcal{V}}_1 = \vec{f} - \mathbb{G} \cdot \vec{\mathcal{P}}_0$. For $k = 1, 2, \dots$, compute

$$\vec{q}_k = \vec{h} - \mathbb{G}^T \cdot \vec{\mathcal{V}}_k \quad (488)$$

$$\vec{p}_k = \mathbb{G} \cdot q_k \quad (489)$$

$$\vec{H}_k = \mathbb{K}^{-1} \cdot \vec{p}_k \quad (490)$$

$$\alpha_k = \frac{\vec{q}_k \cdot \vec{q}_k}{\vec{p}_k \cdot \vec{H}_k} \quad (491)$$

$$\vec{\mathcal{P}}_k = \vec{\mathcal{P}}_{k-1} - \alpha_k \vec{q}_k \quad (492)$$

$$\vec{\mathcal{V}}_{k+1} = \vec{\mathcal{V}}_k + \alpha_k \vec{H}_k \quad (493)$$

 Literature[297, 300]

8.15.3 Conjugate gradient and the Schur complement approach

Since \mathbb{S} is SPD, the Conjugate Gradient (CG) method is very appropriate to solve this system. Indeed, looking at the definition of Wikipedia: "In mathematics, the conjugate gradient method is an algorithm for the numerical solution of particular systems of linear equations, namely those whose matrix is symmetric and positive-definite. The conjugate gradient method is often implemented as an iterative algorithm, applicable to sparse systems that are too large to be handled by a direct implementation or other direct

methods such as the Cholesky decomposition. Large sparse systems often arise when numerically solving partial differential equations or optimization problems.”

A simple Google search tells us that the Conjugate Gradient algorithm is as follows:

```

r0 := b - Ax0
if r0 is sufficiently small, then return x0 as the result
p0 := r0
k := 0
repeat
     $\alpha_k := \frac{\mathbf{r}_k^\top \mathbf{r}_k}{\mathbf{p}_k^\top \mathbf{A} \mathbf{p}_k}$ 
    xk+1 := xk +  $\alpha_k \mathbf{p}_k$ 
    rk+1 := rk -  $\alpha_k \mathbf{A} \mathbf{p}_k$ 
    if rk+1 is sufficiently small, then exit loop
     $\beta_k := \frac{\mathbf{r}_{k+1}^\top \mathbf{r}_{k+1}}{\mathbf{r}_k^\top \mathbf{r}_k}$ 
    pk+1 := rk+1 +  $\beta_k \mathbf{p}_k$ 
    k := k + 1
end repeat
return xk+1 as the result

```

Algorithm as obtained from Wikipedia³⁹

This algorithm is of course explained in detail in many textbooks such as [1419]

[add biblio](#)

Let us look at this algorithm up close. The parts which may prove to be somewhat tricky are those involving the matrix inverse (in our case the Schur complement). We start the iterations with a guess pressure \vec{P}_0 (and an initial guess velocity which could be obtained by solving $\mathbb{K} \cdot \vec{V}_0 = \vec{f} - \mathbb{G} \cdot \vec{P}_0$).

$$\vec{r}_0 = \vec{f} - \mathbb{S} \cdot \vec{P}_0 \quad (494)$$

$$= \mathbb{G}^T \cdot \mathbb{K}^{-1} \cdot \vec{f} - \vec{h} - (\mathbb{G}^T \cdot \mathbb{K}^{-1} \cdot \mathbb{G}) \cdot \vec{P}_0 \quad (495)$$

$$= \mathbb{G}^T \cdot \mathbb{K}^{-1} \cdot (\vec{f} - \mathbb{G} \cdot \vec{P}_0) - \vec{h} \quad (496)$$

$$= \mathbb{G}^T \cdot \mathbb{K}^{-1} \cdot \mathbb{K} \cdot \vec{V}_0 - \vec{h} \quad (497)$$

$$= \mathbb{G}^T \cdot \vec{V}_0 - \vec{h} \quad (498)$$

$$= \mathbb{G}^T \cdot \vec{V}_0 - \vec{h} \quad (499)$$

We now turn to the α_k coefficient:

$$\alpha_k = \frac{\vec{r}_k^T \cdot \vec{r}_k}{\vec{p}_k \cdot \mathbb{S} \cdot \vec{p}_k} = \frac{\vec{r}_k^T \cdot \vec{r}_k}{\vec{p}_k \cdot \mathbb{G}^T \cdot \mathbb{K}^{-1} \cdot \mathbb{G} \cdot \vec{p}_k} = \frac{\vec{r}_k^T \cdot \vec{r}_k}{(\mathbb{G} \cdot \vec{p}_k)^T \cdot \mathbb{K}^{-1} \cdot (\mathbb{G} \cdot \vec{p}_k)}$$

We then define $\tilde{p}_k = \mathbb{G} \cdot \vec{p}_k$, so that α_k can be computed as follows:

1. compute $\tilde{p}_k = \mathbb{G} \cdot \vec{p}_k$
2. solve $\mathbb{K} \cdot \vec{d}_k = \tilde{p}_k$
3. compute $\alpha_k = (\vec{r}_k^T \cdot \vec{r}_k) / (\tilde{p}_k^T \cdot \vec{d}_k)$

Then we need to look at the term $\mathbb{S} \cdot \vec{p}_k$:

$$\mathbb{S} \cdot \vec{p}_k = \mathbb{G}^T \cdot \mathbb{K}^{-1} \cdot \mathbb{G} \cdot \vec{p}_k = \mathbb{G}^T \cdot \mathbb{K}^{-1} \cdot \tilde{p}_k = \mathbb{G}^T \cdot \vec{d}_k$$

We can then rewrite the CG algorithm as follows [1769]:

- $\vec{r}_0 = \mathbb{G}^T \cdot \vec{V}_0 - \vec{h}$

³⁹https://en.wikipedia.org/wiki/Conjugate_gradient_method

- if \vec{r}_0 is sufficiently small, then return $(\vec{\mathcal{V}}_0, \vec{\mathcal{P}}_0)$ as the result
- $\vec{p}_0 = \vec{r}_0$
- $k = 0$
- repeat
 - compute $\tilde{\vec{p}}_k = \mathbb{G} \cdot \vec{p}_k$
 - solve $\mathbb{K} \cdot \vec{d}_k = \tilde{\vec{p}}_k$
 - compute $\alpha_k = (\vec{r}_k^T \cdot \vec{r}_k) / (\tilde{\vec{p}}_k^T \cdot \vec{d}_k)$
 - $\vec{\mathcal{P}}_{k+1} = \vec{\mathcal{P}}_k + \alpha_k \vec{p}_k$
 - $\vec{r}_{k+1} = \vec{r}_k - \alpha_k \mathbb{G}^T \cdot \vec{d}_k$
 - if \vec{r}_{k+1} is sufficiently small, then exit loop
 - $\beta_k = (\vec{r}_{k+1}^T \cdot \vec{r}_{k+1}) / (\vec{r}_k^T \cdot \vec{r}_k)$
 - $\vec{p}_{k+1} = \vec{r}_{k+1} + \beta_k \vec{p}_k$
 - $k = k + 1$
- return $\vec{\mathcal{P}}_{k+1}$ as result

We see that we have managed to solve the Schur complement equation with the Conjugate Gradient method without ever building the matrix \mathbb{S} . Having obtained the pressure solution, we can easily recover the corresponding velocity with $\mathbb{K} \cdot \vec{\mathcal{V}}_{k+1} = \vec{f} - \mathbb{G} \cdot \vec{\mathcal{P}}_{k+1}$. However, this is rather unfortunate because it requires yet another solve with the \mathbb{K} matrix. As it turns out, we can slightly alter the above algorithm to have it update the velocity as well so that this last solve is unnecessary.

We have

$$\vec{\mathcal{V}}_{k+1} = \mathbb{K}^{-1} \cdot (\vec{f} - \mathbb{G} \cdot \vec{\mathcal{P}}_{k+1}) \quad (500)$$

$$= \mathbb{K}^{-1} \cdot (\vec{f} - \mathbb{G} \cdot (\vec{\mathcal{P}}_k + \alpha_k \vec{p}_k)) \quad (501)$$

$$= \mathbb{K}^{-1} \cdot (\vec{f} - \mathbb{G} \cdot \vec{\mathcal{P}}_k) - \alpha_k \mathbb{K}^{-1} \cdot \mathbb{G} \cdot \vec{p}_k \quad (502)$$

$$= \vec{\mathcal{V}}_k - \alpha_k \mathbb{K}^{-1} \cdot \tilde{\vec{p}}_k \quad (503)$$

$$= \vec{\mathcal{V}}_k - \alpha_k \vec{d}_k \quad (504)$$

and we can insert this minor extra calculation inside the algorithm and get the velocity solution nearly for free. The final CG algorithm is then

solver_cg:

- compute $\vec{\mathcal{V}}_0 = \mathbb{K}^{-1} \cdot (\vec{f} - \mathbb{G} \cdot \vec{\mathcal{P}}_0)$
- $\vec{r}_0 = \mathbb{G}^T \cdot \vec{\mathcal{V}}_0 - \vec{h}$
- if \vec{r}_0 is sufficiently small, then return $(\vec{\mathcal{V}}_0, \vec{\mathcal{P}}_0)$ as the result
- $\vec{p}_0 = \vec{r}_0$
- $k = 0$
- repeat
 - compute $\tilde{\vec{p}}_k = \mathbb{G} \cdot \vec{p}_k$
 - solve $\mathbb{K} \cdot \vec{d}_k = \tilde{\vec{p}}_k$
 - compute $\alpha_k = (\vec{r}_k^T \cdot \vec{r}_k) / (\tilde{\vec{p}}_k^T \cdot \vec{d}_k)$
 - $\vec{\mathcal{P}}_{k+1} = \vec{\mathcal{P}}_k + \alpha_k \vec{p}_k$
 - $\vec{\mathcal{V}}_{k+1} = \vec{\mathcal{V}}_k - \alpha_k \vec{d}_k$
 - $\vec{r}_{k+1} = \vec{r}_k - \alpha_k \mathbb{G}^T \cdot \vec{d}_k$

- if \vec{r}_{k+1} is sufficiently small ($\|\vec{r}_{k+1}\|_2 / \|\vec{r}_0\|_2 < tol$), then exit loop
- $\beta_k = (r_{k+1}^T r_{k+1}) / (r_k^T r_k)$
- $\vec{p}_{k+1} = \vec{r}_{k+1} + \beta_k \vec{p}_k$
- $k = k + 1$
- return $\vec{\mathcal{P}}_{k+1}$ as result

This iterative algorithm will converge to the solution with a rate which depends on the condition number of the \mathbb{S} matrix, which is not easy to compute since \mathbb{S} is never built. However, it has been established that large viscosity contrasts in the domain will have a negative impact on the convergence.

Remark. This algorithm requires one solve with matrix \mathbb{K} per iteration but says nothing about the method employed to do so (direct solver, iterative solver, ...)

One thing we know improves the convergence of any iterative solver is the use of a preconditioner matrix and therefore now focus on the Preconditioned Conjugate Gradient (PCG) method. Once again a quick Google search yields:

```

r0 := b - Ax0
z0 := M-1r0
p0 := z0
k := 0
repeat
     $\alpha_k := \frac{\mathbf{r}_k^T \mathbf{z}_k}{\mathbf{p}_k^T \mathbf{A} \mathbf{p}_k}$ 
     $\mathbf{x}_{k+1} := \mathbf{x}_k + \alpha_k \mathbf{p}_k$ 
     $\mathbf{r}_{k+1} := \mathbf{r}_k - \alpha_k \mathbf{A} \mathbf{p}_k$ 
    if  $\mathbf{r}_{k+1}$  is sufficiently small then exit loop end if
     $\mathbf{z}_{k+1} := \mathbf{M}^{-1} \mathbf{r}_{k+1}$ 
     $\beta_k := \frac{\mathbf{z}_{k+1}^T \mathbf{r}_{k+1}}{\mathbf{z}_k^T \mathbf{r}_k}$ 
     $\mathbf{p}_{k+1} := \mathbf{z}_{k+1} + \beta_k \mathbf{p}_k$ 
    k := k + 1
end repeat
The result is xk+1

```

Algorithm obtained from Wikipedia⁴⁰.

Note that in the algorithm above the preconditioner matrix M has to be symmetric positive-definite and fixed, i.e., cannot change from iteration to iteration. We see that this algorithm introduces an additional vector \vec{z} and a solve with the matrix M at each iteration, which means that M must be such that solving $M \cdot \vec{x} = \vec{f}$ where \vec{f} is a given rhs vector must be cheap. Ultimately, the PCG algorithm applied to the Schur complement equation takes the form:

solver_pcg:

- compute $\mathcal{V}_0 = \mathbb{K}^{-1}(f - \mathbb{G}\mathcal{P}_0)$
- $r_0 = \mathbb{G}^T \mathcal{V}_0 - h$
- if \vec{r}_0 is sufficiently small, then return $(\vec{\mathcal{V}}_0, \vec{\mathcal{P}}_0)$ as the result
- $\vec{z}_0 = M^{-1} \cdot \vec{r}_0$
- $\vec{p}_0 = \vec{z}_0$
- $k = 0$

⁴⁰https://en.wikipedia.org/wiki/Conjugate_gradient_method

- repeat
 - compute $\tilde{\vec{p}}_k = \mathbb{G} \cdot \vec{p}_k$
 - solve $\mathbb{K} \cdot \vec{d}_k = \tilde{\vec{p}}_k$
 - compute $\alpha_k = (\vec{r}_k^T \cdot \vec{z}_k) / (\tilde{\vec{p}}_k^T \cdot \vec{d}_k)$
 - $\vec{\mathcal{P}}_{k+1} = \mathcal{P}_k + \alpha_k \vec{p}_k$
 - $\vec{\mathcal{V}}_{k+1} = \mathcal{V}_k - \alpha_k \vec{d}_k$
 - $\vec{r}_{k+1} = \vec{r}_k - \alpha_k \mathbb{G}^T \cdot \vec{d}_k$
 - if r_{k+1} is sufficiently small ($\|r_{k+1}\|_2 / \|r_0\|_2 < tol$), then exit loop
 - $\vec{z}_{k+1} = M^{-1} \cdot r_{k+1}$
 - $\beta_k = (\vec{z}_{k+1}^T \cdot \vec{r}_{k+1}) / (\vec{z}_k^T \cdot \vec{r}_k)$
 - $\vec{p}_{k+1} = \vec{z}_{k+1} + \beta_k \vec{p}_k$
 - $k = k + 1$
- return $\vec{\mathcal{P}}_{k+1}$ as result

Following [1769] one can define the following matrix as preconditioner:

$$M = \text{diag} [\mathbb{G}^T (\text{diag}[\mathbb{K}])^{-1} \mathbb{G}]$$

which is the preconditioner used for the Citcom codes (see appendix ??). It can be constructed while the FEM matrix is being built/assembled and it is trivial to invert.

how to compute M for the Schur complement ?

8.15.4 The Augmented Lagrangian approach

see LaCoDe paper [452].

We start from the saddle point Stokes system:

$$\begin{pmatrix} \mathbb{K} & \mathbb{G} \\ \mathbb{G}^T & 0 \end{pmatrix} \cdot \begin{pmatrix} \vec{\mathcal{V}} \\ \vec{\mathcal{P}} \end{pmatrix} = \begin{pmatrix} \vec{f} \\ \vec{h} \end{pmatrix} \quad (505)$$

The AL method consists of subtracting $\lambda^{-1} \mathbb{M}_p \cdot \vec{\mathcal{P}}$ from the left and right-side of the mass conservation equation (where \mathbb{M}_p is the pressure mass matrix) and introducing the following iterative scheme:

$$\begin{pmatrix} \mathbb{K} & \mathbb{G} \\ \mathbb{G}^T & -\lambda^{-1} \mathbb{M}_p \end{pmatrix} \cdot \begin{pmatrix} \vec{\mathcal{V}}^{k+1} \\ \vec{\mathcal{P}}^{k+1} \end{pmatrix} = \begin{pmatrix} \vec{f} \\ \vec{h} - \lambda^{-1} \mathbb{M}_p \cdot \vec{\mathcal{P}}^k \end{pmatrix} \quad (506)$$

where k is the iteration counter and λ is an artificial compressibility term which has the dimensions of dynamic viscosity. The choice of λ can be difficult as too low or too high a value yields either erroneous results and/or terribly ill-conditioned matrices. LaCoDe paper (!! use such a method and report that $\lambda = \max_{\Omega}(\eta)$) works well. Note that at convergence we have $\|\vec{\mathcal{P}}^{k+1} - \vec{\mathcal{P}}^k\| < \epsilon$ and then Eq.(506) converges to Eq.(505) and the velocity and pressure fields are solution of the unmodified system Eq.(505).

The introduction of this term serves one purpose: allowing us to solve the system in a segregated manner (i.e. computing successive iterates of the velocity and pressure fields until convergence is reached). The second line of Eq. (506) is

$$\mathbb{G}^T \cdot \vec{\mathcal{V}}^{k+1} - \lambda^{-1} \mathbb{M}_p \cdot \vec{\mathcal{P}}^{k+1} = \vec{h} - \lambda^{-1} \mathbb{M}_p \cdot \vec{\mathcal{P}}^k$$

and can therefore be rewritten

$$\vec{\mathcal{P}}^{k+1} = \vec{\mathcal{P}}^k + \lambda \mathbb{M}_p^{-1} \cdot (\mathbb{G}^T \cdot \vec{\mathcal{V}}^{k+1} - \vec{h})$$

We can then substitute this expression of $\vec{\mathcal{P}}^{k+1}$ in the first equation. This yields:

$$\mathbb{K} \cdot \vec{\mathcal{V}}^{k+1} = \vec{f} - \mathbb{G} \cdot \vec{\mathcal{P}}^{k+1}) \quad (507)$$

$$\mathbb{K} \cdot \vec{\mathcal{V}}^{k+1} = \vec{f} - \mathbb{G} \cdot (\vec{\mathcal{P}}^k + \lambda \mathbb{M}_p^{-1} \cdot (\mathbb{G}^T \cdot \vec{\mathcal{V}}^{k+1} - \vec{h})) \quad (508)$$

$$\mathbb{K} \cdot \vec{\mathcal{V}}^{k+1} + \lambda \mathbb{G} \cdot \mathbb{M}_p^{-1} \cdot \mathbb{G}^T \cdot \vec{\mathcal{V}}^{k+1} = \vec{f} - \mathbb{G} \cdot (\vec{\mathcal{P}}^k - \lambda \mathbb{M}_p^{-1} \vec{h}) \quad (509)$$

$$\underbrace{(\mathbb{K} + \lambda \mathbb{G} \cdot \mathbb{M}_p^{-1} \cdot \mathbb{G}^T)}_{\tilde{\mathbb{K}}} \cdot \vec{\mathcal{V}}^{k+1} = \underbrace{\vec{f} - \mathbb{G} \cdot (\vec{\mathcal{P}}^k - \lambda \mathbb{M}_p^{-1} \vec{h})}_{\vec{f}^{k+1}} \quad (510)$$

$$(511)$$

The iterative algorithm goes as follows:

1. if it is the first timestep, set $\vec{\mathcal{P}}^0 = 0$, otherwise set it to the pressure of the previous timestep.
2. calculate $\tilde{\mathbb{K}}$
3. calculate \vec{f}^{k+1}
4. solve $\tilde{\mathbb{K}} \cdot \vec{\mathcal{V}}^{k+1} = \vec{f}^{k+1}$
5. update pressure with $\vec{\mathcal{P}}^{k+1} = \vec{\mathcal{P}}^k + \lambda \mathbb{M}_p^{-1} \cdot (\mathbb{G}^T \cdot \vec{\mathcal{V}}^{k+1} - \vec{h})$

Remark. If discontinuous pressures are used, the pressure mass matrix can be inverted element by element which is cheaper than inverting \mathbb{M}_p as a whole.

Remark. This method has obvious ties with the penalty method.

Remark. If $\lambda >> \max_{\Omega} \eta$ then the matrix $\tilde{\mathbb{K}}$ is ill-conditioned and an iterative solver must be used.

8.15.5 The GMRES approach

The Generalized Minimal Residual method [1420] is an extension of MINRES (which is only applicable to symmetric systems) to unsymmetric systems. Like MINRES, it generates a sequence of orthogonal vectors and combines these through a least-squares solve and update. However, in the absence of symmetry this can no longer be done with short recurrences. As a consequence, all previously computed vectors in the orthogonal sequence have to be retained and for this reason "restarted" versions of the method are used.

It must be said that the (preconditioned) GMRES method is actually much more difficult to implement than the (preconditioned) Conjugate Gradient method. However, since it can deal with unsymmetric matrices, it means that it can be applied directly to the Stokes system matrix (as opposed to the CG method which is used on the Schur complement equation).

 Literature: [507, p208] [1419] [79] [54]

finish GMRES algo description, not sure what to do, hard to explain, not easy to code.

8.16 The consistent boundary flux (CBF)

The Consistent Boundary Flux technique was devised to alleviate the problem of the accuracy of primary variables derivatives (mainly velocity and temperature) on boundaries. These derivatives are important since they are needed to compute the heat flux (and therefore the Nusselt number) or dynamic topography and geoid.

The idea was first introduced in [1191] and later used in geodynamics [1758]. It was finally implemented in the CitcomS code [1761, 1215] and more recently in the ASPECT code (dynamic topography postprocessor). Note that the CBF should be seen as a post-processor step as it does not alter the primary variables values.

The CBF method is implemented and used in Stone ???. It is also discussed but not explicitly named in [1361, p309]. Also see [1018, 742, 1141].

8.16.1 The CBF applied to the Stokes equation

We start from the strong form:

$$\vec{\nabla} \cdot \boldsymbol{\sigma} + \vec{b} = \vec{0} \quad (512)$$

and then write the weak form on an element e :

$$\int_{\Omega_e} N_i^y \vec{\nabla} \cdot \boldsymbol{\sigma} d\Omega + \int_{\Omega_e} N_i^y \vec{b} d\Omega = \vec{0} \quad (513)$$

We then use the two equations:

$$\boldsymbol{\nabla} \cdot (N\boldsymbol{\sigma}) = N\boldsymbol{\nabla} \cdot \boldsymbol{\sigma} + \boldsymbol{\nabla}N \cdot \boldsymbol{\sigma} \quad (\text{chain rule})$$

$$\int_{\Omega} (\boldsymbol{\nabla} \cdot \boldsymbol{\sigma}) dV = \int_{\Gamma} \boldsymbol{\sigma} \cdot \mathbf{n} dS \quad (\text{divergence theorem})$$

and integrate by parts in order to obtain:

$$\int_{\Gamma} N_i^y \boldsymbol{\sigma} \cdot \mathbf{n} dS - \int_{\Omega_e} \vec{\nabla} N_i^y \cdot \boldsymbol{\sigma} d\Omega + \int_{\Omega_e} N_i^y \vec{b} d\Omega = \vec{0} \quad (514)$$

and since the traction vector \vec{t} is given by $\vec{t} = \boldsymbol{\sigma} \cdot \mathbf{n}$ we have:

$$\int_{\Gamma_e} N_i^y t dS = \int_{\Omega_e} \vec{\nabla} N_i^y \cdot \boldsymbol{\sigma} d\Omega - \int_{\Omega_e} N_i^y \vec{b} d\Omega \quad (515)$$

The core idea of the method lies in considering the traction vector as an unknown living on the nodes on the boundary, and assuming we have already solved the Stokes equation and therefore have obtained the velocity and pressure.

Finally, since the traction vector can be expressed as a function of the velocity shape functions on the edges i.e.

$$\vec{t} = \sum_{i=1}^m N_i^y \vec{t}_i$$

the left hand term yields an edge (1D) mass matrix M' (see Section I).

Remark. In Stone ??? an alternative to equation 515 is used. Although somewhat inefficient, the elemental matrices \mathbb{K} and \mathbb{G} and the corresponding body force rhs are built and the rhs of the traction equation is computed as follows:

$$M' \cdot \mathcal{T} = -\mathbb{K}\mathcal{V} - \mathbb{G}\mathcal{P} + f$$

where \mathcal{T} is the vector of assembled tractions which we want to compute and \mathcal{V} and \mathcal{T} are the solutions of the Stokes problem.

Remark. The assembled mass matrix is tri-diagonal and can be easily solved with a Conjugate Gradient method.

Remark. With a trapezoidal integration rule (i.e. Gauss-Lobatto - see Section 4.1.6) the matrix can even be diagonalised and the resulting matrix is simply diagonal, which results in a very cheap solve [1758].

8.16.2 The CBF applied to the heat transport equation

We start from the strong form of the heat transfer equation (without the source terms for simplicity):

$$\rho C_p \left(\frac{\partial T}{\partial t} + \vec{v} \cdot \vec{\nabla} T \right) = \vec{\nabla} \cdot k \vec{\nabla} T$$

The weak form then writes:

$$\int_{\Omega} N^{\theta} \rho C_p \frac{\partial T}{\partial t} dV + \rho C_p \int_{\Omega} N^{\theta} \vec{v} \cdot \vec{\nabla} T dV = \int_{\Omega} N^{\theta} \vec{\nabla} \cdot k \vec{\nabla} T dV$$

Using once again integration by parts and divergence theorem:

$$\int_{\Omega} N \rho C_p \frac{\partial T}{\partial t} dV + \rho C_p \int_{\Omega} N \vec{v} \cdot \nabla T dV = \int_{\Gamma} N k \nabla T \cdot \mathbf{n} d\Gamma - \int_{\Omega} \nabla N \cdot k \nabla T dV$$

On the boundary we are interested in the heat flux $\mathbf{q} = -k \nabla T$

$$\int_{\Omega} N \rho C_p \frac{\partial T}{\partial t} dV + \rho C_p \int_{\Omega} N \vec{v} \cdot \nabla T dV = - \int_{\Gamma} N \mathbf{q} \cdot \mathbf{n} d\Gamma - \int_{\Omega} \nabla N \cdot k \nabla T dV$$

or,

$$\int_{\Gamma} N \mathbf{q} \cdot \mathbf{n} d\Gamma = - \int_{\Omega} N \rho C_p \frac{\partial T}{\partial t} dV - \rho C_p \int_{\Omega} N \vec{v} \cdot \nabla T dV - \int_{\Omega} \nabla N \cdot k \nabla T dV$$

Considering the normal heat flux $q_n = \mathbf{q} \cdot \mathbf{n}$ as an unknown living on the nodes on the boundary,

$$q_n = \sum_{i=1}^2 q_{n|i} N_i$$

so that the left hand term becomes a mass matrix for the shape functions living on the boundary. We have already covered the right hand side terms when building the FE system to solve the heat transport equation, so that in the end

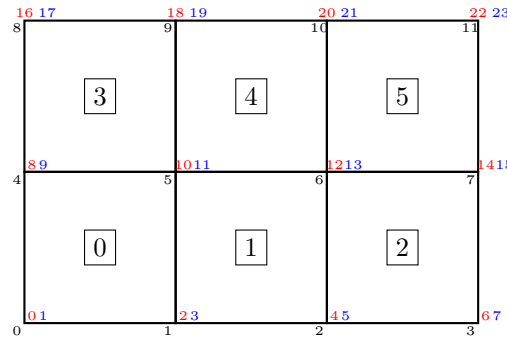
$$M' \cdot \mathcal{Q}_n = -M \cdot \frac{\partial \mathbf{T}}{\partial t} - K_a \cdot \mathbf{T} - K_d \cdot \mathbf{T}$$

where \mathcal{Q}_n is the assembled vector of normal heat flux components. Note that in all terms the assembly only takes place over the elements along the boundary.

Note that the resulting matrix is symmetric.

8.16.3 Some implementation details for the Stokes equation

What follows is relevant for Stone ?? which relies on Q_1 shape functions for the velocity. Let us start with a small example, a 3x2 element FE grid:



Red color corresponds to the dofs in the x direction, blue color indicates a dof in the y direction.

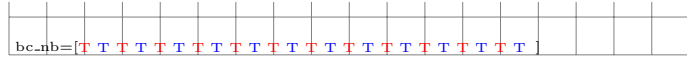
We have nnp=12, nel=6, NfemV=24. Let us assume that free slip boundary conditions are applied. The boundary conditions `fix_bc` array is then:

```
bc_fix=[T T T T T T T T T T T T T T T T T T ]
```

Note that since corners belong to two edges, we effectively prescribed no-slip boundary conditions on those.

[why does array contain only T??](#)

We wish to compute the tractions on the boundaries, and more precisely for the dofs for which a Dirichlet velocity boundary condition has been prescribed. The number of (traction) unknowns NfemTr is then the number of T in the bc_fix array. In our specific case, we have NfemTr=. This means that we need for each targeted dof to be able to find its identity/number between 0 and NfemTr-1. We therefore create the array bc_nb which is filled as follows:



This translates as follows in the code:

```
NfemTr=np.sum(bc_fix)
bc_nb=np.zeros(NfemV,dtype=np.int32)
counter=0
for i in range(0,NfemV):
    if (bc_fix[i]):
        bc_nb[i]=counter
        counter+=1
```

The algorithm is then as follows

- A Prepare two arrays to store the matrix M_{cbf} and its right hand side rhs_{cbf}
- B Loop over all elements
- C For each element touching a boundary, compute the residual vector $R_{el} = -f_{el} + \mathbb{K}_{el}\mathcal{V}_{el} + \mathbb{G}_{el}\mathcal{P}_{el}$
- D Loop over the four edges of the element using the connectivity array
- E For each edge loop over the number of degrees of freedom (2 in 2D)
- F For each edge assess whether the dofs on both ends are target dofs.
- G If so, compute the mass matrix M_{edge} for this edge
- H Extract the 2 values off the element residual vector and assemble these in rhs_{cbf}
- I Assemble M_{edge} into NfemTrxNfemTr matrix using bc_nb

```
M_cbf = np.zeros((NfemTr,NfemTr),np.float64) # A
rhs_cbf = np.zeros(NfemTr,np.float64)

for iel in range(0,nel): # B
    ... compute elemental residual ... # C

    #boundary 0-1 # D
    for i in range(0,ndofV): # E
        idof0=2*icon[0,iel]+i
        idof1=2*icon[1,iel]+i
        if (bc_fix[idof0] and bc_fix[idof1]): # F
            idofTr0=bc_nb[idof0]
            idofTr1=bc_nb[idof1]
            rhs_cbf[idofTr0]+=res_el[0+i] # H
            rhs_cbf[idofTr1]+=res_el[2+i]
            M_cbf[idofTr0,idofTr0]+=M_edge[0,0] # I
            M_cbf[idofTr0,idofTr1]+=M_edge[0,1]
            M_cbf[idofTr1,idofTr0]+=M_edge[1,0]
            M_cbf[idofTr1,idofTr1]+=M_edge[1,1] # I

    #boundary 1-2 # [D]
```

...	
#boundary 2-3	$\#[D]$
...	
#boundary 3-0	$\#[D]$
...	

8.17 The value of the timestep

The chosen time step δt used for time integration is chosen to comply with the Courant-Friedrichs-Lowy condition [31].

$$\delta t = C \min \left(\frac{h}{\max |\mathbf{v}|}, \frac{h^2}{\kappa} \right) \quad (516)$$

where h is a measure of the element size, $\kappa = k/\rho C_p$ is the thermal diffusivity and C is the so-called CFL number chosen in $[0, 1]$.

In essence the CFL condition arises when solving hyperbolic PDEs . It limits the time step in many explicit time-marching computer simulations so that the simulation does not produce incorrect results.

This condition is not needed when solving the Stokes equation but it is mandatory when solving the heat transport equation or any kind of advection-diffusion equation. Note that any increase of grid resolution (i.e. h becomes smaller) yields an automatic decrease of the time step value.

8.18 Mappings

The name isoparametric derives from the fact that the same ('iso') functions are used as basis functions and for the mapping to the reference element.

More generally, if n_e denotes the number of nodes of an element and n_g denotes the number of nodes describing the geometry of the element, then the element is termed subparametric when $n_g < n_e$ and superparametric when $n_g > n_e$.

8.18.1 Linear mapping on a triangle

```

2
|\      s
| \    |_x
|  \
3==1

```

Let us assume that the coordinates of the vertices are (x_1, y_1) , (x_2, y_2) , and (x_3, y_3) . The coordinates inside the reference element are (r, s) . We then simply have the following relationship, i.e. any point of the reference element can be mapped to the physical triangle as follows:

$$x = rx_1 + sx_2 + (1 - r - s)x_3 \quad (517)$$

$$y = ry_1 + sy_2 + (1 - r - s)y_3 \quad (518)$$

There is also an inverse map, which is easily computed:

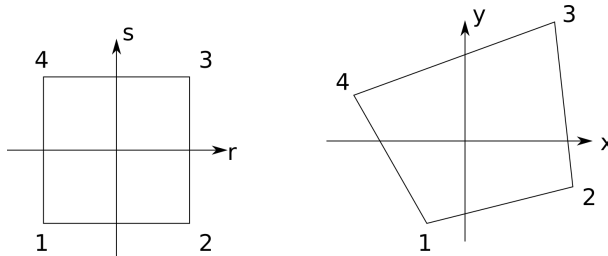
$$r = \frac{(y_2 - y_3)(x - x_3) - (x_2 - x_3)(y - y_3)}{(x_1 - x_3)(y_2 - y_3) - (y_1 - y_3)(x_2 - x_3)} \quad (519)$$

$$s = \frac{-(y_1 - y_3)(x - x_3) + (x_1 - x_3)(y - y_3)}{(x_1 - x_3)(y_2 - y_3) - (y_1 - y_3)(x_2 - x_3)} \quad (520)$$

Remark. The denominator will not vanish, because it is a multiple of the area of the triangle.

8.18.2 Bilinear mapping on a linear quadrilateral

The is in the (r, s) space. It is a square of size 2×2 centered around the origin. We wish to map it to the quadrilateral in the (x, y) space:



The coordinates of the vertices are (x_1, y_1) , (x_2, y_2) , (x_3, y_3) and (x_4, y_4) . We then simply have the following relationship, i.e. any point of the reference element can be mapped to the physical quadrilateral as follows:

$$x = N_1(r, s)x_1 + N_2(r, s)x_2 + N_3(r, s)x_3 + N_4(r, s)x_4 \quad (521)$$

$$y = N_1(r, s)y_1 + N_2(r, s)y_2 + N_3(r, s)y_3 + N_4(r, s)y_4 \quad (522)$$

where the shape functions $N_i(r, s)$ are defined in section 4.4.

In the following example the program randomly generates 10000 points inside the reference element and computes their mapping into the (x, y) space.

```

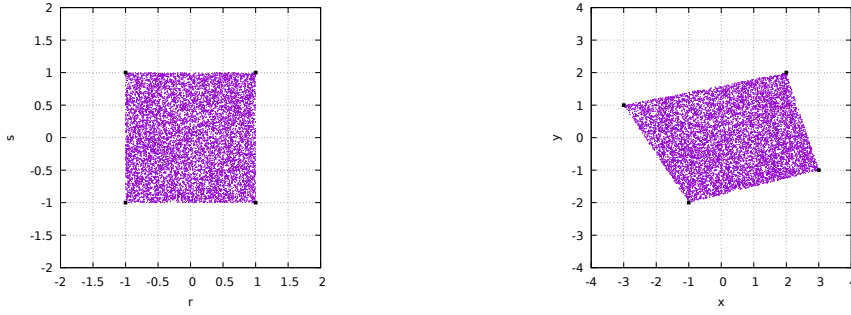
x1=-1 ; y1=-2
x2=3 ; y2=-1
x3=2 ; y3=2
x4=-3 ; y4=1

npts=10000
r=np.zeros(npts,dtype=np.float64)
s=np.zeros(npts,dtype=np.float64)
x=np.zeros(npts,dtype=np.float64)
y=np.zeros(npts,dtype=np.float64)

for i in range(0,npts):
    # compute random r,s coordinates
    r[i]=random.uniform(-1.,+1)
    s[i]=random.uniform(-1.,+1)
    # compute basis function values at r,s
    N1=0.25*(1-r[i])*(1-s[i])
    N2=0.25*(1+r[i])*(1-s[i])
    N3=0.25*(1+r[i])*(1+s[i])
    N4=0.25*(1-r[i])*(1+s[i])
    # compute x,y coordinates
    x[i]=N1*x1+N2*x2+N3*x3+N4*x4
    y[i]=N1*y1+N2*y2+N3*y3+N4*y4

np.savetxt('rs.ascii',np.array([r,s]).T)
np.savetxt('xy.ascii',np.array([x,y]).T)

```



There is also an inverse map, which is not so easily computed (see section 8.21). However, if the quadrilateral in the (x, y) space is a rectangle of size (h_x, h_y) , the inverse mapping is trivial:

$$r = \frac{x - x_1}{x_2 - x_1} \quad (523)$$

$$s = \frac{y - y_1}{y_4 - y_1} \quad (524)$$

Also in this case the shape functions can easily be written as functions of (x, y) :

$$\begin{aligned} N_1(x, y) &= \left(\frac{x_3 - x}{h_x} \right) \left(\frac{y_3 - y}{h_y} \right) \\ N_2(x, y) &= \left(\frac{x - x_1}{h_x} \right) \left(\frac{y_3 - y}{h_y} \right) \\ N_3(x, y) &= \left(\frac{x - x_1}{h_x} \right) \left(\frac{y - y_1}{h_y} \right) \\ N_4(x, y) &= \left(\frac{x_3 - x}{h_x} \right) \left(\frac{y - y_1}{h_y} \right) \end{aligned}$$

On the one hand, any variable defined on the element can be approximated using the shape functions:

$$f_h(r, s) = \sum_i N_i(r, s) f_i. \quad (525)$$

If we treat the coordinate variables x and y themselves as functions, then the shape functions can be used to construct the mapping:

$$x(r, s) = \sum_i N_i(r, s)x_i \quad y(r, s) = \sum_i N_i(r, s)y_i, \quad (526)$$

leading to write

$$\frac{\partial x}{\partial r} = \sum_i \frac{\partial N_i}{\partial r} x_i \quad (527)$$

$$\frac{\partial x}{\partial s} = \sum_i \frac{\partial N_i}{\partial s} x_i \quad (528)$$

$$\frac{\partial y}{\partial r} = \sum_i \frac{\partial N_i}{\partial r} y_i \quad (529)$$

$$\frac{\partial y}{\partial s} = \sum_i \frac{\partial N_i}{\partial s} y_i \quad (530)$$

On the other hand we also have

$$\frac{\partial f}{\partial r} = \frac{\partial f}{\partial x} \frac{\partial x}{\partial r} + \frac{\partial f}{\partial y} \frac{\partial y}{\partial r} \quad (531)$$

$$\frac{\partial f}{\partial s} = \frac{\partial f}{\partial x} \frac{\partial x}{\partial s} + \frac{\partial f}{\partial y} \frac{\partial y}{\partial s} \quad (532)$$

or in matrix form:

$$\begin{pmatrix} \frac{\partial f}{\partial r} \\ \frac{\partial f}{\partial s} \end{pmatrix} = \underbrace{\begin{pmatrix} \frac{\partial x}{\partial r} & \frac{\partial y}{\partial r} \\ \frac{\partial x}{\partial s} & \frac{\partial y}{\partial s} \end{pmatrix}}_{J} \cdot \begin{pmatrix} \frac{\partial f}{\partial x} \\ \frac{\partial f}{\partial y} \end{pmatrix}$$

where J is called the Jacobian of the transformation. By inverting the Jacobian matrix, the desired derivatives with respect to x and y can be obtained:

We have:

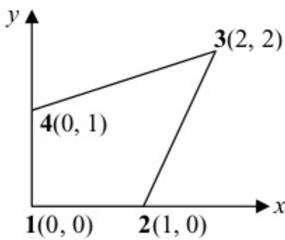
$$\begin{pmatrix} \frac{\partial f}{\partial x} \\ \frac{\partial f}{\partial y} \end{pmatrix} = J^{-1} \cdot \begin{pmatrix} \frac{\partial f}{\partial r} \\ \frac{\partial f}{\partial s} \end{pmatrix}$$

The inverse of the Jacobian matrix can be simply obtained in 2D (Kramer's rule for 2×2 matrices):

$$J^{-1} = \frac{1}{|J|} \begin{pmatrix} \frac{\partial y}{\partial s} & -\frac{\partial y}{\partial r} \\ -\frac{\partial x}{\partial s} & \frac{\partial x}{\partial r} \end{pmatrix}$$

The presence of the determinant in the denominator implies that it cannot be zero anywhere, or in other words: the mapping is not valid if $|J|$ is zero anywhere over the element.

Let us look at this by means of a simple example and let us consider the following element:



Then a Q_1 mapping yields:

$$x(r, s) = \sum_i N_i(r, s)x_i = N_2 + 2N_3 = \frac{1}{4}(3 + 3r + s + rt) \quad (533)$$

$$y(r, s) = \sum_i N_i(r, s)y_i = 2N_3 + N_4 = \frac{1}{4}(3 + r + 3s + rt) \quad (534)$$

The Jacobian matrix is then

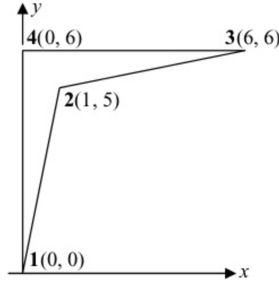
$$\mathbf{J} = \begin{pmatrix} \frac{\partial x}{\partial r} & \frac{\partial x}{\partial s} \\ \frac{\partial y}{\partial r} & \frac{\partial y}{\partial s} \end{pmatrix} = \frac{1}{4} \begin{pmatrix} 3+s & 1+s \\ 1+r & 3+r \end{pmatrix}$$

and its determinant is

$$|\mathbf{J}| = \frac{1}{4}[(3+s)(3+r) - (1+s)(1+r)] = \frac{1}{2} + \frac{1}{8}r + \frac{1}{8}s \quad (535)$$

It is clear that $|\mathbf{J}| > 0$ for $-1 \leq r \leq +1$ and $-1 \leq s \leq +1$.

Let us now consider another example, the following element:



It follows that

$$x(r, s) = \sum_i N_i(r, s)x_i = \frac{1}{4}(1+r)(7+5s) \quad (536)$$

$$y(r, s) = \sum_i N_i(r, s)y_i = \frac{1}{4}(17+5r+7s-5rs) \quad (537)$$

and the determinant:

$$|\mathbf{J}| = \frac{3}{2} - \frac{15r}{4} + \frac{15s}{4}$$

is zero for $r - s = 2/5$. This mapping is invalid!

Remark. Problems also arise when the Jacobian matrix is nearly singular due to round-off errors. To avoid problems linked to badly shaped elements, it is recommended that the inside angles of an element are larger than 15° and less than 165° .

From Eq. 526, we can also write:

$$dx = \frac{\partial x}{\partial r}dr + \frac{\partial x}{\partial s}ds \quad (538)$$

$$dy = \frac{\partial y}{\partial r}dr + \frac{\partial y}{\partial s}ds \quad (539)$$

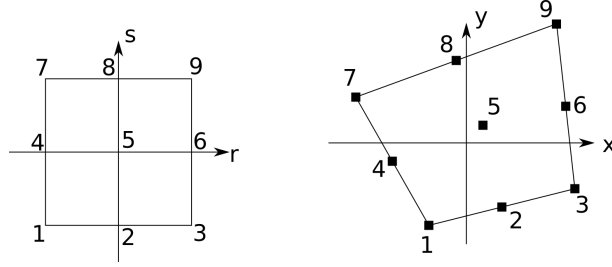
, or,

$$\begin{pmatrix} dx \\ dy \end{pmatrix} = \mathbf{J} \cdot \begin{pmatrix} dr \\ ds \end{pmatrix} \quad (540)$$

This means that

$$\int \int \dots dx dy = \int \int \dots |\mathbf{J}| dr ds \quad (541)$$

8.18.3 biquadratic mapping of a straight-line face Q_2 element



The reference element now contains 9 nodes: 1,3,7,9 are the corners, nodes 2,4,6,8 are the mid-face points and node 5 is in the middle. The mapping from the (r, s) space to the (x, y) space is then as follows:

$$\begin{aligned} \begin{pmatrix} x(r, s) \\ y(r, s) \end{pmatrix} &= N_1(r, s) \begin{pmatrix} x_1 \\ y_1 \end{pmatrix} + N_2(r, s) \begin{pmatrix} x_2 \\ y_2 \end{pmatrix} + N_3(r, s) \begin{pmatrix} x_3 \\ y_3 \end{pmatrix} + N_4(r, s) \begin{pmatrix} x_4 \\ y_4 \end{pmatrix} \\ &+ N_5(r, s) \begin{pmatrix} x_5 \\ y_5 \end{pmatrix} + N_6(r, s) \begin{pmatrix} x_6 \\ y_6 \end{pmatrix} + N_7(r, s) \begin{pmatrix} x_7 \\ y_7 \end{pmatrix} + N_8(r, s) \begin{pmatrix} x_8 \\ y_8 \end{pmatrix} \\ &+ N_9(r, s) \begin{pmatrix} x_9 \\ y_9 \end{pmatrix} \end{aligned}$$

where

$$\begin{aligned} N_1(r, t) &= 0.5r(r-1)0.5t(t-1) \\ N_2(r, t) &= (1-r^2)0.5t(t-1) \\ N_3(r, t) &= 0.5r(r+1)0.5t(t-1) \\ N_4(r, t) &= 0.5r(r-1)(1-t^2) \\ N_5(r, t) &= (1-r^2)(1-t^2) \\ N_6(r, t) &= 0.5r(r+1)(1-t^2) \\ N_7(r, t) &= 0.5r(r-1)0.5t(t+1) \\ N_8(r, t) &= (1-r^2)0.5t(t+1) \\ N_9(r, t) &= 0.5r(r+1)0.5t(t+1) \end{aligned}$$

```

x1=-1 ; y1=-2
x3=3 ; y3=-1
x9=2 ; y9=2
x7=-3 ; y7=1
x2=0.5*(x1+x3) ; y2=0.5*(y1+y3)
x4=0.5*(x1+x7) ; y4=0.5*(y1+y7)
x6=0.5*(x3+x9) ; y6=0.5*(y3+y9)
x8=0.5*(x7+x9) ; y8=0.5*(y7+y9)
x5=0.25*(x1+x3+x7+x9) ; y5=0.25*(y1+y3+y7+y9)

npts=10000
r=np.zeros( npts , dtype=np.float64 )
s=np.zeros( npts , dtype=np.float64 )
xQ1=np.zeros( npts , dtype=np.float64 )
yQ1=np.zeros( npts , dtype=np.float64 )
xQ2=np.zeros( npts , dtype=np.float64 )
yQ2=np.zeros( npts , dtype=np.float64 )

for i in range(0,npts):
    # compute random r, s coordinates
    r[ i ]=random.uniform(-1.,+1)
    s[ i ]=random.uniform(-1.,+1)
    # compute Q2 basis function values at r, s
    N1= 0.5*r[ i ]*( r[ i ]-1. ) * 0.5*s[ i ]*( s[ i ]-1. )

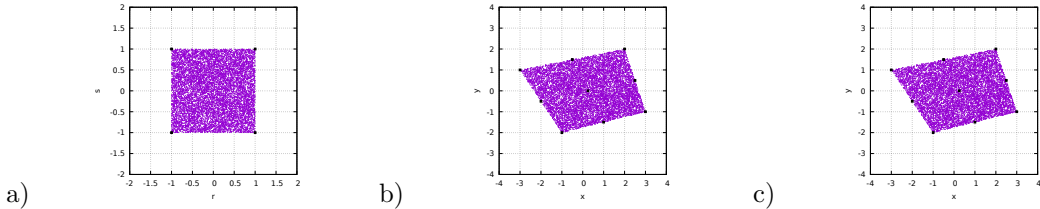
```

```

N2=      (1.-r[i]**2) * 0.5*s[i]*(s[i]-1.)
N3= 0.5*r[i]*(r[i]+1.) * 0.5*s[i]*(s[i]-1.)
N4= 0.5*r[i]*(r[i]-1.) *          (1.-s[i]**2)
N5=      (1.-r[i]**2) *          (1.-s[i]**2)
N6= 0.5*r[i]*(r[i]+1.) *          (1.-s[i]**2)
N7= 0.5*r[i]*(r[i]-1.) * 0.5*s[i]*(s[i]+1.)
N8=      (1.-r[i]**2) * 0.5*s[i]*(s[i]+1.)
N9= 0.5*r[i]*(r[i]+1.) * 0.5*s[i]*(s[i]+1.)
# compute x, y coordinates
xQ2[i]=N1*x1+N2*x2+N3*x3+N4*x4+N5*x5+N6*x6+N7*x7+N8*x8+N9*x9
yQ2[i]=N1*y1+N2*y2+N3*y3+N4*y4+N5*y5+N6*y6+N7*y7+N8*y8+N9*y9
# compute Q1 basis function values at r, s
N1=0.25*(1-r[i])*(1-s[i])
N2=0.25*(1+r[i])*(1-s[i])
N3=0.25*(1+r[i])*(1+s[i])
N4=0.25*(1-r[i])*(1+s[i])
# compute x, y coordinates
xQ1[i]=N1*x1+N2*x3+N3*x9+N4*x7
yQ1[i]=N1*y1+N2*y3+N3*y9+N4*y7

np.savetxt('rs.ascii',np.array([r,s]).T)
np.savetxt('xyQ1.ascii',np.array([xQ1,yQ1]).T)
np.savetxt('xyQ2.ascii',np.array([xQ2,yQ2]).T)

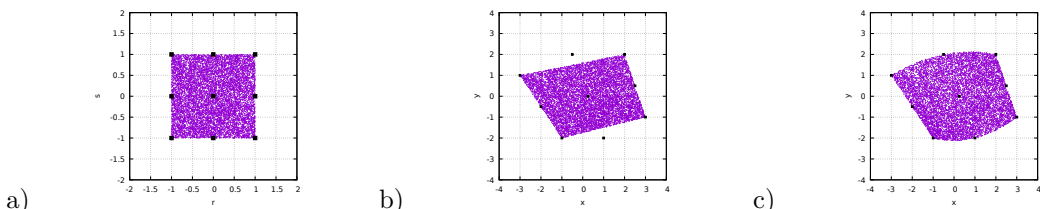
```



a) 10,000 random points in the reference element; b,c) image of these points by means of a bilinear and biquadratic mapping respectively. When the sides of the element are straight we see that a Q_1 mapping is sufficient.

8.18.4 biquadratic mapping of a not-so straight-line face Q_2 element

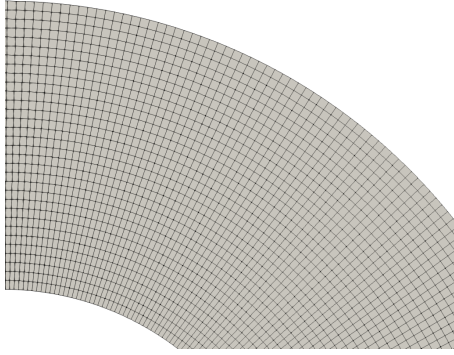
We now carry out the same exercise as before but nodes 2 and 8 are no more in the middle of nodes 1-3 and 7-9 respectively.



a) 10,000 random points in the reference element; b,c) image of these points by means of a bilinear and biquadratic mapping respectively. In this case we see that the Q_2 mapping manages to capture the 'real' shape of the element.

8.18.5 bilinear, biquadratic and bicubic mapping in an annulus

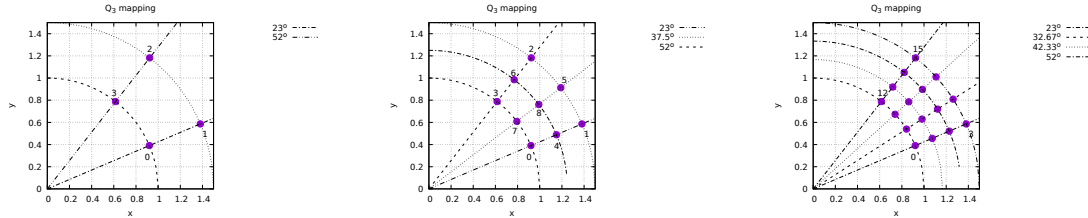
In the light of what precedes, we can now ask ourselves how this translates to a real geodynamic cas. Let us then consider the case of an annular domain, a cross section of a hollow sphere. When using quadrilateral elements, the mesh will look similar to this:



We here focus on Q_1 , Q_2 and Q_3 mappings. We single out an element, and arbitrarily define it as follows in polar coordinates:

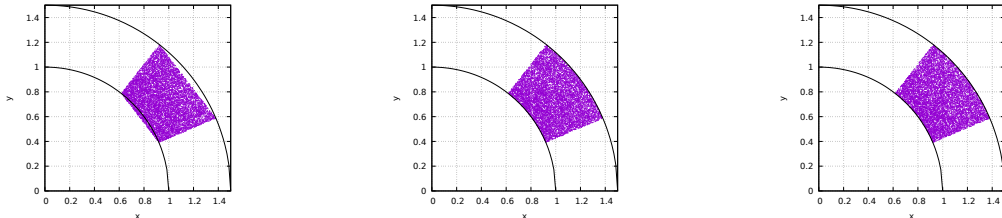
```
theta1=23./180.*np.pi
theta2=52./180.*np.pi
R1=1.
R2=1.5
```

The Q_1 mapping requires four points, the Q_2 nine points and the Q_3 sixteen points. These are placed equidistantly in the r, θ coordinate system, as shown hereunder:



Left to right: position of the nodes for the Q_1 , Q_2 and Q_3 mappings.

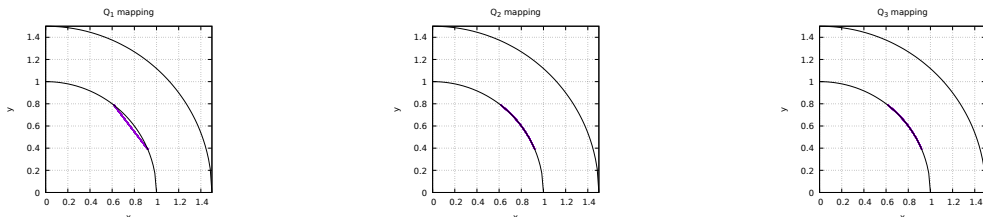
As before, we randomly shoot 10,000 points inside the reference element and map these out in the x, y space. Resulting swarms of points are shown in the following figures:



Left to right: position of the mapped points for the Q_1 , Q_2 and Q_3 mappings.

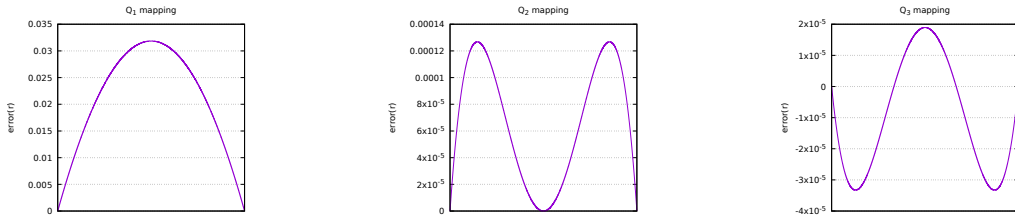
The image of a square with a Q_1 mapping is obviously a quadrilateral so that it looks like quite a few points land outside of the domain $R_1 \leq r \leq R_2$. Note that points are well within $23^\circ \leq \theta \leq 52^\circ$, which can simply be explained by the fact that the faces of the element are straight lines.

However, it looks like the biquadratic and bicubic mappings are doing a much better job at mapping the region of space $R_1 \leq r \leq R_2$. In order to characterise this better, we now place 10,000 points on the bottom face of the reference element (i.e. $s = -1$) and once again compute their coordinates in the the x, y space:



Left to right: position of the mapped points for the Q_1 , Q_2 and Q_3 mappings.

For each point i we now compute ist distance r_i to the origin, which, if the mapping was perfect, whould be exactly equal to $R_1 = 1$. On the following plots are shown the error $r_i - 1$ for all points, from $r = -1$ to $r = +1$.



Left to right: radius error of the mapped points for the Q_1 , Q_2 and Q_3 mappings.

We see that the amplitude of the error decreases with the order of the mapping used, which is why for instance ASPECT uses a Q_4 mapping by default. Actually, in this particular case, the equation which describes the cirle is not a polynomial so that no high-order mapping will ever be able to *exactly* represent the curved boundary of the element!

Another interesting point to keep in mind is that the location of the quadrature points in the x, y space is also determined by the mapping used, which can have consequences on the accuracy of the integration and it will be reflected (for instance) on the error convergence rate.

Finally, the coordinates of the nodes of the element in the x, y are uniquely determined when they are on the convex hull of the element (for instance nodes 0-7 for Q_2) but we need to choose the position of the last nodes which are inside the element. Unfortunately, this choice is not neutral.

re ask Wolfgang about this - correlate with deal.II

8.19 Exporting data to vtk format

This format seems to be the universally accepted format for 2D and 3D visualisation in Computational Geodynamics. Such files can be opened with free softwares such as Paraview⁴¹, MayaVi⁴² or Visit⁴³.

Unfortunately it is my experience that no simple tutorial exists about how to build such files. There is an official document which describes the vtk format⁴⁴ but it delivers the information in a convoluted way. I therefore describe hereafter how **fieldstone** builds the vtk files.

I hereunder show vtk file corresponding to the 3x2 grid presented earlier ???. In this particular example there are:

- 12 nodes and 6 elements
- 1 elemental field: the pressure p)
- 2 nodal fields: 1 scalar (the smoothed pressure q), 1 vector (the velocity field $u, v, 0$)

Note that vtk files are inherently 3D so that even in the case of a 2D simulation the z -coordinate of the points and for instance their z -velocity component must be provided. The file, usually called *solution.vtu* starts with a header:

```
<VTKFile type='UnstructuredGrid' version='0.1' byte_order='BigEndian'>
<UnstructuredGrid>
<Piece NumberOfPoints='12' NumberOfCells='6'>
```

We then proceed to write the node coordinates as follows:

```
<Points>
<DataArray type='Float32' NumberOfComponents='3' Format='ascii'>
0.000000e+00 0.000000e+00 0.000000e+00
3.333333e-01 0.000000e+00 0.000000e+00
6.666667e-01 0.000000e+00 0.000000e+00
1.000000e+00 0.000000e+00 0.000000e+00
0.000000e+00 5.000000e-01 0.000000e+00
3.333333e-01 5.000000e-01 0.000000e+00
6.666667e-01 5.000000e-01 0.000000e+00
1.000000e+00 5.000000e-01 0.000000e+00
0.000000e+00 1.000000e+00 0.000000e+00
3.333333e-01 1.000000e+00 0.000000e+00
6.666667e-01 1.000000e+00 0.000000e+00
1.000000e+00 1.000000e+00 0.000000e+00
</DataArray>
</Points>
```

These are followed by the elemental field(s):

```
<CellData Scalars='scalars'>
<DataArray type='Float32' Name='p' Format='ascii'>
-1.333333e+00
-3.104414e-10
1.333333e+00
-1.333333e+00
8.278417e-17
1.333333e+00
</DataArray>
</CellData>
```

Nodal quantities are written next:

```
<PointData Scalars='scalars'>
<DataArray type='Float32' NumberOfComponents='3' Name='velocity' Format='ascii'>
0.000000e+00 0.000000e+00 0.000000e+00
0.000000e+00 0.000000e+00 0.000000e+00
0.000000e+00 0.000000e+00 0.000000e+00
0.000000e+00 0.000000e+00 0.000000e+00
```

⁴¹<https://www.paraview.org/>

⁴²<https://docs.enthought.com/mayavi/mayavi/>

⁴³<https://wci.llnl.gov/simulation/computer-codes/visit/>

⁴⁴<https://www.vtk.org/wp-content/uploads/2015/04/file-formats.pdf>

```

0.000000e+00 0.000000e+00 0.000000e+00
8.888885e-08 -8.278405e-24 0.000000e+00
8.888885e-08 1.655682e-23 0.000000e+00
0.000000e+00 0.000000e+00 0.000000e+00
1.000000e+00 0.000000e+00 0.000000e+00
</DataArray>
<DataArray type='Float32' NumberOfComponents='1' Name='q' Format='ascii'>
-1.333333e+00
-6.666664e-01
6.666664e-01
1.333333e+00
-1.333333e+00
-6.666664e-01
6.666664e-01
1.333333e+00
-1.333333e+00
-6.666664e-01
6.666664e-01
1.333333e+00
</DataArray>
</PointData>

```

To these informations we must append 3 more datasets. The first one is the connectivity, the second one is the offsets and the third one is the type. The first one is trivial since said connectivity is needed for the Finite Elements. The second must be understood as follows: when reading the connectivity information in a linear manner the offset values indicate the beginning of each element (omitting the zero value). The third simply is the type of element as given in the vtk format document (9 corresponds to a generic quadrilateral with an internal numbering consistent with ours).

```

<Cells>
<DataArray type='Int32' Name='connectivity' Format='ascii'>
0 1 5 4
1 2 6 5
2 3 7 6
4 5 9 8
5 6 10 9
6 7 11 10
</DataArray>
<DataArray type='Int32' Name='offsets' Format='ascii'>
4
8
12
16
20
24
</DataArray>
<DataArray type='Int32' Name='types' Format='ascii'>
9
9
9
9
9
9
</DataArray>
</Cells>

```

The file is then closed with

```

</Piece>
</UnstructuredGrid>
</VTKFile>

```

The *solution.vtu* file can then be opened with ParaView, MayaVi or Visit and the reader is advised to find tutorials online on how to install and use these softwares.

8.20 Runge-Kutta methods

These methods were developed around 1900 by the German mathematicians Carl Runge and Martin Kutta. The RK methods are methods for the numerical integration of ODEs⁴⁵. These methods are well documented in any numerical analysis textbook and the reader is referred to [656, 885]. Any Runge-Kutta method is uniquely identified by its Butcher tableau (REF?) which contains all necessary coefficients to build the algorithm.

The simplest RungeKutta method is the (forward) Euler method. Its tableau is:

0				
	1			

The standard second-order RK method method (also called midpoint method) is:

0				
1/2	1/2			
		0	1	

Another second-order RK method, called Heun's method⁴⁶ is follows:

0				
1	1			
		1/2	1/2	

A third-order RK method is as follows:

0				
1/2	1/2			
1	-1	2		
			1/6	4/6
				1/6

The RK4 method falls in this framework. Its tableau is:

0				
1/2	1/2			
1/2	0	1/2		
1	0	0	1	
	1/6	1/6	1/3	1/6

A slight variation of the standard RK4 method is also due to Kutta in 1901 and is called the 3/8-rule. Almost all of the error coefficients are smaller than in the standard method but it requires slightly more FLOPs per time step. Its Butcher tableau is

0				
1/3	1/3			
2/3	-1/3	1		
1	1	-1	1	
	1/8	3/8	3/8	1/8

The following method is called the Runge-Kutta-Fehlberg method and is commonly abbreviated RKF45⁴⁷. Its Butcher tableau is as follows:

⁴⁵https://en.wikipedia.org/wiki/Runge-Kutta_methods

⁴⁶https://en.wikipedia.org/wiki/Heun%27s_method

⁴⁷https://en.wikipedia.org/wiki/Runge-Kutta-Fehlberg_method

0						
1/4	1/4					
3/8	3/32	9/32				
12/13	1932/2197	-7200/2197	7296/2197			
1	439/216	-8	3680/513	-845/4104		
1/2	-8/27	2	-3544/2565	1859/4104	-11/40	
	16/135	0	6656/12825	28561/56430	-9/50	2/55
	25/216	0	1408/2565	2197/4104	-1/5	0

The first row of coefficients at the bottom of the table gives the fifth-order accurate method, and the second row gives the fourth-order accurate method.

 Literature[548, 778, 474, 475, 1322]

8.20.1 Using RK methods to advect particles/markers

In the context of geodynamical modelling, one is usually confronted to the following problem: now that I have a velocity field on my FE mesh, how can I use it to advect the Lagrangian markers?

Runge-Kutta methods are used to this effect but only their spatial component is used: the velocity solution is not recomputed at the intermediate fractional timesteps, i.e. only the coefficients of the right hand side of the tableaus is used.

The RK1 method is simple. Carry out a loop over markers and

1. interpolate velocity \vec{v}_m onto each marker m
2. compute new position as follows: $\vec{r}_m(t + \delta t) = \vec{r}_m(t) + \vec{v}_m \delta t$

The RK2 method is also simple but requires a bit more work. Carry out a loop over markers and

1. interpolate velocity \vec{v}_m onto each marker m at position \vec{r}_m
2. compute new intermediate position as follows: $\vec{r}_m^{(1)}(t + \delta t) = \vec{r}_m(t) + \vec{v}_m \delta t / 2$
3. compute velocity $\vec{v}_m^{(1)}$ at position $\vec{r}_m^{(1)}$
4. compute new position: $\vec{r}_m(t + \delta t) = \vec{r}_m(t) + \vec{v}_m^{(1)} \delta t$

Note that the intermediate positions could be in a different element of the mesh so extra care must be taken when computing intermediate velocities.

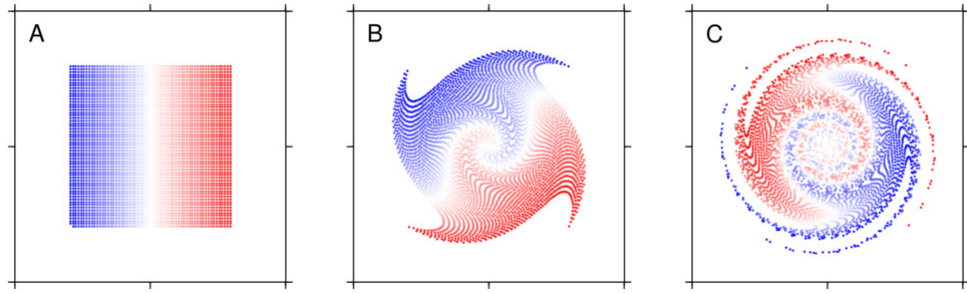
The RK3 method introduces two intermediate steps. Carry out a loop over markers and

1. interpolate velocity \vec{v}_m onto each marker m at position \vec{r}_m
2. compute new intermediate position as follows: $\vec{r}_m^{(1)}(t + \delta t) = \vec{r}_m(t) + \vec{v}_m \delta t / 2$
3. compute velocity $\vec{v}_m^{(1)}$ at position $\vec{r}_m^{(1)}$
4. compute new intermediate position as follows: $\vec{r}_m^{(2)}(t + \delta t) = \vec{r}_m(t) + (2\vec{v}_m^{(1)} - \vec{v}_m) \delta t / 2$
5. compute velocity $\vec{v}_m^{(2)}$ at position $\vec{r}_m^{(2)}$
6. compute new position: $\vec{r}_m(t + \delta t) = \vec{r}_m(t) + (\vec{v}_m + 4\vec{v}_m^{(1)} + \vec{v}_m^{(2)}) \delta t / 6$

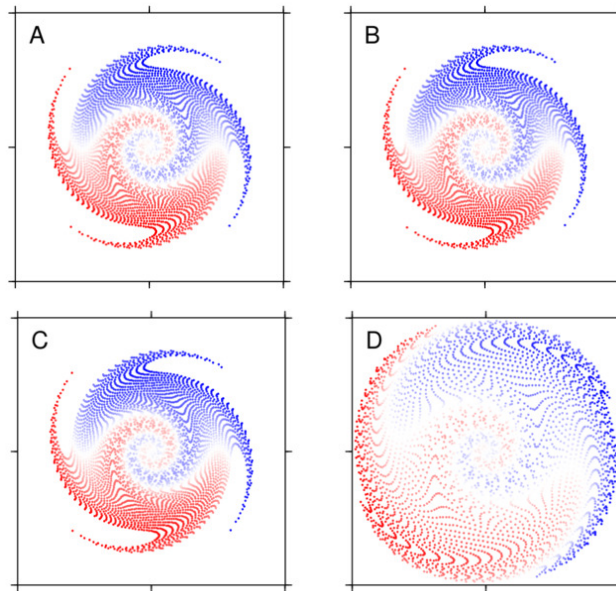
The following example is borrowed from [1113], itself borrowed from Fullsack [614, Section 5.4]. It is a whirl flow [1286], a flow with rotational symmetry in which concentric layers of material rotate around a centre with an angular velocity:

$$\omega(r) = \omega_0 \frac{r}{r_0} \exp\left(-\frac{r}{r_0}\right)$$

The box is $[-0.5, 0.5] \times [-0.5, 0.5]$, $r_0 = 0.25$, $\omega_0 = 0.3$ and $\delta t = 1$. 60×60 particles are regularly positioned inside the $[-0.3, 0.3] \times [-0.3, 0.3]$ square. Maierova [1113] has carried out this experiment for the above Runge-Kutta methods.



Model domain with particles colored at three different time-steps: (A) $t = 0$ (initial position of particles), (B) $t = 50$, and (C) $t = 200$. The advection is computed using the fourth-order Runge-Kutta scheme. Taken from [1113]



The same plot as above, but for different advection schemes at $t = 100$. Advection was computed using (A) the fourth-order Runge-Kutta scheme, (B) the mid-point method, (C) Heuns method and (D) the explicit Euler method. Taken from [1113]

(BSc Thesis)

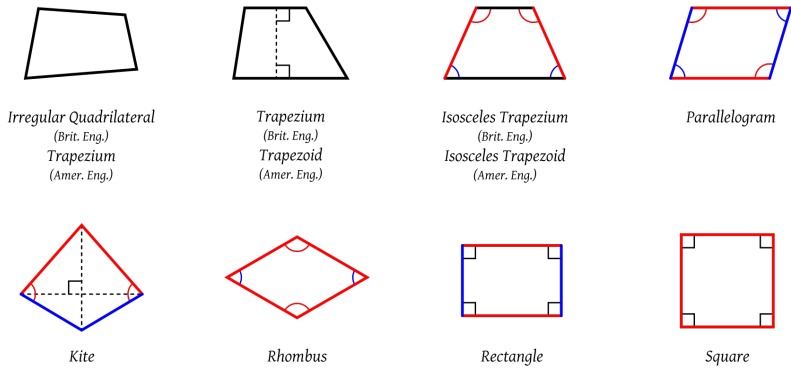
8.21 Am I in or not? - finding reduced coordinates

It is quite common that at some point one must answer the question: "Given a mesh and its connectivity on the one hand, and the coordinates of a point on the other, how do I accurately and quickly determine in which element the point resides?"

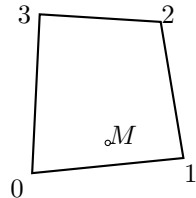
One typical occurrence of such a problem is linked to the use of the Particle-In-Cell technique: particles are advected and move through the mesh, and need to be localised at every time step. This question could arise in the context of a benchmark where certain quantities need to be measured at specific locations inside the domain.

8.21.1 Two-dimensional space

We shall first focus on quadrilaterals. There are many kinds of quadrilaterals as shown hereunder:



I wish to arrive at a single algorithm which is applicable to all quadrilaterals and therefore choose an irregular quadrilateral. For simplicity, let us consider a Q_1 element, with a single node at each corner.



Several rather simple options exist:

- we could subdivide the quadrilateral into two triangles and check whether point M is inside any of them (as it turns out, this problem is rather straightforward for triangles. Simply google it.)
- We could check that point M is always on the left side of segments $0 \rightarrow 1$, $1 \rightarrow 2$, $2 \rightarrow 3$, $3 \rightarrow 0$.
- ...

Any of these approaches will work although some might be faster than others. In three-dimensions all will however become cumbersome to implement and might not even work at all. Fortunately, there is an elegant way to answer the question, as detailed in the following subsection.

8.21.2 Three-dimensional space

If point M is inside the quadrilateral, there exist a set of reduced coordinates $r, s, t \in [-1 : 1]^3$ such that

$$\sum_{i=1}^4 N_i(r_M, s, t) x_i = x_M \quad \sum_{i=1}^4 N_i(r_M, s, t) y_i = y_M \quad \sum_{i=1}^4 N_i(r_M, s, t) z_i = z_M$$

This can be cast as a system of three equations and three unknowns. Unfortunately, each shape function N_i contains a term rst (as well as rs , rt , and st) so that it is not a linear system and standard techniques are not applicable. We must then use an iterative technique: the algorithm starts with a guess for values r, s, t and improves on their value iteration after iteration.

The classical way of solving nonlinear systems of equations is Newton's method. We can rewrite the equations above as $\mathbf{F}(r, s, t) = 0$:

$$\begin{aligned} \sum_{i=1}^8 N_i(r, s, t)x_i - x_M &= 0 \\ \sum_{i=1}^8 N_i(r, s, t)y_i - y_M &= 0 \\ \sum_{i=1}^8 N_i(r, s, t)z_i - z_M &= 0 \end{aligned} \quad (542)$$

or,

$$\begin{aligned} F_r(r, s, t) &= 0 \\ F_s(r, s, t) &= 0 \\ F_t(r, s, t) &= 0 \end{aligned}$$

so that we now have to find the zeroes of continuously differentiable functions $\mathbf{F} : \mathbb{R} \rightarrow \mathbb{R}$. The recursion is simply:

$$\begin{pmatrix} r_{k+1} \\ s_{k+1} \\ t_{k+1} \end{pmatrix} = \begin{pmatrix} r_k \\ s_k \\ t_k \end{pmatrix} - J_F(r_k, s_k, t_k)^{-1} \begin{pmatrix} F_r(r_k, s_k, t_k) \\ F_s(r_k, s_k, t_k) \\ F_t(r_k, s_k, t_k) \end{pmatrix}$$

where J the Jacobian matrix:

$$\begin{aligned} J_F(r_k, s_k, t_k) &= \begin{pmatrix} \frac{\partial F_r}{\partial r}(r_k, s_k, t_k) & \frac{\partial F_r}{\partial s}(r_k, s_k, t_k) & \frac{\partial F_r}{\partial t}(r_k, s_k, t_k) \\ \frac{\partial F_s}{\partial r}(r_k, s_k, t_k) & \frac{\partial F_s}{\partial s}(r_k, s_k, t_k) & \frac{\partial F_s}{\partial t}(r_k, s_k, t_k) \\ \frac{\partial F_t}{\partial r}(r_k, s_k, t_k) & \frac{\partial F_t}{\partial s}(r_k, s_k, t_k) & \frac{\partial F_t}{\partial t}(r_k, s_k, t_k) \end{pmatrix} \\ &= \begin{pmatrix} \sum_{i=1}^8 \frac{\partial N_i}{\partial r}(r_k, s_k, t_k)x_i & \sum_{i=1}^8 \frac{\partial N_i}{\partial s}(r_k, s_k, t_k)x_i & \sum_{i=1}^8 \frac{\partial N_i}{\partial t}(r_k, s_k, t_k)x_i \\ \sum_{i=1}^8 \frac{\partial N_i}{\partial r}(r_k, s_k, t_k)y_i & \sum_{i=1}^8 \frac{\partial N_i}{\partial s}(r_k, s_k, t_k)y_i & \sum_{i=1}^8 \frac{\partial N_i}{\partial t}(r_k, s_k, t_k)y_i \\ \sum_{i=1}^8 \frac{\partial N_i}{\partial r}(r_k, s_k, t_k)z_i & \sum_{i=1}^8 \frac{\partial N_i}{\partial s}(r_k, s_k, t_k)z_i & \sum_{i=1}^8 \frac{\partial N_i}{\partial t}(r_k, s_k, t_k)z_i \end{pmatrix} \end{aligned}$$

In practice, we solve the following system:

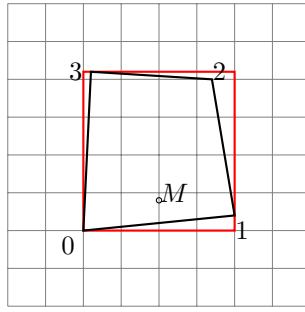
$$J_F(r_k, s_k, t_k) \left[\begin{pmatrix} r_{k+1} \\ s_{k+1} \\ t_{k+1} \end{pmatrix} - \begin{pmatrix} r_k \\ s_k \\ t_k \end{pmatrix} \right] = - \begin{pmatrix} F_r(r_k, s_k, t_k) \\ F_s(r_k, s_k, t_k) \\ F_t(r_k, s_k, t_k) \end{pmatrix}$$

Finally, the algorithm goes as follows:

- set guess values for r, s, t (typically 0)
- loop over $k=0, \dots$
- Compute $\text{rhs} = -\mathbf{F}(r_k, s_k, t_k)$
- Compute matrix $J_F(r_k, s_k, t_k)$

- solve system for (dr_k, ds_k, dt_k)
- update $r_{k+1} = r_k + dr_k, s_{k+1} = s_k + ds_k, t_{k+1} = t_k + dt_k$
- stop iterations when (dr_k, ds_k, dt_k) is small
- if $r_k, s_k, t_k \in [-1, 1]^3$ then M is inside.

This method converges quickly but involves iterations, and multiple solves of 3×3 systems which, when carried out for each marker and at each time step can prove to be expensive. A simple modification can be added to the above algorithm: iterations should be carried out *only* when the point M is inside of a cuboid of size $[\min_i x_i : \max_i x_i] \times [\min_i y_i : \max_i y_i] \times [\min_i z_i : \max_i z_i]$ where the sums run over the vertices of the element. In 2D this translates as follows: only carry out Newton iterations when M is inside the red rectangle!



Note that the algorithm above extends to high degree elements such as Q_2 and higher, even with curved sides.

write about case when element is rectangle/cuboid

8.22 Error measurements and convergence rates

What follows is written in the case of a two-dimensional model. Generalisation to 3D is trivial. What follows is mostly borrowed from [1537].

When measuring the order of accuracy of the primitive variables \vec{v} and p , it is standard to report errors in both the L_1 and the L_2 norm. For a scalar quantity Ψ , the L_1 and L_2 norms are computed as

$$\|\Psi\|_1 = \int_V |\Psi| dV \quad \|\Psi\|_2 = \sqrt{\int_V \Psi^2 dV} \quad (543)$$

For a vector quantity $\vec{k} = (k_x, k_y)$ in a two-dimensional space, the L_1 and L_2 norms are defined as:

$$\|\vec{k}\|_1 = \int_V (|k_x| + |k_y|) dV \quad \|\vec{k}\|_2 = \sqrt{\int_V (k_x^2 + k_y^2) dV} \quad (544)$$

To compute the respective norms the integrals in the above norms can be approximated by splitting them into their element-wise contributions. The element volume integral can then be easily computed by numerical integration using Gauss-Legendre quadrature.

The respective L_1 and L_2 norms for the pressure error can be evaluated via

$$e_p^h|_1 = \sum_{i=1}^{n_e} \sum_{q=1}^{n_q} |e_p^h(\vec{r}_q)| w_q |J_q| \quad e_p^h|_2 = \sqrt{\sum_{i=1}^{n_e} \sum_{q=1}^{n_q} |e_p^h(\vec{r}_q)|^2 w_q |J_q|} \quad (545)$$

where $e_p^h(\vec{r}_q) = p^h(\vec{r}_q) - p(\vec{r}_q)$ is the pressure error evaluated at the q -th quadrature associated with the i th element. n_e and n_q refer to the number of elements and the number of quadrature points per element. w_q and J_q are the quadrature weight and the Jacobian associated with point q .

The velocity error $e_{\vec{v}}^h$ is evaluated using the following two norms

$$e_{\vec{v}}^h|_1 = \sum_{i=1}^{n_e} \sum_{q=1}^{n_q} [|e_u^h(\vec{r}_q)| + |e_v^h(\vec{r}_q)|] w_q |J_q| \quad e_{\vec{v}}^h|_2 = \sqrt{\sum_{i=1}^{n_e} \sum_{q=1}^{n_q} [|e_u^h(\vec{r}_q)|^2 + |e_v^h(\vec{r}_q)|^2] w_q |J_q|} \quad (546)$$

where $e_u^h(\vec{r}_q) = u^h(\vec{r}_q) - u(\vec{r}_q)$ and $e_v^h(\vec{r}_q) = v^h(\vec{r}_q) - v(\vec{r}_q)$.

Another norm is very rarely used in the geodynamics literature but is preferred in the Finite Element literature: the H^1 norm. The mathematical basis for this norm and the nature of the $H^1(\Omega)$ Hilbert space is to be found in many FE books [473, 915, 860]. This norm is expressed as follows for a function f such that $f, |\nabla f| \in L^2(\Omega)$ ⁴⁸

$$\|f\|_{H^1} = \left(\int_{\Omega} (|f|^2 + |\nabla f|^2) d\Omega \right)^{1/2} \quad (547)$$

We then have

$$e_{\vec{v}}^h|_{H^1} = \|\vec{v}^h - \vec{v}\|_{H^1} = \sqrt{\sum_{i=1}^d \int_{\Omega} [(v_i^h - v_i)^2 + \vec{\nabla}(v_i^h - v_i) \cdot \vec{\nabla}(v_i^h - v_i)] d\Omega} \quad (548)$$

where d is the number of dimensions. Note that sometimes the following semi-norm is used [469, 163]:

$$e_{\vec{v}}^h|_{H^1} = \|\vec{v}^h - \vec{v}\|_{H^1} = \sqrt{\sum_{i=1}^d \int_{\Omega} [\vec{\nabla}(v_i^h - v_i) \cdot \vec{\nabla}(v_i^h - v_i)] d\Omega} \quad (549)$$

When computing the different error norms for e_p and $e_{\vec{v}}$ for a set of numerical experiments with varying resolution h we expect the error norms to follow the following relationships:

$$e_{\vec{v}}^h|_1 = Ch^{rvL_1} \quad e_{\vec{v}}^h|_2 = Ch^{rvL_2} \quad e_{\vec{v}}^h|_{H^1} = Ch^{rvH^1} \quad (550)$$

⁴⁸https://en.wikipedia.org/wiki/Sobolev_space

$$e_p^h|_1 = Ch^{rpL_1} \quad e_p^h|_2 = Ch^{rpL_2} \quad (551)$$

where C is a resolution-independent constant and $rpXX$ and $rvXX$ are the convergence rates for pressure and velocity in various norms, respectively. Using linear regression on the logarithm of the respective error norm and the resolution h , one can compute the convergence rates of the numerical solutions.

As mentioned in [469], when finite element solutions converge at the same rates as the interpolants we say that the method is optimal, i.e.:

$$e_v^h|_{L_2} = \mathcal{O}(h^3) \quad e_v^h|_{H^1} = \mathcal{O}(h^2) \quad e_p^h|_{L_2} = \mathcal{O}(h^2) \quad (552)$$

We note that when using discontinuous pressure space (e.g., P_0, P_{-1}), these bounds remain valid even when the viscosity is discontinuous provided that the element boundaries conform to the discontinuity.

8.22.1 About extrapolation

Section contributed by W. Bangerth and part of Thieulot & Bangerth [in prep.]

In a number of numerical benchmarks we want to estimate the error $X_h - X^*$ between a quantity X_h computed from the numerical solution \vec{u}_h, p_h and the corresponding value X computed from the exact solution \vec{u}, p . Examples of such quantities X are the root mean square velocity v_{rms} , but it could also be a mass flux across a boundary, an average horizontal velocity at the top boundary, or any other scalar quantity.

If the exact solution is known, then one can of course compute X from it. On the other hand, we would of course like to assess convergence also in cases where the exact solution is not known. In that case, one can compute an *estimate* X^* for X by way of *extrapolation*. To this end, we make the assumption that asymptotically, X_h converges to X at a fixed (but unknown) rate r , so that

$$e_h = |X_h - X| \approx Ch^r. \quad (553)$$

Here, X , C and r are all unknown constants to be determined, although we are not really interested in C . We can evaluate X_h from the numerical solution on successively refined meshes with mesh sizes h , $h/2$, and $h/4$. Then, in addition to (553) we also have

$$e_{h/2} = |X_{h/2} - X| \approx C \left(\frac{h}{2} \right)^r, \quad (554)$$

$$e_{h/4} = |X_{h/4} - X| \approx C \left(\frac{h}{4} \right)^r. \quad (555)$$

Taking ratios of equations (553)–(555), and replacing the unknown X by an *estimate* X^* , we then arrive at the following equation:

$$\frac{|X_h - X^*|}{|X_{h/2} - X^*|} = \frac{|X_{h/2} - X^*|}{|X_{h/4} - X^*|} = 2^r.$$

If one assumes that X_h converges to X uniformly either from above or below (rather than oscillate around X), then this equation allows us to solve for X^* and r :

$$X^* = \frac{X_h X_{h/2} - X_{h/2}^2}{X_h - 2X_{h/2} + X_{h/4}}, \quad r = \log_2 \frac{X_{h/2} - X^*}{X_{h/4} - X^*}.$$

In the determination of r , we could also have used X_h and $X_{h/2}$, but using $X_{h/2}$ and $X_{h/4}$ is generally more reliable because the higher order terms we have omitted in (553) are less visible on finer meshes.

8.23 The initial temperature field

8.23.1 Single layer with imposed temperature b.c.

Let us take a single layer of material characterised by a heat capacity C_p , a heat conductivity k and a heat production term H .



The Heat transport equation writes

$$\rho C_p \left(\frac{\partial T}{\partial t} + \vec{v} \cdot \vec{\nabla} T \right) = \vec{\nabla} \cdot (k \vec{\nabla} T) + \rho H \quad (556)$$

At steady state and in the absence of a velocity field, assuming that the material properties to be independent of time and space, and assuming that there is no heat production ($H = 0$), this equation simplifies to

$$\Delta T = 0 \quad (557)$$

Assuming the layer to be parallel to the x -axis, the temperature is $T(x, y) = T(y) = \alpha T + \beta$. In order to specify the constants α and β , we need two constraints.

At the bottom of the layer $y = y_b$ a temperature T_b is prescribed while a temperature T_t is prescribed at the top with $y = y_t$. This ultimately yields a temperature field in the layer given by

$$T(y) = \frac{T_t - T_b}{y_t - y_b}(y - y_b) + T_b$$

If now the heat production coefficient is not zero, the differential equation reads

$$k \Delta T + H = 0 \quad (558)$$

The temperature field is then expected to be of the form

$$T(y) = -\frac{H}{2k}y^2 + \alpha y + \beta \quad (559)$$

Supplied again with the same boundary conditions, this leads to

$$\beta = T_b + \frac{H}{2k}y_b^2 - \alpha y_b$$

ie,

$$T(y) = -\frac{H}{2k}(y^2 - y_b^2) + \alpha(y - y_b) + T_b$$

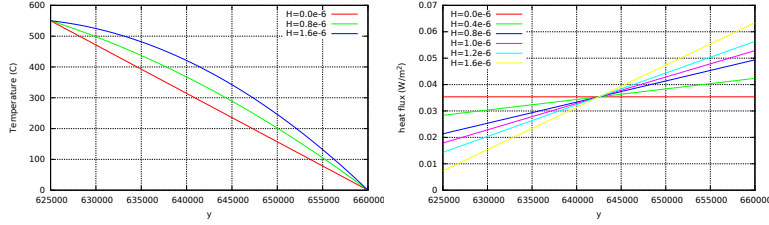
and finally

$$\alpha = \frac{T_t - T_b}{y_t - y_b} + \frac{H}{2k}(y_b + y_t)$$

or,

$$T(y) = -\frac{H}{2k}(y^2 - y_b^2) + \left(\frac{T_t - T_b}{y_t - y_b} + \frac{H}{2k}(y_b + y_t) \right)(y - y_b) + T_b$$

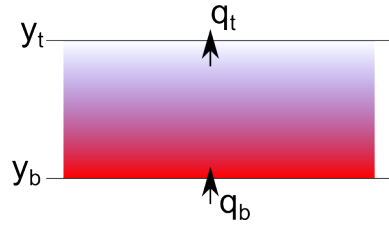
Taking $H = 0$ in this equation obviously yields the temperature field obtained previously. Taking $k = 2.25$, $T_t = 0C$, $T_b = 550C$, $y_t = 660km$, $y_b = 630km$ yields the following temperature profiles and heat fluxes when the heat production H varies:



Looking at the values at the top, which are somewhat estimated to be about $55 - 65 \text{ mW/m}^2$ [910, table 8.6], one sees that value $H = 0.8e-6$ yields a very acceptable heat flux. Looking at the bottom, the heat flux is then about 0.03 W/m^2 which is somewhat problematic since the heat flux at the Moho is reported to be somewhere between 10 and 20 mW/m^2 in [910, table 7.1].

8.23.2 Single layer with imposed heat flux b.c.

Let us now assume that heat fluxes are imposed at the top and bottom of the layer:



We start again from the ODE

$$k\Delta T + H = 0$$

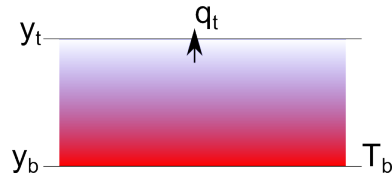
but only integrate it once:

$$k \frac{dT}{dy} + Hy + \alpha = 0$$

At the bottom $q = k(dT/dy)|_{y=y_b} = q_b$ and at the top $q = k(dT/dy)|_{y=y_t} = q_t$ so that

[to finish](#)

8.23.3 Single layer with imposed heat flux and temperature b.c.



[to finish](#)

8.23.4 Half cooling space

TODO.



8.23.5 Plate model

8.23.6 McKenzie slab

When doing thermo-mechanical modelling, the initial temperature field in the domain is of prime importance. This is especially true for the temperature in the slab for subduction modelling as its rheological behaviour is strongly temperature-dependent. One could easily design a simple geometrical initial field but it is unlikely to be close to the field of a slowly subducting slab at an angle in a hot mantle.

McKenzie [1162] derived such approximate initial field from the steady-state energy equation in two dimensions:

$$\rho C_p \vec{v} \cdot \vec{\nabla} T = k \vec{\nabla}^2 T \quad (560)$$

We denote by T_l the temperature at the base of the lithosphere and l its thickness (i.e. the thickness of the slab).

Assuming $\vec{v} = (v_x, 0)$ yields

$$\rho C_p v_x \frac{\partial T}{\partial x} = k \frac{\partial^2 T}{\partial x^2}$$

and substitution of $T' = T/T_l$, $x' = x/l$ and $z' = z/l \in [0, 1]$ in this equation leads to

$$\rho C_p v_x \frac{T_l}{l} \frac{\partial T'}{\partial x'} = k \frac{T_l}{l^2} \left(\frac{\partial^2 T'}{\partial x'^2} + \frac{\partial^2 T'}{\partial z'^2} \right)$$

or

$$\frac{\rho C_p v_x l}{k} \frac{\partial T'}{\partial x'} = \frac{\partial^2 T'}{\partial x'^2} + \frac{\partial^2 T'}{\partial z'^2}$$

and finally (see Eq. 2.3 of [1162]):

$$\frac{\partial^2 T'}{\partial x'^2} - 2R \frac{\partial T'}{\partial x'} + \frac{\partial^2 T'}{\partial z'^2} = 0$$

where R is the thermal Reynolds number

$$R = \frac{\rho C_p v_x l}{2k}$$

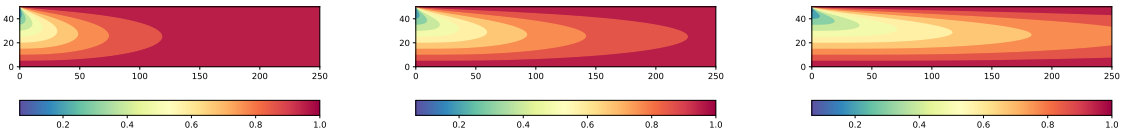
The general solution to this PDE with $T' = 1$ on the top, left and right boundary is

$$T'(x', z') = 1 + \sum_n C_n \exp \left[\left(R - (R^2 + n^2 \pi^2)^{1/2} \right) x' \right] \sin(n \pi z')$$

We now must make an assumption about the temperature on the left boundary ($x' = 0$), which is the temperature of the lithosphere. For simplicity McKenzie assumes that $T'(x' = 0, z') = 1 - z'$ so that $C_n = 2(-1)^n/n\pi$ and finally

$$T'(x', z') = 1 + 2 \sum_n \frac{(-1)^n}{n\pi} \exp \left[\left(R - (R^2 + n^2 \pi^2)^{1/2} \right) x' \right] \sin(n \pi z') \quad (561)$$

Let us build a simple temperature model for a $250\text{km} \times 50\text{km}$ slab, with $\rho = 3000$, $C_p = 1250$, $k = 3$. The python code is available in `images/mckenzie/mckenzie1.py`.

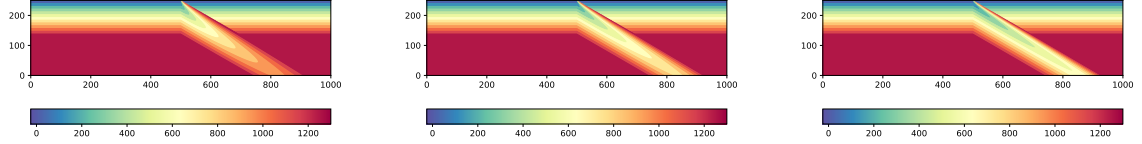


Left to right: Dimensionless temperature T' in a $250\text{km} \times 50\text{km}$ slab for $v_x = 0.5, 1, 2\text{cm/year}$

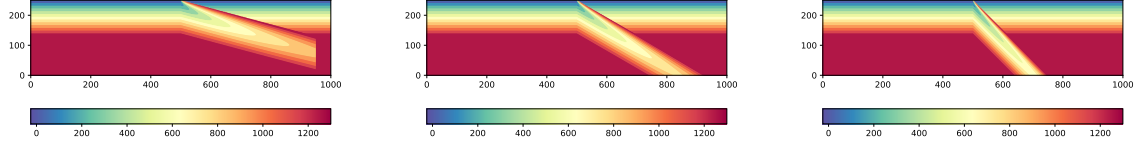
We logically recover the fact that the slower the slab penetrates the mantle the more temperature diffusion dominates over temperature advection. For $v = 0.5\text{cm/year}$ we see that that the slab assumes a constant temperature $T' = 1$ at all depths $0 \leq z' \leq 1$ for $x' \geq 125\text{km}$.

Note that this field is a steady-state field, valid for a constant density, heat conductivity and heat capacity, zero heat production, that it implies that the velocity is constant and that the lithosphere temperature is linear.

One can also embed the slab in a more realistic context, a subduction zone, involving a subducting lithosphere, an over-riding plate and a mantle. The domain is $1000\text{km} \times 250\text{km}$. The mantle temperature is set to 1300° . The slab dip can be varied and so can the velocity. The python code is available in `images/mckenzie/mckenzie2.py`.



Left to right: temperature T for $v_x = 0.5, 1, 2 \text{ cm/year}$ and $\phi = 30^\circ$.



Left to right: temperature T for $v_x = 1 \text{ cm/year}$ and $\phi = 15, 30, 45^\circ$.

8.23.7 Initial temperature for global mantle convection models

This is a difficult topic, and Gottschaldt et al [719] list a few issues or facts to take into account:

- Frequent impacts may have determined the heat structure of the outer layers (Arrhenius and Lepland 2000), leading to an early thermally stable stratification.
- A global magma ocean (Solomatov 2000) or several large scale melting events (Kleine et al. 2004) are also conceivable.
- Fractional crystallisation and subsequent overturn has the potential to result in compositionally or thermally stable layering, too (Elkins-Tanton et al. 2003; Zaranek and Parmentier 2004)

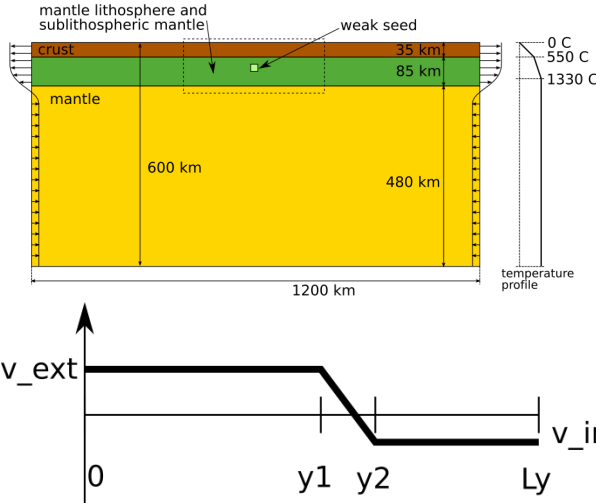
8.24 Kinematic boundary conditions

Boundary conditions come in two basic flavors: essential and natural.

- Essential bcs directly affect DOFs, and are imposed on the FEM matrix.
- Natural bcs do not directly affect DOFs and are imposed on the right-hand side vector.

8.24.1 In-out flux boundary conditions for lithospheric models

C. Thieulot / Physics of the Earth and Planetary Interiors 188 (2011) 47–68



The velocity on the side is given by

$$\begin{aligned} u(y) &= v_{ext} \quad y < L_y \\ u(y) &= \frac{v_{in} - v_{ext}}{y_2 - y_1} (y - y_1) + v_{ext} \quad y_1 < y < y_2 \\ u(y) &= v_{in} \quad y > y_2 \end{aligned}$$

The requirement for volume conservation is:

$$\Phi = \int_0^{L_y} u(y) dy = 0$$

Having chosen v_{in} (the velocity of the plate), one can then compute v_{ext} as a function of y_1 and y_2 .

$$\begin{aligned} \Phi &= \int_0^{y_1} u(y) dy + \int_{y_1}^{y_2} u(y) dy + \int_{y_2}^{L_y} u(y) dy \\ &= v_{ext} y_1 + \frac{1}{2} (v_{in} + v_{ext}) (y_2 - y_1) + (L_y - y_2) v_{in} \\ &= v_{ext} [y_1 + \frac{1}{2} (y_2 - y_1)] + v_{in} [\frac{1}{2} (y_2 - y_1) + (L_y - y_2)] \\ &= v_{ext} \frac{1}{2} (y_1 + y_2) + v_{in} [L_y - \frac{1}{2} (y_1 + y_2)] \end{aligned}$$

and finally

$$v_{ext} = -v_{in} \frac{\frac{1}{2} (y_1 + y_2)}{\frac{1}{2} (y_1 + y_2)}$$

8.25 Computing gradients - the recovery process

write about recovering accurate strain rate components and heat flux components on the nodes.

Let $\vec{g}(\vec{r})$ be the desired nodal field which we want to be the continuous Q_1 representation of the field $\vec{\nabla}f^h$. Since the derivative of the shape function does not exist on the nodes we need to design an algorithm do do so. This problem is well known and has been investigated

refs!

. The main standard techniques are listed hereafter.

8.25.1 Global recovery

The global recovery approach is rather simple: we wish to find \vec{g}^h such that it satisfies

$$\int_{\Omega} \phi \vec{g}^h \, d\Omega = \int_{\Omega} \phi \vec{\nabla} f^h \, d\Omega \quad \forall \phi$$

We will then successively replace ϕ by all the shape functions N_i and since we have $g^h = \sum_j N_i g_i$ we then obtain

$$\sum_j \int N_i N_j d\Omega g_i = \int N_i \vec{\nabla} f^h \, d\Omega$$

or,

$$\mathbb{M} \cdot \vec{\mathcal{G}} = \vec{f}$$

8.25.2 Local recovery - centroid average over patch

8.25.3 Local recovery - nodal average over patch

Let j be the node at which we want to compute \vec{g} . Then

$$\vec{g}_j = \vec{g}(\vec{r}_j) = \frac{\sum_{e \text{ adj. to } j} |\Omega_e| (\vec{\nabla} f)_e(\vec{r}_j)}{\sum |\Omega_e|}$$

where $|\Omega_e|$ is the volume of the element and $(\vec{\nabla} f^h)_e(\vec{r}_j)$ is the gradient of f as obtained with the shape functions inside element e and computed at location \vec{r}_j .

8.25.4 Local recovery - least squares over patch

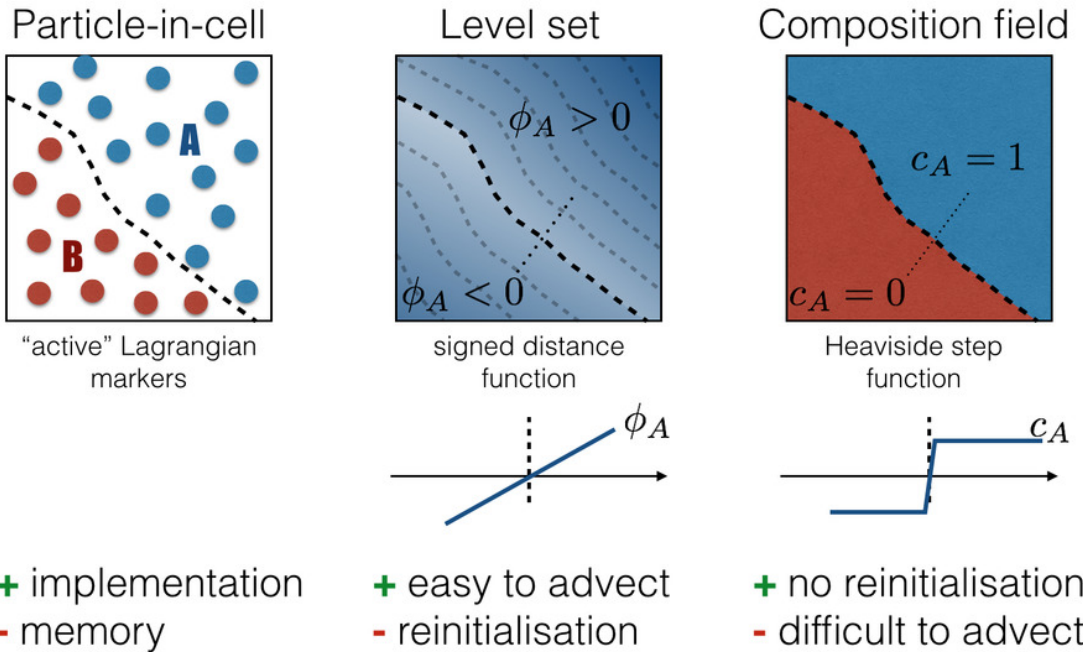
8.25.5 Link to pressure smoothing

When the penalty method is used to solve the Stokes equation, the pressure is then given by $p = -\lambda \vec{\nabla} \cdot \vec{v}$. As explained in section 6.3, the velocity is first obtained and the pressure is recovered by using this equation as a postprocessing step. Since the divergence cannot be computed easily at the nodes, the pressure is traditionally computed in the middle of the elements, yielding an elemental pressure field (remember, we are talking about $Q_1 P_0$ elements here – bi/tri-linear velocity, discontinuous constant pressure)

tie to fieldstone 12

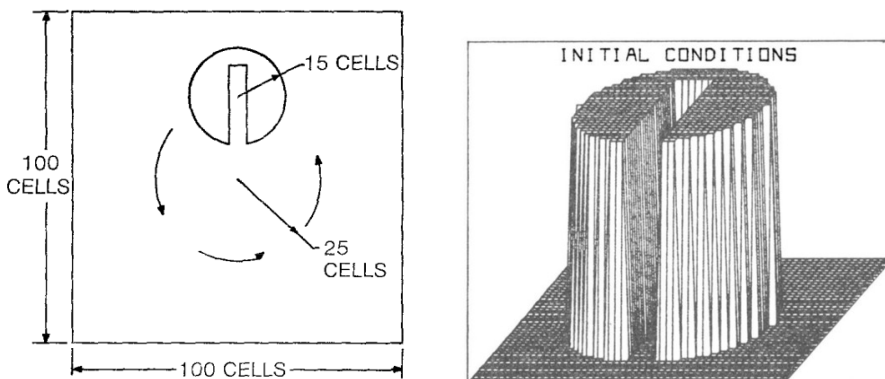
8.26 Tracking materials and/or interfaces

Unless using a fully Lagrangian formulation, one needs an additional numerical method to represent/track the various materials present in an undeformable (Eulerian) mesh. The figure below (by B. Hillebrand) illustrates the three main methods used in geodynamics.



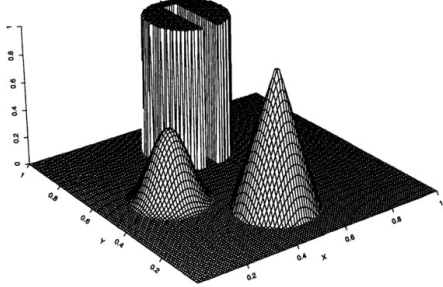
Note that what follows is applicable to FEM, FDM, etc ...

A typical test for advection algorithm is the Zalesak disk [1742]. It is a two dimensional test problem of solid body rotation with a constant angular velocity ω (in rad/sec):



Taken from [1742]. Left: Schematic representation of two dimensional solid body rotation problem. The field inside the cut out has value 3 and it is 1 outside. The rotational speed is such that one full revolution is effected in 628 cycles. The width of the gap separating the two halves of the cylinder, as well as the maximum extent of the “bridge” connecting the two halves, is 5 cells. Right: Perspective view of initial conditions for the two dimensional solid body rotation problem. Note that only a 50×50 portion of the mesh centered on the cylinder is displayed.

This benchmark is widely used in the literature [1493, 1606, 1305, 84, 1753]. Note that the Zalesak disc is often supplemented with a cone and a Gaussian features:



Taken from [1059]. Initial data for solid rotation tests

8.26.1 The Particle-in-cell technique

Remark. The terms 'particle' and 'marker' are commonly (and unfortunately) interchangeably used in the literature in the context of the particle-in-cell technique. However, one should be aware that the marker-and-cell (MAC) technique is something different: it was invented in the early 60's at the Los Alamos Laboratories by Harlow and Welch [798]. For more information on MAC see the review paper by McKee et al [1157].

The Particle-in-cell method is by far the most widely used in computational geodynamics. In its most basic form it is a rather simple method to implement and this probably owes to its success and early adoption [1317] in non-parallel codes such as SOPALE [614], I2VIS [674] or CITCOM [1164] (Appendix B). It has been implemented in ASPECT [633] and the inherent load balancing issues arising from the parallel implementation as well as from the use of Adaptive Mesh Refinement are discussed. It has also been implemented in the MILAMIN code [426] to study LLSVPs [1238].

The basic methodology goes as follows:

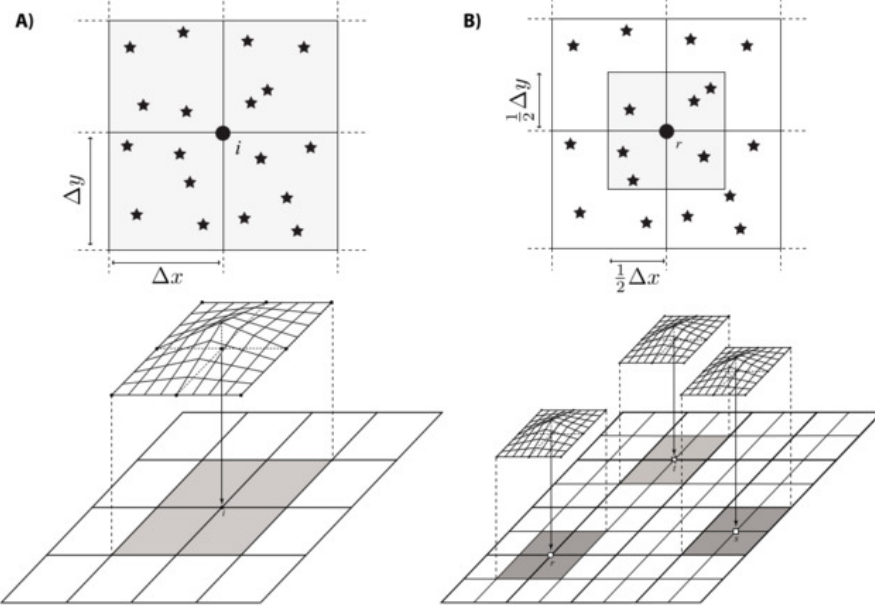
1. distribute particles in the domain
2. assign a material identity (and/or any other quantity) to each of them
3. project particle quantities of the Eulerian nodes of the mesh
4. solve the Stokes equations for a new velocity field
5. interpolate the velocity onto the particles
6. move the particles with their respective velocities
7. go back to step 3

As it turns out each step above needs to be carefully executed and is more difficult than it first looks.

Distributing particles in the domain. Let us assume we wish to distribute N_p particles in the domain. How large must N_p be? To simplify, one end member could be 'as many particles as possible that fit in memory' while the other end member could be 'one per element/cell on average'. While the former does not necessarily guarantee a desired accuracy while being CPU and memory intensive, the latter will certainly lead to zones in the domain void of particles which will be problematic since the projection onto the mesh might yield zero values or very inaccurate values. How many particles (per element/cell) will be enough? Also, should the particles be randomly distributed in the domain or on some kind of regular grid? See fieldstone 13 (Section 9).

Averaging and projection. This is a very critical step. Unfortunately, there is no community-wide agreed-upon method. The problem at hand boils down to: at a given location (\vec{r}) in space I need a quantity which is carried by the particles. The first step is to find the particle(s) close to this point. If done naively, this is a very costly affair, and begs the question what 'close' means. Finding all particles within a radius R of point \vec{r} can be done very efficiently (e.g. with linked lists, Verlet lists, ...) but the choice of R proves to be critical: if too small, there may not be any particle inside the circle, and if too

large there may be many particles inside the circle and the averaging over so many particles in space will prove to be over diffusive. In practice, the FD or FE mesh is used to provide an indication of R . In FDM, the four cells (or quarter cells) around a node represent the volume of space containing the particles whose properties are to be averaged [490] as illustrated in the following figure:



Taken from [490]. The "4-cell" and "1-cell" schemes for projecting properties defined on the markers (denoted by stars) onto a node (denoted by the solid circle). (A) The 4-cell scheme. The support of the interpolating function N_i associated with node i is indicated by the shaded region. Only markers within the support of node i contribute to the projection operation used to define the nodal value at i . The shape of the bilinear interpolation function for node i is indicated in the lower frame. (B) The 1-cell scheme. The thick lines in the lower frame indicate the grid used to discretize the Stokes equations, while the thin lines indicate the grid onto which marker properties are projected. The 1-cell scheme utilizes a compact support of size $\Delta x \times \Delta y$. The support for nodes r, s, t are indicated by the shaded regions. Only markers within the nodal support contribute to the projection operation for that node.

Given that the FEM requires to compute integrals over each element, only the particles inside the element will contribute to the average values assigned to the quadrature points. However, one could also decide to first average the properties onto the nodes before using these nodal values to assign values to the quadrature points. In this case the FDM approach applies.

Finally, in both FDM and FEM bi/trilinear shape functions are used for the interpolation as they can be interpreted as weighing functions. Higher order shape functions could also be used but the standard Q_2 shape functions (Section 4.5) are 2-nd order polynomials which can take negative values (as opposed to the Q_1 shape functions which are strictly positive) and this can pose problems: in some cases, although all values to be averaged are positive, their weighed average can be negative. Q1 projection PUCKETT

it would be nice to have a Q1 and Q2 drawing of a 1D element and show that indeed negative values arise

Assuming that we have established a list of particles, all tracking a field $f(\vec{r})$ and that each particle has an associated weight N_i (function of the location where the average is to be computed or not), we must now compute their average value $\langle f \rangle$. The simplest approach which comes to mind is the (weighted) arithmetic mean (am):

$$\langle f \rangle_{am} = \frac{\sum_{i=1}^n N_i f_i}{\sum_{i=1}^n N_i}$$

In the case where f is the (mass) density ρ , it is indeed what should be used. However, turning now to viscosity η , we know that its value can vary by many orders of magnitude over very short distances. It is then likely that the average runs over values spanning values between 10^{18}Pa s and 10^{25}Pa s . As explained in [1436] the arithmetic averaging tends to 'favour' large values: if the sum runs over 10

particles, 9 carrying the value 10^{25} and 1 carrying the value 10^{19} , the average value (assuming $N_i = 1$ for simplicity) is then

$$\langle \eta \rangle = \frac{9 \cdot 10^{25} + 1 \cdot 10^{19}}{10} \simeq 0.9 \cdot 10^{25}$$

which is much closer to 10^{25} than to 10^{19} . Other averagings are then commonly used, namely the geometric mean (gm) and the harmonic mean (hm), defined as follows:

$$\langle f \rangle_{gm} = \left(\prod_i f_i^{N_i} \right)^{1/\sum_i N_i} \quad \text{or,} \quad \log_{10} \langle f \rangle_{gm} = \frac{\sum_i N_i \log_{10} f_i}{\sum_i N_i}$$

and

$$\langle f \rangle_{hm} = \left(\frac{\sum_{i=1}^n N_i \frac{1}{f_i}}{\sum_i N_i} \right)^{-1} \quad \text{or,} \quad \frac{1}{\langle f \rangle_{hm}} = \frac{\sum_{i=1}^n N_i \frac{1}{f_i}}{\sum_i N_i}$$

The geometric mean can be seen as a form of arithmetic mean of \log_{10} values, while the harmonic mean can be seen as a form of arithmetic mean of the inverse values.

Looking back at the above example, the geometric mean of the viscosities is given by

$$\log \langle \eta \rangle_{gm} = \frac{9 \cdot 25 + 1 \cdot 19}{10} = 24.4 \quad \text{or,} \quad \langle \eta \rangle_{gm} \simeq 2.5 \cdot 10^{24}$$

and the harmonic mean:

$$\langle \eta \rangle_{hm} \simeq \left(\frac{1}{10 \cdot 10^{19}} \right)^{-1} = 10^{20}$$

We see that the harmonic mean tends to favour the small values. Also we recover the known property:

$$\langle f \rangle_{am} \geq \langle f \rangle_{gm} \geq \langle f \rangle_{hm} \tag{562}$$

When all f_i are equal to f_0 their computed average should also be equal to f_0 . As a consequence the weights N_i should fulfill the condition $\sum_{i=1}^n N_i = 1$. If all weights are equal, then $N_i = 1/n$ and the averagings become:

$$\langle f \rangle_{am} = \frac{1}{n} \sum_{i=1}^n f_i \quad \langle f \rangle_{gm} = \prod_i f_i^{1/n} \quad \langle f \rangle_{hm} = \left(\frac{1}{n} \sum_i \frac{1}{f_i} \right)^{-1} \tag{563}$$

There are many papers which have looked at particle averagings and projections. I will for now simply point to the following ones: [1436] [466] [490] [1208] [1320] [1537] [633] [634]. Also check the multiscale PIC in [49]

write more about particle averaging and projection

Interpolation of the velocity onto particles .

Once the particle i has been localised inside a given element (Section 8.21) and its reduced coordinates (r, s, t) determined, the velocity at this location can be computed through the shape functions:

$$\vec{v}_i = \sum_{k=1}^m N_i(r, s, t) \vec{v}_k$$

This approach is not without problem: while the nodal velocities \vec{v}_k are such that⁴⁹ $\vec{\nabla} \cdot \vec{v} = 0$ (in the weak sense), the computed velocity \vec{v}_i is not necessarily divergence-free! In order to remedy this, a Conservative Velocity Interpolation (CVI) has been proposed in [1654].

Moving the particles This is discussed in the context of the Runge-Kutta Methods, see Section 8.20.1.

⁴⁹for incompressible flows, of course

8.26.2 The level set function technique

This method was developed in the 80's by Stanley Osher and James Sethian []

The Level-set Method (LSM), as it is commonly used in Computational Fluid Dynamics – and especially in Computational Geodynamics – represents a close curve Γ (say, in our case, the interface between two fluids or layers) by means of a function ϕ (called the level-set function, or LSF). Γ is then the zero level-set of ϕ :

$$\Gamma = \{(x, y) \mid \phi(x, y) = 0\} \quad (564)$$

The convention is that $\phi > 0$ inside the region delimited by Γ and $\phi < 0$ outside. The function value indicates on which side of the interface a point is located (negative or positive) and this is used to identify materials.

Furthermore, if the curve Γ moves with a velocity \vec{v} , then it satisfies the following equation:

$$\frac{\partial \phi}{\partial t} + \vec{v} \cdot \vec{\nabla} \phi = 0 \quad (565)$$

The level set function is generally chosen to be a signed distance function, i.e. $|\vec{\nabla} \phi| = 1$ everywhere and its value is also the distance to the interface.

As explained in [827], the level-set function ϕ is advected with the velocity \vec{v} which is obtained by solving the Stokes equations. This velocity does not guarantee that after an advection step the signed distance quality of the LSF is preserved. The LSF then needs to be corrected, which is also called reinitialisation. Finally, solving the advection equation must be done in an accurate manner both in time and space, so that so-called ENO (essentially non-oscillatory) schemes are often employed for the space derivative [1284, 1423].

The level set method has not often been used in the geodynamics community with some notable exceptions [181, 182, 780, 752, 1788, 781, 1492, 1491, 827] An overview of the method and applications can be found in [1283].

Several improvements upon the original LSM have been proposed, such as for instance the conservative level set of [1753]. The most notable difference between CLS method originally proposed by Olsson et al. [1276, 1277] and standard LS method lies in the choice of LS function. Instead of the signed distance function, the CLS methods employ the Heaviside function $H(\phi)$

$$H(\phi) = \begin{cases} 1 & \phi > 0 \\ 1/2 & \phi = 0 \\ 0 & \phi < 0 \end{cases}$$

where ϕ is the signed distance function as in the LSM. In practice, a hyperbolic tangent function is used:

$$H(\phi) = \frac{1}{2}(1 + \tanh(\phi/2\epsilon))$$

where ϵ defines the spreading width of H . In the case where there are only two fluids (i.e. a single level set is sufficient), the material properties such as density and viscosity are computed as follows:

$$\rho = \rho_1 + (\rho_2 - \rho_1)H(\phi)$$

$$\eta = \eta_1 + (\eta_2 - \eta_1)H(\phi)$$

8.26.3 The field/composition technique

This is the approach taken by the ASPECT developers [1009, 809]. Each material i is represented by a compositional field c_i , which takes values between 0 and 1. Each compositional field is then advected with the (prescribed or computed) Stokes velocity [343]:

$$\frac{\partial c_i}{\partial t} + \mathbf{v} \cdot \nabla c_i = 0 \quad (566)$$

The value at a point (Finite element node or quadrature point) is 1 if it is in the domain covered by the material i , and 0 otherwise. In one dimension, each compositional field is a Heavyside function. This

approach is somewhat similar to the LSM but the field is essentially discontinuous across the interface, which makes it very difficult to advect. On the plus side, compositional fields need not be reinitialised, as opposed to LSF's.

Accurate numerical advection is a notoriously difficult problem. Unless very specialised techniques are used it often yields undershoot ($c_i < 0$) and overshoot ($c_i > 0$), which ultimately yields mass conservation issues. Also, unless special care is taken, compositional fields tend to become more and more diffuse over time: the SUPG method (Section 8.5) and the entropy viscosity method add small amounts of diffusion to dampen the under- and overshoots. This means that at a given point two or more compositions may have values, which require some form of averaging. If under- and overshoots are present, these averagings can become very problematic and even yield meaningless quantities (e.g. negative viscosities).

One rather old and popular filtering approach is the so-called Lenardic and Kaula filter [1038]:

The filtering algorithm for two-component flow is as follows. An initial step distribution in C is assumed with $C = 0$ and $C = 1$ used to distinguish distinct materials. A high-order upwind solution scheme is applied to equation (2), with prescribed initial conditions, resulting in an uncorrected C field. The field is corrected via the following filtering algorithm:

1. The initial sum of all nodal C values is calculated and is assigned to the variable C_{sum0} .
2. Nodal C values below 0 are set to 0 and the peak value below 0 is assigned to the variable C_{min} .
3. Nodal C values above 1 are set to 1 and the peak value above 1 is assigned to the variable C_{max} .
4. Nodal C values less than or equal to the absolute value of C_{min} are set to 0.
5. Nodal C values greater than or equal to $2 - C_{max}$ are set to 1.
6. The sum of all nodal C values is calculated and assigned to the variable C_{sum1} .
7. The number of nodal C values not 1 or 0 is assigned to the variable NUM.
8. The variable DIST is defined as $(C_{sum0} - C_{sum1})/NUM$ and is added to all C values not 1 or 0.

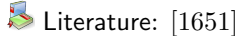
Taken from Lenardic and Kaula [1038]

The basic idea of the filtering algorithm is to ensure that ϕ remains within the bounds $0 \leq \phi \leq 1$, and to minimize dispersion error. We refer the reader to Lenardic and Kaula (1993) for the detailed explanation and here give the outline of the algorithm for a discrete property field $\phi = \{\phi_i\}$.

Algorithm 10 A property filtering algorithm

- (1) Compute the initial sum S_0 of all values of ϕ .
 - (2) Find the minimal value ϕ_{min} below 0.
 - (3) Find the maximal value ϕ_{max} above 1.
 - (4) Set $\phi_i = 0$ if $\phi_i \leq |\phi_{min}|$.
 - (5) Set $\phi_i = 1$ if $\phi_i \geq 2 - \phi_{max}$.
 - (6) Compute the sum S_1 of all values of ϕ .
 - (7) Compute the number num of $0 < \phi_i < 1$.
 - (8) Add $dist = (S_1 - S_0)/num$ to all $0 < \phi_i < 1$.
-

From FENICS book



Literature: [1651]

write about DG approach

8.26.4 The Volume-of-Fluid method

[830]

8.26.5 The method of characteristics

ask Arie to write something

[454]

8.26.6 The Marker Chain method

In two dimensions, the idea is quite simple: each interface is discretised by means of a number of Lagrangian points (which may or may not vary in time). The points are numbered and connected (think of the connectivity array of a 1D FEM code). In the case of small deformations, and in the absence of in/out-flow boundaries, the method is reasonably trivial to implement, and each couple of point defines a segment (and therefore its normal vector too) which can then be used to answer the question: "at this location, am I above or below this interface" or "am I this domain our outside this domain" (in the case that the interface does not reach any of the boundaries).

This method becomes somewhat impractical when large deformation occurs or, for example, when a domain splits into two (think: slab break off). One interface must then become two, and it requires an algorithm capable of detecting the breakup of the surface and capable of rebuilding/patching the new ones so that they can still be used further. Note that in case of large deformation some markers may get further and further apart from each other which makes for a poor representation of the surface. New markers should then be added but the question of when and where must then be addressed.

Also, switching to three dimensions can prove to be very difficult or simply very costly: the generation of the initial marker position is trivial but their connectivity can be complicated to establish at startup: for instance, a Stokes sphere will require a mesh made of triangles which maps exactly the surface of the sphere (see [1541, 1219] for methods on how to efficiently produce such meshes). In the case of more complex 3D geometries this may prove nearly impossible to do. So will the problem of splitting a surface into two (or merging two domains).

This method is usually coupled to Eulerian meshes (typically with FDM, but not only). It was used in [1700] in the context of salt domes analysis and later in [347, 353]. It is also used in [1613] but little details are given about the algorithms used to track and update the chain in the presence of such large deformation. It is also used (although coupled to level set functions) in the DOUAR code[199] (see Section B). Having worked myself on this code and having had to produce complex initial triangulated surfaces for simulations (see for example [1098]) it is easy to understand why later users of this code did implement the marker-in-cell technique. More recently, it is used to track the free surface position in a FDM code [495, 332].

Finally, Christensen [343] makes the following interesting comment: "One might assume that different methods of representing the discontinuity, for example, by a tracer chain [353] or a cloud of tracers, would solve these problems. However, the difficulties arise not only from the way in which material boundaries are represented. Physically, the rate of shear strain parallel to a rheological boundary is discontinuous. Within the finite element scheme such jump can only be realized at an element boundary. In an Eulerian scheme, where the discontinuity will crosscut the elements, the jump in strain rate must be approximated by a continuous variation, and effectively, the rheological properties on both sides of the discontinuity will be averaged in some way within the element."

8.26.7 Hybrid methods

In Braun et al. [199] a level set method is presented which is based on a 3-D set of triangulated points, which makes it a hybrid between tracers and level set functions: in the DOUAR code (Appendix B) the interface is then explicitly tracked by means of the tracers while the LSF is computed on the FE nodes. Although very promising in theory, this method proved to be difficult to use in practice since it requires a) a triangulation of the interfaces at $t = 0$ which is not trivial if the geometries are complex (think about a slab in 3D); b) the addition or removal of tracers because of the interface deformation and the patching of the triangulation; c) the calculation of the distance to the interfaces for each FE node based on the triangle normal vectors. This probably explains why the Particle-In-Cell method was later implemented in this code (pers. comm.). Note that another very similar approach is used in [1423].

8.26.8 Boundary fitted mesh

This method is rather simple to implement and works well for small deformations. It is for instance used by Frehner [594] (see online supplementary material) in which it is stated: "The numerical grid is set up in such a way that the interface between different material phases (two layers in this case) coincides with element boundaries. Hence, each element belongs to a unique material phase and no interpolation

I still have
pics from the
old days using
DOUAR- in-
clude

is necessary.” With such a method, each element is initially attributed a material phase/number and its material properties do not change.

8.27 Static condensation

The idea behind static condensation is quite simple: in some cases, there are dofs belonging to an element which only belong to that element. For instance, the so-called MINI element ($P_1^+ \times P_1$) showcases a bubble function in the middle (see section ??). In the following, \vec{V}^* corresponds to the list of such dofs inside an element. The discretised Stokes equations on any element looks like:

$$\begin{pmatrix} \mathbb{K} & L & \mathbb{G} \\ L^T & \mathbb{K}^* & H \\ \mathbb{G}^T & H^T & 0 \end{pmatrix}_e \begin{pmatrix} \vec{\mathcal{V}} \\ \vec{V}^* \\ \vec{\mathcal{P}} \end{pmatrix}_e = \begin{pmatrix} \vec{f} \\ \vec{f}^* \\ \vec{h} \end{pmatrix}_e \quad (567)$$

This is only a re-writing of the elemental Stokes matrix where the matrix \mathbb{K} has been split in four parts. Note that the matrix \mathbb{K}^* is diagonal.

This can also be re-written in non-matrix form:

$$\mathbb{K} \cdot \vec{\mathcal{V}} + L \cdot \vec{V}^* + \mathbb{G} \cdot \vec{\mathcal{P}} = \vec{f} \quad (568)$$

$$L^T \vec{V} + K^* \cdot \vec{V}^* + H \cdot \vec{\mathcal{P}} = \vec{f}^* \quad (569)$$

$$\mathbb{G}^T \cdot \vec{\mathcal{V}} + H^T \vec{V}^* = \vec{h} \quad (570)$$

The V^* in the second equation can be isolated:

$$\vec{V}^* = \mathbb{K}^{-*} \cdot (\vec{f}^* - L^T \cdot \vec{\mathcal{V}} - H \cdot \vec{\mathcal{P}})$$

and inserted in the first and third equations:

$$\mathbb{K} \cdot \vec{\mathcal{V}} + L \left[\mathbb{K}^{-*} (\vec{f}^* - L^T \cdot \vec{\mathcal{V}} - H \cdot \vec{\mathcal{P}}) \right] + \mathbb{G} \cdot \vec{\mathcal{P}} = \vec{f} \quad (571)$$

$$\mathbb{G}^T \cdot \vec{\mathcal{V}} + H^T \left[\mathbb{K}^{-*} (\vec{f}^* - L^T \cdot \vec{\mathcal{V}} - H \cdot \vec{\mathcal{P}}) \right] = \vec{h} \quad (572)$$

or,

$$(\mathbb{K} - L \cdot \mathbb{K}^{-*} \cdot L^T) \cdot \vec{\mathcal{V}} + (G - L \cdot \mathbb{K}^{-*} \cdot H) \cdot \vec{\mathcal{P}} = \vec{f} - L \cdot \mathbb{K}^{-*} \cdot \vec{f}^* \quad (573)$$

$$(G^T - H^T \cdot \mathbb{K}^{-*} \cdot L^T) \cdot \vec{\mathcal{V}} - (H^T \cdot \mathbb{K}^{-*} \cdot H) \cdot \vec{\mathcal{P}} = \vec{h} - H^T \cdot \mathbb{K}^{-*} \cdot \vec{f}^* \quad (574)$$

i.e.

$$\underline{\mathbb{K}} \cdot \vec{\mathcal{V}} + \underline{\mathbb{G}} \cdot \vec{\mathcal{P}} = \vec{f} \quad (575)$$

$$\underline{\mathbb{G}}^T \cdot \vec{\mathcal{V}} - \underline{\mathbb{C}} \cdot \vec{\mathcal{P}} = \vec{h} \quad (576)$$

with

$$\underline{\mathbb{K}} = K - L \cdot \mathbb{K}^{-*} \cdot L^T \quad (577)$$

$$\underline{\mathbb{G}} = G - L \cdot \mathbb{K}^{-*} \cdot H \quad (578)$$

$$\underline{\mathbb{C}} = H^T \cdot \mathbb{K}^{-*} \cdot H \quad (579)$$

$$\underline{\vec{f}} = \vec{f} - L \cdot \mathbb{K}^{-*} \cdot \vec{f}^* \quad (580)$$

$$\underline{\vec{h}} = \vec{h} - H^T \cdot \mathbb{K}^{-*} \cdot \vec{f}^* \quad (581)$$

Note that $\underline{\mathbb{K}}$ is symmetric, and so is the Stokes matrix.

For instance, in the case of the MINI element, the dofs corresponding to the bubble could be eliminated at the elemental level, which would make the Stokes matrix smaller. However, it is then important to note that static condensation introduces a pressure-pressure term which was not there in the original formulation.

8.28 Measuring incompressibility

The velocity divergence error integrated over the whole element is given by

$$e_{div} = \int_{\Omega} (\vec{\nabla} \cdot \vec{v}^h - \underbrace{\vec{\nabla} \cdot \vec{v}}_{=0}) d\Omega = \int_{\Omega} (\vec{\nabla} \cdot \vec{v}^h) d\Omega \quad (582)$$

where Γ_e is the boundary of element e and \vec{n} is the unit outward normal of Γ_e .

Furthermore, one can show that [469]:

$$e_{div} = \int_{\Gamma_e} \vec{v}^h \cdot \vec{n} d\Gamma$$

The reason is as follows and is called the divergence theorem⁵⁰: suppose a volume V subset of \mathbb{R}^d which is compact and has a piecewise smooth boundary S , and if \vec{F} is a continuously differentiable vector field then

$$\int_V (\vec{\nabla} \cdot \vec{F}) dV = \int_S (\vec{F} \cdot \vec{n}) dS$$

The left side is a volume integral while the right side is a surface integral. Note that sometimes the notation $d\vec{S} = \vec{n} dS$ is used so that $\vec{F} \cdot \vec{n} dS = \vec{F} \cdot d\vec{S}$.

The average velocity divergence over an element can be defined as

$$\langle \vec{\nabla} \cdot \vec{v} \rangle_e = \frac{1}{V_e} \int_{\Omega_e} (\vec{\nabla} \cdot \vec{v}) d\Omega = \frac{1}{V_e} \int_{\Gamma_e} \vec{v} \cdot \vec{n} d\Gamma$$

Note that for elements using discontinuous pressures we shall recover a zero divergence element per element (local mass conservation) while for continuous pressure elements the mass conservation is guaranteed only globally (i.e. over the whole domain), see section 3.13.2 of [743].

Note that one could instead compute $\langle |\vec{\nabla} \cdot \vec{v}| \rangle_e$. Either volume or surface integral can be computed by means of an appropriate Gauss-Legendre quadrature algorithm.

[implement and report](#)

⁵⁰https://en.wikipedia.org/wiki/Divergence_theorem

8.29 Periodic boundary conditions

This type of boundary conditions can be handy in some specific cases such as infinite domains. The idea is simple: when material leaves the domain through a boundary it comes back in through the opposite boundary (which of course presupposes a certain topology of the domain).

For instance, if one wants to model a gas at the molecular level and wishes to avoid interactions of the molecules with the walls of the container, such boundary conditions can be used, mimicking an infinite domain in all directions.

Let us consider the small mesh depicted hereunder:

missing picture

We wish to implement horizontal boundary conditions so that

$$u_5 = u_1 \quad u_{10} = u_6 \quad u_{15} = u_{11} \quad u_{20} = u_{16}$$

One could of course rewrite these conditions as constraints and extend the Stokes matrix but this approach turns out to be not practical at all.

Instead, the method is rather simple: replace in the connectivity array the dofs on the right side (nodes 5, 10, 15, 20) by the dofs on the left side. In essence, we wrap the system upon itself in the horizontal direction so that elements 4, 8 and 12 'see' and are 'made of' the nodes 1, 6, 11 and 16. In fact, this is only necessary during the assembly. Everywhere in the loops nodes 5, 10, 15 and 20 appear one must replace them by their left pendants 1, 6, 11 and 16. This automatically generates a matrix with lines and columns corresponding to the u_5 , u_{10} , u_{15} and u_{20} being exactly zero. The Stokes matrix is the same size, the blocks are the same size and the symmetric character of the matrix is respected. However, there remains a problem. There are zeros on the diagonal of the above mentioned lines and columns. One must then place there 1 or a more appropriate value.

Another way of seeing this is as follows: let us assume we have built and assembled the Stokes matrix, and we want to impose periodic b.c. so that dof j and i are the same. The algorithm is composed of four steps:

1. add col j to col i
2. add row j to row i (including rhs)
3. zero out row j , col j
4. put average diagonal value on diagonal (j, j)

Remark. *Unfortunately the non-zero pattern of the matrix with periodic b.c. is not the same as the matrix without periodic b.c.*

8.30 Removing rotational nullspace

October 23, 2019 - C.T.

When free slip boundary conditions are prescribed in an annulus or hollow sphere geometry there exists a rotational nullspace, or in other words there exists a tangential velocity field ('pure rotation') which, if added or subtracted to the solution, generates a solution which is still the solution of the PDEs.

As in the pressure normalisation case (see section 8.14), the solution is simple:

1. fix the tangential velocity at *one* node on a boundary, and solve the system (the nullspace has been removed)
2. post-process the solution to have the velocity field fulfill the required conditions, i.e. either a zero net angular momentum or a zero net angular velocity of the domain.

Remark. In ASPECT this is available under the option "Remove nullspace = angular momentum" and "Remove nullspace = net rotation". The "angular momentum" option removes a rotation such that the net angular momentum is zero. The "net rotation" option removes the net rotation of the domain.

Angular momentum approach In order to remove the angular momentum, we search for a rotation vector $\vec{\omega}$ such that

$$\int_{\Omega} \rho[\vec{r} \times (\vec{v} - \vec{\omega} \times \vec{r})] dV = \vec{0} \quad (583)$$

The angular momentum of a rigid body can be obtained from the sum of the angular momentums of the particles forming the body⁵¹:

$$\vec{H} = \sum_i \vec{L}_i \quad (584)$$

$$= \sum_i \vec{r}_i \times m_i \vec{v}_i \quad (585)$$

$$= \sum_i \vec{r}_i \times m_i (\vec{\omega}_i \times \vec{r}_i) \quad (586)$$

$$= \sum_i m_i \begin{pmatrix} \sum_i m_i(y_i^2 + z_i^2) & -\sum_i m_i x_i y_i & -\sum_i m_i x_i z_i \\ -\sum_i m_i x_i y_i & \sum_i m_i(x_i^2 + z_i^2) & -\sum_i m_i y_i z_i \\ -\sum_i m_i x_i z_i & -\sum_i m_i y_i z_i & \sum_i m_i(x_i^2 + y_i^2) \end{pmatrix} \cdot \begin{pmatrix} \omega_x \\ \omega_y \\ \omega_z \end{pmatrix} \quad (587)$$

In the continuum limit, we have:

$$\vec{H} = \int_{\Omega} \rho(\vec{r}) \vec{r} \times \vec{v} dV \quad (588)$$

and the 3×3 moment of inertia tensor \mathbf{I} (also called inertia tensor) is given by⁵²

$$\mathbf{I} = \int_{\Omega} \rho(\vec{r}) [\vec{r} \cdot \vec{r} \mathbf{1} - \vec{r} \times \vec{r}] dV \quad (589)$$

so that the above equation writes: $\vec{H} = \mathbf{I} \cdot \vec{\omega}$ and then $\vec{\omega} = \mathbf{I}^{-1} \cdot \vec{H}$.

Ultimately, at each velocity node a rotation about the rotation vector $\vec{\omega}$ is then subtracted from the velocity solution [1761, eq. 26]:

$$\vec{v}_{new} = \vec{v}_{old} - \vec{\omega} \times \vec{r} \quad (590)$$

Angular velocity approach The angular velocity⁵³ vector is given by $\vec{\omega} = \frac{\vec{r} \times \vec{v}}{r^2}$ so that the volume-averaged angular velocity of the cylindrical shell is:

$$\vec{\omega} = \frac{1}{|\Omega|} \int_{\Omega} \frac{\vec{r} \times \vec{v}}{r^2} dV \quad (591)$$

⁵¹<http://www.kwon3d.com/theory/moi/iten.html>

⁵²https://en.wikipedia.org/wiki/Moment_of_inertia

⁵³https://en.wikipedia.org/wiki/angular_velocity

8.30.1 Three dimensions

The angular momentum vector is given by:

$$\vec{H} = \int_{\Omega} \rho(\vec{r}) \begin{pmatrix} yw - zv \\ zu - xw \\ xv - yu \end{pmatrix} d\vec{r} = \begin{pmatrix} \int_{\Omega} \rho(\vec{r})(yw - zv) d\vec{r} \\ \int_{\Omega} \rho(\vec{r})(zu - xw) d\vec{r} \\ \int_{\Omega} \rho(\vec{r})(xv - yu) d\vec{r} \end{pmatrix} = \begin{pmatrix} H_x \\ H_y \\ H_z \end{pmatrix} \quad (592)$$

while the inertia tensor for a continuous body is given by

$$\mathbf{I} = \int_{\Omega} \rho(\vec{r}) [\vec{r} \cdot \vec{r} \mathbf{1} - \vec{r} \times \vec{r}] d\vec{r} \quad (593)$$

$$= \int_{\Omega} \rho(\vec{r}) \left[\begin{pmatrix} x^2 + y^2 + z^2 & 0 & 0 \\ 0 & x^2 + y^2 + z^2 & 0 \\ 0 & 0 & x^2 + y^2 + z^2 \end{pmatrix} - \begin{pmatrix} xx & xy & xz \\ yx & yy & yz \\ zx & zy & zz \end{pmatrix} \right] d\vec{r} \quad (594)$$

$$= \int_{\Omega} \rho(\vec{r}) \begin{pmatrix} y^2 + z^2 & -xy & -xz \\ -yx & x^2 + z^2 & -yz \\ -zx & -zy & x^2 + y^2 \end{pmatrix} d\vec{r} \quad (595)$$

$$= \begin{pmatrix} \int_{\Omega} \rho(\vec{r})(y^2 + z^2) d\vec{r} & -\int_{\Omega} \rho(\vec{r})xy d\vec{r} & -\int_{\Omega} \rho(\vec{r})xz d\vec{r} \\ -\int_{\Omega} \rho(\vec{r})yx d\vec{r} & \int_{\Omega} \rho(\vec{r})(x^2 + z^2) d\vec{r} & -\int_{\Omega} \rho(\vec{r})yz d\vec{r} \\ -\int_{\Omega} \rho(\vec{r})zx d\vec{r} & -\int_{\Omega} \rho(\vec{r})zy d\vec{r} & \int_{\Omega} \rho(\vec{r})(x^2 + y^2) d\vec{r} \end{pmatrix} \quad (596)$$

$$= \begin{pmatrix} I_{xx} & I_{xy} & I_{xz} \\ I_{yx} & I_{yy} & I_{yz} \\ I_{zx} & I_{zy} & I_{zz} \end{pmatrix} \quad (597)$$

8.30.2 Two dimensions

In two dimensions, flow is taking place in the (x, y) plane. This means that $\vec{r} = (x, y, 0)$ and $\vec{v} = (u, v, 0)$ are coplanar, and therefore that $\vec{\omega}$ is perpendicular to the plane. We have then

$$\vec{H} = \int_{\Omega} \rho(\vec{r}) \begin{pmatrix} 0 \\ 0 \\ xv - yu \end{pmatrix} d\vec{r} = \begin{pmatrix} 0 \\ 0 \\ \int_{\Omega} \rho(\vec{r})(xv - yu) d\vec{r} \end{pmatrix} \quad (598)$$

and

$$\mathbf{I} = \begin{pmatrix} I_{xx} & I_{xy} & I_{xz} \\ I_{yx} & I_{yy} & I_{yz} \\ I_{zx} & I_{zy} & I_{zz} \end{pmatrix} = \begin{pmatrix} I_{xx} & I_{xy} & 0 \\ I_{yx} & I_{yy} & 0 \\ 0 & 0 & I_{zz} \end{pmatrix} \quad (599)$$

since $I_{xz} = I_{yz} = 0$ as $z = 0$, and with $I_{xx} = \int_{\Omega} \rho(\vec{r})y^2 d\vec{r}$ and $I_{yy} = \int_{\Omega} \rho(\vec{r})x^2 d\vec{r}$. The solution to $\mathbf{I} \cdot \vec{\omega} = \vec{H}$ can be easily obtained (see Appendix G.2):

$$\omega_x = \frac{1}{\det(\mathbf{I})} \begin{vmatrix} 0 & I_{xy} & 0 \\ 0 & I_{yy} & 0 \\ H_3 & 0 & I_{zz} \end{vmatrix} = 0 \quad (600)$$

$$\omega_y = \frac{1}{\det(\mathbf{I})} \begin{vmatrix} I_{xx} & 0 & 0 \\ I_{yx} & 0 & 0 \\ 0 & H_z & I_{zz} \end{vmatrix} = 0 \quad (601)$$

$$\omega_z = \frac{1}{\det(\mathbf{I})} \begin{vmatrix} I_{xx} & I_{xy} & 0 \\ I_{yx} & I_{yy} & 0 \\ 0 & 0 & H_z \end{vmatrix} \quad (602)$$

$$= \frac{1}{\det(\mathbf{I})} (I_{xx}I_{yy}H_z - I_{yx}I_{xy}H_z) \quad (603)$$

$$= \frac{1}{\det(\mathbf{I})} (I_{xx}I_{yy} - I_{yx}I_{xy}) H_z \quad (604)$$

with $\det(\mathbf{I}) = I_{xx}I_{yy}I_{zz} - I_{yx}I_{xy}I_{zz}$. Concretely, this means that in 2D one does not need to solve the system $\mathbf{I} \cdot \vec{\omega} = \vec{H}$ since only ω_z is not zero.

Likewise, the volume-averaged angular velocity is then simply:

$$\omega_z = \frac{1}{|\Omega|} \int_{\Omega} \frac{xv - yu}{r^2} d\vec{r} \quad (605)$$

8.31 Picard and Newton

explain why our eqs are nonlinear

8.31.1 Picard iterations

Let us consider the following system of nonlinear algebraic equations:

$$\mathbb{A}(\vec{X}) \cdot \vec{X} = \vec{b}(\vec{X})$$

Both matrix and right hand side depend on the solution vector \vec{X} .

For many mildly nonlinear problems, a simple successive substitution iteration scheme (also called Picard method) will converge to the solution and it is given by the simple relationship:

$$\mathbb{A}(\vec{X}^n) \cdot \vec{X}^{n+1} = \vec{b}(\vec{X}^n)$$

where n is the iteration number. It is easy to implement:

1. guess \vec{X}^0 or use the solution from previous time step
2. compute \mathbb{A} and \vec{b} with current solution vector \vec{X}^{old}
3. solve system, obtain \vec{T}^{new}
4. check for convergence (are \vec{X}^{old} and \vec{X}^{new} close enough?)
5. $\vec{X}^{old} \leftarrow \vec{X}^{new}$
6. go back to 2.

There are various ways to test whether iterations have converged. The simplest one is to look at $\|\vec{X}^{old} - \vec{X}^{new}\|$ (in the L_1 , L_2 or maximum norm) and assess whether this term is smaller than a given tolerance ϵ . However this approach poses a problem: in geodynamics, if two consecutively obtained temperatures do not change by more than a thousandth of a Kelvin (say $\epsilon = 10^{-3}$ K) we could consider that iterations have converged but looking now at velocities which are of the order of a cm/year (i.e. $\sim 3 \cdot 10^{-11}$ m/s) we would need a tolerance probably less than 10^{-13} m/s. We see that using absolute values for a convergence criterion is a potentially dangerous affair, which is why one uses a relative formulation (thereby making ϵ a dimensionless parameter):

$$\frac{\|\vec{X}^{old} - \vec{X}^{new}\|}{\|\vec{X}^{new}\|} < \epsilon$$

Another convergence criterion is proposed by Reddy (section 3.7.2) [1361]:

$$\left(\frac{(\vec{X}^{old} - \vec{X}^{new}) \cdot (\vec{X}^{old} - \vec{X}^{new})}{\vec{X}^{new} \cdot \vec{X}^{new}} \right)^{1/2} < \epsilon$$

Yet another convergence criterion is used in [1538]: the means $\langle \vec{X}^{old} \rangle$, $\langle \vec{X}^{new} \rangle$ as well as the variances σ^{old} and σ^{new} are computed, followed by the correlation factor R :

$$R = \frac{\langle (\vec{X}^{old} - \langle \vec{X}^{old} \rangle) \cdot (\vec{X}^{new} - \langle \vec{X}^{new} \rangle) \rangle}{\sqrt{\sigma^{old} \sigma^{new}}}$$

Since the correlation is normalised, it takes values between 0 (very dissimilar velocity fields) and 1 (very similar fields). The following convergence criterion is then used: $1 - R < \epsilon$.

write about nonlinear residual

Note that in some instances and improvement in convergence rate can be obtained by use of a relaxation formula where one first solves

$$\mathbb{A}(\vec{X}^n) \cdot \vec{X}^* = \vec{b}(\vec{X}^n)$$

and then updates \vec{X}^n as follows:

$$\vec{X}^n = \gamma \vec{X}^n + (1 - \gamma) \vec{X}^* \quad 0 < \gamma \leq 1$$

When $\gamma = 1$ we recover the standard Picard iterations formula above.

8.32 Defect correction formulation

Work in progress.

We start from the system to solve:

$$\mathbf{A}(\vec{X}) \cdot \vec{X} = \vec{b}(\vec{X})$$

with the associated residual vector \vec{F}

$$\vec{F}(\vec{X}) = \mathbf{A}(\vec{X}) \cdot \vec{X} - \vec{b}(\vec{X})$$

The Newton-Raphson algorithm consists of two steps:

1. solve $\mathbf{J}_k \cdot \delta \vec{X}_k = -\vec{F}(\vec{X}_k)$, or in the case of the incompressible Stokes equation FEM system:

$$\begin{pmatrix} \mathbf{J}_k^{\mathcal{V}\mathcal{V}} & \mathbf{J}_k^{\mathcal{V}\mathcal{P}} \\ \mathbf{J}_k^{\mathcal{P}\mathcal{V}} & 0 \end{pmatrix} \cdot \begin{pmatrix} \delta \vec{\mathcal{V}}_k \\ \delta \vec{\mathcal{P}}_k \end{pmatrix} = \begin{pmatrix} -\vec{F}_k^{\mathcal{V}} \\ -\vec{F}_k^{\mathcal{P}} \end{pmatrix}$$

2. update $\vec{X}_{k+1} = \vec{X}_k + \alpha_k \delta \vec{X}_k$

The defect correction Picard approach consists of neglecting the derivative terms present in the J terms (Eqs. 16,17,18 of [587]) so that

$$\mathbf{J}_k^{\mathcal{V}\mathcal{V}} \simeq \mathbb{K}_k \quad \mathbf{J}_k^{\mathcal{V}\mathcal{P}} \simeq \mathbb{G} \quad \mathbf{J}_k^{\mathcal{P}\mathcal{V}} \simeq \mathbb{G}^T$$

and step 1 of the above iterations become:

$$\begin{pmatrix} \mathbb{K}_k & \mathbb{G} \\ \mathbb{G}^T & 0 \end{pmatrix} \cdot \begin{pmatrix} \delta \vec{\mathcal{V}}_k \\ \delta \vec{\mathcal{P}}_k \end{pmatrix} = \begin{pmatrix} -\vec{F}_k^{\mathcal{V}} \\ -\vec{F}_k^{\mathcal{P}} \end{pmatrix}$$

(MSc Thesis): implement a simple Newton solver and apply it to a few nonlinear benchmarks.

8.33 Parallel or not?

Let us assume that we want to run a simulation of the whole Earth mantle with a constant resolution of 5km. The volume of the mantle is

$$V_{mantle} = \frac{4}{3}\pi(R_{out}^3 - R_{in}^3) \simeq 10^{12} km^3$$

while the volume of an element is $V_e = 125 km^3$ (this is only an average since the tessellation of a hollow sphere with hexahedra yields elements which are not all similar [1541]). Consequently, the number of cells needed to discretise the mantle is

$$N_{el} = \frac{V_{mantle}}{V_e} \simeq 8 \times 10^9$$

We know that the matrix size is approx. 4 times the number of elements in 3D:

$$N \simeq 25 \times 10^9$$

Using between 9 and 125 particles per element (a very conservative number), the total number of particles is then

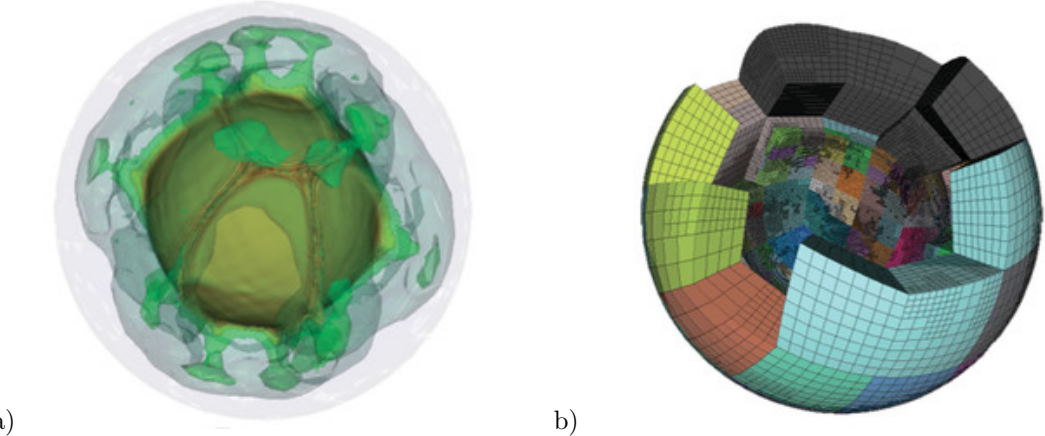
$$N_{particles} \geq 10^{10}$$

The unescapable conclusion is that high-resolution 3D calculations have a very large memory footprint and require extremely long computational times.

The only way to overcome this problem is by resorting to using supercomputers with many processors and large memory capacities.

The idea behind parallel programming is to have each processor carry out only a subset of the total number of operations required. In order to reduce the memory footprint on each processor, only a subset of the computational mesh is known by each: one speaks then of domain decomposition.

An example of such a large parallel calculation of 3D convection with domain decomposition in a spherical shell can be found in [1009]:



a) Isocontours of the temperature field; b) Partitioning of the domain onto 512 proc. The mesh counts 1,424,176 cells. The solution has approximately 54 million unknowns (39 million vel., 1.7 million press., and 13 million temp.)

8.34 Stream function

 Literature[689][1437][353][345]

8.34.1 In Cartesian coordinates

The Stream function (commonly denoted by Φ or Ψ) approach is a useful approach in fluid dynamics as it can provide relatively quick solutions to 2D incompressible flow problems. Lines of constant Φ are called stream lines and give a useful representation of the flow. The definition of the stream function is such that

$$u = -\frac{\partial \Phi}{\partial y} \quad (606)$$

$$v = \frac{\partial \Phi}{\partial x} \quad (607)$$

It then follows that the velocity field based on the above equations automatically fulfills the continuity equation:

$$\vec{\nabla} \cdot \vec{v} = \frac{\partial u}{\partial x} + \frac{\partial v}{\partial y} = -\frac{\partial^2 \Phi}{\partial x \partial y} + \frac{\partial^2 \Phi}{\partial y \partial x} = 0$$

The stream function can also be substituted into the (constant viscosity) Stokes equation $-\vec{\nabla} p + \eta \Delta \vec{v} = \vec{0}$:

$$-\frac{\partial p}{\partial x} - \eta \left(\frac{\partial^3 \Phi}{\partial^2 x \partial y} + \frac{\partial^3 \Phi}{\partial^3 y} \right) = 0 \quad (608)$$

$$-\frac{\partial p}{\partial y} - \eta \left(\frac{\partial^3 \Phi}{\partial^3 x} + \frac{\partial^3 \Phi}{\partial x \partial^2 y} \right) = 0 \quad (609)$$

We can now eliminate the pressure term by taking the partial derivative of the first equation with respect to y and the partial derivative of the second one with respect to x , and subtracting both. We get:

$$\frac{\partial^4 \Phi}{\partial x^4} + \frac{\partial^4 \Phi}{\partial x^2 \partial y^2} + \frac{\partial^4 \Phi}{\partial y^4} = 0 \quad (610)$$

or,

$$\left(\frac{\partial^2}{\partial x^2} + \frac{\partial^2}{\partial y^2} \right) \left(\frac{\partial^2}{\partial x^2} + \frac{\partial^2}{\partial y^2} \right) \Phi = 0 \quad (611)$$

or,

$$\vec{\nabla}^2 \vec{\nabla}^2 \Phi = \vec{\nabla}^4 \Phi = 0$$

which is known as the Biharmonic operator.

8.34.2 In Cylindrical coordinates

TODO

VERIFY THOSE! minus signs ?

$$\mathbf{v}_r = \frac{1}{r} \frac{\partial \Phi}{\partial \theta}$$

$$\mathbf{v}_\theta = -\frac{\partial \Phi}{\partial r}$$

8.35 Corner flow

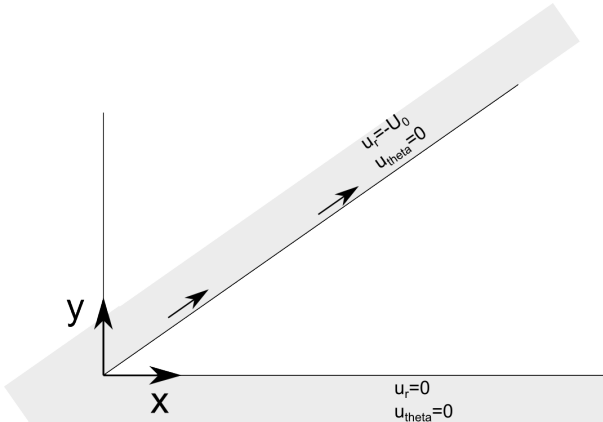
The mantle wedge comprised between the downgoing slab and the overriding plate has been extensively studied since very important geodynamical processes take place in it or right above it (slab dehydration and water transport, melting, over-riding plate deformation, vulcanism, ...).

To first approximation one can approach the problem and simplify it greatly by assuming that both plates kinematic behaviour are independent of what happens in the wedge, that the wedge geometry does not change over time, that the problem is essentially 2D, and that the mantle extends very far away from the actual wedge (plates are infinite).

Under such assumptions, it is possible to derive an analytical solution for incompressible Stokes flow in the wedge as documented at p. 224 in Batchelor [80].

FIND refs. check new version of Vol7 theoretical geophys

A corner flow setup is shown hereunder:



The solution to this problem is arrived at by means of the stream function Φ , defined as $u = -\partial\Phi/\partial y$ and $v = \partial\Phi/\partial x$, so that we automatically have $\vec{\nabla} \cdot \vec{v} = 0$. As shown in Section 8.34, the stream function Φ is then the solution to the biharmonic equation

$$\vec{\nabla}^2 \vec{\nabla}^2 \Phi = \vec{\nabla}^4 \Phi = 0$$

Considering the geometry of the problem has plates of infinite extent with constant relative velocity, the solution for velocity everywhere is expected to be independent of r . This means the equation is separable and we will use a solution of the form

$$\Phi(r, \theta) = R(r)f(\theta)$$

However, given the infinite extent of the domain, the velocity is expected to be independent of r , so we postulate $R(r) = r$ (look at the relationship between velocity components and stream function), or:

$$\Phi(r, \theta) = rf(\theta)$$

and we then have to solve

$$\Delta \left(\frac{1}{r}(f + f'') \right) = \frac{1}{r^3}(f + 2f'' + f''') = 0.$$

The solution of this equation for f is:

$$\begin{aligned} f(\theta) &= A \sin \theta + B \cos \theta + C \theta \sin \theta + D \theta \cos \theta \\ f'(\theta) &= A \cos \theta - B \sin \theta + C(\sin \theta + \theta \cos \theta) + D(\cos \theta - \theta \sin \theta) \end{aligned}$$

with

$$v_r = \frac{1}{r} \frac{\partial \Phi}{\partial \theta} = f'(\theta)$$

$$v_\theta = -\frac{\partial \Phi}{\partial r} = -f(\theta)$$

A, B, C and D are four constants to be determined by means of the boundary conditions which are as follows:

$$\begin{aligned}\mathbf{v}_r(\theta = 0) &= 0 \\ \mathbf{v}_\theta(\theta = 0) &= 0 \\ \mathbf{v}_r(\theta = \theta_0) &= -U_0 \\ \mathbf{v}_\theta(\theta = \theta_0) &= 0\end{aligned}$$

or,

$$f'(0) = A + D = 0 \quad (612)$$

$$f(0) = B = 0 \quad (613)$$

$$f'(\theta_0) = -U_0 \quad (614)$$

$$f(\theta_0) = 0 \quad (615)$$

From the second equation it is trivial to see that $B = 0$, so that:

$$f(\theta) = A \sin \theta + C\theta \sin \theta + D\theta \cos \theta$$

$$f'(\theta) = A \cos \theta + C(\sin \theta + \theta \cos \theta) + D(\cos \theta - \theta \sin \theta)$$

From the first one we obtain $D = -A$ so that

$$f(\theta) = A(\sin \theta - \theta \cos \theta) + C\theta \sin \theta$$

$$f'(\theta) = A(\theta \sin \theta) + C(\sin \theta + \theta \cos \theta)$$

The last two boundary conditions yield:

$$0 = A(\sin \theta_0 - \theta_0 \cos \theta_0) + C\theta_0 \sin \theta_0$$

$$-U_0 = A(\theta_0 \sin \theta_0) + C(\sin \theta_0 + \theta_0 \cos \theta_0)$$

or,

$$A = -U_0 \frac{\theta_0 \sin \theta_0}{\theta_0^2 - \sin^2 \theta_0} \quad C = U_0 \frac{\sin \theta_0 - \theta_0 \cos \theta_0}{\theta_0^2 - \sin^2 \theta_0}$$

Finally:

$$(A, B, C, D) = (-\theta_0 \sin \theta_0, 0, \sin \theta_0 - \theta_0 \cos \theta_0, \theta_0 \sin \theta_0) \frac{U_0}{\theta_0^2 - \sin^2 \theta_0}$$

We have

$$\mathbf{e}_r = \cos \theta \mathbf{e}_x + \sin \theta \mathbf{e}_y \quad (616)$$

$$\mathbf{e}_\theta = -\sin \theta \mathbf{e}_x + \cos \theta \mathbf{e}_y \quad (617)$$

so that the velocity field can be expressed in cartesian coordinates:

$$\begin{aligned}\mathbf{v} &= \mathbf{v}_r \mathbf{e}_r + \mathbf{v}_\theta \mathbf{e}_\theta \\ &= \mathbf{v}_r (\cos \theta \mathbf{u}_x + \sin \theta \mathbf{u}_y) + \mathbf{v}_\theta (-\sin \theta \mathbf{u}_x + \cos \theta \mathbf{u}_y) \\ &= (\mathbf{v}_r \cos \theta - \mathbf{v}_\theta \sin \theta) \mathbf{u}_x + (\mathbf{v}_r \sin \theta + \mathbf{v}_\theta \cos \theta) \mathbf{u}_y\end{aligned} \quad (618)$$

8.36 Surface processes

8.36.1 In 1D - simple nonlinear diffusion a la [268]

The tectonic-scale transport equations describe long term changes in topography $h(x, y, t)$ as a result of simultaneous short- and long-range mass transport processes [93, 987].

The short-range surface processes are represented by cumulative effects of hillslope processes (soil creep, rainsplash, slides) that remove material from uplifted areas down to the valleys. It is then assumed that the horizontal material flux \vec{q}_s is related to local slope $\vec{\nabla}h$ by $\vec{q}_s = -K_s \vec{\nabla}h$ where K_s is the effective diffusivity. Assumption of conservation of mass volume leads to the linear diffusion equation for erosion:

$$\frac{\partial h}{\partial t} = K_s \Delta h$$

This equation can be solved with constant-elevation (fixed h value) boundary conditions simulating local base levels of erosion.

Note that in practice the coefficient K_s might depend on slope and curvature, i.e.

$$\frac{\partial h}{\partial t} = K_s(x, y, h, \vec{\nabla}h) \Delta h$$

Following [717], Burov & Cloetingh use an empirical non linear expression $K_s = k_s(x)(\vec{\nabla}h)^n$.

8.36.2 In 1D - not so simple, a la [33]

The change in surface elevation rate due to surface processes is equal to the divergence of the sediment flux (assuming there is no density difference between the bedrock and sediment and ignoring the effects of compaction):

$$\frac{\partial h}{\partial t} = -\frac{\partial q_s}{\partial x}$$

where h is the topography, t is the time, q_s represents the sediment flux, and x is the horizontal coordinate.

The next step consists in a formulation for the sediment flux. Still following [33], in the subaerial environment, it is possible to define the sediment transport flux q_s in terms of the water flux q_w as

$$q_s = -(K + cq_w^n) \frac{\partial h}{\partial x}$$

where K is the slope diffusivity, c is the transport coefficient, and $n \geq 1$ is the power law that defines the type of relationship between the sediment transport and the water flux (Simpson & Schlunegger, 2003; Smith & Bretherton, 1972).

[get these papers](#)

This model accounts for hillslope diffusion processes where the topography will tend to a dispersive diffusion (Culling, 1960) and fluvial transport processes that result in concentrative diffusion due to water run off (Graf, 1984). For a simple parameterization we choose a linear relationship between sediment transport and water flux ($n = 1$).

The water flux can be related to the water discharge/effective rainfall α as

$$\frac{\partial}{\partial x}(\vec{n}q_w) = -\alpha$$

where \vec{n} is a unit vector directed down the surface gradient (Smith & Bretherton, 1972). By assuming a constant α and integrating equation (12) over the surface in the downstream direction, we obtain

$$q_w = \alpha x_d$$

where x_d is the downstream distance from the drainage divide. By substituting equations (11) and (13) into (10) we obtain the 1-D sediment mass conservation equation for combined hillslope and discharge-dependent fluvial transport

$$\frac{\partial h}{\partial t} = \frac{\partial}{\partial x} \left((K + k\alpha x_d) \frac{\partial h}{\partial x} \right)$$

where the downstream distance x_d is calculated at each time step as the distance from the topographic highs to the valley floors. Because q_w is dependent on the length of the drainage, the model mimics 1-D landscapes similar to river profiles in which fluvial processes are dominant.

8.37 Geometric multigrid

The following is mostly borrowed from the Wikipedia page on multigrid methods⁵⁴.

There are many types of (geometric) multigrid algorithms, but the common features are that a hierarchy of grids is considered. The important steps are:

- *Smoothing*: reducing high frequency errors, for example using a few iterations of the Gauss-Seidel method.
- *Residual Computation*: computing residual error after the smoothing operation(s).
- *Restriction*: downsampling the residual error to a coarser grid.
- *Interpolation or prolongation*: interpolating a correction computed on a coarser grid into a finer grid.
- *Correction*: Adding prolonged coarser grid solution onto the finer grid.

There are many choices of multigrid methods with varying trade-offs between speed of solving a single iteration and the rate of convergence with said iteration. The 3 main types are V-Cycle, F-Cycle, and W-Cycle.

Any geometric multigrid cycle iteration is performed on a hierarchy of grids and hence it can be coded using recursion. Since the function calls itself with smaller sized (coarser) parameters, the coarsest grid is where the recursion stops.

Note that the ratio of the number of nodes between two consecutive levels has to be constant between all the levels. Often powers of 2 are used (especially if the grids are based on quad/octrees) but it is not a requirement.

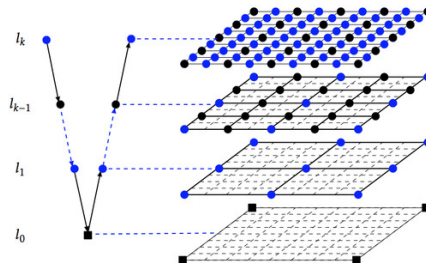


Image from <http://web.utk.edu/~wfeng1/research.html>

What follows is a pseudo-code example of a recursive V-Cycle Multigrid for solving the Poisson equation ($\nabla^2\phi = f$) on a uniform grid of spacing h :

```
function phi = V_Cycle(phi,f,h)
% Pre-Smoothing
phi = smoothing(phi,f,h);
% Compute Residual Errors
r = residual(phi,f,h);
% Restriction
rhs = restriction(r);
eps = zeros(size(rhs));
% stop recursion at smallest grid size
if smallest_grid_size_is_achieved
    eps = smoothing(eps,rhs,2*h);
else
    eps = V_Cycle(eps,rhs,2*h);
end
% Prolongation and Correction
```

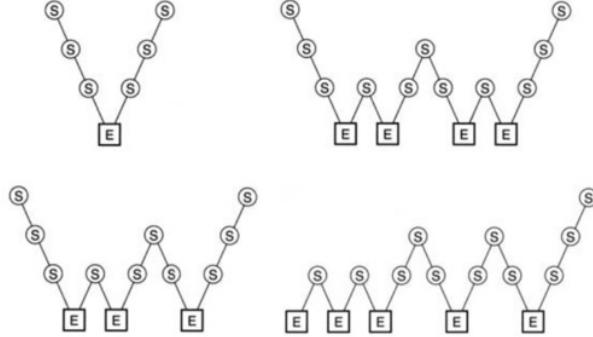
⁵⁴https://en.wikipedia.org/wiki/Multigrid_method

```

phi = phi + prolongation(eps);
% Post-Smoothing
phi = smoothing(phi,f,h);
end

```

A multigrid method with an intentionally reduced tolerance can be used as an efficient preconditioner for an external iterative solver. The solution may still be obtained in $\mathcal{O}(N)$ time as well as in the case where the multigrid method is used as a solver. Multigrid preconditioning is used in practice even for linear systems, typically with one cycle per iteration.



Taken from [885]: Different types of multigrid cycle with four grid levels: (top left) V-cycle, (top right) W-cycle, (bottom left) F-cycle and (bottom right) full multigrid. S denotes smoothing while E denotes exact coarse-grid solution.

Check Kaus BEcker syllabus!

Literature: [885, 656, 1151, 1095, 1569, 1228, 1726, 1728]

8.38 Computing depth

In the case of a perfectly rectangular, cylindrical or spherical domain, computing the depth of any given point inside the domain is trivial. However, when the free surface becomes somewhat distorted, the concept of depth needs to be refined. What follows is an attempt at bringing clarity as to how to compute depth in all cases.

The depth $d(\mathbf{r})$ satisfies the equation:

$$\frac{\mathbf{g}}{|\mathbf{g}|} \cdot \nabla d = 1$$

with $d = 0$ at the surface.

This is a form of steady-state advection equation (the time derivative is zero, there is no diffusion, nor any source term).

Given the boundary conditions, one could solve this equation over the whole domain.

Note that in the case of a cartesian box, $\mathbf{g} = -g\mathbf{u}_z$, we need to solve

$$-\frac{\partial}{\partial z} d = 1$$

For a flat top surface at $d(z = L_z) = 0$ so that in the end

$$d(z) = L_z - z$$

8.39 Imposing boundary conditions

Let us consider a quadrilateral element with one degree of freedom per node and let us assume that we are solving the temperature equation. The local matrix and right-hand side vector are given by

$$A_{el}(4 \times 4) \quad \text{and} \quad B_{el}(4)$$

Let us assume that we want to impose $\tilde{T} = 10$ on the third node (local coordinates numbering). For instance, having built A_{el} and B_{el} , the system looks like :

$$\begin{pmatrix} 3 & 1 & 6 & 9 \\ 5 & 2 & 2 & 8 \\ 7 & 4 & 11 & 2 \\ 9 & 6 & 4 & 3 \end{pmatrix} \begin{pmatrix} T_1 \\ T_2 \\ T_3 \\ T_4 \end{pmatrix} = \begin{pmatrix} 4 \\ 3 \\ 1 \\ 2 \end{pmatrix}$$

which can be rewritten

$$3T_1 + T_2 + 6T_3 + 9T_4 = 4$$

$$5T_1 + 2T_2 + 2T_3 + 8T_4 = 3$$

$$7T_1 + 4T_2 + 11T_3 + 2T_4 = 1$$

$$9T_1 + 6T_2 + 4T_3 + 3T_4 = 2$$

or,

$$3T_1 + T_2 + +9T_4 = 4 - 6T_3$$

$$5T_1 + 2T_2 + +8T_4 = 3 - 2T_3$$

$$7T_1 + 4T_2 + 11T_3 + 2T_4 = 1$$

$$9T_1 + 6T_2 + +3T_4 = 2 - 4T_3$$

- Technique 1: (See [?], p55) Replace the hereabove system by

$$\begin{pmatrix} 3 & 1 & 6 & 9 \\ 5 & 2 & 2 & 8 \\ 7 & 4 & 11 + 10^{12} & 2 \\ 9 & 6 & 4 & 3 \end{pmatrix} \begin{pmatrix} T_1 \\ T_2 \\ T_3 \\ T_4 \end{pmatrix} = \begin{pmatrix} 4 \\ 3 \\ \tilde{T} \times (11 + 10^{12}) \\ 2 \end{pmatrix}$$

- Technique 2: One can choose not to solve for T_3 anymore, i.e. not to consider it as a degree of freedom and therefore write:

$$3T_1 + T_2 + 9T_4 = 4 - 6T_3$$

$$5T_1 + 2T_2 + 8T_4 = 3 - 2T_3$$

$$9T_1 + 6T_2 + 3T_4 = 2 - 4T_3$$

- Technique 3: Since we want to impose $T_3 = 10$, then we can write

$$3T_1 + T_2 + +9T_4 = 4 - 6T_3$$

$$5T_1 + 2T_2 + +8T_4 = 3 - 2T_3$$

$$0 + 0 + T_3 + 0 = 10$$

$$9T_1 + 6T_2 + +3T_4 = 2 - 4T_3$$

and in matrix form :

$$\begin{pmatrix} 3 & 1 & 0 & 9 \\ 5 & 2 & 0 & 8 \\ 0 & 0 & 1 & 0 \\ 9 & 6 & 0 & 3 \end{pmatrix} \begin{pmatrix} T_1 \\ T_2 \\ T_3 \\ T_4 \end{pmatrix} = \begin{pmatrix} 4 - A_{13}T_3 \\ 3 - A_{23}T_3 \\ 10 \\ 2 - A_{43}T_3 \end{pmatrix}$$

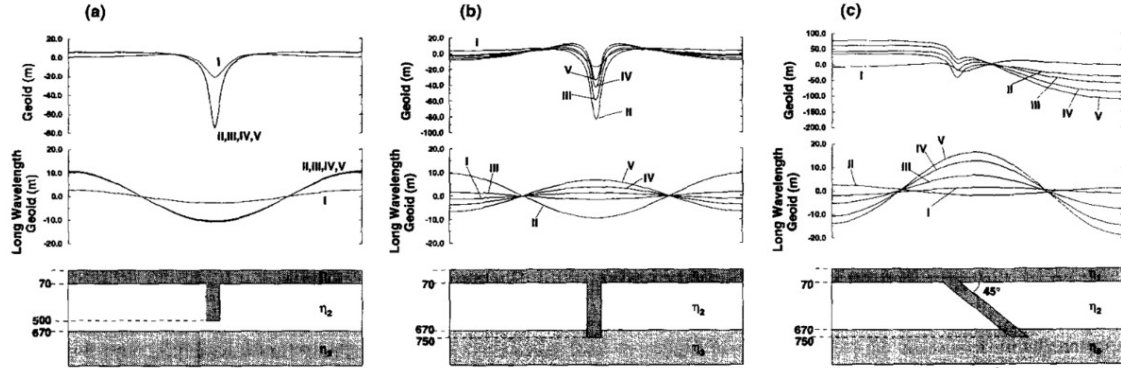
The first technique is not a good idea in practice as it introduces very large values and will likely derail the solver. The second option is somewhat difficult to implement as it means that elemental matrix and rhs sizes will change from element to element and it therefore requires more book-keeping. The third technique is the one adopted throughout this document.

8.40 The Geoid

8.40.1 What is the geoid?

8.40.2 How to compute it?

8.40.3 Interesting modelling



Idealized 2D slab calculations for each viscosity model: geoid and geoid filtered to pass only the longest wavelengths (~ 4000 km). (a) Cold slab extends to 500 km depth in the upper mantle, (b) Slab extends to 750 km so that it is partly supported by the high viscosity lower mantle at 670 km. (c) Slab tilted at 45° to the vertical extending to the top of the lower mantle. Taken from [1209]

9 Gravity and co

WORK in PROGRESS. DUH.

We start from the Poisson equation for the gravity potential:

$$\Delta U = 4\pi\rho\mathcal{G} \quad (619)$$

As a consequence, inside a domain where $\rho = 0$, the equation becomes $\Delta U = 0$.

Let us assume that the spherical coordinates are appropriate for the problem at hand, and that the potential can be decomposed as follows:

$$U(r, \theta, \phi) = U_r(r)U_\perp(\theta, \phi)$$

The full Laplacian operator in spherical coordinates is given by⁵⁵:

$$\Delta U = \underbrace{\frac{1}{r^2}\frac{\partial}{\partial r}\left(r^2\frac{\partial U}{\partial r}\right)}_{\Delta_r} + \underbrace{\frac{1}{r^2\sin\theta}\frac{\partial}{\partial\theta}\left(\sin\theta\frac{\partial U}{\partial\theta}\right)}_{\Delta_\perp} + \frac{1}{r^2\sin^2\theta}\frac{\partial^2 U}{\partial\phi^2}$$

we then have:

$$(\Delta_r + \Delta_\perp)(U_r U_\perp) = 0$$

i.e.,

$$U_\perp \Delta_r U_r + U_r \Delta_\perp U_\perp = 0$$

Assuming $U_\perp = \sum_l \sum_m U_{lm} Y_{lm}$, knowing that spherical harmonics functions verify

$$r^2 \Delta_\perp Y_l^m(\theta, \phi) = -l(l+1)Y_l^m(\theta, \phi)$$

and assuming for now that the problem at hand is 1st degree ($l=1$), then

$$\Delta_\perp Y_l^m(\theta, \phi) = -\frac{2}{r^2} Y_l^m(\theta, \phi)$$

and then

$$\Delta_r U_r - U_r \frac{2}{r^2} = 0$$

make a link with my 2018 paper.

⁵⁵https://en.wikipedia.org/wiki/Laplace_operator

Stone 01: simple analytical solution (D&H)

This fieldstone was developed in collaboration with Job Mos.

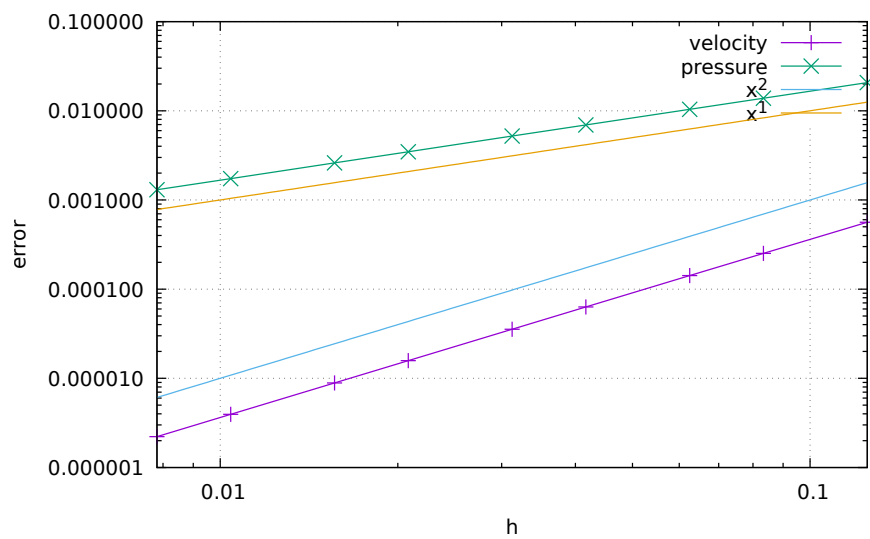
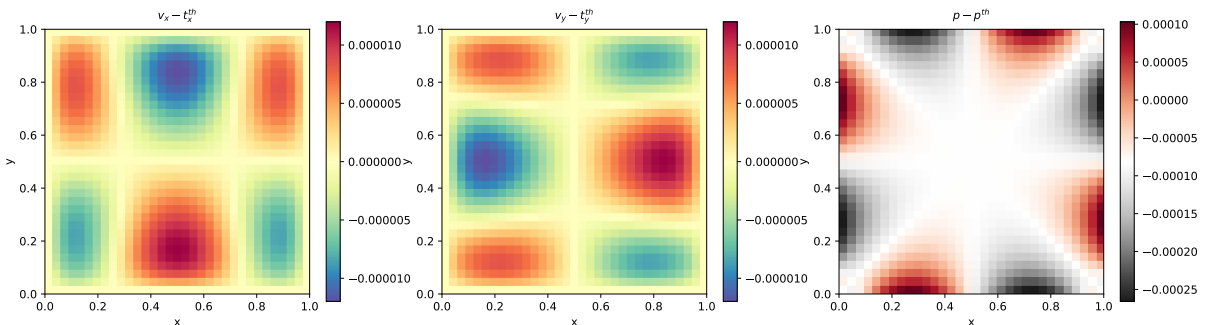
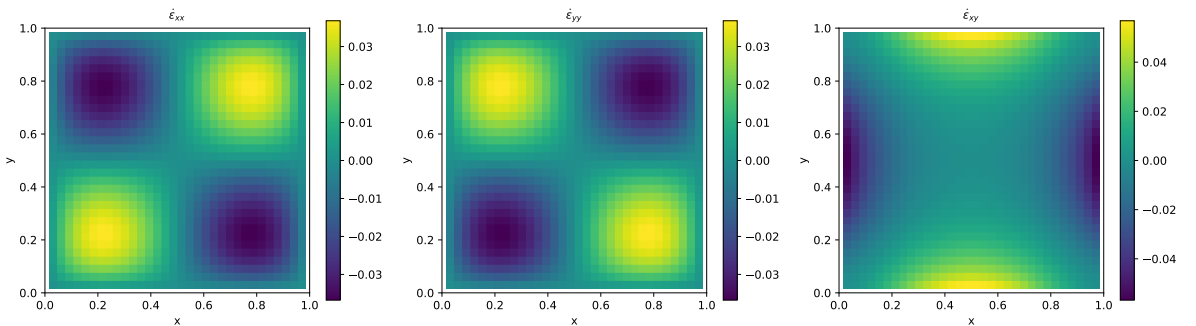
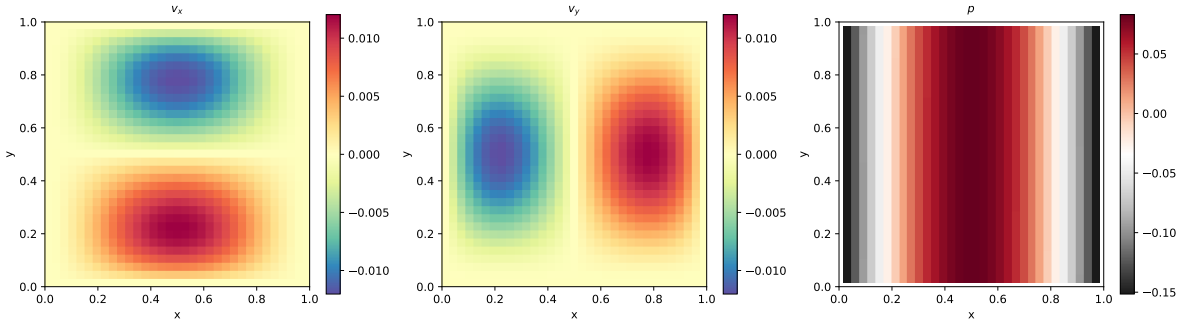
This benchmark is taken from [473] and is described fully in section 8.6. In order to illustrate the behavior of selected mixed finite elements in the solution of stationary Stokes flow, we consider a two-dimensional problem in the square domain $\Omega = [0, 1] \times [0, 1]$, which possesses a closed-form analytical solution. The problem consists of determining the velocity field $\mathbf{v} = (u, v)$ and the pressure p such that

$$\begin{aligned}\eta \Delta \vec{v} - \vec{\nabla} p + \vec{b} &= \vec{0} && \text{in } \Omega \\ \vec{\nabla} \cdot \vec{v} &= 0 && \text{in } \Omega \\ \vec{v} &= \vec{0} && \text{on } \Gamma_D\end{aligned}$$

where the fluid viscosity is taken as $\eta = 1$.

features

- $Q_1 \times P_0$ element
- incompressible flow
- penalty formulation
- Dirichlet boundary conditions (no-slip)
- direct solver
- isothermal
- isoviscous
- analytical solution



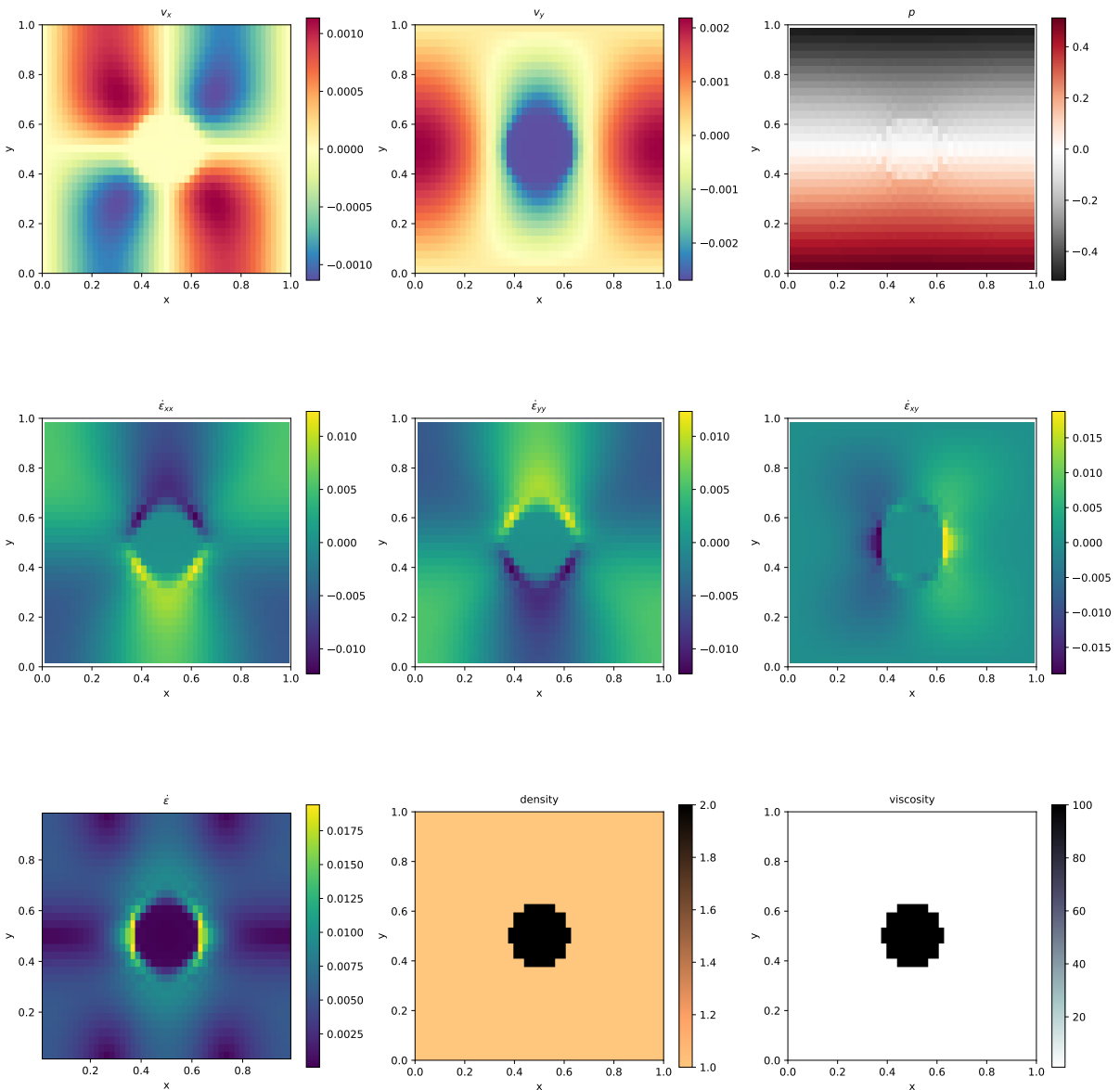
Quadratic convergence for velocity error, linear convergence for pressure error, as expected.

Stone 02: Stokes sphere

Viscosity and density directly computed at the quadrature points.

features

- $Q_1 \times P_0$ element
- incompressible flow
- penalty formulation
- Dirichlet boundary conditions (free-slip)
- isothermal
- non-isoviscous
- buoyancy-driven flow
- Stokes sphere



Stone 03: Convection in a 2D box

This benchmark deals with the 2-D thermal convection of a fluid of infinite Prandtl number in a rectangular closed cell. In what follows, I carry out the case 1a, 1b, and 1c experiments as shown in [158]: steady convection with constant viscosity in a square box.

The temperature is fixed to zero on top and to ΔT at the bottom, with reflecting symmetry at the sidewalls (i.e. $\partial_x T = 0$) and there are no internal heat sources. Free-slip conditions are implemented on all boundaries.

The Rayleigh number is given by

$$Ra = \frac{\alpha g_y \Delta T h^3}{\kappa \nu} = \frac{\alpha g_y \Delta T h^3 \rho^2 C_p}{k \mu} \quad (620)$$

In what follows, I use the following parameter values: $L_x = L_y = 1, \rho_0 = c_P = k = \mu = 1, T_0 = 0, \alpha = 10^{-2}, g = 10^2 Ra$ and I run the model with $Ra = 10^4, 10^5$ and 10^6 .

The initial temperature field is given by

$$T(x, y) = (1 - y) - 0.01 \cos(\pi x) \sin(\pi y) \quad (621)$$

The perturbation in the initial temperature fields leads to a perturbation of the density field and sets the fluid in motion.

Depending on the initial Rayleigh number, the system ultimately reaches a steady state after some time.

The Nusselt number (i.e. the mean surface temperature gradient over mean bottom temperature) is computed as follows [158]:

$$Nu = L_y \frac{\int \frac{\partial T}{\partial y} (y = L_y) dx}{\int T(y = 0) dx} \quad (622)$$

Note that in our case the denominator is equal to 1 since $L_x = 1$ and the temperature at the bottom is prescribed to be 1.

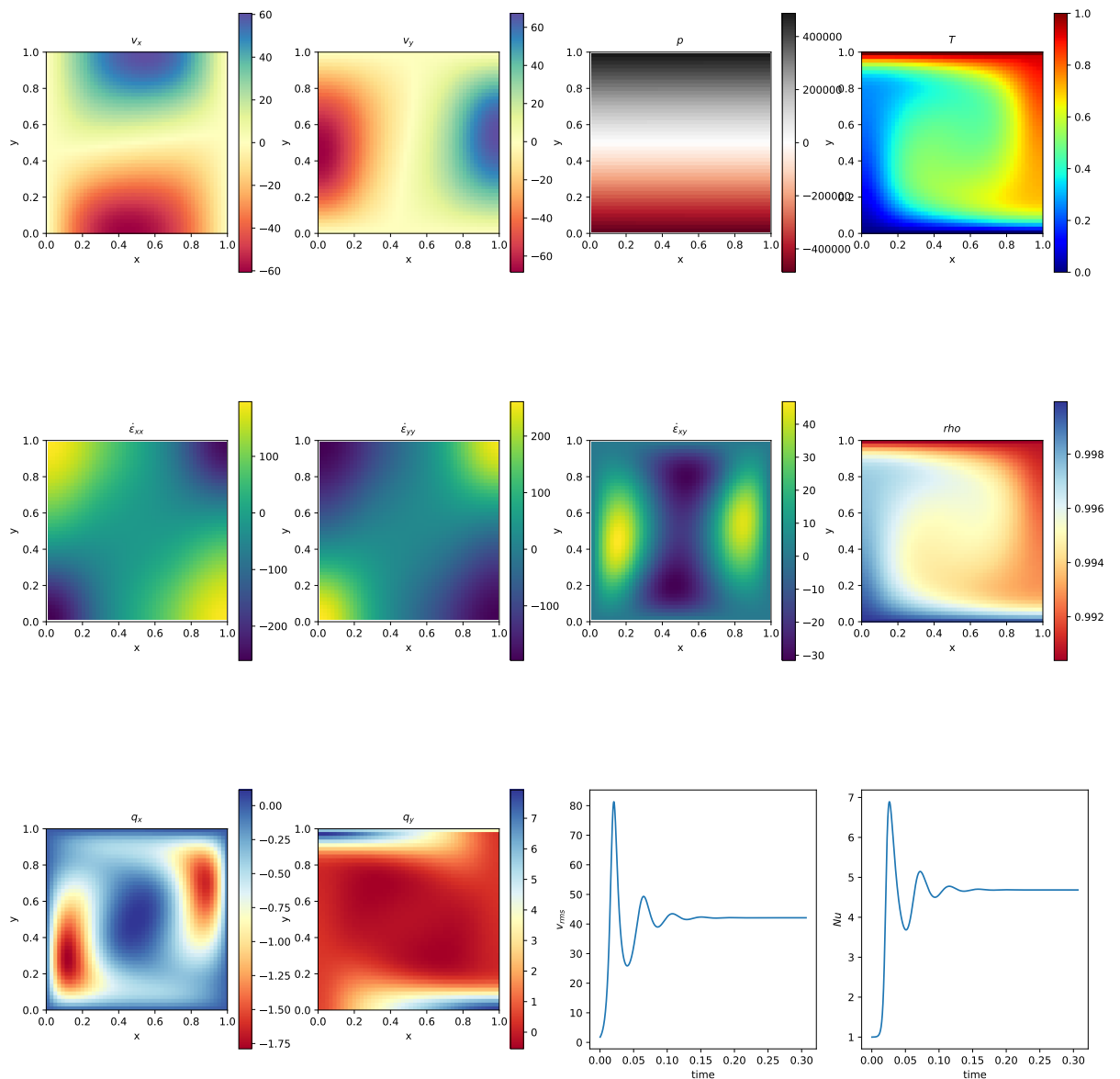
Finally, the steady state root mean square velocity and Nusselt number measurements are indicated in Table ?? alongside those of [158] and [1498]. (Note that this benchmark was also carried out and published in other publications [1567, 13, 656, 440, 1053] but since they did not provide a complete set of measurement values, they are not included in the table.)

		Blankenbach et al	Tackley [1498]
$Ra = 10^4$	V_{rms}	42.864947 ± 0.000020	42.775
	Nu	4.884409 ± 0.000010	4.878
$Ra = 10^5$	V_{rms}	193.21454 ± 0.00010	193.11
	Nu	10.534095 ± 0.000010	10.531
$Ra = 10^6$	V_{rms}	833.98977 ± 0.00020	833.55
	Nu	21.972465 ± 0.000020	21.998

Steady state Nusselt number Nu and V_{rms} measurements as reported in the literature.

features

- $Q_1 \times P_0$ element
- incompressible flow
- penalty formulation
- Dirichlet boundary conditions (free-slip)
- Boussinesq approximation
- direct solver
- non-isothermal
- buoyancy-driven flow
- isoviscous
- CFL-condition



ToDo:

implement steady state criterion

reach steady state

do $\text{Ra}=1\text{e}4, 1\text{e}5, 1\text{e}6$

plot against blankenbach paper and aspect

look at critical Ra number

This benchmark has been carried out in many scientific papers [136].

Stone 04: The lid driven cavity

The lid driven cavity is a famous Computational Fluid Dynamics test case [953, 682, 1290, 176, 228, 746, 1453] and has been studied in countless publications with a wealth of numerical techniques (see [522] for a succinct review) and also in the laboratory [1000].

It models a plane flow of an isothermal isoviscous fluid in a rectangular (usually square) lid-driven cavity. The boundary conditions are indicated in the Fig. ??a. The gravity is set to zero.

the lid driven cavity problem (ldc=0)

In the standard case, the upper side of the cavity moves in its own plane at unit speed, while the other sides are fixed. This thereby introduces a discontinuity in the boundary conditions at the two upper corners of the cavity and yields an uncertainty as to which boundary (side or top) the corner points belong to. In this version of the code the top corner nodes are considered to be part of the lid. If these are excluded the recovered pressure showcases an extremely large checkboard pattern.

This benchmark is usually discussed in the context of low to very high Reynolds number with the full Navier-Stokes equations being solved (with the noticeable exception of [1425, 1426, 324, 506] which focus on the Stokes equation). In the case of the incompressible Stokes flow, the absence of inertia renders this problem instantaneous so that only one time step is needed.

the lid driven cavity problem - regularisation I (ldc=1)

We avoid the top corner nodes issue altogether by prescribing the horizontal velocity of the lid as follows:

$$u(x) = x^2(1-x)^2. \quad (623)$$

In this case the velocity and its first derivative is continuous at the corners. This is the so-called regularised lid-driven cavity problem [1306].

the lid driven cavity problem - regularisation II (ldc=2)

Another regularisation was presented in [451]. Also in Appendix D.4 of [915]. Here, a regularized lid driven cavity is studied which is consistent in the sense that $\nabla \cdot \mathbf{v} = 0$ holds also at the corners of the domain. There are no-slip conditions at the boundaries $x = 0$, $x = 1$, and $y = 0$.

The velocity at $y = 1$ is given by

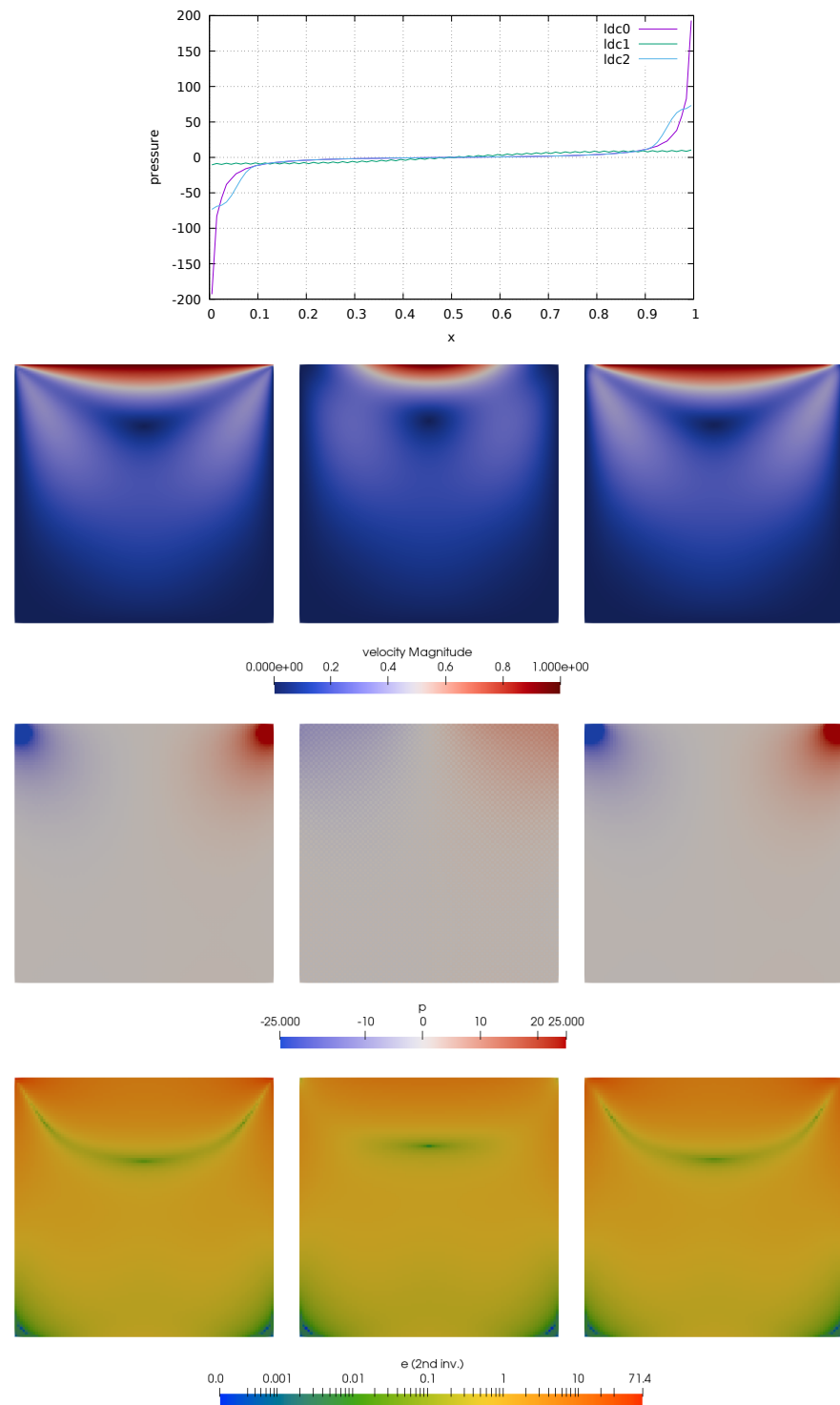
$$\begin{aligned} u(x) &= 1 - \frac{1}{4} \left(1 - \cos\left(\frac{x_1 - x}{x_1}\pi\right) \right)^2 & x \in [0, x_1] \\ u(x) &= 1 & x \in [x_1, 1 - x_1] \\ u(x) &= 1 - \frac{1}{4} \left(1 - \cos\left(\frac{x - (1 - x_1)}{x_1}\pi\right) \right)^2 & x \in [1 - x_1, 1] \end{aligned} \quad (624)$$

Results are obtained with $x_1 = 0.1$.

features

- $Q_1 \times P_0$ element
- incompressible flow
- penalty formulation
- isothermal
- isoviscous

A 100x100 element grid is used. No-slip boundary conditions are prescribed on sides and bottom. A zero vertical velocity is prescribed at the top and the exact form of the prescribed horizontal velocity is controlled by the ldc parameter.



Stone 05: SolCx benchmark

The SolCx benchmark is intended to test the accuracy of the solution to a problem that has a large jump in the viscosity along a line through the domain. Such situations are common in geophysics: for example, the viscosity in a cold, subducting slab is much larger than in the surrounding, relatively hot mantle material.

The SolCx benchmark computes the Stokes flow field of a fluid driven by spatial density variations, subject to a spatially variable viscosity. Specifically, the domain is $\Omega = [0, 1]^2$, gravity is $\mathbf{g} = (0, -1)^T$ and the density is given by

$$\rho(x, y) = \sin(\pi y) \cos(\pi x) \quad (625)$$

Boundary conditions are free slip on all of the sides of the domain and the temperature plays no role in this benchmark. The viscosity is prescribed as follows:

$$\mu(x, y) = \begin{cases} 1 & \text{for } x < 0.5 \\ 10^6 & \text{for } x > 0.5 \end{cases} \quad (626)$$

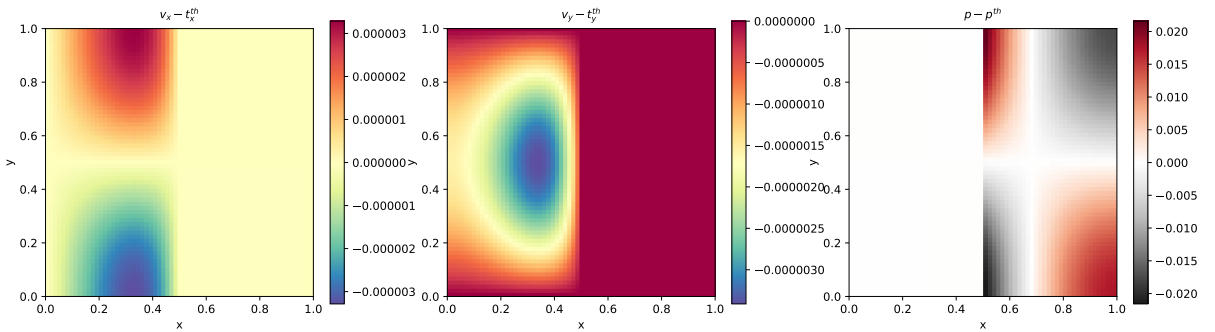
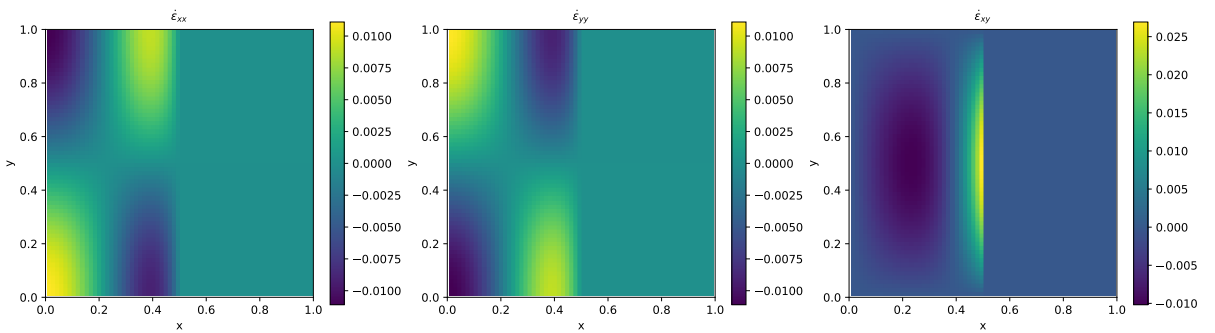
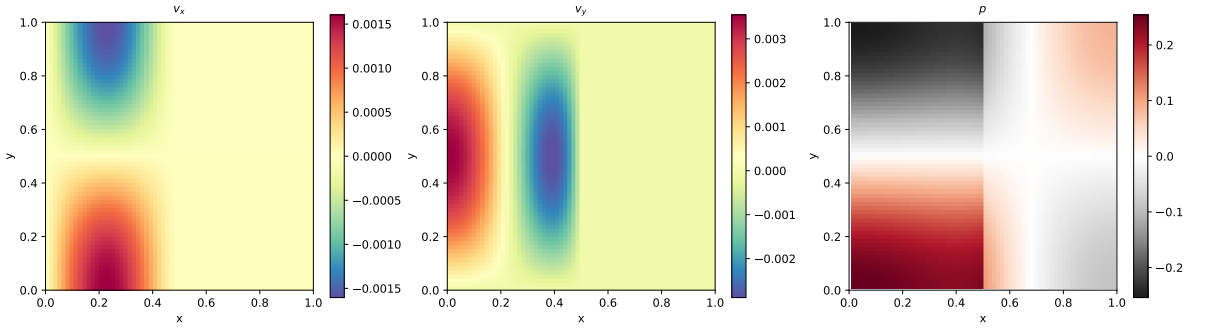
Note the strongly discontinuous viscosity field yields a stagnant flow in the right half of the domain and thereby yields a pressure discontinuity along the interface.

The SolCx benchmark was previously used in [490] (references to earlier uses of the benchmark are available there) and its analytic solution is given in [1768]. It has been carried out in [1009] and [668]. Note that the source code which evaluates the velocity and pressure fields for both SolCx and SolKz is distributed as part of the open source package Underworld ([1212], <http://underworldproject.org>).

In this particular example, the viscosity is computed analytically at the quadrature points (i.e. tracers are not used to attribute a viscosity to the element). If the number of elements is even in any direction, all elements (and their associated quadrature points) have a constant viscosity(1 or 10^6). If it is odd, then the elements situated at the viscosity jump have half their integration points with $\mu = 1$ and half with $\mu = 10^6$ (which is a pathological case since the used quadrature rule inside elements cannot represent accurately such a jump).

features

- $Q_1 \times P_0$ element
- incompressible flow
- penalty formulation
- Dirichlet boundary conditions (free-slip)
- direct solver
- isothermal
- non-isoviscous
- analytical solution



What we learn from this

Stone 06: SolKz benchmark

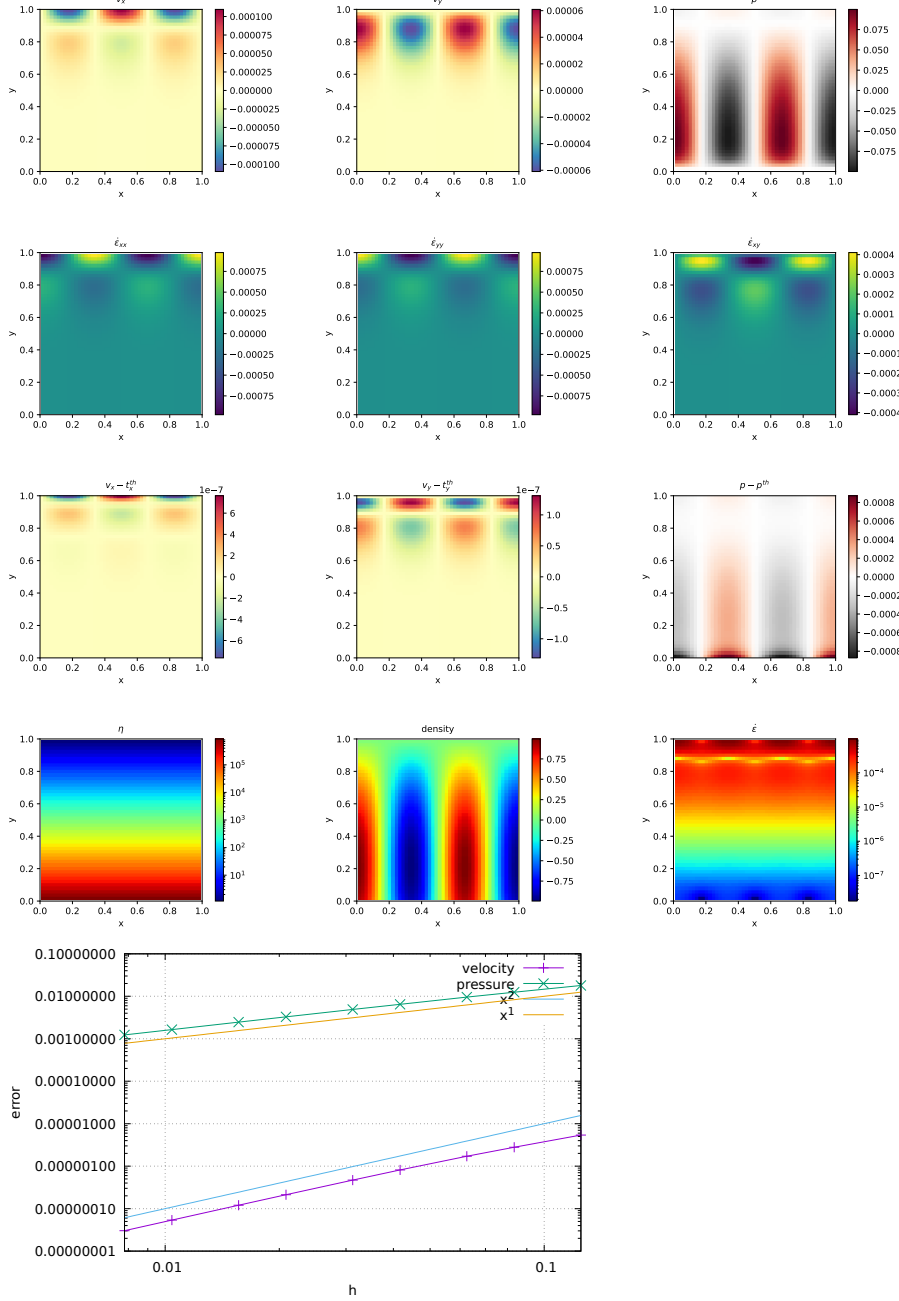
The SolKz benchmark [1376] is similar to the SolCx benchmark, but the viscosity is now a function of the space coordinates:

$$\mu(y) = \exp(By) \quad \text{with} \quad B = 13.8155 \quad (627)$$

It is however not a discontinuous function but grows exponentially with the vertical coordinate so that its overall variation is again 10^6 . The forcing is again chosen by imposing a spatially variable density variation as follows:

$$\rho(x, y) = \sin(2y) \cos(3\pi x) \quad (628)$$

Free slip boundary conditions are imposed on all sides of the domain. This benchmark is presented in [1768] as well and is studied in [490] and [668].



Stone 07: SolVi benchmark

Following SolCx and SolKz, the SolVi inclusion benchmark solves a problem with a discontinuous viscosity field, but in this case the viscosity field is chosen in such a way that the discontinuity is along a circle. Given the regular nature of the grid used by a majority of codes and the present one, this ensures that the discontinuity in the viscosity never aligns to cell boundaries. This in turns leads to almost discontinuous pressures along the interface which are difficult to represent accurately. [1438] derived a simple analytic solution for the pressure and velocity fields for a circular inclusion under simple shear and it was used in [466], [1492], [490], [1009] and [668].

Because of the symmetry of the problem, we only have to solve over the top right quarter of the domain (see Fig. ??a).

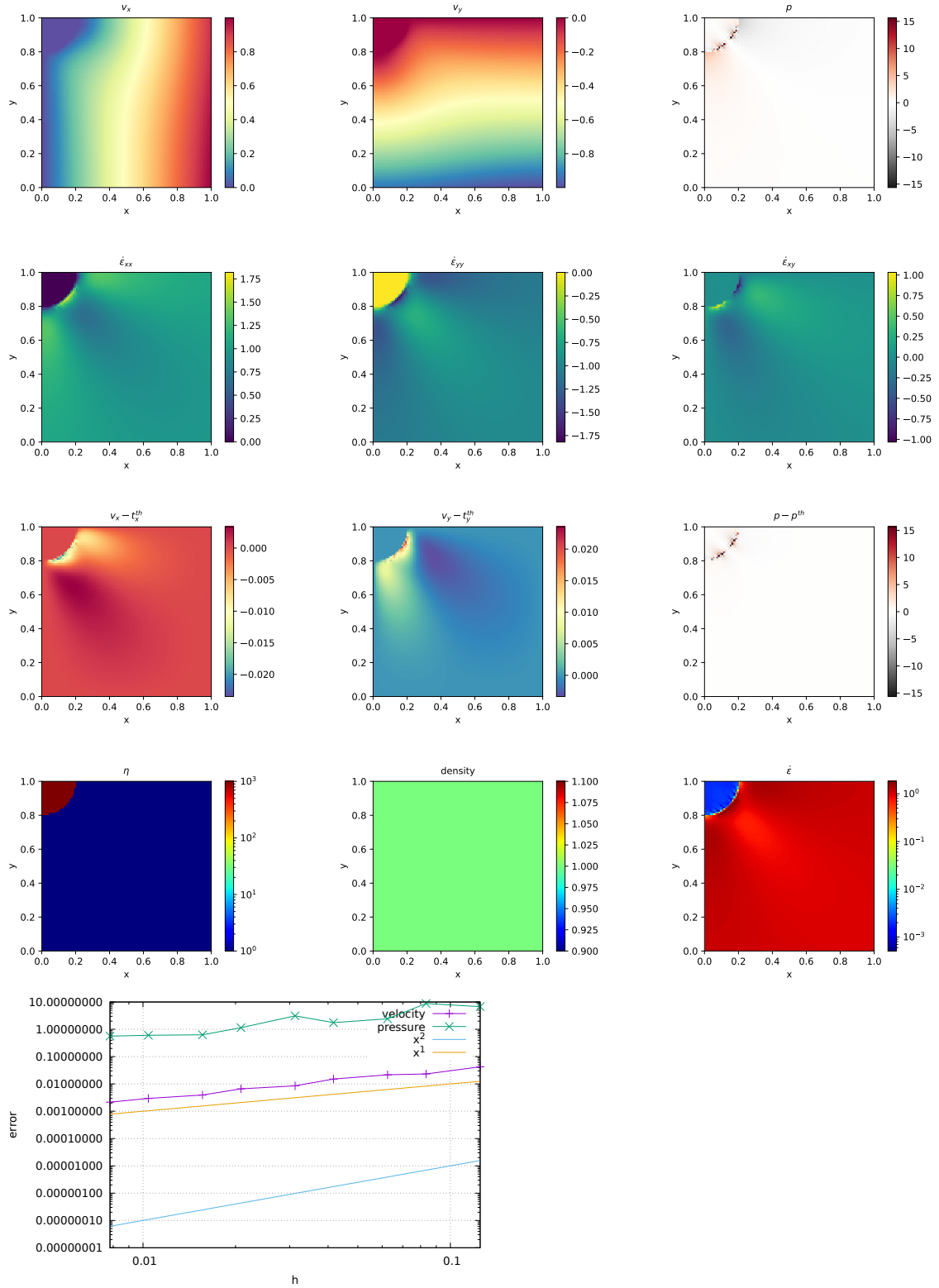
The analytical solution requires a strain rate boundary condition (e.g., pure shear) to be applied far away from the inclusion. In order to avoid using very large domains and/or dealing with this type of boundary condition altogether, the analytical solution is evaluated and imposed on the boundaries of the domain. By doing so, the truncation error introduced while discretizing the strain rate boundary condition is removed.

A characteristic of the analytic solution is that the pressure is zero inside the inclusion, while outside it follows the relation

$$p_m = 4\dot{\epsilon} \frac{\mu_m(\mu_i - \mu_m)}{\mu_i + \mu_m} \frac{r_i^2}{r^2} \cos(2\theta) \quad (629)$$

where $\mu_i = 10^3$ is the viscosity of the inclusion and $\mu_m = 1$ is the viscosity of the background media, $\theta = \tan^{-1}(y/x)$, and $\dot{\epsilon} = 1$ is the applied strain rate.

[466] thoroughly investigated this problem with various numerical methods (FEM, FDM), with and without tracers, and conclusively showed how various averagings lead to different results. [490] obtained a first order convergence for both pressure and velocity, while [1009] and [668] showed that the use of adaptive mesh refinement in respectively the FEM and FDM yields convergence rates which depend on refinement strategies.



Stone 08: the indentor benchmark

The punch benchmark is one of the few boundary value problems involving plastic solids for which there exists an exact solution. Such solutions are usually either for highly simplified geometries (spherical or axial symmetry, for instance) or simplified material models (such as rigid plastic solids) [924].

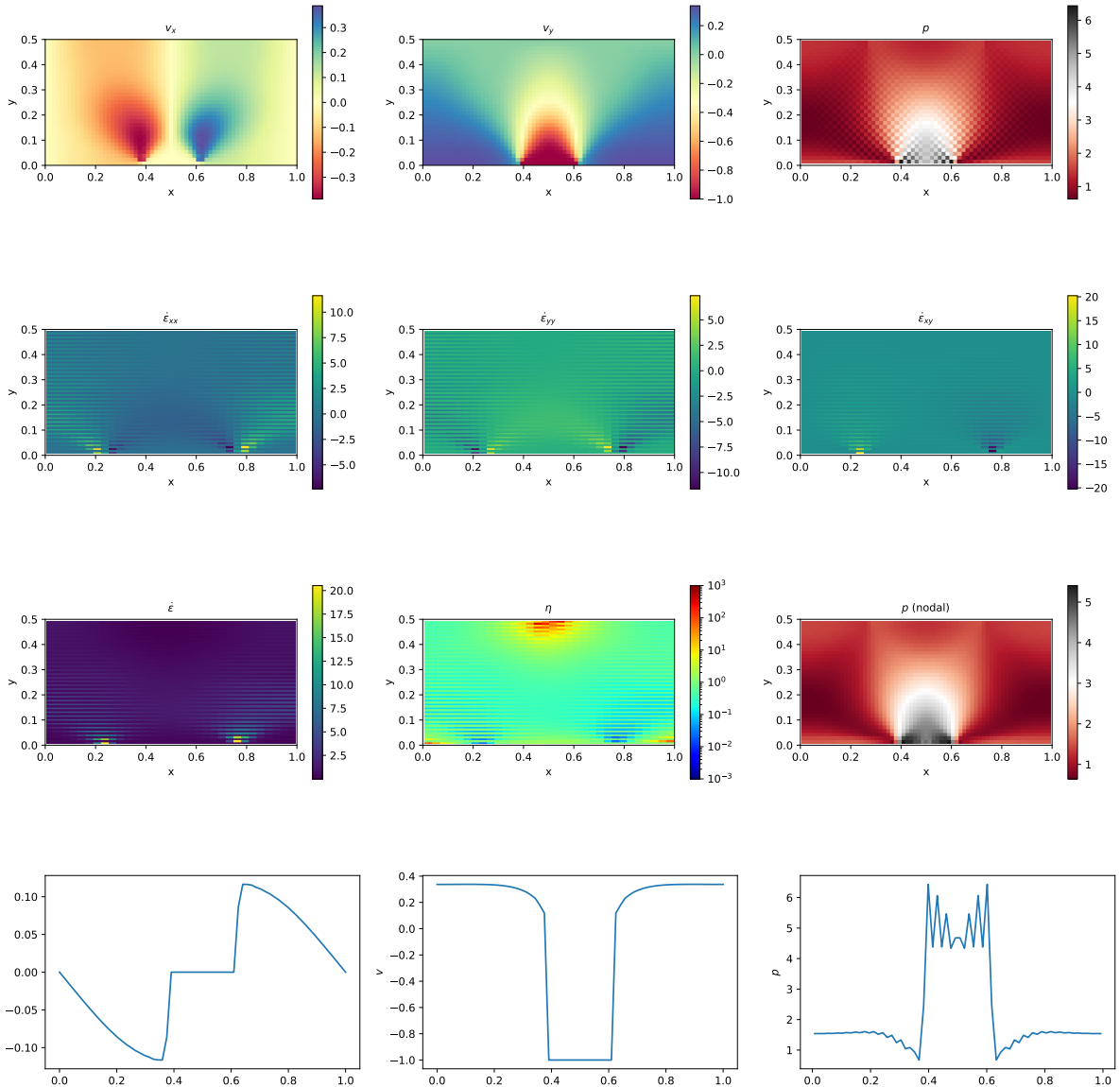
In this experiment, a rigid punch indents a rigid plastic half space; the slip line field theory gives exact solutions as shown in Fig. ??a. The plane strain formulation of the equations and the detailed solution to the problem were derived in the Appendix of [1543] and are also presented in [649].

The two dimensional punch problem has been extensively studied numerically for the past 40 years [1783, 1782, 355, 354, 864, 1736, 236, 1343] and has been used to draw a parallel with the tectonics of eastern China in the context of the India-Eurasia collision [1524, 1196]. It is also worth noting that it has been carried out in one form or another in series of analogue modelling articles concerning the same region, with a rigid indenter colliding with a rheologically stratified lithosphere [1296, 445, 919].

Numerically, the one-time step punch experiment is performed on a two-dimensional domain of purely plastic von Mises material. Given that the von Mises rheology yield criterion does not depend on pressure, the density of the material and/or the gravity vector is set to zero. Sides are set to free slip boundary conditions, the bottom to no slip, while a vertical velocity $(0, -v_p)$ is prescribed at the top boundary for nodes whose x coordinate is within $[L_x/2 - \delta/2, L_x/2 + \delta/2]$.

The following parameters are used: $L_x = 1$, $L_y = 0.5$, $\mu_{min} = 10^{-3}$, $\mu_{max} = 10^3$, $v_p = 1$, $\delta = 0.123456789$ and the yield value of the material is set to $k = 1$.

The analytical solution predicts that the angle of the shear bands stemming from the sides of the punch is $\pi/4$, that the pressure right under the punch is $1 + \pi$, and that the velocity of the rigid blocks on each side of the punch is $v_p/\sqrt{2}$ (this is simply explained by invoking conservation of mass).



ToDo: smooth punch

features

- $Q_1 \times P_0$ element
- incompressible flow
- penalty formulation
- Dirichlet boundary conditions (no-slip)
- isothermal
- non-isoviscous
- nonlinear rheology

Stone 09: the annulus benchmark

keywords: annulus, $Q_1 \times P_0$, penalty, manufactured solution, incompressible flow, Dirichlet boundary conditions, direct solver, isothermal, isoviscous

This fieldstone was developed in collaboration with Prof. E.G.P. Puckett.

This benchmark is based on Thieulot & Puckett [Subm.] in which an analytical solution to the isoviscous incompressible Stokes equations is derived in an annulus geometry. The velocity and pressure fields are as follows:

$$v_r(r, \theta) = g(r)k \sin(k\theta), \quad (630)$$

$$v_\theta(r, \theta) = f(r) \cos(k\theta), \quad (631)$$

$$p(r, \theta) = kh(r) \sin(k\theta), \quad (632)$$

$$\rho(r, \theta) = \aleph(r)k \sin(k\theta), \quad (633)$$

with

$$f(r) = Ar + B/r, \quad (634)$$

$$g(r) = \frac{A}{2}r + \frac{B}{r} \ln r + \frac{C}{r}, \quad (635)$$

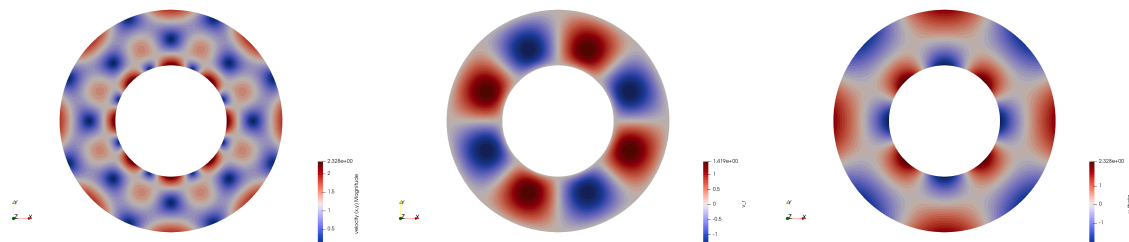
$$h(r) = \frac{2g(r) - f(r)}{r}, \quad (636)$$

$$\aleph(r) = g'' - \frac{g'}{r} - \frac{g}{r^2}(k^2 - 1) + \frac{f}{r^2} + \frac{f'}{r}, \quad (637)$$

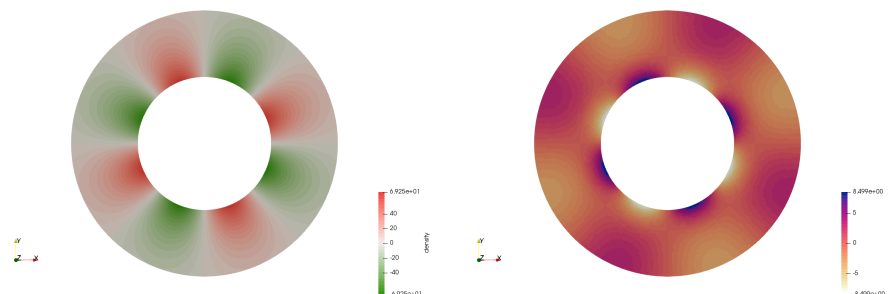
$$A = -C \frac{2(\ln R_1 - \ln R_2)}{R_2^2 \ln R_1 - R_1^2 \ln R_2}, \quad (638)$$

$$B = -C \frac{R_2^2 - R_1^2}{R_2^2 \ln R_1 - R_1^2 \ln R_2}. \quad (639)$$

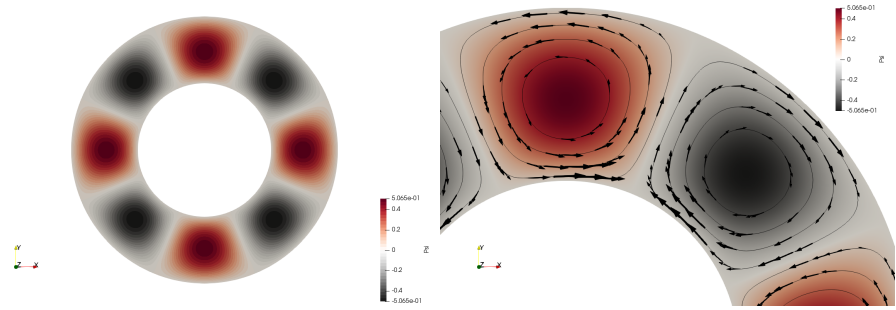
The parameters A and B are chosen so that $v_r(R_1) = v_r(R_2) = 0$, i.e. the velocity is tangential to both inner and outer surfaces. The gravity vector is radial and of unit length. In the present case, we set $R_1 = 1$, $R_2 = 2$ and $C = -1$.



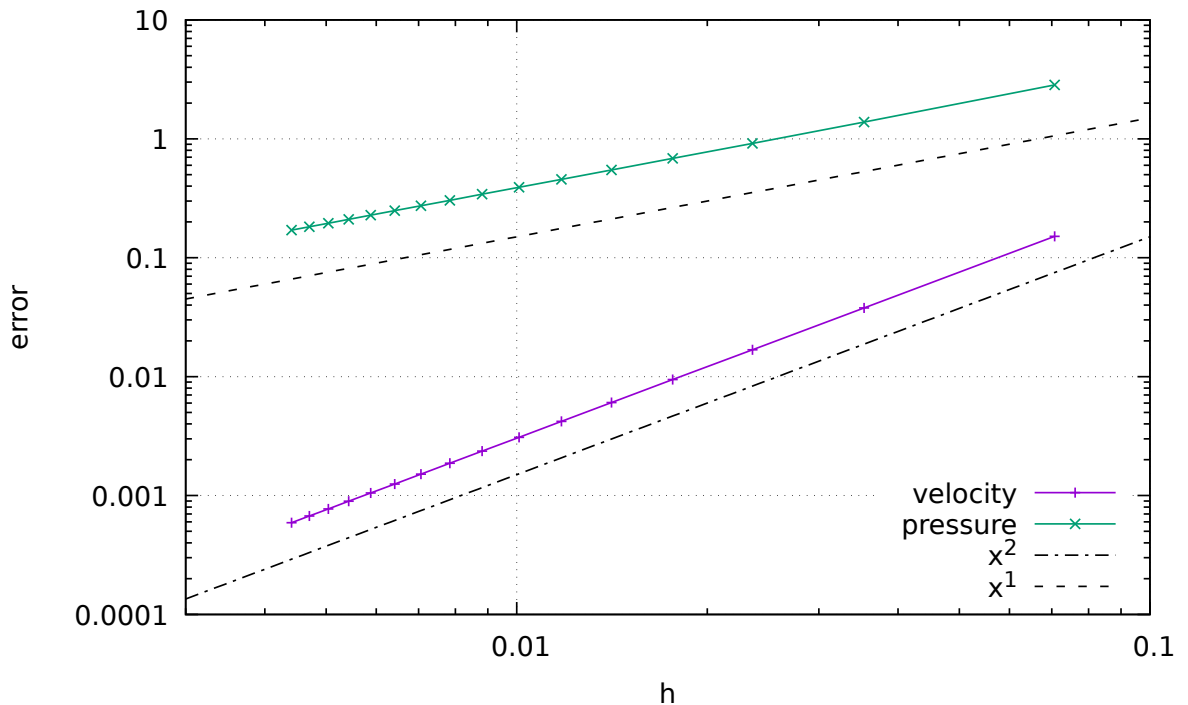
Left to right: velocity norm, r component, θ component



Left: density field; right: pressure field.



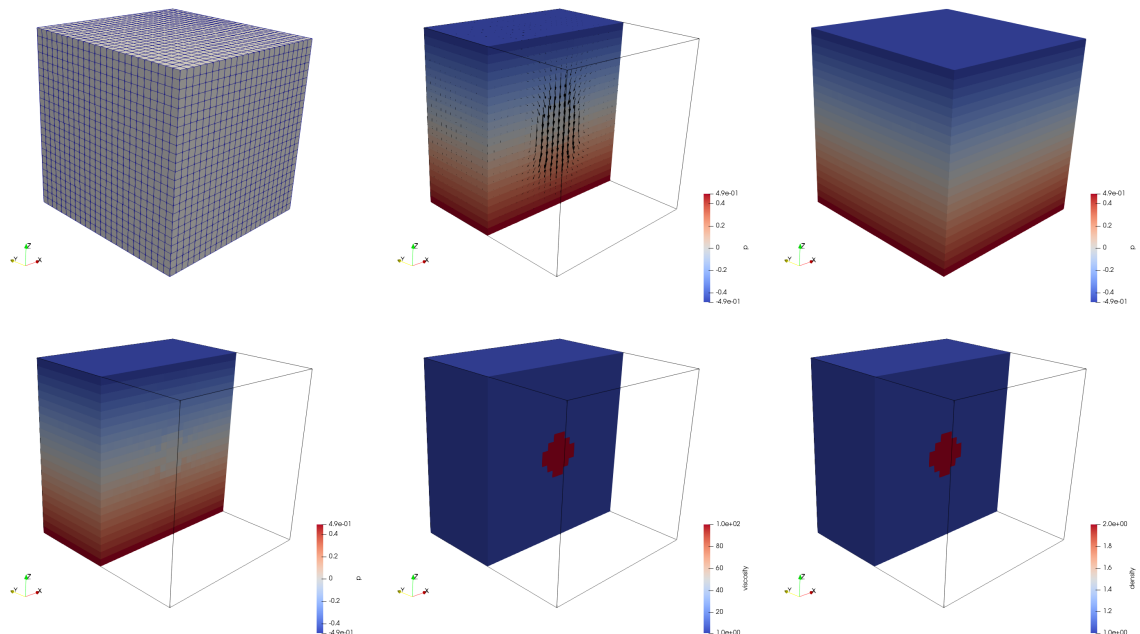
Left: ψ field; right: ψ isolines with velocity arrows.



Stone 10: Stokes sphere (3D) - penalty

features

- $Q_1 \times P_0$ element
- incompressible flow
- penalty formulation
- Dirichlet boundary conditions (free-slip)
- direct solver
- isothermal
- non-isoviscous
- 3D
- elemental b.c.
- buoyancy driven



resolution is 24x24x24

Stone 11: stokes sphere (3D) - mixed formulation

This is the same setup as Section 9.

features

- $Q_1 \times P_0$ element
- incompressible flow
- mixed formulation
- Dirichlet boundary conditions (free-slip)
- direct solver
- isothermal
- non-isoviscous
- 3D
- elemental b.c.
- buoyancy driven

Stone 12: consistent pressure recovery

What follows is presented in [1780]. The second part of their paper wishes to establish a simple and effective numerical method to calculate variables eliminated by the penalisation process. The method involves an additional finite element solution for the nodal pressures using the same finite element basis and numerical quadrature as used for the velocity.

Let us start with:

$$p = -\lambda \nabla \cdot \mathbf{v}$$

which lead to

$$(q, p) = -\lambda(q, \nabla \cdot \mathbf{v})$$

and then

$$\left(\int \mathbf{N} \mathbf{N} d\Omega \right) \cdot \mathbf{P} = - \left(\lambda \int \mathbf{N} \nabla \mathbf{N} d\Omega \right) \cdot \mathbf{V}$$

or,

$$\mathbf{M} \cdot \mathbf{P} = -\mathbf{D} \cdot \mathbf{V}$$

and finally

$$\mathbf{P} = -\mathbf{M}^{-1} \cdot \mathbf{D} \cdot \mathbf{V}$$

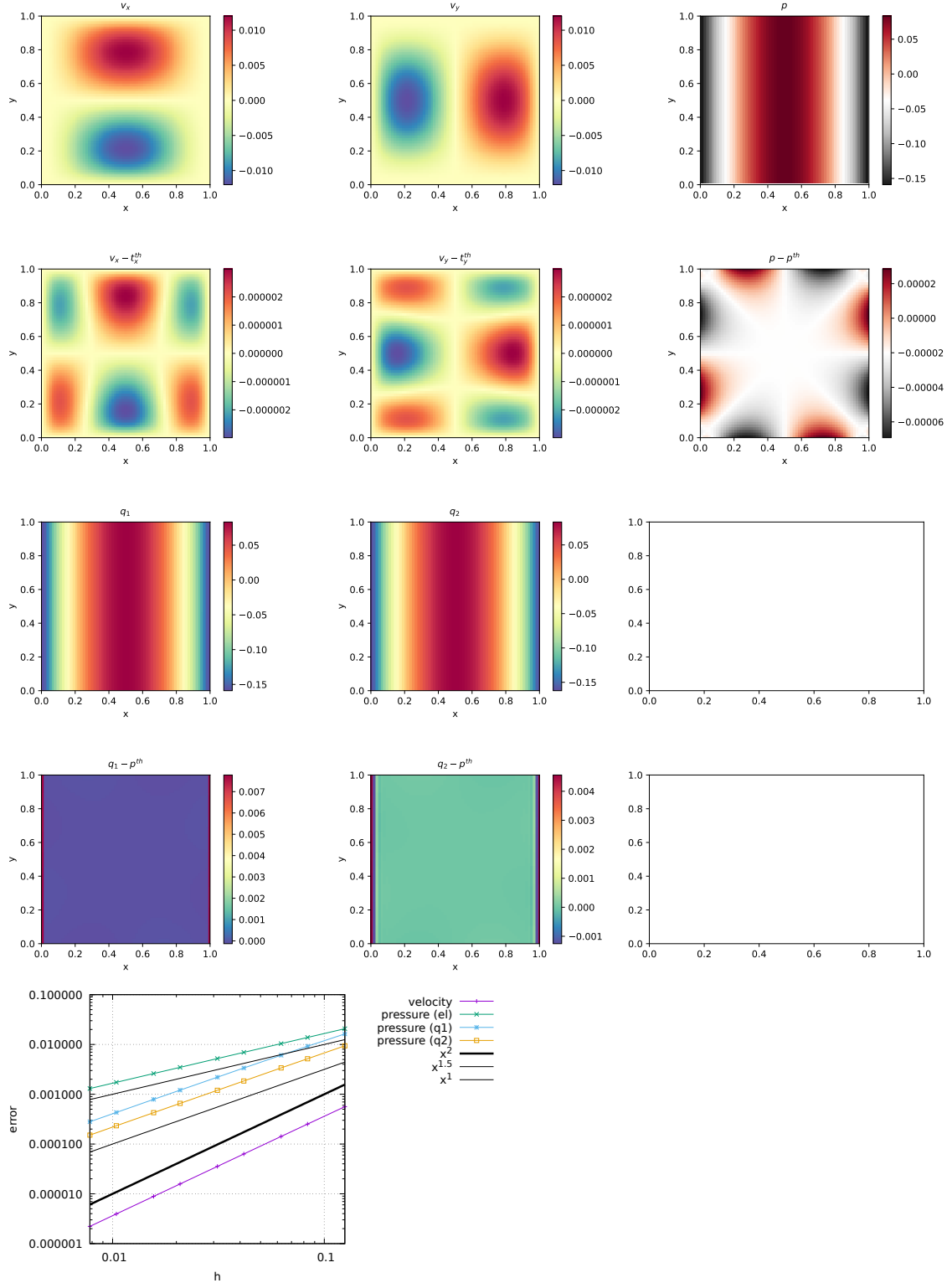
with \mathbf{M} of size $(np \times np)$, \mathbf{D} of size $(np * ndof \times np * ndof)$ and \mathbf{V} of size $(np * ndof)$. The vector \mathbf{P} contains the np nodal pressure values directly, with no need for a smoothing scheme. The mass matrix \mathbf{M} is to be evaluated at the full integration points, while the constraint part (the right hand side of the equation) is to be evaluated at the reduced integration point.

As noted by [1780], it is interesting to note that when linear elements are used and the lumped matrices are used for the \mathbf{M} the resulting algebraic equation is identical to the smoothing scheme based on the averaging method only if the uniform square finite element mesh is used. In this respect this method is expected to yield different results when elements are not square or even rectangular.

q_1 is smoothed pressure obtained with the center-to-node approach.

q_2 is recovered pressure obtained with [1780].

All three fulfill the zero average condition: $\int p d\Omega = 0$.



In terms of pressure error, q_2 is better than q_1 which is better than elemental.

QUESTION: why are the averages exactly zero ?!

TODO:

- add randomness to internal node positions.
- look at elefant algorithms

Stone 13: the Particle in Cell technique (1) - the effect of averaging

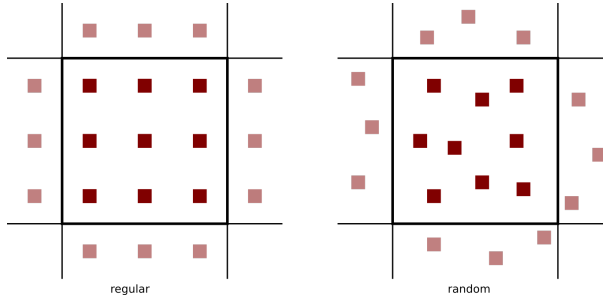
This fieldstone is being developed in collaboration with BSc student Eric Hoogen.

features

- $Q_1 \times P_0$ element
- incompressible flow
- penalty formulation
- Dirichlet boundary conditions (no-slip)
- isothermal
- non-isoviscous
- particle-in-cell

After the initial setup of the grid, markers can then be generated and placed in the domain. One could simply randomly generate the marker positions in the whole domain but unless a *very* large number of markers is used, the chance that an element does not contain any marker exists and this will prove problematic. In order to get a better control over the markers spatial distribution, one usually generates the marker per element, so that the total number of markers in the domain is the product of the number of elements times the user-chosen initial number of markers per element.

Our next concern is how to actually place the markers inside an element. Two methods come to mind: on a regular grid, or in a random manner, as shown on the following figure:



In both cases we make use of the basis shape functions: we generate the positions of the markers (random or regular) in the reference element first (r_{im}, s_{im}), and then map those out to the real element as follows:

$$x_{im} = \sum_i^m N_i(r_{im}, s_{im}) x_i \quad y_{im} = \sum_i^m N_i(r_{im}, s_{im}) y_i \quad (640)$$

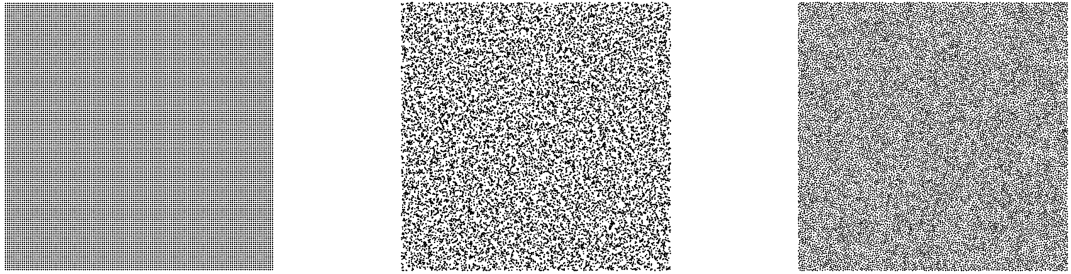
where x_i, y_i are the coordinates of the vertices of the element.

A third option consists in the use of the so-called Poisson-disc sampling which produces points that are tightly-packed, but no closer to each other than a specified minimum distance, resulting in a more natural pattern⁵⁶. Note that the Poisson-disc algorithm fills the whole domain at once, not element after element.

say smthg about avrg dist

insert here theory and link about Poisson disc

⁵⁶<https://en.wikipedia.org/wiki/Supersampling>



Left: regular distribution, middle: random, right: Poisson disc.
16384 markers (32x32 grid, 16 markers per element).

When using *active* markers, one is faced with the problem of transferring the properties they carry to the mesh on which the PDEs are to be solved. As we have seen, building the FE matrix involves a loop over all elements, so one simple approach consists of assigning each element a single property computed as the average of the values carried by the markers in that element. Often in colloquial language "average" refers to the arithmetic mean:

$$\langle \phi \rangle_{am} = \frac{1}{n} \sum_k^n \phi_i \quad (641)$$

where $\langle \phi \rangle_{am}$ is the arithmetic average of the n numbers ϕ_i . However, in mathematics other means are commonly used, such as the geometric mean:

$$\langle \phi \rangle_{gm} = \left(\prod_i^n \phi_i \right) \quad (642)$$

PROBLEM with this formula!!!! and the harmonic mean:

$$\langle \phi \rangle_{hm} = \left(\frac{1}{n} \sum_i^n \frac{1}{\phi_i} \right)^{-1} \quad (643)$$

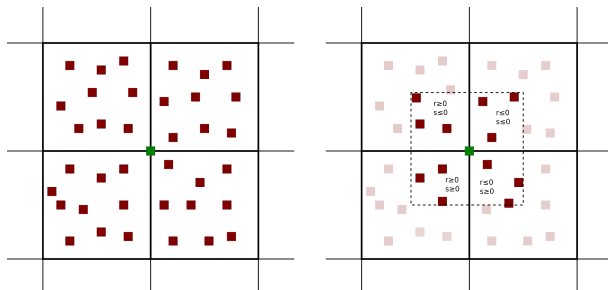
Furthermore, there is a well known inequality for any set of positive numbers,

$$\langle \phi \rangle_{am} \geq \langle \phi \rangle_{gm} \geq \langle \phi \rangle_{hm} \quad (644)$$

which will prove to be important later on.

Let us now turn to a simple concrete example: the 2D Stokes sphere. There are two materials in the domain, so that markers carry the label "mat=1" or "mat=2". For each element an average density and viscosity need to be computed. The majority of elements contains markers with a single material label so that the choice of averaging does not matter (it is trivial to verify that if $\phi_i = \phi_0$ then $\langle \phi \rangle_{am} = \langle \phi \rangle_{gm} = \langle \phi \rangle_{hm} = \phi_0$). Remain the elements crossed by the interface between the two materials: they contain markers of both materials and the average density and viscosity inside those depends on 1) the total number of markers inside the element, 2) the ratio of markers 1 to markers 2, 3) the type of averaging.

This averaging problem has been studied and documented in the literature [1436, 466, 1537, 1326]



Nodal projection. Left: all markers inside elements to which the green node belongs to are taken into account.
Right: only the markers closest to the green node count.

Let k be the green node of the figures above. Let (r, s) denote the coordinates of a marker inside its element. For clarity, we define the follow three nodal averaging schemes:

- nodal type A:

$$f_k = \frac{\text{sum of values carried by markers in 4 neighbour elements}}{\text{number of markers in 4 neighbour elements}}$$

- nodal type B:

$$f_k = \frac{\text{sum of values carried by markers inside dashed line}}{\text{number of markers in area delimited by the dashed line}}$$

- nodal type C

$$f_k = \frac{\text{sum of values carried by markers in 4 neighbour elements} * N_p(r, s)}{\text{sum of } N_p(r, s)}$$

where N_p is the Q_1 basis function corresponding to node p defined on each element. Since these functions are 1 on node k and then linearly decrease and become zero on the neighbouring nodes, this effectively gives more weight to those markers closest to node k .

This strategy is adopted in [1154, 1151] (although it is used to interpolate onto the nodes of Q_2P_{-1} elements. It is formulated as follows:

"We assume that an arbitrary material point property f , is discretized via $f(\mathbf{x}) \simeq \delta(\mathbf{x} - \mathbf{x}_p)f_p$. We then utilize an approximate local L_2 projection of f_p onto a continuous Q_1 finite element space. The corner vertices of each Q_2 finite element define the mesh f_p is projected onto. The local reconstruction for a node i is defined by

$$\hat{f}_i = \frac{\int_{\Omega_i} N_i(\mathbf{x}) f(\mathbf{x})}{\int_{\Omega_i} N_i(\mathbf{x})} \simeq \frac{\sum_p N_i(\mathbf{x}_p) f_p}{\sum_p N_i(\mathbf{x}_p)}$$

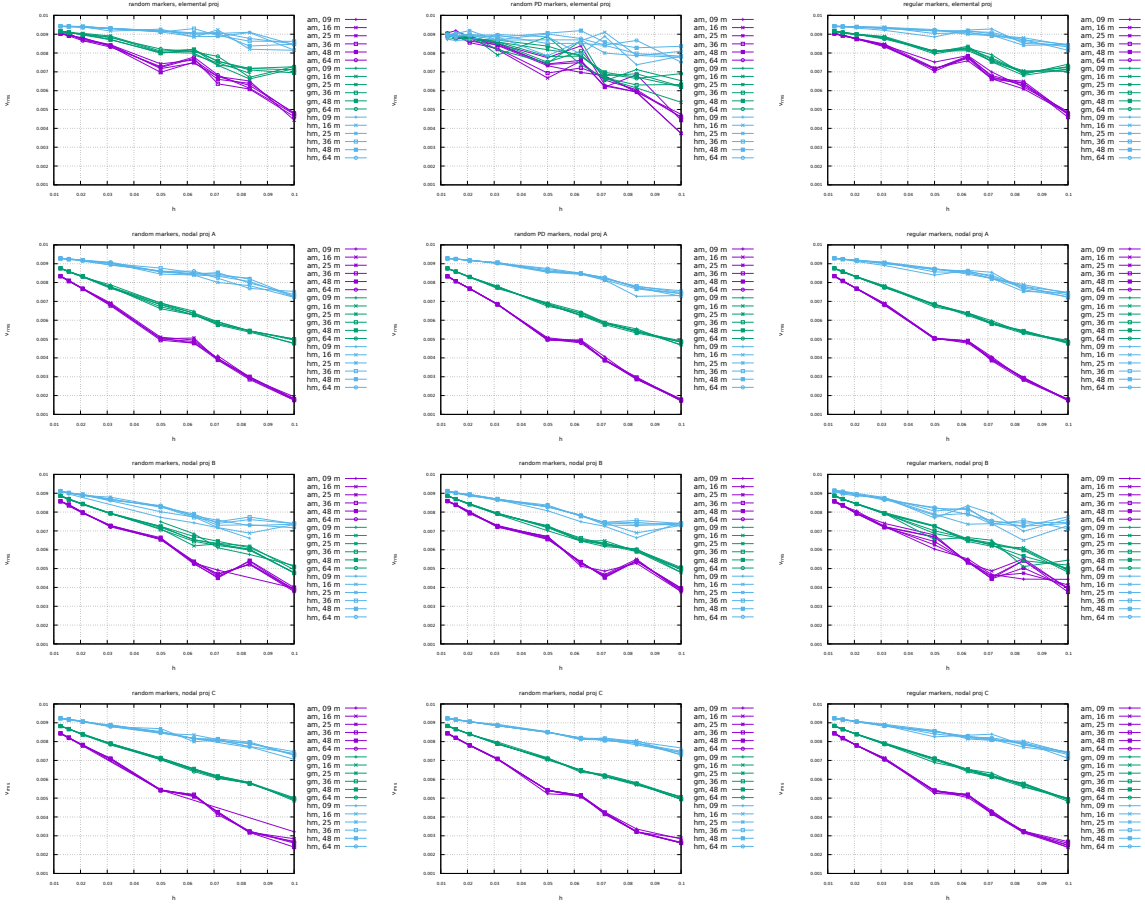
where the summation over p includes all material points contained within the support Ω_i of the trilinear interpolant N_i ".

The setup is identical to the Stokes sphere experiment. The bash script `script_runall` runs the code for many resolutions, both initial marker distribution and all four averaging types. The viscosity of the sphere has been set to 10^3 while the viscosity of the surrounding fluid is 1. The average density is always computed with an arithmetic mean.

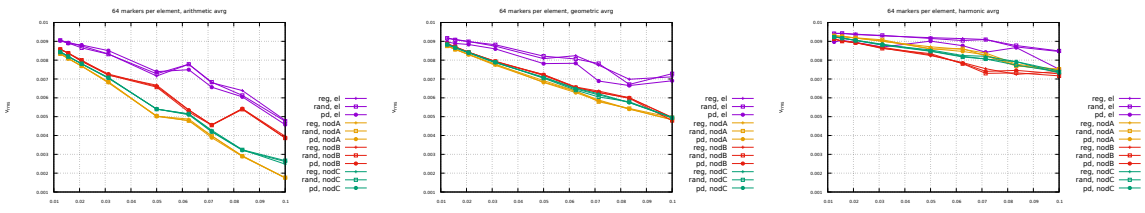
Conclusions:

- With increasing resolution ($h \rightarrow 0$) vrms values seem to converge towards a single value, irrespective of the number of markers.
- At low resolution, say 32x32 (i.e. $h=0.03125$), vrms values for the three averagings differ by about 10%. At higher resolution, say 128x128, vrms values are still not converged.
- The number of markers per element plays a role at low resolution, but less and less with increasing resolution.
- Results for random and regular marker distributions are not identical but follow a similar trend and seem to converge to the same value.
- elemental values yield better results (espcecially at low resolutions)
- harmonic mean yields overal the best results

Root mean square velocity results are shown hereunder:



Left column: random markers, middle column: Poisson disc, right column: regular markers. First row: elemental projection, second row: nodal 1 projection, third row: nodal 2 projection, fourth row: nodal 3 projection.



Left to right: arithmetic, geometric, harmonic averaging for viscosity.

Stone 14: solving the full saddle point problem

The details of the numerical setup are presented in Section ??.

The main difference is that we no longer use the penalty formulation and therefore keep both velocity and pressure as unknowns. Therefore we end up having to solve the following system:

$$\begin{pmatrix} \mathbb{K} & \mathbb{G} \\ \mathbb{G}^T & 0 \end{pmatrix} \cdot \begin{pmatrix} V \\ P \end{pmatrix} = \begin{pmatrix} f \\ h \end{pmatrix} \quad \text{or,} \quad \mathbb{A} \cdot X = rhs$$

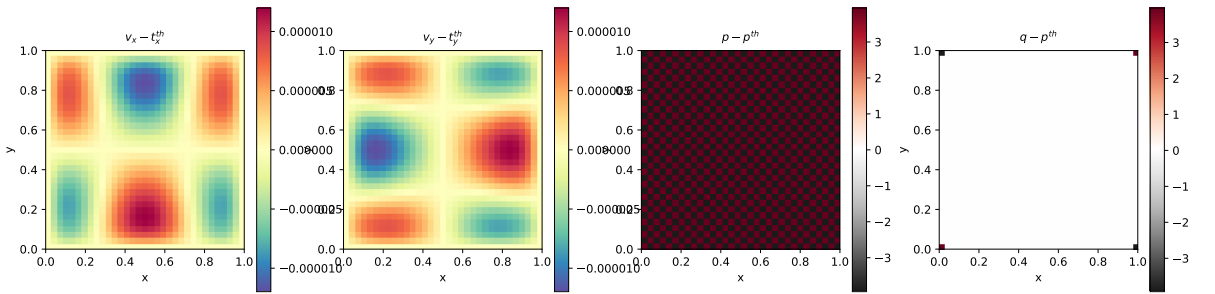
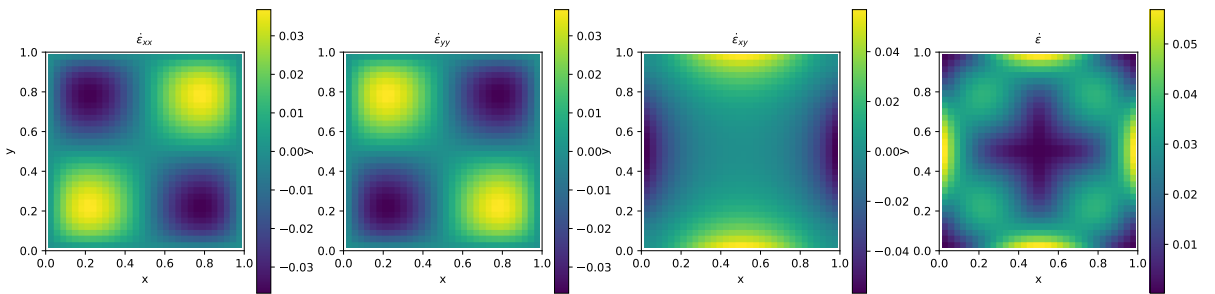
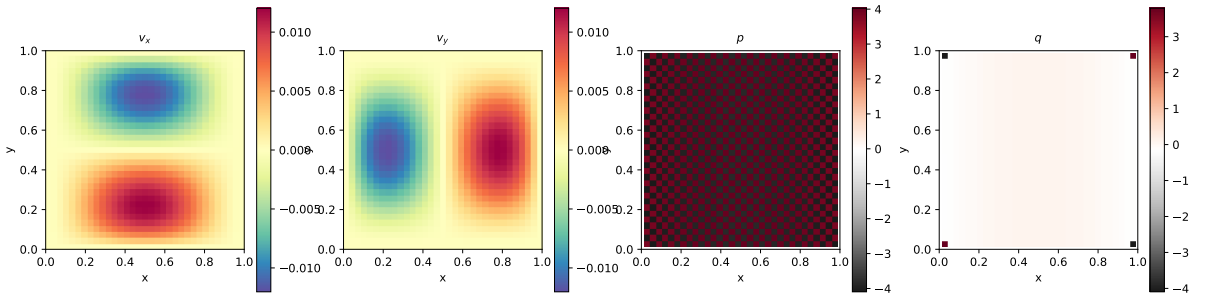
Each block \mathbb{K} , \mathbb{G} and vector f , h are built separately in the code and assembled into the matrix \mathbb{A} and vector rhs afterwards. \mathbb{A} and rhs are then passed to the solver. We will see later that there are alternatives to solve this approach which do not require to build the full Stokes matrix \mathbb{A} .

Each element has $m = 4$ vertices so in total $ndofV \times m = 8$ velocity dofs and a single pressure dof, commonly situated in the center of the element. The total number of velocity dofs is therefore $NfemV = nnp \times ndofV$ while the total number of pressure dofs is $NfemP = nel$. The total number of dofs is then $Nfem = NfemV + NfemP$.

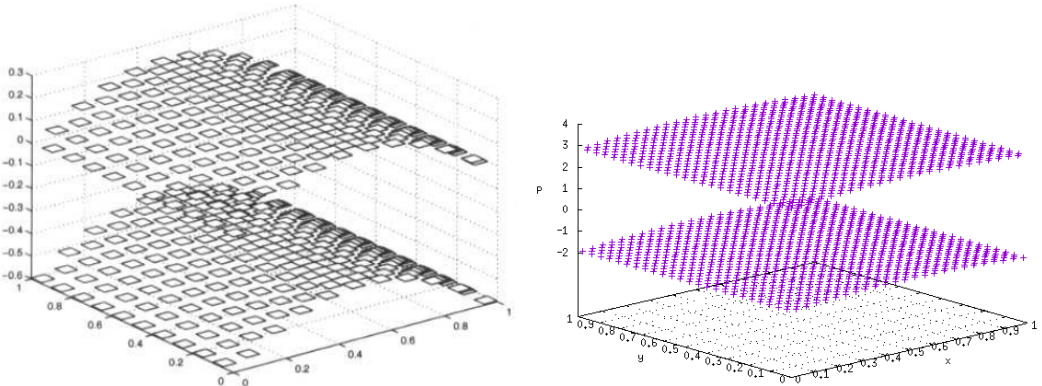
As a consequence, matrix \mathbb{K} has size $NfemV, NfemV$ and matrix \mathbb{G} has size $NfemV, NfemP$. Vector f is of size $NfemV$ and vector h is of size $NfemP$.

features

- $Q_1 \times P_0$ element
- incompressible flow
- mixed formulation
- Dirichlet boundary conditions (no-slip)
- direct solver (?)
- isothermal
- isoviscous
- analytical solution
- pressure smoothing



Unlike the results obtained with the penalty formulation (see Section ??), the pressure showcases a very strong checkerboard pattern, similar to the one in [473].



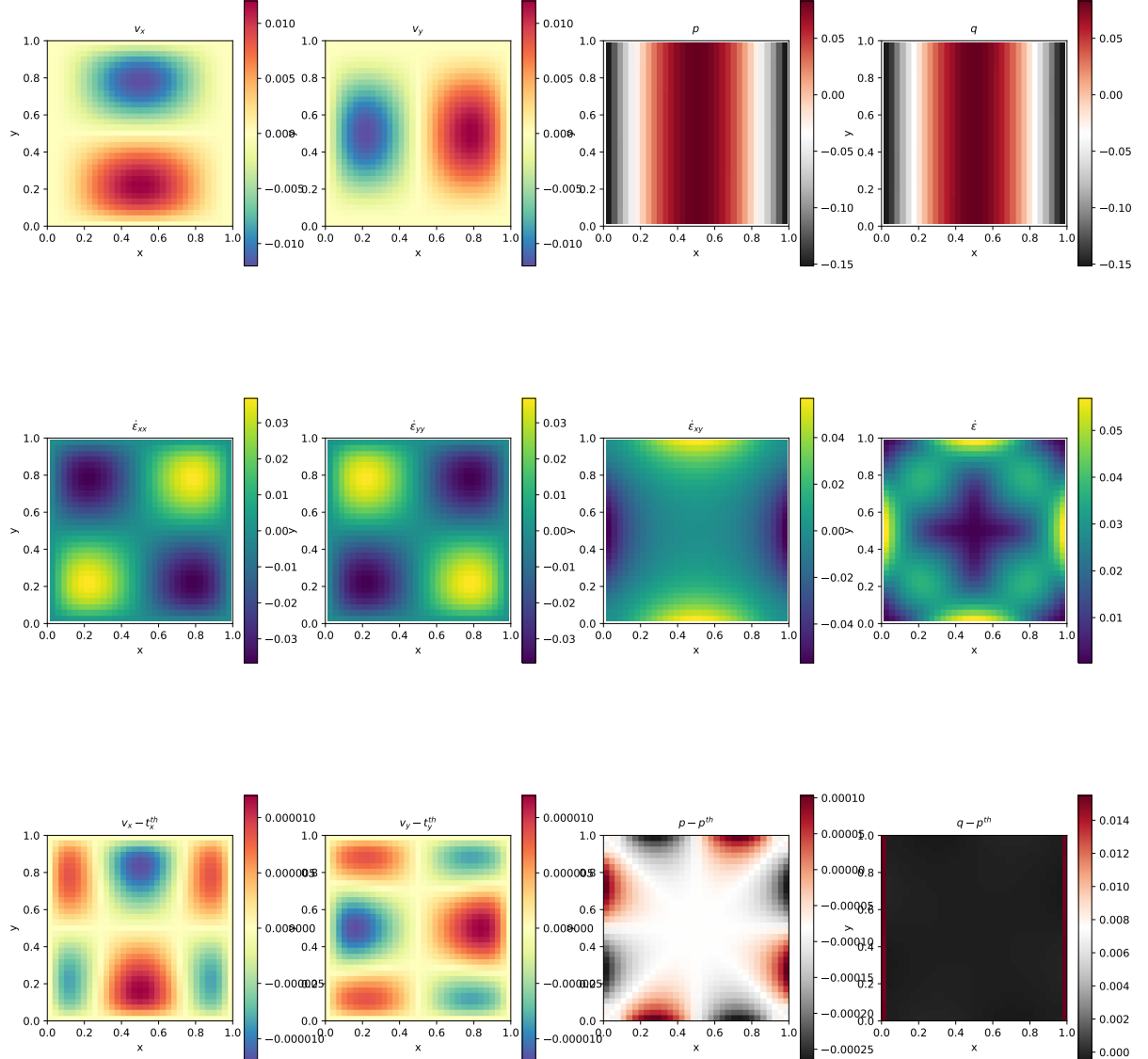
Left: pressure solution as shown in [473]; Right: pressure solution obtained with fieldstone.

Rather interestingly, the nodal pressure (obtained with a simple center-to-node algorithm) fails to recover a correct pressure at the four corners.

Note that the umfpack solver complains a lot about the matrix condition number, even at (very) low resolutions. I believe it does not like the zeros on the (2,2) block of the assembled Stokes matrix.

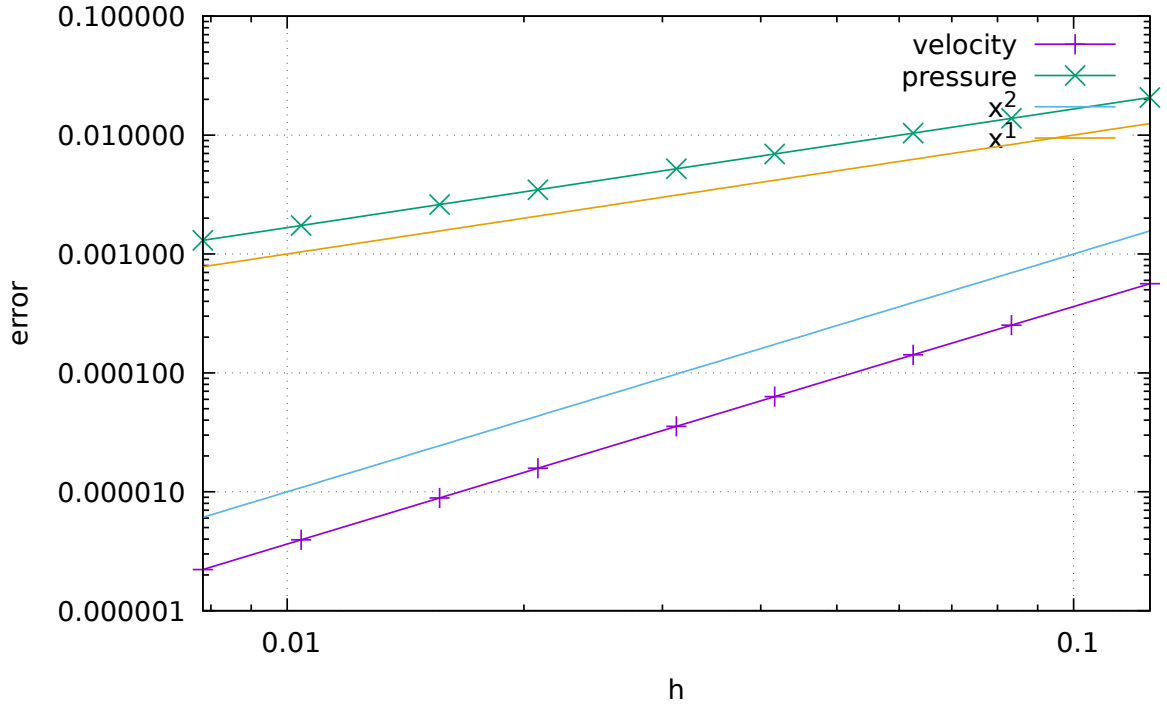
Stone 15: saddle point problem with Schur complement approach - benchmark

The details of the numerical setup are presented in Section ???. The main difference resides in the Schur complement approach to solve the Stokes system, as presented in Section ??? (see `solver_cg`). This iterative solver is very easy to implement once the blocks \mathbb{K} and \mathbb{G} , as well as the rhs vectors f and h have been built.

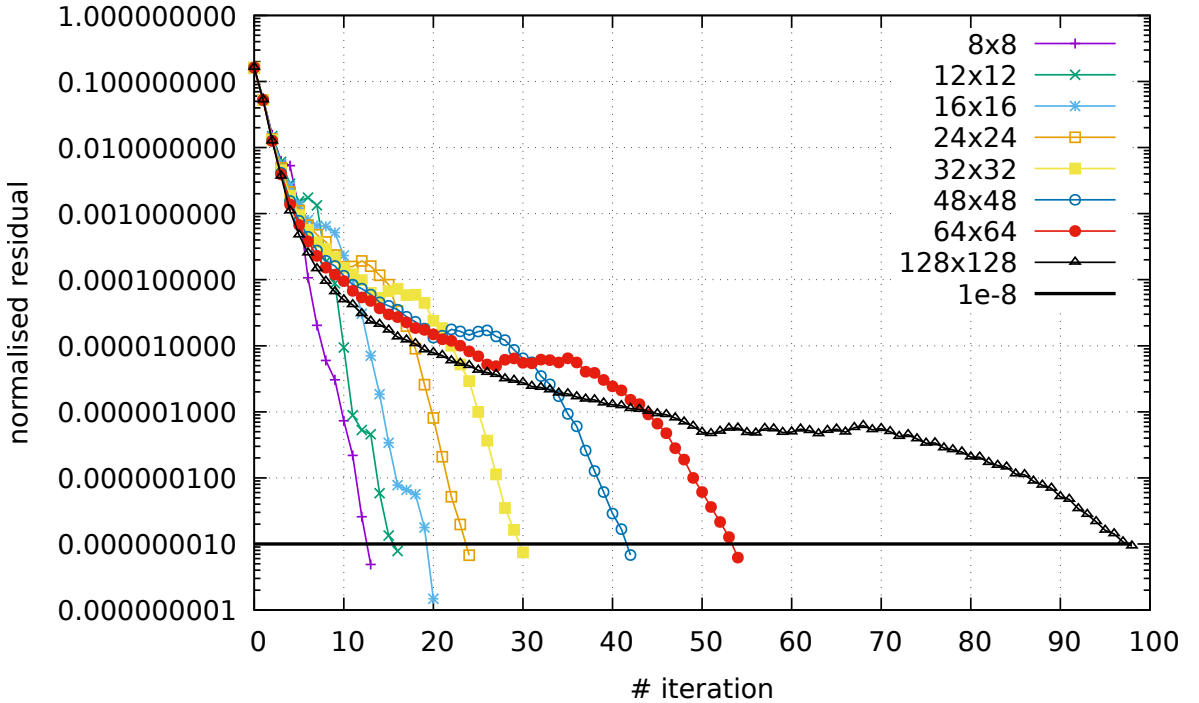


Rather interestingly the pressure checkerboard modes are not nearly as present as in Section ??? which uses a full matrix approach.

Looking at the discretisation errors for velocity and pressure, we of course recover the same rates and values as in the full matrix case.



Finally, for each experiment the normalised residual (see `solver_cg`) was recorded. We see that all things equal the resolution has a strong influence on the number of iterations the solver must perform to reach the required tolerance. This is one of the manifestations of the fact that the $Q_1 \times P_0$ element is not a stable element: the condition number of the matrix increases with resolution. We will see that this is not the case of stable elements such as $Q_2 \times Q_1$.



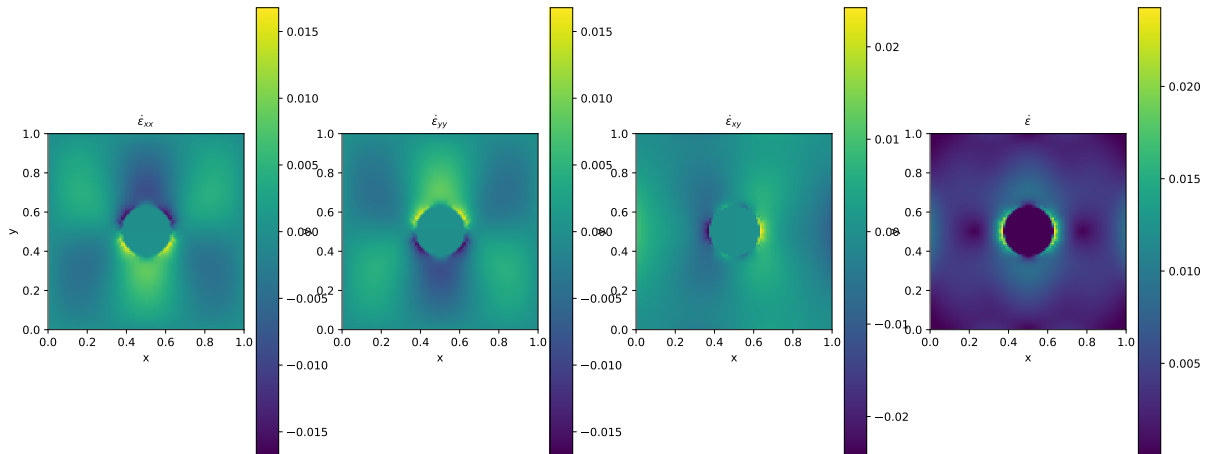
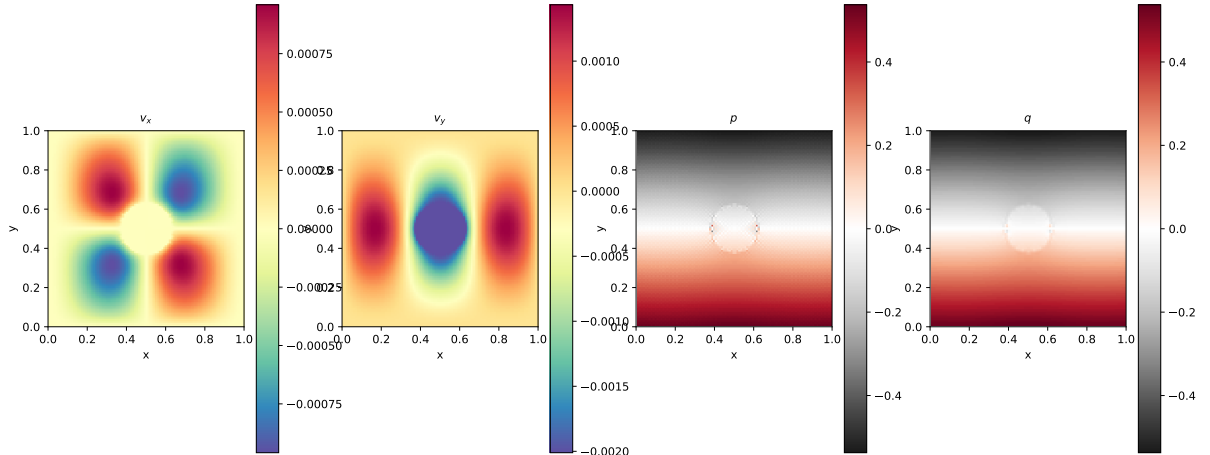
features

- $Q_1 \times P_0$ element
- incompressible flow
- mixed formulation
- Schur complement approach
- isothermal
- isoviscous
- analytical solution

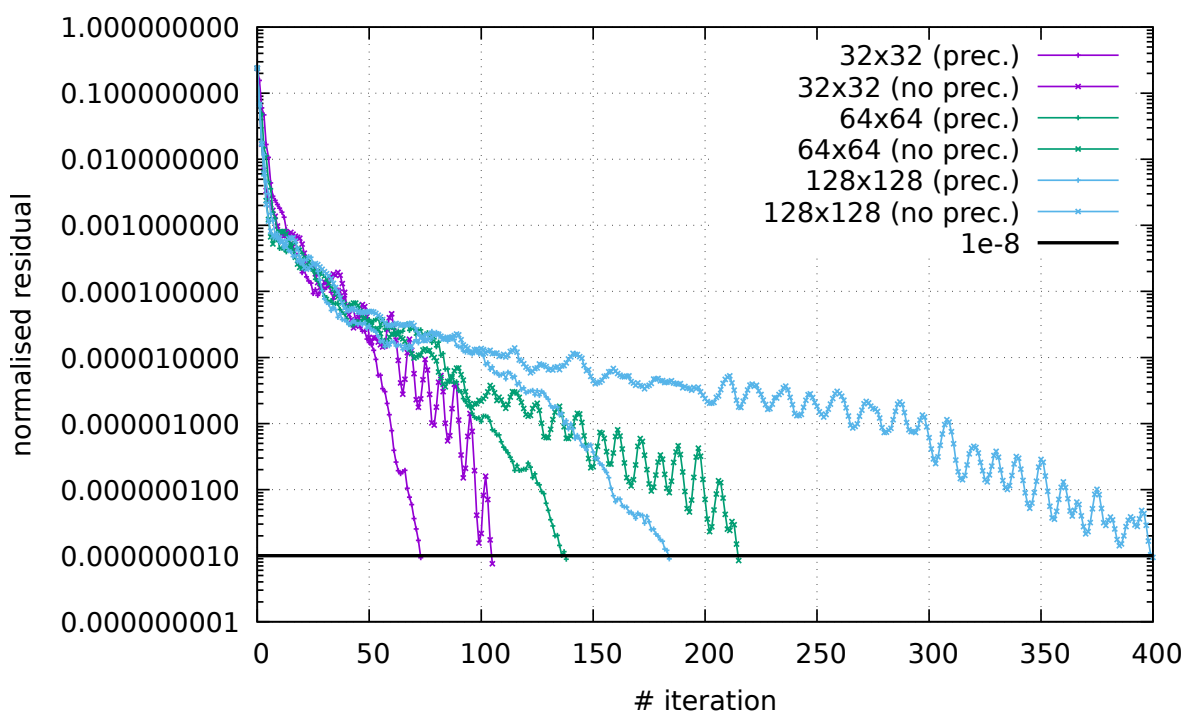
build S and have python compute its smallest and largest eigenvalues as a function of resolution?

Stone 16: saddle point problem with Schur complement approach - Stokes sphere

We are revisiting the 2D Stokes sphere problem, but this time we use the Schur complement approach to solve the Stokes system. Because there are viscosity contrasts in the domain, it is advisable to use the Preconditioned Conjugate Gradient as presented in Section ?? (see `solver_pcg`).



The normalised residual (see `solver_pcg`) was recorded. We see that all things equal the resolution has a strong influence on the number of iterations the solver must perform to reach the required tolerance. However, we see that the use of the preconditioner can substantially reduce the number of iterations inside the Stokes solver. At resolution 128x128, this number is halved.



features

- $Q_1 \times P_0$ element
- incompressible flow
- mixed formulation
- Schur complement approach
- isothermal
- non-isoviscous
- Stokes sphere

Stone 17: solving the full saddle point problem in 3D

When using $Q_1 \times P_0$ elements, this benchmark fails because of the Dirichlet b.c. on all 6 sides and all three components. However, as we will see, it does work well with $Q_2 \times Q_1$ elements. .

This benchmark begins by postulating a polynomial solution to the 3D Stokes equation [469]:

$$\mathbf{v} = \begin{pmatrix} x + x^2 + xy + x^3y \\ y + xy + y^2 + x^2y^2 \\ -2z - 3xz - 3yz - 5x^2yz \end{pmatrix} \quad (645)$$

and

$$p = xyz + x^3y^3z - 5/32 \quad (646)$$

While it is then trivial to verify that this velocity field is divergence-free, the corresponding body force of the Stokes equation can be computed by inserting this solution into the momentum equation with a given viscosity μ (constant or position/velocity/strain rate dependent). The domain is a unit cube and velocity boundary conditions simply use Eq. (645). Following [283], the viscosity is given by the smoothly varying function

$$\mu = \exp(1 - \beta(x(1-x) + y(1-y) + z(1-z))) \quad (647)$$

One can easily show that the ratio of viscosities μ^* in the system follows $\mu^* = \exp(-3\beta/4)$ so that choosing $\beta = 10$ yields $\mu^* \simeq 1808$ and $\beta = 20$ yields $\mu^* \simeq 3.269 \times 10^6$.

We start from the momentum conservation equation:

$$-\nabla p + \nabla \cdot (2\mu \dot{\epsilon}) = \mathbf{f}$$

The x -component of this equation writes

$$f_x = -\frac{\partial p}{\partial x} + \frac{\partial}{\partial x}(2\mu \dot{\epsilon}_{xx}) + \frac{\partial}{\partial y}(2\mu \dot{\epsilon}_{xy}) + \frac{\partial}{\partial z}(2\mu \dot{\epsilon}_{xz}) \quad (648)$$

$$= -\frac{\partial p}{\partial x} + 2\mu \frac{\partial}{\partial x} \dot{\epsilon}_{xx} + 2\mu \frac{\partial}{\partial y} \dot{\epsilon}_{xy} + 2\mu \frac{\partial}{\partial z} \dot{\epsilon}_{xz} + 2 \frac{\partial \mu}{\partial x} \dot{\epsilon}_{xx} + 2 \frac{\partial \mu}{\partial y} \dot{\epsilon}_{xy} + 2 \frac{\partial \mu}{\partial z} \dot{\epsilon}_{xz} \quad (649)$$

Let us compute all the block separately:

$$\begin{aligned} \dot{\epsilon}_{xx} &= 1 + 2x + y + 3x^2y \\ \dot{\epsilon}_{yy} &= 1 + x + 2y + 2x^2y \\ \dot{\epsilon}_{zz} &= -2 - 3x - 3y - 5x^2y \\ 2\dot{\epsilon}_{xy} &= (x + x^3) + (y + 2xy^2) = x + y + 2xy^2 + x^3 \\ 2\dot{\epsilon}_{xz} &= (0) + (-3z - 10xyz) = -3z - 10xyz \\ 2\dot{\epsilon}_{yz} &= (0) + (-3z - 5x^2z) = -3z - 5x^2z \end{aligned}$$

In passing, one can verify that $\dot{\epsilon}_{xx} + \dot{\epsilon}_{yy} + \dot{\epsilon}_{zz} = 0$. We further have

$$\begin{aligned}\frac{\partial}{\partial x} 2\dot{\epsilon}_{xx} &= 2(2 + 6xy) \\ \frac{\partial}{\partial y} 2\dot{\epsilon}_{xy} &= 1 + 4xy \\ \frac{\partial}{\partial z} 2\dot{\epsilon}_{xz} &= -3 - 10xy \\ \frac{\partial}{\partial x} 2\dot{\epsilon}_{xy} &= 1 + 2y^2 + 3x^2 \\ \frac{\partial}{\partial y} 2\dot{\epsilon}_{yy} &= 2(2 + 2x^2) \\ \frac{\partial}{\partial z} 2\dot{\epsilon}_{yz} &= -3 - 5x^2 \\ \frac{\partial}{\partial x} 2\dot{\epsilon}_{xz} &= -10yz \\ \frac{\partial}{\partial y} 2\dot{\epsilon}_{yz} &= 0 \\ \frac{\partial}{\partial z} 2\dot{\epsilon}_{zz} &= 2(0)\end{aligned}$$

$$\frac{\partial p}{\partial x} = yz + 3x^2y^3z \quad (650)$$

$$\frac{\partial p}{\partial y} = xz + 3x^3y^2z \quad (651)$$

$$\frac{\partial p}{\partial z} = xy + x^3y^3 \quad (652)$$

Pressure normalisation Here again, because Dirichlet boundary conditions are prescribed on all sides the pressure is known up to an arbitrary constant. This constant can be determined by (arbitrarily) choosing to normalised the pressure field as follows:

$$\int_{\Omega} p \, d\Omega = 0 \quad (653)$$

This is a single constraint associated to a single Lagrange multiplier λ and the global Stokes system takes the form

$$\begin{pmatrix} \mathbb{K} & \mathbb{G} & 0 \\ \mathbb{G}^T & 0 & \mathcal{C} \\ 0 & \mathcal{C}^T & 0 \end{pmatrix} \begin{pmatrix} V \\ P \\ \lambda \end{pmatrix}$$

In this particular case the constraint matrix \mathcal{C} is a vector and it only acts on the pressure degrees of freedom because of Eq.(653). Its exact expression is as follows:

$$\int_{\Omega} p \, d\Omega = \sum_e \int_{\Omega_e} p \, d\Omega = \sum_e \int_{\Omega_e} \sum_i N_i^p p_i \, d\Omega = \sum_e \sum_i \left(\int_{\Omega_e} N_i^p \, d\Omega \right) p_i = \sum_e \mathcal{C}_e \cdot \mathbf{p}_e$$

where \mathbf{p}_e is the list of pressure dofs of element e . The elemental constraint vector contains the corresponding pressure basis functions integrated over the element. These elemental constraints are then assembled into the vector \mathcal{C} .

Constant viscosity

Choosing $\beta = 0$ yields a constant velocity $\mu(x, y, z) = \exp(1) \simeq 2.718$ (and greatly simplifies the right-hand side) so that

$$\frac{\partial}{\partial x} \mu(x, y, z) = 0 \quad (654)$$

$$\frac{\partial}{\partial y} \mu(x, y, z) = 0 \quad (655)$$

$$\frac{\partial}{\partial z} \mu(x, y, z) = 0 \quad (656)$$

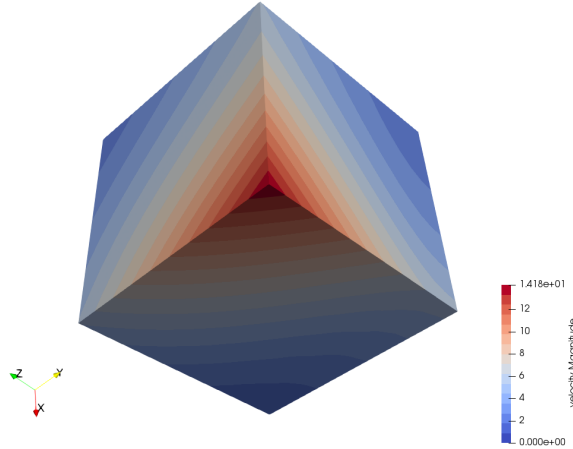
and

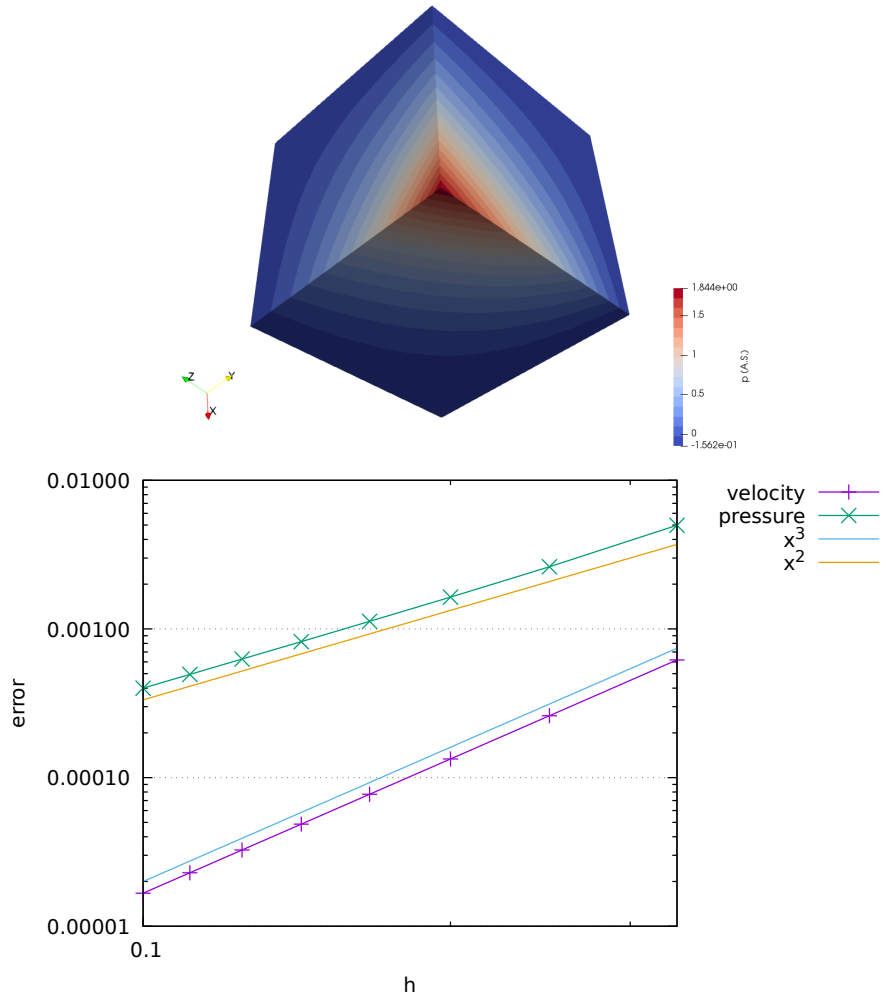
$$\begin{aligned} f_x &= -\frac{\partial p}{\partial x} + 2\mu \frac{\partial}{\partial x} \dot{\epsilon}_{xx} + 2\mu \frac{\partial}{\partial y} \dot{\epsilon}_{xy} + 2\mu \frac{\partial}{\partial z} \dot{\epsilon}_{xz} \\ &= -(yz + 3x^2y^3z) + 2(2 + 6xy) + (1 + 4xy) + (-3 - 10xy) \\ &= -(yz + 3x^2y^3z) + \mu(2 + 6xy) \\ f_y &= -\frac{\partial p}{\partial y} + 2\mu \frac{\partial}{\partial x} \dot{\epsilon}_{xy} + 2\mu \frac{\partial}{\partial y} \dot{\epsilon}_{yy} + 2\mu \frac{\partial}{\partial z} \dot{\epsilon}_{yz} \\ &= -(xz + 3x^3y^2z) + \mu(1 + 2y^2 + 3x^2) + \mu(2(2 + 2x^2) + \mu(-3 - 5x^2)) \\ &= -(xz + 3x^3y^2z) + \mu(2 + 2x^2 + 2y^2) \\ f_z &= -\frac{\partial p}{\partial z} + 2\mu \frac{\partial}{\partial x} \dot{\epsilon}_{xz} + 2\mu \frac{\partial}{\partial y} \dot{\epsilon}_{yz} + 2\mu \frac{\partial}{\partial z} \dot{\epsilon}_{zz} \\ &= -(xy + x^3y^3) + \mu(-10yz) + 0 + 0 \\ &= -(xy + x^3y^3) + \mu(-10yz) \end{aligned}$$

Finally

$$\mathbf{f} = - \begin{pmatrix} yz + 3x^2y^3z \\ xz + 3x^3y^2z \\ xy + x^3y^3 \end{pmatrix} + \mu \begin{pmatrix} 2 + 6xy \\ 2 + 2x^2 + 2y^2 \\ -10yz \end{pmatrix}$$

Note that there seems to be a sign problem with Eq.(26) in [283].





Variable viscosity

The spatial derivatives of the viscosity are then given by

$$\begin{aligned}\frac{\partial}{\partial x} \mu(x, y, z) &= -(1 - 2x)\beta\mu(x, y, z) \\ \frac{\partial}{\partial y} \mu(x, y, z) &= -(1 - 2y)\beta\mu(x, y, z) \\ \frac{\partial}{\partial z} \mu(x, y, z) &= -(1 - 2z)\beta\mu(x, y, z)\end{aligned}$$

and the right-hand side by

$$\begin{aligned}
\mathbf{f} &= - \begin{pmatrix} yz + 3x^2y^3z \\ xz + 3x^3y^2z \\ xy + x^3y^3 \end{pmatrix} + \mu \begin{pmatrix} 2 + 6xy \\ 2 + 2x^2 + 2y^2 \\ -10yz \end{pmatrix} \\
&\quad - (1 - 2x)\beta\mu(x, y, z) \begin{pmatrix} 2\dot{\epsilon}_{xx} \\ 2\dot{\epsilon}_{xy} \\ 2\dot{\epsilon}_{xz} \end{pmatrix} - (1 - 2y)\beta\mu(x, y, z) \begin{pmatrix} 2\dot{\epsilon}_{xy} \\ 2\dot{\epsilon}_{yy} \\ 2\dot{\epsilon}_{yz} \end{pmatrix} - (1 - 2z)\beta\mu(x, y, z) \begin{pmatrix} 2\dot{\epsilon}_{xz} \\ 2\dot{\epsilon}_{yz} \\ 2\dot{\epsilon}_{zz} \end{pmatrix} \\
&= - \begin{pmatrix} yz + 3x^2y^3z \\ xz + 3x^3y^2z \\ xy + x^3y^3 \end{pmatrix} + \mu \begin{pmatrix} 2 + 6xy \\ 2 + 2x^2 + 2y^2 \\ -10yz \end{pmatrix} \\
&\quad - (1 - 2x)\beta\mu \begin{pmatrix} 2 + 4x + 2y + 6x^2y \\ x + y + 2xy^2 + x^3 \\ -3z - 10xyz \end{pmatrix} - (1 - 2y)\beta\mu \begin{pmatrix} x + y + 2xy^2 + x^3 \\ 2 + 2x + 4y + 4x^2y \\ -3z - 5x^2z \end{pmatrix} - (1 - 2z)\beta\mu \begin{pmatrix} -3z - 10xyz \\ -3z - 5x^2z \\ -4 - 6x - 6y - 10xz \end{pmatrix}
\end{aligned}$$

Note that at $(x, y, z) = (0, 0, 0)$, $\mu = \exp(1)$, and at $(x, y, z) = (0.5, 0.5, 0.5)$, $\mu = \exp(1 - 3\beta/4)$ so that the maximum viscosity ratio is given by

$$\mu^* = \frac{\exp(1 - 3\beta/4)}{\exp(1)} = \exp(-3\beta/4)$$

By varying β between 1 and 22 we can get up to 7 orders of magnitude viscosity difference.

features

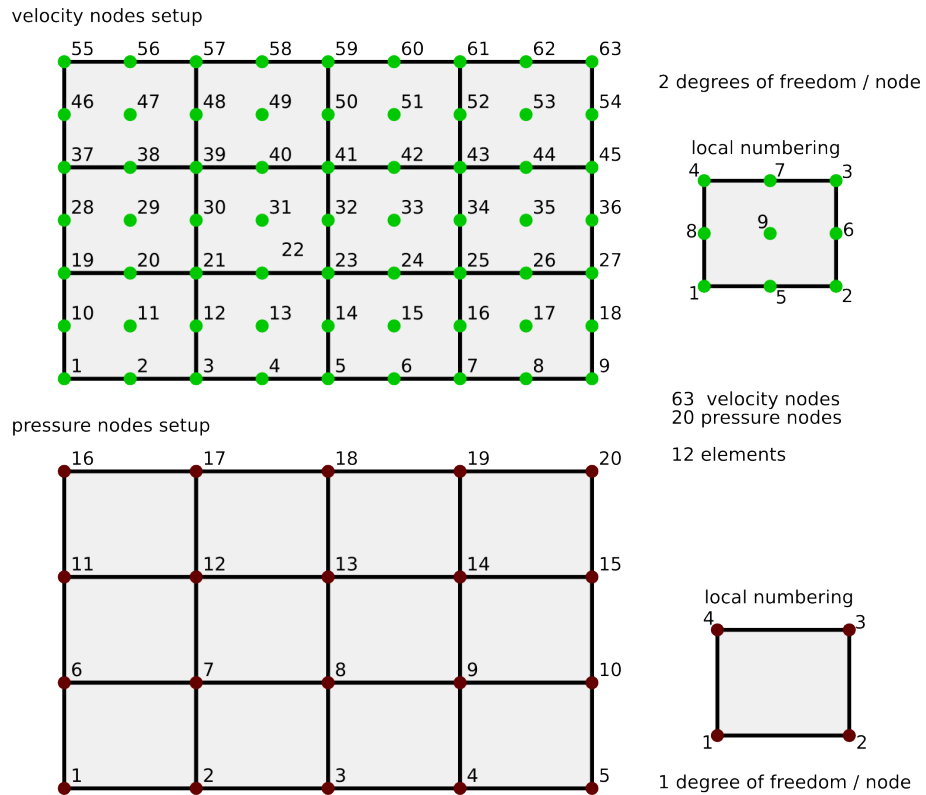
- $Q_1 \times P_0$ element
- incompressible flow
- saddle point system
- Dirichlet boundary conditions (free-slip)
- direct solver
- isothermal
- non-isoviscous
- 3D
- elemental b.c.
- analytical solution

Stone 18: solving the full saddle point problem with $Q_2 \times Q_1$ elements

The details of the numerical setup are presented in Section ??.

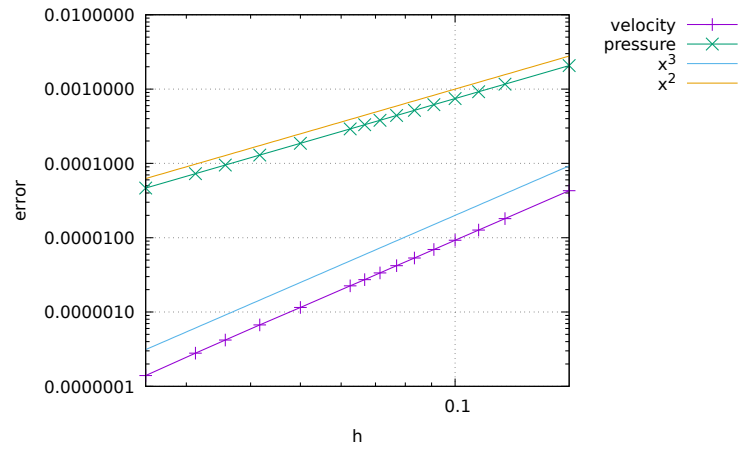
Each element has $m_V = 9$ vertices so in total $ndof_V \times m_V = 18$ velocity dofs and $ndof_P \times m_P = 4$ pressure dofs. The total number of velocity dofs is therefore $NfemV = nnp \times ndofV$ while the total number of pressure dofs is $NfemP = nel$. The total number of dofs is then $Nfem = NfemV + NfemP$.

As a consequence, matrix \mathbb{K} has size $NfemV, NfemV$ and matrix \mathbb{G} has size $NfemV, NfemP$. Vector f is of size $NfemV$ and vector h is of size $NfemP$.



features

- $Q_2 \times Q_1$ element
- incompressible flow
- mixed formulation
- Dirichlet boundary conditions (no-slip)
- isothermal
- isoviscous
- analytical solution



Stone 19: solving the full saddle point problem with $Q_3 \times Q_2$ elements

The details of the numerical setup are presented in Section ??.

Each element has $m_V = 16$ vertices so in total $ndof_V \times m_V = 32$ velocity dofs and $ndof_P \times m_P = 9$ pressure dofs. The total number of velocity dofs is therefore $NfemV = nnp \times ndofV$ while the total number of pressure dofs is $NfemP = nel$. The total number of dofs is then $Nfem = NfemV + NfemP$.

As a consequence, matrix \mathbb{K} has size $NfemV, NfemV$ and matrix \mathbb{G} has size $NfemV, NfemP$. Vector f is of size $NfemV$ and vector h is of size $NfemP$.

```

60====61====62====63====64====65====66====67====68====70
||          ||          ||          ||
50    51    52    53    54    55    56    57    58    59
||          ||          ||          ||
40    41    42    43    44    45    46    47    48    49
||          ||          ||          ||
30====31====32====33====34====35====36====37====38====39
||          ||          ||          ||
20    21    22    23    24    25    26    27    28    29
||          ||          ||          ||
10    11    12    13    14    15    16    17    18    19
||          ||          ||          ||
00====01====02====03====04====05====06====07====08====09

```

Example of 3x2 mesh. $n_{nx}=10$, $n_{ny}=7$, $n_{np}=70$, $n_{elx}=3$, $n_{ely}=2$, $n_{el}=6$

```

12====13====14====15          06=====07=====08
||  ||  ||  ||          ||  ||  ||  ||
08====09====10====11          ||  ||  ||  ||
||  ||  ||  ||          03=====04=====05
04====05====06====07          ||  ||  ||  ||
||  ||  ||  ||          00=====01=====02
00====01====02====03

```

Velocity (Q3)

```

(r,s)_{00}=(-1,-1)          (r,s)_{00}=(-1,-1)
(r,s)_{01}=(-1/3,-1)         (r,s)_{01}=(0,-1)
(r,s)_{02}=(+1/3,-1)         (r,s)_{02}=(+1,-1)
(r,s)_{03}=(+1,-1)           (r,s)_{03}=(-1,0)
(r,s)_{04}=(-1,-1/3)         (r,s)_{04}=(0,0)
(r,s)_{05}=(-1/3,-1/3)       (r,s)_{05}=(+1,0)
(r,s)_{06}=(+1/3,-1/3)       (r,s)_{06}=(-1,+1)
(r,s)_{07}=(+1,-1/3)          (r,s)_{07}=(0,+1)
(r,s)_{08}=(-1,+1/3)          (r,s)_{08}=(+1,+1)
(r,s)_{09}=(-1/3,+1/3)
(r,s)_{10}=(+1/3,+1/3)
(r,s)_{11}=(+1,+1/3)
(r,s)_{12}=(-1,+1)
(r,s)_{13}=(-1/3,+1)
(r,s)_{14}=(+1/3,+1)
(r,s)_{15}=(+1,+1)

```

Pressure (Q2)

```

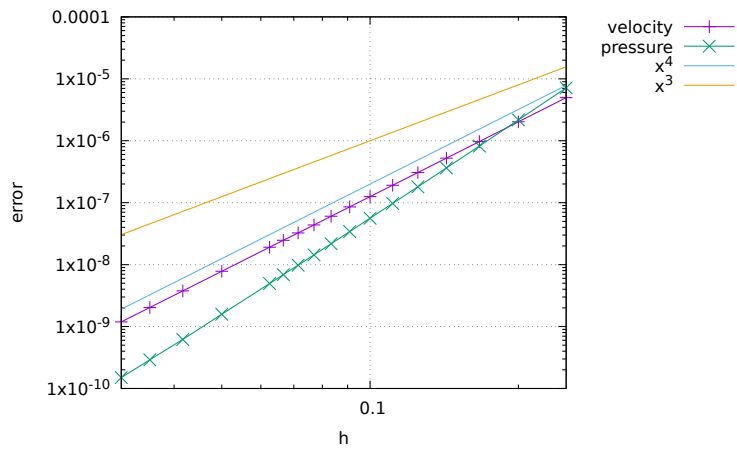
(r,s)_{00}=(-1,-1)
(r,s)_{01}=(0,-1)
(r,s)_{02}=(+1,-1)
(r,s)_{03}=(-1,0)
(r,s)_{04}=(0,0)
(r,s)_{05}=(+1,0)
(r,s)_{06}=(-1,+1)
(r,s)_{07}=(0,+1)
(r,s)_{08}=(+1,+1)

```

Write about 4 point quadrature.

features

- $Q_3 \times Q_2$ element
- incompressible flow
- mixed formulation
- isothermal
- isoviscous
- analytical solution



velocity error rate is cubic, pressure superconvergent since the pressure field is quadratic and therefore lies into the Q_2 space.

Stone 20: the Busse benchmark

This three-dimensional benchmark was first proposed by [288]. It has been subsequently presented in [1498, 1567, 13, 1279, 440, 1009]. We here focus on Case 1 of [288]: an isoviscous bimodal convection experiment at $Ra = 3 \cdot 10^5$.

The domain is of size $a \times b \times h$ with $a = 1.0079h$, $b = 0.6283h$ with $h = 2700\text{km}$. It is filled with a Newtonian fluid characterised by $\rho_0 = 3300\text{kg.m}^{-3}$, $\alpha = 10^{-5}\text{K}^{-1}$, $\mu = 8.0198 \times 10^{23}\text{Pa.s}$, $k = 3.564\text{W.m}^{-1}\text{.K}^{-1}$, $C_p = 1080\text{J.K}^{-1}\text{.kg}^{-1}$. The gravity vector is set to $\mathbf{g} = (0, 0, -10)^T$. The temperature is imposed at the bottom ($T = 3700^\circ\text{C}$) and at the top ($T = 0^\circ\text{C}$).

Note that using these numbers (as provided in the original paper), we arrive at $\text{Ra}=29967.01$, which is not exactly $3 \cdot 10^5$ as announced. Also, the heat diffusivity $\kappa = k/\rho_0 C_p$ is *exactly* 10^{-6} .

The various measurements presented in [288] are listed hereafter:

- The Nusselt number Nu computed at the top surface following Eq. (622):

$$Nu = L_z \frac{\int \int_{z=L_z} \frac{\partial T}{\partial y} dx dy}{\int \int_{z=0} T dx dy}$$

- the root mean square velocity v_{rms} and the temperature mean square velocity T_{rms}
- The vertical velocity w and temperature T at points $\mathbf{x}_1 = (0, 0, L_z/2)$, $\mathbf{x}_2 = (L_x, 0, L_z/2)$, $\mathbf{x}_3 = (0, L_y, L_z/2)$ and $\mathbf{x}_4 = (L_x, L_y, L_z/2)$;
- the vertical component of the heat flux Q at the top surface at all four corners.

Methodology

In what follows I highlight a few important points which are key to understanding how the code is put together and works.

```

load needed modules and functions
define parameters
build V grid (xV,yV,zV)
build V connectivity (iconV)
define b.c. for velocity (bc_fixV,bc_valV)
build T grid (xT,yT,zT)
build T connectivity (iconT)
define b.c. for temperature (bc_fixT,bc_valT)
initial temperature field
.-----> istep -----
| build K,G,f,h
| assemble them in A,rhs
| solve
| split solution vector in u,v,w,p
| {u,v,w}=relax*{u,v,w}+(1-relax)*{u,v,w}
| compute vrms
| build A, rhs for temperature
| solve for temperature T
| T=relax*T+(1-relax)*T
| compute elemental strainrate
| compute nodal strainrate
| compute nodal pressure
| measure V and T at mid side edges, Nu ...
| export to vtu and ascii files
.-----<-----.

```

I first load the shape functions which are in two separate files:

```

from shape_functionsV import NNV, dNNVdr, dNNVds, dNNVdt
from shape_functionsT import NNT, dNNTdr, dNNTds, dNNTdt

```

There are NV=nnx*nny*nnz velocity nodes and NT=NV temperature nodes.

The velocity grid is built: xV, yV, zV, iconV, and these are copied in xT, yT, zT and iconT for the temperature grid.

The initial temperature field is built as follows:

```

for i in range(0,NT):
    T[i] = (Temperature2-Temperature1)/Lz*zT[i]+Temperature1 \
        + 100*(np.pi*cos(np.pi*xT[i]/Lx) + np.pi*cos(np.pi*yT[i]/Ly))*np.sin(np.pi*zT[i]/Lz)

```

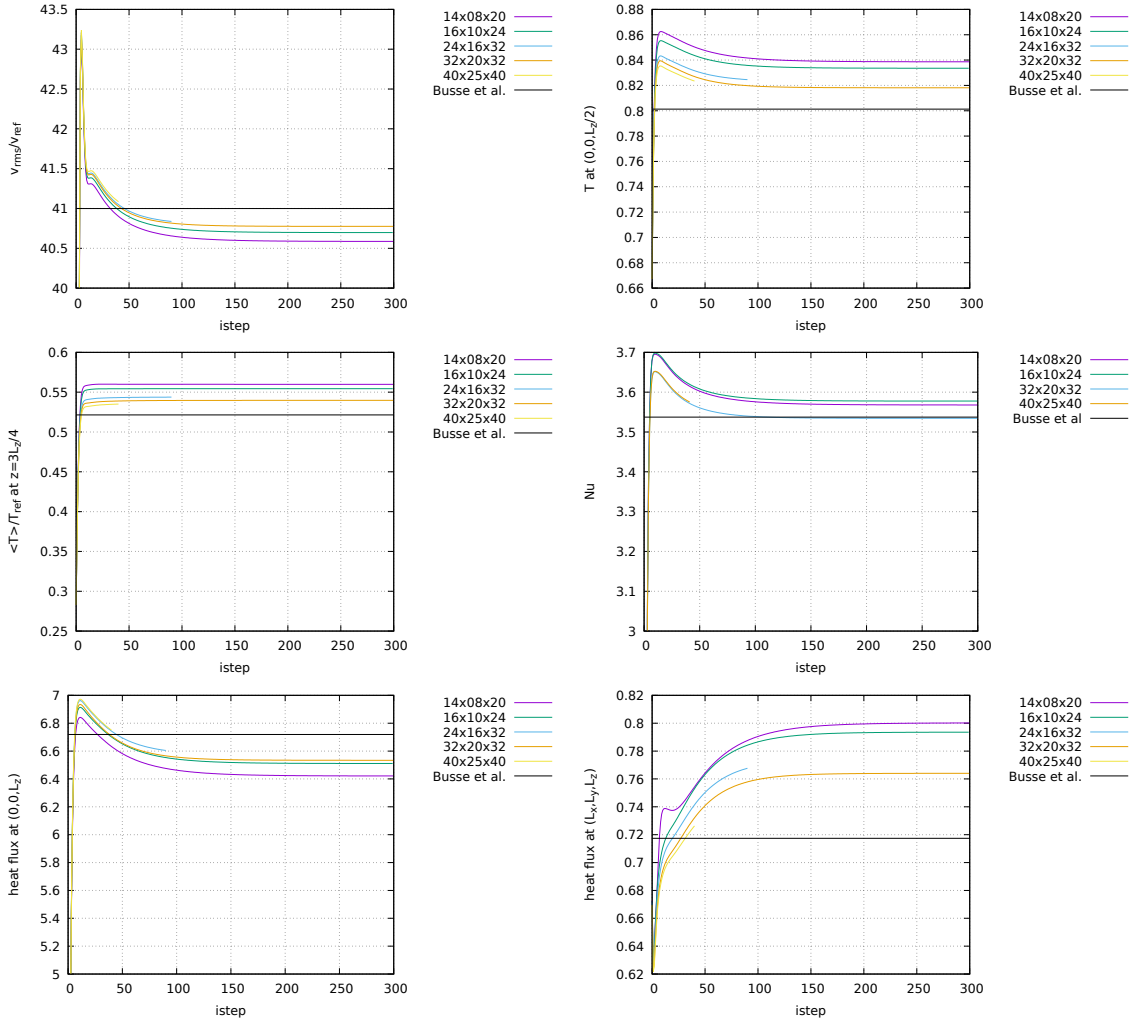
The C matrix of Eq. 303 is then built:

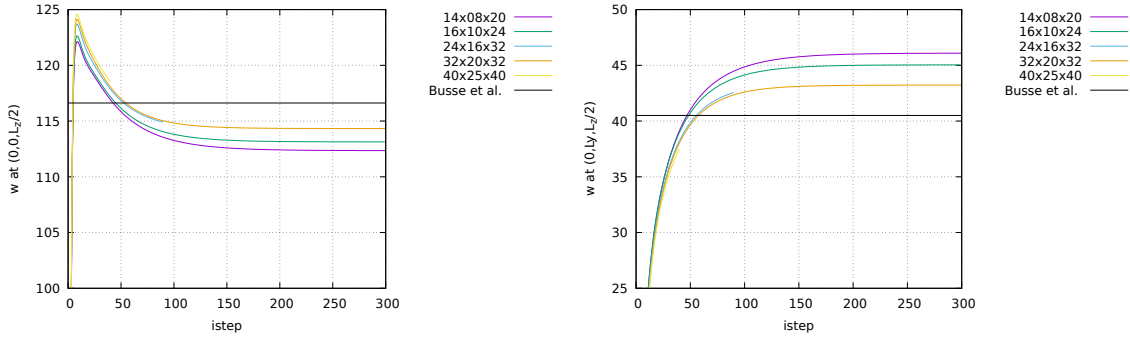
```

c_mat = np.array([[2,0,0,0,0,0], \
                  [0,2,0,0,0,0], \
                  [0,0,2,0,0,0], \
                  [0,0,0,1,0,0], \
                  [0,0,0,0,1,0], \
                  [0,0,0,0,0,1]], dtype=np.float64)

```

Results





The reported values for Busse et al. in the following table are taken from Table 3 of [288]. The reported values for fieldstone are adimensionalised by means of a reference temperature (3700K), a reference lengthscale 2700km, and a reference time $L_z^2/\kappa \sim 7.29e + 18$ s. The steady state is arrived at by solving the steady state Stokes and temperature equations with a relaxation parameter of 1/2.

Mesh size	ASPECT		$(Q_2 \times Q_1/Q_1)$	Busse et al [288]	fieldstone
	$L_z/24$	$L_z/32$	$L_z/48$	(best results)	$14 \times 8 \times 20$
Nu	3.5539	3.5447	3.5397	3.5374 ± 0.0005	
v_{rms}	40.997	40.999	40.999	40.999 ± 0.004	
$\langle T \rangle$ at $0.75 * L_z$	0.52148	0.52148	0.52148	0.52148 ± 0.00003	
$w(0, 0, L_z/2)$	116.605	116.618	116.623	116.625 ± 0.030	
$w(L_x, 0, L_z/2)$	-	-	-	-	
$w(L_x, L_y, L_z/2)$	-	-	-	-	
$w(0, L_y, L_z/2)$				40.500 ± 0.030	
$T(0, 0, L_z/2)$	0.80126	0.80128	0.80129	0.80130 ± 0.00005	
$T(L_x, 0, L_z/2)$	-	-	-	-	
$T(L_x, L_y, L_z/2)$	-	-	-	-	
$T(0, L_y, L_z/2)$				0.61876 ± 0.00005	
$dTdz(0, 0, L_z)$	6.7679	6.7357	6.7189	6.7127 ± 0.0500	
$dTdz(L_x, 0, L_z)$				1.5080 ± 0.0500	
$dTdz(L_x, L_y, L_z)$	0.7237	0.7205	0.7174	0.7140 ± 0.0500	
$dTdz(0, L_y, L_z)$				3.1740 ± 0.0500	

THIS IS NOT FINISHED: I need to run the model at higher resolutions, which will take a few days.

Stone 22: The stabilised $Q_1 \times Q_1$ element

The details of the numerical setup are presented in Section 8.6.

We wish to use $Q_1 \times Q_1$ element, which, unless stabilised, violates the LBB stability condition and therefore is unusable. Stabilisation can be of two types: least-squares [473, 1533, 962, 164], or by means of an additional term in the weak form as first introduced in [469, 163], which is appealing since there is no explicit stabilisation parameter. It is further analysed in [1270, 1063, 862, 1439, 740]. Note that an equal-order velocity-pressure formulation that does not exhibit spurious pressure modes (without stabilisation) has been presented in [1382].

This element corresponds to bilinear velocities, bilinear pressure (equal order interpolation for both velocity and pressure) which is very convenient in terms of data structures since all dofs are colocated.

In geodynamics, it is used in the Rhea code [1476, 283] and in Gale [46]. It is also used in [1053] in its stabilised form, in conjunction with AMR. This element is quickly discussed at page 217 of Volker John's book [915].

The stabilisation term \mathbb{C} enters the Stokes matrix in the (2,2) position:

$$\begin{pmatrix} \mathbb{K} & \mathbb{G} \\ \mathbb{G}^T & -\mathbb{C} \end{pmatrix} \cdot \begin{pmatrix} \mathcal{V} \\ \mathcal{P} \end{pmatrix} = \begin{pmatrix} f \\ h \end{pmatrix}$$

The purpose of the \mathbb{C} term is to stabilise the linear system. It is given by:

$$\mathbb{C}(p, q) = \sum_e \int_{\Omega_e} \frac{1}{\eta} (p - \Pi p)(q - \Pi q) d\Omega$$

where Π is the L^2 -projection onto the space of element-wise constant functions:

$$\Pi p = \frac{1}{|\Omega_e|} \int_{\Omega_e} p d\Omega$$

Because of the stabilisation matrix \mathbb{C} , the numerical solution satisfies the incompressibility condition only approximately. Local mesh refinement helps to control these unwanted effects [282, 283]. Since \mathbb{K} and \mathbb{C} are symmetric matrices, the Stokes system is then an indefinite symmetric system. The Schur complement matrix \mathbb{S} is then given by

$$\mathbb{S} = \mathbb{G}^T \cdot \mathbb{K}^{-1} \cdot \mathbb{G} + \mathbb{C}$$

One can further expand the above expression for the \mathbb{C} term:

$$\begin{aligned} \mathbb{C}(p, q) &= \sum_e \int_{\Omega_e} \frac{1}{\eta} (p - \Pi p)(q - \Pi q) d\Omega \\ &= \sum_e \int_{\Omega_e} \frac{1}{\eta} [pq - (\Pi p)q - (\Pi q)p + (\Pi p)(\Pi q)] d\Omega \\ &= \sum_e \frac{1}{\eta_e} \left[\int_{\Omega_e} pq d\Omega - \int_{\Omega_e} (\Pi p)qd\Omega - \int_{\Omega_e} (\Pi q)pd\Omega + \int_{\Omega_e} (\Pi p)(\Pi q)d\Omega \right] \\ &= \sum_e \frac{1}{\eta_e} \left[\int_{\Omega_e} pq d\Omega - (\Pi p) \int_{\Omega_e} q d\Omega - (\Pi q) \int_{\Omega_e} p d\Omega + (\Pi p)(\Pi q) \int_{\Omega_e} d\Omega \right] \\ &= \sum_e \frac{1}{\eta_e} \left[\int_{\Omega_e} pq d\Omega - (\Pi p)|\Omega_e|(\Pi q) - (\Pi q)|\Omega_e|(\Pi p) + (\Pi p)(\Pi q)|\Omega_e| \right] \\ &= \sum_e \frac{1}{\eta_e} \left[\int_{\Omega_e} pq d\Omega - |\Omega_e|(\Pi p)(\Pi q) \right] \end{aligned} \tag{658}$$

where we have used the fact that on each element Πp^h is constant. The left term will obviously yield a Q_1 mass matrix (scaled by the elemental viscosities). Note that this approach is not used in practice as we'll see hereafter.

The pressure inside an element is given by

$$p^h(\vec{x}) = \sum_k N_k^p(\vec{x}) p_k$$

so that

$$\Pi p^h = \frac{1}{|\Omega_e|} \int_{\Omega_e} \sum_k N_k^p p_k d\Omega = \sum_k \left(\underbrace{\frac{1}{|\Omega_e|} \int_{\Omega_e} N_k^p d\Omega}_{\tilde{N}_k^p} \right) p_k \quad (659)$$

and then

$$p^h - \Pi p^h = \sum_k N_k^p(\vec{x}) p_k - \sum_k \tilde{N}_k^p p_k = \sum_k (N_k^p(\vec{x}) - \tilde{N}_k^p) p_k$$

The algorithm is straightforward and as follows: In the loop over elements, a) Compute the average of each shape function $N_k^p(\vec{x})$ over the element; b) Subtract this average to the shape function; c) Build mass matrix with modified/offset shape functions (taking in account the viscosity).

In the case of rectangular elements of size (h_x, h_y) , \tilde{N}_k^p simplifies even more:

$$\tilde{N}_k^p = \frac{1}{|\Omega_e|} \int_{\Omega_e} N_k^p(\vec{x}) d\Omega = \frac{1}{h_x h_y} \frac{h_x h_y}{4} \int_{-1}^{+1} \int_{-1}^{+1} N_k^p(r, s) dr ds = \frac{1}{4} \int_{-1}^{+1} \int_{-1}^{+1} N_k^p(r, s) dr ds \quad (660)$$

It is easy to show that the average of the Q_1 shape functions over the reference element is 1, so that $\tilde{N}_k^p = 1/4$. This explains why in the code we have:

```
Navrg = np.zeros(m, dtype=np.float64)
Navrg[0]=0.25
Navrg[1]=0.25
Navrg[2]=0.25
Navrg[3]=0.25
```

This also means that $\Pi p^h = (p_1 + p_2 + p_3 + p_4)/4$, i.e. the projected pressure is the mean of the vertex values. It follows, as shown on p.244 of [513] that the elemental \mathbb{C} matrix is (omitting the viscosity term)

$$\mathbb{C}_{el} = \mathbb{M}_{el} - \vec{q}^T \vec{q} |\Omega_e| \quad \vec{q} = \left(\frac{1}{4}, \frac{1}{4}, \frac{1}{4}, \frac{1}{4} \right)$$

The nullspace of \mathbb{C} consists of constant vectors, i.e. $\vec{1} \in \text{null}(\mathbb{C})$ which means that the assembled stabilisation operator is consistent.

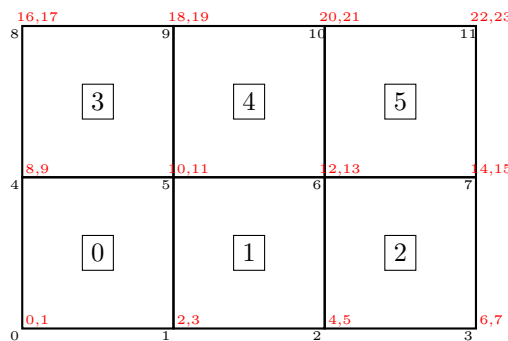
The elemental \mathbb{C}_{el} matrix is then computed like a mass matrix, although with modified shape function vectors. Inside the loop over quadrature points, we do:

```
Nvect[0:0:m]=N[0:m]-Navrg[0:m]
C_el+=Nvect.T.dot(Nvect)*jacob*weightq/viscosity(xq,yq,case)
```

It is then assembled inside the big FEM matrix

```
for k1 in range(0,m):
    for k2 in range(0,m):
        C_mat[icon[k1, ie1], icon[k2, ie1]]+=C_el[k1, k2]
```

Non-zero pattern of the \mathbb{G} matrix: Let us take a simple example: a 3x2 element grid.



The \mathbb{K} matrix is of size $NfemV \times NfemV$ with $NfemV = ndofV \times nnp = 2 \times 12 = 24$. The \mathbb{G} matrix is of size $NfemV \times NfemP$ with $NfemP = ndofP \times nnp = 1 \times 12 = 12$. The \mathbb{C} matrix is of size $NfemP \times NfemP$.

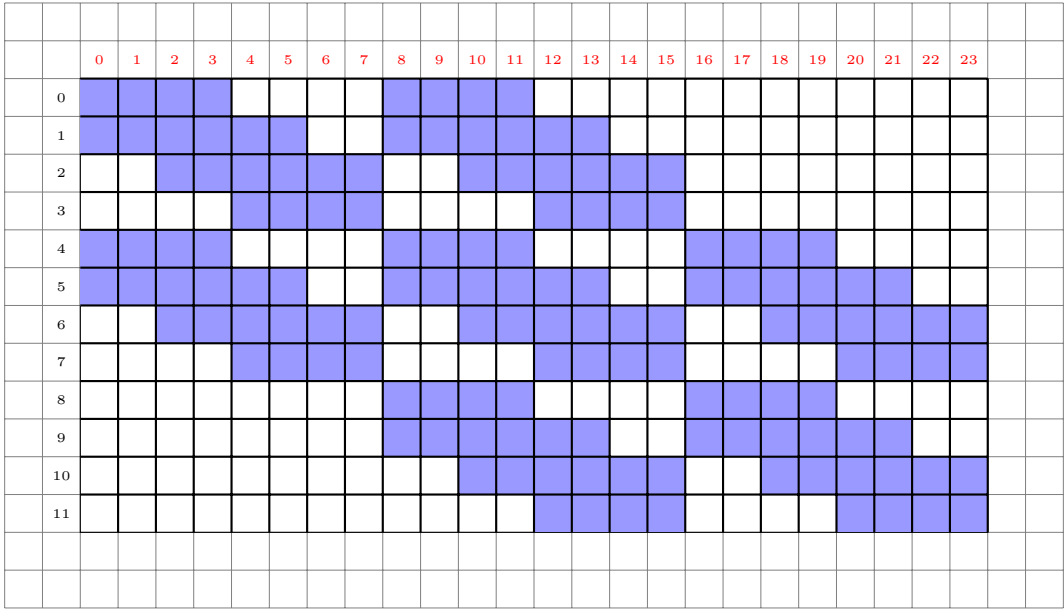
A corner pdof sees 4 vdofs, a side pdof sees 12 vdofs and an inside pdof sees 18 vdofs, so that the total number of nonzeros in \mathbb{G} can be computed as follows:

$$NZ_{\mathbb{G}} = \underbrace{4}_{\text{corners}} + \underbrace{2(nnx - 2) * 12}_{\text{2hor.sides}} + \underbrace{2(nny - 2) * 12}_{\text{2vert.sides}} + \underbrace{(nnx - 2)(nny - 2) * 18}_{\text{insidenodes}}$$

Concretely,

- pdof #0 sees vdofs 0,1,2,3,8,9,10,11
- pdof #1 sees vdofs 0,1,2,3,4,5,8,9,10,11,12,13
- pdof #5 sees vdofs 0,1,2,3,4,5,8,9,10,11,12,13,16,17,18,19,20,21

so that the \mathbb{G}^T matrix non-zero structure then is as follows:



Non-zero pattern of the \mathbb{C} matrix: Let us take a simple example: a 3x2 element grid.

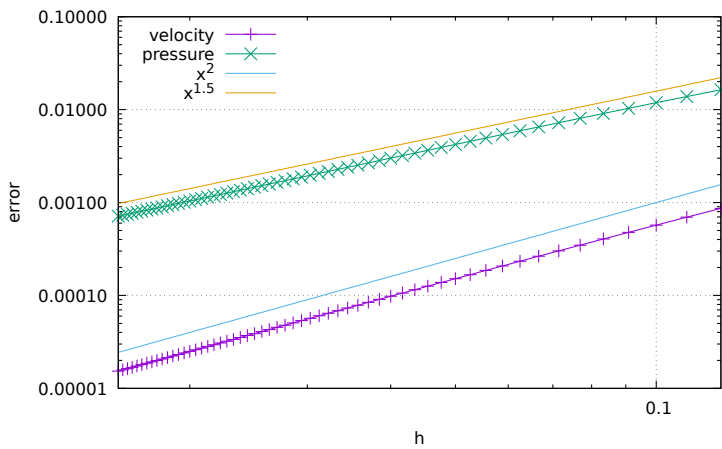
`finish structure of C matrix for q1q1`

We impose $\int pdV = 0$ which means that the following constraint is added to the Stokes matrix:

$$\begin{pmatrix} \mathbb{K} & \mathbb{G} & 0 \\ \mathbb{G}^T & \mathbb{C} & \mathbb{L} \\ 0 & \mathbb{L}^T & 0 \end{pmatrix} \cdot \begin{pmatrix} \mathcal{V} \\ \mathcal{P} \\ \lambda \end{pmatrix} = \begin{pmatrix} f \\ h \\ 0 \end{pmatrix}$$

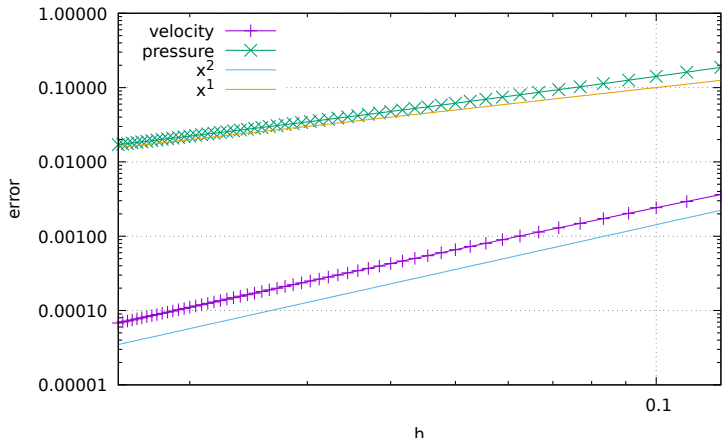
The Donea & Huerta benchmark

As in [473] we solve the benchmark problem presented in section 8.6.1.



The Dohrmann & Bochev benchmark

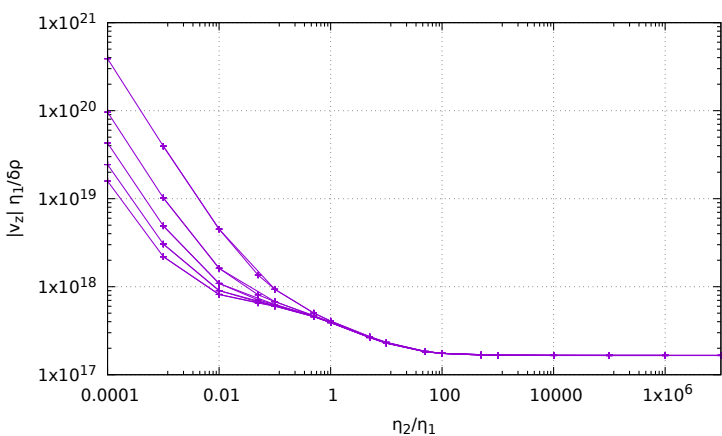
As in [469] we solve the benchmark problem presented in section 8.6.2.



compare my rates with original paper!

The falling block experiment

The setup is described in [1542].



Stone 23: compressible flow (1) - analytical benchmark

This work is part of the MSc thesis of T. Weir (2018).

We first start with an isothermal Stokes flow, so that we disregard the heat transport equation and the equations we wish to solve are simply:

$$-\nabla \cdot \left[2\eta \left(\dot{\epsilon}(\mathbf{v}) - \frac{1}{3}(\nabla \cdot \mathbf{v})\mathbf{1} \right) \right] + \nabla p = \rho \mathbf{g} \quad \text{in } \Omega, \quad (661)$$

$$\nabla \cdot (\rho \mathbf{v}) = 0 \quad \text{in } \Omega \quad (662)$$

The second equation can be rewritten $\nabla \cdot (\rho \mathbf{v}) = \rho \nabla \cdot \mathbf{v} + \mathbf{v} \cdot \nabla \rho = 0$ or,

$$\nabla \cdot \mathbf{v} + \frac{1}{\rho} \mathbf{v} \cdot \nabla \rho = 0$$

Note that this presupposes that the density is not zero anywhere in the domain.

We use a mixed formulation and therefore keep both velocity and pressure as unknowns. We end up having to solve the following system:

$$\begin{pmatrix} \mathbb{K} & \mathbb{G} \\ \mathbb{G}^T + \mathbb{Z} & 0 \end{pmatrix} \cdot \begin{pmatrix} \mathcal{V} \\ \mathcal{P} \end{pmatrix} = \begin{pmatrix} f \\ h \end{pmatrix} \quad \text{or,} \quad \mathbb{A} \cdot X = rhs$$

Where \mathbb{K} is the stiffness matrix, \mathbb{G} is the discrete gradient operator, \mathbb{G}^T is the discrete divergence operator, \mathcal{V} the velocity vector, \mathcal{P} the pressure vector. Note that the term $\mathbb{Z}\mathcal{V}$ derives from term $\mathbf{v} \cdot \nabla \rho$ in the continuity equation.

Each block \mathbb{K} , \mathbb{G} , \mathbb{Z} and vectors f and h are built separately in the code and assembled into the matrix \mathbb{A} and vector rhs afterwards. \mathbb{A} and rhs are then passed to the solver. We will see later that there are alternatives to solve this approach which do not require to build the full Stokes matrix \mathbb{A} .

Remark: the term $\mathbb{Z}\mathcal{V}$ is often put in the rhs (i.e. added to h) so that the matrix \mathbb{A} retains the same structure as in the incompressible case. This is indeed how it is implemented in ASPECT. This however requires more work since the rhs depends on the solution and some form of iterations is needed.

In the case of a compressible flow the strain rate tensor and the deviatoric strain rate tensor are no more equal (since $\nabla \cdot \mathbf{v} \neq 0$). The deviatoric strainrate tensor is given by⁵⁷

$$\dot{\epsilon}^d(\mathbf{v}) = \dot{\epsilon}(\mathbf{v}) - \frac{1}{3} Tr(\dot{\epsilon})\mathbf{1} = \dot{\epsilon}(\mathbf{v}) - \frac{1}{3}(\nabla \cdot \mathbf{v})\mathbf{1}$$

In that case:

$$\dot{\epsilon}_{xx}^d = \frac{\partial u}{\partial x} - \frac{1}{3} \left(\frac{\partial u}{\partial x} + \frac{\partial v}{\partial y} \right) = \frac{2}{3} \frac{\partial u}{\partial x} - \frac{1}{3} \frac{\partial v}{\partial y} \quad (663)$$

$$\dot{\epsilon}_{yy}^d = \frac{\partial v}{\partial y} - \frac{1}{3} \left(\frac{\partial u}{\partial x} + \frac{\partial v}{\partial y} \right) = -\frac{1}{3} \frac{\partial u}{\partial x} + \frac{2}{3} \frac{\partial v}{\partial y} \quad (664)$$

$$2\dot{\epsilon}_{xy}^d = \frac{\partial u}{\partial y} + \frac{\partial v}{\partial x} \quad (665)$$

and then

$$\dot{\epsilon}^d(\mathbf{v}) = \begin{pmatrix} \frac{2}{3} \frac{\partial u}{\partial x} - \frac{1}{3} \frac{\partial v}{\partial y} & \frac{1}{2} \frac{\partial u}{\partial y} + \frac{1}{2} \frac{\partial v}{\partial x} \\ \frac{1}{2} \frac{\partial u}{\partial y} + \frac{1}{2} \frac{\partial v}{\partial x} & -\frac{1}{3} \frac{\partial u}{\partial x} + \frac{2}{3} \frac{\partial v}{\partial y} \end{pmatrix}$$

From $\vec{\tau} = 2\eta \vec{\epsilon}^d$ we arrive at:

$$\begin{pmatrix} \tau_{xx} \\ \tau_{yy} \\ \tau_{xy} \end{pmatrix} = 2\eta \begin{pmatrix} \dot{\epsilon}_{xx}^d \\ \dot{\epsilon}_{yy}^d \\ \dot{\epsilon}_{xy}^d \end{pmatrix} = 2\eta \begin{pmatrix} 2/3 & -1/3 & 0 \\ -1/3 & 2/3 & 0 \\ 0 & 0 & 1/2 \end{pmatrix} \cdot \begin{pmatrix} \frac{\partial u}{\partial x} \\ \frac{\partial v}{\partial y} \\ \frac{\partial u}{\partial y} + \frac{\partial v}{\partial x} \end{pmatrix} = \eta \begin{pmatrix} 4/3 & -2/3 & 0 \\ -2/3 & 4/3 & 0 \\ 0 & 0 & 1 \end{pmatrix} \cdot \begin{pmatrix} \frac{\partial u}{\partial x} \\ \frac{\partial v}{\partial y} \\ \frac{\partial u}{\partial y} + \frac{\partial v}{\partial x} \end{pmatrix}$$

or,

$$\vec{\tau} = \mathbf{C}_\eta \mathbf{B} \mathbf{V}$$

⁵⁷See the ASPECT manual for a justification of the 3 value in the denominator in 2D and 3D.

In order to test our implementation we have created a few manufactured solutions:

- benchmark #1 (ibench=1): Starting from a density profile of:

$$\rho(x, y) = xy \quad (666)$$

We derive a velocity given by:

$$v_x(x, y) = \frac{C_x}{x}, v_y(x, y) = \frac{C_y}{y} \quad (667)$$

With $g_x(x, y) = \frac{1}{x}$ and $g_y(x, y) = \frac{1}{y}$, this leads us to a pressure profile:

$$p = -\eta \left(\frac{4C_x}{3x^2} + \frac{4C_y}{3y^2} \right) + xy + C_0 \quad (668)$$

This gives us a strain rate:

$$\dot{\epsilon}_{xx} = \frac{-C_x}{x^2} \quad \dot{\epsilon}_{yy} = \frac{-C_y}{y^2} \quad \dot{\epsilon}_{xy} = 0$$

In what follows, we choose $\eta = 1$ and $C_x = C_y = 1$ and for a unit square domain $[1 : 2] \times [1 : 2]$ we compute C_0 so that the pressure is normalised to zero over the whole domain and obtain $C_0 = -1$.

- benchmark #2 (ibench=2): Starting from a density profile of:

$$\rho = \cos(x) \cos(y) \quad (669)$$

We derive a velocity given by:

$$v_x = \frac{C_x}{\cos(x)}, v_y = \frac{C_y}{\cos(y)} \quad (670)$$

With $g_x = \frac{1}{\cos(y)}$ and $g_y = \frac{1}{\cos(x)}$, this leads us to a pressure profile:

$$p = \eta \left(\frac{4C_x \sin(x)}{3 \cos^2(x)} + \frac{4C_y \sin(y)}{3 \cos^2(y)} \right) + (\sin(x) + \sin(y)) + C_0 \quad (671)$$

$$\dot{\epsilon}_{xx} = C_x \frac{\sin(x)}{\cos^2(x)} \quad \dot{\epsilon}_{yy} = C_y \frac{\sin(y)}{\cos^2(y)} \quad \dot{\epsilon}_{xy} = 0$$

We choose $\eta = 1$ and $C_x = C_y = 1$. The domain is the unit square $[0 : 1] \times [0 : 1]$ and we obtain C_0 as before and obtain

$$C_0 = 2 - 2 \cos(1) + 8/3 \left(\frac{1}{\cos(1)} - 1 \right) \simeq 3.18823730$$

(thank you WolframAlpha)

- benchmark #3 (ibench=3)
- benchmark #4 (ibench=4)
- benchmark #5 (ibench=5)

features

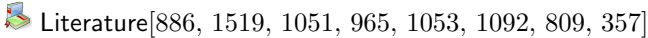
- $Q_1 \times P_0$ element
- incompressible flow
- mixed formulation
- Dirichlet boundary conditions (no-slip)
- isothermal
- isoviscous
- analytical solution
- pressure smoothing

ToDo:

- pbs with odd vs even number of elements
- q is 'fine' everywhere except in the corners - revisit pressure smoothing paper?
- redo A v d Berg benchmark (see Tom Weir thesis)

Stone 24: compressible flow (2) - convection box

This work is part of the MSc thesis of T. Weir (2018).



Literature[886, 1519, 1051, 965, 1053, 1092, 809, 357]

The physics

Let us start with some thermodynamics. Every material has an equation of state. The equilibrium thermodynamic state of any material can be constrained if any two state variables are specified. Examples of state variables include the pressure p and specific volume $\nu = 1/\rho$, as well as the temperature T .

After linearisation, the density depends on temperature and pressure as follows:

$$\rho(T, p) = \rho_0 ((1 - \alpha(T - T_0) + \beta_T p)$$

where α is the coefficient of thermal expansion, also called thermal expansivity:

$$\alpha = -\frac{1}{\rho} \left(\frac{\partial \rho}{\partial T} \right)_p$$

α is the percentage increase in volume of a material per degree of temperature increase; the subscript p means that the pressure is held fixed.

β_T is the isothermal compressibility of the fluid, which is given by

$$\beta_T = \frac{1}{K} = \frac{1}{\rho} \left(\frac{\partial \rho}{\partial P} \right)_T$$

with K the bulk modulus. Values of $\beta_T = 10^{-12} - 10^{-11} \text{ Pa}^{-1}$ are reasonable for Earth's mantle, with values decreasing by about a factor of 5 between the shallow lithosphere and core-mantle boundary. This is the percentage increase in density per unit change in pressure at constant temperature. Both the coefficient of thermal expansion and the isothermal compressibility can be obtained from the equation of state.

The full set of equations we wish to solve is given by

$$-\nabla \cdot [2\eta \dot{\epsilon}^d(\mathbf{v})] + \nabla p = \rho_0 ((1 - \alpha(T - T_0) + \beta_T p) \mathbf{g} \quad \text{in } \Omega \quad (672)$$

$$\nabla \cdot \mathbf{v} + \frac{1}{\rho} \mathbf{v} \cdot \nabla \rho = 0 \quad \text{in } \Omega \quad (673)$$

$$\rho C_p \left(\frac{\partial T}{\partial t} + \mathbf{v} \cdot \nabla T \right) - \nabla \cdot k \nabla T = \rho H + 2\eta \dot{\epsilon}^d : \dot{\epsilon}^d + \alpha T \left(\frac{\partial p}{\partial t} + \mathbf{v} \cdot \nabla p \right) \quad \text{in } \Omega, \quad (674)$$

Note that this presupposes that the density is not zero anywhere in the domain.

The numerics

We use a mixed formulation and therefore keep both velocity and pressure as unknowns. We end up having to solve the following system:

$$\begin{pmatrix} \mathbb{K} & \mathbb{G} + \mathbb{W} \\ \mathbb{G}^T + \mathbb{Z} & 0 \end{pmatrix} \cdot \begin{pmatrix} \mathcal{V} \\ \mathcal{P} \end{pmatrix} = \begin{pmatrix} f \\ h \end{pmatrix} \quad \text{or,} \quad \mathbb{A} \cdot X = rhs$$

Where \mathbb{K} is the stiffness matrix, \mathbb{G} is the discrete gradient operator, \mathbb{G}^T is the discrete divergence operator, \mathcal{V} the velocity vector, \mathcal{P} the pressure vector. Note that the term $\mathbb{Z}\mathcal{V}$ derives from term $\mathbf{v} \cdot \nabla \rho$ in the continuity equation.

As perfectly explained in the step 32 of deal.II⁵⁸, we need to scale the \mathbb{G} term since it is many orders of magnitude smaller than \mathbb{K} , which introduces large inaccuracies in the solving process to the point that

⁵⁸https://www.dealii.org/9.0.0/doxygen/deal.II/step_32.html

the solution is nonsensical. This scaling coefficient is η/L . After building the \mathbb{G} block, it is then scaled as follows: $\mathbb{G}' = \frac{\eta}{L} \mathbb{G}$ so that we now solve

$$\begin{pmatrix} \mathbb{K} & \mathbb{G}' + \mathbb{W} \\ \mathbb{G}'^T + \mathbb{Z} & 0 \end{pmatrix} \cdot \begin{pmatrix} \mathcal{V} \\ \mathcal{P}' \end{pmatrix} = \begin{pmatrix} f \\ h \end{pmatrix}$$

After the solve phase, we recover the real pressure with $\mathcal{P} = \frac{\eta}{L} \mathcal{P}'$.

adapt notes since I should scale \mathbb{W} and \mathbb{Z} too. h should be scaled too !!!!!!!

Each block \mathbb{K} , \mathbb{G} , \mathbb{Z} and vectors f and h are built separately in the code and assembled into the matrix \mathbb{A} and vector rhs afterwards. \mathbb{A} and rhs are then passed to the solver. We will see later that there are alternatives to solve this approach which do not require to build the full Stokes matrix \mathbb{A} .

Remark 1: the terms $\mathbb{Z}\mathcal{V}$ and $\mathbb{W}\mathcal{P}$ are often put in the rhs (i.e. added to h) so that the matrix \mathbb{A} retains the same structure as in the incompressible case. This is indeed how it is implemented in ASPECT, see also appendix A of [1051]. This however requires more work since the rhs depends on the solution and some form of iterations is needed.

Remark 2: Very often the adiabatic heating term $\alpha T(\mathbf{v} \cdot \nabla p)$ is simplified as follows: If you assume the vertical component of the gradient of the dynamic pressure to be small compared to the gradient of the total pressure (in other words, the gradient is dominated by the gradient of the hydrostatic pressure), then $-\rho\mathbf{g} \simeq \nabla p$ and then $\alpha T(\mathbf{v} \cdot \nabla p) \simeq -\alpha\rho T\mathbf{v} \cdot \mathbf{g}$. We will however not be using this approximation in what follows.

We have already established that

$$\vec{\tau} = \mathbf{C}_\eta \mathbf{B} \mathbf{V}$$

The following measurements are carried out:

- The root mean square velocity (**vrms**):

$$v_{rms} = \sqrt{\frac{1}{V} \int_V v^2 dV}$$

- The average temperature (**Tavrg**):

$$\langle T \rangle = \frac{1}{V} \int_V T dV$$

- The total mass (**mass**):

$$M = \int_V \rho dV$$

- The Nusselt number (**Nu**):

$$Nu = -\frac{1}{Lx} \frac{1}{\Delta T} \int_0^{Lx} \frac{\partial T(x, y = L_y)}{\partial y} dx$$

- The kinetic energy (**EK**):

$$E_K = \int_V \frac{1}{2} \rho v^2 dV$$

- The work done against gravity

$$\langle W \rangle = - \int_V \rho g_y v_y dV$$

- The total viscous dissipation (**visc_diss**)

$$\langle \Phi \rangle = \int \Phi dV = \frac{1}{V} \int 2\eta \dot{\epsilon} : \dot{\epsilon} dV$$

- The gravitational potential energy (**EG**)

$$E_G = \int_V \rho g_y (L_y - y) dV$$

- The internal thermal energy (ET)

$$E_T = \int_V \rho_{(0)} C_p T dV$$

Remark 3: Measuring the total mass can be misleading: indeed because $\rho = \rho_0(1 - \alpha T)$, then measuring the total mass amounts to measuring a constant minus the volume-integrated temperature, and there is no reason why the latter should be zero, so that there is no reason why the total mass should be zero...!

The experimental setup

The setup is as follows: the domain is $Lx = Ly = 3000\text{km}$. Free slip boundary conditions are imposed on all four sides. The initial temperature is given by:

$$T(x, y) = \left(\frac{L_y - y}{L_y} - 0.01 \cos\left(\frac{\pi x}{L_x}\right) \sin\left(\frac{\pi y}{L_y}\right) \right) \Delta T + T_{surf}$$

with $\Delta T = 4000\text{K}$, $T_{surf} = T_0 = 273.15\text{K}$. The temperature is set to $\Delta T + T_{surf}$ at the bottom and T_{surf} at the top. We also set $k = 3$, $C_p = 1250$, $|g| = 10$, $\rho_0 = 3000$ and we keep the Rayleigh number Ra and dissipation number Di as input parameters:

$$Ra = \frac{\alpha g \Delta T L^3 \rho_0^2 C_p}{\eta k} \quad Di = \frac{\alpha g L}{C_p}$$

From the second equation we get $\alpha = \frac{Di C_p}{gL}$, which we can insert in the first one:

$$Ra = \frac{Di C_p^2 \Delta T L^2 \rho_0^2}{\eta k} \quad \text{or}, \quad \eta = \frac{Di C_p^2 \Delta T L^2 \rho_0^2}{Ra k}$$

For instance, for $Ra = 10^4$ and $Di = 0.75$, we obtain $\alpha \simeq 3 \cdot 10^{-5}$ and $\eta \simeq 10^{25}$ which are quite reasonable values.

Scaling

Following [965], we non-dimensionalize the equations using the reference values for density ρ_r , thermal expansivity α_r , temperature contrast ΔT_r (`refTemp`), thermal conductivity k_r , heat capacity C_p , depth of the fluid layer L and viscosity η_r . The non-dimensionalization for velocity, u_r , pressure p_r and time, t_r become

$$u_r = \frac{k_r}{\rho_r C_p L} \quad (\text{refvel})$$

$$p_r = \frac{\eta_r k_r}{\rho_r C_p L^2} \quad (\text{refpress})$$

$$t_r = \frac{\rho_r C_p L^2}{k_r} \quad (\text{reftime})$$

In the case of the setup described hereabove, and when choosing $Ra = 10^4$ and $Di = 0.5$, we get:

```
alphaT 2.08333e-05
eta 8.437500e+24
reftime 1.125000e+19
refvel 2.666667e-13
refPress 7.500000e+05
```

Conservation of energy 1

under BA and EBA approximations

Following [1051], we take the dot product of the momentum equation with the velocity \mathbf{v} and integrate over the whole volume⁵⁹:

$$\int_V [-\nabla \cdot \boldsymbol{\tau} + \nabla p] \cdot \mathbf{v} dV = \int_V \rho \mathbf{g} \cdot \mathbf{v} dV$$

or,

$$-\int_V (\nabla \cdot \boldsymbol{\tau}) \cdot \mathbf{v} dV + \int_V \nabla p \cdot \mathbf{v} dV = \int_V \rho \mathbf{g} \cdot \mathbf{v} dV$$

Let us look at each block separately:

$$-\int_V (\nabla \cdot \boldsymbol{\tau}) \cdot \mathbf{v} dV = -\int_S \boldsymbol{\tau} \underbrace{\mathbf{v} \cdot \mathbf{n}}_{=0 \text{ (b.c.)}} dS + \int_V \boldsymbol{\tau} : \nabla \mathbf{v} dV = \int_V \boldsymbol{\tau} : \dot{\boldsymbol{\epsilon}} dV = \int_V \Phi dV$$

which is the volume integral of the shear heating. Then,

$$\int_V \nabla p \cdot \mathbf{v} dV = \int_S p \underbrace{\mathbf{v} \cdot \mathbf{n}}_{=0 \text{ (b.c.)}} dS - \int_V \underbrace{\nabla \cdot \mathbf{v}}_{=0 \text{ (incomp.)}} pdV = 0$$

which is then zero in the case of an incompressible flow. And finally

$$\int_V \rho \mathbf{g} \cdot \mathbf{v} dV = W$$

which is the work against gravity.

Conclusion for an *incompressible* fluid: we should have

$$\int_V \Phi dV = \int_V \rho \mathbf{g} \cdot \mathbf{v} dV \quad (675)$$

This formula is hugely problematic: indeed, the term ρ in the rhs is the full density. We know that to the value of ρ_0 corresponds a lithostatic pressure gradient $p_L = \rho_0 gy$. In this case one can write $\rho = \rho_0 + \rho'$ and $p = p_L + p'$ so that we also have

$$\int_V [-\nabla \cdot \boldsymbol{\tau} + \nabla p'] \cdot \mathbf{v} dV = \int_V \rho' \mathbf{g} \cdot \mathbf{v} dV$$

which will ultimately yield

$$\int_V \Phi dV = \int_V \rho' \mathbf{g} \cdot \mathbf{v} dV = \int_V (\rho - \rho_0) \mathbf{g} \cdot \mathbf{v} dV \quad (676)$$

Obviously Eqs.(675) and (676) cannot be true at the same time. The problem comes from the nature of the (E)BA approximation: $\rho = \rho_0$ in the mass conservation equation but it is not constant in the momentum conservation equation, which is of course inconsistent. Since the mass conservation equation is $\nabla \cdot \mathbf{v} = 0$ under this approximation then the term $\int_V \nabla p \cdot \mathbf{v} dV$ is always zero for any pressure (full pressure p , or overpressure $p - p_L$), hence the paradox. This paradox will be lifted when a consistent set of equations will be used (compressible formulation). On a practical note, Eqs.(675) is not verified by the code, while (676) is.

In the end:

$$\int_V \Phi dV = \underbrace{\int_V}_{\text{visc.diss}} (\rho - \rho_0) \underbrace{\mathbf{g} \cdot \mathbf{v} dV}_{\text{work_grav}}$$

(677)

⁵⁹Check: this is akin to looking at the power, force*velocity, says Arie

under no approximation at all

$$\int_V \nabla p \cdot \mathbf{v} dV = \int_S p \underbrace{\mathbf{v} \cdot \mathbf{n}}_{=0 \text{ (b.c.)}} dS - \int_V \nabla \cdot \mathbf{v} pdV = 0 \quad (678)$$

$$= \int_V \frac{1}{\rho} \mathbf{v} \cdot \nabla \rho pdV = 0 \quad (679)$$

$$(680)$$

ToDo: see section 3 of [1051] where this is carried out with the Adams-Williamson eos.

Conservation of energy 2

Also, following the Reynold's transport theorem [1120], p210, we have for a property A (per unit mass)

$$\frac{d}{dt} \int_V A \rho dV = \int_V \frac{\partial}{\partial t} (A \rho) dV + \int_S A \rho \mathbf{v} \cdot \mathbf{n} dS$$

Let us apply to this to $A = C_p T$ and compute the time derivative of the internal energy:

$$\frac{d}{dt} \int_V \rho C_p T dV = \int_V \frac{\partial}{\partial t} (\rho C_p T) dV + \int_S \rho C_p \underbrace{\mathbf{v} \cdot \mathbf{n}}_{=0 \text{ (b.c.)}} dS = \underbrace{\int_V C_p T \frac{\partial \rho}{\partial t} dV}_I + \underbrace{\int_V \rho C_p \frac{\partial T}{\partial t} dV}_{II} \quad (681)$$

In order to expand I , the mass conservation equation will be used, while the heat transport equation will be used for II :

$$I = \int_V C_p T \frac{\partial \rho}{\partial t} dV = - \int_V C_p T \nabla \cdot (\rho \mathbf{v}) dV = - \int_V C_p T \rho \underbrace{\mathbf{v} \cdot \mathbf{n}}_{=0 \text{ (b.c.)}} dS + \int_V \rho C_p \nabla T \cdot \mathbf{v} dV \quad (682)$$

$$II = \int_V \rho C_p \frac{\partial T}{\partial t} dV = \int_V \left[-\rho C_p \mathbf{v} \cdot \nabla T + \nabla \cdot k \nabla T + \rho H + \Phi + \alpha T \left(\frac{\partial p}{\partial t} + \mathbf{v} \cdot \nabla p \right) \right] dV \quad (683)$$

$$= \int_V \left[-\rho C_p \mathbf{v} \cdot \nabla T + \rho H + \Phi + \alpha T \left(\frac{\partial p}{\partial t} + \mathbf{v} \cdot \nabla p \right) \right] dV + \int_V \nabla \cdot k \nabla T dV \quad (684)$$

$$= \int_V \left[-\rho C_p \mathbf{v} \cdot \nabla T + \rho H + \Phi + \alpha T \left(\frac{\partial p}{\partial t} + \mathbf{v} \cdot \nabla p \right) \right] dV + \int_S k \nabla T \cdot \mathbf{n} dS \quad (685)$$

$$= \int_V \left[-\rho C_p \mathbf{v} \cdot \nabla T + \rho H + \Phi + \alpha T \left(\frac{\partial p}{\partial t} + \mathbf{v} \cdot \nabla p \right) \right] dV - \int_S \mathbf{q} \cdot \mathbf{n} dS \quad (686)$$

Finally:

$$I + II = \underbrace{\frac{d}{dt} \int_V \rho C_p T dV}_{\text{ET}} = \int_V \left[\rho H + \Phi + \alpha T \left(\frac{\partial p}{\partial t} + \mathbf{v} \cdot \nabla p \right) \right] dV - \int_S \mathbf{q} \cdot \mathbf{n} dS \quad (687)$$

$$= \int_V \rho H dV + \underbrace{\int_V \Phi dV}_{\text{visc.diss}} + \underbrace{\int_V \alpha T \frac{\partial p}{\partial t} dV}_{\text{extra}} + \underbrace{\int_V \alpha T \mathbf{v} \cdot \nabla p dV}_{\text{adiab_heating}} - \underbrace{\int_S \mathbf{q} \cdot \mathbf{n} dS}_{\text{heatflux_boundary}} \quad (688)$$

This was of course needlessly complicated as the term $\partial \rho / \partial t$ is always taken to be zero, so that $I = 0$ automatically. The mass conservation equation is then simply $\nabla \cdot (\rho \mathbf{v}) = 0$. Then it follows that

$$0 = \int_V C_p T \nabla \cdot (\rho \mathbf{v}) dV = - \int_V C_p T \rho \underbrace{\mathbf{v} \cdot \mathbf{n}}_{=0 \text{ (b.c.)}} dS + \int_V \rho C_p \nabla T \cdot \mathbf{v} dV \quad (689)$$

$$= \int_V \rho C_p \nabla T \cdot \mathbf{v} dV \quad (690)$$

so that the same term in Eq.(686) vanishes too, and then Eq.(688) is always valid, although one should be careful when computing E_T in the BA and EBA cases as it should use ρ_0 and not ρ .

The problem of the onset of convection

[wiki] In geophysics, the Rayleigh number is of fundamental importance: it indicates the presence and strength of convection within a fluid body such as the Earth's mantle. The mantle is a solid that behaves as a fluid over geological time scales.

The Rayleigh number essentially is an indicator of the type of heat transport mechanism. At low Rayleigh numbers conduction processes dominate over convection ones. At high Rayleigh numbers it is the other way around. There is a so-called critical value of the number with delineates the transition from one regime to the other.

This problem has been studied and approached both theoretically and numerically [1575, e.g.] and it was found that the critical Rayleigh number Ra_c is

$$Ra_c = (27/4)\pi^4 \simeq 657.5$$

in setups similar to ours.

VERY BIG PROBLEM

The temperature setup is built as follows: T_{surf} is prescribed at the top, $T_{surf} + \Delta T$ is prescribed at the bottom. The initial temperature profile is linear between these two values. In the case of BA, the actual value of T_{surf} is of no consequence. However, for the EBA the full temperature is present in the adiabatic heating term on the rhs of the hte, and the value of T_{surf} will therefore influence the solution greatly. This is very problematic as there is no real way to arrive at the surface temperature from the King paper. On top of this, the density uses a reference temperature T_0 which too will influence the solution without being present in the controlling Ra and Di numbers!!

In light thereof, it will be very difficult to recover the values of King et al for EBA!

features

- $Q_1 \times P_0$ element
- compressible flow
- mixed formulation
- Dirichlet boundary conditions (no-slip)
- isoviscous
- analytical solution
- pressure smoothing

Relevant literature: [127, 886, 1519, 1051, 965, 1053, 1092, 809]

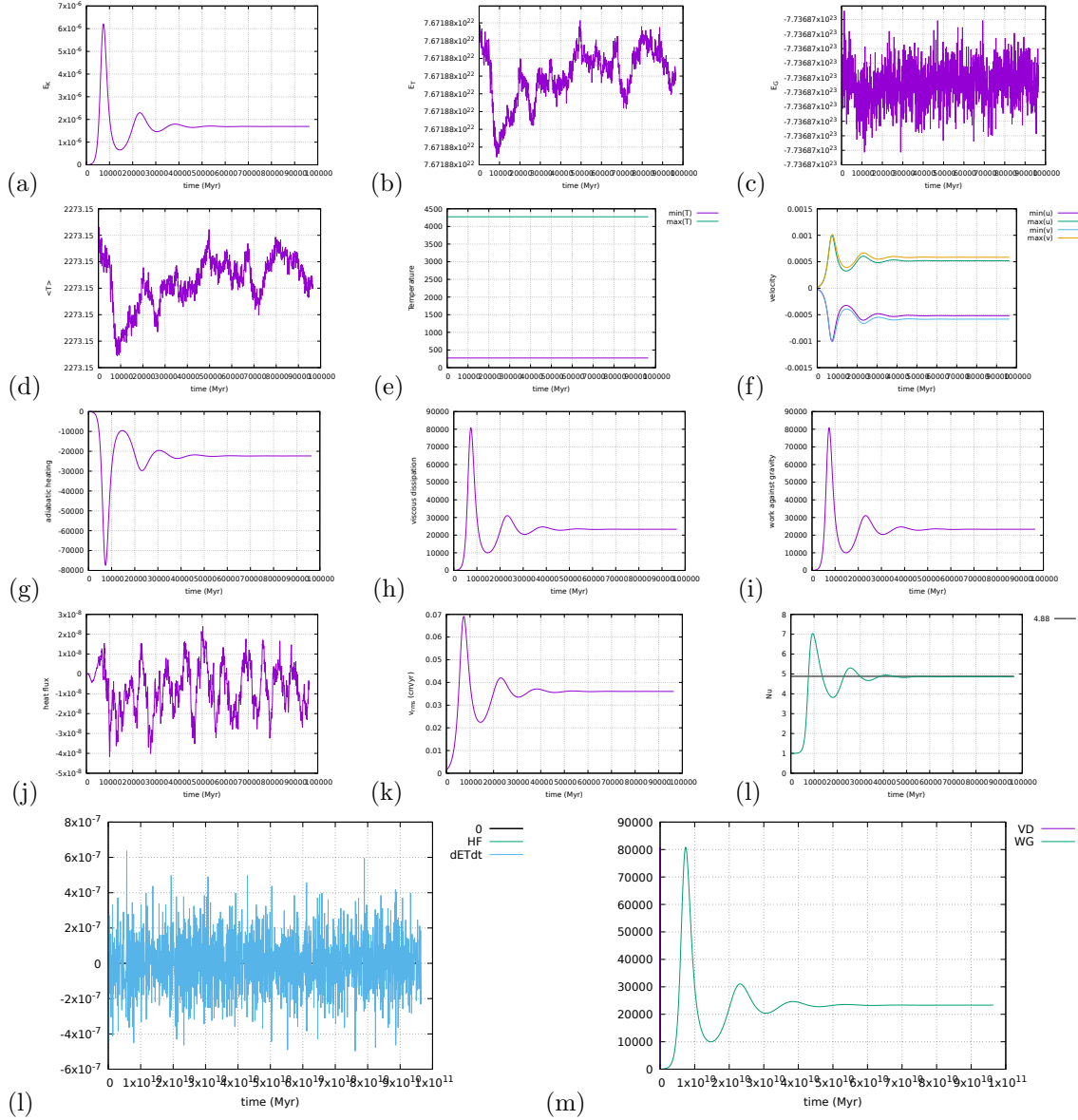
ToDo:

- heat flux is at the moment elemental, so Nusselt and heat flux on boundaries measurements not as accurate as could be.

- implement steady state detection
- do $Ra = 10^5$ and $Ra = 10^6$
- velocity average at surface
- non dimensional heat flux at corners [158]
- depth-dependent viscosity (case 2 of [158])

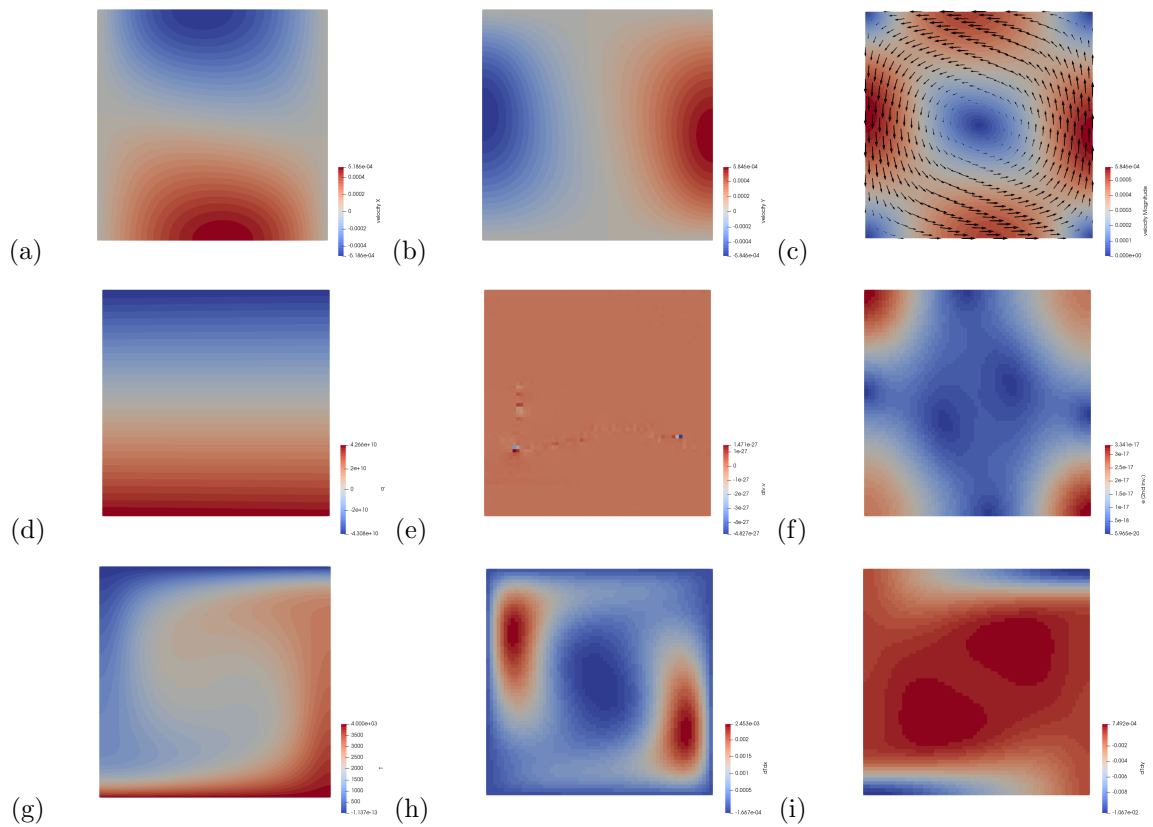
results - BA - $Ra = 10^4$

These results were obtained with a 64x64 resolution, and CFL number of 1. Steady state was reached after about 1250 timesteps.



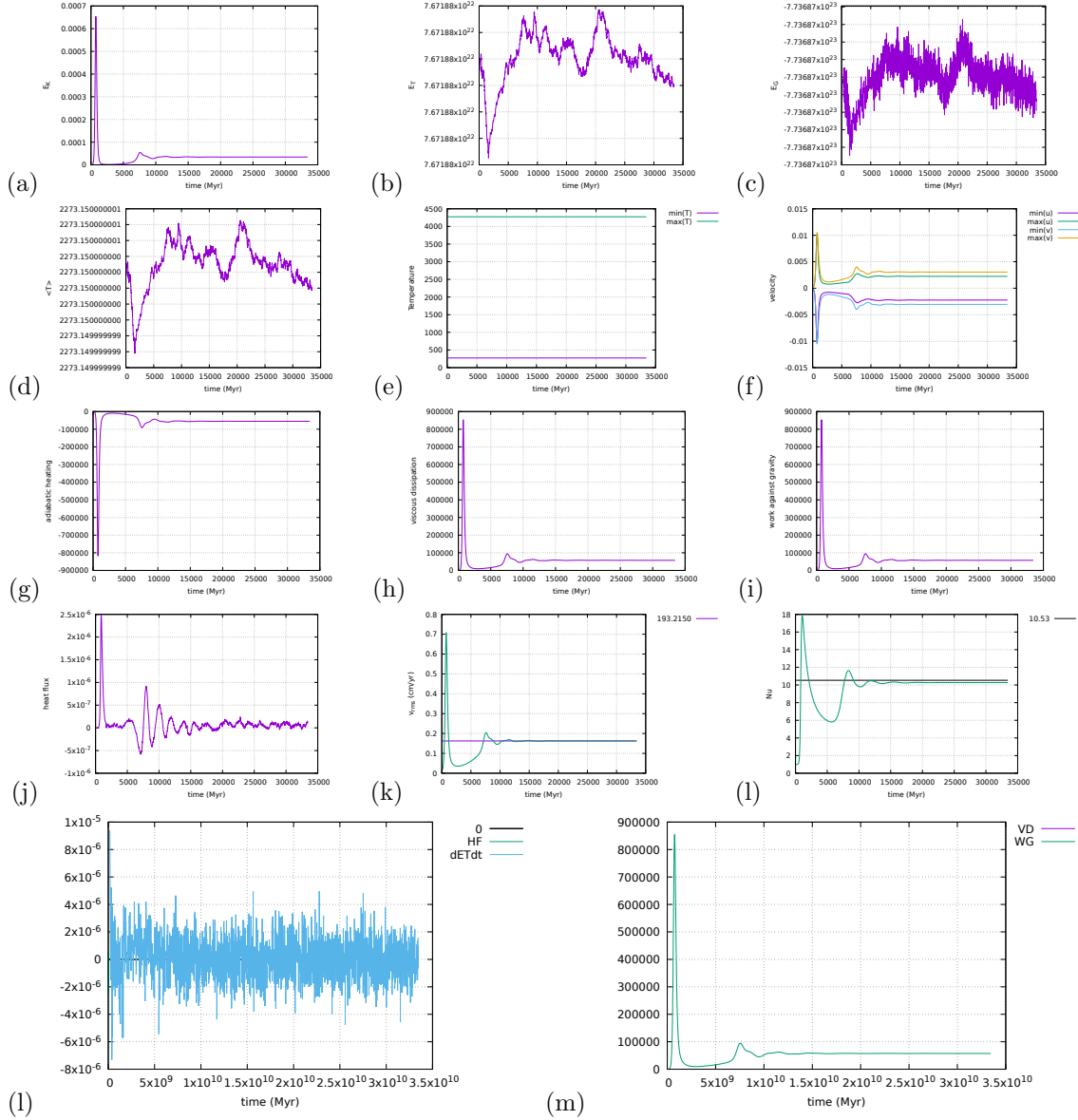
AH: adiabatic heating, VD: viscous dissipation, HF: heat flux, WG: work against gravity

Eq.(688) is verified by (l) and Eq.(677) is verified by (m).



results - BA - $Ra = 10^5$

These results were obtained with a 64x64 resolution, and CFL number of 1. Steady state was reached after about 1250 timesteps.

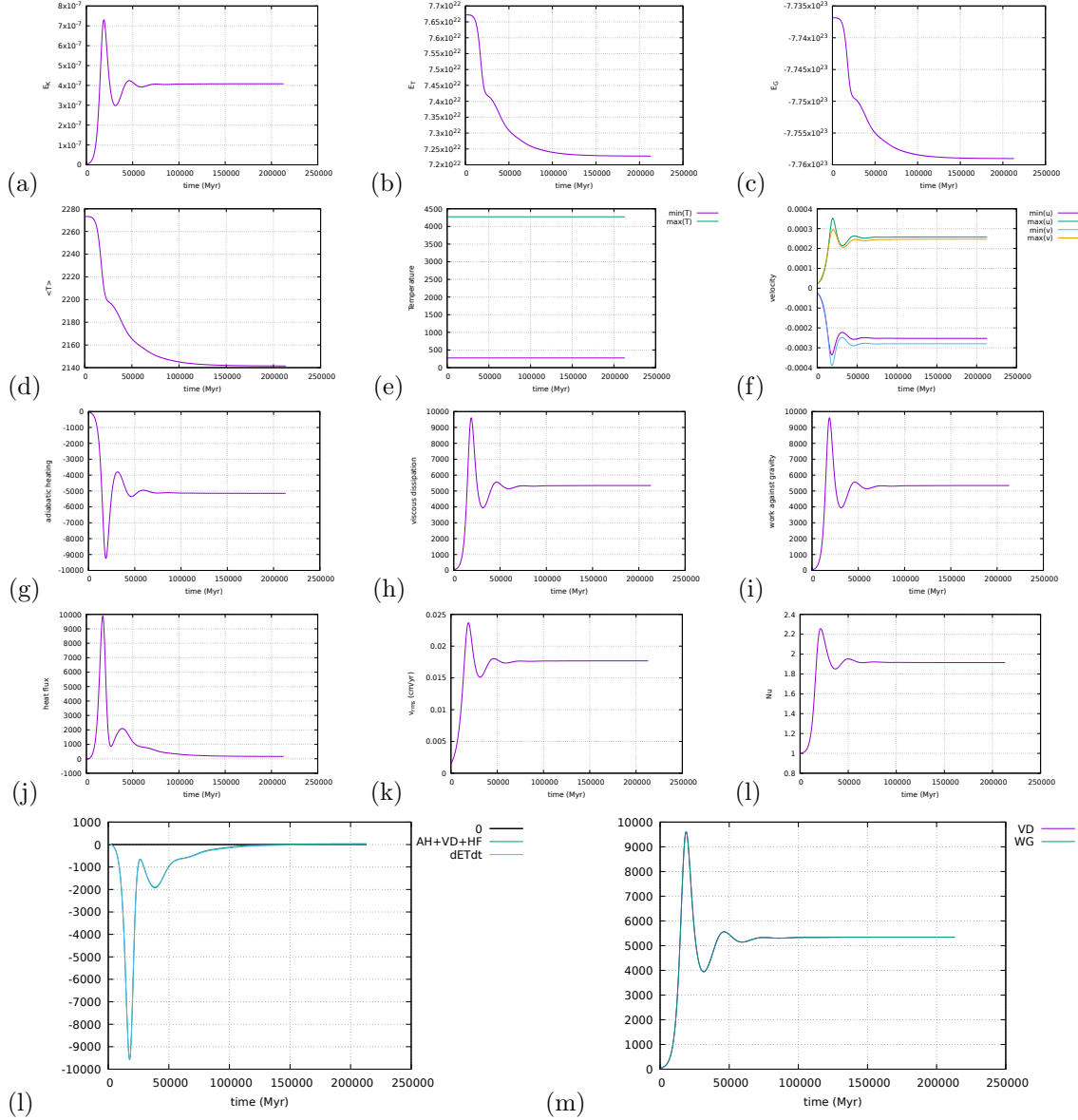


Eq.(688) is verified by (l) and Eq.(677) is verified by (m).

results - BA - $Ra = 10^6$

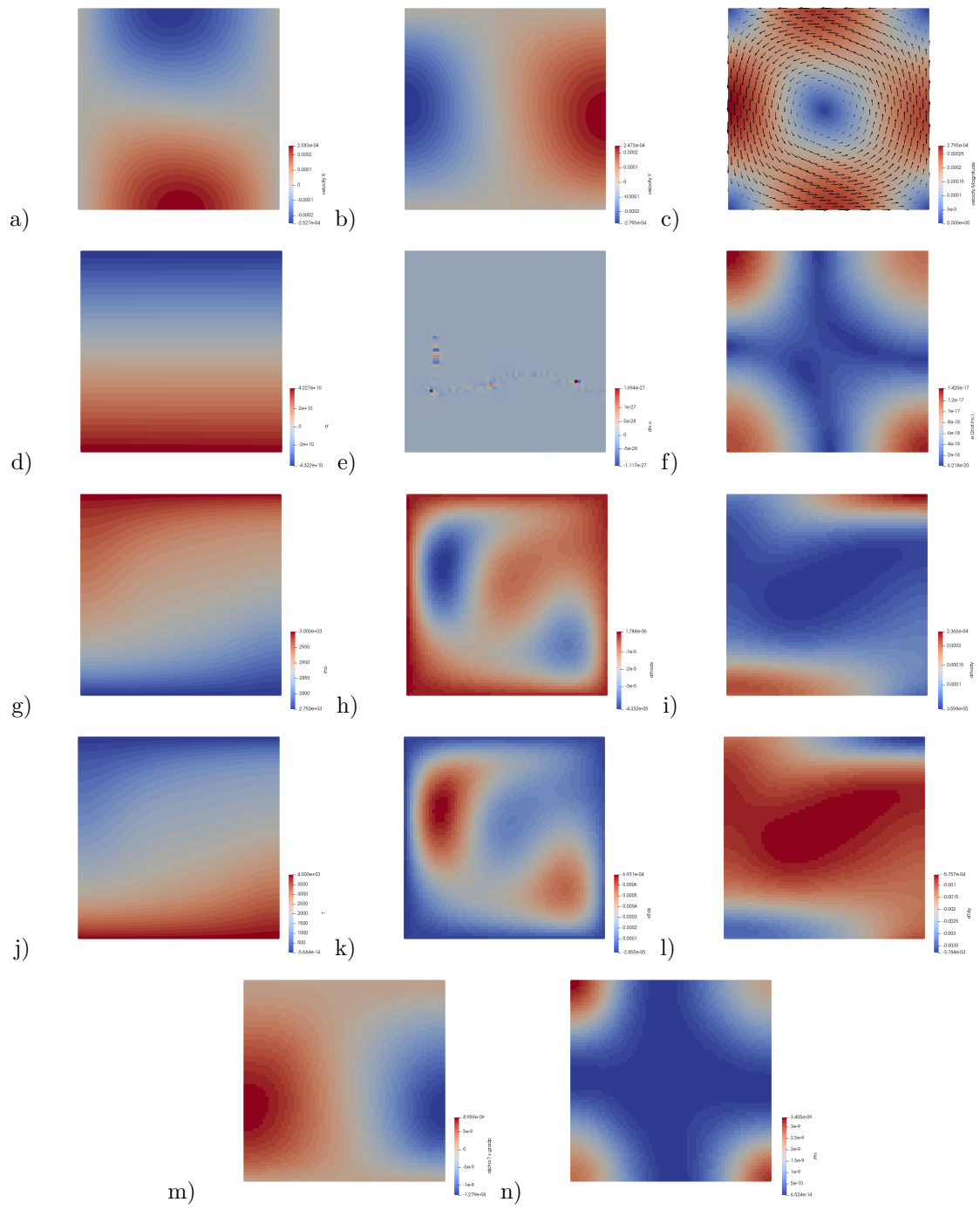
results - EBA - $Ra = 10^4$

These results were obtained with a 64x64 resolution, and CFL number of 1. Steady state was reached after about 2500 timesteps



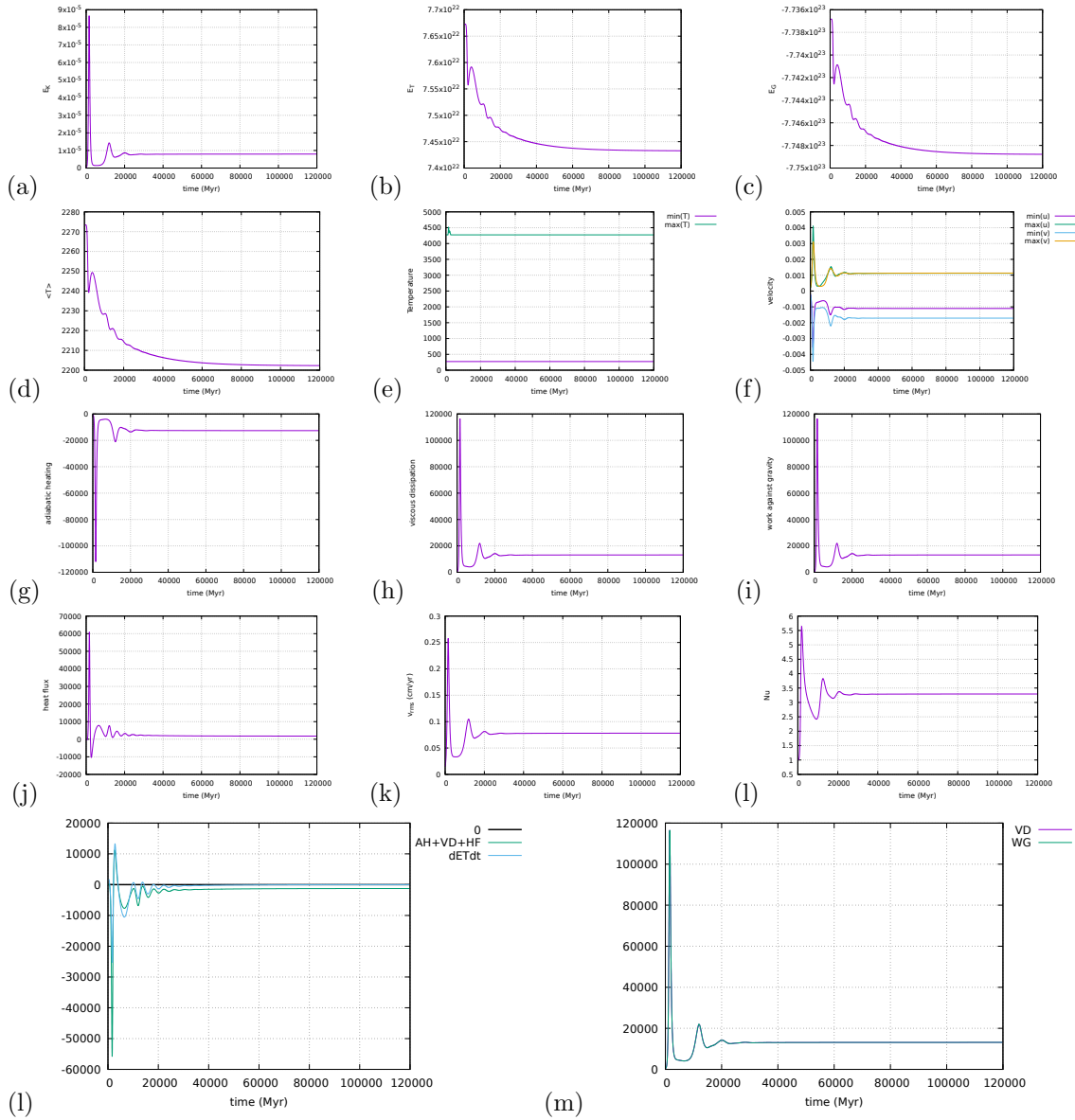
AH: adiabatic heating, VD: viscous dissipation, HF: heat flux, WG: work against gravity

Eq.(688) is verified by (l) and Eq.(677) is verified by (m).



results - EBA - $Ra = 10^5$

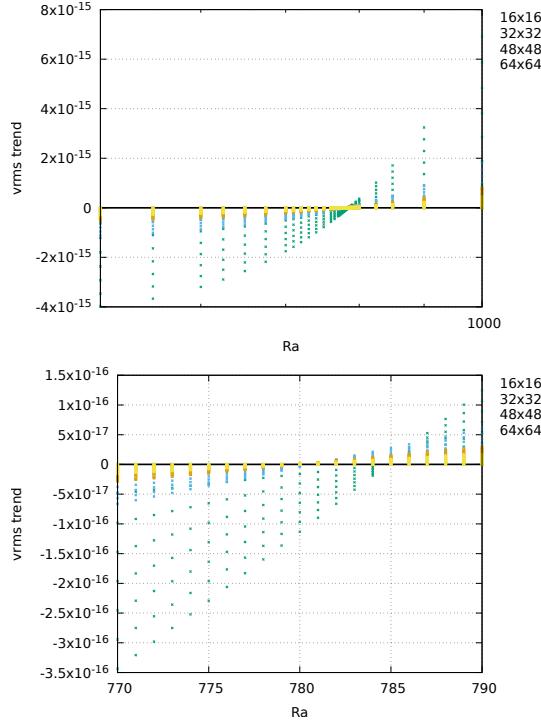
These results were obtained with a 64x64 resolution, and CFL number of 1. Simulation was stopped after about 4300 timesteps.



AH: adiabatic heating, VD: viscous dissipation, HF: heat flux, WG: work against gravity

Onset of convection

The code can be run for values of Ra between 500 and 1000, at various resolutions for the BA formulation. The value $v_{rms}(t) - v_{rms}(0)$ is plotted as a function of Ra and for the 10 first timesteps. If the v_{rms} is found to decrease, then the Rayleigh number is not high enough to allow for convection and the initial temperature perturbation relaxes by diffusion (and then $v_{rms}(t) - v_{rms}(0) < 0$). If the v_{rms} is found to increase, then $v_{rms}(t) - v_{rms}(0) > 0$ and the system is going to showcase convection. The zero value of $v_{rms}(t) - v_{rms}(0)$ gives us the critical Rayleigh number, which is found between 775 and 790.

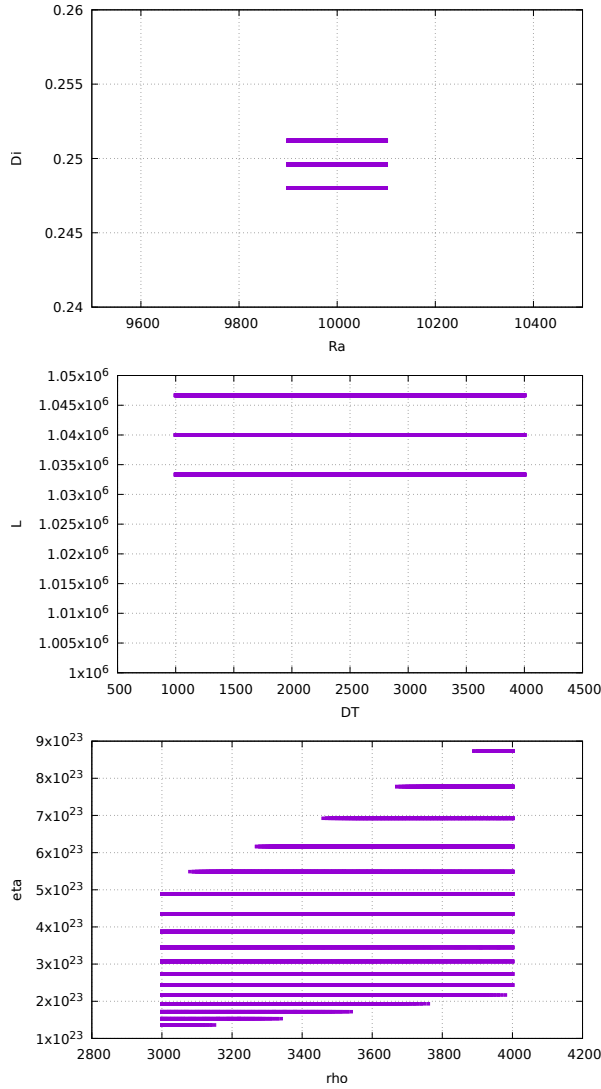


Appendix: Looking for the right combination of parameters for the King benchmark.

I run a quadruple do loop over L , ΔT , ρ_0 and η_0 between plausible values (see code targets.py) and write in a file only the combination which yields the required Rayleigh and Dissipation number values (down to 1% accuracy).

```
alpha=3e-5
g=10
hcapa=1250
hcond=3
DTmin=1000 ; DTmax=4000 ; DTnpts=251
Lmin=1e6 ; Lmax=3e6 ; Lnpts=251
rhomin=3000 ; rhomax=3500 ; rhonpts=41
etamin=19 ; etamax=25 ; etanpts=100
```

On the following plots the 'winning' combinations of these four parameters are shown:



We see that:

- the parameter L (being to the 3rd power in the Ra number) cannot vary too much. Although it is varied between 1000 and 3000km there seems to be a 'right' value at about 1040 km. (why?)
- viscosities are within 10^{23} and 10^{24} which are plausible values (although a bit high?).
- densities can be chosen freely between 3000 and 3500
- ΔT seems to be the most problematic value since it can range from 1000 to 4000K ...

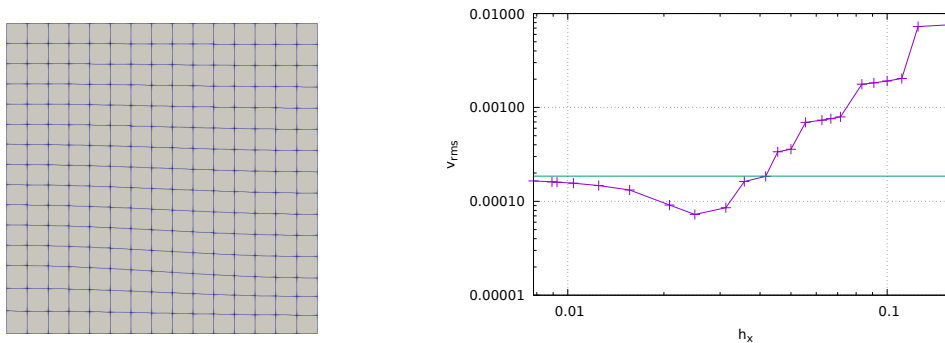
Stone 25: Rayleigh-Taylor instability (1) - instantaneous

This numerical experiment was first presented in [1613]. It consists of an isothermal Rayleigh-Taylor instability in a two-dimensional box of size $L_x = 0.9142$ and $L_y = 1$. Two Newtonian fluids are present in the system: the buoyant layer is placed at the bottom of the box and the interface between both fluids is given by $y(x) = 0.2 + 0.02 \cos\left(\frac{\pi x}{L_x}\right)$. The bottom fluid is parametrised by its mass density ρ_1 and its viscosity μ_1 , while the layer above is parametrised by ρ_2 and μ_2 .

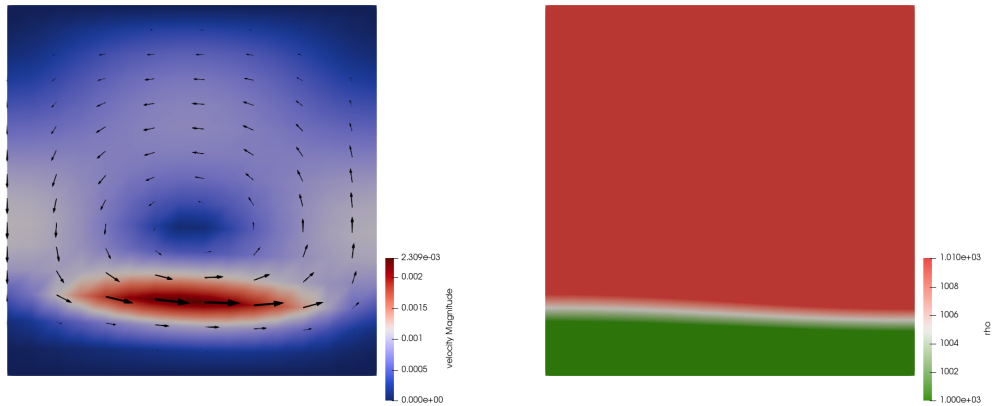
No-slip boundary conditions are applied at the bottom and at the top of the box while free-slip boundary conditions are applied on the sides.

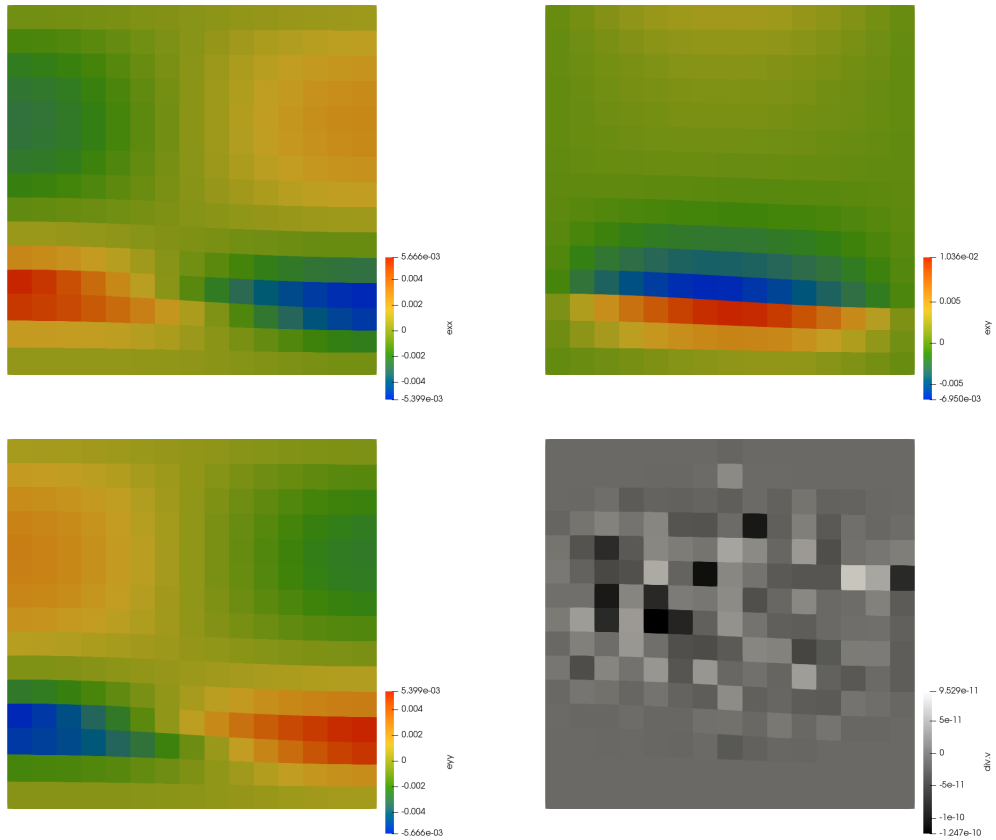
In the original benchmark the system is run over 2000 units of dimensionless time and the timing and position of various upwellings/downwellings is monitored. In this present experiment only the root mean square velocity is measured at $t = 0$: the code is indeed not yet foreseen of any algorithm capable of tracking deformation.

Another approach than the ones presented in the extensive literature which showcases results of this benchmark is taken. The mesh is initially fitted to the fluids interface and the resolution is progressively increased. This results in the following figure:



The green line indicates results obtained with my code ELEFANT with grids up to 2000x2000 with the exact same methodology.





features

- $Q_1 \times P_0$ element
- incompressible flow
- mixed formulation
- isothermal
- numerical benchmark

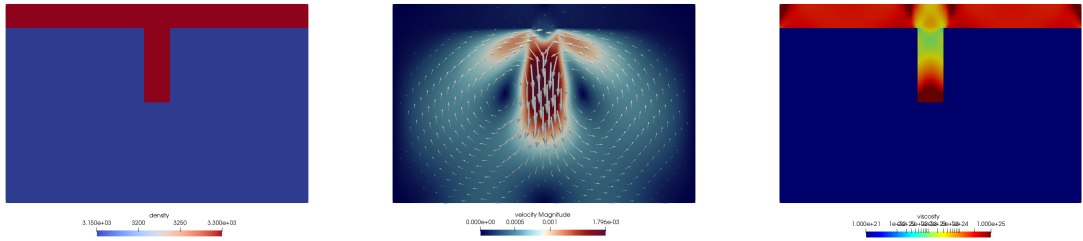
Stone 26: Slab detachment benchmark (1) - instantaneous

As in [1432], the computational domain is $1000\text{km} \times 660\text{km}$. No-slip boundary conditions are imposed on the sides of the system while free-slip boundary conditions are imposed at the top and bottom. Two materials are present in the domain: the lithosphere (mat.1) and the mantle (mat.2). The overriding plate (mat.1) is 80km thick and is placed at the top of the domain. An already subducted slab (mat.1) of 250km length hangs vertically under this plate. The mantle occupies the rest of the domain.

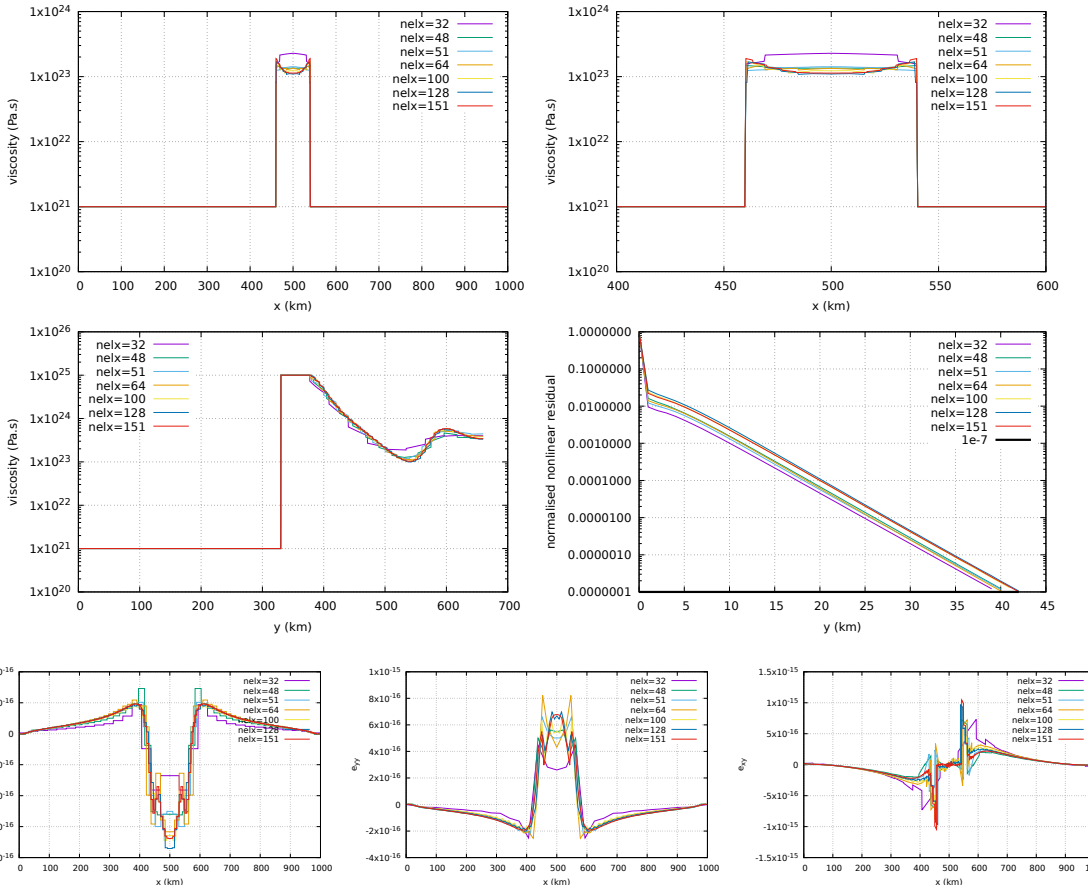
The mantle has a constant viscosity $\eta_0 = 10^{21}\text{Pa.s}$ and a density $\rho = 3150\text{kg/m}^3$. The slab has a density $\rho = 3300\text{kg/m}^3$ and is characterised by a power-law flow law so that its effective viscosity depends on the second invariant of the strainrate I_2 as follows:

$$\eta_{eff} = \frac{1}{2}A^{-1/n_s}I_2^{1/n_s-1} = \frac{1}{2}[(2 \times 4.75 \times 10^{11})^{-n_s}]^{-1/n_s}I_2^{1/n_s-1} = 4.75 \times 10^{11}I_2^{1/n_s-1} = \eta_0 I_2^{1/n_s-1} \quad (691)$$

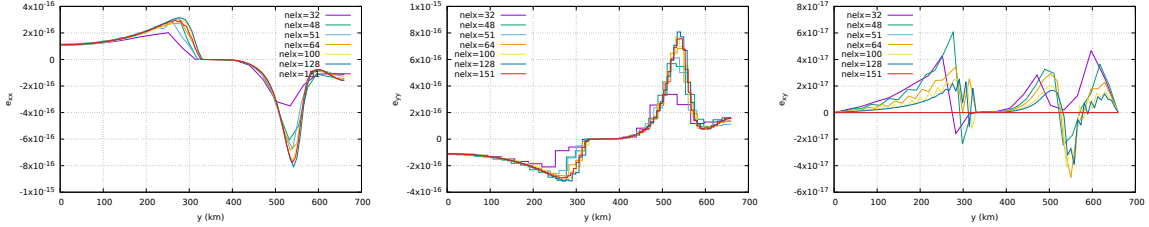
with $n_s = 4$ and $A = (2 \times 4.75 \times 10^{11})^{-n_s}$, or $\eta_0 = 4.75 \times 10^{11}$.



Fields at convergence for 151x99 grid.



Along the horizontal line



Along the vertical line

features

- $Q_1 \times P_0$ element
- incompressible flow
- mixed formulation
- isothermal
- nonlinear rheology
- nonlinear residual

Todo: nonlinear mantle, pressure normalisation

Also check Bellas et al, 2018 [111].

Stone 27: Consistent Boundary Flux

In what follows we will be re-doing the numerical experiments presented in Zhong et al. [1758].

The first benchmark showcases a unit square domain with free slip boundary conditions prescribed on all sides. The resolution is fixed to $64 \times 64 Q_1 \times P_0$ elements. The flow is isoviscous and the buoyancy force \mathbf{f} is given by

$$\begin{aligned} f_x &= 0 \\ f_y &= \rho_0 \alpha T(x, y) \end{aligned}$$

with the temperature field given by

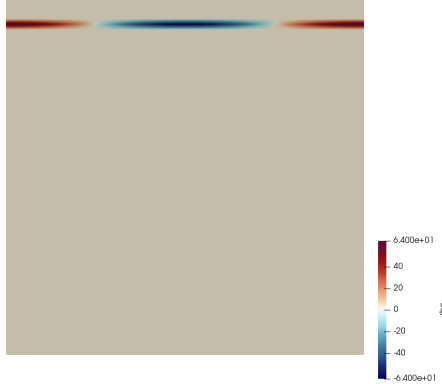
$$T(x, y) = \cos(kx)\delta(y - y_0)$$

where $k = 2\pi/\lambda$ and λ is a wavelength, and y_0 represents the location of the buoyancy strip. We set $g_y = -1$ and prescribe $\rho(x, y) = \rho_0 \alpha \cos(kx)\delta(y - y_0)$ on the nodes of the mesh.

One can prove ([1758] and refs. therein) that there is an analytic solution for the surface stress σ_{zz} ⁶⁰

$$\frac{\sigma_{yy}}{\rho \alpha g h} = \frac{\cos(kx)}{\sinh^2(k)} [k(1 - y_0) \sinh(k) \cosh(ky_0) - k \sinh(k(1 - y_0)) + \sinh(k) \sinh(ky_0)]$$

We choose $\rho_0 \alpha = 64$, $\eta = 1$ (note that in this case the normalising coefficient of the stress is exactly 1 (since $h = L_x/nelx = 1/64$) so it is not implemented in the code). $\lambda = 1$ is set to 1 and we explore $y_0 = \frac{63}{64}, \frac{62}{64}, \frac{59}{64}$ and $y_0 = 32/64$. Under these assumptions the density field for $y_0 = 59/64$ is:

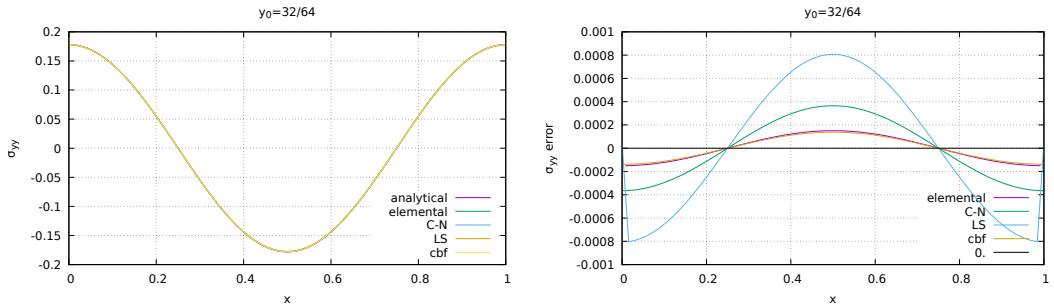


We can recover the stress at the boundary by computing the yy component of the stress tensor in the top row of elements:

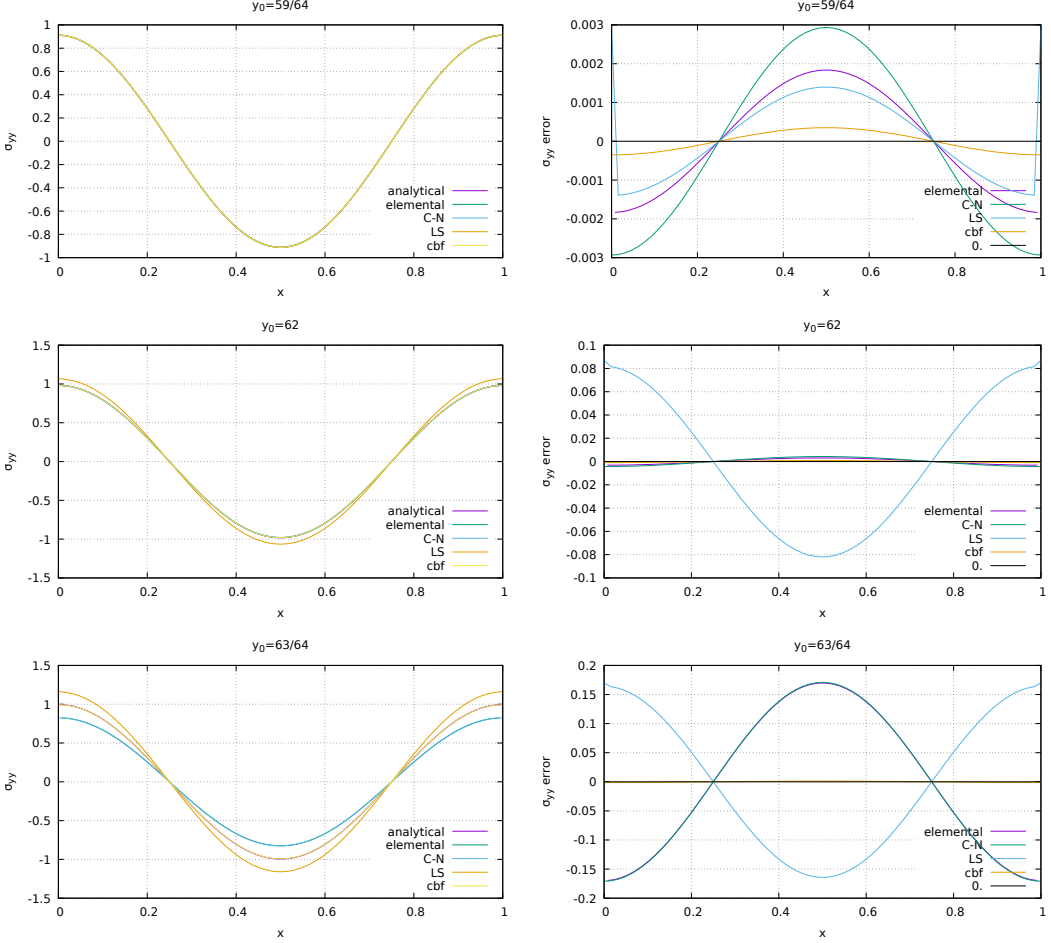
$$\sigma_{yy} = -p + 2\eta\dot{\epsilon}_{yy}$$

Note that pressure is by definition elemental, and that strain rate components are then also computed in the middle of each element.

These elemental quantities can be projected onto the nodes (see section ??) by means of the C→N algorithm or a least square algorithm (LS).



⁶⁰Note that in the paper the authors use $\rho \alpha g$ which does not have the dimensions of a stress



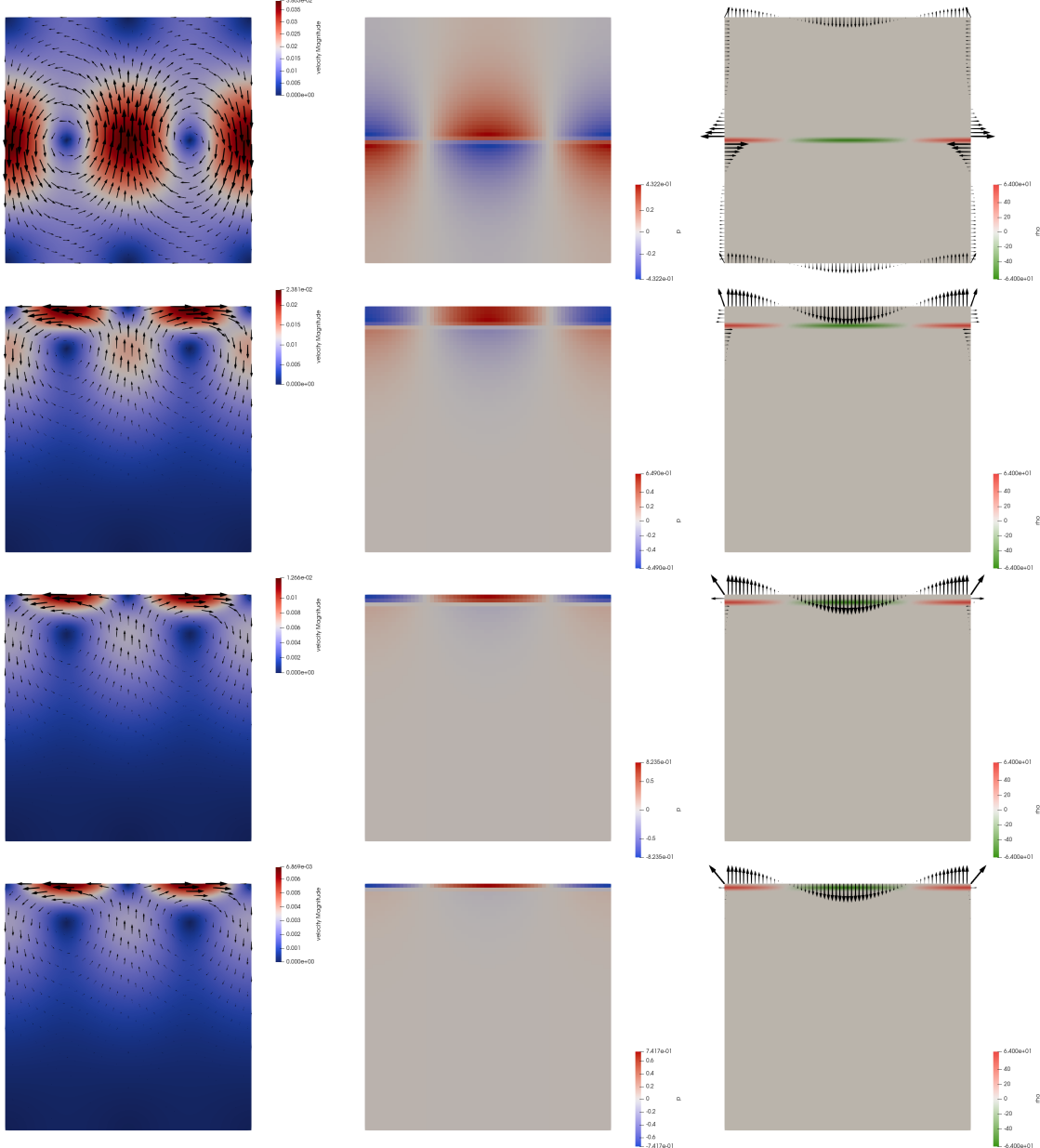
The consistent boundary flux (CBF) method allows us to compute traction vectors $\mathbf{t} = \boldsymbol{\sigma} \cdot \mathbf{n}$ on the boundary of the domain. On the top boundary, $\mathbf{n} = (0, 1)$ so that $\mathbf{t} = (\sigma_{xy}, \sigma_{yy})^T$ and t_y is the quantity we need to consider and compare to other results.

In the following table are shown the results presented in [1758] alongside the results obtained with Fieldstone:

Method	$y_0 = 63/64$	$y_0 = 62/64$	$y_0 = 59/64$ ⁶¹	$y_0 = 32/64$
Analytic solution	0.995476	0.983053	0.912506	0.178136
Pressure smoothing [1758]	1.15974	1.06498	0.911109	n.a.
CBF [1758]	0.994236	0.982116	0.912157	n.a.
fieldstone: elemental	0.824554 (-17.17 %)	0.978744 (-0.44%)	0.909574 (-0.32 %)	0.177771 (-0.20 %)
fieldstone: nodal (C→N)	0.824554 (-17.17 %)	0.978744 (-0.44%)	0.909574 (-0.32 %)	0.177771 (-0.20 %)
fieldstone: LS	1.165321 (17.06 %)	1.070105 (8.86%)	0.915496 (0.33 %)	0.178182 (0.03 %)
fieldstone: CBF	0.994236 (-0.13 %)	0.982116 (-0.10%)	0.912157 (-0.04 %)	0.177998 (-0.08 %)

We see that we recover the published results with the same exact accuracy, thereby validating our implementation. Also rather fascinating is the fact that the original paper carries out the whole study without showing any image of the 2D domain ever.

On the following figures are shown the velocity, pressure and traction fields for two cases $y_0 = 32/64$ and $y_0 = 63/64$.



Here lies the superiority of our approach over the one presented in the original article: our code computes all traction vectors on all boundaries at once.

explain how Medge is arrived at!

compare with ASPECT ???

pressure average on surface instead of volume ?

Remark. The original article on the CBF [1758] uses a penalty-based formulation (see Section 6.3) so that they do not have to worry about pressure normalisation. However, since constant pressure fields lie in the nullspace of \mathbb{G} the pressure normalisation constant does not play a role.

As shown in Appendix I, the Q_1 mass matrix for the reference cell/element is given by:

$$\mathbf{M}^e = \frac{1}{3} \begin{pmatrix} 2 & 1 \\ 1 & 2 \end{pmatrix}$$

This matrix needs to be multiplied by $h/2$ for an element of size h . Following the methodology presented in [1758], one can also use the Gauss-Lobatto quadrature method to arrive at the mass matrix, and in

this case the simple trapezoidal integration rule variant thereof (see Section 4.1.1). We then have:

$$\mathbf{M}_e = \int_{\Omega_e} \vec{N}^T \vec{N} dV = \int_{-1}^{+1} \vec{N}^T \vec{N} dr \quad (692)$$

on the reference element, with

$$\vec{N}^T = \begin{pmatrix} N_1(r) \\ N_2(r) \end{pmatrix} = \frac{1}{2} \begin{pmatrix} 1-r \\ 1+r \end{pmatrix}$$

We know compute the following integrals with the trapezoidal rule:

$$\int_{-1}^{+1} N_1(r) N_1(r) dr = (1 - -1) \frac{N_1(-1) N_1(-1) + N_1(+1) N_1(+1)}{2} = 1 \quad (693)$$

$$\int_{-1}^{+1} N_1(r) N_2(r) dr = (1 - -1) \frac{N_1(-1) N_2(-1) + N_1(+1) N_2(+1)}{2} = 0 \quad (694)$$

$$\int_{-1}^{+1} N_2(r) N_2(r) dr = (1 - -1) \frac{N_2(-1) N_2(-1) + N_2(+1) N_2(+1)}{2} = 1 \quad (695)$$

and finally

$$\mathbf{M}^e = \begin{pmatrix} 1 & 0 \\ 0 & 1 \end{pmatrix}$$

The resulting matrix is diagonal and it is simply the lumped version of the exact mass matrix.

features

- $Q_1 \times P_0$ element
- incompressible flow
- mixed formulation
- isothermal
- isoviscous
- analytical solution
- pressure smoothing
- consistent boundary flux

Stone 28: convection 2D box - Tosi et al, 2015

This fieldstone was developed in collaboration with Rens Elbertsen.

The viscosity field μ is calculated as the harmonic average between a linear part μ_{lin} that depends on temperature only or on temperature and depth d , and a non-linear, plastic part μ_{plast} dependent on the strain rate:

$$\mu(T, z, \dot{\epsilon}) = 2 \left(\frac{1}{\mu_{lin}(T, z)} + \frac{1}{\mu_{plast}(\dot{\epsilon})} \right)^{-1}. \quad (696)$$

The linear part is given by the linearized Arrhenius law (the so-called Frank-Kamenetskii approximation [584]):

$$\mu_{lin}(T, z) = \exp(-\gamma_T T + \gamma_z z), \quad (697)$$

where $\gamma_T = \ln(\Delta\mu_T)$ and $\gamma_z = \ln(\Delta\mu_z)$ are parameters controlling the total viscosity contrast due to temperature ($\Delta\mu_T$) and pressure ($\Delta\mu_z$). The non-linear part is given by [1567, 1566]:

$$\mu_{plast}(\dot{\epsilon}) = \mu^* + \frac{\sigma_Y}{\sqrt{\dot{\epsilon} : \dot{\epsilon}}}, \quad (698)$$

where μ^* is a constant representing the effective viscosity at high stresses [1481] and σ_Y is the yield stress, also assumed to be constant. In 2-D, the denominator in the second term of equation (698) is given explicitly by

$$\sqrt{\dot{\epsilon} : \dot{\epsilon}} = \sqrt{\dot{\epsilon}_{ij}\dot{\epsilon}_{ij}} = \sqrt{\left(\frac{\partial u_x}{\partial x}\right)^2 + \frac{1}{2} \left(\frac{\partial u_x}{\partial y} + \frac{\partial u_y}{\partial x}\right)^2 + \left(\frac{\partial u_y}{\partial y}\right)^2}. \quad (699)$$

The viscoplastic flow law (equation 696) leads to linear viscous deformation at low stresses (equation (697)) and to plastic deformation for stresses that exceed σ_Y (equation (698)), with the decrease in viscosity limited by the choice of μ^* [1481].

In all cases that we present, the domain is a two-dimensional square box. The mechanical boundary conditions are for all boundaries free-slip with no flux across, i.e. $\tau_{xy} = \tau_{yx} = 0$ and $\mathbf{u} \cdot \mathbf{n} = 0$, where \mathbf{n} denotes the outward normal to the boundary. Concerning the energy equation, the bottom and top boundaries are isothermal, with the temperature T set to 1 and 0, respectively, while side-walls are assumed to be insulating, i.e. $\partial T / \partial x = 0$. The initial distribution of the temperature field is prescribed as follows:

$$T(x, y) = (1 - y) + A \cos(\pi x) \sin(\pi y), \quad (700)$$

where $A = 0.01$ is the amplitude of the initial perturbation.

In the following Table ??, we list the benchmark cases according to the parameters used.

Case	Ra	$\Delta\mu_T$	$\Delta\mu_y$	μ^*	σ_Y	Convective regime
1	10^2	10^5	1	—	—	Stagnant lid
2	10^2	10^5	1	10^{-3}	1	Mobile lid
3	10^2	10^5	10	—	—	Stagnant lid
4	10^2	10^5	10	10^{-3}	1	Mobile lid
5a	10^2	10^5	10	10^{-3}	4	Periodic
5b	10^2	10^5	10	10^{-3}	3 – 5	Mobile lid – Periodic – Stagnant lid

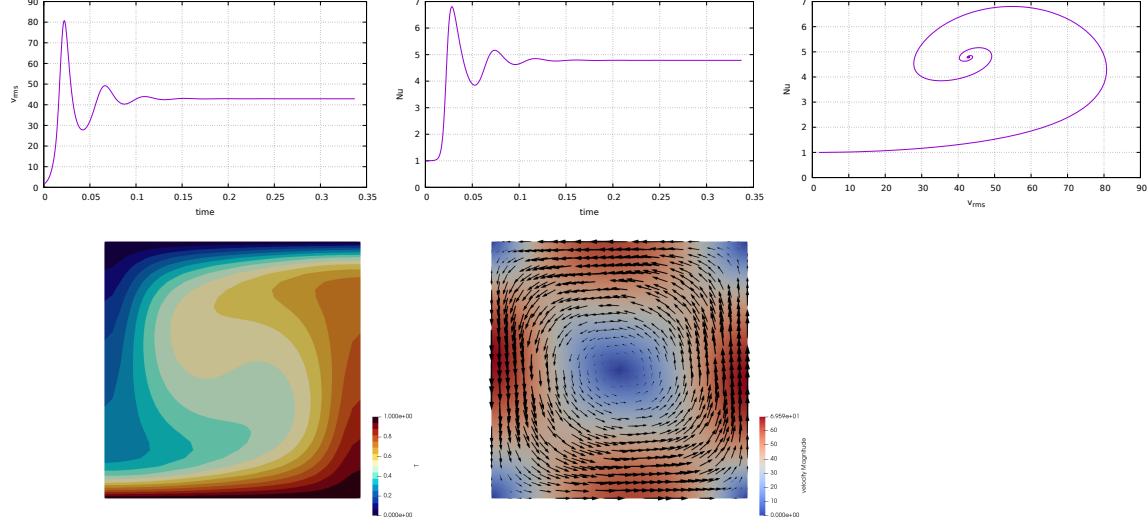
Benchmark cases and corresponding parameters.

In Cases 1 and 3 the viscosity is directly calculated from equation (697), while for Cases 2, 4, 5a, and 5b, we used equation (696). For a given mesh resolution, Case 5b requires running simulations with yield stress varying between 3 and 5

In all tests, the reference Rayleigh number is set at the surface ($y = 1$) to 10^2 , and the viscosity contrast due to temperature $\Delta\mu_T$ is 10^5 , implying therefore a maximum effective Rayleigh number of 10^7 for $T = 1$. Cases 3, 4, 5a, and 5b employ in addition a depth-dependent rheology with viscosity contrast $\Delta\mu_z = 10$. Cases 1 and 3 assume a linear viscous rheology that leads to a stagnant lid regime.

Cases 2 and 4 assume a viscoplastic rheology that leads instead to a mobile lid regime. Case 5a also assumes a viscoplastic rheology but a higher yield stress, which ultimately causes the emergence of a strictly periodic regime. The setup of Case 5b is identical to that of Case 5a but the test consists in running several simulations using different yield stresses. Specifically, we varied σ_Y between 3 and 5 in increments of 0.1 in order to identify the values of the yield stress corresponding to the transition from mobile to periodic and from periodic to stagnant lid regime.

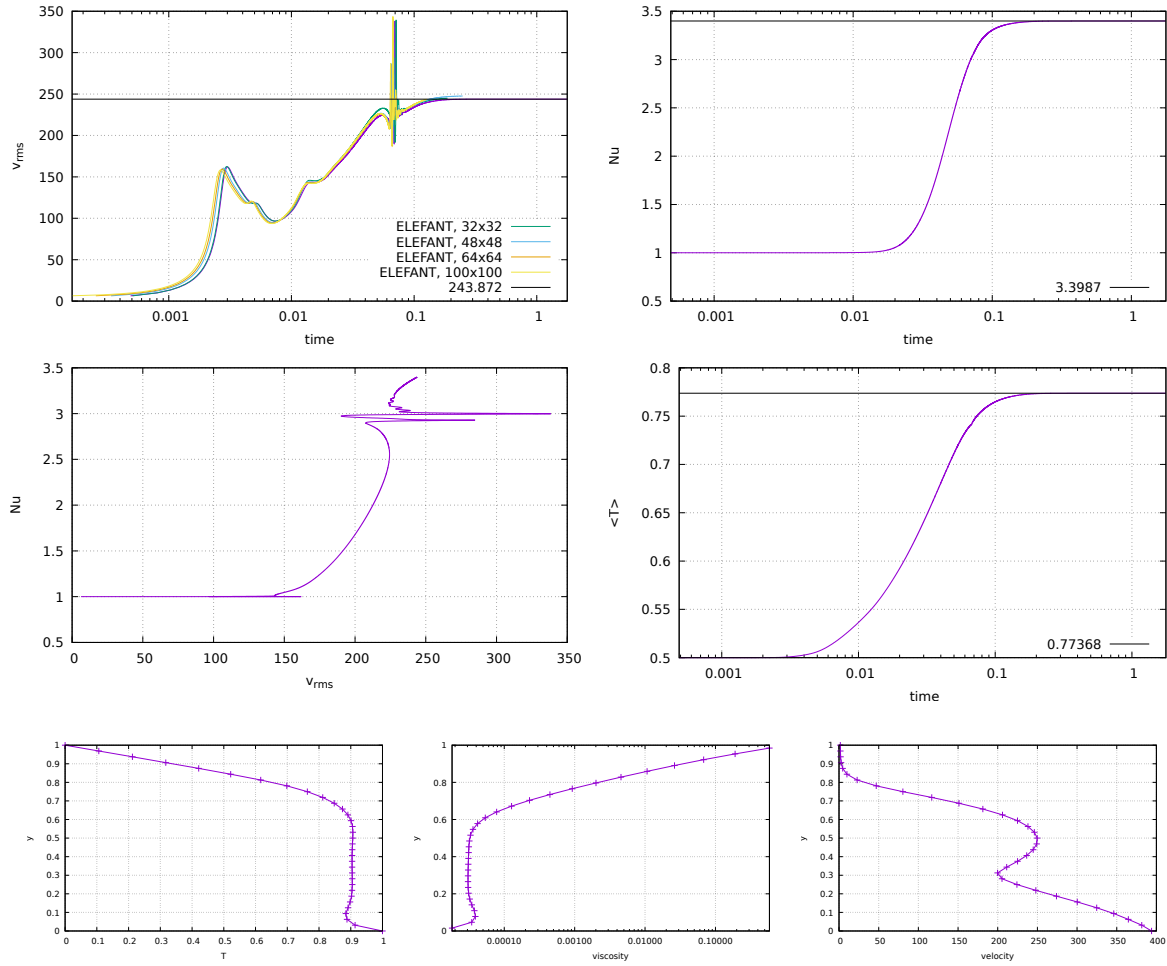
Case 0: Newtonian case, a la Blankenbach et al., 1989

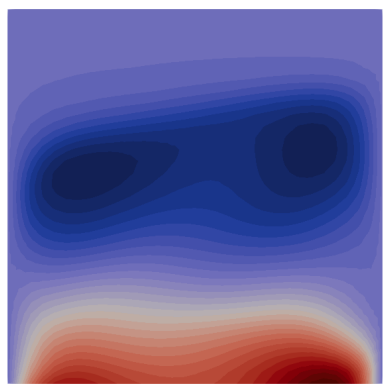


Case 1

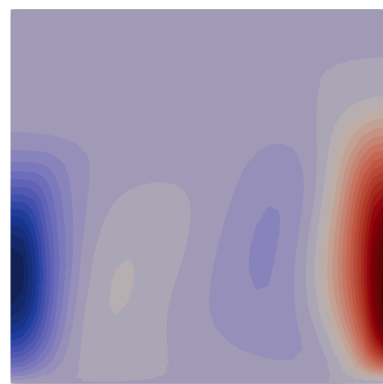
In this case $\mu^* = 0$ and $\sigma_Y = 0$ so that μ_{plast} can be discarded. The CFL number is set to 0.5 and the viscosity is given by $\mu(T, z, \dot{\epsilon}) = \mu_{lin}(T, z)$. And since $\Delta\mu_z = 1$ then $\gamma_z = 0$ so that $\mu_{lin}(T, z) = \exp(-\gamma_T T)$

Code	YACC	Plaatjes	CHIC	GAIA	StreamV	StagYY	FEniCS	Fluidity	ELEFANT	ASPECT	MC3D
Resolution	100 × 100	128×128r	80 × 80	100r×100r	80 × 80	128×128r	80 × 80	128 × 128	100 × 100	64 × 64	100 × 100
<i>Case 1</i>											
$\langle T \rangle$	0.7767	0.7759	0.7758	0.7759	0.776	0.776	0.7759	0.7758	0.7758	0.7768	0.779
Nu_{top}	3.4298	3.4159	3.4260	3.4213	3.4091	3.419	3.5889	3.4253	3.4214	3.4305	3.3129
Nu_{bot}	3.3143	3.4159	3.4259	3.4213	3.4091	3.419	3.4231	3.3795	3.313	3.4142	3.3139
u_{rms}	251.7997	249.54	249.2985	250.0738	252.0906	249.541	249.5730	248.9252	249.134	251.3069	296.6156
u_{surf}^{rms}	1.8298	1.878	1.8999	1.8836	1.8823	1.8723	1.8698	1.8474	1.8642	1.8695	1.1114
u_{surf}^{max}	2.5516	2.618	2.6477	2.6254	2.64	2.6104	2.6066	2.5761	2.6119	2.6064	1.5329
$\langle W \rangle$	2.4583	2.369	2.431	2.4121	2.4071	2.4189	2.4246	2.4148	2.4316	2.4282	2.5548
$\langle \Phi \rangle / Ra$	2.4333	2.4119	2.4189	2.4165	2.392	2.4182	2.4246	2.4148	2.4276	2.4281	2.31916
δ	1.02%	1.78%	0.50%	0.18%	0.63%	0.03%	< 0.01%	< 0.01%	0.16%	< 0.01%	9.22%

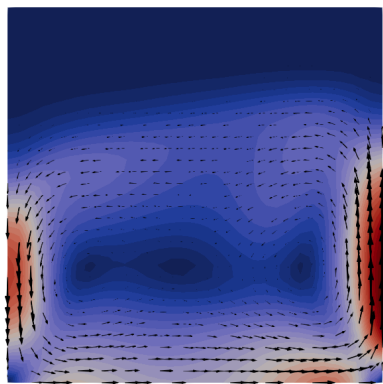




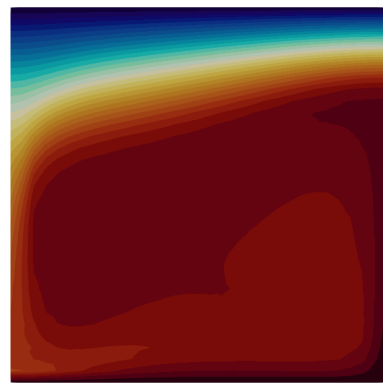
velocity X
-239.722 0 200 400 585.557



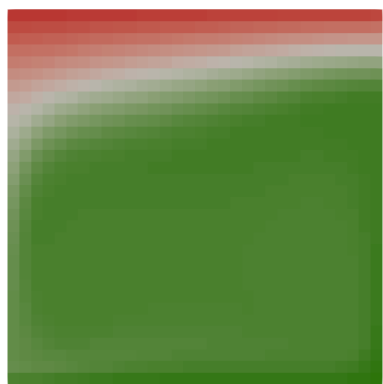
velocity Y
-685.512 0 500 887.230



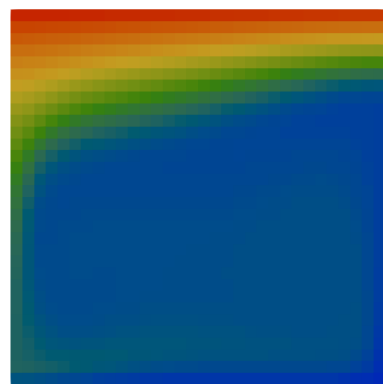
velocity Magnitude
0.000 200 400 600 887.230



T
0.000 0.2 0.4 0.6 0.8 1.000



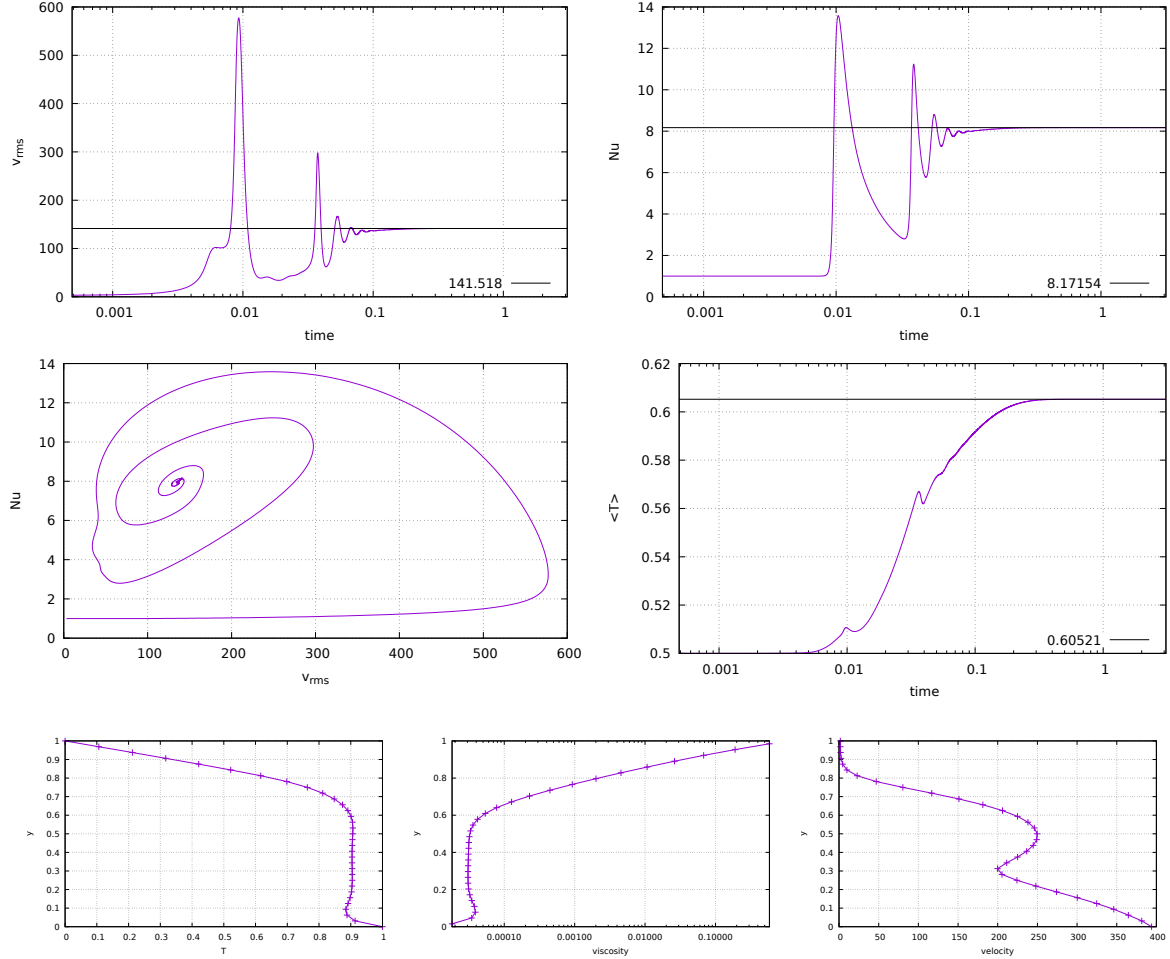
density
-9.900e-05 -6e-5 -4e-5 -3.000e-06

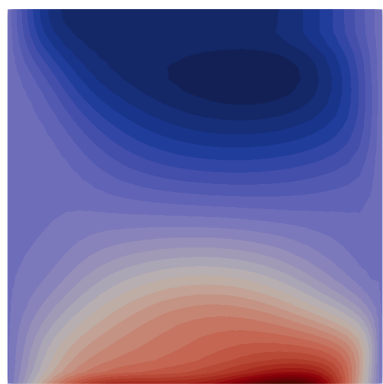


viscosity
1.e-05 f 0.0000000000000002 f 0.0000000000000001 f 7.e-01 f

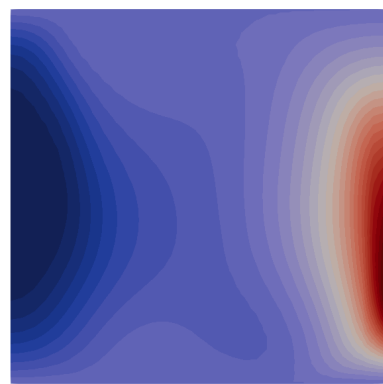
Case 2

$\langle T \rangle$	0.5289	0.5276	0.5276	0.5289	0.5283	0.527304	0.527521	0.5274	0.5277	0.5278	0.5364
Nu_{top}	6.5572	6.6156	6.6074	6.5913	6.6356	6.61082	6.68224	6.6401	6.5912	6.6249	7.4376
Nu_{bot}	6.5243	6.6158	6.6073	6.5913	6.6356	6.61082	6.66899	6.6326	6.5834	6.6267	7.4376
U_{RMS}	79.6202	79.1358	79.0181	78.6652	79.4334	78.9903	79.0684	79.0318	79.1105	79.1996	98.8912
U_{RMS}^{surf}	75.4814	75.1727	75.0434	74.1719	74.8587	75.0606	75.0975	75.0827	74.7596	75.1903	93.5057
U_{max}^{surf}	89.2940	88.9715	88.8130	87.6118	89.1444	88.823	88.8753	88.85	88.9146	88.9848	123.046
η_{min}	1.9174×10^{-4}	1.9220×10^{-4}	1.9448×10^{-4}	1.9204×10^{-4}	1.9900×10^{-4}	1.9574×10^{-4}	1.9167×10^{-4}	1.9200×10^{-4}	1.9860×10^{-4}	1.9178×10^{-4}	1.93×10^{-4}
η_{max}	1.6773	1.9834	1.6508	1.9670	1.1800	1.6665	1.7446	1.8891	1.5200	1.8831	5.67×10^{-3}
$\langle W \rangle$	5.6512	5.6251	5.6076	5.5903	5.629	5.61012	5.61425	5.6136	5.6216	5.6235	6.751
$\langle \Phi \rangle / Ra$	5.6463	5.6174	5.6024	5.5434	5.6325	5.60152	5.61425	5.6136	5.6182	5.6235	7.786
δ	0.09%	0.14%	0.09%	0.84%	0.06%	0.15%	<0.01%	<0.01%	0.06%	<0.01%	13.29%

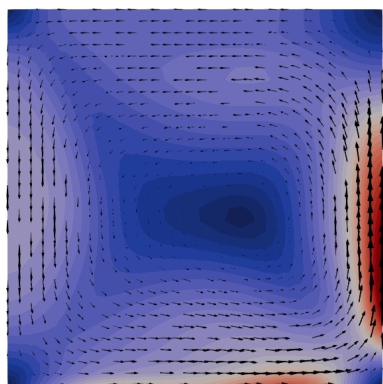




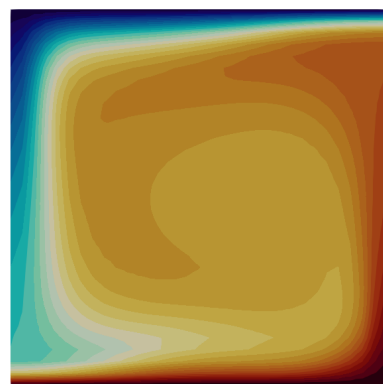
velocity X
-1.437e+02 0 100 200 3.247e+02



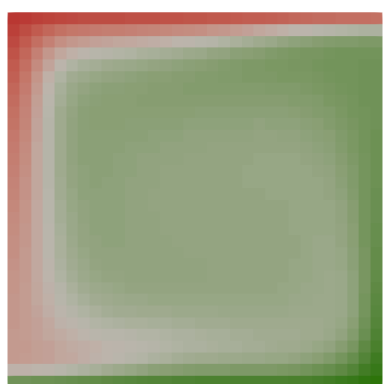
velocity Y
-1.764e+02 0 200 4.549e+02



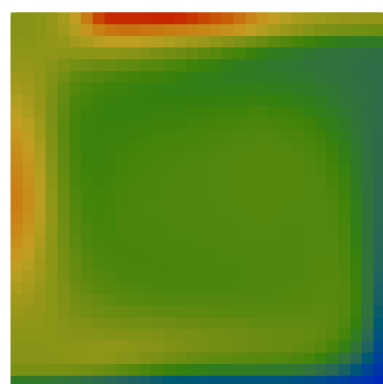
velocity Magnitude
0.000e+00 100 200 300 4.549e+02



T
0.000 0.2 0.4 0.6 0.8 1.000



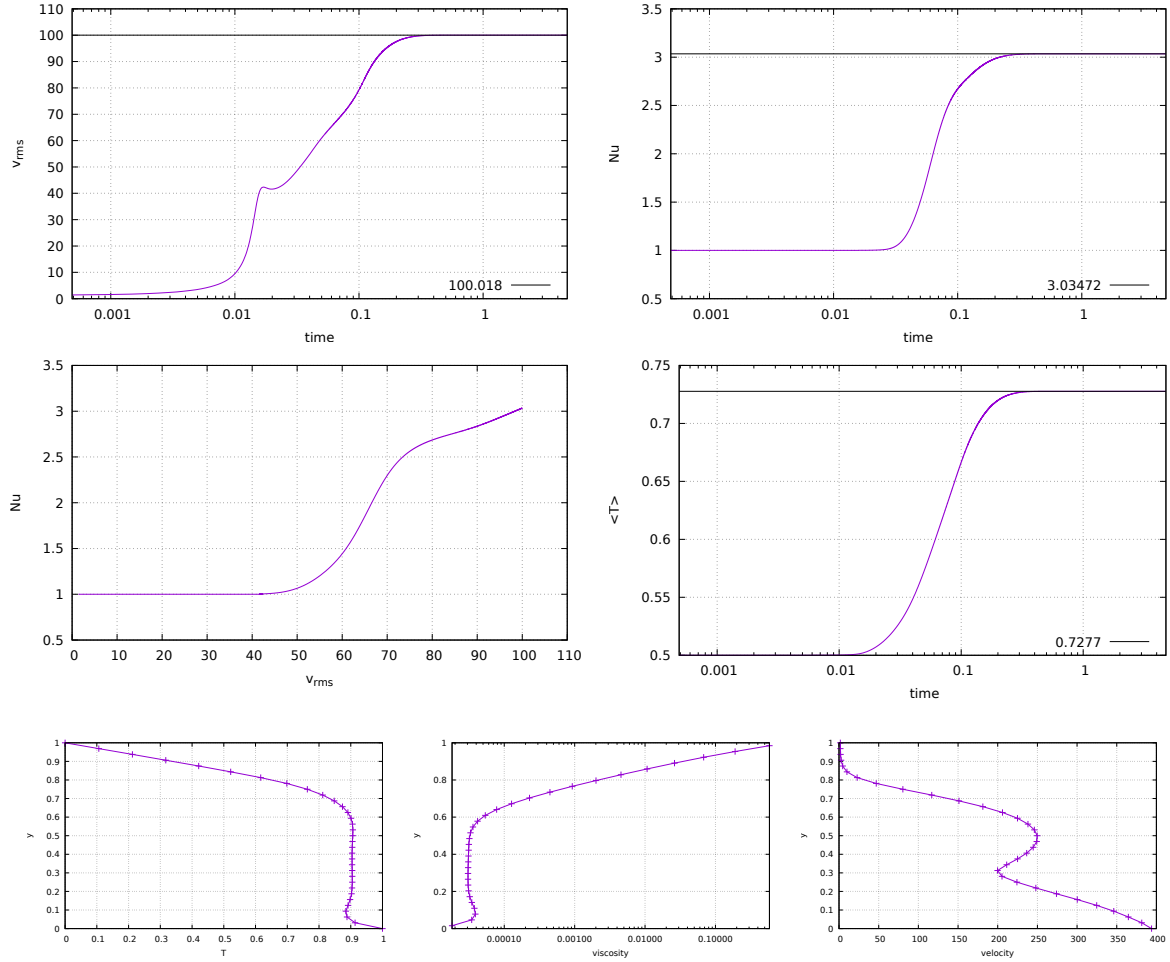
density
-9.900e-05 -6e-5 -4e-5 -2.000e-06

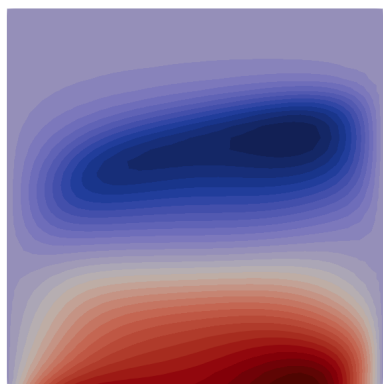


viscosity
2.300e-05 0.00002 0.00003 0.00004 0.00005 6.326e-01

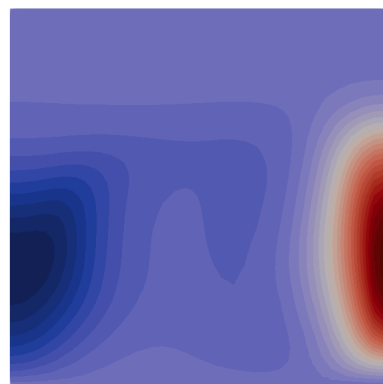
Case 3

$\langle T \rangle$	0.7286	0.7275	0.7271	0.7272	0.7241	0.7274	0.727464	0.7275	0.7275	0.7278	0.7305
Nu_{top}	3.0374	3.0298	3.0324	3.0314	3.0253	3.03025	3.0918	3.0399	3.0347	3.0371	2.9311
Nu_{bot}	2.9628	3.0298	3.0323	3.0314	3.0253	3.03025	3.03487	3.0376	2.9908	3.0410	2.9311
u_{RMS}	100.9467	100.024	99.8701	99.9917	100.197	100.018	100.127	100.0396	100.1208	100.3368	111.6121
u_{surf}^{surf}	2.0374	2.0785	2.0916	2.0835	2.0789	2.07299	2.07301	2.0569	2.0652	2.0727	1.356
u_{max}	2.8458	2.9029	2.9201	2.9094	2.9207	2.89495	2.89501	2.873	2.9019	2.8946	1.8806
η_{min}	4.7907×10^{-5}	4.8140×10^{-5}	4.8014×10^{-5}	4.8047×10^{-5}	4.8400×10^{-5}	4.7951×10^{-5}	4.8081×10^{-5}	4.8000×10^{-5}	4.8080×10^{-5}	4.7972×10^{-5}	10^{-4}
η_{max}	1	0.9987	0.9857	0.9988	0.9010	0.9637	0.9999	1	0.9023	1	1
$\langle W \rangle$	2.0400	2.0028	2.0340	2.0269	2.0235	2.03002	2.03482	2.0298	2.0384	2.0362	2.056
$\langle \Phi \rangle / Ra$	2.0335	2.0277	2.0304	2.0286	2.0164	2.0302	2.03482	2.0298	2.037	2.0362	1.865
δ	0.32%	1.23%	0.18%	0.08%	0.35%	0.01%	<0.01%	<0.01%	0.07%	<0.01%	9.29%

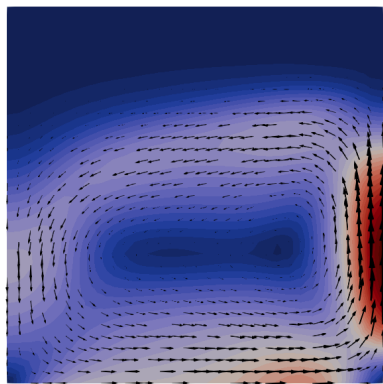




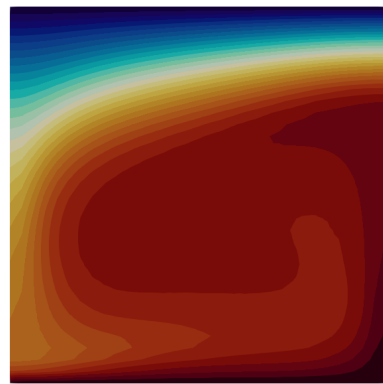
-133.934 0 100 204.210
velocity X



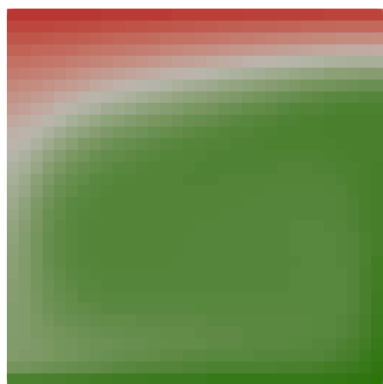
-137.969 0 100 200 330.512
velocity Y



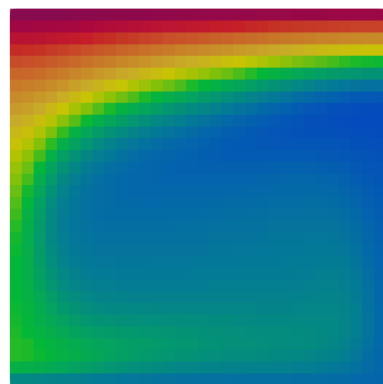
0.000 100 200 330.512
velocity Magnitude



0.000 0.2 0.4 0.6 0.8 1.000
T



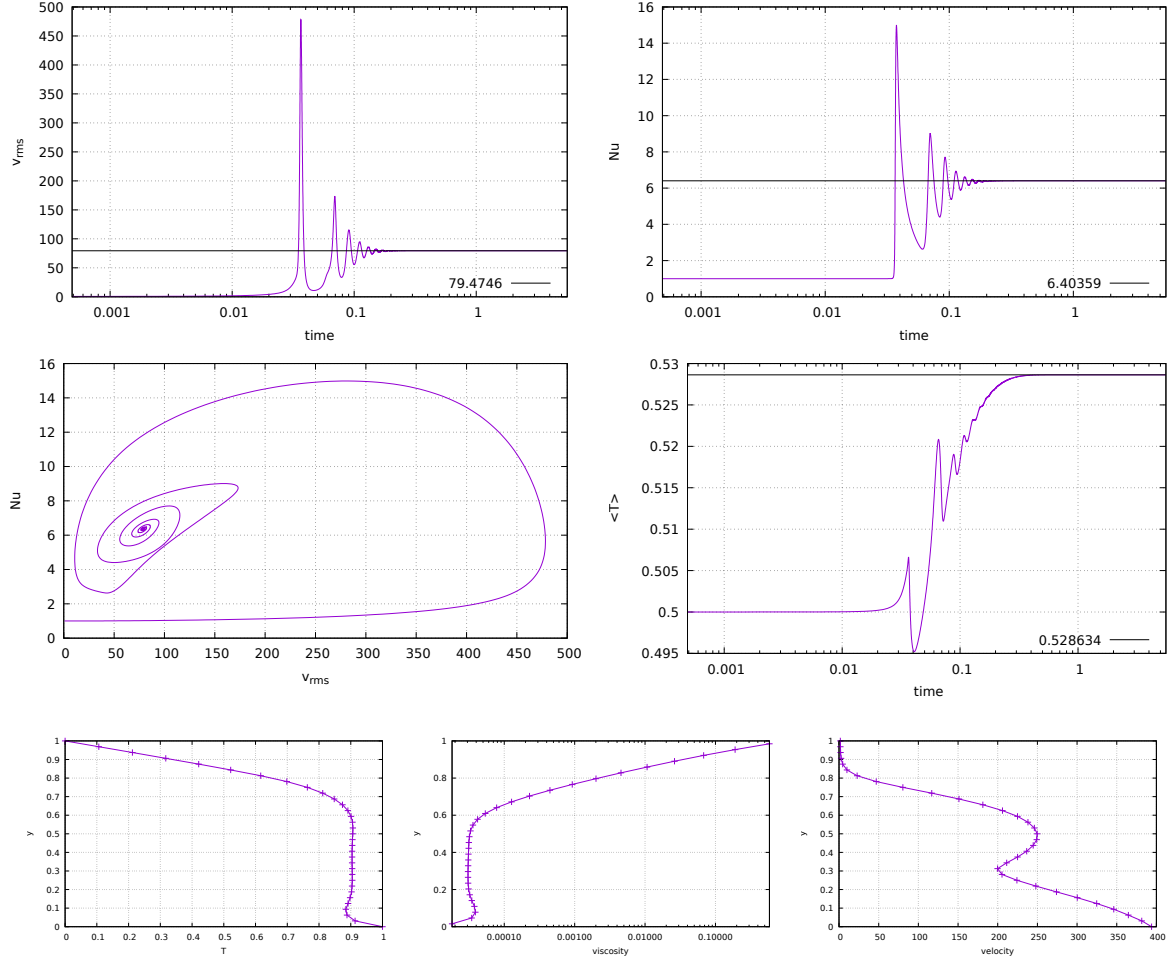
-1.000e-04 -6e-5 -4e-5 -3.000e-06
density

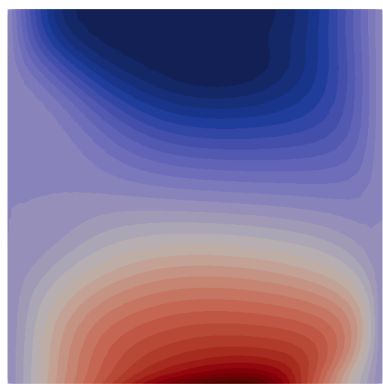


4.800e-05 0.000020000020.001 7.802e-01
viscosity

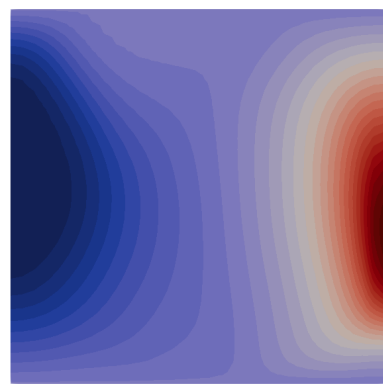
Case 4

$\langle T \rangle$	0.5289	0.5276	0.5276	0.5289	0.5283	0.527304	0.527521	0.5274	0.5277	0.5278	0.5364
Nu_{top}	6.5572	6.6156	6.6074	6.5913	6.6356	6.61082	6.68224	6.6401	6.5912	6.6249	7.4376
Nu_{bot}	6.5243	6.6158	6.6073	6.5913	6.6356	6.61082	6.66899	6.6326	6.5834	6.6267	7.4376
U_{RMS}	79.6202	79.1358	79.0181	78.6652	79.4334	78.9903	79.0684	79.0318	79.1105	79.1996	98.8912
U_{RMS}^{surf}	75.4814	75.1727	75.0434	74.1719	74.8587	75.0606	75.0975	75.0827	74.7596	75.1903	93.5057
U_{max}^{surf}	89.2940	88.9715	88.8130	87.6118	89.1444	88.823	88.8753	88.85	88.9146	88.9848	123.046
η_{min}	1.9174×10^{-4}	1.9220×10^{-4}	1.9448×10^{-4}	1.9204×10^{-4}	1.9900×10^{-4}	1.9574×10^{-4}	1.9167×10^{-4}	1.9200×10^{-4}	1.9860×10^{-4}	1.9178×10^{-4}	1.93×10^{-4}
η_{max}	1.6773	1.9834	1.6508	1.9670	1.1800	1.6665	1.7446	1.8891	1.5200	1.8831	5.67×10^{-3}
$\langle W \rangle$	5.6512	5.6251	5.6076	5.5903	5.629	5.61012	5.61425	5.6136	5.6216	5.6235	6.751
$\langle \Phi \rangle / Ra$	5.6463	5.6174	5.6024	5.5434	5.6325	5.60152	5.61425	5.6136	5.6182	5.6235	7.786
δ	0.09%	0.14%	0.09%	0.84%	0.06%	0.15%	<0.01%	<0.01%	0.06%	<0.01%	13.29%

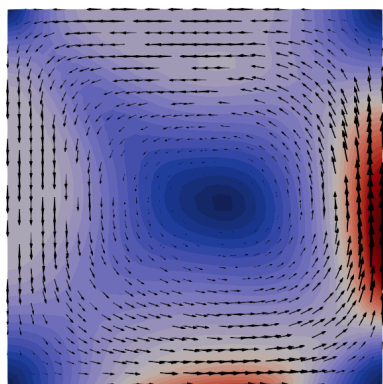




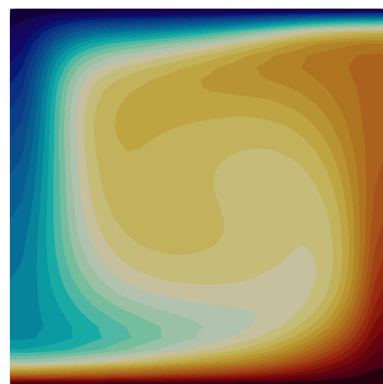
velocity X
-92.305 -50 0 50 100 153.873



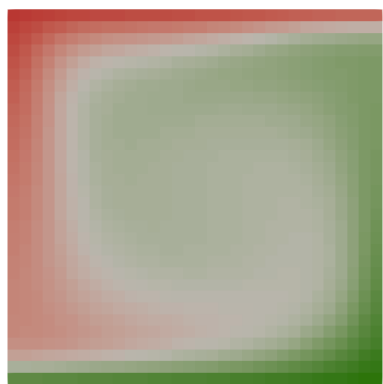
velocity Y
-97.677 0 100 209.053



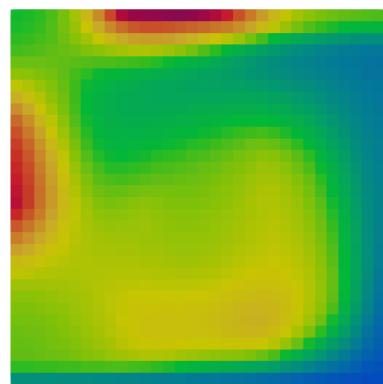
velocity Magnitude
0.000 50 100 150 209.053



T
0.000 0.2 0.4 0.6 0.8 1.000

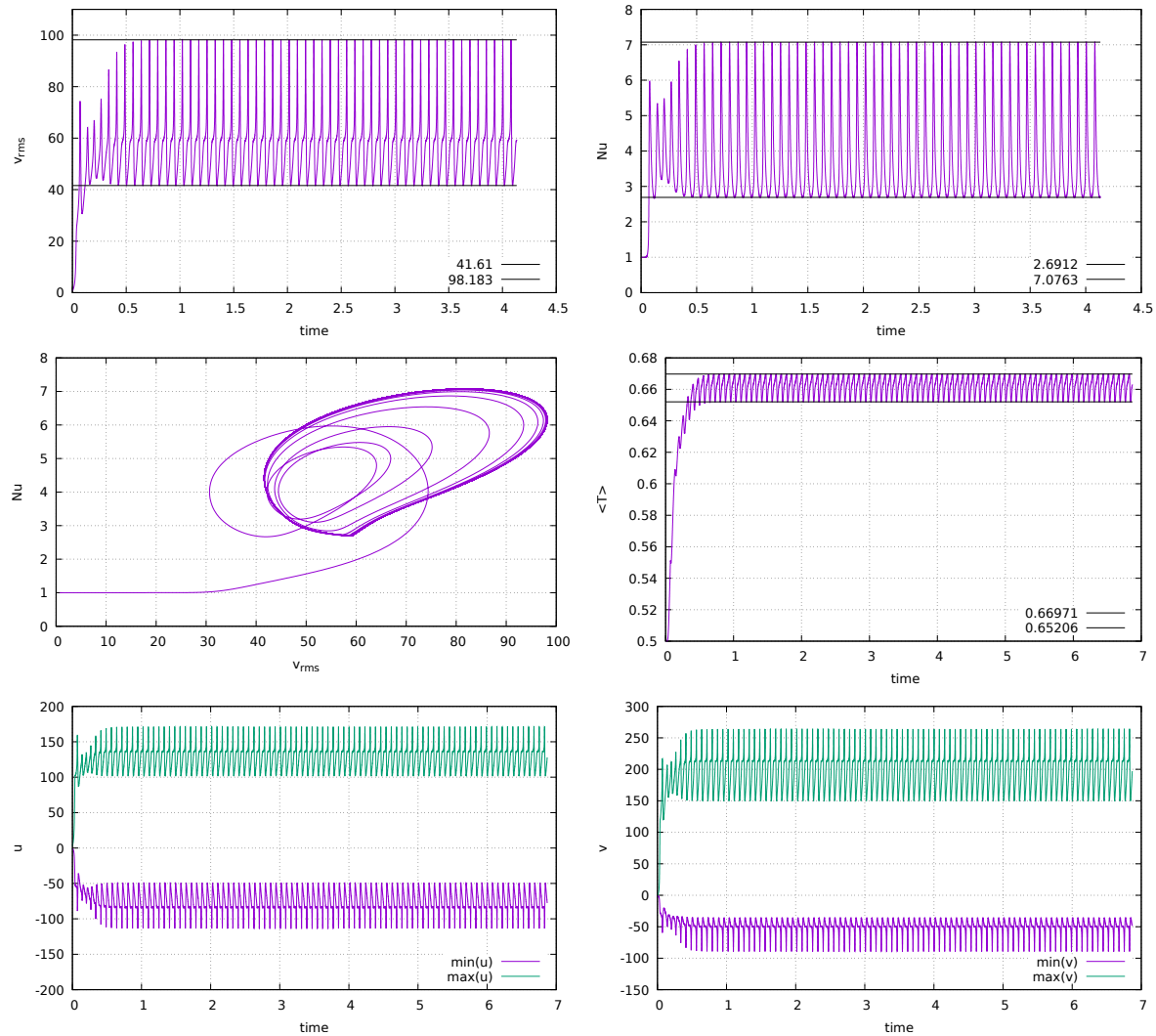


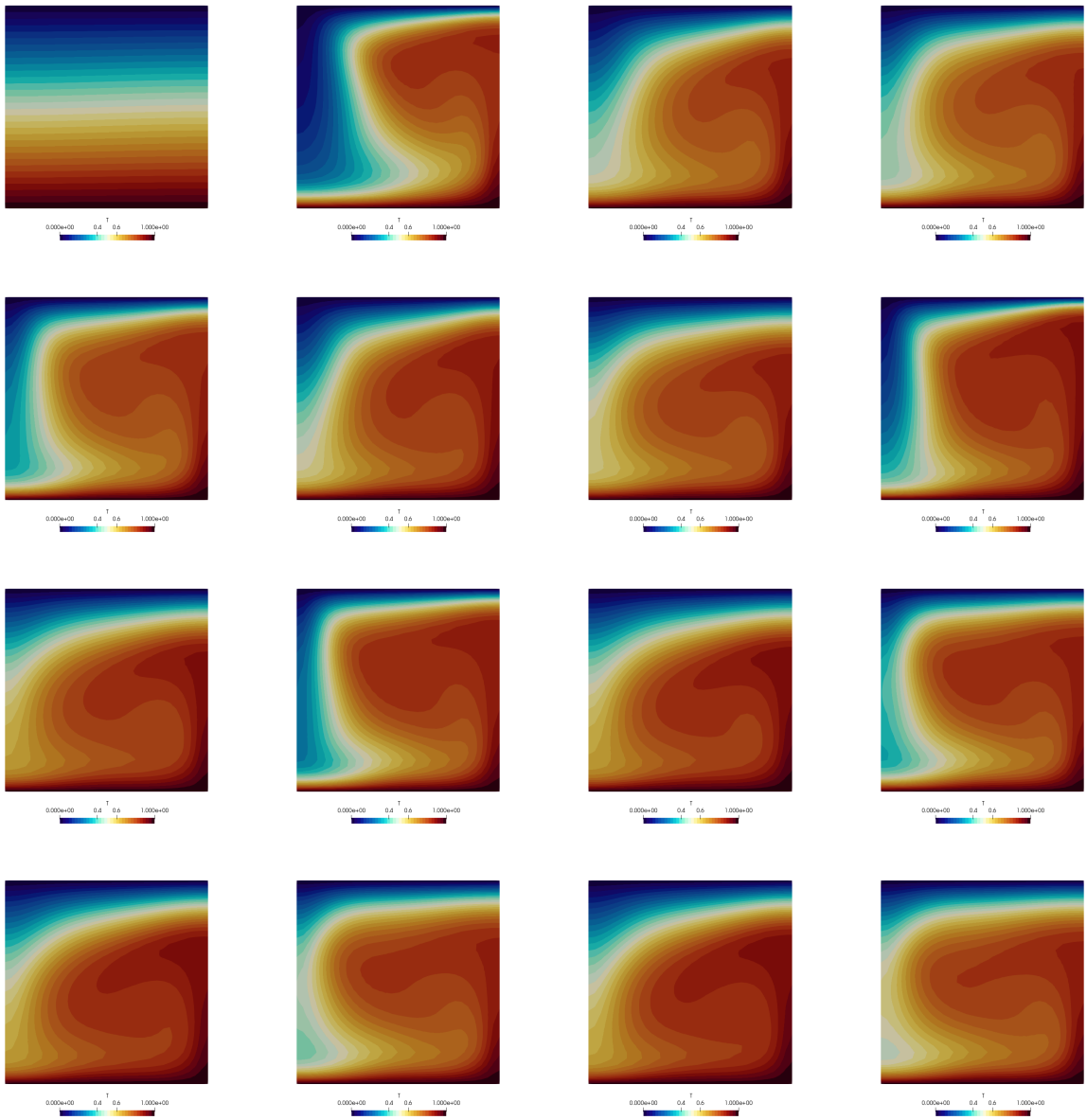
density
-9.900e-05 -5e-05 -4e-05 -1.000e-06



viscosity
0.00021 0.00203 0.00205 0.1 0.75499

Case 5

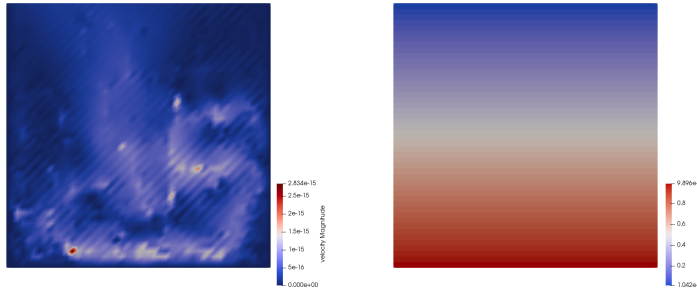




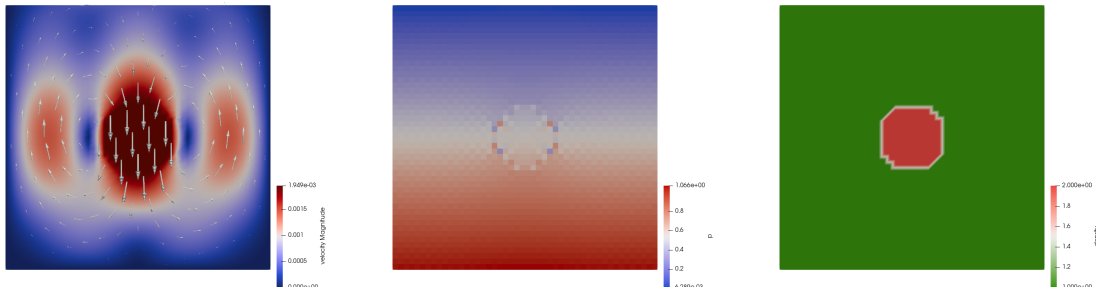
Stone 29: open boundary conditions

In what follows we will investigate the use of the so-called open boundary conditions in the very simple context of a 2D Stokes sphere experiment.

We start with a domain without the sphere. Essentially, it is what people would call an aquarium. Free slip boundary conditions are prescribed on the sides and no-slip conditions at the bottom. The top surface is left free. The fluid has a density $\rho_0 = 1$ and a viscosity $\eta_0 = 1$. In the absence of any density difference in the domain there is no active buoyancy force so that we expect a zero velocity field and a lithostatic pressure field. This is indeed what we recover:



If we now implement a sphere parametrised by its density $\rho_s = \rho_0 + 1$, its viscosity $\eta_s = 10^3$ and its radius $R_s = 0.123$ in the middle of the domain, we see clear velocity field which logically shows the sphere falling downward and a symmetric return flow of the fluid on each side:

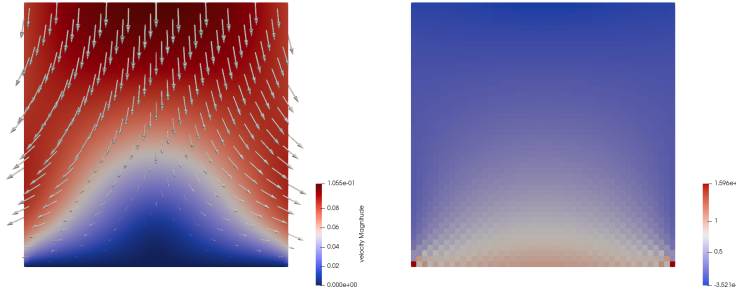


Unfortunately it has been widely documented that the presence of free-slip boundary conditions affects the evolution of subduction [333], even when these are placed rather far from the subduction zone. A proposed solution to this problem is the use of 'open boundary conditions' which are in fact stress boundary conditions. The main idea is to prescribe a stress on the lateral boundaries (instead of free slip) so that it balances out exactly the existing lithostatic pressure inside the domain along the side walls. Only pressure deviations with respect to the lithostatic are responsible for flow and such boundary conditions allow flow across the boundaries.

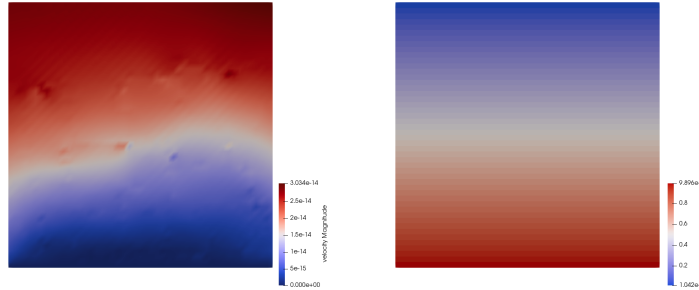
We need the lithostatic pressure and compute it before hand (which is trivial in our case but can prove to be a bit more tedious in real life situations when for instance density varies in the domain as a function of temperature and/or pressure).

```
plith = np.zeros(nnp, dtype=np.float64)
for i in range(0,nnp):
    plith[i]=(Ly-y[i])*rho0*abs(gy)
```

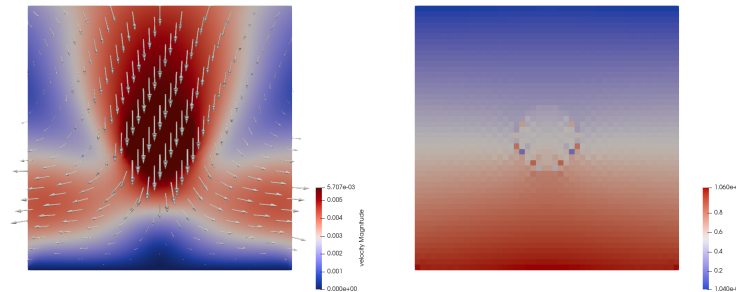
Let us start with a somewhat pathological case: even in the absence of the sphere, what happens when no boundary conditions are prescribed on the sides? The answer is simple: think about an aquarium without side walls, or a broken dam. The velocity field indeed shows a complete collapse of the fluid left and right of the bottom.



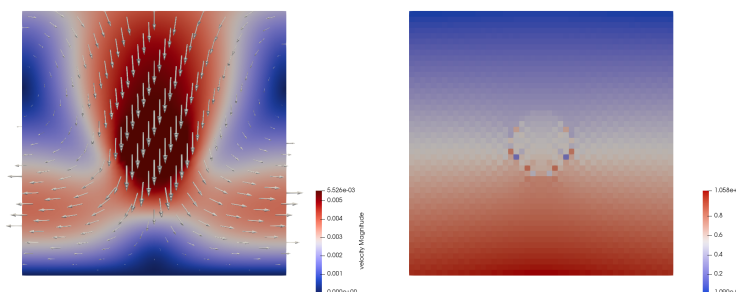
Let us then continue (still with no sphere) but let us now switch on the open boundary conditions. Since the side boundary conditions match the lithostatic pressure we expect no flow at all in the absence of any density perturbation in the system. This is indeed what is recovered:



Finally, let us reintroduce the sphere. This time flow is allowed through the left and right side boundaries:



Finally, although horizontal velocity Dirichlet boundary conditions and open boundary conditions are not compatible, the same is not true for the vertical component of the velocity: the open b.c. implementation acts on the horizontal velocity dofs only, so that one can fix the vertical component to zero, as is shown hereunder:



We indeed see that the in/outflow on the sides is perpendicular to the boundaries.

Turning now to the actual implementation, we see that it is quite trivial, since all element edges are vertical, and all have the same vertical dimension h_x . Since we use a Q_0 approximation for the pressure

we need to prescribe a single pressure value in the middle of the element. Finally because of the sign of the normal vector projection onto the x -axis, we obtain:

```
if open_bc_left and x[icon[0, iel]]<eps: # left side
    pmid=0.5*(plith[icon[0, iel]]+plith[icon[3, iel]])
    f_el[0]+=0.5*hy*pmid
    f_el[6]+=0.5*hy*pmid
if open_bc_right and x[icon[1, iel]]>Lx-eps: # right side
    pmid=0.5*(plith[icon[1, iel]]+plith[icon[2, iel]])
    f_el[2]=-0.5*hy*pmid
    f_el[4]=-0.5*hy*pmid
```

These few lines of code are added after the elemental matrices and rhs are built, and before the application of other Dirichlet boundary conditions, and assembly.

features

- $Q_1 \times P_0$ element
- incompressible flow
- mixed formulation
- open boundary conditions
- isoviscous

Stone 30: conservative velocity interpolation

In this the Stokes equations are not solved. It is a 2D implementation of the cvi algorithm as introduced in [1654] which deals with the advection of markers. Q_1 and Q_2 basis functions are used and in both cases the cvi algorithm can be toggled on/off. Markers can be distributed regularly or randomly at startup.

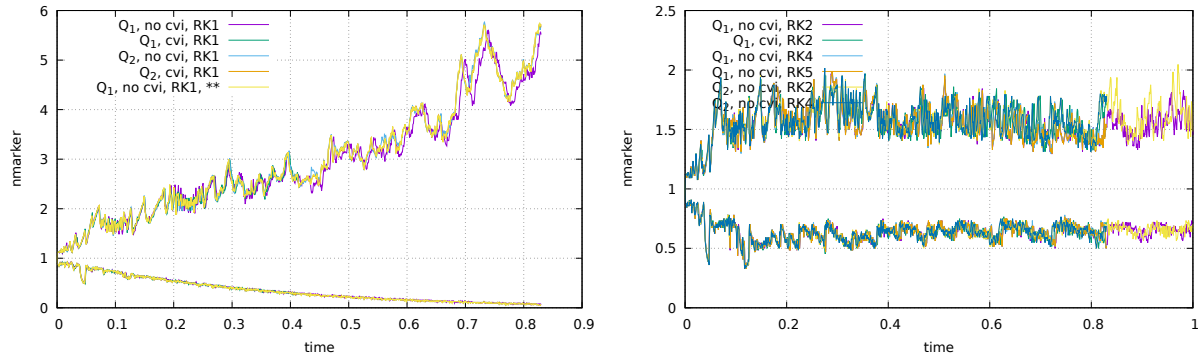
Three velocity fields are prescribed on the mesh:

- the so-called Couette flow of [1654]
- the SolCx solution
- a flow created by means of a stream line function (see fieldstone 32)

Couette flow

SolCx

Streamline flow



In this case RK order seems to be more important than cvi.

Explore why ?!

features

- $Q_1 \times P_0$ element
- incompressible flow
- penalty formulation
- Dirichlet boundary conditions (free-slip)
- direct solver
- isothermal
- non-isoviscous
- analytical solution

Stone 31: conservative velocity interpolation 3D

Stone 32: 2D analytical sol. from stream function

Background theory

The stream function is a function of coordinates and time of an inviscid liquid. It allows to determine the components of velocity by differentiating the stream function with respect to the space coordinates. A family of curves $\Psi = \text{const}$ represent *streamlines*, i.e. the stream function remains constant along a streamline. Although also valid in 3D, this approach is mostly used in 2D because of its relative simplicity

REFERENCES.

In two dimensions the velocity is obtained as follows:

$$\mathbf{v} = \left(\frac{\partial \Psi}{\partial y}, -\frac{\partial \Psi}{\partial x} \right) \quad (701)$$

Provided the function Ψ is a smooth enough function, this automatically insures that the flow is incompressible:

$$\nabla \cdot \mathbf{v} = \frac{\partial u}{\partial x} + \frac{\partial v}{\partial y} = \frac{\partial^2 \Psi}{\partial x \partial y} - \frac{\partial^2 \Psi}{\partial y \partial x} = 0 \quad (702)$$

Assuming constant viscosity, the Stokes equation writes:

$$-\nabla p + \mu \Delta \mathbf{v} = \rho \mathbf{g} \quad (703)$$

Let us introduce the vector \mathbf{W} for convenience such that in each dimension:

$$W_x = -\frac{\partial p}{\partial x} + \mu \left(\frac{\partial^2 u}{\partial x^2} + \frac{\partial^2 u}{\partial x \partial y} \right) = \rho g_x \quad (704)$$

$$W_y = -\frac{\partial p}{\partial y} + \mu \left(\frac{\partial^2 v}{\partial x^2} + \frac{\partial^2 v}{\partial x \partial y} \right) = \rho g_y \quad (705)$$

Taking the curl of the vector \mathbf{W} and only considering the component perpendicular to the xy -plane:

$$\frac{\partial V_y}{\partial x} - \frac{\partial V_x}{\partial y} = \frac{\partial \rho g_y}{\partial x} - \frac{\partial \rho g_x}{\partial y} \quad (706)$$

The advantage of this approach is that the pressure terms cancel out (the curl of a gradient is always zero), so that:

$$\frac{\partial}{\partial x} \mu \left(\left(\frac{\partial^2 v}{\partial x^2} + \frac{\partial^2 v}{\partial x \partial y} \right) - \frac{\partial}{\partial y} \mu \left(\frac{\partial^2 u}{\partial x^2} + \frac{\partial^2 u}{\partial x \partial y} \right) \right) = \frac{\partial \rho g_y}{\partial x} - \frac{\partial \rho g_x}{\partial y} \quad (707)$$

and then replacing u, v by their stream function derivatives yields (for a constant viscosity):

$$\mu \left(\frac{\partial^4 \Psi}{\partial x^4} + \frac{\partial^4 \Psi}{\partial y^4} + 2 \frac{\partial^4 \Psi}{\partial x^2 \partial y^2} \right) = \frac{\partial \rho g_y}{\partial x} - \frac{\partial \rho g_x}{\partial y} \quad (708)$$

or,

$$\nabla^4 \Psi = \left(\frac{\partial^2}{\partial x^2} + \frac{\partial^2}{\partial y^2} \right) \left(\frac{\partial^2}{\partial x^2} + \frac{\partial^2}{\partial y^2} \right) \Psi = \frac{\partial \rho g_y}{\partial x} - \frac{\partial \rho g_x}{\partial y} \quad (709)$$

These equations are also to be found in the geodynamics literature, eee Eq. 1.43 of Tackley book, p 70-71 of Gerya book.

A simple application

I wish to arrive at an analytical formulation for a 2D incompressible flow in the square domain $[-1 : 1] \times [-1 : 1]$. The fluid has constant viscosity $\mu = 1$ and is subject to free slip boundary conditions on all sides. For reasons that will become clear in what follows I postulate the following stream function:

$$\Psi(x, y) = \sin(m\pi x) \sin(n\pi y) \quad (710)$$

We have the velocity being defined as:

$$\mathbf{v} = (u, v) = \left(\frac{\partial \Psi}{\partial y}, -\frac{\partial \Psi}{\partial x} \right) = (n\pi \sin(m\pi x) \cos(n\pi y), -m\pi \cos(m\pi x) \sin(n\pi y)) \quad (711)$$

The strain rate components are then:

$$\dot{\varepsilon}_{xx} = \frac{\partial u}{\partial x} = mn\pi^2 \cos(m\pi x) \cos(n\pi y) \quad (712)$$

$$\dot{\varepsilon}_{yy} = \frac{\partial v}{\partial y} = -mn\pi^2 \cos(m\pi x) \cos(n\pi y) \quad (713)$$

$$2\dot{\varepsilon}_{xy} = \frac{\partial u}{\partial y} + \frac{\partial v}{\partial x} \quad (714)$$

$$= \frac{\partial^2 \Psi}{\partial y^2} - \frac{\partial^2 \Psi}{\partial x^2} \quad (715)$$

$$= -n^2\pi^2\Psi + m^2\pi^2\Psi \quad (716)$$

$$= (m^2 - n^2)\pi^2 \sin(m\pi x) \sin(n\pi y) \quad (717)$$

Note that if $m = n$ the last term is identically zero, which is not desirable (flow is too 'simple') so in what follows we will prefer $m \neq n$.

It is also easy to verify that $u = 0$ on the sides and $v = 0$ at the top and bottom and that the term $\dot{\varepsilon}_{xy}$ is null on all four sides, thereby guaranteeing free slip.

Our choice of stream function yields:

$$\nabla^4 \Psi = \frac{\partial^4 \Psi}{\partial x^4} + \frac{\partial^4 \Psi}{\partial y^4} + 2 \frac{\partial^2 \Psi}{\partial x^2 \partial y^2} = \pi^4 (m^4 \Psi + n^4 \Psi + 2m^2 n^2 \Psi) = (m^4 + n^4 + 2m^2 n^2) \pi^4 \Psi$$

We assume $g_x = 0$ and $g_y = -1$ so that we simply have

$$(m^4 + n^4 + 2m^2 n^2) \pi^4 \Psi = -\frac{\partial \rho}{\partial x} \quad (718)$$

so that (assuming the integration constant to be zero):

$$\rho(x, y) = \frac{m^4 + n^4 + 2m^2 n^2}{m} \pi^3 \cos(m\pi x) \sin(n\pi y)$$

The x -component of the momentum equation is

$$-\frac{\partial p}{\partial x} + \frac{\partial^2 u}{\partial x^2} + \frac{\partial^2 u}{\partial y^2} = -\frac{\partial p}{\partial x} - m^2 n \pi^3 \sin(m\pi x) \cos(n\pi y) - n^3 \pi^3 \sin(m\pi x) \cos(n\pi y) = 0$$

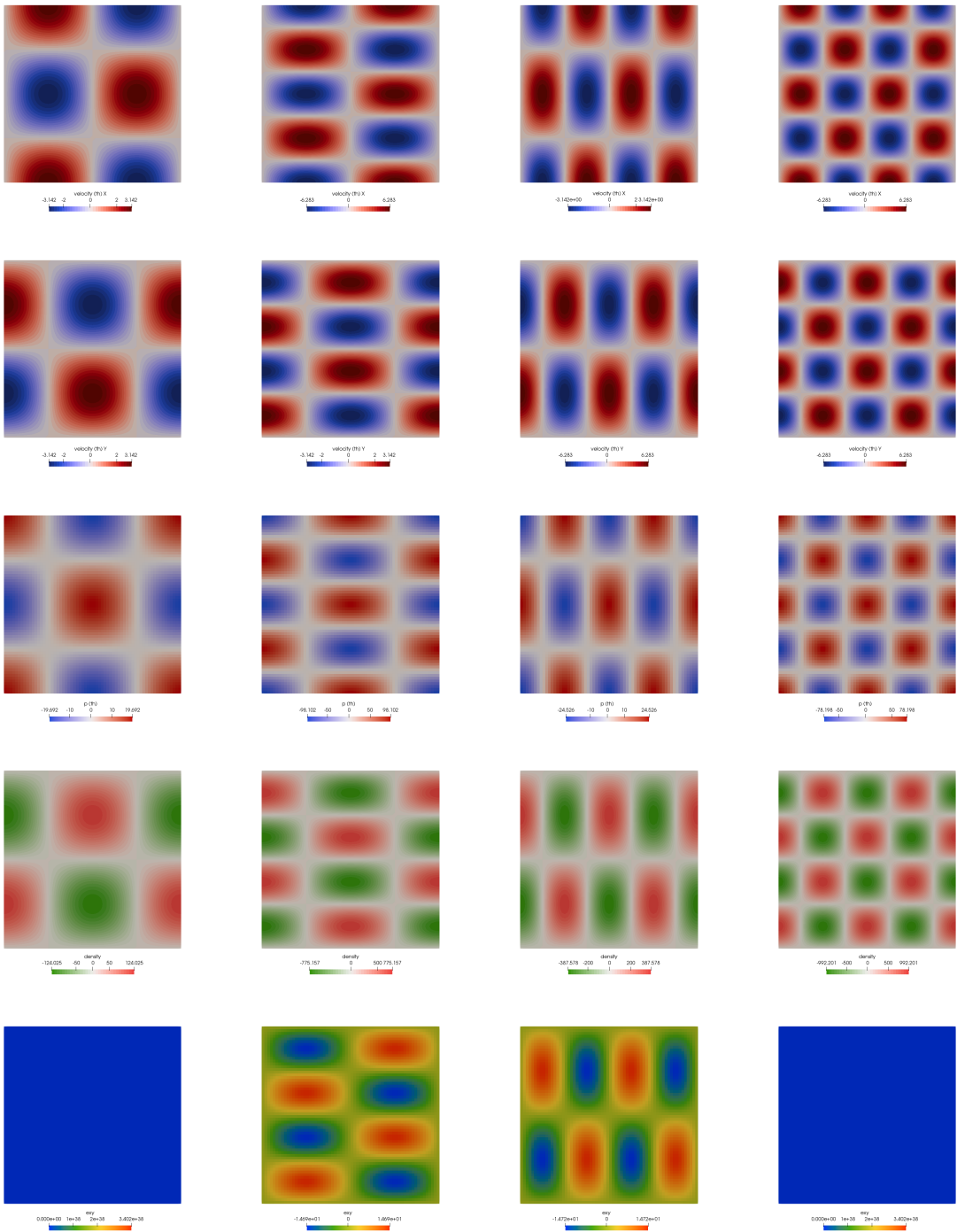
so

$$\frac{\partial p}{\partial x} = -(m^2 n + n^3) \pi^3 \sin(m\pi x) \cos(n\pi y)$$

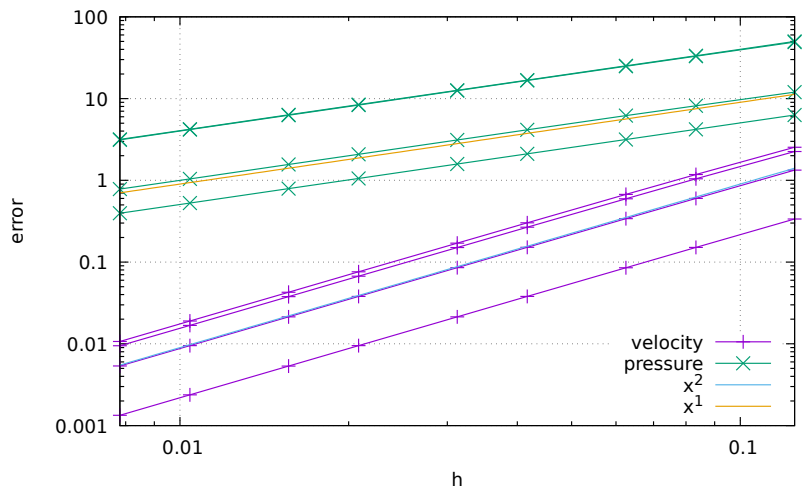
and the pressure field is then (once again neglecting the integration constant):

$$p(x, y) = \frac{m^2 n + n^3}{m} \pi^2 \cos(\pi x) \cos(\pi y)$$

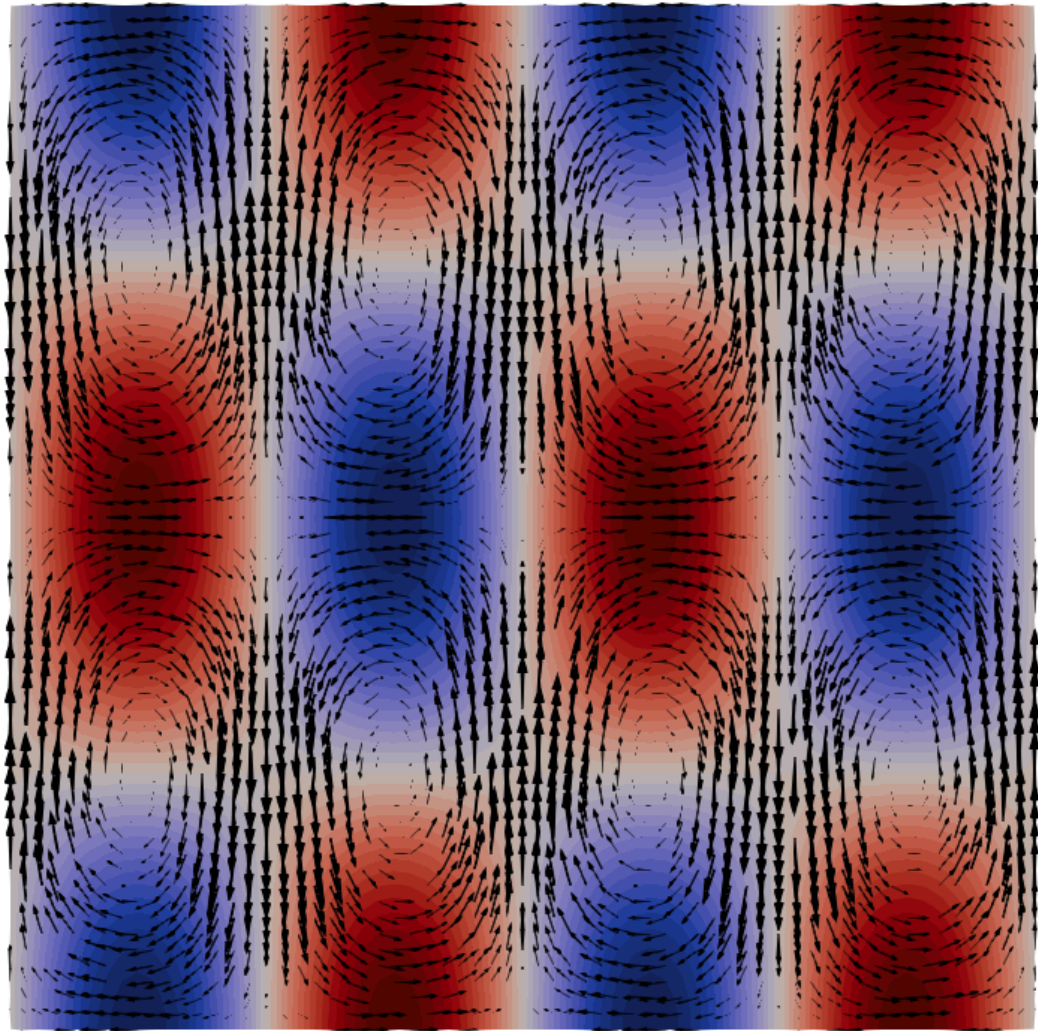
Note that in this case $\int p dV = 0$ so that volume normalisation of the pressure is turned on (when free slip boundary conditions are prescribed on all sides the pressure is known up to a constant and this undeterminacy can be lifted by adding an additional constraint to the pressure field).



Top to bottom: Velocity components u and v , pressure p , density ρ and strain rate $\dot{\epsilon}_{xy}$. From left to right:
 $(m, n) = (1, 1), (m, n) = (1, 2), (m, n) = (2, 1), (m, n) = (2, 2)$



Errors for velocity and pressure for $(m, n) = (1, 1), (1, 2), (2, 1), (2, 2)$



Velocity arrows for $(m, n) = (2, 1)$

Stone 33: Convection in an annulus



This fieldstone was developed in collaboration with Rens Elbertsen.

This is based on the community benchmark for viscoplastic thermal convection in a 2D square box [1558] as already carried out in ??.

In this experiment the geometry is an annulus of inner radius $R_1 = 1.22$ and outer radius $R_2 = 2.22$. The rheology and buoyancy forces are identical to those of the box experiment. The initial temperature is now given by:

$$T(r, \theta) = T_c(r) + A s(1 - s) \cos(N_0 \theta) \quad s = \frac{R_2 - r}{R_2 - R_1} \in [0, 1]$$

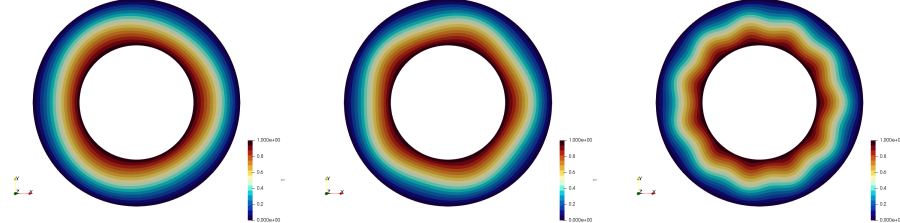
where s is the normalised depth, A is the amplitude of the perturbation and N_0 the number of lobes. In this equation $T_c(r)$ stands for the steady state purely conductive temperature solution which is obtained by solving the Laplace's equation in polar coordinates (all terms in θ are dropped because of radial symmetry) supplemented with two boundary conditions:

$$\Delta T_c = \frac{1}{r} \frac{\partial}{\partial r} \left(r \frac{\partial T}{\partial r} \right) = 0 \quad T(r = R_1) = T_1 = 1 \quad T(r = R_2) = T_2 = 0$$

We obtain

$$T_c(r) = \frac{\log(r/R_2)}{\log(R_1/R_2)}$$

Note that this profile differs from the straight line that is used in [1558] and in section 9.



Examples of initial temperature fields for $N_0 = 3, 5, 11$

Boundary conditions can be either no-slip or free-slip on both inner and outer boundary. However, when free-slip is used on both a velocity null space exists and must be filtered out. In other words, the solver may be able to come up with a solution to the Stokes operator, but that solution plus an arbitrary rotation is also an equally valid solution. This additional velocity field can be problematic since it is used for advecting temperature (and/or compositions) and it also essentially determines the time step value for a chosen mesh size (CFL condition).

For these reasons the nullspace must be removed from the obtained solution after every timestep. There are two types of nullspace removal: removing net angular momentum, and removing net rotations.

We calculate the following output parameters:

- the average temperature $\langle T \rangle$

$$\langle T \rangle = \frac{\int_{\Omega} T d\Omega}{\int_{\Omega} d\Omega} = \frac{1}{V_{\Omega}} \int_{\Omega} T d\Omega \quad (719)$$

- the root mean square velocity v_{rms} as given by equation (55).
- the root mean square of the radial and tangential velocity components as given by equations (57) and (58).

- the heat transfer through both boundaries Q :

$$Q_{inner,outer} = \int_{\Gamma_{i,o}} \mathbf{q} \cdot \mathbf{n} \, d\Gamma \quad (720)$$

- the Nusselt number at both boundaries Nu as given by equations (60) and (61).
- the power spectrum of the temperature field:

$$PS_n(T) = \left| \int_{\Omega} T(r, \theta) e^{in\theta} d\Omega \right|^2. \quad (721)$$

features

- $Q_1 \times P_0$ element
- incompressible flow
- penalty formulation
- Dirichlet boundary conditions
- non-isothermal
- non-isoviscous
- annulus geometry

Stone 34: the Cartesian geometry elastic aquarium

This fieldstone was developed in collaboration with Lukas van de Wiel.

The setup is as follows: a 2D square of elastic material of size L is subjected to the following boundary conditions: free slip on the sides, no slip at the bottom and free at the top. It has a density ρ and is placed in a gravity field $\mathbf{g} = -ge_y$. For an isotropic elastic medium the stress tensor is given by:

$$\boldsymbol{\sigma} = \lambda(\nabla \cdot \mathbf{u})\mathbf{1} + 2\mu\boldsymbol{\varepsilon}$$

where λ is the Lamé parameter and μ is the shear modulus. The displacement field is $\mathbf{u} = (0, u_y(y))$ because of symmetry reasons (we do not expect any of the dynamic quantities to depend on the x coordinate and also expect the horizontal displacement to be exactly zero). The velocity divergence is then $\nabla \cdot \mathbf{u} = \partial u_y / \partial y$ and the strain tensor:

$$\boldsymbol{\varepsilon} = \begin{pmatrix} 0 & 0 \\ 0 & \frac{\partial u_y}{\partial y} \end{pmatrix}$$

so that the stress tensor is:

$$\begin{aligned} \boldsymbol{\sigma} &= \begin{pmatrix} \lambda \frac{\partial u_y}{\partial y} & 0 \\ 0 & (\lambda + 2\mu) \frac{\partial u_y}{\partial y} \end{pmatrix} \\ \nabla \cdot \boldsymbol{\sigma} &= (\partial_x \quad \partial_y) \cdot \begin{pmatrix} \lambda \frac{\partial u_y}{\partial y} & 0 \\ 0 & (\lambda + 2\mu) \frac{\partial u_y}{\partial y} \end{pmatrix} = \begin{pmatrix} 0 \\ (\lambda + 2\mu) \frac{\partial^2 u_y}{\partial y^2} \end{pmatrix} = \begin{pmatrix} 0 \\ \rho g \end{pmatrix} \end{aligned}$$

so that the vertical displacement is then given by:

$$u_y(y) = \frac{1}{2} \frac{\rho g}{\lambda + 2\mu} y^2 + \alpha y + \beta$$

where α and β are two integration constants. We need now to use the two boundary conditions: the first one states that the displacement is zero at the bottom, i.e. $u_y(y=0) = 0$ which immediately implies $\beta = 0$. The second states that the stress at the top is zero (free surface), which implies that $\partial u_y / \partial y(y=L) = 0$ which allows us to compute α . Finally:

$$u_y(y) = \frac{\rho g}{\lambda + 2\mu} \left(\frac{y^2}{2} - Ly \right)$$

The pressure is given by

$$p = -(\lambda + \frac{2}{3}\mu)\nabla \cdot \mathbf{u} = (\lambda + \frac{2}{3}\mu) \frac{\rho g}{\lambda + 2\mu} (L - y) = \frac{\lambda + \frac{2}{3}\mu}{\lambda + 2\mu} \rho g (L - y) = \frac{1 + \frac{2\mu}{3\lambda}}{1 + 2\mu/\lambda} \rho g (L - y)$$

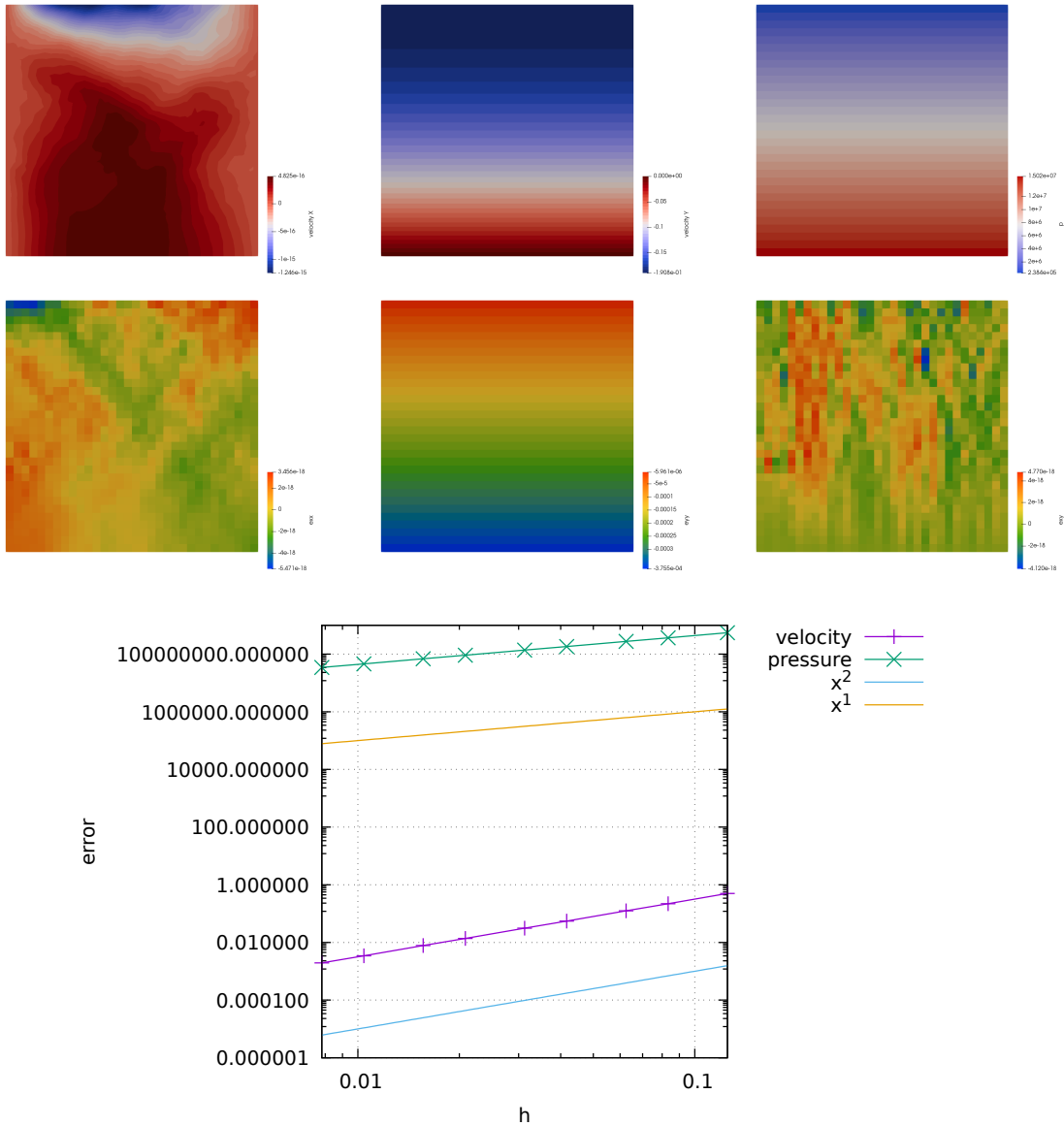
In the incompressible limit, the poisson ratio is $\nu \sim 0.5$. Materials are characterised by a finite Young's modulus E , which is related to ν and λ :

$$\lambda = \frac{E\nu}{(1+\nu)(1-2\nu)} \quad \mu = \frac{E}{2(1+\nu)}$$

It is then clear that for incompressible parameters λ becomes infinite while μ remains finite. In that case the pressure then logically converges to the well known formula:

$$p = \rho g(L - y)$$

In what follows we set $L = 1000\text{m}$, $\rho = 2800$, $\nu = 0.25$, $E = 6 \cdot 10^{10}$, $g = 9.81$.



Stone 35: 2D analytical sol. in annulus from stream function



We seek an exact solution to the incompressible Stokes equations for an isoviscous, isothermal fluid in an annulus. Given the geometry of the problem, we work in polar coordinates. We denote the orthonormal basis vectors by \mathbf{e}_r and \mathbf{e}_θ , the inner radius of the annulus by R_1 and the outer radius by R_2 . Further, we assume that the viscosity μ is constant, which we set to $\mu = 1$ we set the gravity vector to $\mathbf{g} = -g_r \mathbf{e}_r$ with $g_r = 1$.

Given these assumptions, the incompressible Stokes equations in the annulus are [1441]

$$A_r = \frac{\partial^2 v_r}{\partial r^2} + \frac{1}{r} \frac{\partial v_r}{\partial r} + \frac{1}{r^2} \frac{\partial^2 v_r}{\partial \theta^2} - \frac{v_r}{r^2} - \frac{2}{r^2} \frac{\partial u_\theta}{\partial \theta} - \frac{\partial p}{\partial r} = \rho g_r \quad (722)$$

$$A_\theta = \frac{\partial^2 v_\theta}{\partial r^2} + \frac{1}{r} \frac{\partial v_\theta}{\partial r} + \frac{1}{r^2} \frac{\partial^2 v_\theta}{\partial \theta^2} + \frac{2}{r^2} \frac{\partial v_r}{\partial \theta} - \frac{v_\theta}{r^2} - \frac{1}{r} \frac{\partial p}{\partial \theta} = 0 \quad (723)$$

$$\frac{1}{r} \frac{\partial(r v_r)}{\partial r} + \frac{1}{r} \frac{\partial v_\theta}{\partial \theta} = 0 \quad (724)$$

Equations (722) and (723) are the momentum equations in polar coordinates while Equation (724) is the incompressibility constraint. The components of the velocity are obtained from the stream function as follows:

$$v_r = \frac{1}{r} \frac{\partial \Psi}{\partial \theta} \quad v_\theta = - \frac{\partial \Psi}{\partial r}$$

where v_r is the radial component and v_θ is the tangential component of the velocity vector.

The stream function is defined for incompressible (divergence-free) flows in 2D (as well as in 3D with axisymmetry). The stream function can be used to plot streamlines, which represent the trajectories of particles in a steady flow. From calculus it is known that the gradient vector $\nabla \Psi$ is normal to the curve $\Psi = C$. It can be shown that everywhere $\mathbf{u} \cdot \nabla \Psi = 0$ using the formula for \mathbf{u} in terms of Ψ which proves that level curves of Ψ are streamlines:

$$\mathbf{u} \cdot \nabla \Psi = v_r \frac{\partial \Psi}{\partial r} + v_\theta \frac{1}{r} \frac{\partial \Psi}{\partial \theta} = \frac{1}{r} \frac{\partial \Psi}{\partial \theta} \frac{\partial \Psi}{\partial r} - \frac{\partial \Psi}{\partial r} \frac{1}{r} \frac{\partial \Psi}{\partial \theta} = 0$$

In polar coordinates the curl of a vector \mathbf{A} is:

$$\nabla \times \mathbf{A} = \frac{1}{r} \left(\frac{\partial(r A_\theta)}{\partial r} - \frac{\partial A_r}{\partial \theta} \right)$$

Taking the curl of vector \mathbf{A} yields:

$$\frac{1}{r} \left(\frac{\partial(r A_\theta)}{\partial r} - \frac{\partial A_r}{\partial \theta} \right) = \frac{1}{r} \left(- \frac{\partial(\rho g_r)}{\partial \theta} \right)$$

Multiplying on each side by r

$$\frac{\partial(r A_\theta)}{\partial r} - \frac{\partial A_r}{\partial \theta} = - \frac{\partial(\rho g_r)}{\partial \theta}$$

If we now replace A_r and A_θ by their expressions as a function of velocity and pressure, we see that the pressure terms cancel out and assuming the viscosity and the gravity vector to be constant we get: Let us assume the following separation of variables $\boxed{\Psi(r, \theta) = \phi(r)\xi(\theta)}$. Then

$$v_r = \frac{1}{r} \frac{\partial \Psi}{\partial \theta} = \frac{\phi \xi'}{r} \quad v_\theta = - \frac{\partial \Psi}{\partial r} = -\phi' \xi$$

Let us first express A_r and A_θ as functions of Ψ and

$$A_r = \frac{\partial^2 v_r}{\partial r^2} + \frac{1}{r} \frac{\partial v_r}{\partial r} + \frac{1}{r^2} \frac{\partial^2 v_r}{\partial \theta^2} - \frac{v_r}{r^2} - \frac{2}{r^2} \frac{\partial u_\theta}{\partial \theta} \quad (725)$$

$$= \frac{\partial^2}{\partial r^2} \left(\frac{\phi \xi'}{r} \right) + \frac{1}{r} \frac{\partial}{\partial r} \left(\frac{\phi \xi'}{r} \right) + \frac{1}{r^2} \frac{\partial^2}{\partial \theta^2} \left(\frac{\phi \xi'}{r} \right) - \frac{1}{r^2} \left(\frac{\phi \xi'}{r} \right) - \frac{2}{r^2} \frac{\partial}{\partial \theta} (-\phi' \xi) \quad (726)$$

$$= \left(\frac{\phi''}{r} - 2 \frac{\phi'}{r^2} + 2 \frac{\phi}{r^3} \right) \xi' + \left(\frac{\phi'}{r^2} - \frac{\phi}{r^3} \right) \xi' + \frac{\phi}{r^3} \xi''' - \frac{\phi \xi'}{r^3} + \frac{2}{r^2} \phi' \xi' \quad (727)$$

$$= \frac{\phi'' \xi'}{r} + \frac{\phi' \xi'}{r^2} + \frac{\phi \xi'''}{r^3} \quad (728)$$

$$\frac{\partial A_r}{\partial \theta} = \frac{\phi'' \xi''}{r} + \frac{\phi' \xi''}{r^2} + \frac{\phi \xi''''}{r^3} \quad (729)$$

$$(730)$$

$$A_\theta = \frac{\partial^2 v_\theta}{\partial r^2} + \frac{1}{r} \frac{\partial v_\theta}{\partial r} + \frac{1}{r^2} \frac{\partial^2 v_\theta}{\partial \theta^2} + \frac{2}{r^2} \frac{\partial v_r}{\partial \theta} - \frac{v_\theta}{r^2} \quad (731)$$

$$= \frac{\partial^2}{\partial r^2} (-\phi' \xi) + \frac{1}{r} \frac{\partial}{\partial r} (-\phi' \xi) + \frac{1}{r^2} \frac{\partial^2}{\partial \theta^2} (-\phi' \xi) + \frac{2}{r^2} \frac{\partial}{\partial \theta} \left(\frac{\phi \xi'}{r} \right) - \frac{1}{r^2} (-\phi' \xi) \quad (732)$$

$$= -\phi''' \xi - \frac{\phi'' \xi}{r} - \frac{\phi' \xi''}{r^2} + \frac{2\phi \xi''}{r^2} + \frac{\phi' \xi}{r^2} \quad (733)$$

$$\frac{\partial(rA_\theta)}{\partial r} = \quad (734)$$

WRONG:

$$\frac{\partial(r\Delta v)}{\partial r} = \frac{\partial}{\partial r} \left(\frac{\partial}{\partial r} \left(r \frac{\partial v}{\partial r} \right) + \frac{1}{r} \frac{\partial^2 v}{\partial \theta^2} \right) \quad (735)$$

$$= \frac{\partial^2}{\partial r^2} \left(r \frac{\partial v}{\partial r} \right) + \frac{\partial}{\partial r} \left(\frac{1}{r} \frac{\partial^2 v}{\partial \theta^2} \right) \quad (736)$$

$$= \frac{\partial^2}{\partial r^2} \left(r \frac{\partial}{\partial r} \left(-\frac{\partial \Psi}{\partial r} \right) \right) + \frac{\partial}{\partial r} \left(\frac{1}{r} \frac{\partial^2}{\partial \theta^2} \left(-\frac{\partial \Psi}{\partial r} \right) \right) \quad (737)$$

$$= -\frac{\partial^2}{\partial r^2} \left(r \frac{\partial^2 \Psi}{\partial r^2} \right) - \frac{\partial}{\partial r} \left(\frac{1}{r} \frac{\partial^3 \Psi}{\partial \theta^2 \partial r} \right) \quad (738)$$

$$= -2 \frac{\partial^3 \Psi}{\partial r^3} - r \frac{\partial^4 \Psi}{\partial r^4} + \frac{1}{r^2} \frac{\partial^3 \Psi}{\partial \theta^2 \partial r} - \frac{1}{r} \frac{\partial^4 \Psi}{\partial \theta^2 \partial r^2} \quad (739)$$

$$\frac{\partial \Delta u}{\partial \theta} = \frac{\partial}{\partial \theta} \left(\frac{1}{r} \frac{\partial}{\partial r} \left(r \frac{\partial u}{\partial r} \right) + \frac{1}{r^2} \frac{\partial^2 u}{\partial \theta^2} \right) \quad (740)$$

$$= \frac{\partial}{\partial \theta} \left(\frac{1}{r} \frac{\partial}{\partial r} \left(r \frac{\partial u}{\partial r} \right) \right) + \frac{1}{r^2} \frac{\partial^3 u}{\partial \theta^3} \quad (741)$$

$$= \frac{\partial}{\partial \theta} \left(\frac{1}{r} \frac{\partial}{\partial r} \left(r \frac{\partial}{\partial r} \left(\frac{1}{r} \frac{\partial \Psi}{\partial \theta} \right) \right) \right) + \frac{1}{r^2} \frac{\partial^3}{\partial \theta^3} \left(\frac{1}{r} \frac{\partial \Psi}{\partial \theta} \right) \quad (742)$$

$$= \frac{1}{r^3} \frac{\partial^2 \Psi}{\partial \theta^2} - \frac{1}{r^2} \frac{\partial^3 \Psi}{\partial r \partial \theta^2} + \frac{1}{r} \frac{\partial^4 \Psi}{\partial r^2 \partial \theta^2} + \frac{1}{r^3} \frac{\partial^4 \Psi}{\partial \theta^4} \quad (743)$$

Assuming the following separation of variables $\boxed{\Psi(r, \theta) = \phi(r)\xi(\theta)}$:

$$\frac{\partial(r\Delta v)}{\partial r} = -2\phi'''\xi - r\phi''''\xi + \frac{1}{r^2}\phi'\xi'' - \frac{1}{r}\phi''\xi'' \quad (744)$$

$$\frac{\partial \Delta u}{\partial \theta} = \frac{1}{r^3}\phi\xi'' - \frac{1}{r^2}\phi'\xi'' + \frac{1}{r}\phi''\xi'' + \frac{1}{r^3}\phi\xi''' \quad (745)$$

so that

$$\frac{\partial(r\Delta v)}{\partial r} - \frac{\partial \Delta u}{\partial \theta} = -2\phi'''\xi - r\phi''''\xi + \frac{1}{r^2}\phi'\xi'' - \frac{1}{r}\phi''\xi'' - \frac{1}{r^3}\phi\xi'' + \frac{1}{r^2}\phi'\xi'' - \frac{1}{r}\phi''\xi'' - \frac{1}{r^3}\phi\xi'''$$

Further assuming $\boxed{\xi(\theta) = \cos(k\theta)}$, then $\xi'' = -k^2\xi$ and $\xi''' = k^4\xi$ then

$$\frac{\partial(r\Delta v)}{\partial r} - \frac{\partial \Delta u}{\partial \theta} = -2\phi'''\xi - r\phi''''\xi - k^2 \frac{1}{r^2} \phi' \xi + k^2 \frac{1}{r} \phi'' \xi + k^2 \frac{1}{r^3} \phi \xi - k^2 \frac{1}{r^2} \phi' \xi + k^2 \frac{1}{r} \phi'' \xi - k^4 \frac{1}{r^3} \phi \xi$$

By choosing ρ such that $\rho = \lambda(r)\Upsilon(\theta)$ and such that $\partial_\theta \Upsilon = \xi = \cos(k\theta)$ then we have

$$-2\phi'''\xi - r\phi''''\xi - k^2 \frac{1}{r^2} \phi' \xi + k^2 \frac{1}{r} \phi'' \xi + k^2 \frac{1}{r^3} \phi \xi - k^2 \frac{1}{r^2} \phi' \xi + k^2 \frac{1}{r} \phi'' \xi - k^4 \frac{1}{r^3} \phi \xi = -\frac{1}{\eta} \lambda \xi g_r$$

and then dividing by ξ : (IS THIS OK ?)

$$-2\phi'''' - r\phi''''' - k^2 \frac{1}{r^2} \phi' + k^2 \frac{1}{r} \phi'' + k^2 \frac{1}{r^3} \phi - k^2 \frac{1}{r^2} \phi' + k^2 \frac{1}{r} \phi'' - k^4 \frac{1}{r^3} \phi = -\frac{1}{\eta} \lambda g_r$$

$$-2\phi'''' - r\phi''''' - 2k^2 \frac{1}{r^2} \phi' + 2k^2 \frac{1}{r} \phi'' + (k^2 - k^4) \frac{1}{r^3} \phi = -\frac{1}{\eta} \lambda g_r$$

so

$$\lambda(r) = \frac{\eta}{g_r} \left(2\phi'''' + r\phi''''' + 2k^2 \frac{1}{r^2} \phi' - 2k^2 \frac{1}{r} \phi'' - (k^2 - k^4) \frac{1}{r^3} \phi \right)$$

Also not forget $\Upsilon = \frac{1}{k} \sin(k\theta)$

Linking with our paper

We have

$$\phi(r) = -rg(r) \quad (746)$$

$$\phi'(r) = -g(r) - rg'(r) = -f(r) \quad (747)$$

$$\phi''(r) = -f'(r) \quad (748)$$

$$\phi'''(r) = -f''(r) \quad (749)$$

$$\phi''''(r) = -f'''(r) \quad (750)$$

$$f(r) = \frac{\eta_0}{g_0} \left(2f''(r) + rf'''(r) + 2k^2 \frac{1}{r^2} f(r) - 2k^2 \frac{1}{r} f'(r) + (k^2 - k^4) \frac{1}{r^2} g(r) \right)$$

No slip boundary conditions

No-slip boundary conditions inside and outside impose that all components of the velocity must be zero on both boundaries, i.e.

$$\mathbf{v}(r = R_1) = \mathbf{v}(r = R_2) = \mathbf{0}$$

Due to the separation of variables, and since $\xi(\theta) = \cos(k\theta)$ we have

$$u(r, \theta) = \frac{1}{r} \frac{\partial \Psi}{\partial \theta} = \frac{1}{r} \phi \xi' = -\frac{1}{r} \phi(r) k \sin(k\theta) \quad v(r, \theta) = -\frac{\partial \Psi}{\partial r} = -\phi'(r) \xi = -\phi'(r) \cos(k\theta)$$

It is obvious that the only way to insure no-slip boundary conditions is to have

$$\phi(R_1) = \phi(R_2) = \phi'(R_1) = \phi'(R_2) = 0$$

We could then choose

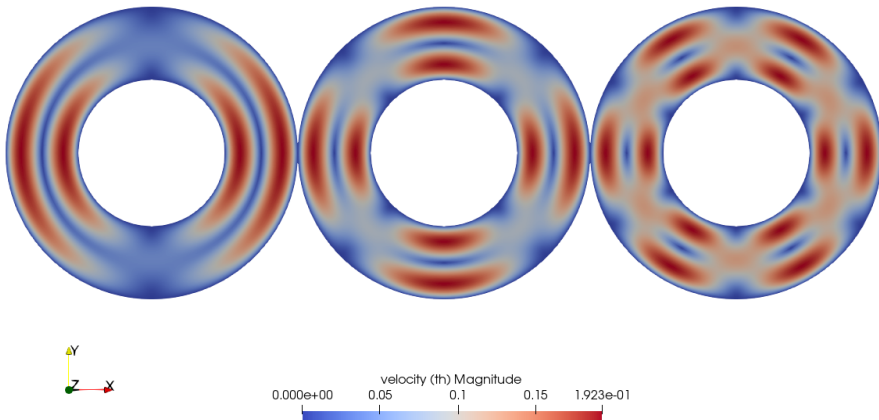
$$\phi(r) = (r - R_1)^2 (r - R_2)^2 \mathcal{F}(r) \quad (751)$$

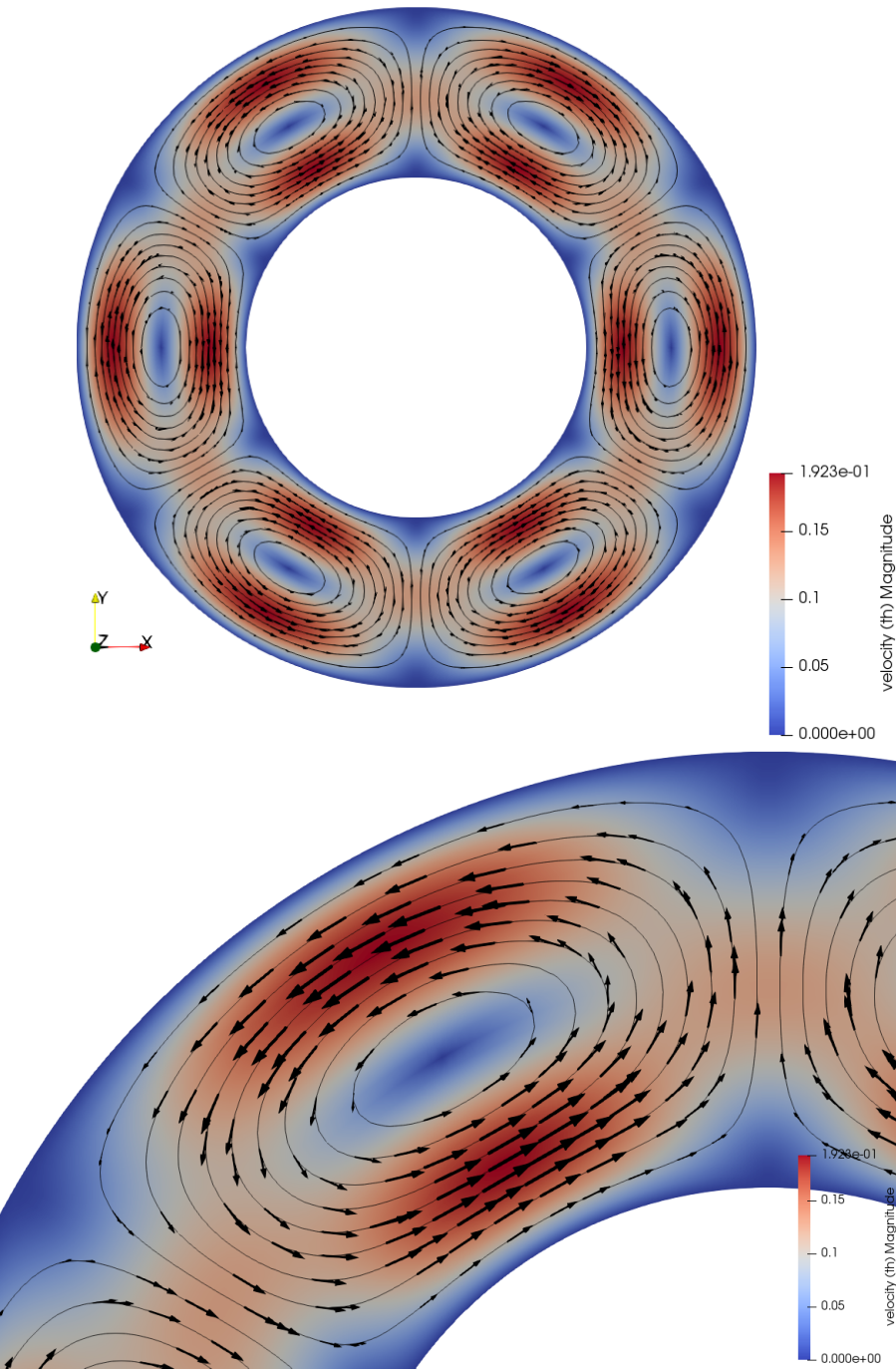
$$\phi'(r) = 2(r - R_1)(r - R_2)^2 \mathcal{F}(r) + 2(r - R_1)^2(r - R_2) \mathcal{F}(r) + (r - R_1)^2(r - R_2)^2 \mathcal{F}'(r) \quad (752)$$

which are indeed identically zero on both boundaries. Here $\mathcal{F}(r)$ is any (smooth enough) function of r . We would then have

$$\boxed{\Psi(r, \theta) = (r - R_1)^2 (r - R_2)^2 \mathcal{F}(r) \cos(k\theta)}$$

In what follows we will take $\mathcal{F}(r) = 1$ for simplicity.





COMPUTE f from ϕ and then the pressure.

Free slip boundary conditions

Before postulating the form of $\phi(r)$, let us now turn to the boundary conditions that the flow must fulfill, i.e. free-slip on both boundaries. Two conditions must be met:

- $\mathbf{v} \cdot \mathbf{n} = 0$ (no flow through the boundaries) which yields $u(r = R_1) = 0$ and $u(r = R_2) = 0$:

$$\frac{1}{r} \frac{\partial \Psi}{\partial \theta}(r = R_1, R_2) = 0 \quad \forall \theta$$

which gives us the first constraint since $\Psi(r, \theta) = \phi(r)\xi(\theta)$:

$$\phi(r = R_1) = \phi(r = R_2) = 0$$

- $(\sigma \cdot n) \times n = \mathbf{0}$ (the tangential stress at the boundary is zero) which imposes: $\sigma_{\theta r} = 0$, with

$$\sigma_{\theta r} = 2\eta \cdot \frac{1}{2} \left(\frac{\partial v}{\partial r} - \frac{v}{r} + \frac{1}{r} \frac{\partial u}{\partial \theta} \right) = \eta \left(\frac{\partial}{\partial r} \left(-\frac{\partial \Psi}{\partial r} \right) - \frac{1}{r} \left(-\frac{\partial \Psi}{\partial r} \right) + \frac{1}{r} \frac{\partial}{\partial \theta} \left(\frac{1}{r} \frac{\partial \Psi}{\partial \theta} \right) \right)$$

Finally Ψ must fulfill (on the boundaries!):

$$-\frac{\partial^2 \Psi}{\partial r^2} + \frac{1}{r} \frac{\partial \Psi}{\partial r} + \frac{1}{r^2} \frac{\partial^2 \Psi}{\partial \theta^2} = 0$$

$$-\phi''\xi + \frac{1}{r}\phi'\xi + \frac{1}{r^2}\phi\xi'' = 0$$

or,

$$-\phi'' + \frac{1}{r}\phi' - k^2 \frac{1}{r^2}\phi = 0$$

Note that this equation is a so-called Euler Differential Equation⁶². Since we are looking for a solution ϕ such that $\phi(R_1) = \phi(R_2) = 0$ then the 3rd term of the equation above is by definition zero on the boundaries. We have to ensure the following equality on the boundary:

$$-\phi'' + \frac{1}{r}\phi' = 0 \quad \text{for } r = R_1, R_2$$

The solution of this ODE is of the form $\phi(r) = ar^2 + b$ and it becomes evident that it cannot satisfy $\phi(r = R_1) = \phi(r = R_2) = 0$.

Separation of variables leads to solutions which cannot fulfill the free slip boundary conditions

⁶²<http://mathworld.wolfram.com/EulerDifferentialEquation.html>

Stone 36: the annulus geometry elastic aquarium

This fieldstone was developed in collaboration with Lukas van de Wiel.

The domain is an annulus with inner radius R_1 and outer radius R_2 . It is filled with a single elastic material characterised by a Young's modulus E and a Poisson ratio ν , a density ρ_0 . The gravity $\mathbf{g} = -g_0 \mathbf{e}_r$ is pointing towards the center of the domain.

The problem at hand is axisymmetric so that the tangential component of the displacement vector v_θ is assumed to be zero as well as all terms containing ∂_θ . The components of the strain tensor are

$$\varepsilon_{rr} = \frac{\partial v_r}{\partial r} \quad (753)$$

$$\varepsilon_{\theta\theta} = \frac{v_r}{r} + \frac{1}{r} \frac{\partial v_\theta}{\partial \theta} = \frac{v_r}{r} \quad (754)$$

$$\varepsilon_{r\theta} = \frac{1}{2} \left(\frac{\partial v_\theta}{\partial r} - \frac{v_\theta}{r} + \frac{1}{r} \frac{\partial v_r}{\partial \theta} \right) = 0 \quad (755)$$

so that the tensor simply is

$$\boldsymbol{\varepsilon} = \begin{pmatrix} \varepsilon_{rr} & \varepsilon_{r\theta} \\ \varepsilon_{r\theta} & \varepsilon_{\theta\theta} \end{pmatrix} = \begin{pmatrix} \frac{\partial v_r}{\partial r} & 0 \\ 0 & \frac{v_r}{r} \end{pmatrix} \quad (756)$$

The pressure is

$$p = -\lambda \nabla \cdot \mathbf{v} = -\lambda \left(\frac{1}{r} \frac{\partial(rv_r)}{\partial r} \right) \quad (757)$$

and finally the stress tensor:

$$\boldsymbol{\sigma} = -p \mathbf{1} + 2\mu \boldsymbol{\varepsilon} = \begin{pmatrix} \lambda \frac{1}{r} \frac{\partial(rv_r)}{\partial r} + 2\mu \frac{\partial v_r}{\partial r} & 0 \\ 0 & \lambda \frac{1}{r} \frac{\partial(rv_r)}{\partial r} + 2\mu \frac{v_r}{r} \end{pmatrix} \quad (758)$$

The divergence of the stress tensor is given by [1441]:

$$\nabla \cdot \boldsymbol{\sigma} = \begin{pmatrix} \frac{\partial \sigma_{rr}}{\partial r} + \frac{\sigma_{rr} - \sigma_{\theta\theta}}{r} + \frac{1}{r} \frac{\partial \sigma_{\theta r}}{\partial \theta} \\ \frac{\partial \sigma_{r\theta}}{\partial r} + \frac{1}{r} \frac{\sigma_{\theta\theta}}{\partial \theta} + \frac{\sigma_{r\theta} + \sigma_{\theta r}}{r} \end{pmatrix} \quad (759)$$

Given the diagonal nature of the stress tensor this simplifies to (also remember that $\partial_\theta = 0$):

$$\nabla \cdot \boldsymbol{\sigma} = \begin{pmatrix} \frac{\partial \sigma_{rr}}{\partial r} + \frac{\sigma_{rr} - \sigma_{\theta\theta}}{r} \\ 0 \end{pmatrix} \quad (760)$$

Focusing on the r -component of the stress divergence:

$$(\nabla \cdot \boldsymbol{\sigma})_r = \frac{\partial \sigma_{rr}}{\partial r} + \frac{\sigma_{rr} - \sigma_{\theta\theta}}{r} \quad (761)$$

$$= \frac{\partial}{\partial r} \left[\lambda \frac{1}{r} \frac{\partial(rv_r)}{\partial r} + 2\mu \frac{\partial v_r}{\partial r} \right] + \frac{1}{r} \left[\lambda \frac{1}{r} \frac{\partial(rv_r)}{\partial r} + 2\mu \frac{\partial v_r}{\partial r} - \lambda \frac{1}{r} \frac{\partial(rv_r)}{\partial r} - 2\mu \frac{v_r}{r} \right] \quad (762)$$

$$= \lambda \frac{\partial}{\partial r} \frac{1}{r} \frac{\partial(rv_r)}{\partial r} + 2\mu \frac{\partial^2 v_r}{\partial r^2} + \lambda \frac{1}{r^2} \frac{\partial(rv_r)}{\partial r} + \frac{2\mu}{r} \frac{\partial v_r}{\partial r} - \lambda \frac{1}{r^2} \frac{\partial(rv_r)}{\partial r} - \frac{2\mu v_r}{r^2} \quad (763)$$

$$= \lambda \left(-\frac{v_r}{r^2} + \frac{1}{r} \frac{\partial v_r}{\partial r} + \frac{\partial^2 v_r}{\partial r^2} \right) + 2\mu \frac{\partial^2 v_r}{\partial r^2} + \frac{2\mu}{r} \frac{\partial v_r}{\partial r} - \frac{2\mu v_r}{r^2} \quad (764)$$

$$= -(2\mu + \lambda) \frac{v_r}{r^2} + (2\mu + \lambda) \frac{1}{r} \frac{\partial v_r}{\partial r} + (2\mu + \lambda) \frac{\partial^2 v_r}{\partial r^2} \quad (765)$$

So the momentum conservation in the r direction is

$$(\nabla \cdot \boldsymbol{\sigma} + \rho_0 \mathbf{g})_r = -(2\mu + \lambda) \frac{v_r}{r^2} + (2\mu + \lambda) \frac{1}{r} \frac{\partial v_r}{\partial r} + (2\mu + \lambda) \frac{\partial^2 v_r}{\partial r^2} - \rho_0 g_0 = 0 \quad (766)$$

or,

$$\frac{\partial^2 v_r}{\partial r^2} + \frac{1}{r} \frac{\partial v_r}{\partial r} - \frac{v_r}{r^2} = \frac{\rho_0 g_0}{\lambda + 2\mu} \quad (767)$$

We now look at the boundary conditions. On the inner boundary we prescribe $v_r(r = R_1) = 0$ while free surface boundary conditions are prescribed on the outer boundary, i.e. $\boldsymbol{\sigma} \cdot \mathbf{n} = 0$ (i.e. there is no force applied on the surface).

The general form of the solution can then be obtained:

$$v_r(r) = C_1 r^2 + C_2 r + \frac{C_3}{r} \quad (768)$$

with

$$C_1 = \frac{\rho_0 g_0}{3(\lambda + 2\mu)} \quad C_2 = -C_1 R_1 - \frac{C_3}{R_1^2} \quad C_3 = \frac{k_1 + k_2}{(R_1^2 + R_2^2)(2\mu + \lambda) + (R_2^2 - R_1^2)\lambda} \quad (769)$$

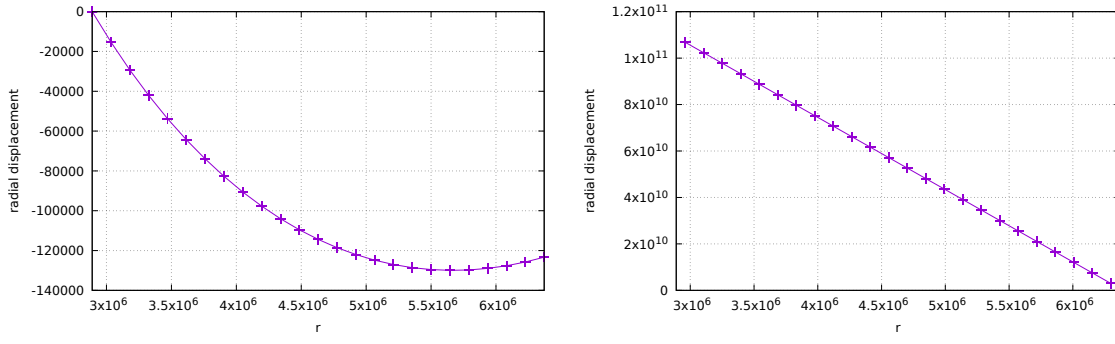
and

$$k_1 = (2\mu + \lambda)C_1(2R_1^2 R_2^3 - R_1^3 R_2^2) \quad k_2 = \lambda C_1(R_1^2 R_2^3 - R_1^3 R_2^2) \quad (770)$$

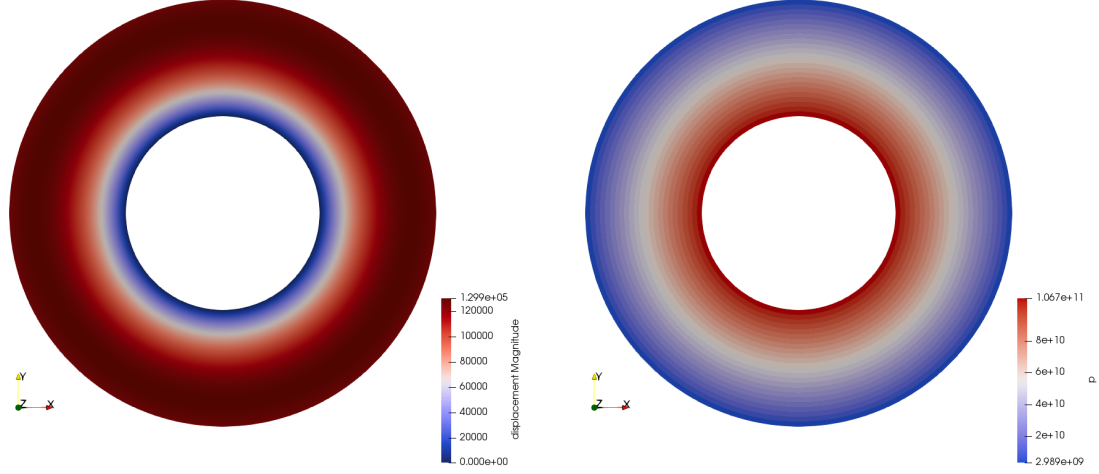
Pressure can then be computed as follows:

$$p = -\lambda \nabla \cdot \mathbf{v} = -\lambda \left(\frac{1}{r} \frac{\partial(r v_r)}{\partial r} \right) = -\lambda \left(\frac{1}{r} (3C_1 r^2 + 2C_2 r) \right) = -\lambda (3C_1 r + 2C_2) \quad (771)$$

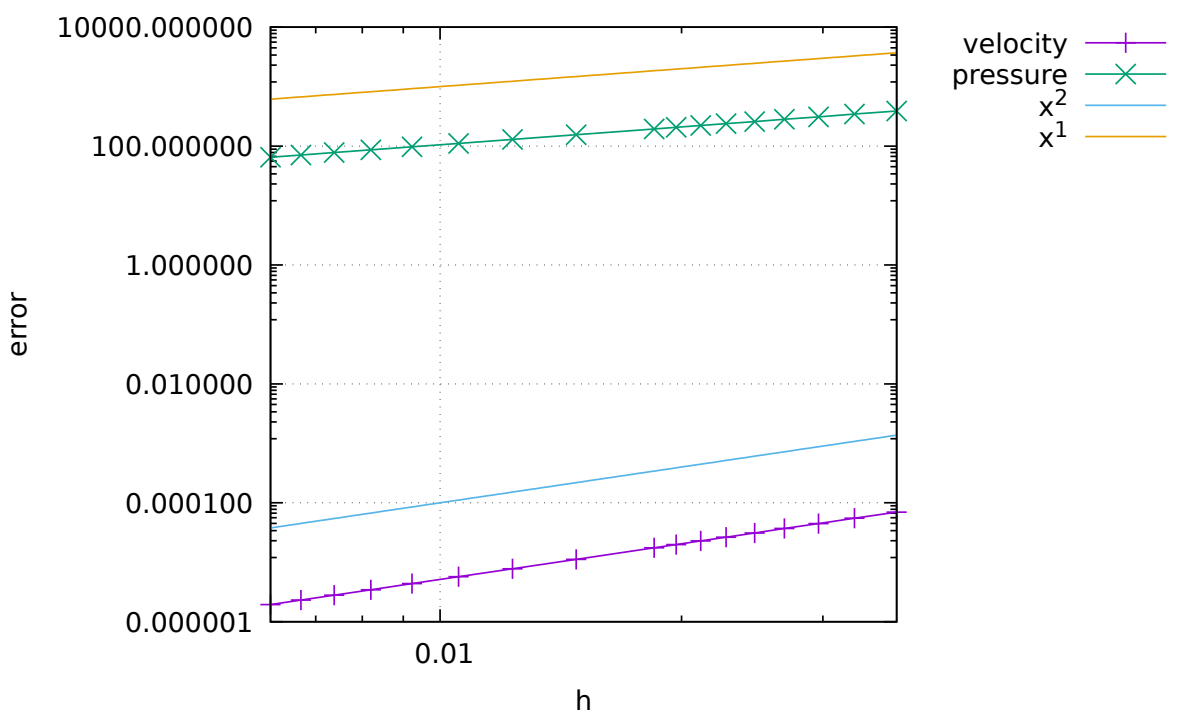
We choose $R_1 = 2890\text{km}$, $R_2 = 6371\text{km}$, $g_0 = 9.81\text{ms}^{-2}$, $\rho_0 = 3300$, $E = 6 \cdot 10^{10}$, $\nu = 0.49$.



radial profiles of the displacement and pressure fields



displacement and pressure fields in the domain



Stone 37: marker advection and population control



The domain is a unit square. The Stokes equations are not solved, the velocity is prescribed everywhere in the domain as follows:

$$u = -(z - 0.5) \quad (772)$$

$$v = 0 \quad (773)$$

$$w = (x - 0.5) \quad (774)$$

At the moment, velocity is computed on the marker itself (rk0 algorithm). When markers are advected outside, they are arbitrarily placed at location (-0.0123,-0.0123).

in construction.

Stone 38: Critical Rayleigh number

This fieldstone was developed in collaboration with Arie van den Berg.

The system is a layer of fluid between $y = 0$ and $y = 1$, with boundary conditions $T(x, y = 0) = 1$ and $T(x, y = 1) = 0$, characterized by ρ , C_p , k , η_0 . The Rayleigh number of the system is

$$\text{Ra} = \frac{\rho_0 g_0 \alpha \Delta T h^3}{\eta_0 \kappa}$$

We have $\Delta T = 1$, $h = 1$ and choose $\kappa = 1$ so that the Rayleigh number simplifies to $\text{Ra} = \rho_0 g_0 \alpha / \eta_0$.

The Stokes equation is $\vec{\nabla} \cdot \boldsymbol{\sigma} + \vec{b} = \vec{0}$ with $\vec{b} = \rho \vec{g}$. Then the components of this equation on the x - and y -axis are:

$$(\vec{\nabla} \cdot \boldsymbol{\sigma})_x = -\rho \vec{g} \cdot \vec{e}_x = 0 \quad (775)$$

$$(\vec{\nabla} \cdot \boldsymbol{\sigma})_y = -\rho \vec{g} \cdot \vec{e}_y = \rho g_0 \quad (776)$$

since \vec{g} and \vec{e}_y are in opposite directions ($\vec{g} = -g_0 \vec{e}_y$, with $g_0 > 0$). The stream function formulation of the incompressible isoviscous Stokes equation is then

$$\nabla^4 \Psi = \frac{g_0}{\eta_0} \frac{\partial \rho}{\partial x}$$

Assuming a linearised density field with regards to temperature $\rho(T) = \rho_0(1 - \alpha T)$ we have

$$\frac{\partial \rho}{\partial x} = -\rho_0 \alpha \frac{\partial T}{\partial x}$$

and then

$$\boxed{\nabla^4 \Psi = -\frac{\rho_0 g_0 \alpha}{\eta_0} g \frac{\partial T}{\partial x} = -Ra \frac{\partial T}{\partial x}} \quad (777)$$

For small perturbations of the conductive state $T_0(y) = 1 - y$ we define the temperature perturbation $T_1(x, y)$ such that

$$T(x, y) = T_0(y) + T_1(x, y)$$

The temperature perturbation T_1 satisfies the homogeneous boundary conditions $T_1(x, y = 0) = 0$ and $T_1(x, y = 1) = 0$. The temperature equation is

$$\rho C_p \frac{DT}{Dt} = \rho C_p \left(\frac{\partial T}{\partial t} + \vec{v} \cdot \vec{\nabla} T \right) = \rho C_p \left(\frac{\partial T_0 + T_1}{\partial t} + \vec{v} \cdot \vec{\nabla}(T_0 + T_1) \right) = k \Delta (T_0 + T_1)$$

and can be simplified as follows:

$$\rho C_p \left(\frac{\partial T_1}{\partial t} + \vec{v} \cdot \vec{\nabla} T_0 \right) = k \Delta T_1$$

since T_0 does not depend on time, $\Delta T_0 = 0$ and we assume the nonlinear term $\vec{v} \cdot \vec{\nabla} T_1$ to be second order (temperature perturbations and coupled velocity changes are assumed to be small). Using the relationship between velocity and stream function $v_y = -\partial_x \Psi$ we have $\vec{v} \cdot \vec{\nabla} T_0 = -v_y = \partial_x \Psi$ and since $\kappa = k/\rho C_p = 1$ we get

$$\boxed{\frac{\partial T_1}{\partial t} - \kappa \Delta T_1 = -\frac{\partial \Psi}{\partial x}} \quad (778)$$

Looking at these equations, we immediately think about a separation of variables approach to solve these equations. Both equations showcase the Laplace operator Δ , and the eigenfunctions of the biharmonic operator and the Laplace operator are the same. We then pose that Ψ and T_1 can be written:

$$\Psi(x, y, t) = A_\Psi \exp(pt) \exp(\pm i k_x x) \exp(\pm i k_y y) = A_\Psi E_\psi(x, y, t) \quad (779)$$

$$T_1(x, y, t) = A_T \exp(pt) \exp(\pm i k_x x) \exp(\pm i k_y y) = A_T E_T(x, y, t) \quad (780)$$

where k_x and k_y are the horizontal and vertical wave number respectively. Note that we then have

$$\nabla^2 \Psi = -(k_x^2 + k_y^2) \Psi \quad \nabla^2 T_1 = -(k_x^2 + k_y^2) T_1$$

The boundary conditions on T_1 , coupled with a choice of a real function for the x dependence yields:

$$E_T(x, y, t) = \exp(pt) \cos(k_x x) \sin(n\pi y).$$

from here onwards check for minus signs!

The velocity boundary conditions are $v_y(x, y=0) = 0$ and $v_y(x, y=1) = 0$ which imposes conditions on $\partial\Psi/\partial x$ and we find that we can use the same y dependence as for T_1 . Choosing again for a real function for the x dependence yields:

$$E_\Psi(x, y, t) = \exp(pt) \sin(k_x x) \sin(n\pi z)$$

We then have

$$\Psi(x, y, t) = A_\Psi \exp(pt) \sin(k_x x) \sin(n\pi z) = A_\Psi E_\Psi(x, y, t) \quad (781)$$

$$T_1(x, y, t) = A_T \exp(pt) \cos(k_x x) \sin(n\pi z) = A_T E_T(x, y, t) \quad (782)$$

In what follows we simplify notations: $k = k_x$. Then the two PDEs become:

$$pT_1 + \kappa(k^2 + n^2\pi^2) - kA_\Psi \exp(pt) \cos(k_x x) \sin(n\pi z) = kA_\Psi E_\theta \quad (783)$$

$$-RaA_T \cos(kx) \sin(n\pi z) + \kappa(k^2 + n^2\pi^2)^2 A_\Psi = -RaA_T E_\Psi + \kappa(k^2 + n^2\pi^2)^2 A_\Psi = 0 \quad (784)$$

These equations must then be verified for all ... which leads to write:

$$\begin{pmatrix} p + (k^2 + n^2\pi^2) & -k \\ -Ra k & (k^2 + n^2\pi^2)^2 \end{pmatrix} \begin{pmatrix} A_\theta \\ A_\Psi \end{pmatrix} = \begin{pmatrix} 0 \\ 0 \end{pmatrix}$$

The determinant of such system must be nul otherwise there is only a trivial solution to the problem, i.e. $A_\theta = 0$ and $A_\Psi = 0$ which is not helpful. CHECK/REPHRASE

$$D = [p + (k^2 + n^2\pi^2)](k^2 + n^2\pi^2)^2 - Ra k^2 = 0$$

or,

$$p = \frac{Ra k^2 - (k^2 + n^2\pi^2)^3}{(k^2 + n^2\pi^2)^2}$$

The coefficient p determines the stability of the system: if it is negative, the system is stable and both Ψ and T_1 will decay to zero (return to conductive state). If $p = 0$, then the system is meta-stable, and if $p > 0$ then the system is unstable and the perturbations will grow. The threshold is then $p = 0$ and the solution of the above system is

Stone 39: chpe15

The Drucker-Prager yield function is given by the function f :

$$f = p \sin \phi + c \cos \phi - \tau$$

where τ is the square root of the second invariant of the deviatoric stress. We have

$$p = \frac{1}{2}(\sigma_1 + \sigma_3)$$

and

$$\tau = \frac{1}{2}(\sigma_1 - \sigma_3)$$

Inserting these into f yields:

$$f = \frac{1}{2}(\sigma_1 + \sigma_3) \sin \phi + c \cos \phi - \frac{1}{2}(\sigma_1 - \sigma_3)$$

The yield condition $f = 0$ can be reworked as follows:

$$\sigma_1 - \frac{1 + \sin \phi}{1 - \sin \phi} \sigma_3 - 2 \frac{\cos \phi}{1 - \sin \phi} c = 0$$

The third term can further be modified as follows:

$$\frac{\cos \phi}{1 - \sin \phi} = \frac{\sqrt{1 - \sin^2 \phi}}{\sqrt{(1 - \sin \phi)^2}} = \frac{\sqrt{(1 - \sin \phi)(1 + \sin \phi)}}{\sqrt{(1 - \sin \phi)^2}} = \sqrt{\frac{1 + \sin \phi}{1 - \sin \phi}}$$

Finally, we define N_ϕ as follows

$$N_\phi = \frac{1 + \sin \phi}{1 - \sin \phi}$$

so that the yield condition becomes:

$$\sigma_1 - N_\phi \sigma_3 - 2\sqrt{N_\phi} c = 0$$

which is Eq. 3 of the article by Choi & Petersen [338].

This paper offers a solution to the problem of the angle of shear bands in geodynamic models. The underlying idea is based on simple modifications brought to existing incompressible flow codes. Note that the codes featured in that paper also implemented elastic behaviour but this can be easily switched off by setting $Z = 1$ in their equations.

Their plasticity implementation starts with a modification of the continuity equation:

$$\vec{\nabla} \cdot \vec{\nabla} = R = 2 \sin \psi \dot{\varepsilon}_p$$

where R is the dilation rate, Ψ is the dilation angle and $\dot{\varepsilon}_p$ is the square root of the second invariant of the plastic strain rate.

Under this assumption, the deviatoric strain rate tensor is given by

$$\dot{\varepsilon}^d(\vec{\nabla}) = \dot{\varepsilon}(\vec{\nabla}) - \frac{1}{3} \text{Tr}[\dot{\varepsilon}(\vec{\nabla})] \mathbf{1} = \dot{\varepsilon}(\vec{\nabla}) - \frac{1}{3} \vec{\nabla} \cdot \vec{\nabla} \mathbf{1} = \dot{\varepsilon}(\vec{\nabla}) - \frac{1}{3} R \mathbf{1}$$

Turning now to the momentum conservation equation:

$$\begin{aligned} -\vec{\nabla} p + \vec{\nabla} \cdot \boldsymbol{\tau} &= -\vec{\nabla} p + \vec{\nabla} \cdot (2\eta \dot{\varepsilon}^d(\vec{\nabla})) \\ &= -\vec{\nabla} p + \vec{\nabla} \cdot \left[2\eta \left(\dot{\varepsilon}(\vec{\nabla}) - \frac{1}{3} R \mathbf{1} \right) \right] \\ &= -\vec{\nabla} p + \vec{\nabla} \cdot (2\eta \dot{\varepsilon}(\vec{\nabla})) - \frac{2}{3} \vec{\nabla} (\eta R) \end{aligned} \tag{785}$$

The last term is then an addition to the right hand side of the momentum equation and its weak form is as follows:

$$\vec{f}' = \int_{\Omega} N_v \frac{2}{3} \vec{\nabla}(\eta R) dV = \frac{4}{3} \sin \Psi \int_{\Omega} N_v \vec{\nabla}(\eta \dot{\varepsilon}_p) dV$$

This formulation proves to be problematic since in order to compute the gradient, we would need the viscosity and the plastic strain rate on the mesh nodes and both these quantities are effectively computed on the quadrature points. One option could be to project those quadrature values onto the nodes, which may introduce interpolation errors/artefacts and/or smoothing. Another option is to resort to integration by parts:

$$\int_{\Omega} N_v \vec{\nabla}(\eta \dot{\varepsilon}_p) dV = [N_v \eta \dot{\varepsilon}_p]_{\Gamma} - \int_{\Omega} \vec{\nabla} N_v (\eta \dot{\varepsilon}_p) dV$$

The last term is now trivial to compute since the shape function derivatives, the viscosity and the plastic strain rate are known at the quadrature points. Remains the surface term. We will neglect it for now to simplify our implementation and note that a) it will not directly affect what happens inside the domain, b) it could be somewhat important when shear bands intersect with the free surface.

$$\vec{f}' = -\frac{4}{3} \sin \psi \int_{\Omega} \vec{\nabla} N_v (\eta \dot{\varepsilon}_p) dV = -\frac{2}{3} \int_{\Omega} \vec{\nabla} N_v (\eta R) dV$$

Although the authors do indicate that they add a term in each rhs, it is not very clear how they deal with the implementation issue above. We then propose an alternative: instead of explicitly removing the deviatoric part of the strain rate as in Eq. 785 and replace the trace of the tensor by R , one could leave the term inside the matrix, thereby using a compressible form of the viscous block of the Stokes matrix. We will recover the same converged solution as before, but the path to convergence will be different than the first approach. In what follows, we denote the original approach by Choi & Petersen 'method 1' and the latter 'method 2'.

Finally, we need to define what the plastic strain rate tensor is. When using a rigid plastic rheology, the only deformation mechanism *is* plasticity so that the plastic strain rate *is* the strain rate. When using a visco-plastic rheology, the plastic strain rate is the strain rate of the zones above/at yield (the shear bands, where the vrm is active).

The 2010 brick

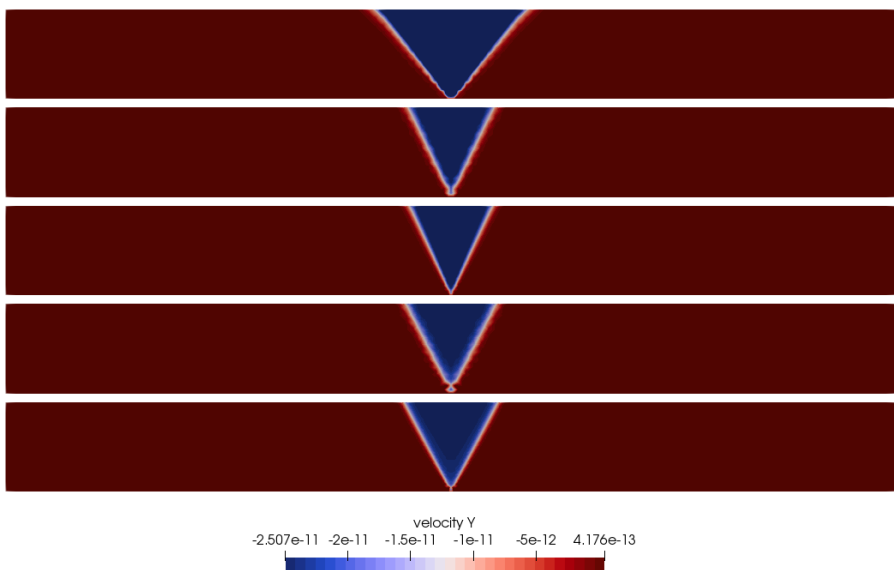
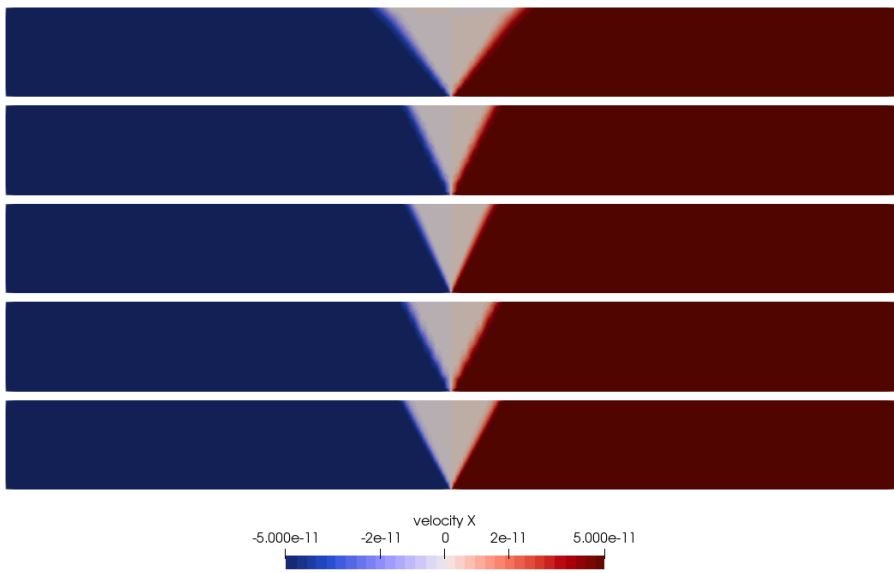
The setup is similar to the one in [944]. It is a 2D Cartesian domain filled with a single rigid-plastic material characterised by a cohesion $c = 10\text{MPa}$, an angle of friction ϕ , a dilation angle ψ and a density $\rho = 2800\text{kg/m}^3$. Extensional boundary conditions are as follows:

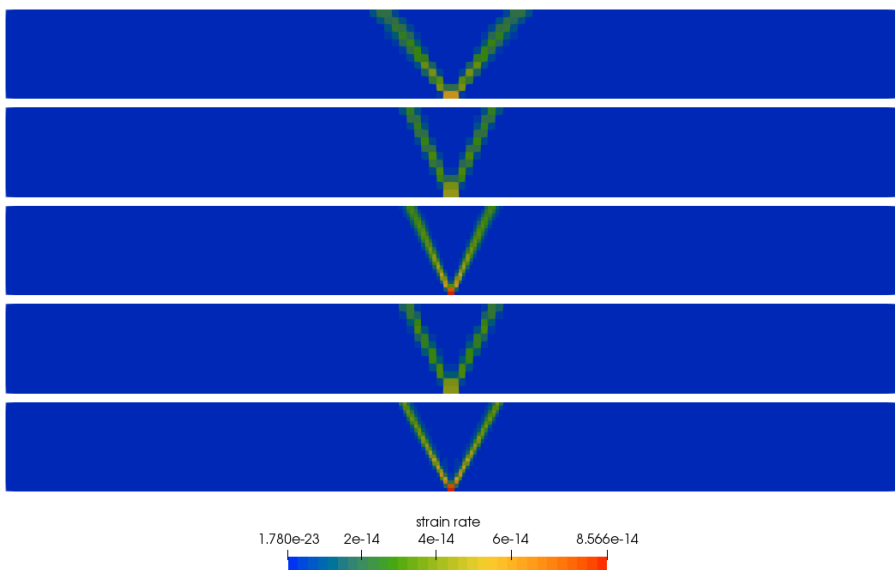
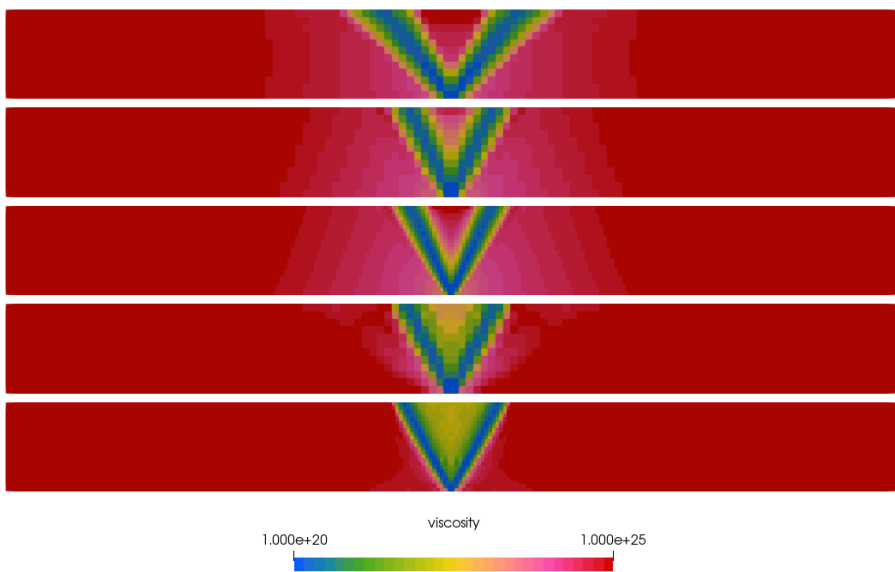
- left boundary: $u = -v_{bc}$;
- right boundary: $u = +v_{bc}$;
- bottom boundary: $v = 0$, $u = -v_{bc}$ for $x < L_x/2$, $u = +v_{bc}$ for $x > L_x/2$, and $u = 0$ if $x = L_x/2$;
- top boundary: zero traction.

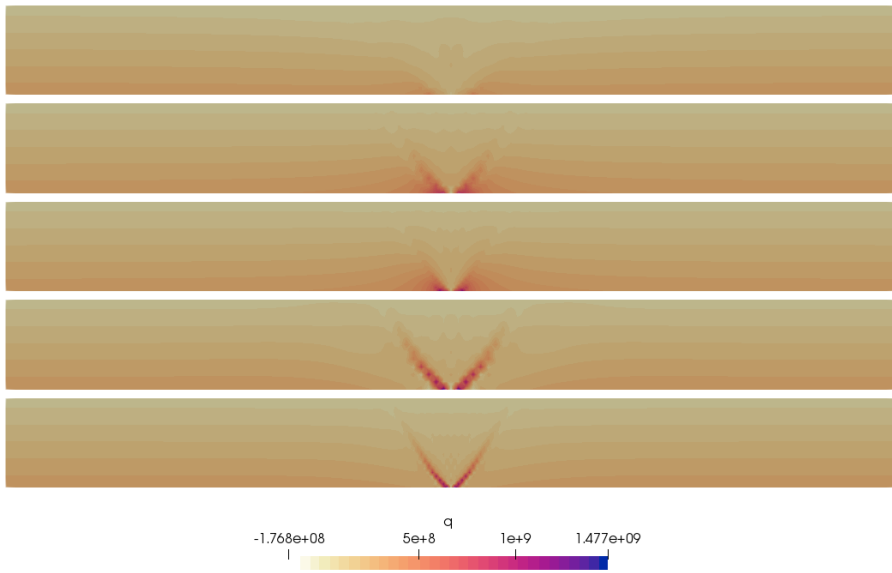
For compressional boundary conditions the signs of all horizontal velocities should be reversed. The nonlinear tolerance is set to $\text{tol} = 10^{-6}$. Nonlinear iterations stop when maximum of the normalised nonlinear residual reaches the desired tolerance.

Following Choi & Petersen [338], we run the experiment with an associative ($\phi = \psi$) plasticity and a non associative one ($\psi = 0$, i.e. $R = 0$). This second approach is essentially what many codes do.

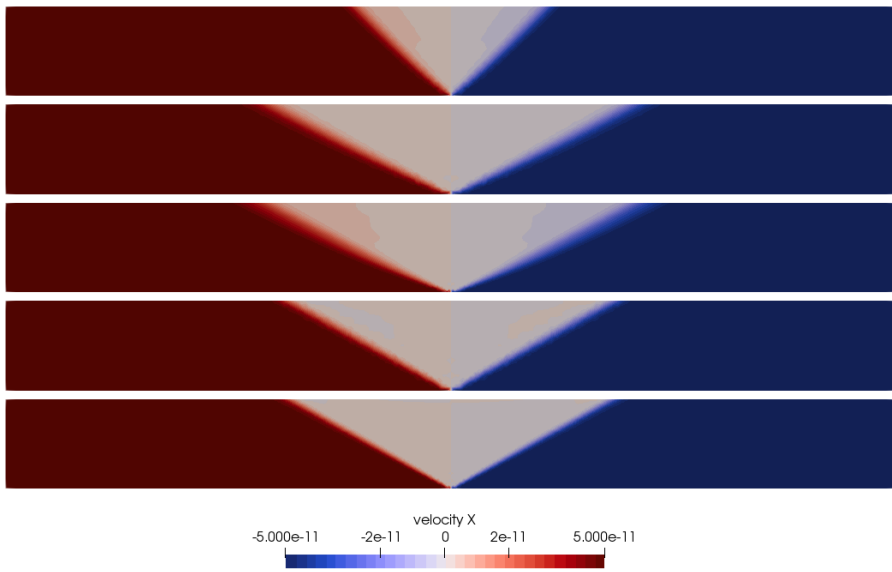
The velocity, pressure, strain rate, dilation rate, and velocity divergence are shown hereunder both in extension and compression.

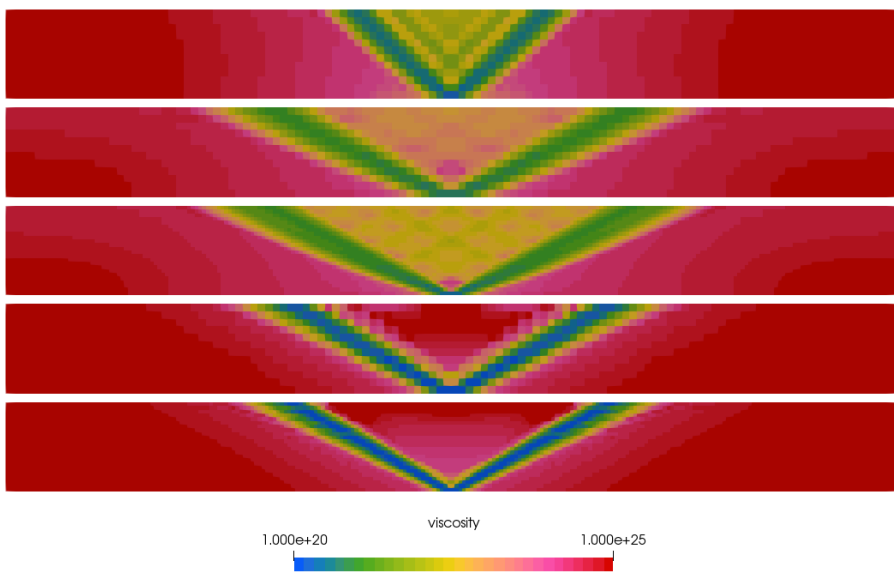
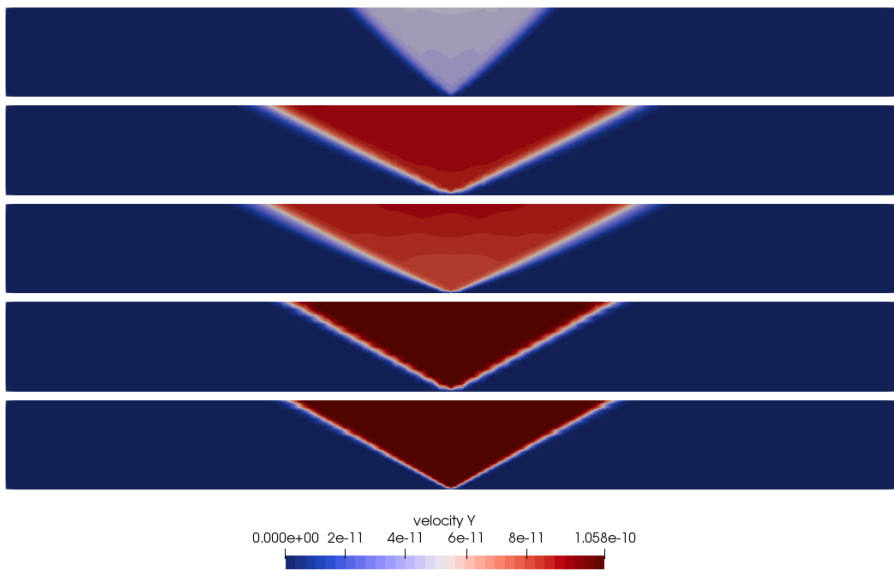


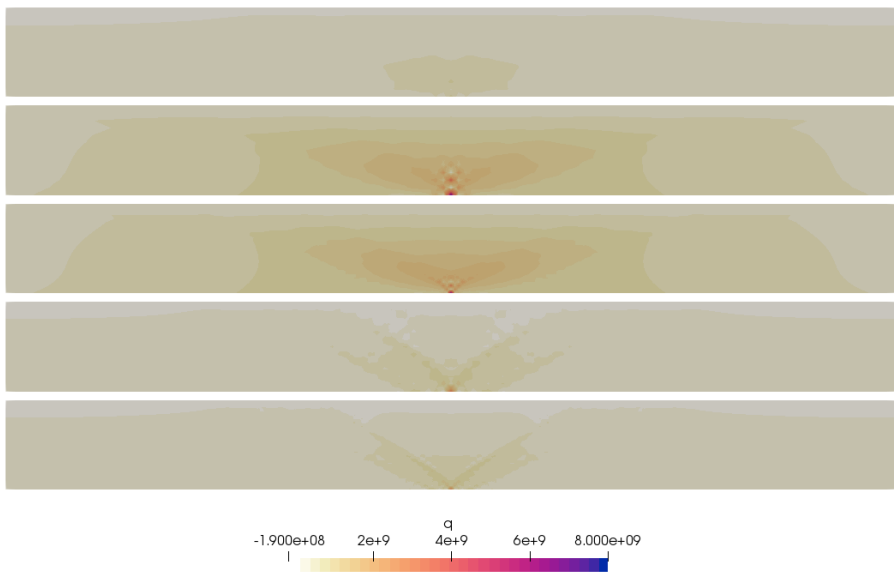
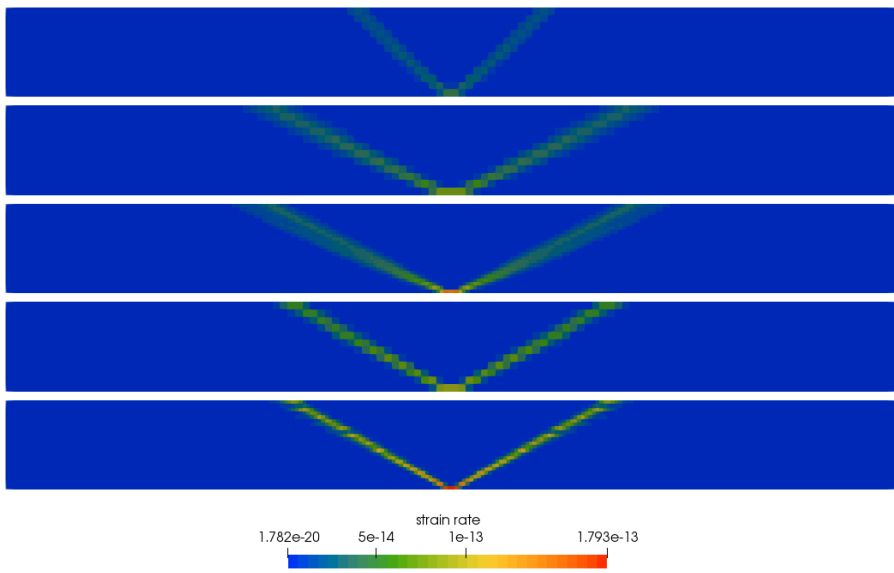




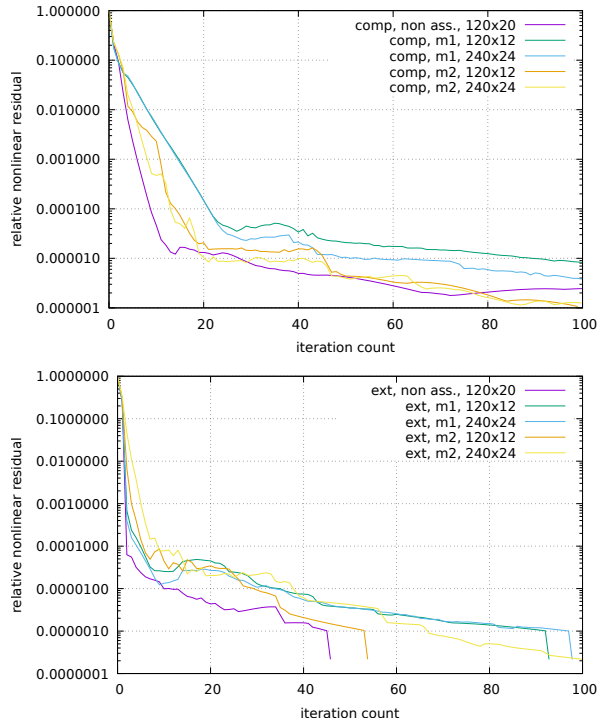
Extension. 1st row: Non-associative plasticity; 2nd and 3rd row: associative plasticity ($\psi = \phi$) with method 1 for two resolutions 120x12 and 240; 4th and 5th row: associative plasticity ($\psi = \phi$) with method 2 for two resolutions 120x12 and 240



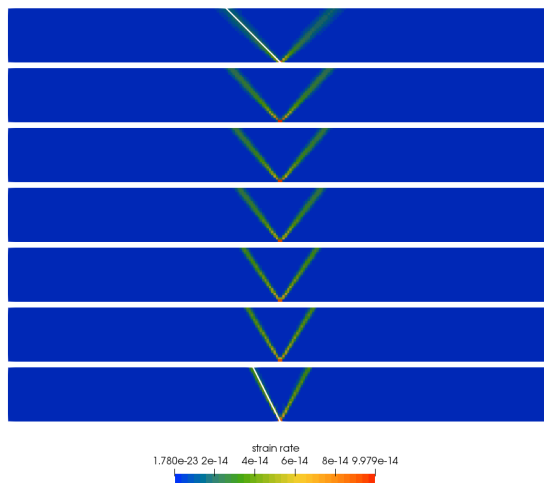


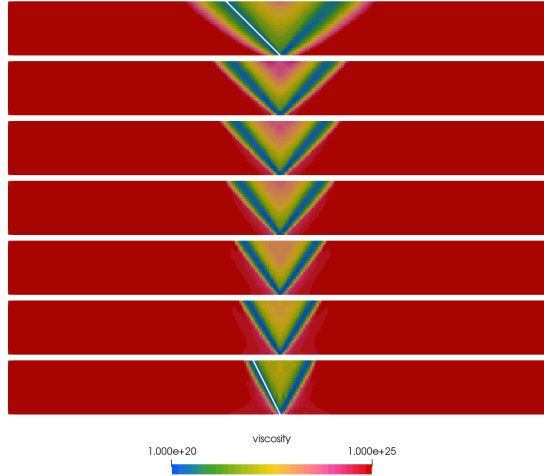


Compression. 1st row: Non-associative plasticity; 2nd and 3rd row: associative plasticity ($\psi = \phi$) with method 1 for two resolutions 120x12 and 240; 4th and 5th row: associative plasticity ($\psi = \phi$) with method 2 for two resolutions 120x12 and 240



One can also run the extension model for $\phi = \psi = 0, 5, 10, 15, 20, 25, 30^\circ$





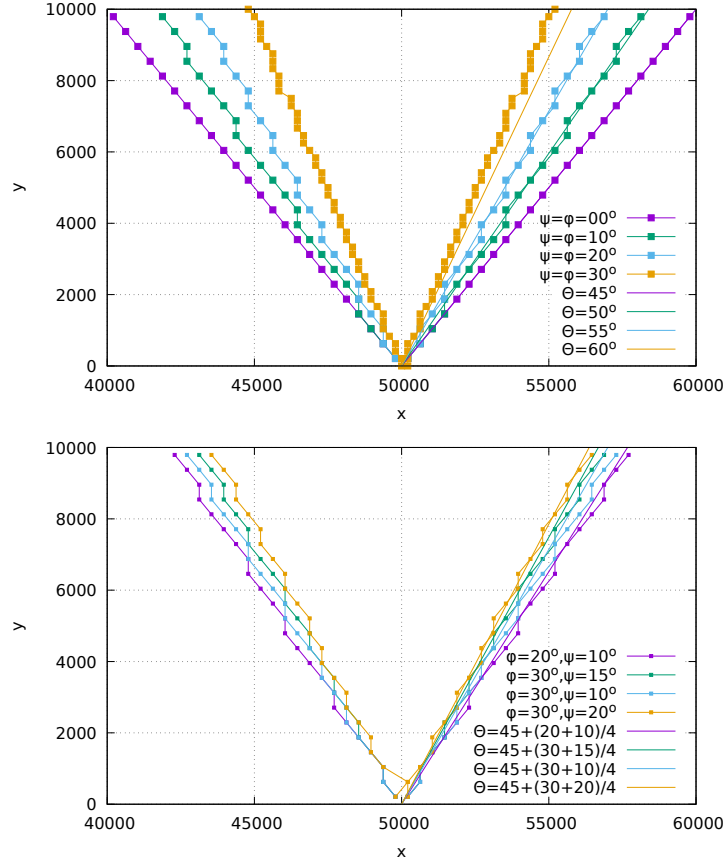
Three angles are mechanically stable (e.g. [944]):

$$\theta = \frac{\pi}{4} \pm \frac{\psi}{2} \quad \text{Roscoe angle}$$

$$\theta = \frac{\pi}{4} \pm \frac{\phi}{2} \quad \text{Coulomb angle}$$

$$\theta = \frac{\pi}{4} \pm \frac{\phi + \psi}{4} \quad \text{Arthur angle}$$

In the case of associative plasticity, $\phi = \psi$, so that all three angles are the same. Per row of elements, and per half of the domain (left and right) we find the element with the highest strain-rate and record their center coordinates on the figure hereunder. These elements are shown for $\phi = \psi = \{0, 10, 20, 30\}^\circ$ alongside a line corresponding to the expected analytical shear band angle value.



Results obtained on a 240x24 grid, max 50 nl iterations.

Note that benchmarking this is not easy. One solution Timo and I found was to add a velocity field $\vec{v} = (x, y, z)$ (with $\nabla \cdot \vec{v} = 3$) to an existing analytical problem, e.g. the Burstedde benchamrk.

The 2016 brick

The setup is similar to the one in [1473]. It is a 2D Cartesian domain filled with an isoviscous layer at the bottom and a visco-plastic material on top, as shown here:

In what follows the nonlinear tolerance is set to 10^{-6} . Due to a lack of resolution, I do not implement the rounded edges of the seed. U_0 is set to 25mm/yr and the background viscosity of the brittle layer is set to $\eta_0 = 10^{24}$ Pa.s. Note that the effective viscosity of the brittle layer is computed as follows:

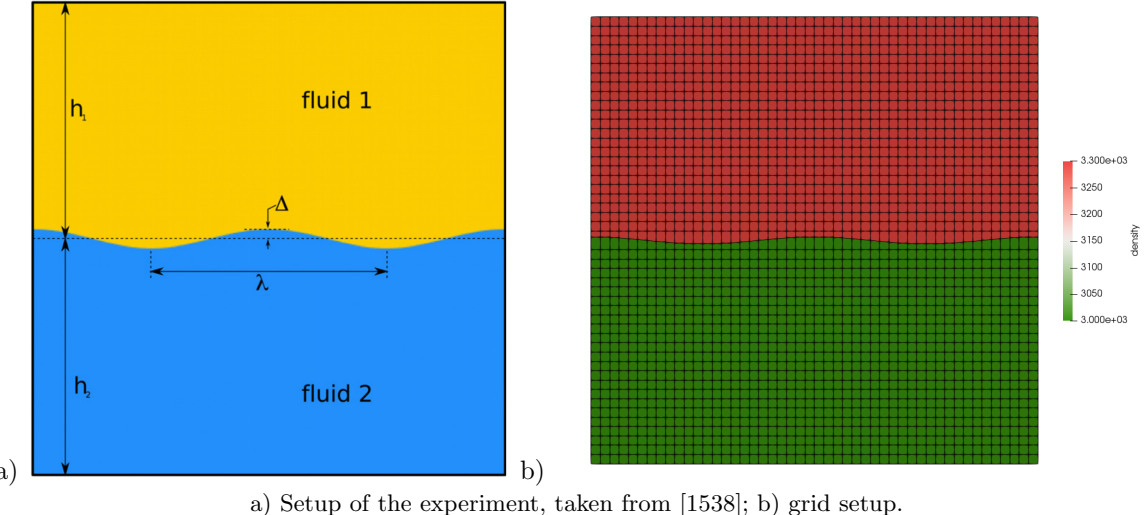
$$\eta_{eff} = \left(\frac{1}{\eta_0} + \frac{1}{\eta_p} \right)^{-1} = \left(\frac{1}{\eta_0} + \frac{2\dot{\epsilon}_{ii}}{Y} \right)^{-1}$$

with $Y = p \sin \phi + c \cos \phi$. Note that the pressure colour bars in Fig(6) of [1473] are most likely not correct at all, and in order for my results to look like theirs I had to change it for VM, DDM and DP.

Stone 40: Rayleigh-Taylor instability

This benchmark is carried out in [466, 656, 1538] and is based on the analytical solution by Ramberg (1968). It consists of a two-layer system driven by gravity. Free slip are imposed on the sides while no-slip boundary conditions are imposed on the top and the bottom of the box.

Fluid 1 (ρ_1, η_1) of thickness h_1 overlays fluid 2 (ρ_2, η_2) of thickness h_2 (with $h_1 + h_2 = L_y$). An initial sinusoidal disturbance of the interface between these layers is introduced and is characterised by an amplitude Δ and a wavelength $\lambda = L_x/2$ as shown in Figure ??.



a) Setup of the experiment, taken from [1538]; b) grid setup.

Under this condition, the velocity of the diapiric growth v_y is given by the relation

$$\frac{v_y}{\Delta} = -K \frac{\rho_1 - \rho_2}{2\eta_2} h_2 g$$

with the dimensionless growth factor K being

$$K = \frac{-d_{12}}{c_{11}j_{22} - d_{12}i_{21}}$$

and

$$c_{11} = \frac{\eta_1 2\phi_1^2}{\eta_2(\cosh 2\phi_1 - 1 - 2\phi_1^2)} - \frac{2\phi_2^2}{\cosh 2\phi_2 - 1 - 2\phi_2^2} \quad (786)$$

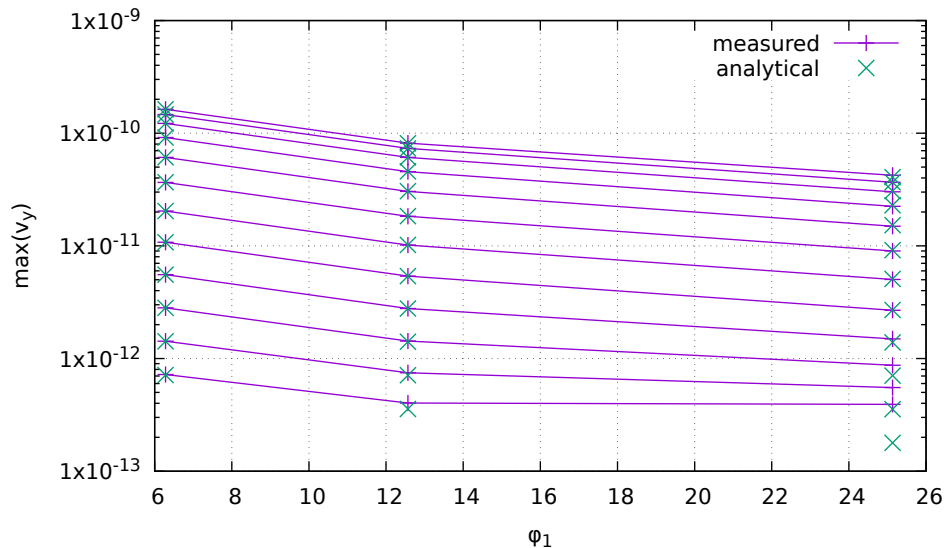
$$d_{12} = \frac{\eta_1(\sinh 2\phi_1 - 2\phi_1)}{\eta_2(\cosh 2\phi_1 - 1 - 2\phi_1^2)} + \frac{\sinh 2\phi_2 - 2\phi_2}{\cosh 2\phi_2 - 1 - 2\phi_2^2} \quad (787)$$

$$i_{21} = \frac{\eta_1 \phi_2 (\sinh 2\phi_1 + 2\phi_1)}{\eta_2(\cosh 2\phi_1 - 1 - 2\phi_1^2)} + \frac{\phi_2 (\sinh 2\phi_2 + 2\phi_2)}{\cosh 2\phi_2 - 1 - 2\phi_2^2} \quad (788)$$

$$j_{22} = \frac{\eta_1 2\phi_1^2 \phi_2}{\eta_2(\cosh 2\phi_1 - 1 - 2\phi_1^2)} - \frac{2\phi_2^3}{\cosh 2\phi_2 - 1 - 2\phi_2^2} \quad (789)$$

$$\phi_1 = \frac{2\pi h_1}{\lambda} \quad (790)$$

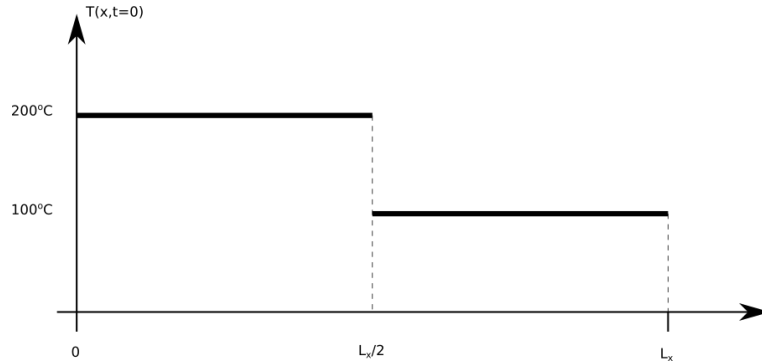
$$\phi_2 = \frac{2\pi h_2}{\lambda} \quad (791)$$



Note that in [1538] I fixed $\lambda = L_x/2$ and varied L_x . Here I keep L_x fixed and vary $\lambda = L_x/2, L_x, 4, L_x/8$. Each line corresponds to a different value of the viscosity η_2 .

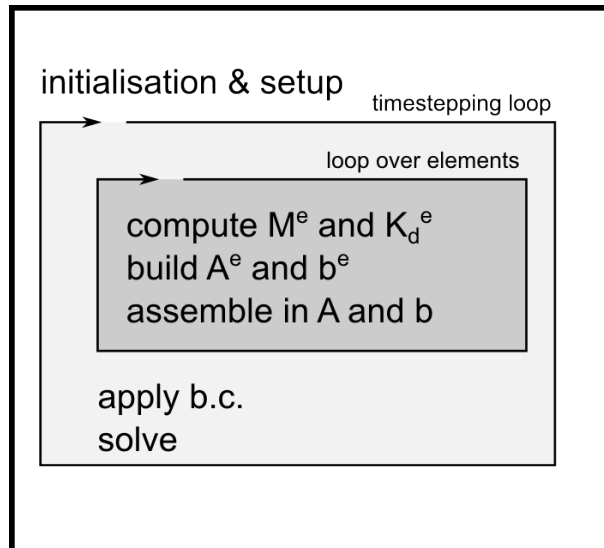
Stone 42: 1D diffusion

This is the simplest case for a FE code: a 1D (temperature) diffusion problem. It puts into practice what is presented in section 5.1. The initial temperature profile is as follows:



$$T(x, t = 0) = 200 \quad x < L_x/2 \quad T(x, t = 0) = 100 \quad x \geq L_x/2$$

The properties of the material are as follows: $\rho = 3000$, $k = 3$, $C_p = 1000$ and the domain size is $L_x = 100\text{km}$. Boundary conditions are $T(t, x = 0) = 200^\circ\text{C}$ and $T(t, x = L_x) = 100^\circ\text{C}$. There are `nelt` elements and `nnx` nodes. All elements are `hx` long. The code will carry out `nstep` timesteps of length `dt` or will stop before that when steady state is reached. The code structure is summarised hereunder:



Stone 43: the rotating cone

This benchmark originates in [473]. It is also carried out in [136]. It considers the advection of a product-cosine hill in a prescribed velocity field. The initial temperature is:

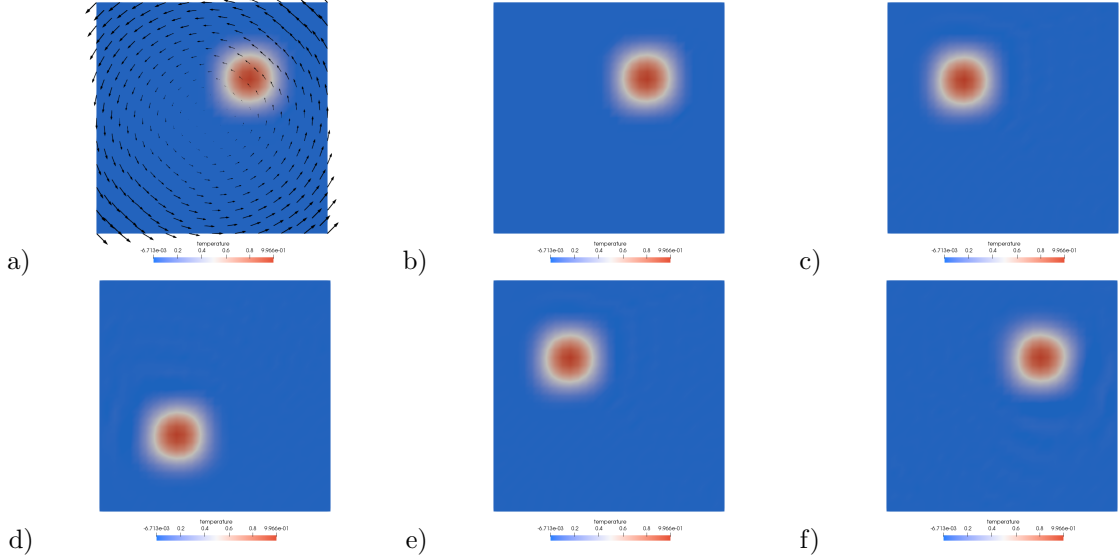
$$T_0(x, y) = \begin{cases} \frac{1}{4} \left(1 + \cos \pi \frac{x-x_c}{\sigma}\right) \left(1 + \cos \pi \frac{y-y_c}{\sigma}\right) & \text{if } (x - x_c)^2 + (y - y_c)^2 \leq \sigma^2 \\ 0 & \text{otherwise} \end{cases} \quad (792)$$

The boundary conditions are $T(x, y) = 0$ on all four sides of the unit square domain. In what follows we set $x_c = y_c = 1/6$ and $\sigma = 0.2$. The velocity field is analytically prescribed: $\vec{v} = (-(y - y_c), +(x - x_c))$.

In what follows we test the time integration scheme by setting $\alpha_T = 1$ (fully implicit formulation), $\alpha = 0$ (fully explicit formulation) and $\alpha_T = 1/2$ (Crank-Nicolson). The timestep is set to $\delta t = 2\pi/200$. The density and heat capacity values are set to 1. We monitor the minimum and maximum value of the temperature field, as well as the total thermal energy E_T in the system during the 200 time steps (2π rotation of the cone):

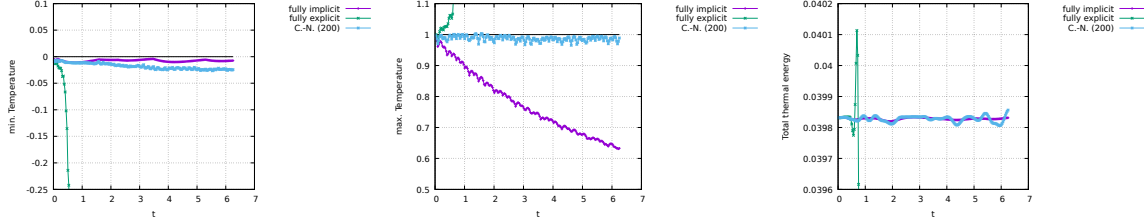
$$E_T = \int_{\Omega} \rho_0 C_p T dV = \int_{\Omega} T dV = |\Omega| \langle T \rangle \quad \text{where} \quad \langle T \rangle = \frac{1}{|\Omega|} \int_{\Omega} T dV$$

The time evolution of the temperature with the Crank-Nicolson algorithm is shown hereunder:



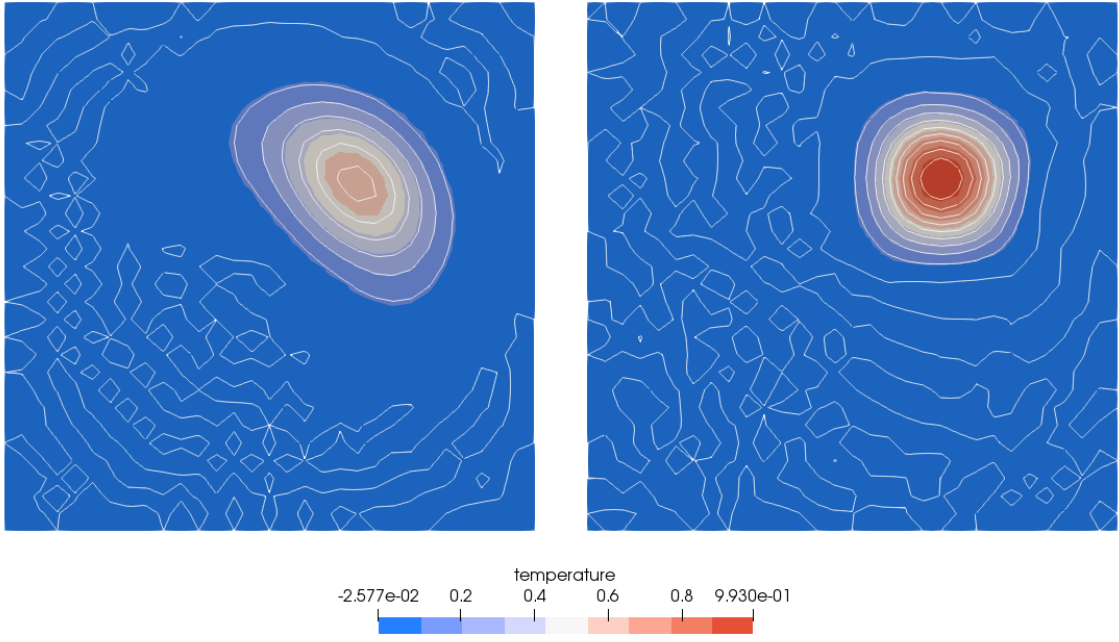
a) Velocity field and initial temperature; b,c,d,e,f) Temperature field at timesteps 0,50,100,150,199.

Turning now to the statistics, we plot $\min(T)$, $\max(T)$ and E_T as a function of time:



Time evolution of the min and max temperature and the total energy

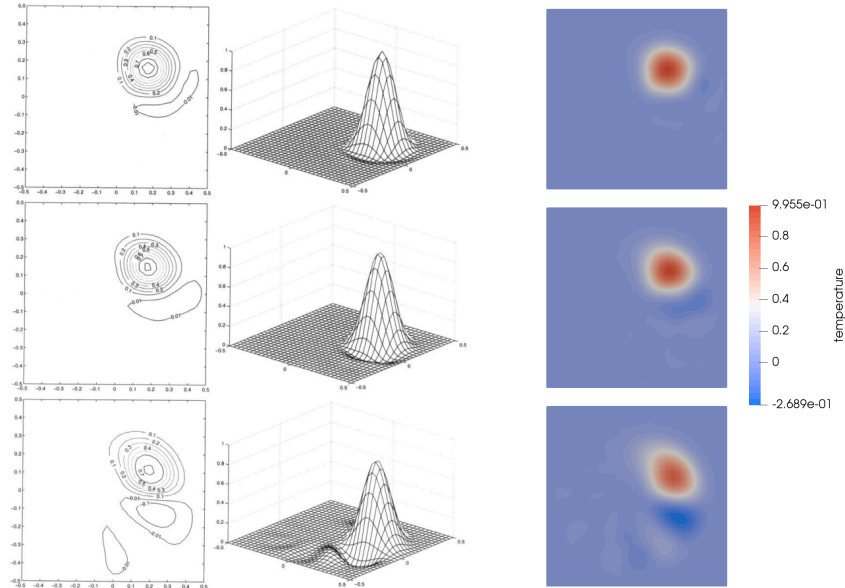
The conclusions are clear: the explicit method diverges quickly and is unusable. The fully implicit and Crank-Nicolson method yield similar energy conservation but the fully-implicit showcases a clear loss in maximum temperature as shown in the following figure:



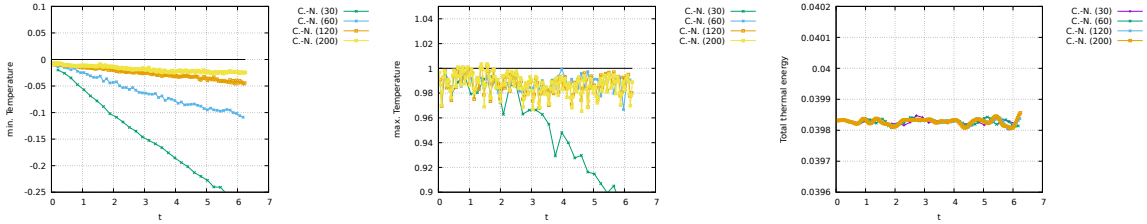
Temperature field after a full rotation with isocontours every 0.1 value.

Left: Fully-implicit; Right: Crank-Nicolson

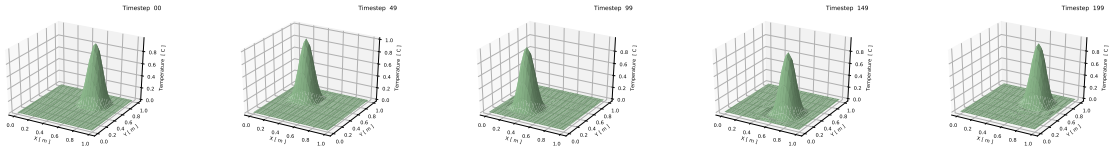
Finally we can run the experiment (still a 2π rotation) with three different time steps ($\delta t = 2\pi/30, 2\pi/60, 2\pi/120$) and we recover very similar results to those presented in [473]:



From top to bottom: $\delta t = 2\pi/120, 2\pi/60, 2\pi/30$ with Crank-Nicolson. Left panel is taken from donea & Huerta [473]



Time evolution of the min and max temperature and the total energy obtained with the Crank-Nicolson algorithm for 4 values of the timestep as indicated by the number between parenthesis.

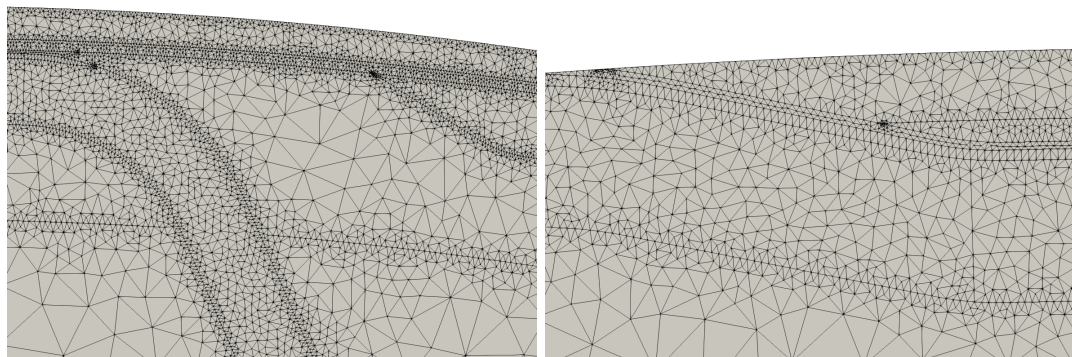
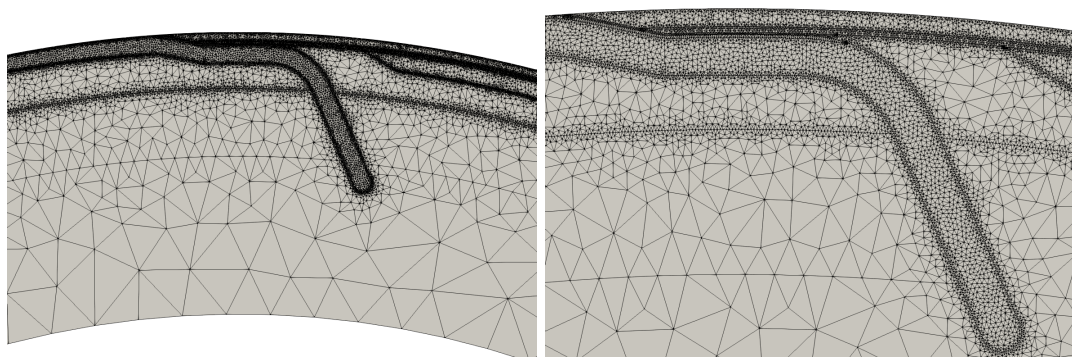
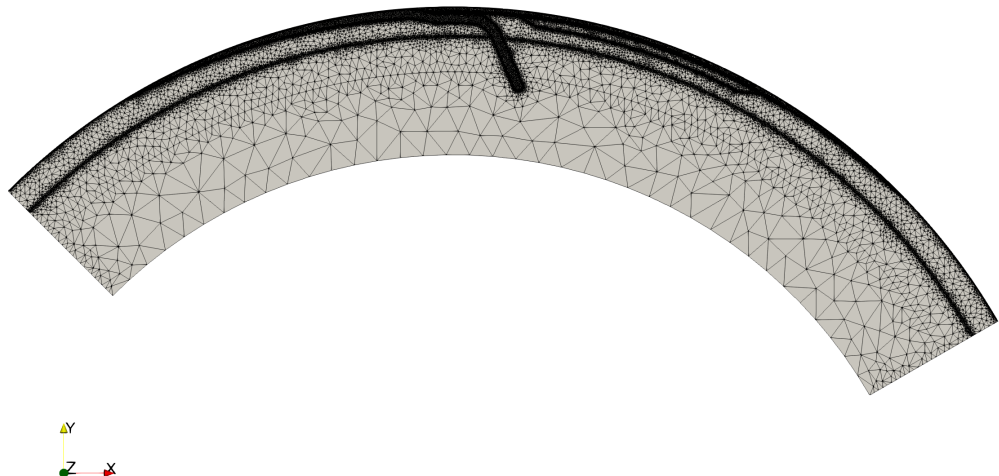


Time evolution of the temperature field for $\delta t = 2\pi/200$ with Crank-Nicolson.

Stone 44: the flat slab

WORK in PROGRESS

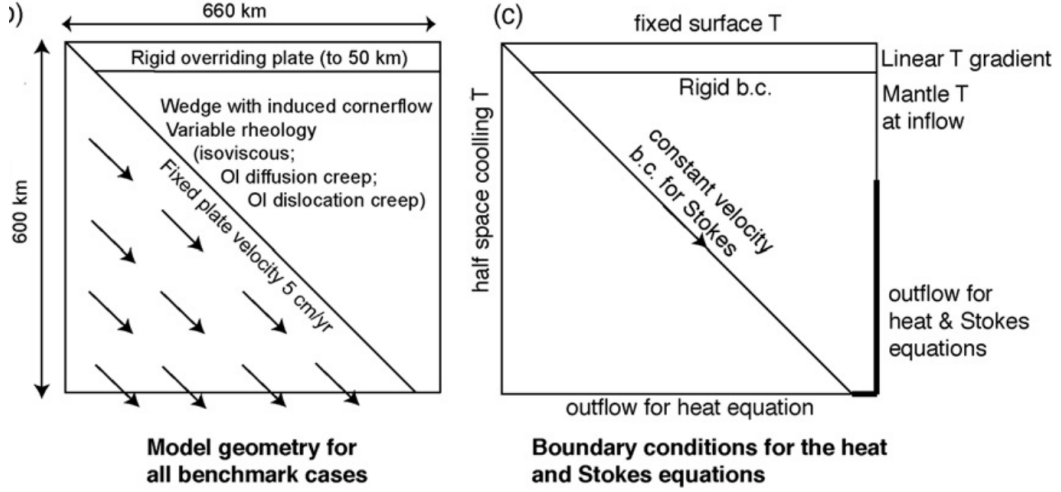
I need a list of nodes on the boundary I need a GCOORD.txt file with more decimals I need an even lower resolution grid I need the scaling factors for rho,eta, ...



Stone 45: the corner flow

This experiment is based on the benchmark paper by van Keken et al, 2008 [1611]. It shares similarities with the time dehydration processes in subduction zones work by Magni et al., 2014 [1110] and the 3D corner flow study of Plunder et al, 2018[1314]. See also Cerpa et al, 2017 [320] for a study of fluid migration in the mantle wedge.

The domain is 660km × 600km. Note that in the original paper the origin of the coordinate system is at the top left while it is at the lower left corner in our code.



As shown in the figure above, the inflow boundaries (at both wedge and trench sides) and top of the model have prescribed temperature. The wedge is assumed to be an incompressible fluid that is driven only by the kinematic forcing of the slab. The wedge is confined by the top of the slab and the base of the rigid overriding plate (located at a depth of 50km). The boundary conditions for the wedge are no-slip below the overriding plate and constant velocity along the top of the slab. The velocity boundary conditions for the boundaries of the wedge are either provided by the Batchelor cornerflow solution (cases 1a and 1b) or based on free inflow/outflow boundaries. The velocity field is discontinuous between the slab and the overriding plate. The velocity in the slab is constant (5cm/yr) and it dips at a 45° angle. There is no radiogenic shear heating.

The flow is assumed to be incompressible and buoyancy effects are neglected. All the experiments shown in the paper are at steady state, i.e. the temperature field satisfies:

$$\rho C_p \vec{v} \cdot \vec{\nabla} T = \vec{\nabla} \cdot (k \vec{\nabla} T) \quad (793)$$

In the paper a simplified diffusion creep formulation is adopted and the effective diffusion creep viscosity is computed as follows:

$$\eta_{\text{diff}} = A_{\text{diff}} \exp \frac{Q_{\text{diff}}}{RT}$$

The dislocation creep effective viscosity is given by

$$\eta_{\text{disl}} = A_{\text{disl}} \dot{\varepsilon}^{(1-n)/n} \exp \frac{Q_{\text{disl}}}{nRT}$$

Note that in both the activation volume has been set to zero, which decouples pressure from the effective viscosities. Both effective viscosities are limited with a maximum viscosity as follows:

$$\eta_{\text{diff}}^* = \left(\frac{1}{\eta_{\text{diff}}} + \frac{1}{\eta_{\text{max}}} \right)^{-1} \quad \eta_{\text{disl}}^* = \left(\frac{1}{\eta_{\text{disl}}} + \frac{1}{\eta_{\text{max}}} \right)^{-1}$$

The top boundary condition is $T_{\text{top}} = T(y = L_y) = 273K$. At the inflow boundary of the wedge (i.e. where $u < 0$)⁶³ temperature is fixed at $T_0 = 1573K$ and a linear geotherm is used at the left hand

⁶³Think about it: it makes little sense to prescribe a temperature where the fluid is leaving the domain

boundary of the overriding plate from 0 to 50 km depth. The temperature at the slab inflow boundary is described by an error-function solution for half-space cooling for 50 Myr:

$$T(x = 0, y) = T_{top} + (T_0 - T_{top}) \operatorname{erf} \frac{L_y - y}{2\sqrt{\kappa t_{50}}}$$

where t_{50} is the age of the slab.

At the slab and wedge outflow boundaries we prescribe the natural boundary condition (zero curvature) for the heat equation.

the original paper considers multiple cases:

- Case 1a: analytical cornerflow model. The wedge flow is prescribed by the analytical expression for cornerflow [80], so that we do not need to solve for the Stokes equations, only the energy equation.
- Case 1b: dynamical flow in isoviscous wedge I This case is the same as 1a, except that the solution for the wedge flow is determined by solving the Stokes equations while the Batchelor solution is imposed on the inflow and outflow boundaries. This case tests the ability of the numerical method to accurately reproduce the corner flow solution.
- Case 1c: dynamical flow in isoviscous wedge II. Same as case 1b, but with stress-free boundary conditions on the mantle wedge.
- Case 2a: dynamical flow with diffusion creep
- Case 2b: dynamical flow with dislocation creep

The temperature field as discreted values T_{ij} on an equidistant grid with 6km spacing, which is a 111×101 matrix stored row-wise starting in the top left corner. From this grid the following measurements are extracted for direct comparison:

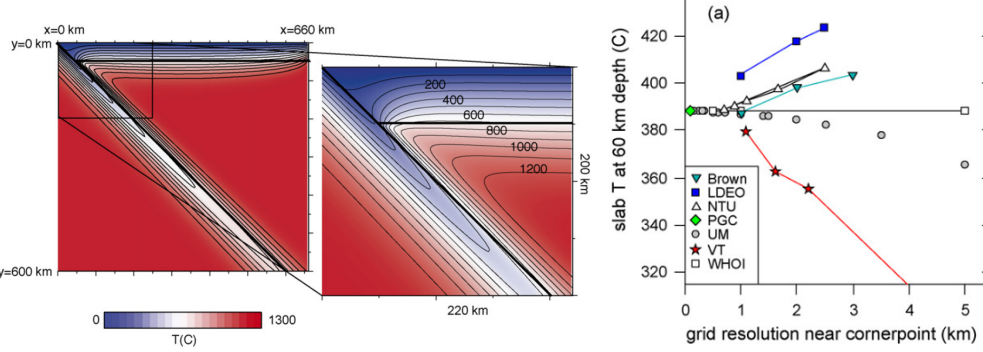
1. the temperature $T_{11,11}$ which is at coordinates (60, 60km) and just down-stream from the corner point. This provides therefore one of the most critical tests of accuracy of the numerical codes;
2. the L2 norm of the slab-wedge interface temperature between 0 and 210 km depth defined by

$$T_{\text{slab}} = \sqrt{\frac{1}{36} \sum_{i=1}^{36} T_{ii}^2}$$

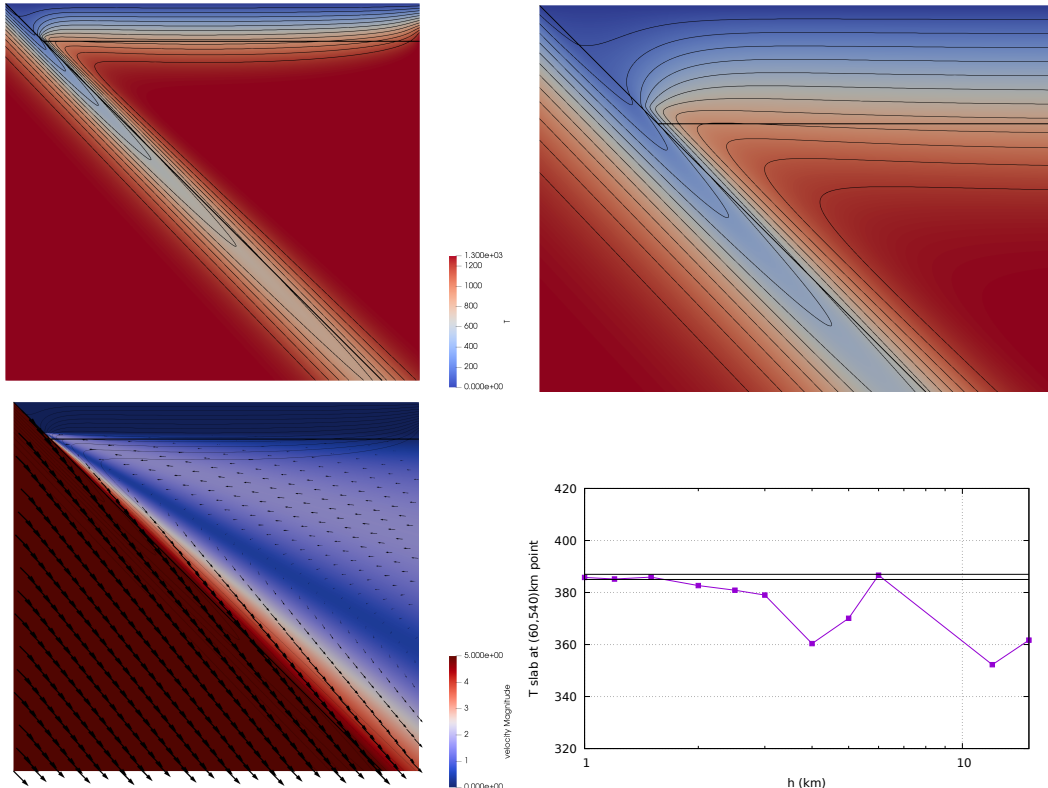
3. the L2 norm of the temperature in the triangular part of the tip of the wedge, between 54 and 120 km depth:

$$T_{\text{wedge}} = \sqrt{\frac{1}{78} \sum_{i=10}^{21} \sum_{j=10}^i T_{ij}^2}$$

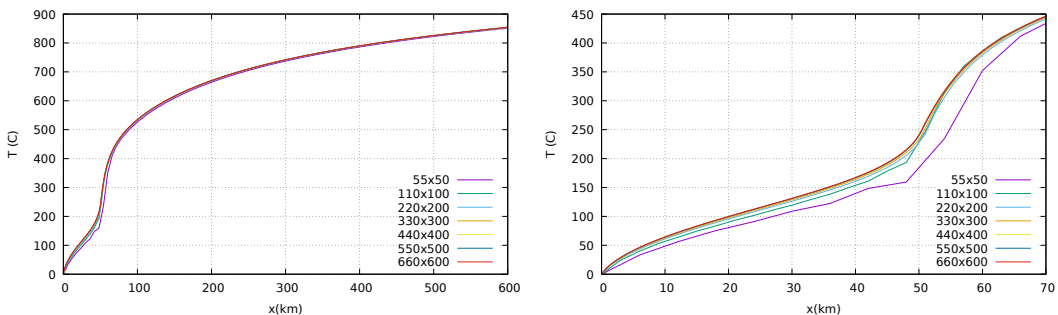
Results for case 1a



(a) Temperature prediction for case 1a. The bold lines indicate the top of the slab and base of the overriding plate. (b) Close up of the top left part of the model. Figures taken from [1611].



Results obtained on mesh 660x600(x2) elements. Black lines on lower right figure correspond to a visible range of values as shown in Fig.3a of [1611].

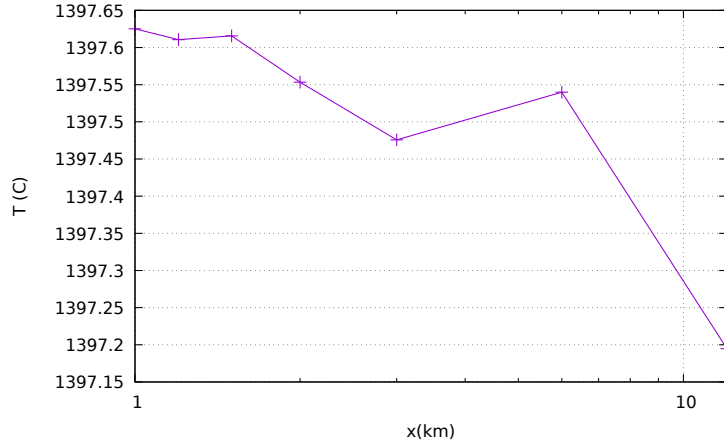


Temperature values on the slab top surface ($y = L_y - x$) plotted as a function of the x coordinate. Left is entire slab, right is zoom on the first 70km

The average temperature

$$\langle T \rangle = \frac{1}{|\Omega|} \int_{\Omega} T \, dV$$

is plotted in the following figure:



Average temperature in the domain.

We see that this measurement is not appropriate to assert whether the resolution is sufficient so that results converge to a single value, as opposed to the point wise temperature measurement presented above. The average temperature changes by about 0.4 for an average value of about 1397, which is not much for a factor 12 increase in resolution (from 55x50 to 660x600).

carry out other two measurements (need interpolation onto other grid for this

Results for case 1b

TODO

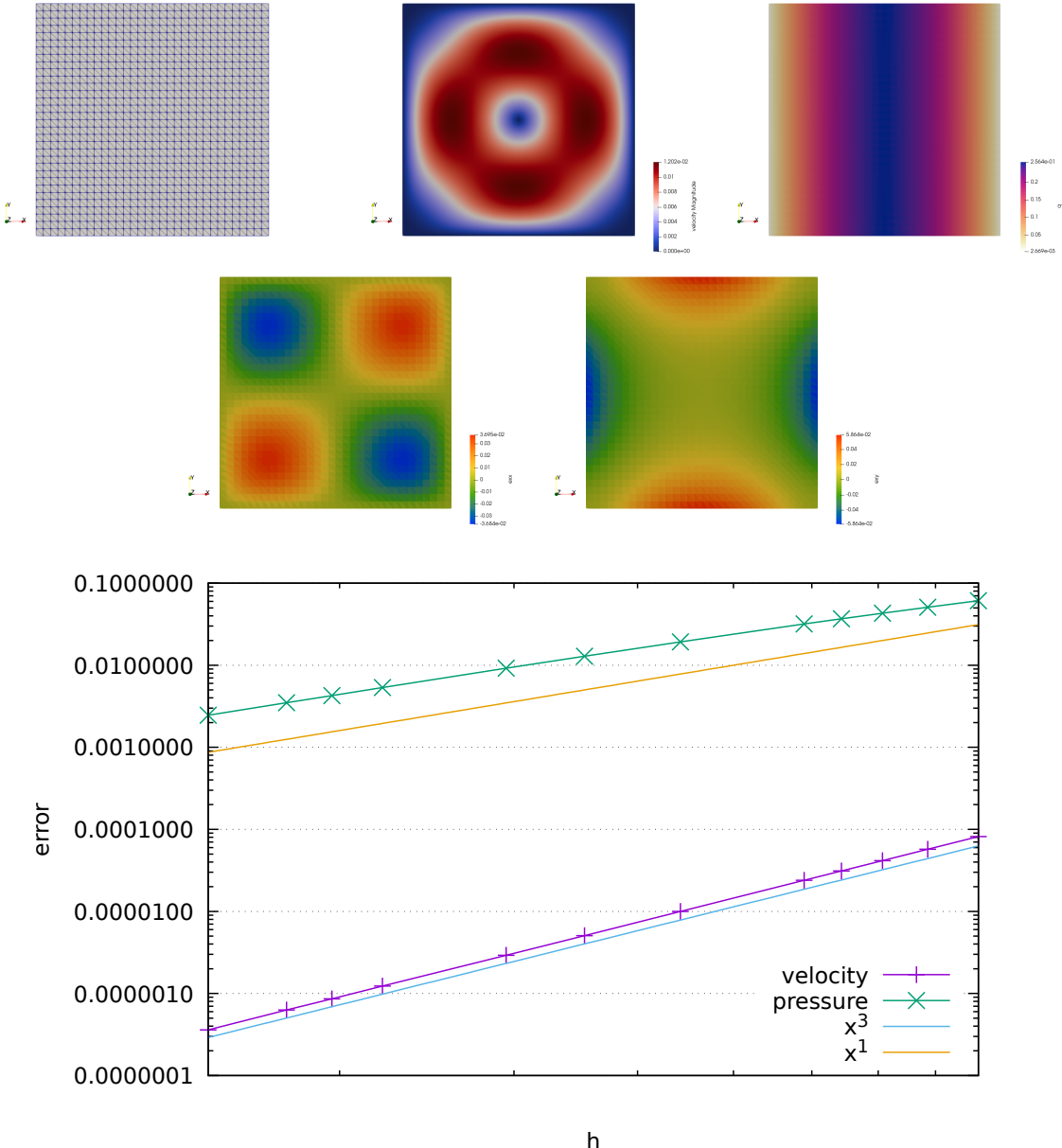
Results for case 1c

TODO

Stone 46: MMS1 with Crouzeix-Raviart ($P_2^+ \times P_{-1}$) elements

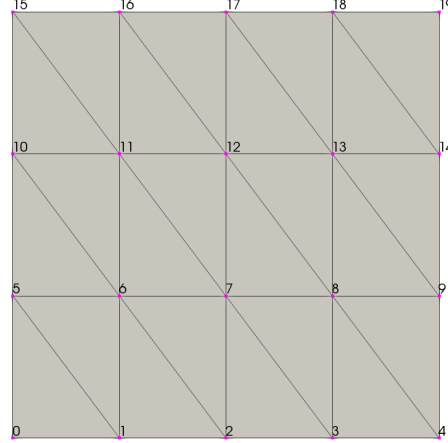
This stone showcases the Crouzeix-Raviart element (see Section 6.2.9) used to solve the analytical problem "Donea & Huerta" (see Section 8.6.1).

Out of convenience the pressure is set to zero at location $(x, y) = (1, 1)$, so that the analytical solution is now $p(x, y) = x(1 - x)$.



Stone 47: MMS1 with MINI ($P_1^+ \times P_1$) elements

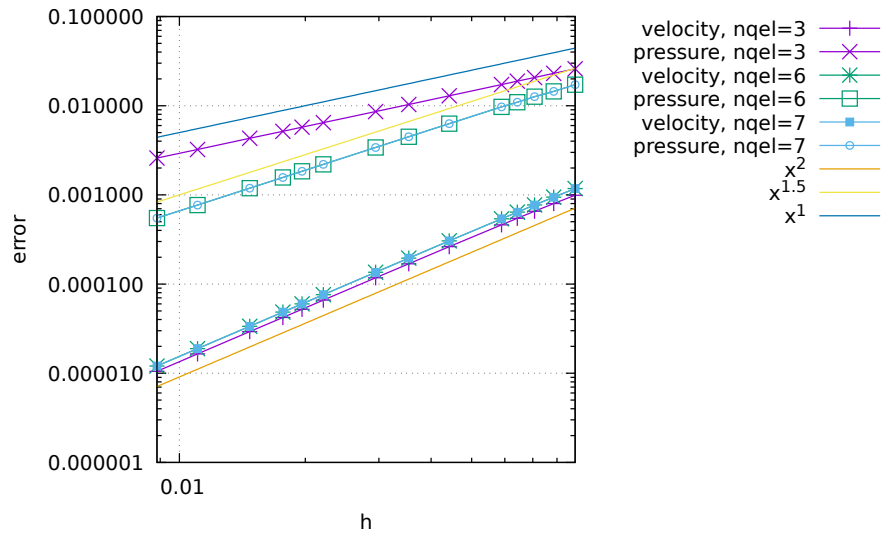
The grid is composed of triangles but for simplicity these are obtained by splitting rectangles in two, as shown hereunder:



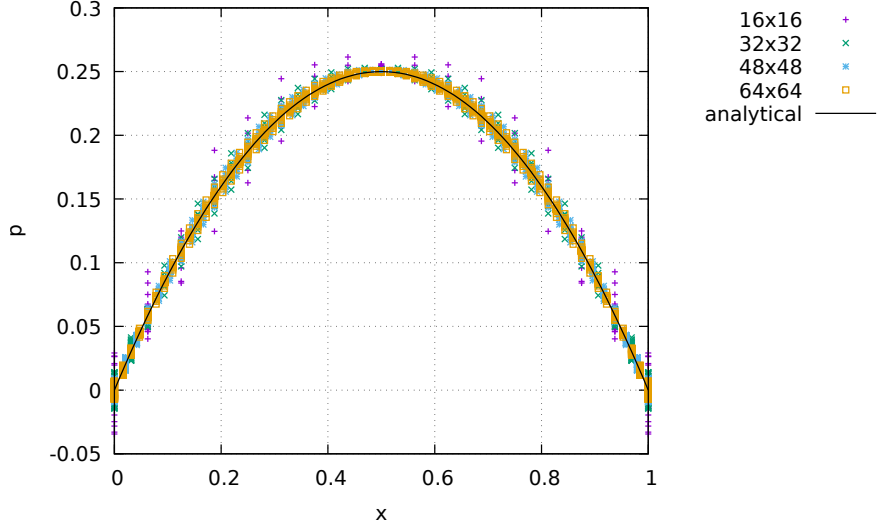
Not shown are the nodes for the bubbles in the middle of each triangle.

This stone showcases the MINI element (see Section 6.2.7) used to solve the analytical problem "Donea & Huerta" (see Section 8.6.1). Out of convenience the pressure is set to zero at location $(x, y) = (1, 1)$, so that the analytical solution is now $p(x, y) = x(1 - x)$.

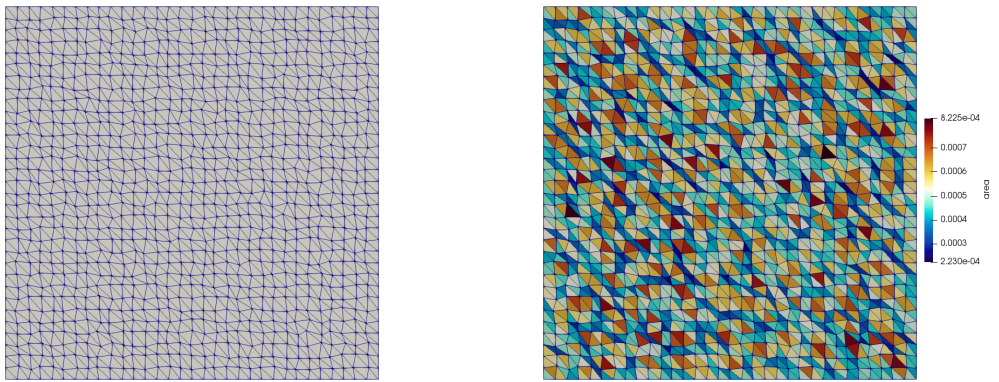
As an experiment I have run convergence tests for two cases: using $nqel=3$ quadrature points and using $nqel=6$ quadrature points. We find that the velocity and pressure errors converge depend on this crucial parameter. For $nqel=3$ the velocity and pressure errors converge quadratically and linearly respectively but for $nqel=6$ they converge as h^2 and $h^{1.5}$ respectively:



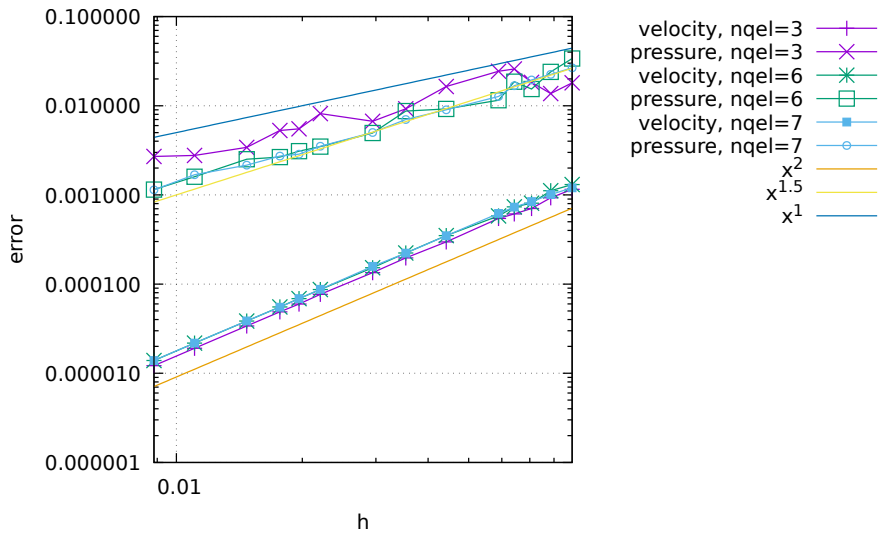
It is worth noticing that although the element is stable, and the error converges at a respectable rate, the pressure solution is not 'clean': as shown on the following figure, there is still some under/overshoot with respect to the analytical solution.



Let us now explore the case where the nodes inside the domain are randomly perturbed, i.e. a random value $(\delta_x, \delta_y) \in [-h_x/5, h_x/5] \times [-h_y/5, h_y/5]$ is added to their position (while preserving the position of the bubble as the barycenter of each triangle), as shown hereunder:



Looking again at the convergence rates of the errors, we see that the velocity errors are virtually unchanged but we observe that the pressure errors no more align on a single line and that the rates are only maintained on average.



Stone 48: D&H with $Q_1 \times P_0$, $Q_2 \times Q_1$, $Q_3 \times Q_2$ and $Q_4 \times Q_3$ elements

In this experiment we consider 4 different finite elements. The idea behind this stone is to build a code which code(the FEM build and assembly) is common to all. The setup is the Donea & HUerta benchmark (Section 8.6.1), which has been modified so that the pressure is zero at the top right corner.

Q4xQ3	Q3xQ2	Q2xQ1	Q1Q0
20====21====22====23====24	12====13====14====15	06=====07=====08	02=====03
20====21====22====23====24			
	08====09====10====11		
20====21====22====23====24			
	03=====04=====05		
	04====05====06====07		
20====21====22====23====24			
20====21====22====23====24	00=====01=====02=====03	00=====01=====02	00=====01
12====13====14====15	06=====07=====08	02=====03	.
08====09====10====11			
	03=====04=====05		00
04====05====06====07			
00=====01=====02=====03	00=====01=====02	00=====01	.
mV=25, mP=16	mV=16, mP=9	mV=9, mP=4	mV=4, mP=1

In the code the 'order' parameter can take values 1,2,3 and 4 which correspond to the polynomial order of the velocity approximation (Q_1 , Q_2 , Q_3 and Q_4).

When both nelx and nely values have been chosen, the total number of element for a regular 2D grid is simply:

```
nel=nelx*nely
```

The number of nodes in each direction is then easily computed:

```
nmx=order*nelx+1
nny=order*nely+1
```

and so is then the total number of velocity nodes:

```
NV=nmx*nny
```

The total number of pressure nodes is as follows:

```

if order==1:
    NP=nelx*nely
if order==2:
    NP=(nelx+1)*(nely+1)
if order==3:
    NP=(2*nelx+1)*(2*nely+1)
if order==4:
    NP=(3*nelx+1)*(3*nely+1)

```

Each velocity node has 2 dofs (ndofV=2) while pressure nodes have one dof (ndofP=1) so that the size of the blocks and the assembled FE matrix are given by:

```

NfemV=NV*ndofV
NfemP=NP*ndofP
Nfem=NfemV+NfemP

```

For the linear element, 2 quadrature points per dimension are enough (nqperdim=2), while 3 are necessary for the quadratic element (nqperdim=3) and 4 are used for the cubic element (nqperdim=4), and 5 for the quartic element, which can be conveniently implemented as follows:

```
nqperdim=order+1
```

The quadrature points location and weight is document in Section 4.1.

Because we wish to use a regular grid, the layout of the points for all three elements can be implemented easily:

```

counter=0
for j in range(0,nny):
    for i in range(0,nnx):
        xV[counter]=i*hx/order
        yV[counter]=j*hy/order
        counter+=1

```

The position of the pressure nodes follows a similar logic.

When it comes to the connectivity array, I first started by building it for each element as follows:

```

if order==1:
    counter=0
    for j in range(0,nely):
        for i in range(0,nelx):
            iconV[0,counter]=(i)*1+0+(j)*1*nnx+nnx*0
            iconV[1,counter]=(i)*1+1+(j)*1*nnx+nnx*0
            iconV[2,counter]=(i)*1+0+(j)*1*nnx+nnx*1
            iconV[3,counter]=(i)*1+1+(j)*1*nnx+nnx*1
            counter += 1

if order==2:
    counter = 0
    for j in range(0,nely):
        for i in range(0,nelx):
            iconV[0,counter]=(i)*2+0+(j)*2*nnx+nnx*0
            iconV[1,counter]=(i)*2+1+(j)*2*nnx+nnx*0
            iconV[2,counter]=(i)*2+2+(j)*2*nnx+nnx*0
            iconV[3,counter]=(i)*2+0+(j)*2*nnx+nnx*1
            iconV[4,counter]=(i)*2+1+(j)*2*nnx+nnx*1
            iconV[5,counter]=(i)*2+2+(j)*2*nnx+nnx*1
            iconV[6,counter]=(i)*2+0+(j)*2*nnx+nnx*2
            iconV[7,counter]=(i)*2+1+(j)*2*nnx+nnx*2
            iconV[8,counter]=(i)*2+2+(j)*2*nnx+nnx*2
            counter += 1

if order==3:
    counter = 0
    for j in range(0,nely):
        for i in range(0,nelx):
            iconV[0,counter]=(i)*3+0+(j)*3*nnx+0*nnx
            iconV[1,counter]=(i)*3+1+(j)*3*nnx+0*nnx
            iconV[2,counter]=(i)*3+2+(j)*3*nnx+0*nnx

```

```

...
iconV[13, counter]=(i)*3+1+(j)*3*nnx+3*nnx
iconV[14, counter]=(i)*3+2+(j)*3*nnx+3*nnx
iconV[15, counter]=(i)*3+3+(j)*3*nnx+3*nnx
counter += 1

```

Having done so, it becomes quickly apparent that the connectivity array can be computed for all elements as follows:

```

counter=0
for j in range(0, nely):
    for i in range(0, nelx):
        counter2=0
        for k in range(0, order+1):
            for l in range(0, order+1):
                iconV[counter2, counter]=i*order+l+j*order*nnx+nnx*k
                counter2+=1
        counter += 1

```

The same approach is taken to build the pressure connectivity array, although the $Q_1 \times P_0$ element requires special attention since the pressure is elemental and attributed to a single node inside the element.

For the other elements I started from:

```

if order==2:
    counter=0
    for j in range(0, nely):
        for i in range(0, nelx):
            iconP[0, counter]=(i)*1+0+(j)*1*(nelx+1)+(nelx+1)*0
            iconP[1, counter]=(i)*1+1+(j)*1*(nelx+1)+(nelx+1)*0
            iconP[2, counter]=(i)*1+0+(j)*1*(nelx+1)+(nelx+1)*1
            iconP[3, counter]=(i)*1+1+(j)*1*(nelx+1)+(nelx+1)*1
            counter += 1

if order==3:
    counter=0
    for j in range(0, nely):
        for i in range(0, nelx):
            iconP[0, counter]=(i)*2+0+(j)*2*(2*nelx+1)+(2*nelx+1)*0
            iconP[1, counter]=(i)*2+1+(j)*2*(2*nelx+1)+(2*nelx+1)*0
            iconP[2, counter]=(i)*2+2+(j)*2*(2*nelx+1)+(2*nelx+1)*0
            iconP[3, counter]=(i)*2+0+(j)*2*(2*nelx+1)+(2*nelx+1)*1
            iconP[4, counter]=(i)*2+1+(j)*2*(2*nelx+1)+(2*nelx+1)*1
            iconP[5, counter]=(i)*2+2+(j)*2*(2*nelx+1)+(2*nelx+1)*1
            iconP[6, counter]=(i)*2+0+(j)*2*(2*nelx+1)+(2*nelx+1)*2
            iconP[7, counter]=(i)*2+1+(j)*2*(2*nelx+1)+(2*nelx+1)*2
            iconP[8, counter]=(i)*2+2+(j)*2*(2*nelx+1)+(2*nelx+1)*2
            counter += 1

if order==4:
    etc ...

```

and quickly arrived at the following compact form:

```

if order >1:
    om1=order-1
    counter=0
    for j in range(0, nely):
        for i in range(0, nelx):
            counter2=0
            for k in range(0, order):
                for l in range(0, order):
                    iconP[counter2, counter]=i*om1+l+j*om1*(om1*nelx+1)+(om1*nelx+1)*k
                    counter2+=1
            counter += 1

```

The core of the code is rather similar if not identical to other stones (i.e. the loop over elements, the calculation of the elemental matrices, their assembly, and the solve).

What is here somewhat elegant is the projection of the pressure field onto the velocity grid nodes (mostly for plotting purposes). For each element I loop over each velocity node, and evaluate the pressure

shape function at this location, compute the pressure with it and add it in the array q while keeping count of how many contributions there are in total per velocity node.

```

for iel in range(0,nel):
    for i in range(0,mV):
        NNNP[0:mP]=NNP(rVnodes[i],sVnodes[i],order)
        q[iconV[i,iel]]+=np.dot(p[iconP[0:mP,iel]],NNNP[0:mP])
        c[iconV[i,iel]]+=1.

q=q/c

```

Finally, since the vtu format does not support higher order elements, I here chose to only extract the corner values for each element, which translates as follows:

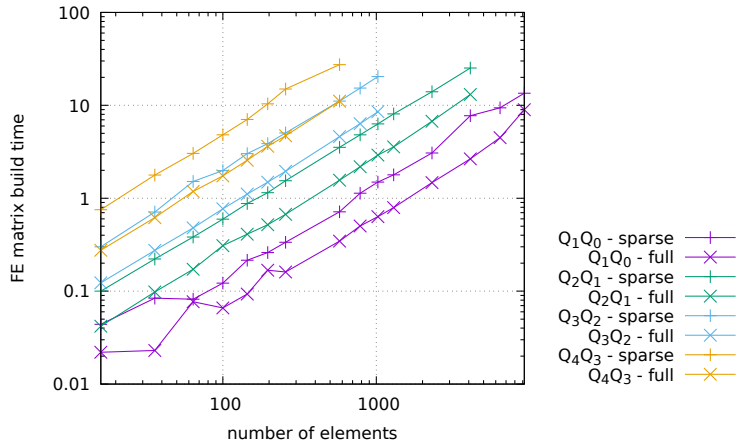
```

vtufile.write("<DataArray _type='Int32' _Name='connectivity' _Format='ascii'>\n")
if order==1:
    for iel in range(0,nel):
        vtufile.write("%d%d%d\n" %(iconV[0,iel],iconV[1,iel],iconV[3,iel],iconV[2,iel]))
if order==2:
    for iel in range(0,nel):
        vtufile.write("%d%d%d%d\n" %(iconV[0,iel],iconV[2,iel],iconV[8,iel],iconV[6,iel]))
if order==3:
    for iel in range(0,nel):
        vtufile.write("%d%d%d%d\n" %(iconV[0,iel],iconV[3,iel],iconV[15,iel],iconV[12,iel]))
if order==4:
    for iel in range(0,nel):
        vtufile.write("%d%d%d%d\n" %(iconV[0,iel],iconV[4,iel],iconV[24,iel],iconV[20,iel]))
vtufile.write("</DataArray>\n")

```

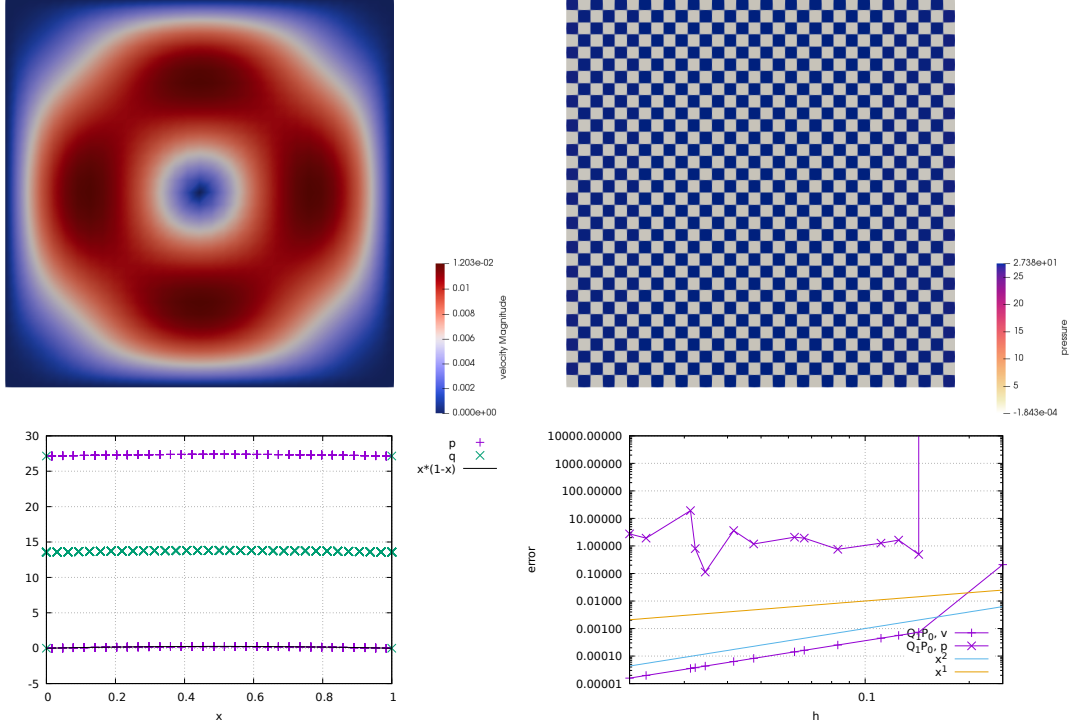
The following results are obtained by running one of the four scripts *script_errorsX* where X=1,2,3,4. The gnuplot script is to be found in the *images* folder.

The stone implements two ways of building the FE matrix. When the flag *sparse* is false, the \mathbb{K} and \mathbb{G} matrices are built as full arrays, later assembled in a larger full array, and then only converted to Compressed Sparse Row before it is passed to the solver. When the flag is true, the global FE matrix is defined as a *lil_matrix* (a List of Lists) and it grows in size/memory every time a new term is added to it. As shown on the following plot, it is about twice as slow compared to the first option, but it uses only a fraction of the memory that the first one does.



Also not very surprising: the cost of building the FE matrix increases with the order of the used elements. A matrix corresponding to 100 $Q_1 \times P_0$ elements can be built in about 1s, while it will take 7s when $Q_4 \times Q_3$ elements are used.

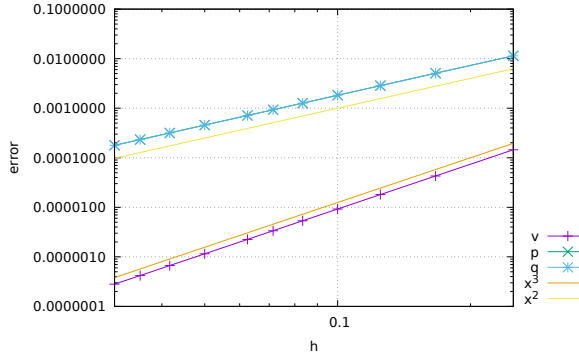
Results with $Q_1 \times P_0$ element



We see that we recover a second order convergence rate for velocity (as expected) but because of the checkerboard pattern the pressure convergence is simply random. The smoothed pressure q shows virtually no checkerboard pattern, except on the boundaries. This is a perfect example for the use of more accurate/ clever smoothing procedure, see Section 8.12.

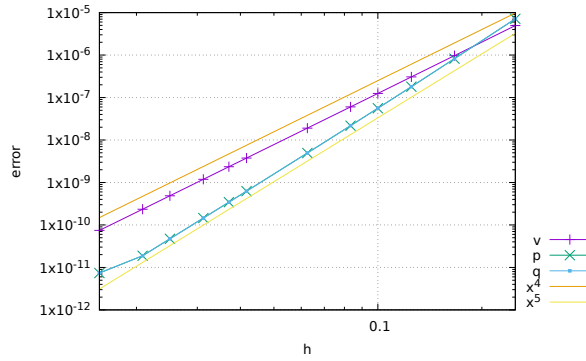
Results with $Q_2 \times Q_1$ element

We recover the cubic convergence for the velocity error and the quadratic convergence for the pressure:



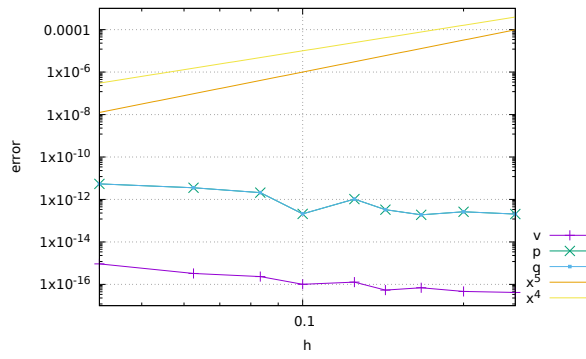
Results with $Q_3 \times Q_2$ element

The analytical solution is a second order polynomial, which means that the pressure shape functions can adequately represent the solution. We recover a fourth-order convergence for the velocity error and a superconvergent (fifth order) pressure error (but why is it 5th order ?).



Results with $Q_4 \times Q_3$ element

Rather interestingly, now both velocity and pressure analytical solutions can be represented exactly by their respective polynomial spaces, so that the errors are at machine precision.

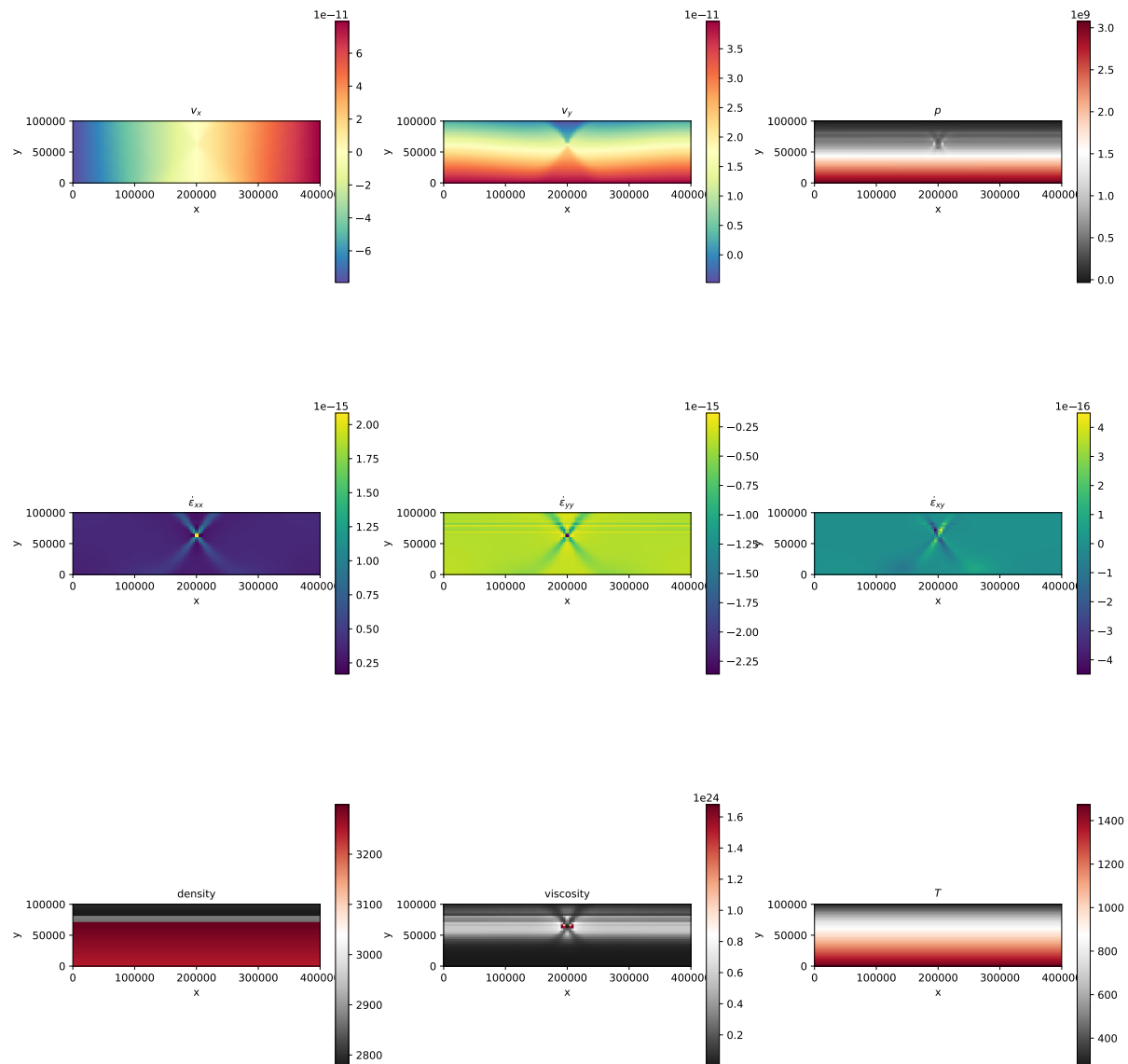


Stone 49: Consistent Boundary Flux method on D&H benchmark with 4 elements

Looking at the four different elements

Looking at the influence of the mas matrix lumping

Stone 50: Lithosphere extension



Stone 51: Triangular domain benchmark with MINI element

This fieldstone was developed in collaboration with L. van de Wiel.

The following problem is studied in [917]. The equations that they solve are the thermo-mechanically coupled steady state equations:

$$-\vec{\nabla}p + \Delta\vec{v} + RaTe_y = 0 \quad (794)$$

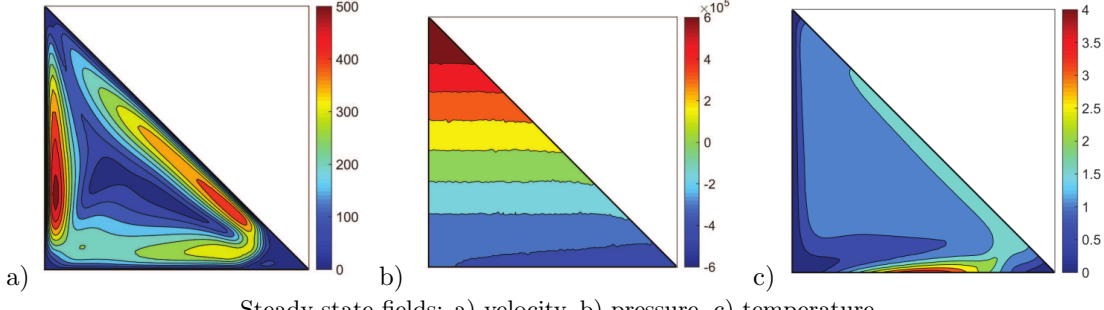
$$\vec{\nabla} \cdot \vec{v} = 0 \quad (795)$$

$$-\Delta T + \vec{v} \cdot \nabla T = 0 \quad (796)$$

In our case the code is based on the MINI element (a.k.a. $P_1^+ \times P_1$), see Section 6.2.7 and we set $Ra = 10^6$.

The domain is chosen to be the right triangle with vertices $(0, 0)$, $(1, 0)$, and $(0, 1)$. The boundary is considered to be solid walls (no-slip). For the temperature, a sinusoidal heat source is enforced on the bottom boundary with a Dirichlet condition ($T(x) = 2(1 - \cos(2\pi x))$), the left wall is set to a constant temperature of zero, and the hypotenuse wall is perfectly insulated so that a Neumann boundary condition is appropriate.

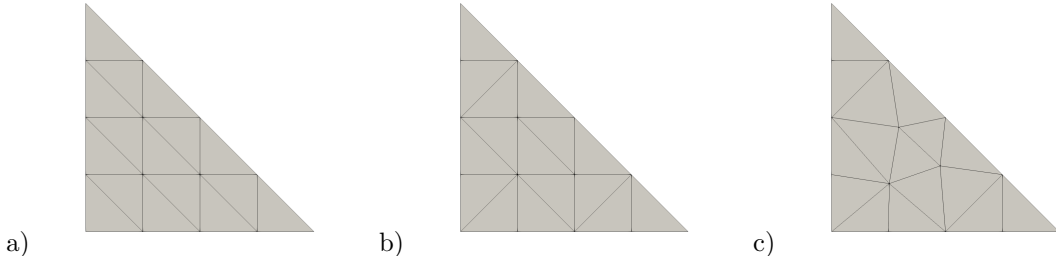
The steady state velocity pressure and temperature fields as shown in [917] are as follows:



Steady state fields: a) velocity, b) pressure, c) temperature.

Although it is not mentioned in the original article it appears that the pressure field has been normalised so that $\langle p \rangle = \int_{\Omega} pdV = 0$.

As opposed to the mesh presented in [917] I build a regular mesh. An example of such a mesh is shown hereunder (a) for $n = 5$ (the number of nodes per side of the triangular domain). In order to generate a mesh which is more isotropic some edges between triangles can be flipped (b). Note that this mesh can also be modified in such a way that the position of nodes inside the domain is perturbed by a small random value (c). In what follows I denote by h the distance between nodes on the horizontal (or vertical) boundaries, i.e. $h = L_x/(n - 1) = L_y/(n - 1)$.



a) regular mesh for $n=5$. b) flipped edges mesh. c) randomized+flipped edges mesh.

Since I am solving for the steady-state solution I set the mass matrix in the heat transport part of the code to zero. However, since I am solving the Stokes equations and the heat transport equation alternatively until convergence is reached, it is well known that this approach does not converge fast (if at all). I then implement a simple relaxation scheme [1651]. After I have solved for velocity (using the most recent temperature field in the rhs), I do:

$$\vec{v}^k = \gamma \vec{v}^k + (1 - \gamma) \vec{v}^{k-1}$$

and after having solved for temperature having used the most recent velocity field, I do the same for temperature:

$$T^k = \gamma T^k + (1 - \gamma) T^{k-1}$$

where the relaxation parameter γ is between 0 and 1.

Additionally I measure:

- the Nusselt number defined by

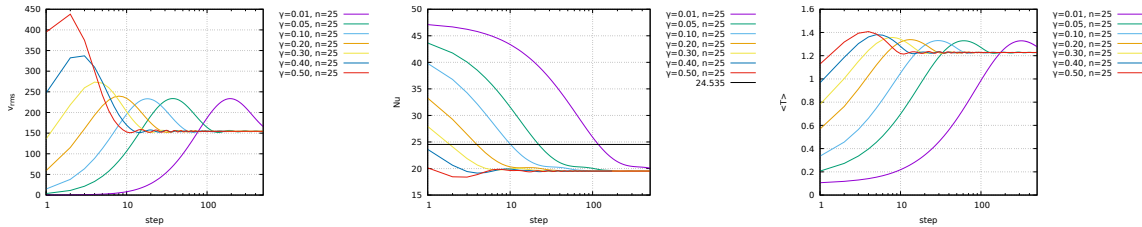
$$Nu = \int_{y=0} \vec{\nabla} T \cdot \vec{n} dS = - \int_{x=0}^{x=1} \frac{\partial T}{\partial y} dx$$

It is reported to be 24.535 in [917].

- the temperature on the hypotenuse.
- the root mean square velocity
- the mean temperature $\langle T \rangle = |\Omega|^{-1} \int_{\Omega} T dV$

On the importance of the relaxation parameter γ

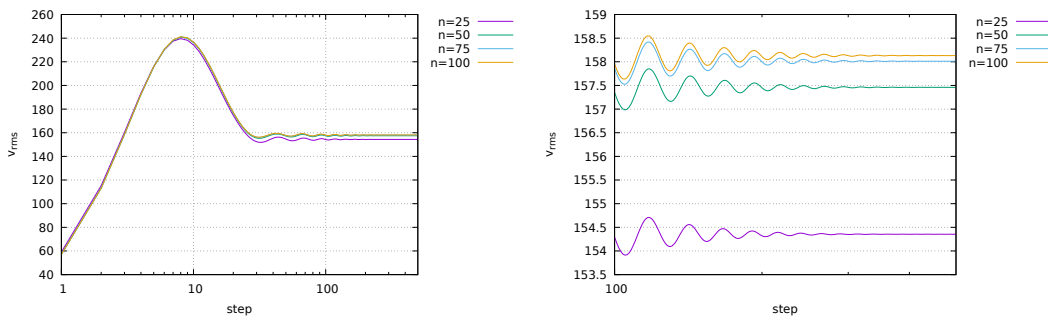
In what follows the internal node coordinate randomness is switched off. I have run the model for various values of γ for $n = 25$, and results are shown on the following figures. We see that all simulations seem to converge to the same steady state, which is very reassuring. However, it looks like too small a value of γ delays greatly the convergence and too large a value also seems detrimental. In light of this, I have chosen $\gamma = 0.2$ for all what follows.

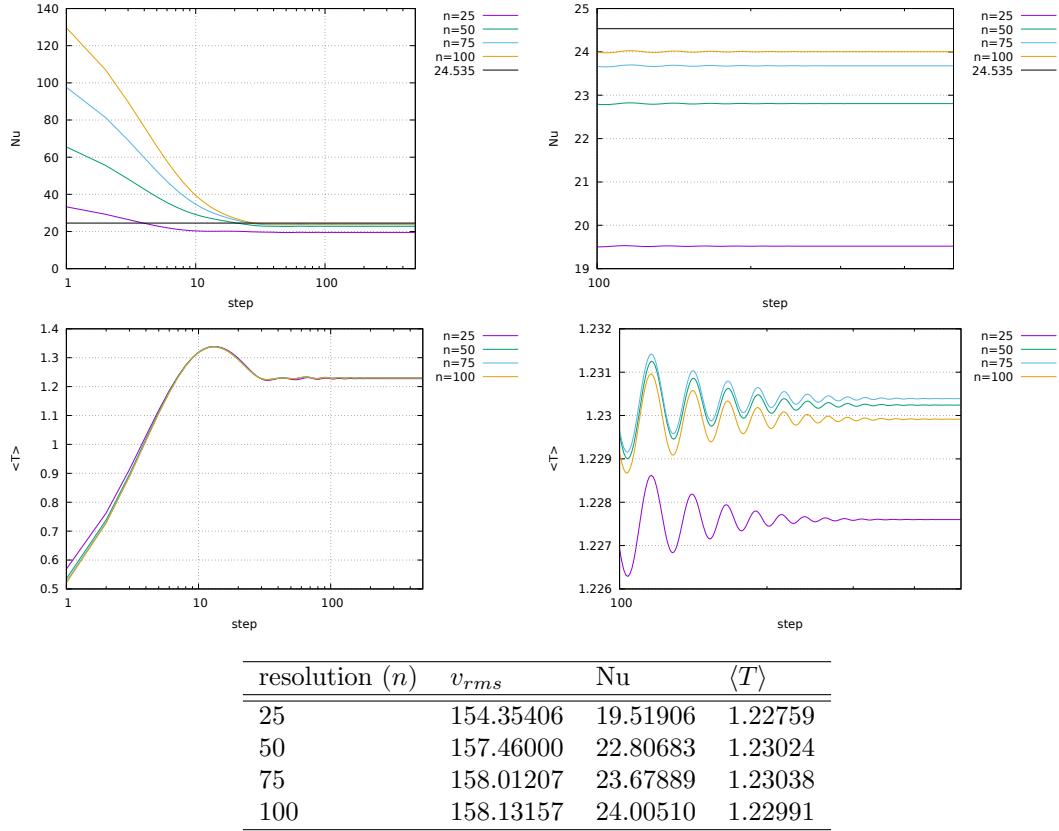


Left to right: Root mean square velocity, Nusselt number and average temperature as a function of the iteration counter.

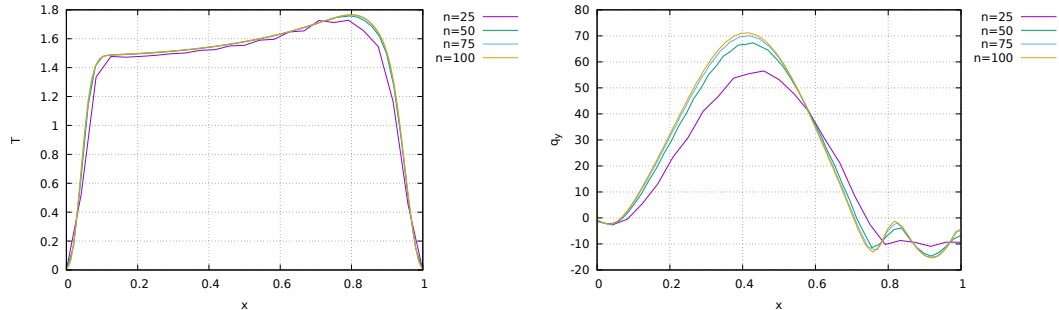
On the influence of mesh resolution

I now explore the influence of the mesh resolution on the results and run steady state calculations for $n = 25, 50, 75, 100$.

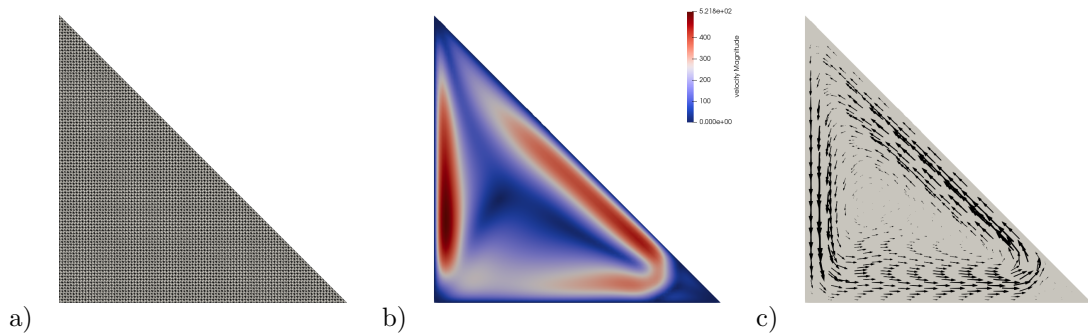


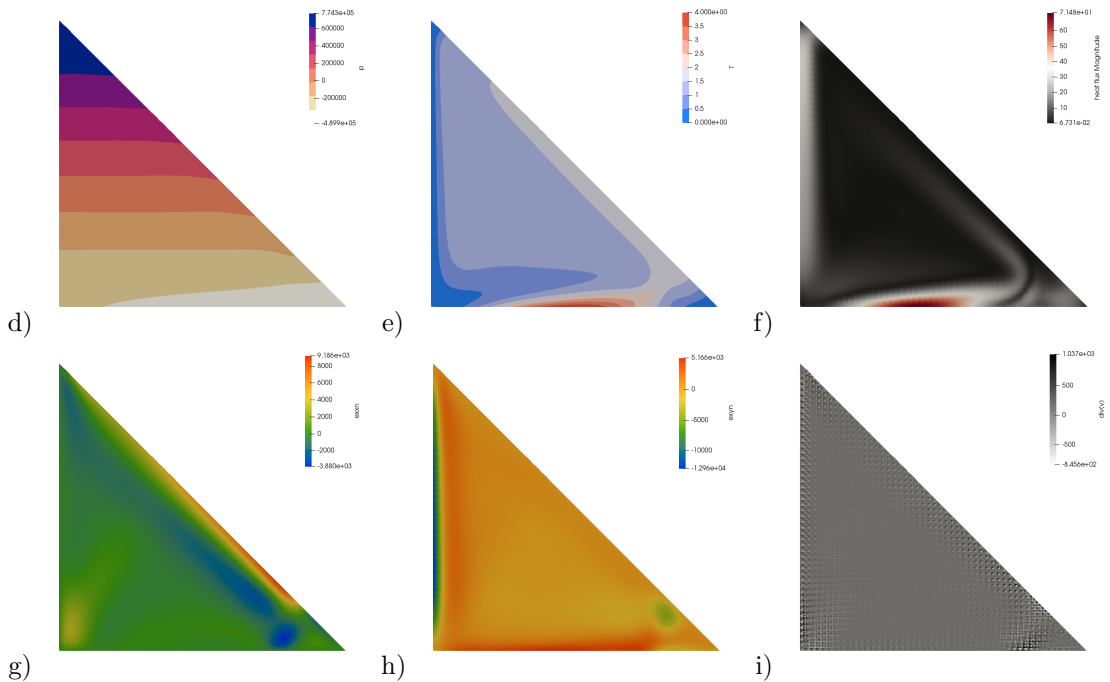


The following two plots show the temperature along the hypotenuse (as a function of x for simplicity) at steady-state and the heat flux measured at the bottom.



Finally, here are the fields for $n = 100$ at steady state:





Steady state fields: a) grid ($n=100$), b,c) velocity, d) pressure, e) temperature, f) heat flux, g) $\dot{\varepsilon}_{xx}$, h) $\dot{\varepsilon}_{xy}$, i) velocity divergence measured in the middle of the element.

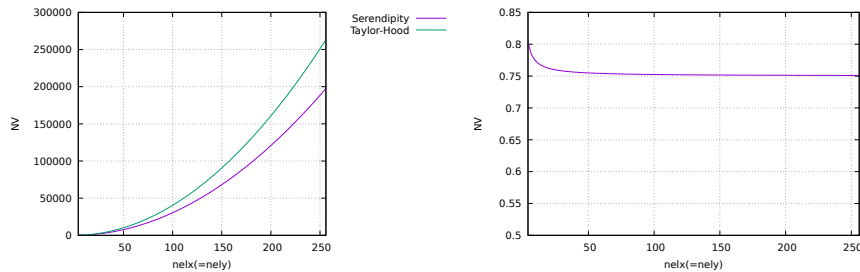
Stone 52: Serendipity element in 2D

In order to test the grid point and connectivity algorithms, we use this simple 4×3 element mesh:

Q_2 X Q1 (serendipity)	Q_2 X Q1 (regular)
15--47--16--48--17--49--18--50--19	54--55--56--57--58--59--60--61--62
	: : : :
42 43 44 45 46	45..46..47..48..49..50..51..52..53
	: : : :
10--38--11--39--12--40--13--41--14	36--37--38--39--40--41--42--43--44
	: : : :
33 34 35 36 37	27..28..29..30..31..32..33..34..35
	: : : :
05--29--06--30--07--31--08--32--09	18--19--20--21--22--23--24--25--26
	: : : :
24 25 26 27 28	09..10..11..12..13..14..15..16..17
	: : : :
00--20--01--21--02--22--03--23--04	00--01--02--03--04--05--06--07--08
iel= 0:	iel= 0
node 0 : 0 at pos. 0.0 0.0	node 0 : 0 at pos. 0.0 0.0
node 1 : 1 at pos. 1.0 0.0	node 1 : 2 at pos. 1.0 0.0
node 2 : 6 at pos. 1.0 1.0	node 2 : 20 at pos. 1.0 1.0
node 3 : 5 at pos. 0.0 1.0	node 3 : 18 at pos. 0.0 1.0
node 4 : 20 at pos. 0.5 0.0	node 4 : 1 at pos. 0.5 0.0
node 5 : 25 at pos. 1.0 0.5	node 5 : 11 at pos. 1.0 0.5
node 6 : 29 at pos. 0.5 1.0	node 6 : 19 at pos. 0.5 1.0
node 7 : 24 at pos. 0.0 0.5	node 7 : 9 at pos. 0.0 0.5
	node 8 : 10 at pos. 0.5 0.5

We see that the serendipity element-based mesh counts only 51 nodes, as opposed to 63 for its counterpart.

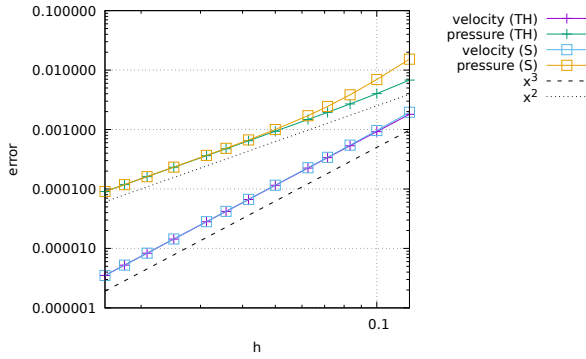
Setting $nelx = nely$, we can look at the number of velocity nodes for each as a function of $nelx$, as shown hereunder:



Looking at the ratio between both, we see that ultimately at high resolution, a mesh composed of serendipity elements will count 25% less nodes than a mesh with Taylor-Hood elements. Since there is not free lunch, what is the price paid in terms of accuracy when using the cheaper serendipity?

The shape functions and their derivatives are in Section 4.5.3.

Although the vtk format does not understand the Q_2 element in 2D or 3D, it surprisingly does understand the serendipity element in 2D (type=23) and 3D (type=25).

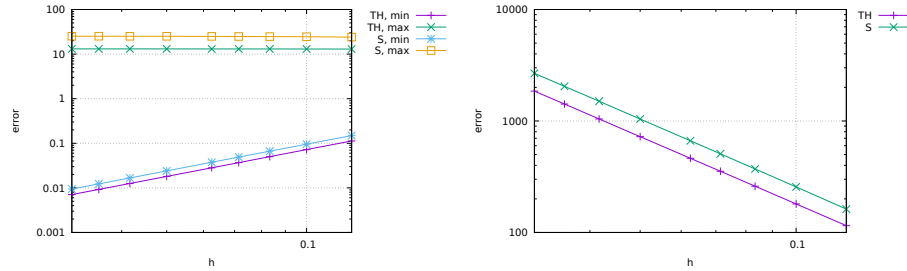


It looks like the serendipity element yields the same errors and error convergence rates as its Taylor-Hood counterpart. Since it is cheaper in terms of dofs, one could think that it should be preferred. However, most modern codes use an iterative solver approach to solve the discretised Stokes problem, and often the \mathbb{K} matrix (which is SPD) is 'solved' with a conjugate gradient solver. The convergence of this type of solver depends on the condition number of the matrix itself, i.e. the ratio of the largest and smallest eigenvalues. Note that this is rather trivial with Python:

```
print('condition_number:', nel, linalg.cond(K_mat))
```

However, since I was also curious about the values of the eigenvalues, I implemented it as follows:

```
eigvals, eigvecs = linalg.eig(K_mat)
print('eigenvalues:', nel, eigvals.min(), eigvals.max())
```



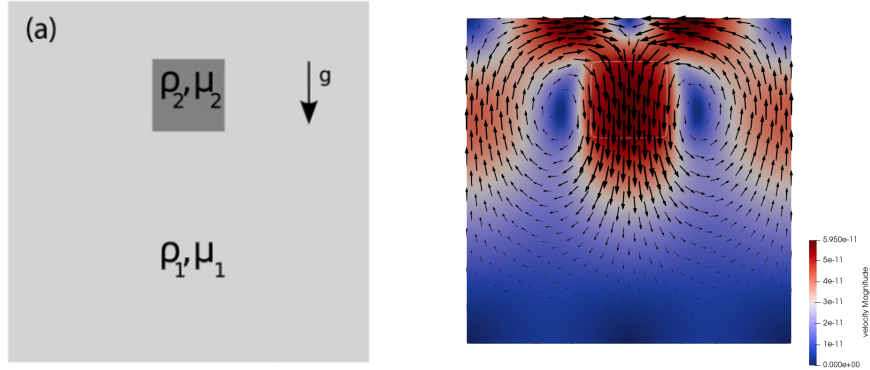
Left: min and max eigenvalues for both types of elements as a function of h ; Right: condition number

As it turns out, the condition number is twice as high for the serendipity element, which means that the CG would have to iterate more to arrive at the solution, thereby offsetting the benefit of less dofs.

Stone 53: the sinking block benchmark

https://github.com/cedrict/fieldstone/tree/master/python_codes/fieldstone_53

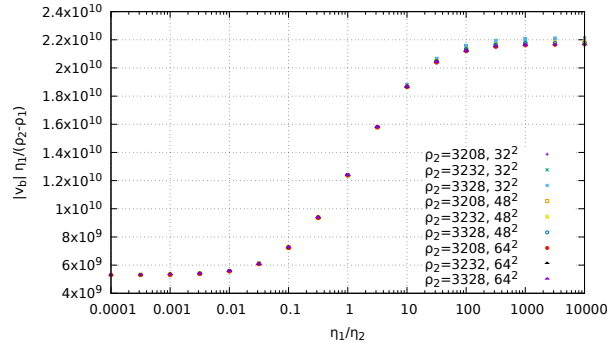
This simple benchmark provides challenging numerical experiments dealing with large viscosity variations within the simulation domain. It appears in [656] and consists of a bulk of fluid 1 (ρ_1, η_1) in which a block of fluid 2 (ρ_2, η_2) falls under its own weight. The domain is a square of size $L_x = L_y = 512\text{km}$ and the block is initially centred at point ($x = 256\text{ km}, y = 384\text{ km}$) with size $128 \times 128\text{ km}$:



Left: setup. Right: velocity field for $\rho_2 = 3208$, $\eta_1 = 10^{21}$ and $\eta_2 = 10^{22}$.

The simulation is carried out on 32×32 , 48×48 and 64×64 grids. Free slip boundary conditions are imposed on all sides of the domain. In all experiments the density of the surrounding fluid is $\rho_1 = 3200\text{kg/m}^3$. The velocity v_b of the falling block is measured in its centre (note that due to symmetry the horizontal component should be zero).

As explained in [1538], following physical intuition, one expects the velocity v_b of the block to (a) decrease when the viscosity of the surrounding medium η_1 increases; (b) increase with the density contrast $\rho_2 - \rho_1$. The quantity $v_b \eta_1 / (\rho_2 - \rho_1)$ is therefore monitored and shown hereunder as a function of the viscosity ratio.



Series of experiments have been conducted with $\rho_2 = 3208, 3232, 3328$, $\log_{10}(\eta_1) = 20, 21, 22$ and $\log_{10}(\eta_2) = 18, 18.5, 19, \dots, 22.5, 23, 23.5, 24$, all with 3 mesh resolutions.

All experimental points line up on a single curve which further indicates that the code can deal with gravity driven simulations in the presence of large viscosity contrasts. These results have been successfully compared with those obtained with ASPECT with the same setup.

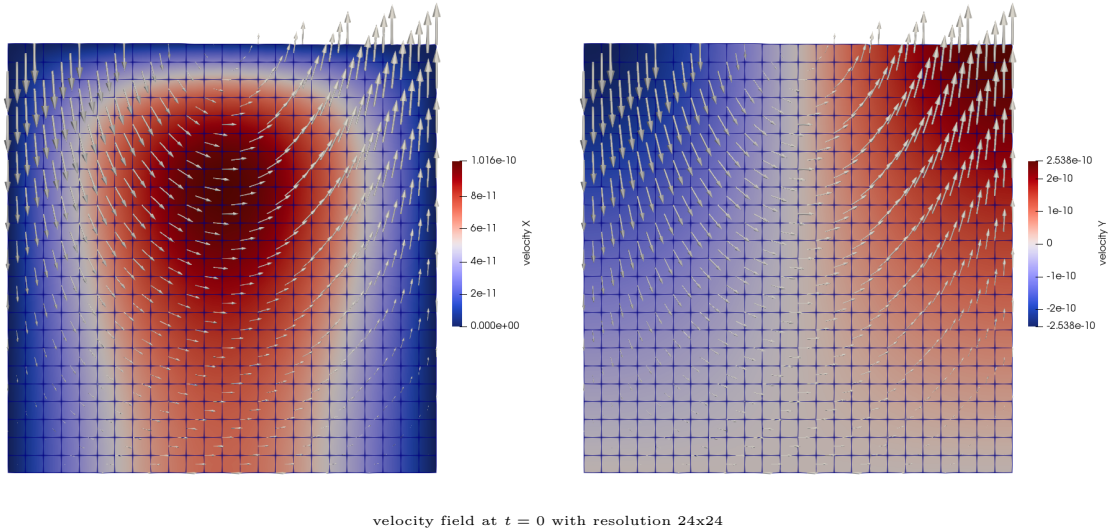
Stone 54: ALEs

https://github.com/cedrikt/fieldstone/tree/master/python_codes/fieldstone_54

This stone implements three different free surface/mesh deformation algorithms. The first one has all the nodes move with the computed velocity (Lagrangian method) and is coined 'method 1'. The second one ('method 2') only has the top row of nodes moving with the computed velocity, while all the nodes underneath are static (this is obviously not a viable method for large deformations). The third one ('method 3') is the method used in ASPECT and described in Rose et al (2017) [1406]. Its implementation is described in Section 8.1.

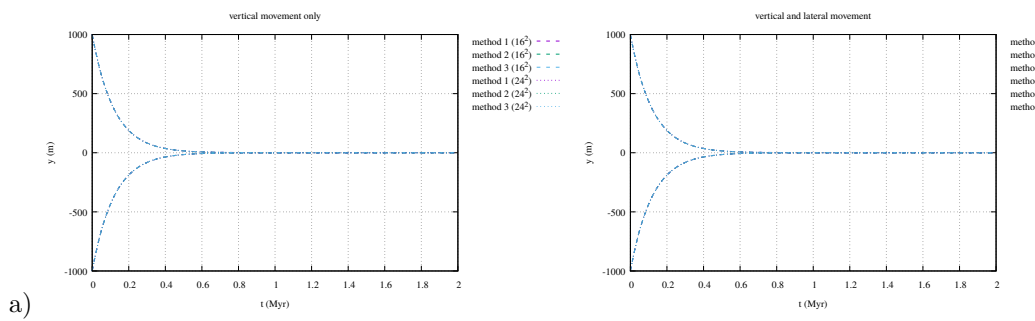
Experiment 1 - relaxation of topography

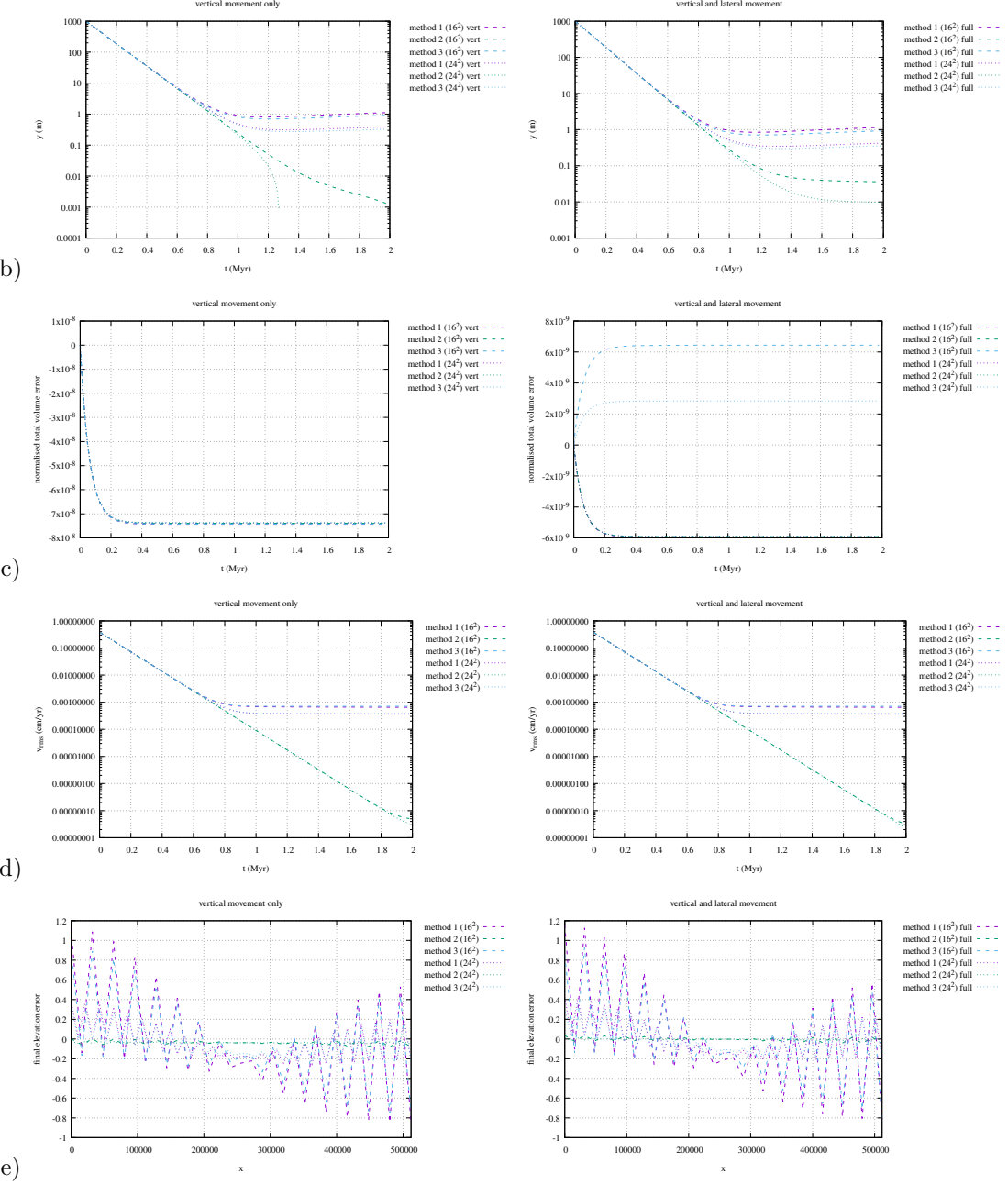
The domain is a 2D Cartesian box of size 512×512 km, with free slip on left, bottom and right sides, free surface at the top. Mantle material characterised by $\rho_m = 3200$ and $\eta_m = 10^{22}$. Gravity is vertical and Earth like. The surface is perturbed at startup by $\delta y = A \cos(\pi x / L_x)$ with $A=1$ km. 200 time steps with $\delta t = 10$ kyr are carried out. The root mean square velocity, the total volume of the domain, the min/max elevation values of the surface are recorded over time.



velocity field at $t = 0$ with resolution 24×24

The results hereunder are obtained for all three methods at two different resolutions (16×16 and 24×24 elements). The plots on the left column are obtained with the movement of the top nodes being constrained in the vertical direction, while the plots on the right column are obtained with nodes being allowed to move in both x and y directions (note that for method 3 the normals are not -yet- computed with the method of Eq. 49 in [1406] but instead by a simple geometric rule).

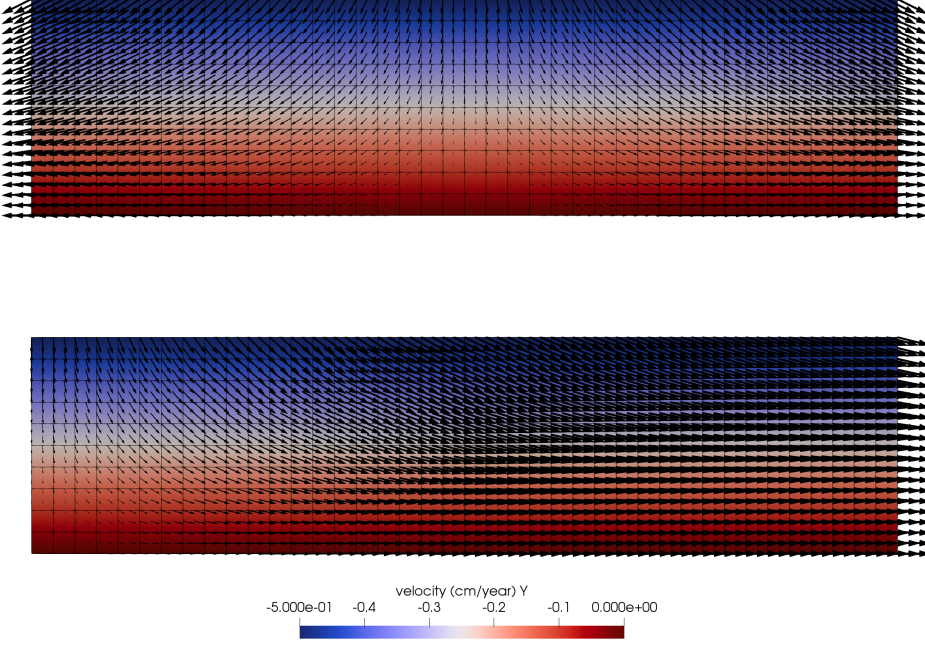




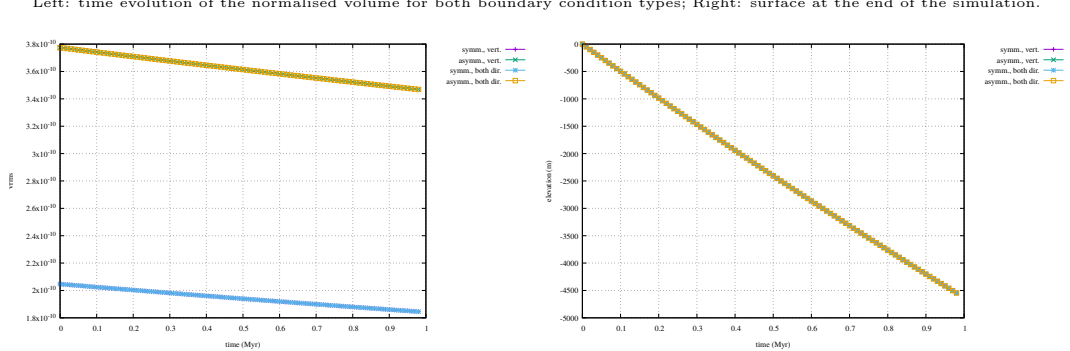
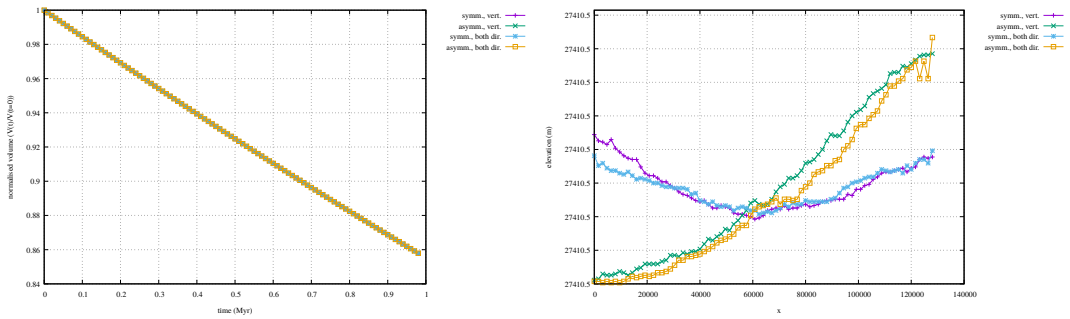
a) min/max of free surface topo as a function of time; b) free surface topo maximum (in log scale) as a function of time; c) measured volume of the domain with numerical quadrature normalised by the expected volume $L_x L_y$; d) root mean square velocity as a function of time; e) final elevation at the 200th time step.

Experiment 2,3 - extension

We now consider a rectangular domain (crust sized) of 128×32 km, discretised by means of 40×10 elements. The fluid is identical to the one above and so is gravity. Extensional boundary conditions are applied. In the first case, a 1 cm/yr horizontal velocity is applied on both sides, while in the second case a 2 cm/yr velocity is applied on the right while 0 is prescribed to the left. Free slip conditions are otherwise prescribed on the sides and bottom. 100 time steps are carried out with $\delta t = 10^4$ yr. Only method 3 is used here.

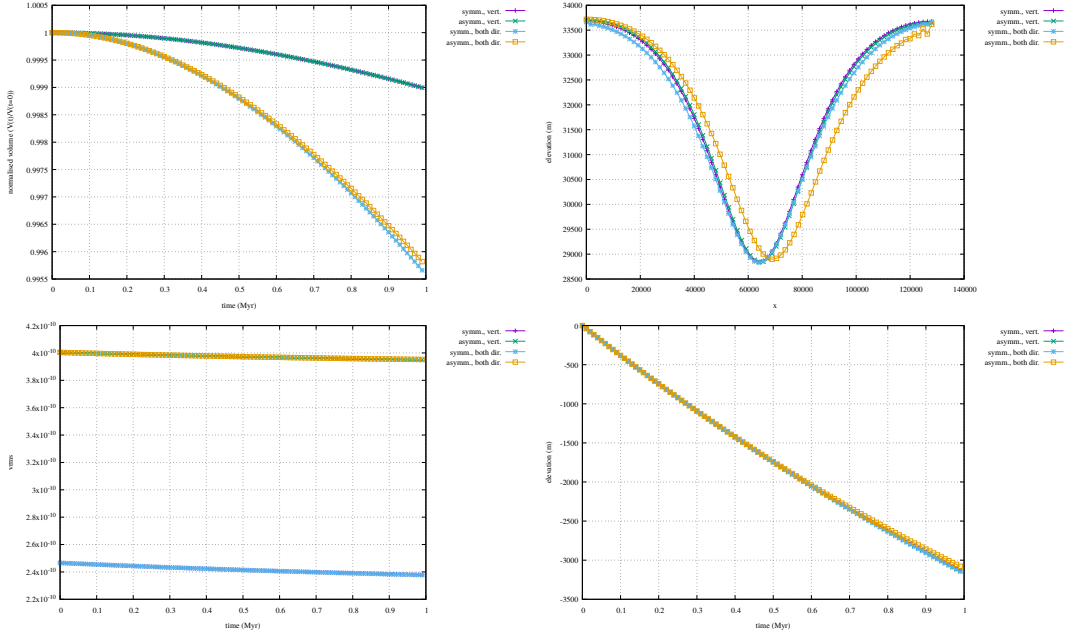


Despite the asymmetry in the boundary conditions, we expect the same evolution of the domain geometry. This is indeed what we recover with surprising accuracy. 'vert' stands for only vertical movement allowed (i.e. $n_x = 0$, $n_y = 1$) while 'both dir' stands for the use of dynamically computed normal vectors (based on geometrical consideration).

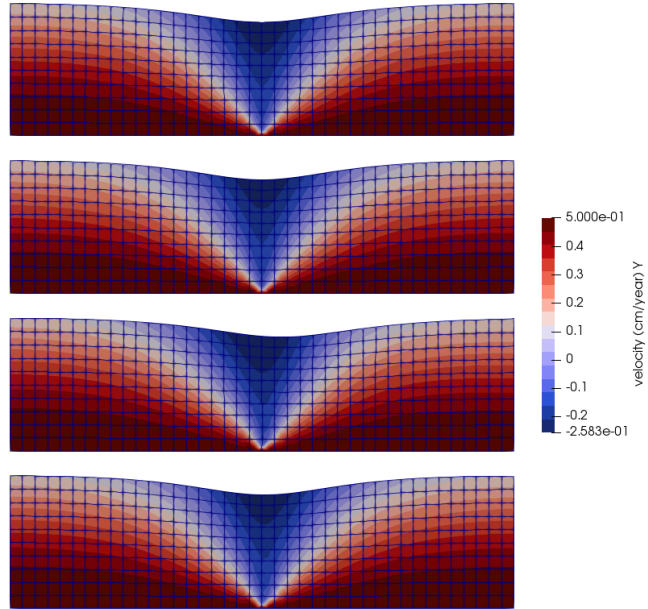


Experiment 4,5 - extension with bottom inflow

This is the same setup as above, but we now impose an influx boundary condition at the bottom: $v = 0.5\text{cm}$ (this balances the outflux exactly) and the horizontal component at the bottom is set to the left value (-1 or 0 cm/yr) for $x \leq L_x/2$ and to the right value +1 or +2 cm/yr for $x \geq L_x/2$.

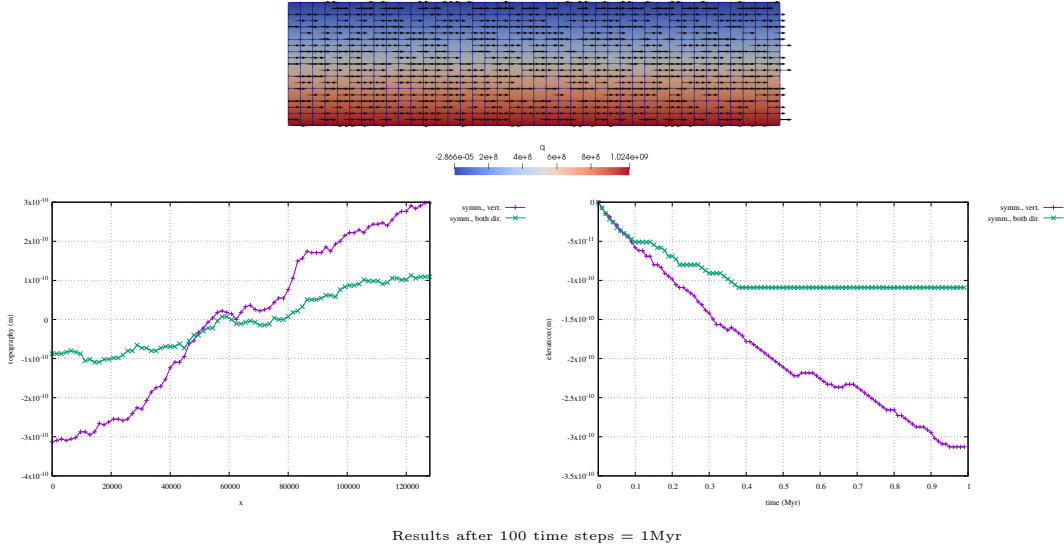


We can conclude that the 'vertical movement only' conserves volume/mass better and the free surface remains symmetrical unless the full normal is used which is simply explained by having $\vec{v} \cdot \vec{n}$ as a boundary condition: in the asymmetric extension case, the velocity is always to the right while the normal has an x component which is negative and positive, therefore introducing an asymmetry in the surface boundary conditions.



Top to bottom: symmetric extension, full normal vector; symmetric extension, vertical normal vector; asymmetric extension, full normal vector; asymmetric extension, vertical normal vector

Experiment 6 - pure advection test



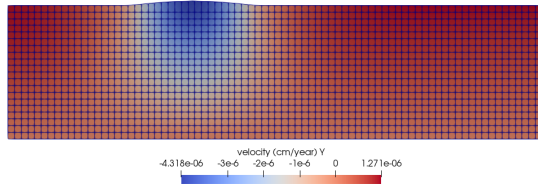
Experiment 7 - pure advection test of a cosine bump

The initial topography bump is given by

$$y(x) = A \left[1 + \cos \left(\frac{x - x_0}{w} \pi \right) \right]$$

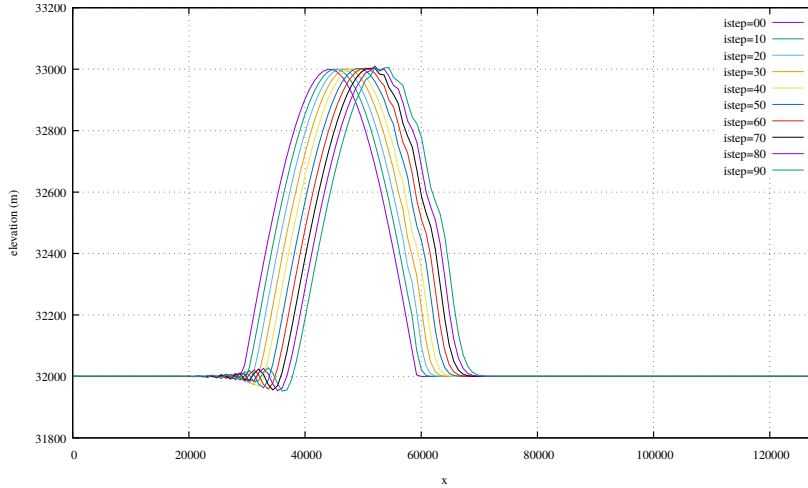
with $A = 1000\text{m}$, $x_0 = 0.345678L_x$ and $w = 15\text{km}$. This is a somewhat ideal case since the transition from flat to bump is very smooth.

The viscosity is set to $10^{26}\text{Pa}\cdot\text{s}$ so that the velocity of the viscous relaxation of the topography is negligible with regards to the advection velocity (+1cm/yr on left and right boundaries). I also choose a resolution of 80x20 elements.

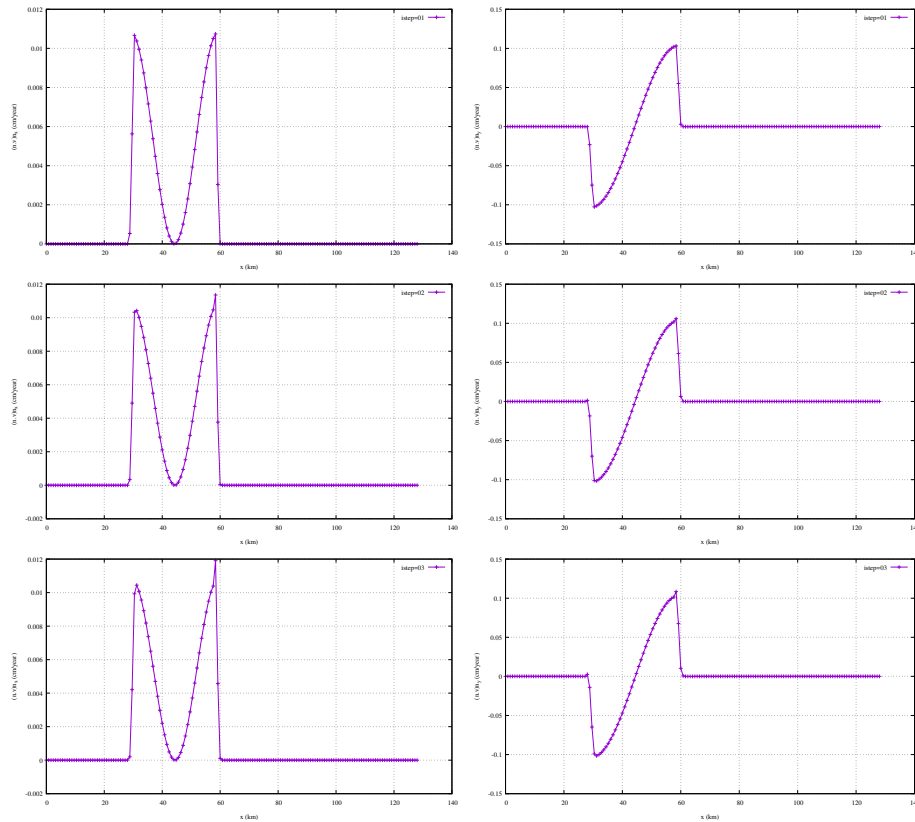


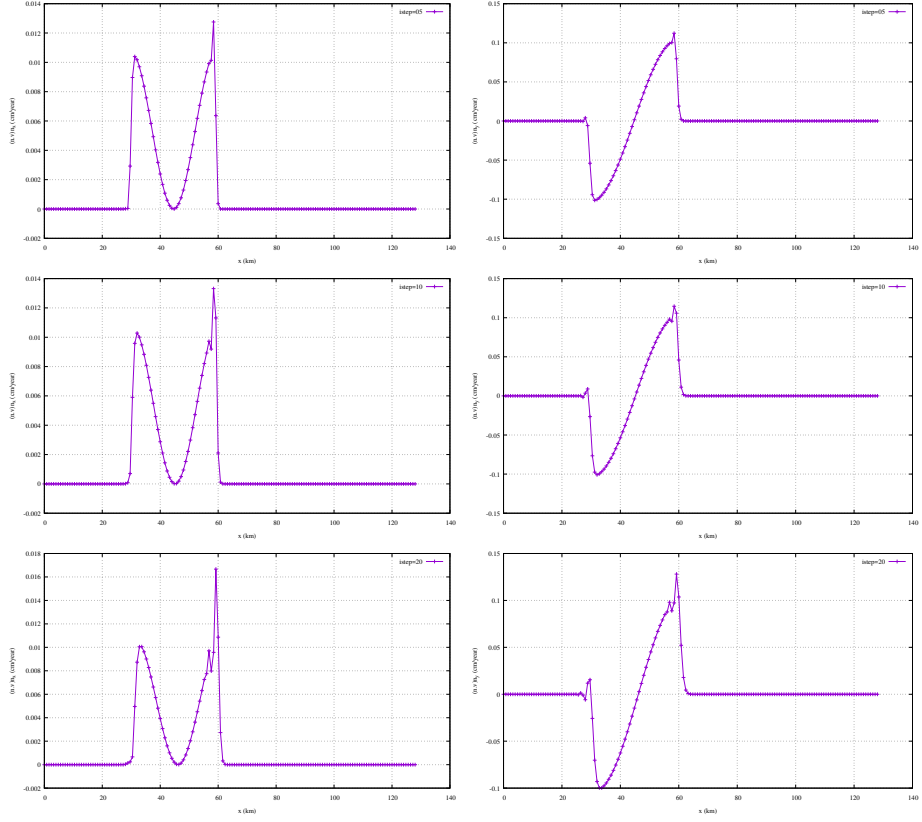
If only the vertical normal is used then *nothing* moves since the velocity is always perpendicular to the normal.

What follows is obtained when the full normal is used. After 20 timesteps the topography has been advected and we already observe some visible asymmetry (and oscillations) on the surface:



On the following plots the left column shows $(\vec{v} \cdot \vec{n})n_x$ as a function of the x -coordinate and the right column shows $(\vec{v} \cdot \vec{n})n_y$, both for timesteps 1,2,3,5,10,20. Both quantities form the boundary conditions for the mesh deformation. Since I have chosen x_0 such that it does not fall on a node, the initial topography is *not* symmetric and therefore the normal vectors at the nodes on the left and right of the peak are not identical. From the second timestep (the first one for which the free surface algo uses a non zero Stokes velocity as boundary condition) we see that both components $(\vec{v} \cdot \vec{n})n_x$ and $(\vec{v} \cdot \vec{n})n_y$ are asymmetric!

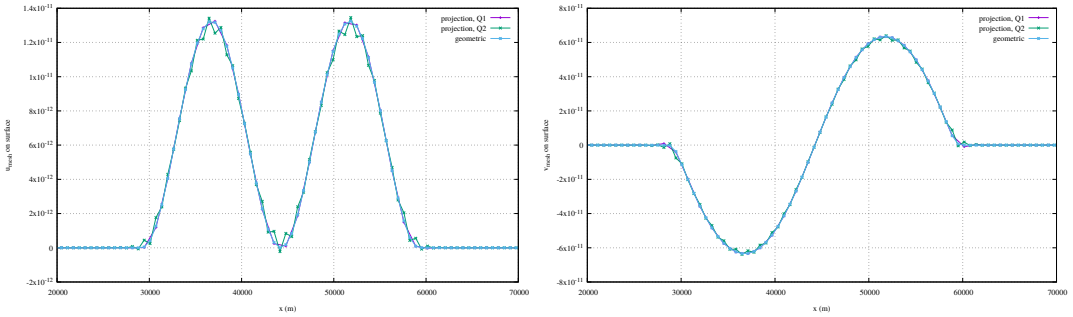


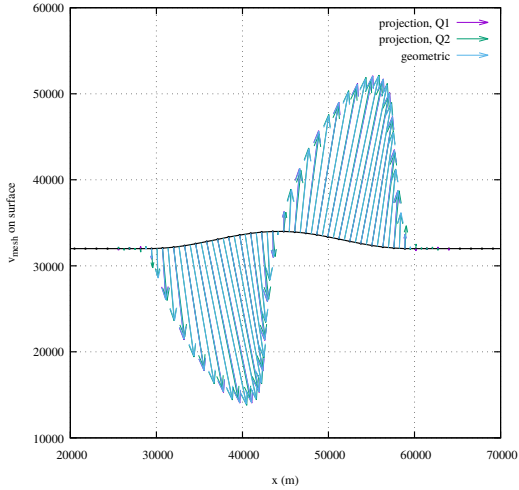


The inescapable conclusion is that the algorithm (as it is now implemented with the normal vector) is incapable of advecting a bump.

In what follows, the Stokes system is solved once, and the obtained velocity is used to compute the mesh velocity boundary condition for the Laplace system. The resolution is set to 100x25. I have implemented the L_2 projection approach of [1406] for both Q1 and Q2 elements. For such a smooth topography the Q1 and geometrical approach (i.e. using geometrically computed normal vectors) are very similar although Q1 produces tiny undershoots. Q2 however generates oscillations which makes the computed velocity not suited as a boundary condition to move surface nodes.

From left to right: horizontal component, vertical component, and vector form of the computed mesh velocity bc.

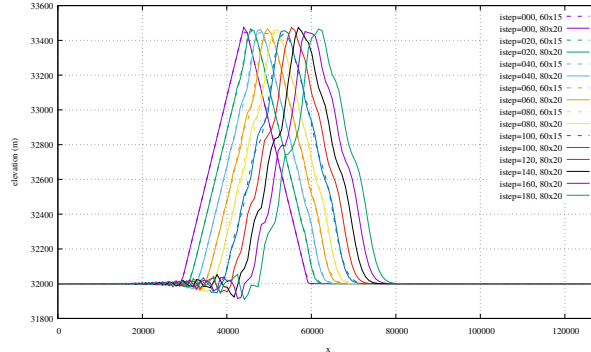
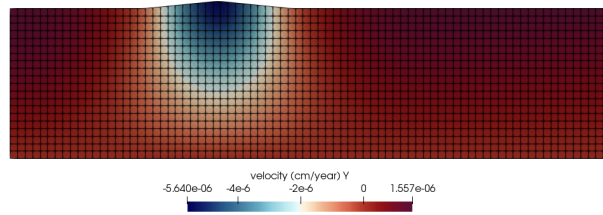


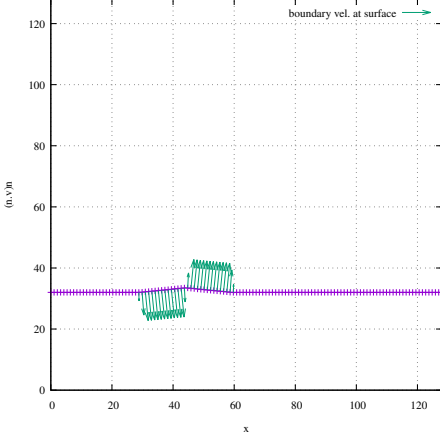


I haven't used any of the projections to carry out timestepping.

Experiment 8 - pure advection test of a pyramidal bump

This is a nearly identical experiment as the previous one, but now the bump is composed of two straight lines, of slopes ± 0.1 . Pyramid centered at $x = 0.345678L_x$, of half width 15km. $\rho = 3000$, $\eta = 10^{26}$. Resolution 60x15. +1cm/yr prescribed on left and right. $dt=10\text{kyr}$.

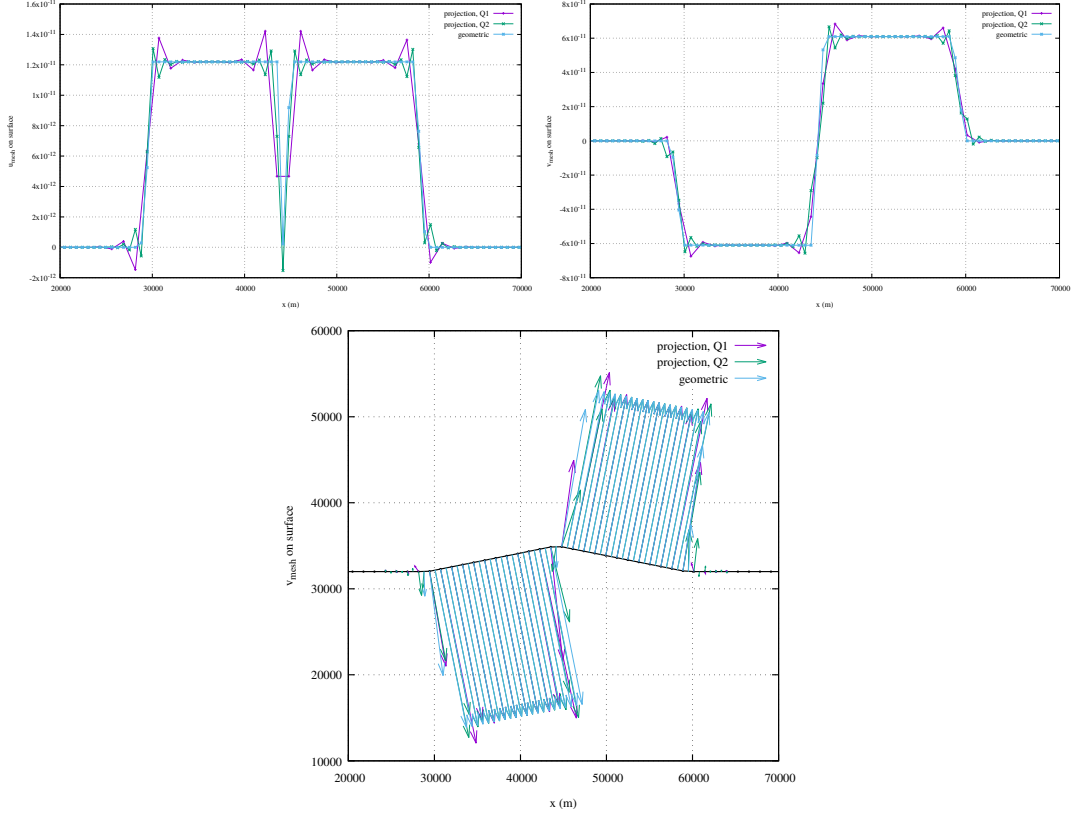




Results are not crazy bad, but we should be able to do better ... the pyramid becomes more and more deformed after only 20km of advection (but surprisingly retains its height).

In what follows, the Stokes system is solved once, and the obtained velocity is used to compute the mesh velocity boundary condition for the Laplace system. The resolution is set to 100x25. I have implemented the L_2 projection approach of [1406] for both Q1 and Q2 elements. For such a broken line topography the geometrical approach (i.e. using geometrically computed normal vectors) is better. Q1 and Q2 both produce under/overshoots/oscillations with no clear winner.

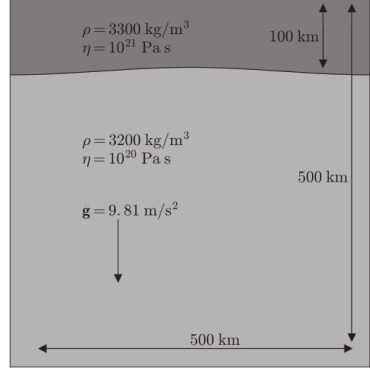
From left to right: horizontal component, vertical component, and vector form of the computed mesh velocity bc.



I haven't used any of the projections to carry out timestepping.

Experiment 9 - Rayleigh-Taylor instability

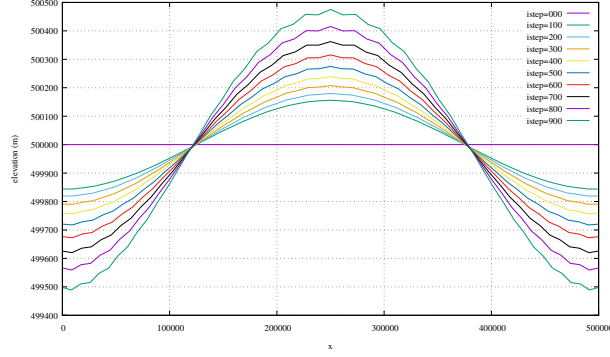
The setup is as follows:



The sinusoidal perturbation is given by

$$y(x) = 400e3 - 500 \cos(2\pi x/L_x)$$

Because I do not have compositional fields or markers implemented in this code I have to align the mesh with the initial sinusoidal perturbation and run the model in Lagrangian mode. Also, as shown in [946], this experiment is prone to drunken sailor instabilities and I have therefore fixed $dt=1000\text{yr}$. As a consequence, the model will run until elements become too distorted.



Stone 55: Subduction as a thin-sheet problem

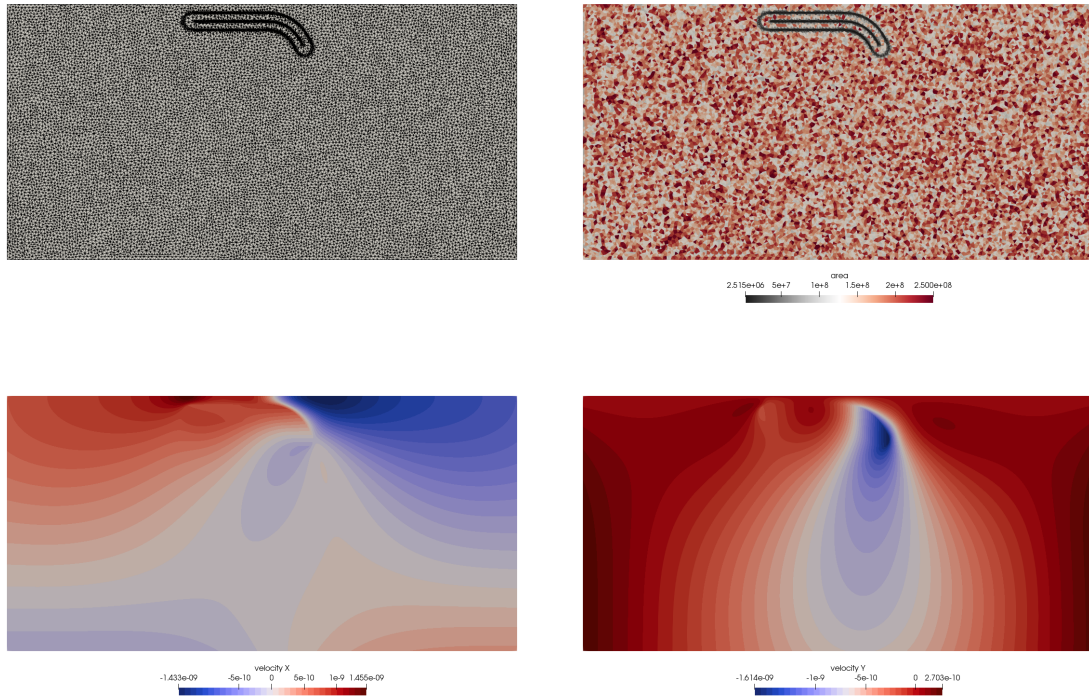
https://github.com/cedriict/fieldstone/tree/master/python_codes/fieldstone_55

Parameters for the setup are defined in *parameters.py*. This file is used in *generate_nodes.py* which produces the *subd.node* file which contains the coordinates of all key points on the boundary of the domain and along the material interfaces. This file is then further processed by the triangle program⁶⁴ as follows:

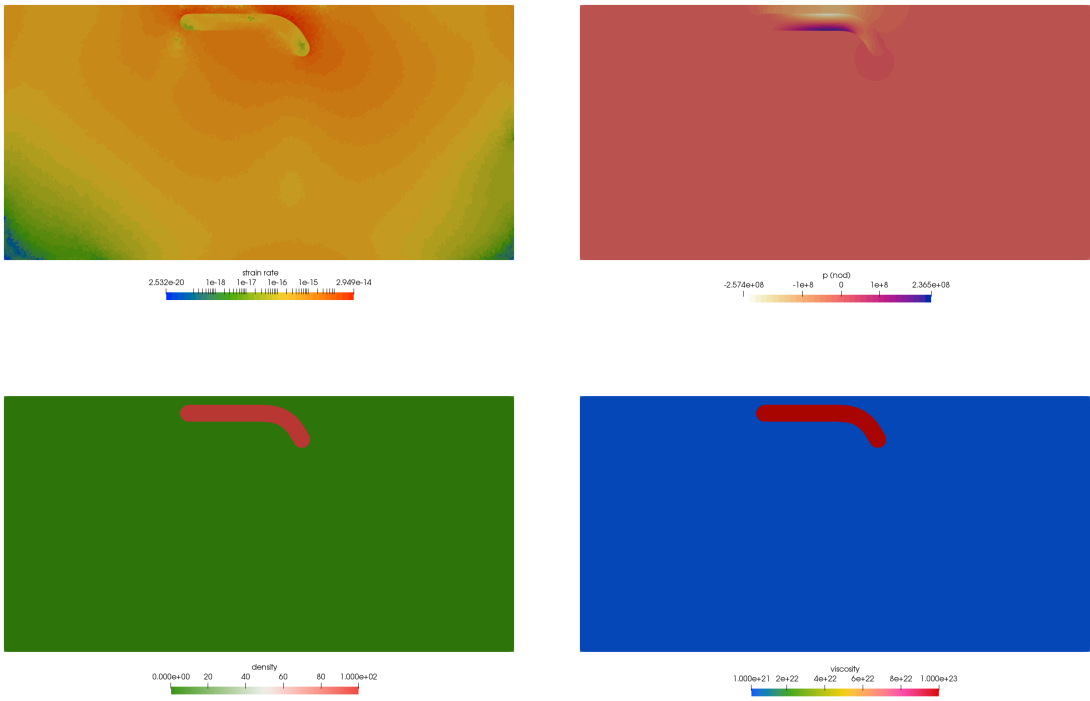
```
./triangle -q -a200000000 -o2 subd.node
```

The '-q' option adds vertices to the mesh to ensure that all angles are between 20 and 140 degrees. The '-a' makes sure that no triangle has an area larger than the supplied number. The '-o2' generates a mesh composed of second order triangles (six nodes per element, rather than three) and the three extra nodes of an element fall at the midpoints of the three edges. This generates two files: 'subd.1.ele' which contains the connectivity of all generated triangles and 'subd.1.node' which contains the coordinates of all nodal points. These two files are then read in *fieldstone.py* and stored in the xV, yV and iconV arrays.

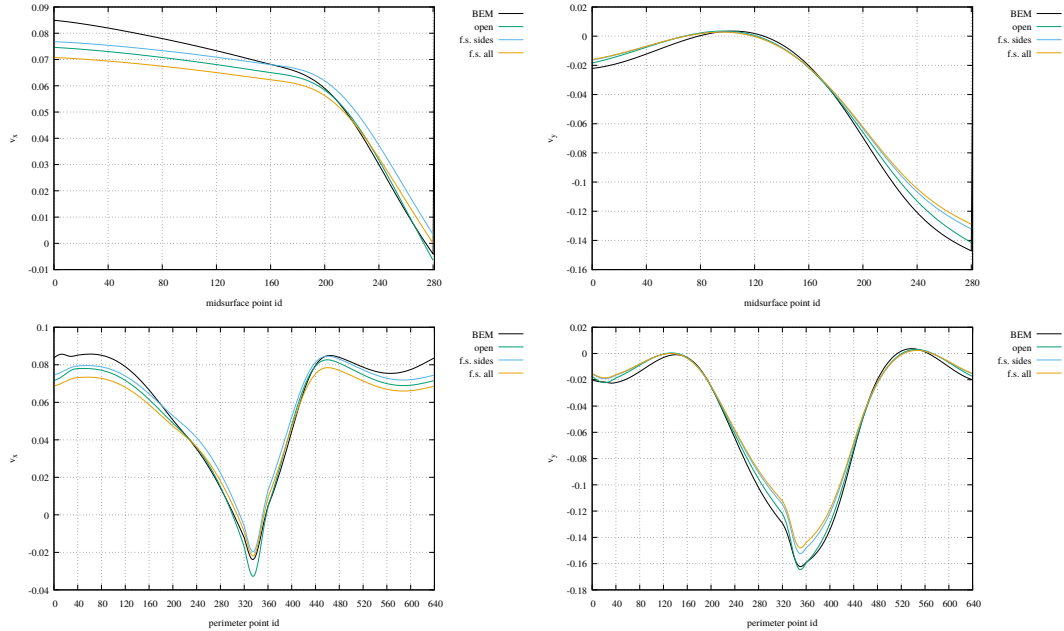
Gravity is vertical and Earth-like. Free-slip boundary conditions are imposed on the top while the other boundaries are free (in/outflow determined freely based on the internal dynamics). In order to remove the horizontal null space the average horizontal velocity is set to zero. Crouzeix-Raviart elements are used, see Section 6.2.9. The density of the mantle is set to zero while the subducting plate has a density $\delta\rho$.



⁶⁴<https://www.cs.cmu.edu/~quake/triangle.html>



Mesh composed of 31,765 triangles. Other parameters: $\theta_0 = 60^\circ$, $\eta_1 = 10^{21}$, $\gamma = 100$, $L_x = 3000\text{km}$, $L_y = 1500\text{km}$, $\delta\rho = 100$, $L = 400\text{km}$, $h = 100\text{km}$, $d = 50\text{km}$.



Top row: midsurface velocity measurements. Bottom row: slab/plate perimeter velocity measurements. 'open' means no b.c. on sides and bottom; 'f.s. sides' means free slip b.c. on left and right sides, open at the bottom; 'f.s. all' means free slip b.c. on sides and bottom.

Literature: [577]

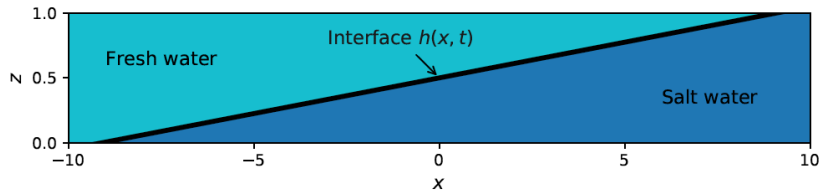
Stone 56: Dynamics of the Salt Water - Fresh Water Interface

Saltwater intrusion in coastal aquifers is a world wide observable phenomena. The mixing of salt and fresh water reduces groundwater quality. It potentially threatens the usability as drinking water. Extensive pumping causing a decrease of groundwater levels amplifies this effect.

Gravity drives salty sea water land inward due to its higher density if an aquifer's water table is lower than sea level. An interface develops between salt and fresh water, which is stable due to the density difference. Along the interface slight mixing occurs due to diffusion. As for most processes in nature, coupled partial differential equations describe the movement of the interface between salt and fresh water.

The target of this exercise is to model a simplified form of the process. Basic assumption hereby are: (i) groundwater flow is mostly horizontal (called *Deput assumption*); (ii) the salt and fresh water interface is sharp, meaning we neglect mixing due to dispersion and diffusion.

We investigate a portion of an aquifer of length L and depth H . Within the aquifer, an interface separates salt water and fresh water as illustrated here under:



The interface $h(x, t)$ is a function of the horizontal location x and time t . For simplicity, we assume an aquifer thickness of $H = 1$. Thus, the values for the position of the interface as a function in the z direction range between zero and one: $h(x, t) \in [0, 1]$.

The differential equation describing the movement of the interface $h(x, t)$ is given by

$$\frac{\partial h(x, t)}{\partial t} = \Gamma \frac{\partial}{\partial x} \left(\frac{h(1-h)\partial h/\partial x}{1 + (\partial h/\partial x)^2} \right) \quad (797)$$

The constant $\Gamma = \frac{\kappa}{\mu g(\rho_{\text{salt}} - \rho_{\text{fresh}})}$ summarizes the physical properties: of the aquifer (permeability κ), of the fluids (viscosity μ , density of salt water ρ_{salt} and density of fresh water ρ_{fresh}) and the gravity constant g .

The differential equation has the character of a non-linear diffusion equation with a non-constant diffusion coefficient $D(h)$:

$$\frac{\partial h}{\partial t} = \Gamma \frac{\partial}{\partial x} \left(D(h) \frac{\partial h}{\partial x} \right) \quad D(h(x, t)) = \frac{h(1-h)}{1 + (\partial h/\partial x)^2} \quad (798)$$

According to the value range of $h \in [0, 1]$, D has the property of $D(0) = D(1) = 0$ (this differential equation is therefore called *degenerate*).

Despite the complexity of the initial differential equation, an analytical solution can be postulated in the form of:

$$h(x, t) = a(t) \cdot x + 0.5 \quad (799)$$

The interface h is a linear function in x with a time-dependent slope $a(t)$. It rotates with time around the fix point $(0; 0.5)$. The slope $a(t)$ can be determined by the ordinary differential equation (REF??):

$$\frac{da(t)}{dt} = -\frac{2a^3}{1 + a^2} \quad (800)$$

The value range of a is limited to $0 < a(t) < 1$ corresponding to a maximal slope angle of 45° . The differential equation in $a(t)$ has an implicit solution:

$$t = \frac{1}{2} \ln \left(\frac{a(0)}{a(t)} \right) + \frac{1}{4} \left(\frac{1}{a(t)^2} - \frac{1}{a(0)^2} \right) \quad (801)$$

We aim to implement a numerical solution of the differential equation 1 which allows us to calculate the location of the interface $h(x, t)$ at specified locations x and times t .

To Do in 2D only

Stone 57: 1D diffusion with DG-FEM

opla

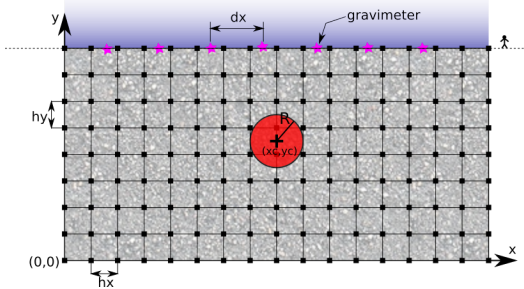
10 fieldstone: Gravity: buried sphere

Before you proceed further, please read :

http://en.wikipedia.org/wiki/Gravity_anomaly

<http://en.wikipedia.org/wiki/Gravimeter>

Let us consider a vertical domain $Lx \times Ly$ where $L_x = 1000\text{km}$ and $L_y = 500\text{km}$. This domain is discretised by means of a grid which counts $nnp = nnx \times nny$ nodes. This grid then counts $nel = nelx \times nely = (nnx - 1) \times (nny - 1)$ cells. The horizontal spacing between nodes is hx and the vertical spacing is hy .



Assume that this domain is filled with a rock type which mass density is given by $\rho_{medium} = 3000\text{kg/m}^3$, and that there is a circular inclusion of another rock type ($\rho_{sphere} = 3200\text{kg/m}^3$) at location $(xsphere, ysphere)$ of radius $rsphere$. The density in the system is then given by

$$\rho(x, y) = \begin{cases} \rho_{sphere} & \text{inside the circle} \\ \rho_{medium} & \text{outside the circle} \end{cases}$$

Let us now assume that we place $nsurf$ gravimeters at the surface of the model. These are placed equidistantly between coordinates $x = 0$ and coordinates $x = Lx$. We will use the arrays $xsurf$ and $ysurf$ to store the coordinates of these locations. The spacing between the gravimeters is $\delta_x = Lx/(nsurf - 1)$.

At any given point (x_i, y_i) in a 2D space, one can show that the gravity anomaly due to the presence of a circular inclusion can be computed as follows:

$$g(x_i, y_i) = 2\pi G(\rho_{sphere} - \rho_0)R^2 \frac{y_i - ysphere}{(x_i - xsphere)^2 + (y_i - ysphere)^2} \quad (802)$$

where r_{sphere} is the radius of the inclusion, $(xsphere, ysphere)$ are the coordinates of the center of the inclusion, and ρ_0 is a reference density.

However, the general formula to compute the gravity anomaly at a given point (x_i, y_i) in space due to a density anomaly of any shape is given by:

$$g(x_i, y_i) = 2G \int \int_{\Omega} \frac{\Delta\rho(x, y)(y - y_i)}{(x - x_i)^2 + (y - y_i)^2} dx dy \quad (803)$$

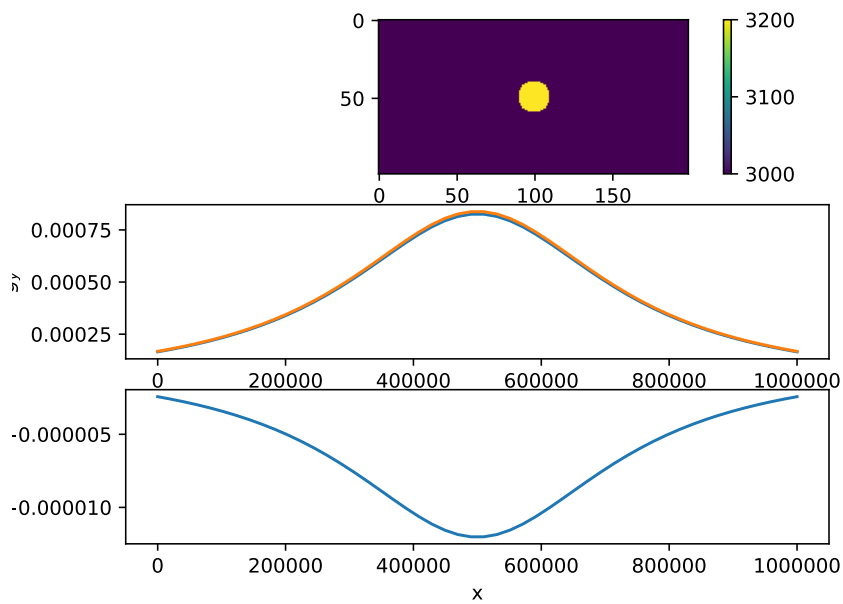
where Ω is the area of the domain on which the integration is to be carried out. Furthermore the density anomaly can be written : $\Delta\rho(x, y) = \rho(x, y) - \rho_0$. We can then carry out the integration for each cell and sum their contributions:

$$g(x_i, y_i) = 2G \sum_{ic=1}^{nel} \int \int_{\Omega_e} \frac{(\rho(x, y) - \rho_0)(y - y_i)}{(x - x_i)^2 + (y - y_i)^2} dx dy \quad (804)$$

where Ω_e is now the area of a single cell. Finally, one can assume the density to be constant within each cell so that $\rho(x, y) \rightarrow \rho(ic)$ and $\int \int_{\Omega_e} dx dy \rightarrow hx \times hy$ and then

$$g(x_i, y_i) = 2G \sum_{ic=1}^{nel} \frac{(\rho(ic) - \rho_0)(y(ic) - y_i)}{(x(ic) - x_i)^2 + (y(ic) - y_i)^2} s_x s_y \quad (805)$$

We will then use the array $gsurf$ to store the value of the gravity anomaly measured at each gravimeter at the surface.



To go further

- explore the effect of the size of the inclusion on the gravity profile.
- explore the effect of the ρ_0 value.
- explore the effect of the grid resolution.
- measure the time that is required to compute the gravity. How does this time vary with nsurf ? how does it vary when the grid resolution is doubled ?
- Assume now that $\rho_2 < \rho_1$. What does the gravity profile look like ?
- what happens when the gravimeters are no more at the surface of the Earth but in a satellite ?
- if you feel brave, redo the whole exercise in 3D...

11 Problems, to do list and projects for students

- Bsc thesis
 - Darcy flow. redo WAFLE (see <http://cedrichieulot.net/wafle.html>)
 - chunk grid
- MSc guided research/thesis
 - surface tension see [1361]p28-29 - see ibuprofem
 - elasticity with markers
 - navier-stokes ? (LUKAS) use dohu matlab code
 - pure shear deformation of inclusions [1565]
 - redo Buck and Sokoutis benchmark for continental convergence [231]
 - redo topo and geoid calculations a la [968]
 - redo Travis study [1564] which is close to Blankenbach [158]. Note that [1113] looks at kinetic energy for [1564]
 - propagator matrix ? what is it ? [1379] (**MSc Thesis**)  Literature[775, 776, 1383, 1768, 392, 1195, 1764, 1051, 1058, 1229, 1709, 1182, 568, 1092, 235]
 - redo early compressional orogen study by Beaumont [100]
- Miscellaneous /to do
 - write about impose bc on el matrix
 - free-slip bc on annulus and sphere . See for example p540 Gresho and Sani book. find book [459]. also check [514] !!
 - constraints [3]
 - formatting of code style
 - Finish nonlinear cavity case5.
 - write about stream functions
 - create stone for layeredflow (see folder one up)
 - in the context of mesh generation on sphere cite [1219]
 - illustrate early boundary fitted static meshes with [1534]
 - [136] spell out the derivation of Jaumann derivative in appendix
 - look at strain-rate softening in [110]
 - write section in features about thermo mechanical simulations and how/why we solve vp, then T.
- carry out critical Rayleigh experiments for various geometries/aspect ratios. Use Arie's notes.
 - Indentor/punch with stress b.c. ?
 - read in crust 1.0 in 2D on chunk
 - compute gravity based on tetrahedra
 - NS a la http://ww2.lacan.upc.edu/huerta/exercises/Incompressible/Incompressible_Ex2.htm
 - write Scott about matching compressible2 setup with his paper
 - including phase changes (w. R. Myhill)
 - GEO1442 indenter setup in plane ?
 - redo puth17 2 layer experiment

- SIMPLE a la p667 [915]
- implement/monitor div v
- shape fct, trial fct, basis fct vs test fct doc
- write/draw the whole FEM process for a 4x3 grid for compgeo
- lukas' 2D and 3D benchmark
- ROTATING disc
- cylindrical footing on (elasto)-viscous medium - analytical solution, Haskell, etc ...
- check the BASIL code by Houseman et al <http://homepages.see.leeds.ac.uk/~eargah/basil/> on which the ELLE code is based <http://elle.ws/>
- try Anderson acceleration for Uzawa [834] with m=1
- $Q_1^+ \times P_0$ Look at fort81 , rota87b and vadvo3
- check [284] for RT0 element use
- deformation around rigid particles [877]
- write about flexural isostasy [1113], bottom Sopale
- mesh containing both quadrilaterals and triangles [28]
- redo/adapt bsc thesis with inversion on stokes sphere
- implementation of fault in FEM codes [1767, 1757]
- https://en.wikipedia.org/wiki/Bernstein_polynomial
- cvi pukp16
- van keken instantane MINI elt
- check $Q_2 \times Q_{-1}$ element, [743] p 697. pressure basis function based at the four 2x2 gauss points.
- look at condition number of \mathbb{K} block for Q1P0 and Q2Q1 as a function of resolution. Insert results in section about why q1p0 should not be used.
- write about splines as shape functions [343]. second or third order shape functions , using extra nodes instead of using more nodes per element. Smaller matrix than Q2 or Q3 but: spline coeffs on nodes are no more unknowns. Plus bc are complicated. Does it work well with visc contrasts ?

`|Cells|, |DataArray type=Int32 Name=connectivity ...|, |DataArray type=Int32 Name=offsets ...|, |DataArray type=UInt8 Name=types ...|, |Cells|`

open questions: what does it mean to have a negative pressure ? should we threshold it when computing yield strength ?

A Three-dimensional applications

In the following table I list many papers which showcase high-resolution models of geodynamical processes (subduction, rifting, mantle flow, plume transport, ...). Given the yearly output of our community and the long list of journal in which research can be disseminated, this list can not be exhaustive.

Ref.	topic	resolution
[169]	Effect of margin curvature on plate deformation in a 3D subduction zones	
[68]	Small-scale sublithospheric convection in the Pacific	$448 \times 56 \times 64$
[1480]	Migration and morphology of subducted slabs in the upper mantle	$50 \times 50 \times 25$
[1334]	Subduction scissor across the South Island of New Zealand	$17 \times 9 \times 9$
[1144]	Influence of a buoyant oceanic plateau on subduction zones	$80 \times 40 \times 80$
[302]	Subduction dynamics, origin of Andean orogeny and the Bolivian orocline	$96 \times 96 \times 64$
[510]	Feedback between rifting and diapirism, ultrahigh-pressure rocks exhumation	$100 \times 64 \times 20$
[20]	Numerical modeling of upper crustal extensional systems	$160 \times 160 \times 12$
[21]	Rift interaction in brittle-ductile coupled systems	$160 \times 160 \times 23$
[1028]	Kinematic interpretation of the 3D shapes of metamorphic core complexes	$67 \times 67 \times 33$
[893]	Role of rheology and slab shape on rapid mantle flow: the Alaska slab edge	$960 \times 648 \times 160$
[301]	Complex mantle flow around heterogeneous subducting oceanic plates	$96 \times 96 \times 64$
[221]	Oblique rifting and continental break-up	$150 \times 50 \times 30$
[135]	Influence of mantle plume head on dynamics of a retreating subduction zone	$80 \times 40 \times 80$
[220]	Rift to break-up evolution of the Gulf of Aden	$83 \times 83 \times 40$
[222]	Thermo-mechanical impact of plume arrival on continental break-up	$100 \times 70 \times 20$
[307]	Subduction and slab breakoff controls on Asian indentation tectonics	$96 \times 96 \times 64$
[530]	Modeling of upper mantle deformation and SKS splitting calculations	$96 \times 64 \times 96$
[1430]	Backarc extension/shortening, slab induced toroidal/poloidal mantle flow	$352 \times 80 \times 64$
[1115]	Sediment transports in the context of oblique subduction modelling	$500 \times 164 \times 100$
[1774]	Crustal growth at active continental margins	$404 \times 164 \times 100$
[1031]	Dynamics of India-Asia collision	$257 \times 257 \times 33$
[1683]	Strain-partitioning in the Himalaya	$256 \times 256 \times 40$
[1068]	Collision of continental corner from 3-D numerical modeling	$500 \times 340 \times 164$
[1327]	Dependence of mid-ocean ridge morphology on spreading rate	$196 \times 196 \times 100$
[529]	Mid mantle seismic anisotropy around subduction zones	$197 \times 197 \times 53$
[808]	Oblique rifting of the Equatorial Atlantic	$120 \times 80 \times 20$
[1206]	Dynamics of continental accretion	$256 \times 96 \times 96$
[1412]	Thrust wedges: infl. of decollement strength on transfer zones	$309 \times 85 \times 149$
[271]	Asymmetric three-dimensional topography over mantle plumes	$500 \times 500 \times 217$
[1544]	modelled crustal systems undergoing orogeny and subjected to surface processes	$96 \times 32 \times 14$
[1076]	Thermo-mechanical modeling of continental rifting and seafloor spreading	$197 \times 197 \times 197$
[134]	Geodynamics of oceanic plateau and plume head accretion	$256 \times 96 \times 96$

B Codes in geodynamics

In what follows I make a quick inventory of the main codes of computational geodynamics, for crust, lithosphere and/or mantle modelling.

in order to find all CIG-codes citations go to: <https://geodynamics.org/cig/news/publications-refbase/>

- ABAQUS

[193] [646] [616] [303] [1013] [1126] [304] [1250] [1299] [1241]

- ADELI

1997: [803]
2004: [699]
2006: [1639]
2008: [168][169]
2012: [645][688]
2013: [1660]
2014: [319]
2015: [317]
2018: [318][647]

- ASPECT

This code is hosted by CIG at <https://geodynamics.org/cig/software/aspect/>. It is an open source community code based on the finite element library deal.II [41]. It is massively parallel, relies on the p4est library for adaptive mesh refinement, uses the Trilinos solver library, and can deal with 2D and 3D geometries.

2012: [1009]
2015: [51][1558]
2016: [429][632][1750]
2017: [807][427][809][1406][1407][50][1540][211] [1278][1515][1746]
2018: [428][1280][697][820][633][1298][1324][210]
2019: [90][1482][402][1091][634][431][1268]

- BASIL/ELLE <http://elle.ws/> [172] [1094]

- BEM [1223] [1226]

- CHIC [1269]

- CitcomS and CITCOMCU

These codes are hosted by CIG at <https://geodynamics.org/cig/software/citcomcu/> and <https://geodynamics.org/cig/software/citcoms/>.

1995: [1216]
1996: [1468][1209]
1997: [1215][1215][261]
1998: [1213][1760][768]
1999: [1218][262][1609][1042]
2000: [1765][763][1041][767]
2001: [143][1046]
2002: [1520]
2003: [1605][394][144][1048][1039]
2004: [1465][592][1049][397]
2005: [145][1166][1165][1047]
2006: [106][1307][1518][109][395][593][398]
2007: [146][1763][1123][69][1390][1229][393]
2008: [693][629][1761][836][1044]
2009: [1075][40][1748][34][566][265][103] [70][1052]

2010: [249][1627][68][266][1747][140]
 [892][1776]
 2011: [107][1040][1602][1054][1089][67]
 2012: [45][893][147][178][872][1769][1466] [828][895][1125]
 2013: [65][185][186][894][1338][1273]
 [46][396]
 2014: [561][248][926][47][1656][1448]
 [11][1110][1777]
 2015: [66][184][179][1452][430][1603]
 [1662][1655][1654][801][1526][1055]
 2016: [1682][1681][891][602][1396]
 2017: [10][1109][591][806]
 2018: [824][969][927][1657][852]
 2019: [1149][604][1108][1104][1129]

[cross check with CIG database](#)

- CONMAN This code is hosted by CIG at <https://geodynamics.org/cig/software/conman/> [973] [886] [970] [971] [887] [108][1042] [1045] [1249] [439] [972]
- CONVRS [1732] [1730]
- DOUAR
[199] [1543] [1718] [201] [1098] [1239] [1683] [1254] [997]
- DYNEARTHSOL [339]
- ELMER Elmer is an open source multiphysical simulation software mainly developed by CSC - IT Center for Science (CSC). Elmer development was started 1995 in collaboration with Finnish Universities, research institutes and industry. Elmer includes physical models of fluid dynamics, structural mechanics, electromagnetics, heat transfer and acoustics, for example. These are described by partial differential equations which Elmer solves by the Finite Element Method (FEM).
<https://www.csc.fi/web/elmer>
[1114]
- LaCoDe [452]
- M-DOODS, Duretz code [1719] [1717] [332][494]
- FENICS [17]
[875] [1256]
- GAIA
[875] [1256]
- GALE
This code is hosted by CIG at <https://geodynamics.org/cig/software/gale/> [547] [729] [137] [420] [1028][1067] [46]
- (G)TECTON
1980: [1171]
1981: [1170]
1993: [723]
1995: [724]
1996: [766][692]
1999: [725][618]
2001: [240][728]
2002: [241]
2005: [726][1626][1628][726]

2006: [581][1093][1435]
2007: [1629]
2008: [450][449]
2009: [1015][1312]
2010: [1582][1311]
2011: [58][59]
2013: [1313][1665]
2014: [1583]
2015: [1131][1260]
2016: [639][1132]
2017: [1287]
2018: [727][1261][811]

- ELEFANT

[1558] [1107] [245] [1023] [1540] [1314] [1701]

- ELLIPSIS

[1208][1687][?] [1686] [1279] [1212][678][497] [1281] [1334] [1054] [1050] [1377]

- FANTOM

[1538] [20] [21] [22] [521] [1544] [519] [520]

FDCON

[518] [606] [605]

- FLUIDITY [440] [628]

- geoFLAC (based on PARAVOZ) [898]

- IFISS: Incompressible Flow Iterative Solution Solver is a MATLAB package that is a very useful tool for people interested in learning about solving PDEs. IFISS includes built-in software for 2D versions of: the Poisson equation, the convection-diffusion equation, the Stokes equations and the Navier-Stokes equations.

<https://personalpages.manchester.ac.uk/staff/david.silvester/ifiss/>

- the I2(3)E(L)VIS code

2003: [674][675][673]

2004: [676][677][671][661]

2005: [258][1130][1490]

2006: [237][654][712][666]

2007: [655][711][664][714][716]

2008: [1436][665][1577][531][1773][259][315][1185][1263][670]

2009: [667][257][1080][533][1074]

2010: [652][1262][85][1069]

2011: [488][490][1070][653][669][157][1264][707][1081]

2012: [409][487][1741][532][715][1578]

2013: [1068][1246][1115][1597][1596][1774][498][668] [1137][326][327][486][316][1078][1645] [662][660][1181]

2014: [489][1327][1412][1644][62][1077][1488][1124] [271][713][1598][1138][63][706][657][663][690]

2015: [485][1579][1413][672][1413][996]

2016: [995][1116][560][1127]

2017: [1128]

2018: [1771]

2019: [994][1072]

- I3MG [529]

- LAMEM [1436] [946] [1030] [1150] [1031] [383] [86] [551] [550] [1325] [552] [382] [950]

- LAPEX2D (LAgrangian Particle EXplicit, based on the prototype code PAROVOZ) [1461] [237][56] [55] [1436] [1462]
- LITMOD [7] [6] [611] [612]
- MARC [1253] [1252]

- MILAMIN

MILAMIN is a finite element method implementation in native MATLAB that is capable of doing one million degrees of freedom per minute on a modern desktop computer. This includes pre-processing, solving, and post-processing. The MILAMIN strategies and package are applicable to a broad class of problems in Earth science. <http://milamin.org/>

2008: [426]
 2009: [705]
 2010: [1011][944]
 2011: [1720]
 2012: [642]
 2014: [918]
 2015: [1101][643][1536][1238]
 2016: [901][1140]
 2018: [493][902][900][406][913][1350][331]
 2019: [33][1460][90]

- PARAVOZ/FLAMAR/FLAC

1989: [422]
 1993: [1316]
 1996: [797]
 1998: [649]
 2000: [1025]
 2001: [273][267]
 2002: [57][366]
 2003: [782][648][1581]
 2004: [762][650][1562][1552][369]
 2005: [272]
 2006: [276]
 2007: [1715][274]
 2008: [1716][1553]
 2009: [651][1718][280]
 2012: [36][645][757][644]
 2013: [1671][583]
 2014: [582][625][270]
 2015: [1710][1142][638][467]

- PINK3D [1649]

- PLASTI [613]

- pTatin3D: A nice succinct description of the code is given in Appendix B of [1029].

2013: [1301]
 2014: [1154]
 2015: [1151]
 2017: [1029]
 2018: [922]
 2019: [921]

- Pylith

[2]

- RHEA [281] [1476] [16] [283]
- SAMOVAR [508]
- SEPRAN
 - 1993: [1586][1591]
 - 1994: [1642][1617]
 - 1995: [1593]
 - 1996: [1592]
 - 2002: [358][1604]
 - 2003: [1620]
 - 2004: [1621][1622][1623]
 - 2005: [1624][1447]
 - 2006: [1082][1083]
 - 2007: [1619][360][192][191]
 - 2008: [1310][190]
 - 2009: [1634]
 - 2010: [1587][1494]
 - 2011: [1612]
 - 2012: [1588][121][333]
 - 2013: [35]
 - 2014: [334][1221]
 - 2015: [1589]
 - 2019: [1755][1590]
- SISTER
 - [1272]
- SLIM3D
 - [1320] [1342] [221] [222] [220] [219] [808] [993] [365] [224] [60]
- SLOMO [943]
 - SNAC [340]
- MICROFEM/SOPALE
 - 1994: [1693][94][100]
 - 1995: [614][509]
 - 1996: [98]
 - 1999: [1691][1689]
 - 2000: [1331][99]
 - 2001: [96]
 - 2002: [869][1332]
 - 2003: [866][1631][1695][1336][243][1699]
 - 2004: [97][1333][1330][512][637]
 - 2005: [636][871]
 - 2006: [1329][1450]
 - 2007: [870][424][1205][1451]
 - 2008: [1449][1668][1669][703][242]
 - 2009: [958][95][244][731][1458]
 - 2010: [15][14][736][1335]
 - 2011: [423][292][865]
 - 2012: [737][738][986][730][896]
 - 2013: [290][330][556][557][718][739][978][1265][897]
 - 2014: [702]
 - 2015: [18][291][819]
 - 2016: [1090]
 - 2017: [289]

- STAG3D/STAGYY

1994: [1508]
 1995: [1440]
 1996: [1509]
 1998: [1203][1550]
 2002: [542][1501]
 2003: [1514]
 2004: [1713][1712]
 2005: [748]
 2006: [1189]
 2007: [750][749][813]
 2008: [462][815][814]
 2009: [463][1242][957]
 2010: [464]
 2011: [1401][707]
 2012: [1400][412][388][465][460][39]
 2013: [1411][1502]

2014: [1727][410][1402][385][112][1066]
 2015: [113] 2016: [1457]
 2017: [384]
 2018: [389][162][386][43]
 2019: [754][44][461]

- SUBMAR

[1135] [1134] [1392]

- SULEC SULEC is a finite element code that solves the incompressible Navier-Stokes equations for slow creeping flows. The code is developed by Susan Ellis (GNS Sciences, NZ) and Susanne Buitner (NGU). <http://www.geodynamics.no/buitner/sulec.html>

2011: [1339][510]
 2012: [239][1529][409][751]
 2013: [679]
 2014: [680][1340]
 2015: [1245]
 2016: [1792]
 2017: [1247]
 2018: [1531]
 2019: [511]

- TERRA: The computational grid is based on a projection of the regular icosahedron onto a sphere and successive dyadic refinements [89]. Concentric copies of such spherical layers of nodes build the domain in radial direction.

[87] [694] [1505] [1506] [254] [253][1725] [251] [1303][1703][719] [1721] [1702] [437] [438] [1599]

- TERRA-NEO: [1680]

- TerraFERMA [1698] [1697] [1473] [320] [321]

- YACC [1558] [1556]

- UNDERWORLD 1&2

2006: [1479][1210]
 2007: [1212][1429]
 2008: [1037][1288][729]
 2010: [308][1144][1480][1478][544][309]

2011: [1174][302]
2012: [301]
2013: [135][1430][530][307][401]
2014: [543]
2015: [1337][134][1431][1454]
2016: [1455][1289][974]
2017: [91]
2018: [1173][1724][92]
2019: [1424][1723][306]

- VEMAN [136]

C Matrix properties

C.1 Symmetric matrices

Any symmetric matrix has only real eigenvalues, is always diagonalizable, and has orthogonal eigenvectors. A symmetric $N \times N$ real matrix \mathbf{M} is said to be

- **positive definite** if $\vec{x} \cdot \mathbf{M} \cdot \vec{x} > 0$ for every non-zero vector \vec{x} of n real numbers. All the eigenvalues of a Symmetric Positive Definite (SPD) matrix are positive. If A and B are positive definite, then so is $A+B$. The matrix inverse of a positive definite matrix is also positive definite. An SPD matrix has a unique Cholesky decomposition. In other words the matrix \mathbf{M} is positive definite if and only if there exists a unique lower triangular matrix \mathbf{L} , with real and strictly positive diagonal elements, such that $\mathbf{M} = \mathbf{LL}^T$ (the product of a lower triangular matrix and its conjugate transpose). This factorization is called the Cholesky decomposition of \mathbf{M} .
- **positive semi-definite** if $\vec{x} \cdot \mathbf{M} \cdot \vec{x} \geq 0$
- **negative definite** if $\vec{x} \cdot \mathbf{M} \cdot \vec{x} < 0$
- **negative semi-definite** if $\vec{x} \cdot \mathbf{M} \cdot \vec{x} \leq 0$

The Stokes linear system

$$\begin{pmatrix} \mathbb{K} & \mathbb{G} \\ \mathbb{G}^T & 0 \end{pmatrix} \cdot \begin{pmatrix} \mathbf{v} \\ \mathbf{p} \end{pmatrix} = \begin{pmatrix} \mathbf{f} \\ \mathbf{g} \end{pmatrix}$$

is **indefinite** (i.e. it has positive as well as negative eigenvalues).

A square matrix that is not invertible is called **singular** or degenerate. A square matrix is singular if and only if its determinant is 0. Singular matrices are rare in the sense that if you pick a random square matrix, it will almost surely not be singular.

C.2 Schur complement

From wiki. In linear algebra and the theory of matrices, the Schur complement of a matrix block (i.e., a submatrix within a larger matrix) is defined as follows. Suppose $\mathbf{A}, \mathbf{B}, \mathbf{C}, \mathbf{D}$ are respectively $p \times p$, $p \times q$, $q \times p$ and $q \times q$ matrices, and \mathbf{D} is invertible. Let

$$\mathbf{M} = \begin{pmatrix} \mathbf{A} & \mathbf{B} \\ \mathbf{C} & \mathbf{D} \end{pmatrix}$$

so that \mathbf{M} is a $(p+q) \times (p+q)$ matrix. Then the Schur complement of the block \mathbf{D} of the matrix \mathbf{M} is the $p \times p$ matrix

$$\mathbf{S} = \mathbf{A} - \mathbf{B} \cdot \mathbf{D}^{-1} \cdot \mathbf{C}$$

Application to solving linear equations: The Schur complement arises naturally in solving a system of linear equations such as

$$\begin{aligned} \mathbf{A} \cdot \vec{x} + \mathbf{B} \cdot \vec{y} &= \vec{f} \\ \mathbf{C} \cdot \vec{x} + \mathbf{D} \cdot \vec{y} &= \vec{g} \end{aligned}$$

where \vec{x}, \vec{f} are p -dimensional vectors, \vec{y}, \vec{g} are q -dimensional vectors, and $\mathbf{A}, \mathbf{B}, \mathbf{C}, \mathbf{D}$ are as above. Multiplying the bottom equation by $\mathbf{B} \cdot \mathbf{D}^{-1}$ and then subtracting from the top equation one obtains

$$(\mathbf{A} - \mathbf{B} \cdot \mathbf{D}^{-1} \cdot \mathbf{C}) \cdot \vec{x} = \vec{f} - \mathbf{B} \cdot \mathbf{D}^{-1} \cdot \vec{g}$$

Thus if one can invert \mathbf{D} as well as the Schur complement of \mathbf{D} , one can solve for \vec{x} , and then by using the equation $\mathbf{C} \cdot \vec{x} + \mathbf{D} \cdot \vec{y} = \vec{g}$ one can solve for \vec{y} . This reduces the problem of inverting a $(p+q) \times (p+q)$ matrix to that of inverting a $p \times p$ matrix and a $q \times q$ matrix. In practice one needs \mathbf{D} to be well-conditioned in order for this algorithm to be numerically accurate.

Considering now the Stokes system:

$$\begin{pmatrix} \mathbb{K} & \mathbb{G} \\ \mathbb{G}^T & -\mathbb{C} \end{pmatrix} \cdot \begin{pmatrix} \vec{v} \\ \vec{p} \end{pmatrix} = \begin{pmatrix} \vec{f} \\ \vec{g} \end{pmatrix}$$

Factorising for \vec{p} we end up with a **velocity-Schur complement**. Solving for \vec{p} in the second equation and inserting the expression for \vec{p} into the first equation we have

$$\mathbb{S}_v \cdot \vec{v} = \vec{f} \quad \text{with} \quad \mathbb{S}_v = \mathbb{K} + \mathbb{G} \cdot \mathbb{C}^{-1} \cdot \mathbb{G}^T$$

Factorising for \vec{v} we get a **pressure-Schur complement**.

$$\mathbb{S}_p \cdot \vec{p} = \mathbb{G}^T \cdot \mathbb{K}^{-1} \cdot \vec{f} \quad \text{with} \quad \mathbb{S}_p = \mathbb{G}^T \cdot \mathbb{K}^{-1} \cdot \mathbb{G} + \mathbb{C}$$

D Dont be a hero - unless you have to

What follows was published online on July 17th, 2017 at <https://blogs.egu.eu/divisions/gd/2017/07/19/dont-be-a-hero-unless-you-have-to/> It was written by me and edited by Iris van Zelst, at the time PhD student at ETH Zürich.

In December 2013, I was invited to give a talk about the ASPECT code [1] at the American Geological Union conference in San Francisco. Right after my talk, Prof. Louis Moresi took the stage and gave a talk entitled: *Underworld: What we set out to do, How far did we get, What did we Learn?*

The abstract went as follows:

"Underworld was conceived as a tool for modelling 3D lithospheric deformation coupled with the underlying / surrounding mantle flow. The challenges involved were to find a method capable of representing the complicated, non-linear, history dependent rheology of the near surface as well as being able to model mantle convection, and, simultaneously, to be able to solve the numerical system efficiently. [] The elegance of the method is that it can be completely described in a couple of sentences. However, there are some limitations: it is not obvious how to retain this elegance for unstructured or adaptive meshes, arbitrary element types are not sufficiently well integrated by the simple quadrature approach, and swarms of particles representing volumes are usually an inefficient representation of surfaces."

Aside from the standard numerical modelling jargon, Louis used a term during his talk which I thought at the time had a nice ring to it: hero codes. In short, I believe he meant the codes written essentially by one or two people who at some point in time spent great effort into writing a code (usually choosing a range of applications, a geometry, a number of dimensions, a particular numerical method to solve the relevant PDEs(1), and a tracking method for the various fields of interest).

In the long list of Hero codes, one could cite (in alphabetical order) CITCOM [1], DOUAR [8], FANTOM [2], IELVIS [5], LaMEM [3], pTatin [4], SLIM3D [10], SOPALE [7], StaggYY [6], SULEC [11], Underworld [9], and I apologise to all other heroes out there whom I may have overlooked. And who does not want to be a hero? The Spiderman of geodynamics, the Superwoman of modelling?

Louis' talk echoed my thoughts on two key choices we (computational geodynamicists) are facing: Hero or not, and if yes, what type?

Hero or not?

Speaking from experience, it is an intense source of satisfaction when peer-reviewed published results are obtained with the very code one has painstakingly put together over months, if not years. But is it worth it?

On the one hand, writing one owns code is a source of deep learning, a way to ensure that one understands the tool and knows its limitations, and a way to ensure that the code has the appropriate combination of features which are necessary to answer the research question at hand. On the other hand, it is akin to a journey; a rather long term commitment; a sometimes frustrating endeavour, with no guarantee of success. Let us not deny it many a student has started with one code only to switch to plan B sooner or later. Ultimately, this yields a satisfactory tool with often little to no perennial survival over the 5 year mark, a scarce if at all existent documentation, and almost always not compliant with the growing trend of long term repeatability. Furthermore, the resulting code will probably bear the marks of its not-all-knowing creator in its DNA and is likely not to be optimal nor efficient by modern computational standards.

This brings me to the second choice: elegance & modularity or taylored code & raw performance? Should one develop a code in a very broad framework using as much external libraries as possible or is there still space for true heroism?

It is my opinion that the answer to this question is: both. The current form of heroism no more lies in writing ones own FEM(2)/FDM(3) packages, meshers, or solvers from scratch, but in cleverly taking advantage of state-of-the-art packages such as for example p4est [15] for Adaptive Mesh Refinement, PetSc [13] or Trilinos [14] for solvers, Saint Germain [17] for particle tracking, deal.ii [12] or Fenics [16] for FEM, and sharing their codes through platforms such as svn, bitbucket or github.

In reality, the many different ways of approaching the development or usage of a (new) code is linked to the diversity of individual projects, but ultimately anyone who dares to touch a code (let alone write one) is a hero in his/her own right: although (super-)heroes can be awesome on their own, they often

complete each other, team up and join forces for maximum efficiency. Let us all be heroes, then, and join efforts to serve Science to the best of our abilities.

Abbreviations

- (1) PDE: Partial Differential Equation
- (2) FEM: Finite Element Method
- (3) FDM: Finite Difference Method

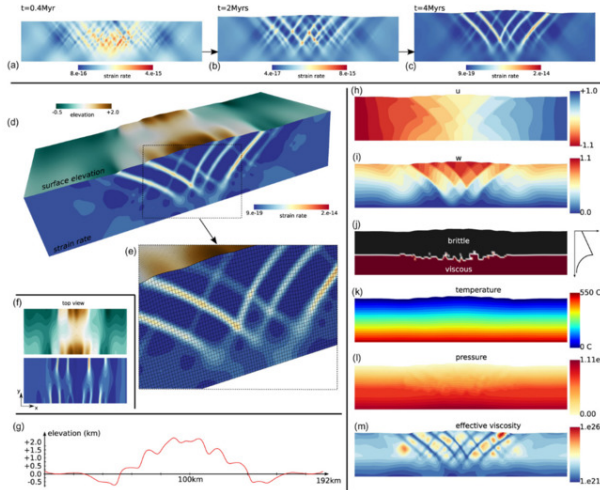
References

- [1] Zhong et al., JGR 105, 2000;
- [2] Thieulot, PEPI 188, 2011;
- [3] Kaus et al., NIC Symposium proceedings, 2016;
- [4] May et al, CMAME 290, 2015
- [5] Gerya and Yuen, PEPI 163, 2007
- [6] Tackley, PEPI 171, 2008
- [7] Fullsack, GJI 120, 1995
- [8] Braun et al., PEPI 171, 2008
- [9] <http://www.underworldcode.org/>
- [10] Popov and Sobolev, PEPI 171, 2008
- [11] <http://www.geodynamics.no/buiter/sulec.html>
- [12] Bangerth et al., J. Numer. Math., 2016; <http://www.dealii.org/>
- [13] <http://www.mcs.anl.gov/petsc/>
- [14] <https://trilinos.org/>
- [15] Burstedde et al., SIAM journal on Scientific Computing, 2011; <http://www.p4est.org/>
- [16] <https://fenicsproject.org/>
- [17] Quenette et al., Proceedings 19th IEEE, 2007

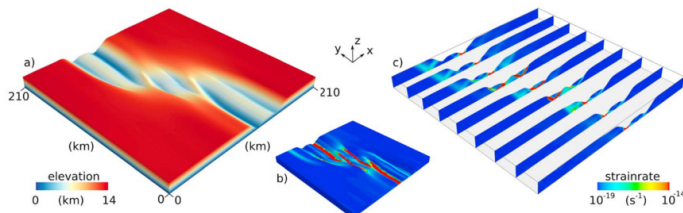
E A FANTOM, an ELEFANT and a GHOST

While a post-doctoral researcher at Bergen University I developed the FANTOM code. Here is what other people and I have published with it:

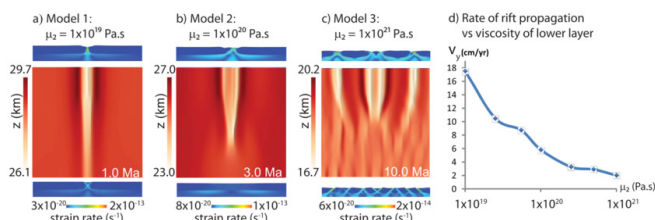
- *FANTOM : two- and three-dimensional numerical modelling of creeping flows for the solution of geological problems*, C. Thieulot, Physics of the Earth and Planetary Interiors, 188, 2011.



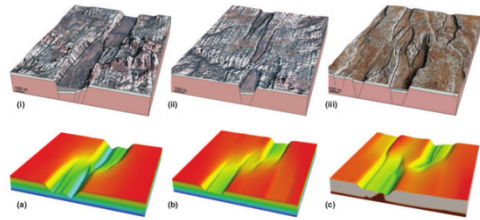
- *Three-dimensional numerical modeling of upper crustal extensional systems*, V. Allken, R.S. Huismans and C. Thieulot, JGR 116, 2011. <https://doi.org/10.1029/2011JB008319>



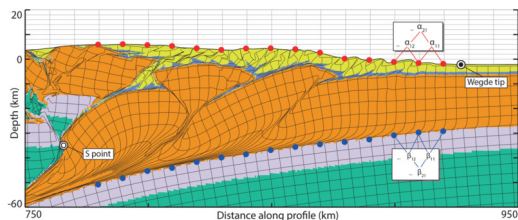
- *Factors controlling the mode of rift interaction in brittle-ductile coupled systems: A 3D numerical study*, V. Allken, R.S. Huismans and C. Thieulot, Geochem. Geophys. Geosyst. 13(5), 2012. <https://doi.org/10.1029/2012GC004077>



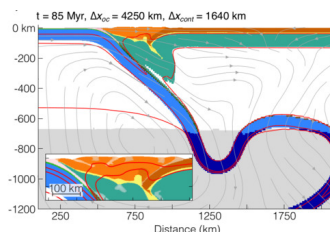
- *3D numerical modelling of graben interaction and linkage: a case study of the Canyonlands grabens, Utah*, V. Allken, R.S. Huismans, Haakon Fossen and C. Thieulot, Basin Research, 25, 1-14, 2013. <https://doi.org/10.1111/bre.12010>



- Three-dimensional numerical simulations of crustal systems undergoing orogeny and subjected to surface processes, C. Thieulot, P. Steer and R.S. Huismans, *Geochem. Geophys. Geosyst.*, 15, 2014. doi:10.1002/2014GC005490
- Extensional inheritance and surface processes as controlling factors of mountain belt structure, Z. Erdős, R.S. Huismans, P. van der Beek, and C. Thieulot, *J. Geophys. Res. Solid Earth*, 119, 2014. doi:10.1002/2014JB011408
- First-order control of syntectonic sedimentation on crustal-scale structure of mountain belts, Z. Erdős, R.S. Huismans, P. van der Beek, *J. Geophys. Res. Solid Earth*, 120, 5362-5377, 2015. doi:10.1002/2014JB011785
- Control of increased sedimentation on orogenic fold-and-thrust belt structure - insights into the evolution of the Western Alps, Z. Erdős, R.S. Huismans and P. van der Beek, *Solid Earth*, 10, 391-404, 2019. <https://doi.org/10.5194/se-10-391-2019>

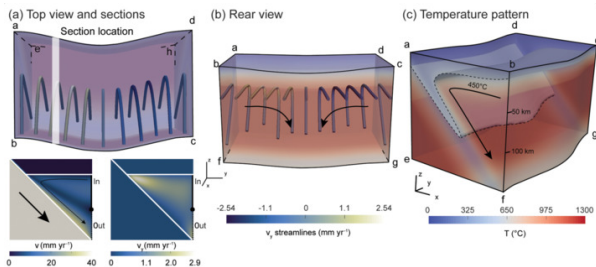


- Mountain building or backarc extension in ocean-continent subduction systems - a function of backarc lithospheric strength and absolute plate velocities, S.G. Wolf and R.S. Huismans, *JGR*, 2019. <https://doi.org/10.1029/2018JB017171>

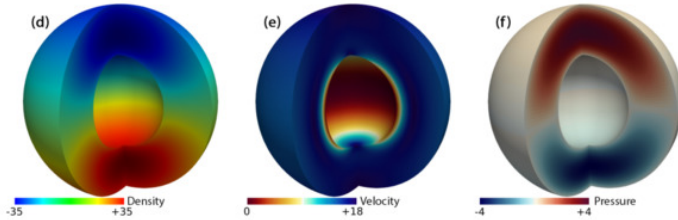


Upon my arrival at Utrecht University in 2012 I started working on a more flexible code, called ELEFANT, which has since very much diverged from FANTOM.

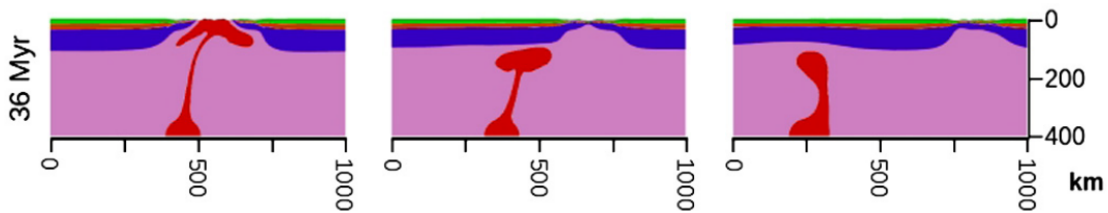
- The effect of obliquity on temperature in subduction zones: insights from 3-D numerical modeling, A. Plunder, C. Thieulot and D.J.J. van Hinsbergen, *Solid Earth* 9, 759-776, 2018. <https://doi.org/10.5194/se-9-759-2018>



- Analytical solution for viscous incompressible Stokes flow in a spherical shell, C. Thieulot, Solid Earth 8, 1181-1191, 2017. <https://doi.org/10.5194/se-8-1181-2017>



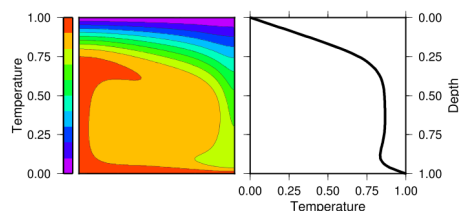
- Lithosphere erosion and continental breakup: interaction of extension, plume upwelling and melting, A. Lavecchia, C. Thieulot, F. Beekman, S. Cloetingh and S. Clark, E.P.S.L. 467, p89-98, 2017.



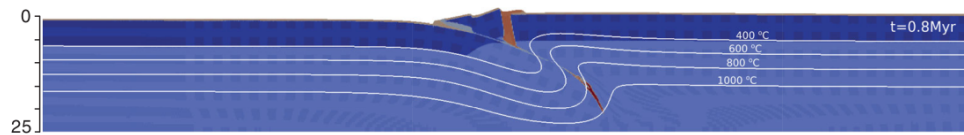
- Benchmarking numerical models of brittle thrust wedges, Susanne J.H. Buiter, Guido Schreurs, Markus Albertz, Taras V. Gerya, Boris Kaus, Walter Landry, Laetitia le Pourhiet, Yury Mishin, David L. Egholm, Michele Cooke, Bertrand Maillot, Cedric Thieulot, Tony Crook, Dave May, Pauline Soulioumiac, Christopher Beaumont Journal of Structural Geology 92, p140-177, 2016. <https://doi:10.1016/j.jsg.2016.03.003>



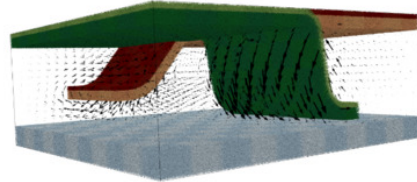
- A community benchmark for viscoplastic thermal convection in a 2-D square box, N. Tosi, C. Stein, L. Noack, C. Huettig, P. Maierova, H. Samuel, D.R. Davies, C.R. Wilson, S.C. Kramer, C. Thieulot, A. Glerum, M. Fraters, W. Spakman, A. Rozel, P.J. Tackley, Geochem. Geophys. Geosyst. 16, doi:10.1002/2015GC005807, 2015.



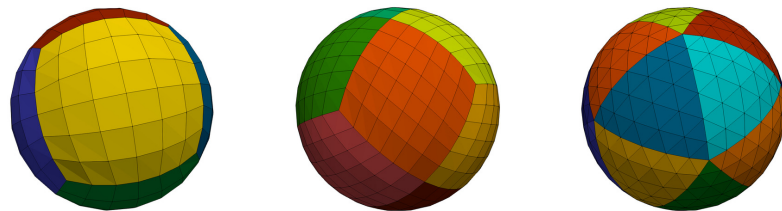
- *Dynamics of intraoceanic subduction initiation: 1. Oceanic detachment fault inversion and the formation of supra-subduction zone ophiolites*, M. Maffione, C. Thieulot, D.J.J. van Hinsbergen, A. Morris, O. Pluempfer and W. Spakman, *Geochem. Geophys. Geosyst.* 16, p1753-1770, 2015.



- *The Geodynamic World Builder: a solution for complex initial conditions in numerical modelling*, M. Fraters, C. Thieulot, A. van den Berg and W. Spakman, *Solid Earth*, <https://doi.org/10.5194/se-2019-24>, 2019.



- *GHOST: Geoscientific Hollow Sphere Tessellation*, C. Thieulot, *Solid Earth*, 9, 11691177, 2018. <https://doi.org/10.5194/se-9-1169-2018>



F Some useful Python commands

F.1 Sparse matrices

So far, the best way I have found to deal with sparse matrices is to declare the matrix as a 'lil_matrix' (linked list).

```
from scipy.sparse import csr_matrix, lil_matrix  
A_mat = lil_matrix((Nfem,Nfem), dtype=np.float64)
```

One then adds terms to it as if it was a full/dense matrix. Once the assembly is done, the conversion to CSR format is trivial:

```
A_mat=A_mat.tocsr()
```

Finally the solver can be called:

```
sol=sps.linalg.spsolve(A_mat,rhs)
```

F.2 condition number

if the matrix has been declared as lil_matrix, first convert it to a dense matrix:

```
A_mat=A_mat.dense()
```

The condition number of the matrix is simply obtained as follows:

```
from numpy import linalg as LA  
print(LA.cond(A_mat))
```

G Some useful maths

G.1 Inverse of a 3x3 matrix

Let us assume we wish to solve the system $\mathbf{A} \cdot \vec{X} = \vec{b}$, with $\vec{X} = (x, y)$. Then the solution is given by
The solution is given by

$$x = \frac{1}{\det(\mathbf{A})} \begin{vmatrix} b_1 & a_{21} \\ b_2 & a_{22} \end{vmatrix} \quad y = \frac{1}{\det(\mathbf{A})} \begin{vmatrix} a_{11} & b_1 \\ a_{21} & b_2 \end{vmatrix}$$

G.2 Inverse of a 3x3 matrix

Let us consider the 3x3 matrix \mathbf{M}

$$\mathbf{M} = \begin{pmatrix} M_{xx} & M_{xy} & M_{xz} \\ M_{yx} & M_{yy} & M_{yz} \\ M_{zx} & M_{zy} & M_{zz} \end{pmatrix}$$

1. Find $\det(\mathbf{M})$, the determinant of the Matrix \mathbf{M} . The determinant will usually show up in the denominator of the inverse. If the determinant is zero, the matrix won't have an inverse.
2. Find \mathbf{M}^T , the transpose of the matrix. Transposing means reflecting the matrix about the main diagonal.

$$\mathbf{M}^T = \begin{pmatrix} M_{xx} & M_{yx} & M_{zx} \\ M_{xy} & M_{yy} & M_{zy} \\ M_{xz} & M_{yz} & M_{zz} \end{pmatrix}$$

3. Find the determinant of each of the 2x2 minor matrices. For instance $\tilde{M}_{xx} = M_{yy}M_{zz} - M_{yz}M_{zy}$, or $\tilde{M}_{xz} = M_{xy}M_{yz} - M_{xz}M_{yy}$.
4. assemble the $\tilde{\mathbf{M}}$ matrix:

$$\tilde{\mathbf{M}} = \begin{pmatrix} +\tilde{M}_{xx} & -\tilde{M}_{xy} & +\tilde{M}_{xz} \\ -\tilde{M}_{yx} & +\tilde{M}_{yy} & -\tilde{M}_{yz} \\ +\tilde{M}_{zx} & -\tilde{M}_{zy} & +\tilde{M}_{zz} \end{pmatrix}$$

5. the inverse of \mathbf{M} is then given by

$$\mathbf{M}^{-1} = \frac{1}{\det(\mathbf{M})} \tilde{\mathbf{M}}$$

Another approach which of course is equivalent to the above is Cramer's rule. Let us assume we wish to solve the system $\mathbf{A} \cdot \vec{X} = \vec{b}$, with $\vec{X} = (x, y, z)$. Then the solution is given by

$$x = \frac{1}{\det(\mathbf{M})} \begin{vmatrix} b_1 & a_{12} & a_{13} \\ b_2 & a_{22} & a_{23} \\ b_3 & a_{32} & a_{33} \end{vmatrix} \quad y = \frac{1}{\det(\mathbf{M})} \begin{vmatrix} a_{11} & b_1 & a_{13} \\ a_{21} & b_2 & a_{23} \\ a_{31} & b_3 & a_{33} \end{vmatrix} \quad z = \frac{1}{\det(\mathbf{M})} \begin{vmatrix} a_{11} & a_{12} & b_1 \\ a_{21} & a_{22} & b_2 \\ a_{31} & a_{32} & b_3 \end{vmatrix}$$

H Topics in (computational) geodynamics

This is a *very* rough attempt at classifying my somewhat extensive bibliography per theme/topic. It goes without saying that this cannot be extensive and that since I started computational geodynamics myself around 2006 these lists are biased towards the last 2 decades or so. In retrospect, the categories I have chosen could have been subdivided into narrower fields. I understand that having 100+ references for 'subduction' or 'mantle convection' is not particularly useful, but it means that all these papers show up in the bibliography section of this book, and the titles of said papers are then searchable per keyword.

Big review papers - very good for students

- Advances and challenges in geotectonic modelling [277]
- Slab breakoff: A critical appraisal of a geological theory as applied in space and time [631]
- Dynamics and evolution of the deep mantle resulting from thermal, chemical, phase and melting effects [1512]
- Subduction
 - From the trench to the core-mantle boundary [963]
 - Modeling the subduction dynamics [141]
 - Slab dynamics in the transition zone [140]
 - Future directions in subduction modeling [653]
 - Controls of subduction geometry, location of magmatic arcs, and tectonics of arc and back-arc regions [417]
 - Stagnant slabs in the upper and lower mantle transition region [608]
- Mantle & plates:
 - Mantle convection models featuring plate tectonic behavior [1100]
 - A mantle convection perspective on global tectonics [384]
 - review of Wilson Cycle plate margins [247]
 - Interior dynamics and long term evolution of habitable planets [1503]
- Computational geodynamics
 - Modelling plate tectonics and convection in the mantle [1217]
- Rheology and strength of the lithosphere [976, 278]
- Rheology of deep upper mantle [936]
- Attributes of a community lithospheric modeling computer code [400]
- Analogue modelling: historical outline [1004]; Approaches, scaling, materials and quantification, with an application to subduction experiments [1427]
- Exhumation of (ultra-)high-pressure terranes: concepts and mechanisms [1667]
- Paradigms, new and old, for ultra-high-pressure tectonism [773]
- The role of solid-solid phase transitions in mantle convection [534]
- Mantle dynamics in the Mediterranean [537]
- Fault linkage and relay structures in extensional settings [574]
- Overview of adaptive finite element analysis in computational geodynamics [1153]

- Verification, validation and confirmation of numerical models [1282]
- Experimental modelling of orogenic wedges [735]
- Vening Meinesz [1641]
- Structure and dynamics of the mantle wedge [1616]
- Mountain building, observations and models of dynamic topography [562, 538]
- Rifted Margins: State of the Art and Future Challenges [1297]
Rifted margin architecture and crustal rheology: Reviewing Iberia-Newfoundland, Central South Atlantic, and South China Sea [226]
- Reconciling laboratory and observational models of mantle rheology in geodynamic modelling [966]
- Controlling parameters, surface expressions and the future directions in delamination modeling [704]
- The structural evolution of the deep continental lithosphere [399]
- What makes computational open source software libraries successful? [74]
- Lithosphere tectonics and thermo-mechanical properties: An integrated modelling approach for Enhanced Geothermal Systems exploration in Europe [370]
- Salt tectonics at passive margins: Geology versus models [218]
- Crustal versus mantle core complexes [217]
- Precambrian geodynamics: concepts and models [657]
- A review of brittle compressional wedge models [239]
- accreted terranes: a compilation of island arcs, oceanic plateaus, submarine ridges, seamounts, and continental fragments [1530]

Analogue modelling

[1251] [785] [923] [371][615] [299][1405] [298] [1308] [1193][1428]

Archean tectonics, early Earth

[306][658]

Anisotropy, Lattice/Crystal preferred orientation, SKS splitting

[1231] [?] [1232] [109] [530] [529]

Benchmark, analytical solutions, code comparisons, methodology, numerical methods, theory

1974: [829]
 1975: [1652][1653]
 1984: [1740]
 1989: [158]
 1990: [1564]
 1993: [1038]
 1994: [207]
 1995: [208][1216][614]
 1996: [1768][1214]
 1997: [1389]

1999: [1084][152]
2002: [1231]
2003: [1513][1208][674][675][1514]
2004: [949][925][928][1232]
2005: [1236]
2006: [948][1224][1279][1235]
2007: [1557][337][945][941][1212][655]
2008: [1761][466][1570][1010][1152][649][1611]
[814][199]
2009: [968][635][1636][1341]
2010: [944][946][508][965]
2011: [490][1580][822][1234]
2012: [409][333][1006][1150][644][49]
2013: [339][956][668]
2014: [1537][1154][1095]
2015: [1036][1410][338][1151]
2016: [495][159]
2017: [1406][1697][1119]
2018: [1173]
2019: [364][1091][452][634][586]

Core dynamics, CMB

[795] [1026][708]

Dataset (gravity, goce, grace, tomography, gps, heat flow) and/or their calculations/use

1977: [1403]
1981: [499]
1998: [139]
2003: [1008][1470]
2006: [1135]
2007: [1178]
2008: [1770][1770]
2012: [805][1372][805][553]
2013: [1373][501][443]
2014: [1292][500][1007]
2015: [180][214]

Computational Structural geology

[559] [4] [1565] [1122] [1121] [597] [1241]

Core complexes

[1028]

Discontinuous Galerkin (DG)

2000: [379]
2002: [314][378]
2003: [381]
2005: [312][376]
2008: [931][1201][471]
2009: [377][375]

2010: [1258][380][1202]
2011: [641][1259]
2012: [942][1257][1097, chapt. 31]
2013: [1651]
2015: [1036]
2017: [549][876][807]
2018: [1324]

(role of) elasticity in geodynamics modelling

1984:[1740]
1995:[279]
1996:[797]
1998:[390]
2001:[1633]
2002:[1233][1207]
2003:[854][1672]
2005:[1236]
2006:[948][1235]
2007:[945]
2008:[55][620]
2009:[1341]
2010:[136]
2012:[644]
2013:[1660]
2014:[543][577]
2015:[1536]
2016:[64][901][1272][64]
2018:[493]

(Geodynamics+) surface processes, erosion, topography evolution

1992: [93]
1994: [850][989][987]
1995: [322][990]
1996: [53][98]
1997: [198][626][82]
1998: [457][1584]
1999: [1691][256][83]
2001: [1744][1574][209][267][407][414]
2002: [1694][1200][627]
2003: [195]
2004: [558][699]
2005: [1021][1696]
2006: [1398][196][170]
2007: [274][1451]
2008: [19][1399]
2009: [1684][1013][1126]
2010: [1692][1573][205][204][201][420]
2011: [1397][734]
2013: [1640][200][556][557][197][326]
2014: [415][383][521][519]
2019: [33]

Geotechnics

[1489] [721] [1772] [720] [722] [277]

Glacier dynamics, ice sheets, ice flow, ice rheology

[744] [592] [48][593] [1745] [1056] [879][598] [1005]

(use of) inverse methods, inversion, adjoint methods, assimilation

[295] [173] [255] [883] [881] [1658] [1708][843] [1661] [681][161] [1061] [162]

Large scale mantle-plate interaction, whole Earth models

[1738] [1666][700][1476] [16][1400][412] [683] [852]

Crust/Lithosphere modelling, plate motion, plate stress

1977: [418]

1981: [213]

1984: [1014]

1988: [445][444]

1990: [328]

1991: [335]

1992: [1194][275]

1993: [1255][202][732]

1994: [231][94]

1995: [119][206][970][279][509]

1996: [98]

1997: [1548][82][268][1215]

1998: [149][1057][971][1133][1143][768]

1999: [1689][152][367][618][1218][1042]

2000: [791][1025][1041][767][1045]

2001: [848][105][947]

2002: [1024][391][57][646]

2003: [1695][1672][673][1581][1631][243][1048]

2004: [1552][650][397]

2005: [783][1686][1159]

2006: [1093][238][56][952][613][398]

2007: [7][998][678]

2008: [6][1553][800][260][371][340][951][547]

2009: [244][1312][1391][257]

2010: [804][544][736][1582][1311]

2011: [1375]

2012: [1664][1618][239][986][715]

2013: [1673][1012][1239][583][1665]

2014: [926][492][1412][1656][1683][1433][1114] [756][623]

2015: [1655][1536][1131]

2017: [1414][1287]

2018: [1657][1261][92]

2019: [997][977]

Delamination

[703] [1627] [1625] [76] [91]

lithospheric stress, intraplate stress

1975: [567]
1976: [1385]
1979: [1387]
1989: [177]
1991: [1705]
1992: [1386][1711][1789][372]
2001: [1483]
2004: [1085]
2005: [1551]
2008: [153][685]
2009: [687][1248]
2010: [136]
2012: [1250][686]
2013: [684]
2014: [1583]

Folding

[1347] [1348] [1349] [564] [565] [599] [1434] [1359] [595] [1357][733] [1358] [594][596] [600]

Geoid

[441][777] [442] [1766] [1749][1381] [1209] [295] [968] [828]

LLSVP, ULVZ

2007: [813]
2008: [629]
2010: [1484]
2012: [1485][437][460]
2013: [1064][185]
2014: [248][1066]
2015: [1238][801][1166]
2016: [476]
2018: [428]
2019: [817]

Magma transport / melting / two phase flow/ volcanism

1984: [1444][1158]
1986: [1445]
1988: [1443]
1993: [1474]
1995: [155]
1998: [1344]
2001: [130]
2003: [129]
2006: [1279]
2007: [1475]
2008: [815][812]
2009: [70]
2010: [68]
2011: [67][1775]
2012: [1719]

2018: [1099]
2019: [431]

Mantle convection/dynamics, whole Earth models, plate interaction

1975: [823]
1976: [1161]
1978: [1141]
1979: [1103][286]
1980: [1274][905]
1981: [287]
1982: [906][847]
1983: [849][846][344][1160]
1984: [1275][907][792][799][441][174][345] [1227][563]
1985: [908][88][349][421]
1986: [442][765]
1987: [1739]
1990: [1564]
1991: [346][1105]
1992: [127][1117][1608]
1993: [1749][909][1499][288][296][1591][1505]
1994: [794][351][1506][1713][1712]
1995: [1757][1593][254]
1996: [1752][838][1417][1418][1509][1571] [154][252][930][766][1592]
1997: [839][888][253][1215]
1998: [29][889][455][1510][1504][1566] [1567][251]
1999: [482]
2000: [13][793][453][1500][1765]
2001: [1607][1384][1046]
2002: [1497][1207][1501]
2003: [784][1039][?]
2004: [1622]
2005: [1507][293][748][1047]
2006: [106]
2007: [1249][1147][192][191][750][749]
2008: [1511][336][190][462]
2009: [1703][566][719][463]
2010: [249][464][1721]
2011: [1100][1401][1702][1040]
2012: [138][387][465] 2013: [837][438][1560][185][283][1190] [538][388][401]
2014: [47][818][410][561][1402][385][112]
2015: [1536][1680][113]
2016: [602][1457]
2018: [386][43][389]
2019: [754][1129]

Mantle rheology, phase transitions, stratification, profile

1982: [1737][347]
1985: [352]
1992: [1754]
1993: [1505][131]
1994: [1617]
1995: [1751][348][1440]
1997: [1186]
1998: [295]

2005: [816]
2007: [1294]
2009: [1242]
2010: [940]
2011: [890][545]
2012: [1512]
2013: [541][1502]

Mantle wedge

1978: [1563]
2001: [143][785]
2003: [1616]
2006: [712][666]
2007: [711]
2008: [979][315]
2009: [1033]
2010: [1392][841]
2014: [1643]

Obduction, ophiolites

[771] [772] [8]

Planets - Mars

[1442] [1266] [1049] [1624] [957] [707] [1411] [1448] [1750]

Planets - Moon

[1755]

Planets - Venus

[1442] [961] [1468] [1106][1213] [1624] [39] [690] [663] [413][435] [969]

Plate motion and mantle, plate tectonic reconstruction

[1163] [1779] [1760] [528][1374] [1075][1594] [873][769] [1225] [1733] [1528]

Plume dynamics

1994: [1244][796]
1997: [1610]
1998: [1550]
1999: [1019]
2002: [542]
2006: [884][1082][1083][1756][1189]
2009: [1634]
2011: [1559][1521][264][1174][436]
2013: [434][1146][30]
2015: [430][801]
2017: [1746]
2018: [433]
2019: [44]

Plume-Lithosphere interaction

1994: [1380]
1996: [1759]
1998: [139][1203]
1999: [1204]
2001: [1633]
2002: [576]
2003: [1605]
2005: [272]
2009: [280][1773][68]
2013: [135][222]
2014: [271][663][247]
2015: [134][672][996][1175]
2016: [560][632]
2017: [78][211][78][122]
2018: [428]

Regenauer-Lieb

2000: [1365]
2003: [1366]
2004: [1371]
2006: [1368][1364]
2008: [1370]
2009: [1369]
2013: [1363]

Rheology, material parameters, rock mechanics

1951: [478][774]
1952: [479]
1968: [294]
1969: [787]
1972: [311]
1974: [984]
1979: [701][527]
1980: [187]
1981: [456]
1984: [1355][342][1638]
1986: [937]
1987: [975]
1990: [1688]
1992: [61][341][934][981]
1993: [935]
1994: [585]
1995: [983][695]
1996: [1659][831]
1997: [524, 523] 1998: [390][1106]
1999: [929]
2000: [1415][1353][1167, 1168]
2001: [1096]
2002: [833]
2003: [832][933][1199]
2005: [468][480]
2006: [1416][276][1210]
2007: [826][982][546]

2008: [1037][263][999][691]
2009: [939][954]
2011: [1032][955]
2012: [1378]
2013: [1027][1180]
2015: [338]
2017: [166]

Rifting, seafloor spreading, ridges, pull-apart basins, extension

1973: [603]
1980: [212]
1985: [175]
1986: [845][1791][1790][1220]
1988: [230]
1989: [1172]
1990: [540]
1991: [1568][232]
1992: [1778][503]
1993: [723]
1995: [724]
1996: [484][120][1148]
1998: [1345]
1999: [216][233][725]
2001: [868][867][588][590][589]
2002: [869][789][432][1630][110]
2003: [866][790][405][1687]
2004: [825]
2005: [871][408][1626][1628]
2006: [1555][404][416]
2007: [857][1139][1629][497]
2008: [403][755][242]
2009: [9][960]
2010: [52][656][575][652]
2011: [20][510]
2012: [21][221]
2013: [22][220][330][978][959][1183][1671] [660][1078][662]
2014: [808][1077][219][993][502][1327][1076]
2015: [1245][365]
2016: [1272][911][1792]
2017: [1029][224][122][1247]
2018: [331][227][223][1531][912]
2019: [1062][1793][33][494][1193]

Salt tectonics

1978: [1700]
1991: [1516]
1992: [1743]
1993: [1251][1614]
1996: [1155]
1998: [689]
2004: [882][637]
2006: [1145]
2007: [855][1145]
2009: [731]

2011: [218]
2012: [555][1067]
2013: [718]
2014: [86][551][550][680]
2015: [552]
2016: [1132]

H.1 Seismo-tectonics, subduction earthquakes

[167] [1597, 1596][1181] [1598] [727] [811]

Subduction

1980: [1171]
1982: [417]
1985: [1534]
1986: [903]
1989: [177]
1990: [851][967]
1992: [1766][1685][764]
1993: [920][496]
1994: [1767][1693][1674][1675][100]
1995: [1136]
1996: [350][692]
1997: [803][964]
1998: [887][246][229]
1999: [786][108][262]
2000: [1532][194][99]
2001: [273][240][323]
2002: [358][366]
2003: [1362][616][648]
2004: [1562][183][97]
2005: [904][1016][726][518][37][726][1130][1490]
2006: [581][1409][1135][654][617]
2007: [38][1715][424][360][1134][303][714][716][1123]
2008: [1716][1288][693][1668][1669][169][1185] [168][55][531][665][615][450][449][670][1263][1449]
2009: [1718][142][535][95][958][651][667]
[533][1074][1223]
2010: [781][1098][1144][304][308][1069][1478]
[1226][1776]
2011: [1070][1089][292][59][302][669][1339]
[157]
2012: [36][896][893][895][1741][737][738]
[1394][1529][1535][178][359][305][301]
[642][1073][121][1578]
2013: [1246][773][35][1243][1730][1774][1068]
[894][880][1102][481][1554][290][1430]
[609][1115][1240][1179][739][1597][1596]
[316][1645]
2014: [1393][840][1395][1206][543][577][582]
[628][1646][1644][1071][183][62][1488]
[63][1598]
2015: [134][179][184][317][972][1603]
2016: [1556][770][1396]
2018: [1724]

Subduction - slab detachment, break-off

1985: [607]
1992: [1706]
1995: [1734][1647]
1997: [1704]
1998: [447][310]
2000: [1707]
2002: [241]
2004: [676]
2006: [536]
2008: [1788]
2009: [34][265]
2010: [266][85]
2011: [488][1602]
2012: [487][491]
2013: [307][1111][679][486]
2014: [489][128][1650]
2015: [1649]
2017: [591]
2018: [631]
2019: [125]

Subduction + water (fluids)

[669] [532] [1340] [320] [321]

Subduction initiation

1978: [151]
1982: [373]
1984: [313]
1989: [368]
1991: [1230]
1998: [1561]
1999: [539]
2000: [1331]
2001: [470][1367][193]
2004: [1487][762]
2003: [782]
2005: [145]
2008: [1577]
2010: [1262][269]
2011: [58][1264]
2013: [498][1137]
2014: [1377][1138]
2015: [1107][1300][1601]
2018: [1771][60]
2019: [101][758]

Subduction - flat slabs - low angle subduction

2011: [423]
2012: [1125]
2015: [643]

Tectonics, small deformation, rock mechanics

[877] [821] [526] [1050]

Wilson cycle, supercontinent cycles

[1572] [1763] [1748] [101]

Meshless methods (SPH, RKPM, ...)

[115] [554] [1267]

Element Free Galerkin Method

[117] [118] [114] [116]

Planetary accretion, exoplanets, planet formation, segregation

[1044] [1080][705] [1081] [706][1727] [1256]

accretionary wedges, nappes

[1699] [1412] [1127] [1128][1414] [511]

Thrust-wrench fault

[1405]

intrusions, diapirism

1981: [213]

1992: [1608][1743][1676][1679]

1993: [1615][1251][1315][1319][1614][1316][1318][1677]

1995: [1678][155][1678]

2003: [673][1620]

2004: [671][882][661]

2007: [664]

2008: [259][1788]

2011: [510]

2013: [606]

2014: [550]

2015: [552][605]

Locations

South America, Andes

[1675] [56] [1396]

North America

[261]

Alps

[258]

New Zealand

[988] [206] [98] [83] [1093] [646][1332] [648][991][1581] [1334] [751]

Zagros

[1639] [804] [1720] [1265] [582] [680] [1414]

Himalayan region, Tibetan plateau, India collision

[151] [1197] [1198] [1693] [322] [1408] [329][362] [96][1022][1744][1525] [992] [1374] [97] [361] [363] [260] [804] [307][1239][326][327] [1683] [289] [1308] [1428]

Pyrenees

[689] [99] [1156] [899] [557] [494]

Carribean**East mediterranean - Aegean region, Turkey**

[309]

Ethiopian and Afar rift

[1178] [403] [960] [137] [1302] [224] [225] [402]

I Elemental mass matrices for simple geometries

In what follows I compute the mass matrix for a variety of reference elements. If you wish to use these in a code, do not forget to take the jacobian of the transformation/mapping into account.

I.1 1D segments

I.1.1 Linear basis functions

Let us start with the mass matrix (which we encountered in Section 5.1 – although we leave the ρC_p term out):

$$\mathbf{M}_e = \int_{\Omega_e} \vec{N}^T \vec{N} dV = \int_{-1}^{+1} \vec{N}^T \vec{N} dr \quad (806)$$

on the reference element, with

$$\vec{N}^T = \begin{pmatrix} N_1(r) \\ N_2(r) \end{pmatrix} = \frac{1}{2} \begin{pmatrix} 1-r \\ 1+r \end{pmatrix}$$

We have

$$\int_{-1}^{+1} N_1(r) N_1(r) dr = 2/3 \quad (807)$$

$$\int_{-1}^{+1} N_1(r) N_2(r) dr = 1/3 \quad (808)$$

$$\int_{-1}^{+1} N_2(r) N_2(r) dr = 2/3 \quad (809)$$

Following the procedure in Section 5.1 we arrive at

$$\mathbf{M}^e = \frac{1}{3} \begin{pmatrix} 2 & 1 \\ 1 & 2 \end{pmatrix}$$

The lumped mass matrix is then

$$\bar{\mathbf{M}}^e = \frac{1}{3} \begin{pmatrix} 2+1 & 0 \\ 0 & 1+2 \end{pmatrix} = \begin{pmatrix} 1 & 0 \\ 0 & 1 \end{pmatrix} \quad (810)$$

Remark. The sum of all the terms in the mass matrix must be equal to 2. Indeed:

$$\begin{aligned} \sum_{ij} M_{ij} &= \sum_{ij} \int_{-1}^{+1} N_i N_j dr \\ &= \int_{-1}^{+1} (N_1 N_1 + N_1 N_2 + N_2 N_1 + N_2 N_2) dr \\ &= \int_{-1}^{+1} [N_1(N_1 + N_2) + N_2(N_1 + N_2)] dr \\ &= \int_{-1}^{+1} (N_1 + N_2) dr \\ &= 2 \end{aligned}$$

I.1.2 Quadratic basis functions

There are now three nodes in the segment so that the mass matrix is now a 3×3 matrix. We have (see Section 4.4.1)

$$\vec{N}^T(r) = \begin{pmatrix} N_1(r) \\ N_2(r) \\ N_3(r) \end{pmatrix} = \begin{pmatrix} \frac{1}{2}r(r-1) \\ 1-r^2 \\ \frac{1}{2}r(r+1) \end{pmatrix} \quad (811)$$

We then have to compute

$$\begin{aligned}
\int_{-1}^{+1} N_1(r)N_1(r)dr &= \frac{8}{30} = 0.26666 \\
\int_{-1}^{+1} N_1(r)N_2(r)dr &= \frac{4}{30} = 0.13333 \\
\int_{-1}^{+1} N_1(r)N_3(r)dr &= -\frac{2}{30} = -0.06666... \\
\int_{-1}^{+1} N_2(r)N_2(r)dr &= \frac{16}{15} = 1.06666 \\
\int_{-1}^{+1} N_2(r)N_3(r)dr &= \frac{4}{30} = 0.13333 \\
\int_{-1}^{+1} N_3(r)N_3(r)dr &= \frac{8}{30} = 0.26666
\end{aligned}$$

and finally

$$\mathbf{M}^e = \frac{1}{30} \begin{pmatrix} 8 & 4 & -2 \\ 4 & 32 & 4 \\ -2 & 4 & 8 \end{pmatrix} \quad (812)$$

The lumped mass matrix is then

$$\begin{aligned}
\bar{\mathbf{M}}^e &= \frac{1}{30} \begin{pmatrix} 8+4-2 & 0 & 0 \\ 0 & 4+32+4 & -2+4+8 \\ 0 & 0 & -2+4+8 \end{pmatrix} \\
&= \frac{1}{30} \begin{pmatrix} 10 & 0 & 0 \\ 0 & 40 & 0 \\ 0 & 0 & 10 \end{pmatrix} \\
&= \frac{1}{3} \begin{pmatrix} 1 & 0 & 0 \\ 0 & 4 & 0 \\ 0 & 0 & 1 \end{pmatrix}
\end{aligned} \quad (813)$$

We can easily verify that

$$\sum_{ij} M_{ij} = 2 \quad \sum_{ij} \bar{M}_{ij} = 2$$

I.1.3 Cubic basis functions

There are now four nodes in the segment so that the mass matrix is now a 4×4 matrix. We have (see Section 4.4.3)

$$\vec{N}^T(r) = \begin{pmatrix} N_1(r) \\ N_2(r) \\ N_3(r) \\ N_4(r) \end{pmatrix} = \frac{1}{16} \begin{pmatrix} -1+r+9r^2-9r^3 \\ 9-27r-9r^2+27r^3 \\ 9+27r-9r^2-27r^3 \\ -1-r+9r^2+9r^3 \end{pmatrix} \quad (814)$$

$$\begin{aligned}
\int_{-1}^{+1} N_1(r)N_1(r)dr &= \frac{1}{256} \frac{4096}{105} \\
\int_{-1}^{+1} N_1(r)N_2(r)dr &= \frac{1}{256} \frac{1056}{35} \\
\int_{-1}^{+1} N_1(r)N_3(r)dr &= -\frac{1}{256} \frac{384}{35} \\
\int_{-1}^{+1} N_1(r)N_4(r)dr &= \frac{1}{256} \frac{608}{105} \\
\int_{-1}^{+1} N_2(r)N_2(r)dr &= \frac{1}{256} \frac{6912}{35} \\
\int_{-1}^{+1} N_2(r)N_3(r)dr &= -\frac{1}{256} \frac{864}{35} \\
\int_{-1}^{+1} N_2(r)N_4(r)dr &= -\frac{1}{256} \frac{384}{35} \\
\int_{-1}^{+1} N_3(r)N_3(r)dr &= \frac{1}{256} \frac{6912}{35} \\
\int_{-1}^{+1} N_3(r)N_4(r)dr &= \frac{1}{256} \frac{1056}{35} \\
\int_{-1}^{+1} N_4(r)N_4(r)dr &= \frac{1}{256} \frac{4096}{105}
\end{aligned}$$

and finally

$$\mathbf{M}^e = \frac{1}{16} \frac{1}{105} \begin{pmatrix} 256 & 198 & -72 & 38 \\ 198 & 1296 & -162 & -72 \\ -72 & -162 & 1296 & 198 \\ 38 & -72 & 198 & 256 \end{pmatrix} \quad (815)$$

The lumped mass matrix is then

$$\begin{aligned}
\bar{\mathbf{M}}^e &= \frac{1}{16} \frac{1}{105} \begin{pmatrix} 256 + 198 - 72 + 38 & 0 & 0 & 0 \\ 0 & 198 + 1296 - 162 - 72 & 0 & 0 \\ 0 & 0 & -72 - 162 + 1296 + 198 & 0 \\ 0 & 0 & 0 & 38 - 72 + 198 + 256 \end{pmatrix} \\
&= \frac{1}{16} \frac{1}{105} \begin{pmatrix} 420 & 0 & 0 & 0 \\ 0 & 1260 & 0 & 0 \\ 0 & 0 & 1260 & 0 \\ 0 & 0 & 0 & 420 \end{pmatrix} \\
&= \frac{1}{4} \begin{pmatrix} 1 & 0 & 0 & 0 \\ 0 & 3 & 0 & 0 \\ 0 & 0 & 3 & 0 \\ 0 & 0 & 0 & 1 \end{pmatrix}
\end{aligned}$$

We can easily verify that

$$\sum_{ij} M_{ij} = 2 \quad \sum_{ij} \bar{M}_{ij} = 2$$

I.1.4 Quartic basis functions

There are now five nodes in the segment so that the mass matrix is now a 5×5 matrix. We have (see Section 4.4.4)

$$\vec{N}^T(r) = \begin{pmatrix} N_1(r) \\ N_2(r) \\ N_3(r) \\ N_4(r) \\ N_5(r) \end{pmatrix} = \frac{1}{6} \begin{pmatrix} r - r^2 - 4r^3 + 4r^4 \\ -8r + 16r^2 + 8r^3 - 16r^4 \\ 6 - 30r^2 + 24r^4 \\ 8r + 16r^2 - 8r^3 - 16r^4 \\ -r - r^2 + 4r^3 + 4r^4 \end{pmatrix} \quad (816)$$

$$\begin{aligned} \int_{-1}^{+1} N_1(r)N_1(r)dr &= \frac{1}{36} \frac{1168}{315} \\ \int_{-1}^{+1} N_1(r)N_2(r)dr &= \frac{1}{36} \frac{1184}{315} \\ \int_{-1}^{+1} N_1(r)N_3(r)dr &= -\frac{1}{36} \frac{232}{105} \\ \int_{-1}^{+1} N_1(r)N_4(r)dr &= \frac{1}{36} \frac{32}{45} \\ \int_{-1}^{+1} N_1(r)N_5(r)dr &= -\frac{1}{36} \frac{116}{315} \\ \int_{-1}^{+1} N_2(r)N_2(r)dr &= \frac{1}{36} \frac{1024}{45} \\ \int_{-1}^{+1} N_2(r)N_3(r)dr &= -\frac{1}{36} \frac{512}{105} \\ \int_{-1}^{+1} N_2(r)N_4(r)dr &= \frac{1}{36} \frac{1024}{315} \\ \int_{-1}^{+1} N_2(r)N_5(r)dr &= \frac{1}{36} \frac{32}{45} \\ \int_{-1}^{+1} N_3(r)N_3(r)dr &= \frac{1}{36} \frac{832}{35} \\ \int_{-1}^{+1} N_3(r)N_4(r)dr &= -\frac{1}{36} \frac{512}{105} \\ \int_{-1}^{+1} N_3(r)N_5(r)dr &= -\frac{1}{36} \frac{232}{105} \\ \int_{-1}^{+1} N_4(r)N_4(r)dr &= \frac{1}{36} \frac{1024}{45} \\ \int_{-1}^{+1} N_4(r)N_5(r)dr &= \frac{1}{36} \frac{1184}{315} \\ \int_{-1}^{+1} N_5(r)N_5(r)dr &= \frac{1}{36} \frac{1168}{315} \end{aligned} \quad (817)$$

$$M^e = \frac{1}{36} \frac{1}{315} \begin{pmatrix} 1168 & 1184 & -696 & 224 & -116 \\ 1184 & 7168 & -1536 & 1024 & 224 \\ -696 & -1536 & 7488 & -1536 & -696 \\ 224 & 1024 & -1536 & 7168 & 1184 \\ -116 & 224 & -696 & 1184 & 1168 \end{pmatrix} \quad (818)$$

The lumped mass matrix is then

$$\bar{\mathbf{M}}^e = \frac{1}{36} \frac{1}{315} \begin{pmatrix} 1764 & 0 & 0 & 0 & 0 \\ 0 & 8064 & 0 & 0 & 0 \\ 0 & 0 & 3024 & 0 & 0 \\ 0 & 0 & 0 & 8064 & 0 \\ 0 & 0 & 0 & 0 & 1764 \end{pmatrix} = \frac{1}{45} \begin{pmatrix} 7 & 0 & 0 & 0 & 0 \\ 0 & 32 & 0 & 0 & 0 \\ 0 & 0 & 12 & 0 & 0 \\ 0 & 0 & 0 & 32 & 0 \\ 0 & 0 & 0 & 0 & 7 \end{pmatrix} \quad (819)$$

We can once again easily verify that

$$\sum_{ij} M_{ij} = 2 \quad \sum_{ij} \bar{M}_{ij} = 2$$

Note that all the integrals above were done very conveniently with the WolframAlpha software/web-site⁶⁵. Example:

The screenshot shows the WolframAlpha interface. At the top, there is a search bar containing the input: `int_-1^1 (r - r^2 - 4r^3 + 4r^4)(r - r^2 - 4r^3 + 4r^4) dr`. Below the search bar are several icons: a star, a square, a grid, and a camera. To the right of the search bar are two buttons: "Browse Examples" and "Surprise Me". In the main result area, it says "Definite integral:" followed by the integral expression $\int_{-1}^{+1} (r - r^2 - 4r^3 + 4r^4)(r - r^2 - 4r^3 + 4r^4) dr = \frac{1168}{315} \approx 3.7079$. There are also buttons for "More digits" and "Step-by-step solution". At the bottom right of the result area, there is a link "Open code" with a small icon.

I.2 Quadrilaterals: rectangular elements

We here assume that each element is a rectangle of size $h_x \times h_y$.

I.3 Hexahedra: cuboid elements

We here assume that each element is a cuboid⁶⁶ of size $h_x \times h_y \times h_z$.

⁶⁵<https://www.wolframalpha.com/>

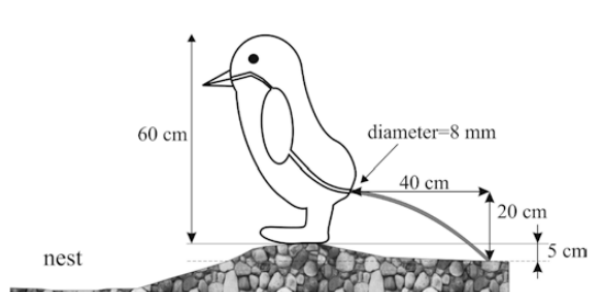
⁶⁶<https://en.wikipedia.org/wiki/Cuboid>

J Finite element terminology in various languages

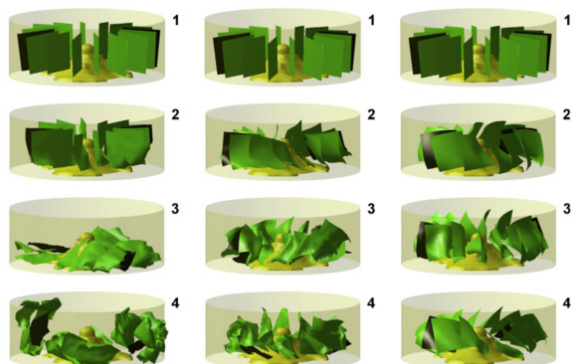
English	French	Dutch
Finite Element Method	Méthode des éléments finis	Eindige-elementenmethode
Finite Difference Method	Méthode des différences finies	Eindige-differentiemethode
Finite Volume Method	Méthode des volumes finis	
Matrix	Matrice	
Heat transport eq.	Equation de transport de la chaleur	Warmtetransport vergelijking
Momentum conservation eq.	équation de conservation du moment	Wet van behoud van impuls
Mass conservation / continuity eq.		Continuïteitsvergelijking
Iterative solver	solveur itératif	
Elemental matrix		
Boundary conditions	conditions aux limites	randvoorwaarden
(In)compressible	(in)compressible	
Surface processes	processus de surface	
an element	un élément	
Computational geodynamics	géodynamique numérique	
Assembly	assemblage	
Strong form		
Weak form	formulation variationnelle / formulation faible	
Basis function		
Shape function		
Partial differential eq. (PDE)	équation aux dérivées partielles (EDP)	partiële differentiaalvergelijking
Node	noeud	knooppunt
Grid, mesh	(la) maille / (le) maillage	rooster
Stiffness matrix	matrice de raideur	stijfheidsmatrix
Displacement vector	vecteur déplacement	verplaatsingsvector
Tessellation	pavage	Betegeling
Mass matrix	matrice de masse	
Classical mechanics	mécanique Newtonienne	(de) klassieke mechanica
Momentum	(le) moment	(de) impuls

K Fun modelling

Because sometimes numerical modelling is fun ...



Pressures produced when penguins pooh - calculations on avian defaecation [1176]



Clothes washing simulations [12]

Computers and Fluids Vol. 9, pp. 223-231
Pergamon Press Ltd., 1981. Printed in Great Britain

0045-7990(81)0001-022\$02.00/0

INTERNATIONAL JOURNAL FOR NUMERICAL METHODS IN FLUIDS, VOL. 9, 99-112 (1989)

DON'T SUPPRESS THE WIGGLES—THEY'RE TELLING YOU SOMETHING!†

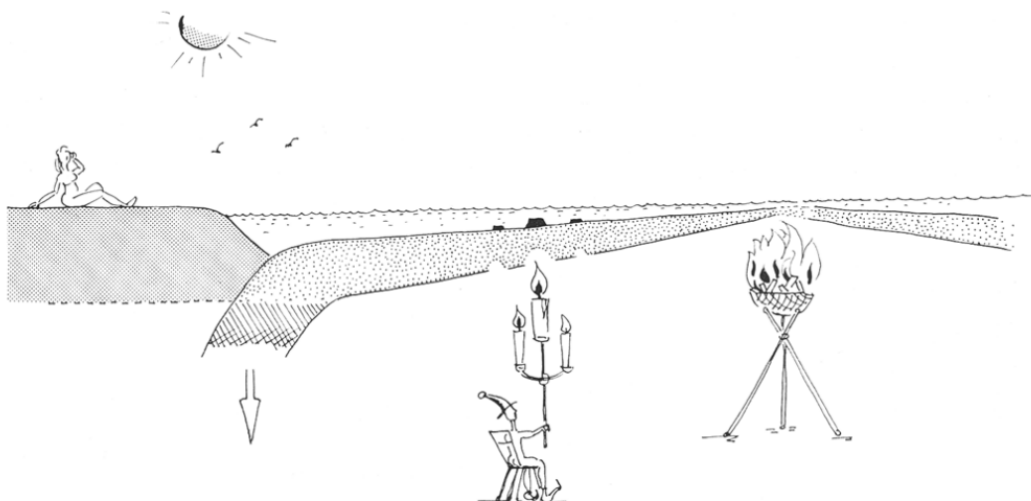
PHILIP M. GRESHO AND ROBERT L. LEE

[741]

ARE FEM SOLUTIONS OF INCOMPRESSIBLE FLOWS REALLY INCOMPRESSIBLE? (OR HOW SIMPLE FLOWS CAN CAUSE HEADACHES!)

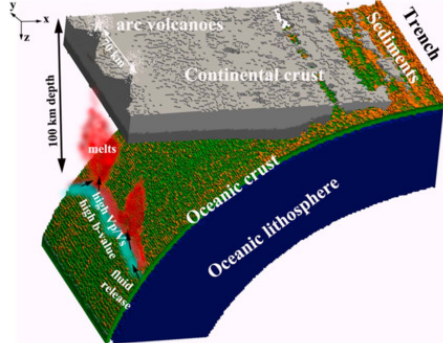
DOMINIQUE PELLETIER, ANDRE FORTIN AND RICARDO CAMARERO

[1295]

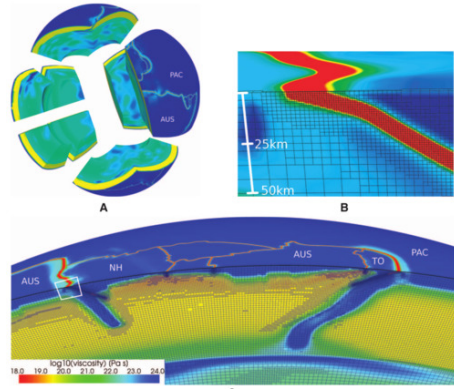


Lithospheric thickness anomaly near the trench and possible driving force of subduction [607]

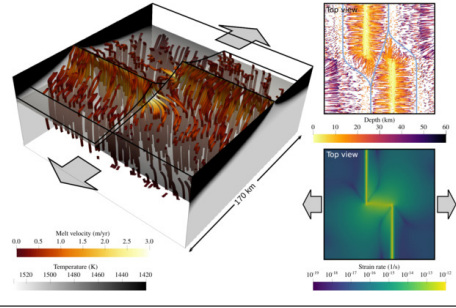
L Beautiful/interesting images from computational geodynamics



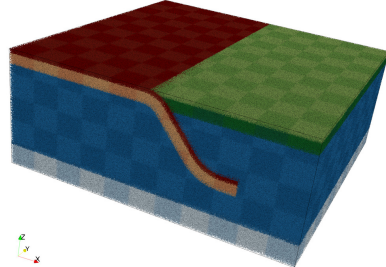
[1774]



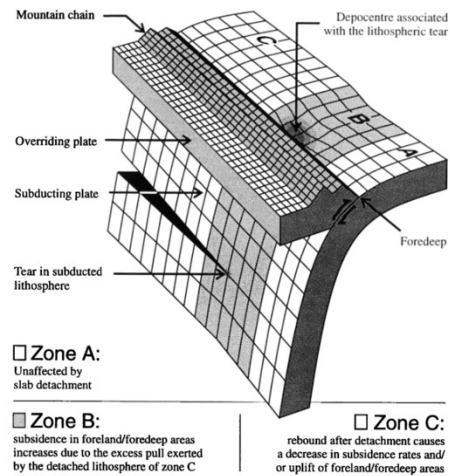
[1476]



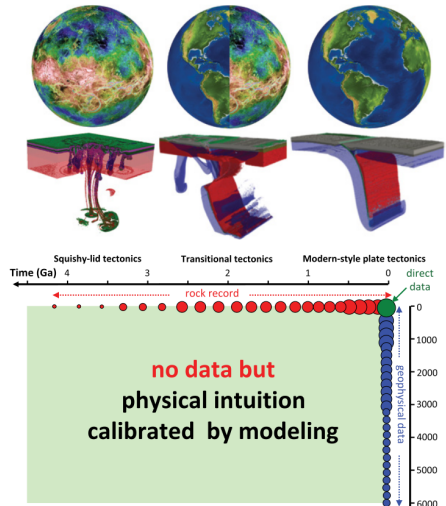
[431]



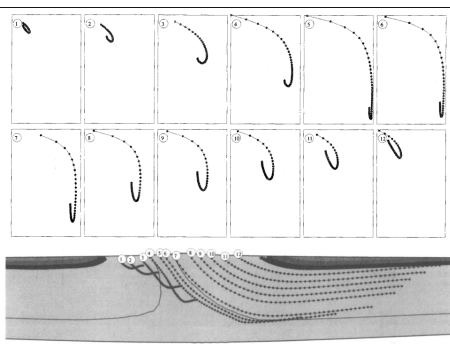
[586]



[1595]



[658]



[82]

M People

This is relevant to me only. Bibliography work.

- Thorsten Becker
- Sascha Brune
- Susanne Buiter. done
- Fabio Crameri
- Fabio Capitanio
- Huw Davies
- Taras Gerya. done
- Gregor Golabek
- Mike Gurnis
- Laurent Husson
- Boris Kaus
- Louis Moresi. done
- Anne Replumaz
- Tobias Rolf
- Paul Tackley. done
- Arie van den Berg
- Peter van Keken
- Ylona van Dinther
- Jeroen van Hunen
- Iris van Zelst

References

- [1] *Three-dimensional spherical shell convection at infinite Prandtl number using the cubed sphere method*, Proceedings Second MIT Conference on Computational Fluid and Solid Mechanics June 1720, 2003. Elsevier, 2003.
- [2] B.T. Aagaard, M.G. Knepley, and C.A. Williams. A domain decomposition approach to implementing fault slip in finite-element models of quasi-static and dynamic crustal deformation. *J. Geophys. Res.*, 118:3059–3079, 2013.
- [3] John F Abel and Mark S Shephard. An algorithm for multipoint constraints in finite element analysis. *International Journal for Numerical Methods in Engineering*, 14(3):464–467, 1979.
- [4] V. Acocella, A. Gudmundsson, and R. Funiciello. Interaction and linkage of extension fractures and normal faults: examples from the rift zone of Iceland. *Journal of Structural Geology*, 22(9):1233–1246, 2000.
- [5] F.J Adewale, A.P. Lucky, A.P. Oluwabunmi, and E.F. Boluwaji. Selecting the most appropriate model for rheological characterization of synthetic based drilling mud. *International Journal of Applied Engineering Research*, 12(18):7614–7649, 2017.
- [6] J. C. Afonso, M. Fernandez, G. Ranalli, W.L. Griffin, and J.A.D. Connolly. Integrated geophysical-petrological modeling of the lithosphere and sublithospheric upper mantle: Methodology and applications. *Geochem. Geophys. Geosyst.*, 9(5):doi:10.1029/2007GC001834, 2008.
- [7] J.C. Afonso, G. Ranalli, and M. Fernandez. Density structure and buoyancy of the oceanic lithosphere revisited. *Geophys. Res. Lett.*, 34(L10302), 2007.
- [8] Ph. Agard, X. Zuo, N. Bellahsen, C. Faccenna, and D. Savva. Obduction: Why, how and where. Clues from analog models. *Earth Planet. Sci. Lett.*, 393:132–145, 2014.
- [9] Andrea Agostini, Giacomo Corti, Antonio Zeoli, and Genene Mulugeta. Evolution, pattern, and partitioning of deformation during oblique continental rifting: Inferences from lithospheric-scale centrifuge models. *Geochem. Geophys. Geosyst.*, 10(11):Q11015, 2009.
- [10] R. Agrusta, S. Goes, and J. van Hunen. Subducting-slab transition-zone interaction: Stagnation, penetration and mode switches. *Earth and Planetary Science Letters*, 464:10–23, 2017.
- [11] R. Agrusta, J. van Hunen, and S. Goes. The effect of metastable pyroxene on the slab dynamics. *Geophys. Res. Lett.*, 41:8800–8808, 2014.
- [12] Deniz Tolga Akcabay, David R Dowling, and William W Schultz. Clothes washing simulations. *Computers & Fluids*, 100:79–94, 2014.
- [13] M. Albers. A local mesh refinement multigrid method for 3D convection problems with strongly variable viscosity. *J. Comp. Phys.*, 160:126–150, 2000.
- [14] M. Albertz and C. Beaumont. An investigation of salt tectonic structural styles in the Scotian Basin, offshore Atlantic Canada: 2. Comparison of observations with geometrically complex numerical models. *Tectonics*, 29(TC4018), 2010.
- [15] M. Albertz, C. Beaumont, J.W. Shimeld, S.J. Ingsand, and S. Gradmann. An investigation of salt tectonic structural styles in the Scotian Basin, offshore Atlantic Canada: Part 1, comparison of observations with geometrically simple numerical models. *Tectonics*, 29, 2010.
- [16] L. Alisic, M. Gurnis, G. Stadler, C. Burstedde, and O. Ghattas. Multi-scale dynamics and rheology of mantle flow with plates. *J. Geophys. Res.*, 117, 2012.
- [17] L. Alisic, J.F. Rudge, R.F. Katz, G.N. Wells, and S. Rhebergen. Compaction around a rigid, circular inclusion in partially molten rock. *J. Geophys. Res.*, 119:5903–5920, 2014.
- [18] J. Allen and C. Beaumont. Continental Margin Syn-Rift Salt Tectonics at Intermediate Width Margins. *Basin Research*, page doi: 10.1111/bre.12123, 2014.
- [19] P.A. Allen. From landscapes into geological history. *Nature*, 451:274–276, 2008.
- [20] V. Allken, R. Huismans, and C. Thieulot. Three dimensional numerical modelling of upper crustal extensional systems. *J. Geophys. Res.*, 116:B10409, 2011.
- [21] V. Allken, R. Huismans, and C. Thieulot. Factors controlling the mode of rift interaction in brittle-ductile coupled systems: a 3d numerical study. *Geochem. Geophys. Geosyst.*, 13(5):Q05010, 2012.
- [22] V. Allken, R.S. Huismans, H. Fossen, and C. Thieulot. 3D numerical modelling of graben interaction and linkage: a case study of the Canyonlands grabens, Utah. *Basin Research*, 25:1–14, 2013.
- [23] P.R. Amestoy and I.S. Duff. Vectorization of a multiprocessor multifrontal code. *International Journal of Supercomputer Applications*, 3:41–59, 1989.

- [24] P.R. Amestoy, I.S. Duff, J.Koster, and J.-Y. LExcellent. A fully asynchronous multifrontal solver using distributed dynamic scheduling. *SIAM Journal of Matrix Analysis and Applications*, 23(1):15–41, 2001.
- [25] P.R. Amestoy, I.S. Duff, and J.-Y. L'Excellent. Multifrontal parallel distributed symmetric and unsymmetric solvers. *Computer Methods in Applied Mechanics and Engineering*, 184:501–520, 2000.
- [26] P.R. Amestoy, A. Guermouche, J.-Y. LExcellent, and S. Pralet. Hybrid scheduling for the parallel solution of linear systems. *Parallel Computing*, 32(2):136–156, 2006.
- [27] Christophe Ancey and Steve Cochard. The dam-break problem for herschel–bulkley viscoplastic fluids down steep flumes. *Journal of Non-Newtonian Fluid Mechanics*, 158(1-3):18–35, 2009.
- [28] C.A. Anderson and R.J. Bridwell. A finite element method for studying the transient non-linear thermal creep of geological structures. *International Journal for Numerical and Analytical Methods in Geomechanics*, 4:255–276, 1980.
- [29] D.L. Anderson. The scales of mantle convection. *Tectonophysics*, 284(1-2):1–17, 1998.
- [30] DL Anderson. The persistent mantle plume myth. *Australian Journal of Earth Sciences*, 60(6-7):657–673, 2013.
- [31] J.D. Anderson. *Computational Fluid Dynamics*. McGraw-Hill, 1995.
- [32] Miguel Andrés-Martínez, Jason P Morgan, Marta Pérez-Gussinyé, and Lars Rüpke. A new free-surface stabilization algorithm for geodynamical modelling: Theory and numerical tests. *Physics of the Earth and Planetary Interiors*, 246:41–51, 2015.
- [33] Miguel Andrés-Martínez, Marta Pérez-Gussinyé, John Armitage, and Jason P Morgan. Thermomechanical implications of sediment transport for the architecture and evolution of continental rifts and margins. *Tectonics*, 38(2):641–665, 2019.
- [34] E.R. Andrews and M.I. Billen. Rheologic controls on the dynamics of slab detachment. *Tectonophysics*, 464:60–69, 2009.
- [35] A. Androvicova, H. Čížková, and A. van den Berg. The effects of rheological decoupling on slab deformation in the Earth's upper mantle. *Stud. Geophys. Geod.*, 57:460–481, 2013.
- [36] S. Angiboust, S. Wolf, E. Burov, P. Agard, and P. Yamato. Effect of fluid circulation on subduction interface tectonic processes: Insights from thermo-mechanical numerical modelling. *Earth Planet. Sci. Lett.*, 357–358:238–248, 2012.
- [37] D. Arcay, E. Tric, and M.-P. Doin. Numerical simulations of subduction zones. effect of slab dehydration on the mantle wedge dynamics. *Phys. Earth. Planet. Inter.*, 149:133–153, 2005.
- [38] D. Arcay, E. Tric, and M.-P. Doin. Slab surface temperature in subduction zones: influence of the interplate decoupling depth and upper plate thinning processes. *Earth Planet. Sci. Lett.*, 255:324–338, 2007.
- [39] M. Armann and P.J. Tackley. Simulating the thermochemical magmatic and tectonic evolution of Venus' mantle and lithosphere: Two-dimensional models. *J. Geophys. Res.*, 117(E12003), 2012.
- [40] J.J. Armitage, T.J. Henstock, T.A. Minshull, and J.R. Hopper. Lithospheric controls on melt production during continental breakup at slow rates of extension: Application to the North Atlantic. *Geochem. Geophys. Geosyst.*, 10(6), 2009.
- [41] D. Arndt, W. Bangerth, T. C. Clevenger, D. Davydov, M. Fehling, D. Garcia-Sanchez, G. Harper, T. Heister, L. Heltai, M. Kronbichler, R. M. Kynch, M. Maier, J.-P. Pelteret, B. Turcksin, and D. Wells. The **deal.II** library, version 9.1. *Journal of Numerical Mathematics*, 2019. accepted.
- [42] D.N. Arnold, F. Brezzi, and M. Fortin. A stable finite element for the Stokes equation. *Calcolo*, XXI(IV):337–344, 1984.
- [43] M Arnould, Nicolas Coltice, Nicolas Flament, V Seigneur, and RD Müller. On the scales of dynamic topography in whole-mantle convection models. *Geochemistry, Geophysics, Geosystems*, 19(9):3140–3163, 2018.
- [44] Maëlis Arnould, Jérôme Ganée, Nicolas Coltice, and Xiaojun Feng. Northward drift of the azores plume in the earths mantle. *Nature communications*, 10(1):3235, 2019.
- [45] K. M. Arredondo and M. I. Billen. Rapid weakening of subducting plates from trench-parallel estimates of flexural rigidity. *Physics of the Earth and Planetary Interiors*, 196-197:1–13, 2012.
- [46] P.-A. Arrial and M.I. Billen. Influence of geometry and eclogitization on oceanic plateau subduction . *Earth Planet. Sci. Lett.*, 363:34–43, 2013.
- [47] P.A. Arrial, N. Flyer, G.B. Wright, and L.H. Kellogg. On the sensitivity of 3-D thermal convection codes to numerical discretization: a model intercomparison. *Geosci. Model Dev.*, 7:2065–2076, 2014.

- [48] A. Aschwanden and H. Blatter. Numerical modeling of glacier flow. *COMSOL Users Conference*, 2006.
- [49] Alireza Asgari and LN Moresi. Multiscale particle-in-cell method: from fluid to solid mechanics. *Advanced Methods for Practical Applications in Fluid Mechanics*. InTech, Croatia, pages 185–208, 2012.
- [50] J. Austermann, J. X. Mitrovica, P. Huybers, and A. Rovere. Detection of a dynamic topography signal in last interglacial sea-level records. *Science Advances*, 3(7):1700457, 2017.
- [51] J. Austermann, D. Pollard, J. X. Mitrovica, R. Moucha, A. M. Forte, R. M. DeConto, D. B. Rowley, and M. E. Raymo. The impact of dynamic topography change on antarctic ice sheet stability during the mid-pliocene warm period. *Geology*, 43(10):927–930, 2015.
- [52] J. Autin, N. Bellahsen, L. Husson, M.O. Beslier, S. Leroy, and E. d’Acremont. Analog models of oblique rifting in a cold lithosphere. *Tectonics*, 29(6):TC6016, 2010.
- [53] JP Avouac and EB Burov. Erosion as a driving mechanism of intracontinental mountain growth. *J. Geophys. Res.*, 101(B8):17747, 1996.
- [54] EH Ayachour. A fast implementation for gmres method. *Journal of Computational and Applied Mathematics*, 159(2):269–283, 2003.
- [55] A. Babeyko and S. Sobolev. High-resolution numerical modeling of stress distribution in visco-elasto-plastic subducting slabs. *Lithos*, 103:205–216, 2008.
- [56] Andrey Y Babeyko, Stephan V Sobolev, Tim Vietor, Onno Oncken, and Robert B Trumbull. Numerical study of weakening processes in the central andean back-arc. In *The Andes*, pages 495–512. Springer, 2006.
- [57] A.Yu. Babeyko, S.V. Sobolev, R.B. Trumbull, O. Oncken, and L.L. Lavier. Numerical models of crustal scale convection and partial melting beneath the Altiplano-Puna plateau. *Earth Planet. Sci. Lett.*, 199:373–388, 2002.
- [58] M. Baes, R. Govers, and R. Wortel. Subduction initiation along the inherited weakness zone at the edge of a slab: Insights from numerical models. *Geophys. J. Int.*, 184:991–1008, 2011.
- [59] M. Baes, R. Govers, and R. Wortel. Switching between alternative responses of the lithosphere to continental collision. *Geophys. J. Int.*, 2011.
- [60] Marzieh Baes, Stephan V Sobolev, and Javier Quinteros. Subduction initiation in mid-ocean induced by mantle suction flow. *Geophysical Journal International*, 215(3):1515–1522, 2018.
- [61] Quan Bai and DL Kohlstedt. High-temperature creep of olivine single crystals, 2. dislocation structures. *Tectonophysics*, 206(1-2):1–29, 1992.
- [62] B. Baitsch-Ghirardello, Taras V. Gerya, and J.-P. Burg. Geodynamic regimes of intra-oceanic subduction: Implications for arc extension vs. shortening processes. *Gondwana Research*, 25:546–560, 2014.
- [63] Bettina Baitsch-Ghirardello, Andreas Stracke, James AD Connolly, Ksenia M Nikolaeva, and Taras V Gerya. Lead transport in intra-oceanic subduction zones: 2d geochemical–thermo-mechanical modeling of isotopic signatures. *Lithos*, 208:265–280, 2014.
- [64] R.R. Bakker, M. Frehner, and M. Lupi. How temperature-dependent elasticity alters host rock/magmatic reservoir models: A case study on the effects of ice-cap unloading on shallow volcanic systems. *epsl*, 456:16–25, 2016.
- [65] M. D. Ballmer, C. P. Conrad, E. I. Smith, and N. Harmon. Non-hotspot volcano chains produced by migration of shear-driven upwelling toward the east pacific rise. *Geology*, 41(4):479–482, 2013.
- [66] M. D. Ballmer, C. P. Conrad, E. I. Smith, and R. Johnsen. Intraplate volcanism at the edges of the colorado plateau sustained by a combination of triggered edge-driven convection and shear-driven upwelling. *Geochemistry, Geophysics, Geosystems*, 16(2):366–379, 2015.
- [67] Maxim D Ballmer, Garrett Ito, Jeroen Van Hunen, and Paul J Tackley. Spatial and temporal variability in hawaiian hotspot volcanism induced by small-scale convection. *Nature Geoscience*, 4(7):457, 2011.
- [68] M.D. Ballmer, G. Ito, J. van Hunen, and P.J. Tackley. Small-scale sublithospheric convection reconciles geochemistry and geochronology of ‘Superplume’ volcanism in th western and south pacific. *Earth Planet. Sci. Lett.*, 290:224–232, 2010.
- [69] M.D. Ballmer, J. van Hunen, G. Ito, P.J. Tackley, and T.A. Bianco. Non-hotspot volcano chains originating from small-scale sublithospheric convection. *Geophys. Res. Lett.*, 34(L23310):doi:10.1029/2007GL031636, 2007.
- [70] MD v Ballmer, J Van Hunen, G Ito, TA Bianco, and PJ Tackley. Intraplate volcanism with complex age-distance patterns: A case for small-scale sublithospheric convection. *Geochemistry, Geophysics, Geosystems*, 10(6), 2009.

- [71] NJ Balmforth, RV Craster, P Perona, AC Rust, and R Sassi. Viscoplastic dam breaks and the bostwick consistometer. *Journal of non-newtonian fluid mechanics*, 142(1-3):63–78, 2007.
- [72] N.J. Balmforth, Y. Forterre, and O. Pouliquen. The viscoplastic stokes layer. *Journal of Non-Newtonian Fluid Mechanics*, 158:46–53, 2009.
- [73] N.J. Balmforth and A.C. Rust. Weakly nonlinear viscoplastic convection. *Journal of Non-Newtonian Fluid Mechanics*, 158:36–45, 2009.
- [74] W. Bangerth and T. Heister. What makes computational open source software libraries successful? *Computational Science & Discovery*, 6, 2013.
- [75] W. Bangerth, T. Heister, et al. ASPECT: *Advanced Solver for Problems in Earth's Convection*. Computational Infrastructure for Geodynamics, 2019.
- [76] Xuewei Bao, David W Eaton, and Bernard Guest. Plateau uplift in western canada caused by lithospheric delamination along a craton edge. *Nature Geoscience*, 7(11):830, 2014.
- [77] H.A. Barnes. The yield stress - everything flows? *J. Non-Newtonian Fluid Mech.*, 81:133–178, 1999.
- [78] N. Barnett-Moore, R. Hassan, N. Flament, and D. Müller. The deep Earth origin of the Iceland plume and its effects on regional surface uplift and subsidence. *Solid Earth*, 8:235–254, 2017.
- [79] R. Barrett, M. Berry, T.F. Chan, J. Demmel, J.M. Donato, J. Dongarra, V. Eijkhout, R. Pozo, C. Romine, and H. van der Vorst. *Templates for the solution of linear systems: building blocks for iterative methods*. SIAM, 1994.
- [80] G.K. Batchelor. *An introduction to fluid dynamics*. Cambridge University Press, 1967.
- [81] K.-J. Bathe. *Finite Element Procedures in Engineering Analysis*. Prentice-Hall, 1982.
- [82] GE Batt and J Braun. On the thermomechanical evolution of compressional orogens. *Geophysical Journal International*, 128(2):364–382, 1997.
- [83] Geoffrey E Batt and Jean Braun. The tectonic evolution of the southern alps, new zealand: insights from fully thermally coupled dynamical modelling. *Geophysical Journal International*, 136(2):403–420, 1999.
- [84] L. Battaglia, M.A. Storti, and J. D'Elia. An interface capturing finite element approach for free surface flows using unstructured grids. *Mecanica Computational*, XXVII:33–48, 2008.
- [85] Cyrill Baumann, Taras V Gerya, and James AD Connolly. Numerical modelling of spontaneous slab breakoff dynamics during continental collision. *Geological Society, London, Special Publications*, 332(1):99–114, 2010.
- [86] T.S. Baumann, B.J.P. Kaus, and A.A. Popov. Constraining effective rheology through parallel joint geodynamic inversion. *Tectonophysics*, 631:197–211, 2014.
- [87] JR Baumgardner. *A Three-Dimensional Finite Element Model for Mantle Convection*. PhD thesis, UCLA, 1983.
- [88] J.R. Baumgardner. Three-Dimensional treatment of convective flow in the Earth's mantle. *Journal of Statistical Physics*, 39(5/6):501–511, 1985.
- [89] J.R. Baumgardner and P.O. Frederickson. Isocahedral discretisation of the two-sphere. *SIAM J. Numer Anal.*, 22(6):1107–1115, 1985.
- [90] A. Bauville and T. S. Baumann. geomio: an open-source matlab toolbox to create the initial configuration of 2d/3d thermo-mechanical simulations from 2d vector drawings. *Geochemistry, Geophysics, Geosystems*, 2019.
- [91] Adam P Beall, Louis Moresi, and Tim Stern. Dripping or delamination? a range of mechanisms for removing the lower crust or lithosphere. *Geophysical Journal International*, 210(2):671–692, 2017.
- [92] AP Beall, Louis Moresi, and Catherine M Cooper. Formation of cratonic lithosphere during the initiation of plate tectonics. *Geology*, 46(6):487–490, 2018.
- [93] C. Beaumont, P. Fullsack, and J. Hamilton. Erosional control of active compressional orogens. *Thrust Tectonics*, 99:1–18, 1992.
- [94] C. Beaumont, P. Fullsack, and J. Hamilton. Styles of crustal deformation in compressional orogens caused by subduction of the underlying lithosphere. *Tectonophysics*, 232:119–132, 1994.
- [95] C. Beaumont, R.A. Jamieson, J.P. Butler, and C.J. Warren. Crustal structure: A key constraint on the mechanism of ultra-high-pressure rock exhumation. *Earth Planet. Sci. Lett.*, 287:116–129, 2009.
- [96] C. Beaumont, R.A. Jamieson, M.H. Nguyen, and B. Lee. Himalayan tectonics explained by extrusion of a low-viscosity crustal channel coupled to focused surface denudation. *Nature*, 414:738–742, 2001.

- [97] C. Beaumont, R.A. Jamieson, M.H. Nguyen, and S. Medvedev. Crustal channel flows: 1. Numerical models with applications to the tectonics of the Himalayan-Tibetan orogen. *J. Geophys. Res.*, 109(B06406), 2004.
- [98] C. Beaumont, P.J. Kamp, J. Hamilton, and P. Fullsack. The continental collision zone, south island, new zealand: comparison of geodynamical models and observations. *J. Geophys. Res.*, 101:3333–3359, 1996.
- [99] C. Beaumont, J.A. Munoz, J. Hamilton, and P. Fullsack. Factors controlling the alpine evolution of the central pyrenees inferred from a comparison of observations and geodynamical models. *J. Geophys. Res.*, 105:8121–8145, 2000.
- [100] Christopher Beaumont and Garry Quinlan. A geodynamic framework for interpreting crustal-scale seismic-reflectivity patterns in compressional orogens. *Geophysical Journal International*, 116(3):754–783, 1994.
- [101] Stéphane J Beaussier, Taras V Gerya, and Jean-Pierre Burg. Near-ridge initiation of intraoceanic subduction: Effects of inheritance in 3d numerical models of the wilson cycle. *Tectonophysics*, 763:1–13, 2019.
- [102] J.M. Becker and M. Bevis. Love’s problem. *Geophys. J. Int.*, 156:171–178, 2004.
- [103] T. W. Becker and C. Faccenna. *Subduction Zone Geodynamics*, chapter A Review of the Role of Subduction Dynamics for Regional and Global Plate Motions, pages 3–34. Springer Berlin Heidelberg, 2009.
- [104] Thorsten Becker. Fine-scale modeling of global plate tectonics. *Science*, 329(5995):1020–1021, 2010.
- [105] Thorsten W Becker and Richard J O’Connell. Predicting plate velocities with mantle circulation models. *Geochemistry, Geophysics, Geosystems*, 2(12), 2001.
- [106] T.W. Becker. On the effect of temperature and strain-rate dependent viscosity on global mantle flow, net rotation, and plate-driving forces. *Geophys. J. Int.*, 167:943–957, 2006.
- [107] T.W. Becker and C. Faccenna. Mantle conveyor beneath the Tethyan collisional belt. *Earth Planet. Sci. Lett.*, 310:453–461, 2011.
- [108] T.W. Becker, C. Faccenna, R. O’Connell, and D. Giardini. The development of slabs in the upper mantle: Insights from numerical and laboratory experiments. *J. Geophys. Res.*, 104(B7):15,207–15,226, 1999.
- [109] T.W. Becker, V. Schulte-Pelkum, D.K. Blackman, J.B. Kellogg, and R.J. O’Connell. Mantle flow under the western United States from shear wave splitting. *Earth Planet. Sci. Lett.*, 247:235–251, 2006.
- [110] M.D. Behn, J. Lin, and M.T. Zuber. A continuum mechanics model for normal faulting using a strain-rate softening rheology: implications for thermal and rheological controls on continental and oceanic rifting. *Earth Planet. Sci. Lett.*, 202:725–740, 2002.
- [111] A. Bellas, Sh. Zhong, D. Bercovici, and E. Mulyukova. Dynamic weakening with grain-damage and implications for slab detachment. *Phys. Earth. Planet. Inter.*, 285:76–90, 2018.
- [112] Léa Bello, Nicolas Coltice, Tobias Rolf, and Paul J Tackley. On the predictability limit of convection models of the earth’s mantle. *Geochemistry, Geophysics, Geosystems*, 15(6):2319–2328, 2014.
- [113] Léa Bello, Nicolas Coltice, Paul J Tackley, R Dietmar Müller, and John Cannon. Assessing the role of slab rheology in coupled plate-mantle convection models. *Earth and Planetary Science Letters*, 430:191–201, 2015.
- [114] T. Belytschko, Y. Krongauz, M. Fleming, D. Organ, and W.K.S. Liu. Smoothing and accelerated computations in the element free galerkin method. *Journal of Computational and Applied Mathematics*, 74:111–126, 1996.
- [115] T. Belytschko, Y. Krongauz, D. Organ, M. Fleming, and P. Krysl. Meshless methods: an overview and recent developments. *Comput. Methods Appl. Mech. Engrg.*, 139:3–47, 1996.
- [116] T. Belytschko, P. Krysl, and Y. Krongauz. A three-dimensional explicit element-free galerkin method. *International journal for numerical methods in fluids*, 24:1253–1270, 1997.
- [117] T. Belytschko, Y.Y. Lu, and L. Gu. Crack propagation by element-free galerkin methods. *Engineering Fracture Mechanics*, 51:295–315, 1995.
- [118] T. Belytschko, Y.Y. Lu, and M. Tabbara. Element-free galerkin methods for static and dynamic fracture. *International Journal of Solids and Structures*, 32:2547–2570, 1995.
- [119] Z Ben-Avraham, V Lyakhovsky, and M Grasso. Simulation of collision zone segmentation in the central mediterranean. *Tectonophysics*, 243(1-2):57–68, 1995.
- [120] Vladimir Benes and Philippe Davy. Modes of continental lithospheric extension: experimental verification of strain localization processes. *Tectonophysics*, 254(1-2):69–87, 1996.
- [121] A.K. Bengtson and P.E. van Keeken. Three-dimensional thermal structure of subduction zones: effects of obliquity and curvature. *Solid Earth*, 3:365–373, 2012.

- [122] A Beniest, A Koptev, and Evgenii Burov. Numerical models for continental break-up: Implications for the south atlantic. *Earth and Planetary Science Letters*, 461:176–189, 2017.
- [123] David J Benson. An efficient, accurate, simple ale method for nonlinear finite element programs. *Computer methods in applied mechanics and engineering*, 72(3):305–350, 1989.
- [124] M. Benzi, G.H. Golub, and J. Liesen. Numerical solution of saddle point problems. *Acta Numerica*, 14:1–137, 2005.
- [125] D. Bercovici, E. Mulyukova, and M.D. Long. A simple toy model for coupled retreat and detachment of subducting slabs. *Journal of Geodynamics*, 129:275–289, 2019.
- [126] D. Bercovici and G. Schubert. *Treatise on geophysics: Mantle dynamics. Vol. 7*. Elsevier, 2009.
- [127] D. Bercovici, G. Schubert, and G.A. Glatzmaier. Three-dimensional convection of an infinite Prandtl-number compressible fluid in a basally heated spherical shell. *J. Fluid Mech.*, 239:683–719, 1992.
- [128] D. Bercovici, G. Schubert, and Yanick Ricard. Abrupt tectonics and rapid slab detachment with grain damage. *Proceedings of the National Academy of Sciences*, 2014.
- [129] David Bercovici and Yanick Ricard. Energetics of a two-phase model of lithospheric damage, shear localization and plate-boundary formation. *Geophysical Journal International*, 152(3):581–596, 2003.
- [130] David Bercovici, Yanick Ricard, and Gerald Schubert. A two-phase model for compaction and damage: 1. general theory. *Journal of Geophysical Research: Solid Earth*, 106(B5):8887–8906, 2001.
- [131] David Bercovici, Gerald Schubert, and Paul J Tackley. On the penetration of the 660 km phase change by mantle downflows. *Geophysical research letters*, 20(23):2599–2602, 1993.
- [132] M. Bercovier and M. Engelman. A finite-element for the numerical solution of viscous incompressible flows. *J. Comp. Phys.*, 30:181–201, 1979.
- [133] M. Bercovier and M. Engelman. A finite-element method for incompressible Non-Newtonian flows. *J. Comp. Phys.*, 36:313–326, 1980.
- [134] Peter G Betts, Louis Moresi, Meghan S Miller, and David Willis. Geodynamics of oceanic plateau and plume head accretion and their role in phanerozoic orogenic systems of china. *Geoscience Frontiers*, 6(1):49–59, 2015.
- [135] P.G. Betts, W.G. Mason, and L. Moresi. The influence of a mantle plume head on the dynamics of a retreating subduction zone. *Geology*, 40(8):739–742, 2012.
- [136] M.J. Beuchert and Y.Y. Podladchikov. Viscoelastic mantle convection and lithospheric stresses. *GJI*, 183:35–63, 2010.
- [137] E. Beutel, J. van Wijk, C. Ebinger, D. Keir, and A. Agostini. Formation and stability of magmatic segments in the Main Ethiopian and Afar rifts. *Earth Planet. Sci. Lett.*, 293:225–235, 2010.
- [138] Andrew J Biggin, Bernard Steinberger, Julien Aubert, Neil Suttie, Richard Holme, Trond Helge Torsvik, Douwe G van der Meer, and DJJ van Hinsbergen. Possible links between long-term geomagnetic variations and whole-mantle convection processes. *Nature Geoscience*, 5(8):526, 2012.
- [139] Harmen Bijwaard and Wim Spakman. Tomographic evidence for a narrow whole mantle plume below iceland. *Earth and Planetary Science Letters*, 166(3-4):121–126, 1999.
- [140] M. I. Billen. Slab dynamics in the transition zone. *Physics of the Earth and Planetary Interiors*, 183(1-2):296–308, 2010.
- [141] Magali I Billen. Modeling the dynamics of subducting slabs. *Annu. Rev. Earth Planet. Sci.*, 36:325–356, 2008.
- [142] Magali I Billen. Tectonics: Soaking slabs. *Nature Geoscience*, 2(11):744, 2009.
- [143] M.I. Billen and M. Gurnis. A low wedge in subduction zones. *Earth Planet. Sci. Lett.*, 193:227–236, 2001.
- [144] M.I. Billen and M. Gurnis. Comparison of dynamic flow models for the Central Aleutian and Tonga-Kermadec subduction zones. *Geochem. Geophys. Geosyst.*, 4(4), 2003.
- [145] M.I. Billen and G. Hirth. Newtonian versus non-Newtonian upper mantle viscosity: Implications for subduction initiation. *Geophys. Res. Lett.*, 32(L19304):doi:10.1029/2005GL023457, 2005.
- [146] M.I. Billen and G. Hirth. Rheologic controls on slab dynamics. *Geochem. Geophys. Geosyst.*, 8(8):doi:10.1029/2007GC001597, 2007.
- [147] M.I. Billen and M. Jadamec. Origin of localized fast mantle flow velocity in numerical models of subduction. *Geochem. Geophys. Geosyst.*, 13(1), 2012.
- [148] E.C. Bingham. *Fluidity and Plasticity*. McGraw-Hill, New York, 1922.

- [149] P. Bird. Testing hypotheses on plate-driving mechanisms with global lithosphere models including topography, thermal structure, and faults. *J. Geophys. Res.*, 103(B5):10,115–10,129, 1998.
- [150] Peter Bird. Finite element modeling of lithosphere deformation: the zagros collision orogeny. *Tectonophysics*, 50(2-3):307–336, 1978.
- [151] Peter Bird. Initiation of intracontinental subduction in the himalaya. *Journal of Geophysical Research: Solid Earth*, 83(B10):4975–4987, 1978.
- [152] Peter Bird. Thin-plate and thin-shell finite-element programs for forward dynamic modeling of plate deformation and faulting. *Computers & Geosciences*, 25(4):383–394, 1999.
- [153] Peter Bird, Zhen Liu, and William Kurt Rucker. Stresses that drive the plates from below: Definitions, computational path, model optimization, and error analysis. *Journal of Geophysical Research: Solid Earth*, 113(B11), 2008.
- [154] BI Birger. Rheological model of the earth's and the terrestrial planets' mantles. *Computational Seismology and Geodynamics*, 3:1–7, 1996.
- [155] D. Bittner and H. Schmeling. Numerical modelling of melting processes and induced diapirism in the lower crust. *Geophy. J. Int.*, 123:59–70, 1995.
- [156] J Blackery and E Mitsoulis. Creeping motion of a sphere in tubes filled with a bingham plastic material. *Journal of non-newtonian fluid mechanics*, 70(1-2):59–77, 1997.
- [157] I.F. Blanco-Quintero, T.V. Gerya, A. Garcia-Casco, and A. Castro. Subduction of young oceanic plates: A numerical study with application to aborted thermalchemical plumes. *Geochem. Geophys. Geosyst.*, 12(10), 2011.
- [158] B. Blankenbach, F. Busse, U. Christensen, L. Cserepes, D. Gunkel, U. Hansen, H. Harder, G. Jarvis, M. Koch, G. Marquart, D. Moore, P. Olson, H. Schmeling, and T. Schnaubelt. A benchmark comparison for mantle convection codes. *Geophys. J. Int.*, 98:23–38, 1989.
- [159] Irina Blinova, Ilya Makeev, and Igor Popov. Benchmark solutions for stokes flows in cylindrical and spherical geometry. *Bulletin of the Transilvania University of Brasov. Mathematics, Informatics, Physics. Series III*, 9(1):11, 2016.
- [160] AM Bobrov and AA Baranov. Thermochemical mantle convection with drifting deformable continents: Main features of supercontinent cycle. *Pure and Applied Geophysics*, pages 1–21, 2019.
- [161] M Bocher, Nicolas Coltice, Alexandre Fournier, and Paul J Tackley. A sequential data assimilation approach for the joint reconstruction of mantle convection and surface tectonics. *Geophysical Journal International*, 204(1):200–214, 2016.
- [162] Marie Bocher, Alexandre Fournier, and Nicolas Coltice. Ensemble kalman filter for the reconstruction of the earth's mantle circulation. *Nonlinear Processes in Geophysics*, 25(1):99–123, 2018.
- [163] P. B. Bochev, C. R. Dohrmann, and M. D. Gunzburger. Stabilization of low-order mixed finite elements for the stokes equations. *SIAM Journal on Numerical Analysis*, 44(1):82–101, 2006.
- [164] Pavel B Bochev, Max D Gunzburger, and Richard B Lehoucq. On stabilized finite element methods for the stokes problem in the small time step limit. *International Journal for Numerical Methods in Fluids*, 53(4):573–597, 2007.
- [165] D. Boffi and L. Gastaldi. On the quadrilateral Q2-P1 element for the Stokes problem. *Int. J. Num. Meth. Fluids*, 39:1001–1011, 2002.
- [166] Francesca Boioli, Philippe Carrez, Patrick Cordier, Benoit Devincre, Karine Gouriet, Pierre Hirel, Antoine Kraych, and Sebastian Ritterbex. Pure climb creep mechanism drives flow in earths lower mantle. *Science advances*, 3(3):e1601958, 2017.
- [167] Marco Bonini, Giacomo Corti, Dimitrios Sokoutis, Gianfranco Vannucci, Paolo Gasperini, and Sierd Cloetingh. Insights from scaled analogue modelling into the seismotectonics of the iranian region. *Tectonophysics*, 376(3-4):137–149, 2003.
- [168] M.-A. Bonnardot, R. Hassani, and E. Tric. Numerical modelling of lithosphereasthenosphere interaction in a subduction zone. *Earth Planet. Sci. Lett.*, 272:698–708, 2008.
- [169] M.-A. Bonnardot, R. Hassani, E. Tric, E. Ruellan, and M. Regnier. Effect of margin curvature on plate deformation in a 3-D numerical model of subduction zones. *Geophy. J. Int.*, 173:1084–1094, 2008.
- [170] Stephane Bonnet and Alain Crave. Macroscale dynamics of experimental landscapes. *Geological Society, London, Special Publications*, 253(1):327–339, 2006.
- [171] Alain Bonneville and Patrick Capolsini. Thermic: a 2-d finite-element tool to solve conductive and advective heat transfer problems in earth sciences. *Computers & Geosciences*, 25(10):1137–1148, 1999.

- [172] P.D. Bons, D. Koehn, and M.W. Jessell, editors. *Microdynamics Simulation*. Lecture Notes in Earth Sciences. Springer, 2008.
- [173] F. Boschetti and Louis Moresi. Interactive inversion in geosciences. *Geophysics*, 66(4):1226–1234, 2001.
- [174] AP Boss, CL Angevine, and IS Sacks. Finite-amplitude models of convection in the early mantle. *Physics of the earth and planetary interiors*, 36(3-4):328–336, 1984.
- [175] William Bosworth. Geometry of propagating continental rifts. *Nature*, 316(6029):625, 1985.
- [176] O. Botella and R. Peyret. Benchmark spectral results on the lid-driven cavity flow. *Computers and Fluids*, 27(4):421–433, 1998.
- [177] MHP Bott, GD Waghorn, and A Whittaker. Plate boundary forces at subduction zones and trench-arc compression. *Tectonophysics*, 170(1-2):1–15, 1989.
- [178] A.D. Bottrill, J. van Hunen, and M.B. Allen. Insight into collision zone dynamics from topography: numerical modelling results and observations. *Solid Earth*, 3:387–399, 2012.
- [179] P. Bouilhol, V. Magni, J. van Hunen, and L. Kaislaniemi. A numerical approach to melting in warm subduction zones. *Earth Planet. Sci. Lett.*, 411:37–44, 2015.
- [180] Johannes Bouman, Jörg Ebbing, Sjef Meekes, Rader Abdul Fattah, Martin Fuchs, Sofie Gradmann, Roger Haagmans, Verena Lieb, Michael Schmidt, Denise Dettmering, et al. Goce gravity gradient data for lithospheric modeling. *International Journal of Applied Earth Observation and Geoinformation*, 35:16–30, 2015.
- [181] L. Bourgouin, H.-B. Mühlhaus, A.J. Hale, and A. Arsac. Towards realistic simulations of lava dome growth using the level set method. *Acta Geotechnica*, 1:225–236, 2006.
- [182] L. Bourgouin, H.-B. Mühlhaus, A.J. Hale, and A. Arsac. Studying the influence of a solid shell on lava dome growth and evolution using the level set method. *Geophys. J. Int.*, 170:1431–1438, 2007.
- [183] D. Boutelier, A. Chemenda, and C. Jorand. Continental subduction and exhumation of high-pressure rocks: insights from thermo-mechanical laboratory modelling. *Earth Planet. Sci. Lett.*, 222:209–216, 2004.
- [184] D.J. Bower, M. Gurnis, and N. Flament. Assimilating lithosphere and slab history in 4-D Earth models. *Phys. Earth. Planet. Inter.*, 238:8–22, 2015.
- [185] D.J. Bower, M. Gurnis, and M. Seton. Lower mantle structure from paleogeographically constrained dynamic Earth models. *Geochem. Geophys. Geosyst.*, 14(1):44–63, 2012.
- [186] D.J. Bower, M. Gurnis, and D. Sun. Dynamic origins of seismic wavespeed variation in D''. *Phys. Earth. Planet. Inter.*, 214:74–86, 2013.
- [187] W.F. Brace and D.L. Kohlstedt. Limits on lithospheric stress imposed by laboratory experiments. *J. Geophys. Res.*, 85:6248–6252, 1980.
- [188] D. Braess. *Finite Elements*. Cambridge, 2007.
- [189] Henning Braess and Peter Wriggers. Arbitrary lagrangian eulerian finite element analysis of free surface flow. *Computer Methods in Applied Mechanics and Engineering*, 190(1-2):95–109, 2000.
- [190] J.P. Brandenburg, E.H. Hauri, P.E. van Keken, and C.J. Ballentine. A multiple-system study of the geochemical evolution of the mantle with force-balanced plates and thermochemical effects. *Earth Planet. Sci. Lett.*, 276:1–13, 2008.
- [191] J.P. Brandenburg and P.E. van Keken. Deep storage of oceanic crust in a vigorously convecting mantle. *J. Geophys. Res.*, 112(B06403), 2007.
- [192] J.P. Brandenburg and P.E. van Keken. Methods for thermochemical convection in Earth's mantle with force-balanced plates. *Geochem. Geophys. Geosyst.*, 8(11), 2007.
- [193] J.M. Branholt, K. Regenauer-Lieb, and D.A. Yuen. Weak zone formation for initiating subduction from thermo-mechanical feedback of low-temperature plasticity. *Earth Planet. Sci. Lett.*, 190:237–250, 2001.
- [194] Joy M Branholt, Masanori C Kameyama, David A Yuen, and Yoshiyuki Kaneda. Effects of temperature-dependent thermal diffusivity on shear instability in a viscoelastic zone: implications for faster ductile faulting and earthquakes in the spinel stability field. *Earth and Planetary Science Letters*, 182(2):171–185, 2000.
- [195] J. Braun. Pecube: a new finite-element code to solve the 3D heat transport equation including the effects of a time-varying, finite amplitude surface topography. *Computers and Geosciences*, 29:787–794, 2003.
- [196] J. Braun. Recent advances and current problems in modelling surface processes and their interaction with crustal deformation. *Analogue and Numerical Modelling of Crustal-Scale Processes. Geological Society, London. Special Publications*, 253:307–325, 2006.

- [197] J Braun, Xavier Robert, and T Simon-Labrec. Eroding dynamic topography. *Geophysical Research Letters*, 40(8):1494–1499, 2013.
- [198] J. Braun and M. Sambridge. Modelling landscape evolution on geological time scales: a new method based on irregular spatial discretisation. *Basin Research*, 9:27–52, 1997.
- [199] J. Braun, C. Thieulot, P. Fullsack, M. DeKool, and R.S. Huismans. DOUAR: a new three-dimensional creeping flow model for the solution of geological problems. *Phys. Earth. Planet. Inter.*, 171:76–91, 2008.
- [200] J. Braun and S.D. Willett. A very efficient O(n), implicit and parallel method to solve the stream power equation governing fluvial incision and landscape evolution. *Geomorphology*, 180–181:170–179, 2013.
- [201] J. Braun and P. Yamato. Structural evolution of a three-dimensional, finite-width crustal wedge. *Tectonophysics*, 484:181–192, 2010.
- [202] Jean Braun. Three-dimensional numerical modeling of compressional orogenies: Thrust geometry and oblique convergence. *Geology*, 21(2):153–156, 1993.
- [203] Jean Braun. Three-dimensional numerical simulations of crustal-scale wrenching using a non-linear failure criterion. *Journal of Structural Geology*, 16(8):1173–1186, 1994.
- [204] Jean Braun. Earth science: glaciers shield mountain tops. *Nature*, 467(7313):281, 2010.
- [205] Jean Braun. The many surface expressions of mantle dynamics. *Nature Geoscience*, 3(12):825, 2010.
- [206] Jean Braun and Christopher Beaumont. Three-dimensional numerical experiments of strain partitioning at oblique plate boundaries: Implications for contrasting tectonic styles in the southern Coast Ranges, California, and central South Island, New Zealand. *J. Geophys. Res.*, 100(B9):18,059–18,074, 1995.
- [207] Jean Braun and Malcolm Sambridge. Dynamical lagrangian remeshing (dlr): a new algorithm for solving large strain deformation problems and its application to fault-propagation folding. *Earth and Planetary Science Letters*, 124(1-4):211–220, 1994.
- [208] Jean Braun and Malcolm Sambridge. A numerical method for solving partial differential equations on highly irregular evolving grids. *Nature*, 376(6542):655, 1995.
- [209] Jean Braun and Russell Shaw. A thin-plate model of palaeozoic deformation of the australian lithosphere: implications for understanding the dynamics of intracratonic deformation. *Geological Society, London, Special Publications*, 184(1):165–193, 2001.
- [210] E. Bredow and B. Steinberger. Variable melt production rate of the kerguelen hotspot due to long-term plume-ridge interaction. *Geophysical Research Letters*, 45(1):126–136, 2018.
- [211] E. Bredow, B. Steinberger, R. Gassmöller, and J. Dannberg. How plume-ridge interaction shapes the crustal thickness pattern of the réunion hotspot track. *Geochemistry, Geophysics, Geosystems*, 2017.
- [212] RJ Bridwell and CA Anderson. Thermomechanical models of the rio grande rift. Technical report, Los Alamos Scientific Lab., NM (USA), 1980.
- [213] RJ Bridwell and C Potzick. Thermal regimes, mantle diapirs and crustal stresses of continental rifts. *Tectonophysics*, 73(1-3):15–32, 1981.
- [214] Taco Broerse, Riccardo Riva, Wim Simons, Rob Govers, and Bert Vermeersen. Postseismic GRACE and GPS observations indicate a rheology contrast above and below the Sumatra slab. *Journal Of Geophysical Research*, 120:5343–5361, 2015.
- [215] A.N. Brooks and T.J.R. Hughes. Streamline Upwind/Petrov-Galerkin formulations for convection dominated flows with particular emphasis on the incompressible Navier-Stokes equations. *Computer Methods in Applied Mechanics and Engineering*, 32:199–259, 1982.
- [216] J.-P. Brun. Narrow rifts versus wide rifts: inferences for the mechanics of rifting from laboratory experiments. *Philosophical Transactions of the Royal Society A*, 357:695–712, 1999.
- [217] J.-P. Brun, D. Sokoutis, C. Tirel, F. Gueydan, J. van Den Driessche, and M.-O. Beslier. Crustal versus mantle core complexes. *Tectonophysics*, 746:22–45, 2018.
- [218] Jean-Pierre Brun and Xavier Fort. Salt tectonics at passive margins: Geology versus models. *Marine and Petroleum Geology*, 28(6):1123–1145, 2011.
- [219] S. Brune. Evolution of stress and fault patterns in oblique rift systems: 3-D numerical lithospheric-scale experiments from rift to breakup. *Geochem. Geophys. Geosyst.*, 15:3392–3415, 2014.
- [220] S. Brune and J. Autin. The rift to break-up evolution of the Gulf of Aden: Insights from 3D numerical lithospheric-scale modelling. *Tectonophysics*, 607:65–79, 2013.
- [221] S. Brune, A.A. Popov, and S. Sobolev. Modeling suggests that oblique extension facilitates rifting and continental break-up. *J. Geophys. Res.*, 117(B08402), 2012.

- [222] S. Brune, A.A. Popov, and S. Sobolev. Quantifying the thermo-mechanical impact of plume arrival on continental break-up. *Tectonophysics*, 604:51–59, 2013.
- [223] Sascha Brune. Modelling continental rift dynamics, 2018.
- [224] Sascha Brune, Giacomo Corti, and Giorgio Ranalli. Controls of inherited lithospheric heterogeneity on rift linkage: Numerical and analog models of interaction between the kenyan and ethiopian rifts across the turkana depression. *Tectonics*, 36(9):1767–1786, 2017.
- [225] Sascha Brune, Giacomo Corti, and Giorgio Ranalli. Controls of inherited lithospheric heterogeneity on rift linkage: Numerical and analog models of interaction between the kenyan and ethiopian rifts across the turkana depression. *Tectonics*, 36(9):1767–1786, 2017.
- [226] Sascha Brune, Christian Heine, Peter D Clift, and Marta Pérez-Gussinyé. Rifted margin architecture and crustal rheology: reviewing iberia-newfoundland, central south atlantic, and south china sea. *Marine and Petroleum Geology*, 79:257–281, 2017.
- [227] Sascha Brune, Simon E Williams, and R Dietmar Müller. Oblique rifting: the rule, not the exception. *Solid Earth*, 9(5):1187–1206, 2018.
- [228] C.-H. Bruneau and M. Saad. The 2D lid-driven cavity problem revisited. *Computers & Fluids*, 35:326–348, 2006.
- [229] David Brunet, Philippe Machetel, and David A Yuen. Slab weakening by the exothermic olivine-spinel phase change. *Geophysical research letters*, 25(17):3231–3234, 1998.
- [230] W Roger Buck, Fernando Martinez, Michael S Steckler, and James R Cochran. Thermal consequences of lithospheric extension: pure and simple. *Tectonics*, 7(2):213–234, 1988.
- [231] W Roger Buck and Dimitrios Sokoutis. Analogue model of gravitational collapse and surface extension during continental convergence. *Nature*, 369(6483):737, 1994.
- [232] W.R. Buck. Modes of Continental Lithospheric Extension. *J. Geophys. Res.*, 96(B2):20,161–20,178, 1991.
- [233] W.R. Buck, L.L. Lavier, and A.N.B. Poliakov. How to make a rift wide. *Phil. Trans. R. Soc. Lond. A*, 357:671–693, 1999.
- [234] Richard Gordon Budynas. *Advanced strength and applied stress analysis*. McGraw-Hill, 1999.
- [235] B.A. Buffet, C.W. Gable, and R.J. R.J. OConnell. Linear stability of a layered fluid with mobile surface plates. *J. Geophys. Res.*, 99(B10):19,885–19,900, 1994.
- [236] H.H. Bui, R. Fukugawa, K. Sako, and S. Ohno. Lagrangian meshfree particles method (SPH) for large deformation and failure flows of geomaterial using elasticplastic soil constitutive model. *Int. J. Numer. Anal. Geomech.*, 32(12):1537–1570, 2008.
- [237] S. Buitner, A.Y. Babeyko, S. Ellis, T.V. Gerya, B.J.P. Kaus, A. Kellner, G. Schreurs, and Y. Yamada. The numerical sandbox: comparison of model results for a shortening and an extension experiment. *Analogue and Numerical Modelling of Crustal-Scale Processes. Geological Society, London. Special Publications*, 253:29–64, 2006.
- [238] S. Buitner, A.Y. Babeyko, S. Ellis, T.V. Gerya, B.J.P. Kaus, A. Kellner, G. Schreurs, and Y. Yamada. The numerical sandbox: comparison of model results for a shortening and an extension experiment. *Analogue and Numerical Modelling of Crustal-Scale Processes. Geological Society, London. Special Publications*, 253:29–64, 2006.
- [239] S.J.H. Buitner. A review of brittle compressional wedge models. *Tectonophysics*, 530:1–17, 2012.
- [240] S.J.H. Buitner, R. Govers, and M.J.R. Wortel. A modelling study of vertical surface displacements at convergent plate margins. *Geophys. J. Int.*, 147:415–427, 2001.
- [241] S.J.H. Buitner, R. Govers, and M.J.R. Wortel. Two-dimensional simulations of surface deformation caused by slab detachment. *Tectonophysics*, 354:195–210, 2002.
- [242] S.J.H. Buitner, R.S. Huismans, and C. Beaumont. Dissipation analysis as a guide to mode selection during crustal extension and implications for the styles of sedimentary basins. *J. Geophys. Res.*, 113(B06406):B06406, 2008.
- [243] S.J.H. Buitner and O.A. Pfiffner. Numerical models of the inversion of half-graben basins. *Tectonics*, 22, 2003.
- [244] S.J.H. Buitner, O.A. Pfiffner, and C. Beaumont. Inversion of extensional sedimentary basins: A numerical evaluation of the localisation of shortening. *Earth Planet. Sci. Lett.*, 288:492–504, 2009.
- [245] S.J.H. Buitner, G. Schreurs, M. Albertz, T.V. Gerya, B. Kaus, W. Landry, L. le Pourhiet, Y. Mishin, D.L. Egholm, M. Cooke, B. Maillet, C. Thieulot, T. Crook, D. May, P. Souloumiac, and C. Beaumont. Benchmarking numerical models of brittle thrust wedges. *Journal of Structural Geology*, 92:140–177, 2016.

- [246] SJH Buiter, MJR Wortel, and R Govers. The role of subduction in the evolution of the apennines foreland basin. *Tectonophysics*, 296(3-4):249–268, 1998.
- [247] Susanne JH Buiter and Trond H Torsvik. A review of wilson cycle plate margins: A role for mantle plumes in continental break-up along sutures? *Gondwana Research*, 26(2):627–653, 2014.
- [248] A.L. Bull, M. Domeier, and T.H. Torsvik. The effect of plate motion history on the longevity of deep mantle heterogeneities. *Earth Planet. Sci. Lett.*, 401:172–182, 2014.
- [249] A.L. Bull, A.K. McNamara, T.W. Becker, and J. Ritsema. Global scale models of the mantle flow field predicted by synthetic tomography models. *Phys. Earth. Planet. Inter.*, 182:129–138, 2010.
- [250] P.S. Bullen. *Handbook of Means and Their Inequalities*. Springer; 2nd edition, 2003.
- [251] H.-P. Bunge, M. Richards, C. Lithgow-Bertelloni, J.R. Baumgardner, S.P. Grand, and B. Romanowicz. Time scales and heterogeneous structure in geodynamic Earth models. *Science*, 280:91–95, 1998.
- [252] H.-P. Bunge, M.A. Richards, and J.R. Baumgardner. Effect of depth-dependent viscosity on the planform of mantle convection. *Nature*, 379:436–438, 1996.
- [253] H.-P. Bunge, M.A. Richards, and J.R. Baumgardner. A sensitivity study of three-dimensional spherical mantle convection at 10^8 Rayleigh number: Effects of depth-dependent viscosity, heating mode, and endothermic phase change. *J. Geophys. Res.*, 102(B6):11,991–12,007, 1997.
- [254] Hans-Peter Bunge and John R Baumgardner. Mantle convection modeling on parallel virtual machines. *Computers in physics*, 9(2):207–215, 1995.
- [255] Hans-Peter Bunge, CR Hagelberg, and BJ Travis. Mantle circulation models with variational data assimilation: inferring past mantle flow and structure from plate motion histories and seismic tomography. *Geophysical Journal International*, 152(2):280–301, 2003.
- [256] DW Burbank and N Pinter. Landscape evolution: the interactions of tectonics and surface processes. *Basin Research*, 11(1):1–6, 1999.
- [257] J.-P. Burg, J.-L. Bodinier, T. Gerya, R.-M. Bedini, F. Boudier, J.-M. Dautria, V. Prikhodko, A. Efimov, E. Pupier, and J.-L. Balanec. Translithospheric mantle diapirism: Geological evidence and numerical modelling of the kondyor zoned ultramafic complex (russian far-east). *Journal of Petrology*, 50(2), 2009.
- [258] J.-P. Burg and T.V. Gerya. The role of viscous heating in Barrovian metamorphism of collisional orogens: thermomechanical models and application to the Lepontine Dome in the Central Alps. *J. Metamorphic Geology*, 23:75–95, 2005.
- [259] J.-P. Burg and T.V. Gerya. Modelling intrusion of mafic and ultramafic magma into the continental crust: numerical methodology and results . *Boll. Soc. Geol. It.*, 127(2), 2008.
- [260] J.-P. Burg and S.M. Schmalholz. Viscous heating allows thrusting to overcome crustal-scale buckling: Numerical investigation with application to the Himalayan syntaxes. *Earth Planet. Sci. Lett.*, 274:189–203, 2008.
- [261] Peter M Burgess, Michael Gurnis, and Louis Moresi. Formation of sequences in the cratonic interior of north america by interaction between mantle, eustatic, and stratigraphic processes. *Geological Society of America Bulletin*, 109(12):1515–1535, 1997.
- [262] PM Burgess and LN Moresi. Modelling rates and distribution of subsidence due to dynamic topography over subducting slabs: is it possible to identify dynamic topography from ancient strata? *Basin Research*, 11(4):305–314, 1999.
- [263] Roland Bürgmann and Georg Dresen. Rheology of the lower crust and upper mantle: Evidence from rock mechanics, geodesy, and field observations. *Annu. Rev. Earth Planet. Sci.*, 36:531–567, 2008.
- [264] Kevin Burke. Plate tectonics, the wilson cycle, and mantle plumes: geodynamics from the top. *Annual Review of Earth and Planetary Sciences*, 39:1–29, 2011.
- [265] E.R. Burkett and M.I. Billen. Dynamics and implications of slab detachment due to ridge-trench collision. *J. Geophys. Res.*, 114(B12402), 2009.
- [266] E.R. Burkett and M.I. Billen. Three-dimensionality of slab detachment due to ridge-trench collision: Laterally simultaneous boudinage versus tear propagation. *Geochem. Geophys. Geosyst.*, 11(11), 2010.
- [267] E. Burov and A.Poliakov. Erosion and rheology controls on synrift and postrift evolution: Verifying old and new ideas using a fully coupled numerical model. *J. Geophys. Res.*, 106(B8):16,461–16,481, 2001.
- [268] E. Burov and S. Cloetingh. Erosion and rift dynamics: new thermomechanical aspects of post-rift evolution of extensional basins. *Earth Planet. Sci. Lett.*, 150:7–26, 1997.
- [269] E. Burov and S. Cloetingh. Plume-like upper mantle instabilities drive subduction initiation. *Geophys. Res. Letters*, 37(L03309), 2010.

- [270] E. Burov, T. Francois, P. Agard, L. Le Pourhiet, B. Meyer, C. Tirel, S. Lebedev, P. Yamato, and J.-P. Brun. Rheological and geodynamic controls on the mechanisms of subduction and HP/UHP exhumation of crustal rocks during continental collision: Insights from numerical models. *Tectonophysics*, 2014.
- [271] E. Burov and T. Gerya. Asymmetric three-dimensional topography over mantle plumes. *Nature*, 513:doi:10.1038/nature13703, 2014.
- [272] E. Burov and L. Guillou-Frottier. The plume head-continental lithosphere interaction using a tectonically realistic formulation for the lithosphere. *Geophys. J. Int.*, 161:469–490, 2005.
- [273] E. Burov, L. Jolivet, L. Le Pourhiet, and A. Poliakov. A thermomechanical model of exhumation of high pressure (HP) and ultra-high pressure (UHP) metamorphic rocks in Alpine-type collision belts. *Tectonophysics*, 342:113–136, 2001.
- [274] E. Burov and G. Toussaint. Surface processes and tectonics: Forcing of continental subduction and deep processes. *Global and Planetary Change*, 58:141–164, 2007.
- [275] EB Burov and Michel Diament. Flexure of the continental lithosphere with multilayered rheology. *Geophysical Journal International*, 109(2):449–468, 1992.
- [276] EB Burov, AB Watts, et al. The long-term strength of continental lithosphere:” jelly sandwich” or” crème brûlée”? *GSA today*, 16(1):4, 2006.
- [277] Evgene Burov, Thomas François, Philippe Yamato, and Sylvie Wolf. Advances and challenges in geotectonic modelling. *Bulletin de la Société Géologique de France*, 185(3):147–168, 2014.
- [278] Evgene Burov. Rheology and strength of the lithosphere. *Marine and Petroleum Geology*, 28(8):1402–1443, 2011.
- [279] Evgene Burov and Michel Diament. The effective elastic thickness (t_e) of continental lithosphere: what does it really mean? *Journal of Geophysical Research: Solid Earth*, 100(B3):3905–3927, 1995.
- [280] Evgueni Burov and Sierd Cloetingh. Controls of mantle plumes and lithospheric folding on modes of intraplate continental tectonics: differences and similarities. *Geophysical Journal International*, 178(3):1691–1722, 2009.
- [281] C. Burstedde, O. Ghattas, M. Gurnis, G. Stadler, E. Tan, T. Tu, L.C. Wilcox, and S. Zhong. Scalable Adaptive Mantle Convection Simulation on Petascale Supercomputers. *ACM/IEEE SC Conference Series, 2008*, 2008.
- [282] C. Burstedde, O. Ghattas, G. Stadler, T. Tu, and L.C. Wilcox. Parallel scalable adjoint-based adaptive solution of variable-viscosity Stokes flow problems. *Computer Methods in Applied Mechanics and Engineering*, 198:1691–1700, 2009.
- [283] C. Burstedde, G. Stadler, L. Alisic, L.C. Wilcox, E. Tan, M. Gurnis, and O. Ghattas. Large-scale adaptive mantle convection simulation. *Geophys. J. Int.*, 192:889–906, 2013.
- [284] Carsten Burstedde, Jose A Fonseca, and Bram Metsch. An amg saddle point preconditioner with application to mixed poisson problems on adaptive quad/cube meshes. *arXiv preprint arXiv:1901.05830*, 2019.
- [285] Carsten Burstedde, Omar Ghattas, Michael Gurnis, Tobin Isaac, Georg Stadler, Tim Warburton, and Lucas Wilcox. Extreme-scale amr. In *Proceedings of the 2010 ACM/IEEE International Conference for High Performance Computing, Networking, Storage and Analysis*, pages 1–12. IEEE Computer Society, 2010.
- [286] FH Busse. High prandtl number convection. *Physics of the Earth and Planetary Interiors*, 19(2):149–157, 1979.
- [287] FH Busse. On the aspect ratios of two-layer mantle convection. *Physics of the Earth and Planetary Interiors*, 24(4):320–324, 1981.
- [288] F.H. Busse, U. Christensen, R. Clever, L. Cserepes, C. Gable, E. Giannandrea, L. Guillou, G. Houseman, H.-C. Nataf, M. Ogawa, M. Parmentier, C. Sotin, and B. Travis. 3D convection at infinite Prandtl number in Cartesian geometry - a benchmark comparison. *Geophys. Astrophys. Fluid Dynamics*, 75:39–59, 1993.
- [289] J.P. Butler and C. Beaumont. Subduction zone decoupling/retreat modeling explains south Tibet (Xigaze) and other supra-subduction zone ophiolites and their UHP mineral phases. *Earth Planet. Sci. Lett.*, 463:101–117, 2017.
- [290] J.P. Butler, C. Beaumont, and R.A. Jamieson. The Alps 1: A working geodynamic model for burial and exhumation of (ultra)high-pressure rocks in Alpine-type orogens. *Earth Planet. Sci. Lett.*, 337–378:114–131, 2013.

- [291] J.P. Butler, C. Beaumont, and R.A. Jamieson. Paradigm lost: Buoyancy thwarted by the strength of the Western Gneiss Region (ultra)high-pressure terrane, Norway. *Lithosphere*, page doi:10.1130/L426.1, 2015.
- [292] J.P. Butler, C. Veumont, and R.A. Jamieson. Crustal emplacement of exhuming (ultra)high-pressure rocks: Will that be pro- or retro-side ? *Geology*, 39:635–638, 2011.
- [293] SL Butler, WR Peltier, and SO Costin. Numerical models of the earths thermal history: Effects of inner-core solidification and core potassium. *Physics of the Earth and Planetary Interiors*, 152(1-2):22–42, 2005.
- [294] James D Byerlee. Brittle-ductile transition in rocks. *Journal of Geophysical Research*, 73(14):4741–4750, 1968.
- [295] O Čadek and AP van den Berg. Radial profiles of temperature and viscosity in the earth’s mantle inferred from the geoid and lateral seismic structure. *Earth and Planetary Science Letters*, 164(3-4):607–615, 1998.
- [296] Ondřej Čadek, Yanick Ricard, Zdeněk Martinec, and Ctirad Matyska. Comparison between newtonian and non-newtonian flow driven by internal loads. *Geophysical Journal International*, 112(1):103–114, 1993.
- [297] J. Cahouet and J.-P. Chabard. Some fast 3D finite element solvers for the generalized Stokes problem. *Int. J. Num. Meth. Fluids*, 8:869–895, 1988.
- [298] Elisa Calignano, Dimitrios Sokoutis, E Willingshofer, J-P Brun, Frédéric Gueydan, and S Cloetingh. Oblique contractional reactivation of inherited heterogeneities: Cause for arcuate orogens. *Tectonics*, 36(3):542–558, 2017.
- [299] Elisa Calignano, Dimitrios Sokoutis, Ernst Willingshofer, Frédéric Gueydan, and Sierd Cloetingh. Strain localization at the margins of strong lithospheric domains: Insights from analog models. *Tectonics*, 34(3):396–412, 2015.
- [300] Z.-H. Cao. Fast Uzawa algorithm for generalized saddle point problems . *Applied Numerical Mathematics*, 46:157–171, 2003.
- [301] F.A. Capitanio and M. Faccenna. Complex mantle flow around heterogeneous subducting oceanic plates. *Earth Planet. Sci. Lett.*, 353-354:29–37, 2012.
- [302] F.A. Capitanio, C. Faccenna, S. Zlotnik, and D.R. Stegman. Subduction dynamics and the origin of Andean orogeny and the Bolivian orocline. *Nature*, 480:doi:10.1038/nature10596, 2011.
- [303] FA Capitanio, G Morra, and S Goes. Dynamic models of downgoing plate-buoyancy driven subduction: Subduction motions and energy dissipation. *Earth and Planetary Science Letters*, 262(1-2):284–297, 2007.
- [304] FA Capitanio, G Morra, S Goes, RF Weinberg, and L Moresi. India–asia convergence driven by the subduction of the greater indian continent. *Nature Geoscience*, 3(2):136, 2010.
- [305] FA Capitanio and Gabriele Morra. The bending mechanics in a dynamic subduction system: Constraints from numerical modelling and global compilation analysis. *Tectonophysics*, 522:224–234, 2012.
- [306] FA Capitanio, O Nebel, PA Cawood, RF Weinberg, and F Clos. Lithosphere differentiation in the early earth controls archean tectonics. *Earth and Planetary Science Letters*, 525:115755, 2019.
- [307] F.A. Capitanio and A. Replumaz. Subduction and slab breakoff controls on Asian indentation tectonics and Himalayan western syntaxis formation . *Geochem. Geophys. Geosyst.*, 14(9):doi:10.1002/ggge.20171, 2013.
- [308] F.A. Capitanio, D.R. Stegman, L.N. Moresi, and W. Sharples. Upper plate controls on deep subduction, trench migrations and deformations at convergent margins. *Tectonophysics*, 483:80–92, 2010.
- [309] F.A. Capitanio, S. Zlotnik, and C. Faccenna. Controls on subduction reorganization in the Hellenic margin, eastern Mediterranean. *Geophys. Res. Lett.*, 37(L14309), 2010.
- [310] E. Carminati, M.J.R. Wortel, W. Spakman, and R. Sabadini. The role of slab detachment processes in the opening of the westerncentral Mediterranean basins: some geological and geophysical evidence. *Earth Planet. Sci. Lett.*, 160:651–665, 1998.
- [311] P.J. Carreau. Rheological Equations from Molecular Network Theories. *Transactions of the Society of rheology*, 16(1):99–127, 1972.
- [312] J. Carrero, B. Cockburn, and D. Schötzau. Hybridized globally divergence-free LDG methods. Part I: The Stokes problem. *Mathematics of Computation*, 75(254):533–563, 2005.
- [313] JF Casey and JF Dewey. Initiation of subduction zones along transform and accreting plate boundaries, triple-junction evolution, and forearc spreading centresimplications for ophiolitic geology and obduction. *Geological Society, London, Special Publications*, 13(1):269–290, 1984.
- [314] P. Castillo, B. Cockburn, I. Perugia, and D. Schötzau. Local discontinuous Galerkin methods for elliptic problems. *Commun. Numer. Meth. Engng*, 18:69–75, 2002.

- [315] A. Castro and T.V. Gerya. Magmatic implications of mantle wedge plumes: Experimental study. *Lithos*, 103:138–148, 2008.
- [316] Antonio Castro, Katharina Vogt, and Taras Gerya. Generation of new continental crust by sublithospheric silicic-magma relamination in arcs: a test of taylor’s andesite model. *Gondwana Research*, 23(4):1554–1566, 2013.
- [317] N.G. Cerpa, R. Araya, M. Gerbault, and R. Hassani. Relationship between slab dip and topography segmentation in an oblique subduction zone: Insights from numerical modeling. *Geophys. Res. Lett.*, 41:10.1002/2015GL064047, 2015.
- [318] N.G. Cerpa, B. Guillaume, and J.Martinod. The interplay between overriding plate kinematics, slab dip and tectonics. *Geophys. J. Int.*, 215:1789–1802, 2018.
- [319] N.G. Cerpa, R. Hassani, M. Gerbault, and J.-H. Prévost. A fictitious domain method for lithosphere–asthenosphere interaction: Application to periodic slab folding in the upper mantle. *Geochem. Geophys. Geosyst.*, 15, 2014.
- [320] N.G. Cerpa, I. Wada, and C.R. Wilson. Fluid migration in the mantle wedge: Influence of mineral grain size and mantle compaction. *J. Geophys. Res.*, 122:6247–6268, 2017.
- [321] N.G. Cerpa, I. Wada, and C.R. Wilson. Effects of fluid influx, fluid viscosity, and fluid density on fluid migration in the mantle wedge and their implications for hydrous melting. *Geosphere*, 15(1):1–23, 2019.
- [322] Edouard Chalaron, Jean Louis Mugnier, and Georges Mascle. Control on thrust tectonics in the himalayan foothills: a view from a numerical model. *Tectonophysics*, 248(1-2):139–163, 1995.
- [323] AI Chemenda, R-K Yang, J-F Stephan, EA Konstantinovskaya, and GM Ivanov. New results from physical modelling of arc–continent collision in taiwan: evolutionary model. *Tectonophysics*, 333(1-2):159–178, 2001.
- [324] J.S. Chen, C. Pan, and T.Y.P. Chang. On the control of pressure oscillation in bilinear-displacement constant-pressure element. *Comput. Methods Appl. Mech. Engrg.*, 128:137–152, 1995.
- [325] L Chen, H Nguyen-Xuan, T Nguyen-Thoi, KY Zeng, and SC Wu. Assessment of smoothed point interpolation methods for elastic mechanics. *International Journal for Numerical Methods in Biomedical Engineering*, 26(12):1635–1655, 2010.
- [326] Lin Chen, Taras Gerya, Zhongjie Zhang, GuiZhi Zhu, Thibault Duretz, and Wolfgang R Jacoby. Numerical modeling of eastern tibetan-type margin: influences of surface processes, lithospheric structure and crustal rheology. *Gondwana Research*, 24(3-4):1091–1107, 2013.
- [327] Lin Chen, Taras V Gerya, Zhong-Jie Zhang, Alan Aitken, Zhong-Hai Li, and Xiao-Feng Liang. Formation mechanism of steep convergent intracontinental margins: Insights from numerical modeling. *Geophysical Research Letters*, 40(10):2000–2005, 2013.
- [328] Yongshun Chen and W Jason Morgan. A nonlinear rheology model for mid-ocean ridge axis topography. *Journal of Geophysical Research: Solid Earth*, 95(B11):17583–17604, 1990.
- [329] Z. Chen, B.C. Burchfiel, Y. Liu, R.W. King, L.H. Royden, W. Tang, E. Wang, J. Zhao, and X. Zhang. Global positioning system measurements from eastern tibet and their implications for india/eurasia inter-continental deformation. *J. Geophys. Res.*, 105:16,215–16,227, 2000.
- [330] P. Chenin and C. Beaumont. Influence of offset weak zones on the development of rift basins: Activation and abandonment during continental extension and breakup. *J. Geophys. Res.*, 118:1–23, 2013.
- [331] P. Chenin, S.M. Schmalholz, G. Manatschal, and G.D. Karner. Necking of the lithosphere: A reappraisal of basic concepts with thermo-mechanical numerical modeling. *Journal of Geophysical Research: Solid Earth*, 123(6):5279–5299, 2018.
- [332] Pauline Chenin, Gianreto Manatschal, Alessandro Decarlis, Stefan M Schmalholz, Thibault Duretz, and Marco Beltrando. Emersion of distal domains in advanced stages of continental rifting explained by asynchronous crust and mantle necking. *Geochemistry, Geophysics, Geosystems*, 2019.
- [333] M.V. Chertova, T. Geenen, A. van den Berg, and W. Spakman. Using open sidewalls for modelling self-consistent lithosphere subduction dynamics . *Solid Earth*, 3:313–326, 2012.
- [334] M.V. Chertova, W. Spakman, T. Geenen, A.P. van den Berg, and D.J.J. van Hinsbergen. Underpinning tectonic reconstructions of the western Mediterranean region with dynamic slab evolution from 3-D numerical modeling. *J. Geophys. Res.*, 119:10.1002/ 2014JB011150, 2014.
- [335] Jean Chery, Alain Bonneville, Jean Pierre Vilotte, and Dave Yuen. Numerical modelling of caldera dynamical behaviour. *Geophysical Journal International*, 105(2):365–379, 1991.
- [336] S. Chiu-Webster, E.J. Hinch, and J.R. Lister. Very viscous horizontal convection. *J. Fluid Mech.*, 611:395–426, 2008.

- [337] G. Choblet, O. Cadek, F. Couturier, and C. Dumoulin. OEDIPUS: a new tool to study the dynamics of planetary interiors. *Geophys. J. Int.*, 170:9–30, 2007.
- [338] E. Choi and K.D. Petersen. Making Coulomb angle-oriented shear bands in numerical tectonic models. *Tectonophysics*, 657:94–101, 2015.
- [339] E. Choi, E. Tan, L.L. Lavier, and V.M. Calo. DynEarthSol2D: An efficient unstructured finite element method to study long-term tectonic deformation. *J. Geophys. Res.*, 118:1–16, 2013.
- [340] Eunseo Choi, Luc Lavier, and Michael Gurnis. Thermomechanics of mid-ocean ridge segmentation. *Phys. Earth Planet. Interiors*, 171:374–386, 2008.
- [341] A. Chopelas and R. Boehler. Thermal expansivity in the lower mantle. *Geophysical Research Letters*, 19(19):1983–1986, 1992.
- [342] PN Chopra and MS Paterson. The role of water in the deformation of dunite. *Journal of Geophysical Research: Solid Earth*, 89(B9):7861–7876, 1984.
- [343] R.R. Christensen. An Eulerian technique for thermomechanical modeling of lithospheric extension. *J. Geophys. Res.*, 97(B2):2015–2036, 1992.
- [344] U. Christensen. Convection in a variable-viscosity fluid: Newtonian versus power-law rheology. *Earth and Planetary Science Letters*, 64(1):153–162, 1983.
- [345] U. Christensen. Convection with pressure-and temperature-dependent non-newtonian rheology. *Geophysical Journal International*, 77(2):343–384, 1984.
- [346] U. Christensen and H. Harder. 3-D convection with variable viscosity. *Geophys. J. Int.*, 104:213–226, 1991.
- [347] Ulrich Christensen. Phase boundaries in finite amplitude mantle convection. *Geophysical Journal International*, 68(2):487–497, 1982.
- [348] Ulrich Christensen. Effects of phase transitions on mantle convection. *Annual Review of Earth and Planetary Sciences*, 23(1):65–87, 1995.
- [349] Ulrich R. Christensen. Thermal evolution models for the earth. *Journal of Geophysical Research: Solid Earth*, 90(B4):2995–3007, 1985.
- [350] Ulrich R. Christensen. The influence of trench migration on slab penetration into the lower mantle. *Earth and Planetary Science Letters*, 140(1–4):27–39, 1996.
- [351] Ulrich R. Christensen and Albrecht W. Hofmann. Segregation of subducted oceanic crust in the convecting mantle. *Journal of Geophysical Research: Solid Earth*, 99(B10):19867–19884, 1994.
- [352] Ulrich R. Christensen and David A. Yuen. Layered convection induced by phase transitions. *Journal of Geophysical Research: Solid Earth*, 90(B12):10291–10300, 1985.
- [353] U.R. Christensen and D.A. Yuen. The interaction of a subducting lithospheric slab with a chemical or phase boundary. *J. Geophys. Res.*, 89(B6):4389–4402, 1984.
- [354] Edmund Christiansen and Knud D. Andersen. Computation of collapse states with von mises type yield condition. *International Journal for Numerical Methods in Engineering*, 46:1185–1202, 1999.
- [355] Edmund Christiansen and Ole S. Pedersen. Automatic mesh refinement in limit analysis. *International Journal for Numerical Methods in Engineering*, 50:1331–1346, 2001.
- [356] M.A. Christon, P.M. Gresho, and S.B. Sutton. Computational predictability of time-dependent natural convection flows in enclosures (including a benchmark solution). *Int. J. Num. Meth. Fluids*, 40:953–980, 2002.
- [357] H. Ciskova, A. van den Berg, and M. Jacobs. Impact of compressibility on heat transport characteristics of large terrestrial planets. *Phys. Earth. Planet. Inter.*, 268:65–77, 2017.
- [358] H. Ciskova, J. van Hunen, A.P. van den Berg, and N.J. Vlaar. The influence of rheological weakening and yield stress on the interaction of slabs with the 670 km discontinuity. *Earth Planet. Sci. Lett.*, 199:447–457, 2002.
- [359] H. Čížková, A.P. van den Berg, W. Spakman, and Ctirad Matyska. The viscosity of the earth's lower mantle inferred from sinking speed of subducted lithosphere. *Phys. Earth. Planet. Inter.*, 200–201:56–62, 2012.
- [360] Hana Čížková, Jeroen van Hunen, and Arie van den Berg. Stress distribution within subducting slabs and their deformation in the transition zone. *Physics of the Earth and Planetary Interiors*, 161(3–4):202–214, 2007.
- [361] Marin K Clark, John WM Bush, and Leigh H Royden. Dynamic topography produced by lower crustal flow against rheological strength heterogeneities bordering the tibetan plateau. *Geophysical Journal International*, 162(2):575–590, 2005.

- [362] Marin Kristen Clark and Leigh Handy Royden. Topographic ooze: Building the eastern margin of tibet by lower crustal flow. *Geology*, 28(8):703–706, 2000.
- [363] M.K. Clark, LH Royden, KX Whipple, BC Burchfiel, X Zhang, and W Tang. Use of a regional, relict landscape to measure vertical deformation of the eastern tibetan plateau. *Journal of Geophysical Research: Earth Surface*, 111(F3), 2006.
- [364] Thomas C Clevenger and Timo Heister. Comparison between algebraic and matrix-free geometric multigrid for a stokes problem on adaptive meshes with variable viscosity. *arXiv preprint arXiv:1907.06696*, 2019.
- [365] P.D. Clift, S. Brune, and J. Quinteros. Climate changes control offshore crustal structure at South China Sea continental margin. *Earth Planet. Sci. Lett.*, 420:66–72, 2015.
- [366] S. Cloetingh, E. Burov, F. Beekman, B. Andeweg, P.A.M. Andriessen, D. Garcia-Castellanos, G. de Vicente, and R. Vegas. Lithospheric folding in Iberia. *Tectonics*, 21(5):10.1029/2001TC901031, 2002.
- [367] S. Cloetingh, E. Burov, and A. Poliakov. Lithospehre folding: Primary response to compression? (from central asia to paris basin). *Tectonics*, 18:1064–1083, 1999.
- [368] S. Cloetingh, R. Wortel, and N.J. Vlaar. On the Initiation of Subduction Zones. *Pure and Applied Geophysics*, 129(1/2):7–25, 1989.
- [369] S.A.P.L. Cloetingh, E. Burov, L. Matenco, G. Toussaint, G. Bertotti, P.A.M. Andriessen, M.J.R. Wortel, and W. Spakman. thermo-mechanical controls on the mode of continental collision in the se carpathians (romania). *Earth Planet. Sci. Lett.*, 218:57–76, 2004.
- [370] SAPL Cloetingh, Jan Diederik Van Wees, PA Ziegler, L Lenkey, F Beekman, M Tesauro, A Förster, B Norden, M Kaban, N Hardebol, et al. Lithosphere tectonics and thermo-mechanical properties: An integrated modelling approach for Enhanced Geothermal Systems exploration in Europe. *Earth-Science Reviews*, 102:159, 2010.
- [371] Sierd Cloetingh, Fred Beekman, Peter A Ziegler, Jan-Diederik van Wees, and Dimitrios Sokoutis. Post-rift compressional reactivation potential of passive margins and extensional basins. *Geological Society, London, Special Publications*, 306(1):27–70, 2008.
- [372] Sierd Cloetingh and Henk Kooi. Intraplate stresses and dynamical aspects of rifted basins. *Tectonophysics*, 215(1-2):167–185, 1992.
- [373] Sierd Auke Pieter Leonard Cloetingh, MJR Wortel, and NJ Vlaar. Evolution of passive continental margins and initiation of subduction zones. *Nature*, 297(5862):139, 1982.
- [374] S Cochard and C Ancey. Experimental investigation of the spreading of viscoplastic fluids on inclined planes. *Journal of Non-Newtonian Fluid Mechanics*, 158(1-3):73–84, 2009.
- [375] B. Cockburn and J. Gopalakrishnan. The derivation of hybridizable discontinuous Galerkin methods for Stokes flow. *SIAM J. Numer. Anal.*, 47(2):1092–1125, 2009.
- [376] B. Cockburn, G. Kanschat, and D. Schötzau. The local discontinuous Galerkin method for linearized incompressible fluid flow: a review. *Computers and Fluids*, 34:491–506, 2005.
- [377] B. Cockburn, G. Kanschat, and D. Schötzau. An Equal-Order DG Method for the Incompressible Navier-Stokes Equations. *J. Sci. Comput.*, 40:188–210, 2009.
- [378] B. Cockburn, G. Kanschat, D. Schoetzau, and C. Schwab. Local discontinuous Galerkin methods for the Stokes system. *SIAM J. Numer. Anal.*, 40(1):319–343, 2002.
- [379] B. Cockburn, G.E. Karniadakis, and C.W. Shu. The Development of Discontinuous Galerkin Methods. *Discontinuous Galerkin Methods. Lecture Notes in Computational Science and Engineering*, 11, 2000.
- [380] B. Cockburn, N.C. Nguyen, and J. Peraire. A Comparison of HDG Methods for Stokes Flow. *J. Sci. Comput.*, 45:215–237, 2010.
- [381] Bernardo Cockburn. Discontinuous galerkin methods. *ZAMM-Journal of Applied Mathematics and Mechanics*, 83(11):731–754, 2003.
- [382] M. Collignon, N. Fernandez, and B.J.P. Kaus. Influence of surface processes and initial topography on lateral fold growth and fold linkage mode. *Tectonics*, 34:1622–1645, 2015.
- [383] M. Collignon, B.J.P. Kaus, D.A. May, and N. fernandez. Influences of surface processes on fold growth during 3-D detachment folding. *Geochem. Geophys. Geosyst.*, 15:doi:10.1002/2014GC005450, 2014.
- [384] N. Coltice, M. Gerault, and M. Ulvrova. A mantle convection perspective on global tectonics. *Earth-Science Reviews*, 165:120–150, 2017.
- [385] N Coltice, T Rolf, and PJ Tackley. Seafloor spreading evolution in response to continental growth. *Geology*, 42(3):235–238, 2014.

- [386] Nicolas Coltice, Gaspard Larroutuou, Eric Debayle, and Edward J Garnero. Interactions of scales of convection in the earth's mantle. *Tectonophysics*, 746:669–677, 2018.
- [387] Nicolas Coltice, Tobias Rolf, Paul J Tackley, and Stéphane Labrosse. Dynamic causes of the relation between area and age of the ocean floor. *Science*, 336(6079):335–338, 2012.
- [388] Nicolas Coltice, Maria Seton, Tobias Rolf, RD Müller, and Paul J Tackley. Convergence of tectonic reconstructions and mantle convection models for significant fluctuations in seafloor spreading. *Earth and Planetary Science Letters*, 383:92–100, 2013.
- [389] Nicolas Coltice and Grace E Shephard. Tectonic predictions with mantle convection models. *Geophysical Journal International*, 213(1):16–29, 2018.
- [390] JAD Connolly and Yu Yu Podladchikov. Compaction-driven fluid flow in viscoelastic rock. *Geodinamica Acta*, 11(2-3):55–84, 1998.
- [391] Clinton P Conrad and Carolina Lithgow-Bertelloni. How mantle slabs drive plate tectonics. *Science*, 298(5591):207–209, 2002.
- [392] Clinton P Conrad and Peter Molnar. The growth of rayleightaylor-type instabilities in the lithosphere for various rheological and density structures. *Geophysical Journal International*, 129(1):95–112, 1997.
- [393] C.P. Conrad, M.D. Behn, and P.G. Silver. Global mantle flow and the development of seismic anisotropy: Differences between the oceanic and continental upper mantle. *J. Geophys. Res.*, 112(B07317), 2007.
- [394] C.P. Conrad and M. Gurnis. Seismic tomography, surface uplift, and the breakup of Gondwanaland: Integrating mantle convection backwards in time. *Geochem. Geophys. Geosyst.*, 4(3), 2003.
- [395] C.P. Conrad and C. Lithgow-Bertelloni. Influence of continental roots and asthenosphere on plate-mantle coupling. *Geophys. Res. Lett.*, 33(L05312), 2006.
- [396] C.P. Conrad, B. Steinberger, and T.H. Torsvik. Stability of active mantle upwelling revealed by net characteristics of plate tectonics. *Nature*, 498:479, 2013.
- [397] Catherine M Cooper, Adrian Lenardic, and L Moresi. The thermal structure of stable continental lithosphere within a dynamic mantle. *Earth and Planetary Science Letters*, 222(3-4):807–817, 2004.
- [398] Catherine M Cooper, Adrian Lenardic, and L Moresi. Effects of continental insulation and the partitioning of heat producing elements on the earth's heat loss. *Geophysical Research Letters*, 33(13), 2006.
- [399] CM Cooper, Meghan S Miller, and Louis Moresi. The structural evolution of the deep continental lithosphere. *Tectonophysics*, 695:100–121, 2017.
- [400] CM Cooper, Eric Mittelstaedt, Claire A Currie, Jolante van Wijk, Louise H Kellogg, Lorraine Hwang, and Ramon Arrowsmith. Moving lithospheric modeling forward: Attributes of a community computer code. *GSA Today*, 25(6):42–43, 2015.
- [401] C.M. Cooper, L.-N. Moresi, and A. Lenardic. Effects of continental configuration on mantle heat loss. *Geophys. Res. Lett.*, 40:2647–2651, 2013.
- [402] G. Corti, R. Cioni, Z. Franceschini, F. Sani, Stéphane Scaillet, P. Molin, I. Isola, F. Mazzarini, S. Brune, D. Keir, A. Erbello, A. Muluneh, F. Illsley-Kemp, and A. Glerum. Aborted propagation of the ethiopian rift caused by linkage with the kenyan rift. *Nature Communications*, 10, 2019.
- [403] Giacomo Corti. Control of rift obliquity on the evolution and segmentation of the main ethiopian rift. *Nature Geoscience*, 1(4):258, 2008.
- [404] Giacomo Corti and Piero Manetti. Asymmetric rifts due to asymmetric mohos: An experimental approach. *Earth and Planetary Science Letters*, 245(1-2):315–329, 2006.
- [405] Giacomo Corti, Jolante van Wijk, Marco Bonini, Dimitrios Sokoutis, Sierd Cloetingh, Fabrizio Innocenti, and Piero Manetti. Transition from continental break-up to punctiform seafloor spreading: How fast, symmetric and magmatic. *Geophysical Research Letters*, 30(12), 2003.
- [406] N.J. Cosentino, J.P. Morgan, and T.E. Jordan. Modeling trench sediment-controlled flow in subduction channels: Implications for the topographic evolution of the central andean fore arc. *Journal of Geophysical Research: Solid Earth*, 123(10):9121–9135, 2018.
- [407] T.J. Coulthard. Landscape evolution models: a software review. *Hydrological processes*, 15:165–173, 2001.
- [408] Patience A Cowie, John R Underhill, Mark D Behn, Jian Lin, and Caroline E Gill. Spatio-temporal evolution of strain accumulation derived from multi-scale observations of late jurassic rifting in the northern north sea: A critical test of models for lithospheric extension. *Earth and Planetary Science Letters*, 234(3-4):401–419, 2005.

- [409] F. Crameri, H. Schmeling, G.J. Golabek, T. Duretz, R. Orendt, S.J.H. Buitier, D.A. May, B.J.P. Kaus, T.V. Gerya, and P.J. Tackley. A comparison of numerical surface topography calculations in geodynamic modelling: an evaluation of the 'sticky air' method. *Geophys. J. Int.*, 189:38–54, 2012.
- [410] F. Crameri and P.J. Tackley. Spontaneous development of arcuate single-sided subduction in global 3-D mantle convection models with a free surface. *J. Geophys. Res.*, 119:doi:10.1002/2014JB010939, 2014.
- [411] F. Crameri and P.J. Tackley. Subduction initiation from a stagnant lid and global overturn: new insights from numerical models with a free surface. *Progress in Earth and Planetary Science*, 3, 2016.
- [412] F. Crameri, P.J. Tackley, I. Meilick, T.V. Gerya, and B.J.P. Kaus. A free plate surface and weak oceanic crust produce single-sided subduction on earth. *Geophys. Res. Lett.*, 39, 2012.
- [413] Fabio Crameri. Sinking plates on venus. *Nature Geoscience*, 2017.
- [414] A Crave and Ph Davy. A stochastic precipiton model for simulating erosion/sedimentation dynamics. *Computers & Geosciences*, 27(7):815–827, 2001.
- [415] T. Croissant and J. Braun. Constraining the stream power law: a novel approach combining a landscape evolution model and an inversion method. *Earth Surf. Dynam.*, 2:155–166, 2014.
- [416] AJL Crook, SM Willson, JG Yu, and DRJ Owen. Predictive modelling of structure evolution in sandbox experiments. *Journal of Structural Geology*, 28(5):729–744, 2006.
- [417] Timothy A Cross and Rex H Pilger Jr. Controls of subduction geometry, location of magmatic arcs, and tectonics of arc and back-arc regions. *Geological Society of America Bulletin*, 93(6):545–562, 1982.
- [418] S Thomas Crough. Approximate solutions for the formation of the lithosphere. *Physics of the Earth and Planetary Interiors*, 14(4):365–377, 1977.
- [419] M. Crouzeix and P.-A. Raviart. Conforming and nonconforming finite element methods for solving the stationary Stokes equations I. *R.A.I.R.O.*, 7(3):33–75, 1973.
- [420] L. Cruz, J. Malinski, A. Wilson, W.A. Take, and G. Hillel. Erosional control of kinematics and geometry of fold-and-thrust belts imaged in a physical and numerical sandbox. *J. Geophys. Res.*, 115(B09404):doi:10.1029/2010JB007472, 2010.
- [421] L Cserepes and M Rabinowicz. Gravity and convection in a two-layer mantle. *Earth and Planetary Science Letters*, 76(1-2):193–207, 1985.
- [422] Peter A Cundall. Numerical experiments on localization in frictional materials. *Ingenieur-archiv*, 59(2):148–159, 1989.
- [423] C.A. Currie and C. Beaumont. Are diamond-bearing Cretaceous kimberlites related to low-angle subduction beneath western North America. *Earth Planet. Sci. Lett.*, 303:59–70, 2011.
- [424] C.A. Currie, C. Beaumont, and R.S. Huismans. The fate of subducted sediments: a case for backarc intrusion and underplating. *Geology*, 35(12):1111–1114, 2007.
- [425] C. Cuvelier, A. Segal, and A.A. van Steenhoven. *Finite Element Methods and Navier-Stokes Equations*. D. Reidel Publishing Company, 1986.
- [426] M. Dabrowski, M. Krotkiewski, and D.W. Schmid. Milamin: Matlab based finite element solver for large problems. *Geochem. Geophys. Geosyst.*, 9(4):Q04030, 2008.
- [427] J. Dannberg, Z. Eilon, U. Faul, R. Gassmöller, P. Moulik, and R. Myhill. The importance of grain size to mantle dynamics and seismological observations. *Geochem. Geophys. Geosyst.*, 18:3034–3061, 2017.
- [428] J. Dannberg and R. Gassmöller. Chemical trends in ocean islands explained by plume-slab interaction. *PNAS*, 115(17):4351–4356, 2018.
- [429] J. Dannberg and T. Heister. Compressible magma/mantle dynamics: 3-D, adaptive simulations in ASPECT. *Geophys. J. Int.*, 207:1343–1366, 2016.
- [430] J. Dannberg and S.V. Sobolev. Low-buoyancy thermochemical plumes resolve controversy of classical mantle plume concept. *Nature Communications*, 6(6960):doi:10.1038/ncomms7960, 2015.
- [431] Julianne Dannberg, Rene Gassmöller, Ryan Grove, and Timo Heister. A new formulation for coupled magma/mantle dynamics. *Geophysical Journal International*, 219(1):94–107, 2019.
- [432] O Dauteuil, O Bourgeois, and T Mauduit. Lithosphere strength controls oceanic transform zone structure: insights from analogue models. *Geophysical Journal International*, 150(3):706–714, 2002.
- [433] A. Davaille, Ph. Carrez, and P. Cordier. Fat plumes may reflect the complex rheology of the lower mantle. *Geophys. Res. Lett.*, 45, 2018.
- [434] A. Davaille, B. Guesclin, A. Massmeyer, and E. Di Giuseppe. Thermal instabilities in a yield stress fluid: Existence and morphology. *Journal of Non-Newtonian Rheology*, 193:144–153, 2013.

- [435] A Davaille, SE Smrekar, and S Tomlinson. Experimental and observational evidence for plume-induced subduction on venus. *Nature Geoscience*, 10(5):349, 2017.
- [436] Anne Davaille, Angela Limare, Floriane Touitou, Ichiro Kumagai, and Judith Vatteville. Anatomy of a laminar starting thermal plume at high prandtl number. *Experiments in Fluids*, 50(2):285–300, 2011.
- [437] D Rhodri Davies, Saskia Goes, JH Davies, BSA Schuberth, H-P Bunge, and J Ritsema. Reconciling dynamic and seismic models of earth’s lower mantle: The dominant role of thermal heterogeneity. *Earth and Planetary Science Letters*, 353:253–269, 2012.
- [438] D.R. Davies, J.H. Davies, P.C. Bollada, O. Hassan, K. Morgan, and P. Nithiarasu. A hierarchical mesh refinement technique for global 3-D spherical mantle convection modelling. *Geosci. Model Dev.*, 6:1095–1107, 2013.
- [439] DR Davies, JH Davies, O Hassan, K Morgan, and P Nithiarasu. Investigations into the applicability of adaptive finite element methods to two-dimensional infinite prandtl number thermal and thermochemical convection. *Geochemistry, Geophysics, Geosystems*, 8(5), 2007.
- [440] D.R. Davies, C.R. Wilson, and S.C. Kramer. Fluidity: A fully unstructured anisotropic adaptive mesh computational modeling framework for geodynamics. *Geochem. Geophys. Geosyst.*, 12(6), 2011.
- [441] Geoffrey F Davies. Lagging mantle convection, the geoid and mantle structure. *Earth and planetary science letters*, 69(1):187–194, 1984.
- [442] Geoffrey F Davies. Mantle convection under simulated plates: effects of heating modes and ridge and trench migration, and implications for the core-mantle boundary, bathymetry, the geoid and benioff zones. *Geophys. J. R. astr. Soc.*, 84(1):153–183, 1986.
- [443] J.H. Davies. Global map of solid Earth surface heat flow. *Geochem. Geophys. Geosyst.*, 14(10), 2013.
- [444] P. Davy and P. Cobbold. Indentation tectonics in nature and experiment. 1. central asia. *Bulletin of the Geological Institutions of Uppsala*, 14:143–162, 1988.
- [445] P. Davy and P. Cobbold. Indentation tectonics in nature and experiment. 1. experiments scaled for gravity. *Bulletin of the Geological Institutions of Uppsala*, 14:129–141, 1988.
- [446] B. Deglo de Besses, A. Magnin, and P. Jay. Sphere drag in a viscoplastic fluid. *AIChE Journal*, 50(10):2627–2629, 2004.
- [447] H. de Boorder, W. Spakman, S.H. White, and M.J.R. Wortel. Late Cenozoic mineralization, orogenic collapse and slab detachment in the European Alpine Belt. *Earth Planet. Sci. Lett.*, 164:569–575, 1998.
- [448] Arne De Coninck, Bernard De Baets, Drosos Kourounis, Fabio Verbosio, Olaf Schenk, Steven Maenhout, and Jan Fostier. Needles: Toward large-scale genomic prediction with marker-by-environment interaction. *203(1):543–555*, 2016.
- [449] R De Franco, Rob Govers, and R Wortel. Nature of the plate contact and subduction zones diversity. *Earth And Planetary Science Letters*, 271(1-4):245–253, 2008.
- [450] Roberta De Franco, Rob Govers, and Rinus Wortel. Dynamics of continental collision: influence of the plate contact. *Geophysical Journal International*, 174(3):1101–1120, 2008.
- [451] J. de Frutos, V. John, and J. Novo. Projection methods for incompressible ow problems with WENO nite difference schemes. *J. Comp. Phys.*, 309:368–386, 2016.
- [452] Albert de Montserrat, Jason P Morgan, and Jörg Hasenclever. Lacode: a lagrangian two-dimensional thermo-mechanical code for large-strain compressible visco-elastic geodynamical modeling. *Tectonophysics*, page 228173, 2019.
- [453] J De Smet, AP van den Berg, and NJ Vlaar. Early formation and long-term stability of continents resulting from decompression melting in a convecting mantle. *Tectonophysics*, 322(1-2):19–33, 2000.
- [454] Jeroen H De Smet, Arie P van Den Berg, Nico J Vlaar, and David A Yuen. A characteristics-based method for solving the transport equation and its application to the process of mantle differentiation and continental root growth. *Geophysical Journal International*, 140(3):651–659, 2000.
- [455] JH De Smet, AP van den Berg, and NJ Vlaar. Stability and growth of continental shields in mantle convection models including recurrent melt production. *Tectonophysics*, 296(1-2):15–29, 1998.
- [456] Carlos A Dengo and John M Logan. Implications of the mechanical and frictional behavior of serpentinite to seismogenic faulting. *Journal of Geophysical Research: Solid Earth*, 86(B11):10771–10782, 1981.
- [457] Alexander L Densmore, Michael A Ellis, and Robert S Anderson. Landsliding and the evolution of normal-fault-bounded mountains. *Journal of geophysical research: solid earth*, 103(B7):15203–15219, 1998.

- [458] S Dequand, JFH Willems, M Leroux, R Vullings, M van Weert, C Thieulot, and Abraham Hirschberg. Simplified models of flue instruments: Influence of mouth geometry on the sound source. *The Journal of the Acoustical Society of America*, 113(3):1724–1735, 2003.
- [459] C.S. Desai and J.F. Abel. *Introduction to the Finite Element Method: A Numerical Method for Engineering Analysis*. Van Nostrand Reinhold, 1972.
- [460] Frédéric Deschamps, Laura Cobden, and Paul J Tackley. The primitive nature of large low shear-wave velocity provinces. *Earth and Planetary Science Letters*, 349:198–208, 2012.
- [461] Frédéric Deschamps and Yang Li. Core-mantle boundary dynamic topography: influence of post-perovskite viscosity. *Journal of Geophysical Research: Solid Earth*, 2019.
- [462] Frédéric Deschamps and Paul J Tackley. Searching for models of thermo-chemical convection that explain probabilistic tomography: I. principles and influence of rheological parameters. *Physics of the Earth and Planetary Interiors*, 171(1-4):357–373, 2008.
- [463] Frédéric Deschamps and Paul J Tackley. Searching for models of thermo-chemical convection that explain probabilistic tomography. iiinfluence of physical and compositional parameters. *Physics of the Earth and Planetary Interiors*, 176(1-2):1–18, 2009.
- [464] Frédéric Deschamps, Paul J Tackley, and Takashi Nakagawa. Temperature and heat flux scalings for isoviscous thermal convection in spherical geometry. *Geophysical Journal International*, 182(1):137–154, 2010.
- [465] Frédéric Deschamps, Chloé Yao, Paul J Tackley, and C Sanchez-Valle. High rayleigh number thermal convection in volumetrically heated spherical shells. *Journal of Geophysical Research: Planets*, 117(E9), 2012.
- [466] Y. Deubelbeiss and B.J.P. Kaus. Comparison of Eulerian and Lagrangian numerical techniques for the Stokes equations in the presence of strongly varying viscosity. *Phys. Earth Planet. Interiors*, 171:92–111, 2008.
- [467] A.E. Svartman Dias, L.L. Lavier, and N.W. Hayman. Conjugate rifted margins width and asymmetry: The interplay between lithospheric strength and thermomechanical processes. *J. Geophys. Res.*, 120:8672–8700, 2015.
- [468] Alexandre Dimanov and Georg Dresen. Rheology of synthetic anorthite-diopside aggregates: Implications for ductile shear zones. *Journal of Geophysical Research: Solid Earth*, 110(B7), 2005.
- [469] C.R. Dohrmann and P.B. Bochev. A stabilized finite element method for the Stokes problem based on polynomial pressure projections. *Int. J. Num. Meth. Fluids*, 46:183–201, 2004.
- [470] Marie-Pierre Doin and Pierre Henry. Subduction initiation and continental crust recycling: the roles of rheology and eclogitization. *Tectonophysics*, 342(1-2):163–191, 2001.
- [471] Vít Dolejší. Analysis and application of the iipg method to quasilinear nonstationary convection–diffusion problems. *Journal of Computational and Applied Mathematics*, 222(2):251–273, 2008.
- [472] J. Donea, A. Huerta, J.Ph. Ponthot, and A. Rodriguez-Ferran. Arbitrary Lagrangian-Eulerian Methods. *Encyclopedia of Computational Mechanics*, 1, 2004.
- [473] Jean Donea and Antonio Huerta. *Finite Element Methods for Flow Problems*. John Wiley & Sons, 2003.
- [474] J.R. Dormand and P.J. Prince. A family of embedded runge-kutta formulae. *Journal of Computational and Applied Mathematics*, 6(1):19–26, 1980.
- [475] J.R. Dormand and P.J. Prince. A reconsideration of some embedded runge-kutta formulae. *Journal of Computational and Applied Mathematics*, 15:203–211, 1986.
- [476] Pavel V Doubrovine, Bernhard Steinberger, and Trond H Torsvik. A failure to reject: Testing the correlation between large igneous provinces and deep mantle structures with edf statistics. *Geochemistry, Geophysics, Geosystems*, 17(3):1130–1163, 2016.
- [477] M van Driel, Lion Krischer, Simon C Stähler, Kambod Hosseini, and Tarje Nissen-Meyer. Instaseis: Instant global seismograms based on a broadband waveform database. *Solid Earth*, 6(2):701–717, 2015.
- [478] Daniel Charles Drucker. A more fundamental approach to plastic stress-strain relations. In *Proc. of 1st US National Congress of Applied Mechanics, 1951*, pages 487–491, 1951.
- [479] D.C. Drucker and W. Prager. Soil mechanics and plastic analysis or limit design. *Quarterly of Applied Mathematics*, 10(2):157–165, 1952.
- [480] Martyn R Drury. Dynamic recrystallization and strain softening of olivine aggregates in the laboratory and the lithosphere. *Geological Society, London, Special Publications*, 243(1):143–158, 2005.

- [481] J.C. Duarte, W.P. Schellart, and A.R. Cruden. Three-dimensions dynamic laboratory models of subduction with an overriding plate and variable interplate rheology . *Geophys. J. Int.*, 2013.
- [482] F Dubuffet, DA Yuen, and M Rabinowicz. Effects of a realistic mantle thermal conductivity on the patterns of 3-d convection. *Earth and Planetary Science Letters*, 171(3):401–409, 1999.
- [483] D.A. Dunavant. High-degree efficient symmetrical Gaussian quadrature rules for the triangle. *Int. J. Num. Meth. Eng.*, 21:1129–1148, 1985.
- [484] J.A. Dunbar and D.S. Sawyer. Three-dimensional dynamical model of continental rift propagation and margin plateau formation. *J. Geophys. Res.*, 101(B12):27,845–27,863, 1996.
- [485] T. Duretz, Ph. Agard, Ph. Yamato, C. Ducassou, E.B. Burov, and T.V. Gerya. Thermo-mechanical modeling of the obduction process based on the Oman Ophiolite case. *Gondwana Research*, 2015.
- [486] T. Duretz and T.V. Gerya. Slab detachment during continental collision: Influence of crustal rheology and interaction with lithospheric delamination. *Tectonophysics*, 602:124–140, 2013.
- [487] T. Duretz, T.V. Gerya, B.J.P. Kaus, and T.B. Andersen. Thermomechanical modeling of slab eduction. *J. Geophys. Res.*, 117(B08411), 2012.
- [488] T. Duretz, T.V. Gerya, and D.A. May. Numerical modelling of spontaneous slab breakoff and subsequent topographic response. *Tectonophysics*, 502:244–256, 2011.
- [489] T. Duretz, T.V. Gerya, and W. Spakman. Slab detachment in laterally varying subduction zones: 3-D numerical modeling. *Geophys. Res. Lett.*, 41:1951–1956, 2014.
- [490] T. Duretz, D.A. May, T.V. Gerya, and P.J. Tackley. Discretization errors and free surface stabilisation in the finite difference and marker-in-cell method for applied geodynamics: A numerical study. *Geochem. Geophys. Geosyst.*, 12(Q07004), 2011.
- [491] T. Duretz, S.M. Schmalholz, and T.V. Gerya. Dynamics of slab detachment. *Geochem. Geophys. Geosyst.*, 13(3):doi:10.1029/2011GC004024, 2012.
- [492] T. Duretz, S.M. Schmalholz, and Y.Y. Podladchikov. Physics-controlled thickness of shear zones caused by viscous heating: Implications for crustal shear localization. *Geophys. Res. Lett.*, page doi: 10.1002/2014GL060438, 2014.
- [493] T. Duretz, A. Souche, R. de Borst, and L. Le Pourhiet. The Benefits of Using a Consistent Tangent Operator for Viscoelastoplastic Computations in Geodynamics. *Geochem. Geophys. Geosyst.*, 19, 2018.
- [494] Thibault Duretz, Riccardo Asti, Yves Lagabrielle, Jean-Pierre Brun, Anthony Jourdon, Camille Clerc, and Benjamin Corre. Numerical modelling of cretaceous pyrenean rifting: The interaction between mantle exhumation and syn-rift salt tectonics. *Basin Research*, 2019.
- [495] Thibault Duretz, Dave A May, and Philippe Yamato. A free surface capturing discretization for the staggered grid finite difference scheme. *Geophysical Journal International*, 204(3):1518–1530, 2016.
- [496] Jack Dvorkin, Amos Nur, Gary Mavko, and Zvi Ben-Avraham. Narrow subducting slabs and the origin of backarc basins. *Tectonophysics*, 227(1-4):63–79, 1993.
- [497] S. Dyksterhuis, P. Rey, R.D. Mueller, and L. Moresi. Effects of initial weakness on rift architecture. *Geological Society, London, Special Publications*, 282:443–455, 2007.
- [498] D Dymkova and T Gerya. Porous fluid flow enables oceanic subduction initiation on earth. *Geophysical Research Letters*, 40(21):5671–5676, 2013.
- [499] A.M. Dziewonski and D.L. Anderson. Preliminary reference Earth model. *Phys. Earth. Planet. Inter.*, 25:297–356, 1981.
- [500] J Ebbing, J Bouman, M Fuchs, S Gradmann, and R Haagmans. Sensitivity of goce gravity gradients to crustal thickness and density variations: Case study for the northeast atlantic region. In *Gravity, Geoid and Height Systems*, pages 291–298. Springer, 2014.
- [501] Jörg Ebbing, Johannes Bouman, Martin Fuchs, Verena Lieb, Roger Haagmans, JAC Meekes, and Rader Abdul Fattah. Advancements in satellite gravity gradient data for crustal studies. *The Leading Edge*, 32(8):900–906, 2013.
- [502] C. Ebinger and J. van Wijk. Roadmap to continental rupture: Is obliquity the route to success? *Geology*, 42(3):271–272, 2014.
- [503] SS Egan. The flexural isostatic response of the lithosphere to extensional tectonics. *Tectonophysics*, 202(2-4):291–308, 1992.
- [504] David L. Egholm. A new strategy for discrete element numerical models: 1. Theory. *J. Geophys. Res.*, 112:B05203, doi:10.1029/2006JB004557, 2007.

- [505] David L. Egholm, Mike Sandiford, Ole R. Clausen, and Søren B. Nielsen. A new strategy for discrete element numerical models: 2. Sandbox applications. *J. Geophys. Res.*, 112:B05204, doi:10.1029/2006JB004558, 2007.
- [506] R. Eid. Higher order isoparametric finite element solution of Stokes flow . *Applied Mathematics and Computation*, 162:1083–1101, 2005.
- [507] V. Eijkhout. *Introduction to High Performance Scientific Computing*. Creative Commons, 2013.
- [508] Y. Elesin, T. Gerya, I.M. Artemieva, and H. Thybo. Samovar: a thermomechanical code for modeling of geodynamic processes in the lithosphere – application to basin evolution. *Arabian Journal of Geosciences*, 3:477–497, 2010.
- [509] S. Ellis, P. Fullsack, and C. Beaumont. Oblique convergence of the crust driven by basal forcing: implications for length-scales of deformation and strain partitioning in orogens. *Geophys. J. Int.*, 120:24–44, 1995.
- [510] S.M. Ellis, T.A. Little, L.M. Wallace, B.R. Hacker, and S.J.H. Buiter. Feedback between rifting and diapirism can exhume ultrahigh-pressure rocks. *Earth Planet. Sci. Lett.*, 311:427–438, 2011.
- [511] Susan Ellis, Francesca Ghisetti, Philip M Barnes, Carolyn Boulton, Åke Fagereng, and Susanne Buiter. The contemporary force balance in a wide accretionary wedge: numerical models of the southcentral hikurangi margin of new zealand. *Geophysical Journal International*, 219(2):776–795, 2019.
- [512] Susan Ellis, Guido Schreurs, and Marion Panien. Comparisons between analogue and numerical models of thrust wedge development. *Journal of Structural Geology*, 26(9):1659–1675, 2004.
- [513] H. Elman, D. Silvester, and A. Wathen. *Finite Elements and Fast Iterative Solvers*. Oxford Science Publications, 2014.
- [514] M.S. Engelman and R.L. Sani. The implementation of normal and/or tangential boundary conditions in finite element codes for incompressible fluid flow. *Int. J. Num. Meth. Fluids*, 2:225–238, 1982.
- [515] P. England. Some numerical investigations of large scale continental deformation. In *Mountain Building Processes*, pages 129–189. Academic Press, 1982.
- [516] P. England and G. Houseman. A dynamical model of lithosphere extension and sedimentary basin formation. *J. Geophys. Res.*, 91(B3):3664–3676, 1986.
- [517] Philip England and Peter Molnar. Active deformation of asia: From kinematics to dynamics. *Science*, 278(5338):647–650, 1997.
- [518] A. Enns, T.W. Becker, and H. Schmeling. The dynamics of subduction and trench migration for viscosity stratification. *Geophys. J. Int.*, 160:761–775, 2005.
- [519] Z. Erdos, R.S. huismans, and P. van der Beek. First-order control of syntectonic sedimentation on crustal-scale structure of mountain belts . *J. Geophys. Res.*, 120:doi:10.1002/2014JB011785, 2015.
- [520] Z. Erdos, R.S. Huismans, and P. van der Beek. Control of increased sedimentation on orogenic fold-and-thrust belt structure - insights into the evolution of the Western Alps. *Solid Earth*, 10:391–404, 2019.
- [521] Z. Erdos, R.S. huismans, P. van der Beek, and C. Thieulot. Extensional inheritance and surface processes as controlling factors of mountain belt structure. *J. Geophys. Res.*, 119:doi:10.1002/2014JB011408, 2014.
- [522] E. Erтурk. Discussions on Driven Cavity Flow. *Int. J. Num. Meth. Fluids*, 60:275–294, 2009.
- [523] J. Escartin, G. Hirth, and B. Evans. Effects of serpentization on the lithospheric strength and the style of normal faulting at slow-spreading ridges . *Earth Planet. Sci. Lett.*, 151:181–189, 1997.
- [524] J. Escartin, G. Hirth, and B. Evans. Nondilatant brittle deformation of serpentinites: Implications for Mohr-Coulomb theory and the strength of faults. *J. Geophys. Res.*, 102(B2):2897–2913, 1997.
- [525] Pep Espanol and Cedric Thieulot. Microscopic derivation of hydrodynamic equations for phase-separating fluid mixtures. *The Journal of chemical physics*, 118(20):9109–9127, 2003.
- [526] Nicolas Espurt, Francesca Funiciello, Joseph Martinod, Benjamin Guillaume, Vincent Regard, Claudio Faccenna, and Stéphane Brusset. Flat subduction dynamics and deformation of the south american plate: Insights from analog modeling. *Tectonics*, 27(3), 2008.
- [527] Brian Evans and Christopher Goetze. The temperature variation of hardness of olivine and its implication for polycrystalline yield stress. *Journal of Geophysical Research: Solid Earth*, 84(B10):5505–5524, 1979.
- [528] D.A.D. Evans. True polar wander and supercontinents. *Tectonophysics*, 362:303–320, 2003.
- [529] M. Faccenda. Mid mantle seismic anisotropy around subduction zones. *Phys. Earth. Planet. Inter.*, 227:1–19, 2014.

- [530] M. Faccenda and F.A. Capitanio. Seismic anisotropy around subduction zones: Insights from three-dimensional modeling of upper mantle deformation and SKS splitting calculations . *Geochem. Geophys. Geosyst.*, 14(1):doi:10.1029/2012GC004451, 2013.
- [531] M. Faccenda, T.V. Gerya, and S. Chakraborty. Styles of post-subduction collisional orogeny: Influence of convergence velocity, crustal rheology and radiogenic heat production. *Lithos*, 103:257–287, 2008.
- [532] M. Faccenda, T.V. Gerya, N.S. Mancktelow, and L. Moresi. Fluid flow during slab unbending and dehydration: Implications for intermediate-depth seismicity, slab weakening and deep water recycling. *Geochem. Geophys. Geosyst.*, 13(1):doi:10.1029/2011GC003860, 2012.
- [533] M Faccenda, G Minelli, and TV Gerya. Coupled and decoupled regimes of continental collision: numerical modeling. *Earth and Planetary Science Letters*, 278(3-4):337–349, 2009.
- [534] Manuele Faccenda and Luca Dal Zilio. The role of solid–solid phase transitions in mantle convection. *Lithos*, 268:198–224, 2017.
- [535] Manuele Faccenda, Taras V Gerya, and Luigi Burlini. Deep slab hydration induced by bending-related variations in tectonic pressure. *Nature Geoscience*, 2(11):790, 2009.
- [536] C. Faccenna, O. Bellier, J. Martinod, C. Piromallo, and V. Regard. Slab detachment beneath eastern Anatolia: A possible cause for the formation of the North Anatolian fault. *Earth Planet. Sci. Lett.*, 242:85–97, 2006.
- [537] Claudio Faccenna, Thorsten W Becker, Ludwig Auer, Andrea Billi, Lapo Boschi, Jean Pierre Brun, Fabio A Capitanio, Francesca Funiciello, Ferenc Horváth, Laurent Jolivet, Claudia Piromallo, Leigh Royden, Federico Rossetti, and Enrico Serpelloni. Mantle dynamics in the mediterranean. *Reviews of Geophysics*, 52(3):283–332, 2014.
- [538] Claudio Faccenna, Thorsten W Becker, Clinton P Conrad, and Laurent Husson. Mountain building and mantle dynamics. *Tectonics*, 32(1):80–93, 2013.
- [539] Claudio Faccenna, Domenico Giardini, Philippe Davy, and Alessio Argentieri. Initiation of subduction at atlantic-type margins: Insights from laboratory experiments. *Journal of Geophysical Research: Solid Earth*, 104(B2):2749–2766, 1999.
- [540] K Fadaie and Giorgio Ranalli. Rheology of the lithosphere in the east african rift system. *Geophysical Journal International*, 102(2):445–453, 1990.
- [541] Robert JM Farla, Shun-ichiro Karato, and Zhengyu Cai. Role of orthopyroxene in rheological weakening of the lithosphere via dynamic recrystallization. *Proceedings of the National Academy of Sciences*, 110(41):16355–16360, 2013.
- [542] Cinzia G Farnetani, Bernard Legras, and Paul J Tackley. Mixing and deformations in mantle plumes. *Earth and Planetary Science Letters*, 196(1-2):1–15, 2002.
- [543] R.J. Farrington, L.-N. Moresi, and F.A. Capitanio. The role of viscoelasticity in subducting plates. *Geochem. Geophys. Geosyst.*, 15:4291–4304, 2014.
- [544] R.J. Farrington, D.R. Stegman, L.N. Moresi, M. Sandiford, and D.A. May. Interactions of 3D mantle flow and continental lithosphere near passive margins. *Tectonophysics*, 483:20–28, 2010.
- [545] U.H. Faul, J.D. Fitz Gerald, R. J.M. Farlai, R. Ahlefeldt, and I. Jackson. Dislocation creep of finegrained olivine. *J. Geophys. Res.*, 116(B01203,:doi:10.1029/2009JB007174, 2011.
- [546] Ulrich H Faul and Ian Jackson. Diffusion creep of dry, melt-free olivine. *Journal of Geophysical Research: Solid Earth*, 112(B4), 2007.
- [547] N.P. Fay, R.A. Bennett, J.C. Spinler, and E.D. Humphreys. Small-scale upper mantle convection and crustal dynamics in southern California. *Geochem. Geophys. Geosyst.*, 9(8), 2008.
- [548] E. Fehlberg. Some old and new Runge-Kutta formulas with stepsize control and their error coefficients. *Computing*, 34:265–270, 1985.
- [549] N. Fehn, W.A. Wall, and M. Kronbichler. On the stability of projection methods for the incompressible NavierStokes equations based on high-order discontinuous Galerkin discretizations. *J. Comp. Phys.*, 351:392–421, 2017.
- [550] N. Fernandez and B. Kaus. Influence of pre-existing salt diapirs on 3D folding patterns . *Tectonophysics*, 637:354–369, 2014.
- [551] N. Fernandez and B. Kaus. Fold interaction and wavelength selection in 3D models of multilayer detachment folding. *Tectonophysics*, 632:199–217, 2014.
- [552] N. Fernandez and B. Kaus. Pattern formation in 3-D numerical models of down-built diapirs initiated by a RayleighTaylor instability. *Geophy. J. Int.*, 202:1253–1270, 2015.

- [553] Javier Fernández-Lozano, Dimitrios Sokoutis, Ernst Willingshofer, Endre Dombrádi, Alfonso M Martín, Gerardo De Vicente, and Sierd Cloetingh. Integrated gravity and topography analysis in analog models: Intraplate deformation in iberia. *Tectonics*, 31(6), 2012.
- [554] Sonia Fernández-Méndez, Javier Bonet, and Antonio Huerta. Continuous blending of sph with finite elements. *Computers & structures*, 83(17-18):1448–1458, 2005.
- [555] O. Ferrer, M.P.A. Jackson, E. Roca, and M. Rubinat. Evolution of salt structures during extension and inversion of the Offshore Parentis Basin (Eastern Bay of Biscay) . *Salt Tectonics, Sediments and Prospectivity. Geological Society, London, Special Publications*, 363:361–379, 2012.
- [556] C. Fillon, R.S. Huismans, and P. van der Beek. Syntectonic sedimentation effects on the growth of fold-and-thrust belts . *Geology*, 41(1):83–86, 2013.
- [557] C. Fillon, R.S. Huismans, P. van der Beek, and J.A. Mu noz. Syntectonic sedimentation controls on the evolution of the southern Pyrenean fold-and-thrust belt: Inferences from coupled tectonic-surface processes models. *J. Geophys. Res.*, 118:5665–5680, 2013.
- [558] KD Fischer, T Jahr, and G Jentzsch. Evolution of the variscan foreland-basin: modelling the interactions between tectonics and surface processes. *Physics and Chemistry of the Earth, Parts A/B/C*, 29(10):665–671, 2004.
- [559] Mark P Fischer, Michael R Gross, Terry Engelder, and Roy J Greenfield. Finite-element analysis of the stress distribution around a pressurized crack in a layered elastic medium: implications for the spacing of fluid-driven joints in bedded sedimentary rock. *Tectonophysics*, 247(1-4):49–64, 1995.
- [560] R. Fischer and T. Gerya. Early Earth plume-lid tectonics: A high-resolution 3D numerical modelling approach. *Journal of Geodynamics*, 100:198–214, 2016.
- [561] N. Flament, M. Gurnis, S. Williams, M. Seton, J. Skogseid, C. Heine, and D. Müller. Topographic asymmetry of the South Atlantic from global models of mantle flow and lithospheric stretching. *Earth Planet. Sci. Lett.*, 387:107–119, 2014.
- [562] Nicolas Flament, Michael Gurnis, and R Dietmar Müller. A review of observations and models of dynamic topography. *Lithosphere*, 5(2):189–210, 2013.
- [563] Luce Fleitout and David A Yuen. Secondary convection and the growth of the oceanic lithosphere. *Physics of the earth and planetary interiors*, 36(3-4):181–212, 1984.
- [564] Raymond C Fletcher. Three-dimensional folding of an embedded viscous layer in pure shear. *Journal of Structural Geology*, 13(1):87–96, 1991.
- [565] Raymond C Fletcher. Three-dimensional folding and necking of a power-law layer: are folds cylindrical, and, if so, do we understand why? *Tectonophysics*, 247(1-4):65–83, 1995.
- [566] B.J. Foley and T.W. Becker. Generation of plate-like behavior and mantle heterogeneity from a spherical, viscoplastic convection model. *Geochem. Geophys. Geosyst.*, 10(8):doi:10.1029/2009GC002378, 2009.
- [567] Donald Forsyth and Seiya Uyeda. On the relative importance of the driving forces of plate motion. *Geophysical Journal International*, 43(1):163–200, 1975.
- [568] A.M. Forte and W.R. Peltier. Viscous flow models of global geophysical observables. 1. forward problems. *J. Geophys. Res.*, 96:20,131–20,159, 1991.
- [569] A. Fortin, M. Jardak, J.J. Gervais, and R. Pierre. Old and new results on the two-dimensional poiseuille flow. *J. Comp. Phys.*, 115(2):455–469, 1994.
- [570] M. Fortin. Old and new finite elements for incompressible flows. *Int. J. Num. Meth. Fluids*, 1:347–364, 1981.
- [571] M. fortin and S. Boivin. Iterative stabilisation of the bilinear velocity-constant pressure element. *Int. J. Num. Meth. Fluids*, 10:125–140, 1990.
- [572] M. Fortin and A. Fortin. Experiments with several elements for viscous incompressible flows. *Int. J. Num. Meth. Fluids*, 5:911–928, 1985.
- [573] Michel Fortin and F Thomasset. Mixed finite-element methods for incompressible flow problems. *Journal of Computational Physics*, 31(1):113–145, 1979.
- [574] Haakon Fossen and Atle Rotevatn. Fault linkage and relay structures in extensional settingsa review. *Earth-Science Reviews*, 154:14–28, 2016.
- [575] Haakon Fossen, Richard A Schultz, Egil Rundhovde, Atle Rotevatn, and Simon J Buckley. Fault linkage and graben stepovers in the canyonlands (utah) and the north sea viking graben, with implications for hydrocarbon migration and accumulation. *AAPG bulletin*, 94(5):597–613, 2010.

- [576] GR Foulger. Plumes, or plate tectonic processes? *Astronomy & Geophysics*, 43(6):6–19, 2002.
- [577] L. Fourel, S. Goes, and G. Morra. The role of elasticity in slab bending. *Geochem. Geophys. Geosyst.*, 15:4507–4525, 2014.
- [578] Marc Fournier, Laurent Jolivet, Philippe Davy, and Jean-Charles Thomas. Backarc extension and collision: an experimental approach to the tectonics of asia. *Geophysical Journal International*, 157(2):871–889, 2004.
- [579] L.P. Franca and S.P. Oliveira. Pressure bubbles stabilization features in the Stokes problem. *Computer Methods in Applied Mechanics and Engineering*, 192:1929–1937, 2003.
- [580] L.P. Franca, S.P. Oliveira, and M. Sarkis. Continuous q1q1 stokes elements stabilised with non-conforming null edge average velocity functions. *Mathematical Models and Methods in Applied Sciences*, 17:439–459, 2007.
- [581] R. De Franco, R. Govers, and R. Wortel. Numerical comparison of different convergent plate contacts: subduction channel and subduction fault. *Geophys. J. Int.*, pages 10.1111/j.1365–246X.2006.03498.x, 2006.
- [582] T. Francois, E. Burov, P. Agard, and B. Meyer. Buildup of a dynamically supported orogenic plateau: Numerical modeling of the Zagros/Central Iran case study. *Geochem. Geophys. Geosyst.*, 15:doi:10.1002/2013GC005223, 2014.
- [583] Thomas François, Evgueni Burov, Bertrand Meyer, and Philippe Agard. Surface topography as key constraint on thermo-rheological structure of stable cratons. *Tectonophysics*, 602:106–123, 2013.
- [584] DA Frank-Kamenetskii. *Diffusion and heat transfer in chemical kinetics*. New York: Plenum Press, 1969.
- [585] Raymond CMW Franssen. The rheology of synthetic rocksalt in uniaxial compression. *Tectonophysics*, 233(1-2):1–40, 1994.
- [586] M. Fraters, C. Thieulot, A. van den Berg, and W. Spakman. The geodynamic world builder: a solution for complex initial conditions in numerical modelling. *Solid Earth*, 2019.
- [587] M.R.T. Fraters, W. Bangerth, C. Thieulot, A.C. Glerum, and W. Spakman. Efficient and Practical Newton Solvers for Nonlinear Stokes Systems in Geodynamic Problems. *Geophys. J. Int.*, 2019.
- [588] S. Frederiksen and J. Braun. Numerical modelling of strain localisation during extension of the continental lithosphere. *Earth Planet. Sci. Lett.*, 188:241–251, 2001.
- [589] Susanne Frederiksen, Søren Bom Nielsen, and Niels Balling. A numerical dynamic model for the norwegian–danish basin. *Tectonophysics*, 343(3-4):165–183, 2001.
- [590] Susanne Frederiksen, Søren Bom Nielsen, and Niels Balling. Post-permian evolution of the central north sea: a numerical model. *Tectonophysics*, 343(3-4):185–203, 2001.
- [591] R. Freeburn, P. Bouilhol, B. Maunder, V. Magni, and J. van Hunen. Numerical models of the magmatic processes induced by slab breakoff. *Earth Planet. Sci. Lett.*, 478:203–213, 2017.
- [592] J. Freeman, L. Moresi, and D.A. May. Evolution into the stagnant lid convection regime with a non-newtonian water ice rheology. *Geophys. Res. Lett.*, 31, 2004.
- [593] J Freeman, L Moresi, and DA May. Thermal convection with a water ice i rheology: Implications for icy satellite evolution. *Icarus*, 180(1):251–264, 2006.
- [594] M. Frehner. 3D fold growth rates. *Terra Nova*, 26:417–424, 2014.
- [595] Marcel Frehner. The neutral lines in buckle folds. *Journal of Structural Geology*, 33(10):1501–1508, 2011.
- [596] Marcel Frehner and Ulrike Exner. Strain and foliation refraction patterns around buckle folds. *Geological Society, London, Special Publications*, 394(1):21–37, 2014.
- [597] Marcel Frehner, Ulrike Exner, Neil S Mancktelow, and Djordje Grujic. The not-so-simple effects of boundary conditions on models of simple shear. *Geology*, 39(8):719–722, 2011.
- [598] Marcel Frehner, Anna Hui Mee Ling, and Isabelle Gärtner-Roer. Furrow-and-ridge morphology on rock-glaciers explained by gravity-driven buckle folding: A case study from the murtèl rockglacier (switzerland). *Permafrost and Periglacial Processes*, 26(1):57–66, 2015.
- [599] Marcel Frehner and Stefan M Schmalholz. Numerical simulations of parasitic folding in multilayers. *Journal of Structural Geology*, 28(9):1647–1657, 2006.
- [600] Marcel Frehner and Timothy Schmid. Parasitic folds with wrong vergence: How pre-existing geometrical asymmetries can be inherited during multilayer buckle folding. *Journal of Structural Geology*, 87:19–29, 2016.
- [601] P.J. Frey and P.-L. George. *Mesh generation*. Hermes Science, 2000.
- [602] EH Fritzell, AL Bull, and GE Shephard. Closure of the mongol–okhotsk ocean: Insights from seismic tomography and numerical modelling. *Earth and Planetary Science Letters*, 445:1–12, 2016.

- [603] C. Froidevaux. Energy dissipation and geometric structure at spreading plate boundaries. *Earth Planet. Sci. Lett.*, 20:419–424, 1973.
- [604] L. Fuchs and Th.W. Becker. Role of strain-dependent weakening memory on the style of mantle convection and plate boundary stability. *Geophys. J. Int.*, 218:601–618, 2019.
- [605] L. Fuchs, H. Koyi, and H. Schmeling. Numerical modeling of the effect of composite rheology on internal deformation in down-built diapirs. *Tectonophysics*, 646:79–95, 2015.
- [606] L. Fuchs and H. Schmeling. A new numerical method to calculate inhomogeneous and time-dependent large deformation of two-dimensional geodynamic flows with application to diapirism. *Geophys. J. Int.*, 194(2):623–639, 2013.
- [607] Hiromi Fujimoto and Yoshibumi Tomoda. Lithospheric thickness anomaly near the trench and possible driving force of subduction. *Tectonophysics*, 112(1-4):103–110, 1985.
- [608] Y. Fukao, S. Widjiantoro, and M. Obayashi. Stagnant slabs in the upper and lower mantle transition region. *Reviews of Geophysics*, 39:291–323, 2001.
- [609] Yoshio Fukao and Masayuki Obayashi. Subducted slabs stagnant above, penetrating through, and trapped below the 660 km discontinuity. *Journal of Geophysical Research: Solid Earth*, 118(11):5920–5938, 2013.
- [610] T. Fukuchi. Numerical calculation of fully-developed laminar flows in arbitrary cross-sections using finite difference method. *AIP Advances*, 1:042109, 2011.
- [611] J. Fullea, J.C. Afonso, J.A.D. Connolly, M. Fernandez, D. Garcia-Castellanos, and H. Zeyen. LitMod3D: An interactive 3-D software to model the thermal, compositional, density, seismological, and rheological structure of the lithosphere and sublithospheric upper mantle. *Geochem. Geophys. Geosyst.*, 10(8):doi:10.1029/2009GC002391, 2009.
- [612] J. Fullea, M. Fernandez, J.C. Afonso, J. Verges, and H. Zeyen. iThe structure and evolution of the lithosphereasthenosphere boundary beneath the AtlanticMediterranean Transition Region. *Lithos*, 2010.
- [613] Ch.W. Fuller, S.D. Willett, and M.T. Brandon. Formation of forearc basins and their influence on subduction zone earthquakes. *Geology*, 34(2):65–68, 2006.
- [614] P. Fullsack. An arbitrary Lagrangian-Eulerian formulation for creeping flows and its application in tectonic models. *Geophys. J. Int.*, 120:1–23, 1995.
- [615] F Funiciello, C Faccenna, Arnauld Heuret, Serge Lallemand, Erika Di Giuseppe, and TW Becker. Trench migration, net rotation and slab–mantle coupling. *Earth and Planetary Science Letters*, 271(1-4):233–240, 2008.
- [616] F. Funiciello, K. Regenauer-Lieb G. Morra, and D. Giardini. Dynamics of retreating slabs: 1. Insights from two-dimensional numerical experiments. *J. Geophys. Res.*, 108(B4):2206, 2003.
- [617] F. Funiciello, M. Moroni, C. Piromallo, C. Faccenna, A. Cenedese, and H.A. Bui. Mapping mantle flow during retreating subduction: Laboratory models analyzed by feature tracking. *J. Geophys. Res.*, 111(B03402), 2006.
- [618] KP Furlong and Rob Govers. Ephemeral crustal thickening at a triple junction: The Mendocino crustal conveyor. *GEOLOGY*, 27(2):127, 1999.
- [619] Mikito Furuchi. Numerical modeling of three dimensional self-gravitating stokes flow problem with free surface. *Procedia Computer Science*, 4:1506–1515, 2011.
- [620] M. Furuichi, M. Kameyama, and A. Kageyama. Three-dimensional Eulerian method for large deformation of viscoelastic fluid: Toward plate-mantle simulation. *J. Comp. Phys.*, 227:4977–4997, 2008.
- [621] M. Furuichi and D. Nishiura. Robust coupled fluid-particle simulation scheme in Stokes-flow regime: Toward the geodynamic simulation including granular media. *Geochem. Geophys. Geosyst.*, 15:2865–2882, 2014.
- [622] Mikito Furuichi, Dave A May, and Paul J Tackley. Development of a stokes flow solver robust to large viscosity jumps using a schur complement approach with mixed precision arithmetic. *Journal of Computational Physics*, 230(24):8835–8851, 2011.
- [623] Sébastien Gac, Ritske S Huismans, Nina SC Simon, Jan Inge Faleide, and Yuri Y Podladchikov. Effects of lithosphere buckling on subsidence and hydrocarbon maturation: a case-study from the ultra-deep east barents sea basin. *Earth and Planetary Science Letters*, 407:123–133, 2014.
- [624] Sashikumaar Ganesan, Gunar Matthies, and Lutz Tobiska. Local projection stabilization of equal order interpolation applied to the stokes problem. *Mathematics of Computation*, 77(264):2039–2060, 2008.

- [625] J. Ganne, M. Gerbault, and S. Block. Thermo-mechanical modeling of lower crust exhumation – Constraints from the metamorphic record of the Palaeoproterozoic Eburnean orogeny, West African Craton. *Precambrian Research*, 243:88–109, 2014.
- [626] D Garcia-Castellanos, M Fernàndez, and M Torne. Numerical modeling of foreland basin formation: a program relating thrusting, flexure, sediment geometry and lithosphere rheology. *Computers & Geosciences*, 23(9):993–1003, 1997.
- [627] Daniel Garcia-Castellanos. Interplay between lithospheric flexure and river transport in foreland basins. *Basin Research*, 14(2):89–104, 2002.
- [628] F. Garel, S. Goes, D.R. Davies, J.H. Davies, S.C. Kramer, and C.R. Wilson. Interaction of subducted slabs with the mantle transition-zone: A regime diagram from 2-D thermo-mechanical models with a mobile trench and an overriding plate. *Geochem. Geophys. Geosyst.*, 15(1739–1765):doi:10.1002/2014GC005257, 2014.
- [629] E.J. Garnero and A.K. McNamara. Structure and Dynamics of Earths Lower Mantle. *Science*, 320:626–628, 2008.
- [630] D.K. Gartling. Nachos - a finite element computer program for incompressible flow problems. Technical Report Sand77-1333, Sandia Laboratories, 1978.
- [631] E. Garzanti, G. Radeff, and M.G. Malus. Slab breakoff: A critical appraisal of a geological theory as applied in space and time. *Earth-Science Reviews*, 177:303–319, 2018.
- [632] R. Gassmöller, J. Dannberg, E. Bredow, B. Steinberger, and T. H. Torsvik. Major influence of plume-ridge interaction, lithosphere thickness variations, and global mantle flow on hotspot volcanism-the example of tristan. *Geochem. Geophys. Geosyst.*, 17(4):1454–1479, 2016.
- [633] R. Gassmöller, H. Lokavarapu, E. M. Heien, E. G. Puckett, and W. Bangerth. Flexible and scalable particle-in-cell methods with adaptive mesh refinement for geodynamic computations. *Geochem. Geophys. Geosyst.*, 19(9):3596–3604, 2018.
- [634] Rene Gassmöller, Harsha Lokavarapu, Wolfgang Bangerth, and Gerry Puckett. Evaluating the accuracy of hybrid finite element/particle-in-cell methods for modelling incompressible stokes flow. *Geophy. J. Int.*, 2019.
- [635] T. Geenen, M. ur Rehman, S.P. MacLahlan, G. Segal, C. Vuik, A.P. van den Berg, and W. Spakman. Scalable robust solvers for unstructured FE geodynamic modeling applications: Solving the Stokes equation for models with large localized viscosity contrasts. *Geochem. Geophys. Geosyst.*, 10(9), 2009.
- [636] L. Gemmer, C. Beaumont, and S. Ings. Dynamic modelling of passive margin salt tectonics: effects of water loading, sediment properties and sedimentation patterns. *Basin Research*, 17:383–402, 2005.
- [637] L. Gemmer, S.J. Ings, S. Medvedev, and C. Beaumont. Salt tectonics driven by differential sediment loading: stability analysis and finite-element experiments. *Basin Research*, 16:199–218, 2004.
- [638] L. Geoffroy, E.B. Burov, and P. Werner. Volcanic passive margins: another way to break up continents. *Scientific Reports*, 5:DOI:10.1038/srep14828, 2015.
- [639] O A George, R Malservisi, Rob Govers, C B Connor, and L J Connor. Is uplift of volcano clusters in the Tohoku Volcanic Arc, Japan, driven by magma accumulation in hot zones? A geodynamic modeling study. *Journal Of Geophysical Research*, 121:4780–4796, 2016.
- [640] P.-L. George and H. Borouchaki. *Delaunay Triangulation and Meshing*. Hermes, 1998.
- [641] E.H. Georgoulis. Discontinuous Galerkin Methods for Linear Problems: An Introduction. In E.H. Georgoulis, A. Iske, and J. Levesley, editors, *Approximation algorithms for Complex Systems*. Springer-Verlag, Berlin Heidelberg, 2011.
- [642] M. Gérault, T.W. Becker, B.J.P. Kaus, C. Faccenna, L. Moresi, and L. Husson. The role of slabs and oceanic plate geometry in the net rotation of the lithosphere, trench motions, and slab return flow. *Geochem. Geophys. Geosyst.*, 13(4):Q04001, doi:10.1029/2011GC003934, 2012.
- [643] M. Gérault, L. Husson, M.S. Miller, and E.D. Humphreys. Flat-slab subduction, topography, and mantle dynamics in southwestern Mexico. *Tectonics*, 34:10.1002/2015TC003908, 2015.
- [644] M. Gerbault. Pressure conditions for shear and tensile failure around a circular magma chamber; insight from elasto-plastic modelling. *Geological Society, London, Special Publications*, 367:111–130, 2012.
- [645] M. Gerbault, F. Cappa, and R. Hassani. Elasto-plastic and hydromechanical models of failure around an infinitely long magma chamber. *Geochem. Geophys. Geosyst.*, 13(3):doi:10.1029/2011GC003917, 2012.
- [646] M. Gerbault, F. Davey, and S. Henrys. Three-dimensional lateral crustal thickening in continental oblique collision: an example from the Southern Alps, New Zealand. *Geophy. J. Int.*, 150:770–779, 2002.

- [647] M. Gerbault, R. Hassani, C. Novoa Lizama, and A. Souche. Three-Dimensional Failure Patterns Around an Inflating Magmatic Chamber. *Geochem. Geophys. Geosyst.*, 19:749–771, 2018.
- [648] M. Gerbault, S. Henrys, and F. Davey. Numerical models of lithospheric deformation forming the Southern Alps of New Zealand. *J. Geophys. Res.*, 108(B7), 2003.
- [649] M. Gerbault, A.N.B. Poliakov, and M. Daignieres. Prediction of faulting from the theories of elasticity and plasticity: what are the limits? *Journal of Structural Geology*, 20:301–320, 1998.
- [650] M. Gerbault and W. Willingshofer. Lower crust indentation or horizontal ductile flow during continental collision? *Tectonophysics*, 387:169–187, 2004.
- [651] Muriel Gerbault, José Cembrano, C Mpodozis, M Farias, and M Pardo. Continental margin deformation along the andean subduction zone: Thermo-mechanical models. *Physics of the Earth and Planetary Interiors*, 177(3-4):180–205, 2009.
- [652] T. Gerya. Dynamical instability produces transform faults at mid-ocean ridges. *Science*, 329:1047–1050, 2010.
- [653] T. Gerya. Future directions in subduction modeling. *Journal of Geodynamics*, 52:344–378, 2011.
- [654] T. Gerya and B. Stöckhert. Two-dimensional numerical modeling of tectonic and metamorphic histories at active continental margins. *Int J Earth Sci (Geol Rundsch)*, 95:250–274, 2006.
- [655] T. Gerya and D.A. Yuen. Robust characteristics method for modelling multiphase visco-elasto-plastic thermo-mechanical problems. *Phys. Earth. Planet. Inter.*, 163:83–105, 2007.
- [656] Taras Gerya. *Numerical Geodynamic Modelling*. Cambridge University Press, 2010.
- [657] Taras Gerya. Precambrian geodynamics: concepts and models. *Gondwana Research*, 25(2):442–463, 2014.
- [658] Taras Gerya. Geodynamics of the early earth: Quest for the missing paradigm. *Geology*, 47(10):1006–1007, 2019.
- [659] Taras Gerya. *Numerical Geodynamic Modelling - 2nd edition*. Cambridge University Press, 2019.
- [660] Taras V Gerya. Three-dimensional thermomechanical modeling of oceanic spreading initiation and evolution. *Physics of the Earth and Planetary Interiors*, 214:35–52, 2013.
- [661] Taras V Gerya, Ronald Uken, Juergen Reinhardt, Michael K Watkeys, Walter V Maresch, and Brendan M Clarke. "cold" diapirs triggered by intrusion of the bushveld complex: Insight from two-dimensional numerical modeling. *Special Papres – Geological Society of America*, pages 117–128, 2004.
- [662] TV Gerya. Initiation of transform faults at rifted continental margins: 3d petrological-thermomechanical modeling and comparison to the woodlark basin. *Petrology*, 21(6):550–560, 2013.
- [663] TV Gerya. Plume-induced crustal convection: 3d thermomechanical model and implications for the origin of novae and coronae on venus. *Earth and Planetary Science Letters*, 391:183–192, 2014.
- [664] T.V. Gerya and J.-P. Burg. Intrusion of ultramafic magmatic bodies into the continental crust: Numerical simulation. *Phys. Earth. Planet. Inter.*, 160:124–142, 2007.
- [665] T.V. Gerya, J.A.D. Connolly, and D.A. Yuen. Why is terrestrial subduction one-sided ? *Geology*, 36(1):43–46, 2008.
- [666] T.V. Gerya, J.A.D. Connolly, D.A. Yuen, W. Gorczyk, and A.M. Capel. Seismic implications of mantle wedge plumes. *Phys. Earth. Planet. Inter.*, 156:59–74, 2006.
- [667] T.V. Gerya, D. Fossati, C. Cantieni, and D. Seward. Dynamic effects of aseismic ridge subduction: numerical modelling. *Eur. J. Mineral*, 21:649–661, 2009.
- [668] T.V. Gerya, D.A. May, and T. Duretz. An adaptive staggered grid finite difference method for modeling geodynamic Stokes flows with strongly variable viscosity. *Geochem. Geophys. Geosyst.*, 14(4), 2013.
- [669] T.V. Gerya and F.I. Meilick. Geodynamic regimes of subduction under an active margin: effects of rheological weakening by fluids and melts. *Journal of Metamorphic Geology*, 29:7–31, 2011.
- [670] TV Gerya, LL Perchuk, and J-P Burg. Transient hot channels: perpetrating and regurgitating ultrahigh-pressure, high-temperature crust–mantle associations in collision belts. *Lithos*, 103(1-2):236–256, 2008.
- [671] T.V. Gerya, L.L. Perchuk, W.V. Maresch, and A.P. Willner. Inherent gravitational instability of hot continental crust: Implications for doming and diapirism in granulite facies terrains. *Geological Society of America*, 380:97–115, 2004.
- [672] T.V. Gerya, R.J. Stern, M.Baes, S.V. Sobolev, and S.A. Whattam. Plate tectonics on the Earth triggered by plume-induced subduction initiation. *Nature*, 527, 2015.

- [673] T.V. Gerya, R. Uken, J. Reinhardt, M. Watkeys, W.V. Maresch, and B.M. Clarke. Cold fingers in a hot magma: Numerical modeling of country-rock diapirs in the Bushveld Complex, South Africa. *Geology*, 31(9):753–756, 2003.
- [674] T.V. Gerya and D.A. Yuen. Characteristics-based marker-in-cell method with conservative finite-differences schemes for modeling geological flows with strongly variable transport properties. *Phys. Earth. Planet. Inter.*, 140:293–318, 2003.
- [675] T.V. Gerya and D.A. Yuen. Rayleigh-Taylor instabilities from hydration and melting propel 'cold plumes' at subduction zones. *Earth Planet. Sci. Lett.*, 212:47–62, 2003.
- [676] T.V. Gerya, D.A. Yuen, and W.V. Maresch. Thermomechanical modelling of slab detachment. *Earth Planet. Sci. Lett.*, 226:101–116, 2004.
- [677] T.V. Gerya, D.A. Yuen, and E.O.D. Sevre. Dynamical causes for incipient magma chambers above slabs. *Geology*, 32(1):89–92, 2004.
- [678] Klaus Gessner, Chris Wijns, and Louis Moresi. Significance of strain localization in the lower crust for structural evolution and thermal history of metamorphic core complexes. *Tectonics*, 26(2), 2007.
- [679] R.K. Ghazian and S.J.H. Buiter. A numerical investigation of continental collision styles. *GJI*, 2013.
- [680] R.K. Ghazian and S.J.H. Buiter. Numerical modelling of the role of salt in continental collision: An application to the southeast Zagros fold-and-thrust belt. *Tectonophysics*, 632:96–110, 2014.
- [681] Siavash Ghelichkhan and Hans-Peter Bunge. The compressible adjoint equations in geodynamics: derivation and numerical assessment. *GEM-International Journal on Geomathematics*, 7(1):1–30, 2016.
- [682] U. Ghia, K.N. Ghia, and C.T. Shin. High-Re Solutions for incompressible flow using the Navier-Stokes equations and a multigrid method. *J. Comp. Phys.*, 48:387–411, 1982.
- [683] A Ghosh, TW Becker, and ED Humphreys. Dynamics of the north american continent. *Geophysical Journal International*, 194(2):651–669, 2013.
- [684] A Ghosh, WE Holt, and L Wen. Predicting the lithospheric stress field and plate motions by joint modeling of lithosphere and mantle dynamics. *Journal of Geophysical Research: Solid Earth*, 118(1):346–368, 2013.
- [685] A Ghosh, WE Holt, L Wen, AJ Haines, and LM Flesch. Joint modeling of lithosphere and mantle dynamics elucidating lithosphere-mantle coupling. *Geophysical Research Letters*, 35(16), 2008.
- [686] Attreyee Ghosh and William E Holt. Plate motions and stresses from global dynamic models. *Science*, 335(6070):838–843, 2012.
- [687] Attreyee Ghosh, William E Holt, and Lucy M Flesch. Contribution of gravitational potential energy differences to the global stress field. *Geophysical Journal International*, 179(2):787–812, 2009.
- [688] G. Gibert, M. Gerbault, R. Hassani, and E. Tric. Dependency of slab geometry on absolute velocities and conditions for cyclicity: insights from numerical modelling. *Geophys. J. Int.*, 189:747–760, 2012.
- [689] JA Gil and Maria José Jurado. Geological interpretation and numerical modelling of salt movement in the barbastro-balaguer anticline, southern pyrenees. *Tectonophysics*, 293(3-4):141–155, 1998.
- [690] Cedric Gillmann and Paul Tackley. Atmosphere/mantle coupling and feedbacks on venus. *Journal of Geophysical Research: Planets*, 119(6):1189–1217, 2014.
- [691] Daniele Giordano, James K Russell, and Donald B Dingwell. Viscosity of magmatic liquids: a model. *Earth and Planetary Science Letters*, 271(1-4):123–134, 2008.
- [692] Carlo Giunchi, Roberto Sabadini, Enzo Boschi, and Paolo Gasperini. Dynamic models of subduction: geophysical and geological evidence in the tyrrhenian sea. *Geophysical Journal International*, 126(2):555–578, 1996.
- [693] E. Di Giuseppe, J. van Hunen, F. Funiciello, C. Faccenna, and D. Giardini. Slab stiffness control of trench motion: Insights from numerical models. *Geochem. Geophys. Geosyst.*, 9(2), 2008.
- [694] G.A. Glatzmaier. Numerical simulations of mantle convection: Time-dependent, three-dimensional, compressible, spherical shell. *Geophys. Astrophys. Fluid Dyn.*, 43:223–264, 1988.
- [695] G.C. Gleason and J. Tullis. A flow law for dislocation creep of quartz aggregates determined with the molten salt cell. *Tectonophysics*, 247:1–23, 1995.
- [696] John W Glen. The creep of polycrystalline ice. *Proceedings of the Royal Society of London. Series A. Mathematical and Physical Sciences*, 228(1175):519–538, 1955.
- [697] A. Glerum, C. Thieulot, M. Fraters, C. Blom, and W. Spakman. Nonlinear viscoplasticity in ASPECT: benchmarking and applications to subduction. *Solid Earth*, 9(2):267–294, 2018.

- [698] R. Glowinski. *Handbook of Numerical Analysis, vol IX: Numerical methods for fluids*. North-Holland, 2003.
- [699] Vincent Godard, R Cattin, and J Lavé. Numerical modeling of mountain building: Interplay between erosion law and crustal rheology. *Geophysical Research Letters*, 31(23), 2004.
- [700] S Goes, JJP Loohuis, MJR Wortel, and Rob Govers. The effect of plate stresses and shallow mantle temperatures on tectonics of northwestern Europe. *Global and Planetary Change*, 27(1-4):23–38, 2000.
- [701] C. Goetze and B. Evans. Stress and temperature in the bending lithosphere as constrained by experimental rock mechanics. *GJI*, 59(3):463–478, 1979.
- [702] Oguz H. Gogus. Rifting and subsidence following lithospheric removal in continental back arcs. *Geology*, page doi:10.1130/G36305.1, 2014.
- [703] Oğuz H Göğüş and Russell N Pysklywec. Mantle lithosphere delamination driving plateau uplift and synconvergent extension in eastern anatolia. *Geology*, 36(9):723–726, 2008.
- [704] Oğuz H Göğüş and Kosuke Ueda. Peeling back the lithosphere: Controlling parameters, surface expressions and the future directions in delamination modeling. *Journal of Geodynamics*, 117:21–40, 2018.
- [705] GJ Golabek, TV Gerya, BJP Kaus, R Ziethe, and PJ Tackley. Rheological controls on the terrestrial core formation mechanism. *Geochemistry, Geophysics, Geosystems*, 10(11), 2009.
- [706] Gregor J Golabek, Bernard Bourdon, and Taras V Gerya. Numerical models of the thermomechanical evolution of planetesimals: Application to the acapulcoite-lodranite parent body. *Meteoritics & Planetary Science*, 49(6):1083–1099, 2014.
- [707] Gregor J Golabek, Tobias Keller, Taras V Gerya, Guizhi Zhu, Paul J Tackley, and James AD Connolly. Origin of the martian dichotomy and tharsis from a giant impact causing massive magmatism. *Icarus*, 215(1):346–357, 2011.
- [708] Gregor J Golabek, Harro Schmeling, and Paul J Tackley. Earth’s core formation aided by flow channelling instabilities induced by iron diapirs. *Earth and Planetary Science Letters*, 271(1-4):24–33, 2008.
- [709] DL Goldsby and DL Kohlstedt. Superplastic deformation of ice: Experimental observations. *Journal of Geophysical Research: Solid Earth*, 106(B6):11017–11030, 2001.
- [710] G.H. Golub and C.F. van Loan. *Matrix Computations, 4th edition*. John Hopkins University Press, 2013.
- [711] W. Gorczyk, T.V. Gerya, J.A.D. Connolly, and D.A. Yuen. Growth and mixing dynamics of mantle wedge plumes. *Geology*, 35(7):587–590, 2007.
- [712] W. Gorczyk, T.V. Gerya, J.A.D. Connolly, D.A. Yuen, and M. Rudolph. Large-scale rigid-body rotation in the mantle wedge and its implications for seismic tomography . *Geochem. Geophys. Geosyst.*, 7(5):10.1029/2005GC001075, 2006.
- [713] W. Gorczyk, H. Smithies, F. Korhonen, H. Howard, and R. Quentin De Gromard. Ultra-hot Mesoproterozoic evolution of intracontinental central Australia. *Geoscience Frontiers*, 6(1):23–37, 2014.
- [714] Weronika Gorczyk, Stéphane Guillot, Taras V Gerya, and Kéiko Hattori. Asthenospheric upwelling, oceanic slab retreat, and exhumation of uhp mantle rocks: Insights from greater antilles. *Geophysical Research Letters*, 34(21), 2007.
- [715] Weronika Gorczyk, Bruce Hobbs, and Taras Gerya. Initiation of rayleigh–taylor instabilities in intra-cratonic settings. *Tectonophysics*, 514:146–155, 2012.
- [716] Weronika Gorczyk, Arne P Willner, Taras V Gerya, James AD Connolly, and Jean-Pierre Burg. Physical controls of magmatic productivity at pacific-type convergent margins: Numerical modelling. *Physics of the Earth and Planetary Interiors*, 163(1-4):209–232, 2007.
- [717] H Gossman. Slope modelling with changing boundary conditions-effects of climate and lithology. *Z. Geomoph. NF*, 25:72–88, 1976.
- [718] R. Goteti, C. Beaumont, and S.J. Ings. Factors controlling early stage salt tectonics at rifted continental margins and their thermal consequences. *J. Geophys. Res.*, 117:1–31, 2013.
- [719] Klaus-D Gottschaldt, Uwe Walzer, Dave R Stegman, John R Baumgardner, and Hans B Mühlhaus. Mantle dynamics—a case study. In *Advances in Geocomputing*, pages 139–181. Springer, 2009.
- [720] S. Gourvenec. Bearing capacity under combined loading. In *9th Australia New Zealand Conference on Geomechanics, Auckland, New Zealand, 8-11 february 2004.*, 2004.
- [721] S. Gourvenec and M. Randolph. Effect of strength non-homogeneity on the shape of failure envelopes for combined loading of strip and circular foundations on clay. *Géotechnique*, 53:575–586, 2003.

- [722] S. Gourvenec, M. Randolph, and O. Kingsnorth. Undrained bearing capacity of square and rectangular footings. *International Journal of Geomechanics*, 6:147–157, 2006.
- [723] R. Govers and M.J.R. Wortel. Initiation of asymmetric extension in continental lithosphere. *Tectonophysics*, 223(1-2):75–96, 1993.
- [724] R. Govers and M.J.R. Wortel. Extension of stable continental lithosphere and the initiation of lithospheric scale faults. *Tectonics*, 14(4):1041–1055, 1995.
- [725] R. Govers and M.J.R. Wortel. Some remarks on the relation between vertical motions of the lithosphere during extension and the necking depth parameter inferred from kinematic modeling studies. *J. Geophys. Res.*, 104:23,245–23,253, 1999.
- [726] R. Govers and M.J.R. Wortel. Lithosphere tearing at STEP faults: Response to edges of subduction zones. *Earth Planet. Sci. Lett.*, 236:505–523, 2005.
- [727] Rob Govers, K P Furlong, L van de Wiel, M W Herman, and T Broerse. The Geodetic Signature of the Earthquake Cycle at Subduction Zones: Model Constraints on the Deep Processes. *Reviews Of Geophysics*, 85(7):457–44, 2018.
- [728] Rob Govers and PT Meijer. On the dynamics of the Juan de Fuca plate. *Earth And Planetary Science Letters*, 189(3-4):115–131, 2001.
- [729] Shea Goyette, Masa Takatsuka, Stuart Clark, R Dietmar Müller, Patrice Rey, and Dave R Stegman. Increasing the usability and accessibility of geodynamic modelling tools to the geoscience community: Underworldgui. *Visual Geosciences*, 13(1):25–36, 2008.
- [730] S. Gradmann and C. Beaumont. Coupled fluid flow and sediment deformation in margin-scale salt-tectonic systems: 2. Layered sediment models and application to the northwestern Gulf of Mexico. *Tectonics*, 31(TC4011), 2012.
- [731] S. Gradmann, C. Beaumont, and M. Albertz. Factors controlling the evolution of the Perdido Fold Belt, northwestern Gulf of Mexico, determined from numerical models. *Tectonics*, 28(TC2002), 2009.
- [732] Bernhard Grasemann and Neil S Mancktelow. Two-dimensional thermal modelling of normal faulting: the simplon fault zone, central alps, switzerland. *Tectonophysics*, 225(3):155–165, 1993.
- [733] Bernhard Grasemann and Stefan M Schmalholz. Lateral fold growth and fold linkage. *Geology*, 40(11):1039–1042, 2012.
- [734] Fabien Graveleau, J-E Hurtrez, Stéphane Dominguez, and Jacques Malavieille. A new experimental material for modeling relief dynamics and interactions between tectonics and surface processes. *Tectonophysics*, 513(1-4):68–87, 2011.
- [735] Fabien Graveleau, Jacques Malavieille, and Stéphane Dominguez. Experimental modelling of orogenic wedges: A review. *Tectonophysics*, 538:1–66, 2012.
- [736] R. Gray and R.N. Pysklywec. Geodynamic models of Archean continental collision and the formation of mantle lithosphere keels. *Geophys. Res. Lett.*, 37(L19301), 2010.
- [737] R. Gray and R.N. Pysklywec. Geodynamic models of mature continental collision: Evolution of an orogen from lithospheric subduction to continental retreat/delamination. *J. Geophys. Res.*, 117(B03408), 2012.
- [738] R. Gray and R.N. Pysklywec. Influence of sediment deposition on deep lithospheric tectonics. *Geophys. Res. Lett.*, 39(L11312), 2012.
- [739] R. Gray and R.N. Pysklywec. Influence of viscosity pressure dependence on deep lithospheric tectonics during continental collision. *J. Geophys. Res.*, 118, 2013.
- [740] P.M. Gresho, S.T. Chan, M.A. Christon, and A.C. Hindmarsch. A little more on stabilised $Q_1 Q_1$ for transient viscous incompressible flow. *Int. J. Num. Meth. Fluids*, 21:837–856, 1995.
- [741] P.M. Gresho and R.L. Lee. Don't suppress the wiggles - They're telling you something! *Computers and Fluids*, 9:223–253, 1981.
- [742] P.M. Gresho, R.L. Lee, R.L. Sani, M.K. Maslanik, and B.E. Eaton. The consistent Galerkin FEM for computing derived boundary quantities in thermal and/or fluid problems. *Int. J. Num. Meth. Fluids*, 7:371–394, 1987.
- [743] P.M. Gresho and R.L. Sani. *Incompressible flow and the Finite Element Method, vol II*. John Wiley and Sons, Ltd, 2000.
- [744] Ralf Greve. Application of a polythermal three-dimensional ice sheet model to the greenland ice sheet: response to steady-state and transient climate scenarios. *Journal of Climate*, 10(5):901–918, 1997.
- [745] Ralf Greve and Heinz Blatter. *Dynamics of ice sheets and glaciers*. Springer Science & Business Media, 2009.

- [746] M. Griebel, T. Dornseifer, and T. Neunhoeffer. *Numerical simulation in Fluid Dynamics*. SIAM, 1997.
- [747] D. Griffiths and D. Silvester. Unstable modes of the q1-p0 element. Technical Report 257, University of Manchester/UMIST, 1994.
- [748] Cécile Grigné, Stéphane Labrosse, and Paul J Tackley. Convective heat transfer as a function of wavelength: Implications for the cooling of the earth. *Journal of Geophysical Research: Solid Earth*, 110(B3), 2005.
- [749] Cécile Grigné, Stéphane Labrosse, and PJ Tackley. Convection under a lid of finite conductivity: Heat flux scaling and application to continents. *Journal of Geophysical Research: Solid Earth*, 112(B8), 2007.
- [750] Cécile Grigné, Stéphane Labrosse, and PJ Tackley. Convection under a lid of finite conductivity in wide aspect ratio models: Effect of continents on the wavelength of mantle flow. *Journal of Geophysical Research: Solid Earth*, 112(B8), 2007.
- [751] S.G. Grigull, S.M. Ellis, T.A. Little, M.P. Hill, and S.J.H. Buiter. Rheological constraints on quartz derived from scaling relationships and numerical models of sheared brittle-ductile quartz veins, central Southern alps, New Zealand. *Journal of Structural Geology*, 37:200–222, 2012.
- [752] L. Gross, L. Bourgouin, A. Hale, and H.-B. Mühlhaus. Interface modeling in incompressible media using level sets in Escript. *Phys. Earth. Planet. Inter.*, 163:23–34, 2007.
- [753] J.-L. Guermond, R. Pasquetti, and Bojan Popov. Entropy viscosity method for nonlinear conservation laws. *J. Comp. Phys.*, page doi:10.1016/j.jcp.2010.11.043, 2011.
- [754] JM Guerrero, Julian P Lowman, and Paul J Tackley. Spurious transitions in convective regime due to viscosity clipping: ramifications for modeling planetary secular cooling. *Geochemistry, Geophysics, Geosystems*, 20(7):3450–3468, 2019.
- [755] F. Gueydan, C. Morency, and J.-P. Brun. Continental rifting as a function of lithosphere mantle strength. *Tectonophysics*, 460:83–93, 2008.
- [756] Frédéric Gueydan, Jacques Précigout, and Laurent GJ Montesi. Strain weakening enables continental plate tectonics. *Tectonophysics*, 631:189–196, 2014.
- [757] L. Guillou-Frottier, E. Burov, S. Cloetingh, E. Le Goff, Y. Deschamps, B. Huet, and V. Bouchot. Plume-induced dynamic instabilities near cratonic blocks: Implications for PTt paths and metallogeny. *Global and Planetary Change*, 90-91:37–50, 2012.
- [758] A.J.P. Gürlicher, S.J. Beaussier, and T.V. Gerya. On the formation of oceanic detachment faults and their influence on intra-oceanic subduction initiation: 3D thermomechanical modeling. *Earth Planet. Sci. Lett.*, 506:195–208, 2019.
- [759] M. Gunzburger. *Finite Element Methods for Viscous Incompressible Flows: A Guide to Theory, Practice and Algorithms*. Academic, Boston, 1989.
- [760] Anshul Gupta, George Karypis, and Vipin Kumar. Highly scalable parallel algorithms for sparse matrix factorization. *IEEE Transactions on Parallel and Distributed Systems*, 8(5):502–520, May 1997.
- [761] Anshul Gupta, Seid Koric, and Thomas George. Sparse matrix factorization on massively parallel computers. In *SC09 (International Conference for High Performance Computing, Networking, Storage and Analysis)*, 2009.
- [762] M. Gurnis, C. Hall, and L. Lavie. Evolving force balance during incipient subduction. *Geochem. Geophys. Geosyst.*, 5(7), 2004.
- [763] M. Gurnis, J.X. Mitrovica, J. Ritsema, and H.-J. van Heijst. Constraining mantle density structure using geological evidence of surface uplift rates: The case of the African superplume. *Geochem. Geophys. Geosyst.*, 1, 2000.
- [764] Michael Gurnis. Rapid continental subsidence following the initiation and evolution of subduction. *Science*, 255(5051):1556–1558, 1992.
- [765] Michael Gurnis and Geoffrey F Davies. Numerical study of high rayleigh number convection in a medium with depth-dependent viscosity. *Geophysical Journal International*, 85(3):523–541, 1986.
- [766] Michael Gurnis, Christophe Eloy, and Shijie Zhong. Free-surface formulation of mantle convectionii. implication for subduction-zone observables. *Geophysical Journal International*, 127(3):719–727, 1996.
- [767] Michael Gurnis, Louis Moresi, and R Dietmar Müller. Models of mantle convection incorporating plate tectonics: The australian region since the cretaceous. 2000.
- [768] Michael Gurnis, R Dietmar Müller, and Louis Moresi. Cretaceous vertical motion of australia and the australianantarctic discordance. *Science*, 279(5356):1499–1504, 1998.

- [769] Michael Gurnis, Mark Turner, Sabin Zahirovic, Lydia DiCaprio, Sonja Spasojevic, R Dietmar Müller, James Boyden, Maria Seton, Vlad Constantin Manea, and Dan J Bower. Plate tectonic reconstructions with continuously closing plates. *Computers & Geosciences*, 38(1):35–42, 2012.
- [770] M-A Gutscher, F Klingelhoefer, T Theunissen, W Spakman, Théo Berthet, TK Wang, and C-S Lee. Thermal modeling of the sw ryukyu forearc (taiwan): Implications for the seismogenic zone and the age of the subducting philippine sea plate (huatung basin). *Tectonophysics*, 692:131–142, 2016.
- [771] B.R. Hacker. Simulation of the metamorphic and deformational history of the metamorphic sole of the Oman ophiolite. *J. Geophys. Res.*, 95(B4):4895–4907, 1990.
- [772] B.R. Hacker. The role of deformation in the formation of metamorphic gradients: ridge subduction beneath the Oman ophiolite. *Tectonics*, 10(2):455–473, 1991.
- [773] B.R. Hackley and T.V. Gerya. Paradigms, new and old for ultrahigh-pressure tectonism. *Tectonophysics*, 603:79–88, 2013.
- [774] W. Hafner. Stress distributions and faulting. *Bulletin of the Geological Society of America*, 62:373–398, 1951.
- [775] B.H. Hager and R.J. O'Connell. Subduction zone dip angles and flow driven by plate motion. *Tectonophysics*, 50:111–133, 1978.
- [776] B.H. Hager and R.J. O'Connell. A simple global model of plate dynamics and mantle convection. *J. Geophys. Res.*, 86(B6):4843–4867, 1981.
- [777] Bradford H Hager. Subducted slabs and the geoid: Constraints on mantle rheology and flow. *Journal of Geophysical Research: Solid Earth*, 89(B7):6003–6015, 1984.
- [778] E. Hairer, S.P. Nørsett, and G. Wanner. *Solving Ordinary Differential Equations I*. Springer, 1993.
- [779] E. Hairer and G. Wanner. *Solving Ordinary Differential Equations II. Stiff and Differential-Algebraic Problems*. Springer-Verlag, Berlin, 1991.
- [780] A.J. Hale, L. Bourgouin, and H.B. Muehlhaus. Using the level set method to model endogenous lava dome growth . *J. Geophys. Res.*, 112(B03213), 2007.
- [781] A.J. Hale, K.-D. Gottschaldt, G. Rosenbaum, L. Bourgouin, M. Bauchy, and Hans Mühlhaus. Dynamics of slab tear faults: Insights from numerical modelling. *Tectonophysics*, 483:58–70, 2010.
- [782] C.E. Hall, M. Gurnis, M. Sdrolias, L.L. Lavie, and R.D. Mueller. Catastrophic initiation of subduction following forced convergence across fracture zones. *Earth Planet. Sci. Lett.*, 212:15–30, 2003.
- [783] Chad E Hall and Michael Gurnis. Strength of fracture zones from their bathymetric and gravitational evolution. *Journal of Geophysical Research: Solid Earth*, 110(B1), 2005.
- [784] Chad E Hall and EM Parmentier. Influence of grain size evolution on convective instability. *Geochemistry, Geophysics, Geosystems*, 4(3), 2003.
- [785] Paul S Hall and Chris Kincaid. Diapiric flow at subduction zones: A recipe for rapid transport. *Science*, 292(5526):2472–2475, 2001.
- [786] Lijie Han and Michael Gurnis. How valid are dynamic models of subduction and convection when plate motions are prescribed? *Physics of the Earth and Planetary Interiors*, 110(3-4):235–246, 1999.
- [787] J. Handin. On the Coulomb-Mohr failure criterion. *J. Geophys. Res.*, 74(22):5343, 1969.
- [788] D.L. Hansen. A meshless formulation for geodynamic modeling. *J. Geophys. Res.*, 108:doi:10.1029/2003JB002460, 2003.
- [789] D.L. Hansen and S.B. Nielsen. Does thermal weakening explain basin inversion? Stochastic modelling of the thermal structure beneath sedimentary basins. *Earth Planet. Sci. Lett.*, 198:113–127, 2002.
- [790] D.L. Hansen and S.B. Nielsen. Why rifts invert in compression. *Tectonophysics*, 373:5–24, 2003.
- [791] D.L. Hansen, S.B. Nielsen, and H. Lykke-Andersen. The post-Triassic evolution of the SorgenfreiTornquist Zone - results from thermo-mechanical modelling. *Tectonophysics*, 328:245–267, 2000.
- [792] U Hansen and A Ebel. Experiments with a numerical model related to mantle convection: boundary layer behaviour of small-and large scale flows. *Physics of the earth and planetary interiors*, 36(3-4):374–390, 1984.
- [793] U Hansen and DA Yuen. Extended-boussinesq thermal-chemical convection with moving heat sources and variable viscosity. *Earth and Planetary Science Letters*, 176(3-4):401–411, 2000.
- [794] Ulrich Hansen and Adolf Ebel. Time-dependent thermal convection-a possible explanation for a multiscale flow in the earth's mantle. *Geophysical Journal International*, 94(2):181–191, 1988.

- [795] Ulrich Hansen and David A Yuen. Potential role played by viscous heating in thermal-chemical convection in the outer core. *Geochimica et cosmochimica acta*, 60(7):1113–1123, 1996.
- [796] Ulrich Hansen, David A Yuen, and Sherri E Kroening. Effects of depth-dependent thermal expansivity on mantle circulations and lateral thermal anomalies. *Geophysical Research Letters*, 18(7):1261–1264, 1991.
- [797] H. Harder and U.R. Christensen. A one-plume model of martian mantle convection. *Nature*, 380:507–509, 1996.
- [798] F.H. Harlow and J.E. Welch. Numerical calculation of time-dependent viscous incompressible flow of fluid with free surface. *The physics of fluids*, 8(12):2182, 1965.
- [799] JF Harper. Mantle flow due to internal vertical forces. *Physics of the Earth and Planetary Interiors*, 36(3-4):285–290, 1984.
- [800] E.H. Hartz and Y.Y. Podlachikov. Toasting the jelly sandwich: The effect of shear heating on lithospheric geotherms and strength . *Geology*, 36(4):331–334, 2008.
- [801] R. Hassan, N. Flament, M. Gurnis, D.J. Bower, and D. Müller. Provenance of plumes in global convection models. *Geochem. Geophys. Geosyst.*, 16:1465–1489, 2015.
- [802] R. Hassani and J Chéry. Anelasticity explains topography associated with basin and range normal faulting. *Geology*, 24(12):1095–1098, 1996.
- [803] R. Hassani, D. Jongmans, and Jean Chéry. Study of plate deformation and stress in subduction processes using two-dimensional numerical models. *J. Geophys. Res.*, 102(B8):17,951–17,96, 1997.
- [804] Denis Hatzfeld and Peter Molnar. Comparisons of the kinematics and deep structures of the zagros and himalaya and of the iranian and tibetan plateaus and geodynamic implications. *Reviews of Geophysics*, 48(2), 2010.
- [805] G.P. Hayes, D.J. Wald, and R.L. Johnson. Slab1.0: A threedimensional model of global subduction zone geometries. *J. Geophys. Res.*, 117(B01302), 2012.
- [806] K.L. Haynie and M.A. Jadamec. Tectonic drivers of the Wrangell block: Insights on fore-arc sliver processes from 3-D geodynamic models of Alaska. *Tectonics*, 36, 2017.
- [807] Y. He, E.G. Puckett, and M.I. Billen. A discontinuous Galerkin method with a bound preserving limiter for the advection of non-diffusive fields in solid Earth geodynamics. *Phys. Earth. Planet. Inter.*, 263:23–37, 2017.
- [808] C. Heine and S. Brune. Oblique rifting of the Equatorial Atlantic: Why there is no Saharan Atlantic Ocean. *Geology*, 42(3):211–214, 2014.
- [809] T. Heister, J. Dannberg, R. Gassmöller, and W. Bangerth. High Accuracy Mantle Convection Simulation through Modern Numerical Methods. II: Realistic Models and Problems. *Geophy. J. Int.*, 210(2):833–851, 2017.
- [810] Heinrich Hencky. Zur theorie plastischer deformationen und der hierdurch im material hervorgerufenen nachspannungen. *ZAMM-Journal of Applied Mathematics and Mechanics/Zeitschrift für Angewandte Mathematik und Mechanik*, 4(4):323–334, 1924.
- [811] Matthew W Herman, Kevin P Furlong, and Rob Govers. The Accumulation of Slip Deficit in Subduction Zones in the Absence of Mechanical Coupling: Implications for the Behavior of Megathrust Earthquakes. *Journal Of Geophysical Research*, 123(9):8260–8278, 2018.
- [812] John W Hernlund, David J Stevenson, and Paul J Tackley. Buoyant melting instabilities beneath extending lithosphere: 2. linear analysis. *Journal of Geophysical Research: Solid Earth*, 113(B4), 2008.
- [813] John W Hernlund and Paul J Tackley. Some dynamical consequences of partial melting in earths deep mantle. *Physics of the Earth and Planetary Interiors*, 162(1-2):149–163, 2007.
- [814] John W Hernlund and Paul J Tackley. Modeling mantle convection in the spherical annulus. *Physics of the Earth and Planetary Interiors*, 171(1-4):48–54, 2008.
- [815] John W Hernlund, Paul J Tackley, and David J Stevenson. Buoyant melting instabilities beneath extending lithosphere: 1. numerical models. *Journal of Geophysical Research: Solid Earth*, 113(B4), 2008.
- [816] John W Hernlund, Christine Thomas, and Paul J Tackley. A doubling of the post-perovskite phase boundary and structure of the earth’s lowermost mantle. *Nature*, 434(7035):882, 2005.
- [817] John William Hernlund and Irene Bonati. Modeling ultralow velocity zones as a thin chemically distinct dense layer at the core-mantle boundary. *Journal of Geophysical Research: Solid Earth*, 2019.
- [818] Philip J Heron and Julian P Lowman. The impact of rayleigh number on assessing the significance of supercontinent insulation. *Journal of Geophysical Research: Solid Earth*, 119(1):711–733, 2014.

- [819] P.J. Heron, R.N. Pysklywec, and R. Stephenson. Intraplate orogenesis within accreted and scarred lithosphere: Example of the Eurekan Orogeny, Ellesmere Island. *Tectonophysics*, 2015.
- [820] P.J. Heron, R.N. Pysklywec, R. Stephenson, and J. van Hunen. Deformation driven by deep and distant structures: Influence of a mantle lithosphere suture in the ouachita orogeny, southeastern united states. *Geology*, 2018.
- [821] H.J. Herrmann, A.N.B. Poliakov, and F. Tzschichholz. Examples of fractals in rock mechanics. *Size-Scale Effects in the Failure Mechanisms of Materials and Structures*, page 58, 1996.
- [822] G. Hetényi, V. Godard, R. Cattin, and J.A.D. Connolly. Incorporating metamorphism in geodynamic models: the mass conservation problem. *Geophys. J. Int.*, 186:6–10, 2011.
- [823] J.M. Hewitt, D.P. McKenzie, and N.O. Weiss. Dissipative heating in convective flows. *J. Fluid Mech.*, 68(4):721–738, 1975.
- [824] B.H. Heyn, C.P. Conrad, and R.G. Tronnes. Stabilizing Effect of Compositional Viscosity Contrasts on Thermochemical Piles. *Geophys. Res. Lett.*, 45:7523–7532, 2018.
- [825] Christoph F Hieronymus. Control on seafloor spreading geometries by stress-and strain-induced lithospheric weakening. *Earth and Planetary Science Letters*, 222(1):177–189, 2004.
- [826] N. Hilairat, B. Reynard, Y. Wang, I. Daniel, S. Merkel, N. Nishiyama, and S. Petitgirard. High-Pressure creep of Serpentinite, interseismic deformation, and initiation of subduction. *Science*, 318:1910–1913, 2007.
- [827] B. Hillebrand, C. Thieulot, T. Geenen, A. P. van den Berg, and W. Spakman. Using the level set method in geodynamical modeling of multi-material flows and earth’s free surface. *Solid Earth*, 5(2):1087–1098, 2014.
- [828] J.M. Hines and M.I. Billen. Sensitivity of the short- to intermediate-wavelength geoid to rheologic structure in subduction zones. *J. Geophys. Res.*, 117(B05410), 2012.
- [829] C.W. Hirt, A. Amsden, and J.L. Cook. An Arbitrary Lagrangian-Eulerian computing method for all flow speeds. *J. Comp. Phys.*, 14:227–253, 1974.
- [830] C.W. Hirt and B.D. Nichols. Volume of Fluid (VOF) Method for the dynamics of Free Boundaries. *J. Comp. Phys.*, 39:201–225, 1981.
- [831] G. Hirth and D. L. Kohlstedt. Water in the oceanic upper mantle: Implications for rheology, melt extraction and the evolution of the lithosphere. *Earth Planet. Sci. Lett.*, 144:93–108, 1996.
- [832] G. Hirth and D.L. Kohlstedt. Rheology of the upper mantle and the mantle wedge: A view from the experimentalists. *in Inside the Subduction Factory*, ed. J. Eiler, *Geophysical Monograph American Geophysical Union, Washington, D.C.*, 138:83–105, 2003.
- [833] Greg Hirth. Laboratory constraints on the rheology of the upper mantle. *Reviews in Mineralogy and Geochemistry*, 51(1):97–120, 2002.
- [834] N. Ho, S.D. Olson, and H.F. Walker. Accelerating the Uzawa algorithm. *SIAM J. Sci. Comput.*, 39(5):S461–S476, 2017.
- [835] AJ Hogg and GP Matson. Slumps of viscoplastic fluids on slopes. *Journal of Non-Newtonian Fluid Mechanics*, 158(1-3):101–112, 2009.
- [836] T. Höink and A. Lenardic. Three-dimensional mantle convection simulations with a low-viscosity asthenosphere and the relationship between heat flow and the horizontal length scale of convection. *Geophys. Res. Lett.*, 35(L10304), 2008.
- [837] T. Höink, A. Lenardic, and A.M. Jellinek. Earth’s thermal evolution with multiple convection modes: A Monte-Carlo approach. *Phys. Earth. Planet. Inter.*, 221:22–26, 2013.
- [838] S Honda. Local rayleigh and nusselt numbers for cartesian convection with temperature-dependent viscosity. *Geophysical research letters*, 23(18):2445–2448, 1996.
- [839] S Honda. A possible role of weak zone at plate margin on secular mantle cooling. *Geophysical research letters*, 24(22):2861–2864, 1997.
- [840] S. Honda. Strength of slab inferred from the seismic tomography and geologic history around the Japanese Islands. *Geochem. Geophys. Geosyst.*, 15:1333–1347, 2014.
- [841] Satoru Honda, Taras Gerya, and Guizhi Zhu. A simple three-dimensional model of thermo-chemical convection in the mantle wedge. *Earth and Planetary Science Letters*, 290(3-4):311–318, 2010.
- [842] P. Hood and C. Taylor. NavierStokes equations using mixed interpolation. In J.T. Oden, R.H. Gallagher, O.C. Zienkiewicz, and C. Taylor, editors, *Finite element methods in flow problems*. Huntsville Press, University of Alabama, 1974.

- [843] André Horbach, Hans-Peter Bunge, and Jens Oeser. The adjoint method in geodynamics: derivation from a general operator formulation and application to the initial condition problem in a high resolution mantle circulation model. *GEM-International Journal on Geomathematics*, 5(2):163–194, 2014.
- [844] C.O. Horgan. Korn’s inequalities and their applications in continuum mechanics. *SIAM Review*, 37(4):491–511, 1995.
- [845] G. Houseman and P. England. A dynamical model of lithosphere extension and sedimentary basin formation. *J. Geophys. Res.*, 91(B1):719–729, 1986.
- [846] Greg Houseman. Large aspect ratio convection cells in the upper mantle. *Geophysical Journal International*, 75(2):309–334, 1983.
- [847] Greg Houseman and Dan P McKenzie. Numerical experiments on the onset of convective instability in the earth’s mantle. *Geophysical Journal International*, 68(1):133–164, 1982.
- [848] Gregory Houseman and Peter Molnar. Mechanisms of lithospheric rejuvenation associated with continental orogeny. *Geological Society, London, Special Publications*, 184(1):13–38, 2001.
- [849] Gregory A Houseman. The deep structure of ocean ridges in a convecting mantle. *Earth and Planetary Science Letters*, 64(2):283–294, 1983.
- [850] Alan D Howard. A detachment-limited model of drainage basin evolution. *Water resources research*, 30(7):2261–2285, 1994.
- [851] Albert T Hsui, Tang Xiao-Ming, and M Nafi Toksöz. On the dip angle of subducting plates. *Tectonophysics*, 179(3-4):163–175, 1990.
- [852] JiaShun Hu, LiJun Liu, and Quan Zhou. Reproducing past subduction and mantle flow using high-resolution global convection models. *Earth and Planetary Physics*, 2(3):189–207, 2018.
- [853] Ch. Huber, A. Parmigiani, B. Chopard, M. Manga, and O. Bachmann. Lattice Boltzmann model for melting with natural convection. *International Journal of Heat and Fluid Flow*, 29:1469–1480, 200.
- [854] Aurélia Hubert-Ferrari, Geoffrey King, Isabelle Manighetti, Rolando Armijo, Bertrand Meyer, and Paul Tapponnier. Long-term elasticity in the continental lithosphere; modelling the aden ridge propagation and the anatolian extrusion process. *Geophysical Journal International*, 153(1):111–132, 2003.
- [855] M.R. Hudec and M.P.A. Jackson. Terra infirma: Understanding salt tectonics. *Earth-Science Reviews*, 82:1–28, 2007.
- [856] A. Huerta and W.K. Liu. Viscous flow with large free surface motion. *Computer Methods in Applied Mechanics and Engineering*, 69:277–324, 1988.
- [857] Audrey D Huerta and Dennis L Harry. The transition from diffuse to focused extension: Modeled evolution of the west antarctic rift system. *Earth and Planetary Science Letters*, 255(1-2):133–147, 2007.
- [858] Thomas JR Hughes, Wing Kam Liu, and Thomas K Zimmermann. Lagrangian-eulerian finite element formulation for incompressible viscous flows. *Computer methods in applied mechanics and engineering*, 29(3):329–349, 1981.
- [859] Thomas JR Hughes, Michel Mallet, and Akira Mizukami. A new finite element formulation for computational fluid dynamics: II. beyond supg. *Computer methods in applied mechanics and engineering*, 54(3):341–355, 1986.
- [860] T.J.R. Hughes. *The Finite Element Method. Linear Static and Dynamic Finite Element Analysis*. Dover Publications, Inc., 2000.
- [861] T.J.R. Hughes and A. Brooks. A theoretical framework for petrov-galerkin methods with discontinuous weighting functions: application to the streamline-upwind procedure. *Finite Elements in Fluids*, 4:47–65, 1982.
- [862] T.J.R. Hughes, L.P. Franca, and M. Balestra. A new finite element formulation for computational fluid dynamics: V. Circumventing the Babuška-Brezzi condition: A stable Petrov-Galerkin formulation of the Stokes problem accommodating equal-order interpolations. *Computer Methods in Applied Mechanics and Engineering*, 59(1):85–99, 1986.
- [863] T.J.R. Hughes, W.K. Liu, and A. Brooks. Finite element analysis of Incompressible viscous flows by the penalty function formulation. *J. Comp. Phys.*, 30:1–60, 1979.
- [864] Hoon Huh, Choong Ho Lee, and Wei H. Yang. A general algorithm for plastic flow simulation by finite element limit analysis. *International Journal of Solids and Structures*, 36:1193–1207, 1999.
- [865] R. Huismans and C. Beaumont. Depth-dependent extension, two-stage breakup and cratonic underplating at rifted margins. *Nature*, 473:74–79, 2011.

- [866] R. S. Huismans and C. Beaumont. Symmetric and asymmetric lithospheric extension: Relative effects of frictional-plastic and viscous strain softening. *J. Geophys. Res.*, 108 (B10)(2496), 2003.
- [867] Ritske S Huismans, Yuri Y Podladchikov, and Sierd Cloetingh. Dynamic modeling of the transition from passive to active rifting, application to the pannonian basin. *Tectonics*, 20(6):1021–1039, 2001.
- [868] Ritske S Huismans, Yuri Y Podladchikov, and Sierd Cloetingh. Transition from passive to active rifting: Relative importance of asthenospheric doming and passive extension of the lithosphere. *Journal of Geophysical Research: Solid Earth*, 106(B6):11271–11291, 2001.
- [869] R.S. Huismans and C. Beaumont. Complex rifted continental margins explained by dynamical models of depth-dependent lithospheric extension. *Geology*, 30(3):211–214, 2002.
- [870] R.S. Huismans and C. Beaumont. Roles of lithospheric strain softening and heterogeneity in determining the geometry of rifts and continental margins. In *Imaging, Mapping and Modelling Continental Lithosphere Extension and Breakup*, volume 282, pages 111–138. Geological Society, London, Special Publications, 2007.
- [871] R.S. Huismans, S.J.H. Buiter, and C. Beaumont. Effect of plastic-viscous layering and strain softening on mode selection during lithospheric extension. *J. Geophys. Res.*, 110:B02406, 2005.
- [872] L. Husson, C.P. Conrad, and C. Faccenna. Plate motions, Andean orogeny, and volcanism above the South Atlantic convection cell. *Earth Planet. Sci. Lett.*, 317–318:126–135, 2012.
- [873] Laurent Husson. Trench migration and upper plate strain over a convecting mantle. *Physics of the Earth and Planetary Interiors*, 212:32–43, 2012.
- [874] C. Hüttig and K. Stemmer. The spiral grid: A new approach to discretize the sphere and its application to mantle convection. *Geochem. Geophys. Geosyst.*, 9(2), 2008.
- [875] C. Hüttig, N. Tosi, and W.B. Moore. An improved formulation of the incompressible NavierStokes equations with variable viscosity. *Phys. Earth. Planet. Inter.*, 220:11–18, 2013.
- [876] I. Igrelja and A.F.D. Loula. Stabilized velocity and pressure mixed hybrid DGFEM for the stokes problem. *Int. J. Num. Meth. Eng.*, 112:603–628, 2017.
- [877] Benoit Ildefonse and Neil S Mancktelow. Deformation around rigid particles: the influence of slip at the particle/matrix interface. *Tectonophysics*, 221(3-4):345–359, 1993.
- [878] F. Ilinca and D. Pelletier. Computation of accurate nodal derivatives of finite element solutions: The finite node displacement method. *Int. J. Num. Meth. Eng.*, 71:1181–1207, 2007.
- [879] Tobin Isaac, Georg Stadler, and Omar Ghattas. Solution of nonlinear stokes equations discretized by high-order finite elements on nonconforming and anisotropic meshes, with application to ice sheet dynamics. *SIAM Journal on Scientific Computing*, 37(6):B804–B833, 2015.
- [880] A. Ismail-Zadeh, S. Honda, and I. Tsepelev. Linking mantle upwelling with the lithosphere descent and the Japan Sea evolution: a hypothesis. *Scientific Reports*, 3(1137):doi://10.1038/srep01137, 2013.
- [881] A Ismail-Zadeh, A Korotkii, G Schubert, and I Tsepelev. Quasi-reversibility method for data assimilation in models of mantle dynamics. *Geophysical Journal International*, 170(3):1381–1398, 2007.
- [882] A. Ismail-Zadeh, I. Sepelev, C. Talbot, and A. Korotkii. Three-dimensional forward and backward modelling of diapirism: numerical approach and its applicability to the evolution of salt structures in the Priscaspian basin. *Tectonophysics*, 387:81–103, 2004.
- [883] Alik Ismail-Zadeh, Gerald Schubert, Igor Tsepelev, and Alexander Korotkii. Inverse problem of thermal convection: numerical approach and application to mantle plume restoration. *Physics of the Earth and Planetary Interiors*, 145(1-4):99–114, 2004.
- [884] Alik Ismail-Zadeh, Gerald Schubert, Igor Tsepelev, and Alexander Korotkii. Three-dimensional forward and backward numerical modeling of mantle plume evolution: Effects of thermal diffusion. *Journal of Geophysical Research: Solid Earth*, 111(B6), 2006.
- [885] Alik Ismail-Zadeh and Paul Tackley. *Computational Methods for Geodynamics*. Cambridge University Press, 2010.
- [886] J. Ita and S.D. King. Sensitivity of convection with an endothermic phase change to the form of governing equations, initial conditions, boundary conditions, and equation of state. *J. Geophys. Res.*, 99(B8):15,919–15,938, 1994.
- [887] J. Ita and S.D. King. The influence of thermodynamic formulation on simulations of subduction zone geometry and history. *Geophys. Res. Lett.*, 25(9):1463–1466, 1998.
- [888] Yasuyuki Iwase and Satoru Honda. An interpretation of the nusselt-rayleigh number relationship for convection in a spherical shell. *Geophysical journal international*, 130(3):801–804, 1997.

- [889] Yasuyuki Iwase and Satoru Honda. Effects of geometry on the convection with core-cooling. *Earth, planets and space*, 50(5):387–395, 1998.
- [890] M.H.G. Jacobs and A.P. van den Berg. Complex phase distribution and seismic velocity structure of the transition zone: Convection model predictions for a magnesium-endmember olivinepyroxene mantle. *Phys. Earth. Planet. Inter.*, 186:36–48, 2011.
- [891] M. A. Jadamec. Insights on slab-driven mantle flow from advances in three-dimensional modelling. *Journal of Geodynamics*, 2016.
- [892] M.A. Jadamec and M.I. Billen. Reconciling surface plate motions with rapid three-dimensional mantle flow around a slab edge. *Nature*, 465:338–341, 2010.
- [893] M.A. Jadamec and M.I. Billen. The role of rheology and slab shape on rapid mantle flow: Three-dimensional numerical models of the Alaska slab edge. *J. Geophys. Res.*, 117(B02304), 2012.
- [894] M.A. Jadamec, M.I. Billen, and S.M. Roeske. Three-dimensional numerical models of flat slab subduction and the Denali fault driving deformation in south-central Alaska. *Earth Planet. Sci. Lett.*, 376:29–42, 2013.
- [895] Margarete A Jadamec, Magali I Billen, and Oliver Kreylos. Three-dimensional simulations of geometrically complex subduction with large viscosity variations. In *Proceedings of the 1st Conference of the Extreme Science and Engineering Discovery Environment: Bridging from the eXtreme to the campus and beyond*, page 31. ACM, 2012.
- [896] S. Jammes and R.S. Huismans. Structural styles of mountain building: Controls of lithospheric rheologic stratification and extensional inheritance. *J. Geophys. Res.*, 117, 2012.
- [897] S. Jammes, R.S. Huismans, and J.A. Muñoz. Lateral variation in structural style of mountain building: controls of rheological and rift inheritance. *Terra Nova*, 0:doi:10.1111/ter.12087, 2013.
- [898] S. Jammes and L.L. Lavier. Effect of contrasting strength from inherited crustal fabrics on the development of rifting margins. *Geosphere*, 15(2):407–422, 2019.
- [899] S. Jammes, G. Manatschal, and L. Lavier. Interaction between prerift salt and detachment faulting in hyperextended rift systems: The example of the Parentis and Mauléon basins (Bay of Biscay and western Pyrenees). *AAPG Bulletin*, 94(7):957–975, 2010.
- [900] Y. Jaquet, T. Duretz, D. Grujic, H. Masson, and S.M. Schmalholz. Formation of orogenic wedges and crustal shear zones by thermal softening, associated topographic evolution and application to natural orogens. *Tectonophysics*, 746:512–529, 2018.
- [901] Y. Jaquet, Th. Duretz, and S.M. Schmalholz. Dramatic effect of elasticity on thermal softening and strain localization during lithospheric shortening. *Geophys. J. Int.*, 204:780–784, 2016.
- [902] Y. Jaquet and S.M. Schmalholz. Spontaneous ductile crustal shear zone formation by thermal softening and related stress, temperature and strain rate evolution. *Tectonophysics*, 746:384–397, 2018.
- [903] Richard D Jarrard. Relations among subduction parameters. *Reviews of Geophysics*, 24(2):217–284, 1986.
- [904] Gary T Jarvis and Julian P Lowman. Sinking slabs below fossil subduction zones. *Physics of the Earth and Planetary Interiors*, 152(1-2):103–115, 2005.
- [905] Gary T. Jarvis and Dan P. McKenzie. Convection in a compressible fluid with infinite prandtl number. *Journal of Fluid Mechanics*, 96(3):515–583, 1980.
- [906] Gary T Jarvis and WR Peltier. Mantle convection as a boundary layer phenomenon. *Geophysical Journal International*, 68(2):389–427, 1982.
- [907] GT Jarvis. Time-dependent convection in the earth's mantle. *Physics of the earth and planetary interiors*, 36(3-4):305–327, 1984.
- [908] GT Jarvis. The long wavelength component of mantle convection. *Physics of the earth and planetary interiors*, 40(1):24–42, 1985.
- [909] G.T. Jarvis. Effects of curvature on two-dimensional models of mantle convection: cylindrical polar coordinates. *J. Geophys. Res.*, 98(B3):4477–4485, 1993.
- [910] C. Jaupart and J.-C. Mareschal. *Heat Generation and Transport in the Earth*. Cambridge, 2011.
- [911] L. Jeanniot, N. Kusznir, G. Mohn, G. Manatschal, and L. Cowie. Constraining lithosphere deformation modes during continental breakup for the IberiaNewfoundland conjugate rifted margins. *Tectonophysics*, 680:28–49, 2016.
- [912] Ludovic Jeanniot and Susanne JH Buitier. A quantitative analysis of transtensional margin width. *Earth and Planetary Science Letters*, 491:95–108, 2018.

- [913] K.E. Jensen. Topology optimization of stokes flow on dynamic meshes using simple optimizers. *Computers and Fluids*, 174:66–77, 2018.
- [914] V. John. A posteriori L2-error estimates for the nonconforming P1/P0-finite element discretization of the Stokes equations. *Journal of Computational and Applied Mathematics*, 96:99–116, 1998.
- [915] V. John. *Finite Element Methods for Incompressible Flow Problems*. Springer, 2016.
- [916] Volker John. Higher order finite element methods and multigrid solvers in a benchmark problem for the 3d navier–stokes equations. *International Journal for Numerical Methods in Fluids*, 40(6):775–798, 2002.
- [917] Volker John, Alexander Linke, Christian Merdon, Michael Neilan, and Leo G Rebholz. On the divergence constraint in mixed finite element methods for incompressible flows. *SIAM review*, 59(3):492–544, 2017.
- [918] T.E. Johnson, M. Brown, B.J.P. Kaus, and J.A. VanTongeren. Delamination and recycling of Archaean crust caused by gravitational instabilities. *Nature Geoscience*, 7:47–52, 2014.
- [919] L. Jolivet, P. Davy, and P. Cobbold. Right-lateral shear along the Northwest Pacific margin and the India-Eurasia collision. *Tectonics*, 9(6):1409–1419, 1990.
- [920] FW Jones, F Pascal, and ME Ertman. The thermal regime of a three-dimensional subducting lithospheric slab and its electromagnetic response: a numerical model. *Tectonophysics*, 225(1-2):35–48, 1993.
- [921] A. Jourdon, L. Le Pourhiet, Mouthereau F, and E. Masini. Role of rift maturity on the architecture and shortening distribution in mountain belts. *Earth Planet. Sci. Lett.*, 512:89–99, 2019.
- [922] A. Jourdon, L. Le Pourhiet, C. Petit, and Y. Rolland. Impact of range-parallel sediment transport on 2D thermo-mechanical models of mountain belts: Application to the Kyrgyz Tien Shan. *Terra Nova*, 30:279–288, 2018.
- [923] D Jurine, C Jaupart, G Brandeis, and PJ Tackley. Penetration of mantle plumes through depleted lithosphere. *Journal of Geophysical Research: Solid Earth*, 110(B10), 2005.
- [924] L.M. Kachanov. *Fundamentals of the Theory of Plasticity*. Dover Publications, Inc., 2004.
- [925] A. Kageyama and T. Sato. Yin-Yang grid: An overset grid in spherical geometry. *Geochem. Geophys. Geosyst.*, 5(9):DOI:10.1029/2004GC000734, 2004.
- [926] L. Kaislaniemi and J. van Hunen. Dynamics of lithospheric thinning and mantle melting by edge-driven convection: Application to Moroccan Atlas mountains. *Geochem. Geophys. Geosyst.*, 15:3175–3189, 2014.
- [927] L. Kaislaniemi, J. van Hunen, and P. Bouilhol. Lithosphere destabilization by melt weakening and crust-mantle interactionsâimplications for generation of granite-migmatite belts. *Tectonics*, 2018.
- [928] M. Kameyama, A. Kageyamab, and T. Sato. Multigrid-based simulation code for mantle convection in spherical shell using YinYang grid. *Phys. Earth. Planet. Inter.*, 171:19–32, 2008.
- [929] M. Kameyama, D.A. Yuen, and S.-I. Karato. Thermal-mechanical effects of low-temperature plasticity (the Peierls mechanism) on the deformation of a viscoelastic shear zone. *Earth Planet. Sci. Lett.*, 168:159–172, 1999.
- [930] Masanori Kameyama, Hiromi Fujimoto, and Masaki Ogawa. A thermo-chemical regime in the upper mantle in the early earth inferred from a numerical model of magma-migration in a convecting upper mantle. *Physics of the earth and planetary interiors*, 94(3-4):187–215, 1996.
- [931] G. Kanschat. Divergence-free discontinuous Galerkin schemes for the Stokes equations and the MAC scheme. *Int. J. Num. Meth. Fluids*, 56:941–950, 2008.
- [932] S. Karato, M.R. Riedel, and D.A. Yuen. Rheological structure and deformation of subducted slabs in the mantle transition zone: implications for mantle circulation and deep earthquakes. *Phys. Earth. Planet. Inter.*, 127:83–108, 2001.
- [933] S.-I. Karato and H. Jung. Effects of pressure on high-temperature dislocation creep in olivine. *Philosophical Magazine*, 83(3):401–414, 2003.
- [934] S.-I. Karato and P. Li. Diffusion Creep in Perovskite: Implications for the Rheology of the Lower Mantle. *Science*, 255(5049):1238, 1992.
- [935] S.-I. Karato and P. Wu. Rheology of the Upper Mantle: A synthesis. *Science*, 260:771–778, 1993.
- [936] Shun-ichiro Karato. Rheology of the deep upper mantle and its implications for the preservation of the continental roots: A review. *Tectonophysics*, 481(1-4):82–98, 2010.
- [937] Shun-Ichiro Karato, Mervyn S Paterson, and John D FitzGerald. Rheology of synthetic olivine aggregates: influence of grain size and water. *Journal of Geophysical Research: Solid Earth*, 91(B8):8151–8176, 1986.
- [938] I. Katayama and S. Karato. Low-temperature, high-stress deformation of olivine under water-saturated conditions. *Phys. Earth. Planet. Inter.*, 168(3-4):125–133, 2008.

- [939] Tomoo Katsura, Sho Yokoshi, Kazuaki Kawabe, Anton Shatskiy, MA Geeth M Manthilake, Shuangmeng Zhai, Hiroshi Fukui, HA Chamathni I Hegoda, Takashi Yoshino, Daisuke Yamazaki, et al. P-v-t relations of mgsio₃ perovskite determined by in situ x-ray diffraction using a large-volume high-pressure apparatus. *Geophysical Research Letters*, 36(1), 2009.
- [940] Tomoo Katsura, Akira Yoneda, Daisuke Yamazaki, Takashi Yoshino, and Eiji Ito. Adiabatic temperature profile in the mantle. *Physics of the Earth and Planetary Interiors*, 183(1-2):212–218, 2010.
- [941] Richard F Katz, Matthew G Knepley, Barry Smith, Marc Spiegelman, and Ethan T Coon. Numerical simulation of geodynamic processes with the portable extensible toolkit for scientific computation. *Physics of the Earth and Planetary Interiors*, 163(1-4):52–68, 2007.
- [942] Peter Kaufmann. *Discontinuous Galerkin FEM in Computer Graphics*. PhD thesis, ETH Zurich, 2012.
- [943] B. Kaus. *Modelling approaches to geodynamic processes*, PhD thesis. PhD thesis, ETH Zurich, 2005.
- [944] B.J.P. Kaus. Factors that control the angle of shear bands in geodynamic numerical models of brittle deformation. *Tectonophysics*, 484:36–47, 2010.
- [945] B.J.P. Kaus and T.W. Becker. Effects of elasticity on the RayleighTaylor instability: implications for large-scale geodynamics. *Geophys. J. Int.*, 168(843–862), 2007.
- [946] B.J.P. Kaus, H. Mühlhaus, and D.A. May. A stabilization algorithm for geodynamic numerical simulations with a free surface. *Phys. Earth. Planet. Inter.*, 181:12–20, 2010.
- [947] B.J.P. Kaus and Y.Y. Podlachikov. Forward and Reverse Modeling of the Three-Dimensional Viscous Rayleigh-Taylor Instability. *Geophys. Res. Lett.*, 28(6):1095–1098, 2001.
- [948] B.J.P. Kaus and Y.Y. Podlachikov. Initiation of localized shear zones in viscoelastoplastic rocks. *J. Geophys. Res.*, 111(B04412), 2006.
- [949] B.J.P. Kaus, Y.Yu. Podladchikov, and D.W. Schmid. Eulerian Spectral/Finite Difference Method for Large Deformation Modelling of Visco-Elasto-Plastic Geomaterials. *Bulletino di Geofisica*, 45:346–349, 2004.
- [950] B.J.P. Kaus, A.A. Popov, T.S. Baumann, A.E. Pusok, A. Bauville, N. Fernandez, and M. Collignon. Forward and Inverse Modelling of Lithospheric Deformation on Geological Timescales. *NIC Symposium 2016*, pages 299–307, 2016.
- [951] B.J.P. Kaus, C. Steedman, and T.W. Becker. From passive continental margin to mountain belt: insights from analytical and numerical models and application to Taiwan. *Phys. Earth. Planet. Inter.*, 171:235–251, 2008.
- [952] Boris J. P. Kaus and Stefan M. Schmalholz. 3d finite amplitude folding: Implications for stress evolution during crustal and lithospheric deformation. *Geophys. Res. Lett.*, 33, 2006.
- [953] M. Kawaguti. Numerical solution of the Navier-Stokes equations for the flow in a two-dimensional cavity. *Journal of the Physical Society of Japan*, 16(12):2307–2315, 1961.
- [954] Takaaki Kawazoe, Shun-ichiro Karato, Kazuhiko Otsuka, Zhicheng Jing, and Mainak Mookherjee. Shear deformation of dry polycrystalline olivine under deep upper mantle conditions using a rotational drickamer apparatus (rda). *Physics of the Earth and Planetary Interiors*, 174(1-4):128–137, 2009.
- [955] JW Keefner, SJ Mackwell, DL Kohlstedt, and F Heidelbach. Dependence of dislocation creep of dunite on oxygen fugacity: implications for viscosity variations in earth's mantle. *Journal of Geophysical Research: Solid Earth*, 116(B5), 2011.
- [956] T. Keller, D.A. May, and B.J.P. Kaus. Numerical modelling of magma dynamics coupled to tectonic deformation of lithosphere and crust. *Geophys. J. Int.*, page doi:10.1093/gji/ggt306, 2013.
- [957] Tobias Keller and Paul J Tackley. Towards self-consistent modeling of the martian dichotomy: The influence of one-ridge convection on crustal thickness distribution. *Icarus*, 202(2):429–443, 2009.
- [958] D.F. Keppie, C.A. Currie, and C. Warren. Subduction erosion modes: comparing finite element numerical models with the geological record. *Earth Planet. Sci. Lett.*, 287:241–254, 2009.
- [959] R Keppler, FM Rosas, and TJ Nagel. Thin viscous middle-crust and evolving fault distribution during continental rifting: Insights from analog modeling experiments. *Tectonophysics*, 608:161–175, 2013.
- [960] Katie M Keranen, Simon L Klemperer, Jordi Julia, Jesse F Lawrence, and Andy A Nyblade. Low lower crustal velocity across ethiopia: Is the main ethiopian rift a narrow rift in a hot craton? *Geochemistry, Geophysics, Geosystems*, 10(5), 2009.
- [961] W.S. Kiefer and B. Hager. Geoid anomalies and dynamic topography from convection in cylindrical geometry: applications to mantle plumes on Earth and Venus. *Geophys. J. Int.*, 108:198–214, 1992.
- [962] Madlen Kimmritz and Malte Braack. Equal-order finite elements for the hydrostatic stokes problem. *Computational Methods in Applied Mathematics Comput. Methods Appl. Math.*, 12(3):306–329, 2012.

- [963] Chris Kincaid. Subduction dynamics: From the trench to the core-mantle boundary. *Reviews of Geophysics*, 33(S1):401–412, 1995.
- [964] Chris Kincaid and I Selwyn Sacks. Thermal and dynamical evolution of the upper mantle in subduction zones. *Journal of Geophysical Research: Solid Earth*, 102(B6):12295–12315, 1997.
- [965] S. King, C. Lee, P. van Keken, W. Leng, S. Zhong, E. Tan, N. Tosi, and M. Kameyama. A community benchmark for 2D Cartesian compressible convection in the Earths mantle. *Geophys. J. Int.*, 180:7387, 2010.
- [966] Scott D King. Reconciling laboratory and observational models of mantle rheology in geodynamic modelling. *Journal of Geodynamics*, 100:33–50, 2016.
- [967] Scott D King and Bradford H Hager. The relationship between plate velocity and trench viscosity in newtonian and power-law subduction calculations. *Geophysical Research Letters*, 17(13):2409–2412, 1990.
- [968] S.D. King. On topography and geoid from 2-D stagnant lid convection calculations. *Geochem. Geophys. Geosyst.*, 10(3), 2009.
- [969] S.D. King. Venus Resurfacing Constrained by Geoid and Topography. *JGR: Planets*, 123:1041–1060, 2018.
- [970] S.D. King and D.L. Anderson. An alternative mechanism of flood basalt formation. *Earth Planet. Sci. Lett.*, 136:269–279, 1995.
- [971] S.D. King and D.L. Anderson. Edge-driven convection. *Earth Planet. Sci. Lett.*, 160:289–296, 1998.
- [972] S.D. King, D.J. Frost, and D.C. Rubie. Why cold slabs stagnate in the transition zone. *Geology*, page doi:10.1130/G36320.1, 2015.
- [973] S.D. King, A. Raefsky, and B.H. Hager. ConMan: Vectorizing a finite element code for incompressible two-dimensional convection in the Earths mantle. *Phys. Earth. Planet. Inter.*, 59:195–208, 1990.
- [974] A. Kiraly, F.A. Capitanio, F. Funiciello, and C. Faccenna. Subduction zone interaction: Controls on arcuate belts. *Geology*, 2016.
- [975] S.H. Kirby and A.K. Kronenberg. Rheology of the lithosphere: Selected topics. *Reviews of Geophysics*, 25(6), 1987.
- [976] Stephen H Kirby. Rheology of the lithosphere. *Reviews of Geophysics*, 21(6):1458–1487, 1983.
- [977] Dániel Kiss, Yuri Podladchikov, Thibault Duretz, and Stefan M Schmalholz. Spontaneous generation of ductile shear zones by thermal softening: Localization criterion, 1d to 3d modelling and application to the lithosphere. *Earth and Planetary Science Letters*, 519:284–296, 2019.
- [978] Erik A. Kneller, Markus Albertz, Garry D. Karner, , and Christopher A. Johnson. Testing inverse kinematic models of paleocrustal thickness in extensional systems with high-resolution forward thermo-mechanical models. *Geochem. Geophys. Geosyst.*, 2013.
- [979] Erik A Kneller and Peter E van Keken. Effect of three-dimensional slab geometry on deformation in the mantle wedge: Implications for shear wave anisotropy. *Geochemistry, Geophysics, Geosystems*, 9(1), 2008.
- [980] P. Knobloch. On Korn's inequality for nonconforming Finite Elements. *Technische Mechanik*, 20(3):205–214, 2000.
- [981] David L Kohlstedt. Role of water and melts on upper mantle viscosity and strength. *Mantle Flow and Melt Generation at Mid-Ocean Ridges. Am. Geophys. Union, Washington DC*, pages 103–121, 1992.
- [982] David L Kohlstedt. Properties of rocks and minerals-constitutive equations, rheological behavior, and viscosity of rocks. In *Treatise on Geophysics*, pages 389–417. Elsevier, 2007.
- [983] D.L. Kohlstedt, B. Evans, and S.J. Mackwell. Strength of the lithosphere: Constraints imposed by laboratory experiments. *J. Geophys. Res.*, 100:17587–17602, 1995.
- [984] D.L. Kohlstedt and C. Goetze. Low-StressHigh-Temperature Creep in Olivine Single Crystals. *J. Geophys. Res.*, 79(14):2045, 1974.
- [985] Dimitri Komatitsch, Seiji Tsuboi, Jeroen Tromp, A Levander, and G Nolet. The spectral-element method in seismology. *GEOPHYSICAL MONOGRAPH-AMERICAN GEOPHYSICAL UNION*, 157:205, 2005.
- [986] T. Komut, R. Gray, R. Pysklywec, and O. Gogus. Mantle flow uplift of western Anatolia and the Aegean: Interpretation from geophysical analyses and geodynamic modeling. *J. Geophys. Res.*, 117(B11412), 2012.
- [987] Henk Kooi and Christopher Beaumont. Escarpment evolution on high-elevation rifted margins: Insights derived from a surface processes model that combines diffusion, advection, and reaction. *Journal of Geophysical Research: Solid Earth*, 99(B6):12191–12209, 1994.
- [988] P.O. Koons. Two-sided orogen: Collision and erosion from the sandbox to the Southern Alps, New Zealand. *Geology*, 18:679–682, 1990.

- [989] P.O. Koons. Three-dimensional critical wedges: Tectonics and topography in oblique collisional orogen. *J. Geophys. Res.*, 99(B6):12,301–12,315, 1994.
- [990] P.O. Koons. Modeling the topographic evolution of collisional belts. *Annu. Rev. Earth Planet. Sci.*, 23:375–408, 1995.
- [991] P.O. Koons, R.J. Norris, D. Craw, and A.F. Cooper. Influence of exhumation on the structural evolution of transpressional plate boundaries: An example from the Southern Alps, New Zealand. *Geology*, 31(1):3–6, 2003.
- [992] P.O. Koons, P.K. Zeitler, C.P. Chamberlain, D. Craw, and A.S. Meltzer. Mechanical links between erosion and metamorphism in Nanga Parbat, Pakistan Himalaya. *American Journal of Science*, 302:749–733, 2002.
- [993] H. Koopmann, S. Brune, D. Franke, and S. Breuer. Linking rift propagation barriers to excess magmatism at volcanic rifted margins. *Geology*, page doi:10.1130/G36085.1, 2014.
- [994] A. Koptev, A. Beniest, L. Jolivet, and S. Leroy. PlumeInduced Breakup of a Subducting Plate: Micro-continent Formation Without Cessation of the Subduction Process. *Geophys. Res. Lett.*, 46:3663–3675, 2019.
- [995] A. Koptev, E. Burov, E. Calais, S. Leroy, T. Gerya, L. Guillou-Frottier, and S. Cloetingh. Contrasted continental rifting via plume-craton interaction: Applications to Central East African Rift. *Geoscience Frontiers*, 7:221–236, 2016.
- [996] A. Koptev, E. Calais, E. Burov, S. Leroy, and T. Gerya. Dual continental rift systems generated by plumelithosphere interaction. *Nature Geoscience*, page DOI: 10.1038/NGEO2401, 2015.
- [997] Alexander Koptev, Todd A Ehlers, Matthias Nettesheim, and David Whipp. Response of a rheologically stratified lithosphere to subduction of an indenter-shaped plate: Insights into localized exhumation at orogen syntaxes. *Tectonics*, 2019.
- [998] J. Korenaga. Thermal cracking and the deep hydration of oceanic lithosphere: A key to the generation of plate tectonics? *J. Geophys. Res.*, 112(B05408), 2007.
- [999] J. Korenaga and S.-I. Karato. A new analysis of experimental data on olivine rheology. *J. Geophys. Res.*, 113(B02403), 2008.
- [1000] J.R. Koseff and R.L. Street. The Lid-Driven Cavity Flow: A Synthesis of Qualitative and Quantitative Observations. *J. Fluids Eng.*, 106:390–398, 1984.
- [1001] D. Kourounis, A. Fuchs, and O. Schenk. Towards the next generation of multiperiod optimal power flow solvers. *IEEE Transactions on Power Systems*, PP(99):1–10, 2018.
- [1002] L.I.G. Kovasznay. Laminar flow behind a two-dimensional grid. *Mathematical Proceedings of the Cambridge Philosophical Society*, 44(1):58–62, 1948.
- [1003] Peter Kovesi. Good colour maps: How to design them. *CoRR*, abs/1509.03700, 2015.
- [1004] Hemin Koyi. Analogue modelling: from a qualitative to a quantitative techniquea historical outline. *Journal of Petroleum Geology*, 20(2):223–238, 1997.
- [1005] M. Krabbendam. Sliding of temperate basal ice on a rough, hard bed: creep mechanisms, pressure melting, and implications for ice streaming. *The Cryosphere*, 10:1915–1932, 2016.
- [1006] Stephan C Kramer, Cian R Wilson, and D Rhodri Davies. An implicit free surface algorithm for geodynamical simulations. *Physics of the Earth and Planetary Interiors*, 194:25–37, 2012.
- [1007] Corné Kreemer, Geoffrey Blewitt, and Elliot C Klein. A geodetic plate motion and global strain rate model. *Geochemistry, Geophysics, Geosystems*, 15(10):3849–3889, 2014.
- [1008] Corné Kreemer, William E Holt, and A John Haines. An integrated global model of present-day plate motions and plate boundary deformation. *Geophysical Journal International*, 154(1):8–34, 2003.
- [1009] M. Kronbichler, T. Heister, and W. Bangerth. High accuracy mantle convection simulation through modern numerical methods . *Geophys. J. Int.*, 191:12–29, 2012.
- [1010] M Krotkiewski, M Dabrowski, and YY Podladchikov. Fractional steps methods for transient problems on commodity computer architectures. *Physics of the Earth and Planetary Interiors*, 171(1-4):122–136, 2008.
- [1011] Marcin Krotkiewski and Marcin Dabrowski. Parallel symmetric sparse matrix–vector product on scalar multi-core cpus. *Parallel Computing*, 36(4):181–198, 2010.
- [1012] Neil J Krystopowicz and Claire A Currie. Crustal eclogitization and lithosphere delamination in orogens. *Earth and Planetary Science Letters*, 361:195–207, 2013.
- [1013] D. Kurfess and O. Heidbach. CASQUS: A new simulation tool for coupled 3D finite element modeling of tectonic and surface processes based on ABAQUS and CASCADE. *Computers and Geosciences*, 35:1959–1967, 2009.

- [1014] NJ Kusznir and RG Park. The strength of intraplate lithosphere. *Physics of the Earth and Planetary Interiors*, 36(3-4):224–235, 1984.
- [1015] Peter Lafemina, Timothy H Dixon, Rob Govers, Edmundo Norabuena, Henry Turner, Armando Saballos, Glen Mattioli, Marino Protti, and Wilfried Strauch. Fore-arc motion and Cocos Ridge collision in Central America. *Geochemistry Geophysics Geosystems*, 10(5), 2009.
- [1016] Serge Lallemand, Arnauld Heuret, and David Boutelier. On the relationships between slab dip, back-arc stress, upper plate absolute motion, and crustal nature in subduction zones. *Geochemistry, Geophysics, Geosystems*, 6(9), 2005.
- [1017] W. Landry, L. Hodkinson, and S. Kientz. Gale user manual. Technical report, CIG, VPAC, 2011.
- [1018] BE Larock and LR Herrmann. Improved flux prediction using low order finite elements. In *International Conference on Finite Elements in Water Resources, Part II*, 1976.
- [1019] Tine B Larsen, David A Yuen, and Michael Storey. Ultrafast mantle plumes and implications for flood basalt volcanism in the northern atlantic region. *Tectonophysics*, 311(1-4):31–43, 1999.
- [1020] Gautier Laurent, Guillaume Caumon, and Mark Jessell. Interactive editing of 3d geological structures and tectonic history sketching via a rigid element method. *Computers & geosciences*, 74:71–86, 2015.
- [1021] J Lavé. Analytic solution of the mean elevation of a watershed dominated by fluvial incision and hillslope landslides. *Geophysical research letters*, 32(11), 2005.
- [1022] J. Lavé and JP Avouac. Fluvial incision and tectonic uplift across the Himalayas of central Nepal. *J. Geophys. Res.*, 106(B11):26561, 2001.
- [1023] A. Lavecchia, C. Thieulot, F. Beekman, S. Cloetingh, and S. Clark. Lithosphere erosion and continental breakup: Interaction of extension, plume upwelling and melting. *Earth Planet. Sci. Lett.*, 467:89–98, 2017.
- [1024] Luc L Lavier and W Roger Buck. Half graben versus large-offset low-angle normal fault: Importance of keeping cool during normal faulting. *Journal of Geophysical Research: Solid Earth*, 107(B6):ETG–8, 2002.
- [1025] Luc L Lavier, W Roger Buck, and Alexei NB Poliakov. Factors controlling normal fault offset in an ideal brittle layer. *Journal of Geophysical Research: Solid Earth*, 105(B10):23431–23442, 2000.
- [1026] Thorne Lay, John Hernlund, and Bruce A Buffett. Core–mantle boundary heat flow. *Nature geoscience*, 1(1):25, 2008.
- [1027] L. Le Pourhiet. Strain Localization Due to Structural Softening During Pressure Sensitive Rate Independent Yielding. *Bull. Soc. Geol. France*, 184:357–371, 2013.
- [1028] L. Le Pourhiet, B. Huet, D.A. May, L. Labrousse, and L. Jolivet. Kinematic interpretation of the 3D shapes of metamorphic core complexes. *Geochem. Geophys. Geosyst.*, 13(Q09002), 2012.
- [1029] Laetitia Le Pourhiet, Dave A May, Lucas Huille, Louise Watremez, and Sylvie Leroy. A genetic link between transform and hyper-extended margins. *Earth and Planetary Science Letters*, 465:184–192, 2017.
- [1030] S.M. Lechmann, D.A. May, B.J.P. Kaus, and S.M. Schmalholz. Comparing thin-sheet models with 3-D multilayer models for continental collision. *Geophys. J. Int.*, 187:10–33, 2011.
- [1031] S.M. Lechmann, S.M. Schmalholz, G. Hetenyi, D.A. May, and B.J.P. Kaus. Quantifying the impact of mechanical layering and underthrusting on the dynamics of the modern India-Asia collisional system with 3-D numerical models. *J. Geophys. Res.*, 119:doi:10.1002/2012JB009748, 2014.
- [1032] E. Lecomte, L. Le Pourhiet, O. Lacombe, and L. Jolivet. A continuum mechanics approach to quantify brittle strain on weak faults: application to the extensional reactivation of shallow dipping discontinuities. *Geophys. J. Int.*, 184:1–11, 2011.
- [1033] Changyeol Lee and Scott D King. Effect of mantle compressibility on the thermal and flow structures of the subduction zones. *Geochemistry, Geophysics, Geosystems*, 10(1), 2009.
- [1034] E-S Lee, Charles Moulinec, Rui Xu, Damien Violeau, Dominique Laurence, and Peter Stansby. Comparisons of weakly compressible and truly incompressible algorithms for the sph mesh free particle method. *Journal of computational Physics*, 227(18):8417–8436, 2008.
- [1035] R. Lee, P. Gresho, and R. Sani. Smoothing techniques for certain primitive variable solutions of the Navier-Stokes equations. . *Int. J. Num. Meth. Eng.*, 14:1785–1804, 1979.
- [1036] R.S. Lehmann, M. Lukacova-Medvidova, B.J.P. Kaus, and A.A. Popov. Comparison of continuous and discontinuous Galerkin approaches for variable-viscosity Stokes flow. *Z. Angew. Math. Mech.*, pages 1–14, 2015.
- [1037] V. Lemiale, H.-B. Mühlhaus, L. Moresi, and J. Stafford. Shear banding analysis of plastic models formulated for incompressible viscous flows. *Phys. Earth. Planet. Inter.*, 171:177–186, 2008.

- [1038] A. Lenardic and W.M. Kaula. A numerical treatment of geodynamic viscous flow problems involving the advection of material interfaces. *J. Geophys. Res.*, 98(B5):8243–8260, 1993.
- [1039] A Lenardic and L Moresi. Thermal convection below a conducting lid of variable extent: heat flow scalings and two-dimensional, infinite prandtl number numerical simulations. *Physics of Fluids*, 15(2):455–466, 2003.
- [1040] A. Lenardic, L. Moresi, A.M. Jellinek, C.J. O'Neill, C.M. Cooper, and C.T. Lee. Continents, supercontinents, mantle thermal mixing, and mantle thermal isolation: Theory, numerical simulations, and laboratory experiments. *Geochem. Geophys. Geosyst.*, 12(10), 2011.
- [1041] A Lenardic, L Moresi, and H Mühlhaus. The role of mobile belts for the longevity of deep cratonic lithosphere: the crumple zone model. *Geophysical Research Letters*, 27(8):1235–1238, 2000.
- [1042] A Lenardic and L-N Moresi. Some thoughts on the stability of cratonic lithosphere: Effects of buoyancy and viscosity. *Journal of Geophysical Research: Solid Earth*, 104(B6):12747–12758, 1999.
- [1043] Adrian Lenardic, CM Cooper, and L Moresi. A note on continents and the earths urey ratio. *Physics of the Earth and Planetary Interiors*, 188(1-2):127–130, 2011.
- [1044] Adrian Lenardic, AM Jellinek, and L-N Moresi. A climate induced transition in the tectonic style of a terrestrial planet. *Earth and Planetary Science Letters*, 271(1-4):34–42, 2008.
- [1045] Adrian Lenardic and L Moresi. A new class of equilibrium geotherms in the deep thermal lithosphere of continents. *Earth and Planetary Science Letters*, 176(3-4):331–338, 2000.
- [1046] Adrian Lenardic and L Moresi. Heat flow scaling for mantle convection below a conducting lid: Resolving seemingly inconsistent modeling results regarding continental heat flow. *Geophysical research letters*, 28(7):1311–1314, 2001.
- [1047] Adrian Lenardic, L-N Moresi, AM Jellinek, and M Manga. Continental insulation, mantle cooling, and the surface area of oceans and continents. *Earth and Planetary Science Letters*, 234(3-4):317–333, 2005.
- [1048] Adrian Lenardic, L-N Moresi, and H Mühlhaus. Longevity and stability of cratonic lithosphere: insights from numerical simulations of coupled mantle convection and continental tectonics. *Journal of Geophysical Research: Solid Earth*, 108(B6), 2003.
- [1049] Adrian Lenardic, Francis Nimmo, and L Moresi. Growth of the hemispheric dichotomy and the cessation of plate tectonics on mars. *Journal of Geophysical Research: Planets*, 109(E2), 2004.
- [1050] W. Leng, M. Gurnis, and P. Asimov. From basalts to boninites: The geodynamics of volcanic expression during induced subduction initiation. *Initiation and Termination of Subduction: Rock Record, Geodynamic Models, Modern Plate Boundaries*, 2012.
- [1051] W. Leng and S. Zhong. Viscous heating, adiabatic heating and energetic consistency in compressible mantle convection. *Geophy. J. Int.*, 173:693–702, 2008.
- [1052] W. Leng and S. Zhong. More constraints on internal heating rate of the earth's mantle from plume observations: Constraining mantle internal heating. *Geophysical Research Letters*, 36(2):n/a–n/a, 2009.
- [1053] W. Leng and S. Zhong. Implementation and application of adaptive mesh refinement for thermochemical mantle convection studies. *Geochem. Geophys. Geosyst.*, 12(4), 2011.
- [1054] Wei Leng and Michael Gurnis. Dynamics of subduction initiation with different evolutionary pathways. *Geochem. Geophys. Geosyst.*, 12(12):Q12018, doi:10.1029/2011GC003877, 2011.
- [1055] Wei Leng and Michael Gurnis. Subduction initiation at relic arcs. *Geophys. Res. Lett.*, 42:7014–7021, 2015.
- [1056] Wei Leng, Lili Ju, Yan Xie, Tao Cui, and Max Gunzburger. Finite element three-dimensional stokes ice sheet dynamics model with enhanced local mass conservation. *Journal of Computational Physics*, 274:299–311, 2014.
- [1057] O Lesne, E Calais, and J Deverchere. Finite element modelling of crustal deformation in the baikal rift zone: new insights into the active–passive rifting debate. *Tectonophysics*, 289(4):327–340, 1998.
- [1058] Einat Lev and Bradford H Hager. Rayleigh–taylor instabilities with anisotropic lithospheric viscosity. *Geophysical Journal International*, 173(3):806–814, 2008.
- [1059] R.J. Leveque. High-resolution conservative algorithms for advection in incompressible flow. *SIAM J. Numer. Anal.*, 33(2):627–665, 1996.
- [1060] Ben Q Li. *Discontinuous finite elements in fluid dynamics and heat transfer*. Springer Science & Business Media, 2006.
- [1061] D. Li, M. Gurnis, and G. Stadler. Towards adjoint-based inversion of time-dependent mantle convection with nonlinear viscosity. *Geophy. J. Int.*, 209:86–105, 2017.

- [1062] Fucheng Li, Zhen Sun, Xiong Pang, Jie Liao, Hongfeng Yang, Hui Xie, Haiteng Zhuo, and Zhongxian Zhao. Low-viscosity crustal layer controls the crustal architecture and thermal distribution at hyper-extended margins: Modeling insight and application to the northern south china sea margin. *Geochemistry, Geophysics, Geosystems*, 2019.
- [1063] J. Li, Y. He, and Z. Chen. Performance of several stabilized finite element methods for the Stokes equations based on the lowest equal-order pairs. *Computing*, 86:37–51, 2009.
- [1064] Mingming Li and Allen K McNamara. The difficulty for subducted oceanic crust to accumulate at the earth’s core-mantle boundary. *Journal of Geophysical Research: Solid Earth*, 118(4):1807–1816, 2013.
- [1065] S. Li and W.K. Liu. *Meshfree Particle Methods*. Springer, 2004.
- [1066] Yang Li, Frédéric Deschamps, and Paul J Tackley. The stability and structure of primordial reservoirs in the lower mantle: insights from models of thermochemical convection in three-dimensional spherical geometry. *Geophysical Journal International*, 199(2):914–930, 2014.
- [1067] Yanyou Li and Jiafu Qi. Salt-related contractional structure and its main controlling factors of kelasu structural zone in kuqa depression: insights from physical and numerical experiments. *Procedia Engineering*, 31:863–867, 2012.
- [1068] Z.-H. Li, Z. Xu, T. Gerya, and J.-P. Burg. Collision of continental corner from 3-D numerical modeling. *Earth Planet. Sci. Lett.*, 380:98–111, 2013.
- [1069] ZH Li, TV Gerya, and J-P Burg. Influence of tectonic overpressure on p-t paths of hp-uhp rocks in continental collision zones: thermomechanical modelling. *Journal of Metamorphic Geology*, 28(3):227–247, 2010.
- [1070] Z.H. Li, Z.Q. Xu, and T.V. Gerya. Flat versus steep subduction: Contrasting modes for the formation and exhumation of high- to ultrahigh-pressure rocks in continental collision zones. *Earth Planet. Sci. Lett.*, 301:65–77, 2011.
- [1071] Zhong-Hai Li, Jeanette F Di Leo, and Neil M Ribe. Subduction-induced mantle flow, finite strain, and seismic anisotropy: Numerical modeling. *Journal of Geophysical Research: Solid Earth*, 119(6):5052–5076, 2014.
- [1072] Zhong-Hai Li, Taras Gerya, and James AD Connolly. Variability of subducting slab morphologies in the mantle transition zone: Insight from petrological-thermomechanical modeling. *Earth-Science Reviews*, 2019.
- [1073] Zhong-Hai Li and Neil M Ribe. Dynamics of free subduction from 3-d boundary element modeling. *Journal of Geophysical Research: Solid Earth*, 117(B6), 2012.
- [1074] Zhonghai Li and Taras V Gerya. Polyphase formation and exhumation of high-to ultrahigh-pressure rocks in continental subduction zone: Numerical modeling and application to the sulu ultrahigh-pressure terrane in eastern china. *Journal of Geophysical Research: Solid Earth*, 114(B9), 2009.
- [1075] Z.-X. Lia and S. Zhong. Supercontinentsuperplume coupling, true polar wander and plume mobility: Plate dominance in whole-mantle tectonics. *Phys. Earth. Planet. Inter.*, 176:143–156, 2009.
- [1076] J. Liao and T. Gerya. From continental rifting to seafloor spreading: Insight from 3D thermo-mechanical modeling. *Gondwana Research*, 2014.
- [1077] J. Liao and T. Gerya. Influence of lithospheric mantle stratification on craton extension: Insight from two-dimensional thermo-mechanical modeling. *Tectonophysics*, 2014.
- [1078] J Liao, T Gerya, and Q Wang. Layered structure of the lithospheric mantle changes dynamics of craton extension. *Geophysical Research Letters*, 40(22):5861–5866, 2013.
- [1079] A. Limache, S. Idelsohn, R. Rossi, and E. Oñate. The violation of objectivity in Laplace formulations of the NavierStokes equations. *Int. J. Num. Meth. Fluids*, 54:639–664, 2007.
- [1080] Ja-Ren Lin, Taras V Gerya, Paul J Tackley, David A Yuen, and Gregor J Golabek. Numerical modeling of protocore destabilization during planetary accretion: Methodology and results. *Icarus*, 204(2):732–748, 2009.
- [1081] Ja-Ren Lin, Taras V Gerya, Paul J Tackley, David A Yuen, and Gregor J Golabek. Protocore destabilization in planetary embryos formed by cold accretion: Feedbacks from non-newtonian rheology and energy dissipation. *Icarus*, 213(1):24–42, 2011.
- [1082] S.-C. Lin and P.E. van Keken. Dynamics of thermochemical plumes: 1. Plume formation and entrainment of a dense layer. *Geochem. Geophys. Geosyst.*, 7(2), 2006.
- [1083] S.-C. Lin and P.E. van Keken. Dynamics of thermochemical plumes: 2. Complexity of plume structures and its implications for mapping mantle plumes . *Geochem. Geophys. Geosyst.*, 7(3), 2006.

- [1084] E. Rune Lindgren. The motion of a sphere in an incompressible viscous fluid at Reynolds numbers considerably less than one. *Physica Scripta*, 60:97–110, 1999.
- [1085] C. Lithgow-Bertelloni and J.H. Guynn. Origin of the lithospheric stress field. *J. Geophys. Res.*, 109(B01408), 2004.
- [1086] G.R. Liu. *Mesh Free Methods*. CRC press, 2003.
- [1087] G.R. Liu and Y.T. Gu. *An introduction to meshfree methods and their programming*. Springer, 2005.
- [1088] G.R. Liu and M.B. Liu. *Smoothed Particle Hydrodynamics*. World Scientific, 2003.
- [1089] L. Liu and D.R. Stegman. Segmentation of the Farallon slab. *Earth Planet. Sci. Lett.*, 311:1–10, 2011.
- [1090] S. Liu and C.A. Currie. Farallon plate dynamics prior to the Laramide orogeny: Numerical models of flat subduction. *Tectonophysics*, 666:33–47, 2016.
- [1091] S. Liu and S.D. King. A benchmark study of incompressible Stokes flow in a 3-D spherical shell using ASPECT. *Geophys. J. Int.*, 217:650–667, 2019.
- [1092] X. Liu and S. Zhong. Analyses of marginal stability, heat transfer and boundary layer properties for thermal convection in a compressible fluid with infinite Prandtl number. *Geophys. J. Int.*, 194:125–144, 2013.
- [1093] Z. Liu and P. Bird. Two-dimensional and three-dimensional finite element modelling of mantle processes beneath central South Island, New Zealand. *Geophys. J. Int.*, 165:1003–1028, 2006.
- [1094] M.-G. Llorens. Stress and strain evolution during single-layer folding under pure and simple shear. *Journal of Structural Geology*, 126:245–257, 2019.
- [1095] IS Lobanov, I Yu Popov, AI Popov, and TV Gerya. Numerical approach to the stokes problem with high contrasts in viscosity. *Applied Mathematics and Computation*, 235:17–25, 2014.
- [1096] J. Lof and A.H. van den Boogaard. Adaptive return mapping algorithms for J_2 elasto-viscoplastic flow. *Int. J. Num. Meth. Eng.*, 51:1283–1298, 2001.
- [1097] Anders Logg, Kent-Andre Mardal, and Garth Wells. *Automated solution of differential equations by the finite element method: The FEniCS book*, volume 84. Springer Science & Business Media, 2012.
- [1098] C. Loiselet, J. Braun, L. Husson, C. Le Carlier de Veslud, C. Thieulot, P. Yamato, and D. Grujic. Subducting slabs: Jellyfishes in the Earth’s mantle. *Geochem. Geophys. Geosyst.*, 11(8):doi:10.1029/2010GC003172, 2010.
- [1099] Diogo L Lourenço, Antoine B Rozel, Taras Gerya, and Paul J Tackley. Efficient cooling of rocky planets by intrusive magmatism. *Nature Geoscience*, 11(5):322, 2018.
- [1100] Julian P Lowman. Mantle convection models featuring plate tectonic behavior: An overview of methods and progress. *Tectonophysics*, 510(1-2):1–16, 2011.
- [1101] G. Lu, B.J.P. Kaus, L. Zhao, and T. Zheng. Self-consistent subduction initiation induced by mantle flow. *Terra Nova*, page doi: 10.1111/ter.12140, 2015.
- [1102] Stefan Luth, Ernst Willingshofer, Dimitrios Sokoutis, and Sierd Cloetingh. Does subduction polarity changes below the alps? inferences from analogue modelling. *Tectonophysics*, 582:140–161, 2013.
- [1103] Richard A Lux, Geoffrey F Davies, and John H Thomas. Moving lithospheric plates and mantle convection. *Geophysical Journal International*, 58(1):209–228, 1979.
- [1104] P. Ma, S. Liu, M. Gurnis, and B. Zhang. Slab Horizontal Subduction and Slab Tearing Beneath East Asia. *Geophys. Res. Lett.*, 46:5161–5169, 2019.
- [1105] Philippe Machetel and Patrice Weber. Intermittent layered convection in a model mantle with an endothermic phase change at 670 km. *Nature*, 350(6313):55, 1991.
- [1106] S.J. Mackwell, M. E. Zimmerman, and D. L. Kohlstedt. High-temperature deformation of dry diabase with application to tectonics on Venus. *J. Geophys. Res.*, 103:975–984, 1998.
- [1107] M. Maffione, C. Thieulot, D.J.J. van Hinsbergen, A. Morris, O. Plümper, and W. Spakman. Dynamics of intraoceanic subduction initiation: 1. Oceanic detachment fault inversion and the formation of supra-subduction zone ophiolites. *Geochem. Geophys. Geosyst.*, 16:1753–1770, 2015.
- [1108] V. Magni. The effects of back-arc spreading on arc magmatism. *Earth Planet. Sci. Lett.*, 519:141–151, 2019.
- [1109] V. Magni, M.B. Allen, J. van Hunen, and P. Bouilhol. Continental underplating after slab break-off. *Earth Planet. Sci. Lett.*, 474:59–67, 2017.
- [1110] V. Magni, P. Bouilhol, and J. van Hunen. Deep water recycling through time. *Geochem. Geophys. Geosyst.*, 15:4203–4216, 2014.

- [1111] Valentina Magni, Claudio Faccenna, Jeroen van Hunen, and Francesca Funiciello. Delamination vs. break-off: the fate of continental collision. *Geophysical Research Letters*, 40(2):285–289, 2013.
- [1112] R. Mahmood, N. Kousar, M. Yaqub, and K. Jabeen. Numerical Simulations of the Square Lid Driven Cavity Flow of Bingham Fluids Using Nonconforming Finite Elements Coupled with a Direct Solver. *Advances in Mathematical Physics*, 2017.
- [1113] P. Maierová. *Evolution of the Bohemian Massif: Insights from numerical modeling*. PhD thesis, Charles University in Prague, 2012.
- [1114] P. Maierova, O. Lexa, K. Schulmann, and P. Stipska. Contrasting tectono-metamorphic evolution of orogenic lower crust in the Bohemian Massif: A numerical model. *Gondwana Research*, 25:509–521, 2014.
- [1115] C. Malatesta, T. Gerya, L. Crispini, L. Federico, and G. Capponi. Oblique subduction modelling indicates along-trench tectonic transport of sediments. *Nature Communications*, 4, 2013.
- [1116] C. Malatesta, T. Gerya, L. Crispini, L. Federico, and G. Capponi. Interplate deformation at early-stage oblique subduction: 3-D thermomechanical numerical modeling. *Tectonics*, 35:1610–1625, 2016.
- [1117] Andrei V Malevsky, David A Yuen, and LM Weyer. Viscosity and thermal fields associated with strongly chaotic non-newtonian thermal convection. *Geophysical research letters*, 19(2):127–130, 1992.
- [1118] D.S. Malkus and T.J.R. Hughes. Mixed finite element methods - reduced and selective integration techniques: a unification of concepts. *Comput. Meth. Appl. Mech. Eng.*, 15:63–81, 1978.
- [1119] C Mallard, B Jacquet, and N Coltice. Adopt: A tool for automatic detection of tectonic plates at the surface of convection models. *Geochemistry, Geophysics, Geosystems*, 18(8):3197–3208, 2017.
- [1120] L.E. Malvern. *Introduction to the mechanics of a continuous medium*. Prentice-Hall, Inc., 1969.
- [1121] N.S. Mancktelow. Tectonic pressure: Theoretical concepts and modelled examples. *Lithos*, 103:149–177, 2008.
- [1122] N Mandal, Susanta Kumar Samanta, and Chandan Chakraborty. Numerical modeling of heterogeneous flow fields around rigid objects with special reference to particle paths, strain shadows and foliation drag. *Tectonophysics*, 330(3-4):177–194, 2001.
- [1123] V. Manea and M. Gurnis. Subduction zone evolution and low viscosity wedges and channels. *Earth Planet. Sci. Lett.*, 264:22–45, 2007.
- [1124] V.C. Manea, W.P. Leeman, T. Gerya, M. Manea, and G. Zhu. Subduction of fracture zones controls mantle melting and geochemical signature above slabs. *Nature Communications*, page doi:10.1038/ncomms6095, 2014.
- [1125] Vlad C Manea, Marta Pérez-Gussinyé, and Marina Manea. Chilean flat slab subduction controlled by overriding plate thickness and trench rollback. *Geology*, 40(1):35–38, 2012.
- [1126] G. Maniatis, D. Kurfess, A. Hampel, and O. Heidbach. Slip acceleration on normal faults due to erosion and sedimentation Results from a new three-dimensional numerical model coupling tectonics and landscape evolution. *Earth Planet. Sci. Lett.*, 284:570–582, 2009.
- [1127] Utsav Mannu, Kosuke Ueda, Sean D Willett, Taras V Gerya, and Michael Strasser. Impact of sedimentation on evolution of accretionary wedges: Insights from high-resolution thermomechanical modeling. *Tectonics*, 35(12):2828–2846, 2016.
- [1128] Utsav Mannu, Kosuke Ueda, Sean D Willett, Taras V Gerya, and Michael Strasser. Stratigraphic signatures of forearc basin formation mechanisms. *Geochemistry, Geophysics, Geosystems*, 18(6):2388–2410, 2017.
- [1129] Wei Mao and Shijie Zhong. Controls on global mantle convective structures and their comparison with seismic models. *Journal of Geophysical Research: Solid Earth*, 2019.
- [1130] Walter V Maresch and Taras V Gerya. Blueschists and blue amphiboles: How much subduction do they need? *International Geology Review*, 47(7):688–702, 2005.
- [1131] G. Marketos, R. Govers, and C.J. Spiers. Ground motions induced by a producing hydrocarbon reservoir that is overlain by a viscoelastic rocksalt layer: a numerical model. *Geophys. J. Int.*, 203:228–242, 2015.
- [1132] G Marketos, C J Spiers, and Rob Govers. Impact of rock salt creep law choice on subsidence calculations for hydrocarbon reservoirs overlain by evaporite caprocks. *Journal Of Geophysical Research*, 121(6):4249–4267, 2016.
- [1133] AM Marotta, M Fernandez, and R Sabadini. Mantle unrooting in collisional settings. *Tectonophysics*, 296(1-2):31–46, 1998.
- [1134] A.M. Marotta and M.I. Spalla. Permian-Triassic high thermal regime in the Alps: Result of late Variscan collapse or continental rifting? Validation by numerical modeling. *Tectonics*, 26(TC4016):oi:10.1029/2006TC002047, 2007.

- [1135] A.M. Marotta, E. Spelta, and C. Rizzetto. Gravity signature of crustal subduction inferred from numerical modelling. *Geophys. J. Int.*, 166:923–938, 2006.
- [1136] Anna Maria Marotta and Roberto Sabadini. The style of the tyrrhenian subduction. *Geophysical research letters*, 22(7):747–750, 1995.
- [1137] Fernando O Marques, Ksenia Nikolaeva, Marcelo Assumpção, Taras V Gerya, Francisco HR Bezerra, Aderson F do Nascimento, and Joaquim M Ferreira. Testing the influence of far-field topographic forcing on subduction initiation at a passive margin. *Tectonophysics*, 608:517–524, 2013.
- [1138] F.O. Marques, F.R. Cabral, T.V. Gerya, G. Zhu, and D.A. May. Subduction initiates at straight passive margins. *geology*, 2014.
- [1139] FO Marques, PR Cobbold, and N Lourenço. Physical models of rifting and transform faulting, due to ridge push in a wedge-shaped oceanic lithosphere. *Tectonophysics*, 443(1-2):37–52, 2007.
- [1140] F.O. Marques and B.J.P. Kaus. Speculations on the impact of catastrophic subduction initiation on the Earth System. *Journal of Geodynamics*, 93:1–16, 2016.
- [1141] Robert S Marshall, Juan C Heinrich, and OC Zienkiewicz. Natural convection in a square enclosure by a finite-element, penalty function method using primitive fluid variables. *Numerical Heat Transfer, Part B: Fundamentals*, 1(3):315–330, 1978.
- [1142] J. Martinod, V. Regard, Y. Letourmy, H. Henry, R. Hassani, S. Baratchart, and S. Carretier. How do subduction processes contribute to forearc Andean uplift? Insights from numerical models. *Journal of Geodynamics*, 2015.
- [1143] J.G. Masek and C. Duncan. Minimum-work mountain building. *J. Geophys. Res.*, 103(B1):907–917, 1998.
- [1144] W.G. Mason, L. Moresi, P.G. Betts, and M.S. Miller. Three-dimensional numerical models of the influence of a buoyant oceanic plateau on subduction zones. *Tectonophysics*, 483:71–79, 2010.
- [1145] P. Massimi, A. Quarteroni, F. Saleri, and G. Scrofani. Modeling of salt tectonics. *Comput. Methods Appl. Mech. Engrg.*, 197:281–293, 2007.
- [1146] A. Massmeyer, E. Di Giuseppe, A. Davaille, T. Rolf, and P.J. Tackley. Numerical simulation of thermal plumes in a Herschel-Bulkley fluid. *Journal of Non-Newtonian Rheology*, 195:32–45, 2013.
- [1147] Ctirad Matyska and David A Yuen. Lower-mantle material properties and convection models of multiscale plumes. *Special Papers – Geological Society of America*, 430:137, 2007.
- [1148] T. Mauduit and O. Dauteuil. Small-scale models of oceanic transform zones. *J. Geophys. Res.*, 101(B9):20,195–20,209, 1996.
- [1149] B. Maunder, J. van Hunen, P. Bouilhol, and V. Magni. Modeling Slab Temperature: A Reevaluation of the Thermal Parameter. *Geochem. Geophys. Geosyst.*, 2019.
- [1150] D.A. May. Volume reconstruction of point cloud data sets derived from computational geodynamic simulations. *Geochem. Geophys. Geosyst.*, 13(5):Q05019, 2012.
- [1151] D.A. May, J. Brown, and L. Le Pourhiet. A scalable, matrix-free multigrid preconditioner for finite element discretizations of heterogeneous Stokes flow. *Computer Methods in Applied Mechanics and Engineering*, 290:496–523, 2015.
- [1152] D.A. May and L. Moresi. Preconditioned iterative methods for Stokes flow problems arising in computational geodynamics. *Phys. Earth. Planet. Inter.*, 171:33–47, 2008.
- [1153] D.A. May, W.P. Schellart, and L. Moresi. Overview of adaptive finite element analysis in computational geodynamics. *Journal of Geodynamics*, 70:1–20, 2013.
- [1154] Dave A May, Jed Brown, and Laetitia Le Pourhiet. ptatin3d: High-performance methods for long-term lithospheric dynamics. In *Proceedings of the international conference for high performance computing, networking, storage and analysis*, pages 274–284. IEEE Press, 2014.
- [1155] RA Mazariegos, MJ Andrews, and JE Russell. Modeling the evolution of salt structures using nonlinear rocksalt flow laws. *Tectonophysics*, 256(1-4):129–143, 1996.
- [1156] K. McClay, J.-A. Muñoz, and J. García-Senz. Extensional salt tectonics in a contractional orogen: A newly identified tectonic event in the Spanish Pyrenees . *Geology*, 32:373–740, 2004.
- [1157] S. McKee, M.F. Tome, V.G. Ferreira, J.A. Cuminato, A. Castelo, F.S. Sousa, and N. Mangiavacchi. The MAC method. *Computers and Fluids*, 37:907–930, 2008.
- [1158] Dan McKenzie. The generation and compaction of partially molten rock. *Journal of Petrology*, 25:713–765, 1984.

- [1159] Dan McKenzie, James Jackson, and Keith Priestley. Thermal structure of oceanic and continental lithosphere. *Earth and Planetary Science Letters*, 233(3-4):337–349, 2005.
- [1160] Dan P McKenzie. The earth’s mantle. *Scientific American*, 249(3):66–81, 1983.
- [1161] Di P McKenzie and Frank Richter. Convection currents in the earth’s mantle. *Scientific American*, 235(5):72–89, 1976.
- [1162] D.P. McKenzie. Speculations on the consequences and causes of plate motions. *Geophys. J. R. astr. Soc.*, 18:1–32, 1969.
- [1163] DP McKenzie and JG Selater. The evolution of the indian ocean. *Scientific American*, 228(5):62–74, 1973.
- [1164] A.K. McNamara and S. Zhong. Thermochemical structures within a spherical mantle: Superplumes or piles? *J. Geophys. Res.*, 109(B07402), 2004.
- [1165] A.K. McNamara and S. Zhong. Degree-one mantle convection: Dependence on internal heating and temperature-dependent rheology. *Geophys. Res. Lett.*, 32(L01301), 2005.
- [1166] A.K. McNamara and S. Zhong. Thermochemical structures beneath Africa and the Pacific Ocean. *Nature*, 437:1136, 2005.
- [1167] S. Mei and D.L. Kohlstedt. Influence of water on plastic deformation of olivine aggregates 1. Diffusion creep regime. *J. Geophys. Res.*, 105(B9):21,457–21,469, 2000.
- [1168] S. Mei and D.L. Kohlstedt. Influence of water on plastic deformation of olivine aggregates 2. Dislocation creep regime. *J. Geophys. Res.*, 105(B9):21,471–21,481, 2000.
- [1169] S. Mei, A.M. Suzuki, D.L. Kohlstedt, N.A. Dixon, and W.B. Durham. Experimental constraints on the strength of the lithospheric mantle. *J. Geophys. Res.*, 115(B08204), 2010.
- [1170] HJ Melosh and A Raefsky. A simple and efficient method for introducing faults into finite element computations. *Bulletin of the Seismological Society of America*, 71(5):1391–1400, 1981.
- [1171] HJ Melosh and Arthur Raefsky. The dynamical origin of subduction zone topography. *Geophysical Journal International*, 60(3):333–354, 1980.
- [1172] HJ Melosh and CA Williams Jr. Mechanics of graben formation in crustal rocks: A finite element analysis. *Journal of Geophysical Research: Solid Earth*, 94(B10):13961–13973, 1989.
- [1173] C.A. Mériaux, A. May D, J. Mansour, Z. Chen, and O. Kaluza. Benchmark of three-dimensional numerical models of subduction against a laboratory experiment. *Phys. Earth. Planet. Inter.*, 283:110–121, 2018.
- [1174] CA Mériaux, JA Mansour, Louis N Moresi, RC Kerr, and David Alexander May. On the rise of strongly tilted mantle plume tails. *Physics of the Earth and Planetary Interiors*, 184(1-2):63–79, 2011.
- [1175] Catherine A Mériaux, João C Duarte, Wouter P Schellart, and Anne-Sophie Mériaux. A two-way interaction between the hainan plume and the manila subduction zone. *Geophysical Research Letters*, 42(14):5796–5802, 2015.
- [1176] Victor Benno Meyer-Rochow and Jozsef Gal. Pressures produced when penguins poohcalculations on avian defaecation. *Polar Biology*, 27(1):56–58, 2003.
- [1177] K. Michibayashi and D. Mainprice. The role of pre-existing mechanical anisotropy on shear zone development within oceanic mantle lithosphere: an example from the oman ophiolite. *J. Petrol.*, 45(2):405–414, 2004.
- [1178] K Mickus, Ketsela Tadesse, GR Keller, and Befekadu Oluma. Gravity analysis of the main ethiopian rift. *Journal of African Earth Sciences*, 48(2-3):59–69, 2007.
- [1179] Ivar Midtkandal, Jean-Pierre Brun, Roy H Gabrielsen, and Ritske S Huismans. Control of lithosphere rheology on subduction polarity at initiation: Insights from 3d analogue modelling. *Earth and Planetary Science Letters*, 361:219–228, 2013.
- [1180] C. Miehe, F. Aldakheel, and S. Mauthe. Mixed variational principles and robust finite element implementations of gradient plasticity at small strains. *Int. J. Num. Meth. Eng.*, 94:1037–1074, 2013.
- [1181] V Mikhailov, V Lyakhovsky, I v Panet, Y Van Dinther, M Diament, T d Gerya, O deViron, and E Timoshkina. Numerical modelling of post-seismic rupture propagation after the sumatra 26.12.2004 earthquake constrained by grace gravity data. *Geophysical Journal International*, 194(2):640–650, 2013.
- [1182] K. Milner, T.W. Becker, L. Boschi, J. Sain, D. Schorlemmer, and H. Waterhouse. New software framework to share research tools. *Eos Trans. AGU*, 90(12):104–104, 2009.
- [1183] A.N. Minakov, Y.Y. Podlachikov, J.I. Faleide, and R.S. Huismans. Rifting assisted by shear heating and formation of the Lomonosov ridge. *Earth Planet. Sci. Lett.*, 373:31–40, 2013.

- [1184] Y. Mishin. *Adaptive multiresolution methods for problems of computational geodynamics*. PhD thesis, ETH Zurich, 2011.
- [1185] Y.A. Mishin, T.V. Gerya, J.-P. Burg, and J.A.D. Connolly. Dynamics of double subduction: Numerical modeling. *Phys. Earth. Planet. Inter.*, 171:280–295, 2008.
- [1186] Jerry X Mitrovica and Alessandro M Forte. Radial profile of mantle viscosity: results from the joint inversion of convection and postglacial rebound observables. *Journal of Geophysical Research: Solid Earth*, 102(B2):2751–2769, 1997.
- [1187] E. Mitsoulis and S. Galazoulias. Simulation of viscoplastic flow past cylinders in tubes. *Journal of Non-Newtonian Fluid Mechanics*, 158:132–141, 2009.
- [1188] E. Mitsoulis and Th. Zisis. Flow of Bingham plastics in a lid-driven square cavity. *Journal of Non-Newtonian Fluid Mechanics*, 101:173–180, 2001.
- [1189] Eric Mittelstaedt and Paul J Tackley. Plume heat flow is much lower than cmb heat flow. *Earth and Planetary Science Letters*, 241(1-2):202–210, 2006.
- [1190] Arata Miyauchi and Masanori Kameyama. Influences of the depth-dependence of thermal conductivity and expansivity on thermal convection with temperature-dependent viscosity. *Physics of the Earth and Planetary Interiors*, 223:86–95, 2013.
- [1191] A. Mizukami. A mixed Finite Element method for boundary flux computation. *Computer Methods in Applied Mechanics and Engineering*, 57:239–243, 1986.
- [1192] P.K. Mohapatra, V. Eswaran, and S. Murty Bhallamudi. Two-dimensional analysis of dam-break flow in vertical plane. *Journal of Hydraulic Engineering*, 125(2):183–192, 1999.
- [1193] Nicolas E Molnar, Alexander R Cruden, and Peter G Betts. Interactions between propagating rifts and linear weaknesses in the lower crust. *Geosphere*, 2019.
- [1194] P. Molnar. *Brace-Goetze strength profiles, the partitioning of strike-slip and thrust faulting at zones of oblique convergence, and the stress-heat flow paradox of the San Andreas Fault*. Academic Press Ltd, 1992.
- [1195] P. Molnar, G.A. Houseman, and C.P. Conrad. RayleighTaylor instability and convective thinning of mechanically thickened lithosphere: effects of non-linear viscosity decreasing exponentially with depth and of horizontal shortening of the layer. *Geophys. J. Int.*, 133:568–584, 1998.
- [1196] P. Molnar and P. Tapponnier. Relation of the tectonics of eastern China to the India-Eurasia collision: Application of the slip-line field theory to large-scale continental tectonics. *Geology*, 5:212–216, 1977.
- [1197] Peter Molnar. The geologic evolution of the tibetan plateau. *American Scientist*, 77:350–360, 1989.
- [1198] Peter Molnar, Philip England, and Joseph Martinod. Mantle dynamics, uplift of the tibetan plateau, and the indian monsoon. *Reviews of Geophysics*, 31(4):357–396, November 1993.
- [1199] Laurent GJ Montési and Greg Hirth. Grain size evolution and the rheology of ductile shear zones: from laboratory experiments to postseismic creep. *Earth and Planetary Science Letters*, 211(1-2):97–110, 2003.
- [1200] D.R. Montgomery and M.T. Brandon. Topographic controls on erosion rates in tectonically active mountain ranges. *Earth Planet. Sci. Lett.*, 201:481–489, 2002.
- [1201] A. Montlaur, S. Fernandez-Mendez, and A. Huerta. Discontinuous Galerkin methods for the Stokes equations using divergence-free approximations. *Int. J. Num. Meth. Fluids*, 57(08):1071–1092, 2008.
- [1202] A. Montlaur, S. Fernandez-Mendez, J. Peraire, and A. Huerta. Discontinuous Galerkin methods for the NavierStokes equations using solenoidal approximations. *Int. J. Num. Meth. Fluids*, 64:549–564, 2010.
- [1203] William B Moore, Gerald Schubert, and Paul Tackley. Three-dimensional simulations of plume-lithosphere interaction at the hawaiian swell. *Science*, 279(5353):1008–1011, 1998.
- [1204] William B Moore, Gerald Schubert, and Paul J Tackley. The role of rheology in lithospheric thinning by mantle plumes. *Geophysical Research Letters*, 26(8):1073–1076, 1999.
- [1205] C. Morency, R.S. Huismans, C. Beaumont, and P. Fullsack. A numerical model for coupled fluid flow and matrix deformation with applications to disequilibrium compaction and delta stability. *J. Geophys. Res.*, 112(B10407), 2007.
- [1206] L. Moresi, P.G. Betts, M.S. Miller, and R.A. Cayley. Dynamics of continental accretion. *Nature*, 2014.
- [1207] L. Moresi, F. Dufour, and H.B. Muhlhaus. Mantle Convection Modeling with Viscoelastic/Brittle Lithosphere: Numerical Methodology and Plate Tectonic Modeling. *Pure and Applied Geophysics*, 159:159, 2002.
- [1208] L. Moresi, F. Dufour, and H.B. Mühlhaus. A Lagrangian integration point finite element method for large deformation modeling of visco-elastic geomaterials. *J. Comp. Phys.*, 184(2):476–497, 2003.

- [1209] L. Moresi and M. Gurnis. Constraints on the lateral strength of slabs from three-dimensional dynamic flow models. *Earth and Planetary Science Letters*, 138(1):15–28, 1996.
- [1210] L Moresi and H-B Mühlhaus. Anisotropic viscous models of large-deformation mohr–coulomb failure. *Philosophical Magazine*, 86(21-22):3287–3305, 2006.
- [1211] L Moresi, H-B Mühlhaus, Vincent Lemiale, and D May. Incompressible viscous formulations for deformation and yielding of the lithosphere. *Geological Society, London, Special Publications*, 282(1):457–472, 2007.
- [1212] L. Moresi, S. Quenette, V. Lemiale, C. Mériaux, B. Appelbe, and H.-B. Mühlhaus. Computational approaches to studying non-linear dynamics of the crust and mantle. *Phys. Earth. Planet. Inter.*, 163:69–82, 2007.
- [1213] L. Moresi and V. Solomatov. Mantle convection with a brittle lithosphere: thoughts on the global tectonics styles of the earth and venus. *Geophys. J. Int.*, 133:669–682, 1998.
- [1214] L. Moresi, S. Zhong, and M. Gurnis. The accuracy of finite element solutions of stokes' flow with strongly varying viscosity. *Phys. Earth. Planet. Inter.*, 97:83–94, 1996.
- [1215] L-N Moresi and A Lenardic. Three-dimensional numerical simulations of crustal deformation and subcontinental mantle convection. *Earth and Planetary Science Letters*, 150(3-4):233–243, 1997.
- [1216] L.-N. Moresi and V.S. Solomatov. Numerical investigation of 2D convection with extremely large viscosity variations. *Physics of Fluids*, 7(9):2154–2162, 1995.
- [1217] Louis Moresi, Michael Gurnis, and Shijie Zhong. Plate tectonics and convection in the earths mantle: Toward a numerical simulation. *Computing in Science & Engineering*, 2(3):22, 2000.
- [1218] Louis Moresi and Adrian Lenardic. Three-dimensional mantle convection with continental crust: first-generation numerical simulations. *Earth Interactions*, 3(2):1–14, 1999.
- [1219] Louis Moresi and Ben Mather. Stripy: A python module for (constrained) triangulation in cartesian coordinates and on a sphere. *Journal of Open Source Software*, 2019.
- [1220] Isabelle Moretti and Claude Froidevaux. Thermomechanical models of active rifting. *Tectonics*, 5(4):501–511, 1986.
- [1221] M. Morishige and P.E. van Keken. Along-arc variation in the 3-D thermal structure around the junction between the Japan and Kurile arcs. *Geochem. Geophys. Geosyst.*, 15:2225–2240, 2014.
- [1222] Gabriele Morra. Pythonic geodynamics. *Lecture Notes in Earth System Sciences*, 2018.
- [1223] Gabriele Morra, Philippe Chatelain, Paul Tackley, and Petros Koumoutsakos. Earth curvature effects on subduction morphology: Modeling subduction in a spherical setting. *Acta Geotechnica*, 4(2):95–105, 2009.
- [1224] Gabriele Morra and K Regenauer-Lieb. A coupled solid–fluid method for modelling subduction. *Philosophical magazine*, 86(21-22):3307–3323, 2006.
- [1225] Gabriele Morra, Maria Seton, Leonardo Quevedo, and R Dietmar Müller. Organization of the tectonic plates in the last 200 myr. *Earth and Planetary Science Letters*, 373:93–101, 2013.
- [1226] Gabriele Morra, David A Yuen, L Boschi, P Chatelain, P Koumoutsakos, and PJ Tackley. The fate of the slabs interacting with a density/viscosity hill in the mid-mantle. *Physics of the Earth and Planetary Interiors*, 180(3-4):271–282, 2010.
- [1227] S Morris and D Canright. A boundary-layer analysis of benard convection in a fluid of strongly temperature-dependent viscosity. *Physics of the Earth and planetary interiors*, 36(3-4):355–373, 1984.
- [1228] K.W. Morton and D.F. Mayers. *Numerical Solution of Partial Differential Equations: An Introduction*. Cambridge, 2005.
- [1229] R. Moucha, A.M. Forte, J.X. Mitrovica, and A. Daradich. Lateral variations in mantle rheology: implications for convection related surface observables and inferred viscosity models. *Geophys. J. Int.*, 169:113–135, 2007.
- [1230] S. Mueller and R.J. Phillips. On the initiation of subduction. *J. Geophys. Res.*, 96(B1):651–665, 1991.
- [1231] H-B Mühlhaus, Frédéric Dufour, Louis Moresi, and Bruce Hobbs. A director theory for visco-elastic folding instabilities in multilayered rock. *International Journal of Solids and Structures*, 39(13-14):3675–3691, 2002.
- [1232] H-B Mühlhaus, L Moresi, and Miroslav Cada. Emergent anisotropy and flow alignment in viscous rock. *pure and applied geophysics*, 161(11-12):2451–2463, 2004.
- [1233] H.-B. Mühlhaus, L. Moresi, B. Hobbs, and F. Dufour. Large amplitude folding in finely layered viscoelastic rock structures. *Pure appl. Geophys.*, 159:2311–2333, 2002.

- [1234] Hans B Mühlhaus, Jingyu Shi, Louise Olsen-Kettle, and Louis Moresi. Effects of a non-coaxial flow rule on shear bands in viscous-plastic materials. *Granular Matter*, 13(3):205–210, 2011.
- [1235] Hans-Bernd Mühlhaus, Matt Davies, and Louis Moresi. Elasticity, yielding and episodicity in simple models of mantle convection. In *Computational Earthquake Physics: Simulations, Analysis and Infrastructure, Part I*, pages 2031–2047. Springer, 2006.
- [1236] H.B. Muhlhaus and K. Regenauer-Lieb. Towards a self-consistent plate mantle model that includes elasticity: simple benchmarks and application to basic modes of convection. *Geophys. J. Int.*, 163:788–800, 2005.
- [1237] E. Mulyukova and D. Bercovici. Collapse of passive margins by lithospheric damage and plunging grain size. *Earth Planet. Sci. Lett.*, 484:341–352, 2018.
- [1238] E. Mulyukova, B. Steinberger, M. Dabrowski, and S.V. Sobolev. Survival of LLSVPs for billions of years in a vigorously convecting mantle: Replenishment and destruction of chemical anomaly. *J. Geophys. Res.*, 120:3824–3847, 2015.
- [1239] M.A. Murphy, M.H. Taylor, J. Gosse, C.R.P. Silver, D.M. Whipp, and C. Beaumont. Limit of strain partitioning in the Himalaya marked by large earthquakes in western Nepal. *Nature Geoscience*, 2013.
- [1240] Jun Muto, Bunichiro Shibasaki, Yoshihiro Ito, Takeshi Iinuma, Mako Ohzono, Takumi Matsumoto, and Tomomi Okada. Two-dimensional viscosity structure of the northeastern japan islands arc-trench system. *Geophysical Research Letters*, 40(17):4604–4608, 2013.
- [1241] Seyed Tohid Nabavi, Seyed Ahmad Alavi, Soheil Mohammadi, Mohammad Reza Ghassemi, and Marcel Frehner. Analysis of transpression within contractional fault steps using finite-element method. *Journal of Structural Geology*, 96:1–20, 2017.
- [1242] Takashi Nakagawa, Paul J Tackley, Frederic Deschamps, and James AD Connolly. Incorporating self-consistently calculated mineral physics into thermochemical mantle convection simulations in a 3-d spherical shell and its influence on seismic anomalies in earth’s mantle. *Geochemistry, Geophysics, Geosystems*, 10(3), 2009.
- [1243] Tomoeki Nakakuki and Erika Mura. Dynamics of slab rollback and induced back-arc basin formation. *Earth Planet. Sci. Lett.*, 361:287–297, 2013.
- [1244] Tomoeki Nakakuki, Hiroki Sato, and Hiromi Fujimoto. Interaction of the upwelling plume with the phase and chemical boundary at the 670 km discontinuity: Effects of temperature-dependent viscosity. *Earth Planet. Sci. Lett.*, 121(3–4):369–384, 1994.
- [1245] J. Naliboff and S.J.H. Buiter. Rift reactivation and migration during multiphase extension. *Earth Planet. Sci. Lett.*, 421:58–67, 2015.
- [1246] J.B. Naliboff, M.I. Billen, T. Gerya, and J. saunders. Dynamics of outer-rise faulting in oceanic-continental subduction systems. *Geochem. Geophys. Geosyst.*, 14(7):10.1002/ggge.20155, 2013.
- [1247] J.B. Naliboff, S.J.H. Buiter, G. Péron-Pinvidic, P.T. Osmundsen, and J. Tetraault. Complex fault interaction controls continental rifting. *Nature Communications*, 8:1179, 2017.
- [1248] J.B. Naliboff, C.P. Conrad, and C. Lithgow-Bertelloni. Modification of the lithospheric stress field by lateral variations in plate-mantle coupling. *Geophys. Res. Lett.*, 36(L22307), 2009.
- [1249] J.B. Naliboff and L.H. Kellogg. Can large increases in viscosity and thermal conductivity preserve large-scale heterogeneity in the mantle? *Phys. Earth. Planet. Inter.*, 161:86–102, 2007.
- [1250] J.B. Naliboff, C. Lithgow-Bertelloni, L.J. Ruff, and N. de Koker. The effects of lithospheric thickness and density structure on Earths stress field. *Geophys. J. Int.*, 188:1–17, 2012.
- [1251] T Nalpas and J-P Brun. Salt flow and diapirism related to extension at crustal scale. *Tectonophysics*, 228(3–4):349–362, 1993.
- [1252] A.M. Negredo, R. Sabadini, G. Bianco, and M. Fernandez. Three-dimensional modelling of crustal motions caused by subduction and continental convergence in the central Mediterranean. *Geophys. J. Int.*, 136:261–274, 1999.
- [1253] A.M. Negredo, R. Sabadini, and C. Giunchi. Interplay between subduction and continental convergence:a three- dimensional dynamic model for the Central Mediterranean. *Geophys. J. Int.*, 131:F9–F13, 1997.
- [1254] M. Nettesheim, T.A. Ehlers, D.M. Whipp, and A. Koptev. The influence of upper-plate advance and erosion on overriding plate deformation in orogen syntaxes. *Solid Earth*, 9:1207–1224, 2018.
- [1255] Gregory A Neumann and Donald W Forsyth. The paradox of the axial profile: Isostatic compensation along the axis of the mid-atlantic ridge? *Journal of Geophysical Research: Solid Earth*, 98(B10):17891–17910, 1993.

- [1256] Wladimir Neumann. Towards 3d modelling of convection in planetesimals and meteorite parent bodies. *Monthly Notices of the Royal Astronomical Society: Letters*, 490(1):L47–L51, 2019.
- [1257] N.C. Nguyen and J. Peraire. Hybridizable discontinuous Galerkin methods for partial differential equations in continuum mechanics. *J. Comp. Phys.*, 231:5955–5988, 2012.
- [1258] N.C. Nguyen, J. Peraire, and B. Cockburn. A hybridizable discontinuous Galerkin method for Stokes flow. *Comput. Methods Appl. Mech. Engrg.*, 199:582–597, 2010.
- [1259] N.C. Nguyen, J. Peraire, and B. Cockburn. An implicit high-order hybridizable discontinuous Galerkin method for the incompressible NavierStokes equations. *J. Comp. Phys.*, 230:1147–1170, 2011.
- [1260] Nicolai Nijholt and Rob Govers. The role of passive margins on the evolution of Subduction-Transform Edge Propagators (STEPS). *Journal Of Geophysical Research*, 120(10):7203–7230, 2015.
- [1261] Nicolai Nijholt, Rob Govers, and Rinus Wortel. On the forces that drive and resist deformation of the south-central Mediterranean: a mechanical model study. *Geophys. J. Int.*, 214(2):876–894, 2018.
- [1262] K. Nikolaeva, T.V. Gerya, and F.O. Marques. Subduction initiation at passive margins: numerical modeling. *J. Geophys. Res.*, 115(B03406), 2010.
- [1263] Ksenia Nikolaeva, Taras V Gerya, and James AD Connolly. Numerical modelling of crustal growth in intraoceanic volcanic arcs. *Physics of the Earth and Planetary Interiors*, 171(1-4):336–356, 2008.
- [1264] Ksenia Nikolaeva, Taras V Gerya, and Fernando O Marques. Numerical analysis of subduction initiation risk along the atlantic american passive margins. *Geology*, 39(5):463–466, 2011.
- [1265] F. Nilforoushan, R. Pysklywec, A. Cruden, and H. Koyi. Thermal-mechanical modeling of salt-based mountain belts with pre-existing basement faults: Application to the Zagros fold and thrust belt, southwest Iran. *Tectonics*, 32:1212–1226, 2013.
- [1266] F Nimmo and DJ Stevenson. Estimates of martian crustal thickness from viscous relaxation of topography. *Journal of Geophysical Research: Planets*, 106(E3):5085–5098, 2001.
- [1267] Daisuke Nishiura, Mikito Furuichi, and Hide Sakaguchi. Computational performance of a smoothed particle hydrodynamics simulation for shared-memory parallel computing. *Computer Physics Communications*, 194:18–32, 2015.
- [1268] Emmanuel A. Njinju, Estella A. Atekwana, D. Sarah Stamps, Mohamed G. Abdelsalam, Eliot A. Atekwana, Kevin L. Mickus, Stewart Fishwick, Folarin Kolawole, Tahiry A. Rajaonarison, and Victor N. Nyalugwe. Lithospheric structure of the malawi rift: Implications for magma-poor rifting processes. *Tectonics*, 2019.
- [1269] L. Noack, A. Rivoldini, and T. van Hoolst. CHIC Coupling Habitability, Interior and Crust. *INFOCOMP 2015 : The Fifth International Conference on Advanced Communications and Computation*, 2015.
- [1270] S. Norburn and D. Silvester. Fourier analysis of stabilized Q1-Q1 mixed finite element approximation. *SIAM J. Numer. Anal.*, 39:817–833, 2001.
- [1271] D. Oldham, J.H. Davies, and T.N. Phillips. Generic polyhedron grid generation for solving partial differential equations on spherical surfaces. *Computers and Geosciences*, 39:11–17, 2012.
- [1272] J.-A. Olive, M.D. Behn, E. Mittelstaedt, G. Ito, and B.Z. Klein. The role of elasticity in simulating long-term tectonic extension. *Geophy. J. Int.*, 205:728–743, 2016.
- [1273] P. Olson, R. Deguen, L.A. Hinnov, and S. Zhong. Controls on geomagnetic reversals and core evolution by mantle convection in the Phanerozoic. *Phys. Earth. Planet. Inter.*, 214:87–103, 214.
- [1274] Peter Olson and GM Corcos. A boundary layer model for mantle convection with surface plates. *Geophysical Journal International*, 62(1):195–219, 1980.
- [1275] Peter Olson, David A. Yuen, and Derick Balsiger. Convective mixing and the fine structure of mantle heterogeneity. *Phys. Earth. Planet. Inter.*, 36(3–4):291–304, 1984.
- [1276] E. Olsson and G. Kreiss. A conservative level set method for two phase flow. *J. Comp. Phys.*, 210:225–246, 2005.
- [1277] E. Olsson, G. Kreiss, and S. Zahedi. A conservative level set method for two phase flow ii. *J. Comp. Phys.*, 225:785–807, 2007.
- [1278] C. O'Neill, S. Marchi, S. Zhang, and W. Bottke. Impact-driven subduction on the hadean earth. *Nature Geoscience*, 10(10):793, 2017.
- [1279] C. O'Neill, L. Moresi, D. Müller, R. Albert, and F. Dufour. Ellipsis 3D: a particle-in-cell finite element hybrid code for modelling mantle convection and lithospheric deformation. *Computers and Geosciences*, 32:1769–1779, 2006.

- [1280] C. J. O'Neill and S. Zhang. Lateral mixing processes in the hadean. *Journal of geophysical research.*, 123:7074–7089, 2018.
- [1281] C.J. O'Neill, A. Lenardic, W.L. Griffin, and S.Y. O'Reilly. Dynamics of cratons in an evolving mantle. *Lithos*, 102:12–24, 2008.
- [1282] Naomi Oreskes, Kristin Shrader-Frechette, and Kenneth Belitz. Verification, validation, and confirmation of numerical models in the earth sciences. *Science*, 263(5147):641–646, 1994.
- [1283] S. Osher and R. Fedkiw. Level set methods: an overview and some recent results. *J. Comp. Phys.*, 169:463–502, 2001.
- [1284] S. Osher and C.-W. Shu. High-order essentially non-oscillatory schemes for HamiltonJacobi equations. *SIAM J. Numer. Anal.*, 28:907–922, 1991.
- [1285] Tim A Osswald and Natalie Rudolph. *Polymer rheology: fundamentals and applications*. Carl Hanser Verlag GmbH Co KG, 2014.
- [1286] J.M. Ottino. *The kinematics of mixing: stretching, chaos, and transport*, volume 3. Cambridge university press, 1989.
- [1287] Ali Değer Özbȧkir, Rob Govers, and Rinus Wortel. Active faults in the anatolian-aegean plate boundary region with nubia. *Turkish Journal Of Earth Sciences*, pages 30–56, 2017.
- [1288] M. OzBench, K. Regenauer-Lieb, D.R. Stegman, G. Morra, R. Farrington, A. Hale, D.A. May, J. Freeman, L. Bourgois, H.-B. Mühlhaus, and L. Moresi. A model comparison study of large-scale mantle-lithosphere dynamics driven by subduction. *Phys. Earth. Planet. Inter.*, 171:224–234, 2008.
- [1289] C. O'Neill, A. Lenardic, M. Weller, L. Moresi, S. Quenette, and S. Zhang. A window for plate tectonics in terrestrial planet evolution? *Phys. Earth. Planet. Inter.*, 255(80–92), 2016.
- [1290] F. Pan and A. Acrivos. Steady flows in rectangular cavities. *J. Fluid Mech.*, 28(4):643–655, 1967.
- [1291] Tasos C Papanastasiou. Flows of materials with yield. *Journal of Rheology*, 31(5):385–404, 1987.
- [1292] M.E. Pasyanos, T.G. Masters, G. Laske, and Z. Ma. Litho1.0: An updated crust and lithospheric model of the earth. *J. Geophys. Res.*, 119:2153–2173, 03 2014.
- [1293] WSB Paterson and WF Budd. Flow parameters for ice sheet modeling. *Cold Regions Science and Technology*, 6(2):175–177, 1982.
- [1294] Archie Paulson, Shijie Zhong, and John Wahr. Inference of mantle viscosity from grace and relative sea level data. *Geophysical Journal International*, 171(2):497–508, 2007.
- [1295] D. Pelletier, A. Fortin, and R. Camarero. Are fem solutions of incompressible flows really incompressible ? (or how simple flows can cause headaches!). *International journal for numerical methods in fluids*, 9:99–112, 1989.
- [1296] G. Peltzer and P. Tapponnier. Formation and evolution of strike-slip faults, rifts, and basins during the india-asia collision: an experimental approach. *J. Geophys. Res.*, 93(B12):15085–15177, 1988.
- [1297] Gwenn Peron-Pinvidic, Gianreto Manatschal, et al. Rifted margins: state of the art and future challenges. *Frontiers in Earth Science*, 7:218, 2019.
- [1298] J. Perry-Houts and L. Karlstrom. Anisotropic viscosity and time-evolving lithospheric instabilities due to aligned igneous intrusions. *Geophysical Journal International*, 216(2):794–802, 2018.
- [1299] M. Peters, M. Veveakis, T. Poulet, A. Karrech, M. Herwegh, and K. Regenauer-Lieb. Boudinage as a material instability of elasto-visco-plastic rocks. *Journal of Structural Geology*, 78:86–102, 2015.
- [1300] Kenni Dinesen Petersen and W Roger Buck. Eduction, extension, and exhumation of ultrahigh-pressure rocks in metamorphic core complexes due to subduction initiation. *Geochemistry, Geophysics, Geosystems*, 16(8):2564–2581, 2015.
- [1301] Thomas Philippe. *Single viscous layer fold interplay and linkage*. PhD thesis, ETH Zurich, 2013.
- [1302] M. Philippon, G. Corti, F. Sani, M. Bonini, M.-L. Balestrieri, P. Molin, E. Willingshofer, D. Sokoutis, and S. Cloetingh. Evolution, distribution, and characteristics of rifting in southern Ethiopia. *Tectonics*, 33, 2014.
- [1303] B.R. Phillips, H.-P. Bunge, and K. Schaber. True polar wander in mantle convection models with multiple, mobile continents. *Gondwana Research*, 15:288–296, 2009.
- [1304] E. Pichelin and T. Coupez. Finite element solution of the 3D mold filling problem for viscous incompressible fluid. *Computer Methods in Applied Mechanics and Engineering*, 163:359–371, 1998.
- [1305] D.A. Di Pietro, S. Lo Forte, and N. Parolini. Mass preserving finite element implementations of the level set method. *Applied Numerical Mathematics*, 56:1179–1195, 2006.

- [1306] A. Pinelli and A. Vacca. Chebyshev collocation method and multidomain decomposition for the incompressible Navier-Stokes equations. *International Journal for numerical methods in fluids*, 18:781–799, 1994.
- [1307] C. Piromallo, T.W. Becker, F. Funiciello, and C. Faccenna. Three-dimensional instantaneous mantle flow induced by subduction. *Geophys. Res. Lett.*, 33(L08304), 2006.
- [1308] Paul Pitard, Anne Replumaz, Francesca Funiciello, Laurent Husson, and Claudio Faccenna. Mantle kinematics driving collisional subduction: Insights from analogue modeling. *Earth and Planetary Science Letters*, 502:96–103, 2018.
- [1309] J. Pitkäranta and T. Saarinen. A Multigrid Version of a Simple Finite Element Method for the Stokes Problem. *Mathematics of Computation*, 45(171):1–14, 1985.
- [1310] T. Plank and P.E. van Keken. The ups and downs of sediments. *Nature Geoscience*, 1:17, 2008.
- [1311] C Plattner, R Malservisi, K P Furlong, and Rob Govers. Development of the Eastern California Shear Zone — Walker Lane belt: The effects of microplate motion and pre-existing weakness in the Basin and Range. *Tectonophysics*, 485(1-4):78–84, 2010.
- [1312] C Plattner, R Malservisi, and Rob Govers. On the plate boundary forces that drive and resist Baja California motion. *GEOLOGY*, 37(4):359–362, 2009.
- [1313] Christina Plattner, Falk Amelung, Scott Baker, Rob Govers, and Michael Patrick Poland. The role of viscous magma mush spreading in volcanic flank motion at Kīlauea Volcano, Hawai’i. *Journal of Geophysical Research*, 118(5):2474–2487, 2013.
- [1314] A. Plunder, C. Thieulot, and D.J.J. van Hinsbergen. The effect of obliquity on temperature in subduction zones: insights from 3D numerical modeling. *Solid Earth*, 9:759–776, 2018.
- [1315] Yu. Podlachikov, C. Talbot, and A.N.B. Poliakov. Numerical models of complex diapirs. *Tectonophysics*, 228:189–198, 1993.
- [1316] A. Poliakov, P. Cundall, P. Podlachikov, and V. Lyakhovsky. An explicit inertial method for the simulation of viscoelastic flow: an evaluation of elastic effects on diapiric flow in two- and three-layers models. In *Flow and creep in the solar system: Observations, Modeling and theory*, pages 175–195. Kluwer Academic Publishers, 1993.
- [1317] A. Poliakov and Y. Podlachikov. Diapirism and topography. *Geophy. J. Int.*, 109:553–564, 1992.
- [1318] A.N.B. Poliakov, Yu. Podlachikov, and C. talbot. Initiation of salt diapirs with frictional overburdens: numerical experiments. *Tectonophysics*, 228:199–210, 1993.
- [1319] A.N.B. Poliakov, R. van Balen, Yu. Podladchikov, B. Daudre, S. Cloetingh, and C. Talbot. Numerical analysis of how sedimentation and redistribution of surficial sediments affects salt diapirism. *Tectonophysics*, 226:199–216, 1993.
- [1320] A.A. Popov and S.V. Sobolev. SLIM3D: a tool for three-dimensional thermomechanical modelling of lithospheric deformation with elasto-visco-plastic rheology. *Phys. Earth. Planet. Inter.*, 171(1):55–75, 2008.
- [1321] I.Yu. Popov, I.S. Lobanov, S.I. Popov, A.I. Popov, and T. Gerya. Practical analytical solutions for benchmarking of 2D and 3D geodynamic Stokes problems with variable viscosity. *Solid Earth*, 5:461–476, 2014.
- [1322] P.J. Prince and J.R. Dormand. High order embedded runge-kutta formulae. *Journal of Computational and Applied Mathematics*, 7(1):67–75, 1981.
- [1323] A. Prosperetti. Motion of two superposed viscous fluids. *Phys. Fluids*, 24(7):1217–1223, 1981.
- [1324] E.G. Puckett, D.L. Turcotte, Y. He, H. Lokavarapu, J.M. Robey, and L.H. Kellogg. New numerical approaches for modeling thermochemical convection in a compositionally stratified fluid. *Phys. Earth. Planet. Inter.*, 276:10–35, 2018.
- [1325] A.E. Pusok and B.J.P. Kaus. Development of topography in 3D continental collision models. *Geochem. Geophys. Geosyst.*, page doi:10.1002/2015GC005732, 2015.
- [1326] A.E. Pusok, B.J.P. Kaus, and A.A. Popov. On the Quality of Velocity Interpolation Schemes for Marker-in-Cell Method and Staggered Grids. *Pure and Applied Geophysics*, pages doi:10.1007/s00024-016-1431-8, 2016.
- [1327] C. Pütthe and T. Gerya. Dependence of mid-ocean ridge morphology on spreading rate in numerical 3-D models. *Gondwana Research*, 25:270–283, 2014.
- [1328] W.M. Putman and S.-J. Lin. Finite-Volume transport on various cubed-sphere grids. *J. Comp. Phys.*, 227:55–78, 2007.

- [1329] R.N. Pysklywec. Surface erosion control on the evolution of the deep lithosphere. *Geology*, 34:225–228, 2006.
- [1330] R.N. Pysklywec and C. Beaumont. Intraplate tectonics: feedback between radioactive thermal weakening and crustal deformation driven by mantle lithosphere instabilities. *Earth Planet. Sci. Lett.*, 221:275–292, 2004.
- [1331] R.N. Pysklywec, C. Beaumont, and P. Fullsack. Modeling the behavior of continental mantle lithosphere during plate convergence. *Geology*, 28(7):655–658, 2000.
- [1332] R.N. Pysklywec, C. Beaumont, and P. Fullsack. Lithospheric deformation during the early stages of continental collision: Numerical experiments and comparison with South Island, New Zealand. *J. Geophys. Res.*, 107(B72133), 2002.
- [1333] R.N. Pysklywec and A.R. Cruden. Coupled crust-mantle dynamics and intraplate tectonics: Two-dimensional numerical and three-dimensional analogue modeling. *Geochem. Geophys. Geosyst.*, 5(10), 2004.
- [1334] R.N. Pysklywec, S.M. Ellis, and A.R. Gorman. Three-dimensional mantle lithosphere deformation at collisional plate boundaries: A subduction scissor across the South Island of New Zealand. *Earth Planet. Sci. Lett.*, 289:334–346, 2010.
- [1335] R.N. Pysklywec, O. Gogus, J. Percival, A.R. Cruden, and C. Beaumont. Insights from geodynamical modeling on possible fates of continental mantle lithosphere: collision, removal, and overturn. *Can. J. Earth Sci.*, 47:541–563, 2010.
- [1336] R.N. Pysklywec, J.X. Mitrovica, and M. Ishii. Mantle avalanche as a driving force for tectonic reorganization in the southwest Pacific. *Earth Planet. Sci. Lett.*, 209:29–38, 2003.
- [1337] S. Quenette, Y. Xi, J. Mansour, L. Moresi, and D. Abramson. Underworld-GT Applied to Guangdong, a Tool to Explore the Geothermal Potential of the Crust. *Journal of Earth Sciences*, 26(1):78–88, 2015.
- [1338] S. Quere, J.P. Lowman, J. Arkani-Hamed, J.H. Roberts, and R. Moucha. Subcontinental sinking slab remnants in a spherical geometry mantle model. *J. Geophys. Res.*, 118:1760–1777, 2013.
- [1339] Matthieu E.T. Quinquis, Suzanne J.H. Buiter, and Susan Ellis. The role of boundary conditions in numerical models of subduction zone dynamics. *Tectonophysics*, 497:57–70, 2011.
- [1340] M.E.T. Quinquis and S.J.H. Buiter. Testing the effects of basic numerical implementations of water migration on models of subduction dynamics. *Solid Earth*, 5:537–555, 2014.
- [1341] J. Quinteros, V.A. Ramos, and P.M. Jacobakis. An elasto-visco-plastic model using the finite element method for crustal and lithospheric deformation. *Journal of Geodynamics*, 48:83–94, 2009.
- [1342] J. Quinteros, S.V. Sobolev, and A.A. Popov. Viscosity in transition zone and lower mantle: Implications for slab penetration . *Geophys. Res. Lett.*, 37(L09307,), 2010.
- [1343] T. Rabczuk, P.M.A. Areias, and T. Belytschko. A simplified mesh-free method for shear bands with cohesive surfaces . *Int. J. Num. Meth. Eng.*, 69:993–1021, 2007.
- [1344] M Rabinowicz, J Boulegue, and P Genton. Two-and three-dimensional modeling of hydrothermal convection in the sedimented middle valley segment, juan de fuca ridge. *Journal of Geophysical Research: Solid Earth*, 103(B10):24045–24065, 1998.
- [1345] Bret Rahe, David A Ferrill, and Alan P Morris. Physical analog modeling of pull-apart basin evolution. *Tectonophysics*, 285(1-2):21–40, 1998.
- [1346] A. Ramachandran. Parallel adaptive finite element simulation using distributed quad-tree/octree forest. Master’s thesis, Institute for Structural Mechanics, Ruhr University Bochum, 2016.
- [1347] Hans Ramberg. Instability of layered systems in the field of gravity. *Phys. Earth. Planet. Inter.*, 1:427–447, 1968.
- [1348] Hans Ramberg. Folding of laterally compressed multilayers in the field of gravity, i. *Physics of the Earth and Planetary Interiors*, 2(4):203–232, 1970.
- [1349] Hans Ramberg. Folding of laterally compressed multilayers in the field of gravity, ii numerical examples. *Physics of the Earth and Planetary Interiors*, 4(2):83–120, 1971.
- [1350] H. Ran, P.D. Bons, G. Wang, F. Steinbach, M.A. Finch, A. Griera, E. Gomez-Rivas, M.-G. Llorens, S. Ran, X. Liang, and J. Zhou. High-strain deformation of conglomerates: Numerical modelling, strain analysis, and an example from the wutai mountains, north china craton. *Journal of Structural Geology*, 114:222–234, 2018.
- [1351] G. Ranalli. *Rheology of the Earth*. Springer, 1995.

- [1352] G. Ranalli. Rheology of the lithosphere in space and time. *Geological Society Special Publications*, 121:19–37, 1997.
- [1353] G. Ranalli. Rheology of the crust and its role in tectonic reactivation. *Journal of Geodynamics*, 30:3–15, 2000.
- [1354] Giorgio Ranalli. Rheology and deep tectonics. *Annals of Geophysics*, 40(3), 1997.
- [1355] Giorgio Ranalli and B Fischer. Diffusion creep, dislocation creep, and mantle rheology. *Physics of the earth and planetary interiors*, 34(1-2):77–84, 1984.
- [1356] J.T. Ratcliff, G. Schubert, and A. Zebib. Steady tetrahedral and cubic patterns of spherical shell convection with temperature-dependent viscosity. *J. Geophys. Res.*, 101(B11):25,473–25,484, 1996.
- [1357] J.E. Reber, M. Dabrowski, and D.W. Schmid. Sheath fold formation around slip surfaces. *Terra Nova*, pages doi:10.1111/j.1365-3121.2012.01081.x, 2012.
- [1358] J.E. Reber, O. Galland, P.R. Cobbold, and C. Le Carlier de Veslud. Experimental study of sheath fold development around a weak inclusion in a mechanically layered matrix. *Tectonophysics*, 586:130–144, 2013.
- [1359] JE Reber, Stefan M Schmalholz, and J-P Burg. Stress orientation and fracturing during three-dimensional buckling: Numerical simulation and application to chocolate-tablet structures in folded turbidites, sw portugal. *Tectonophysics*, 493(1-2):187–195, 2010.
- [1360] J.N. Reddy. On penalty function methods in the finite element analysis of flow problems. *Int. J. Num. Meth. Fluids*, 2:151–171, 1982.
- [1361] J.N. Reddy and D.K. Gartling. *The Finite Element Method in Heat Transfer and Fluid Dynamics*. CRC Press, 2010.
- [1362] V. Regard, C. Faccenna, J. Martinod, O. Bellier, and J.-C. Thomas. From subduction to collision: Control of deep processes on the evolution of convergent plate boundary. *J. Geophys. Res.*, 108(B4):doi:10.1029/2002JB001943, 2003.
- [1363] K. Regenauer-Lieb, M. Veveakis, T. Poulet, F. Wellmann, A. Karrech, J. Liu, J. Hauser, C. Schrank, O. Gaede, and M. Trefry. Multiscale coupling and multiphysics approaches in earth sciences: Theory. *J. Coupled Syst. Multiscale Dyn.*, 1(1):doi:10.1166/jcsmd.2013.1012, 2013.
- [1364] K. Regenauer-Lieb, R.F. Weinberg, and G. Rosenbaum. The effect of energy feedbacks on continental strength. *Nature*, 442:67–70, 2006.
- [1365] K Regenauer-Lieb and DA Yuen. Fast mechanisms for the formation of new plate boundaries. *Tectonophysics*, 322(1-2):53–67, 2000.
- [1366] K. Regenauer-Lieb and D.A. Yuen. Modeling shear zones in geological and planetary sciences: solid- and fluid-thermalmechanical approaches. *Earth-Science Reviews*, 63:295–349, 2003.
- [1367] K. Regenauer-Lieb, D.A. Yuen, and J. Bralund. The initiation of subduction: Criticality by addition of water ? *Science*, 294:578–580, 2001.
- [1368] Klaus Regenauer-Lieb, Bruce Hobbs, David A Yuen, Alison Ord, Yanhua Zhang, Hans B Mulhaus, and Gabriele Morra. From point defects to plate tectonic faults. *Philosophical Magazine*, 86(21-22):3373–3392, 2006.
- [1369] Klaus Regenauer-Lieb, Thomas Poulet, Delphine Siret, Florian Fusseis, Jie Liu, Klaus Gessner, Oliver Gaede, Gabriele Morra, Bruce Hobbs, Alison Ord, et al. First steps towards modeling a multi-scale earth system. In *Advances in Geocomputing*, pages 1–25. Springer, 2009.
- [1370] Klaus Regenauer-Lieb, Gideon Rosenbaum, and Roberto F Weinberg. Strain localisation and weakening of the lithosphere during extension. *Tectonophysics*, 458(1-4):96–104, 2008.
- [1371] Klaus Regenauer-Lieb and Dave Yuen. Positive feedback of interacting ductile faults from coupling of equation of state, rheology and thermal-mechanics. *Physics of the Earth and Planetary Interiors*, 142(1-2):113–135, 2004.
- [1372] Mirko Reguzzoni and Daniele Sampietro. Moho estimation using goce data: a numerical simulation. In *Geodesy for Planet Earth*, pages 205–214. Springer, 2012.
- [1373] Mirko Reguzzoni, Daniele Sampietro, and Fernando Sansò. Global moho from the combination of the crust2. 0 model and goce data. *Geophysical Journal International*, 195(1):222–237, 2013.
- [1374] Anne Replumaz and P Tapponnier. Reconstruction of the deformed collision zone between india and asia by backward motion of lithospheric blocks. *Journal of Geophysical Research: Solid Earth*, 108(B6), 2003.
- [1375] TJ Reston and César R Ranero. The 3-d geometry of detachment faulting at mid-ocean ridges. *Geochemistry, Geophysics, Geosystems*, 12(7), 2011.

- [1376] J. Revenaugh and B. Parsons. Dynamic topography and gravity anomalies for fluid layers whose viscosity varies exponentially with depth. *Geophysical Journal of the Royal Astronomical Society*, 90(2):349–368, 1987.
- [1377] Patrice F Rey, Nicolas Coltice, and Nicolas Flament. Spreading continents kick-started plate tectonics. *Nature*, 513(7518):405, 2014.
- [1378] B. Reynard. Serpentine in active subduction zones . *Lithos*, 2012.
- [1379] Neil M Ribe. *Theoretical Mantle Dynamics*. Cambridge University Press, 2018.
- [1380] NM Ribe and UR Christensen. Three-dimensional modeling of plume-lithosphere interaction. *Journal of Geophysical Research: Solid Earth*, 99(B1):669–682, 1994.
- [1381] Y. Ricard, M. Richards, C. Lithgow-Bertelloni, and Y. Le Stunff. a geodynamic model of mantle density heterogeneity. *J. Geophys. Res.*, 98:21,895–21,909, 1993.
- [1382] J.G. Rice and R.J. Schnipke. An equal-order velocity-pressure formulation that does not exhibit spurious pressure modes. *Computer Methods in Applied Mechanics and Engineering*, 58:135–149, 1986.
- [1383] M.A. Richards and B.H. Hager. Geoid anomalies in a dynamic Earth. *J. Geophys. Res.*, 89(B7):5987–6002, 1984.
- [1384] M.A. Richards, W.-S. Yang, J.R. Baumgardner, and H.-P. Bunge. Role of a low-viscosity zone in stabilizing plate tectonics: Implications for comparative terrestrial planetology. *Geochem. Geophys. Geosyst.*, 2, 2001.
- [1385] Randall M Richardson, Sean C Solomon, and Norman H Sleep. Intraplate stress as an indicator of plate tectonic driving forces. *Journal of geophysical research*, 81(11):1847–1856, 1976.
- [1386] R.M. Richardson. Ridge Forces, Absolute Plate Motions, and the Intraplate Stress Field. *J. Geophys. Res.*, 97(B8):11,739–11,748, 1992.
- [1387] R.M. Richardson and S.C. Solomon. Tectonic stress in the plates. *Reviews of Geophysics and Space Physics*, 17(5):981, 1979.
- [1388] F.M. Richter and S.F. Daly. Convection models having a multiplicity of large horizontal scales. *J. Geophys. Res.*, 83:4951–4956, 1978.
- [1389] G.H. Ristow. Wall correction for sinking cylinders in fluids. *Physical Review E*, 55(3):2808–2813, 1997.
- [1390] J. Ritsema, A.K. McNamara, and A.L. Bull. Tomographic filtering of geodynamic models: Implications for model interpretation and large-scale mantle structure. *J. Geophys. Res.*, 112(B01303), 2007.
- [1391] Riccardo E M Riva and Rob Govers. Relating viscosities from postseismic relaxation to a realistic viscosity structure for the lithosphere. *Geophys. J. Int.*, 176(2):614–624, 2009.
- [1392] M. Roda, A.M. Marotta, and M.I. Spalla. Numerical simulations of an oceancontinent convergent system: Influence of subduction geometry and mantle wedge hydration on crustal recycling. *Geochem. Geophys. Geosyst.*, 11(5):10.1029/2009GC003015, 2010.
- [1393] J. Rodriguez-González, M.I. Billen, and A.M. Negredo. Non-steady-state subduction and trench-parallel flow induced by overriding plate structure . *Earth Planet. Sci. Lett.*, 401:227–235, 2014.
- [1394] J. Rodriguez-González, A.M. Negredo, and M.I. Billen. The role of the overriding plate thermal state on slab dip variability and on the occurrence of flat subduction. *Geochem. Geophys. Geosyst.*, 13(1):10.1029/2011GC003859, 2012.
- [1395] J. Rodriguez-Gonzalez, A.M. Negredo, and E. Carminati. Slab-mantle flow interaction: influence on subduction dynamics and duration. *Terra Nova*, 0:1–8, 2014.
- [1396] Juan Rodríguez-González, Magali I Billen, Ana M Negredo, and Laurent GJ Montesi. Along-strike variation in subducting plate velocity induced by along-strike variation in overriding plate structure: Insights from 3d numerical models. *Journal of Geodynamics*, 100:175–183, 2016.
- [1397] Gerard H Roe and Mark T Brandon. Critical form and feedbacks in mountain-belt dynamics: Role of rheology as a tectonic governor. *Journal of Geophysical Research: Solid Earth*, 116(B2), 2011.
- [1398] Gerard H Roe, Drew B Stolar, and Sean D Willett. Response of a steady-state critical wedge orogen to changes in climate and tectonic forcing. *SPECIAL PAPERS-GEOLOGICAL SOCIETY OF AMERICA*, 398:227, 2006.
- [1399] Gerard H Roe, Kelin X Whipple, and Jennifer K Fletcher. Feedbacks among climate, erosion, and tectonics in a critical wedge orogen. *American Journal of Science*, 308(7):815–842, 2008.
- [1400] T Rolf, Nicolas Coltice, and PJ Tackley. Linking continental drift, plate tectonics and the thermal state of the earth’s mantle. *Earth and Planetary Science Letters*, 351:134–146, 2012.

- [1401] T. Rolf and P.J. Tackley. Focussing of stress by continents in 3D spherical mantle convection with selfconsistent plate tectonics. *Geophys. Res. Lett.*, 38(L18301):10.1029/2011GL048677, 2011.
- [1402] Tobias Rolf, Nicolas Coltice, and Paul J Tackley. Statistical cyclicity of the supercontinent cycle. *Geophysical Research Letters*, 41(7):2351–2358, 2014.
- [1403] Barbara Romanowicz and Kurt Lambeck. The mass and moment of inertia of the earth. *Physics of the Earth and Planetary Interiors*, 15(1):P1–P4, 1977.
- [1404] C. Ronchi, R. Iacono, and P.S. Paolucci. The "Cubed Sphere": A New Method for the Solution of Partial Differential Equations in Spherical Geometry. *J. Comp. Phys.*, 124:93–114, 1996.
- [1405] Filipe M Rosas, João C Duarte, Wouter Pieter Schellart, Ricardo Tomas, Vili Grigorova, and Pedro Terrinha. Analogue modelling of different angle thrust-wrench fault interference in a brittle medium. *Journal of Structural Geology*, 74:81–104, 2015.
- [1406] I. Rose, B. Buffet, and T. Heister. Stability and accuracy of free surface time integration in viscous flows. *Phys. Earth. Planet. Inter.*, 262:90–100, 2017.
- [1407] I. Rose and B. Buffet. Scaling rates of true polar wander in convecting planets and moons. *Physics of the Earth and Planetary Interiors*, 2017.
- [1408] Leigh H Royden, B Clark Burchfiel, Robert W King, Erchie Wang, Zhiliang Chen, Feng Shen, and Yuping Liu. Surface deformation and lower crustal flow in eastern tibet. *science*, 276(5313):788–790, 1997.
- [1409] Leigh H Royden and Laurent Husson. Trench motion, slab geometry and viscous stresses in subduction systems. *Geophysical Journal International*, 167(2):881–905, 2006.
- [1410] Johann Rudi, A Cristiano I Malossi, Tobin Isaac, Georg Stadler, Michael Gurnis, Peter WJ Staar, Yves Ineichen, Costas Bekas, Alessandro Curioni, and Omar Ghattas. An extreme-scale implicit solver for complex pdes: highly heterogeneous flow in earth's mantle. In *Proceedings of the international conference for high performance computing, networking, storage and analysis*, page 5. ACM, 2015.
- [1411] Thomas Ruedas, Paul J. Tackley, and Sean C. Solomon. Thermal and compositional evolution of the martian mantle: Effects of phase transitions and melting. *Phys. Earth. Planet. Inter.*, 216:32–58, 2013.
- [1412] J.B. Ruh, T. Gerya, and J.-P. Burg. High-resolution 3D numerical modeling of thrust wedges: Influence of décollement strength on transfer zones. *Geochem. Geophys. Geosyst.*, 14(4):1131–1155, 2014.
- [1413] J.B. Ruh, L. Le Pourhiet, Ph. Agard, E. Burov, and T. Gerya. Tectonic slicing of subducting oceanic crust along plate interfaces: Numerical modeling. *Geochem. Geophys. Geosyst.*, 16:10.1002/2015GC005998, 2015.
- [1414] Jonas B Ruh, Taras Gerya, and Jean-Pierre Burg. Toward 4d modeling of orogenic belts: Example from the transpressive zagros fold belt. *Tectonophysics*, 702:82–89, 2017.
- [1415] E Rybacki and G Dresen. Dislocation and diffusion creep of synthetic anorthite aggregates. *Journal of Geophysical Research: Solid Earth*, 105(B11):26017–26036, 2000.
- [1416] E Rybacki, M Gottschalk, R Wirth, and G Dresen. Influence of water fugacity and activation volume on the flow properties of fine-grained anorthite aggregates. *Journal of Geophysical Research: Solid Earth*, 111(B3), 2006.
- [1417] VV Rykov and VP Trubitsyn. 3-d model of mantle convection incorporating moving continents. *Computational Seismology and Geodynamics*, 3:23–32, 1996.
- [1418] VV Rykov and VP Trubitsyn. Numerical technique for calculation of three-dimensional mantle convection and tectonics of continental plates. *Computational Seismology and Geodynamics*, 3:17–22, 1996.
- [1419] Y. Saad. *Iterative methods for sparse linear systems*. SIAM, 2003.
- [1420] Y. Saad and M.H. Schultz. GMRES: A Generalized Minimal Residual Algorithm for Solving Nonsymmetric Linear Systems. *SIAM Journal on Scientific and Statistical Computing*, 7(3):856–869, 1986.
- [1421] R. Sadourny. Conservative Finite-Difference Approximations of the Primitive Equations on Quasi-Uniform Spherical Grids. *Monthly Weather Review*, 100(2):136–144, 1972.
- [1422] M. Saito and Y. Abe. Consequences of anisotropic viscosity in the earths mantle (in japanese, with english abstract). *Zisin*, 37:237–245, 1984.
- [1423] H. Samuel and M. Evonuk. Modeling advection in geophysical flows with particle level sets. *Geochem. Geophys. Geosyst.*, 11(8):doi:10.1029/2010GC003081, 2010.
- [1424] D. Sandiford and L. Moresi. Improving subduction interface implementation in dynamic numerical models. *Solid Earth*, 10:969–985, 2019.

- [1425] R.L. Sani, P.M. Gresho, R.L. Lee, and D.F. Griffiths. The cause and cure (?) of the spurious pressures generated by certain FEM solutions of the incompressible Navier-Stokes equations: part 1. *Int. J. Num. Meth. Fluids*, 1:17–43, 1981.
- [1426] R.L. Sani, P.M. Gresho, R.L. Lee, D.F. Griffiths, and M. Engelman. The cause and cure (?) of the spurious pressures generated by certain fem solutions of the incompressible navier-stokes equations: part 2. *Int. J. Num. Meth. Fluids*, 1:171–204, 1981.
- [1427] Wouter P Schellart and Vincent Strak. A review of analogue modelling of geodynamic processes: Approaches, scaling, materials and quantification, with an application to subduction experiments. *Journal of Geodynamics*, 100:7–32, 2016.
- [1428] W.P. Schellart, Z. Chen, V. Strak, J.C. Duarte, and F.M. Rosas. Pacific subduction control on asian continental deformation including tibetan extension and eastward extrusion tectonics. *Nature Communications*, 10, 2019.
- [1429] W.P. Schellart, J. Freeman, D.R. Stegman, L. Moresi, and D. May. Evolution and diversity of subduction zones controlled by slab width. *Nature*, 446:308–311, 2007.
- [1430] W.P. Schellart and L. Moresi. A new driving mechanism for backarc extension and backarc shortening through slab sinking induced toroidal and poloidal mantle flow: Results from dynamic subduction models with an overriding plate. *J. Geophys. Res.*, 118:1–28, 2013.
- [1431] W.P. Schellart and W. Spakman. Australian plate motion and topography linked to fossil New Guinea slab below Lake Eyre. *Earth Planet. Sci. Lett.*, 421:107–116, 2015.
- [1432] S.M. Schmalholz. A simple analytical solution for slab detachment. *Earth Planet. Sci. Lett.*, 304:45–54, 2011.
- [1433] S.M. Schmalholz, S. Medvedev, S.M. Lechmann, and Y. Podladchikov1. Relationship between tectonic overpressure, deviatoric stress, driving force, isostasy and gravitational potential energy. *Geophy. J. Int.*, 2014.
- [1434] Stefan M Schmalholz. 3d numerical modeling of forward folding and reverse unfolding of a viscous single-layer: Implications for the formation of folds and fold patterns. *Tectonophysics*, 446(1-4):31–41, 2008.
- [1435] G Schmalzle, T Dixon, R Malservisi, and Rob Govers. Strain accumulation across the Carrizo segment of the San Andreas Fault, California: Impact of laterally varying crustal properties. *Journal Of Geophysical Research*, 111, 2006.
- [1436] H. Schmeling, A.Y. Babeyko, A. Enns, C. Faccenna, F. Funiciello, T. Gerya, G.J. Golabek, S. Grigull, B.J.P. Kaus, G. Morra, S.M. Schmalholz, and J. van Hunen. A benchmark comparison of spontaneous subduction models - Towards a free surface. *Phys. Earth. Planet. Inter.*, 171:198–223, 2008.
- [1437] H. Schmeling and W.R. Jacoby. On modelling the lithosphere in mantle convection with non-linear rheology. *Journal of Geophysics*, 50:89–100, 1981.
- [1438] D.W. Schmid and Y.Y. Podlachikov. Analytical solutions for deformable elliptical inclusions in general shear. *Geophy. J. Int.*, 155:269–288, 2003.
- [1439] G.E. Schneider, G.D. Raithby, and M.M. Yovanovich. Finite-element solution procedures for solving the incompressible Navier-Stokes equations using equal order variable interpolation. *Numerical Heat Transfer*, 1:433–451, 1978.
- [1440] G Schubert and PJ Tackley. Mantle dynamics: The strong control of the spinel-perovskite transition at a depth of 660 km. *Journal of geodynamics*, 20(4):417–428, 1995.
- [1441] G. Schubert, D.L. Turcotte, and P. Olson. *Mantle Convection in the Earth and Planets*. Cambridge University Press, 2001.
- [1442] Gerald Schubert, D Bercovici, and GA Glatzmaier. Mantle dynamics in mars and venus: Influence of an immobile lithosphere on three-dimensional mantle convection. *Journal of Geophysical Research: Solid Earth*, 95(B9):14105–14129, 1990.
- [1443] David R Scott. The competition between percolation and circulation in a deformable porous medium. *Journal of Geophysical Research: Solid Earth*, 93(B6):6451–6462, 1988.
- [1444] David R Scott and David J Stevenson. Magma solitons. *Geophysical Research Letters*, 11(11):1161–1164, 1984.
- [1445] David R Scott and David J Stevenson. Magma ascent by porous flow. *Journal of Geophysical Research: Solid Earth*, 91(B9):9283–9296, 1986.
- [1446] A. Segal. *Finite element methods for the incompressible Navier-Stokes equations*. Delft University of Technology, 2012.

- [1447] A. Segal and N.P. Praagman. The sepran fem package. Technical report, Technical Report, Ingenieursbureau Sepra, The Netherlands. <http://ta.twi.tudelft.nl/sepran/sepran.html>, 2005.
- [1448] P. Sekhar and S.D. King. 3D spherical models of Martian mantle convection constrained by melting history. *Earth Planet. Sci. Lett.*, 388:27–37, 2014.
- [1449] C. Selzer, S.J.H. Buiter, and O.A. Pfiffner. Numerical modeling of frontal and basal accretion at collisional margins. *Tectonics*, 27(TC3001):doi:10.1029/2007TC002169, 2008.
- [1450] Cornelia Selzer. *Tectonic accretion styles at convergent margins: A numerical modelling study*. PhD thesis, University of Bern, 2006.
- [1451] Cornelia Selzer, Susanne JH Buiter, and O Adrian Pfiffner. Sensitivity of shear zones in orogenic wedges to surface processes and strain softening. *Tectonophysics*, 437(1-4):51–70, 2007.
- [1452] Maria Seton, Nicolas Flament, Joanne Whittaker, R Dietmar Müller, Michael Gurnis, and Dan J Bower. Ridge subduction sparked reorganization of the pacific plate-mantle system 60–50 million years ago. *Geophysical Research Letters*, 42(6):1732–1740, 2015.
- [1453] P.N. Shankar and M.D. Deshpande. Fluid mechanics in the driven cavity. *Annu. Rev. Fluid Mech.*, 32:93–136, 2000.
- [1454] W. Sharples, L.-N. Moresi, and M. A. Jadamec andJ. Revote. Styles of rifting and fault spacing in numerical models of crustal extension. *J. Geophys. Res.*, 120:4379–4404, 2015.
- [1455] W. Sharples, L.N. Moresi, M. Velic, M.A. Jadamec, and D.A. May. Simulating faults and plate boundaries with a transversely isotropic plasticity model. *Phys. Earth. Planet. Inter.*, 252:77–90, 2016.
- [1456] J.R. Shewchuk. Triangle: Engineering a 2D Quality Mesh Generator and Delaunay Triangulator. In Ming C. Lin and Dinesh Manocha, editors, *Applied Computational Geometry: Towards Geometric Engineering*, volume 1148 of *Lecture Notes in Computer Science*, pages 203–222. Springer-Verlag, May 1996. From the First ACM Workshop on Applied Computational Geometry.
- [1457] Shi J Sim, Dave R Stegman, and Nicolas Coltice. Influence of continental growth on mid-ocean ridge depth. *Geochemistry, Geophysics, Geosystems*, 17(11):4425–4437, 2016.
- [1458] K. Simon, R.S. Huismans, and C. Beaumont. Dynamical modelling of lithospheric extension and small-scale convection: implications for magmatism during the formation of volcanic rifted margins. *Geophy. J. Int.*, 176:327–350, 2009.
- [1459] Guy Simpson. *Practical Finite Element Modelin in Earth Science Using Matlab*. Wiley-Blackwell, 2017.
- [1460] Gaia Siravo, Claudio Faccenna, Mélanie Gérault, Thorsten W Becker, Maria Giuditta Fellin, Frédéric Herman, and Paola Molin. Slab flattening and the rise of the eastern cordillera, colombia. *Earth and Planetary Science Letters*, 512:100–110, 2019.
- [1461] S.V. Sobolev, A. Petrunin, Z. Garfunkel, and A.Y. Babeyko. Thermo-mechanical model of the Dead Sea Transform. *Earth Planet. Sci. Lett.*, 238:78–95, 2005.
- [1462] S.V. Sobolev, A.V. Sobolev, D.V. Kuzmin, N.A. Krivolutskaya, A.G. Petrunin, N.T. Arndt, V.A. Radko, and Y.R. Vasiliev. Linking mantle plumes, large igneous provinces and environmental catastrophes. *Nature*, 477:312, 2011.
- [1463] F. Soboutia, A. Ghods, and J. Arkani-Hamed. On the advection of sharp material interfaces in geodynamic problems: entrainment of the D” layer. *Journal of Geodynamics*, 31:459–479, 2001.
- [1464] VS Solomatov. Grain size-dependent viscosity convection and the thermal evolution of the earth. *Earth and Planetary Science Letters*, 191(3-4):203–212, 2001.
- [1465] V.S. Solomatov. Initiation of subduction by small-scale convection. *J. Geophys. Res.*, 109(B01412), 2004.
- [1466] V.S. Solomatov. Localized subcritical convective cells in temperature-dependent viscosity fluids. *Phys. Earth. Planet. Inter.*, 200-201:63–71, 2012.
- [1467] VS Solomatov, R El-Khozondar, and V Tikare. Grain size in the lower mantle: constraints from numerical modeling of grain growth in two-phase systems. *Physics of the Earth and planetary interiors*, 129(3-4):265–282, 2002.
- [1468] V.S. Solomatov and L.-N. Moresi. Stagnant lid convection on Venus. *J. Geophys. Res.*, 101(E2):4737–4753, 1996.
- [1469] VS Solomatov and CC Reese. Grain size variations in the earth’s mantle and the evolution of primordial chemical heterogeneities. *Journal of Geophysical Research: Solid Earth*, 113(B7), 2008.
- [1470] Teh-Ru Alex Song and Mark Simons. Large trench-parallel gravity variations predict seismogenic behavior in subduction zones. *Science*, 301(5633):630–633, 2003.

- [1471] M. Souli and J.P. Zolesio. Arbitrary Lagrangian-Eulerian and free surface methods in fluid mechanics. *Comput. Methods Appl. Mech. Engrg.*, 191:451–466, 2001.
- [1472] Edward A Spiegel and G Veronis. On the boussinesq approximation for a compressible fluid. *The Astrophysical Journal*, 131:442, 1960.
- [1473] M. Spiegelman, D.A. May, and C. Wilson. On the solvability of incompressible Stokes with viscoplastic rheologies in geodynamics. *Geochem. Geophys. Geosyst.*, 17:2213–2238, 2016.
- [1474] Marc Spiegelman. Flow in deformable porous media. part 2 numerical analysis—the relationship between shock waves and solitary waves. *Journal of Fluid Mechanics*, 247:39–63, 1993.
- [1475] Ondřej Šrámek, Yanick Ricard, and David Bercovici. Simultaneous melting and compaction in deformable two-phase media. *Geophysical Journal International*, 168(3):964–982, 2007.
- [1476] G. Stadler, M. Gurnis, C. Burstedde, L.C. Wilcox, L. Alisic, and O. Ghattas. The dynamics of plate tectonics and mantle flow: from local to global scales. *Science*, 329:1033–1038, 2010.
- [1477] Ph. Steer, R. Cattin, J. Lavé, and V. Godard. Surface Lagrangian Remeshing: A new tool for studying long term evolution of continental lithosphere from 2D numerical modelling. *Computers and Geosciences*, 37(8):1067–1074, 2010.
- [1478] D.R. Stegman, R. Farrington, F.A. Capitanio, and W.P. Schellart. A regime diagram for subduction styles from 3-D numerical models of free subduction. *Tectonophysics*, 483:29–45, 2010.
- [1479] D.R. Stegman, J. Freeman, W.P. Schellart, L. Moresi, and D. May. Influence of trench width on subduction hinge retreat rates in 3-D models of slab rollback. *Geochem. Geophys. Geosyst.*, 7(3):doi:10.1029/2005GC001056, 2006.
- [1480] D.R. Stegman, W.P. Schellart, and J. Freeman. Competing influences of plate width and far-field boundary conditions on trench migration and morphology of subducted slabs in the upper mantle. *Tectonophysics*, 483:46–57, 2010.
- [1481] C. Stein, J. Lowman, and U. Hansen. A comparison of mantle convection models featuring plates. *Geochem. Geophys. Geosyst.*, 15:2689–2698, 2014.
- [1482] B. Steinberger, E. Bredow, S. Lebedev, A. Schaeffer, and T. H. Torsvik. Widespread volcanism in the greenland-north atlantic region explained by the iceland plume. *Nature Geoscience*, 12(1):61, 2019.
- [1483] B. Steinberger, H. Schmeling, and G. Marquart. Large-scale lithospheric stress field and topography induced by global mantle circulation. *Earth Planet. Sci. Lett.*, 186:75–91, 2001.
- [1484] Bernard Steinberger and Trond H Torsvik. Toward an explanation for the present and past locations of the poles. *Geochemistry, Geophysics, Geosystems*, 11(6), 2010.
- [1485] Bernhard Steinberger and Trond H Torsvik. A geodynamic model of plumes from the margins of large low shear velocity provinces. *Geochemistry, Geophysics, Geosystems*, 13(1), 2012.
- [1486] K. Stemmer, H. Harder, and U. Hansen. A new method to simulate convection with strongly temperature- and pressure-dependent viscosity in a spherical shell: Applications to the Earth's mantle. *Phys. Earth. Planet. Inter.*, 157:223–249, 2006.
- [1487] R.J. Stern. Subduction initiation: spontaneous and induced. *Earth Planet. Sci. Lett.*, 226:275–292, 2004.
- [1488] P. Sternai, L. Jolivet, A. Menant, and T. Gerya. Driving the upper plate surface deformation by slab rollback and mantle flow. *Earth Planet. Sci. Lett.*, 405:110–118, 2014.
- [1489] D. Sterpi. An analysis of geotechnical problems involving strain softening effects. *International Journal for Numerical and Analytical Methods in Geomechanics*, 23:1427–1454, 1999.
- [1490] Bernhard Stöckhert and Taras V Gerya. Pre-collisional high pressure metamorphism and nappe tectonics at active continental margins: A numerical simulation. *Terra Nova*, 17(2):102–110, 2005.
- [1491] J. Suckale, B.H. Hager, L.T. ElkinsTanton, and J.Ch. Nave. It takes three to tango: 2. Bubble dynamics in basaltic volcanoes and ramifications for modeling normal Strombolian activity. *J. Geophys. Res.*, 115(B7), 2010.
- [1492] J. Suckale, J.-C. Nave, and B.H. Hager. It takes three to tango: 1. Simulating buoyancy-driven flow in the presence of large viscosity contrasts. *J. Geophys. Res.*, 115(B07409), 2010.
- [1493] M. Sussman and E.G. Puckett. A Coupled Level Set and Volume-of-Fluid Method for Computing 3D and Axisymmetric Incompressible Two-Phase Flows. *J. Comp. Phys.*, 162:301–337, 2000.
- [1494] E.M. Syracuse, P.E. van Keeken, and G.A. Abers. The global range of subduction zone thermal models. *Phys. Earth. Planet. Inter.*, 183:73–90, 2010.

- [1495] A. Syrakos, G.C. Georgiou, and A.N. Alexandrou. Performance of the finite volume method in solving regularised Bingham flows: Inertia effects in the lid-driven cavity flow. *Journal of Non-Newtonian Fluid Mechanics*, 208–209:88–107, 2014.
- [1496] M. Tabata and A. Suzuki. Mathematical modeling and numerical simulation of Earth's mantle convection. *Mathematical modeling and numerical simulation in continuum mechanics, lecture notes in computational science and engineering*, 19:219–231, 2002.
- [1497] Masahisa Tabata and Atsushi Suzuki. Mathematical modeling and numerical simulation of earths mantle convection. In *Mathematical Modeling and Numerical Simulation in Continuum Mechanics*, pages 219–231. Springer, 2002.
- [1498] P. Tackley. *Three-dimensional models of mantle convection: Influence of phase transitions and temperature-dependent viscosity*. PhD thesis, California Institute of Technology, 1994.
- [1499] Paul J Tackley. Effects of strongly temperature-dependent viscosity on time-dependent, three-dimensional models of mantle convection. *Geophysical Research Letters*, 20(20):2187–2190, 1993.
- [1500] Paul J Tackley. Mantle convection and plate tectonics: Toward an integrated physical and chemical theory. *Science*, 288(5473):2002–2007, 2000.
- [1501] Paul J Tackley. Strong heterogeneity caused by deep mantle layering. *Geochemistry, Geophysics, Geosystems*, 3(4):1–22, 2002.
- [1502] Paul J Tackley, Michael Ammann, John P Brodholt, David P Dobson, and Diana Valencia. Mantle dynamics in super-earths: Post-perovskite rheology and self-regulation of viscosity. *Icarus*, 225(1):50–61, 2013.
- [1503] Paul J Tackley, Michael M Ammann, John P Brodholt, David P Dobson, and Diana Valencia. Habitable planets: Interior dynamics and long-term evolution. *Proceedings of the International Astronomical Union*, 8(S293):339–349, 2012.
- [1504] Paul J Tackley et al. Three-dimensional simulations of mantle convection with a thermo-chemical basal boundary layer: D. *The Core-Mantle Boundary Region, Geodyn. Ser.*, 28:231–253, 1998.
- [1505] Paul J Tackley, David J Stevenson, Gary A Glatzmaier, and Gerald Schubert. Effects of an endothermic phase transition at 670 km depth in a spherical model of convection in the earth's mantle. *Nature*, 361(6414):699, 1993.
- [1506] Paul J Tackley, David J Stevenson, Gary A Glatzmaier, and Gerald Schubert. Effects of multiple phase transitions in a three-dimensional spherical model of convection in earth's mantle. *Journal of Geophysical Research: Solid Earth*, 99(B8):15877–15901, 1994.
- [1507] Paul J Tackley, Shunxing Xie, Takashi Nakagawa, and John W Hernlund. Numerical and laboratory studies of mantle convection: Philosophy, accomplishments, and thermochemical structure and evolution. *GEOPHYSICAL MONOGRAPH-AMERICAN GEOPHYSICAL UNION*, 160:83, 2005.
- [1508] P.J. Tackley. *Three-dimensional models of mantle convection: influence of phase transitions and temperature-dependent viscosity*. PhD thesis, California Institute of Technology, 1994.
- [1509] P.J. Tackley. Effects of strongly variable viscosity on three-dimensional compressible convection in planetary mantles. *J. Geophys. Res.*, 101(B2):3311–3332, 1996.
- [1510] P.J. Tackley. Self-consistent generation of tectonic plates in three-dimensional mantle convection. *Earth Planet. Sci. Lett.*, 157:9–22, 1998.
- [1511] P.J. Tackley. Modelling compressible mantle convection with large viscosity contrasts in a three-dimensional spherical shell using the yin-yang grid. *Phys. Earth. Planet. Inter.*, 171:7–18, 2008.
- [1512] P.J. Tackley. Dynamics and evolution of the deep mantle resulting from thermal, chemical, phase and melting effects. *Earth-Science Reviews*, 110:1–25, 2012.
- [1513] P.J. Tackley and S.D. King. Testing the tracer ratio method for modeling active compositional fields in mantle convection simulations. *Geochem. Geophys. Geosyst.*, 4(4), 2003.
- [1514] PJ Tackley and S Xie. Stag3d: a code for modeling thermo-chemical multiphase convection in earth's mantle. In *Computational Fluid and Solid Mechanics 2003*, pages 1524–1527. Elsevier, 2003.
- [1515] K. Takeyama, T. R. Saitoh, and J. Makino. Variable inertia method: A novel numerical method for mantle convection simulation. *New Astronomy*, 2017.
- [1516] Christopher J Talbot, Peter Rönnlund, H Schmeling, Hemin Koyi, and MPA Jackson. Diapiric spoke patterns. *Tectonophysics*, 188(1-2):187–201, 1991.
- [1517] E. Taliadorou, G.C. Georgiou, and I. Moultsas. Weakly compressible poiseuille flows of a herschelbulkley fluid. *Journal of Non-Newtonian Fluid Mechanics*, 158:162–169, 2009.

- [1518] E. Tan, E. Choi, P. Thoutireddy, M. Gurnis, and M. Aivazis. GeoFramework: Coupling multiple models of mantle convection within a computational framework. *Geochem. Geophys. Geosyst.*, 7(6):10.1029/2005GC001155, 2006.
- [1519] E. Tan and M. Gurnis. Compressible thermochemical convection and application to lower mantle structures. *J. Geophys. Res.*, 112(B06304), 2007.
- [1520] E. Tan, M. Gurnis, and L. Han. Slabs in the lower mantle and their modulation of plume formation. *Geochem. Geophys. Geosyst.*, 3(11), 2002.
- [1521] Eh Tan, Wei Leng, Shijie Zhong, and Michael Gurnis. On the location of plumes and lateral movement of thermochemical structures with high bulk modulus in the 3-d compressible mantle. *Geochemistry, Geophysics, Geosystems*, 12(7), 2011.
- [1522] A. Tanaka, Y. Sanada, Y. Yamada, T. Matsuoka, and Y. Ashida. Discretree element simulations of continental collision in asia. *Exploration Geophysics*, 36(1):1–6, 2005.
- [1523] R.I. Tanner and E. Tanner. Heinrich hencky: a rheological pioneer. *Rheol. Acta*, 42:93–101, 2003.
- [1524] Paul Tapponnier and Peter Molnar. Slip-line field theory and large-scale continental tectonics. *Nature*, 264:319–324, November 1976.
- [1525] Paul Tapponnier, Xu Zhiqin, Françoise Roger, Bertrand Meyer, Nicolas Arnaud, Gerard Wittlinger, and Yang Jingsui. Oblique stepwise rise and growth of the tibet plateau. *Science*, 294:1671–1677, 2001.
- [1526] J.M. Taramon, J. Rodriguez-Gonzalez, A.M. Negredo, and M.I. Billen. Influence of cratonic lithosphere on the formation and evolution of flat slabs: Insights from 3-D time-dependent modeling. *Geochem. Geophys. Geosyst.*, 16:doi:10.1002/2015GC005940, 2015.
- [1527] C. Tayloor and P. Hood. A numerical solution of the Navier-Stokes equations using the finite element technique. *Comput. Fluids*, 1:73–100, 1973.
- [1528] Michael G Tetley, Simon E Williams, Michael Gurnis, Nicolas Flament, and R Dietmar Müller. Constraining absolute plate motions since the triassic. *Journal of Geophysical Research: Solid Earth*, 2019.
- [1529] J.L. Tetreault and S.J.H. Buiter. Geodynamic models of terrane accretion: Testing the fate of island arcs, oceanic plateaus, and continental fragments in subduction zones. *J. Geophys. Res.*, 2012.
- [1530] JL Tetreault and SJH Buiter. Future accreted terranes: a compilation of island arcs, oceanic plateaus, submarine ridges, seamounts, and continental fragments. *Solid Earth*, 5(2):1243–1275, 2014.
- [1531] J.L. Tetreault and S.J.H. Buiter. The influence of extension rate and crustal rheology on the evolution of passive margins from rifting to break-up. *Tectonophysics*, 746:155–172, 2018.
- [1532] M Tetzlaff and H Schmeling. The influence of olivine metastability on deep subduction of oceanic lithosphere. *Physics of the Earth and Planetary Interiors*, 120(1-2):29–38, 2000.
- [1533] T.E. Tezduyar, S. Mittal, S.E. Ray, and R. Shih. Incompressible flow computations with stabilized bilinear and linear equal-order-interpolation velocity-pressure elements. *Comput. Methods Appl. Mech. Engrg.*, 95:221–242, 1992.
- [1534] Thomas M Tharp. Numerical models of subduction and forearc deformation. *Geophysical Journal International*, 80(2):419–437, 1985.
- [1535] M. Thielmann and B.J.P. Kaus. Shear heating induced lithospheric-scale localization: Does it result in subduction? . *Earth Planet. Sci. Lett.*, 359-360:1–13, 2012.
- [1536] M. Thielmann, B.J.P. Kaus, and A.A. Popov. Lithospheric stresses in RayleighBenard convection: effects of a free surface and a viscoelastic Maxwell rheology. *Geophy. J. Int.*, 203:2200–2219, 2015.
- [1537] M. Thielmann, D.A. May, and B.J.P. Kaus. Discretization errors in the Hybrid Finite Element Particle-In-Cell Method. *Pure and Applied Geophysics*, 171(9):2164–2184, 2014.
- [1538] C. Thieulot. FANTOM: two- and three-dimensional numerical modelling of creeping flows for the solution of geological problems. *Phys. Earth. Planet. Inter.*, 188(1):47–68, 2011.
- [1539] C. Thieulot. ELEFANT: a user-friendly multipurpose geodynamics code. *Solid Earth Discussions*, 6:1949–2096, 2014.
- [1540] C. Thieulot. Analytical solution for viscous incompressible stokes flow in a spherical shell. *Solid Earth Discussions*, 2017:1–19, 2017.
- [1541] C. Thieulot. GHOST: Geoscientific Hollow Sphere Tesselation. *Solid Earth*, 9(1–9), 2018.
- [1542] C. Thieulot and W. Bangerth. On the use of equal order elements in geodynamics. *Solid Earth*, 2019.
- [1543] C. Thieulot, P. Fullsack, and J. Braun. Adaptive octree-based finite element analysis of two- and three-dimensional indentation problems. *J. Geophys. Res.*, 113:B12207, 2008.

- [1544] C. Thieulot, P. Steer, and R.S. Huismans. Three-dimensional numerical simulations of crustal systems undergoing orogeny and subjected to surface processes. *Geochem. Geophys. Geosyst.*, 15, 2014.
- [1545] Cedric Thieulot and Pep Español. Non-isothermal diffusion in a binary mixture with smoothed particle hydrodynamics. *Computer physics communications*, 169(1-3):172–176, 2005.
- [1546] Cedric Thieulot, LPBM Janssen, and Pep Español. Smoothed particle hydrodynamics model for phase separating fluid mixtures. i. general equations. *Physical Review E*, 72(1):016713, 2005.
- [1547] Cedric Thieulot, LPBM Janssen, and Pep Español. Smoothed particle hydrodynamics model for phase separating fluid mixtures. ii. diffusion in a binary mixture. *Physical Review E*, 72(1):016714, 2005.
- [1548] Alan Bruce Thompson, Karel Schulmann, and Josef Jezek. Thermal evolution and exhumation in obliquely convergent (transpressive) orogens. *Tectonophysics*, 280(1-2):171–184, 1997.
- [1549] J.F. Thompson, B.K. Soni, and N.P. Weatherill. *Handbook of grid generation*. CRC press, 1998.
- [1550] Paul F Thompson and Paul J Tackley. Generation of mega-plumes from the core-mantle boundary in a compressible mantle with temperature-dependent viscosity. *Geophysical research letters*, 25(11):1999–2002, 1998.
- [1551] M. Tingay, B. Mueller, and J. Reinecker. Understanding tectonic stress in the oil patch: The World Stress Map Project. *The leading edge*, page 1276, 2005.
- [1552] C. Tirel, J.-P. Brun, and E. Burov. Thermomechanical modeling of extensional gneiss domes. *Geological Society of America Special Papers*, 380:67–78, 2004.
- [1553] C. Tirel, J.-P. Brun, and E. Burov. Dynamics and structural development of metamorphic core complexes. *J. Geophys. Res.*, 113(B04403), 2008.
- [1554] C. Tirel, J.-P. Brun, E. Burov, M.J.R. Wortel, and S. Lebedev. A plate tectonics oddity: Caterpillar-walk exhumation of subducted continental crust. *Geology*, 41(5):555–558, 2013.
- [1555] C. Tirel, J.-P. Brun, and D. Sokoutis. Extension of thickened and hot lithospheres: Inferences from laboratory modeling. *Tectonics*, 25(1), 2006.
- [1556] N. Tosi, P. Maierová, and D.A. Yuen. Influence of Variable Thermal Expansivity and Conductivity on Deep Subduction. In *Subduction Dynamics: From Mantle Flow to Mega Disasters*, *Geophysical Monograph* 211, pages 115–133. John Wiley & Sons, Inc., 2016.
- [1557] N. Tosi and Z. Martinec. Semi-analytical solution for viscous Stokes flow in two eccentrically nested spheres. *Geophys. J. Int.*, 170:1015–1030, 2007.
- [1558] N. Tosi, C. Stein, L. Noack, C. Huettig, P. Maierova, H. Samuel, D.R. Davies, C.R. Wilson, S.C. Kramer, C. Thieulot, A. Glerum, M. Fraters, W. Spakman, A. Rozel, and P.J. Tackley. A community benchmark for viscoplastic thermal convection in a 2-D square box. *Geochem. Geophys. Geosyst.*, 16(7):21752196, 2015.
- [1559] Nicola Tosi and David A Yuen. Bent-shaped plumes and horizontal channel flow beneath the 660 km discontinuity. *Earth and Planetary Science Letters*, 312(3-4):348–359, 2011.
- [1560] Nicola Tosi, David A Yuen, Nico de Koker, and Renata M Wentzcovitch. Mantle dynamics with pressure- and temperature-dependent thermal expansivity and conductivity. *Physics of the Earth and Planetary Interiors*, 217:48–58, 2013.
- [1561] J. Toth and M. Gurnis. Dynamics of subduction initiation at preexisting fault zones. *J. Geophys. Res.*, 103(B8):18,053–18,067, 1998.
- [1562] G. Toussaint, E. Burov, and J.-P. Avouac. Tectonic evolution of a continental collision zone: A thermo-mechanical numerical model. *Tectonics*, 23(TC6003):doi:10.1029/2003TC001604, 2004.
- [1563] Aaron Tovich, Gerald Schubert, and Bruce P Luyendyk. Mantle flow pressure and the angle of subduction: Non-newtonian corner flows. *Journal of Geophysical Research: Solid Earth*, 83(B12):5892–5898, 1978.
- [1564] B.J. Travis, C. Anderson, J. Baumgardner, C.W. Gable, B.H. Hager, R.J. O’Connell, P. Olson, A. Raefsky, and G. Schubert. A benchmark comparison of numerical methods for infinite Prandtl number thermal convection in two-dimensional Cartesian geometry. *Geophysical & Astrophysical Fluid Dynamics*, 55(3-4):137–160, 1990.
- [1565] S.H. Treagus and L. Lan. Pure shear deformation of square objects, and applications to geological strain analysis. *Journal of Structural Geology*, 22:105–122, 2000.
- [1566] R.A. Trompert and U. Hansen. Mantle convection simulations with rheologies that generate plate-like behaviour . *Nature*, 395:686–689, 1998.
- [1567] R.A. Trompert and U. Hansen. On the Rayleigh number dependence of convection with a strongly temperature-dependent viscosity. *Physics of Fluids*, 10(2):351–360, 1998.

- [1568] Virginie Tron and Jean-Pierre Brun. Experiments on oblique rifting in brittle-ductile systems. *Tectonophysics*, 188(1-2):71–84, 1991.
- [1569] Ulrich Trottenberg, Cornelius W. Oosterlee, and Anton Schuller. *Multigrid*. 2001.
- [1570] VP Trubitsyn. Equations of thermal convection for a viscous compressible mantle of the earth including phase transitions. *Izvestiya, Physics of the Solid Earth*, 44(12):1018–1026, 2008.
- [1571] VP Trubitsyn and AM Bobrov. Thermal and mechanical interaction of continents with the mantle. *Computational Seismology and Geodynamics*, 3:33–41, 1996.
- [1572] VP Trubitsyn and VV Rykov. A 3-d numerical model of the wilson cycle. *Journal of geodynamics*, 20(1):63–75, 1995.
- [1573] G.E. Tucker and G.R. Hancock. Modelling landscape evolution. *Earth Surface Processes and Landforms*, 35:28–50, 2010.
- [1574] Gregory E Tucker, Stephen T Lancaster, Nicole M Gasparini, Rafael L Bras, and Scott M Rybarczyk. An object-oriented framework for distributed hydrologic and geomorphic modeling using triangulated irregular networks. *Computers & Geosciences*, 27(8):959–973, 2001.
- [1575] D.L. Turcotte and G. Schubert. *Geodynamics, 2nd edition*. Cambridge, 2012.
- [1576] S. Turek. *Efficient Solvers for Incompressible Flow Problems*. Springer, 1999.
- [1577] K. Ueda, T. Gerya, and S.V. Sobolev. Subduction initiation by thermalchemical plumes: Numerical studies. *Phys. Earth. Planet. Inter.*, 171:296–312, 2008.
- [1578] K Ueda, Taras V Gerya, and J-P Burg. Delamination in collisional orogens: Thermomechanical modeling. *Journal of Geophysical Research: Solid Earth*, 117(B8), 2012.
- [1579] K. Ueda, S.D. Willett, T. Gerya, and J. Ruh. Geomorphologicalthermo-mechanical modeling: Application to orogenic wedge dynamics. *Tectonophysics*, 659:12–30, 2015.
- [1580] Leonardo Uieda, Everton P Bomfim, Carla Braatenberg, and Eder Molina. Optimal forward calculation method of the marussi tensor due to a geologic structure at goce height. In *Proceedings of the 4th International GOCE User Workshop*. Munich Germany, 2011.
- [1581] Phædra Upton, Peter O Koons, and Donna Eberhart-Phillips. Extension and partitioning in an oblique subduction zone, new zealand: Constraints from three-dimensional numerical modeling. *Tectonics*, 22(6), 2003.
- [1582] S van Benthem and Rob Govers. The Caribbean plate: Pulled, pushed, or dragged? *Journal Of Geophysical Research*, 115(B10):B10409, 2010.
- [1583] S van Benthem, Rob Govers, and Rinus Wortel. What drives microplate motion and deformation in the northeastern Caribbean plate boundary region? *TECTONICS*, 33, 2014.
- [1584] P van de Beek and Jean Braun. Numerical modelling of landscape evolution on geological time-scales: A parameter analysis and comparison with the south-eastern highlands of australia. *Basin Research*, 10(1):49–68, 1998.
- [1585] F.N. van de Vosse, A.A. van Steenhoven, A. Segal, and J.D. Janssen. A finite element analysis of the steady laminar entrance flow in a 90° curved tube. *Int. J. Num. Meth. Fluids*, 9:275–287, 1989.
- [1586] A. van den Berg, P.E. van Keeken, and D.A. Yuen. The effects of a composite non-Newtonian and Newtonian rheology on mantle convection. *Geophys. J. Int.*, 115:62–78, 1993.
- [1587] A.P. van den Berg, M.V. De Hoop, D.A. Yuen, A. Duchkov, R.D. van der Hilst, and M.H.G. Jacobs. Geodynamical modeling and multiscale seismic expression of thermo-chemical heterogeneity and phase transitions in the lowermost mantle. *Phys. Earth. Planet. Inter.*, 180:244–257, 2010.
- [1588] A.P. van den Berg, G. Segal, and D. Yuen. SEPRAN: A Versatile Finite-Element Package for Realistic Problems in Geosciences. *International Workshop of Deep Geothermal Systems, Wuhan, China, June 29-30*, 2012.
- [1589] A.P. van den Berg, G. Segal, and D.A. Yuen. SEPRAN: A Versatile Finite-Element Package for a Wide Variety of Problems in Geosciences. *Journal of Earth Science*, 26(1):089–095, 2015.
- [1590] A.P. van den Berg, D.A. Yuen, K. Umamoto, M.H.G. Jacobs, and R.M. Wentzcovitch. Mass-dependent dynamics of terrestrial exoplanets using ab initio mineral properties. *Icarus*, 317:412–426, 2019.
- [1591] Arie P van den Berg, Peter E van Keeken, and David A Yuen. The effects of a composite non-newtonian and newtonian rheology on mantle convection. *Geophysical Journal International*, 115(1):62–78, 1993.
- [1592] Arie P van den Berg and David A Yuen. Is the lower-mantle rheology newtonian today? *Geophysical research letters*, 23(16):2033–2036, 1996.

- [1593] Arie P van Den Berg, David A Yuen, and Peter E van Keken. Rheological transition in mantle convection with a composite temperature-dependent, non-newtonian and newtonian rheology. *Earth and Planetary Science Letters*, 129(1-4):249–260, 1995.
- [1594] Douwe G van Der Meer, Wim Spakman, Douwe JJ van Hinsbergen, Maisha L Amaru, and Trond H Torsvik. Towards absolute plate motions constrained by lower-mantle slab remnants. *Nature Geoscience*, 3(1):36, 2010.
- [1595] M.J. van der Meulen, S.J.H. Buiter, J.E. Meulenkamp, and M.J.R. Wortel. An early pliocene uplift of the central apenninic foredeep and its geodynamic significance. *Tectonics*, 19:300–313, 2000.
- [1596] Y. van Dinther, T.V. Gerya, L.A. Dalguer, F. Corbi, F. Funiciello, and P.M. Mai. The seismic cycle at subduction thrusts: 2. Dynamic implications of geodynamic simulations validated with laboratory models. *J. Geophys. Res.*, 118:1502–1525, 2013.
- [1597] Y. van Dinther, T.V. Gerya, L.A. Dalguer, P.M. Mai, G. Morra, and D. Giardini. The seismic cycle at subduction thrusts: Insights from seismo-thermo-mechanical models. *J. Geophys. Res.*, 118:1–20, 2013.
- [1598] Y. van Dinther, P.M. Mai, L.A. Dalguer, and T.V. Gerya. Modeling the seismic cycle in subduction zones: The role and spatiotemporal occurrence of off-megathrust earthquakes. *Geophys. Res. Lett.*, 41:1194–1201, 2014.
- [1599] H.J. van Heck, J.H. Davies, T. Elliott, and D. Porcelli. Global-scale modelling of melting and isotopic evolution of Earths mantle: melting modules for TERRA. *Geosci. Model Dev.*, 9:1399–1411, 2016.
- [1600] HJ van Heck and PJ Tackley. Plate tectonics on super-earths: equally or more likely than on earth. *Earth and Planetary Science Letters*, 310(3-4):252–261, 2011.
- [1601] Douwe JJ van Hinsbergen, Kalijn Peters, Marco Maffione, Wim Spakman, Carl Guilmette, Cedric Thieulot, Oliver Plümper, Derya Güner, Frauke M Brouwer, Ercan Aldanmaz, et al. Dynamics of intraoceanic subduction initiation: 2. suprasubduction zone ophiolite formation and metamorphic sole exhumation in context of absolute plate motions. *Geochemistry, Geophysics, Geosystems*, 16(6):1771–1785, 2015.
- [1602] J. van Hunen and M.B. Allen. Continental collision and slab break-off: A comparison of 3-D numerical models with observations. *Earth Planet. Sci. Lett.*, 302:27–37, 2011.
- [1603] J. van Hunen and M.S. Miller. Collisional processes and links to episodic changes in subduction zones. *Elements*, 11:119–124, 2015.
- [1604] J. van Hunen, A.P. van den Berg, and N.J. Vlaar. On the role of subducting oceanic plateaus in the development of shallow flat subduction. *Tectonophysics*, 352(3-4):317–333, 2002.
- [1605] J. van Hunen and S. Zhong. New insight in the Hawaiian plume swell dynamics from scaling laws. *Geophys. Res. Lett.*, 30(15):doi:10.1029/2003GL017646,, 2003.
- [1606] J. van Kan, A. Segal, and F. Vermolen. *Numerical Methods in Scientific Computing*. VSSD, 2005.
- [1607] P. van Keken. Cylindrical scaling for dynamical cooling models of the Earth. *Phys. Earth. Planet. Inter.*, 124:119–130, 2001.
- [1608] P. van Keken, D.A. Yuen, and A. van den Berg. Pulsating diapiric flows: Consequences of vertical variations in mantle creep laws. *Earth Planet. Sci. Lett.*, 112:179–194, 1992.
- [1609] P. van Keken and S. Zhong. Mixing in a 3D spherical model of present-day mantle convection. *Earth Planet. Sci. Lett.*, 171:533–547, 1999.
- [1610] P.E. van Keken. Evolution of starting mantle plumes: a comparison between numerical and laboratory models. *Earth Planet. Sci. Lett.*, 148:1–11, 1997.
- [1611] P.E. van Keken, C. Currie, S.D. King, M.D. Behn, Amandine Cagnioncle, J. Hee, R.F. Katz, S.-C. Lin, E.M. Parmentier, M. Spiegelman, and K. Wang. A community benchmark for subduction zone modelling. *Phys. Earth. Planet. Inter.*, 171:187–197, 2008.
- [1612] P.E. van Keken, B.R. Hacker, E.M. Syracuse, and G.A. Abers. Subduction factory: 4. Depthdependent flux of H₂O from subducting slabs worldwide. *J. Geophys. Res.*, 116(B01401), 2011.
- [1613] P.E. van Keken, S.D. King, H. Schmelting, U.R. Christensen, D. Neumeister, and M.-P. Doin. A comparison of methods for the modeling of thermochemical convection. *J. Geophys. Res.*, 102(B10):22,477–22,495, 1997.
- [1614] P.E. van Keken, C.J. Spiers, A.P. van den Berg, and E.J. Muyzert. The effective viscosity of rocksalt: implementation of steady-state creep laws in numerical models of salt diapirism. *Tectonophysics*, 225:457–476, 1993.

- [1615] P.E. van Keken, C.J. Spiers, A.P. van den Berg, and E.J. Muyzert. The effective viscosity of rocksalt: implementation of steady-state creep laws in numerical models of salt diapirism. *Tectonophysics*, 225:457–476, 1993.
- [1616] Peter E van Keken. The structure and dynamics of the mantle wedge. *Earth and planetary science letters*, 215(3-4):323–338, 2003.
- [1617] Peter E van Keken, David A Yuen, and Arie P van den Berg. Implications for mantle dynamics from the high melting temperature of perovskite. *Science*, 264(5164):1437–1439, 1994.
- [1618] J. van Summeren, C.P. Conrad, and C. Lithgow-Bertelloni. The importance of slab pull and a global asthenosphere to plate motions. *Geochem. Geophys. Geosyst.*, 13(1):10.1029/2011GC003873, 2012.
- [1619] P. van Thienen. Convective vigour and heat flow in chemically differentiated systems. *Geophys. J. Int.*, 169(2):747–766, 2007.
- [1620] P. van Thienen, A.P. van den Berg, J.H. de Smet, J. van Hunen, and M.R. Drury. Interaction between small-scale mantle diapirs and a continental root. *Geochem. Geophys. Geosyst.*, 4(2):doi:10.1029/2002GC000338, 2003.
- [1621] P. van Thienen, A.P. van den Berg, and N.J. Vlaar. On the formation of continental silicic melts in thermochemical mantle convection models: implications for early Earth. *Tectonophysics*, 394(1-2):111–124, 2004.
- [1622] P. van Thienen, AP van den Berg, and NJ Vlaar. Production and recycling of oceanic crust in the early earth. *Tectonophysics*, 386(1-2):41–65, 2004.
- [1623] P. van Thienen, N.J. Vlaar, and A.P. van den Berg. Plate tectonics on the terrestrial planets. *Phys. Earth. Planet. Inter.*, 142:61–74, 2004.
- [1624] P. van Thienen, N.J. Vlaar, and A.P. van den Berg. Assessment of the cooling capacity of plate tectonics and flood volcanism in the evolution of Earth, Mars and Venus. *Phys. Earth. Planet. Inter.*, 150:287–315, 2005.
- [1625] J van Wijk, J van Hunen, and S Goes. Small-scale convection during continental rifting: Evidence from the rio grande rift. *Geology*, 36(7):575–578, 2008.
- [1626] J.W. van Wijk. Role of weak zone orientation in continental lithosphere extension. *Geophys. Res. Lett.*, 32(L02303), 2005.
- [1627] J.W. van Wijk, W.S. Baldridge, J. van Hunen, S. Goes, R. Aster, D.D. Coblenz, S.P. Grand, and J. Ni. Small-scale convection at the edge of the Colorado Plateau: Implications for topography, magmatism, and evolution of Proterozoic lithosphere. *Geology*, 38:611–614, 2010.
- [1628] J.W. van Wijk and D.K. Blackman. Dynamics of continental rift propagation: the end-member modes. *Earth Planet. Sci. Lett.*, 229:247–258, 2005.
- [1629] J.W. van Wijk and D.K. Blackman. Development of en echelon magmatic segments along oblique spreading ridges. *Geology*, 35(7):599–602, 2007.
- [1630] J.W. van Wijk and S.A.P.L. Cloetingh. Basin migration caused by slow lithospheric extension. *Earth Planet. Sci. Lett.*, 198:275–288, 2002.
- [1631] O. Vanderhaeghe, S. Medvedev, P. Fullsack, C. Beaumont, and R.A. Jamieson. Evolution of orogenic wedges and continental plateaux: insights from crustal thermal-mechanical overlying subduction mantle lithosphere. *Geophys. J. Int.*, 153:27–51, 2003.
- [1632] R.S. Varga. *Matrix Iterative Analysis*. Prentice-Hall, Inc., 1963.
- [1633] Oleg V. Vasilyev, Yuri Yu. Podladchikov, and David A. Yuen. Modelling of viscoelastic plume-lithosphere interaction using the adaptive multilevel wavelet collocation method. *Geophys. J. Int.*, 147:579–589, 2001.
- [1634] J. Vattelle, P.E. van Keken, A. Limare, and A. Davaille. Starting laminar plumes: Comparison of laboratory and numerical modeling. *Geochem. Geophys. Geosyst.*, 10(12):doi:10.1029/2009GC002739, 2009.
- [1635] A. Vauchez, A. Tomassi, and G. Barroul. Rheological heterogeneity, mechanical anisotropy and deformation of the continental lithosphere. *Tectonophysics*, 296:61–86, 1998.
- [1636] Mirko Velić, Dave May, and Louis Moresi. A fast robust algorithm for computing discrete voronoi diagrams. *Journal of Mathematical Modelling and Algorithms*, 8(3):343–355, 2009.
- [1637] Fabio Verbosio, Arne De Coninck, Drosos Kourounis, and Olaf Schenk. Enhancing the scalability of selected inversion factorization algorithms in genomic prediction. *Journal of Computational Science*, 22(Supplement C):99 – 108, 2017.
- [1638] P.A. Vermeer and R. de Borst. Non-associated plasticity for soils, concrete and rock. *Heron*, 29:1–62, 1984.

- [1639] Ph. Vernant and J. Chery. Mechanical modelling of oblique convergence in the Zagros, Iran. *Geophys. J. Int.*, 165:991–1002, 2006.
- [1640] Philippe Vernant, F. Hivert, Jean Chery, Philippe Steer, Rodolphe Cattin, and Alexis Rigo. Erosion-induced isostatic rebound triggers extension in low convergent mountain ranges. *Geology*, 41(4):467–470, 2013.
- [1641] Nicolaas J Vlaar. Vening meinesza student of the earth. *Eos, Transactions American Geophysical Union*, 70(9):129–140, 1989.
- [1642] N.J. Vlaar, P.E. van Keken, and A.P. van den Berg. Cooling of the Earth in the Archean: Consequences of pressure-release melting in a hotter mantle. *Earth Planet. Sci. Lett.*, 121:1–18, 1994.
- [1643] G. Le Voci, D.R. Davies, S. Goes, S.C. Kramer, and C.R. Wilson. A systematic 2-D investigation into the mantle wedges transient flow regime and thermal structure: Complexities arising from a hydrated rheology and thermal buoyancy. *Geochem. Geophys. Geosyst.*, 15(1), 2014.
- [1644] K. Vogt and T. Gerya. Deep plate serpentinization triggers skinning of subducting slabs. *Geology*, page doi:10.1130/G35565.1, 2014.
- [1645] Katharina Vogt, Antonio Castro, and Taras Gerya. Numerical modeling of geochemical variations caused by crustal relamination. *Geochemistry, Geophysics, Geosystems*, 14(2):470–487, 2013.
- [1646] Katharina Vogt and Taras V Gerya. From oceanic plateaus to allochthonous terranes: numerical modelling. *Gondwana Research*, 25(2):494–508, 2014.
- [1647] F. von Blanckenburg and J.H. Davies. Slab breakoff: A model for syncollisional magmatism and tectonics in the Alps. *Tectonics*, 14(1):120–131, 1995.
- [1648] R. von Mises. Mechanik der festen korper im plastisch deformablen zustand. *Nachrichten der Koniglichen Gesellschaft der Wissenschaften*, page 582, 1913.
- [1649] M. von Tscharner and S. M. Schmalholz. A 3-D Lagrangian finite element algorithm with remeshing for simulating large-strain hydrodynamic instabilities in power law viscoelastic fluids. *Geochem. Geophys. Geosyst.*, 16:215–245, 2015.
- [1650] M. von Tscharner, S.M. Schmalholz, and T. Duretz. Three-dimensional necking during viscous slab detachment. *Geophys. Res. Lett.*, 41:10.1002/2014GL060075, 2014.
- [1651] L. Vynnytska, M.E. Rognes, and S.R. Clark. Benchmarking FEniCS for mantle convection simulations. *Computers & Geosciences*, 50:95–105, 2013.
- [1652] Shoichi Wakiya. Application of bipolar coordinates to the two-dimensional creeping motion of a liquid. i. flow over a projection or a depression on a wall. *Journal of the Physical Society of Japan*, 39(4):1113–1120, 1975.
- [1653] Shoichi Wakiya. Application of bipolar coordinates to the two-dimensional creeping motion of a liquid. ii. some problems for two circular cylinders in viscous fluid. *Journal of the Physical Society of Japan*, 39(6):1603–1607, 1975.
- [1654] H. Wang, R. Agrusta, and J. van Hunen. Advantages of a conservative velocity interpolation (CVI) scheme for particle-in-cell methods with application in geodynamic modeling. *Geochem. Geophys. Geosyst.*, 16:doi:10.1002/2015GC005824, 2015.
- [1655] H. Wang, J. van Hunen, , and D.G. Pearson. The thinning of subcontinental lithosphere: The roles of plume impact and metasomatic weakening. *Geochem. Geophys. Geosyst.*, 16:1156–1171, 2015.
- [1656] H. Wang, J. van Hunen, D.G. Pearson, and M.B. Allen. Craton stability and longevity: The roles of composition-dependent rheology and buoyancy. *Earth Planet. Sci. Lett.*, 391:224–233, 2014.
- [1657] Hongliang Wang, Jeroen van Hunen, and D Graham Pearson. Making archean cratonic roots by lateral compression: a two-stage thickening and stabilization model. *Tectonophysics*, 746:562–571, 2018.
- [1658] Li Wang and Dimitri J Mavriplis. Adjoint-based h–p adaptive discontinuous galerkin methods for the 2d compressible euler equations. *Journal of Computational Physics*, 228(20):7643–7661, 2009.
- [1659] W.M. Wang, L.J. Sluys, and R. de Borst. Interaction between material length scale and imperfection size for localisation phenomena in viscoplastic media. *Eur. J. Mech. A/Solids*, 15(3):447–464, 1996.
- [1660] X. Wang, J. He, L. Ding, and R. Gao. A possible mechanism for the initiation of the Yinggehai Basin: A visco-elasto-plastic model. *Journal of Asian Earth Sciences*, 74:25–36, 2013.
- [1661] Xinguo Wang, William E Holt, and Attreyee Ghosh. Joint modeling of lithosphere and mantle dynamics: Evaluation of constraints from global tomography models. *Journal of Geophysical Research: Solid Earth*, 120(12):8633–8655, 2015.

- [1662] Y. Wang, J. Huang, and S. Zhong. Episodic and multistaged gravitational instability of cratonic lithosphere and its implications for reactivation of the North China Craton. *Geochem. Geophys. Geosyst.*, 16:815–833, 2015.
- [1663] G.H. Wannier. A contribution to the hydrodynamics of lubrication. *Quarterly of Applied Mathematics*, VIII:1–32, 1950.
- [1664] Karin N Warners-Ruckstuhl, Rob Govers, and Rinus Wortel. Lithosphere–mantle coupling and the dynamics of the eurasian plate. *Geophysical Journal International*, 189(3):1253–1276, 2012.
- [1665] Karin N Warners-Ruckstuhl, Rob Govers, and Rinus Wortel. Tethyan collision forces and the stress field of the Eurasian Plate. *Geophys. J. Int.*, 195(1):1–15, 2013.
- [1666] KN Warners-Ruckstuhl, P Th Meijer, Rob Govers, and MJR Wortel. A lithosphere-dynamics constraint on mantle flow: Analysis of the Eurasian plate. *Geophysical Research Letters*, 37:L18308, 2010.
- [1667] C.J. Warren. Exhumation of (ultra-)high-pressure terranes: concepts and mechanisms . *Solid Earth*, 4:75–92, 2013.
- [1668] C.J. Warren, C. Beaumont, and R.A. Jamieson. Formation and exhumation of ultra-high-pressure rocks during continental collision: Role of detachment in the subduction channel. *Geochem. Geophys. Geosyst.*, 9, 2008.
- [1669] C.J. Warren, C. Beaumont, and R.A. Jamieson. Modelling tectonic styles and ultra-high pressure (UHP) rock exhumation during the transition from oceanic subduction to continental collision. *Earth Planet. Sci. Lett.*, 267:129–145, 2008.
- [1670] Clare J Warren, Christopher Beaumont, and Rebecca A Jamieson. Deep subduction and rapid exhumation: Role of crustal strength and strain weakening in continental subduction and ultrahigh-pressure rock exhumation. *Tectonics*, 27(6), 2008.
- [1671] Louise Watremez, Evgenii Burov, Elia d’Acremont, Sylvie Leroy, Benjamin Huet, Laetitia Le Pourhiet, and Nicolas Bellahsen. Buoyancy and localizing properties of continental mantle lithosphere: Insights from thermomechanical models of the eastern gulf of aden. *Geochemistry, Geophysics, Geosystems*, 14(8):2800–2817, 2013.
- [1672] AB Watts and EB Burov. Lithospheric strength and its relationship to the elastic and seismogenic layer thickness. *Earth and Planetary Science Letters*, 213(1-2):113–131, 2003.
- [1673] AB Watts, SJ Zhong, and J Hunter. The behavior of the lithosphere on seismic to geologic timescales. *Annual Review of Earth and Planetary Sciences*, 41:443–468, 2013.
- [1674] Shimon Wdowinski and Yehuda Bock. The evolution of deformation and topography of high elevated plateaus: 1. model, numerical analysis, and general results. *Journal of Geophysical Research: Solid Earth*, 99(B4):7103–7119, 1994.
- [1675] Shimon Wdowinski and Yehuda Bock. The evolution of deformation and topography of high elevated plateaus: 2. application to the central andes. *Journal of Geophysical Research: Solid Earth*, 99(B4):7121–7130, 1994.
- [1676] R.F. Weinberg. Internal circulation in a buoyant two-fluid Newtonian sphere: implications for composed magmatic diapirs. *Earth Planet. Sci. Lett.*, 110:77–94, 1992.
- [1677] R.F. Weinberg. The upward transport of inclusions in Newtonian and power-law salt diapirs. *Tectonophysics*, 228:141–150, 1993.
- [1678] R.F. Weinberg. The rise of solid-state diapirs. *Journal of Structural Geology*, 17(8):1183–1195, 1995.
- [1679] R.F. Weinberg and H. Schmeling. Polydiapirs: multiwavelength gravity structures. *Journal of Structural Geology*, 14(4):425–436, 1992.
- [1680] Jens Weismüller, Björn Gmeiner, Siavash Ghelichkhan, Markus Huber, Lorenz John, Barbara Wohlmuth, Ulrich Rüde, and Hans-Peter Bunge. Fast asthenosphere motion in high-resolution global mantle flow models. *Geophysical Research Letters*, 42(18):7429–7435, 2015.
- [1681] M.B. Weller and A. Lenardic. The energetics and convective vigor of mixed-mode heating: Velocity scalings and implications for the tectonics of exoplanets. *Geophys. Res. Lett.*, 43, 2016.
- [1682] M.B. Weller, A. Lenardic, and W.B. Moore. Scaling relationships and physics for mixed heating convection in planetary interiors: Isoviscous spherical shells. *J. Geophys. Res.*, 121, 2016.
- [1683] D.M. Whipp, C. Beaumont, and J. Braun. Feeding the aneurysm: Orogen-parallel mass transport into Nanga Parbat and the western Himalayan syntaxis. *J. Geophys. Res.*, 119:doi:10.1002/2013JB010929, 2014.

- [1684] Kelin X Whipple. The influence of climate on the tectonic evolution of mountain belts. *Nature geoscience*, 2(2):97, 2009.
- [1685] A Whittaker, MHP Bott, and GD Waghorn. Stresses and plate boundary forces associated with subduction plate margins. *Journal of Geophysical Research: Solid Earth*, 97(B8):11933–11944, 1992.
- [1686] C. Wijns, R. Weinberg, K. Gessner, and L. Moresi. Mode of crustal extension determined by rheological layering. *Earth Planet. Sci. Lett.*, 236:120–134, 2005.
- [1687] Chris Wijns, Fabio Boschetti, and Louis Moresi. Inverse modelling in geology by interactive evolutionary computation. *Journal of Structural Geology*, 25:1615–1621, 2003.
- [1688] K.R. Wilks and N.L. Carter. Rheology of some continental lower crustal rocks. *Tectonophysics*, 182(1-2):57–77, 1990.
- [1689] S. D. Willett. Rheological dependence of extension in wedge models of convergent orogens. *Tectonophysics*, 305:419–435, 1999.
- [1690] S.D. Willett. Dynamic and kinematic growth and change of a coulomb wedge. In K.R. McClay, editor, *Thrust Tectonics*, pages 19–31. Chapman and Hall, 1992.
- [1691] S.D. Willett. Orogeny and orography: The effects of erosion on the structure of mountain belts. *J. Geophys. Res.*, 104(B12):28957, 1999.
- [1692] S.D. Willett. Erosion on a line. *Tectonophysics*, 484:168–180, 2010.
- [1693] S.D. Willett and C. Beaumont. Subduction of Asian lithosphere mantle beneath Tibet inferred from models of continental collision. *Nature*, 369:642–645, 1994.
- [1694] Sean D Willett and Mark T Brandon. On steady states in mountain belts. *Geology*, 30(2):175–178, 2002.
- [1695] Sean D. Willett and Daniel C. Pope. Thermo-mechanical models of convergent orogenesis: Thermal and rheologic dependence of crustal deformation. In *Rheology and deformation of the lithosphere at continental margins.*, pages 166–222. Columbia University Press, 2003.
- [1696] Garry Willgoose. Mathematical modeling of whole landscape evolution. *Annual Review of Earth and Planetary Sciences*, 33(1):443–459, 2005.
- [1697] C.R. Wilson, M. Spiegelman, and P.E. van Keken. TerraFERMA: The Transparent Finite Element Rapid Model Assembler for multiphysics problems in Earth sciences. *Geochem. Geophys. Geosyst.*, 18:769–810, 2017.
- [1698] C.R. Wilson, M. Spiegelman, P.E. van Keken, and B.R. Hacker. Fluid flow in subduction zones: The role of solid rheology and compaction pressure. *Earth Planet. Sci. Lett.*, 401:261–274, 2014.
- [1699] SB Wissing, S Ellis, and Othmar-Adrian Pfiffner. Numerical models of alpine-type cover nappes. *Tectonophysics*, 367(3-4):145–172, 2003.
- [1700] W.-D. Woidt. Finite element calculations applied to salt dome analysis. *Tectonophysics*, 50:369–386, 1978.
- [1701] Sebastian G Wolf and Ritske S Huismans. Mountain building or backarc extension in ocean-continent subduction systems-a function of backarc lithospheric strength and absolute plate velocities. *Journal of Geophysical Research: Solid Earth*, 2019.
- [1702] M. Wolstencroft and J.H. Davies. Influence of the Ringwoodite-Perovskite transition on mantle convection in spherical geometry as a function of Clapeyron slope and Rayleigh number. *Solid Earth*, 2:315–326, 2011.
- [1703] M. Wolstencroft, J.H. Davies, and D.R. Davies. NusseltRayleigh number scaling for spherical shell Earth mantle simulation up to a Rayleigh number of 10^9 . *Phys. Earth. Planet. Inter.*, 176:132–141, 2009.
- [1704] S.Y.N. Wong-A-Ton and M.J.R. Wortel. Slab detachment in continental collision zones: An analysis of controlling parameters. *Geophys. Res. Lett.*, 24(16):2095–2098, 1997.
- [1705] MJR Wortel, MJN Remkes, R Govers, SAPL Cloetingh, and P Th Meijer. Dynamics of the lithosphere and the intraplate stress field. *Philosophical Transactions of the Royal Society of London. Series A: Physical and Engineering Sciences*, 337(1645):111–126, 1991.
- [1706] MJR Wortel and W Spakman. Structure and dynamics of subducted lithosphere in the mediterranean region. *Proceedings of the Koninklijke Nederlandse Akademie van Wetenschappen*, 95(3):325–347, 1992.
- [1707] M.J.R. Wortel and W. Spakman. Subduction and slab detachment in the Mediterranean-Carpathian region. *Science*, 290:1910–1917, 2000.
- [1708] Jennifer Worthen, Georg Stadler, Noemi Petra, Michael Gurnis, and Omar Ghattas. Towards adjoint-based inversion for rheological parameters in nonlinear viscous mantle flow. *Physics of the Earth and Planetary Interiors*, 234:23–34, 2014.

- [1709] Benjun Wu, Clinton P Conrad, Arnauld Heuret, Carolina Lithgow-Bertelloni, and Serge Lallemand. Reconciling strong slab pull and weak plate bending: The plate motion constraint on the strength of mantle slabs. *Earth and Planetary Science Letters*, 272(1-2):412–421, 2008.
- [1710] G. Wu, L.L. Lavier, and E. Choi. Modes of continental extension in a crustal wedge. *Earth Planet. Sci. Lett.*, 421:89–97, 2015.
- [1711] B. Wuming, C. Vigny, Y. ricard, and C. Froidevaux. On the origin of deviatoric stresses in the lithosphere. *J. Geophys. Res.*, 97(B8):11,729–11,737, 1992.
- [1712] Shunxing Xie and Paul J Tackley. Evolution of helium and argon isotopes in a convecting mantle. *Physics of the Earth and Planetary Interiors*, 146(3-4):417–439, 2004.
- [1713] Shunxing Xie and Paul J Tackley. Evolution of u-pb and sm-nd systems in numerical models of mantle convection and plate tectonics. *Journal of Geophysical Research: Solid Earth*, 109(B11), 2004.
- [1714] H. Xing, W. Yu, and J. Zhang. 3d mesh generation in geocomputing. In *Advances in Geocomputing, Lecture Notes in Earth Sciences*. Springer-Verlag, Berlin Heidelberg, 2009.
- [1715] P. Yamato, P. Agard, E. Burov, L. Le Pourhiet, L. Jolivet, and C. Tiberi. Burial and exhumation in a subduction wedge: Mutual constraints from thermomechanical modeling and natural P-T-t data (Schistes Lustres, western Alps). *J. Geophys. Res.*, 112(B07410):doi:10.1029/2006JB004441, 2007.
- [1716] P. Yamato, E. Burov, P. Agard, L. Le Pourhiet, and L. Jolivet. HP-UHP exhumation during slow continental subduction: Self-consistent thermodynamically and thermomechanically coupled model with application to the Western Alps. *Earth Planet. Sci. Lett.*, 271:63–74, 2008.
- [1717] P. Yamato, L. Husson, T.W. Becker, and K. Pedoja. Passive margins getting squeezed in the mantle convection vice. *Tectonics*, 2013.
- [1718] P. Yamato, L. Husson, J. Braun, C. Loiselet, and C. Thieulot. Influence of surrounding plates on 3D subduction dynamics. *Geophys. Res. Lett.*, 36(L07303), 2009.
- [1719] P. Yamato, R. Tartese, T. Duretz, and D.A. May. Numerical modelling of magma transport in dykes . *Tectonophysics*, 526-529:97–109, 2012.
- [1720] Ph. Yamato, B.J.P. Kaus, F. Mouthereau, and S. Castelltort. Dynamic constraints on the crustal-scale rheology of the Zagros fold belt, Iran. *Geology*, 39(9):815–818, 2011.
- [1721] Takatoshi Yanagisawa, Yasuko Yamagishi, Yozo Hamano, and Dave R Stegman. Mechanism for generating stagnant slabs in 3-d spherical mantle convection models at earth-like conditions. *Physics of the Earth and Planetary Interiors*, 183(1-2):341–352, 2010.
- [1722] S. Yang and Y. Shi. Three-dimensional numerical simulation of glacial trough forming process. *Science China: Earth Sciences*, pages 10.1007/s11430-015-5120-8, 2015.
- [1723] T. Yang, L. Moresi, M. Gurnis, S. Liu, D. Sandiford, S. Williams, and F.A. Capitanio. Contrasted East Asia and South America tectonics driven by deep mantle flow. *Earth Planet. Sci. Lett.*, 517:106–116, 2019.
- [1724] Ting Yang, Louis Moresi, Dapeng Zhao, Dan Sandiford, and Joanne Whittaker. Cenozoic lithospheric deformation in northeast asia and the rapidly-aging pacific plate. *Earth Planet. Sci. Lett.*, 492:1–11, 2018.
- [1725] Woo-Sun Yang. *Variable viscosity thermal convection at infinite Prandtl number in a thick spherical shell*. PhD thesis, University of Illinois, 1997.
- [1726] Woo-Sun Yang and John R Baumgardner. A matrix-dependent transfer multigrid method for strongly variable viscosity infinite prandtl number thermal convection. *Geophysical & Astrophysical Fluid Dynamics*, 92(3-4):151–195, 2000.
- [1727] C. Yao, F. Deschamps, J.P. Lowman, C. Sanchez-Valle, and P.J. Tackley. Stagnant lid convection in bottom-heated thin 3-D spherical shells: Influence of curvature and implications for dwarf planets and icy moons. *J. Geophys. Res.*, 119:1895–1913, 2014.
- [1728] Irad Yavneh. Why multigrid methods are so efficient. *Computing in science & engineering*, 8(6):12, 2006.
- [1729] Tao Ye, Rajat Mittal, HS Udaykumar, and Wei Shyy. An accurate cartesian grid method for viscous incompressible flows with complex immersed boundaries. *Journal of computational physics*, 156(2):209–240, 1999.
- [1730] M. Yoshida. The role of harzburgite layers in the morphology of subducting plates and the behavior of oceanic crustal layers. *Geophys. Res. Lett.*, 40:5387–5392, 2013.
- [1731] M. Yoshida and A. Kageyama. Application of the Yin-Yang grid to a thermal convection of a Boussinesq fluid with infinite Prandtl number in a three-dimensional spherical shell. *Geophys. Res. Lett.*, 31(L12609), 2004.

- [1732] M. Yoshida, F. Tajima, S. Honda, and M. Morishige. The 3D numerical modeling of subduction dynamics: Plate stagnation and segmentation, and crustal advection in the wet mantle transition zone. *J. Geophys. Res.*, 117(B04104), 2012.
- [1733] Masaki Yoshida and Yozo Hamano. Pangea breakup and northward drift of the indian subcontinent reproduced by a numerical model of mantle convection. *Scientific reports*, 5:8407, 2015.
- [1734] S. Yoshioka and M.J.R. Wortel. Three-dimensional numerical modeling of detachment of subducted lithosphere. *J. Geophys. Res.*, 100(B10):20,223–20,244, 1995.
- [1735] Warren Clarence Young and Richard Gordon Budynas. *Roark's formulas for stress and strain*, volume 7. McGraw-Hill New York, 2002.
- [1736] X. Yu and F. Tin-Loi. A simple mixed finite element for static limit analysis. *Computers and Structures*, 84:1906–1917, 2006.
- [1737] DA Yuen, R Sabadini, and E Boschi. Mantle rheology from a geodynamical standpoint. *La Rivista del Nuovo Cimento (1978-1999)*, 5(8):1–35, 1982.
- [1738] David A Yuen and Luce Fleitout. Thinning of the lithosphere by small-scale convective destabilization. *Nature*, 313(5998):125, 1985.
- [1739] David A Yuen, Francesca Quarenici, and H-J Hong. Effects from equation of state and rheology in dissipative heating in compressible mantle convection. *Nature*, 326(6108):67, 1987.
- [1740] David A Yuen and Roberto Sabadini. Secular rotational motions and the mechanical structure of a dynamical viscoelastic earth. *Physics of the earth and planetary interiors*, 36(3-4):391–412, 1984.
- [1741] Z. Xu Z. Li and T.V. Gerya. Numerical Geodynamic Modeling of Continental Convergent Margins, Earth Sciences. In Dr. Imran Ahmad Dar, editor, *Earth Sciences*. InTech, 2012.
- [1742] S.T. Zalesak. Fully Multidimensional Flux-Corrected Transport Algorithms for Fluids. *J. Comp. Phys.*, 31:335–362, 1979.
- [1743] S. Zaleski and P. Julien. Numerical simulation of Rayleigh-Taylor instability for single and multiple salt diapirs. *Tectonophysics*, 206:55–69, 1992.
- [1744] Peter K Zeitler, Anne S Meltzer, Peter O Koons, David Craw, Bernard Hallet, C Page Chamberlain, William SF Kidd, Stephen K Park, Leonardo Seeber, Michael Bishop, et al. Erosion, himalayan geodynamics, and the geomorphology of metamorphism. *GSA Today*, 11(1):4–9, 2001.
- [1745] Huai Zhang, Lili Ju, Max Gunzburger, Todd Ringler, and Stephen Price. Coupled models and parallel simulations for three-dimensional full-stokes ice sheet modeling. *Numerical Mathematics: Theory, Methods and Applications*, 4(3):396–418, 2011.
- [1746] N. Zhang and Z-X Li. Formation of mantle "lone plumes" in the global downwelling zone – A case for subduction-controlled plume generation beneath the South China Sea. *Tectonophysics*, 2017.
- [1747] N. Zhang, S. Zhong, W. Leng, , and Z.X. Li. A model for the evolution of the Earths mantle structure since the Early Paleozoic. *J. Geophys. Res.*, 115(B06401), 2010.
- [1748] N. Zhang, S. Zhong, and A.K. McNamara. Supercontinent formation from stochastic collision and mantle convection models. *Gondwana Research*, 15:267–275, 2009.
- [1749] S. Zhang and U. Christensen. Some effects of lateral viscosity variations on geoid and surface velocities induced by density anomalies in the mantle. *Geophys. J. Int.*, 114:531–547, 1993.
- [1750] S. Zhang and C. O'Neill. The early geodynamic evolution of mars-type planets. *Icarus*, 265:187–208, 2016.
- [1751] S. Zhang and D.A. Yuen. The influences of lower mantle viscosity stratification on 3D spherical-shell mantle convection. *Earth Planet. Sci. Lett.*, 132:157–166, 1995.
- [1752] S Zhang and DA Yuen. Intense local toroidal motion generated by variable viscosity compressible convection in 3-d spherical-shell. *Geophysical research letters*, 23(22):3135–3138, 1996.
- [1753] L. Zhao, X. Bai, T. Li, and J.J.R. Williams. Improved conservative level set method. *Int. J. Num. Meth. Fluids*, 2014.
- [1754] W Zhao. Da yuen s. honda. *Multiple phase transitions and the style of mantle convection*, *Phys. Earth Planet. Int.*, 72:185–210, 1992.
- [1755] Y. Zhao, J. de Vries, A.P. van den Berg, M.H.G. Jacobs, and W. van Westrenen. The participation of ilmenite-bearing cumulates in lunar mantle overturn. *Earth Planet. Sci. Lett.*, 511:1–11, 2019.
- [1756] S. Zhong. Constraints on thermochemical convection of the mantle from plume heat flux, plume excess temperature, and upper mantle temperature. *Journal of Geophysical Research*, 111(B4), 2006.

- [1757] S. Zhong and M. Gurnis. Mantle convection with plates and Mobile, Faulted Plate Margins. *Science*, 267(5199):838–843, 1995.
- [1758] S. Zhong, M. Gurnis, and G. Hulbert. Accurate determination of surface normal stress in viscous flow from a consistent boundary flux method. *Phys. Earth. Planet. Inter.*, 78:1–8, 1993.
- [1759] S. Zhong, M. Gurnis, and L. Moresi. Free-surface formulation of mantle convection - I. Basic theory and application to plumes. *Geophys. J. Int.*, 127:708–718, 1996.
- [1760] S. Zhong, M. Gurnis, and L. Moresi. Role of faults, nonlinear rheology, and viscosity structure in generating plates from instantaneous mantle flow models. *J. Geophys. Res.*, 103(B7):15,255–15,268, 1998.
- [1761] S. Zhong, A. McNamara, E. Tan, L. Moresi, and M. Gurnis. A benchmark study on mantle convection in a 3-D spherical shell using CitcomS. *Geochem. Geophys. Geosyst.*, 9(10), 2008.
- [1762] S. Zhong and A.B. Watts. Lithospheric deformation induced by loading of the Hawaiian Islands and its implications for mantle rheology. *J. Geophys. Res.*, 118:6025–6048, 2013.
- [1763] S. Zhong, N. Zhang, Z.-X. Li, and J.H. Roberts. Supercontinent cycles, true polar wander, and very long-wavelength mantle convection. *Earth Planet. Sci. Lett.*, 261:551–564, 2007.
- [1764] S. Zhong and M.T. Zuber. Long-wavelength topographic relaxation for self-gravitating planets and implications for the time-dependent compensation of surface topography. *J. Geophys. Res.*, 105:4153–4164, 2000.
- [1765] S. Zhong, M.T. Zuber, L.N. Moresi, and M. Gurnis. The role of temperature-dependent viscosity and surface plates in spherical shell models of mantle convection. *J. Geophys. Res.*, 105(B5):11,063–11,082, 2000.
- [1766] Sh. Zhong and M. Gurnis. Viscous flow model of a subduction zone with a faulted lithosphere: long and short wavelength topography, gravity and geoid. *Geophys. Res. Lett.*, 19(18):1891–1894, 1992.
- [1767] Sh. Zhong and M. Gurnis. Controls on trench topography from dynamic models of subducted slabs. *J. Geophys. Res.*, 99(B8):15,683–15,695, 1994.
- [1768] Shijie Zhong. Analytic solutions for Stokes flow with lateral variations in viscosity. *Geophys. J. Int.*, 124(1):18–28, 1996.
- [1769] S.J. Zhong, D.A. Yuen, L.N. Moresi, and M.G. Knepley. 7.05 - numerical methods for mantle convection. In Gerald Schubert, editor, *Treatise on Geophysics (Second Edition)*, pages 197 – 222. Elsevier, Oxford, second edition edition, 2015.
- [1770] X. Zhou. 2D vector gravity potential and line integrals for the gravity anomaly caused by a 2D mass of depth-dependent density contrast. *Geophysics*, 73(6):143–150, 2008.
- [1771] X. Zhou, Z.-H. Li, T.V. Gerya, R.J. Stern, Z. Xu, and J. Zhang. Subduction initiation dynamics along a transform fault control trench curvature and ophiolite ages. *Geology*, 46(7):607–610, 2018.
- [1772] D.Y. Zhu, C.F. Lee, and K.T. Law. Determination of bearing capacity of shallow foundations without using superposition approximation. *Can. Geotech. J.*, 40:450–459, 2003.
- [1773] G. Zhu, T. Gerya, D.A. Yuen, S. Honda, T. Yoshida, and T. Connolly. Three-dimensional dynamics of hydrous thermal-chemical plumes in oceanic subduction zones. *Geochem. Geophys. Geosyst.*, 10:doi:10.1029/2009GC002625, 2009.
- [1774] G. Zhu, T.V. Gerya, P.J. Tackley, and E. Kissling. Four-dimensional numerical modeling of crustal growth at active continental margins. *J. Geophys. Res.*, 118:4682–4698, 2013.
- [1775] Guizhi Zhu, Taras Gerya, and David A Yuen. Melt evolution above a spontaneously retreating subducting slab in a three-dimensional model. *Journal of Earth Science*, 22(2):137–142, 2011.
- [1776] Guizhi Zhu, Yaolin Shi, and Paul Tackley. Subduction of the western pacific plate underneath northeast china: implications of numerical studies. *Physics of the Earth and Planetary Interiors*, 178(1-2):92–99, 2010.
- [1777] T. Zhu. Tomography-based mantle flow beneath Mongolia-Baikal area. *Phys. Earth. Planet. Inter.*, 237:40–50, 2014.
- [1778] Peter A Ziegler. Geodynamics of rifting and implications for hydrocarbon habitat. *Tectonophysics*, 215(1-2):221–253, 1992.
- [1779] Peter A Ziegler. Plate tectonics, plate moving mechanisms and rifting. *Tectonophysics*, 215(1-2):9–34, 1992.
- [1780] O. Zienkiewicz and S. Nakazawa. The penalty function method and its application to the numerical solution of boundary value problems. *The American Society of Mechanical Engineers*, 51, 1982.

- [1781] O.C. Zienkiewicz and I.C. Cormeau. Visco-plasticity and creep in elastic solids - a unified numerical solution approach. *Int. J. Num. Meth. Eng.*, 8:821–845, 1974.
- [1782] O.C. Zienkiewicz, M. Huang, and M. Pastor. Localization problems in plasticity using finite elements with adaptive remeshing. *International Journal for Numerical and Analytical Methods in Geomechanics*, 19:127–148, 1995.
- [1783] O.C. Zienkiewicz, C. Humpheson, and R.W. Lewis. Associated and non-associated visco-plasticity and plasticity in soil mechanics . *Géotechnique*, 25(4):671–689, 1975.
- [1784] O.C. Zienkiewicz and R.L. Taylor. *The Finite Element Method. Vol. 2: Solid Mechanics*. Butterworth and Heinemann, 2002.
- [1785] O.C. Zienkiewicz, R.L. Taylor, and D.D. Fox. *The Finite Element Method for solid and structural mechanics*. Elsevier B.H., 2014.
- [1786] O.C. Zienkiewicz, J.P. Vilotte, and S. Toyoshima. Iterative method for constrained and mixed approximation. An inexpensive improvement of FEM performance. *Computer Methods in Applied Mechanics and Engineering*, 51:3–29, 1985.
- [1787] F. Zinani and S. Frey. Galerkin Least-Squares Solutions for Purely Viscous Flows of Shear- Thinning Fluids and Regularized Yield Stress Fluids. *J. of the Braz. Soc. of Mech. Sci. & Eng.*, XXIX:432–443, 2007.
- [1788] S. Zlotnik, M. Fernandez, P. Diez, and J. Verges. Modelling gravitational instabilities: slab break-off and Rayleigh-Taylor diapirism. *Pure appl. geophys.*, 165:1491–1510, 2008.
- [1789] M.L. Zoback. First- and second-order patterns of stress in the lithosphere: the World Stress Map project. *J. Geophys. Res.*, 97(B8):11,703–11,728, 1992.
- [1790] M.T. Zuber and E.M. Parmentier. Lithospheric necking: a dynamic model for rift morphology. *Earth Planet. Sci. Lett.*, 77:373–383, 1986.
- [1791] M.T. Zuber, E.M. Parmentier, and R.C. Fletcher. Extension of Continental Lithosphere: A Model for Two Scales of Basin and Range Deformation. *J. Geophys. Res.*, 91(B5):4826–4838, 1986.
- [1792] F. Zwaan, G. Scheurs, J. Naliboff, and S.J.H. Buiter. Insights into the effects of oblique extension on continental rift interaction from 3D analogue and numerical models. *Tectonophysics*, 2016.
- [1793] F. Zwaan, G. Schreurs, and S.J.H. Buiter. A systematic comparison of experimental set-ups for modelling extensional tectonics. *Solid Earth*, 10:1063–1097, 2019.

Index

- H^1 norm, 230
- H^1 semi-norm, 230
- $H^1(\Omega)$ space, 230
- L_1 norm, 230
- L_2 norm, 230
- P_1 , 77, 79, 85, 89
- $P_1 \times P_0$, 108
- P_1^+ , 80, 86
- P_2 , 82
- P_2^+ , 83, 89
- P_3 , 85
- $P_m \times P_n$, 63
- $P_m \times P_{-n}$, 63
- $Q_1 \times P_0$, 105, 266, 272, 274, 280, 287, 291, 296, 298, 316, 323, 335, 337, 341, 356, 357
- Q_1 , 64, 71
- $Q_1 \times P_0$, 281
- $Q_1^+ \times Q_1$, 108
- $Q_2 \times P_0$, 108
- $Q_2 \times Q_1$, 63, 299, 304
- Q_2 , 65, 73, 88
- $Q_2^{(20)}$, 90
- $Q_2^{(8)}$, 74
- $Q_3 \times Q_2$, 307
- Q_3 , 65, 76
- Q_4 , 68, 77
- $Q_m \times P_{-n}$, 63
- $Q_m \times Q_n$, 63
- $Q_m \times Q_{-n}$, 63
- , 439, 441
- Accretionary Wedge, 466
- Adaptive Mesh Refinement, 188
- Advection-Diffusion, 98
- Aegean region, 467
- Afar rift, 467
- ALE, 132
- Alps, 466
- AMR, 188
- Analogue Modelling, 455
- analytical solution, 266, 274, 291, 296, 304, 307, 316, 323, 341, 357
- Andes, 466
- angular momentum, 249
- angular velocity, 249
- Anisotropy, 455
- annulus, 281
- Arbitrary Lagrangian Eulerian, 132
- Archean tectonics, 455
- arithmetic mean, 288
- Arrhenius law, 52
- Augmented Lagrangian, 207
- Backward Euler, 101
- Barycentric Coordinates, 80
- basis functions, 71
- BDF-2, 102
- Biharmonic Operator, 255, 256
- Bingham model, 40
- Bird-Carreau model, 40
- Bird-Carreau-Yasuda model, 40
- Boussinesq Approximation, 27
- Bow-tied element, 129
- BSc Thesis, 150, 153, 159, 226
- Bubble Function, 63, 80
- bulk modulus, 28, 318
- bulk viscosity, 26
- buoyancy-driven flow, 268
- Capacitance matrix, 94
- Carreau model, 40
- Caribbean region, 467
- CBF, 341
- CG, 203
- chain rule, 209
- checkerboard, 197
- cohesion, 196
- compositional Field, 242
- Compressed Sparse Column, 180
- Compressed Sparse Row, 180
- compressibility, 318
- compressible flow, 323
- Conforming Element, 64
- conjugate gradient, 203
- Connectivity Array, 183
- Convex Polygon, 183
- Core Dynamics, 456
- Crank-Nicolson, 101
- Critical Rayleigh Number, 32
- Crouzeix-Raviart, 83
- CSC, 180
- CSR, 180, 406
- Degenerate Diffusion Equation, 430
- Diffusion creep, 42
- Dirichlet boundary condition, 31
- Dislocation creep, 42
- divergence theorem, 209
- Divergence-free, 25
- Divergence-free Flow, 104
- Domain Decomposition, 254
- Drucker-Prager, 49, 196
- dynamic viscosity, 26
- Early Earth, 455
- ENO, 242
- Erosion, 457

Essential Boundary Conditions, 236
 Extension, 463
 Extrapolation, 231
 FANTOM, 439
 FLUIDITY, 439
 Forward Euler, 101
 Frank-Kamenetskii, 53
 Free Surface, 129
 Gauss quadrature, 58
 Gauss-Lobatto, 62
 Generalized Newtonian Fluid, 39
 geoFLAC, 439
 Geoid, 459
 geometric mean, 288
 Geotechnics, 458
 Griffith-Murrell, 51
 GTECTON, 438
 Haigh-Westergaard Coordinates, 37
 harmonic mean, 288
 Herschel-Bulkley model, 41
 Heun's emthod, 224
 Himalayan region, 467
 hyperbolic PDE, 213
 IFISS, 439
 incompressible flow, 274, 280, 287, 291, 296, 298, 304, 307, 316, 335, 337, 341, 356, 357
 Isoparametric, 214
 isothermal, 266, 272, 274, 280, 287, 291, 296, 298, 304, 307, 316, 335, 337, 341, 357
 Isotropic, 103
 isoviscous, 266, 272, 291, 296, 304, 307, 316, 323, 341, 356
 Lamé parameter, 28
 LBB, 104
 Legendre polynomial, 58
 Level-set Function, 242
 Level-set Method, 242
 LLSVP, 459
 Lode Angle, 37
 Lode Coordinates, 37
 LSF, 242
 LSM, 242
 MAC, 239
 Magma Transport, 459
 manufactured solution, 281
 Marker Chain method, 244
 Marker-and-Cell, 239
 Mars, 461
 Mass matrix, 94
 Maximum Shear Stress, 34
 Melting, 459
 Meshless, 183
 Method of Manufactured Solutions, 144
 Midpoint Method, 224
 midpoint rule, 57
 MINI element, 106
 mixed formulation, 291, 296, 298, 304, 307, 316, 323, 335, 337, 341, 356
 MMS, 144
 Mohr-Coulomb, 50
 Moment Invariant, 195
 moment of inertia, 249
 Moon, 461
 MSc Thesis, 41, 54, 103, 163, 164, 253, 434
 Natural Boundary Conditions, 236
 Neumann boundary condition, 31
 New Zealand, 467
 Newton's method, 228
 Newton-Cotes, 58
 Newtonian fluid, 39
 Non-Conforming Element, 64
 non-isoviscous, 274, 280, 287, 298, 357
 nonlinear, 252, 337
 nonlinear rheology, 280
 Normal Stress, 22
 North America, 466
 nullspace, 200
 numerical benchmark, 335
 Nusselt Number, 33
 Obduction, 461
 open boundary conditions, 356
 Ophiolites, 461
 optimal rate, 104, 231
 Orthotropic, 103
 Particle-in-Cell, 239
 particle-in-cell, 287
 Peierls creep, 52
 penalty, 281
 penalty formulation, 108, 266, 268, 272, 274, 280, 287, 357
 PIC, 239
 Picard iterations, 252
 Piecewise, 63
 Plume Dynamics, 461
 Plume-Lithosphere Interaction, 462
 Poiseuille flow, 150
 Poisson ratio, 28
 Power-law model, 39
 Prandtl Number, 33
 preconditioned conjugate gradient, 206
 pressure normalisation, 300
 pressure nullspace, 151
 pressure scaling, 199
 pressure smoothing, 197, 291, 316, 323, 341

Principal Stress, 34
Pyrenees, 467
quadrature, 58
Rayleigh Number, 32
rectangle rule, 57
reference element, 214
relaxation, 252
Rens Elbertsen, 342, 363
Rheology, 462
Richardson iterations, 202
Rifting, 463
RK2, 224
RK3, 224
RK4, 224
RK45, 224
Runge-Kutta-Fehlberg method, 224

Schur complement, 202
Schur complement approach, 296, 298
Seafloor spreading, 463
second viscosity, 26
Serendipity element, 74, 90
Shear Heating, 150
shear modulus, 28
Shear Stress, 22
Solenoidal Field, 104
Solenoidal field, 25
SPD, 202
spin tensor, 23
Static Condensation, 107, 246
Sticky Air, 130
Stokes sphere, 268, 298
strain rate, 23
Strain rate tensor, 32
Strain tensor, 32
strain tensor, 28
Stream Function, 255, 256
Stress Tensor, 22, 32
Stress Vector, 22
strong form, 104
Structured Grid, 183
Subparametric, 214
Superparametric, 214
Surface Processes, 457
Symmetric Positive Definite, 444

Taylor-Hood, 104
TECTON, 438
tensor invariant, 195
TERRA-NEO, 442
TerraFERMA, 442
thermal expansion, 318
Thrust-Wrench Fault, 466
Tibetan plateau, 467
Traction, 22
trapezoidal rule, 57
Tresca, 48
Two Phase Flow, 459
Unstructured Grid, 183
velocity gradient, 23
Venus, 461
Viscosity Rescaling Method, 196
von Mises, 47, 196
VRM, 196
weak form, 104, 110
work against gravity, 321
Young's modulus, 28

Notes

finish. not happy with definition. Look at literature	33
derive formula for Earth size R1 and R2	34
check aspect manual The 2D cylindrical shell benchmarks by Davies et al. 5.4.12	34
SOMETHING missing HERE	37
Channel flow of wikipedia with analytical solution!	41
look at folder, codes, clean up, change labels new and old	47
insert here figure	57
insert here figure	57
citation needed	73
find reference	83
VERIFY that when $\eta_1 = 1 - r - s$, $\eta_2 = r$ and $\eta_3 = s$ we find the above r, s shape functions	85
verify those	85
REFS ??? better definition of functions !	89
find/build shape functions!	90
NOT happy with this statement!!	91
add source term!!	101
find literature	104
Check Cuvelier book chapter 8 for modified element	107
list codes which use this approach	109
reduced integration	111
write about 3D to 2D	111
insert here link(s) to manual and literature	112
surface terms arising from the integration by parts are neglected. EXPLAIN WHY!	136
sort out mess wrt Eq 26 of busa13	148
go through my papers and add relevant ones here	159
there are discrepancies between [1346] and [325]	164
finish vrms calculation of benchmark	169
produce drawing of node numbering	184
mention stripack, plus paper moresi with it, and lithos1.0	187
write about gmesh	187
insert here the rederivation 2.1.1 of spmw16	196
produce figure to explain this	198
link to proto paper	198
link to least square and nodal derivatives	198
check this, and report page number	203
add biblio	204
how to compute M for the Schur complement ?	207
finish GMRES algo description. not sure what to do, hard to explain, not easy to code.	208
why does array contain only T??	211
finish	211
re ask Wolfgang about this - correlate with deal.ii	221
missing refs for Butcher tableau	224
write about case when element is rectangle/cuboid	229
to finish	233
to finish	233
refs!	237
tie to fieldstone 12	237
it would be nice to have a Q1 and Q2 drawing of a 1D element and show that indeed negative values arise	240
write more about particle averaging and projection	241
write about DG approach	243
ask Arie to write something	243
I still have pics from the old days using DOUAR- include	244
check	246

implement and report	247
missing picture	248
explain why our eqs are nonlinear	252
write about nonlinear residual	252
FIND refs. check new version of Vol7 theoretical geophys	256
get these papers	258
build S and have python compute its smallest and largest eigenvalues as a function of resolution?	296
finish structure of C matrix for q1q1	313
compare my rates with original paper!	314
explain how Medge is arrived at!	340
compare with ASPECT ??!	340
pressure average on surface instead of volume ?	340
carry out other two measurements (need interpolation onto other grid for this	399
cross check with CIG database	438